Effects of RADIATION on Materials

17th International Symposium

David S. Gelles, Randy K. Nanstad,
Arvind S. Kumar, and Edward A. Little
editors

ASTM
STP 1270

STP 1270

Effects of Radiation on Materials: 17th International Symposium

David S. Gelles, Randy K. Nanstad, Arvind S. Kumar, and Edward A. Little, Editors

ASTM Publication Code Number (PCN):
04-012700-35

ASTM
100 Barr Harbor Drive
West Conshohocken, PA 19428-2959
Printed in the U.S.A.

ISBN: 0-8031-2016-8
PCN: 04-012700-35
ISSN: 1050-7515

Copyright © 1996 AMERICAN SOCIETY FOR TESTING AND MATERIALS, West Conshohocken, PA. All rights reserved. This material may not be reproduced or copied, in whole or in part, in any printed, mechanical, electronic, film, or other distribution and storage media, without the written consent of the publisher.

Photocopy Rights

Authorization to photocopy items for internal, personal, or educational classroom use, or the internal, personal, or educational classroom use of specific clients, is granted by the American Society for Testing and Materials (ASTM) provided that the appropriate fee is paid to the Copyright Clearance Center, 222 Rosewood Drive, Danvers, MA 01923; Tel: (508) 750-8400; online: http://www.copyright.com/.

Peer Review Policy

Each paper published in this volume was evaluated by three peer reviewers. The authors addressed all of the reviewers' comments to the satisfaction of both the technical editor(s) and the ASTM Committee on Publications.

To make technical information available as quickly as possible, the peer-reviewed papers in this publication were prepared "camera-ready" as submitted by the authors.

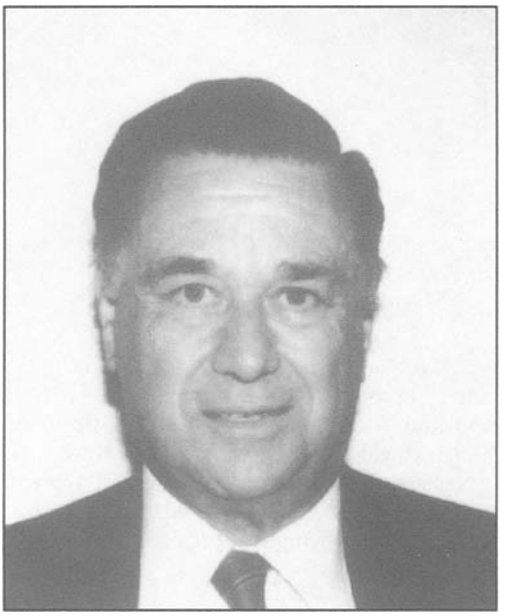
The quality of the papers in this publication reflects not only the obvious efforts of the authors and the technical editor(s), but also the work of these peer reviewers. The ASTM Committee on Publications acknowledges with appreciation their dedication and contribution to time and effort on behalf of ASTM.

Printed in Ann Arbor, MI
August 1996

Foreword

This publication, *Effects of Radiation on Materials: 17th International Symposium,* contains papers presented at the symposium of the same name, held in Sun Valley, Idaho on 20-23 June 1994. The symposium was sponsored by ASTM Committee E-10 on Nuclear Technology and Applications. David S. Gelles of Pacific Northwest National Laboratory in Richland, WA; Randy K. Nanstad of the Oak Ridge National Laboratory in Oak Ridge, TN; Arvind S. Kumar of the University of Missouri in Rolla, MO; and Edward A. Little of University College in Swansea, United Kingdom presided as symposium chairmen and are editors of the resulting publication.

DEDICATION



Peter Hedgecock
1931–1992

Peter D. Hedgecock contributed significantly to the success of ASTM Committee E-10 on Nuclear Technology and Applications. Peter has been the Chairman of Subcommittee E10.02, on Radiation Effects on Structural Materials until the time of his sudden death. His colleagues within ASTM acknowledge his high degree of professionalism, organization, and enthusiasm.

Peter was trained as a metallurgical engineer at the University of London and was licensed in the United States as a metallurgical, corrosion, and nuclear engineer. His knowledge and experience extended beyond that of nuclear structural materials, since he had extensive exposure in the aerospace industry and as an expert witness in accident reconstruction and component failures.

Peter was a gentleman and a friend. We will miss him.

Contents

Overview—D. S. GELLES, R. K. NANSTAD, A. E. KUMAR, AND E. A. LITTLE xiii

MODELING OF CONTROLLING MECHANISMS IN RPV STEELS

Mechanisms Controlling the Composition Influence on Radiation Hardening and Embrittlement of Iron-Base Alloys—V. A. NIKOLAEV AND V. V. RYBIN 3

Pressure Vessel Embrittlement Predictions Based on a Composite Model of Copper Precipitation and Point Defect Clustering—R. E. STOLLER 25

The B&W Owners Group Program for Microstructural Characterization and Radiation Embrittlement Modeling of Linde 80 Reactor Vessel Welds—W. A. PAVINICH AND L. S. HARBISON 59

Irradiation Embrittlement Modeling of Linde 80 Weld Metals—R. J. McELROY AND A. L. LOWE, JR. 68

Modeling of Irradiation Embrittlement and Annealing/Recovery in Pressure Vessel Steels—R. G. LOTT AND P. D. FREYER 86

The Modeling of Irradiation Embrittlement in Submerged-Arc Welds—C. J. BOLTON, J. T. BUSWELL, R. B. JONES, R. MOSKOVIC, AND R. H. PRIEST 103

The Modeling of Irradiation-Enhanced Phosphorus Segregation in Neutron Irradiated Reactor Pressure Vessel Submerged-Arc Welds—S. G. DRUCE, C. A. ENGLISH, A. J. E. FOREMAN, R. J. McELROY, I. A. VATTER, C. J. BOLTON, J. T. BUSWELL, AND R. B. JONES 119

Research to Understand the Embrittlement Behavior of Yankee/BR3 Surveillance Plate and Other Outlier RPV Steels—A. FABRY, J. VAN DE VELDE, J. L. PUZZOLANTE, T. VAN RANSBEECK, A. VERSTREPEN, E. C. BIEMILLER, R. G. CARTER, AND T. PETROVA 138

MICROSTRUCTURE STUDIES ON RPV STEELS

Electron Microscopy and Small Angle Neutron Scattering Study of Precipitation in Low Alloy Steel Submerged-Arc Welds—T. J. WILLIAMS AND W. J. PHYTHIAN 191

Radiation Damage Studies Using Small-Angle Neutron Scattering—G. ALBERTINI, F. CARSUGHI, R. COPPOLA, F. RUSTICHELLI, AND M. STEFANON 206

Damage Structures of Proton Irradiated Fe-0.3wt.%Cu Alloy—A. KIMURA, H. SHIBAMOTO, H. YUYA, M. HASEGAWA, S. YAMAGUCHI, AND H. MATSUI 220

Mitigation of Irradiation Embrittlement by Annealing—A. D. AMAYEV, A. M. KRYUKOV, V. I. LEVIT, P. A. PLATONOV, AND M. A. SOKOLOV 232

Microstructure and Mechanical Properties of WWER-440 Reactor Vessel Metal After Service Life Expiration and Recovery Anneal—I. V. GORYNIN, E. V. NESTEROVA, V. A. NIKOLAEV, AND V. V. RYBIN 248

A Microstructural Study of Phosphorus Segregation and Intergranular Fracture in Neutron Irradiated Submerged-Arc Welds—P. J. E. BISCHLER AND R. K. WILD 260

CHARPY IMPACT RESPONSE OF RPV STEELS

Effects of Annealing Time on the Recovery of Charpy V-Notch Properties of Irradiated High-Copper Weld Metal—S. K. ISKANDER, M. A. SOKOLOV, AND R. K. NANSTAD 277

In-Service Embrittlement of the Pressure Vessel Welds at the Doel I and II Nuclear Power Plants—R. GERARD, A. FABRY, J. VAN DE VELDE, J.-L. PUZZOLANTE, A. VERSTREPEN, T. VAN RANSBEECK, AND E. VAN WALLE 294

The Toughness of Irradiated Pressure Water Reactor (PWR) Vessel Shell Rings and the Effect of Segregation Zones—M. BETHMONT, J.-M. FRUND, B. HOUSIN, AND P. SOULAR 320

Low Temperature Embrittlement of RPV Support Structure Steel—F. M. D. BOYDON, R. J. McELROY, G. GAGE, AND W. J. PHYTHIAN 331

Effects of Neutron Flux and Irradiation Temperature on Irradiation Embrittlement of A533B Steels—M. SUZUKI, K. ONIZAWA, AND M. KIZAKI 351

The Interpretation of Charpy Impact Test Data Using Hyper-Logistic Fitting Functions—J. L. HELM 363

Uncertainty Evaluation in Transition Temperature Measurements—C. BRILLAUD, H. AUGENDRE, AND M. BETHMONT 375

On Impact Testing of Subsize Charpy V-Notch Type Specimens— M. A. SOKOLOV AND R. K. NANSTAD 384

Reconstitution: Where Do We Stand?—E. VAN WALLE 415

The Reconstitution of Charpy-Size Tensile Specimens—T. VAN RANSBEECK, E. VAN WALLE, A. FABRY, J. L. PUZZOLANTE, AND J. VAN DE VELDE 442

Notch Reorientation of Charpy-V Specimens of the BWR Philippsburg 1 Through Reconstitution—E. VAN WALLE, A. FABRY, T. VAN RANSBEECK, J.-L. PUZZOLANTE, J. VAN DE VELDE, K. TULKE, AND W. BACKFISCH 458

Variations in Charpy Impact Data Evaluated by a Round-Robin Testing Program—A Summary—A. L. LOWE, JR. 487

The Embrittlement Data Base (EDB) and Its Applications—J. A. WANG, F. B. K. KAM, AND F. W. STALLMANN 500

Surveillance Programme for WWER-440/Type 213 Reactor Pressure Vessels—Standard Programme, Re-Evaluation of Results, Supplementary Programme—M. BRUMOVSKY, P. NOVOSAD, AND J. ZDAREK 522

STRENGTH AND TOUGHNESS ISSUES IN RPV STEELS

Application of Micromechanical Models of Ductile Fracture Initiation to Reactor Pressure Vessel Materials—R. CHAOUADI, P. DE MEESTER, E. VAN WALLE, A. FABRY, AND J. VAN DE VELDE 531

On the Effect of Flux and Composition on Irradiation Hardening at 60°C— G. R. ODETTE, G. E. LUCAS, R. D. KLINGENSMITH, AND R. E. STOLLER 547

The Dependence of Radiation Hardening and Embrittlement on Irradiation Temperature—R. B. JONES AND T. J. WILLIAMS 569

HFIR Steels Embrittlement: The Possible Effect of Gamma Field Contribution—I. REMEC, J.-A. WANG, AND F. B. K. KAM 591

The Influence of Metallurgical Variables on the Temperature Dependence of Irradiation Hardening in Pressure Vessel Steels—G. R. ODETTE, G. E. LUCAS, AND R. D. KLINGENSMITH 606

Effects of Proton Irradiation on Positron Annihilation and Micro-Vickers Hardness of Fe-C-Cu Model Alloys—H. SHIBAMOTO, K. KOYAMA, H. YUYA, M. HASEGAWA, A. KIMURA, H. MATSUI, AND S. YAMAGUCHI 623

Ductile Fracture Mechanisms in an A302B Modified Reactor Pressure Vessel Steel—L. J. CUDDY, M. P. MANAHAN, G. BRAUER, AND J. MARTINKO 637

Fracture Toughness Test Results of Thermal Aged Reactor Vessel Materials—M. J. DeVAN, A. J. LOWE, JR., AND J. B. HALL 660

The Effect of Constraint on Toughness of a Pressure Vessel Steel—K. EDSINGER, G. R. ODETTE, G. E. LUCAS, AND B. WIRTH 670

The Effects of Thermal Annealing on Fracture Toughness of Low Upper-Shelf Welds—M. A. SOKOLOV, R. K. NANSTAD, AND S. K. ISKANDER 690

Evaluation of Embrittlement in a Pressure Vessel Steel by Fracture Reconstruction—B. WIRTH, K. EDSINGER, G. R. ODETTE, AND G. E. LUCAS 706

FERRITIC AND MARTENSITIC STEELS

The Microstructural Stability and Mechanical Properties of Two Low Activation Martensitic Steels—M. VICTORIA, E. BATAWI, C. BRIGUET, D. GAVILLET, P. MARMY, J. PETERS, AND F. REZAI-ARIA 721

Influence of Thermomechanical Treatment on Irradiation Microstructures in an ODS Ferritic Steel—E. A. LITTLE 739

Effect of Boron on Post Irradiation Tensile Properties of Reduced Activation Ferritic Steel (F-82H) Irradiated in HFIR—K. SHIBA, M. SUZUKI, A. HISHINUMA, AND J. E. PAWEL 753

Irradiation Effects on Base Metal and Welds of 9Cr-1Mo (EM10) Martensitic Steel—A. ALAMO, J. L. SERAN, O. RABOUILLE, J. C. BRACHET, A. MAILLARD, H. TOURON, AND J. ROYER 761

Evaluation of the Upper Shelf Energy for Ferritic Steels from Miniaturized Charpy Specimen Data—H. KURISHITA, I. SHIBAHARA, M. NARUI, S. MIZUTA, AND H. KAYANO 775

On the Role of Strain Rate, Size and Notch Acuity on Toughness: A Comparison of Two Martensitic Stainless Steels—G. E. LUCAS, G. R. ODETTE, K. EDSINGER, B. WIRTH, AND J. W. SHECKHERD 790

AUSTENITIC STEELS

Microstructural Evolution of Austenitic Stainless Steels Irradiated In a Fast Reactor—O. V. BORODIN, V. V. BRYK, V. N. VOYEVODIN, I. M. NEKLYUDOV, V. K. SHAMARDIN, AND V. S. NEYSTROEV 817

Effects of Helium/DPA Ratio, Alloy Composition and Cold Work on Microstructural Evolution and Hardening of ^{59}Ni-Doped Fe-Cr-Ni Alloys Neutron-Irradiated at 465°C—H. KAWANISHI, M. L. HAMILTON, AND F. A. GARNER 831

Swelling, Mechanical Properties and Structure of Austenitic High-Nickel Alloy Irradiated in a Fast Reactor—V. K. SHAMARDIN, V. S. NEUSTROEV, A. V. POVSTYANKO, T. M. BULANOVA, Z. E. OSTROVSKY, A. A. KUZNETZOV, I. P. KURSEVITCH, AND V. A. NIKOLAEV 842

Effects of Metallurgical Variables on Swelling of Modified 316 and Higher Ni Austenitic Stainless Steels—I. SHIBAHARA, N. AKASAKA, AND S. ONOSE 858

On the Fundamentals of Radiation Damage in FCC Materials: A Review—W. SCHULE 874

An Investigation of Microstructures and Yield Strengths in Irradiated Austenitic Stainless Steels Using Small Specimen Techniques—M. B. TOLOCZKO, G. E. LUCAS, G. R. ODETTE, R. E. STOLLER, AND M. L. HAMILTON 902

Irradiation Hardening and Loss of Ductility of Type 316L(N) Stainless Steel Plate Material Due to Neutron-Irradiation—M. G. HORSTEN AND M. I. DE VRIES 919

Fatigue Crack Propagation by Channel Fracture in Irradiated 316 Stainless Steel—S. JITSUKAWA, A. HISHINUMA, AND M. SUZUKI 933

Fracture Toughness of Irradiated Candidate Materials for ITER First Wall/Blanket Structures—D. J. ALEXANDER, J. E. PAWEL, M. L. GROSSBECK, A. F. ROWCLIFFE, AND K. SHIBA 945

Irradiation Behavior of Weldments of Austenitic Stainless Steel Made by Various Welding Techniques—K. SHIBA, T. SAWAI, S. JITSUKAWA, A. HISHINUMA, AND J. E. PAWEL 971

Helium Effects on the Reweldability and Low Cycle Fatigue Properties of Welded Joints for Type Cr16Ni11Mo3Ti and 316L(N) Stainless Steels—S. A. FABRITSIEV AND J. G. VAN DER LAAN 980

Data Collection on the Effect of Irradiation on the Mechanical Properties of Austenitic Stainless Steels and Weld Metals—A.-A. TAVASSOLI, C. PICKER, AND J. WAREING 995

OTHER MATERIALS

Bubble Microstructure Evolution and Helium Behavior in He^+ Implanted Ni-Base Alloys—B. A. KALIN, I. I. CHERNOV, A. N. KALASHNIKOV, AND B. G. SOLOVYEV 1013

Saturation of Swelling in Neutron Irradiated Pure Nickel and Its Dependence on Temperature and Starting Dislocation Microstructure—J. F. STUBBINS AND F. A. GARNER 1038

Effect of Irradiation in a Spallation Neutron Environment on Tensile Properties and Microstructure of Aluminum Alloys 5052 and 6061—J. A. DUNLAP, M. J. BORDEN, W. F. SOMMER, AND J. F. STUBBINS 1047

Correlation Between Shear Punch and Tensile Data for Neutron-Irradiated Aluminum Alloys—M. L. HAMILTON, M. B. TOLOCZKO, D. J. EDWARDS, W. F. SOMMER, M. J. BORDEN, J. A. DUNLAP, J. F. STUBBINS, AND G. E. LUCAS 1057

Effect of Dynamically Charged Helium on Mechanical Properties of Vanadium-Base Alloys—H. M. CHUNG, B. A. LOOMIS, AND D. L. SMITH 1068

Swelling and Structure of Vanadium-Base Alloys Irradiated in the Dynamic Helium Charging Experiment—H. M. CHUNG, B. A. LOOMIS, AND D. L. SMITH 1077

Corrosion Response of Pre-Irradiated Zr-2.5Nb Pressure Tube Material—V. F. URBANIC AND M. GRIFFITHS 1088

SPECIAL PROCEDURES AND TECHNIQUES

The Development of Structural Materials for Reduced Long-Term Activation—K. EHRLICH, S. W. CIERJACKS, S. KELZENBERG, AND A. MOSLANG 1109

Characterization of Irradiation-Induced Precipitates by Small Angle X-Ray and Neutron Scattering Experiments—M. GROSSE, F. EICHHORN, J. BOHMERT, AND G. BRAUER 1123

Variable Energy Positron Measurements at Nitrogen Ion Bombarded Steel Surfaces—G. BRAUER, A. KOLITSCH, H. SCHUT, AND A. VAN VEEN 1134

Use of Laser Extensometer for Mechanical Tests on Irradiated Materials—
C. BRILLAUD, T. MEYLOGAN, AND P. SALATHE 1144

Author Index 1155

Subject Index 1159

Overview

ASTM Committee E-10 on Nuclear Technology and Applications sponsors a biennial series of symposia on the effects of radiation on materials. The first symposium was held in 1960 and followed an earlier series begun in 1956 by ASTM Committee E-10, then called the Committee on Radioisotopes and Radiation Effects. Since that first meeting, these symposia have continued to grow in importance as nuclear energy has provided an increasingly larger fraction of the world's electrical capacity. The meetings have become a major international forum for the presentation and discussion of research on the influence of radiation on the microstructure and mechanical properties on structural materials. The proceedings of the Seventeenth International Symposium on the Effects of Radiation on Materials are published in two parts, in this ASTM special technical publication (STP) 1270 and in a special issue of the *Journal of Nuclear Materials,* Volume 225 (1995). The symposium was held in Sun Valley, Idaho on 20–23 June 1994.

The Seventeenth International Symposium is distinguished by the very large attendance attained. One hundred seventy-seven abstracts were submitted for presentation at the symposium, and 104 are now being published in the combined proceedings of the symposium. The size of this publication effort has proven to be too large to fit in an ASTM STP, and therefore, it was necessary to split the publication between two publishers. The basis chosen for the split was relevance to ASTM standards, with the underlying intent to include in each publication examples of the wide range of topics covered. As a result, the papers being published in this volume represent the full range of topics covered at the symposium, but emphasize those topics that are most closely related to ASTM standards.

The papers published in this STP have been organized into eight sections. The first four sections are devoted to behavior of low alloy reactor pressure vessel steels. Papers on pressure vessel steels constituted approximately half of the papers submitted, and topics range from discussions of modeling and mechanisms, to microstructure and welding effects, but the greatest number describe mechanical property response or mechanical property data base information. The next two sections describe research on two other major classes of material: ferritic and martensitic steels and austenitic steels and the seventh section includes papers on the remaining materials of interest. The final section contains papers concerning special procedures, such as development of low long-term activation steels for fusion applications, and special techniques, such as positron measurements, laser extensometry, and small angle neutron scattering measurements.

Recent improvement in our understanding of reactor pressure vessel steel embrittlement has advanced rapidly, so that this proceedings contains seven papers in section one that describe mechanisms controlling behavior and model the processes of radiation embrittlement and segregation. Section two focuses on the precipitation process that controls embrittlement, including reports on electron microscopy and small angle neutron scattering, and the improvements available from annealing procedures to recover properties by altering precipitate distributions. Section three includes thirteen papers that expand and organize the mechanical properties data base on irradiation embrittlement. Topics include the effects of annealing on properties, properties of irradiated welds and specific reactor parts, consequences of flux, irradiation temperature and gamma radiation, interpretation of data by

specialized data analysis procedures, use of small specimen technology and reconstitution, and data base summaries including round robin test results. Section four expands the mechanical properties data base on reactor pressure vessel steels, providing six papers with improved understanding of irradiation hardening, one paper concerned with ductile fracture mechanisms and finally four important papers on fracture toughness results including new techniques used to understand the fracture process in these steels.

Section five provides a shift in attention to steels with higher chromium levels for use at higher temperatures. Papers include development of Martensitic steels for fusion, effects of radiation on the microstructure of an oxide dispersion strengthened alloy, and four papers on the mechanical properties of this class of steels. Section six is concerned with austenitic ferrous alloys, with four papers covering microstructural response, a paper on the fundamentals of radiation damage in this class of materials, six papers on mechanical properties, and one paper concerned with development of a materials data base. Section seven includes two papers on microstructural evolution in nickel, two papers on mechanical properties of aluminum alloys, two papers on helium effects in vanadium, one on microstructure, the second on mechanical properties, and finally a paper on corrosion of a zirconium alloy. The last section includes four specialized papers on development of structural materials for fusion to avoid long-term radioactivity, and on use of neutron scattering for precipitate characterization, positron measurements, and laser extensometry.

It should also be noted that this proceedings contains a series of excellent papers concerned with the development of small specimen technology and understanding of fractographic information for assessment of fracture toughness response. Papers on these topics are included in sections three, four, and five. Together, they demonstrate that our understanding of the propagation of a crack tip is increasing rapidly.

A photograph of attendees is provided in Fig. 1.

Finally, in order to be fair to those authors at this symposium whose papers could not be



FIG. 1—*Symposium attendees.*

published in this volume, we have provided the following section that lists authors and titles of papers that have appeared in the companion volume of this proceedings, Volume 225 of the *Journal of Nuclear Materials*.

David S. Gelles

Battelle Pacific Northwest National Laboratory
Richland, WA
Symposium Chairman and Editor

Randy K. Nanstad

Oak Ridge National Laboratory
Oak Ridge, TN
Symposium Cochairman and Editor

Arvind E. Kumar

University of Missouri-Rolla
Rolla, MO
Symposium Cochairman and Editor

Ted A. Little

Dept. of Materials Engineering
University College, Swansea, UK
Symposium Cochairman and Editor

Papers Included in the *Journal of Nuclear Materials*—Volume 225, 1995

Calculation of Radiation-Induced Creep and Stress Relaxation—J. NAGAKAWA, p. 1.

Correlation Between Void Swelling and SIPA Creep—C. H. WOO, p. 8.

The Effect of Swelling on SIPA Irradiation Creep—V. A. BORODIN, p. 15.

Critical Parameters Controlling Irradiation Swelling in Beryllium—V. L. DUBINKO AND V. R. BARABASH, p. 22.

Theory of Irradiation Swelling in Materials with Elastic and Diffusional Anisotropy—V. L. DUBINKO, p. 26.

The Effect of Internal Stress Fields on Fracture of Structural Materials under Irradiation—V. M. MANICHEV AND V. A. BORODIN, p. 33.

Interstitial Cluster Formation in Metals under Intense Irradiation—E. A. KOPTELOC, S. ISHINO, S. IWATA, AND N. SEKIRMURA, p. 38.

Post-Irradiation Deformation Characteristics of Heavy-Ion Irradiated 304L 55—J. I. COLE AND S. M. BRUEMMER, p. 53.

Threshold Helium Concentration Required to Initiate Cracking During Welding of Irradiated Stainless Steel—C. A. WANG, M. L. GROSSBECK, AND B. A. CHIN, p. 59.

Welding Irradiated Stainless Steel—W. R. KANNE, JR., G. T. CHANDLER, D. Z. NELSON, AND E. A. FRANCO-FERREIRA, p. 69.

The Influence of Silicon and Phosphorus Additions on Neutron Induced Microstructural Evolution of Fe-Cr-Ni Ternary Alloys at 646-703 K—H. WATANABE, F. A. GARNER, T. MUROGA, AND N. YOSHIDA, p. 76.

Radiation-Enhanced Diffusion in Nickel-10.6% Chromium Alloys—M. GIEB, I. HEIECK, AND W. SCHULE, p. 85.

Dependence of Radiation-Induced Segregation on Dose, Temperature and Alloy Composition in Austenitic Alloys—D. L. DAMCOTT, T. R. ALLEN, AND G. S. WAS, p. 97.

A Model for Radiation-Induced Segregation in FCC Binary Alloys—T. HASHIMOTO, Y. ISOLE, AND N. SHIGENAKA, p. 108.

Quantification of Defect-Solute Coupling from Inverse-Kirkendall Segregation—E. P. SIMONEN, L. A. CHARLOT, AND S. M. BRUEMMER, p. 117.

Microstructure of Copper and Nickel Irradiated with Fission Neutrons Near 230°C—S. J. ZINKLE AND L. L. SNEAD, p. 23.

Low Activation Braze Joint of Dispersion-Strengthened Copper—S. CHEN AND B. A. CHIN, p. 132.

Microstructure and Tensile Properties of Neutron Irradiated Cu and Cu-5Ni Containing Isotopically Controlled Boron—T. MUROGA, H. WATANABE, N. YOSHIDA, H. KURISHITA, AND M. L. HAMILTON, p. 137.

Microstructure Investigation of Cr and Cr Alloys Irradiated with Heavy Ions—V. V. BRYK, V. N. VOYEVODIN, L. M. NEKLYUDOV, AND A. N. RAKITSKIJ, p. 146.

Swelling and Dislocation Evolution in Simple Ferritic Alloys Irradiated to High Fluence in FFTF/MOTA—Y. KATOH, A. KOHYAMA, AND D. S. GELLES, p. 154.

Void Swelling in Binary Fe-Cr Alloys at 200 dpa—D. S. GELLES, p. 163.

Microstructure-Mechanical Properties Correlation of Irradiated Conventional and Reduced-Activation Martensitic Steels—R. L. KLUEH, J.-J. KAI, AND D. J. ALEXANDER, p. 175.

Hardness of 12Cr-8Mo Ferritic Steels Irradiated by Ni Ions—T. OHTA, T. OHMURA, K. KAKO, M. TOKIWAI, AND T. SUZUKI, p. 187.

Experimental Evidence of Several Contributions to the Radiation Damage in Ferritic Alloys—M. AKAMATSU, I. C. VAN DUYSEN, P. PAREIGE, AND P. AUGER, p. 192.

Irradiation-Induced Microstructural Changes, and Hardening Mechanisms, in Model PWR Reactor Pressure Vessel Steels—J. T. BUSWELL, W. J. PHYTHIAN, R. I. McELROY, S. DUMBILL, P. H. N. RAY, J. MACE, AND R. N. SINCLAIR, p. 196.

Characterization of Phosphorus Segregation in Neutron-Irradiated Russian Pressure Vessel Steel Weld—M. K. MILLER, R. JAYARAM, AND K. F. RUSSELL, p. 215.

APFIM Investigation of Clustering in Neutron-Irradiated Fe-Cu Alloys and Pressure Vessel Steels—P. AUGER, P. PAREIGE, M. AKAMATSU, AND D. BLAVETTE, p. 225.

Effect of Specimen Size on the Impact Properties of Neutron Irradiated A533B Steel—L. E. SCHUBERT, A. S. KUMAR, S. T. ROSINSKI, AND M. L. HAMILTON, p. 231.

Size Effects on the Upper Shelf Energy of a Neutron Irradiated Pressure Vessel Weld Metal—A. S. KUMAR, L. E. SCHUBERT, M. L. HAMILTON, AND N. S. CANNON, p. 238.

Microstructural Aspects of Accelerated Deformation of Zircaloy Nuclear Reactor Components During Service—M. GRIFFITHS, R. A. HOLT, AND A. ROGERSON, p. 245.

Tensile Behavior and Microstructure of Neutron-Irradiated Mo-5% Re Alloy—A. HASEGAWA, K. ABE, M. SATOU, AND C. NAMBA, p. 259.

Change in Physical Properties of High Density Isotropic Graphites Irradiated in the "JOYO" Fast Reactor—I. MARUYAMA, T. KAITO, S. ONOSE, AND I. SHIBAHARA, p. 267.

Radiation Damage of Graphite and Carbon-Graphite Materials—YAI SHTROMBAKH, B. A. GUROVICH, P. A. PLATONOV, AND V. M. ALEKSEEV, p. 273.

Inert Gas Release from Metals and UO_2 During High Temperature Annealing: The Role of Thermal Vacancies—J. H. EVANS, p. 302.

A Mechanistic Model for Radiation-Induced Crystallization and Amorphization in U_3Si—J. REST, p. 308.

Effect of Irradiation on the Microhardness of the LEC Grown Semi-Insulating GaAs Single Crystals—M. UDHAYASANKAR, S. ARULKUMARAN, I. AROKIARAJ, P. SANTHANARAGHAVAN, B. SUNDARAKANNAN, I. KUMAR, P. RAMASAMY, K. G. M. NAIR, P. MAGUDAPATHY, N. S. THAMPI, AND K. KRISHAN, p. 314.

Structural Damage in Spinel After Ion Irradiation—N. BORDES, K. E. SICKAFUS, C. A. COOPER, AND R. C. EWING, p. 318.

Optical Properties in Fibers During Irradiation in a Fission Reactor—T. SHIKAMA, T. KAKUTA, M. NAMI, T. SAGAWA, AND H. KAYANO, p. 324.

Radiation Induced Conductivity in Alumina—C. PATUWATHAVITHANE, W. Y. WU, AND R. H. ZEE, p. 328.

Modeling of Controlling Mechanisms in RPV Steels

V. A. Nikolaev[1] and V. V. Rybin[2]

MECHANISMS CONTROLLING THE COMPOSITION INFLUENCE ON RADIATION HARDENING AND EMBRITTLEMENT OF IRON-BASE ALLOYS

REFERENCE: Nikolaev, V. A. and Rybin, V. V., **"Mechanisms Controlling the Composition Influence on Radiation Hardening and Embrittlement of Iron-Base Alloys,"** *Effects of Radiation on Materials: 17th International Symposium, ASTM STP 1270,* David S. Gelles, Randy K. Nanstad, Arvind S. Kumar, and Edward A. Little, Eds., American Society for Testing and Materials, 1996.

ABSTRACT: Classification and ranking of the solid solution on thier reaction to the irradiation is suggested on the basis of binary system structure controlling by mixing enthalpy sign, melting temperatures relation of components and solidus curves slope. Several combinations of these characteristics permit to pick out three groups of substitutional elements capable to form the vacancy-solute atom complexes either low-mobile or fast-mobile ones as compared to monovacancies migration. The radiation hardening (and embrittlement) of binary alloys should be intensified respectively either due to heterogeneous point defect clusters nucleation on solute traps or due to solute atom clusters/precipitate formation. A local cohesion decrease may also occur especially if low-melting elements (characterized by low surface energy) are segregating on internal sinks or grain boundaries. The predicted specifics of diffrent alloy group under irradiation and during post-irradiation annealing were experimentally examined using a wide set of Fe-base alloys. A good agreement was find between expected and really observed behaviour of alloys.

KEYWORDS: radiation, hardening, embrittlement, defect, cluster, solid solution, segregation, annealing, iron, binary alloy.

1. Binary Alloys Classification On Their Possible Reaction On Irradiation

Simplified qualitative models of the point defect - solution atom complex formation and migration were analysed to build a classification and ranking of the Fe-

[1] Laboratory Chief, CRISM "Prometey", St.petersburg, Russia
[2] Department Chief, CRISM "Prometey", St.Petersburg, Russia

Copyright© 1996 by ASTM International www.astm.org

alloys on their sensitivity to radiation hardening and embrittlement [1]. Some thermodynamic characteristics of the binary systems and individual element properties were suggested as prediction parameters, namely:

- a sign of partial enthalpy of mixing

$\Delta U = U_{AB} - {}^{1}/_{2}(U_{AA}+U_{BB})$

where U_{AA}, U_{BB},U_{AB} are energies of the paired interaction of A and B (solute) element atoms:

- a relation of melting temperatures of B and A atoms $\chi = T_m^B/T_m^A$;
- a solidus parameter $\theta = (dT_s/dC_B) - (T_m^B - T_m^A)$,
where (dT_s/dC_B) is the slope of the solidus curve at B element content, C_B, equal to zero;
- a dimension misfit factor, δ, of atoms A and B.

Three groups of substitutional elements were picked out from the position of their predicted behaviour under irradiation.

Group 1. $\Delta U<0$, $\chi>1$. In these systems the solute atoms are capable to trap the migrating vacancies forming the low-mobile complexes (as compared with monovacancies migration). The heterogeneous point defect cluster nucleation should lead to the growth of radiation hardening and, respectively, barrier-induced embrittlement of similar alloys. The irradiation temperature elevation should decrease this effect. The post-irradiation annealing should completely recover alloys properties after defect annihilation. In the case of the Fe-base systems the following elements are appertained to this group: Hf, Ta, Nb, Zr, Ti, W, Mo. The order in row of these elements corresponds to parameter θ decrease pointing to the direction of the effect weakening.

Group 2. $\Delta U>0$, $\chi<1$. This type of binary systems is predisposed to the solid solution separation or to precipitation of the structurally free phase. The solutes in such alloys should form the fast-mobile vacancy complexes. The latter should enhance the radiation hardening (embrittlement) due to clustering of the solute atoms or mixed defect-solute cluster formation. The irradiation temperature elevation and annealing treatment can either weaken or enhance second component influence depending on its content in relation to the solubility limit. The following elements belong to this group in Fe-base systems: Au, Cu, Mn, Ni (for the latter $\Delta U>0$ condition is valid just in the case of BCC modification). This series of elements is arranged for the parameter χ growth and solubility increase.

Group 3. $|U_{AA}|>>|U_{BB}|$, $\chi << 1$. This is a group of especially low-melting and low surface energy elements. The atoms of these elements can also form fast-mobile complexes despite of ΔU sign. Their segregation on internal sinks or grain boundaries

should cause a local decrease in cohesion and thereby will lead to the embrittlement effect out of direct connection with the barrier-induced hardening. The effects of irradiation temperature and annealing should depend on individual element properties and solution concentration. For Fe-base alloys this group can be presented by the following elements: P, Sb, Sn, As, Ga, Zn. The arrangement in the series corresponds to the parameter θ diminution. Phosphorus takes also especial place in this row being only element that has a smaller atom size than iron. This feature makes it capable for fast diffusion on mechanisms of mixed dumbbell migration.

Thus, the experimental observation of specifics of radiation induced changes in mechanical properties and following behaviour of alloys during the post-irradiation annealing enables to reveal a meaningful difference in their nature and to get the described concept confirmation (or to refuse it).

2. Experimental Study of Iron Model Alloys

2.1. Experimental Procedure

Model alloys were melted under laboratory conditions using high purity iron (0.003% C, 0.008% Si, 0.0017% P, 0.005% Mn, 0.015% Cu, less than 0.002% Ni, Cr, Mo, V). Alloying additions were made to the furnace in the form of pure elements with increasing concentration during overflow. The concentration of the second component, C_B, varied with regard to its solubility, but was no more than 3 at.%. The alloys contained nitrogen (0.01..0.03% by weight) which was present either in the completely bound condition (in alloys with Ta, Ni, Ti) or partially in the solid solution which was controlled by the effect of dynamic strain ageing. In order to evaluate the possible secondary influence of the dissolved nitrogen in the Fe-Cu alloys, one of the two serieses was melted with addition of about 0.15% Ti for bonding the nitrogen. A total of about 50 alloys and 12 binary systems were prepared.

The resulting alloys in the form of blanks (bars and plates) were treated on a solid solution with heating to 925°C (for alloys with Ta and Nb up to 1225°C) with subsequent cooling in water (for supersaturated alloys) or in air.

The tensile properties were mainly defined at room temperature on 3 mm dia specimens. In order to determine T_t shift the sub-size Charpy type specimens were used (5x5x27.5 mm). The electrical resistance measurements were fulfilled also for some alloys using flat 0.2 mm thick specimens.

The specimens were irradiated by neutrons predominantly at temperature of the coolant of reactor WWR-M (50°C) or in some cases in the range of 250-300°C. The fluence of fast (E>0.5 MeV) neutrons in several experiments was within the range of $3..5x10^{23}$ m^{-2}

2.2 Effect of Solute Concentration on Radiation Hardening and Embrittlement

The test results were treated in the form of dependence of concentration of the irradiation-induced increase in yield stress $\Delta\sigma_y$ and its ΔT_t (Fig 1). We will discuss the experimental data that characterize the behaviour of the alloys with elements belonging to each classification group.

Group I. Alloys with elements of this group have radiation hardening dependence similar to those of radiation embrittlement. The sharpest rise in the quantities $\Delta\sigma_y$ and T_t with rise in concentration of the second component is observed in alloys Fe-Ta and Fe-Nb (Fig 1). Alloys Fe-Ti and Fe-W occupy an intermediate position. Alloys of the latter system even for the content of 3 at.% W do not reach a hardening level essential alloys Fe 0.25 at. %Ta and Fe - 0.35 at. %Nb. Alloys Fe-Mo in the interval of concentrations studied show very weak dependences of radiation hardening and radiation embrittlement on dissolved element content.

As it follows from a comparison of Figs 1a,b, the effectiveness of elements in the I group on radiation hardening and radiation embrittlement of alloys actually is controlled by parameter θ. One can be qualitatively convinced of this after comparing Figs 1a, b with Fig 1c which shows the solidus curves of the same binary systems. The order of arrangement of the curves in these pictures essentially coincides. Only curves for pairs of elements W-Mo and Nb-Ta change places. These discrepancies are explained by the fact that the order of arrangement of curves $T_s(C_B)$ are determined by the slope dT_S / dC_B, while curves $\Delta\sigma_y(C_B)$ are determined by parameter θ. The latter differs from dT_S/dC_B by the quantity $T^B_m - T^A_m$, which for W and Ta is especially great.

The type of concentration dependence $\Delta\sigma_y(C_B)$ and $\Delta T_t(C_B)$ obtained from the experiment agrees well with the predictions [1]. With small C_B the dependence of radiation hardening and radiation embrittlement on concentration is close to linear. The linearity interval is conditioned by the vacancy-solute atom complex binding energy, i.e., the value θ. Therefore, in alloys of the system Fe-W an approximately linear relationship is revealed $\Delta\sigma_y(C_B)$ and $\Delta T_t(C_B)$ in the range of concentrations studied, while for alloys Fe-Nb and Fe-Ta, only at the initial section of curves $\Delta\sigma_y(C_B)$. At $C_B > 2x10^{-3}$ the corresponding relationship is described better by the formula of type $\Delta\sigma_y \sim C_B^{0.4}$, which does not contradict to the permissible interval of change in the exponent, which changes from 1 to 0.33 in the case of three-dimensional clusters [1].

Group II. For two series of copper-containing alloys with dissolved nitrogen (further called Fe-Cu-N) and with addition of 0.15% Ti the results of several independent experiments (each point at 50°C corresponds to the main result of an individual experiment) shows (Fig 2) an essentially linear dependence of $\Delta\sigma_y$ and ΔT_t on concentration in limits up to 1.2 at.%. In this case the slope of the curves for alloys of the series Fe-Cu-0.15 Ti is considerably steeper.

With a rise of the irradiation temperature up to 250°C the linear relationship is preserved, moreover, the slope of the corresponding curves for alloys of the series Fe-

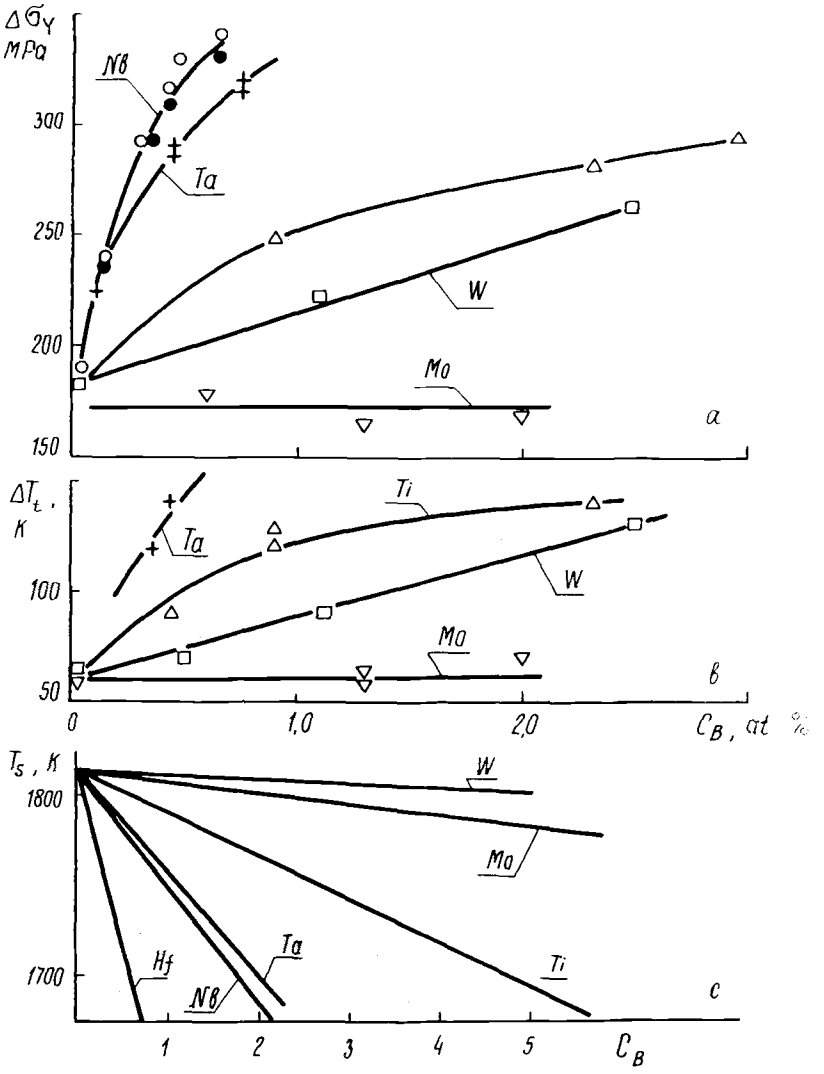


Fig 1. Effect of the refractory element content on radiation hardening (a), embrittlement (b) and solidus curve slope (c) of binary iron alloys.

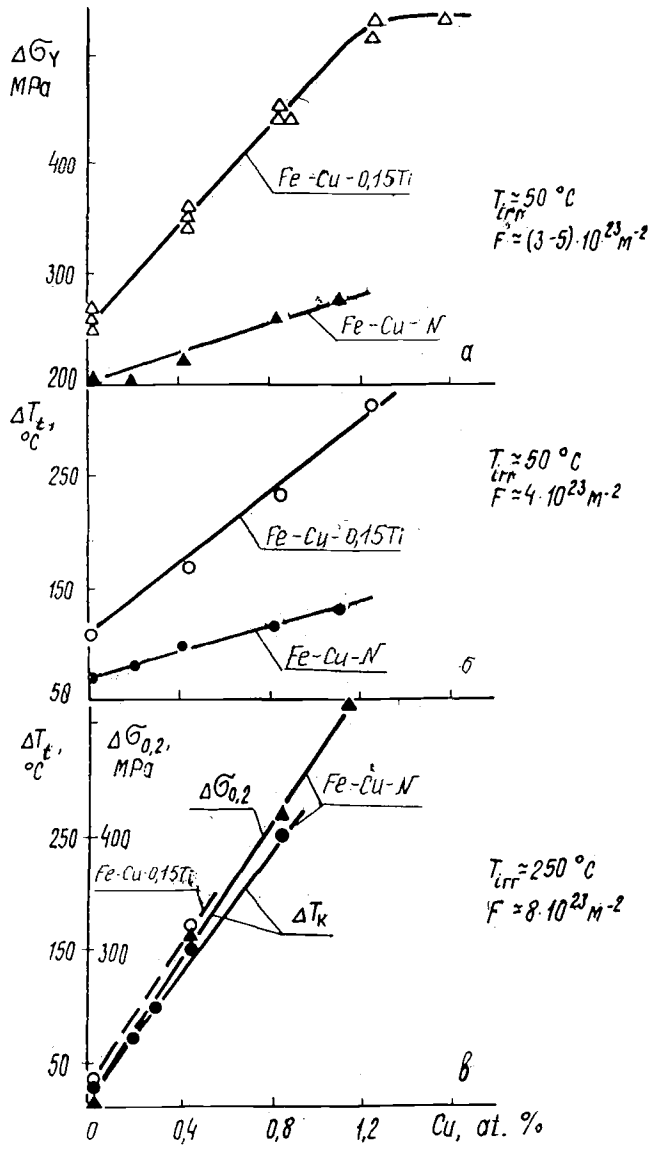


Fig 2. Concentration dependence of radiation hardening (a,b) and embrittlement (c) of iron-copper alloys.

Cu-0.15 Ti. Thus, in the nitrogen-free solid solution the influence of copper reveals weak sensitivity to the change in irradiation temperature in the studied interval. This relationship is explicitly impacted by the presence of dissolved nitrogen, apparently because of bonding of the vacancies.

The linear relationship $\Delta\sigma_y(C_B)$, according to the analysis [1], is possible in the case of a mechanism similar to solid-solution hardening, or under the influence of "vacancy pump". The last case corresponds to the critical nucleus of the cluster made of 2 - 3 atoms of copper.

The results of testing the Fe-Ni and Fe- Mn alloys are presented in Fig 3 in the form of concentration dependence of the increment in σ_y and T_t for irradiation temperature of 50°C. The findings unequivocally indicate that with a rise in the content of nickel and manganese in the studied interval of concentrations, changes in σ_y and T_t rise by linear law. At this temperature of irradiation the influence of these elements is essentially equivalent since the slope of the curve is almost the same (it is noticeable smaller than the alloys Fe-Cu).

The interrelationship between radiation hardening and radiation embrittlement for alloys Fe-Ni and Fe-Nn at an irradiation temperature of 50°C is confirmed as for alloys Fe-Cu by the same type of relationships $\Delta\sigma_y(C_B)$ and $\Delta T_t(C_B)$ and approximately the same ratio of angular coefficients of the corresponding curves.

Increase in irradiation temperature to 250C means that the influence of the nickel content is significantly weakened. The influence of manganese to the contrary rises. The last effect that was not predicted beforehand but correlates with the behavioural features of alloys detected in anealing experiments.

Group III. Concentration dependences for alloys Fe-P, -Sb, -Sn, -Ga and -Se are shown in Fig 4. It is clear from these data that starting from a certain concentration the alloys with phosphorus, antimony and tin are severely embrittled. Additions of phosphorus are especially deleterious. With a content of 0.3 at.%, the magnitude of ΔT_t exceeds 300°C. A similar effect is observed for alloys Fe-Sb and Fe-Sn, but with concentration 0.5 and 0.6 at.% respectively. For alloys Fe-Ga and Fe-Se the dependence of values ΔT_t on the content of the second component in the studied concentration interval of 0..1 at.% has not been revealed.

Comparison shows that in this group of alloys mutual arrangement of the curves $\Delta T_t(C_B)$ correlates with that for the family of solidus curves (Fig 4c), i.e., the solidus criterion in this case correctly ranks the relative effectiveness of the elements. It is indicative that the only element with small atomic diameter, phosphorus, for which the theory predicts the possibility of segregation due to diffusion by the mechanism "relay-race" interstitial migration is not isolated by its position among the remaining elements characterized by the parameter $\Delta\varepsilon > 0$, and therefore potentially prone to migration by the vacancy mechanism. This fact indicates the high diagnostic rank of the parameter θ.

As for the influence of the III group on hardening, for alloys Fe-P one can indicate a weak tendency for intensification of radiation hardening with concentration

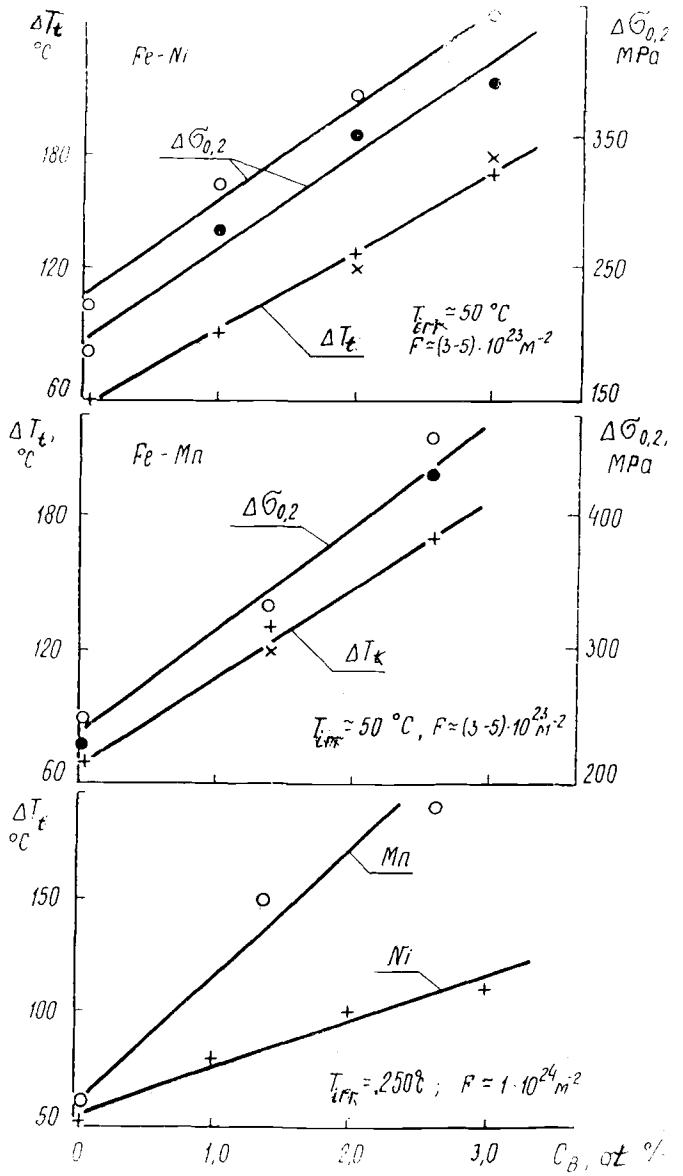


Fig 3. Effect of nickel and manganese content on radiation embrittlement and hardening of binary iron alloys.

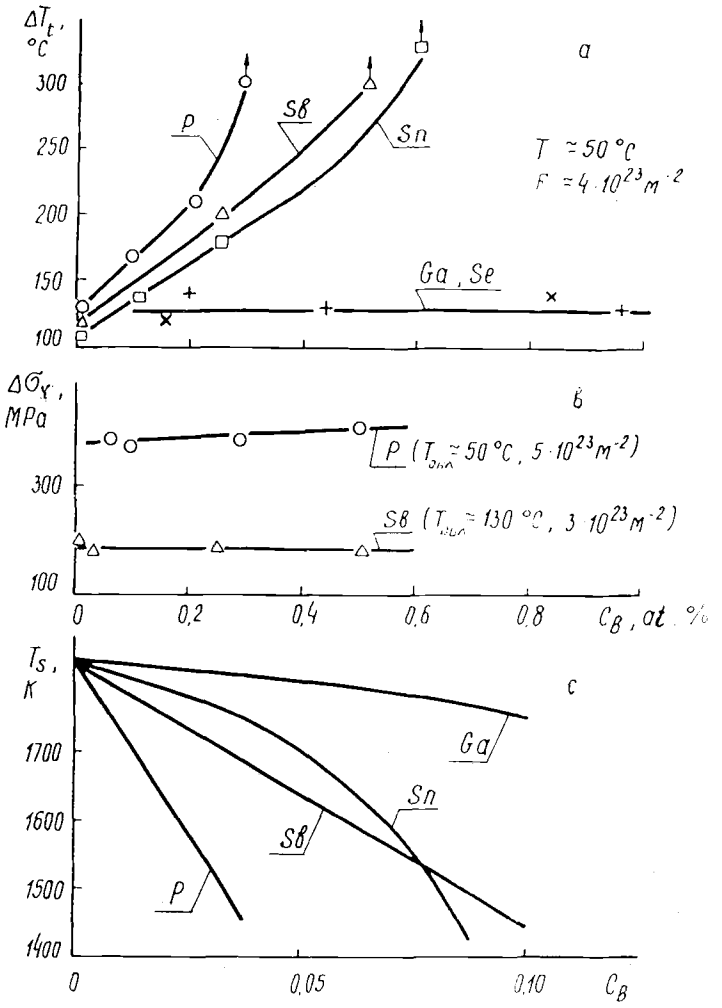


Fig 4. Effect of the refractory element content on radiation hardening (a), embrittlement (b) and solidus curve slope (c) of binary iron alloys.

in the interval 0 - 0.5 at.% (Fig 4b) but this does not at all explain the sharp concentration relationship of their embrittlement. For alloys of the series Fe-Sb the dependence of $\Delta\sigma_y$ on concentration is altogether missing. Thus, the fact of disruption in proportionality between he quantities $\Delta\sigma_y$ and ΔT_t as a classification sign of elements of the III group is fairly clear.

2.4. Post-Irradiation Annealing

The recovery of mechanical properties of alloys has been studied during isochronal annealing during 1 h after irradiation at the temperature of 50°C. The results of experiments on recovery of the yield stress and T_t of alloys of the I group presented in Fig 5 agree well with the theory. In fact, for alloys of the system Fe-Nb, -Ta, -Ti for which this study was made it was found that the recovery begins at the temperature about 170°, and with $T_a = 350°$ (~0.35 T_m of iron) the process ends completely. The residual effect of hardening or embrittlement after annealing at temperatures above this is missing. One should note a certain slowing down in the recovery for alloy Fe - 1.1 at.% W compared to the remaining materials, which is linked to the presence of free nitrogen in the solid solution.

The experiments on isochronal annealing of irradiated Fe-Cu alloys revealed complex kinetics for changes in the increment in the yield stress depending on the annealing temperature, T_a (Fig 6a). Its main feature is that the beginning of softening is preceded by an additional increase in the yield limit, the effect of radiation-thermal hardening, especially noticeable in alloys Fe-Cu-N. This process is observed in the temperature region of 175..325°C, i.e., it occurs simultaneously with annealing of the radiation defects. In order to separate these effects, for alloys of the series Fe-Cu - 0.15 Ti differential (in relationship to the curve for iron) curves were constructed (Fige 6b). They obviously confirm both the actual existence of radiation-anneal hardening in the temperature range of 175 - 325°C, and its dependence on copper concentration.

Another not less important fact is that after high-temperature annealing (T_a = 500°C) the initial strength level of the alloys is not reached. In this case the residual effect of hardening is essentially proportional to the copper concentration (Fig 7).

The solubility limit of copper in iron at 450°C amount to 0.15 at.% [2], thus, both radiation-thermal hardening and residual hardening and brittleness of alloys at the annealing temperature of 500°C is naturally explained by the precipitation of copper atoms from the supersaturated solid solution during irradiation and subsequent annealing. The hardening peak is reached at the annealing temperature of 325°C, while at T_a = 450°C the alloys are already in overaged condition. Similar processes occur under the initial conditions as well, but for equal concentrations, the magnitude of hardening of the nonirradiated alloys is significantly lower (Fig 6b). This indicates the deeper copper separation from the solid solution in the case of preirradiated

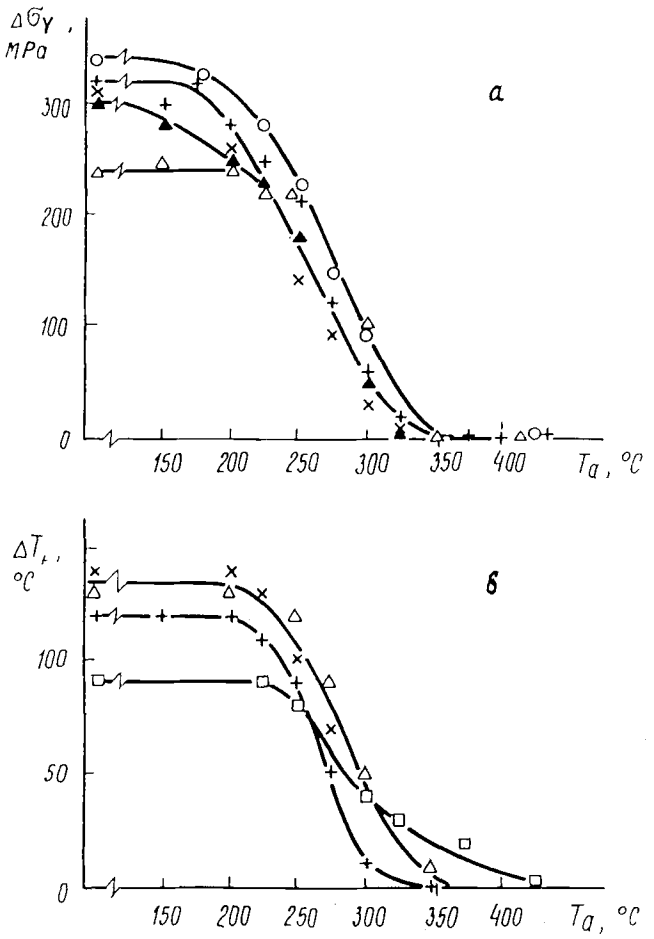


Fig 5. Isochronal annealing recovery of the yield stress (a) and the transition temperature shift (b) of binary iron-refractory element alloys irradiated at 50°C (- 0.44 at.% Nb, - 0.35 at.% Ta, -0.45 at.% Ta, - 0.9 at.% Ti, - 1.1 at.%W).

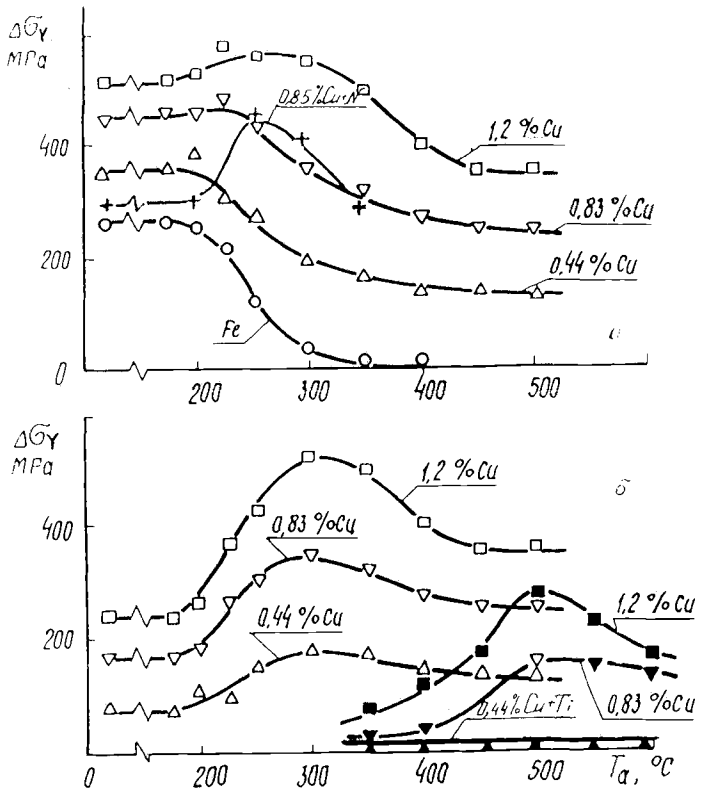


Fig 6. Changes in the yield stress of irradiated iron-copper alloys during isochronal annealing (a), (b) - differential curves (Δ,▽,□) related to iron and hardening of non-irradiated alloys during thermal ageing (▼,■).

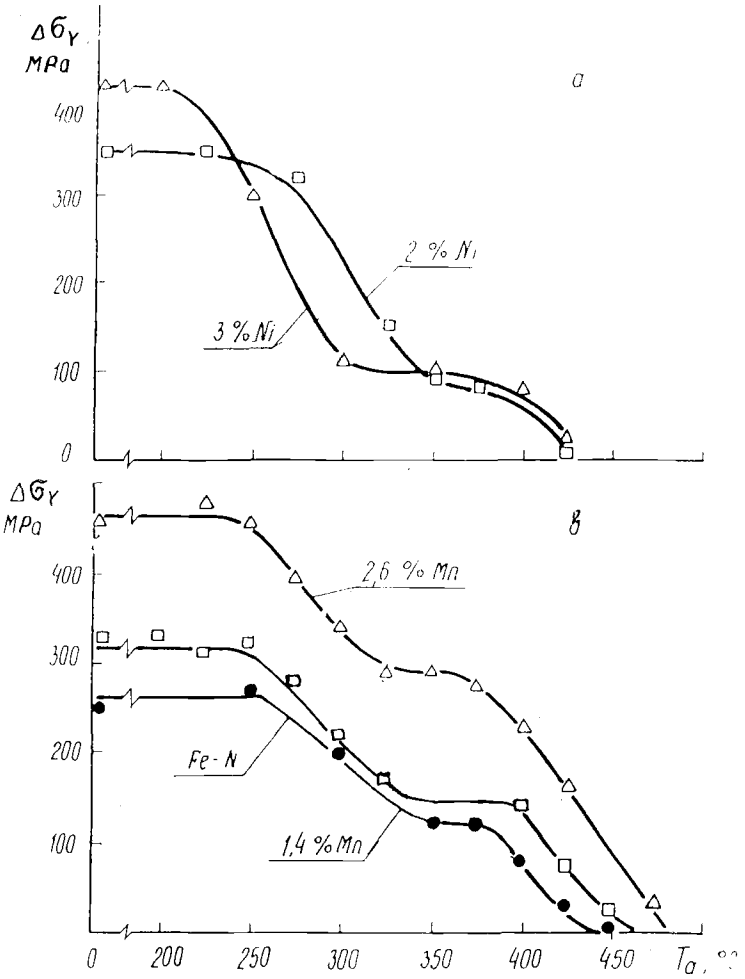


Fig 7. Isochronal annealing recovery of the yield stress of Fe-Ni and Fe-Mn (b) alloys irradiated at 50°C (a).

alloys. In fact, it is apparent from a comparison of the curves in Fig 6b that even with copper content of 0.44 at.% the irradiated and annealed alloy detects noticeably hardening, while in the nonirradiated condition it does not manifest any signs of hardening.

For Fe-Ni alloys the isochrone $\Delta\sigma_y(T_a)$ exhibits a two-stage form (Fig 7) like for the Fe-N alloys, differing from the latter by more developed first substage whose share depends on nickel concentration. Recovery of the properties ends completely at an annealing temperature of 425°C. This result can designate that radiation-induced separation of the dissolved component in the Fe-Ni alloys, if it does occur, is nonequilibrium and is eliminated together with the radiation defects annihilation.

Data on the influence of annealing on the yield stress of Fe-Mn alloys also indicates the two-stage nature of the isochronals (Fig 7b). But in contrast to the Fe-Ni alloys, increase in manganese concentration results in a rise in specific weight and temperature boundaries of the second substage. In other words, manganese intensifies the residual admixture (nitrogen) effect and improves its thermal stability, probably because of the formation of manganese nitrides. However, this does not prevent reaching the complete recovery of the initial strength level at $T_a = 475°C$.

Changes in T_t of the Fe-Mn alloys during annealing in the range 225 - 325°C (Fig 8) are characterized be the effect of radiation-anneal embrittlement, which is not accompanied by change in the mode of cleavage brittle fracture inherent to these alloys in the irradiated condition. In contrast to a similar effect in Fe-Cu alloys, radiation-anneal embrittlement of alloy Fe-Mn occurs on the background of yield stress reduction. Special experiments to investigate the temperature dependence of strength and ductility properties of irradiated and annealed alloy Fe - 2.6% Mn in the interval of -196..+20°C demonstrate (Fig 9) that the reason for this is most likely related to a decrease in cleavage fracture stress, σ_{bf} (Fig 9). This unpredicted effect, judging from complete recovery of T_t at annealing temperatures of 450..475°C is also reversible, and probably caused by some nonequilibrium process whose nature is still unclear.

The influence of annealing on T_t recovery of alloys of the III group was studied on irradiated samples of alloys Fe-0.5 at.% P and Fe-0.6 at.% Sn (Fig 10). Experiments showed that after annealing at temperature 400°C the residual T_t shift for alloys is only 20..40°, while at the temperature of 450° (0.39 T_m) the values of T_t are completely restored. Consequently, for alloys of this group on the condition that $\Delta U < 0$ reversibility of radiation embrittlement also occurs at $T_a \sim 0.4\ T_m$.

A rather special behaviour was detected during annealing of alloy Fe-0.5 at.% Sb (Fig 10), for which the tendency for T_t return noted at T_a=400..450°C is replaced by intensification of embrittlement at 500°, while embrittlement is only eliminated after annealing at temperature over 600°C. This result, however, does not refuse the concept regarding intracrystalline nonequilibrium segregation of the antimony atoms, insofar as cleavage fracture, predominantly characteristic for the brittle fracture of irradiated alloy, after annealing at temperatures of 450..550°C is replaced by typically

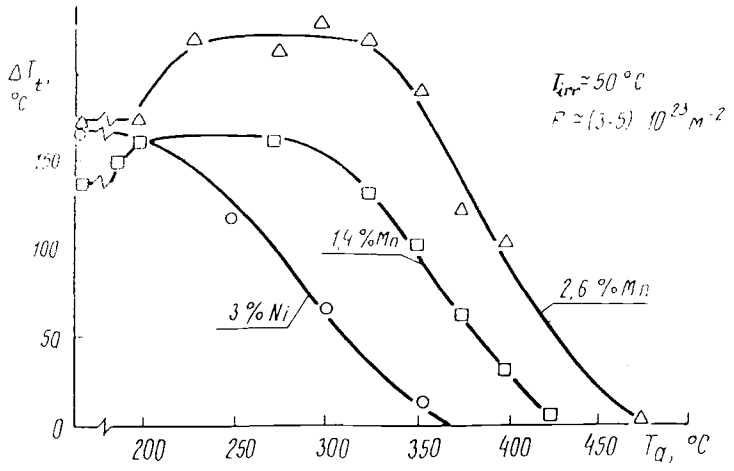


Fig 8. Recovery of radiation embrittlement during annealing of Fe-Ni and Fe-Mn alloys.

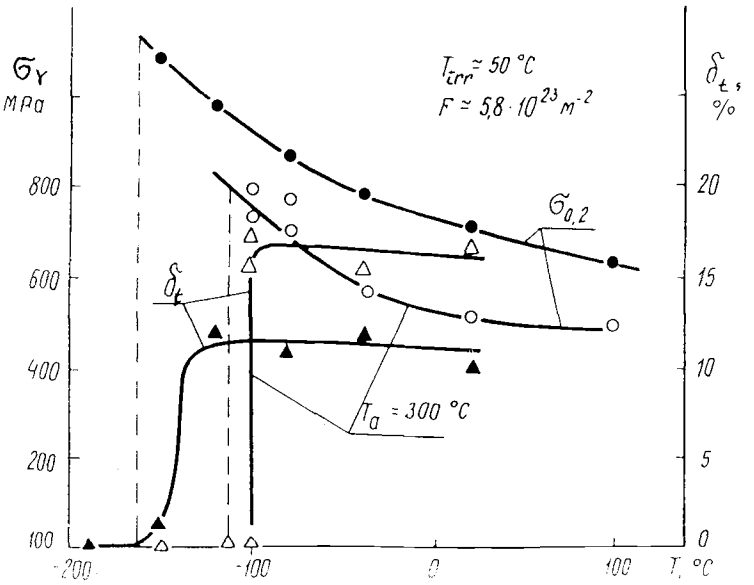


Fig 9. Influence of the post-irradiation annealing at 300°C on the mechanical property demperature dependence of Fe-2.6%Mn alloy.

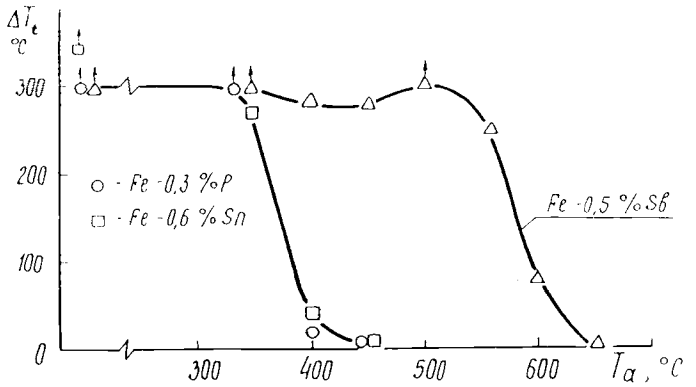


Fig 10. Isochronal annealing recovery of the transition temperature shift of irradiated iron alloys with phosphorus, tin and antimony.

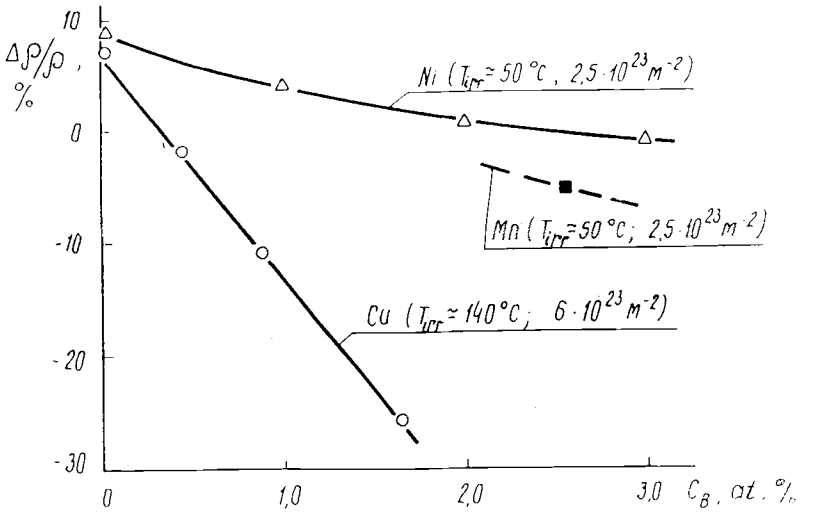


Fig 11. Effect of neutron irradiation on electrical resistivity changes of iron alloys with different copper, nickel and manganese contents.

intergranular failure. The isochrone $\Delta T_t(T_a)$ obtained for this alloy consequently reflects superposition of the radiation embrittlement recovery and the effect of temper embrittlement, to which this material is prone in contrast to the others.

2.5. Electrical Resistance Measurements

Concentration dependence. The influence of irradiation on changes in electrical resistance (ρ) has been studied on alloys of the series Fe-Cu, Fe-Ni and Fe-Mn (one composition). For alloys with copper irradiation at temperature 140°C led to a decrease in ρ for all compositions, with the exception of iron and was greater the higher the copper content (Fig 11). Taking into consideration that intensive decrease in electrical resistance of the supersaturated alloys Fe-Cu is caused by precipitation of the δ-phase during ageing in the interval of 400..600°C, a similar effect during irradiation could be unequivocally related to the solid solution separation.

For electrical resistance of Fe-Ni alloys which were irradiated was conducted at a temperature of 50°C, there is a characteristic drop in the magnitude of the radiation effect as the concentration increases (Fig 11). Increment in ρ equal to 9.5% in iron monotonously diminishes in alloys with 1 and 2% Ni, being replaced as a result by a negative quantity (~ 0.25%) with 3% Ni content. It is doubtless that the radiation defects are also forming in Fe-Ni alloys. The corresponding resitometric effect should be present in alloys of any concentration in completely or partially latent form because the opposite effect appears due to another mechanism action. It is clear that the integral changes observed for the Fe-Ni alloys indicate a perceptible development of the process of the nickel atoms redistribution.

A similar effect, but even more clearly pronounced was obtained for the Fe-2.6% Mn alloy ($\Delta\rho/\rho$ = -5.5%).

Annealing. In the series of Fe-Cu alloys irradiated at a temperature of 140°C, the isochronal (20 min) annealing causes a drop in electrical resistance in the interval 200 - 400°C (Fig 12). This drop is apparently governed by annealing of radiation defects. An explicit trend is observed for rise in the annealing part with higher copper content. This circumstance, if only it is not linked to deepening of the process of copper precipitation, can be viewed as proof for the increased concentration of the preserved defects. In this case one should take into consideration the effect of a certain mechanism not discussed above that promotes survival of the defects in the solid solution. This type of mechanism [3] could be based on the effect of the type of "masking" of the vacancies on the composition of the complex with dissolved atom because of smaller size of the recombination zone of the bound vacancy as comared with the recombination zone of isolated defect.

The drop in electrical resistance during annealing of the irradiated specimens of the Fe-Ni series is also observed in all compositions, including the alloy of maximum Ni concentration (3%) in which irradiation led to a decrease in ρ (Fig 13). The simplest type of isochrone is observed for iron whose electrical resistance is

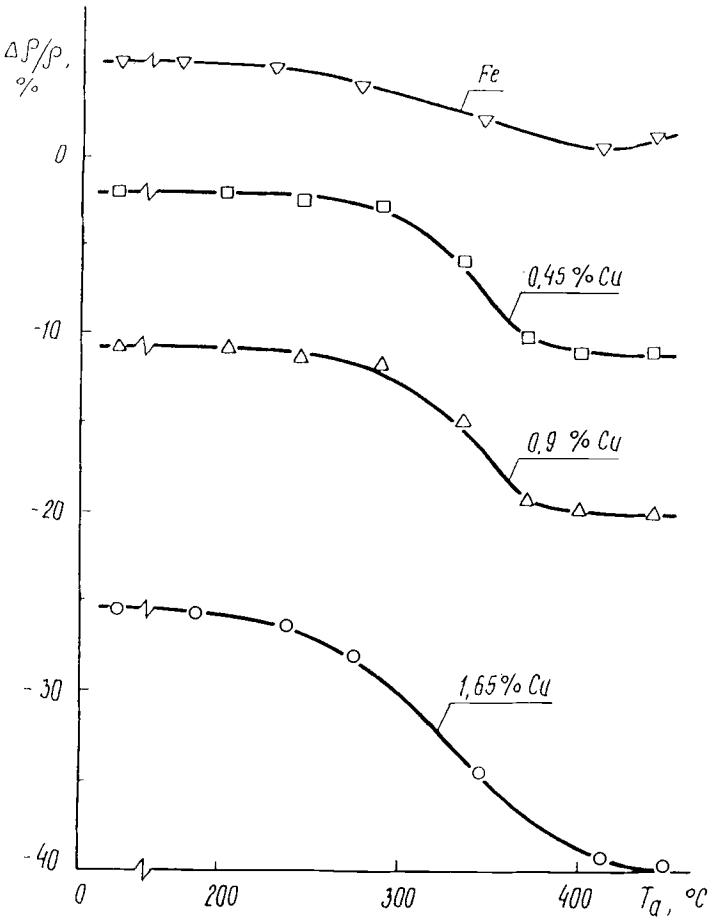


Fig 12. Isochronal annealing changes of the electrical resistivity of Fe-Cu alloy irradiated at 140°C.

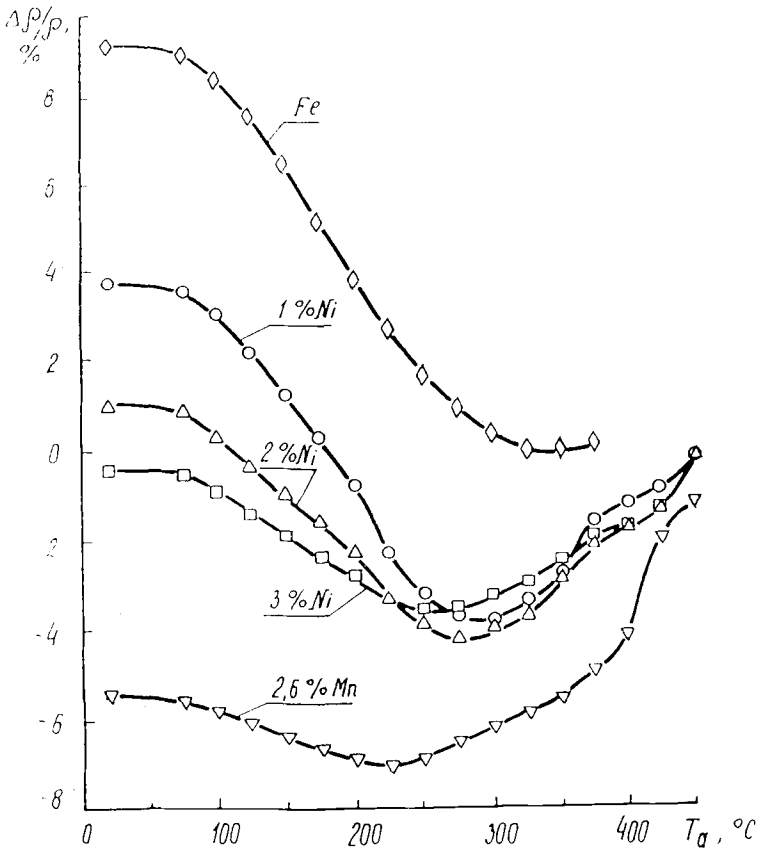


Fig 13. Isochronal annealing recovery of the electrical resistivity of Fe-Ni and Fe-Mn alloys irradiated at 50°C.

TABLE

PHYSICO-CHEMICAL PROPERTIES OF ELEMENTS IN ALLOYS BASED ON α-Fe

'	Element	T_m^B/T_M^{Fe}	q 10^3 K	?B / ?A - 1 (from data of different sources)		Type of secondary phase	g_B/g_{Fe}
1	Ti	1.08	-2.5	0.14	0.327	Fe_2Ti	0.89
2	Zr	1.18	-5.3	-	1.10	Fe_2Zr	0.92
3	Hf	1.23	-18.0	-	1.18	Fe_2Hf	0.96
4	V	1.22	-0.6	0.105	0.127	FeV	1.16
5	Nb	1.54	-6.8	0.176	0.727	Fe_2Nb	1.37
6	Ta	1.82	-6.5	-	0.589	Fe_2Ta	1.47
7	Cr	1.21	0	0.043	0.096	FeCr	0.98
8	Mo	1.60	-1.5	0.275	0.399	Fe_3Mo_2	1.38
9	W	2.02	-1.5	0.330	0.389	Fe2W	1.50
10	Mn	0.84	-0.3	0.049	0.096	g-Fe**	0.98^x
11	Ni	0.95	-0.6	0.046	0.125	-"-	0.89
12	Cu	0.75	-0.5	0.175	0.569	e(Cu)**	0.69
13	Au	0.74	-2.5	0.441	-	e(Au)**	0.75
14	P	0.17	-12.0	-0.13	-	Fe_3P	-
15	Zn	0.38	-0.9	0.21	0.156	$FeZn_3$	0.065
16	Ga	0.17	0	-	-		0.395^x
17	As	0.60	-8.0	0.237	0.181	Fe_2As	-
18	Se	0.27	-	-	-	FeSe	0.059^x
19	Sn	0.28	-0.9	0.677	0.328	Fe_3Sn	0.43
20	Sb	0.50	-2.5	0.364	-	Fe_3Sb_2	0.214^x

* For liquid phase
** solid solution

restored at T_a=350°C as a result of defects annealing. The nonmonotonous nature of the isochrones for alloys indicates parallel occurrence of two processes, one of which is related to the rise in ρ and definitely governed by the presence of nickel. The amplitude of changes $\rho(T_a)$ decreases in the interval of 75..350°C as the nickel concentration rises. Together with this fact the return of ρ at 450°C indicates that homogeneity of the solid solution disrupted by irradiation is restored as a result of annealing at mentioned temperature. This also confirms the nonequilibrium nature of the structural changes observed in the Fe-Ni alloys, which is natural for nonsaturated solutions.

A pattern similar in the main features was obtained during annealing of alloy Fe-2.6% Mn (Fig 13) which makes it possible to use these consideration for it.

Conclusion

The results of this experimental study agree with the predictions regarding the diversity of factors that determine the influence of chemical composition on radiation hardening and embrittlement of reactor pressure vessel materials.

Classification of binary alloys based on the concepts regarding interaction of point defects with dissolved atoms and analysis of the thermodynamic properties of the corresponding systems, reflected in the structure of their patterns of state in experimentally confirmed for model alloys of iron in all the studied aspects: in type of concentration relationship of radiation hardening, in correlation between the magnitudes $\Delta\sigma_y$ and ΔT_t, for ranking of effectiveness of the influence of elements based on the solidus criterion, in capacity of alloys for return of properties when defects are eliminated. One can see in this not only proof for the important role of interaction between the point defects and solute atoms in the change in mechanical properties of alloys under the influence of low-temperature irradiation, but also confirmation of the correctness of the developed basis for the approach to influence of solute atoms on the formation of structures of irradiated materials. In this case the set of experimental factors corresponds to the conclusion that vacancy-solute atom reactions are very important in these processes.

It should also be stressed that increase in the number of components in the alloy significantly complicates the situation, introducing an additional factor of chemical interaction. Therefore it should be kept in mind that the influence of certain element may not be completely the same in binary alloy and in steel.

References

1. Rybin V.V., Nikolaev V.A., In: Voprosy materialovedenia (in Russian), 1995, N1, pp. 28-40.
2. Royen, P.; Reinhardt, H. Zeitschr. anorg. Chemie, 281, 1955, p.18.

3. Alekseenko, N. N.; Amaev, A. D.; Gorynin, I. V.; Nikolaev, V. A. Radiatsionnoye poverzhdeniye stali korpusov vodo-vodyanykh reaktorov [Radiation Damage of Steel in Vessels of Water-Moderated Water-Cooled Reactors], Moscow, Energoizdat, 1981.

Roger E. Stoller[1]

PRESSURE VESSEL EMBRITTLEMENT PREDICTIONS BASED ON A COMPOSITE MODEL OF COPPER PRECIPITATION AND POINT DEFECT CLUSTERING

REFERENCE: Stoller, R. E., **"Pressure Vessel Embrittlement Predictions Based on a Composite Model of Copper Precipitation and Point Defect Clustering,"** *Effects of Radiation on Materials: 17th International Symposium, ASTM STP 1270,* David S. Gelles, Randy K. Nanstad, Arvind S. Kumar, and Edward A. Little, Eds., American Society for Testing and Materials, 1996.

Abstract: A theoretical model is used to investigate the relative importance of point defect clusters (PDC) and copper-rich precipitates CRP) in reactor pressure vessel (RPV) embrittlement and to examine the influence of a broad range of irradiation and material parameters on predicted yield strength changes. The results indicate that there are temperature and displacement rate regimes wherein either CRP or PDC can dominate the material's response to irradiation, with both interstitial and vacancy type defects contributing to the PDC component. The different dependencies of the CRP and PDC on temperature and displacement rate indicate that simple data extrapolations could lead to poor predictions of RPV embrittlement. It is significant that the yield strength changes predicted by the composite PDC/CRP model exhibit very little dependence on displacement rate below about 10^{-9} dpa/s. If this result is confirmed, concerns about accelerated displacement rates in power reactor surveillance programs should be minimized. The sensitivity of the model to microstructural parameters highlights the need for more detailed microstructural characterization of RPV steels.

KEYWORDS: pressure vessel steels, modeling, hardening, embrittlement, point defect clusters, copper precipitates, irradiation temperature, displacement rate

[1] Senior research staff member, Metals and Ceramics Division, Oak Ridge National Laboratory, Oak Ridge, TN 37831-6376, USA

Copyright© 1996 by ASTM International www.astm.org

INTRODUCTION

Much of the radiation-induced embrittlement observed in commercial reactor pressure vessel (RPV) steels has been attributed to the formation of copper-rich precipitates (CRP), and this phenomenon has been extensively investigated [1-9]. Theoretical models have been developed that show good agreement with a broad range of data [1-4,10,11]. The use of high-resolution transmission electron microscopy (TEM) imaging and analysis techniques, small-angle neutron scattering (SANS), and the atom probe/field ion microscope (AP/FIM) have clearly revealed the presence of CRP, as well as a broad range of other fine-scale precipitates in both irradiated and unirradiated material [5-9]. Such work provides estimates of the size and density of the CRP. A combination of high-resolution TEM and molecular dynamics (MD) simulations has demonstrated that the CRP are coherent, bcc at small sizes and pass through an intermediate structure prior to becoming fcc [12]. The MD work also provided an estimate for the shear modulus of the bcc CRP.

Small clusters of point defects (vacancies and interstitials) have also been recognized as contributing to radiation-induced hardening in irradiated metals and alloys [10,11,13-22]. In fcc materials such as copper, the size distributions of these point defect clusters (PDC) can be characterized at very small sizes by TEM. The contribution of these PDC to the yield strength change following irradiation can be computed using standard hardening models [19-24] and the computed values compare favorably with the measured values [18]. It has proven difficult to apply this same sort of analysis to bcc ferritic alloys such as RPV steels. Ferritic steels exhibit significant hardening at low doses, well before any corresponding microstructural change can be observed by TEM. Fine-scale TEM characterization is inhibited by the magnetic nature of ferritic steels and by the oxide layers that quickly form on the specimen surfaces. The overall complex microstructure exhibited by commercial RPV steels can also obscure small defects in the TEM. MD simulations of displacement cascades suggest that there may be some inherent differences in primary damage formation between fcc and bcc materials [25-27] as well.

Although the PDC are not easily observed, there is considerable indirect evidence for embrittlement arising from these defects. This evidence includes the embrittlement observed in model and engineering alloys that include little or no copper, the post-irradiation annealing behavior of these steels [28,29], and the fact that the incremental change in precipitation under irradiation does not always seem adequate to account for the observed changes in mechanical properties. Low temperature embrittlement, i.e. below about 150°C, such as that observed in the pressure vessel of the High Flux Isotope Reactor (HFIR) [30], is also unlikely to be due to copper precipitation since diffusion rates are much slower at such temperatures. Finally, there is evidence that one influence of solutes such as copper is to refine the PDC size distribution [16,31].

The potential significance of PDCs in RPV embrittlement was investigated using a theoretical model described in previous papers [21,22]. This work indicated that the formation of both interstitial and vacancy clusters could lead to significant hardening.

However, the values for the dislocation barrier strengths of the PDC used in Ref. 21 were near the maximum plausible and the level of assumed in-cascade clustering of point defects was rather high. Thus, the calculations represented the upper limit of the possible hardening. These severe limits are relaxed in the work presented here in order to examine the influence of a more reasonable set of model parameters and to include the concurrent effects of CRP. A simple copper precipitation model is adapted from those in the literature in order to determine the relative magnitude of hardening induced by CRP and PDC. A range of irradiation temperatures and displacement rates is examined, and the sensitivity of the model to variations in key parameters is determined. Several assumptions commonly made in the use of CRP models are also examined. Additional results obtained with the composite PDC/CRP model are reported in Ref. 32.

MODEL DESCRIPTION

The details of the numerical model for PDC are contained in Refs. 21 and 22 and will not be repeated here; the discussion will emphasize the changes required to implement the CRP model. Briefly, the model integrates the rate equations describing the time (dose) dependence of the interstitial and vacancy concentrations, the interstitial cluster population, the number of vacancy clusters, and the CRP radius. The hardening increment due to the PDC populations is computed assuming that they act as weak dispersed barriers to dislocation motion, while the Russell-Brown model [33] is used to compute the hardening due to the CRP.

Point Defect Concentrations

The equations describing the spatially-averaged point defect concentrations (C_i and C_v) can be written as:

$$\frac{dC_{i,v}}{dt} = G_{i,v} - RC_iC_v - D_{i,v}C_{i,v}S_{i,v}^T \qquad (1)$$

where the subscripts i and v denote interstitial and vacancy, respectively. The constants in Eq. (1) are: G_i, the interstitial generation rate; G_v, the vacancy generation rate; R, the recombination rate coefficient; D_i, the interstitial diffusivity; and D_v, the vacancy diffusivity. The $S_{i,v}^T$ are the total sink strengths of all the extended defects in the material. These sinks can include dislocations, grain boundaries and other interfaces, and the interstitial and vacancy clusters discussed below. The total sink strength should also include that of the CRP, although this has been neglected in most previous work. The influence of the CRP sink strength will be discussed below. The sink strengths of the extended defects are calculated to lowest order [21, 34].

In the general case, the interstitial and vacancy generation rates include the displacement rate, G_{dpa}, and the point defects produced by thermal emission from extended defects. In addition, the dpa rate is reduced by the cascade efficiency, η, to account for in-cascade recombination and terms that account for in-cascade clustering. The interstitial formation energy is sufficiently high in these materials that interstitial emission from extended defects such as dislocations can be neglected in practice and even vacancy emission is small at the temperatures of interest to this work. Interstitial emission can occur from the small interstitial clusters for which the binding energy is sufficiently low.

Point Defect Clustering

Interstitial clustering is treated in greater detail than is vacancy clustering. Interstitial clusters can be formed directly in the displacement cascade, or by essentially classical, homogeneous nucleation due to random collisions between diffusing defects. Although clusters with up to 8 interstitials have been observed in recent MD simulations of high energy cascades in iron, most of the in-cascade interstitial clusters are smaller [26,27]. Thus the model assumes that in-cascade formation occurs only for the smallest three cluster sizes. The total in-cascade cluster fraction, f_{icl}, is then the sum of three components: the fraction forming di-(f_{icl}^2), tri-(f_{icl}^3), and tetra-interstitials (f_{icl}^4).

For simplicity, homogeneous nucleation of vacancy clusters is neglected and vacancy cluster formation is assumed to happen only as the result of cascade collapse. The vacancy clusters are assumed to form directly in the cascade as microvoids with a radius r_{vcl}. The vacancy cluster generation rate is determined by the fraction of the vacancies that are assumed to collapse into the clusters, f_{vcl}, and the number of vacancies contained in a cluster of size r_{vcl}. For the irradiation conditions of interest here, these microvoids are generally unstable and shrink at a rate determined by the absorption of point defects and vacancy emission [21].

Hardening Due to Point Defect Clusters

A dispersed barrier model has been used to calculate matrix hardening due to the interstitial and vacancy clusters. Such models are derived from the theory developed by Orowan to describe hardening due to precipitates and involve a calculation of the shear stress required to move a dislocation past an obstacle in its glide plane, leaving behind a dislocation loop [19,24]. A related change in the yield stress can be computed from this shear stress. The Orowan-looping mechanism may not be appropriate for small point defect clusters since they may be sheared before the dislocation has bowed completely around them. Its use here provides a simple expedient way of examining the possible importance of these clusters.

Although more complex forms are generally appropriate [35], the simplest expression of Orowan's dispersed barrier equation for the change in the shear stress, $\Delta\tau$, can be written as:

$$\Delta\tau = \frac{\mu b}{\beta \ell} \qquad (2)$$

in which μ is the shear modulus and b is the magnitude of the Burgers vector. The average barrier spacing, $\ell=(Nd)^{-0.5}$, is computed from the number density (N) and the diameter (d) of the obstacles. The factor β in Eq. (2) is a measure of the barrier strength. For example, $\beta=1$ for a periodic array of strong barriers, such as incoherent precipitates. In a polycrystalline material, the Taylor factor can be used to convert the calculated change in shear stress to a change in the uniaxial yield stress, i.e. $\Delta\sigma_y \sim 3.1\Delta\tau$ [23]. When computing the shear strength, a root-square summation (rss) of the CRP and the interstitial and vacancy cluster contributions was assumed, i.e. $\Delta\tau=(\Delta\tau_{CRP}^2 + \Delta\tau_{icl}^2 + \Delta\tau_{vcl}^2)^{0.5}$ [19,24].

A number of values for the barrier strength term in Eq. (2) are discussed in Refs. 19 to 21. However, there are only limited experimental data available to guide the choice of β for very small defects. Estimates of β for small PDC and interstitial loops in bcc materials range from 1.5 to 5 [20]. Recent measurements of tensile properties and detailed TEM examination of fcc copper irradiated to low doses indicated a value of $\beta=4$ [18]. This value was derived for PDC with mean diameters below 3 nm, which is comparable to the size of those calculated here. Although the crystal structure of RPV steels is bcc, rather than fcc, $\beta=4$ was used to obtain the results presented here.

Evolution of Copper-Rich Precipitates

The copper precipitation model employed here shares common features with those developed by Odette [1] and by Fisher and co-workers [11]. Precipitate nucleation is not modeled. The assumption is made that nucleation occurs quickly under irradiation [1] and that precipitate growth is the rate limiting process. A fixed density (N_{ppt}) of small precipitates is included in the calculations from the beginning. The initial precipitate radius (r_{ppt}) is taken as equal to the magnitude of the Burgers vector, ~0.249 nm. Assuming diffusion-limited growth, the growth rate of these precipitates can be computed as:

$$\frac{dr_{ppt}}{dt} = 4\pi r_{ppt} N_{ppt} D_{Cu}^{*} (Cu^{\circ} - f_{Cu}) \qquad (3)$$

where D_{Cu}^{*} is the radiation-enhanced copper diffusion coefficient, Cu° is the initial concentration of copper in solution, and f_{Cu} is the concentration of copper contained in precipitates that formed during irradiation. The term ($Cu^{\circ} - f_{Cu}$) in Eq. (3) is the concentration of copper in solution at any given time. If the precipitates are pure copper, f_{Cu} is equal to the volume fraction of the precipitates. In the case of RPV steels, Cu° is generally less than the concentration obtained by bulk chemistry since copper also

precipitates during post-fabrication heat treatment [5,11]. These coarser copper precipitates are neglected in the following analysis.

The available diffusion data for copper in iron is consistent with diffusion by a vacancy mechanism [36, 37]. In this case, the radiation-copper diffusion coefficient (REDC) for copper can be computed as:

$$D^{*}_{Cu} = D_{Cu}(C_v/C_v^e) \ , \qquad (4)$$

where D_{Cu} is the thermal diffusion coefficient of copper, C_v is the total vacancy concentration (radiation-induced plus thermal) and C_v^e is the thermal equilibrium vacancy concentration. Specific values for the various parameters are listed in Table 1. Eq. 4 is integrated along with Eq. 1 and the related equations for the interstitial and vacancy cluster concentrations [21].

Hardening Due to Copper-Rich Precipitates

The model that is most commonly used [1,11] to compute the hardening caused by the CRP is that of Russell and Brown [33], which differs from the Orowan model in that the hardening arises from a difference between the shear modulus of the precipitate and the shear modulus of the iron matrix. The Russell-Brown model is also employed here. The incremental increase in the shear stress due to precipitates in this model is given as:

$$\Delta\tau = \frac{0.8\mu b}{\ell}\left(1 - \frac{E_{ppt}}{E}\right)^{1/2} ; \sin^{-1}(E_{ppt}/E) < 50 \qquad (5a)$$

$$\Delta\tau = \frac{\mu b}{\ell}\left(1 - \frac{E_{ppt}}{E}\right)^{0.75} ; \sin^{-1}(E_{ppt}/E) > 50 \qquad (5b)$$

where:

$$\frac{E_{ppt}}{E} = \frac{1}{\ell n(r_c/r_o)}\left[\frac{E^{\infty}_{ppt}}{E^{\infty}}\ \ell n\left(\frac{r_{ppt}}{r_o}\right) + \ell n\left(\frac{r_c}{r_{ppt}}\right)\right] \qquad (6)$$

The ratio $E^{\infty}_{ppt}/E^{\infty}$ in Eq. 6 is equal to the ratio of the precipitate shear modulus to the matrix shear modulus for a screw dislocation. $E^{\infty}_{ppt}/E^{\infty}=[(1-\nu)\mu_{ppt}]/[(1-\nu_{ppt})/\mu]$ for an edge dislocation, where ν is Poisson's ratio in the matrix and ν_{ppt} is Poisson's ratio in the precipitate. Other variables in Eqs. 5 and 6 are: μ, the matrix (Fe) shear modulus; μ_{ppt}, the precipitate shear modulus; r_o, the inner cut-off or dislocation core radius; r_c the outer cut-

TABLE 1--Material parameters for base case model calculations

Parameter	Symbol	Value
Cascade efficiency	η	0.1
Interstitial clustering parameters:		
total interstitial clustering fraction	f_{icl}^{T}	0.3
di, tri, and tetra interstitial clustering fractions	f_{icl}^{2}, f_{icl}^{3}, f_{icl}^{4}	0.15, 0.1, 0.05
cluster binding energies (eV)	E_{2i}^{B}, E_{3i}^{B}, E_{4i}^{B}	0.75, 1.00, 1.50
Vacancy clustering fraction	f_{vcl}	0.6
Vacancy cluster radius (nm)	r_{vcl}	0.5
Diffusivity pre-exponential (m^2/s):		
interstitial	D_io	$5.0x10^{-6}$
vacancy	D_vo	$5.0x10^{-5}$
copper	$D_{cu}o$	$3.0x10^{-2}$
Interstitial migration energy (eV)	E_im	0.25
Vacancy migration energy (eV)	E_v^m	1.25
Vacancy formation energy (eV)	E_if	1.55
Copper migration energy (eV)	E_{cu}^m	2.94
Lattice parameter (nm)	a_o	0.287
Recombination radius (nm)	r_R	0.574
Surface free energy (J/m^2), [temperature (°C) dependent]	γ	$2.947-4.5x10^{-4}*T$
Dislocation capture efficiencies:		
Interstitial	Z_i^d	1.25
Vacancy	Z_v^d	1.00
Network dislocation density (m^{-2})	ρ_n	$(0.5 \text{ to } 5.0)x10^{14}$
Effective grain size (μm)	d_g	10.
Dislocation barrier strength of point defect clusters	β	4.
Precipitate density (m^{-3}), [temperature (K) and copper dependent]	N_{ppt}	$8.0x10^{23}*(\text{at-\%Cu})^{0.5}*$ $\{\exp[0.35/k(1/T-1/561.16)]\}$
Copper shear modulus (MPa), [temperature (K) dependent]	μ_{ppt}	$5.328x10^4 - 18.6*T$

off radius used to compute the dislocation energy; and b, the magnitude of the Burgers vector. Differences in Poisson's ratio for the matrix and precipitate were neglected here; $\nu=\nu_{ppt}=0.3$ was used. Temperature-dependent values for the shear modulus of the ferritic steel matrix and the copper precipitates were taken from the literature [38,39]. An MD-based calculation indicated that the shear modulus of bcc copper should be lower than that of fcc copper [12]; the use of the lower value would increase the calculated hardening.

Two alternate hardening models, those of Weeks and Knowles and Kelly, were investigated to examine their sensitivity to the relevant parameters. A summary description of these models is given by Kelly [35], along with a full description of the Orowan equation. A comparison of the three modulus hardening models and the Orowan equation is shown in Figure 1. The hardening has been normalized using the square root of the precipitate volume fraction in order to eliminate the dependence on precipitate number density. For purposes of this comparison, $\mu_{ppt}/\mu=0.6$, $r_o=2b$, and $r_c=1000\ r_o$. All of the modulus-dependent models yield less hardening than does the Orowan model; with the latter corresponding to a precipitate modulus of zero. The radius dependencies of the Russell-Brown models is more similar to the Orowan equation than are the others. The overall differences among the three modulus hardening models are not large; less than a factor of two at most sizes. More details on this comparison can be found in Ref. 32.

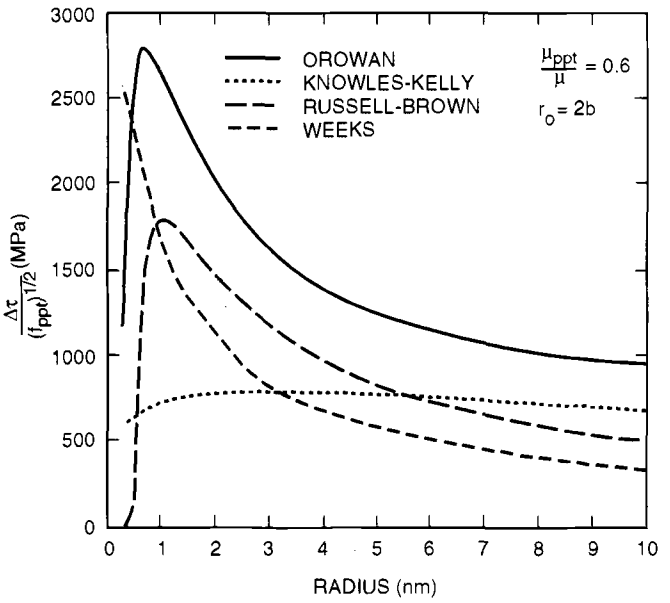


Figure 1. Comparison of hardening predicted by three modulus hardening models and that from the Orowan equation.

The models tend to be strongly sensitive to the precipitate radius at small sizes due to arithmetic limits such as that which can be found by examination of Eqs. 5 and 6. In

this case, r_{ppt} must be greater than r_o. Similar limits for the other models are discussed in Ref. 32. In this work, a polynomial fit was used to smoothly extrapolate the radius dependence of the Russell-Brown model for radii less than r_o. This is in some sense only a formality since the computed hardening drops off very rapidly as the precipitate radius approaches r_o.

The dependence of the Russell-Brown model on r_o and r_c is shown in Figures 2(a) and 2(b), respectively. Relatively modest changes are observed for reasonable variations of these parameters. A value of r_o=2.5b [33] was used in the calculations described below. Although Russell and Brown used r_c=1000 r_o, such a value seems physically unreasonable for engineering materials since it is larger than the mean spacing of dislocations. Here, r_c has been set equal to this mean dislocation spacing [40], $r_c=(\pi\rho_n)^{-0.5}$, where ρ_n is the network dislocation density.

RESULTS OF MODEL CALCULATIONS

One observation from Ref. 21 should be recalled before the current results are discussed. It is commonly assumed that the steady state point defect concentrations can be used in radiation damage modeling. This is generally a good assumption for elevated temperatures, but not at low temperatures. The point defect concentrations do reach steady state quite rapidly at 285°C, but the steady state concentrations are not reached at 60°C until about 30 years [21]. The time required for the vacancies to diffuse to sinks typically determines the duration of the transient approach to steady state.

The steady state point defect concentrations should not be used when the irradiation temperature is much below 200°C without examining the impact of the long point defect transient. Extrapolations based on data obtained at higher temperatures could be misleading. This transient accounts for some of the differences observed in the results discussed below. The results will focus on the temperatures of 60 and 288°C since these two temperatures bracket the service conditions of pressure vessel steels and similar alloys in light water reactors (LWR). Displacement rates from $1x10^{-13}$ dpa/s to $1x10^{-7}$ dpa/s will be discussed. The lower end of this range includes the exposure conditions of the HFIR pressure vessel and commercial LWR support structures; the upper limit is similar to that in high flux materials test reactors. The displacement rate in commercial LWR pressure vessels is in the range of 10^{-11} to 10^{-10} dpa/s.

The primary material parameters that were used in computing the results presented here are listed in Table 1. These values generally represent best estimates obtained from the literature or from other simulations [21]. These values were used to compute a set of "base case" predictions and the sensitivity of the results to variations in these parameters was explored. The next section will examine the role of PDC with no copper precipitation to demonstrate the conditions for which PDC should be important. With these results as a baseline, the role of CRP will be shown by comparison.

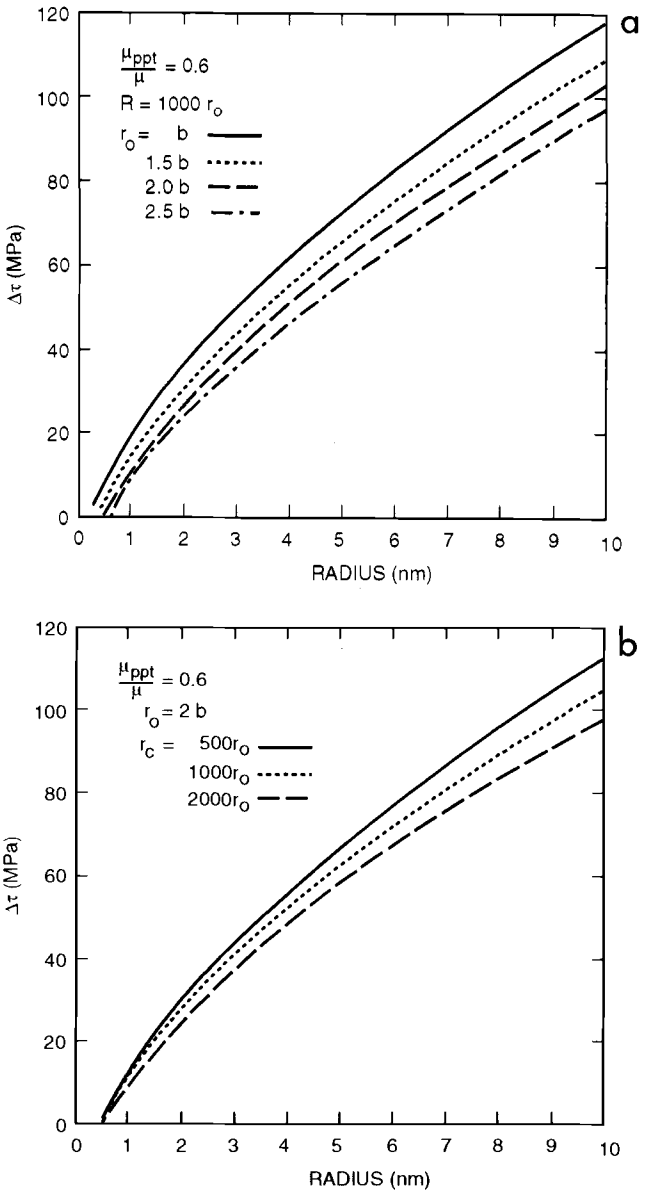


Figure 2. Dependence of the Russell-Brown hardening model on: (a) the dislocation core radius, r_o and (b) the dislocation capture radius, r_c.

Role of Point Defect Clusters

The predicted changes in the yield strength at 60 and 288°C are shown as a function of displacement dose in Figure 3 for calculations using the base parameter set from Table 1. Results are displayed at the low and high displacement rate limits. The calculated yield strength change includes increments from both the interstitial and vacancy clusters; their relative contributions will be examined below. Representative data are included for comparison. The A212B data shown at 60°C in Figure 3(a) includes those from the HFIR surveillance program [41] and this same material irradiated in the Oak Ridge Research reactor (ORR) at a higher displacement rate [42]. The data shown in Figure 3(b) for 288°C are from an experiment conducted in a research reactor at the University of Virginia [43]. Since the displacement rate in this experiment lies between the predicted curves at 10^{-13} and 10^{-7} dpa/s, a partial curve for the model predictions for a 10^{-9} dpa/s displacement rate are also indicated in Figure 3(b).

There are several notable features in Figure 3. First, the dependence on displacement rate is much greater at the higher temperature. This is a result of thermal instability of the PDC. For low displacement rates at 288°C the PDC populations reach steady state very quickly and little fluence dependence is observed. At low temperatures and high displacement rates the PDC densities continue to build up at a rate that is roughly proportional to the square root of the fluence. The effect of the point defect transient can be seen in Figure 3(a). At 60°C, the low and high displacement rate curves begin to diverge at about 10^{-5} dpa since the point defect concentrations are approaching steady state at the lower displacement rate. The time required to reach steady state is about 10^{8} s for these conditions. For a displacement rate of 10^{-13} dpa/s, a dose of 10^{-5} dpa is accumulated in this time; at 10^{-7} dpa/s, 10^{-5} dpa is reached in only 100 s. For conditions where PDC are a major contributor to hardening, the predictions indicate that accelerated irradiations should give a conservative estimate of the mechanical property changes at lower displacement rates.

Although the absolute values of the predicted yield strength changes are certainly subject to the assumptions of the model and the specific choices of model parameters, the comparison between the model's predictions and the yield strength data in Figure 3 indicates that PDC could be responsible for much of the hardening observed in irradiated RPV steels. At 288°C the model predictions lie within the data band for a displacement rate of 10^{-9} dpa/s, while at 60°C the model predictions exceed the observations. Some of the model parameters that influence the predictions will be discussed shortly.

The displacement rate dependence of the yield strength change due to PDC at a dose of 0.01 dpa is shown in Figure 4 for three irradiation temperatures. Although much greater hardening is predicted at lower temperatures, the dependence on displacement rate is greater at higher temperatures. Recent experimental results appear to confirm that hardening at 60°C is relatively insensitive to displacement rate [44]. For each of the three temperatures, the curves exhibit regions which are more sensitive to changes in the

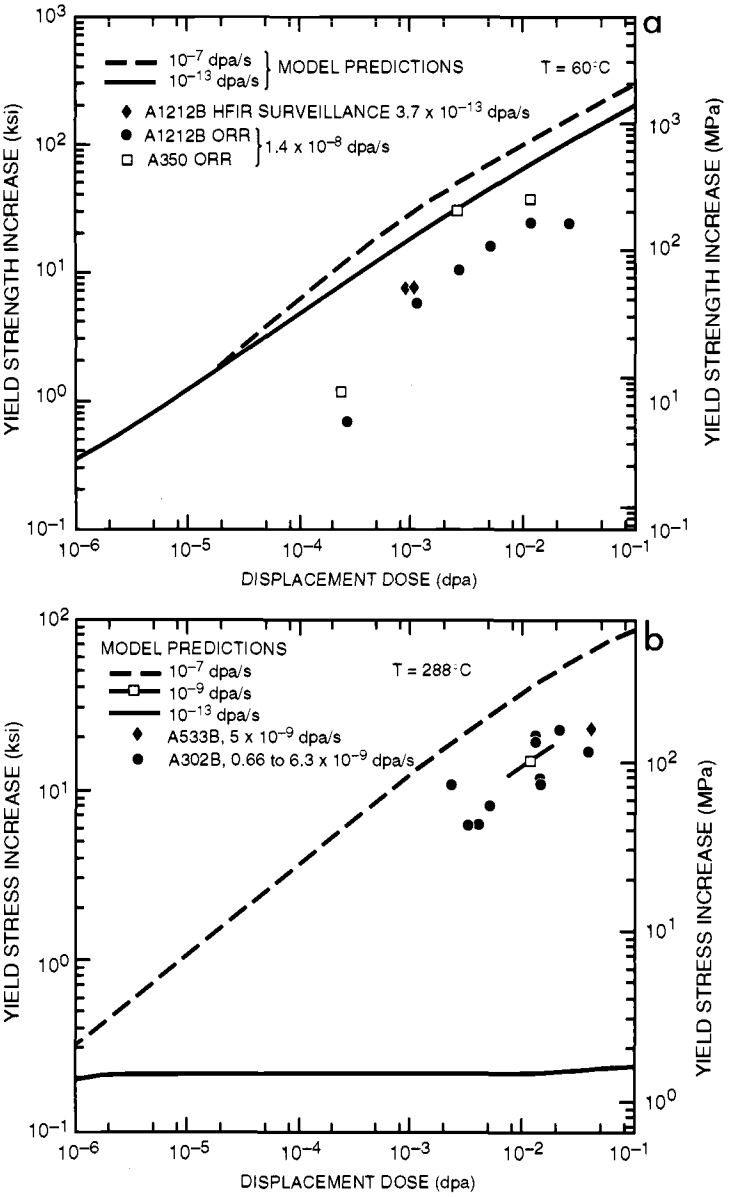


Figure 3. Fluence dependence of the predicted yield strength change due to PDC at: (a) 60 and (b) 288 °C using the base parameter set in Table 1. Typical data is shown for purposes of comparison. The shift in the HFIR surveillance data reflects previously uncounted displacements due to gamma rays.

displacement rate than others. At 288°C the displacement rate dependence is largely due to the competition between formation and annealing of the PDC. The point defect transient is important in the behavior at 60°C. The time to reach 0.01 dpa is comparable to or longer than the transient at the lower displacement rates; however, the point defect concentrations are far from steady state at the higher displacement rates. The behavior at 175°C is influenced by both the point defect transient and PDC annealing.

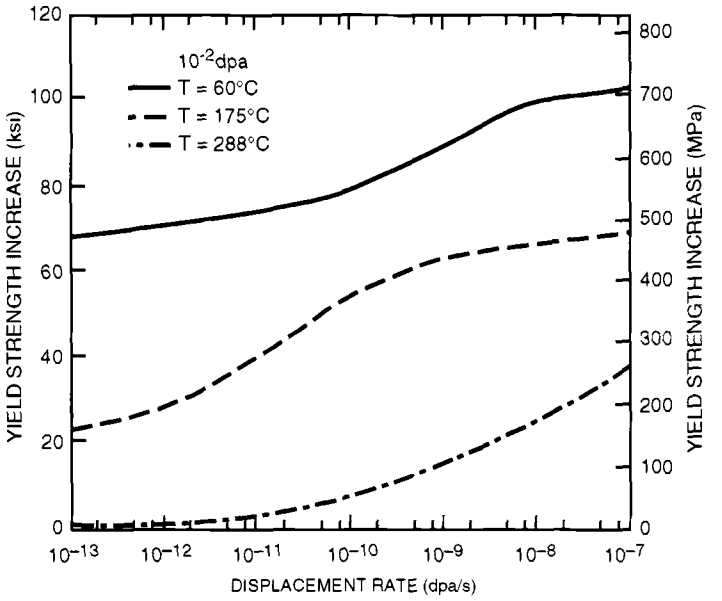


Figure 4. Total yield strength change due to PDC predicted at 0.01 dpa as a function of displacement rate for irradiation temperatures of 60, 175 and 288°C.

The existence of these different regimes requires that caution be used in data extrapolation and interpolation. While an experiment conducted at a high displacement rate will apparently give a conservative estimate of the yield strength change expected at the same dose for a lower displacement rate, extrapolations using data at several high displacement rates could be either conservative or nonconservative. For example, an extrapolation down to 10^{-11} dpa/s using the predicted curves in the range of 10^{-9} to 10^{-7} dpa/s would be conservative at 175 and nonconservative at 288°C.

Parameters Influencing Vacancy Clustering

For some time, vacancy clusters formed by the collapse of displacement cascades have been assumed to play an important role in RPV steel embrittlement [10,17]. Some MD simulations of displacement cascades in fcc metals have demonstrated this

phenomenon [45]. However, there is only limited experimental support for their existence in RPV steels. As mentioned above, the difficulty in imaging small defects in ferritic alloys may have contributed to this lack of experimental observation. In the base set of parameters, the relatively large vacancy cluster radius of 1 nm was used. This is larger than any vacancy cluster expected to form by cascade collapse, but it represents a probable upper limit to how large these clusters could be and still remain undetected by TEM. The use of this large initial size almost certainly overestimates the hardening increment attributed to vacancy-type PDCs, but could be seen as compensating for the lack of detail in the vacancy clustering model. This size was reduced to a more realistic 0.5 nm for the comparison between PDC and CRP discussed below.

In order to examine the influence of the vacancy cluster parameters, Figure 5 compares the results of three sets of calculations. The total yield strength increase as a function of displacement rate is shown in this figure for: (1) the base parameter set, (2) the result of reducing the vacancy cluster radius to the size of a 10-vacancy microvoid (0.304 nm), and (3) the result of using the smaller radius and also reducing the vacancy cluster fraction from 0.6 to 0.15. The total hardening is reduced significantly for either of these changes at those conditions where vacancy clusters provide an appreciable fraction of the total. The change due to reducing the cluster radius is more modest than that due to reducing the clustering fraction, particularly at 60°C. However, the overall change is greater than that due to the lost vacancy clusters alone since the resulting higher concentration of free vacancies reduces the interstitial cluster population.

Reducing the impact of vacancy clusters appears to be reasonable. The use of a lower vacancy clustering fraction or smaller vacancy cluster radius would reduce the predicted curves shown in Figure 3. This would provide better agreement with the data at 60°C where PDC are dominant and would make allowance for precipitation-induced hardening to contribute to the total at 288°C. Recent MD simulations of cascades in bcc iron with primary knock-on atom (PKA) energies up to 10 keV showed essentially no in-cascade vacancy cluster formation [26,27]. Higher energy PKAs may yet provide evidence of such clustering, but a 10 kev PKA is about the average energy for a 0.3 MeV neutron. Thus, a significant fraction of the PKA spectrum for an LWR pressure vessel has been sampled. However, the MD results obtained for pure iron may not be representative of the clustering behavior in alloys. One effect of alloying elements and residual impurities such as copper and phosphorus may be to aid in the formation of vacancy clusters [10,16].

Parameters Influencing Interstitial Clustering

The influence of the interstitial clustering fraction is shown in Figure 6. The interstitial clustering fraction was decreased from the base value of 0.3 to 0.15 for one set of curves, and increased to 0.5 for the other. The corresponding di-, tri-, and tetra-interstitial fractions were 0.1, 0.03, and 0.02 at 0.15; and 0.25, 0.15, and 0.1 at 0.5. The base set are listed in Table 1. The expected trends are observed in the results. The impact is greater at 60°C where interstitial-type PDC are dominant. In an analogous fashion to

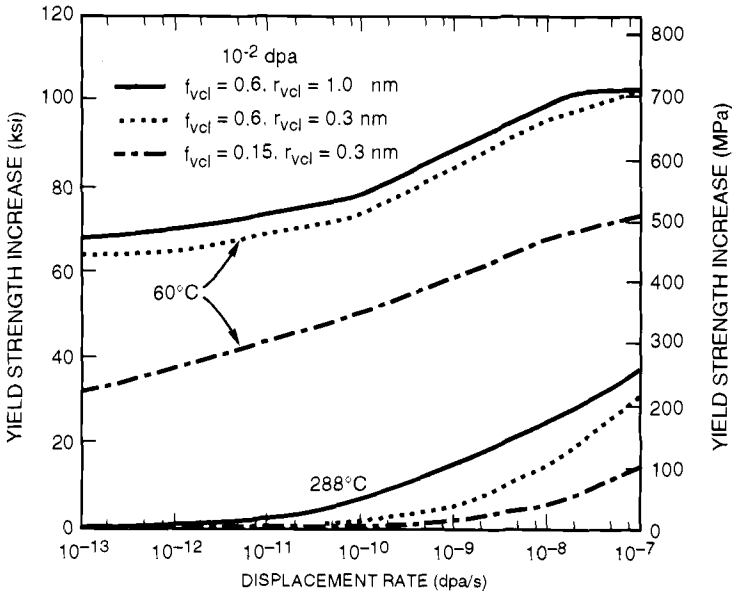


Figure 5. Influence of the vacancy clustering fraction and vacancy clusters radius on the yield strength change due to PDC at 0.01 dpa.

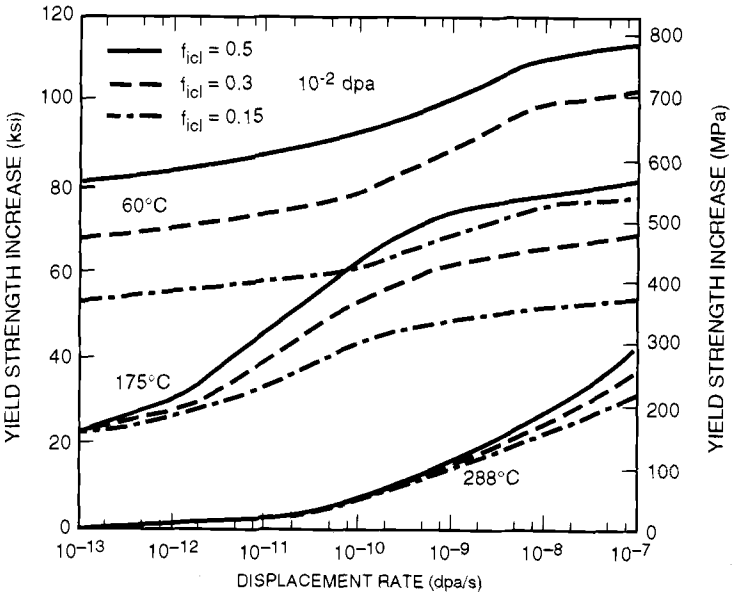


Figure 6. Influence of the interstitial clustering fraction on the yield strength change due to PDC at 0.01 dpa.

the changes in the vacancy clustering fraction discussed above, a reduction in the interstitial clustering fraction reduces the hardening from both types of PDC.

In the case of the interstitial clusters, the MD results are in general agreement with the cluster fractions used here. For example, when the results of seven 10 kev cascades conducted at 100K are averaged, the fraction of interstitials in clusters is 0.46. Of these, 0.2 are in di-interstitials, 0.11 are in tri-interstitials, and 0.03 are in tetra-interstitials [27]. The cluster fraction is relatively insensitive to temperature between 100 and 600K [26], and the fraction will increase with PKA energy. The influence of other parameters which influence interstitial and vacancy clustering is discussed in Refs. 21 and 22. Overall, the implication of the MD results and the present calculations is that more attention should be paid to the potential role of interstitial cluster formation in RPV steels.

Influence of Clustering and Recombination on Radiation-Enhanced Diffusion

It has been pointed out that separate changes in either the interstitial or vacancy clustering parameters influences the evolution of both types of PDC. This comes about because a reduction in the fraction of clustered point defects increases the population of the corresponding mono-defects. These point defects can then impact the evolution of the PDC in two ways. First, by diffusing to and annihilating with clusters of the opposite type defect, they can reduce their growth. Secondly, they can reduce the concentration of the opposite mono-defect by recombination reactions in the matrix. This matrix recombination reduces the nucleation and growth of both types of clusters by reducing the defect supersaturation and reducing the point defect flux to stable defects. The overall effect is determined by the competition between matrix recombination, point defect absorption at fixed sinks such as dislocations, and point defect absorption at the two types of PDC.

In a similar way, the presence of PDC should help to limit precipitate formation. A high density of PDC will reduce the driving force for radiation-induced precipitate formation by reducing the point defect fluxes that drive solute segregation. One measure of the ability of a material to support segregation is the radiation-enhanced diffusion coefficient (REDC). As mentioned above, the simplest formulation of this coefficient is essentially proportional to the ratio of the vacancy concentration under irradiation to the thermal equilibrium value. In order to demonstrate the impact of PDC on the driving force for radiation-induced precipitation, the calculated ratio of the REDC with no clustering to the REDC when clustering is included is shown in Figure 7. A related set of curves shows the further impact of a reduction in matrix recombination. In this case, the recombination radius was reduced from two to one times the lattice parameter.

The different displacement rate dependence for different temperatures shown in Figure 7 can be explained along lines similar to that used in discussing Figure 4. This variation is due to a combination of the point defect transient, the competition between matrix recombination and point defect absorption at sinks, and the relative importance of PDC versus the fixed sinks (dislocations and grain boundaries). The trend is simple at

288°C, where the point defect transient is very short, matrix recombination is insignificant, and PDC become increasingly important at higher displacement rates but their sink strength doesn't exceed that of the fixed sinks. At 60°C, the PDC sink strength exceeds that of the fixed sinks at all displacement rates and matrix recombination becomes important above 10^{-12} dpa/s. In addition, the time to reach 0.01 dpa is greater than the point defect transient at all but the lowest displacement rates.

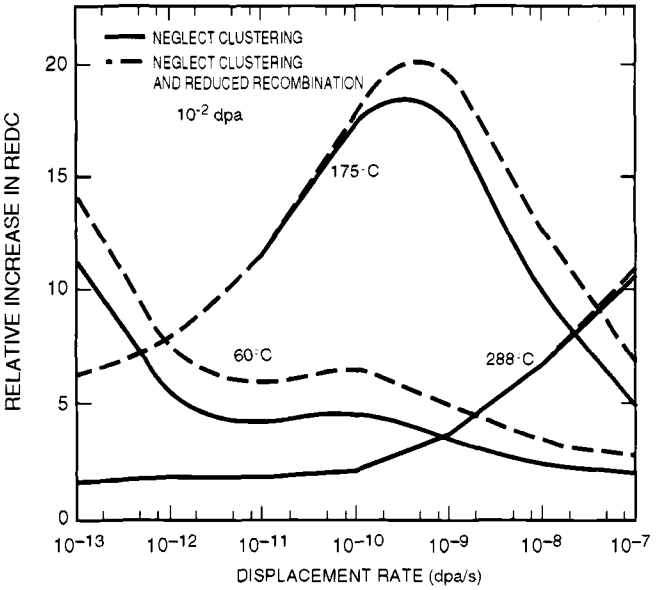


Figure 7. Influence of PDC and matrix recombination on the radiation-enhanced diffusion coefficient (REDC) at 0.01 dpa. Results are normalized using the REDC for the base parameter set.

The behavior is more involved at 175°C. Matrix recombination is only important at the highest displacement rates. The fixed sinks are more important than the PDC at the lowest displacement rates, comparable to the PDC at intermediate rates, and less important than the PDC at the highest rates. There is also a small residual effect of the point defect transient in the total partitioning of point defects at the highest displacement rates.

Because of this complex balance between the various microstructural components, it is difficult to make reliable, predictions about the response of a material to changes in temperature or displacement rate without detailed calculations of the type discussed here. However, the model predicts that neglecting the influence of PDC can lead to an overestimate of the REDC by more than a factor of 20 and by a minimum of about two with the current model parameters. The time required for significant copper precipitation to occur in most models would then be underestimated by a similar factor. In a similar

way, it is important to include realistic estimates of the other point defect sinks in Eq. (1) when computing the point defect concentrations.

Role of Copper-Rich Precipitates

An extensive set of calculations was carried out to determine the dependence of CRP hardening on irradiation temperature, displacement rate, material sink strength, and the possible chemical effects of copper on the other microstructural components. These results are broadly consistent with previous work [1,11], but they have also identified several areas that require additional attention.

Typical results for an irradiation temperature of 288°C are shown in Figure 8 where the dose dependence of hardening due to PDC and CRP is plotted for displacement rates of 10^{-11} and 10^{-6} dpa/s. The shear stress increment for each component is shown in (a) and the total (rss) change in the yield strength is shown in (b). Several observations can be made from the results shown in Figure 8. Each of the defect types (interstitial clusters, vacancy clusters, and CRP) has a regime in which it provides most of the hardening. While both types of PDC build up monotonically, a clear threshold is observed for the CRP at 10^{-11} dpa/s. This threshold dose is increased for higher displacement rates. In addition, the displacement rate dependence of CRP hardening is opposite that for PDC hardening. Because of the behavior of the individual components shown in Figure 8(a), Figure 8(b) indicates simple extrapolations in either dose or displacement rate could be misleading. For example, the results of accelerated irradiations would be conservative at low doses, but not at high doses. Such behavior has been experimentally observed [2,46]. The dose at which the two curves in Figure 8(b) crossover is reduced if the difference between the two displacement rates is reduced.

The explicit copper dependence in the model is contained in the precipitate density. As listed in Table 1, N_{ppt} is assumed to scale with the square root of the copper concentration available in the matrix at the beginning of the irradiation. This dependence is consistent with simple homogeneous nucleation models [4]. It should be noted that the available copper may be much less than the value obtained from bulk chemical analysis [3,5,11]. The copper concentration dependence of CRP hardening will be shown below. First, a potential indirect effect of copper as a solute on the PDC will be examined.

There is evidence that the presence of copper increases the nucleation of PDC [16,31]. This could be a result of copper stabilizing vacancy clusters by reducing the surface energy. A more stable vacancy cluster could enhance the formation of interstitial clusters since this would promote differential partitioning of the two types of point defects. Copper could also stabilize interstitial clusters directly by reducing the stacking fault energy. A fairly strong dependence of the surface tension on solute content has been observed in binary iron alloys [47,48]. The data includes copper, phosphorus, nickel, and silicon. Similar data on stacking fault energies indicates that it is also reduced [47]. Guided by this data, the surface energy was reduced by an amount equal to [250*(atom-% Cu)] and the tetra-interstitial binding energy was increased by 0.1 eV to approximately

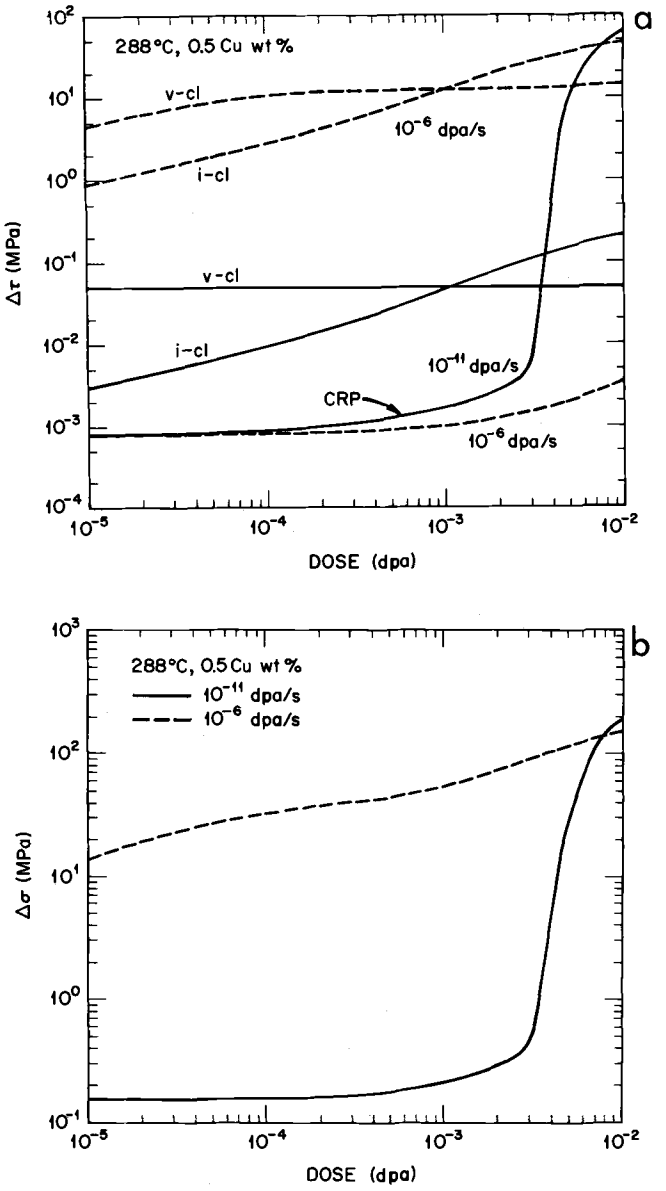


Figure 8. Dose dependence of hardening due to PDC and CRP at 288°C for displacement rates of 10^{-11} and 10^{-6} dpa/s. The shear stress increment for each component is shown in (a) and the total (rss) change in the yield strength is shown in (b).

account for the effects of copper. The influence of these changes in the basic set of mode· parameters is shown in Figure 9 for an irradiation temperature of 288°C. To limit the number of curves, results are shown for displacement rates of 10^{-11} and 10^{-6} dpa/s.

Figure 9 compares the total predicted yield strength change with and without the parameter changes just mentioned. For the conditions where PDC are dominant (higher displacement rate and lower doses), the yield strength increase can change by a factor of about two. When CRP dominate the hardening, the effect is relatively small. CRP growth is somewhat reduced by the higher PDC densities since they reduce radiation-enhanced diffusion. The increase in the shear strength is about a factor of two for both vacancy and interstitial type defects. The results shown in Figure 9 provide one explanation for the nickel contribution to RPV embrittlement. Nickel also reduces the surface energy in Fe-Ni binary alloys [47] and it should play a similar role in RPV steels. In such a case the effect of nickel would appear to be stronger when PDC are dominant and less important when CRP are dominant. The effect of nickel was examined parametrically with the present model by increasing the change in surface energy and tetra-interstitial binding energy for a fixed copper content. This led to the expected increases in the PDC contribution relative to the CRP contribution.

The possible impact of the CRP or other precipitate sink strength is shown in Figure 10. As mentioned above, CRP growth is assumed to proceed by diffusion-limited kinetics with a precipitate sink strength of $4\pi r_{ppt} N_{ppt}$, c.f. Eq. (3). If these precipitates were efficient sinks for point defects, this same sink strength should be included in the total system sink strength used in Eq. 1 to compute the vacancy and interstitial concentrations. If this was done, it appears that the CRP could be the dominant sink strength for many conditions. For a precipitate radius of 1 nm and a precipitate density of 1×10^{23} m^{-3}, the sink strength is 1.3×10^{15} m^{-2}. However, the use of the diffusion-limited sink strength leads to an overestimate of the effect of the CRP. The results of AP/FIM studies suggest that some of the small CRP responsible for hardening do not have a well developed interface [5]. Such solute "atmospheres" would not absorb point defects in the conventional sense. Similarly, this sink strength will continue to be an overestimate of the CRP sink strength as long as the CRP remain fully coherent with the bcc iron matrix [12]. In addition, there is some evidence that even incoherent precipitate interfaces may not be good sinks for vacancies [49].

The coherent CRP should exhibit a reduced "effective" sink strength due to the reduced ability of the interface to trap point defects. Although it is difficult to provide a quantitative estimate of this sink strength, Figure 10 shows the impact of including one-

half of the CRP sink strength in Eq. 1. Even this reduced sink strength is sufficient to limit radiation-enhanced diffusion to such an extent that hardening due to copper precipitates is prevented up to a dose of 0.01 dpa ($\sim 7 \times 10^{22}$ n/m^2 fast fluence) at 288°C and a displacement rate of 10^{-11} dpa/s. The interstitial cluster contribution to hardening is reduced by about a factor of two. Vacancy clusters were not significantly affected since their formation was assumed to occur directly within the displacement cascades. In fact

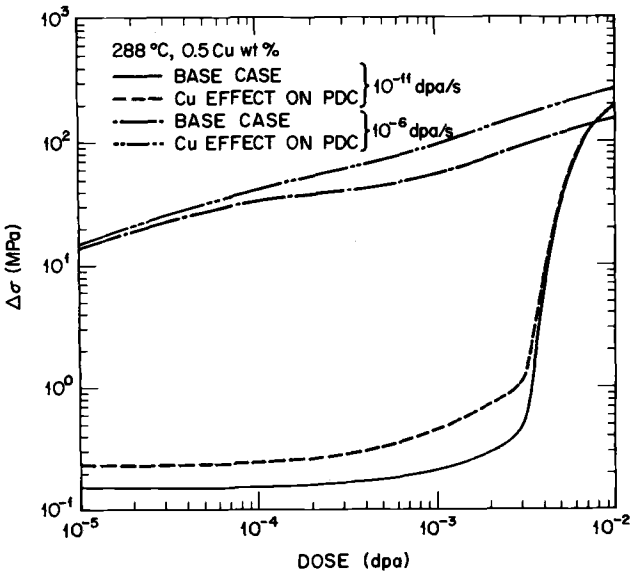


Figure 9. Dose dependence of composite PDC/CRP model predictions at 288 °C on the assumed surface energy and tetra-interstitial binding energy for displacement rates of 10^{-11} and 10^{-6} dpa/s. The total (rss) change in the yield strength is shown.

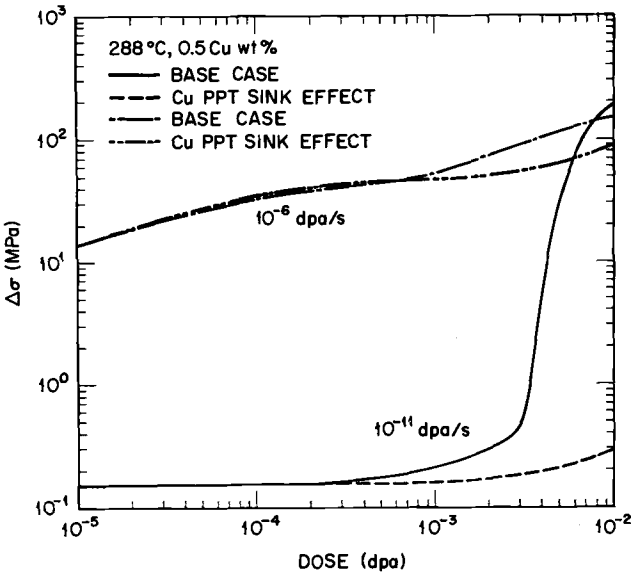


Figure 10. Influence of CRP sink strength on the predicted dose dependence of hardening at 288 °C for displacement rates of 10^{-11} and 10^{-6} dpa/s. The total (rss) change in the yield strength is shown.

the vacancy cluster contribution increased slightly at the higher displacement rate since the interstitial flux was reduced by the precipitate sink strength.

The issue of the CRP sink strength requires further discussion. The influence of this precipitate sink strength can be explained along the same lines as that of the PDC influence on the REDC discussed above. If the irradiation conditions are right to form a precipitate density high enough to give the expected hardening, the sink strength of the evolving precipitates could be high enough to delay precipitate growth. The 50% reduction in the CRP sink strength used to obtain the results shown in Figure 10 may still represent an overestimate of the CRP influence. However, this evolving CRP sink strength can be thought of as a surrogate for other precipitate phases and microstructural evolution that takes place during irradiation.

The calculated PDC hardening was compared with relevant yield strength data in Figure 3 above. The predictions of the composite PDC/CRP model at 288 °C have been compared to Charpy transition temperature (CTT) shifts obtained in commercial LWR surveillance programs. It is necessary to convert the calculated yield strength changes to CTT shifts in order to make a direct comparison. Odette and co-workers [1,2] report yield strength to CTT correlation factors ranging from 0.5 (plate) to 0.65 (weld) °C/MPa. The uncertainty in this correlation factor is probably smaller than that due to other model parameters. For the present purpose of comparing model predictions with CTT data contained in the Power Reactor Embrittlement Data Base (PR-EDB) [50], these two values have been used for their respective materials. The predictions of the model are compared with the LWR surveillance data [50] in Figure 11 and 12.

The computed embrittlement curves shown in Figure 11 were obtained with the base parameter set, a dislocation density of $2x10^{14}$ m^{-2}, a displacement rate of 10^{-10} dpa/s, and matrix copper contents of 0.01, 0.05, 0.1, 0.2, and 0.5 atom percent. No attempt was made to optimize the material parameters in order to improve the agreement between the computed values and the data. The computed dose was converted to neutron fluence (E>1.0 MeV) using a displacement cross-section of 1500 barns. This displacement rate and cross-section are typical of the data in the PR-EDB. The data shown in Figure 11 consist of essentially all the A533B and A302B 41-J Charpy shifts contained in the PR-EDB. Plate material is shown in Figure 11a and weld material in Figure 11b. The copper content for the data is shown in the figure legend in weight percent. The calculations were based on the copper concentrations given above in atomic percent, but they have been converted to the weight percent values shown in the figures for the purpose of comparison with the data.

The threshold dose for CRP embrittlement mentioned above can be seen in Figure 11 and little embrittlement is predicted for copper values less than about 0.088 weight percent (0.1 atom percent) for fast neutron fluences below $1x10^{23}$ n/m^2. The apparent saturation in the embrittlement at high doses occurs when all of the available copper has been extracted from the matrix. The predicted total PDC contribution to embrittlement is small for these conditions, but the contribution of interstitial clusters

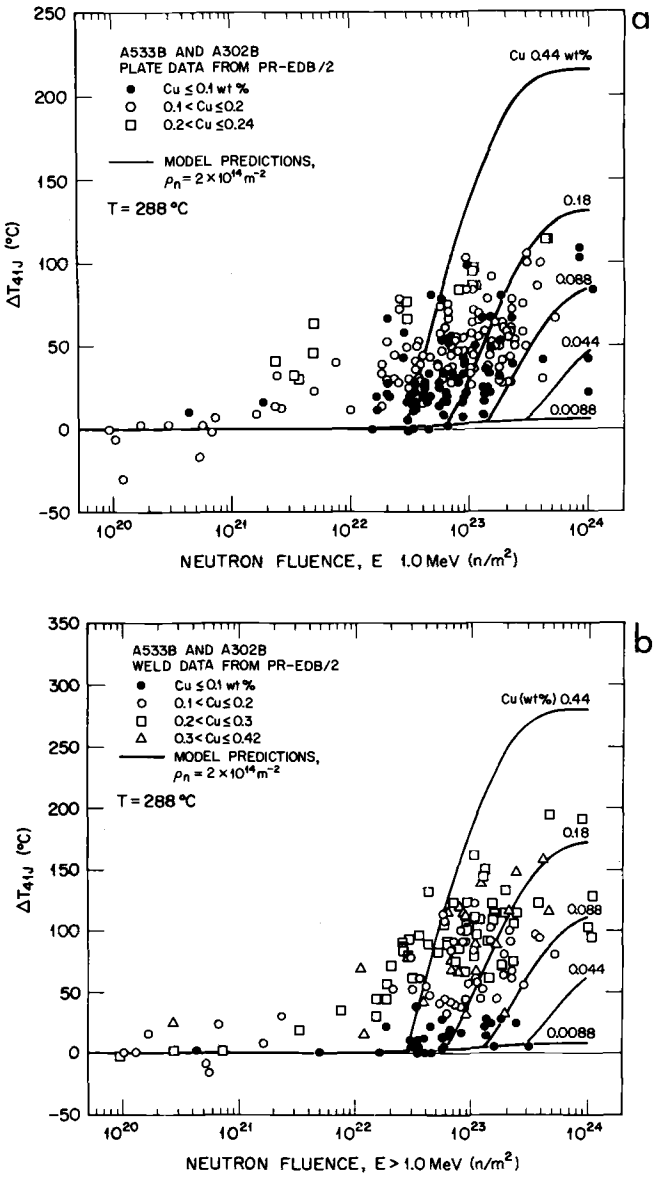


Figure 11. Comparison between model predictions at 288°C and Charpy transition temperature shift data for: (a) plate and (b) weld material from the PR-EDB [49]. Model copper content as indicated and other material parameters from Table 1.

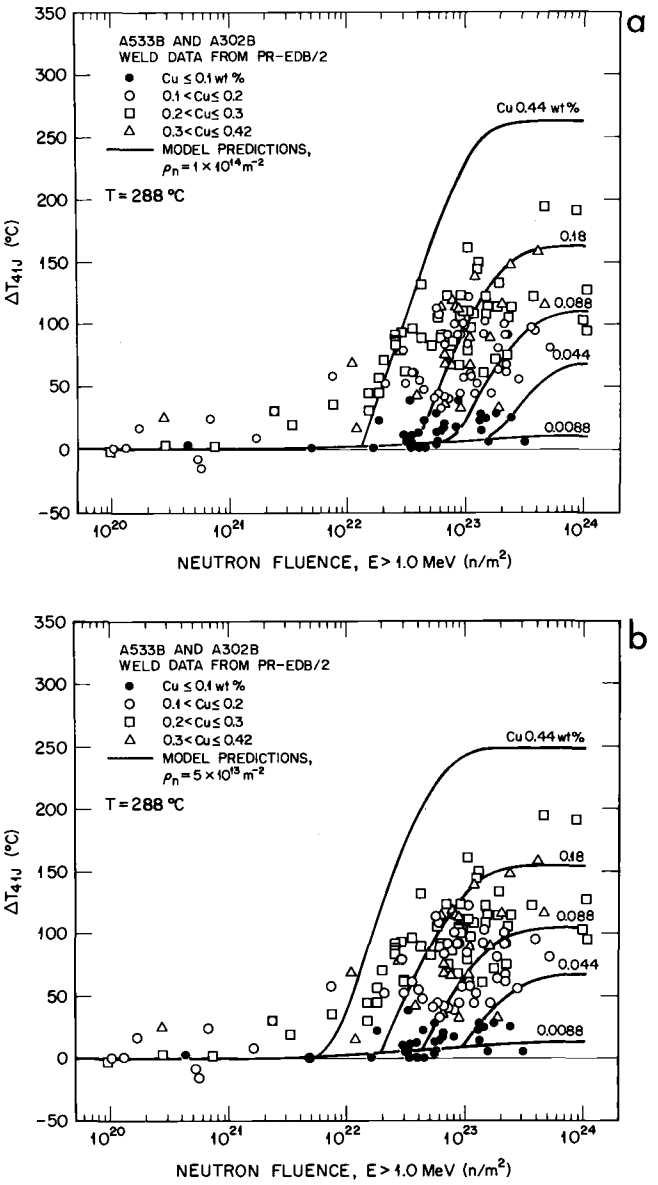


Figure 12. Influence of dislocation density on predictions of composite PDC/CRP model at 288°C and comparison with Charpy transition temperature shift data for weld material from the PR-EDB [49].

continues to slowly increase at the higher doses. The model predictions obtained with the base parameter set show a somewhat higher threshold dose than the data. At high doses, the predictions are comparable, but somewhat higher than the observed CTT shifts for both the plate and weld material for similar copper levels. Overall, the dependence of the model's predictions on the copper content appears to be greater that the dependence exhibited by the data. The copper dependence of the data will be addressed further below.

The difference between the CTT shifts measured for weld and plate with the same copper content highlights the importance of other variables that influence embrittlement. For example, differences in other alloying elements such as nickel and manganese are neglected in these figures. In addition, heat treatment differences that lead to a variation in microstructural parameters such as the grain size and dislocation density are likely to be important. The influence of the dislocation density on the predicted embrittlement can be seen by comparing Figure 11b with Figures 12a and 12b. Reported measurements of the dislocation density in RPV steels range from about $3x10^{13}$ to $3x10^{14}$ m^{-2} [43,46,51], with little effect of irradiation observed [52]. A reduction of the dislocation density in the model from $2x10^{14}$ m^{-2} (Figure 11b) to $1x10^{14}$ m^{-2} (Figure 12a) reduces the threshold dose for CRP embrittlement by about a factor of two. The lower dislocation density leads to a higher vacancy concentration; this increases the radiation-enhanced diffusion of copper. Reducing the dislocation density to $5x10^{13}$ m^{-2} results in another factor of two. In this latter case, the threshold fluence for significant copper precipitation at the low copper value of 0.044 weight percent is reduced to about $1x10^{23}$ n/m^2. The saturation level of embrittlement is somewhat reduced for the lower dislocation densities due to the dependence of Russell-Brown model on the outer dislocation cut-off radius mentioned above.

The calculated dependence on dislocation density could contribute to the overall data scatter shown in Figure 11 and could also be partially responsible for the higher sensitivity of welds to irradiation. Although there are only a limited number of dislocation density measurements reported in the literature, there is one report of welds having lower dislocation densities than plate materials [43]. A correlation between weld nickel content and dislocation density [46] has also been reported. These observations indicate that it may be significant that improved agreement with the weld data from the PR-EDB is obtained when the lower dislocation densities are used in the calculations.

The influence of the displacement rate on the predicted yield strength change at 288°C is shown in Figure 13 for doses of 0.02 and 0.1 dpa. Values are plotted for three different copper levels. For low copper or high displacement rates, the yield strength change tends to be dominated by the PDC and it increases at higher displacement rates. The CRP dominate for mid to high copper steels and the yield strength change decreases at higher displacement rates. This is particularly true for lower doses. The behavior shown in Figure 13 re-emphasizes a point discussed above in reference to Figure 8. Safe extrapolation of data from high to low displacement rates requires that a number of other variables be considered, including irradiation temperature, displacement dose, and copper content. Fortunately, these results also indicate that the dependence on displacement rate

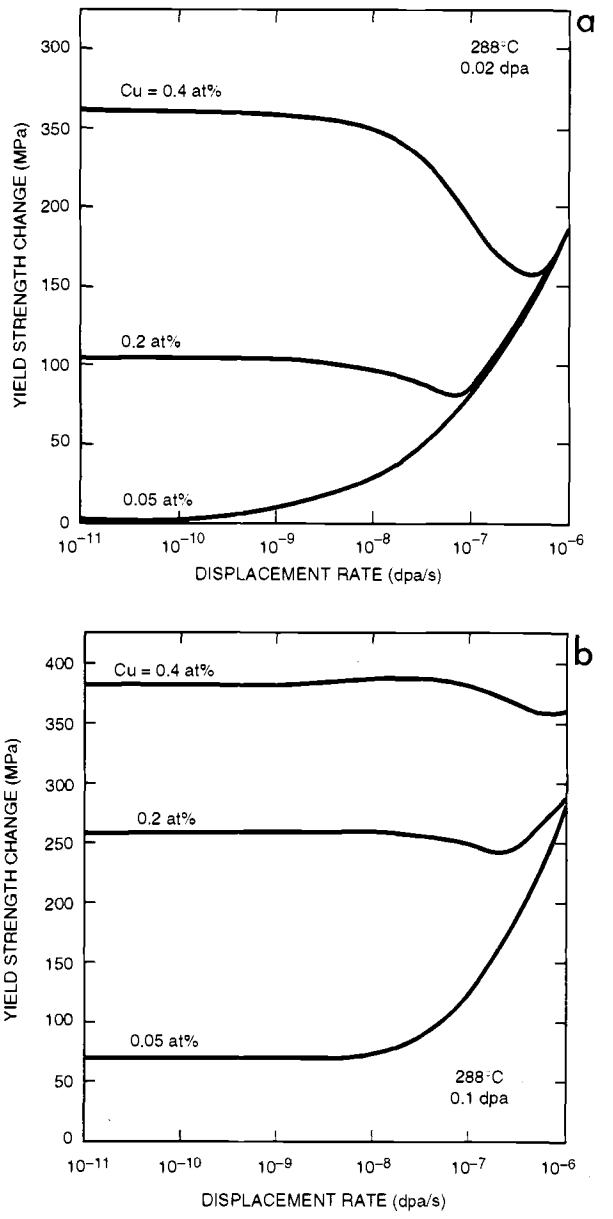


Figure 13. Displacement rate dependence of predicted yield strength change at 288°C for doses of: (a) 0.02 dpa and (b) 0.1 dpa.

is rather weak below about $5x10^{-9}$ dpa/s, corresponding to a fast flux (E>1.0 MeV) of about $5x10^{16}$ n/m^2/s. This effect arises from the dependence of the CRP model on REDC. Higher displacement rates would be expected to lead to greater REDC, but they also lead to higher sink densities which tend to reduce REDC by absorbing point defects. If these predictions can be confirmed by experiments, it should reduce concerns about lead factors in commercial reactor surveillance programs and provide for broader use of some test reactor data.

Additional parametric studies with the composite PDC/CRP model are discussed in Ref. 32. They include the effect of surface energy, vacancy migration energy, and irradiation temperature. Notably, the results of simulations at 60°C appeared to confirm the previous conclusion [21] that PDC rather than CRP were responsible for the embrittlement of the HFIR pressure vessel. In contrast with earlier work suggesting that CRP could be responsible for the embrittlement [3], the model discussed here indicates that there should be little copper precipitation for the HFIR pressure vessel irradiation conditions. In fact, no radiation-induced copper precipitates were observed in the initial examination of specimens fabricated from the HFIR surveillance specimens [42].

The fact that the model seems to exhibit a greater dependence on copper content than does the LWR surveillance data is probably due to the neglect of the effects of post-fabrication heat treatments on the matrix copper content. As mentioned above, copper in excess of the solubility limit can begin to precipitate out during such heat treatments. AP/FIM measurements of alloy composition in A533B welds indicate that the matrix copper content is unlikely to exceed about 0.25 atom percent after a typical post-weld stress relief at 600 to 650°C [5]. This is consistent with the copper dependence of the data in the PR-EDB 50]. Figures 14 and 15 show the CTT shifts for plate and weld material from the PR-EDB as a function of the bulk copper content. Both low and high fluence data are shown. Although the data scatter is significant, there is an apparent saturation of the effect of copper near about 0.25 weight percent. This indicates that the matrix copper content, rather than a value obtained from bulk chemistry measurements, controls the embrittlement.

SUMMARY

A model based on the kinetic rate theory has been developed to determine the relative importance of point defect clusters and copper-rich precipitates in the hardening and embrittlement that is observed in irradiated RPV steels. Guidance in the choice of clustering parameters was provided by current work investigating cascade evolution in iron using molecular dynamics simulation. The interaction between the components of the PDC model and the CRP model has provided new insight into radiation-induced embrittlement mechanisms and identified areas that require further attention. The predictions of the composite PDC/CRP model exhibited very little dependence on displacement rate below about $5x10^{-9}$ dpa/s. This suggests that currently accepted lead

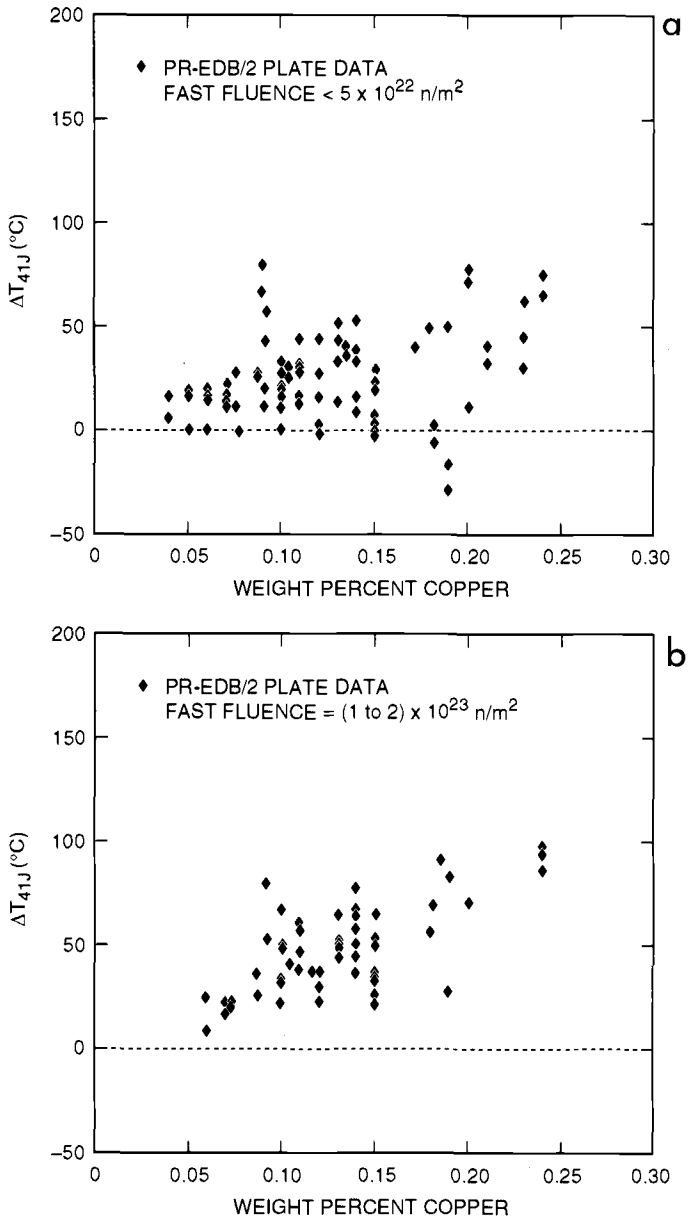


Figure 14. Dependence of Charpy transition temperature shift on copper content at: (1) low and (b) high fluence for plate material from the PR-EDB [49].

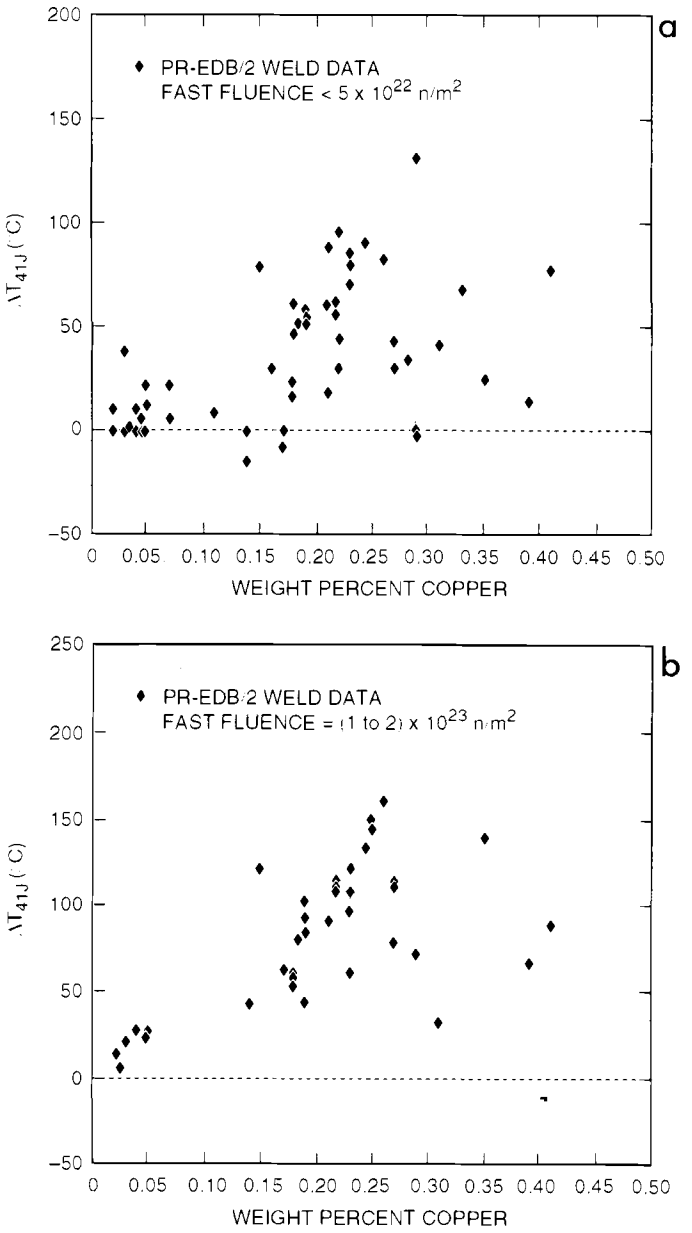


Figure 15. Dependence of Charpy transition temperature shift on copper content at: (a) low and (b) high fluence for weld material from the PR-EDB [49].

factors in reactor surveillance programs are quite conservative and that some test reactor data could find broader use.

The results of the calculations indicate that PDC could provide a major source of matrix hardening, particularly at low irradiation temperatures, high displacement rates, and low doses. CRP appear to be more important at high temperatures, low displacement rates, and high doses. Because these two classes of defects exhibit such different dependencies on these major variables, any extrapolation of data that involves a significant variation in one of these variables should be carried out with caution. Although the model parameters were not adjusted to fit the data, reasonable agreement was obtained between the model's predictions and yield strength and Charpy transition temperature shift data over a range of temperatures and displacement rates. The absolute magnitude of the model's predictions are sensitive to a number of uncertain parameters [21,22,32]; however, the predicted trends in the dose, displacement rate, and temperature dependence of hardening should be valid.

The magnitude of the predicted changes in yield strength due to the formation of PDC is sufficiently large to warrant more investigation of their influence. Their behavior could be particularly important in understanding and predicting the behavior of RPV steels under annealing and under subsequent re-irradiation. The relative contribution of PDC and radiation-induced precipitates, and their thermal stability needs to be determined for all the radiation/annealing conditions of interest to LWR pressure vessels. Experimental confirmation of the presence of PDC in the numbers and sizes predicted by the current model does not presently exist. Experiments are currently underway to address this need. These same experiments are intended to investigate the uncertainty in determining the dislocation obstacle strength for small PDC in iron-based alloys and hardening superposition laws in multicomponent microstructures.

The dependence of the model on the CRP sink strength and the dislocation density is significant. A CRP density high enough to give rise to the observed hardening could significantly limit CRP growth by suppressing radiation-enhanced diffusion. The simple estimate of the effect of the CRP sink strength shown in Figure 10 can also be used to infer that the impact of other radiation-induced and radiation-enhanced phases could be significant. This observation, along with the effect of dislocation density shown in Figs. 11 and 12, highlights the need for more detailed microstructural characterization of RPV steels. High-resolution TEM and AP/FIM work are needed to better quantify the microstructure in both irradiated and unirradiated materials because of the sensitivity of the calculations to the sink strengths.

ACKNOWLEDGMENTS

The author would like to acknowledge helpful reviews by Drs. K. Farrell, L. K. Mansur and R. K. Nanstad. This research was sponsored by the Office of Nuclear Regulatory Research, U.S. Nuclear Regulatory Commission under inter-agency agreement DOE

1886-8109-8L with the U.S. Department of Energy and by the Division of Materials Sciences, U.S. Department of Energy under contract DE-AC05-84OR21400 with Martin Marietta Energy Systems, Inc.

REFERENCES

1. G. R. Odette, Scripta Metallurgica 17 (1983) 1183-1188.
2. G. E. Lucas, G. R. Odette, P. M. Lombrozo, and J. W. Sheckherd, "Effects of Composition, Microstructure, and Temperature on Irradiated Hardening of Pressure Vessel Steels," Effects of Radiation on Materials, ASTM STP 870, F. A. Garner and J. S. Perrin, Eds., American Society of Testing and Materials, Philadelphia, 1985, pp. 900-930.
3. S. G. Druce, "Application of the United Kingdom Magnox Steel Irradiation Model to the HFIR Pressure Vessel," Effects of Radiation on Materials, ASTM STP 1046, N. H. Packan, R. E. Stoller, and A. S. Kumar, Eds., American Society of Testing and Materials, Philadelphia, 1990, pp. 30-44.
4. G. R. Odette, "Modeling Irradiation Embrittlement in Reactor Pressure Vessel Steels," L. E. Steele, Ed., IAEA, Vienna, 1993.
5. M. K. Miller and M. G. Burke, Journal of Nuclear Materials 195 (1992) 68-82.
6. P. A. Beaven, F. Frisius, R. Kampmann, and R. Wagner, "SANS/TEM Studies of the Defect Microstructure of Test Reactor Irradiated Fe-Cu Alloys and Cu-Containing RPV Steels," Environmental Degradation of Materials in Nuclear Power Systems-Water Reactors, Second International Symposium, The American Nuclear, La Grange Park, IL, 1986, pp. 400-408.
7. J. T. Buswell, C. A. English, M. G. Hetherington, W. J. Phythian, G. D. W. Smith, and G. M. Worrall, "An Analysis of Small Clusters Formed in Thermally Aged and Irradiated FeCu and FeCuNi Model Alloys," Effects of Radiation on Materials, ASTM STP 1046, N. H. Packan, R. E. Stoller, and A. S. Kumar, Eds., American Society of Testing and Materials, Philadelphia, 1990, pp. 127-153.
8. M. K. Miller and M. G. Burke, "Fine-Scale Microstructural Characterization of Pressure Vessel Steels and Related Materials using APFIM", Effects of Radiation on Materials, ASTM STP 1046, N. H. Packan, R. E. Stoller, and A. S. Kumar, Eds., American Society of Testing and Materials, Philadelphia, 1990, pp. 107-126.
9. G. M. Worrall, J. T. Buswell, C. A. English, M. G. Hetherington, and G. D. W. Smith, Journal of Nuclear Materials 148 (19787) 107-114.
10. G. R. Odette and C. K. Sheeks, "A Model for Displacement Cascade Induced Microvoid and Precipitate Formation in Dilute Iron-Copper Alloys," Phase Stability During Irradiation, J. R. Holland, L. K. Mansur, and D. I. Potter, Eds., The Metallurgical Society of the AIME, Warrendale, PA, 1981, pp. 415-436.
11. S. B. Fisher, J. E. Harbottle, and N. Aldridge, Philosophical Transactions of the Royal Society of London A315 (1985) 301-322.
12. W. J. Phythian, A. J. E. Foreman, C. A. English, J. T. Buswell, M. Hetherington, K. Roberts, and S. Pizzini, "The Structure and Hardening Mechanism of Copper

Precipitation in Thermally Aged or Irradiated Fe-Cu and Fe-Cu-Ni Model Alloys," AEA-TRS-2004, Harwell Laboratory, Harwell, UK, 1990.
13. M. J. Makin and T. H. Blewitt, Acta Metallurgica 10 (1962) 241-246.
14. B. L. Eyre, "A Study of Neutron Irradiation in Alpha Iron and a 1Cr-0.5Mo Pressure Vessel Steel," Radiation Effects on Metals and Neutron Dosimetry, ASTM STP 341, J. R. Hawthorne, Ed., American Society of Testing and Materials, Philadelphia, 1963, pp. 294-304.
15. D. R. Harries and B. L. Eyre, "Effects of Irradiation in Iron and Steels," Flow and Fracture of Metals and Alloys in Nuclear Environments, ASTM STP 389, C. E. Weber, Ed., American Society of Testing and Materials, Philadelphia, 1965, pp. 105-119.
16. F. A. Smidt, Jr. and J. A. Sprague, "Property Changes Resulting from Impurity-Defect Interactions in Iron and Pressure Vessel Steel Alloys," Effects of Radiation on Substructure and Mechanical Properties of Metals and Alloys, ASTM STP 529, J. Moteff, Ed., American Society of Testing and Materials, Philadelphia, 1973, pp. 78-91.
17. R. L. Simons, "Damage Rate and Spectrum Effects in Ferritic Steel ΔNDTT Data," Influence of Radiation on Material Properties, 13th International Symposium (Part II), ASTM STP 956, F. A. Garner, C. H. Henager, Jr., and N. Igata, Eds., American Society of Testing and Materials, Philadelphia, 1987, pp. 535-551.
18. S. Kojima, S. J. Zinkle, and H. L. Heinisch, Journal of Nuclear Materials 179-181 (1991) 982-985.
19. A. L. Bement, Jr., "Fundamental Materials Problems in Nuclear Reactors," Strength of Metals and Alloys, Proceedings of Second International Conference, American Society for Metals, Metals Park, OH, 1970, pp. 693-728.
20. J. Moteff, D. J. Michel, and V. K. Sikka, "The Influence of Irradiation temperature on the Hardening Behavior of the Refractory BCC Metals and Alloys," Defects and Defect Clusters in BCC Metals and Their Alloys, Proceedings of International Conference, R. J. Arsenault, Ed., U. S. National Bureau of Standards, 1973, pp. 198-215.
21. R. E. Stoller, "Modeling the Influence of Irradiation Temperature and Displacement Rate on Hardening Due to Point Defect Clusters in Ferritic Steels", Effects of Radiation on Materials, ASTM STP 1175, A. S. Kumar, D. S. Gelles, R. K. Nanstad, and E. A. Little, Eds., American Society of Testing and Materials, Philadelphia, 1993, pp. 394-423; see also NUREG/CR-5859, Oak Ridge National Laboratory, 1992.
22. Stoller, R. E., "The Role of Point Defect Clusters in Reactor Pressure Vessel Embrittlement," Environmental Degradation of Materials in Nuclear Power Systems-Water Reactors, Sixth International Symposium, The Metallurgical Society, Warrendale, PA, 1993, pp. 747-754.
23. U. F. Kocks, Metallurgical Transactions 1 (1970) 1121-1143.
24. J. W. Martin, Micromechanisms in Particle-Hardened Alloys (Cambridge University Press, Cambridge, U.K., 1980).

25. A. J. E. Foreman, W. J. Phythian, and C. A. English, Philosphical Magazine A 66 (1992) 671-695.
26. A. F. Calder and D. J. Bacon, "A Molecular Dynamics Study of Displacement Cascades in α-Iron", Journal of Nuclear Materials 207 (1993) 25-45.
27. R. E. Stoller, A. F. Calder, A. J. E. Foreman, W. J. Phythian, and D. J. Bacon, to be published.
28. D. Pachur, "Apparent Embrittlement Saturation and Radiation Mechanisms of Reactor Pressure Vessel Steels," Effects of Radiation on Materials, ASTM STP 725, D. Kramer, H. R. Brager, and J. S. Perrin, Eds., American Society of Testing and Materials, Philadelphia, 1981, pp. 5-19.
29. G. R. Odette, E. V. Mader, G. E. Lucas, W. J. Phythian, and C. A. English, "The Effect of Flux on the Irradiation Hardening of Pressure Vessel Steels," Effects of Radiation on Materials, ASTM STP 1175, A. S. Kumar, D. S. Gelles, R. K. Nanstad, and E. A. Little, Eds., American Society of Testing and Materials, Philadelphia, 1993, pp. 373-393.
30. R. K. Nanstad, K. Farrell, D. N. Braski, and W. R. Corwin, Journal of Nuclear Materials 158 (1988) 1-6.
31. F. Frisius, R. Kampmann, P. A. Beaven, and R. Wagner, "Influence of Copper on the Defect Microstructure and Radiation Strengthening of Iron," Dimensional Stability and Mechanical Behavior of Irradiated Metals and Alloys, Proc. of BNES Conference, British Nuclear Energy Society, London, 1983, pp. 171-174.
32. "A Comparison of the Relative Importance of Copper Precipitates and Point Defect Clusters in Reactor Pressure Vessel Steel," Stoller, R. E., NUREG/CR-6231, ORNL-6811, Oak Ridge National Laboratory, Oak Ridge, TN, 1994.
33. K. C. Russell and L. M. Brown, Acta Metallurgica 20 (1972) 969-974.
34. A. D. Brailsford and R. Bullough, Philosophical Transactions of the Royal Society of London 302 (1981) 87-137.
35. P. M. Kelly, International Metallurgical Reviews 18 (1973) 31-36
36. G. Salje and M. Feller-Kniepmeier, Journal of Applied Physics 48 (1977) 1833-1839.
37. S. J. Rothman, N. L. Peterson, C. M. Walter, and L. J. Nowicki, Journal of Applied Physics 39 (1968) 5041-5044.
38. ASME Section III, Nuclear Vessels," 1968 and ASME Section III "Nuclear Power Plant Components," 1971, American Society of Mechanical Engineers, New York.
39. "Single Crystal Elastic Constants and Calculated Aggregate Properties: A Handbook," G. Simmons and H. Wang, M.I.T. Press, Cambridge, MA, 1971.
40. "The Theory of Dislocations," J. R. Hirth and J. Lothe, McGraw-Hill, New York, NY, 1968.
41. Remec, I and Kam, F. B. K., "HFIR Steels Embrittlement: The Possible Effect of Gamma Field Contribution," Effects of Radiation on Materials, 17th International Symposium, American Society of Testing and Materials, Philadelphia, PA (these proceedings).
42. "Evaluation of HFIR Pressure Vessel Integrity Considering Radiation Embrittlement", R. D. Cheverton, J. G. Merkle, and R. K. Nanstad, ORNL TM-10444, Oak Ridge National Laboratory, Oak Ridge, TN, 1988.

43. "Irradiation Embrittlement of LWR Pressure Vessel Steels," G. R. Odette and G. E. Lucas, EPRI NP-6114, Electric Power Research Institute, Palo Alto, CA, 1989.
44. G. R. Odette, G. E. Lucas, D. Klingensmith, R. E. Stoller, and W. J. Phythian, "On the Effect of Flux and Composition on Irradiation Hardening at 60°C," Effects of Radiation on Materials, 17th International Symposium, American Society of Testing and Materials, Philadelphia, PA (these proceedings).
45. T. Diaz de la Rubia and W. J. Phythian, Journal of Nuclear Materials 191-194 (1992) 108-115.
46. T. J. Williams, P. R. Burch, C. A. English, and P. H. N. de la cour Ray, "The Effect of Irradiation Dose Rate and Temperature, and Copper and Nickel Content, on the Irradiation Shift of Low Alloy Steel Submerged Arc Welds," Environmental Degradation of Materials in Nuclear Power Systems-Water Reactors, Third International Symposium, The Metallurgical Society, Warrendale, PA, 1988, pp. 121-131.
47. "Interfacial Phenomena in Metals and Alloys," L. E. Murr, Addison-Wesley, Reading, MA, 1975.
48. E. D. Hondros, Proceedings of the Royal Society of London 286 (1965) 479-498.
49. J. E. Harris, Metal Science Journal 7 (1973) 1-6.
50. "PR-EDB: Power Reactor Embrittlement Data Base, Version 2," F. W. Stallman, J. A. Wang, F. B. K. Kam, and B. J. Taylor, NUREG/CR-4816 Revision 2, ORNL/TM-10328/R2, Oak Ridge National Laboratory, Oak Ridge, TN, 1994.
51. L. M. Davies, T. Ingham, and R. L. Squires, "Evaluation of Advanced Reactor Pressure Vessel Steels Under Neutron Irradiation," Effects of Radiation on Materials, ASTM STP 782, H. R. Brager, and F. A. Garner, Eds., American Society of Testing and Materials, Philadelphia, 1982, pp. 433-463.
52. J. C. Van Duysen, J. Bourgoin, C. Janot, and J. M. Penisson, "Evolution of the Microstructure of PWR Pressure Vessel Steels from the CHOOZ A Reactor Surveillance Program after Long-Term Irradiations," Effects of Radiation on Materials, ASTM STP 1125, R. E. Stoller, A. S. Kumar, and D. S. Gelles, Eds., American Society of Testing and Materials, Philadelphia, 1992, pp. 117-130.

Wayne A. Pavinich[1] and Lance S. Harbison[2]

THE B&W OWNERS GROUP PROGRAM FOR MICROSTRUCTURAL CHARACTERIZATION AND RADIATION EMBRITTLEMENT MODELLING OF LINDE 80 REACTOR VESSEL WELDS

REFERENCE: Pavinich, W. A. and Harbison, L. S., **"The B&W Owners Group Program for Microstructural Characterization and Radiation Embrittlement Modelling of Linde 80 Reactor Vessel Welds,"** *Effects of Radiation on Materials: 17th International Symposium, ASTM STP 1270,* David S. Gelles, Randy K. Nanstad, Arvind S. Kumar, and Edward A. Little, Eds., American Society for Testing and Materials, 1996.

ABSTRACT: The Babcock and Wilcox Owners Group (B&WOG) is sponsoring an on-going study to develop an understanding of radiation embrittlement of Linde 80 reactor vessel welds from a micro-mechanical viewpoint. Previous work that focused on characterizing the large microstructural features indicated that a large portion of the bulk copper content is in precipitate/inclusion/carbide form. This result indicates that copper in solid solution is considerably less than the bulk composition. Field-ion microscope atom probe investigations on unirradiated weld metals with bulk copper contents ranging from 0.22 to 0.38 wt%, also indicate significant amount of copper are tied up in precipitate/inclusion/carbide form. This results is significant since the bulk copper content (which includes both copper in solid solution and copper contained in precipitates, inclusions, and carbides) is used in Regulatory Guide 1.99, Revision 2 to determine radiation damage. This paper reviews these results.

Existing radiation embrittlement models superpose the changes in yield strength due to defect clusters and copper-rich precipitates induced by neutron irradiation. Low-copper Linde 80 welds display little or no increase in the 41 joule (30 ft-lb) transition temperature as a result of neutron irradiation which indicates that precipitation is the dominant component of radiation embrittlement for Linde 80 welds. Future work will include further microstructural characterizations of Linde 80 reactor vessel welds and applying the existing radiation embrittlement models to Linde 80 welds. This paper describes the detailed plans for future work.

KEYWORDS: submerged-arc welds, neutron irradiation, copper precipitation, reactor vessel, transmission electron microscopy, optical microscopy, small-angle neutron scattering, field-ion microscopy.

The study of the microstructure of the Mn-Mo-Ni/Linde 80 weld metals was initiated to identify the microstructural characteristics which caused this class of weld metals to behave differently from other weld metals. Numerous studies in the past characterized materials on microscopic levels to attempt to identify the causes of neutron embrittlement sensitivity [1, 2, 3]. This approach was followed for the Mn-Mo-Ni/Linde 80 weld metal. It was decided to characterize the larger microstructural features first and then employ state-of-the-art techniques to evaluate the very fine features in the weld metals.

[1]Principal Consultant, Grove Engineering, Knoxville, TN 37923 and [2]Engineer B&W Nuclear Technologies, P. O. Box 10935, Lynchburg, VA 24506-0935.

Copyright© 1996 by ASTM International www.astm.org

A number of techniques are available to examine the microstructural characteristics of weld metals. The methods that were used throughout this program include optical microscopy, transmission electron microscopy, small-angle neutron scattering, and field-ion microscopy. Each technique was used to determine a specific feature of the weld metal, whether it was grain size, precipitate size, or solute concentration. The following sections describe each technique and the significant results.

OPTICAL MICROSTRUCTURAL ANALYSES

The goal of the optical microstructural analysis was to evaluate microstructural constituents that may affect initial, as well as post-irradiation fracture toughness. The weld metals examined included ten WF-70 specimens and three WF-209-1 specimens originating from tested Charpy specimens and eight other specimens (SA-1107, SA-1135, SA-1484, SA-1526, SA-1585, WF-25, WF-67, and WF-182-1) originating from small blocks of weld metal. The WF-70 and WF-209-1 material was originally fabricated with weld wire 72105 and Linde 80 weld flux [2]. The WF-70 material came from a nozzle dropout weld and the Midland Unit 1 beltline weld; the WF-209-1 material came from a surveillance weld. The 13 specimens generally received a stress relief heat treatment at 607 $\pm$14°C (1125 $\pm$ 25°F) between 20 and 50 hours; however, one specimen was stress relieved for only 1/4 hour. Specimens were examined to characterize inclusion distribution and inclusion geometry using optical microscopy and quantitative metallurgical techniques. Inclusion chemical composition and matrix chemical composition were determined using energy dispersive spectrometry and electron microprobe analysis.

All welds were found to contain a mixture of acicular ferrite and ferrite-carbide aggregate comprising between 84 and 99% of the microstructural features. Grain boundary ferrite, ferrite with aligned martensite, austenite, or carbide, and intergranular polygonal ferrite were also present in minor amounts. In the WF-70 materials (which include the surrogate WF 209-1 material) inclusions were present having mean diameters between 1.96 and 2.69 μm. The eight non-WF-70 samples contained smaller inclusions with mean diameters between 0.98 and 1.68 μm. Minor inclusion contents were noted for inclusions with diameters as small as 0.26 μm and as large as 7 μm for the WF-70 welds and as large as 5.9 μm for the non-WF-70 welds. No differences in inclusion characteristics were identified by optical microscopy as a result of different post-weld heat treatment (PWHT) times.

Chemical analysis of the inclusions was completed using energy dispersive spectrometry (EDS). All analyzed inclusions were classified to be in one of eight categories based on chemical composition. Manganese, silicon, sulfur, chromium, aluminum, copper, nickel, titanium, phosphorous, and potassium were found in the inclusions in varying concentrations. Chemical analysis of the weld metal matrices was completed for each specimen using electron microprobe X-ray analysis. Copper content varied between 0.18 and 0.37 wt% for the WF-70 samples and between 0.14 and 0.32 wt% for the remaining samples.

A second microstructural analysis program has recently been completed [4]. This project analyzed five weld metal samples and ten plate samples. The weld metal samples (including WF-193 and WF-209-1) contained similar inclusion contents as the welds examined in the earlier research. The plate material samples had inclusion contents significantly less than that of the weld materials (100 to 10,000 times less).

TRANSMISSION ELECTRON MICROSCOPY

A microstructural study was completed on four Mn-Mo-Ni/Linde 80 weld metals using transmission electron microscopy (TEM) [1, 2, 3]. The four weld metals were WF-25, WF-70, WF-193, and WF-209-1, each having similar copper contents (0.35, 0.42, 0.28, and 0.36 wt%, respectively) but different stress relief times (48, 48, 29, and 33 hrs, respectively) at 607°C (1125°F). TEM was used to examine and characterize the microstructural features on a finer scale than that available from optical microscopy techniques.

TEM identified all four welds as containing large, randomly distributed spherical inclusions comprised primarily of Mn and Si. M_3C and M_2C carbides were also detected primarily on grain boundaries [1, 2]. Very small copper particles were detected usually in the vicinity of other precipitates. Each type of inclusion and precipitate were evaluated to establish an average chemical composition. This work, however, did not establish average precipitate densities.

In a subsequent TEM study, specimens of the above four weld metals irradiated on the order of 10^{19} n/cm^2 (E > 1 MeV) were examined [3]. In this study, inclusions and precipitates that were characterized in the previous study were compared to the specimens in the irradiated and irradiated/annealed conditions. The only anomalous behavior to be noted is in the characterization of the copper precipitates. In the previous TEM study of the unirradiated weld metals, copper precipitates were detected in all welds except for WF-193. After irradiation, TEM did not find copper precipitates in the WF-209-1, WF-25, and WF-193 welds while copper precipitates were again found in the WF-70 weld.

Since copper precipitation is believed to occur with irradiation, the absence of copper precipitates in the three weld metals may be the result of an inhomogeneous distribution of copper in the microstructure. Since TEM is a small area sampling technique, the absence of a particular microstructural feature may not be representative of the bulk material. In the case of weld metals, the absence of copper from areas of the weld is not unexpected.

SMALL-ANGLE NEUTRON SCATTERING

Small-angle neutron scattering (SANS) was used to characterize copper precipitate size and density. Ten WF-70 weld metal specimens, taken from unirradiated tested Charpy specimens, were analyzed by SANS. Nominal copper contents of the specimens ranged from 0.22 to 0.39 at.%. All specimens were stress relieved at 607°C (1125°F) for 20 to 50 hours prior to the SANS analysis [5].

Of the 10 tested specimens, 7 exhibited similar scattering characteristics regardless of copper content. Of the remaining 3 specimens, 2 did not show scattering while 1 exhibited a greater magnitude of scattering. For the 7 specimens with similar scattering, average copper precipitate size was found to be approximately 18Å with an average precipitate density of approximately 10^{15}cm^{-3}; the specimen exhibiting greater scattering was found to have the same average copper precipitate size, but an average precipitate density of approximately 10^{16}cm^{-3}, believed to be a result of fewer copper atoms in solid solution. The lack of scattering in two of the specimens indicates that weld metals have varying amounts of precipitates and copper in solid solution.

FIELD-ION MICROSCOPY

Recent microstructural characterizations using the field-ion microscope atom probe (FIM/AP) were performed to determine the concentration of copper, nickel, and phosphorus in solid solution of WF-70 weld metal [6]. To date, two unirradiated specimens were examined by the FIM/AP technique: solution-treated and as-received. Solution treated specimens were heat treated at 1000°C (1832°F) for 2 hours followed by quenching. For the solution treated material, results of the FIM/AP showed the matrix copper to be identical to the nominal copper content of the WF-70 material (0.31 at%). In the as-received material, matrix copper concentration was determined to be about two-thirds (0.21 at%) of the nominal copper content. The remaining copper is believed to be in the form of precipitates, inclusions, or carbides. Since the purpose of this study was to determine the matrix copper concentration, no estimates can be given on the size or chemical composition of the second phase particles.

A similar FIM/AP study has recently been completed at Oak Ridge National Laboratory (ORNL) on WF-70 welds from the canceled Midland Unit 1 nuclear plant [7]. Weldments were taken from the beltline and nozzle belt regions of the reactor vessel. From a microstructural standpoint, a goal of this research was to determine the variation in copper throughout the welds. Copper in solid solution was determined to be 0.06 to 0.11 at % depending on through-wall location. This result appears to contrary to that of the B&W results. However, the solubility of copper in iron is very sensitive to temperature at the post-weld heat treatment (PWHT) temperature of 607°C (1125°F). The PWHT temperature was controlled to ±14°C(±25°F) which corresponds to copper solubility levels of approximately 0.12 at% and 0.20 at% for PWHT temperatures of 593°C (1100°F) and 621°C (1150°F) respectively. Therefore the difference in copper in solid solution for the ORNL and B&W measurements can be expected.

Preceding the FIM/AP study, bulk chemical analyses found copper to range between 0.21 and 0.34 wt% (0.25 wt% ave.) in the four beltline weld sections examined and between 0.37 and 0.46 wt% (0.39 wt% ave.) in the two nozzle belt weld sections examined [8]; electron microprobe analyses confirmed the bulk copper.

FIM/AP was used to examine the welds for the presence of copper-base precipitates. FIM/AP was also used to compare the matrix copper content with the bulk copper content. Unlike the SANS experiments, FIM/AP did not detect copper precipitates or clusters. However, ultrafine refractory carbides (approximately 1 nm in diameter) were found in the microstructure.

FIM/AP was used to determine the amount of copper in the matrix of the welds. Of five samples taken from one beltline weld section, matrix copper was found to range between 0.07 and 0.13 wt% (0.11 wt% ave.). Compared to the bulk copper analysis as given above, it appears that a significant portion of the copper is contained in either precipitates, inclusions, or carbides. This result is significant since the bulk copper content (which includes both copper in solid solution and copper contained in precipitates, inclusions, and carbides) is used in Regulatory Guide 1.99, Revision 2 to determine radiation damage. However, only copper in solid solution is free to precipitate/segregate, during irradiation, and form new precipitates that further degrade fracture toughness.

MICROSTRUCTURAL CHARACTERIZATION

To date, the microstructural characterization performed on Mn-Mo-Ni/Linde 80 weld materials has primarily focused on the location of copper in the various microstructural features. Since Regulatory Guide 1.99, Revision 2, calculates the change in reference temperature based on the nominal copper content, it is important to establish the location of copper in the weld metals. Previous work sponsored by the BWOG has shown that some of the copper is tied up in the form of precipitates, inclusions or carbides, rather than being completely in solid solution. Therefore, an argument against using nominal copper content in the Regulatory Guide calculations is warranted. It can be argued that if a copper atom is not in solid solution, then it will not be available to form a toughness degrading second phase particle at a later time. Only the copper that remains in solid solution (after processing) is available for precipitation at a later time.

Present microstructural characterization of Linde 80 weld metals is focusing on identifying the dominant mechanisms of radiation embrittlement. To achieve this goal, the appropriate microstructural characterization techniques have been selected to quantify the following microstructural features.

- Composition of ultra fine copper-rich precipitates (approximately 1 to 2 nm in diameter) and composition of the matrix is being characterized using AP/FIM for irradiated and unirradiated materials. Comparison of the irradiated and unirradiated conditions will identify the microstructural changes that will guide the customization of the embrittlement model. These changes include: 1) the depletion of copper in solid solution and, 2) the change in precipitate size.

- The size and distribution of the ultra fine precipitates will be characterized for irradiated and unirradiated materials to quantify the radiation induced changes in these parameters. The candidate technique for this characterization is SANS. Some SANS data are presently available. This task will build on the available data.

- The dislocation density will be quantified using TEM. characterization.

The test matrix identified in Table 1 covers a wide range of neutron fluence and bulk copper content. The largest fluence represents the inside wall fluence at 48 effective full power years (EFPY) for B&W designed reactor vessels and 32 EFPY at 1/4T for Westinghouse designed reactor vessels. Nickel, phosphorus, silicon, and manganese contents for these materials are equivalent, and therefore, copper is an isolated variable in the matrix. The mid-level copper content material was chosen since 0.24 wt% Cu is approximately the solubility limit for copper in iron at the post-weld heat treatment temperature of 607°C (1125°F). The objective of this work is to provide physical evidence to support observed mechanical test data trends including

- saturation/stabilization of radiation embrittlement

- neutron flux effects

- irradiation temperature effects

- the effect of copper solid solution on radiation embrittlement

Table 1 - Microstructural Characterization Matrix

Material	Neutron Fluences x 10^{19}, n/cm^2 (E > 1.0 MeV)				Copper Content, wt%
WF 209-1	0	0.25	1.3	1.6	0.35
WF 182-1	0	0.59	0.96	1.3	0.24
WF 447	0	0.40	1.7		0.03

SHIFT TREND BASED ON COPPER IN SOLID SOLUTION

A shift trend will be developed for Linde 80 welds that will be based on the percentage of copper in solid solution and not on bulk copper content. Measurements of copper in solid solution that will be statistically correlated with various Charpy shift parameters for Linde 80 welds including upper shelf, yield strength, fracture appearance, and 41 joule (30 ft-lb) shifts. The optimum shift parameter will be identified. Results will be compared with trends of Reg. Guide 1.99, Rev 2 and B&W generated correlations.

EMBRITTLEMENT SATURATION

Linde 80 welds apparently display radiation embrittlement saturation at high neutron fluences. Figure 1 is a typical plot of Linde 80 weld metal yield strength data showing an apparent saturation trend. This trend can be explained considering the fundamental aspects of radiation embrittlement. Radiation embrittlement of RPV steels has been attributed to the following processes.

- Defect production (i. e. vacancies, interstitials, dislocation loops, and vacancy clusters) caused by neutron displacement cascades
- Radiation assisted formation of ultra-fine, copper-rich, coherent precipitates
- Radiation assisted formation of ultra-fine phosphides
- Radiation assisted formation of ultra-fine carbides
- Temper embrittlement caused by radiation assisted phosphorous segregation

Existing embrittlement models consider only the first two processes by superposing the changes in yield strength due to defect production and age hardening [9, 10, 11, 12]. The last three processes have not been modelled since there is no hard evidence that these processes are caused by or enhanced by neutron irradiation in US RPVs. Modelling these processes will be pursued if evidence of their existence is produced by microstructural characterization. The existing models have the following mathematical form.

$$\Delta\sigma_y = \Delta\sigma_{dam} + \Delta\sigma_p$$

where:

$\Delta\sigma_y$ = change in yield strength
$\Delta\sigma_{dam}$ = change in yield strength due to defects
$\Delta\sigma_p$ = change in yield strength due to precipitation

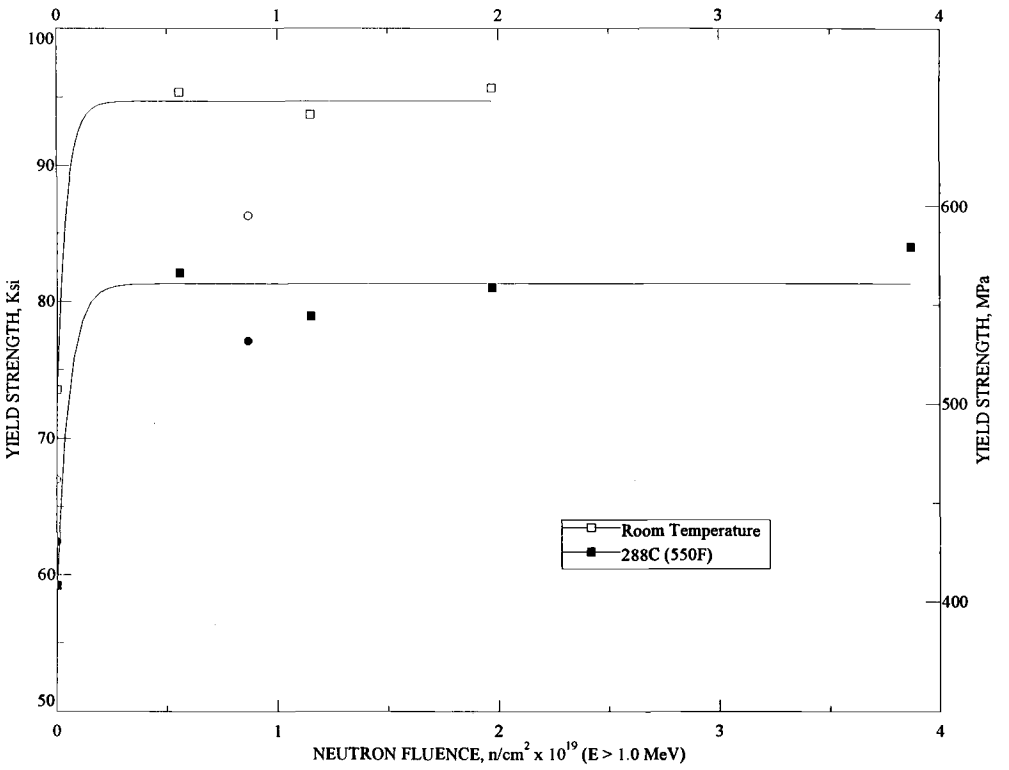


FIG. 1--Apparent Saturation Trend of Linde 80 Welds.

Figure 2 is a schematic of the contributors to radiation embrittlement based on the work of Odette, et al [13]. Unstable matrix damage has been postulated to be small voids or vacancy clusters that are not thermodynamically stable while stable matrix damage has been postulated to be stable nanovoids or radiation induced phosphides and carbo-nitrides. It is clear that if the contributions of unstable and stable matrix damage are small then radiation embrittlement saturation is expected. The 41 joule (30 ft-lb) shifts at 3.5 x 10^{18} n/cm^2 and 1.4 x 10^{19} n/cm^2 are 0°F and 35°F respectively for the low-copper weld. This indicates that the matrix damage is only a small component of radiation embrittlement for Linde 80 welds thus supporting the observed saturation trend. Microstructural characterizations will demonstrate whether or not microstructures stabilize at higher neutron fluences where mechanical properties apparently do not further degrade at even higher neutron fluences.

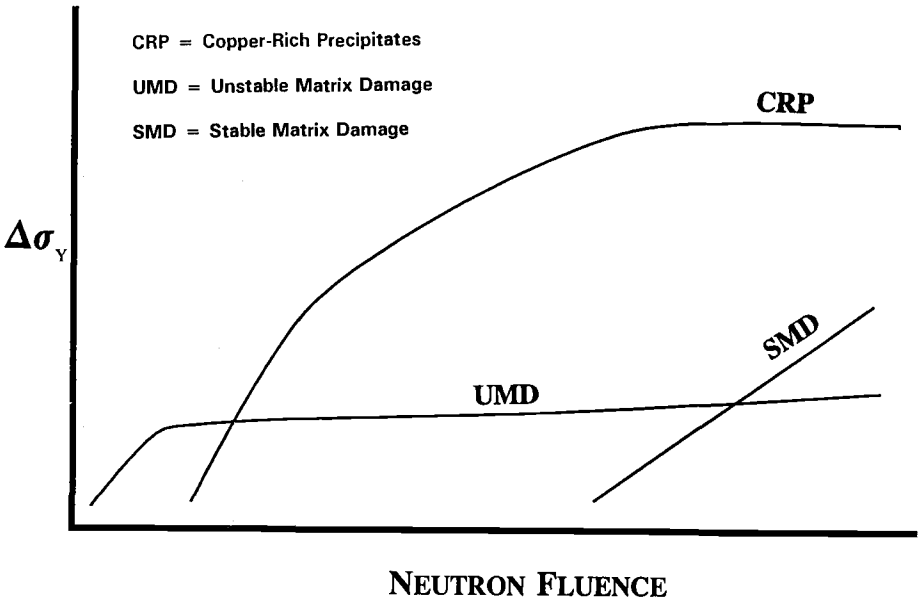


FIG. 2--Contributors to Radiation Embrittlement of Linde 80 Welds.

CONCLUSIONS

Two conclusions can be drawn from the information presented in this paper.

- o The amount of copper in solid solution which is available for precipitation is significantly less than the bulk copper content for high copper Linde 80 welds.
- o Saturation of radiation embrittlement for Linde 80 welds is a plausible trend.

REFERENCES

[1] Lawless, K. R., Pavinich, W. A., Lowe, A. L., "Microstructural Characterization of Submerged-Arc Weld Metals," Effects of Radiation on Materials: 13th International Symposium, ASTM STP 956, F. A. Garner, C. H. Henager, Jr., and N. Igata, Eds., American Society for Testing and Materials, Philadelphia, 1987, pp. 321-332.

[2] Lawless, K. R., Lowe, A. L., "Further Microstructural Characterization of Submerged-Arc Weld Metals," Effects of Radiation on Materials: 15th International Symposium, ASTM STP 1125, R. E. Stoller, A. S. Kumar, and D. S. Gelles, Eds., American Society for Testing and Materials, Philadelphia, 1992, pp. 186-199.

[3] Lawless, K. R., Lowe, A. L., "Further Microstructural Characterization of Submerged-Arc Weld Metals - II," Effects of Radiation on Materials: 16th International Symposium, ASTM STP 1175, A. S. Kumar, D. S. Gelles, R. K. Nanstad, and E. A. Little, Eds., American Society for Testing and Materials, Philadelphia, 1993, pp. 292-305.

[4] Sarver, L. W., unpublished work performed on behalf of the B&W Owners Group, Babcock & Wilcox Co., Alliance, Ohio, 1993.

[5] Vlak, W. A. H. M., unpublished work performed on behalf of the B&W Owners Group.

[6] Brenner, S. S., Kowalik, J., unpublished work performed on behalf of the B&W Owners Group, University of Pittsburgh, Pittsburgh, Pa., November 15, 1989.

[7] Nanstad, R. K., D. E. McCabe, and Swain, R. L., "Irradiation Effects in a Commercial LUS Weld," Heavy-Section Steel Irradiation Program, Semiannual Progress Report for October 1990 - March 1991, NUREG/CR-5591, Prepared by W. R. Corwin, April 1994.

[8] Moore, K. E., Heller, A. S., "B&W 177-FA Reactor Vessel Beltline Weld Chemistry Study," BAW-1799, Babcock and Wilcox Utility Power Generation Division, Lynchburg, Va., July 1983.

[9] Fisher, S. B., Harbottle, J. E., Aldridge, N. B., "Copper Precipitation in Pressure Vessel Steels," CEGB Report in 3 Parts, TPRD/B/0396/N84, TPRD/B/0397/N84, TPRD/B/0398/N84, 1984.

[10] Fisher, S. B., Buswell, J. T., "A Model for PWR Vessel Embrittlement," CEGB Report, TPRD/B/0745/R86, January 1986.

[11] Lucas, G. E., Odette, G. R., "Recent Advances in Understanding Radiation Hardening and Embrittlement Mechanisms in Pressure Vessel Steels" Proceedings of the Second International Symposium on Environmental Degradation of Materials in Nuclear Power Systems - Water Reactors, American Nuclear Society, La Grange Park, Illinois, 1986, pp345-360.

[12] Odette, G. R., Lucas, G. E., "Irradiation Embrittlement of LWR Pressure Vessel Steels," EPRI NP-6114, Final Report, Electric Power Research Institute, Palo Alto, CA, January 1986.

[13] Odette, G. R., et al, "The Effect of Flux on the Irradiation Hardening of Pressure Vessel Steels," Effects of Radiation on Materials: 16th International Symposium, ASTM STP 1175, A. S. Kumar, D. S. Gelles, R. K. Nanstad, and E. A. Little, Eds., American Society for Testing and Materials, Philadelphia, 1993, pp. 292-305.

Ron J. McElroy[1] and Arthur L. Lowe, Jr[2]

IRRADIATION EMBRITTLEMENT MODELLING OF LINDE 80 WELD METALS

REFERENCE: McElroy, R. J. and Lowe, Jr., A. L., **"Irradiation Embrittlement Modelling of Linde 80 Weld Metals,"** *Effects of Radiation on Materials: 17th International Symposium, ASTM STP 1270,* David S. Gelles, Randy K. Nanstad, Arvind S. Kumar, and Edward A. Little, Eds., American Society for Testing and Materials, 1996.

ABSTRACT: Linde 80 weld metals are characterised by a narrow range of chemical compositions, except for copper content, which varies from 0.2 - 0.42 wt%. The surveillance database for Linde 80 weld metals constitutes a unique and large database on a single class of material for evaluating embrittlement models and property correlations used in the assessment of RPV embrittlement.

Correlations between Charpy transition temperature shifts and yield strength, which best characterises the hardening behaviour, were tested and it was concluded that fracture appearance transition temperature (FATT) provided less scatter and a more representative indicator than either lateral expansion or Charpy 30 ft-lb energy. This is believed to be a consequence of the low upper shelf of Linde 80 weld metals distorting the latter two transition temperatures, especially after irradiation, which induces a significant reduction in upper-shelf to levels approaching the indexing values.

The main purpose of the present study has been to obtain a simple two component barrier hardening model form which best describes the behaviour of Linde 80 weld metal. To this end, the UK Magnox Embrittlement Model, often referred to as the Fisher Model, has been used and the key parameters, such as activation energies, dislocation densities and damage cross sections, were used as fitting parameters. Good agreement was found between model predictions and the surveillance yield strength data following optimisation of model parameters. Applying the latter optimised form produced equally good prediction of HSSI results at a significantly higher damage rate demonstrating the "rate effect" inherent in the irradiation enhanced copper precipitation process. The best agreement was obtained assuming a matrix copper content of about 0.23 wt% which is consistent with recent solubility data for Linde 80 welds. For these materials an insensitivity to bulk copper content was demonstrated even though this varied from 0.21 - 0.42 wt%. Additionally, the parameters optimised for high copper welds provided a good prediction for low-copper materials indicating that the matrix hardening component was correctly specified. The low matrix hardening and predicted completion of copper precipitation by doses of about $1x10^{19}ncm^{-2}$ support the notion of embrittlement saturation at high doses.

KEYWORDS: neutron irradiation hardening, embrittlement, pressure vessel steels, weld metal, mechanistic modelling, copper precipitation.

[1] Research Scientist, AEA Technology, Harwell Laboratory, Didcot, Oxon. OX11 ORA, UK.
[2] Consultant, Lowe Associates, Lynchburg, USA.

Copyright© 1996 by ASTM International www.astm.org

INTRODUCTION

Linde 80 weld metals are characterised by their narrow range of composition in all respects except for copper content, which has a 0.2-0.42wt% range in the vast majority of welds used in the fabrication of older LWR RPVs and can be as low as 0.03wt% in modern welds. This class of weld metal is notorious for its low upper shelf energy (USE), which has been the main area of research in recent years, but it is the basic embrittlement behaviour, characterised by Charpy shift and irradiation hardening, which is the subject of the present paper. A comprehensive surveillance database is available for all of the vessels in US nuclear plant fabricated with Linde 80 welds in their beltline. This constitutes a uniquely large database on a single class of material for testing and evaluating embrittlement models and materials property correlations used in the assessment of RPV embrittlement.

The purpose of the present paper is to present the initial phase in the development of a phenomenologically based modelling approach for RPV embrittlement assessment. This phase of the work concentrates on the application of barrier hardening models to describe irradiation hardening, the first step in the development programme. The next phase of the work will necessitate translation of the present hardening predictions into fracture toughness predictions, a step requiring new insights and further development. To assist in this process, some observations and comments regarding property correlations derived from the present database will also be presented.

LINDE 80 SURVEILLANCE AND SUPPORTING DATABASES

All the surveillance data for this class of weld metal, including the reference Charpy 30ft-lb, 35mils lateral expansion and fracture appearance transition temperature (FATT) and the yield strength have been collated and evaluated in a self-consistent manner. The reference 30ft-lb (ΔRT_{NDT}), 35mils lateral expansion (ΔT_{LE}) and FATT ($\Delta FATT$) transition temperature shifts and the yield strength increases[3] ($\Delta\sigma_y$) for each surveillance capsule are summarised in TABLE 1, together with materials and relevant irradiation parameters. The tabulated ΔRT_{NDT} and $\Delta FATT$ values were determined by manual assessment and ΔT_{LE} by computer least squares fitting using the familiar Oldfield tanh function [1] to data in the Power Reactor Embrittlement Database (PREDB). Similar computer fitting has been employed for ΔRT_{NDT} and $\Delta FATT$ in order to assess the statistics in a more uniform manner and the computed shifts were generally within $\pm 10°F$ of the manually derived values. Also presented in the table are the low unirradiated upper shelf energies (USE) which distinguish this class of weld metal.

It is also apparent from the data that a further characteristic of Linde 80 weld metal is the narrow range of bulk nickel content (0.54-70wt%) which, given the concern regarding the possible synergistic role of nickel in hardening and embrittlement, is sufficiently small to justify ignoring this element as a second order factor in the analysis. The bulk copper content on the other hand varies over a wide range (0.21-0.42) and constitutes the principal compositional variable. The impressive extent of the database, consisting as it does of 52 surveillance capsules, provides a unique opportunity for model testing and validation.

In addition to the irradiation dose, a key environmental variable for modelling purposes is the capsule irradiation temperature. The latter parameter is generally quoted in terms of behaviour of melt wire temperature monitors which can be misleading. Consequently, an alternative approach has been employed here and, instead, the coolant inlet temperature during normal operation has been used and these values are included in the table.

---

[3] The room temperature yield stress is used where this is available. Otherwise the nearest temperature data is used.

TABLE 1- -Linde 80 weld metal surveillance irradiation database employed in present study

Plant	Capsule	Weld Metal	Ni	Cu	Unirr. USE	Irr. Temp.	Fluence[4] [E>1MeV]	ΔRT_{NDT}	ΔT_{LE}	$\Delta FATT$	$\Delta\sigma_y$
			wt%	wt%	ft-lb	°F	10^{19}ncm^{-2}	°F	°F	°F	MPa
Oconee 1	E	WF-112	0.59	0.32	64	556	0.150	78	112	87	108
Oconee 1	A						0.895	191	184	161	126
Oconee 1	C						0.986	185	186	108	168
Oconee 2	C	WF-209-1A	0.58	0.36	67	556	0.102	45	137	26	52
Oconee 2	A						0.337	114	67	49	113
Oconee 2	E						1.210	179	236	73	139
Oconee 3	A	WF-209-1B	0.58	0.30	66	556	0.081	48	67	41	30
Oconee 3	B						0.312	64	63	59	108
Oconee 3	D						1.450	140	158	102	159
TMI 1	E	WF-25	0.66	0.33	81	556	0.107	124	199	57	92
TMI 1	C						0.866	203	189	109	148
TMI 2	C	WF-182-1	0.63	0.28	...	556	0.168	117	...	...	34
TMI 2	E						0.174	99	...	...	74
Arkansas 1	E	WF-193A	0.59	0.28	73	556	0.073	105	122	77	59
Arkansas 1	A						1.030	151	136	122	114
Arkansas 1	C						1.460	185	183	...	111
Rancho Seco	B	WF-193B	0.59	0.27	68	556	0.399	99	131	104	134
Rancho Seco	D						0.660	152	174	96	132
Rancho Seco	F						1.420	166	176	116	113
Davis-Besse	F	WF-182-1	0.63	0.21	70	556	0.196	127	101	83	85
Davis-Besse	B						0.592	125	148	89	105
Davis-Besse	D						0.962	150	144	106	118
Davis-Besse	A						1.290	175	192	119	128
Crystal River	C1	WF-25	0.70	0.35	73	556	0.779	214	222	178	148
Crystal River	C1	WF-67	0.60	0.22	72	556	0.609	160	73	143	52
Crystal River	C1	SA-1585	0.59	0.21	77	556	0.510	148	172	171	92
Davis-Besse	D1	WF-70	0.59	0.42	56	556	0.663	135	170	88	114
Davis-Besse	D1	WF-112	0.59	0.32	79	556	0.821	204	98	135	171
Davis-Besse	D1	SA-1135	0.59	0.27	76	556	1.030	142	190	132	134
Pt. Beach 1	V	SA-1263	0.57	0.21	65	542	0.620	110	114	88	122
Pt. Beach 1	S						0.758	165	210	157	...
Pt. Beach 1	R						2.100	165	202	145	172
Pt. Beach 1	T						2.110	175	236	130	143
Pt. Beach 2	V	WF-193C	0.59	0.25	66	542	0.614	165	147	134	122
Pt. Beach 2	T						0.836	150	188	145	...
Pt. Beach 2	R						2.150	235	256	157	161
Pt. Beach 2	S						3.470	231	249	195	172
R.E. Ginna	V	SA-1036	0.56	0.23	80	545	0.653	140	...	...	151
R.E. Ginna	R						1.020	165	162	171	140
R.E. Ginna	T						1.780	150	250	130	153
Turkey Pt 3	T	SA-1101	0.54	0.26	66	546	0.710	164	218	194	151
Turkey Pt 3	V						1.230	178	201	193	99
Turkey Pt 4	T	SA-1094	0.60	0.30	68	546	0.754	224	245	202	151
Zion 1	T	WF-209-1D	0.57	0.35	64	529	0.253	112	112	109	93
Zion 1	U						0.849	199	222	162	74
Zion 1	X						1.260	199	222	213	83
Zion 1	Y						1.560	205	239	156	141
Zion 2	U	WF-209-1E	0.57	0.35	68	529	0.257	145	146	125	129
Zion 2	T						0.804	191	200	177	123
Zion 2	Y						1.480	231	257	239	125
Surry 1	T	SA-1526	0.70	0.35	70	543	0.286	167	162	133	139
Surry 1	V						1.940	240	312	148	145
Braidwood 1	U	WF-562	0.65	0.03	70	558	0.379	10	...	...	...
Braidwood 2	U	WF-562	0.65	0.03	71	558	0.391	0	...	...	12
Byron 1	U	WF-336	0.46	0.03	74	558	0.350	0	...	...	...
Byron 2	U	WF-447	0.62	0.05	67	558	0.396	0	...	...	13

[4] Fluences typically ±10%.

Also included in the table are four additional data sets from surveillance irradiations of modern, low copper Linde 80 weld metals. These additional data, which will not be employed in the modelling exercise, provide the opportunity to test the predictions of the model for low copper materials where the hardening is dominated by radiation damage alone.

Data from Heavy Section Steel Irradiation (HSSI) Series 2 and 3 programmes [2] on a number of similar Linde 80 welds, 61W-67W, has been used to provide tests at higher damage rates of predictions and correlations derived from the surveillance database. This provides a test of the sensitivity to so-called "rate effects" and provides an independent test of the predictive capability of the model parameters derived from the analysis of surveillance database.

PROPERTY CORRELATIONS

Property correlations are an integral part of most current approaches to facilitate understanding and prediction of irradiation embrittlement in reactor pressure vessels and their structural materials. While this is of value to extend databases and provide intercomparisons between disparate measurements, it can equally be counterproductive if the basis of the correlations is flawed or of dubious physical significance.

Most regulatory approaches still employ Charpy 30ft-lb (41J) transition temperature shift as a surrogate for static and dynamic fracture toughness shift because, historically, only Charpy specimens were used in the surveillance programmes of most existing plants. An increasing appreciation of the physical complexity of the nominally simple Charpy test is bringing into question the tenability of this approach. Unfortunately, at the present time there is insufficient irradiated fracture toughness data to provide clear guidance on alternatives to this approach and the tendency is to compensate for the large uncertainties by use of large margins in regulatory prescriptions for embrittlement prediction. It is noted that tensile specimens have been included in all surveillance capsules, but this information, which provides a more precise indication of irradiation hardening, has, until recently, been largely ignored.

In a similar vein, attempts to model irradiation embrittlement invariably concentrate on the physics of barrier hardening, characterised by the yield strength change accompanying irradiation. The latter modelling, often supported by high quality yield strength data for which good agreement can be obtained, is then translated into Charpy shift prediction using poorly supported correlation factors with large scatter due to the poorer relative quality of Charpy shift data. An alternative approach of linking the higher quality yield strength information directly to fracture toughness is being actively pursued and, though not the subject of the present study, consideration of property correlations in the present material might assist this process and is therefore presented here.

Transition Temperature Shift Parameters

The main transition temperature shift parameter employed for regulatory and research activities is the 30ft-lb (41J) shift. It is generally assumed that this should correlate linearly with shifts in lateral expansion indexed at the 35mils (0.9mm) level and the FATT at 50% shear (fibrosity). Comparisons between 30ft-lb and, respectively, lateral expansion and FATT shifts for the Linde 80 database are presented in FIG. 1 and 2 from which it is apparent that neither correlation is particularly good in this class of material. Of the two correlations, that with lateral expansion appears to be the closest (FIG. 1), though even here there is a general tendency for the lateral expansion shift to exceed the 30ft-lb shift. In the case of the FATT shift the opposite tendency is evident, namely the FATT shift is consistently less than the 30ft-lb shift, in many cases by more than 50°F (28°C).

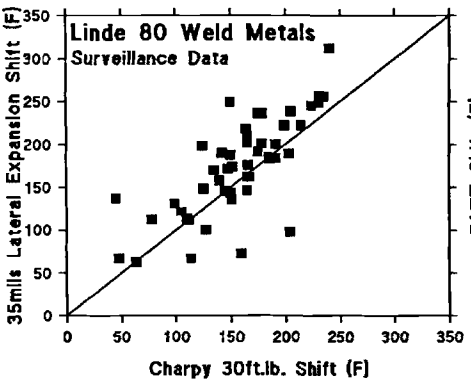


FIG. 1 Correlation between 35mils Lateral Expansion and Charpy 30ft.lb. Shifts for Linde 80.

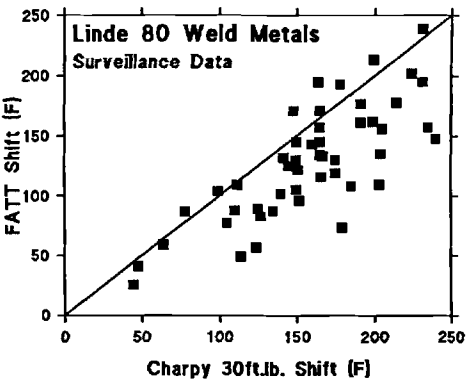


FIG. 2 Correlation between Fracture Appearance Transition Temperature (FATT) and Charpy 30ft.lb. Shifts for Linde 80.

It is instructive to pursue further the reason for the poor correlation between the various transition temperature shifts in the case of Linde 80 weld metals. At the root of this lies the nature of the transition addressed by the various definitions of transition temperature and the central issue of the already low unirradiated upper shelf energy and lateral expansion of the materials. This is best illustrated by the following example, which is quite typical of the behaviour exhibited for particular weld metals throughout the database. The example chosen is weld SA-1263 from the surveillance programme of Point Beach Unit 1, for which four irradiation capsules are available. Charpy data for this case are presented in FIG. 3, 4 and 5, respectively, showing the Charpy energy, lateral expansion and fracture appearance results and fitted tanh curves for each.

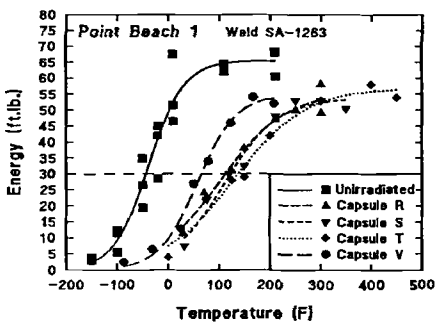


FIG. 3 Charpy Energy Curves for Weld Metal SA-1263 from Surveillance Programme of Point Beach 1.

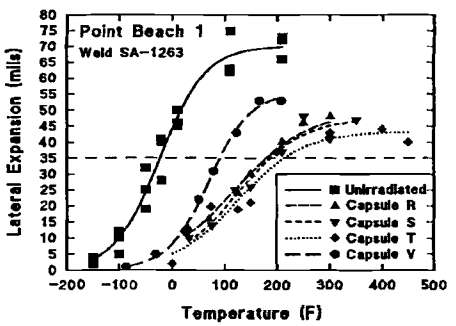


FIG. 4 Charpy Lateral Expansion Curves for Weld Metal SA-1263 from Surveillance Programme of Point Beach 1.

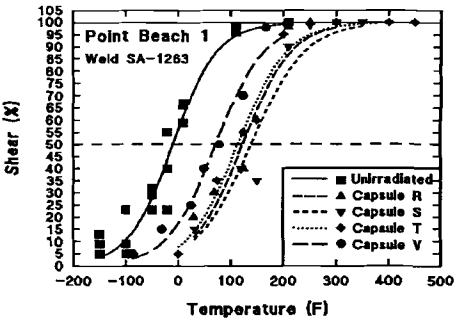


FIG. 5 Charpy Percent Shear Curves for Weld Metal SA-1263 from Surveillance Programme of Point Beach 1.

Both the Charpy energy and lateral expansion show familiar behaviour, namely the reduction in upper shelf level and reduction in slope in the transition region with irradiation. Indexation of the transition temperature at any arbitrary level will consequently provide different measures of irradiation shifts. Indeed it is even possible to set an indexing level where the difference between irradiations apparently disappears. The reason for the lateral expansion shift being greater than the 30ft-lb shift is now immediately obvious, namely the close proximity of the upper shelf lateral expansion to the indicated indexing level of 35mils in the heavily irradiated condition.

Fracture appearance, on the other hand, provides a much clearer representation of the transition behaviour, in that each curve is closely parallel to the others and shifted by a similar amount over the majority of the transition range. Such behaviour is consistent with the classical transition between two physical states, in this case fully brittle and fully ductile behaviour. Comparison of FIG. 3 and 5 indicates clearly the trend observed in FIG. 2, that the 30ft-lb shift will generally be greater than the FATT shift. This tendency is further exaggerated in those cases where the USE approaches the indexing level of 30ft-lb, as it does in some Linde 80 weld metals which exhibit reductions in irradiated USE to as low as 42ft-lb.

It is therefore concluded that the fracture appearance may provide a more physically meaningful description of ductile-brittle transition than either the Charpy energy or the lateral expansion, both of which are strongly influenced by the proximity of the upper shelf. Use of fracture appearance data has often been criticised for introducing larger scatter into transition temperature data than the use of absorbed energy, which it is argued can be measured to greater accuracy. Comparison of the standard deviations of 30ft-lb transition temperature and FATT for the present database shows that this is not generally true (FIG. 6), the FATT showing the lower scatter. This is probably a result of the constraints imposed on the fitting procedure, since the measurement of percent shear is highly subjective. Additionally, the accuracy of defining the transition is primarily determined by the frequency of measurements at varying temperature in the region of 0 and 100% shear rather than the measurement of absolute percent shear.

Finally, it is worth noting that the maintenance of the shape of the transition in fracture appearance is more in keeping with the assumed invariance of the shape of the ASME reference toughness curve with irradiation than is the gross change occurring in the shape of the absorbed energy curves usually employed to index the toughness shift. The latter gross changes might be expected to provide over conservative estimates of toughness shift in this class of low upper shelf material. This is an area which merits further theoretical and experimental investigation and one which could provide significantly reduced embrittlement predictions for this class of weld metal.

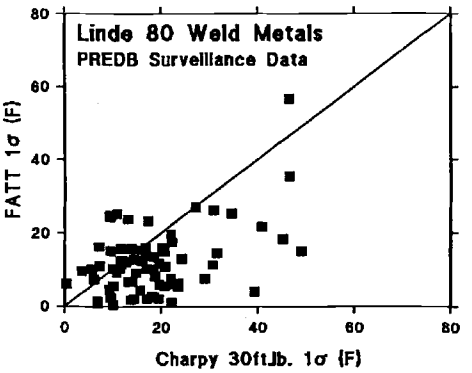


FIG. 6 Comparison of Standard Deviations from Charpy Energy and Percent Shear Curves for all Charpy Tests on Linde 80 Weld Metals in TABLE 1.

Transition Temperature Shifts and Yield Strength Change

The correlation of transition temperature shift with yield strength change due to irradiation is central to the modelling exercise which follows. It is therefore important to investigate the correlation for Linde 80 weld metal from the present database.

The variation of yield strength change with Charpy 30ft-lb shift is presented in FIG. 7 from which it can be concluded that an approximately linear correlation though with a large degree of scatter. The correlation between Charpy shift (ΔT) and the increase in yield strength ($\Delta\sigma$) generally given by

$$\Delta T/\Delta\sigma = F_1 \qquad \text{.....(1)}$$

where F_1 is a material constant in the range (0.5-0.7) $C.MPa^{-1}$ depending on product form (plate, weld or heat-affected zone). Linear regression of the data in FIG. 7 gave $F_1 = 0.73°C.MPa^{-1}$, which is somewhat higher than the $0.65°C.MPa^{-1}$ found by Odette et al [3] for all US RPV steel weld metals.

Following the above conclusions regarding FATT shift, the correlation with yield strength has been tested in this case also and this is presented in FIG. 8. Fitting to all the data gave $F_1 = 0.58°C.MPa^{-1}$ and $F_1 = 0.52°C.MPa^{-1}$ if the three apparent outlier points are excluded from the regression. Only one of the latter could be interpreted as an outlier in FIG. 7. The latter relation is represented by the line plotted in the figure and it is apparent that with the exception of the outliers the correlation is considerably less scattered (R=0.72) than for the 30ft-lb shift (R=0.62).

The principal reason for the poor correlations between yield strength change and Charpy shift parameters lies in the fact that they are essentially empirical in nature, with only a weak physical basis. The latter physical basis for the correlation arises from the effect of hardening on the temperature dependent yield strength in the presence of an irradiation insensitive, temperature independent fracture stress as expressed in the familiar Davidenkov diagram. Odette and coworkers [3] have studied this in some detail and concluded, from analysis of instrumented Charpy data, that the energy indexation level at which transition temperature shift should be adjudged should be about 10J (7ft-lb) instead of the 41J (30ft-lb) commonly employed. This is essentially a correlation based on a criterion for brittle fracture and corresponds to the point at which the Charpy energy rises from the lower shelf, at which point the general yield point corresponds to the critical fracture stress. The latter point is extremely difficult to define since it usually corresponds to the region of the Charpy transition curve at which least data is available and an energy

level which is within the material scatter and measurement accuracy. In this respect, the FATT probably provides the best indication due to the relative insensitivity of the transition curve shape to irradiation in this case, unlike those for Charpy energy and lateral expansion in which significant changes in shape occur.

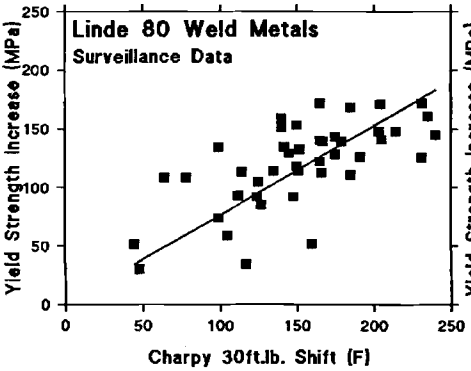


FIG. 7 Correlation between Charpy 30ft.lb. Shift and Yield Strength for Linde 80 Weld Metals.

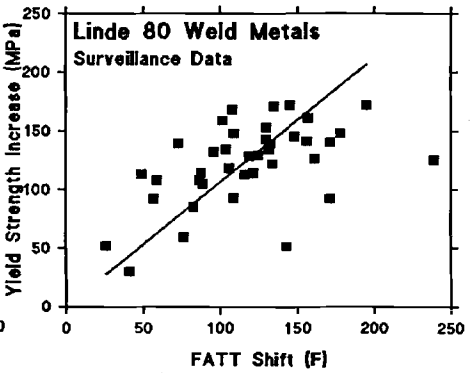


FIG. 8 Correlation between FATT Shift and Yield Strength for Linde 80 Weld Metals.

Other factors, such as the strain rate, probably contribute to the poor correlations, the tensile testing having generally been performed quasi-statically compared to the very high strain rates in Charpy testing. Additionally, yield strength is a simple, well defined material property of a material, whereas Charpy energy, lateral expansion and, to a lesser extent, fracture appearance are complex combinations of several material properties with considerably more scatter.

Notwithstanding the latter comment concerning FATT shift, it is suggested that this is a more representative indicator of toughness shift than either of the alternative Charpy shift parameters. However, for the purpose of modelling embrittlement, the first step is to describe irradiation hardening which is represented by the change in yield strength and it is with this that the main body of the paper, which follows, is concerned.

EMBRITTLEMENT MODELLING

Two well established and widely accepted models are available for irradiation embrittlement. These were developed independently at about the same time by Fisher et al [4] and Odette and coworkers [5-7], referred to in the following as the Fisher and Odette models respectively. Considerable parallel development of the original Odette model has also been performed by Williams and coworkers [8]. The essential features of the two models are similar in that irradiation embrittlement is postulated to arise from two principal irradiation hardening processes; matrix hardening, due to irradiation damage cluster/loop formation, and irradiation enhanced/induced precipitation of copper-rich particles. However, the models differ in detail particularly with respect to the matrix hardening component. The Odette et al [5-7] model has undergone considerable theoretical development over the intervening years [10] making it complex to use for trend curves, due the incorporation of sophisticated rate theory and cluster modelling features. The Fisher Model, on the other hand, has retained its essential simplicity and relies heavily on empirical and readily available information, particularly in relation to the matrix hardening component. It was

therefore decided to use the Fisher Model as the basis of the present embrittlement modelling activity and this model is described in detail below.

The Fisher Model

As with all such models, the starting point is an assumption that the irradiation induced embrittlement arises from the increase in yield strength of the material due to the introduction of obstacles to dislocation motion. It is further assumed that a simple proportionality exists between the irradiation induced increase in Charpy transition temperature shift (ΔT) and the increase in yield strength ($\Delta\sigma$) given by equation (1) above. The latter is principally an empirical correlation with large scatter and only a rather tenuous physical basis, as pointed out above. Consequently, it is best to apply the following physical barrier hardening model, wherever possible, if yield strength data is available, which it is for Linde 80 welds.

The net increase in yield strength, $\Delta\sigma_{tot}(t)$, assumed to arise from the linear superposition of two hardening components after irradiation time, t, is given by

$$\Delta\sigma_{tot}(t) = \Delta\sigma_{dam}(t) + \Delta\sigma_{Cu}(t) \qquad .....(2)$$

where $\Delta\sigma_{dam}(t)$ and $\Delta\sigma_{Cu}(t)$ are respectively the hardening induced by the accumulation of irradiation produced point defect clusters and radiation enhanced copper precipitation respectively.

The first component, $\Delta\sigma_{dam}(t)$, often referred to as the matrix damage term, is assumed to be dependent only on the total accumulated fast neutron fluence (ϕt), regardless of neutron flux (ϕ), and has the familiar square root of fluence dependence

$$\Delta\sigma_{dam}(t) = A\,(\phi t)^{1/2} \qquad .....(3)$$

where A is a parameter often referred to as the Barton coefficient since, in the Magnox steels analysis of Fisher et al [4], values for this parameter were obtained from the work of Barton et al [11]. It should be noted that the Barton coefficient will be a function of composition, particularly free nitrogen content, heat treatment and product form, irradiation temperature and, finally, neutron spectrum through its influence on effective displacement cross-section. Barton coefficients obtained in one reactor environment should be corrected when applied to another using the square root of the ratio of displacement cross-sections. This will not be necessary for the light-water reactor surveillance data in the present study, since neutron spectra are unlikely to vary appreciably.

A temperature dependence has recently been assigned to the matrix damage component [12] by including a temperature correction parameter, F_T, in equation (3)

$$\Delta\sigma_{dam}(t) = A\,F_T\,(\phi t)^{1/2} \qquad .....(4)$$

such that

$$F_T = 1.869 - 4.57\text{x}10^{-3}\,T \qquad .....(5)$$

where F_T has a value of unity at a temperature, T, of 190°C. The assumed square root dose dependency, Barton coefficient and the temperature dependence are all empirical parameters. The latter temperature correction has been shown to apply for a range of typical RPV plate and weld materials, but insufficient data is available to substantiate it for Linde 80 weld metals. It is therefore desirable to provide a firmer physical basis or alternative form for this component of the hardening.

The second component, $\Delta\sigma_{Cu}(t)$, generally referred to as the copper precipitation term, arises from the irradiation induced formation of fine copper precipitates of a size (~2nm) such that they produce maximum modulus hardening. This component may be calculated from the peak or maximum hardening

for the given copper content, the time to peak hardening and time dependence of hardening derived from empirical fitting to experimental thermal ageing data. This approach assumes that irradiation, while changing the rate of precipitation, does not change the underlying kinetics. It is noted here that the latter fitting procedure is potentially flawed in that recent microchemical analysis indicates that the peak hardening due to copper precipitation during thermal ageing corresponds to only 50-70% of the copper available for precipitation.

The peak hardening of ferrite due to copper precipitation is given by

$$\Delta\sigma_{Cu}^{max} = 4.5\text{x}10^3\ V_f^{1/2} - 90 \text{ (MPa)} \qquad \text{.....(6)}$$

where V_f is the volume fraction of copper. This differs slightly from the relationship in the original Fisher Model formulation, having recently been modified [12]. A detailed description of the radiation enhanced copper precipitation formalism has been presented extensively elsewhere [13] and will not be discussed further here.

Because thermal ageing data was fitted in the original formulation of the model, an overageing stage was included and it is this form that was used until recently. However, there is no strong evidence that an overageing stage exists during irradiation, so the latter term has not been included in the version of the model used here and in other recent assessments [12]. Instead, hardening is assumed to increase with time or dose to a plateau rather than a peak, the plateau level corresponding to $\Delta\sigma_{Cu}^{max}$. Recent SANS data supports this exclusion of an overageing stage [14].

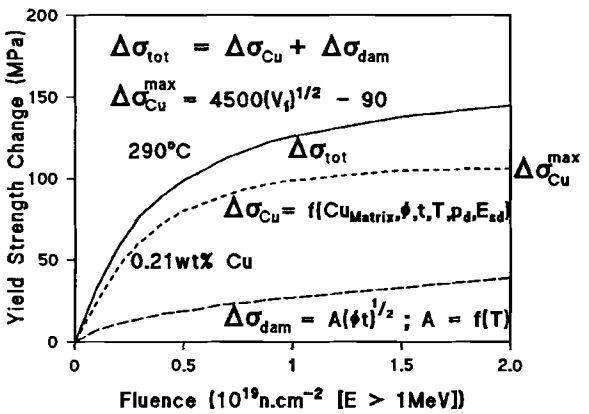


FIG. 9 Prediction of Embrittlement Model for a 0.21wt% Cu Steel Showing the Dose Dependence of the Matrix and Copper Precipitation Components.

The two components of the model are illustrated in FIG. 9 for irradiation of a steel with 0.21wt% copper content at 290°C. The saturation of the copper hardening component at the higher doses is apparent from the figure. The matrix hardening ($\Delta\sigma_{dam}$) following its root dose dependence does not saturate, though, at this temperature, it comprises a relatively small fraction of the total hardening. Based on this prediction, complete hardening saturation should not occur until significantly higher doses, though to a reasonable approximation it can be considered to have effectively occurred by the highest dose shown, which corresponds to the peak end-of-life dose of many reactor vessels. This will not be true at lower temperatures since the matrix hardening increases with decreasing temperature. At higher temperatures

the behaviour approaches more closely true saturation as the matrix hardening reduces further with increasing temperature.

MODELLING IRRADIATION HARDENING OF LINDE 80 WELD METAL

The above model has been applied to the data of TABLE 1 for all high copper weld metals by manual fitting using a spreadsheet, which permits detailed assessment of the effect and importance of all the possible model variables, and by non-linear least-squares fitting techniques. Within the model the following variables are identified as having significance and, while it is desirable to employ values which are physically realistic, within these limits they may be used as fitting parameters:

(1) Activation energy for diffusion ($E_m + E_f$);	range 2.4-2.6eV;
(2) Dislocation density (ρ_d);	range 1-5x10^{14}m^{-2};
(3) Effective displacement cross section (S_{eff});	range 200-2000barns;
(4) Matrix hardening Barton coefficient (A);	range 10-25.

Additionally, as will become apparent, the copper content employed in the model can be treated as a fitting parameter given certain constraints. It is known that for high copper materials the amount of copper in solid solution and thereby available for precipitation during irradiation can be significantly below the bulk copper content due principally to the limited solubility that exists at the post-weld heat treatment (PWHT) temperature. Excess copper, above the solubility limit, will be dispersed in coarse copper precipitates and take no part in the embrittlement process. Some copper, particularly in welds, may also be associated with inclusions, further reducing the amount of copper available in low and intermediate copper welds. Of the latter two factors, by far the most important is the effect of heat treatment and this will be considered in detail below.
An important parameter, not included in the summary TABLE 1, is the neutron flux. This was generally obtained by dividing the fluence by the elapsed time at full power and where, in a few cases, data was not readily available a default value (8x10^{10}ncm^{-2}s^{-1}) has been employed based on an average of the rest of the database.

High Copper Weld Metals

Bulk Copper Content

The first step in the current modelling process was to apply the model to hardening using the bulk chemical analysis values from the high copper database of TABLE 1 as input, in order to provide a baseline for subsequent comparisons. Manual and free data fitting was employed to assess the sensitivity to the above fitting parameters and determine their importance. It was found that allowing completely free fitting of the parameters resulted in unrealistic values, in particular, for displacement cross section and dislocation density. Since dislocation density is a well defined quantity it was decided to fix its value at 2.0x10^{14}m^{-2} a value typical of stress-relieved RPV steels. Similarly, it was decided to fix the value of the effective displacement cross-section to 1750barns, the average from a large database of surveillance dosimetry re-evaluations performed recently by Lippincott [15]. This leaves two fitting parameters, the activation energy and Barton coefficient, which were then optimised using the non-linear least-squares technique.

The resulting optimised model fit is compared with the measured yield strength increases in FIG. 10, together with the main curve fitting parameters. This comparison indicates that the data is reasonably well correlated with the model predictions but the scatter is significant particularly the overprediction at large yield strength changes. This is to be expected if the levels of soluble copper are significantly lower than the bulk copper content due to heat treatment effects. It is also noted that the Barton coefficient is lower than might be expected for this irradiation temperature range and again may reflect an

overprediction of the copper hardening component resulting from the use of bulk copper values. Never-the-less the agreement was sufficiently encouraging to justify more detailed assessment.

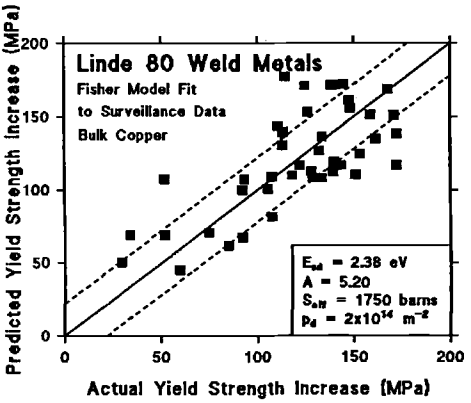


FIG. 10 Comparison of Measured and Predicted Yield Strength Increases Based on the Bulk Copper Content.

Soluble Copper Content

Recent measurements of equilibrium copper solubility at temperatures in the range 550-650°C in model steels using the Field Emission Gun Scanning Electron Microscope (FEGSTEM) [16] suggest that only 0.23±0.04wt% copper should be in solid solution at the nominal PWHT temperature, 1125°F (607°C), of all the weld metals in the present database. For the nominal range for PWHT, ±25°F (148°C), the amount of copper in solid solution could therefore vary between 0.16 and 0.29wt%, given the error of 0.04wt% in the analysis. Using this information as a guide to the possible range of dissolved copper in Linde 80 weld metals the manual fitting procedures employed earlier were performed. In this case an upper bound, Cu_{sol}, was set for the copper content used in the model, such that weld metals having bulk copper contents, Cu_{bulk}, greater than this level were assigned the bounding value and those containing lower bulk copper contents were assigned the bulk value, ie.

$$Cu_{bulk} < Cu_{sol}\,;\ Cu = Cu_{bulk}$$
$$Cu_{bulk} > Cu_{sol}\,;\ Cu = Cu_{sol}.$$

Constraining the effective displacement cross section and dislocation density as before the optimum fit to the data was obtained for a bounding solubility of 0.23wt% copper, the mean solubility from the FEGSTEM study. The much improved quality of the fit to the yield strength data is apparent from FIG. 11, where the fitting parameters are once again summarised. Also included on the figure is a band, actually ±22MPa, corresponding approximately to a ±1σ band on the fit to bulk copper data in FIG. 10, to illustrate the improved quality of the model fit to the data. Only two data points now lie significantly outside the correlation and these correspond to "outliers" in the Charpy-FATT correlation of FIG. 2. Furthermore the latter points constitute an overprediction of the model and not an underprediction. The model is therefore conservative in these cases.

The improved prediction based on the soluble copper content, rather than bulk copper content, suggests that hardening in Linde 80 weld metals is independent of copper content for copper contents in excess of about 0.23wt%, which constitutes the majority of welds in the database and, therefore, those welds of most concern regarding irradiation embrittlement shift. Earlier empirical studies [17,18] have suggested likewise. For example, in their recent study Lowe and Pegram [18] found that one of the best empirical Chemistry Factor fits to the data contained no bulk copper term. This prediction of the model should be tested by high resolution microchemical analysis techniques such as Atom Probe Field Ion Microscopy (APFIM) and/or Field Emission Gun Scanning Transmission Microscopy (FEGSTEM). This could be accomplished most efficiently on a small number of bounding materials identified by the present analysis. One such measurement [19], using APFIM, on a 0.31wt% Linde 80 weld metal indicated a soluble copper content of 0.21wt%, in fair agreement with the model prediction.

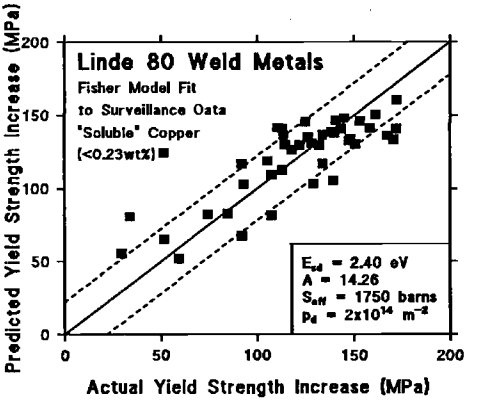


FIG. 11 Comparison of Measured and Predicted Yield Strength Increases Based on the Soluble Copper Content.

While the above agreement is impressive it is prudent to test the capability of the model to predict behaviour outside the database employed in the fitting procedures. Two such opportunities exist to accomplish this, as discussed below.

HSSI Series 2 and 3 Weld Metals

The HSSI Series 3 and 3 programme studied the irradiation response of a series of Linde 80 weld metals, designated 61W to 67W, in MTR irradiations at neutron fluxes more than an order of magnitude higher than in the average surveillance irradiation and at temperatures in the range 278-345°C. The summarised yield strength data is presented in TABLE 2.

The predictions of the model for the HSSI weld metals using the same modelling parameters as in FIG. 11 and similar input copper content procedure, namely Cu_{sol} = 0.23wt%, are compared with the experimental values in FIG. 12. It is apparent that the model provides as good a prediction as above for all but one of the data.

In addition to providing an independent test of the model, the latter good prediction of HSSI results at a significantly higher damage rate is consistent with the contention that a damage "rate effect" should arise from the irradiation enhanced copper precipitation process.

TABLE 2 - - Data from HSSI Series 2 and 3 Programmes

Weld Metal	Cu (wt%)	Temp (°C)	Fluence [E>1MeV] 10^{19}ncm^{-2}	$\Delta\sigma_y$ (MPa)
61W	0.28	345	0.78	100
61W	0.28	329	0.96	114
61W	0.28	325	0.70	103
61W	0.28	304	0.41	125
61W	0.28	288	1.48	151
61W	0.28	288	1.19	152
62W	0.20	290	1.38	129
62W	0.20	278	1.55	148
62W	0.20	303	0.82	103
62W	0.20	306	0.83	120
62W	0.20	310	1.10	102
63W	0.30	316	0.81	99
63W	0.30	288	0.38	127
63W	0.30	285	1.28	146
63W	0.30	310	0.90	121
63W	0.30	285	1.31	143
63W	0.30	303	0.72	116
64W	0.35	281	0.46	145
64W	0.35	289	0.24	129
65W	0.21	279	0.76	125
65W	0.21	287	0.20	105
66W	0.42	279	0.40	101
66W	0.42	281	0.87	137
67W	0.26	288	0.18	151

Low Copper Linde 80 Weld Metals

A further test of the model predictions can be made using the small quantity of low copper weld metal data included at the bottom of TABLE 1. In these weld metals, the copper hardening effect should be negligible and the hardening should be due solely to the matrix hardening, $\Delta\sigma_{dam}$. The yield strength increases for the four cases should be similar since the capsule fluences were very close to one another. Using the Barton coefficient derived in the above analysis and indicated in FIG. 11, the predicted yield strength increase lies in the range 14-16MPa, which is in agreement with the measured values, 12-13MPa. This agreement is particularly encouraging since the model parameters were derived for high copper material in which the copper hardening dominates the behaviour. The low level of matrix hardening implied by this prediction and confirmatory observation, amounting as it does to only 35MPa increase at near end-of-life doses of $2x10^{19}$ncm^{-2} (E>1MeV), and the saturation in precipitated copper below this dose, provide strong support for the concept of embrittlement saturation at high doses. This prediction of the model should be tested by confirming full copper precipitation using a combination of APFIM/FEGSTEM and small-angle neutron scattering (SANS) on bounding materials identified in the present analysis.

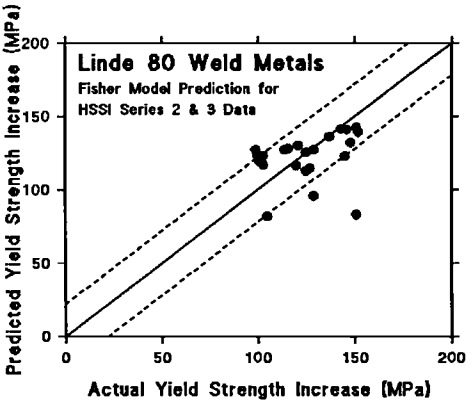


FIG. 12 Comparison of Measured and Predicted Yield Strength Increases for the HSSI Series Linde 80 Weld Metals Using the Optimised Model Parameters Based on Soluble Copper.

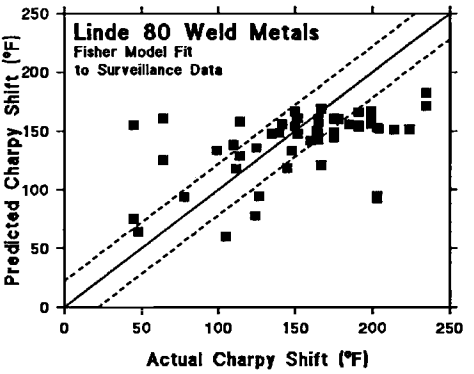


FIG. 13 Comparison of Measured and Predicted Charpy 30ft.lb. Shift Based on the Soluble Copper Content and Charpy-Yield Strength Correlation from FIG 1.

MODELLING IRRADIATION EMBRITTLEMENT OF LINDE 80 WELD METAL

The eventual objective of the present approach is to provide a model based prediction of embrittlement. At the present time this is achieved through correlations between yield strength change and Charpy shift which have been shown to be inadequate for the present weld metals, especially in the case of the 30ft-lb shift, which is the generally accepted parameter. Not surprisingly, this leads to considerable scatter in the predictions compared to the Charpy shift data, as is apparent from FIG. 13, for which the correlation parameter from FIG. 1 has been used. In addition to the much increased scatter, there is a strong tendency for underprediction at high shifts, which is consistent with the behaviour of 30ft-lb shift relative to FATT shift already commented upon above. In the absence of the latter observation, the underprediction of shift by the model might have been interpreted as the intervention of a so-called non-hardening embrittlement process in those cases where the underprediction is greatest. The FATT shift

should, however, also reveal a similar tendency and the fact that it does not rules out the latter possibility. It is concluded that the poor prediction of 30ft-lb Charpy shift is a consequence of the failure of Charpy data to correctly reflect the irradiation hardening process and the arbitrary nature of the Charpy indexation procedure, which is aggravated by the low USE of Linde 80 weld metals.

DISCUSSION

The success of the hardening model suggests that yield strength provides the most suitable starting point for modelling irradiation embrittlement. In the present case of Linde 80 weld metals, the inadequacies of the semi-empirical correlations with Charpy shift indicate that the present method based on 30 ft-lb Charpy shift is likely to be overconservative and, because of the large scatter in the correlation, is likely to lead to excessive margins. There are strong theoretical arguments for establishing a direct link between yield strength and fracture toughness transition temperature shift through the Ritchie-Knott-Rice [20] and other more recent deterministic and probabilistic microscopical fracture models. This could eliminate a significant source of scatter introduced by use of the present pseudo-physical correlation between true fracture toughness shift and Charpy shift. However, significant experimental verification and theoretical development is still required to reach this desirable position.

The present study suggests that in the case of Linde 80 weld metals 30ft-lb Charpy shift is probably overconservative and an alternative to the use of this parameter should be sought to minimise its impact on the safe, economic operation of nuclear plant in which this is the limiting weld material. An acceptable parameter is suggested by the present study, namely FATT. It is required by surveillance standards, such as ASTM E185, that fracture appearance data be taken, but its use in assessing the condition of RPV materials has largely been ignored, even though there is a strong historical and technical precedent for its universal usage instead of arbitrary energy or lateral expansion indexation procedures. In other situations, such as modern high upper shelf RPV steels there is evidence [21] that 30ft-lb Charpy shift is not conservative in respect of fracture toughness shift, in which case it has been found that FATT shift remains a more representative parameter. It is believed that the latter trend may be reversed for low upper shelf materials, the 30ft-lb shift being overconservative, but the FATT shift still providing a representative indication. Support for this view is contained in the detailed analysis of instrumented Charpy data by Fabry and coworkers [22].

CONCLUSIONS

Correlations between Charpy transition temperature shifts and yield strength, which best characterises the hardening behaviour of Linde 80 weld metals, were tested and it was concluded that FATT provided a less scattered and more representative indicator than either lateral expansion or Charpy energy indexed at 30ftlb. This is thought to be a consequence of the low USE and USLE of Linde 80 weld metals which distort the latter two transition temperatures, especially after irradiation which induces a significant reduction in upper shelf to levels approaching the indexing level. It is suggested that FATT provides a more representative indication of embrittlement for this class of material.

Excellent agreement was found between model predictions and the surveillance yield strength data following optimisation of the model parameters. Furthermore, applying the latter optimised form produced equally good prediction of HSSI results at a significantly higher damage rate demonstrating the "rate effect" inherent in the irradiation enhanced copper precipitation process. In the latter context best agreement was obtained assuming a soluble (matrix) copper content of about 0.23wt% in all cases consistent with recent solubility data and the reported PWHT for Linde 80 welds (10-50h at 1125$\pm$25°F). In other words, for these materials an insensitivity to bulk copper content was demonstrated even though the copper varied from 0.21-0.42wt%. Additionally, the parameters optimised for high copper welds provided a good prediction for modern low copper materials indicating that the matrix hardening

component had been correctly specified. The low level of matrix hardening indicated by this analysis provides strong support for the concept of embrittlement saturation at high doses in these high copper materials, where the hardening is dominated by the irradiation enhanced/induced precipitation of copper, which is predicted to saturate by doses of $1x10^{19}ncm^{-2}$.

REFERENCES

[1] W. Oldfield, ASTM Standardisation News, Vol. 14, No. 11, 1975, p.24.

[2] R.K. Nanstad and R.G. Berggren, "Irradiation Effects on Charpy Impact and Tensile Properties of Low Upper-Shelf Welds, HSSI Series 2 and 3", USNRC Report NUREG/CR-5696 (ORNL/TM-11804), August 1991.

[3] G.R. Odette, P.M. Lombrozo and R.A. Wullaert, "Relationship between Irradiation Hardening and Embrittlement of Pressure Vessel Steels", Effects of Radiation on Metallic Materials: 12th International Symposium, ASTM STP 870, F.A. Garner and J.S. Perrin, Eds., American Society for Testing and Materials, Philadelphia, 1985, pp. 840-860.

[4] S.B. Fisher, J.E. Harbottle and N. Aldridge, "Radiation Hardening in MAGNOX Pressure Vessel Steels", Phil. Trans. Roy. Soc. Lond., Vol. A 315, 1983, p.301.

[5] G.R. Odette, "On the Dominant Mechanism of Irradiation Embrittlement of Reactor Pressure Steels", Scripta Met., Vol. 17, 1983, p.1183.

[6] G.E. Lucas, G.R. Odette, P.M. Lombrozo and J. Sheckherd, "Effects of Radiation on Materials: 12th International Symposium", ASTM STP 870, F.A. Garner and J.S. Perrin, Eds., American Society for Testing and Materials, Philadelphia, 1985, p.900.

[7] G.R. Odette and G.E. Lucas (1986) "Radiation Embrittlement of Nuclear Reactor Pressure Vessel Steels: An International Review (Second Volume)", ASTM STP 870, L.E. Steele, Ed., American Society for Testing and Materials, Philadelphia, 1986, p.206.

[8] T.J. Williams, P.R. Burch, C.A. English and P.H.N. Ray, "Proc. Third International Symposium on Environmental Degradation of Materials in Nuclear Power Systems - Water Reactors", G.J. Theus and J.R. Weeks, Eds., The Metallurgical Society, Warrendale, PA., 1988, p.121.

[9] T.J. Williams and W.J. Phythian, "Electron Microscopy and SANS Study of the Effect of Irradiation Dose and Dose Rate on Copper Precipitation in Low Alloy Steel Submerged-Arc Welds", Effects of Radiation on Materials: 17th International Symposium, ASTM STP 1270, David S. Gelles, Randy K. Nanstad, Arvind S. Kumar and Edward A. Little, Eds., American Society for Testing and Materials, Philadelphia, 1996, this volume.

[10] G.R. Odette, "Neutron Irradiation Effects in Reactor Pressure Vessel Steels", L.M. Davies, Ed., IAEA Technical Series, to be published.

[11] P.J. Barton, D.R. Harries and I.L. Mogford, "Effects of Neutron Dose Rate and Irradiation Temperature on Radiation Hardening in Mild Steels", J. Iron Steel Inst., Vol. 203, 1965, p.507.

[12] J.T. Buswell and R.B. Jones, "The Modelling of Radiation Hardening and Embrittlement in MAGNOX Mild Steel Submerged-Arc Welds", Effects of Radiation on Materials: 16th International Symposium, ASTM STP 1175, A.S. Kumar, D.S. Gelles, R.K. Nanstad and E.A. Little, Eds., American Society for Testing and Materials, Philadelphia, 1993, pp.424-443.

[13] R.J. McElroy, T.J. Williams, F.M.D. Boydon and B. Hemsworth, "Low Temperature Embrittlement of LWR RPV Support Structures", Int. J. Pres. Ves. & Piping, Vol. 54, 1993, pp.171-211.

[14] Buswell, J.T., Bischler, P.J.E., Fenton, S.T. and Ward, A.E., "Microstructural Developments in Neutron-Irradiated Mild Steel Submerged-Arc Weld Metal", J. Nucl. Mat., Vol. 205, 1993, pp.198-205.

[15] E.P. Lippincott, "Westinghouse Surveillance Capsule Neutron Fluence Reevaluation", WCAP-14044, April 1994.

[16] W.J. Phythian, AEA Technology, Harwell, private communication, 1994.

[17] A.L. Lowe, Jr., "Irradiation Characterisation of Wire Heat Number 72105", Effects of Radiation on Materials: 15th International Symposium, ASTM STP 1125, R.E. Stoller, A.S. Kumar and D.S. Gelles, Eds., American Society for Testing and Materials, Philadelphia, 1992, pp. 292-308.

[18] A.L. Lowe, Jr. and J.W. Pegram, "Improved Correlations for Predicting the Effects of Neutron Radiation on Linde 80 Submerged-Arc Weld Metals", Effects of Radiation on Materials: 14th International Symposium, ASTM STP 1046, N.H. Packan, R.E. Stoller and A.S. Kumar, Eds., American Society for Testing and Materials, Philadelphia, 1990, pp. 234-250.

[19] W.S. Pavinich and L.S. Harbison, "Microstructural Characterisation and Modelling of Radiation Embrittlement of Linde 80 Reactor Vessel Welds", Effects of Radiation on Materials: 17th International Symposium, ASTM STP ####, David S. Gelles, Randy K. Nanstad, Arvind S. Kumar and Edward A. Little, Eds., American Society for Testing and Materials, Philadelphia, 199#, this volume.

[20] R.O. Ritchie, K.F. Knott and J.R. Rice, "On the Relationship between Critical Fracture Stress and Fracture Toughness in Mild Steel", J. Mech. Phys. Solids, Vol. 21, 1973, pp. 395-410.

[21] R.J. McElroy, A.J.E. Foreman, G. Gage, W.J. Phythian, P.H.N. Ray and I.A. Vatter, "UK Contribution to the IAEA Phase 3 Coordinated Research Programme on Optimisation of Reactor Pressure Vessel Surveillance Programmes and their Analysis", AEA Technology Report AEA-RS-2426, December 1993.

[22] R. Gerard, A. Fabry, J. Van de Velde, J. Puzzolante, A. Verstrepen, T. Van Ransbeeck and E. van Walle, "In-Service Embrittlement of the Pressure Vessel Welds at the Doel I and II Nuclear Plants", Effects of Radiation on Materials: 17th International Symposium, ASTM STP 1270, David S. Gelles, Randy K. Nanstad, Arvind S. Kumar and Edward A. Little, Eds., American Society for Testing and Materials, Philadelphia, 1996, this volume.

Randy G. Lott[1] and Paula D. Freyer[1]

MODELING OF IRRADIATION EMBRITTLEMENT AND ANNEALING/RECOVERY IN PRESSURE VESSEL STEELS

REFERENCE: Lott, R. G. and Freyer, P. D., **"Modeling of Irradiation Embrittlement and Annealing/Recovery in Pressure Vessel Steels,"** *Effects of Radiation on Materials: 17th International Symposium, ASTM STP 1270,* David S. Gelles, Randy K. Nanstad, Arvind S. Kumar, and Edward A. Little, Eds., American Society for Testing and Materials, 1996.

ABSTRACT: The results of reactor pressure vessel (RPV) annealing studies are interpreted in light of the current understanding of radiation embrittlement phenomena in RPV steels. An extensive RPV irradiation embrittlement and annealing database has been compiled and the data reveal that the majority of annealing studies completed to date have employed test reactor irradiated weldments. Although test reactor and power reactor irradiations result in similar embrittlement trends, subtle differences between these two damage states can become important in the interpretation of annealing results. Microstructural studies of irradiated steels suggest that there are several different irradiation-induced microstructural features that contribute to embrittlement. The amount of annealing recovery and the post-anneal re-embrittlement behavior of a steel are determined by the annealing response of these microstructural defects. The active embrittlement mechanisms are determined largely by the irradiation temperature and the material composition. Interpretation and thorough understanding of annealing results require a model that considers the underlying physical mechanisms of embrittlement. This paper presents a framework for the construction of a physically based mechanistic model of irradiation embrittlement and annealing behavior.

KEYWORDS: pressure vessel steel, irradiation, embrittlement, annealing, recovery, models, microstructure, mechanisms, coarsening, microhardness, precipitates

1.0 INTRODUCTION

As U.S. commercial nuclear power plants continue to age, causing the material properties of some reactor pressure vessel steels (RPV) to slowly degrade, thermal annealing the reactor pressure vessel has become an increasingly more attractive option. Although many technologies are available to slow the rate of vessel embrittlement, thermal annealing is the only viable option that restores the material properties, i.e., Charpy upper shelf energy (USE) and ductile-to-brittle transition temperature (DBTT) of an already embrittled vessel. Restoration of vessel material properties not only relaxes restrictions on vessel operating pressure and temperature limits, it also relieves immediate concerns regarding vessel performance during postulated pressurized thermal shock transients.

[1]Senior engineer/scientist and engineer/scientist, respectively, Westinghouse Science and Technology Center, 1310 Beulah Road, Pittsburgh, PA 15235, USA.

Copyright© 1996 by ASTM International www.astm.org

It has been repeatedly demonstrated that thermally annealing irradiated RPV steels at temperatures 100-150°C above the irradiation temperature recovers most of the degraded mechanical properties of the material [1,2,3,4]. The effectiveness of the anneal and the materials' post-anneal behavior upon reirradiation depend on a large number of factors including the irradiation temperature, the annealing temperature, the time at annealing temperature, the material form and the material composition. Because RPV annealing programs cannot rely solely on surveillance data due to the impracticality of compiling comprehensive sets of data on annealed materials, the ability to reliably predict the post-anneal properties of irradiated steels is a critical factor in the consideration and implementation of RPV thermal annealing. To accurately predict anneal and post-anneal material behavior, the development of models that incorporate all of the major influencing factors is essential.

2.0 THE DATABASE FOR ANNEALING STUDIES

To provide the foundation for advanced modeling efforts, a computerized database of embrittlement, annealing and reembrittlement data was compiled by combining data from a comprehensive literature review with existing computerized databases on embrittlement. This strategy of combining new data with existing Westinghouse databases, and the Oak Ridge National Laboratory PR-EDB Database [5] produced an extensive database containing information from over 2200 test cases. The database was constructed using an effective relational database and consists of nine interrelated tables of data that include various material types, irradiation conditions, and anneal conditions. The database currently contains approximately 475 different materials (including plate, forging, and weld material), 480 different irradiation conditions, i.e., various combinations of fluence and irradiation temperature, and 26 different anneal conditions, i.e., various combinations of anneal time and temperature. Specifically, the database includes material properties and data, i.e., material chemistries, upper shelf energies, ductile-to-brittle transition temperatures, irradiation sources (test vs. power), etc., for the first, second, and third irradiation states, and for the first and second anneal states. These data are provided in a format that can be used to test existing models of embrittlement and annealing and to develop new models.

3.0 MODELING STRATEGY

The modeling strategy incorporated the development of three separate models: 1.) irradiation embrittlement, 2.) annealing recovery, and 3.) reirradiation embrittlement. The objective of this effort was to develop models that are consistent with current industry practice for predicting irradiation embrittlement, i.e., the industry standard for the prediction of changes in the Charpy transition temperature per US NRC Regulatory Guide 1.99 Rev. 2 [6]. In addition, the models must incorporate recent data on embrittlement and embrittlement mechanisms. The irradiation embrittlement and annealing models developed in this study are based on the form outlined in the Regulatory Guide.

Two limiting cases for reirradiation embrittlement were originally proposed by Server and Taboada [7]. These two cases, which are included in ASTM Standard Guide for In-Service Annealing of Light Water Cooled Nuclear Reactor Vessels (E509-86) [8], are generally described as the lateral shift model and the vertical shift model. A lateral shift in the prediction curve results in a post anneal embrittlement rate that reflects the high rates normally observed in the early stages of irradiation. With a vertical shift model, annealing results in a permanent downward (vertical) shift in the embrittlement trend curve causing no change between the embrittlement and reembrittlement rates. These lateral and vertical shift models provide upper and lower bound estimates, respectively, for the reirradiation embrittlement rate. Both cases describe the state of the annealed and reirradiated material in terms of existing pre-anneal embrittlement trend curves. This strategy of using existing pre-anneal embrittlement trend curves to develop annealing response and reembrittlement trend curves was also used in this study.

4.0 DATA ANALYSIS AND TREND CURVE DEVELOPMENT

4.1 Irradiation Embrittlement

4.1.1 Evaluation of NRC Reg. Guide 1.99 Rev. 2

The annealing and reirradiation response of nine pressure vessel steel weldments has been extensively reported in the literature [9,10,11,12,13]. These particular welds were selected from the database for detailed studies because the complete irradiation, annealing, and reirradiation histories were available. The compositions of these materials are listed in Table 1. Although these weldments are representative of a critical set of materials that are relevant to annealing in several reactor vessels, they are all also representative of a relatively narrow class of high copper, radiation sensitive steels. Recent observations that radiation sensitivity is determined by the amount of copper in solution at the onset of irradiation rather than by the gross copper content of the steel [14] suggest that increasing the copper content beyond the solubility limit at the post weld heat treatment temperature (approximately 0.3%) will have little effect on the radiation sensitivity. Therefore, the range of radiation sensitivity in these steels may be much smaller than originally expected.

Table 1. Compositions (wt %) of Pressure Vessel Steel Weldments

Weld Flux	Weld	Cu	P	C	Mn	S	Si	Ni	Cr	Mo	Sn
Linde 80	EP19	0.40	0.005	0.12	1.36	0.013	0.50	0.59	0.044	0.45	...
Linde 80	EP23	0.23	0.007	0.12	1.40	0.013	0.50	0.59	0.044	0.45	...
Linde 0091	EP24	0.35	0.005	0.16	1.30	0.010	0.17	0.59	0.039	0.442	...
Linde 80	W8A	0.37	0.010	0.079[1]	1.27	0.012	0.71	0.55	0.10	0.42	0.002
Linde 0091	W9A	0.35	0.008	0.191[1]	1.21	0.005	0.23	0.64	0.10	0.49	0.003
Linde 80	WW7	0.35	0.013	0.08	1.56	0.008	0.60	0.10	0.12	0.54	0.002
Linde 124	WW4	0.16	0.013	0.08	1.38	0.018	0.49	0.65	0.10	0.44	0.004
Linde 1092	V84	0.35	0.013	0.14	1.56	0.011	0.14	0.62	0.03	0.53	...
Linde 80	V86	0.35	0.016	0.08	1.60	0.013	0.55	0.69	...	0.40	...

[1] minimum value

These nine weldments have all been irradiated in test reactors at fast neutron fluxes approximately 100 times higher than that normally experienced in reactor surveillance programs. To ascertain the effects of this higher flux on the embrittlement of these materials, the shifts in ductile-to-brittle transition temperatures predicted by Reg. Guide 1.99 Rev. 2 were compared to the measured values contained in the database. The results of this comparison are presented in Figure 1, where the data have been plotted as a function of fast neutron fluence. As expected, the prediction residuals are evenly distributed around zero for the surveillance materials showing that the Reg. Guide model accurately predicts the DBTT for materials irradiated in power reactors. However, it is equally evident that the Reg. Guide consistently over-predicts the embrittlement in the nine test reactor irradiated weldments. Because available annealing and reembrittlement data have been obtained using test reactor irradiations and the application of the reembrittlement prediction procedure requires an accurate embrittlement trend curve, it was necessary to develop a new model and modified trend curve for the test reactor irradiated materials.

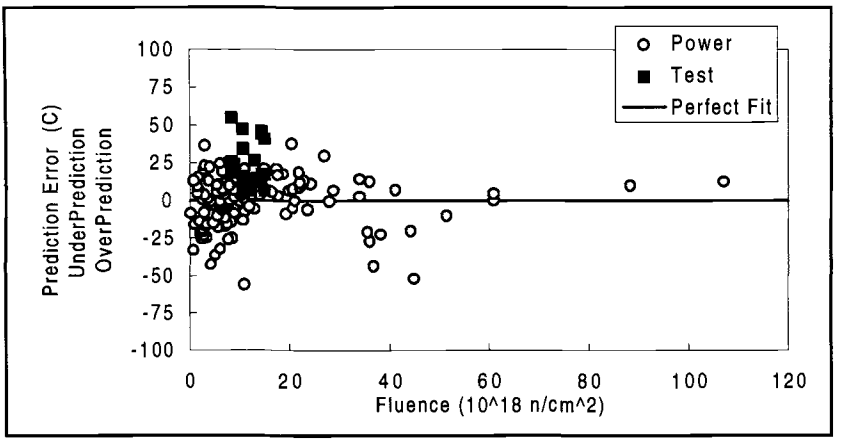


Figure 1. Reg. Guide 1.99 Rev. 2 Predictions for Transition Temperature Shifts of Welds for Test and Power Reactor Irradiations

4.1.2. Modification of NRC Reg. Guide for Test Reactor Data

The test reactor data contained in the database was fit using the fluence factor provided in Reg. Guide 1.99 Rev. 2. Effective chemistry factors were determined for each material by dividing the observed shifts by the fluence factor calculated in the Regulatory Guide. Multiple linear regressions were performed on a series of models with different combinations of compositional variables to determine a reasonable predictive equation for the test reactor data. With this new model for the effective chemistry factor, the transition temperatures were predicted by an equation of the form:

$$\Delta T = (A_0 \cdot Cu + A_1 \cdot Cu \cdot Ni + A_2 \cdot Si) \cdot \phi t^{(0.28-0.1\log(\phi t))} \quad (1)$$

where

A_0, A_1, A_2 = fitting constants

As indicated in Figure 2, this equation provides a reasonable estimate of the shift for the test reactor data contained in the database and, as expected, under-predicts the power reactor data. Although it has been suggested that the fluence dependence of embrittlement may be different in high flux irradiations, [15] the amount of available test reactor data is not currently sufficient to evaluate this effect. These trend curves, with modified chemistry factors, were the basis for further analysis.

4.2 Annealing Response Model

The effectiveness of annealing may be expressed as the percentage recovery, R, of the shift in transition temperature. The recovery is defined as:

$$R = 100\left(1 - \frac{\Delta T_a}{\Delta T_i}\right) \quad (2)$$

where

ΔT_i = Charpy shift prior to annealing
ΔT_a = Charpy shift after annealing

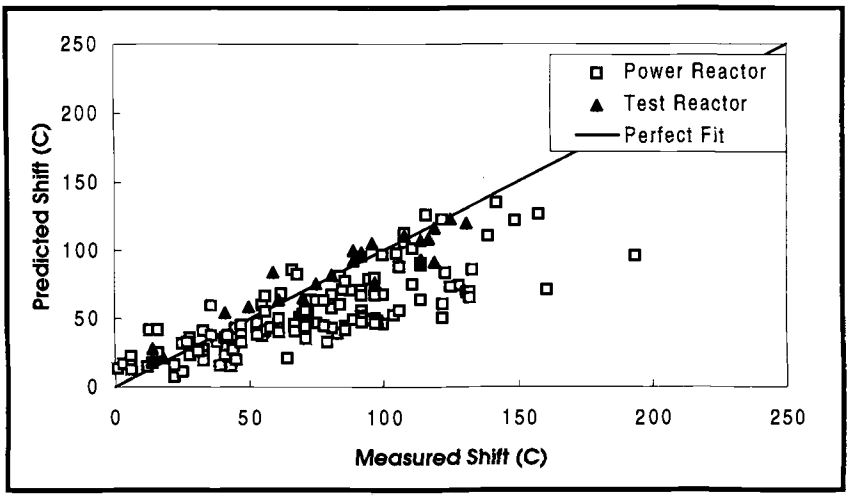


Figure 2. Modified Chemistry Factor Model Applied to Weld Materials for Test and Power Reactor Irradiations

The response of the nine weldments for one week anneals can be described as a linear function of annealing temperature. Although there is considerable scatter in the data, no other significant variables other than annealing temperature were found to affect recovery. This response is in agreement with a previous Westinghouse study where a similar linear function was used to describe the annealing response of microhardness values [16].

Although a simple linear function can be used to fit the observed shifts in transition temperature, it is informative to consider how the assumption of multiple annealing mechanisms might affect the analysis of the same set of data. In a series of isochronal annealing studies, Pachur [17,18] has demonstrated that four distinct annealing stages are present in pressure vessel steels irradiated at 150°C. Recovery of each defect type followed the relationship:

$$R_n = R_{no} e^{\{-\lambda_o t e^{(-U_n/kT)}\}} \quad (3)$$

where

R_{no} = contribution of mechanism n to recovery
λ_o = frequency factor (1.4×10^{10}/sec)
U_n = activation energy for mechanism n
t = annealing time
T = annealing temperature

Each of the four defect types and hence, each annealing stage is characterized by an activation energy for annealing, i.e., 1.5 eV, 1.68 eV, 1.85 eV and 2.06 eV. At an irradiation temperature of 290°C, the first two types of defects are thermally unstable and only the two high activation energy stages are subsequently observed during annealing. The absence of the first two annealing stages at this higher irradiation temperature may be attributed to the recovery of microcavities and vacancy complexes during irradiation. Positron annihilation (PA) results support this presumption since these two defect types have been observed in steels irradiated at 150°C, but not in steels irradiated at 290°C [18]. The activation energy for the third stage of annealing is apparently a function of the

irradiation fluence, increasing from 1.85 eV at 10^{19} n/cm^2 to 1.91 eV at 10^{20} n/cm^2. This third annealing stage is active at annealing temperatures between 350°C and 400°C.

Calculations based on Pachur's parameters would predict complete recovery of the most stable, high activation energy mechanism after 168 hours at 400°C. The measured annealing data does not show complete recovery under these anneal conditions; therefore, an additional component of annealing must be present which is not included in Pachur's analysis. Insight into this additional component can be obtained from small-angle neutron scattering (SANS) results which indicate that, in addition to the dissolution of small defects, there is coarsening of the precipitate size distribution and a possible evolution in the composition and structure of the precipitates. This coarsening may be described by a bulk diffusion controlled Ostwald ripening model [12]. For a constant precipitate volume, the precipitation hardening of the material is roughly proportional to the inverse of the precipitate radius. For this copper coarsening portion of the embrittlement, the particle growth kinetics should then follow the form:

$$r_a^3 - r_i^3 = Kt_a \tag{4}$$

where

r_i = radius of precipitate in irradiated material

r_a = radius of precipitate in annealed material

t_a = annealing time

$K = \dfrac{8\gamma D\omega C_o}{9kT}$

where

γ = precipitate/matrix interfacial surface energy

ω = atomic volume of precipitate

C_o = concentration of copper in solution

D = copper diffusion coefficient

k = Boltzmann's constant

T = annealing temperature

This copper coarsening model requires estimates of the diffusion coefficient D, the copper solubility C_o, and the interfacial energy γ, at the annealing temperature of interest. Although there are no reliable measurements of these values at typical annealing temperatures, which are in the range of 350°C to 450°C, it is possible to make reasonable estimates from high temperature measurements. The diffusion coefficient and copper solubility may be estimated from the measurements of Salje and Feller-Kniepmeier [19]. However, to fit the annealing data, a slight adjustment in the activation energy for diffusion is required (from 68 kcal/mole to 60 kcal/mole). Such a decrease in activation energy has previously been attributed to the presence of excess vacancies during studies of heavily cold worked Fe-Cu alloys [20]. The interfacial surface energy is estimated as 100 erg/cm^2, using procedures originally outlined by Goodman and colleagues [21].

By combining Pachur's annealing model with the copper coarsening model, the total annealing response of the pressure vessel steels weldments under investigation in this study can be approximated. If it is assumed that 1/3 of the recovery can be attributed to the Pachur dissolution mechanisms and 2/3 of the recovery can be attributed to copper precipitate coarsening, recovery should follow the form:

$$R = 100\left[0.33\left(e^{\left\{-\lambda_o te^{(-1.91/kT)}\right\}} + e^{\left\{-\lambda_o te^{(-2.06/kT)}\right\}}\right) + 0.67\left(\frac{r_i}{\left(Kt_a + r_i^3\right)^{1/3}}\right)\right] \tag{5}$$

This multi-component annealing model is compared to the annealing data in Figure 3. Although this model provides no better fit than the simple linear function discussed previously, it is certainly consistent with the data. In addition, the form of this model is in

agreement with numerous microstructural studies that suggest that multiple embrittlement mechanisms are operative in these steels. Due to the large extent of scatter in the data, refinement of the fitting constants beyond the simple 1:2 ratio implied here is not justified.

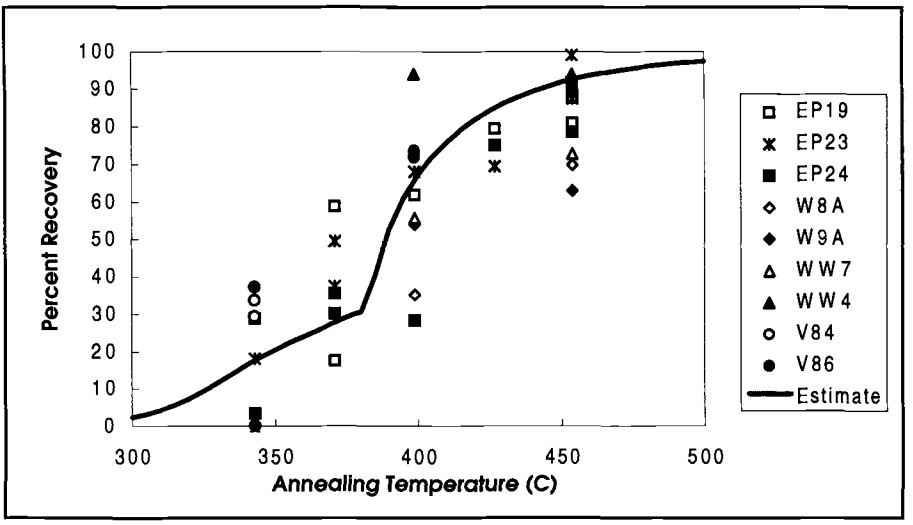


Figure 3. Annealing Response of Weldments Showing Multi-Component Annealing Model Fit

To test this multi-component annealing model, Equation 5 was used to re-evaluate microhardness annealing results previously reported by Westinghouse for welds EP-19, EP-23, and EP-24 [11]. The comparison between these microhardness data, which are contained in the database, and the multi-component annealing model predictions are summarized in Figure 4. In this particular microhardness study, anneals were conducted at 315°C, 371°C and 427°C. At each temperature, the initial recovery was apparently rapid, with little additional recovery occurring between 20 and 168 hours. The multi-component annealing model described by Equation 5 predicts that at 371°C, recovery of the Pachur mechanisms is rapid and no significant recovery of the copper coarsening component is expected. Therefore, the recovery at 371°C should approach 33% in the early stages of annealing, as is indicated from the measured data shown in Figure 4. At 427°C, copper precipitate coarsening contributes to embrittlement and Equation 5 predicts approximately 80% recovery after annealing for 168 hours. As can be seen from Figure 4, the model prediction again matches the observed microhardness data trends relatively well. At 315°C, a small radiation anneal hardening (RAH) peak (an increase in hardness during the initial stages of post irradiation annealing) was observed after 1 hour. Following the RAH peak, very little additional recovery was observed. Again, the multi-component model predicts the observed data trends relatively well.

4.3 Reembrittlement Model

Previous Westinghouse annealing and reembrittlement models developed by Lott and Mager [12] were based upon the assumption that annealing can be attributed to coarsening of irradiation produced copper precipitates. Copper precipitate coarsening results in a stable microstructure after annealing by immobilizing the copper in large

precipitates. In this way, the Cu is not able to further contribute to the embrittlement of the material following an anneal. Precipitate coarsening should therefore result in a vertical shift in the embrittlement trend curve. Ensuing analyses of microhardness data [22] led to the development of semi-empirical models of embrittlement and reirradiation embrittlement that incorporated many of the features of the copper coarsening model, but assumed that there was a second additional embrittlement mechanism. The annealing and reembrittlement semi-empirical model assumed that 80% of the embrittlement resulted from copper precipitation that recovered by coarsening and 20% of the embrittlement resulted from a second mechanism that was easily recovered during annealing, but quickly reestablished during subsequent irradiation.

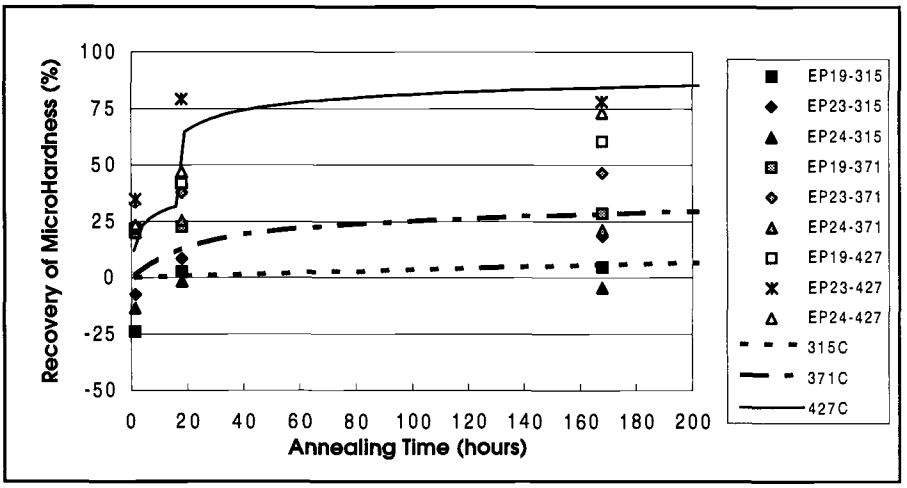


Figure 4. Multi-Component Model Fit to Microhardness Recovery of Weldments Following Annealing

The form of the newly developed multi-component annealing model, as presented in Equation 5, suggests that the 80%-20% split outlined in the original semi-empirical annealing and reembrittlement model might more properly be described as a 67%-33% split where the copper coarsening component causes a vertical shift in the embrittlement curve. Although the exact nature of the microstructural features related to Pachur's annealing mechanisms is not known, it seems reasonable to assume that they do not recover by coarsening and that reembrittlement of this component occurs by a lateral shift of the embrittlement curve. In this case, the relative contributions of lateral shifts and vertical shifts to the reembrittlement curves is a function of the annealing temperature. The vertical shift fraction (VSF) and lateral shift fraction (LSF) can be determined by examining Equation 5 to determine the contribution of each factor to annealing. Figure 5 illustrates the dependence of LSF and VSF on the annealing temperature for a series of one week anneals. For example, annealing at low temperatures (<380°C) results in a lateral shift of the annealing curve while annealing at higher temperatures results in a combination of lateral and vertical shifts.

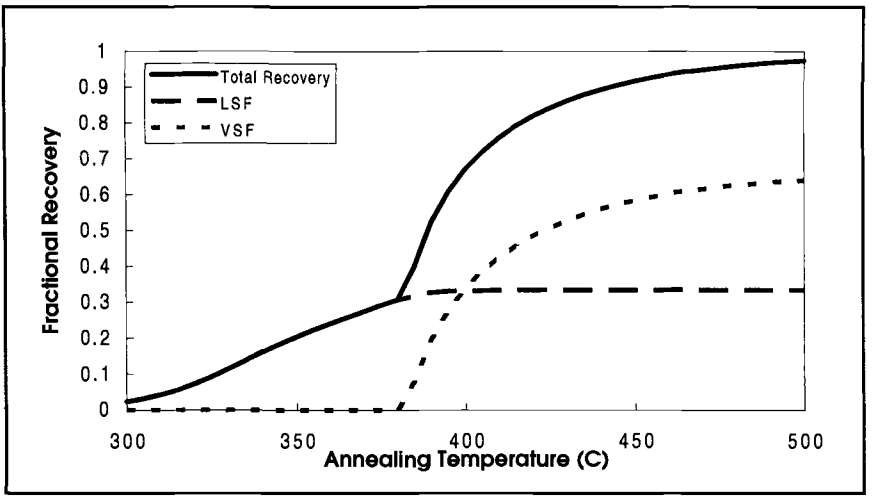


Figure 5. Dependence of Lateral Shift Factor (LSF) and Vertical Shift Factor (VSF) on Annealing Temperature

The post anneal embrittlement curve is determined from the sum of the vertical shift (ΔT_{VS}) and lateral shift (ΔT_{LS}) contributions. The shift after irradiation (i), annealing (a), and reirradiation (r) should then be:

$$\Delta T_{iar} = \Delta T_{VS} + \Delta T_{LS} \quad (6)$$

The individual lateral and vertical shift contributions can be expressed in terms of the original embrittlement curve. According to the multi-component annealing model, 67% of the reembrittlement should follow the vertical shift model. In this case, the post anneal shift in transition temperature is:

$$\Delta T_{VS} = 0.67\Delta T_{ii} - VSF\Delta T_i \quad (7)$$

where

ΔT_{VS} = contribution of copper precipitation to shift
ΔT_i = shift prior to anneal
ΔT_{ii} = shift predicted with continued irradiation and no anneal
VSF = vertical shift factor

For the determination of the lateral shift contribution to the reembrittlement trend curve, the fluence necessary to produce a state of embrittlement equivalent to the annealed material is required. As described previously, the shape of the embrittlement curves used in this study is determined by the fluence factor as outlined in NRC Regulatory Guide 1.99 Rev. 2. At the equivalent fluence for the annealed material, ϕt_s, the remaining fraction of embrittlement should equal the fraction of the fluence factor such that:

$$\frac{(0.33 - LSF)}{0.33} = \frac{F(\phi t_s)}{F(\phi t_i)} \quad (8)$$

where

LSF = lateral shift factor
ϕt_s = equivalent fluence for annealed material
ϕt_i = fluence at point of anneal
$F(\phi t) = \phi t^{(0.28-0.1\log(\phi t))}$ where fluence is in units of 10^{19}n/cm^2

The equivalent fluence, ϕt_s, may be determined either graphically or by examining a fluence factor table. The lateral shift contribution to reembrittlement is then:

$$\Delta T_{LS} = 0.33(CF)F(\phi t_s + \phi t_{ii} - \phi t_i) \quad (9)$$

where

CF = chemistry factor from Reg. Guide
ϕt_{ii} = irradiation fluence + reirradiation fluence

The predicted values of ΔT_{jar}, obtained from equation 6, are compared to the measured values in Figure 6. It is important to note that these predictions are based on the assumptions outlined above, with no additional fitting parameters required for the reembrittlement data. The prediction errors are plotted as a function of annealing temperature in Figure 7; most of the measured data fall within ± 20°C of the predicted values. In addition, the data continue to show a significant long term benefit of annealing.

5.0 DISCUSSION

5.1 Embrittlement Model

The analysis of the radiation embrittlement data in this program required the development of a separate prediction curve for test reactor irradiated welds because industry standard trend curves developed on the basis of reactor surveillance program materials consistently over-estimate the embrittlement in test reactor irradiated materials. Guthrie and Simonen [23] reached a similar conclusion in an analysis of a NRC developed database. Because the differences between the Regulatory Guide prediction and the measured test reactor data fall within the normal scatter band for this type of Charpy data, the over-prediction of the test reactor shifts is not apparent unless the test data are observed as a group and not on a single data point basis. Therefore, comparisons of individual pairs of test reactor and surveillance capsule data points (i.e., same material irradiated to the same fluence in both test and power reactors) may be misleading since the power reactor shift may, in some instances, be greater than the test reactor shift.

To investigate the fluence rate dependence of embrittlement, several flux effect studies have been conducted. For instance, Amayev et al. [24] noted that increasing the neutron flux from $4x10^{11}$ n/cm^2•s to $4x10^{12}$ n/cm^2•s (E > 0.5 MeV) reduced the apparent embrittlement rate in highly irradiated specimens of VVER type pressure vessel steels. Williams and coworkers [25] found that low flux irradiations of high copper steels produced larger Charpy transition temperature shifts than equivalent high flux irradiations at low doses (< 0.01 dpa). However, this difference between the low flux and high flux data was diminished at higher fluences. Odette and Lucas [15] also reported larger transition temperature shifts in low flux irradiations at fluences below 0.03 dpa (approximately 2 x 10^{19} n/cm^2 ≥ fluence of test reactor data used in this study, E > 1 MeV). However Odette and Lucas found that at doses above 0.03 dpa this relationship was reversed, with higher shifts noted in the low flux irradiations. All of these results imply that the same fluence factor should not be applied to both the test reactor and power reactor data. The data analyzed in this study did not support the development of a separate fluence factor for the test reactor irradiations. The choice of the Regulatory Guide fluence factor, which exhibits relatively low embrittlement rates at high fluences,

assured that subsequent conclusions indicating low reembrittlement rates were not an artifact of an unnecessarily conservative embrittlement curve. The use of a test reactor fluence factor with higher embrittlement rate at high fluences, would have accentuated the lower embrittlement rates noted during reirradiation of annealed materials. As more high fluence test reactor data becomes available, alternative fluence factors will be evaluated.

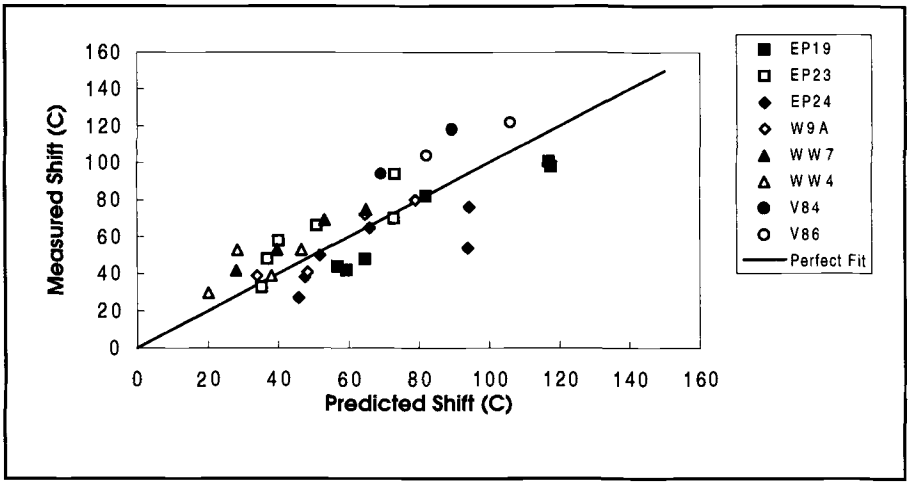


Figure 6. Comparison of Multi-Component Annealing Model Predicted Shifts vs. Measured Shifts in Annealed and Reirradiated Materials

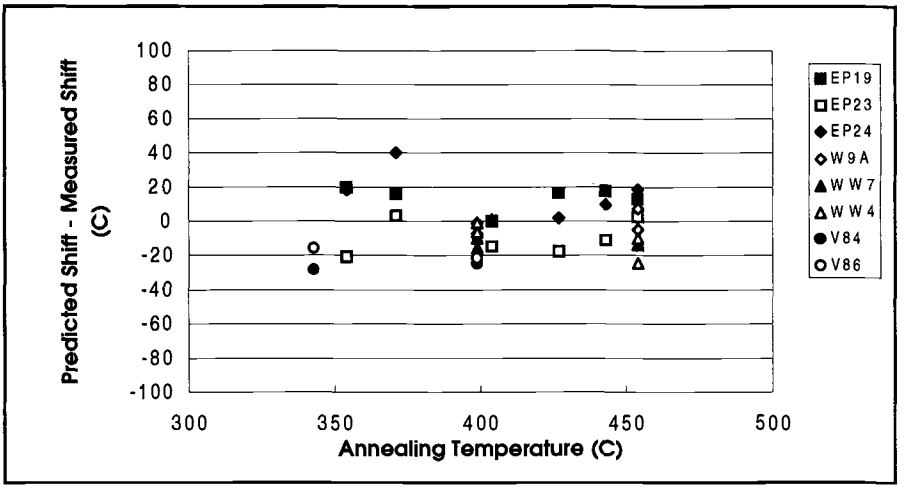


Figure 7. Residuals of Multi-Component Model Predictions as a Function of Annealing Temperature for Annealed and Reirradiated Materials

5.2 Annealing Model

The annealing recovery data included in Figure 3 indicates that recovery is a strong function of temperature. Although these data have been examined in some detail, no additional material related variables were found to strongly influence recovery. However, some of the scatter apparent in the data shown in Figure 3 can be eliminated by considering the fluence at the point of anneal as a variable. The effect of preirradiation fluence on annealing and reirradiation was not modeled in this study. The annealing behavior can be satisfactorily modeled with a simple linear regression. The multi-component annealing model described in this study is also consistent with the data, but is not statistically superior to the model developed using simple regressions. The primary arguments for the multi-component model are drawn from detailed annealing kinetics studies and microstructural examinations.

The isochronal annealing kinetics studies conducted by Pachur [17,18] form an integral part of the multi-component model. However, Pachur's activation energies would imply complete annealing for all specimens annealed at temperatures greater than 390°C which is contradictory to measured values for the materials evaluated in this study. This discrepancy may be attributable to compositional differences between the materials evaluated here and the A533B plate analyzed by Pachur. Specifically, Pachur's material contained a relatively low Cu (0.12 wt%) content, while the concentrations of C (0.22 wt%) and P (0.012 wt%) were relatively high. These variations in composition may account for the small copper coarsening component contribution to the embrittlement observed by Pachur as compared to that observed for the materials studied in this program.

The microhardness annealing kinetics [11] data presented in Figure 4 also supports the multi-component model. These data indicate that relatively little recovery occurs at an annealing temperature of 315°C, a temperature only 25°C higher than the irradiation temperature. At an annealing temperature of 371°C, there is a rapid recovery of approximately 1/3 of the embrittlement, following the recovery kinetics described by Pachur. The remaining 2/3 of the embrittlement is apparently stable in the 371°C anneals, but recovers at a rate consistent with copper coarsening when annealed at 427°C.

A growing body of evidence exists that suggests that multiple mechanisms contribute to the process of pressure vessel steel embrittlement. Mader and coworkers [26] have provided a detailed review of this evidence. Early studies [27,28, 29] indicated that changes in mechanical properties can be directly related to fine scale microstructural features. These fine scale microstructural features can be observed using such advanced characterization techniques as small angle neutron scattering (SANS), positron annihilation (PA), and atom probe-field ion microscopy (APFIM). SANS and APFIM studies have provided the strongest evidence for a precipitate component to embrittlement in irradiated steels. APFIM studies [30,31, 32] reported the observation of a wide variety of copper-rich precipitates, clusters and "pre-clusters", demonstrating the complex nature of irradiation-induced precipitation in RPV steels. These copper-rich regions often contain other alloying elements, particularly Mn, P, Ni and Si. In addition, small P clusters have also been reported in the irradiated steels. SANS has provided useful information on fine-scale microstructural features, [33,34,35]. However, interpretation of SANS data is extremely difficult because of the complex nature of the features present. Because Mn atoms and vacancies produce similar SANS data, the incorporation of Mn and other elements into the irradiation-produced defects makes it difficult to differentiate between vacancy-rich features and precipitates. However, the high magnetic component to scattering observed in SANS results indicates the presence of small irradiation-produced precipitates that are approximately 1-2 nm in diameter and occur at a density of approximately $5 \times 10^{17}/cm^3$.

As indicated above, the complex nature of the microstructure in irradiated steels makes quantitative analysis of SANS data difficult. However, Kampmann et al. [36] used SANS analysis of extremely low Cu steels to demonstrate that there are void-like defects

in the microstructure, which are reduced in size and volume fraction by annealing at 399°C. The same study found that precipitate-like defects in higher Cu steels were stable under the same annealing conditions. SANS data analysis of steels annealed at temperatures between 400°C and 450°C generally shows an increase in the magnetic component of scattering, an increase in the average defect size and a decrease in the defect volume fraction. This SANS behavior may be attributed to a variety of factors including a decrease in the vacancy component of the microstructure, a change in the precipitate structure or composition, and a coarsening of the precipitate size distribution. While these microstructural studies suggest a complicated combination of mechanisms are responsible for annealing recovery of irradiation damage, they are generally consistent with the multi-component annealing model.

5.3 Reembrittlement Model

Annealing of these welds is modeled as a combination of overaging of copper precipitates and dissolution of at least two secondary neutron-induced components of the microstructure. Because overaging results in a thermally stable microstructure, it is reasonable to assume that this component is permanently removed from subsequent considerations of embrittlement, resulting in a vertical shift of the embrittlement curve. Dissolution is a reversible process, returning the material to its original state. In this case, a lateral shift of the embrittlement curve would be expected. The reembrittlement model incorporates elements of both mechanisms. The model explains the low reembrittlement rates that are routinely observed after high temperature annealing of high copper weldments. Annealing at temperatures below 380°C does not produce copper coarsening and does result in a vertical shift of the embrittlement curve.

The annealing model used in this study assumed that the 67%-33% split for embrittlement mechanisms was valid for all materials. It would seem reasonable to expect that this split would be a function of the material composition. In particular, it would be reasonable to expect that the copper precipitation component of annealing and embrittlement would be smaller for low copper steels. Unfortunately, there is practically no annealing and reembrittlement data for low copper content steels; most studies to date have concentrated on higher copper welds to ensure that a reasonably large transition temperature shift would be obtained. Some recent results, however, have been reported on VVER-type low Cu, high P steels. These materials exhibit high reembrittlement rates consistent with the lateral shift model after high temperature annealing [37] indicating that the microstructural features formed during annealing are not thermally stable. An APFIM analysis of similar low Cu, high P steels indicates that the predominant features of the microstructure are small carbides and phosphides [38]. Therefore, as expected, recovery by copper coarsening is not as significant a factor in the annealing of these low Cu materials.

The irradiation temperature may also drastically affect the relative contribution of each embrittlement mechanism. Pachur found an annealing stage in materials irradiated at 150°C that was active at annealing temperatures between 290°C and 350°C. This annealing stage was not observed in materials irradiated at 290°C. Data generated in support of the annealing of the Army SM-1A reactor vessel indicated that annealing at 300°C for one week was sufficient to produce 70% recovery in a steel irradiated at 221°C [4]. The SM-1A data also indicated the presence of a microstructural feature that is present in low temperature irradiations that is not stable at normal power reactor pressure vessel operating temperatures. Low temperature anneals (343°C) were also successful in producing recovery of pressure vessel steel properties in the Belgian BR-3 reactor, which had an operating temperature of 260°C [39]. The VVER steels discussed above which were irradiated at 270°C were subsequently annealed and reirradiated by Amayev et al. [37]. This lower irradiation temperature may also have contributed to the larger lateral shift fraction observed in these VVER steels.

6.0 CONCLUSIONS AND OUTSTANDING ISSUES

A model of annealing and reirradiation embrittlement behavior based on the analysis of nine high copper pressure vessel steel welds has been developed. These models assume the existence of multiple embrittlement mechanisms. Annealing is described as a combination of copper coarsening along with the dissolution of other secondary irradiation-induced features. The kinetics of the annealing model have been determined from isochronal annealing studies and from an Ostwald ripening model applied to small Cu precipitates. The copper coarsening results in permanent recovery because the large precipitates formed during annealing are stable during subsequent irradiation, thus, the copper coarsening portion of the recovery results in a vertical shift of the original embrittlement curve. The secondary mechanisms are presumed to anneal in a reversible manner, resulting in a lateral shift in the original embrittlement curve. The reembrittlement model describes the post-anneal embrittlement as a combination of vertical shift and lateral shift models where the relative contributions of the vertical and lateral shifts are determined from the annealing model.

The model described in this paper provides a linkage between the fundamental mechanistic understanding of embrittlement in pressure vessel steels and the existing data on annealing and reirradiation embrittlement. To provide a connection to industry standards, US NRC Regulatory Guide 1.99 Rev.2 was used as a starting point for the modeling effort. Both the chemistry factor used to model the test reactor data and the relative importance of copper coarsening to annealing were determined by empirical observations. Although the existing database on irradiated and annealed pressure vessel steels is not sufficient to conclusively demonstrate the validity of this model for a variety of material compositions, the model predictions are consistent with both the values in the database and with results of numerous microstructural studies. Several important observations and implications concerning embrittlement, annealing and reirradiation embrittlement can be drawn from this modeling effort:

1. The embrittlement rates in the test reactor irradiated materials used in reactor vessel annealing studies are generally lower than predicted by trend curves based on surveillance data.
2. Annealing temperatures below 380°C, can be described by annealing recovery curves originally proposed by Pachur [17,18].
3. Annealing at temperatures greater than 380°C includes a copper coarsening contribution.
4. For the high copper weldments that are included in the annealing database, copper precipitation is responsible for approximately 2/3's of the transition temperature shift.
5. The reirradiation embrittlement rate is a strong function of annealing temperature because the contributions of lateral shift and vertical shift to the post-annealing embrittlement curve are determined by the relative significance of copper coarsening and the recovery of the secondary embrittlement components.

The annealing and reirradiation embrittlement model also provides a framework for addressing two outstanding reactor pressure vessel steel annealing issues. The first issue is the apparent difference between the power reactor and test reactor embrittlement data. A difference in the original embrittlement curve implies that there is some difference in the underlying embrittlement mechanisms. To apply this model to power reactor irradiations, the relative importance of copper precipitation to embrittlement must be determined. Test results and APFIM results from reactor surveillance capsule materials clearly indicate that copper precipitation continues to be a major contributor to embrittlement in power reactor materials. The second issue is raised by the relatively narrow range of high copper weldments evaluated to date. Because of this lack of low Cu steel data, it is difficult to

determine if the relative importance of copper precipitation decreases for lower copper steels. Low Cu VVER steels exhibit large lateral shift contributions to reembrittlement after high temperature anneals, suggesting that copper coarsening is not an important annealing mechanism in these steels. Unfortunately, there are several subtle differences between the experience with VVER steels and US RPV steels that make direct comparisons difficult. Additional data from US RPV steels is required to expand this model beyond the range of high copper weldments included in this analysis.

From the multi-component model, the critical information required to determine the post-anneal embrittlement rate is the fractional contribution of copper coarsening to the annealing recovery. This model, which incorporates an underlying mechanistic understanding of irradiation embrittlement and annealing, is consistent with the existing data on high copper weldments. This type of weldment is the plant limiting material for many reactors currently considering reactor vessel annealing. In addition, the available data continues to indicate that reactor vessel thermal annealing can provide long term benefit for these plants. This mutli-component model not only can be used as a tool for predicting the benefits of annealing in these specific plants, it also provides a framework for the analysis of annealing reirradiation in other types of steels.

ACKNOWLEDGMENTS

The authors gratefully acknowledge T. R. Mager, W. G. Clark, Jr., R. P. Shogan, M. G. Burke, and N. Pessall of Westinghouse Electric Corporation for their encouragement and valuable contributions.

REFERENCES

[1] Spitznagel, J. A., Shogan, R. P., and Phillips, J. H., **"Annealing of Irradiation Damage in High-Copper Ferritic Steels,"** *Irradiation Effects on the Microstructure and Properties of Metals, ASTM STP 611*, American Society for Testing and Materials, 1976, pp. 434-448.

[2] Hawthorne, J. R., Watson, H. E., and Loss, F. J., **"Exploratory Investigations of Cyclic Irradiation and Annealing Effects on Notch Ductility of A533-B Weld Deposits,"** *Irradiation Effects on the Microstructure and Properties of Metals, ASTM STP 683*, J.A. Sprague, and D. Kramer, Eds., American Society for Testing and Materials, 1978, pp. 278-294.

[3] Macdonald, B., **"Post-Irradiation Annealing Recovery of Commercial Pressure Vessel Steels,"** *Effects of Radiation on Materials: Twelfth International Symposium, ASTM STP 870,* F. A. Garner and J. S. Perrin, Eds., American Society for Testing and Materials, Philadelphia, 1985, pp. 972-978.

[4] Potapovs, U. and Hawthorne, J. R., **"Notch Ductility Properties of SM-1A Reactor Pressure Vessel Following the In-Place Annealing Operation,"** *Nuclear Applications*, Vol. 5, Dec. 1968, pp. 389-409.

[5] Miller, R. B., and F. W., Stallmann, Reactor Pressure Vessel Steel Embrittlement Data Base, Version 1.1.

[6] U.S. NRC Regulatory Guide 1.99 Rev. 2, May 1988.

[7] Server, W. L. and Taboada, A., **"An Approach for Estimating Post-Anneal Reirradiation Embrittlement of Reactor Vessel Steels,"** *Environmental Degradation of Materials in Nuclear Power Systems - Water Reactors*, American Nuclear Society, Sept. 1985, pp. 496-501.

[8] Standard Guide for "In-Service Annealing of Light-Water Cooled Nuclear Reactor Vessels," American Society for Testing and Materials, Designation: E509-86.

[9] Hawthorne, J. R., **"Irradiation-Anneal-Reirradiation (IAR) Studies of Prototypic Reactor Vessel Weldments,"** NUREG/CR-5469, MEA-2364, Oct. 1989.

[10] Hawthorne, J. R., **"Survey of Postirradiation Heat Treatment as a Means to Mitigate Radiation Embrittlement of Reactor Vessel Steels,"** Meeting of IAEA International Working Group on Reliability of Reactor Pressure Components, March 1979, pp. 181-194.

[11] Mager, T. R., et al., **"Feasibility of and Methodology for Thermal Annealing an Embrittled Reactor Vessel,"** EPRI NP-2712, EPRI Project RP1021-1 Final Report, Jan. 1983.

[12] Lott, R. G., Mager, T. R., Shogan, R. P., and Yanichko, S. E., "**Annealing and Reirradiation Response of Irradiated Pressure Vessel Steels,**" *Radiation Embrittlement of Nuclear Reactor Pressure Vessel Steels: An International Review (Second Volume), ASTM STP 909*, L. E. Steele, Ed., American Society for Testing and Materials, Philadelphia, 1986, pp. 242-259.

[13] Hawthorne, J. R., Watson, H. E., and Loss, F. J., "**Experimental Investigation of Multicycle Irradiation and Annealing Effects on Notch Ductility of A533-B Weld Deposits,**" *Effects of Radiation on Materials: Tenth Conference, ASTM STP 725*, D. Kramer, H. R. Brager, and J. S. Perrin, Eds., American Society for Testing and Materials, 1981, pp. 63-75.

[14] Miller, M. K., and Burke, M. G., "**Fine-Scale Microstructural Characterization of Pressure Vessel Steels and Related Materials Using APFIM,**" *Effects of Radiation on Materials: 14th International Symposium (Volume II), ASTM STP 1046*, N. H. Packan, R. E. Stoller, and A. S. Kumar, Eds., American Society for Testing and Materials, Philadelphia, 1990, pp. 107-126.

[15] Odette, G. R. and Lucas, G. E., "**Irradiation Embrittlement of Reactor Pressure Vessel Steels: Mechanisms, Models, and Data Correlations,**" *Radiation Embrittlement of Nuclear Reactor Pressure Vessel Steels: An International Review (Second Volume), ASTM STP 909*, L. E. Steele, Ed., American Society for Testing and Materials, Philadelphia, 1986, pp. 206-241.

[16] Lott, R. G. and Mager, T. R., "**A Determination of the Benefits of Annealing Irradiated Pressure Vessel Weldments,**" *Int. J. Pres. Ves. & Piping*, Vol. 34, 1988, 155-170.

[17] Pachur, D., "**Radiation Annealing Mechanisms of Low-Alloy Reactor Pressure Vessel Steels Dependent on Irradiation Temperature and Neutron Fluence,**" *Nuclear Technology*, Vol. 59, Dec. 1982, pp. 463-475.

[18] Pachur, D., "**Radiation and Annealing Mechanisms of Low Alloyed Reactor Pressure Vessel Steel,**" *Environmental Degradation of Materials in Nuclear Power Systems - Water Reactor*, American Nuclear Society, 1985, pp. 502.

[19] Salje, G. and Feller-Kniepmeier, M., "**The Diffusion and Solubility of Copper in Iron,**" *Journal of Applied Physics*, Vol. 48, No. 5, May 1977, pp. 1833.

[20] Soeno, K., "**Effect of Cold Work on the Precipitation of Copper from Alpha-Iron,**" *Trans. Japan Inst. Metals*, Vol. 11, (3), May 1970, pp. 185-189.

[21] Goodman, S. R., Brenner, S. S., and Low, J. R., Jr., "**An FIM-Atom Probe Study of the Precipitation of Copper from Iron-1.4 At. Pct Copper. Part II: Atom Probe Analysis,**" *Met. Trans.*, Vol. 4, Oct. 1973, pp. 2371.

[22] Mager, T. R. and Lott, R. G., "**Semiempirical Model for Annealing and Reirradiation Embrittlement in Pressure Vessel Steels,**" *Radiation Embrittlement of Nuclear Reactor Pressure Vessel Steels: An International Review (Third Volume), ASTM STP 1011*, L. E. Steele, Ed., American Society for Testing and Materials, Philadelphia, 1989, pp. 206-216.

[23] Guthrie, G.L. and Simonen, E.P., "**Correlations Between Power and Test Reactor Databases,**" NUREG CR 5328, 1989.

[24] Amayev, A. D., Kryukov, A. M., Levit, V. I., and Sokolov, M. A., "**Radiation Stability of WWER-440 Vessel Materials,**" *Radiation Embrittlement of Nuclear Reactor Pressure Vessel Steels: An International Review (Fourth Volume), ASTM STP 1170*, L. E. Steele, Ed., American Society for Testing and Materials, Philadelphia, 1993, pp. 9-29.

[25] Williams, T. J., Burch, P. R., English, C. A., and de la cour Ray, P. H. N., "**The Effect of Irradiation Dose Rate and Temperature, and Copper and Nickel Content, on the Irradiation Shift of Low Alloy Steel Submerged Arc Welds,**" *Environmental Degradation of Materials in Nuclear power Systems - Water Reactors*, G. J. Theus and J. R. Weeks, Eds., The Metallurgical Society, 1988, pp. 121.

[26] Mader, E., Lucas, G. E., and Odette, G. R., "**The Effects of Metallurgical and Irradiation Variables on the Postirradiation Annealing Kinetics of Pressure Vessel Steels,**" *Effects of Radiation on Materials: 15th International Symposium, ASTM STP 1125*, R. E. Stoller, A. S. Kumar, and D. S. Gelles, Eds., American Society for Testing and Materials, Philadelphia, 1992, pp. 151-171.

[27] Harbottle, J. E. and Fisher, S. B., "**Copper Sulphide $Cu_{1.8}S$ (Digenite I) Precipitation in Mild Steel",** *Nature*, Vol. 299, 1982, pp. 139-140.

[28] Odette, G. R., **"On the Dominant Mechanism of Embrittlement of Reactor Pressure Vessel Steels,"** *Scripta Met.*, Vol. 17, 1983, pp. 1183-1188.

[29] Lott, R. G., **"A Microstructural Basis for the Prediction of Embrittlement in Pressure Vessel Steels,"** *Topical Conference on Ferritic Alloys for use in Nuclear Energy Technologies*, J.W. Davis and D. J. Michel, Ed., The Metallurgical Society of AIME, 1983, pp. 37-44.

[30] Burke, M. G. and Brenner, S.S., **"Microstructural Investigation of Irradiated Pressure Vessel Steel Weld Metal,"** *Journal de Physique*, Vol. 47, 1986, pp. C2-239-C2-244..

[31] Miller, M. K. and Burke, M. G., **"An Atom Probe Field Ion Microscopy Study of Neutron-Irradiated Pressure Vessel Steels,"** *Journal of Nuclear Materials* 195, 1992, pp. 68-82.

[32] Burke, M. G., Grant, S. P., and Miller, M. K., **"APFIM Investigations of Solute Clustering and Precipitation in Irradiated RPV Steels,"** *Environmental Degradation of Materials in Nuclear Power Systems - Water Reactors*, D. Cubicciotti, Ed., National Association of Corrosion Engineers, 1990, pp. 2-53.

[33] Ukpong, I. E., Krawitz, A. D., Milder, D. F. R., and Leighly, H. P., Jr., **"A Study of Radiation Induced Voids and Precipitates and Their Annealing Behavior by Small-Angle Neutron Scattering,"** *Influence of Radiation on Material Properties: 13th International Symposium (Part II), ASTM STP 956*, F. A. Garner, C. H. Henager, Jr., and N. Igata, Eds., American Society for Testing and Materials, Philadelphia, 1987, pp. 480-493.

[34] Solt, G., Frisius, F., Waeber, W. B., and Buhrer, W., **"SANS and DENS Study of Irradiation Damage in A Reactor Pressure Vessel Material with a Systematic Variation of Irradiation Dose and Heat Treatments,"** *Effects of Radiation on Materials: 14th International Symposium (Volume II), ASTM STP 1046*, N. H. Packan, R. E. Stoller, and A. S. Kumar, Eds., American Society for Testing and Materials, Philadelphia, 1990, pp. 154-164.

[35] Van Duysen, J. C., Bourgoin, J., Janot, Christian, and Penisson, J. M., **"Evolution of the Microstructure of PWR Pressure Vessel Steels from the CHOOZ A Reactor Surveillance Program after Long-Term Irradiation,"** *Effects of Radiation on Materials: 15th International Symposium, ASTM STP 1125*, R. E. Stoller, A. S. Kumar, and D. S. Gelles, Eds., American Society for Testing and Materials, Philadelphia, 1992, pp. 117-130.

[36] Kampmann, R., Frisius, F., Hackbarth, H., Beaven, P. A., Wagner, R., and Hawthorne, J. R., **"SANS Investigations of Low Alloy Steels in Neutron Irradiated, Annealed and Reirradiated Conditions,"** *Environmental Degradation of Materials in Nuclear Power Systems - Water Reactors*, American Nuclear Society, 1991, pp.679.

[37] Amayev, A. D., Kryukov, A. M., and Sokolov, M. A., **"Recovery of the Transition Temperature of Irradiated WWER-440 Vessel Metal by Annealing,"** *Radiation Embrittlement of Nuclear Reactor Pressure Vessel Steels: An International Review (Fourth Volume), ASTM STP 1170*, L. E. Steele, Ed., American Society for Testing and Materials, Philadelphia, 1993, pp. 369-379.

[38] Miller, M. K., Jayaram, J., Othen, P. J. and Brauer, G., **"Atom Probe Field Ion Microscopy Characterization of VVER Steels,"** *Environmental Degradation of Materials in Nuclear Power Systems - Water Reactors*, R. E. Gold and E. P. Simonen, Eds., The Minerals, Metals & Materials Society, 1993, pp. 161-163.

[39] Fabry, A., Motte, F., Stiennon, G., Debrue, J., Gubel, P., Van de Velde, J., Minsart, G., and Van Asbroeck, Ph., **"Annealing of the BR3 Reactor Pressure Vessel,"** *Twelfth Water Reactor Safety Research Information Meeting*, Vol. 4, 1984, pp. 144.

Christopher J. Bolton[1], John T. Buswell[1], R. Barry Jones[1], Robert Moskovic[1] and Robert H. Priest[1]

THE MODELLING OF IRRADIATION EMBRITTLEMENT IN SUBMERGED-ARC WELDS

REFERENCE: Bolton, C. J., Buswell, J. T., Jones, R. B., Moskovic, R., and Priest, R. H., **"The Modelling of Irradiation Embrittlement in Submerged-Arc Welds,"** *Effects of Radiation on Materials: 17th International Symposium, ASTM STP 1270,* David S. Gelles, Randy K. Nanstad, Arvind S. Kumar, and Edward A. Little, Eds., American Society for Testing and Materials, 1996.

ABSTRACT: Until very recently, the irradiation embrittlement behaviour of submerged-arc welds has been interpreted in terms of two mechanisms, namely a matrix damage component and an additional component due to the irradiation-enhanced production of copper-rich precipitates .

However, some of the weld specimens from a recent accelerated re-irradiation experiment have shown high Charpy shifts which exceeded the values expected from the measured shift in yield stress. Microstructural examination has revealed the occurrence of intergranular fracture (IGF) in these specimens, accompanied by grain boundary segregation of phosphorus.

Theoretical models were developed to predict the parametric dependence of irradiation-enhanced phosphorus segregation on experimental variables. Using these parametric forms, along with the concept of a critical level of segregation for the onset of IGF instead of cleavage, a three mechanism trend curve has been developed. The form of this trend curve, taking into account IGF as well as matrix and copper embrittlement, is thus mechanistically based. The constants in the equation, however, are obtained by a statistical fit to the actual Charpy shift database.

KEYWORDS: pressure vessels, irradiation, embrittlement, intergranular fracture

A number of theoretical models have been developed for the prediction

(1) Nuclear Electric plc, Berkeley Technology Centre, Berkeley, Gloucestershire, U.K.

Copyright© 1996 by ASTM International www.astm.org

of embrittlement effects in reactor pressure vessel (RPV) steels, e.g. [1-6]. These models are based on a mechanistic interpretation of the processes occurring as a result of the disruption of the steel by neutron-atom interactions. The Nuclear Electric model was initially derived for the assessment of Magnox RPV surveillance data [2]. Later a slightly modified version of the model was used to interpret embrittlement in PWR steels irradiated under surveillance and accelerated conditions [4].

Until recently, the irradiation embrittlement behaviour of high copper submerged-arc welds has been interpreted in terms of two mechanisms, namely a matrix damage component and an additional component due to the irradiation-enhanced production of copper-rich precipitates [6]. The data have been fitted to embrittlement trend curves whose form is based on this mechanistic understanding.

However, some of the weld specimens from a recent accelerated re-irradiation experiment have shown high Charpy shifts which exceeded the values expected from the measured shift in yield stress. Microstructural examination has revealed the occurrence of intergranular fracture (IGF) in these specimens, accompanied by grain boundary segregation of phosphorus [7]. These results indicate the existence of a third, non-hardening, embrittlement mechanism.

This paper describes how a mechanistic understanding of the third mechanism can be applied to the derivation of a trend curve which takes into account all three mechanisms.

DAMAGE MECHANISMS IN SUBMERGED-ARC WELD

We review first the three damage mechanisms referred to briefly in our introductory paragraphs, namely matrix damage, copper precipitation and intergranular fracture.

Matrix damage

Matrix damage is produced by the coalescence of point defects resulting from the neutron damage. This creates obstacles to the free movement of dislocations and thus increases the yield stress, or transition temperature, of the steel.

Based on studies of low-copper materials, it is concluded that this component of the damage increases with the square root of the dose and is independent of the dose-rate [8]. Its magnitude is, however, influenced by the fabrication practice (in particular the presence of free interstitials), and by the irradiation temperature [9].

Thus, the shift in yield stress due to matrix damage, $\Delta\sigma_{y,Matrix}$, is described by

$$\Delta\sigma_{y,Matrix} = A' F_T \sqrt{D} \quad (1)$$

where

D = dose, measured in dpa,
A′ = a material-specific constant, and
F_T is a factor depending on irradiation temperature, given by

$$F_T = 1.869 - 4.57 \times 10^{-3} T \quad (2)$$

where

T = irradiation temperature, °C.

F_T has a value of unity at 190°C. Eq 2 was derived from an analysis of the radiation hardening of mild steel plates subjected to accelerated irradiation [9]. The relationship is valid over the temperature range from 100°C to 350°C.

The shift in Charpy 40J transition temperature due to matrix damage, $\Delta T_{40J,Matrix}$, can be calculated from an equation identical to eq 1, but replacing the constant A′ with a different value, A. This is consistent with the experimental observation that Charpy shifts are linearly proportional to yield stress shifts [6], within the scatter on the data.

Copper Precipitation

The irradiation-enhanced precipitation of small (typically 2nm diameter) copper-rich particles gives rise to the second component of the hardening/embrittlement. For a full description of the mechanistic understanding of this component as it occurs in submerged-arc welds, the reader is referred to [6], but the principal features are as follows.

The modelling is based on that for thermal ageing of copper-containing steels and alloys, in which the rate of precipitation is dramatically increased by the presence of large excesses of radiation-induced point defects. As a result the development of the copper component is dependent not only on time and temperature, but also on dose-rate.

The maximum copper contribution to the yield stress shift, $\Delta\sigma_{y,Cu}(max)$, in MPa, is given by [4]

$$\Delta\sigma_{y,Cu}(max) = 4.5 \times 10^{-3}(f_{Cu})^{0.5} - 90 \quad (3)$$

where

f_{Cu} = volume fraction of copper in solution in the steel.

$\Delta\sigma_{y,Cu}(max) = 0$ for $f_{Cu} \leq 4 \times 10^{-4}$ (0.046wt%)

The volume fraction of copper in solution may be lower than the bulk content in a weld owing to the precipitation of copper during the stress relief heat treatment, and also to the precipitation of some copper sulphide during welding, see Ref. 6.

During irradiation, the copper component rises to a peak given by eq 3. The equivalent transition temperature shift, $\Delta T_{40J,Cu}$, may again be calculated at any dose by application of a similar equation but with different numerical factors, because of the proportionality of transition shifts to yield stress shifts.

Once the peak copper contribution has been reached, (at a typical dose, for Magnox surveillance specimens, of approximately 1mdpa), no overageing is invoked in the modelling. This is consistent with a number of experimental observations referred to in [6] for specimens exposed at temperatures below about 300°C. Therefore, after peak precipitation is achieved, $\Delta T_{40J,Cu}$ is set equal to a constant, B, and for the combined matrix and copper contributions we have

$$\Delta T_{40J} = \Delta T_{40J,Matrix} + \Delta T_{40J,Cu} = AF_T\sqrt{D} + B \quad (4)$$

Arguments justifying the approximation of linear additivity of the two processes represented in eq 4 are presented in [2] and [4].

If good justification can be provided (see [6]) that the copper precipitation in a particular dataset is 'post-peak', then a trend curve of the form of eq 4 can be fitted to experimental data, and values of the constants A and B may be determined. In predicting RPV shifts using such a trend curve, it would be important to consider whether the vessel itself is also 'post-peak'.

Intergranular Fracture

So far, the mechanistic understanding of embrittlement assumes that irradiation-induced transition temperature shifts result from the increments in yield stress produced by two 'barrier hardening' mechanisms: matrix irradiation

damage and irradiation-assisted precipitation processes. Support for this has come from the observed linear relationship between Charpy shifts and yield stress shifts which is found for the accelerated irradiation samples reported in [6]. However, as indicated in our introductory paragraphs, some recent results from accelerated re-irradiation of surveillance samples indicate that this relationship is not always obeyed. In particular, some high dose welds show transition temperature shifts (a) greater than expected for the irradiation dose and temperature experienced, and (b) greater than calculated from the measured yield stress shifts using the normal proportionality constant relating ΔT_{40J} to $\Delta\sigma_y$. These data suggest the operation of an additional embrittlement mechanism.

In order to investigate the existence of a third mechanism, detailed fractographic and metallographic studies have been undertaken on failed Charpy samples [7]. Scanning electron fractography revealed significant amounts of intergranular fracture (IGF) in the fine-grained regions of some specimens, with more in a weld showing high Charpy shifts than in another, lower shift weld. Furthermore, small 'matchstick' specimens were removed from embrittled regions and fractured in a scanning Auger microscope. Significant levels of grain boundary phosphorus segregation were found, and these levels were found to increase with dose. No other element known to embrittle grain boundaries was found to be segregated to any significant level. Thus, a link has been made between phosphorus segregation and the observation of IGF. In subsequent sections of the paper we consider how to incorporate an allowance for IGF in the derivation of trend curves. It is emphasised that significant IGF did not occur in all specimens; consideration is also given later in the paper to the accommodation of this variability.

INCORPORATION OF INTERGRANULAR EFFECTS

Modelling of Grain Boundary Segregation

Theoretical modelling of irradiation-enhanced intergranular segregation of phosphorus [10] has been carried out. The modelling uses two approaches. In the first approach, the kinetic model of Murphy, and Murphy and Perks [11,12] for irradiation-enhanced segregation of phosphorus in nickel has been applied to phosphorus segregation in iron; and in the second, the thermal equilibrium model of McLean, as applied to phosphorus in steel [13] has been modified for the irradiation situation by incorporating effective vacancy diffusion coefficients.

The models predict the dependence of phosphorus segregation, expressed as a fractional monolayer coverage on the boundary (P_g), as functions of the irradiation exposure parameters and materials variables such as the neutron dose, the dose rate, the irradiation temperature, the dislocation density, the bulk phosphorus level and the pre-irradiation monolayer coverage ($P_{g,0}$). With realistic values for the physical parameters in the models, reasonable agreement is obtained with the available data on phosphorus segregation in submerged-arc welds, as measured in field emission gun scanning transmission electron

microscopy (FEGSTEM) and Scanning Auger investigations. At this stage of development, however, it is considered that the models should be relied on more for the parametric dependencies that are indicated than for the detailed prediction of levels of phosphorus segregation. The next few paragraphs summarise the qualitative predictions of the models.

As far as the irradiation temperature dependence of segregation is concerned, both models produce similar indications of the response under surveillance and accelerated conditions. These are illustrated by the results of the first model shown in Figures 1 and 2.

The conclusion depicted in Figure 1 is that at surveillance dose rates there is essentially no effect of irradiation temperature over the range 150°C to about 300°C, but at higher temperatures segregation effects due to purely thermal diffusion begin to dominate.

Figure 2 shows that at the higher doses (approximately 10mdpa) and dose-rates typical of accelerated irradiation and re-irradiation experiments there is an enhancement of grain boundary coverage compared with that predicted at typical surveillance doses (approximately 2mdpa maximum) and dose rates, with the enhancement reaching a maximum at irradiation temperatures of about 275°C. The further rise shown beginning at about 400°C is due to the onset of thermal effects; these are delayed to higher temperature by the large reduction in exposure time resulting from the use of accelerated irradiation tests.

Comparing the predictions for a dose of 10mdpa at a high dose-rate in Figure 2 with those for a dose of 5mdpa at a low dose-rate in Figure 1, it is apparent that a similar amount of segregation is predicted for these two conditions. The implication of this is that in the temperature range 150 - 300°C there is a dose-rate effect, such that a given dose at the low dose-rate produces more segregation than the same dose at the high dose-rate. This arises because the segregation depends on the free defects and there are fewer defects lost by mutual recombination at the lower dose rate than at the higher dose rate. Further consideration is given later to the question of how to allow for this effect when dealing with an experimental database.

As far as the effect of dose is concerned, the grain boundary segregation of phosphorus is predicted by the models to depend on dose raised to a power significantly greater than the value of 0.5 appropriate to matrix hardening. The kinetic model calculations have been analysed [10] and segregation is found to be proportional to $D^{0.87}$ in the dose and temperature ranges of interest so that

$$P_g - P_{g,0} = \alpha D^{0.87} \qquad (5)$$

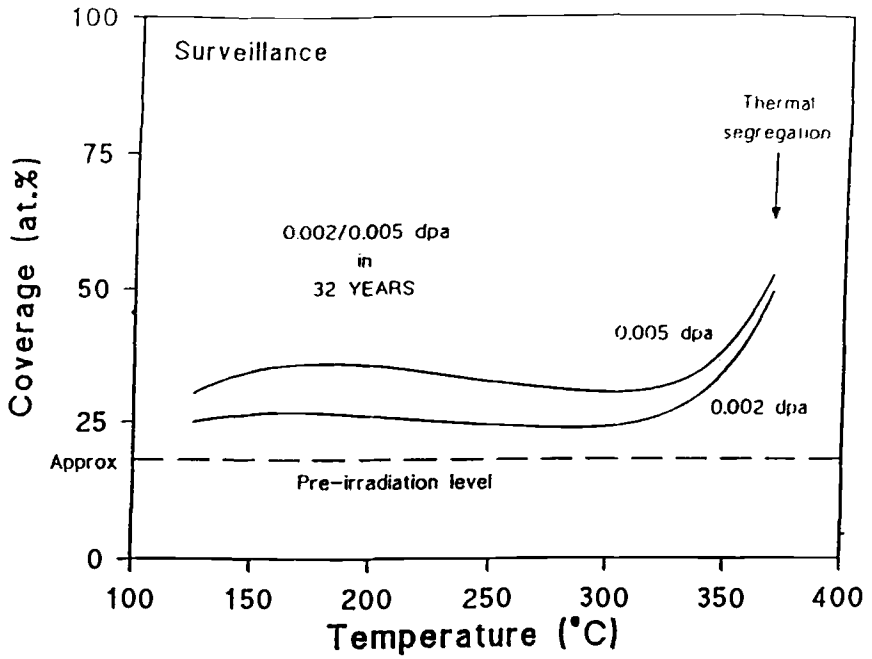


Fig. 1 Modelling of Phosphorus Segregation at Surveillance Dose-rates (see [10])

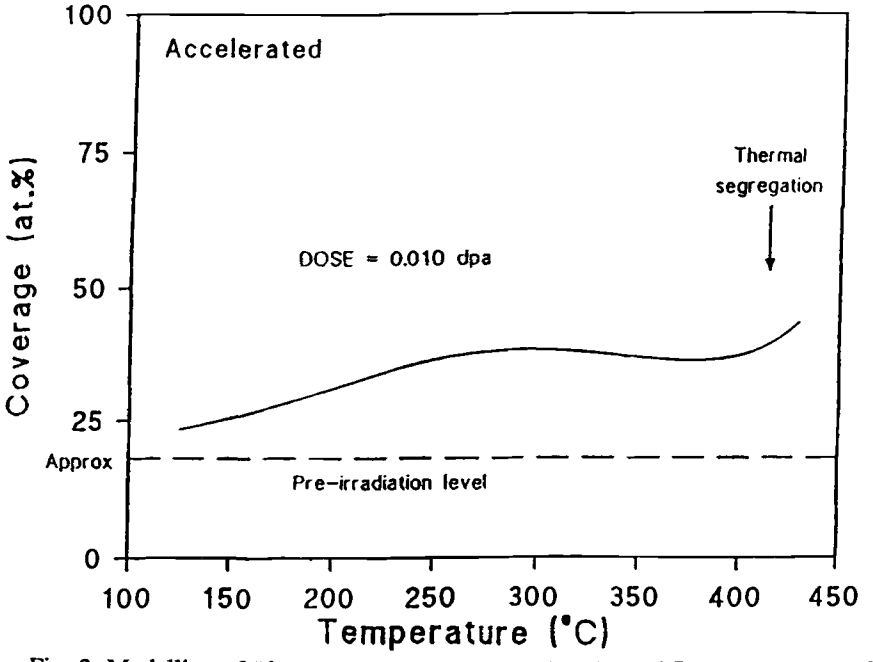


Fig. 2 Modelling of Phosphorus Segregation at Accelerated Dose-rates (see [10])

Segregation and Intergranular Fracture

The above predictions of the theoretical model apply to segregation, but we are of course concerned with IGF. Segregation may be necessary for IGF, but what level of segregation is required to initiate IGF in a steel? A conceptual model is provided by the idea of a critical stress for IGF, as depicted schematically in Figure 3. The absence of IGF in the unirradiated material implies that the intergranular fracture stress at start-of-life ($\sigma_{g,0}$) lies above the cleavage fracture stress (σ_c).

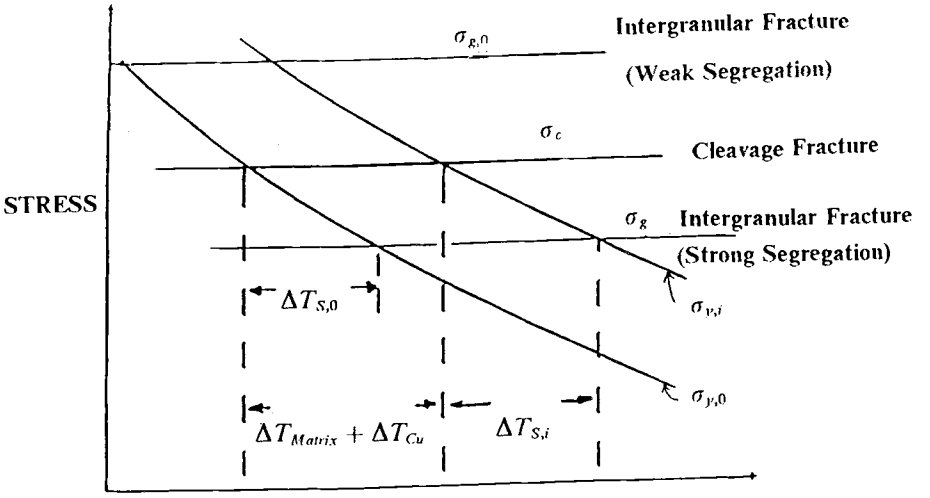


Fig. 3 Schematic Diagram of Intergranular Fracture Criterion. See text for details

It is convenient to consider two cases; first, segregation arising from thermal ageing, and second, segregation due to irradiation exposure. Under thermal exposure conditions in service the intergranular fracture stress will gradually reduce as phosphorus segregation proceeds. Assuming that the reduction is linear with phosphorus coverage then

$$\sigma_{g,0} - \sigma_g = \beta(P_g - P_{g,0}) \qquad (6)$$

where β is a constant. When σ_g has fallen to a critical value $\sigma_{g,c}$ equal to the fracture stress for cleavage (σ_c) then the brittle fracture mode will change from cleavage to intergranular. At this critical stress

$$\sigma_{g,0} - \sigma_{g,c} = \beta(P_{g,c} - P_{g,0}) \quad (7)$$

where $P_{g,c}$ is the critical monolayer coverage of phosphorus required to change the fracture mode. Any further decrease in σ_g below $\sigma_{g,c}$ due to additional segregation beyond $P_{g,c}$ will cause an increase in transition temperature ($\Delta T_{S,0}$), as shown in Figure 3, which will be given by

$$\Delta T_{S,0} = \kappa(\sigma_{g,c} - \sigma_g) \quad (8)$$

where κ is related to the dependence of the yield stress on the test temperature. Eq 8 may be expressed in terms of the monolayer coverage of phosphorus

$$\Delta T_{S,0} = \beta\kappa(P_g - P_{g,c}) \quad (9)$$

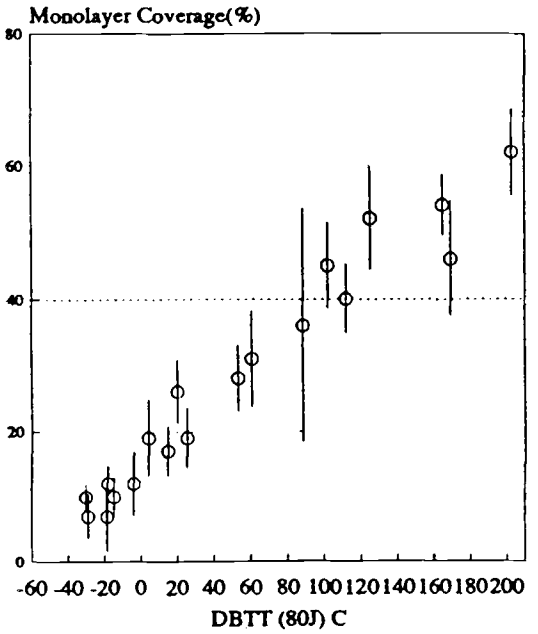


Fig.4 Shifts in 80J impact transition temperature (DBTT(80J)) as a function of surface phosphorus coverage (see Ref.14)

For a particular steel microstructure $P_{g,c}$ will have a constant value and for relatively large ranges of test temperature and phosphorus surface coverage κ and β respectively also will be constant. Hence the increase in Charpy transition temperature will be linearly dependent on the additional intergranular segregation above $P_{g,c}$. Evidence supporting these assumptions is shown in Figure 4 (from [14]) for specially heat treated model A533B alloys with a constant yield strength thermally aged at 450°C. In Figure 4 the transition temperature increase is a linear function of the phosphorus coverage over a temperature range of almost 200°C with a tendency towards a higher rate of change at high transition temperatures.

For the case of irradiation-enhanced segregation the shift in transition temperature due to segregation will be additional to the conventional shift arising from irradiation-induced increases in the yield strength of the steel. In Figure 3 the latter effect comes from matrix irradiation hardening and irradiation-enhanced copper precipitation hardening which result in transition shifts of ΔT_m and ΔT_{Cu} respectively. The shift arising from IGF ($\Delta T_{s,i}$), shown in Figure 3, can be obtained in a similar way to the shift from thermal ageing given above. From equation 7 a critical level of grain boundary phosphorus ($P_{g,c}$) will be required to initiate IGF at $\sigma_{g,c}$. This critical level of phosphorus is generated by a threshold dose (D_0) such that

$$P_{g,c} = P_{g,0} + \alpha D_0^{0.87} \tag{10}$$

Similarly, the intergranular shift is given by

$$\Delta T_{S,i} = \kappa(\sigma_{g,c} - \sigma_g) \tag{11}$$

Through equations (5), (6), (7), (10) and (11) the intergranular shift can be related back to irradiation dose so that

$$\Delta T_{s,i} = \alpha\beta\kappa(D^{0.87} - D_0^{0.87}) \tag{12}$$

For the present submerged-arc weld database, the mean value of D_0 is taken to be 2mpda, which is slightly less than the highest dose seen by the surveillance specimens. Up to this dose, there is no evidence of a significant effect of IGF on the mechanical properties - i.e. in excess of the normal data scatter.

The idea that in irradiated steel, the extra Charpy shift due to grain boundary embrittlement effects is proportional to the extra phosphorus segregation above $P_{g,c}$ is supported by the limited evidence currently available on irradiated submerged-arc weld samples.

In summary, the Charpy shifts arising from intergranular segregation are considered to be proportional to ($D^{0.87} - D_0^{0.87}$) for doses greater than D_0.

Form of Trend Curve

On the basis of the last two Sections, the form of the trend curve taking into account the three embrittlement mechanisms (matrix damage, copper precipitation, and intergranular segregation) is:

$$\Delta T_{40J} = AF_T\sqrt{D} + B + CD_{gb} \quad (13)$$

where

$$D_{gb} = D^{0.87} - D_0^{0.87} \quad (14)$$

The third term in eq 13 represents the contribution of IGF, and combines the ideas that this type of embrittlement is independent of irradiation temperature, is proportional to $D^{0.87}$, and has a threshold dose, D_0. The third term is ignored for values of D below D_0, where the intergranular fracture stress is still above that for cleavage.

The final stage in deriving a trend curve is to fit the experimental data from surveillance and accelerated experiments to the form of eq 13. To do this, two further issues have to be addressed.

FITTING DATA TO OBTAIN THE TREND CURVE

Dose-rate effects

In incorporating data from accelerated irradiation experiments into a database for trend curve determination, it is necessary to consider the possible effects of the differences in dose-rate.

As far as matrix damage is concerned, it was noted earlier that this is found to be independent of dose-rate over a wide range of dose-rates, including those of interest here; so there is no requirement to make any correction for this term.

In general, copper precipitation is dose-rate dependent. However, provided that the copper precipitation contribution is fully developed, then the term B is a constant and no corrections are required. The accelerated data in the Nuclear Electric submerged-arc weld database are of two types, namely irradiation of virgin material, and re-irradiation of withdrawn surveillance specimens. In the former case, care is required to exclude pre-peak specimens, while in the latter case, it can be demonstrated that the copper component is fully developed in all the re-irradiated specimens (which emphasises a major advantage of this type of experiment).

Where the IGF term is concerned, it is important to note that a dose-rate effect on segregation needs to be taken into account, especially since ignoring it would be non-conservative. In the Nuclear Electric data-base, a correction has been applied on the basis of modelling calculations which showed that the segregation produced by a dose D at the high dose-rate appropriate to the accelerated irradiations was approximately equal to the segregation produced by a dose of 0.65D at a low dose-rate (in the surveillance range). Thus, since we are developing a trend curve for application to low dose-rate situations, data from specimens subjected to accelerated exposures are incorporated into the database by applying a correction factor of 0.65 to the dose D in eq 14 - or if the experiment is a re-irradiation, then D is replaced by $D_1 + 0.65\ D_2$ where D_1 is the surveillance dose and D_2 is the accelerated dose.

Variability in Specimen Behaviour Beyond the Threshold Dose

Having rationalised the form of the trend curve, eq 13, and identified a method for the treatment of dose-rate effects in specimens which show IGF, the next step is to establish how to take account of the fact, noted earlier, that some results exhibit effects of IGF beyond D_0, while others do not. First, however, it is worth pointing out that there are good mechanistic reasons for this variability. Among the factors which work to reduce IGF effects in individual welds are low bulk phosphorus content (segregation is proportional to phosphorus content), and high carbon content (carbon strengthens grain boundaries and may compete with phosphorus atoms for grain boundary sites).

The method adopted to allow for this variability in the database is standard multiple regression, where a dummy, or censoring, variable, z, is used, with the value 1 for those data where intergranular effects are present, and 0 for data which do not show intergranular effects. Thus the regression becomes

$$\Delta T_{40J} = AF_T\sqrt{D} + B + CzD_{gb} \qquad (15)$$

When ascribing values of the dummy variable, z, a number of criteria have been used. The most obvious method is to determine the post-irradiation fracture process occurring in the Charpy samples for the particular irradiation exposures considered. However, establishing the incidence of intergranular fracture is not straightforward and because of variability in the microstructure the sample areas may not be optimal for detecting intergranular effects. Moreover, it is highly unlikely that a few intergranular facets observed in a fracture surface can have a measurable effect on the mechanical properties. Consequently, criteria based on mechanical properties response have been employed as a primary test. If these criteria were met then direct confirmation, by microscopy, of the occurrence of intergranular fracture effects was required before the result could be classified with the factor $z=1$.

In the present submerged-arc weld database, there are three ways in which

conclusions may be drawn as to whether or not mechanical properties are being affected by intergranular features observed on the fracture surfaces.

(1) Charpy shifts in a particular set of specimens may be compared with yield stress measurements on mini-tensile specimens made from the failed Charpy halves. Specimens failing by cleavage show a linear relation between ΔT_{40J} and $\Delta\sigma_y$ (or, equivalently, between T_{40J} and σ_y). Intergranular phosphorus segregation, by contrast, would be expected to affect T_{40J} without affecting σ_y. Thus, a *significant* deviation *i.e.* outside the normal scatter from the linear relation in specimens showing intergranular fracture features implies a significant effect on the mechanical properties.

(2) Charpy properties in a particular set of specimens showing intergranular features may be compared to the Charpy properties of a similarly exposed set of specimens which show no intergranular features. If there is no significant deterioration then it can be argued that the intergranular features are not impairing the impact properties.

(3) Arguments may be developed for particular specimens based on the proportion of the susceptible region of the fracture surface exhibiting intergranular features. It can be argued that there is no effect on the mechanical properties if this proportion is less than that on other specimens for which no effect on mechanical properties can be detected as in (1) and (2) above.

Trend Curve

Using the above methodology it is now possible to derive a trend curve from the database, and Fig 5 shows a graphical presentation of the trend curves fitted for $z=0$ and $z=1$. The best estimate trend curves are shown, along with upper bound curves representing the top of the 90% prediction interval. It is to be noted that, because of the form of eq 13, trend curves for different irradiation temperatures do not coincide when plotted as in Fig 5. The graph plotted is for an irradiation temperature of 190°C, which is close to that experienced by the majority of the surveillance specimens, so it is easy to see from Fig 5 that the trend curve and upper bound are a reasonable description of this part of the database. The irradiation temperatures for the accelerated experiments, however, are not 190°C, nor are they all the same. In order to show the fit to individual data points, it would be necessary to display trend curves for each appropriate temperature

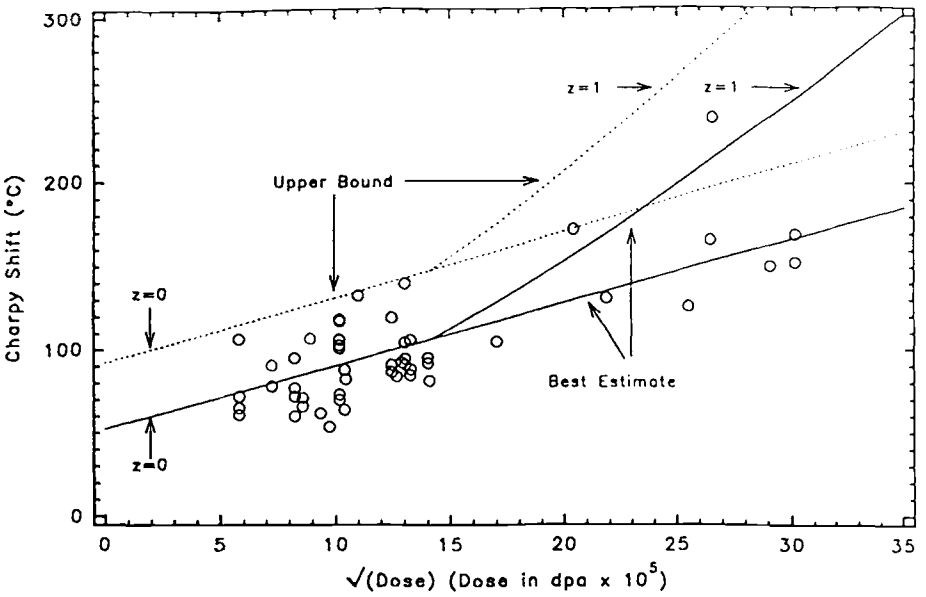


Fig. 5 Trend Curve and Upper Bound for z = 0 and z = 1 at 190°C

In applying such a trend curve to predictions of RPV embrittlement, it is necessary to know what value of z to ascribe to the RPV. In practice, this question may only be approached by making the conservative assumption that all RPV submerged-arc welds are susceptible to IGF - i.e. the trend curve for z=1 would be used.

CONCLUSIONS

(1) A three-term embrittlement trend curve has been developed, describing for the first time a contribution from intergranular fracture, as well as matrix and copper embrittlement.

(2) The parametric form of the trend curve takes into account the features of theoretical models of irradiation-enhanced intergranular phosphorus segregation, which are described in a companion paper.

(3) A threshold dose is incorporated, to reflect the idea that the intergranular embrittlement contribution only occurs when sufficient segregation has occurred to cause the critical stress for intergranular fracture to fall below that for cleavage fracture.

ACKNOWLEDGEMENT

This paper is published by permission of Nuclear Electric plc.

REFERENCES

[1] Lucas, G. E., Odette, G. R., Lombrozo, P. M., and Sheckherd, J. W., "Effects of Composition, Microstructure, and Temperature on Irradiation Hardening of Pressure Vessel Steels", Effects of Radiation on Materials: Twelfth International Symposium, ASTM STP 870, American Society for Testing and Materials, Philadelphia, 1985, p 900.

[2] Fisher, S. B., Harbottle, J. E., and Aldridge, N., "Radiation Hardening in Magnox Pressure Vessel Steels", Philosophical Transactions of the Royal Society of London, Vol.A315, 1985, p 301.

[3] Odette, G. R., and Lucas, G. E., "Irradiation Embrittlement of Reactor Pressure Vessel Steels: Mechanisms, Models and Data Correlations", Radiation Embrittlement of Nuclear Reactor Pressure Vessel Steels: An International Review (Second Volume), ASTM STP 909, American Society for Testing and Materials, Philadelphia, 1986, p 206.

[4] Fisher, S. B., and Buswell, J. T., "A Model for PWR Pressure Vessel Embrittlement", International Journal of Pressure Vessels and Piping, Vol. 27, 1987, p 91.

[5] Williams, T. J., Burch, P. R., English, C. A., and Ray, P. H. N., "The Effect of Irradiation Dose Rate and Temperature, and Copper and Nickel Content, on the Irradiation Shift of Low Alloy Steel Submerged Arc Welds", Proceedings of the Third International Symposium on Environmental Degradation of Materials in Nuclear Power Systems - Water Reactors, Travers City, 1987. The Metallurgical Society, 1988, p 121.

[6] Buswell, J.T., and Jones, R.B., "The Modelling of Radiation Hardening and Embrittlement in Magnox Mild Steel Submerged-Arc Welds", Effects of Radiation on Materials: 16th International Symposium, ASTM STP 1175, American Society for Testing and Materials, Philadelphia, 1993, p 424.

[7] Bischler, P. J. E., and Wild, R. K., "A Microstructural Study of Phosphorus Segregation and Interganular Fracture in Neutron Irradiated Submerged-Arc Welds", Effects of Radiation on Materials: 17th Volume, ASTM STP 1270, American Society for Testing and Materials, Philadelphia, 1995, this Publication.

[8] Jones, R. B., and Buswell, J. T., "The Influence of Neutron Dose Rate on the Irradiation Hardening of C-Mn Reactor Pressure Vessel Steels", Effects of Radiation on Materials: 17th Volume, ASTM STP 1270, American Society for Testing and Materials, Philadelphia, 1995, this Publication.

[9] Jones, R. B., and Williams, T. J., "The Dependence of Radiation Hardening and Embrittlement on Irradiation Temperature", Effects of Radiation on Materials: 17th Volume, ASTM STP 1270, American Society for Testing and Materials, Philadelphia, 1995, this Publication.

[10] Druce, S.G., English, C.A., Foreman, A.J.E., McElroy, R.J., Vatter, I.A., Bolton, C.J., Buswell, J.T., and Jones, R.B., "The Modelling of Irradiation-Enhanced Phosphorus Segregation in Neutron-Irradiated Sumberged-Arc Welds", Effects of Radiation on Materials: 17th Volume, ASTM STP 1270, American Society for Testing and Materials, Philadelphia, 1995, this Publication.

[11] Murphy, S.M., "A Model for Segregation in Dilute Alloys During Irradiation", AEA Report AERE R 13405, 1989.

[12] Murphy, S.M., and Perks J.M., "Analysis of Phosphorus Segregation in Ion-Irradiated Nickel", J. Nucl. Mat., Vol. 171, p.360, 1990.

[13] Vatter, I.A., and Hippsley, C.A., "Final Report of Thermal Ageing Studies and Segregation Modelling of Model Mn-Mo-Ni Steels", AEA Report AEA-RS-2092, 1991.

[14] Vatter, I.A., Hippsley, C.A., and Druce, S.G., "Review of Thermal Ageing Data and its Application to Operating Reactor Pressures Vessels", NEA/CSNI Workshop, Safety Assessment of RPVs, Espoo, Finland, p.39, 1990.

Stephen G. Druce[1], Colin A. English[1], Alan J.E. Foreman[1], Ron J. McElroy[1], Ian A. Vatter[1], Chris J. Bolton[2], John T. Buswell[2] and R. Barry Jones[2].

The Modelling of Irradiation-Enhanced Phosphorus Segregation in Neutron Irradiated Reactor Pressure Vessel Submerged-Arc Welds

REFERENCE: Druce, S. G., English, C. A., Foreman, A. J. E., McElroy, R. J., Vatter, I. A., Bolton, C. J., Buswell, J. T., and Jones, R. J., **"The Modelling of Irradiation-Enhanced Phosphorus Segregation in Neutron Irradiated RPV Submerged-Arc Welds,"** *Effects of Radiation on Materials: 17th International Symposium, ASTM STP 1270,* David S. Gelles, Randy K. Nanstad, Arvind S. Kumar, and Edward A. Little, Eds., American Society for Testing and Materials, 1996.

ABSTRACT: Recent results on neutron-irradiated RPV submerged-arc welds have revealed grain boundary segregation of phosphorus during irradiation, which may lead to intergranular fracture. However, the experimental database is insufficient to define the dependence of the process on variables such as dose, dose-rate and temperature. This paper describes work in which two existing models of phosphorus segregation, under thermal or irradiation conditions, have been developed to obtain predictions of these dependencies.

The critical parameters in the models have been adjusted to give consistency with the available reference data, and predictions have been made of the dependence of segregation on a number of variables.

KEYWORDS: Irradiation damage, welds, segregation, phosphorus, inter-granular failure.

INTRODUCTION

The segregation of impurities to grain interfaces during component life is known to be a cause of in-service embrittlement and, in ferritic based components, commonly leads to a rise in the material ductile to brittle transition temperature (DBTT) and an increase in the propensity to failure by intergranular fracture. This

[1]AEA Technology, Harwell Laboratory, UK,
[2]Nuclear Electric, Berkeley Technology Centre, UK.

Copyright© 1996 by ASTM International www.astm.org

segregation can be caused by the action of thermal ageing, neutron irradiation or a combination of the two mechanisms.

More specifically, recent data [1]on the failure of C-Mn mild steel RPV submerged-arc weld surveillance samples subjected to an accelerated irradiation have highlighted the potential importance of a non-hardening irradiation embrittlement mechanism. This is in contrast to the conventional barrier hardening mechanisms from irradiation-produced clusters observed in the majority of other irradiated steels. Microstructural examination has pointed to the importance of grain boundary segregation of phosphorus during thermal ageing or irradiation, which may lead to an inter-granular failure mechanism [2]. However, the irradiation data base is insufficient to allow the dependence on parameters such as dose rate and component temperature to be determined and, thus, it is not possible from existing experimental studies to provide guidance on conditions under which this failure mechanism is important.

An approach that can provide mechanistic insight and guidance on the parametric dependence on any irradiation-induced segregation is that of applying theoretical models of thermal or irradiation-induced segregation to this situation. In this paper we describe the application of two models, developed by AEA-Technology, that describe phosphorus segregation under either thermal ageing or irradiation. Firstly, the kinetic minor element model for segregation of phosphorus in austenitic steels at high doses and temperatures, developed by Murphy and co-workers [3, 4], has been used to describe phosphorus segregation in iron. It makes a detailed analysis of the diffusive movements of all the defects, including the coupled interactions between the point defects and phosphorus atoms. This permits an evaluation of the level of phosphorus on the boundary plane from both random walk interactions and also from coupling of the phosphorus with either interstitial (I) or vacancy (V) point defects. Secondly, the equilibrium McLean type model developed by Druce and co-workers [5] to predict segregation during thermal ageing has been modified for the irradiation situation by incorporating effective vacancy diffusion coefficients. In the McLean equilibrium model the segregation is driven by the reduction in free energy of the system resulting from segregation of phosphorus to the grain boundary.

In both cases the physical conditions under which the models can be applied have been established, the critical parameters in the models have been examined, the models have been fitted against the available reference data, and the models have been used to describe the temperature dependence of segregation expected in material irradiated under surveillance and accelerated test conditions.

REFERENCE DATA

A key aspect of validating the models is the comparison with the available reference data on phosphorus segregation before and after irradiation. Experimental measurements have been made, using a Perkins Elmer 595 Scanning Auger Microscope and a Vacuum Generators HB501 (100kV) field emission gun scanning transmission electron microscopy (FEGSTEM), on the levels of grain boundary phosphorus prior to and after neutron

irradiation at temperatures between 160°C and 310°C. The data encompass materials irradiated under surveillance conditions (10^{-12} dpa/sec) and tests under accelerated conditions (10^{-9} dpa/sec), (see Buswell et al [6] for details of the irradiation). These are presented in Table 1. All the FEGSTEM data was obtained on the Harwell HB501. The segregation data shown in Table 1 are for welds irradiated under surveillance (10^{-12} dpa/sec) and under accelerated irradiation temperatures (10^{-9} dpa/sec) conditions at the irradiation temperatures and nominal doses indicated. The compositions of welds HS, LS and of the cut-out are given in [2] and [6] respectively; weld HT lay within the compositional range quoted in [6]. Pre-irradiation post-weld heat treatments were typically in the range 580 to 600C for 6 to 10 hours followed by slow cooling at 4 to 10C/hour [6]. The level of segregation measured has been converted to monolayer coverages using the method of Titchmarsh and Vatter [7] assuming a full-width half maximum (FWHM) of the X-ray profile of 3.5 nm. The Auger data was obtained on matchstick (2 x 2 x 10 mm miniature notch bend) samples specimens removed from the embrittled regions. It is important to note that in the Auger analysis no other embrittling species were found in significant levels [2].

It is to be noted that some phosphorus segregation occurred at the start-of-life, presumably during the post-weld heat treatment. Significant increases in the level of grain boundary segregation were observed in the high dose accelerated irradiations.

TABLE 1-- Reference Segregation data

MATERIAL	TEMP. (°C)	BULK PHOSPHORUS CONTENT wt%	MONOLAYER COVERAGE	CONDITION
LS	--	0.039	0.18	Unirradiated
LS	198	0.039	0.20	Surveillance 0.00094 dpa
LS	251	0.039	0.37 (mean) 0.54 (max)	Accelerated 0.0092 dpa
LS*	251	0.039	0.29	Accelerated 0.0092 dpa
HS*	286	0.040	0.42	Accelerated 0.0095 dpa
HT	290-310	0.028	0.27	Surveillance 0.00152 dpa
Cut-out	--	0.036	0.13 (mean) 0.20 (max)	Unirradiated
Cut-out	252	0.036	0.27 (mean) 0.49 (max)	Accelerated 0.00861 dpa
Cut-out	166	0.036	0.18 (mean) 0.25 (max)	Accelerated 0.00911 dpa

* Auger Data

KINETIC MINOR ELEMENT MODEL

Background

The kinetic model of Murphy [3, 4] was initially set up to analyse the transport of manganese or phosphorus in fcc nickel. The model does not take into account irradiation-induced segregation of the major alloying elements. It makes a detailed analysis of the diffusive movements of all the defects, including the coupled interactions between the point defects and phosphorus atoms. The corresponding treatment for a bcc material has not yet been made. The diffusion equations are solved numerically with a discrete grain boundary sink to determine the time dependent concentration profiles of the three components, namely vacancies, interstitials and phosphorus atoms. In the case of vacancies, the concentration is the sum of both thermal and irradiation-produced vacancies. The temperature at which thermal vacancies become important is dependent on dose rate and is discussed in the context of Figure 5. The normal irradiation-induced concentrations of the point defects are enhanced because of their interactions with the phosphorus atoms. Thus at any moment of time an appreciable fraction of the interstitial atoms will be diffusing as bound interstitial-phosphorus pairs, whilst a smaller fraction of the vacancies will also be interacting with the phosphorus atoms.

The diffusion of phosphorus atoms during irradiation is, in principle, induced by both the vacancies and interstitial atoms, which can move phosphorus atoms by simple replacement events. However the interstitials should produce a larger effect, because they are expected to have an appreciable binding energy with the undersized phosphorous atoms. Thus phosphorus atoms will form bound solute-interstitial pairs that can migrate over appreciable distances before dissociating. The distance travelled by each pair is determined essentially by the magnitude of the binding energy relative to the migration energy of the pair. This ratio appears to be a critical parameter in modelling the segregation of phosphorus in iron.

The internal dislocations are represented in these calculations by a continuum sink, as in standard rate theory calculations. The purpose of this continuum sink is to represent the average point defect trapping power of the dislocation network, which will be in a state of continuous motion during irradiation. We assume here that the dislocation density remains constant up to the grain boundaries. The dislocation density has been modified for the ferritic steels, which typically contain an average density of 10^{14} m^{-2} during irradiations up to ~0.01 dpa [6]. The additional fine-scale microstructure that is generated during these irradiations may enhance the sink density, particularly if it is produced near the boundaries, but this is not taken into account.

The grain boundaries are generally assumed to be good sinks for the point defects, so that a steep gradient of defect concentration is established near the boundaries. The concentration of irradiation produced defects greatly exceeds the level of the thermal vacancies at temperatures of interest, so that thermal segregation is negligible. At the accelerated rate there is appreciable recombination of the irradiation produced vacancies and

interstitial atoms, which modifies the shape of the profile near the boundary. The precise level of this recombination depends on the choice of the vacancy migration energy E_m^V and a range of acceptable values has been investigated, see below.

The flux of interstitial atoms towards the grain boundary from both sides produces a localised phosphorus segregation peak. The Murphy model allows phosphorus atoms to accumulate on the pair of atom planes immediately adjoining the boundary on each side. Thus we define the total boundary coverage produced by the calculations to be the sum of the segregation on both planes, i.e. double that on each. An important point is that phosphorus binding to the boundary was not specifically included in the original model, but this feature has now been added. The work of Vatter and Hippsley [8] indicates that, within the range of the present calculations, the phosphorus should be fully adhesive; that is for temperatures up to about 400C and a coverage not exceeding 50%. The underlying physical reason is that the binding energy of the phosphorus to the boundary is sufficiently high such that the desorption of the phosphorus can be neglected under these conditions.

Parameter Assignment

The results of the kinetic model will be compared with the available data on phosphorus segregation. The important parameters and assumptions made in applying the model are set out below. The values of the parameters are set out in Table 2.

(i) Choice of E_m^V

We take $E_m^V + E_f^V = 2.56$ eV in accord with the measured activation energy for thermal segregation obtained by Vatter and Hippsley [8] for ferritic steels. The vacancy migration energy, E_m^V, is believed to lie between 1.2 and 1.3 eV for ferritic steels and is usually slightly less than the vacancy formation energy, E_f^V. Thus we take $E_m^V = 1.24$ eV and $E_f^V = 1.32$ eV, although the choice is not critical within this range.

(ii) Rate of production of point defects.

The rate of production of point defects is assumed to be that given by the accepted formula due to Norgett Robinson and Torrens [9], NRT, but the effect of modifying this has been briefly assessed since there is evidence that it may be smaller.

(iii) Dumb-bell rotation energy.

The dumbell rotation energy has been shown to be the principal fitting parameter in this model. This rotation is easier in bcc than fcc metals (Deiderichs et al, [10]) and the energy barrier has been reduced from the Ni value of 0.75 eV. The value of the dumb-bell rotation energy is not well-known for Fe, but nevertheless an estimate has been made. Johnson [11] has calculated the relative energies of a large number of interstitial atom configurations in fcc Fe. He finds that in no case does this exceed that of the lowest energy configuration by more than 0.5 eV, so that the energy to rotate a dumb-bell is likely to be of this magnitude. The effect of one atom in the dumb-bell being an undersized phosphorus atom is estimated to reduce this rotation energy by ~15%. Thus the mixed dumb-bell rotation energy is likely to be ~0.4eV, which is comparable with its binding energy. This allows a

phosphorus atom to execute multiple jumps whilst associated with an interstitial atom, with a corresponding increase in the rate of segregation. We find that a value of 0.42eV gives a good overall fit to the measured segregation of phosphorus, as described below.

(iv) Nature of the grain boundary sink.

The grain boundaries are assumed here to be very good sinks for the point defects. However, the boundary sink efficiency can be varied in the Murphy model and the effect of this is also demonstrated. The segregation could be appreciably enhanced if they were to become 'poisoned' in some way against point defects, whilst still readily accepting phosphorus atoms. However such effects are difficult to quantify. This effect is illustrated in Figure 2(a).

(v) Initial distribution of the phosphorus.

The phosphorus is assumed to be distributed uniformly throughout the grains at the start of the irradiation. No allowance is made for any pre-existing denudation of the phosphorus near the boundaries due to the thermal ageing treatment of the steel. This local denudation is unlikely to affect the segregation when the phosphorus is being carried towards the boundary by an extended flux of point defects. However a pre-existing phosphorus profile could readily be included in the calculations, if it were to be considered an important effect.

Model Fit To Experimental Segregation Data

The accompanying Figs. 1and 2 show the comparison between the calculated and FEGSTEM measurements of the phosphorous segregation on boundaries. The calculated segregation represents the total segregation after irradiation, i.e. the sum of two components; the segregation during iradiation and the level of segregation at start of life. The measured values for the level of segregation in the unirradiated material are used (Table 1), except for HT and HS where no measured value are available and the value for LS was assumed.

Fig. 1 shows the agreement between the calculated and measured coverage for accelerated tests of LS. Figs. 1(a) and (c) show the calculated results for the accelerated tests of the Cut-Out Weld at 250°C and 166°C. The agreement is very satisfactory in both cases. In Fig. 1(b) the lower curve shows the accelerated test of LS. The upper curve is a similar calculation, but this has been continued from the end of the surveillance test on LS, taking into account the phosphorus denudation near the boundary from that test. There is good agreement with the mean coverage, but the maximum experimental coverage stands high. In Fig. 1(d) similar good agreement is shown for the Auger data from the accelerated irradiation of HS. The effect of reducing the bulk phosphorus content of HS from 0.04 to 0.02 Wt% is to almost halve the calculated rate of phosphorus segregation (not shown). Fig. 2 (a) shows the calculated coverage for surveillance irradiation of LS at 198°C, while Fig. 2(b) shows the result for the surveillance test of HT at 300°C, where the temperature dependence is too small to warrant using temperatures of 290 and 310°C. However we note that at 350°C thermal segregation is starting to occur. The agreement here is well within the uncertainties in the measured values.

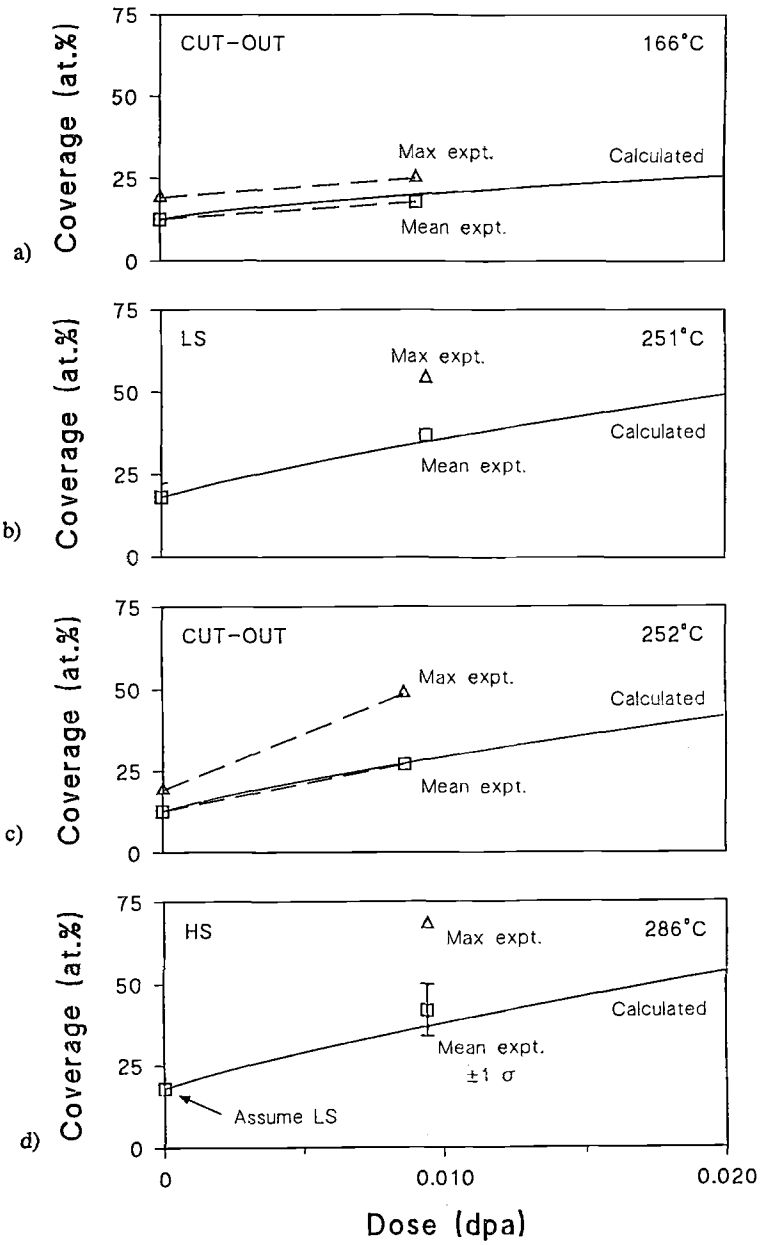


Fig. 1. Comparison of the calculated and measured phosphorus monolayer coverage versus dose for an accelerated irradiation (2×10^{-9} dpa/s), using the measured bulk concentration of phosphorus in each case.

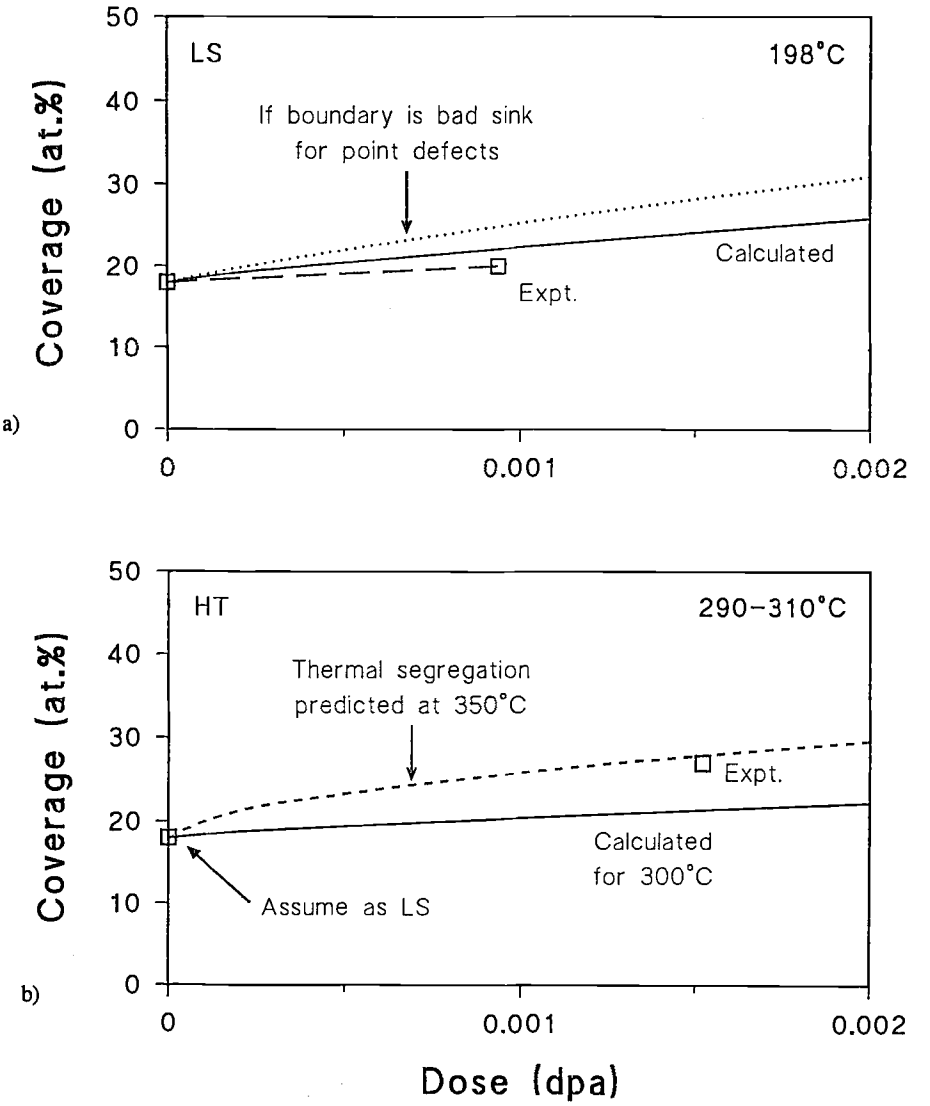


Fig. 2. Comparison of the calculated and measured phosphorus monolayer coverage versus dose for a surveillance irradiation (2 x 10^{-12} dpa/s) of (a) LS at 198°C, and (b) HT at 290 -300 °C, using the measured bulk concentration of phosphorus in each case.

To summarise, the fit obtained with the model is reasonably consistent, which gives confidence in the present modelling and suggests that irradiation is significantly enhancing the segregation. The agreement is most obvious in the accelerated tests at 250°C, where doses of up to 0.01 dpa have been attained.

TABLE 2-- Values of Physical Parameters Employed.

Dislocation density	10^{14} m^{-2}	*
Vacancy formation entropy	3 k	
Vacancy formation energy	1.32 eV	*
Vacancy migration energy	1.24 eV	*
Vacancy pre-exponential	$5x10^{13}$ s^{-1}	
SIA migration energy	0.15 eV	
SIA pre-exponential	$5x10^{12}$ s^{-1}	
Mixed dumbbell association energy	0.15 eV	
Mixed dumbbell dissociation energy	0.40 eV	
Mixed dumbbell rotation energy	0.42 eV	*
Mixed dumbbell migration energy	0.06 eV	
a-type SIA association energy	0.15 eV	
a-type SIA dissociation energy	0.32 eV	
a-type SIA migration around solute	0.15 eV	
b-type SIA association energy	0.24 eV	
b-type SIA dissociation energy	0.15 eV	
b-type SIA migration around solute	0.15 eV	

* Modified from Murphy-Perks values for Ni

MCLEAN EQUILIBRIUM SEGREGATION MODEL

Model Description

In the McLean model, the driving force for segregation is the reduction of free energy, ΔG_p, associated with moving solute atoms to the grain boundary [12]. The model

predicts that saturation level of grain boundary segregation, given sufficient time to allow equlibrium conditions, increases with decreasing temperature. However, the rate of segregation, being dependent on bulk diffusion, decreases with decreasing temperature. The model has been successfully applied to a wide range of materials including Fe-P-Cr alloys, Cr-Mo steels and Mn MoNi pressure vessel steels [13].

Model Parameters

The value of free energy change on segregation chosen for this report has been calculated using an equation derived from previous studies on model MoMnNi steels (Vatter and Hippsley [8]). These data represent the most comprehensive data base known, they have been derived using well-defined experimental procedures and have been shown to fit well with the McLean model predictions. The equation predicts the following temperature dependence of ΔG_p:

$$-\Delta G_p = 50.55 - 0.00474\ T \qquad (1)$$

where ΔG_p in kJ/mol
T in degrees K

Other equations have been suggested for phosphorus segregating in iron and other MoMnNi steels. e.g.

$-\Delta G_p = 56.7 - 0.0124\ T$	P in MoMnNi steel	Gage et al [14]	(2)
$-\Delta G_p = 44 + 0.01025\ T$	P in Iron	Druce et al [13]	(3)
$-\Delta G_p = 34.3 + 0.0215\ T$	P in Iron	Briant et al [15]	(4)

Over the temperature range that this model has been applied (190°C - 400°C) all of these equations give similar values for the free energy change on segregation. At 190°C the calculated ΔG_p values range from - 44 to - 51 kJ/mol. At 410°C ΔG_p ranges from -47.3 to -51 kJ/mol. The effect of these variations on the equilibrium segregation is as follows. At 190°C the predicted equilibrium coverage varies by approximately 1% (98.5 - 99.5%), and at 400°C the range is from 75 to 85% of a monolayer, with the equation used here giving a value of 75%. As can be seen the model is not particularly sensitive to the choice of free energy data obtained from a study of MoMnNi steel.

The diffusion rate for use in the McLean kinetic formula has been calculated from a fit to thermal ageing data for phosphorus in iron and low alloy steels and can be expressed as

$$D = D_0 \exp - ((E_f^V + E_m^V)/ kT) = D_v C_v^e \qquad (5)$$

where E_f^V = Energy of vacancy formation
E_m^V = Energy of vacancy migration
For thermal diffusion $E_m^V + E_f^V = 2.56$ eV
D_v = Vacancy diffusivity
C_v^e = Thermal vacancy concentration

In modelling the irradiation enhanced diffusion the E_f^V term has been replaced by the vacancy concentration as calculated by the kinetic model, this is equivalent to replacing C_v^e by the irradiation-induced concentration, C_v. The increased concentration of vacancies produced by irradiation enhances the diffusion rate but does not affect the equilibrium level. In addition it is assumed that the vacancy concentration is uniform up to the boundary.

Model Fit to Experimental Segregation Data

In Figs. 3 and 4 the data are presented as segregation versus dose and the segregation predicted by the model is compared with the available experimental data. The initial level of grain boundary coverage of phosphorus has been taken as the mean of the unirradiated values available (i.e. 0.15 monolayers). The initial segregation, taken from the unirradiated condition, has been treated in two ways which are considered to bound the actual behaviour. In the "zero time" case subsequent segregation has simply been added to the initial segregation. This will provide an upper bound to the predicted segregation levels. In the "equivalent time" case it is assumed that the boundary is initially free of segregation (i.e. coverage = 0) and the time required to achieve the measured initial segregation is calculated for the relevant subsequent ageing conditions of irradiation temperature and dose rate. Subsequent segregation is then calculated extending from this period. This will provide a lower bound to the predicted segregation levels. The mean value of the experimental data has been plotted on the graphs and the error bar extended to the maximum value and a similar distance below the experimental point. The predicted effect of surveillance irradiation on the segregation of phosphorus in a material containing 390 wtppm phosphorus, (Fig. 4 (a)), agrees well with the experimental observation from LS surveillance data. In the other cases the experimental points lie above the prediction. However the theoretical predictions are close to or within the range of scatter of experimental data.

PREDICTIONS OF THE MODELS

Both model predict similiar trends:

1. For an equivalent time the accelerated irradiation dose rate enhances segregation compared with the surveillance dose rate. However, the segregation per unit dose is less in the accelerated irradiation.
2. High fractional monolayer coverage is predicted for extended irradiation times at the accelerated dose rate but not at the surveillance dose rate.
3. In both models there is no appreciable effect of irradiation temperature at the surveillance dose rate over the range 190° C- 310°C.
4. In both models increasing the irradiation temperature at the accelerated dose rate over the range 190°C - 310°C increases the degree of segregation.
5. The additional segregation levels at the surveillance dose rate are approximately proportional to bulk phosphorus levels.

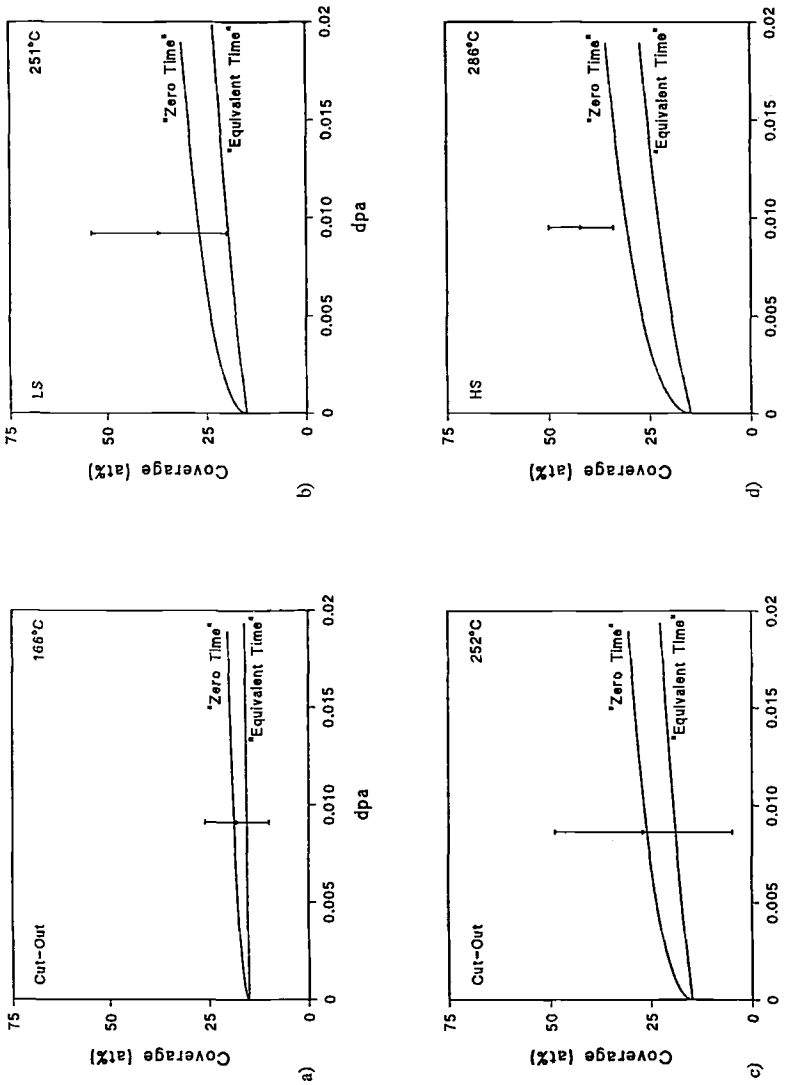


Fig. 3. Comparison of irradiation enhanced McLean model with experimental data using E_m V=1.24 eV and an accelerated dose rate (2×10^{-9}dpa/s).

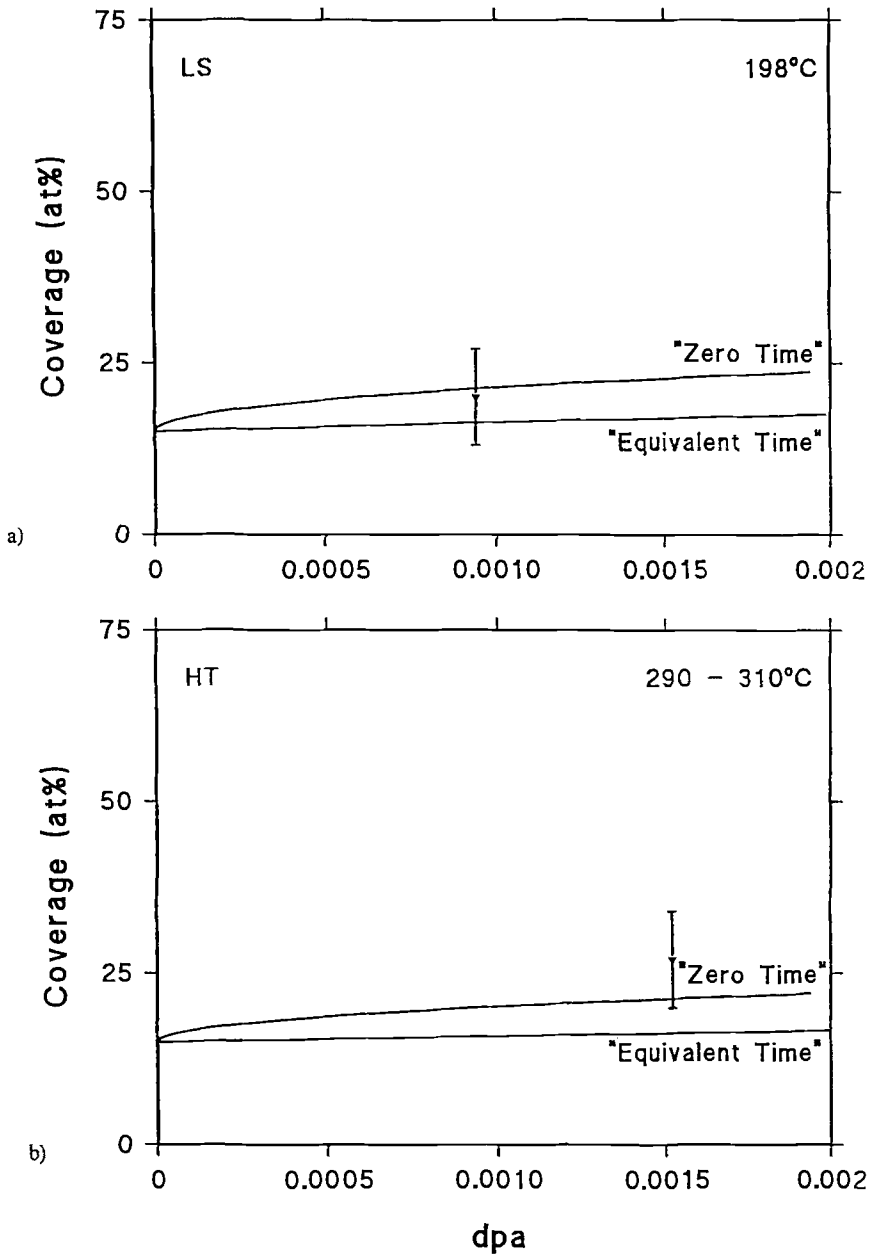


Fig. 4. Comparison of irradiation enhanced McLean model with experimental data. using E_m^V=1.24 eV and at a surveillance dose rate (2 x 10^{-12}dpa/s).

6. In both models the initial segregation level is likely to dominate the final segregation level at the surveillance dose rate. At the accelerated dose rate the initial segregation level will only dominate for the first few thousand hours.
7. The "equivalent time" thermodynamic model predicts lower levels of segregation but the "zero time" approximation shows reasonable agreement with the kinetic model.

This is illustrated for the kinetic model in Figure.5.

1. Fig. 5(a) shows temperature dependence of the segregation under surveillance calculated for two surveillance doses (0.002 and 0.005 dpa after 32 years, corresponding to damage rates of $2x10^{-12}$ and $5x10^{-12}$ dpa/s). The results, show a modest peak in the region 150°C to 200°C and a sharp rise above ~310°C due to the thermal vacancies. At a surveillance dose of 0.002 dpa relatively little irradiation-induced segregation is observed at temperatures below 310°C. The approximately linear increase of segregation with dose is also apparent from the Fig..

2. At the accelerated dose rate (Fig. 5(b)) at a dose of 0.01 dpa the segregation exhibits a progressive rise up to 300°C, which is the result of a steady reduction in the point defect recombination, followed by a plateau and then a rapid increase above 400°C from thermal segregation. From the present calculations we cannot identify, at this dose, a temperature below which the segregation is likely to be negligible. However, there is a possibility that the enhanced density of the irradiation-produced microstructure at the lower temperatures, which has not been included here, might introduce an additional temperature dependence.

DISCUSSION AND CONCLUSIONS

The models have been fitted to the available experimental data and predictions made to the temperature and dose rate dependence of the observed segregation. The conclusions from comparing the two sets of predictions are presented later. Before undertaking a comparison of the two sets of predictions the impact of the major assumptions in each model are assessed.

Assessment of the Models

Kinetic model -- There are several possible limitations in the present application of this kinetic model, which need to be discussed. These are set out below:

(i) The present code is set up to describe diffusive mechanisms in fcc metals. The precise atomic jumps leading to diffusion of solute-point defect complexes will be different in bcc metals, and have not as yet been formally set out in the literature. Thus, an uncertainty in approach here is how it will be modified on going to a bcc model. However it is highly likely that, provided the rotational energy is low, then the insight developed here will still hold true for a more exact model.

(ii) In modelling the dislocation density no allowance has been made for the effect of the fine-scale irradiation-produced microstructure on the amount of phosphorus available or on the quasi-steady state concentrations of vacancies and interstitials. However for the low doses at present being considered this should not be a serious limitation. The effect of such a microstructure must be to reduce the amount of segregation, especially towards the lower temperatures, and so the calculations here are likely to be conservative in this respect.

(iii) The nature of the grain boundary sink is clearly important, as it has been assumed to be a perfect sink for point defects. If it is not able to absorb all the defects reaching it then the amount of segregation will be enhanced, see later.

(iv) The model assumes that the phosphorus will remain uniformly distributed on the boundary.

(v) The rate of production of point defects is assumed to be given by the NRT value. Preliminary calculations indicate that the effect of introducing a 25% efficiency factor, as suggested by computer simulations of damage cascades, can be offset by reducing the dumbell rotation energy to 0.36 eV, which is still within the range of physically reasonable values.

Irradiation Enhanced McLean Model-- The model is theoretically well founded for binary Fe-P alloys and has been well validated empirically for model and commercial MnMoNi and Cr Mo steels under thermal ageing. The MnMoNi model alloy data have provided data to determine the free energy of phosphorus segregation and its associated temperature dependence. Under thermal ageing the segregation kinetics are controlled by the diffusion coefficient which in turn is dependent on the sum of E_f^V and E_m^V. Empirical data have been used to confirm and slightly modify values of diffusion coefficient taken from the literature. These data taken from MnMoNi steels have been assumed to apply to the submerged-arc steel weldmetals.

In addition to the possible effects of changing alloy type there are two principal uncertainties in the modelling as applied under irradiation: the treatment of non-zero initial segregation levels and the assumed vacancy concentration.

The treatment of the initial segregation level and the related effect of two stage ageing presents some uncertainty in predicted levels of segregation. Neither of the two cases presented are totally rigorous but they are considered to provide bounding solutions. The trends in the predicted segregation dependence on irradiation temperature and dose rate (Fig.5) are not affected by the choice of treatment of initial coverage

The vacancy concentration calculated under irradiation, and used in this model to define an effective E_f^V, is dependent on the assumed value of E_m^V. The exact value of E_m^V is not known for this material but is thought to be in the range 1.0 to 1.3 eV. Reducing the value of E_m^V from 1.28 to 1.0 eV does not affect the predicted segregation at the

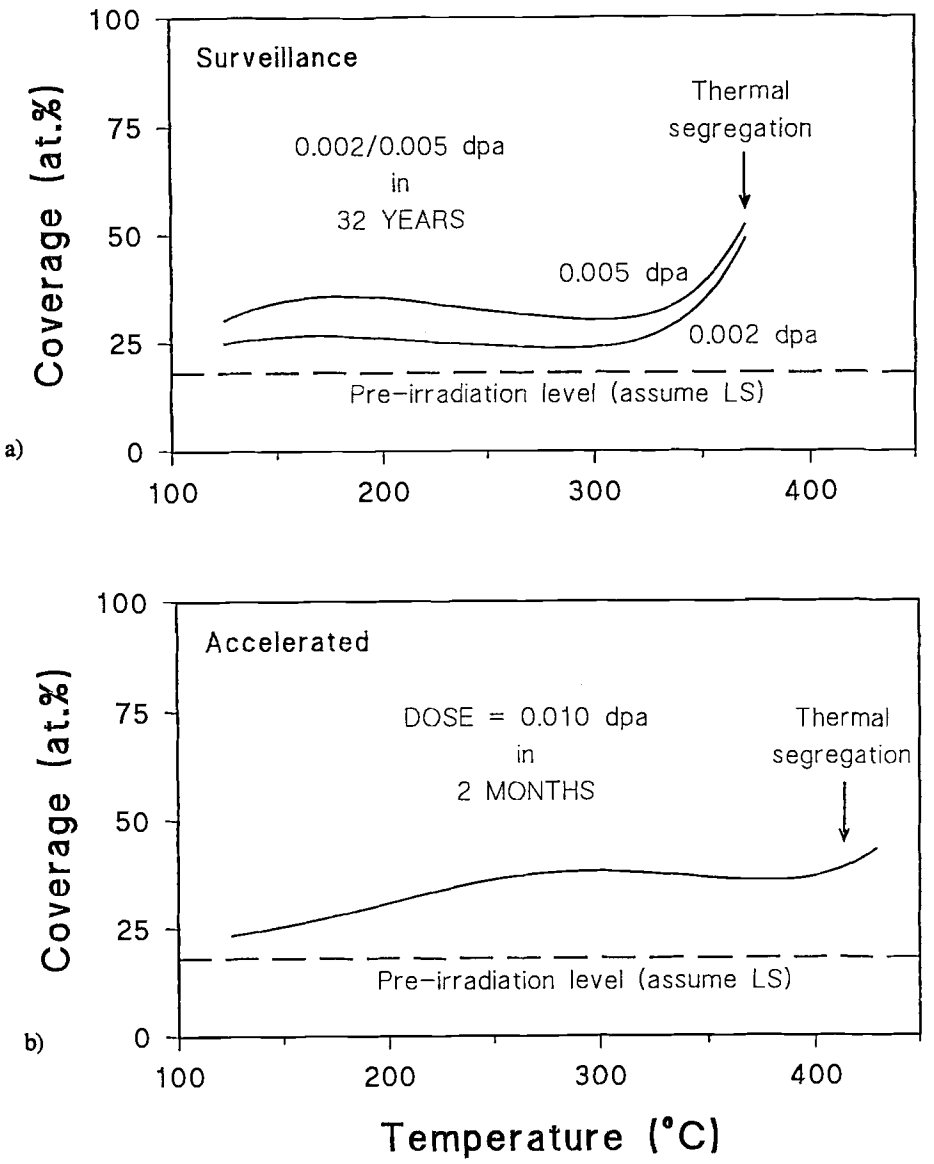


Fig. 5. Calculated temperature dependence of the grain boundary coverage for (a) surveillance irradiations (for a bulk concentration of 0.04 Wt% phosphorus) at both 2 x 10^{-12} and 5 x 10^{-12} dpa/s after 32 years, and (b) for accelerated irradiations (for a bulk concentration of 0.04 Wt% phosphorus) at 2 x 10^{-9} dpa/s to 0.010 dpa, assuming the pre-irradiation level to be as measured for LS.

surveillance dose rate over the temperature range 190°C - 300°C or at the accelerated dose rate for T>300°C. However for T<300°C the predicted segregation is increased.

No attempt has been made to model the vacancy gradient predicted by the kinetic model to occur close to the grain boundary if the boundary is assumed to be an effective vacancy sink. The vacancy concentration used in the McLean model predictions is that appropriate to the grain interior. Reducing the vacancy concentration to simulate vacancy gradients close to the boundary would proportionately increase the time to reach a particular segregation level.

Comparison of Physical Processes Underlying the Two Models

It is important to distinguish between the dominant physical processes underlying each model. For the kinetic model the grain boundary is a perfect sink for point defects but it has been made "adhesive" so that all phosphorus atoms reaching the boundary are trapped there. The physical process that gives rise to segregation at the boundary is the strong coupling of the phosphorus to the flux of interstitial point defects going to the boundary down the concentration gradient. The low concentration of defects close to the boundary reduces the rate at which the phosphorus atoms will arrive by random walk processes and appreciable segregation can only occur if there is this strong coupling between phosphorus and interstitial point defect. If the grain boundary becomes a negligible sink for point defects and steep concentrations gradients are not built up then there will not be a net flux of point defects to the boundary. In this case phosphorus atoms will arrive by random walk processes involving exchange with either vacancy or interstitial point defects. It is the segregation in this situation due to vacancy exchange that is described by the McLean thermodynamic model employed here. The grain boundary has been poisoned and does not absorb the point defects arriving at it, and the segregation is occasioned by random walk processes involving the interchange of vacancies and phosphorus atoms. Thus, each model represents a limiting case of processes likely to control the movement of phosphorus to the boundary under the influence of the irradiation-produced point defects.

The effect on the predictions of the kinetic model of the grain boundary acting as a very bad sink for the point defects, whilst still accepting phosphorus has been explored for the surveillance and accelerated irradiation conditions. As explained above, the segregation is occasioned by random walk processes (in this instance the kinetic model accounts for exchange between interstitials and vacancies). In both cases the segregation is similar but slightly greater than the segregation predicted for the "good" boundary condition when the point defects are absorbed at the boundary. It is important to note that in performing these calculations the phosphorus has been denuded adjacent to the boundary prior to irradiation to simulate the segregation occurring during thermal ageing, as in the McLean model. Otherwise the high density of irradiation produced defects close to the boundary would effectively repeat the thermal ageing segregation.

Conclusions on the Predictions of the Two Models

(i) The preliminary attempts to use both models to predict the segregation occurring in C-Mn submerged arc welds has met with some success. The models have been fitted to the available experimental data and predictions made on the temperature and dose rate dependence of the segregation.

(ii) It is to be emphasised that both models make major assumptions on the physical processes occurring and the results of the calculations must in each case be regarded as indicative rather than a detailed prediction which can be applied to individual steels. The assumptions are likely to encompass the actual segregation mechanisms.

(iii) In each model one set of physically reasonable parameters can be chosen which are consistent with the data in Table 1. A controlling factor in each case is that the movement of P at temperatures below that required for appreciable thermal vacancy concentrations is controlled by the irradiation-produced vacancy or interstitial concentrations. It is this that generates the similar dependence on irradiation temperature and dose rate.

(iv) Predictions have been made of the temperature dependence to be expected under surveillance and accelerated irradiation conditions. For both models the segregation under surveillance conditions does not show a strong temperature dependence until the segregation becomes dominated by the thermal vacancies i.e temperatures above 310°C. Under accelerated conditions some dependence on temperature is predicted in the region at 190-300°C.

ACKNOWLEDGEMENTS

This paper is published by permission of Nuclear Electric plc.

REFERENCES

[1] C.J. Bolton, J.T. Buswell, R.B. Jones, R. Muskovic, and R.H. Priest, this publication.
[2] P.J.E Bischler and R.K.Wild. Proceedings of this conference (1994)
[3] S.M. Murphy, Harwell Report AERE R 13405 (1989).
[4] S.M. Murphy and J.M Perks, J. Nucl. Mater. **171** (1990) 360.
[5] S.G. Druce, G Gage, and G R Jordan, Acta Met **34** (1986) 641.
[6] J.T. Buswell, C.J.Bolton, M.R. Wooton, P.E.J. Bischler, R.B. Jones, L.T. Jones, W.J. Phythian, and R. Sinclair. Proceedings of the 16th International Symposium on Effects of Radiation on Materials. (Editors Gelles, Nanstead and Little) ASTM, Philadelphia, 1993, p 332-351.
[7] J.M. Titchmarsh, I.A. Vatter, Proceedings of NATO advanced workshop on 'The evaluation of advanced semiconductor materials by electron microscopy' Ed. D Churns, Bristol University Sept 1989.
[8] I.A. Vatter and C.A. Hippsley, Harwell Report AEA-RS-2092 (1991).

[9] M.J.Norgett, M.T.Robinson, and I.M.Torrens, Nucl Eng Design, **33** (1975) 50
[10] P.H. Dederichs, C. Lehmann, H.R. Scrober, A. Scholz and R. Zeller, J. Nucl. Mater. **69 & 70** (1978) 176.
[11] R.A. Johnson, Phys. Rev. **145** (1966) 423.
[12] D McLean in "Grain Boundaries in Metals", Clarenden Press, Oxford (1957).
[13] S G Druce, G Gage, G Jordon, "Effect of Ageing on Properties of Pressure Vessel Steels" Acta Metall Vol 34 No 4 pp. 141-252, 1986
[14] G. Gage, PhD Thesis Univ of Leeds England 1984.
[15] C.L. Briant and H. J. Grabke, Mat Sci Forum, **46**, (1989) 253.

A. Fabry[1], J. Van de Velde[1], J.L. Puzzolante[1], T. Van Ransbeeck[1], A. Verstrepen[1], E.C. Biemiller[2] , R.G. Carter[3] , T. Petrova[4]

RESEARCH TO UNDERSTAND THE EMBRITTLEMENT BEHAVIOR OF YANKEE/BR3 SURVEILLANCE PLATE AND OTHER OUTLIER RPV STEELS

REFERENCE: Fabry, A., Van de Velde, J., Puzzolante, J. L., Van Ransbeeck, T., Verstrepen, A., Biemiller, E. C., Carter, R. G., and Petrova, T., **"Research to Understand the Embrittlement Behavior of Yankee/BR3 Surveillance Plate and Other Outlier RPV Steels,"** *Effects of Radiation on Materials: 17th International Symposium, ASTM STP 1270,* David S. Gelles, Randy K. Nanstad, Arvind S. Kumar, and Edward A. Little, Eds., American Society for Testing and Materials, 1996.

ABSTRACT: The reactor pressure vessels at the Yankee Rowe and Belgian BR3 nuclear plants were constructed by Babcock & Wilcox in 1958. The plates of an open-hearth fabrication were welded using a submerged-arc process with Linde 80 flux as the filler. The original surveillance programs at the two plants were limited to representative A302B specimens; they feature similar chemistries as the ASTM reference plate, but coarser microstructure. The present testing program includes sixteen Charpy-V and four tensile specimens of the surveillance plate, irradiated at BR3 at a dose rate of ≈ 7 E10 $cm^{-2}.s-1$ (>1MeV) over a period of 25 years; the investigation also addresses annealing and notch orientation effects. The new experimental results are compared to previously published data for the same and/or related melts. The Yankee/BR3 surveillance plate displays an anomalously large 41J C_v-shift as compared to the ASTM reference plate and to Regulatory predictions. Some of the Linde 80 welds investigated by the BR3 program are also found to behave as outliers. The data are evaluated in the light of state-of-the-art damage modeling and fracture micro-mechanics concepts, which are currently being incorporated into a new, consolidated strategy for improved RPV surveillance. The approach makes extensive use of the information contained in the load-deflection response of the instrumented C_v test. The implications of such analysis in terms of RPV steel embrittlement trend curve development are discussed.

KEYWORDS: Reactor pressure vessel steel, irradiation embrittlement, surveillance, reconstitution, fracture toughness, micromechanics, damage modeling, safety.

[1]Lead scientist, manager, senior engineer, senior engineer and technician, Boeretang 200, 2400 Mol (Belgium)

[2]Principal engineer, Yankee Atomic Electric Company, Bolton, USA.

[3]Project manager, Electric Power Research Institute, Charlotte, USA.

[4]Research scientist, INRNE, Sofia, Bulgaria

Copyright© 1996 by ASTM International www.astm.org

1. BACKGROUND: THE APPARENT OUTLIER BEHAVIOR OF SOME LWR REACTOR PRESSURE VESSEL STEELS

Yankee/BR3 Surveillance Plate Embrittlement Dilemma

The reactor pressure vessels at the Yankee Rowe (YR) and Belgian BR3 nuclear plants were built in 1958, by Babcock and Wilcox Company, to the ASME Section VIII design requirements. The hot formed plates, of an open-hearth fabrication, were welded using high Mn-Mo wires and a submerged-arc process with Linde 80 flux as the filler. The plates are clad with spot resistance welded 304 stainless steel, and the welds are clad by 308L deposits. The final stress relief temperatures were in the range 590-620°C (for an accumulated time of ~31h. at BR3). The single BR3 plate is made of nickel modified A-302 grade B steel, similar to the Yankee Rowe lower shell plate; there was no nickel addition in the case of the upper shell plate at Yankee, and the surveillance specimens (C_v and tensile) prepared by the plant vendor (Westinghouse) are representative of this plate only, at both Yankee and BR3 [1]. No weld specimens were included in the surveillance capsules at either plant, but this was later done at BR3.

Table 1 gathers the chemistries of the plates under consideration. Also included are the chemistries of the ASTM reference plate and of surrogate surveillance plates procured for accelerated irradiations in support of license renewal programmes: either by Yankee Atomic (YA1,YA9) [2] or by SCK-CEN (PT-A, BR3 anneal) [3].

TABLE 1-- Chemical composition (wt.%) of base metals relevant to Yankee Rowe and BR3 vessels and their surveillance programs.

	C	Mn	P	S	Si	Cr	Ni	Mo	Cu
BR3 Shell	0.28	1.25	0.020	0.020	0.26	0.06	0.56	0.47	0.19
YR Lower Shell	0.19	1.18	0.016	0.026	0.20	-	0.63	0.48	0.20
YR Upper Shell	0.20	1.27	0.020	0.028	0.21	-	0.21	0.48	0.18
YR Surv. Plate	0.20	1.20	0.018	0.028	0.22	0.14	0.19	0.42	0.19
ASTM Ref. Plate	0.23	1.36	0.012	0.025	0.24	0.11	0.18	0.50	0.20
YA9	0.17	1.28	0.026	0.022	0.22	-	0.19	0.50	0.24
YA1	0.25	1.40	0.008	0.011	0.23	-	0.62	0.59	0.24
PT-A	0.22	1.44	0.011	0.021	0.24	0.10	0.55	0.59	0.19

The Yankee Rowe and BR3 vessel plates were austenitized at 954-982°C [1]; this exceeds the range typical of the base metals represented in the USNRC Regulatory Guide 1.99 by about 70 °C [4] and results in coarser prior austenite grains: ASTM n°7, diameter ~ 36μ, as compared for instance to ~ 15μ for the ASTM A302-B

reference plate. Larger austenite grains promote the formation of larger laths of ferrite during quenching, and because ferrite is generally considered as the governing hardenable phase [8], it did not seem unreasonable that the Yankee surveillance plate might be more sensitive to irradiation than the reference plate [5]-[7]. It had also been found in another study [9] that large-grained ferrite-bainite structures can exhibit significantly greater embrittlement than fine-grained ones; the anomalously coarse ferrite grains in this case were traced to the fact that these high sensitivity heats were not renormalized subsequent to a high temperature (1290°C) roll-bond cladding [10]; the C_v- shift anomaly was however proportionately reflected by the yield strength increase, which is not the case for the Yankee/BR3 surveillance plate (see Section 3).

It is important to point-out that the vessel beltline materials at both Yankee Rowe and BR3 are operated at an average temperature of 260°C (500°F).[1]

The outlier behavior of the Yankee/BR3 surveillance plate is illustrated by Figures 1 and 2. Here, the data for the ASTM reference plate have been taken from Stallmann's evaluation [11]. The surveillance plate 41J shift data at BR3 lie well above the reference plate and Regulatory Guide trend curves, even allowing for the slightly lower irradiation temperature for the surveillance plate (274-282 °C); and while the FATT data fall within the Regulatory margin, they lie near the upper bound, consistent with the lower irradiation temperature. The C_v -upper shelf drops of the surveillance and reference plates are also consistent with one another (for ex., Figure 2).

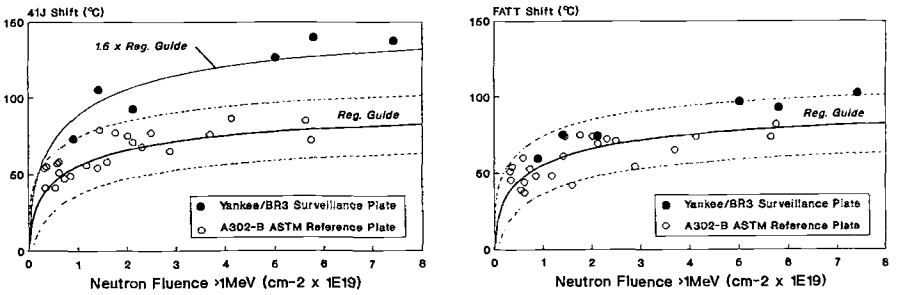


FIG. 1-- Outlier behavior of Yankee Rowe surveillance plate.

Figure 3 summarizes an evaluation of this situation as performed in Spring 1991 [12]. This was done before completion of Ford Nuclear Reactor (FNR) accelerated irradiations of the Yankee Rowe YA1 and YA9 surrogate plates [2]. Whenever applicable, the preliminary FNR results have been plotted here on the original figures (3b, c) forcomparison. It is reminded that YA1 and YA9 were heat treated to simulate the Yankee vessel (coarse grain) and Regulatory Guide 1.99 data base materials (fine grain); specimens taken from plate surface locations (vs. 1/4T) were included, as well

[1]Regulatory Guide 1.99 refers to an irradiation temperature of 288°C (550 °F); the Guide suggests a correction (penalty) of 1°C toughness shift for 1°C difference in irradiation temperature.

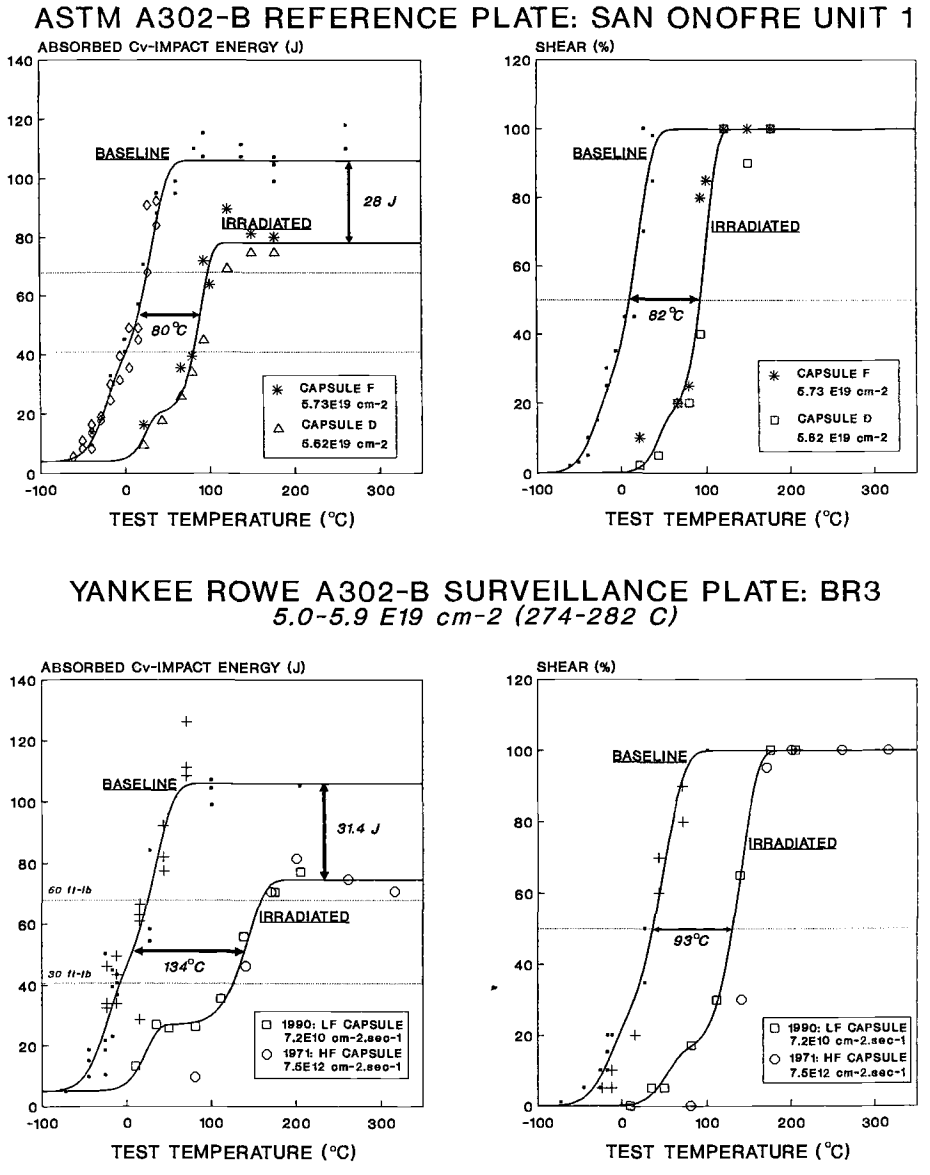


FIG. 2-- Outlier behavior of Yankee surveillance plate.

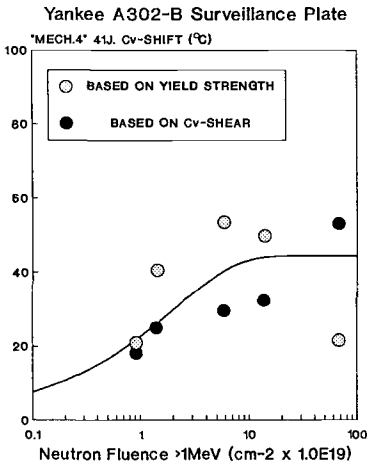


Fig. 3.a

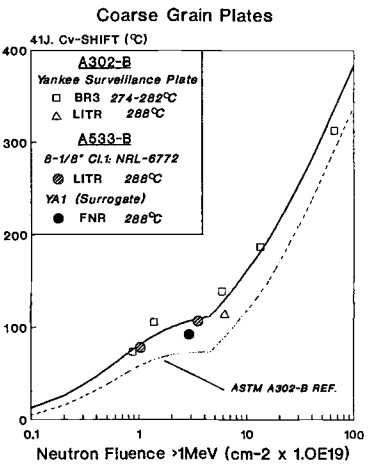


Fig. 3.b

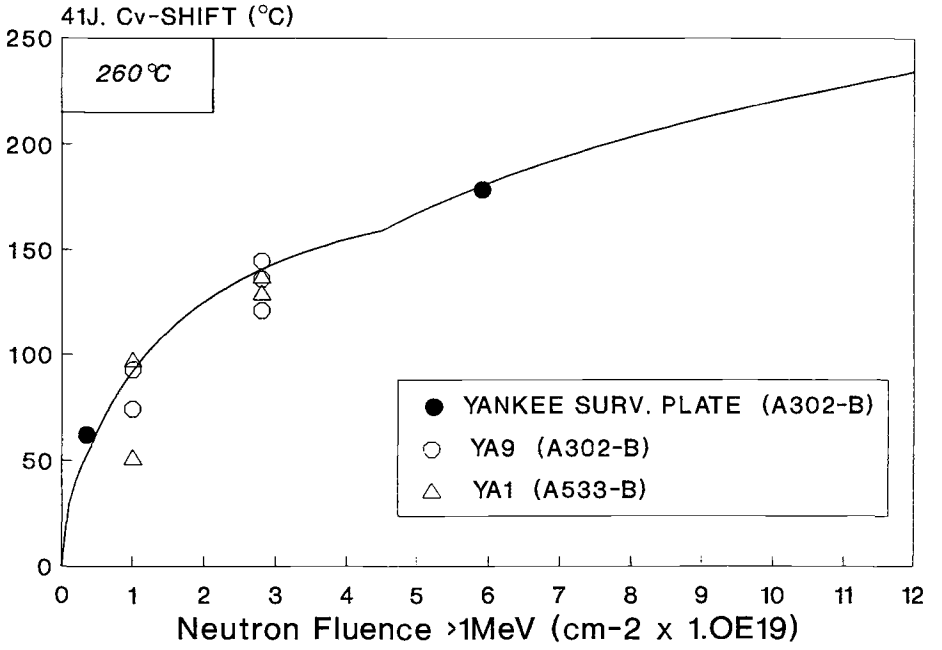


Fig. 3.c

FIG. 3-- Evaluation of the embrittlement of Yankee Rowe lower and upper beltline plates.

as correlation monitor HSST-02. The 1991 evaluation relied on the similarity of composition between the Yankee/BR3 A302-B surveillance plate, the ASTM reference A302-B plate and the Yankee vessel upper shell plate (Table I); a trend curve for the vessel upper plate was derived by applying two corrections to the reference plate trend curve (Figure 1 and Section 3):

1) Projection to the lower irradiation temperature of 260 °C prevailing at vessel beltline; this correction was fluence dependent and slightly larger than recommended in the Regulatory Guide; it was considered unaffected by the microstructure and the nickel content of the plate (these two views have been confirmed, see Section 3).

2) Correction for the high austenitization temperature and coarser-than-usual microstructure (Figure 3a); this microstructure influence was treated as an additional damage mechanism, found unannealable and labelled "mechanism 4", along a nomenclature introduced by Pachur [16]; the fluence dependency was estimated from the tensile yield strength and C_V-FATT (fracture appearance) shift data obtained for the A302-B surveillance plate at BR3.

In order to derive a trend curve for the Yankee lower shell plate, the influence of the nickel modification needed to be estimated. The 1991 evaluation concluded that there is no nickel influence. This is shown by Figure 3.b. The Figure gathers one LITR result for the Yankee surveillance plate (L-T, 1/4T) [13], the oldier BR3 surveillance data (summarized in Section 4, and confirmed by the new experiments, also described in Section 4), and two LITR results for a 8 1/8" A533-B class 1 plate (Cu: 0.19%; Ni: 0.48%) [14]; this plate is most relevant because it does feature the same austenitization conditions as the Yankee A302-B surveillance plate and does behave in similar manner: no anomaly of the irradiation effect on tensile nor C_v- upper shelf properties, but an excessive 41J. shift [14], [15]. It is proposed in Section 3 that fine grain plates are not affected by nickel either, in the compositional range considered here.

The 41J.-shift trend curve believed applicable to the Yankee Rowe upper *and* lower beltline plates, as well as to the BR3 plate, is shown on Figure 3.c. It is noteworthy that never do enter into this scheme the actual surveillance data developed by NRL using the Yankee Rowe capsules [1] [13], but they are plotted on Figure 3.c and are seen to agree with the evaluation; note that, despite in-depth transport theory re-evaluation of the dosimetry for the Yankee Rowe capsules [1], it is possible that the higher fluence datum, plotted at 5.9 E19 cm-2 (>1MeV), could have seen a fluence of 10.6 E19 cm-2 (best value for *nominal* location of this capsule). In any event, the evaluation [12] stated that the trend curve of Figure 3.c is an **upper bound**. The Yankee Atomic accelerated irradiation and test data (YA1, YA9) have later confirmed the evaluation (Fig. 3c). It was also suggested that the microstructure effect had not to do with some additional irradiation-induced defect, but was accountable for as a micromechanical effect: "Mechanism 4" was assumed to act on the plastic strain energy absorption as enhanced by the lack of constraint (triaxiality) at the notch of a conventional Cv- specimen; such influence, it was contended, would eventually

disappear under the plane strain field within a reactor vessel. A supportive analogy was found in the systematics of C_v- reconstitution entailing small inserts [17],[18]: increased constraint due to localized blockage of the plastic flow by the hard welded zones caused significant energy loss without any modification of fracture appearance curves; also, the precracking and side-grooving of similar reconstituted specimens provided upper shelf static initiation fracture toughness values equal to the ones measured with the original samples [18]. It was concluded that the FATT shift must be a better indicator of fracture toughness shift than the Regulatory 41J. shift.

Test Reactor Irradiations in Support of the 1984 BR3 Vessel Anneal

The BR3 reactor was operated from 1962 to 1987. In 1984, the BR3 vessel was successfully wet-annealed during 168h. at 343°C [3] [19], and re-licensed; the maximum inner surface neutron fluence at the time of this anneal was ~3.3 E19 cm-2 (> 1MeV), corresponding to ~72000 efph. At the time of final plant shutdown, the vessel fluence reached ~4.0 E19 cm-2 (> 1MeV), after ~86000 efph.

The licensing of the BR3 vessel anneal has largely been based on an accelerated irradiation program conducted at the UBR test reactor [20],[21], using commercial "archive" steels chosen to be representative of the vessel. After 1978, the longitudinal, low upper shelf Linde 80 submerged-arc weld has been considered governing in terms of vessel integrity considerations, and five old vintage Linde 80 welds have been the focus of the investigations. The archive plate PT-A (Table 1) was also selected because its chemistry matches the BR3 plate chemistry, but as its upper shelf level is larger, 0.5T-CT and C_v specimens of the ASTM reference A302-B plate in its weak (T-L) orientation were used to verify the extrapolation, to very low toughness levels [21]. Table 2 provides excerpts of the chemistry data for the BR3-related Linde 80 welds considered in this paper. They were obtained from B&W (courtesy: A.L. Lowe, Jr.) and were specially heat-treated to be representative of the vessel weld (stress relief: 31h., 590-620°C), except the material labelled W-E, cut from a coupon of the Quad Cities II surveillance weld (courtesy: T.U. Marston, EPRI).

TABLE 2-- Chemical composition (wt.%) of Linde 80 weld metals relevant to BR3 vessel and its anneal/post-anneal surveillance program.

	C	Mn	P	S	Si	Cr	Ni	Mo	Cu
BR3 Weld	0.12	1.20	0.018	0.019	0.32	0.06	0.70	0.49	0.18
W3	0.09	1.55	0.017	0.021	0.44	0.09	0.67	0.41	0.32
W1	0.09	1.40	0.021	0.020	0.54	0.07	0.56	0.40	0.31
W2	0.10	1.42	0.020	0.021	0.52	0.07	0.56	0.41	0.26
W-E	0.10	1.68	0.013	0.016	0.56	0.07	0.56	0.39	0.23
W-D	0.03	1.74	0.014	0.013	0.41	0.14	0.60	0.41	0.19

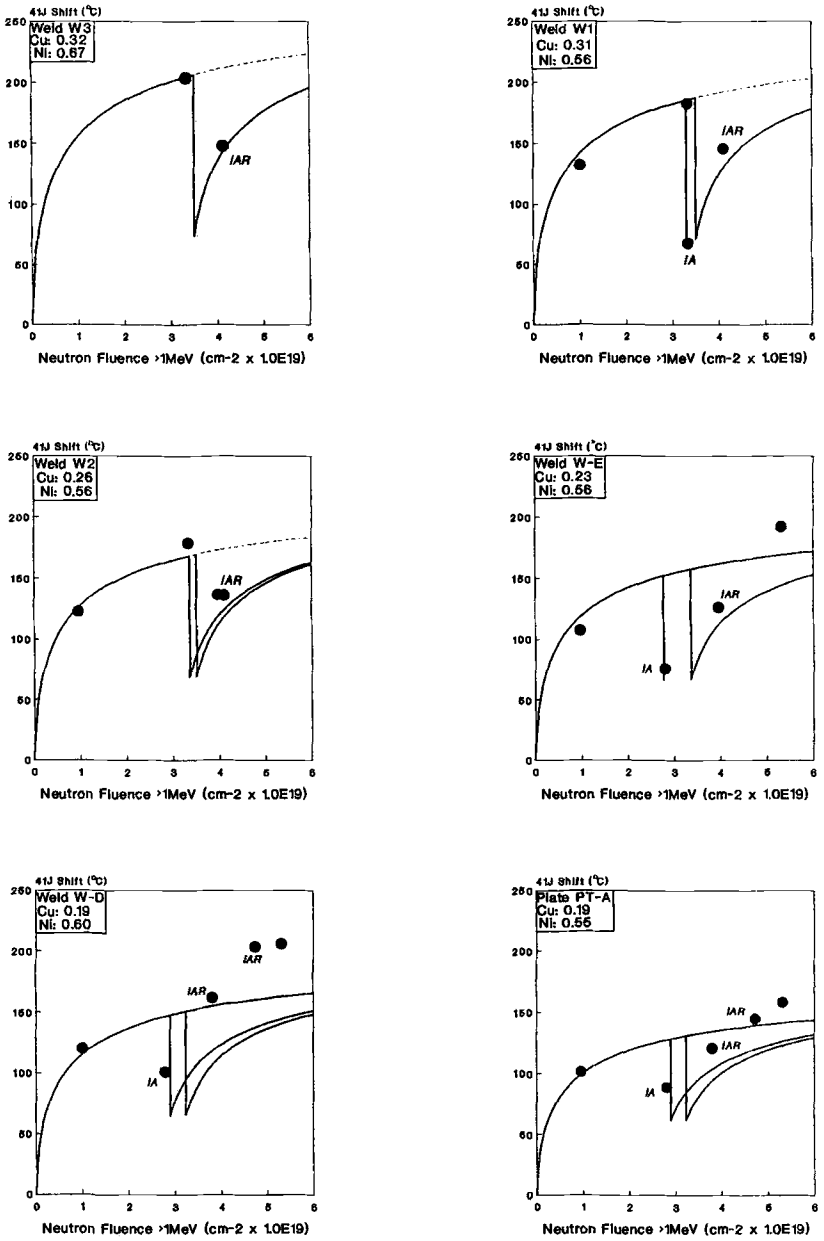


FIG. 4--Accelerated irradiation and test program in support of BR3 vessel wet anneal.

Most of the results of irradiated (I), irradiated-annealed (IA) and irradiated-annealed-reirradiated (IAR) 260°C exposures are summarized on Figure 4; annealing was at 343°C for 168h. The data relative to the plate PT-A (Table 1) have been included. The welds W3, W1 and W2 were also irradiated to ~3.3 E19 cm-2 (> 1MeV) at a temperature of 288°C: the corresponding 41J. C_v-shifts agreed well with the predictions of Regulatory Guide 1.99 Rev. 2 [4]. For the I- condition, the trend lines on Figure 4 have also been derived from the Guide, including for the correction from 288°C to 260°C irradiation. The IA and IAR paths have been constructed according to the specifications of ASTM Guide E509-86 [22].

It can be seen that the agreement observed for the high copper welds on Figure 4 (W3, W1) tends to deteriorate as the copper content decreases (W-E, W-D). Across-the-board, it seems that the behaviour of the five welds depends little on their copper content; in particular, W-D (0.19%) shifts as much as W3 (0.32%).
All these data are being re-analyzed on basis of the load diagram approach of Section 2. Some preliminary conclusions are presented in Section 3.

2. FRACTURE TOUGHNESS INDEXING AND DAMAGE MODELING BY USE OF INSTRUMENTED C_v LOAD-TIME TRACES

Load Diagram, Characteristic Temperatures and Energy Partitioning

The most fundamental information embodied in the *C_v impact test* is the *load diagram* [23]-[31], as derived from the instrumented load versus time (deflection) traces recorded by strain gages on the hammer tup. This is shown schematically in Fig. 5.

Considering a typical signal in the transition temperature range, left-hand part of the Figure, it is well known [32] [33] that at least four characteristic loads can be defined: F_y: General Yield Load; F_m: Maximum Load; F_u: Brittle Crack Initiation Load; F_a: Crack Arrest Load.

Some energy partitioning can be associated to the C_v load diagram, and if done according to the characteristic loads identified by the testing standards, this leads to four distinct fractions, labelled LSE, A, B and C. Their definition, similar to an earlier proposal by Pachur [29], is illustrated by the left-hand side of Fig.5. For each of the main fractions, one can also define a transition temperature, TTA,..., taken at 50% of the corresponding shelf. In this work, all energies are corrected for elastic interaction at the load points. The energy fraction LSE, Lower Shelf Energy, is composed of elastic energy and brittle crack propagation energy. It is largely insensitive to service exposure, and normally never exceeds 5-6 J.
Ductile initiation occurs at point marked i on Fig. 5, left. The energy fraction C is called "post arrest "energy and involves comparatively large deflections accompanied by shear lip formation.

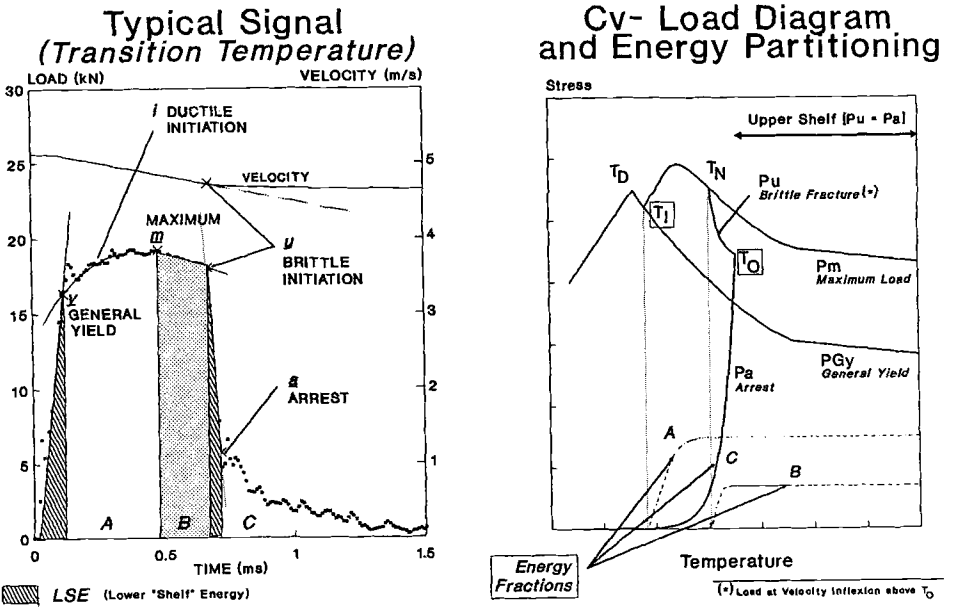


FIG. 5--Use of instrumented Charpy impact load-time traces.

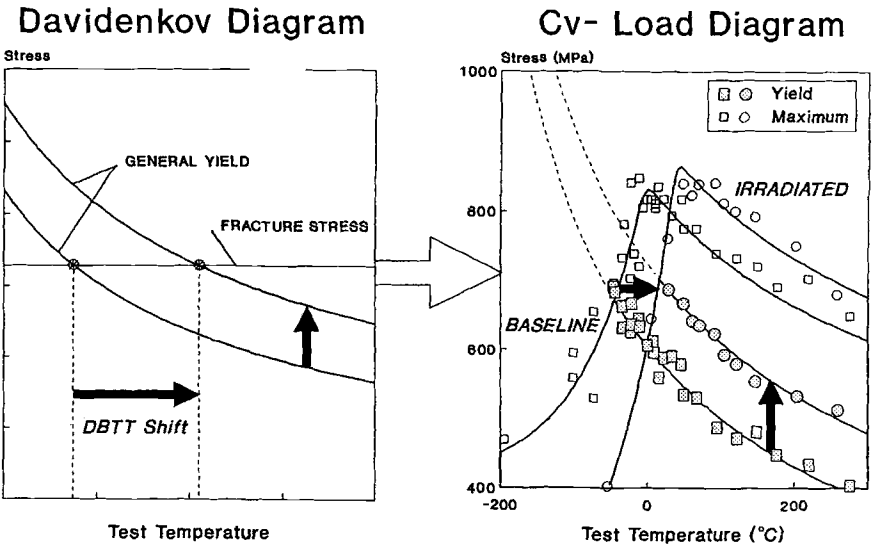


FIG. 6--Modeling of irradiation effects on RPV steels and the Charpy impact load diagram.

Concerning the transition temperature concept, the ***emphasis*** in this work lies generally on the characteristic temperatures marked T_I and T_0, right-hand side of Fig. 5. The onset of C_v impact upper shelf regime begins at Characteristic Temperature T_0, above which the load curves $F_u(T)$ and $F_a(T)$ coincide, i. e. there is no brittle crack initiation. We can further identify: T_N, "Ductility Temperature", onset of Energy Fraction B, a fraction entailing ductile tearing, under more or less plane strain conditions (deteriorating as the crack advances); T_I, "Ductile Crack Initiation Temperature", onset of actual ductility, i.e. temperature at which the shear fracture appearance in the C_v test begins to exceed 0% (see below); T_D, "Brittleness Temperature": in a nutshell, the maximum temperature of "elastic fracture". This is also the temperature relevant to the 'plastic collapse' failure analysis approach.

More accurately, T_D is the temperature corresponding to the load at which plastically induced cleavage coincides with general yielding (yielding spread over the entire ligament under the notch, with associated plastic hinge [34], [35]). Most significantly, this is the characteristic temperature for the OROWAN [36] cleavage fracture criterion; fracture occurs when the maximum value of the maximum principal tensile stress σ_{yy}^{max} exceeds the microcleavage fracture stress σ_f^*

$$\sigma_{yy}^{max} = K_{\sigma p}\, \sigma_{y_{|T,\dot{\varepsilon}}} \geq \sigma_f^* \qquad (1)$$

Here,

$\sigma_{y_{|T,\dot{\varepsilon}}}$ is the uniaxial yield stress at the temperature T and strain rate $\dot{\varepsilon}$ of interest and $K_{\sigma p}$ is the plastic constraint factor.

In the older literature, T_D has often been considered a good definition for the ductile-brittle transition temperature DBTT. The present views are that T_I is actually the most adequate. A criterion similar to (1) can in any case also be applied at T_I; this is usually done in this work. Between T_D and T_I, the failure load is slightly larger than, and more or less parallel to the general yield load , while strain hardening primarily occurs in the space between the net and the gross specimen sections, causing some deflection, but only minor energy increase. At high strain rates, such as in the C_v test, T_D is generally close to T_I. On another hand, it has been recently shown that T_I is a more universal characteristics of the materials than T_D [37]-[39]; it is also rather insensitive to specimen thickness and notch angle [40] (but it depends on notch acuity and strain rate). Certainly, the increase ΔT_I under service conditions (thermal and strain ageing, irradiation) is a good measure of the corresponding shift of the initiation fracture toughness for the same strain rate - assuming the temperature dependency (shape) to be invariant, as also done in the Regulatory, ASME XI based framework. In other words, ΔT_I is a *good index for the shift of the dynamic initiation fracture toughness* K_{Id}.

Early work by Kobayashi & al. [41] shows that T_0 may correspond to the crack arrest

temperature (CAT) of the Robertson test. A recent study by Pachur [42] does conclude that the Pellini drop weight nil ductility temperature (NDT) does correlate with the onset of the post-arrest energy fraction C. The NDT shift by irradiation is found significantly less than the 41J C_v shift, for the investigated steels. The possibility of experimental bias due to the brittle bead deposition method [43] does not seem a problem in this case, nor in a similar German study by Schmitt et. al. [44].

Very recently, Wallin [45] has proposed an alternate K_{Ia} indexation using the temperature at which the C_v crack arrest load reaches a level of 4 kN (a level aimed at providing sufficient ligament); he has obtained a defendable correlation of this temperature with the temperature at which K_{Ia} reaches 100 MPa$\sqrt{m}$ and has suggested that the same, exponential "master curve" can be used to represent the temperature dependence of both K_{Ic} and K_{Ia}. In our work, we also use an exponential master curve to fit the C_v crack arrest load in function of test temperature, but it is significantly steeper than Wallin's function; for this reason, and given the metallurgical scatter, the two proposed indices differ little; the T_O index is somewhat more conservative, but can be estimated from fracture appearance data in absence of load-time records.

Damage Modeling Using the C_v Impact Load Diagram

In general, in-service steel embrittlement can be accounted for by matrix hardening alone: namely, by the increase of the flow stress through the creation of new obstacles to the mobility of dislocations; this is reflected by an increase of hardness (Vickers, Rockwell, ...) - proportional whenever work hardening is not affected by irradiation. The fracture stress corresponds to the microcleavage fracture stress - which is generally independent of temperature, strain rate and irradiation. The resulting increase (shift) of DBTT is roughly proportional to the increase of the uniaxial yield stress and to the increase of the C_v general yield stress.

Service exposure can sometimes also lower interboundary cohesive energies, causing a decrease of fracture stress and resulting in easier microcrack propagation beyond the hard particles in which they form. One example is the occurrence of irradiation enhanced segregation at grain boundaries, leading to mixed mode fracture (intergranular cracking and transgranular cleavage). This 'non-hardening' embrittlement may compound with hardening-induced embrittlement or, albeit very seldomly, be found in isolation : in such case, the yield stress, the hardness and the C_v upper shelf do not change, but the transition temperature shift can be sizeable.

This brief outline shows that the mechanical data important for damage modeling are the flow properties and the microscopic fracture stresses; these can be obtained from the load signals of the instrumented C_v notch impact test, in combination with conventional, static tensile tests.

The C_v load diagram does thus provide a rather straightforward experimental expression of the Davidenkov diagram, by which DBTT shifts (ΔT_I) are linked to matrix hardening: this is illustrated by Figure 6 for the case of irradiation-induced

embrittlement. In the considered example, the microcleavage fracture stress is seen to be unaffected by the reactor exposure (intersection of maximum and yield loads essentially unchanged) and one has:

$$\Delta T_I = K \ \Delta \ \sigma_y \qquad (2)$$

where $\Delta \sigma_y$ (MPa) is the dynamic yield stress increase
K (°C/MPa) is a proportionality factor depending on unirradiated properties and on the irradiation effect on the strain hardening; it is generally close to 0.63 for PWR exposure (260- 310°C).

It is interesting to note that the proportionality factor K in (2) is similar (0.63) for the Pellini drop weight NDT and the Cv- FATT shifts, for 290°C exposure. It is important to **emphasize** again that the Davidenkov diagram must be interpreted and applied [18] in terms of the ductile initiation temperature T_I, as distinct from the "brittleness temperature" of earlier textbooks and publications on the topic.

The C_v load diagram analysis also provides a mesure of the microcleavage fracture stress [18]; and therefore allows to probe for the possibility that non- hardening embrittlement may have taken place.

Correlation between C_v Impact Load Diagram and Fracture Appearance

Systematic application of the Fraunhofer Magnetic Emission (ME) detector [46] to unirradiated and irradiated steel samples broken at a number of temperatures has allowed to conclude that ductile crack initiation in the C_v impact test occurs at a load

$$F_i = F_y + (1-k) \ (F_m - F_y) \qquad (3)$$

where, generally, $k \approx 0.5$.

This work has also confirmed that the bulk of absorbed C_v energy is unrelated to ductile crack initiation (which consumes only 6 to 14 J.). *The C_v test is primarily a propagation one*, and the best use of its energy information may be in trying to derive the tearing modulus for dynamic ductile stable crack growth, as exemplified in ref. [47]-[49].

The implication of (3) is that the shear fracture appearance (SFA) of C_v impact specimens can always be determined from the load diagram through the relationship

$$SFA(\%) = \left[1 - \frac{F_u - F_a}{F_m + k(F_m - F_y)} \right] \times 100 \qquad (4)$$

The best value for k is most accurately defined, *on a case-to-case basis*, by means of simultaneous fit to both the load diagram and to *planimetry* measurements on the

fracture surfaces.

Cv- reconstitution and miniaturization work summarized elsewhere [18] may yet provide the strongest evidence in favour of our emphasis on the load diagram approach. Indeed, the link between the load diagram and the fracture appearance provided by relation (4) is valid irrespective of specimen size, notch acuity and constraint. An illustration is given by Figure 7 for the case of Cv- miniaturization to the standard DIN 50115 (3x4x27 mm specimens). The loads measured for the reference - E23 size- specimens are not shown for clarity of the figure, but can be found on Figure 8 (as well as in a companion paper [50] figure 11). Figure 8 is obtained after correction for the estimated strain rate differences[1] between the two types of tests (the abscissa is defined by equation (7) below): $\mathbf{T_o}$ is found here to be independent on specimen size, and this re-inforces the view that it is adequate for $\mathbf{K_{Ia}}$ **indexation,** whereas $\mathbf{T_I}$ can only be used to index $\mathbf{K_{Id}}$ **shifts.**

Combination of C_v Impact and Static Tensile Tests

The general yield load, PGy, (kN) for a notched specimen tested in three or four point bending can be related to the uniaxial yield stress σ_y (MPa) by considering slip-line field solutions [51] for the form of the plane strain plastic zone below the notch [52-54]:

$$PG_y = \frac{2\,\mathfrak{q}\,(W-a)^2\,B\,\tau_y}{S} \qquad (5)$$

where

	W	=	Specimen width
	a	=	Notch depth
	W-a	=	Ligament below the notch
	B	=	Specimen thickness
	τ_y	=	Shear yield stress
	S	=	Loading span (For C_v testing: S/W= 4).
	$\mathfrak{q}$	=	Constraint factor (dependent on tup indenter width)

and the tensile yield stress σ_y can be inferred from τ_y using either a Tresca or Von Mises yield criterion.

It has been our practice to scale the entire C_v load diagram according to (5), in order to allow its evaluation in combination with uniaxial static tensile test data.

The equation used to describe the shear stress τ in function of strain rate $\dot{\varepsilon}$ and temperature T is as follows [18]:

[1]Estimate accounts for the influence of hammer velocity and specimen size on the rate of loading in the plastic hinge.

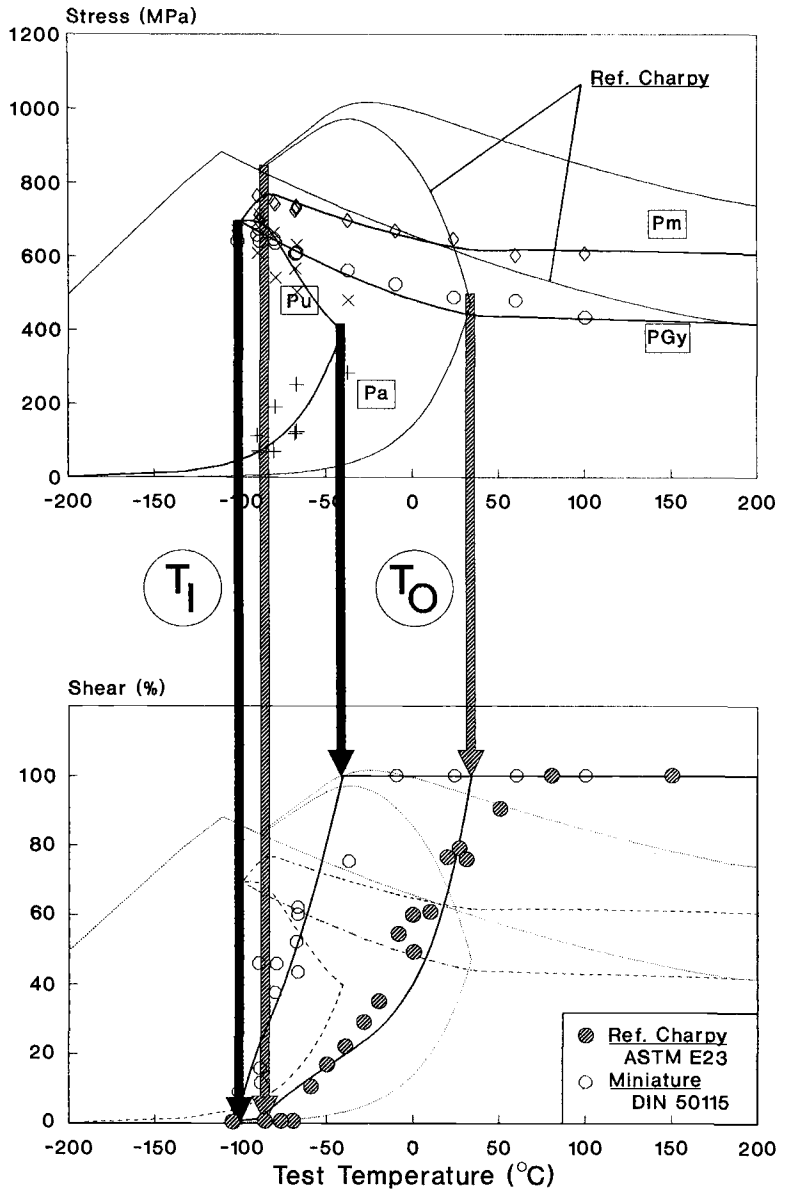


FIG. 7--C_V-load diagram and fracture appearance define indexation temperatures for dynamic fracture toughness.

$$\tau(T,\dot{\varepsilon}) = \tau_0(1-\alpha T) + \tau_P\left[1-\left(\frac{kT}{H_c}\ln\frac{\dot{\varepsilon}_0}{\dot{\varepsilon}}\right)^{\frac{1}{m}}\right]^{m'} \quad (6)$$

τ_0 = athermal stress at 0 K
α = slope (2.8E-04 K^{-1})
τ_P = "effective" Peierls stress
k = Boltzmann constant
H_c = activation energy
ε_0 = intrinsic strain rate sensitivity
m, m' = constants for description of lattice energy barrier.

A more exact form of the equation is actually used, in which the entropy is accounted for by the temperature dependence of the shear modulus $\mu(T)$.

The stress calculated by means of Equation (6) can be plotted, either relatively to the temperature, or relatively to the activation enthalpy (energy). The strain rate - temperature sensitivity is lumped into the activation energy (enthalpy) parameter

$$H = kT\ln\frac{\dot{\varepsilon}_0}{\dot{\varepsilon}} \quad (7)$$

which brings together into a single trend all experimental data at the various strain rates. The Peierls' component vanishes at $H = H_c$, the "Activation Energy". To this does correspond a critical temperature above which the measurements provide the athermal stress component. The construction of Figure 8 is based on this description.

Accuracy of the C_v Impact Load Diagram

Extensive attention has been devoted at scrutinizing the procedure to establish C_v load diagrams to accuracies suitable for engineering, surveillance applications. Various testing installations have been directly or indirectly intercompared. A particular concern in the present context was to decide whether sufficiently reliable use could be made of data recorded with older machines, featuring maybe slower electronics than required by more modern standards. To this respect, accurate definition of the general yield load is the most critical to achieve. A favourable conclusion has been reached, which should allow to reanalyze many PWR surveillance and test reactor experiments along the lines of the present approach. An example of such quality insurance effort is displayed on Figure 9. (The LHMA machine is of old vintage with slow electronics while the VITO and FhG machines comply strictly with the standards). In addition to bringing together static and dynamic yields, important features of such diagrams are:

1) Small scatter,
2) Insensitivity to notch orientation
3) Insensitivity to hammer geometry
4) Insensitivity to reconstitution, even for small inserts causing energy losses [18].

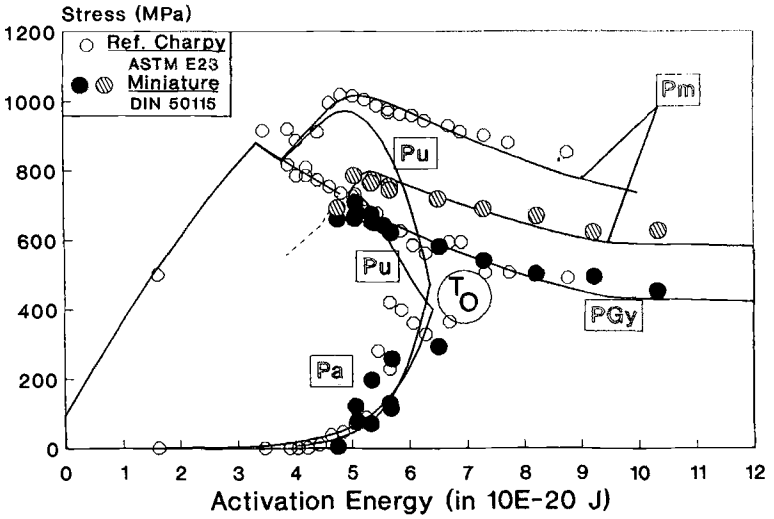


FIG. 8--Size-independence of T_0 indexation temperature.

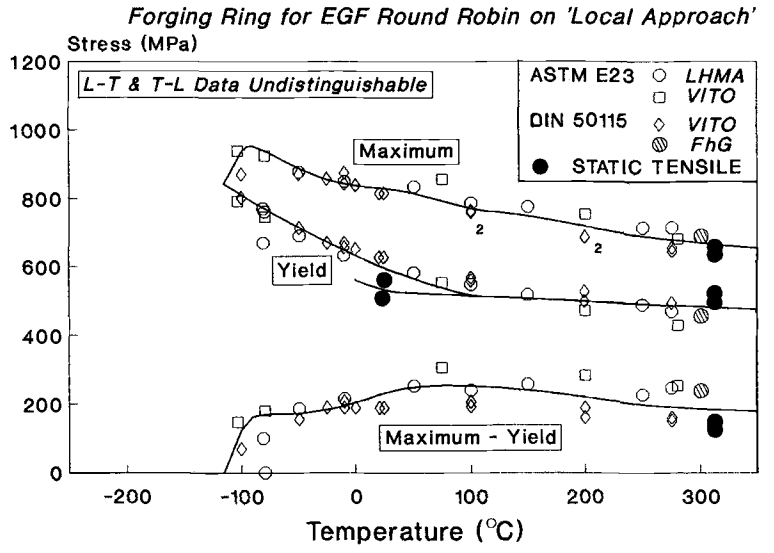


FIG. 9--Quality assurance for C_V-impact load diagram procedure.

These properties are due to the fact that a load diagram such as the one on Figure 9 does simply reflect the *material flow properties*. The first two items however do not necessarily apply so well to the brittle initiation and crack arrest loads of the complete diagram, Figure 7: here, the scatter can be larger; while in certain steels, T_0 may depend *slightly* on notch orientation.

Summary

The proposed ***Charpy-V Impact Load Diagram approach*** allows **to assess the influence of service exposure on the dynamic initiation and crack arrest fracture toughness of pressure vessel steels. The load diagram is intimately correlated to the shear fracture appearance and it also embodies the Davidenkov diagram, so useful to anyone concerned with the modeling of irradiation effects.**

Figure 10 illustrates some of the features highlighted in this paper.

3. PROGRESS IN THE MODELING OF RPV EMBRITTLEMENT TREND CURVES

The modeling of RPV embrittlement trend curves requires damage modeling and fracture mechanics. The property of interest for structural integrity assurance is of course fracture toughness: in RPV surveillance practice, "indexation" of toughness to the C_v test is the prevailing approach. The more recent trends aimed at reducing conservatism while enhancing safety lead to "indexation" through the insights brought by "micromechanics" ([55]-[63]).

Radiation-Enhanced Precipitation

A major contribution to the hardening and embrittlement of RPV steels involves the radiation-enhanced diffusion and precipitation of copper impurities. Various phenomenological models [64]-[68] have been developed to predict the increase in yield stress associated with these precipitates. These models are rather consistent with one another and we have adopted here the Nuclear Electric description by Fisher et. al. [65], [66].

Copper diffusion at PWR (and lower) irradiation temperatures is possible because the steady state concentration of mobile vacancies is largely increased by neutron irradiation. Only copper in solid solution contributes to embrittlement; this can be significantly less than the bulk copper content, especially in welds due to the precipitation of copper sulphide during welding and to the precipitation of copper during stress relief. This is accounted for by using an "effective copper" content (Cu_{eff}), the matrix content available for in-pile precipitation. This can be estimated or adjusted to fit the mechanical data, or measured by a combination of high resolution techniques: e.g., FEGSTEM [69], APFIM [70], SANS [71]. The experimental determination can be vital for accurate modeling. The precipitates in commercial steels are not pure copper, but

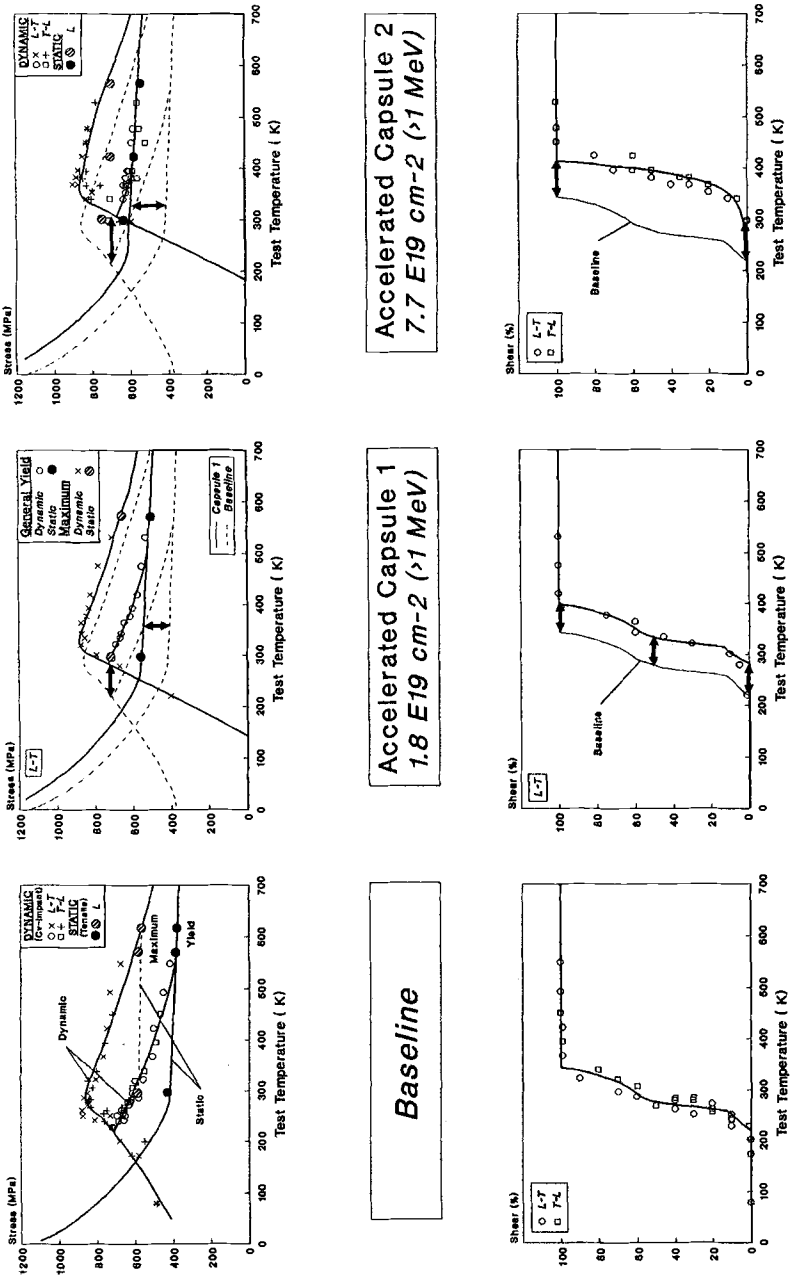


FIG. 10--Irradiation effect on C_V-load diagram and fracture appearance (Maine Yankee surveillance plate).

complex mixtures[1] (Cu, Ni, Mn, Si,...) possibly associated to vacancy aggregates that they stabilize. For the base metals examined herein, we have assumed that Cu_{eff} = bulk copper and that the increase of yield strength at "saturation" (i.e., after complete precipitation) can be represented as

$$\Delta \sigma_y^{\infty} = 216 \text{ (MPa)} \{1\text{-exp}(-3.3(Cu_{eff}-0.03)\} \quad (8)$$

where Cu_{eff} is expressed in weight percent.

The kinetics of copper precipitation is described in the model by reference to the thermal ageing behavior [65], except that no overageing is assumed to take place beyond peak hardening (thus, we speak of "saturation") [66b]. The main parameters used to describe this kinetics are the temperature, the neutron flux, the dislocation density, the spectrum-averaged cross-section for production of mobile vacancies and the activation energy for diffusion of copper. The *most sensitive* kinetics parameter is the ***activation energy for copper diffusion***: we have adjusted it, for 290 °C exposure conditions, as an ***unique linear function of the logarithm of the neutron dose rate.*** Copper diffusivity also changes with irradiation temperature, but below 290 °C, embrittlement becomes by far more sensitive to the damage features discussed next and the present approximation to the copper component probably causes comparatively small uncertainties.

Other Components to Matrix Hardening

It is generally assumed at present that there is a second contribution to matrix hardening, stemming from the formation of radiation-induced point defect clusters. We believe that this "matrix damage" is strongly affected by the irradiation temperature and may depend on the free nitrogen content of the steel. But we contend on another hand that the physical nature of "matrix damage" is actually rather complex, and we harbor no doubt that "matrix damage" entails at least two components, not one - as also shown by Odette and co-workers [67b].. These components *may* entail small vacancy clusters and precipitates mediated by carbide/nitride formers (Cr, V,...) in competition with austenitizers (primarily nickel) [72]. We have found evidence from our annealing work that the superposition law [73] describing the lattice strengthening due to these two defects and to the copper-related component is not simply linear, but that summation of these three components under the approximation of dispersed barrier hardening is reasonably accurate for irradiation of the considered steels in the temperature range ~260-300°C; this approximation is adopted here.

Further microstructural characterization work coupled to parametric irradiation and annealing studies is needed to clarify the physical nature of "matrix" damage. We follow the idea of Pachur [16] and designate the components of "matrix damage" as "damage mechanisms n° 2 and 2A"; this is exemplified by the left-hand side of Figure 11. In our present formulation, we represent each of these components by

[1]The role of precipitate composition is illustrated in reference [50].

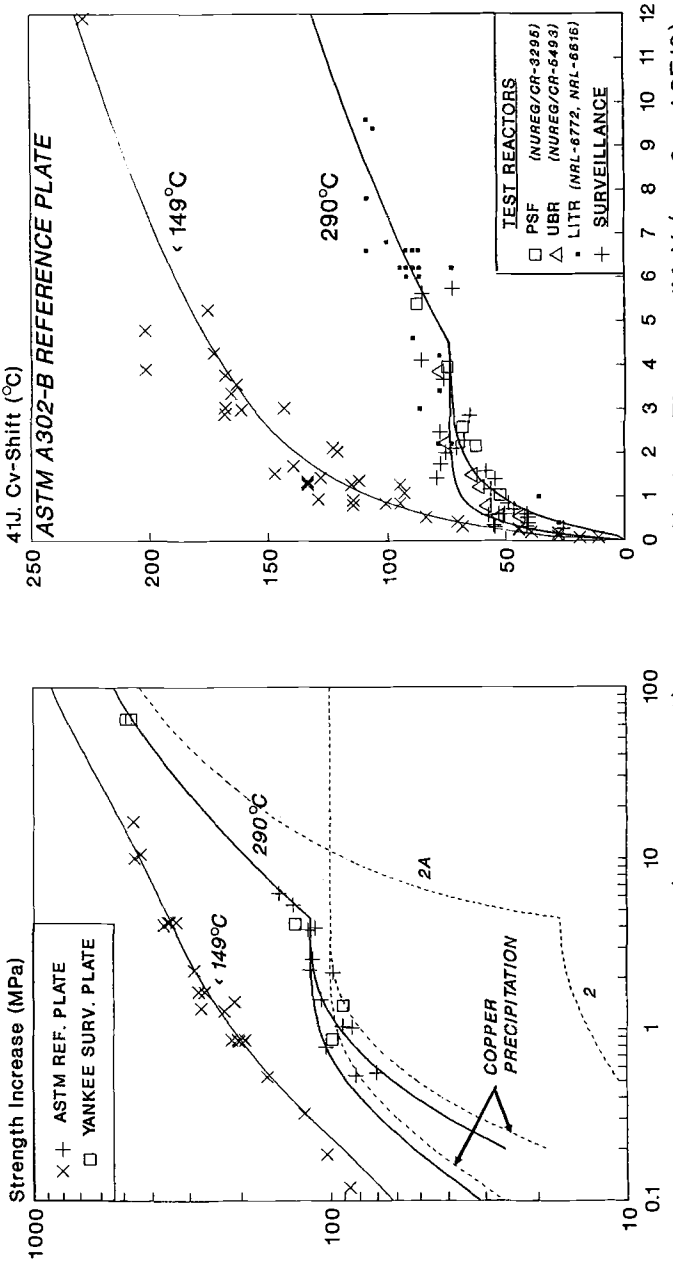


FIG. 11--A302-B plate tensile yield strength and transition temperature shift are affected by three distinct damage mechanisms.

$$\Delta \sigma_y^j = Wj \sqrt{(1-\exp(-Lj(\Phi-\Phi j)))} \quad j: 2, 2A \qquad (9)$$

where

Wj= saturated strengthening (MPa)
Lj= kinetics exponent (cm2)
Φ = neutron fluence (cm-2 >1MeV)
Φj = incubation fluence (cm-2 >1MeV)

The various embrittlement trend curves displayed in this paper are all obtained by assigning a fixed value to the parameters in (9) (see Table 3), except for what concerns W2 and Φ2A: both are found to depend on the irradiation temperature, but W2 does not seem to depend on chemistry for the steels examined here; while Φ2A depends on the nickel content if this exceeds ~0.7-1%.

TABLE 3-- Parameters used to describe damage mechanisms 2 and 2A for the considered steels.

Parameter	Irradiation temperature 260 °C	290 °C
L_2 ($cm^2 \times 10^{-19}$)	1.0	
ϕ_2 ($cm^{-2} \times 10^{19}$)	0-0.1	
W_2 (MPa)*	110 ± 10	30 ± 10
L_{2A} ($cm^2 \times 10^{-19}$)	0.01	
ϕ_{2A} ($cm^{-2} \times 10^{19}$)	4.0-4.5**	
W_{2A} (MPa)*	300 ± 100	

*To obtain temperature shift, multiply by 0.63 °C/MPa (in this irradiation temperature range).
**For Ni < 0.7 wt % and for MoMnNi low alloy steels; decreases rapidly below 250°C.

Embrittlement Trend Curve for ASTM Reference A302-B Plate Exposed at 290°C

The present evaluation is illustrated in Figure 11. The low irradiation temperature data (<149°C) are taken from reference [74].
In addition to the well pedigreed experiments in PSF [75] and at the UBR [76], and to the surveillance capsule data compiled by Stallmann [11], Figure 11 also contains older 288°C LITR results [13] [14]. Reference [14] and a companion paper in reference [15]

have been used in Section 1 (Figure 3.b) to examine the role of nickel for the austenitization conditions of the Yankee Rowe/BR3 surveillance plate.
The tensile data at 288°C [75] [76] have been complemented by BR3 measurements for the Yankee surveillance plate [77], obtained at irradiation temperatures in the range 274-282°C. Within experimental uncertainties- as already mentionned in Section 1-, both plates display a similar strength increase: no heat treatment/microstructure influence is detected. The Fisher model predicts a saturated yield strength increase of about 100 MPa due to copper precipitation, assuming all copper to be in solid solution prior to irradiation; the predicted dose rate effect brackets reasonably well the experimental results, which cover the range of 8.0 E10 to 3.0 E13 cm^{-2} sec^{-1} (> 1 MeV). After substraction of the copper contribution, the residual yield strength increase shows the contribution of damage mechanisms 2 and 2A: at ~290°C, the first one is quite small while the second one has an incubation fluence of ϕ_{2A} ~4.5 E19 cm-2 (>1MeV). The parameters of these fits are also consistent with isochronal annealing experiments. In practice, the trend lines on Figure 11 were obtained by simultaneous least-squares fits to both the 41J. shift and yield strength increase data, accounting for their proportionality per equation (2), as well as for the Fisher model prediction of the copper contribution to the yield. The proportionality constant is found equal to:

Irradiation temperature range 260-290°C: K= 0.63°C/MPa
Irradiation temperature range ≤ 150°C: K= 0.50°C/MPa

This variation of K with temperature is due to changes of work hardening capability [72].
An important comment needs to be made concerning ***dosimetry biases*** in older test reactor (and in older power reactor) experiments. In the mid-seventies, the USNRC Materials Research Branch has established the LWR Surveillance Dosimetry Improvement program (SDIP) [78], a program which soon became international and was quite successful. In Figures 11 and 12 older neutron fluences have been rescaled as appropriate on grounds of the SDIP findings. For instance, the fluences in reference [74] are readjusted to provide consistency with the re-evaluation by Simons [79] of low temperature experiments; the average dosimetry bias of ~1.7 is close to our own derivation of a bias of ~2.0 on all LITR neutron fluences, e.g. references [13], [74], [14],[15],.... The neutron fluences for the earlier BR3 surveillance experiments [77] have also been re-evaluated in 1978; the revised best estimates are given in Section 4, Table 4. The Yankee Rowe dosimetry data were similarly adjusted [1].

The Influence of Irradiation Temperature and of Nickel

Figure 12.a shows that the largest effect of irradiation temperature in the range 260-290°C is due to "mechanism 2". The interplay between this component and the copper related component leads to a fluence dependency of the effect, as illustrated by Figure 12.b. Note that the effect is not influenced by the nickel content nor microstructure of the considered plates (it is similar for the Linde 80 welds of the BR3 program).

Figure 12.c compares the data of Figure 11 to a thermodynamically-based Russian

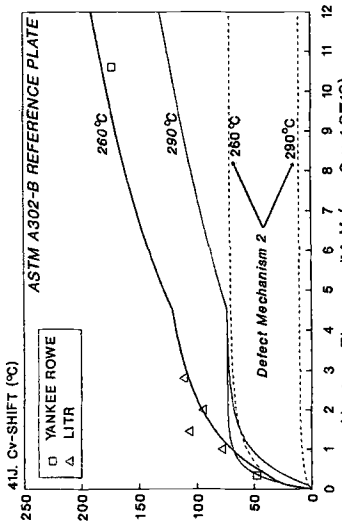


FIG. 12.a

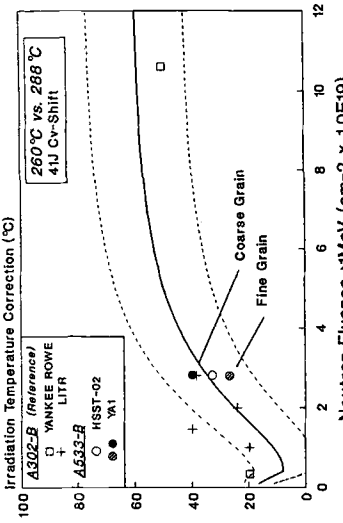


FIG. 12.b

FIG. 12.c

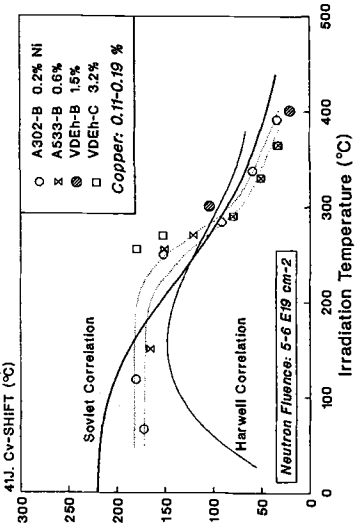


FIG. 12.d

FIG. 12--Influence of irradiation temperature on RPV steel embrittlement.

correlation (solid line) [80]. The simplified equation, which lumps together the various damage mechanisms, is as follows:

$$(1/\Delta TT) = (1/\Delta TT^{\infty}) + 22.4\ (1/\Phi)\ \exp(-U/kT) \qquad \textbf{(10)}$$

where
ΔTT = shift at neutron fluence Φ and irradiation temperature T
ΔTT^{∞} = saturated shift
U = activation energy (0.305 eV)
k = Boltzmann constant

The fit to A302-B data on Figure 12.c considers ΔTT^{∞} to be the only adjustable parameter; this fit is quite remarkable, as the activation energy and slope parameter (adjusted to the neutron fluence unit >1Mev, vs. >0.5 MeV in the reference) have been derived for high Cr-V Russian steels. The deviations from experiment are traceable to the fact that copper precipitation effects have not been explicitely accounted for. Figure 12.c seems to support our view [72] that the major difference in embrittlement between Western and Russian steels probably entails "mechanism 2A".

Figure 12.d is provided to substantiate our position of a ***lack of nickel influence on* MoMnNi base *metals up to neutron fluences of 5-6 E19 cm-2 (>1MeV) and up to a nickel content of 0.6 %.*** The A302-B data on this Figure are taken from reference [6]; the other results have been provided by D. Pachur [81]. The VDEh-B and VDEh-C steels display somewhat larger shifts than A302-B and A533-B probably due to their metallurgical difference and the much larger nickel content (mechanism 2A). Also shown is the Russian correlation of equation (10), as well as a preliminary Harwell evaluation [82], similar in many respects to this work; it encompasses A302-B and A212-B plate data [74], as well as independent Swedish experiments [83], but neglects the dosimetry biases and mismatch between the A302-B reference ASTM and Yankee Rowe surveillance plate in reference [74].

Figures 13 and 14 are added to complete this outline. The model predictions are obtained from the Fisher model for the copper contribution and from relation (9) for "matrix damage" (Table 3). Thus, the lack of nickel influence for these base metals is again confirmed up to 4-6 E19 cm-2 (>1MeV).

Unravelling the Apparent Outlier Behaviour of BR3 Surrogate Surveillance Melts

The accelerated irradiation and test data shown on Fig. 4 for W-D and PT-A have been evaluated using the damage modeling and micromechanics-based approach described here and the results are shown in Figure 15.

Within experimental uncertainties, Figure 15 demonstrates a complete consistency of behavior between the Linde 80 weld W-D and the A533-B plate PT-A. Predicted dynamic and static yield data are consistent with data as are the shifts. All parameters

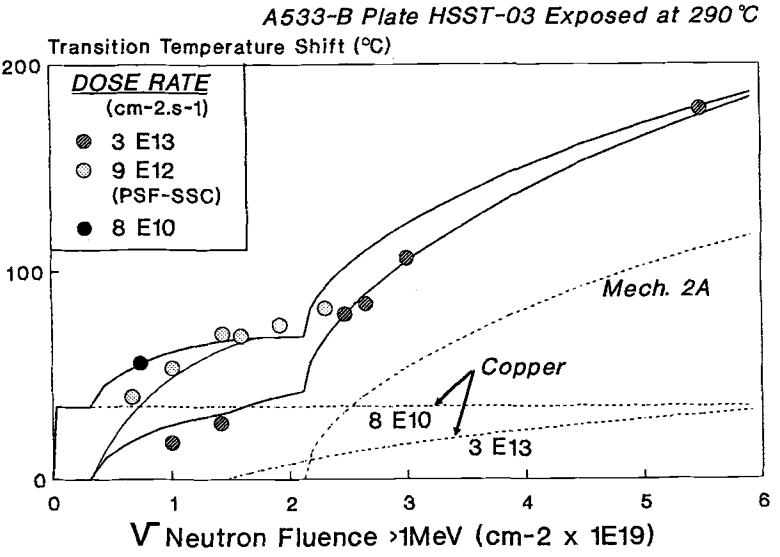


FIG. 13--Dose rate effect on embrittlement.

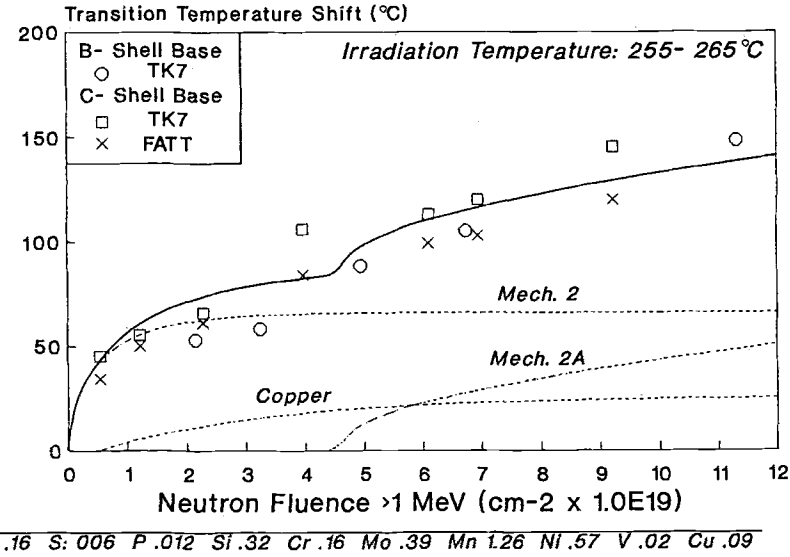


FIG. 14--Embrittlement of Chooz A surveillance base metal is well predicted by model.

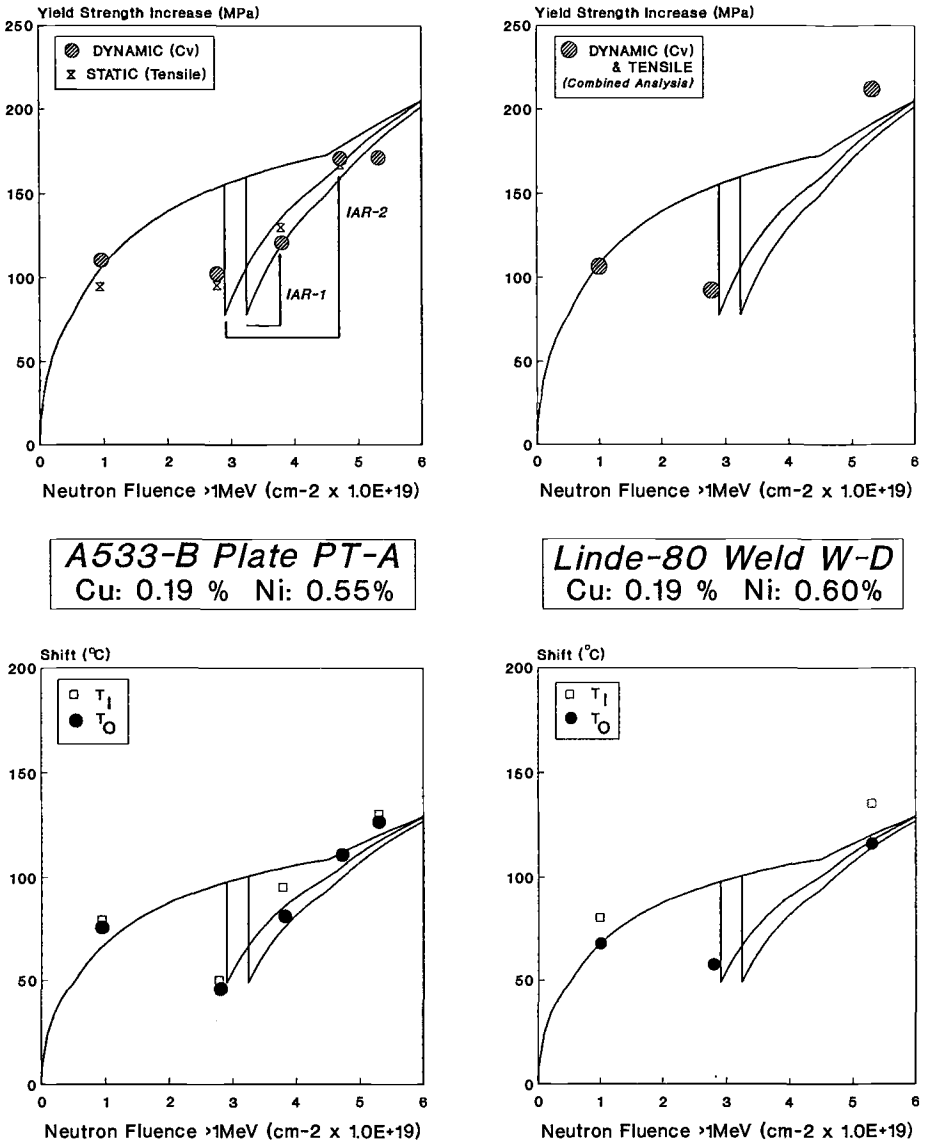


FIG. 15--Behaviour of outlier BR3 surrogate surveillance melts is rationalized by micromechanics and damage modeling evaluation.

for the model trend curves are the same as for the A302-B reference plate on Figure 11. In other words, there is **no weld-versus-plate difference for these materials, nor any nickel influence up to contents of 0.6 %, in the neutron fluence range of the experiments.** This is confirmed by the similar evaluation of all other welds on Figure 4: only the Fisher model description needs to be adapted to account for differences of copper content.

4. UNRAVELLING THE APPARENT OUTLIER BEHAVIOR OF YANKEE/BR3 SURVEILLANCE PLATE

Use of Yankee Rowe Surveillance Plate for Early BR3 Vessel Surveillance

As already explained in Section 1, the early BR3 vessel surveillance program was limited to C_v and tensile specimens from the same batch of A302-B plate as used for the Yankee Rowe vessel surveillance. There were two types of capsules at BR3:

1) Accelerated ones (HF: high flux), located in the radial reflector, and exposed at a dose rate of ~7.5 E12 cm-2.sec-1; the irradiation temperature was believed to be ~310°C, but the initial gamma heating estimate was later revised, based on coupled neutron-gamma transport theory calculations, benchmarked at the Venus critical facility [84] ; the final best estimate is 282°C.

2) "Low flux" (LF) capsules, located in the vertical reflector above the reactor core; here, gamma heating is low, but the cooling water emerging from the core is at a higher temperature than the average operation value of 260°C; similar capsules later built to supplement the vendor's surveillance program were instrumented with melt wires and found to run at a temperature of ~274°C. The dose rate for these capsules is ~ 7.2 E10 cm-2.sec-1 (>1MeV).

The neutron fluences quoted in the initial documentation [77] have been up-dated in 1978 [Internal SCK-CEN memo, Fabry A., ref. AF/sa.380/78-11] and the revised values are quoted in Table 4. It must be noted that each individual capsule is small and contained only four Charpy and one tensile specimen.; furthermore, the LF specimens are exposed to a vertical neutron flux gradient and the fluence at the C_v- notches of the upper level of the capsules is about 2.5 less than at the lower level; this fact was not given any attention during the first tests, nor could the actual positions of the individual samples be ascertained for the first test campaigns, performed in the U.K.. Furthermore, only one C_v- specimen was broken in the transition range for LF capsules 3, 9 and 16, so that the only useful information from these capsules is that the upper shelf is not degraded by irradiation below a fluence of ~6E18 cm-2. Finally, it must be noted that the tensile tests performed at Culcheth, U.K. were found severely biased, for undocumented reasons. The present summary is directed at avoiding possible misinterpretation of this early BR3 surveillance work; Table 4 is limited to report the C_v-information deemed useable (This does not include the tensile data shown on Figure 11 nor the Vickers hardness data). Finally, it must be noted that all these C_v- tests were unfortunately un-instrumented.

TABLE 4-- Summary of Early BR3 Results Using Yankee Rowe Surveillance Plate

Capsule I.D.	Neutron Fluence (>1MeV) (cm^{-2})	USE (J)	ΔTT41J (°C)	ΔFATT (°C)	Testing Site (if not LHMA, Mol) Dosimetry Accuracy
Baseline	0	107	_	_	
LF 3,9	2.7 E18	107	_	_	Tests at Culcheth, U.K. ± 30-50%
LF 16	6.2 E18	107	_	_	Tests at Culcheth, U.K. ± 30-50%
LF 5,11,15	8.7 E18	106	73	60	± 20-25%
LF 12	1.4 E19	76.6	105	75	± 15%
HF 1	5.8 E19	75.6	139	93	Tests at Culcheth, U.K. ± 10%
HF 14	1.3 E20	63.4	187	_	Tests at Culcheth,U.K. ± 10%
HF 4,7	6.5 E20	36.7	313	_	± 10%

Test Matrix for the 1991 Yankee/BR3 Surveillance Plate Investigation

Four BR3 capsules of type LF were left from the original program just outlined, and provide a total inventory of 16 Cv- and 4 tensile specimens, exposed over the entire BR3 life (25 y., ~9.5 efpy)- but kept on hold out of the vessel during the 1984 vessel anneal. Upon request from Yankee Atomic Electric Company, SCK/CEN did contractually accomplish the testing program shown schematically on Figure 16. This study accounts for the neutron fluence and resulting hardening gradient, Figure 17.[1] The neutron fluence at the notch level of the two layers of specimens are respectively 5.0 and 2.1 E19 cm-2 (>1MeV). These specimens were tested in their "as-received" condition, then reconstituted according to the illustrated scheme. The reconstitution technique was first validated for the desired minimum insert length of 10mm. This

[1]The line on Figure 17 has been obtained by scaling the corresponding transition temperature trend curve (x 0.5 kg mm^{-2}/°C).

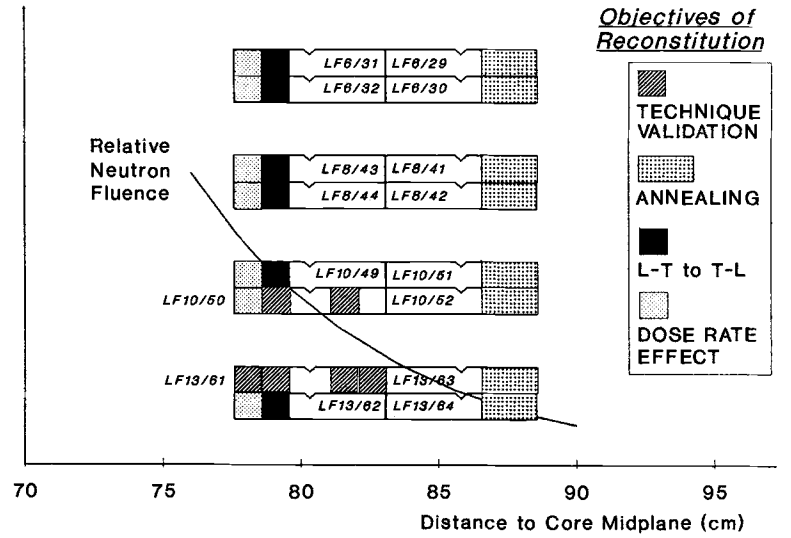


FIG. 16--Schematic layout of C_V-specimens at BR3 and reconstitution schedule.

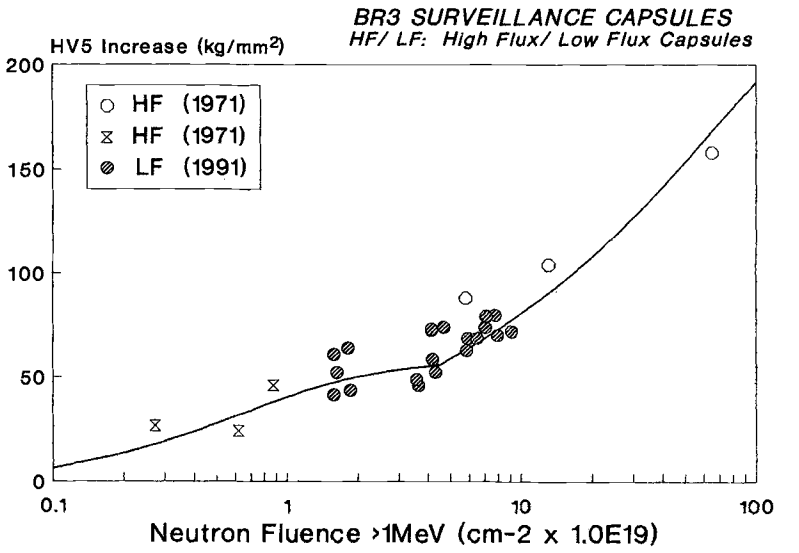


FIG. 17--Hardening of Yankee surveillance plate at BR3.

included carefully documented work on un-irradiated plate HSST-03 [17] and led to the establishment of the first correlation for the energy loss due to plastic flow perturbation by the welded zones. As a result, it was clear that the tests of reconstituted specimens exposed to 7.4 E19 cm-2 would not entail any loss; these tests were specifically aimed at verifying whether embrittlement "mechanism 2A" is sensitive to dose rate. It was clear also that the L-T to T-L notch re-orientation study could be performed without need for any energy loss correction, but as some correction may be needed for the anneal recovery evaluation, it was decided to keep the insert length to ~20 mm for this experiment.

Comments on Data Interpretation and Data Scatter

All fits to C_v data in this paper intend to characterize the ***mean*** behaviour of a set of specimens corresponding to a given material condition. Bounding intervals can also be defined.

It has been found (Figure 18) that the most significant scatter in the C_v test entails the deflection, thus also the energy, of fraction B. Closer inspection reveals that what fluctuates the most widely is the amount of stable crack growth between the appearance of a ductile crack front under the notch and the subsequent onset of brittle cleavage. The competition between fracture modes is strongly affected by the inhomogeneous distribution of trigger particles and this leads to much larger energy spreads than the ones caused by the same particles under lower shelf regimes.This is presumably because large deformations, thus large deflections, can be accommodated by unit crack length propagation, owing to the enhanced plasticity in the transition range. This is reminiscent of the amplification of K_{Jc} scatter by stable crack growth prior to brittle failure in the upper transition temperature regime .

The increase of Fraction B with increasing test temperature is generally the steepest one as compared to the other fractions, i.e. energy B goes from zero to its shelf value over a small temperature interval (10 to 30°C), at least compared to the interval between lower and upper shelf for the total energy (typically 120 ± 25 °C). Fraction B is often the one most affected by irradiation. The smaller scatter often associated with the C_v testing of specimens subject to substantial in-pile embrittlement,- as is the case for the present Yankee/BR3 plate- is due to the significant decrease of this fraction, and/or to its shift to higher temperatures (sometimes even exceeding T_0).

The major difference between C_v transverse orientation (T-L) and strong orientation (L-T) data in base metals stems from the reduction of energy B in the former case. Upper shelf orientation effects are linked to the spacing, shape and distribution of inclusions (sulphides, oxides, ...), which govern microvoid coalescence and the critical strain for ductile fracture. Thus, energy B is totally unrelated whatsoever to stress-controlled brittle fracture, and to DBTT.

Finally, energy partitioning has been found most useful to help identify outlier specimens, an important issue in surveillance applications - given the usually limited test

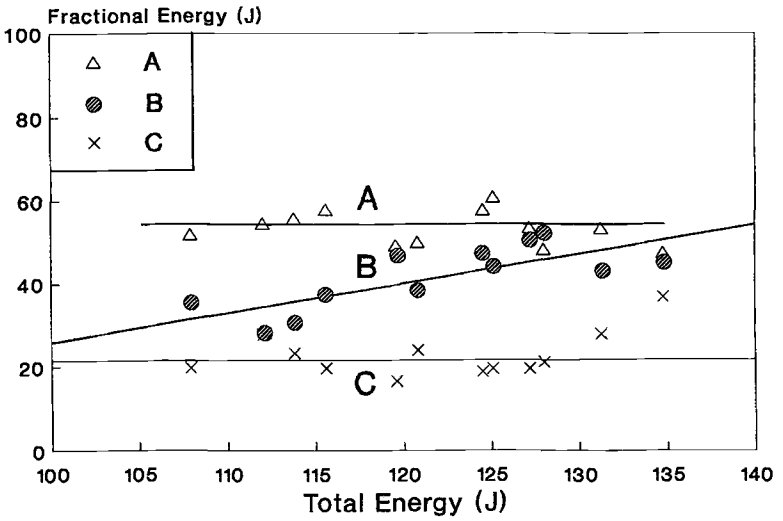


FIG. 18--Fraction B of load-time signal governs C_V data scatter in transition temperature range.

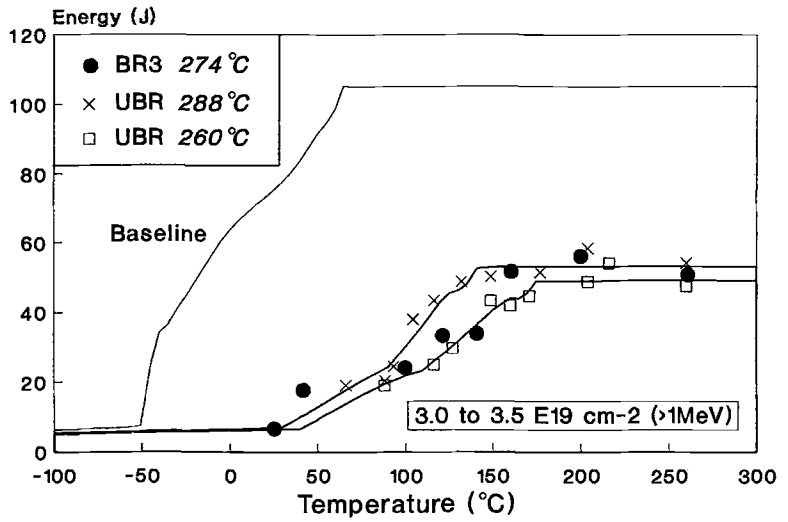


FIG. 19--Embrittlement of weld W1 at BR3 LF capsules is consistent with UBR test reactor results.

matrix. In particular, a fraction A or fraction C abnormality may not be obvious from total energy, lateral expansion and fracture appearance alone. The approach, extended to encompass deflection and expansion data, is a very powerful evaluation tool.

Quality Assurance of BR3 Surveillance Capsules

A supplementary surveillance program has been installed in BR3 after the 1984 vessel anneal. The new capsule design was similar to the old, LF type one, and the exposure locations were also similar. Various relevant steels were irradiated. Figure 19 shows the results for Linde 80 weld W1 (Table 2). Good concurrence is observed with the UBR test reactor data [20].

Evaluation of the Results

The results of these 1991 experiments have been evaluated by means of the load diagram approach described in Section 2. Figures 20 to 22 illustrate, in part, this analysis; the shifts ΔT_I and ΔT_O are compared in Table 5 to the shifts ΔTT41J and ΔFATT.

TABLE 5-- Engineering versus Physically-Based Transition Temperature Shifts for Yankee/BR3 Surveillance Plate Exposed at BR3.

Neutron Fluence (cm^{-2} >1MeV)	ΔTT41J (°C)	ΔFATT (°C)	ΔT_I (°C)	ΔT_0 (°C)
I-condition				
2.1 E19 L-T	92.3	74.4	35	64
5.0 E19 L-T	126	96.6	75	80
7.4 E19 L-T	137	102	_	89
6.2 E19 T-L	118	105	_	86
IA-condition				
1.6 E19 L-T	54.4	54.4	22	47

Good agreement is obtained between reconstituted and as-received test results for the L-T notch orientation; this is true not only in terms of total absorbed energy and fracture appearance (Figure 20, left), lateral expansion and load diagram (not shown), but also for the individual energy fractions (Figure 22, left)-if one accounts for the previous discussion of the sources of data scatter. It is also seen that the "tearing" energy fraction B has become quite small after 5.0 E19 cm-2; no energy reconstitution loss is expected under such conditions.

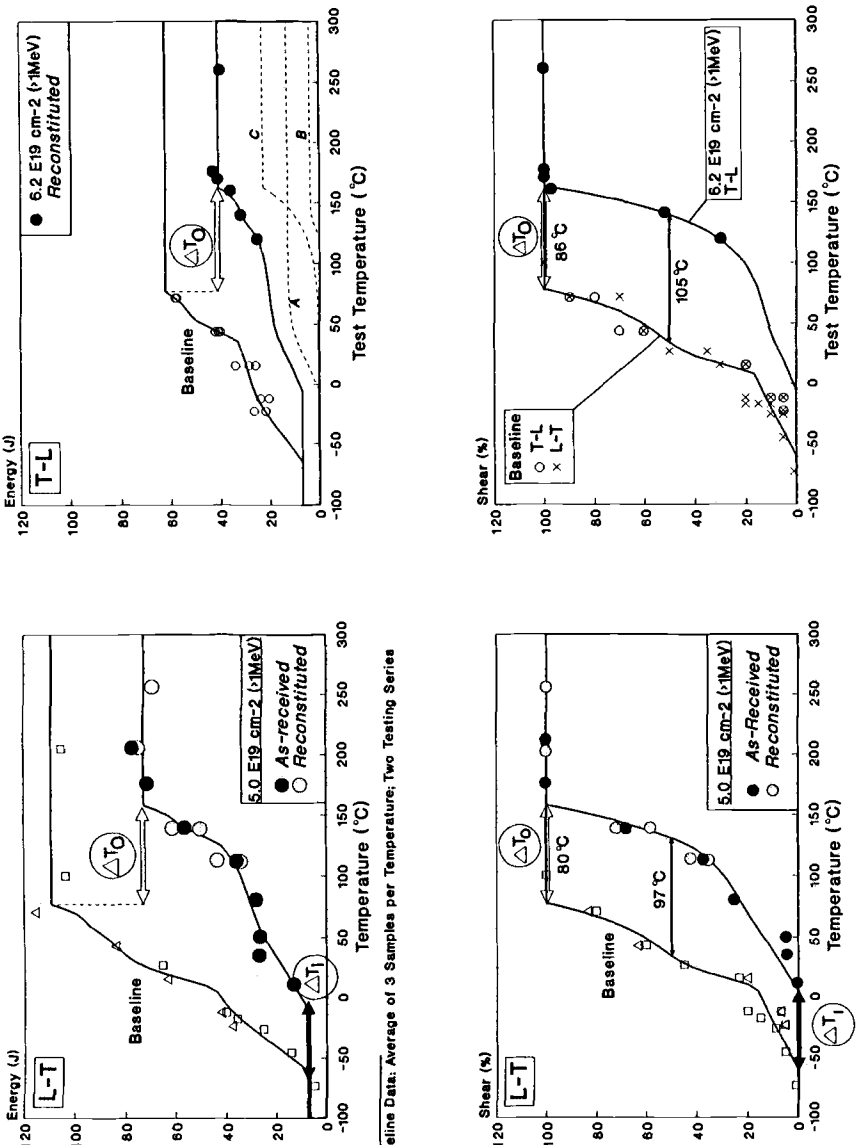


FIG. 20--Effect of notch orientation on Yankee surveillance plate at BR3.

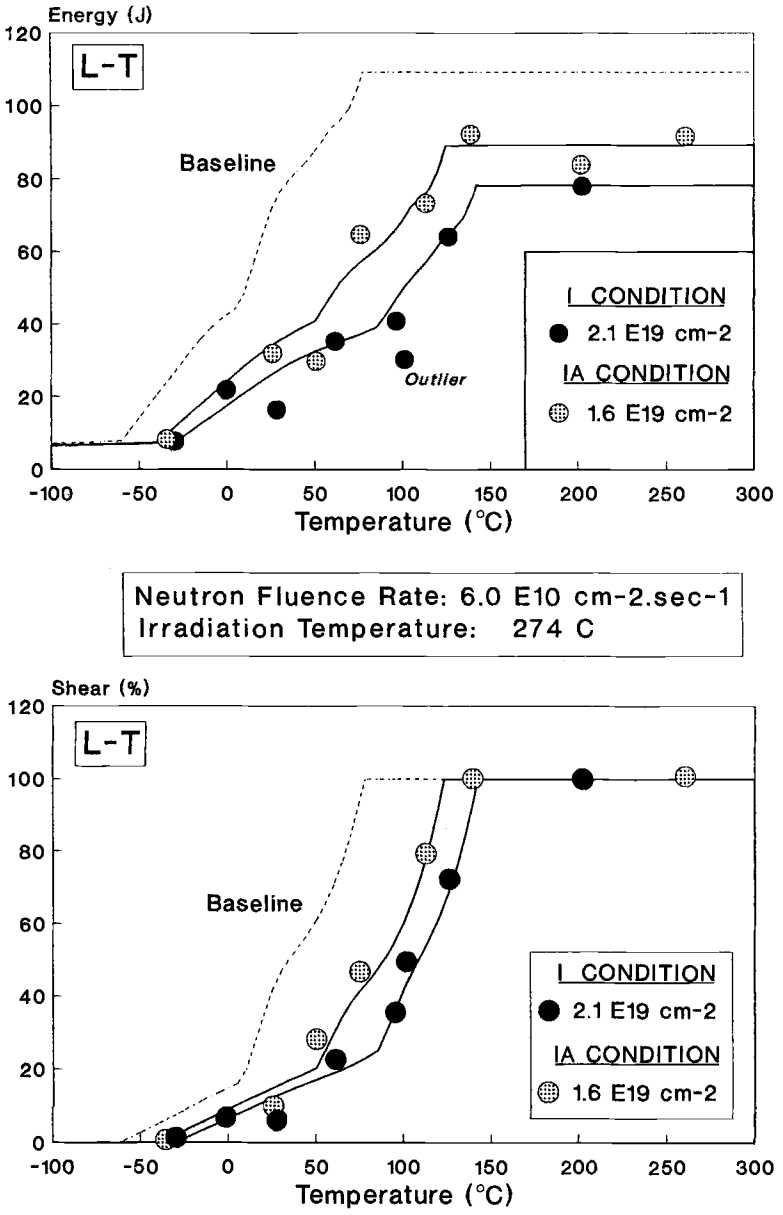


FIG. 21--Anneal recovery of Yankee surveillance plate at BR3: 2 weeks at 343 °C.

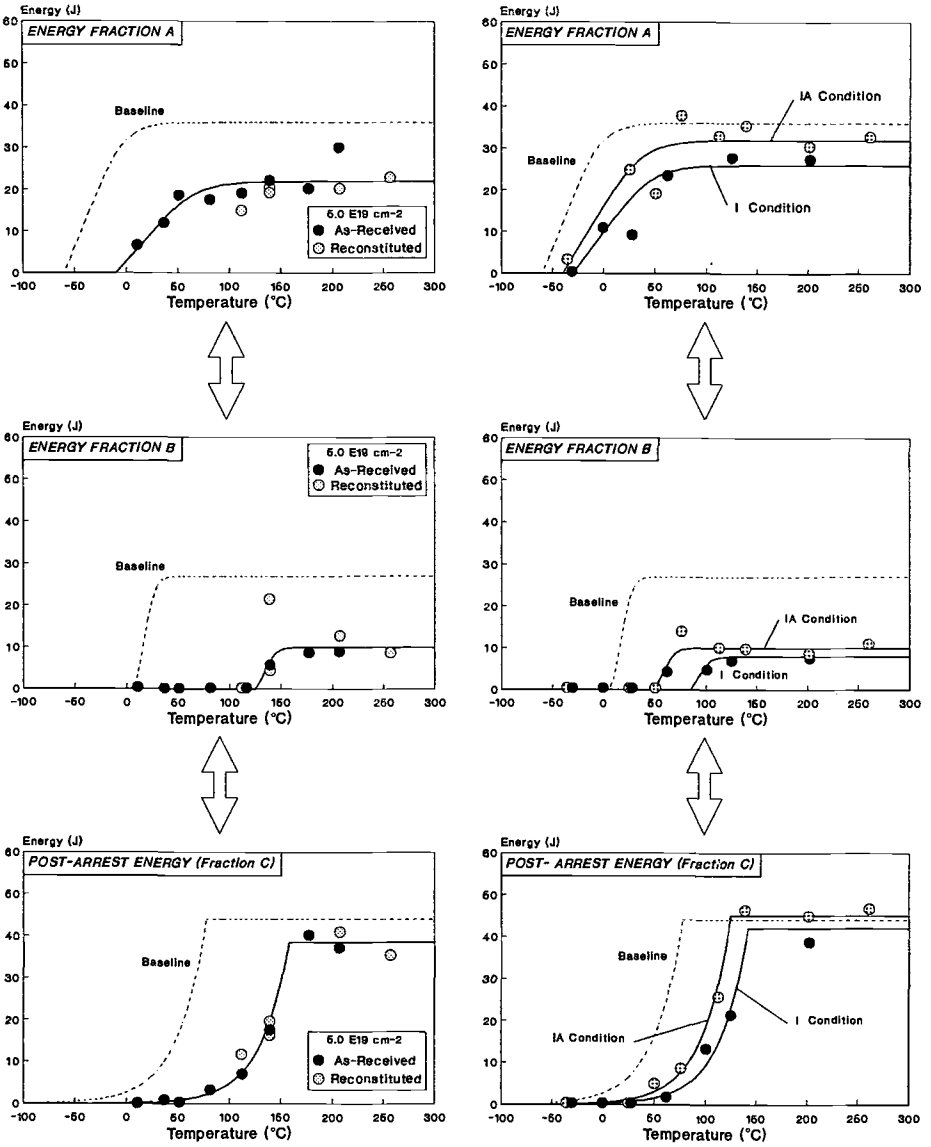


FIG. 22--Energy partitioning of C_V-impact energy curves: typical results for Yankee surveillance plate at BR3.

From the point of view of reconstitution losses,the T-L notch configuration is even more favourable than the L-T one.Because fraction B in the T-L orientation is so small at 6.2 E19 cm-2, data scatter is also small and the results can be considered reliable,despite the limited number of specimens (6 only,which does not allow to define ΔT_I, as the testing has been optimized to ascertain ΔT_O and the upper shelf level). Keeping in mind the differences in neutron fluences, one can see that the L-T and T-L transition temperature shifts ΔT_O are about the same; this is true also for the fracture appearance shifts, but ΔFATT exceeds somewhat ΔT_O (as was the case for the Maine Yankee plate at high neutron fluence, Figure 10). The 41J. shifts are the largest ones, but are meaningless, as will be explained below. It is most telling that here,the *L-T shift ΔTT41 exceeds the T-L one, even though the T-L upper shelf is significantly less than the L-T one: barely 42J., as compared to ~73J.* This particular experiment shows that a significant lowering of the C_v-upper shelf by irradiation does not necessarily cause a larger transition temperature shift than if the shelf remained high.

For the neutron fluence range of 5 to 6 E19 cm-2, the relative C_v- upper shelf drop is ~34%, independent of notch orientation. Due to the rather large sulphur content of this material (Table 1), the T-L/L-T upper shelf ratio is low,i.e. it is barely 0.6 for the baseline;as we have seen,this does not adversely affect the transition temperature shift because it is stress controlled, but this leads to low shelf values for energy fraction B, because deflection is strain controlled.For the same reasons, the enhancement of fraction B by nickel addition is not prone to affect the DBTT shift;this probably explains the lack of nickel effect below ~4.5 E19 cm-2, as reported in section 3.

The low Charpy upper shelf of this A302-B plate could be a concern for vessels of more recent design (ASME III).

Also incorporated into the test matrix of Figure 16 is an investigation to specifically examine whether the importance of damage mechanism 2A could be reduced or whether the mechanism could altogether vanish at low dose rate, surveillance exposure conditions. The answer is: no. The load diagram clearly reveals a shift of the crack arrest load to higher temperature, consistent with the FATT shift (Table 5). Moreover, the presence of 2A is apparent in the Vickers hardness data of Figure 17. The conclusion is further supported by the Chooz-A results of Figure 14.

Recovery of Charpy properties after annealing at 343°C during 2 weeks is very poor, as shown by Figure 21 and by the right hand-side of Figure 22. Isothermal Vickers hardness experiments at various temperatures up to 450°C suggest a significant dose rate effect on annealing.

Inadequacy of Fracture Toughness Indexation to a Fixed C_v Impact Absorbed Energy Level and Physically-Based C_v Impact Indexation Temperatures

Intuitively, it is difficult to believe that the DBTT shift upon service could ever exceed the shift of either T_I or T_0. This view is reinforced by the fact that one generally observes that $\Delta T_I \approx \Delta T_0$. Yet, it may happen that the 41J shift ΔTT41 significantly

exceeds ΔT_I and ΔT_0. In such case, ΔTT41 is certainly inadequate for fracture toughness indexation.

The non-physical behaviour of ΔTT41 for the Yankee/BR3 surveillance plate is explained by Fig. 23. It is seen that the 41J temperature in the baseline is controlled by the plane strain, pre-maximum energy fraction, A+LSE, while some amount of post-arrest energy fraction C - i.e., of plane stress, shear lip formation energy - is needed to reach the same 41J level after irradiation; this represents a mismatch of totally unrelated physical phenomena, which furthermore do each shift by about the same amount upon service exposure. The 41J shift is strongly affected by the shelf levels and mid-shelf temperatures of the fractions in the steel baseline: it is NOT independent of the un-irradiated condition; for ex., when A+LSE exceeds 41J both before and after service, the 41J shift is considerably less than otherwise, and agrees with the physically grounded shift. So, two plates of same chemistry may shift quite differently at 41J, under identical environmental conditions, depending on their baseline. This guarantees that unwarranted scatter and distortion does affect empirical, engineering or Regulatory embrittlement correlations, such as the ones in [4]. Furthermore, some steels may be considered as "outliers", while they actually are not.

The 50% FATT shift is often closer to the shifts of TI and TO than the TT41 shift, but occasionally, it may also be too large (as on Fig. 20). Nevertheless, C_v FATT has been shown to be superior to the Pellini drop weight NDT for toughness indexation of a variety of unirradiated steels [85] [86], and *to first approximation*, one generally finds that upon reactor exposure, Δ FATT $\approx \Delta$TI $\approx \Delta$T0. Thus, to first approximation, FATT should provide a reasonable indexation of the dynamic initiation and crack arrest fracture toughness; although this is more conservative than the C_v fracture arrest parameter proposed by Wallin [45], an advantage is that FATT is generally available from existing data bases.

Figure 24 compares the modeling-based trend curve for the Yankee/BR3 surveillance plate at BR3 to the corresponding FATT-shift data. The model trend curve is the same as for the A302-B reference plate under similar exposure conditions. In other words, the real influence of service exposure on the Yankee/BR3 surveillance plate is the same as for other A302-B plates of similar composition; the only influence of its coarser microstructure is on its baseline properties: as Figure 2 indicates, the unirradiated crack arrest capability of this material is less favourable than is the case for the A302-B reference plate (i.e., its T_0 is higher), but the difference does not change upon irradiation.

5. IMPLICATIONS

Methodology to Estimate the Regulatory Implications of the Proposed Fracture Toughness Indexation Approach

The logic followed in this *scoping* examination is to bring together $0.63\ \Delta\ \sigma_y$ ΔFATT and Damage Modeling

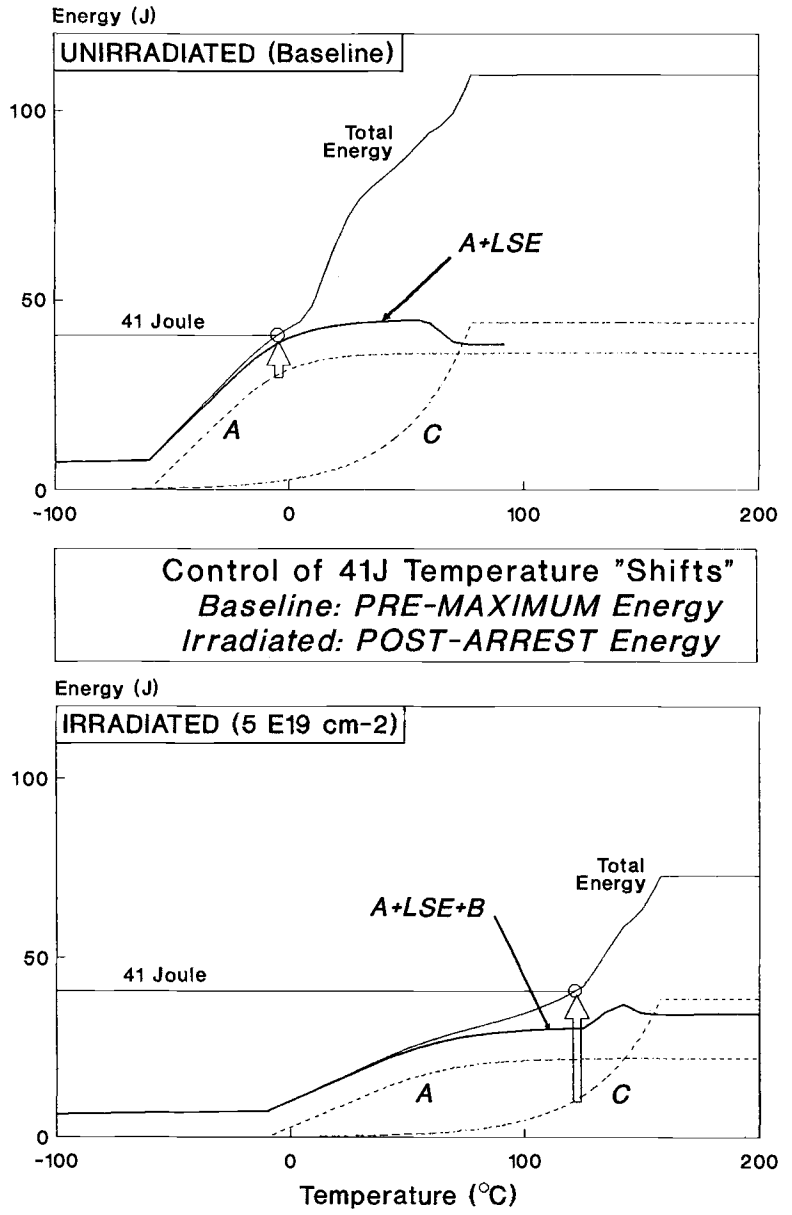


FIG. 23--The physical reason for the outlier engineering shift of the Yankee Rowe surveillance plate.

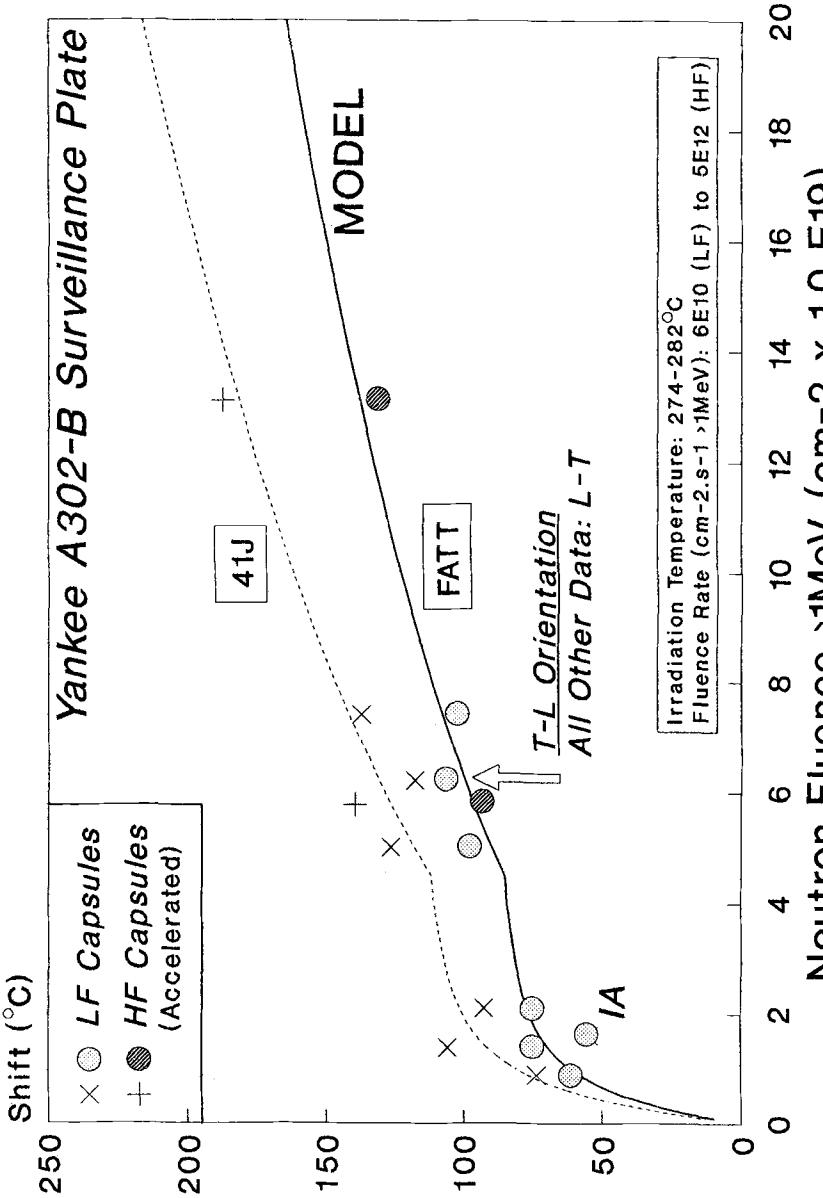


FIG. 24--Modeling-based embrittlement trend curve of Yankee Rowe surveillance plate at BR3.

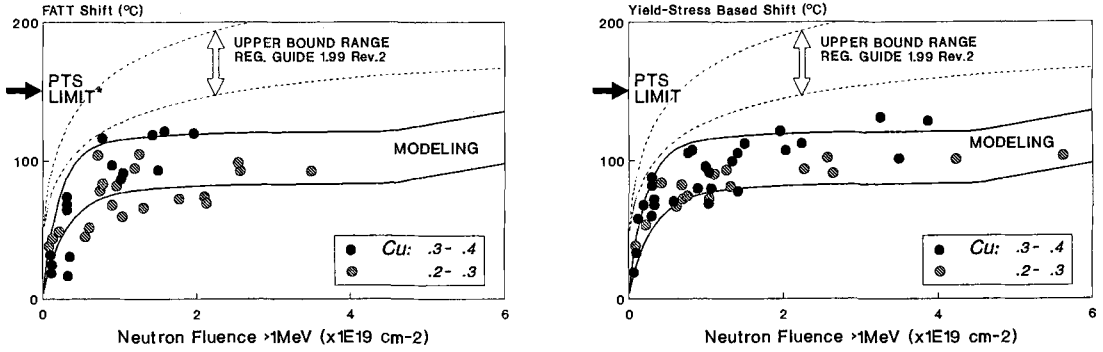
The purpose is to try quantifying, ***to first approximation*** (conservatively), the influence- if any- of a physically-grounded definition of DBTT shifts in terms of metallurgical embrittlement trend curves. This is done by comparing to the more empirical, Regulatory correlations [4] of the "engineering" shifts $\Delta TT41$ (i.e. C_v- shifts at an absorbed energy of 41 Joules). It will be seen that the influence is large, in many respects.

Conservatism of Regulatory RPV Embrittlement Trend Curves

The approach has been applied "across-the-board" to examine ***upper bound shifts*** for the available data base relative to the Linde-80 low upper shelf energy welds, Figure 25 (as well as data for other materials, not discussed herein). This was done to propose that no U.S. pressure vessel would need to be annealed in the foreseeable future [87]. The Linde 80 weld data include U.S. power reactor surveillance [88], as well as some test reactor experiments at 288°C (such as the weld codes W8A [76][89] and W1 [20]). The FATT shifts were not determined in some cases, but tensile properties were generally available for at least one test temperature; this is the reason why the right part of Figure 25 contains more points than the left one. The FATT shifts for the copper range 0.2-0.3% tend to be somewhat lower than the shifts based on tensile yield strength increases; full-fledged application of the load diagram approach may allow to clarify this difference, but this has not been attempted for this scoping of bounds. The modeling curves were calculated so as to bracket the dose rate, irradiation temperature and copper content ranges in these experiments; no eventual nickel influence was accounted for, given our findings for the archive welds in support of BR3 anneal (Section 3). The main reasons for the conservatism of the Regulatory upper bounds on Figure 25 are the shift definition (indexation) and, as importantly, the fluence function adopted by the Guide: it is too steep in the neutron fluence range ~1-4.5 E19 cm-2 (>1MeV), simply because it lumps together the various damage mechanisms.

It is interesting to note how huge the scatter of embrittlement data can be for reference steels such as plates HSST-02 and HSST-03, Figure 26; the data base displayed here, which gathers power reactor surveillance and test reactor experiments, has been carefully scrubbed for baseline variability and dosimetry biases. Yet, this scatter exceeds the one for Linde 80 welds on Figure 25. This is because the HSST plate data encompass a somewhat wider range of dose rates and irradiation temperatures. These results can be rationalized and the scatter removed by damage modeling: this is illustrated by Figure 13 for a selected subset of the data on Figure 26.

Summarizing: an **arbitrary indexation of transition temperature shifts to 41J. absorbed C_v-energy can cause the embrittlement behavior of certain steels to appear "outlier"**: Yankee/BR3 surveillance plate, Belgian Doel-I,-II welds [50][90], some Linde 80 welds,... These outliers do significantly contribute to the ***mismatch*** and ***scatter*** of embrittlement trend curves based on engineering correlations:



Generic, Axial Welds

FIG. 25-- Combined micromechanics and damage modeling show conservatism of Regulation for Linde-80 welds.

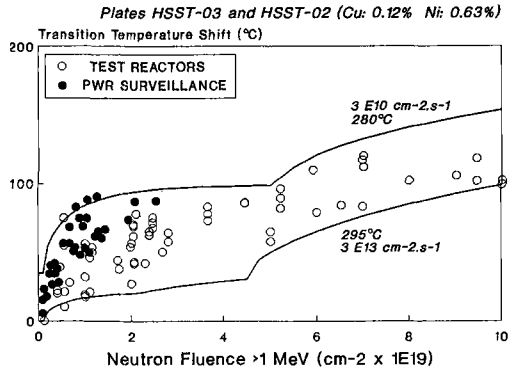


FIG. 26-- Test and power reactor data for reference A533-B plates.

- Mean trend curves too high
- Margins too high
- Chemistry factors distorded
- Fluence dependency too steep in range 1-4 E19 cm-2 (>1MeV).

As a result, unwarranted penalties can be imposed on vessel heat-up and cooldown operation limits (which are controlled by K_{Id}, K_{Ia}).

On another hand, our micromechanical modeling work does also predict that the shift of the static initiation fracture toughness upon service exposure must normally be larger than the shift of the corresponding dynamic toughness - namely, whenever the steel is not an outlier, in the sense of this paper. Both curves *tend* towards one another with the reduction of the strain hardening exponent associated with the increase of the yield stress [18]. The maximum difference of about 30 °C between dynamic and static shift is not expected to invalidate our views regarding both annealing and the conservatism of current embrittlement projection methods. For outlier steels, the K_{Ic}-shift can be less than the 41J. C_v-shift.

Recommendation

For plants involving outlier steel behavior, or otherwise limited according to current Regulation, it has been recommended in [18] to implement **"Enhanced RPV Surveillance Strategy"** based on the present concepts and on supplementary fracture toughness measurements using small precracked specimens reconstituted from broken surveillance remnants. The technology is available and the basic Regulatory framework for actual application does exist, pending final adoption of Test Practices and Standards under consideration at this time.

REFERENCES

[1] Biemiller, E.C., "Reference Temperature," Chapter 5 in "Reactor Pressure Vessel Evaluation Report for Yankee Nuclear Power Station", Yankee Atomic Electric Company, Report YAEC n° 1735, July 1990.

[2] Biemiller, E.C., Fyfitch, S., and Campbell, C. A.,"Preliminary Irradiation Test Results from the Yankee Atomic Electric Company Reactor Vessel Test Irradiation Program," ASME Pressure Vessel & Piping Conference, Denver, July 25-29, 1993, and SMIRT12, Paper No. F09/1, Stuttgart, Germany, August 15-20, 1993.

[3] Fabry, A., et.al., "Annealing of the BR3 Reactor Pressure Vessel", in Transactions of the Twelfth Water Reactor Safety Information Meeting, NUREG/CP-0058, Vol.4, 1984, pp.144-175.

[4] U. S. Nuclear Regulatory Commission, Regulatory Guide 1.99 Revision 2, Office of Nuclear Regulatory Research, May 1988.

[5] Steele, L.E., and Serpan, C.Z., "Analysis of Reactor Vessel Radiation Effects Surveillance Programs," ASTM STP 481, American Society for Testing and Materials, Philadelphia, PA, 1970.

[6] Steele, L.E., "Neutron Irradiation Embrittlement of Reactor Pressure Vessel Steels", IAEA Technical Report Series, n° 163, 1975.

[7] Steele, L.E., et al. "Irradiation Effects on Reactor Structural Materials," NRL Memorandum Report 1593, U.S. Naval Research Laboratory, Washington, D.C., February 15, 1965.

[8] Little, E.A., "Neutron-irradiation hardening in irons and ferritic steels," Int. Metals Reviews, 21, 1976, pp. 25-60.

[9] Carpenter, G.F., Knopf, N.R., and Byron, E.S., "Anomalous Embrittling Effects Observed During Irradiation Studies on Pressure Vessel Steels," Nucl. Sci. and Eng. 19, 1964, pp.18-38.

[10] Wessel, E.T., and Eichelberger, T.W., "Variations in the Embrittlement of Irradiated Pressure Vessel Steels, Part 1," Report WERL-8844-4, Westinghouse Research Laboratories, 1965.

[11] Stallmann, F. W., "Analysis of the A302B and A533B Standard Reference Materials in Surveillance Capsules of Commercial Power Reactors", Report NUREG/CR-4947, ORNL/TM-10459, 1987.

[12] Fabry, A., "Peer Review of the Reactor Pressure Vessel Evaluation Report for Yankee Nuclear Power Station, Chapter 5: Reference Temperature," Memorandum AF/ivb-61.B3110 313/91-16, SCK-CEN, April 15, 1991.

[13] Serpan, C.Z., and Hawthorne, J.R., "Yankee Reactor Pressure Vessel Surveillance: Notch Ductility Performance of Vessel Steel and Maximum Service Fluence Determined from Exposure During Cores II, III and IV," Report NRL 6616, Naval Research Laboratory, 1967.

[14] Hawthorne, J.R., and Potapovs, U., "Initial assessments of Notch Ductility Behavior of A533 Pressure Vessel Steel with Neutron Irradiation", Report NRL 6772, Naval Research Laboratory, and ASTM STP 457, 1968, pp. 113-134.

[15] Hawthorne, J.R., "Trends in Charpy-v Shelf Energy Degradation and Yield Strength Increase of Neutron-Embrittled Pressure Vessel Steels," Nucl. Eng. and Design, 11, 1970, pp. 427-446.

[16] Pachur, D., "Radiation Annealing Mechanisms of Low-Alloy Reactor Pressure Vessel Steels Dependent on Irradiation Temperature and Neutron Fluence," Nucl. Techn., Vol. 59, 1982, pp. 463-475.

[17] Vandermeulen, W., Fabry, A., Puzzolante, J.L., Van de Velde, J., Van Ransbeeck, Th., and van Walle, E., "Charpy Specimen Reconstitution as a Means of Providing Data for Plex Licencing Purposes," Int. Journ. Pres. Ves. & Piping, 54, 1993, pp. 89-98.

[18] Fabry, A., van Walle, E., Chaouadi, R., Wannijn, J.P., Verstrepen, A., Puzzolante, J. L., Van Ransbeeck, Th. and Van de Velde, J., "RPV Steel Embrittlement: Damage Modeling and Micromechanics in an Engineering Perspective," presented at The IAEA/OECD Specialists Meeting on Irradiation Embrittlement and Optimization of Annealing, Paris, September 20-23 , 1993, and Report BLG-649, SCK-CEN, October 1993.

[19] Motte, F., Fabry, A., Gubel, P., and Minsart, G., "Safety Evaluation of a Highly Irradiated PWR Vessel," NUCSAFE 88, Session 20, Paper 157, 1988.

[20] Hawthorne, J.R., and Hiser, A.L., "Irradiation and Irradiation-Anneal-Reirradiation Studies of RPV Steels and Welds in Support of the BR3 Reactor," Report MEA-2218, 1988.

[21] Hiser, A.L., and Hawthorne, J.R., "Fracture Toughness (J-R Curve) Characterization of IAR (Irradiate-Anneal-Reirradiate) Cycled A302-B Plate and Weld," Report MEA-2204, 1987.

[22] Standard Guide for "In-service Annealing of Light-Water Cooled Nuclear Vessels," ASTM E509-86, American Society for Testing and Materials, Philadelphia, 1986.

[23] Fearnehough, G.D., and Hoy, C.J., "Mechanism of Deformation and Fracture in the Charpy Test as Revealed by Dynamic Recording of Impact Loads," Journal of the Iron and Steel Institute, 1964, pp. 912-920.

[24] Wilshaw, T.R., "Deformation and Fracture of Mild Steel Charpy Specimens," Journal of the Iron and Steel Institute, Vol. 204, 1966, pp. 936-942.

[25] Wullaert, R.A., Ireland, D.R., and Tetelman, A.S., "Radiation Effects on the Metallurgical Fracture Parameters and Fracture Toughness of Pressure Vessel Steels," Irradiation Effects on Structural Alloys for Nuclear Reactor Applications, ASTM STP 484, American Society for Testing and Materials, 1970, pp. 20-41.

[26] Radon, J.C., and Turner, C.E., "Fracture Toughness Measurement by Instrumented Impact Test," Engineering Fracture Mechanics, Vol. 1, 1969, pp. 411-428.

[27] Rintamaa, R., and Zimmermann, C., "Advanced Instrumented Impact Testing Facility for Characterization of Dynamic Fracture Behavior," Nuclear Engineering and Design, Vol. 96, 1986, pp. 159-166.

[28] Ray, S.K., Sreenivasan, P.R., Samuel, K.G., and Rodriguez, P., "Characterization of Irradiation-Induced Embrittlement in a ASTM A 203D Steel Using Instrumented Impact Testing," Int. J. Pres. Ves. & Piping, Vol. 54, 1993, pp. 481-496.

[29] Pachur, D., "Influence of Radiation Damage Mechanisms on the Load Signal and on the Transition Curve of Instrumented Impact Testing", J. Nucl. Mat., Vol. 160, 1988, pp. 24 -33.

[30] Krompholz, K., Tipping, P., and Ullrich, G., "Results from Investigations with an Instrumented Impact Machine on a Molybdenum Base Alloy, Nickel Base Alloys, and Incoloy 800", Z. Werkstofftech., Vol. 15, 1984, pp. 117-123.

[31] Chatterjee, S., Anantharaman, S., Viswanathan,U.K., and Sivaramakrishnan, K.S., "Evaluation of Irradiation Embrittlement by Instrumented Impact Testing", Effects of Radiation on Materials: 14th International Symposium (Volume II), ASTM STP 1046, N.H. Packan, R.E. Stoller, and A.S. Kumar, Eds., American Society for Testing and Materials, Philadelphia, 1990, pp. 496-514.

[32] "Proposed Standard Method for the Instrumented Charpy-V Impact Test on Metallic Materials," ESIS Instrumented Charpy-V Standard, Draft 9, 1993.

[33] "Standard Guide for Conducting Supplemental Surveillance Tests for Nuclear Power Reactor Vessels, E706(1H)," ASTM Committee E10, Revision of E0636-83, in Preparation.

[34] Tetelman, A.S. and McEvily Jr., A.J., "Fracture of Structural Materials," John Wiley & Sons, Inc., 1967.

[35] Knott, J.F., "Fundamentals of Fracture Mechanics", Edited by Butterworths, 1973.

[36] Orowan, F., "Fracture and Strength of Solids," Rep. Prog. Phys., Vol. 12, 1948, pp. 185-232.

[37] Yao, M., He, Y.K., Li, D.M., and Zhou, C.Z., "A Mechanics-Metallurgy Approach to Cleavage behavior in Mild Steel," Advances in Fracture Research, Proc. 6th. Intern. Conf. on Fracture (ICF6), New Delhi, India, Vol. 2, 1984, pp. 1423-1430.

[38] Li, D.M. and Yao, M., "Effect of Notch Depth on Low-Temperature Fracture Behavior of Mild Steel," Scripta Metallurgica, Vol.21, 1987, pp. 593-596.

[39] Huang, Z. and Yao, M., "Research into Brittle/Ductile Transition Temperature", Scripta Metallurgica, Vol. 23, 1989, pp. 2137-2142.

[40] Helms, R., Veith, H. and Ziebs, J., "Correlation between Charpy Test Results and those from Larger Specimens and Structures on the Basis of General Yield," CSNI Specialists Meeting on Instrumented Precracked Charpy Testing Palo Alto, Cal., 1980, pp. 5/45-5/56.

[41] Kobayaski, ,T., Takai, K., and Maniwa, H., "Transition Behaviour and Evaluation of Fracture Toughness in Charpy Impact Test," Trans. Iron and Steel Institute of Japan, Vol. 7, 1967, pp. 115-125.

[42] Pachur, D., "Comparison of Drop-Weight and Instrumented Charpy Impact Test Results for Irradiated RPV Steels, Effects of Radiation on Materials: 16th International Symposium, ASTM STP 1175, A.S. Kumar, D.S. Gelles, R.K. Nanstad and E.A. Little, Eds., American Society for Testing and Materials, Philadelphia, 1993.

[43] Onodera, S., Ohnishi, K., Tsukada, H., Suzuki, K., Iwadate, T. and Tanaka, Y., "Effect of Crack-Starter Bead Application on the Drop-Weight NDT Temperature," Drop-Weight Test for Determination of Nil-Ductility Transition Temperature: User's Experience with ASTM Method E208, ASTM STP 919, J.M. Holt and P.P. Puzak, Eds., American Society for Testing and Materials, Philadelphia, 1986, pp. 34-55.

[44] Schmitt, F.J., "Correlation of Cv and Drop-Weight Transition Temperature Increase Caused by Irradiation," Effects of Radiation on Materials: 14th International Symposium (Vol.II), ASTM STP 1046, N.H. Packan,, R.E. Stoller and A.S. Kumar, Eds., American Society for Testing and Materials, Philadelphia, 1990, pp. 373-384.

[45] Wallin, K., "Descriptive Potential of Charpy-V Fracture Arrest Parameter with Respect to Crack Arrest KIa," presented at the ESIS 2nd TC5 Workshop, SCK-CEN, Mol, Belgium, April 28, 1994, and to be published.

[46] Winkler, S.R., "Magnetic Emission Detection of Crack Initiation," Fracture Mechanics: Twenty-First Symposium, ASTM STP 1074, J.P. Gudas, J.A. Joyce and E.M. Hackett, Eds., ASTM, Philadelphia, 1990, pp. 178-192.

[47] Aurich, D., Helms, R., Kühn, H.J. and Ziebs, J., "The Influence of Loading Rate on Fracture Resistance of Notched and Precracked ISO-V Specimens", Nuclear Eng. and Design, Vol. 96, 1986, pp. 149-157.

[48] Aurich, D., Helms, R., Kühn, H.J., Wobst, K., and Ziebs, J., "Charpy Upper Shelf Energy and Crack Resistance," Nucl. Eng. and Design, Vol. 87, 1985, pp. 109-121.

[49] Brüninghaus, K., Falk, J., Twickler, M., and Dahl, W., "Determination of Crack Resistance Curves under Static and Dynamic Loading by Analysis of Load Displacement Relationship," Eng. Fract. Mech., Vol. 34, 1989, pp. 989-1000.

[50] Gérard, R., Fabry, A., Van de Velde, J., Puzzolante, J.L., Verstrepen, A., Van Ransbeeck, T., and van Walle, E., "In-Service Embrittlement of the Pressure Vessel Welds at the Doel I and II Nuclear Power Plants," 17th Symposium on Effects of Radiation on Materials, Sun Valley, Idaho, American Society for Testing and Materials, USA, June 20-23, 1994.

[51] Green, A.P., and Hundy, B.B., "Initial Plastic Yielding in Notch Bend Tests," J. Mech. Phys. Solids, Vol. 4, 1956, pp. 128-144.

[52] Alexander, J.M., and Komoly, T.J., "On The Yielding of a Rigid/Plastic Bar with an Izod Notch," J. Mech. Phys. Solids, Vol. 10, 1962, pp. 265-275.

[53] Wu, S.X., Cotterell, B. and Mai, Y.W., "Slip-line Field Solutions for Three-Point Notch-Bend Specimens," Int. Journ. of Fract., Vol. 37, 1988, pp. 13-29.

[54] Ewing, D.J.F., "Calculations on the Bending of Rigid/Plastic Notched Bars", J. Mech. Phys. Solids, Vol. 16, 1968, pp. 205-213.

[55] Ritchie, R.O., Knott, J.F. and Rice, J.R., "On the Relationship between Critical Tensile Stress and Fracture Toughness in Mild Steel," J. Mech. Phys. Solids, Vol. 21, 1973, pp. 395-410.

[56] Ritchie, R.O., Server, W.L. and Wullaert, R.A. "Critical Fracture Stress and Fracture Strain Models for the Prediction of Lower and Upper Shelf Toughness in Nuclear Pressure Vessel Steels," Metallurgical Transactions, Vol. 10A, 1979, pp. 1557-1570.

[57] Curry, D.A., "Comparison Between Two Models of Cleavage Fracture," Metal Science, Vol. 14, 1980, pp. 78-80.

[58] Evans, A.G., "Statistical Aspects of Cleavage Fracture in Steel," Metallurgical Transactions, Vol. 14A, 1983, pp. 1349-1355.

[59] Beremin, F.M., "A Local Criterion for Cleavage Fracture of a Nuclear Pressure Vessel Steel," Metallurgical Transactions, Vol. 14A, 1983, pp. 2277-2287.

[60] Wallin, K., Saario, T., and Törrönen, K., "Statistical Model for Carbide Induced Brittle Fracture in Steel," Metal Science, Vol. 18, 1984, pp. 13-16.

[61] Lin, T., Evans, A.G., Ritchie, R.O., "Stochastic Modeling of the Independent Roles of Particle Size and Grain Size in Transgranular Cleavage Fracture," Metallurgical Transactions, Volume 18A, 1987, pp. 641-651.

[62] Godse, R., and Gurland, J. "A Statistical Model for Low Temperature Cleavage Fracture in Mild Steels," Acta Metallurgica, Vol. 37, 1989, pp. 541-548.

[63] Xu, X.X., Cai, Q.G., Su, Y., Hou, C.X. and Ma, W.D. , "Statistical Model of Cleavage Fracture in Granular Bainite in Simulated Weld Heat Affected Zone," Materials Science and Technology, Vol. 5, 1989, pp. 913-917

[64] Odette, G.R., "On the Dominant Mechanism of Irradiation Embrittlement of Reactor Pressure Vessel Steels," Scripta Metallurgica, Vol. 17, 1983, pp. 1183-1188.

[65] Fisher, S.B., Harbottle, J.E., and Aldridge, N.," Radiation Hardening in Magnox Pressure-Vessel Steels," Phil. Trans. R. Soc. Lond., A315, 1985, pp. 301-332.

[66a] Fisher, S.B., and Buswell, J.T., "A Model for PWR Pressure Vessel Embrittlement," Int. J. Press. Vessel and Piping, Vol. 27, 1987, pp. 91-135.

[66b] Buswell J.T. and Jones R.B., "The Modelling of Radiation Hardening and Embrittlement in Magnox Mild Steel Submerged - Arc Welds" ASTM STP 1175, A.S. Kumar, D.S. Gelles, R.K. Nanstad and E.A. Little, Eds., American Society for Testing and Materials, Philadelphia, 1993, pp. 424-443.

[67a] Odette, G.R., and Lucas, G.E., "The Effect of Heat Treatment on Irradiation Hardening of Pressure Vessel Steels: Data Trends and Mechanisms," Environmental Degradation of Materials in Nuclear Power Systems-Water Reactors, G.J.Theus and J.R. Weeks, Eds., The Metallurgical Society, 1988, pp. 95-104.

[67b] Odette, G.R. and Lucas, G.E., "Irradiation Embrittlement of Reactor Pressure Vessel Steels: Mechanisms, Models and Data Correlations", ASTM STP 909, L.E. Steele, Ed., American Society for Testing and Materials, Philadelphia, 1986, pp. 206-241.

[67c] Lucas, G.E., Odette, G.R., Lombrozo, P.M., and Sheckherd, J.W., ASTM STP 870, F. Garner and J. Perrin, Eds., American Society for Testing and Materials, Philadelphia, 1985, pp. 900-930.

[68] Williams, T.J., Burch, P.R., English, C.A., and de la cour Ray, P.H.N.,"The Effect of Irradiation Dose Rate and Temperature, and Copper and Nickel Content, on the Irradiation Shift of Low Alloy Steel Submerged Arc Welds," Environmental Degradation of Materials in Nuclear Power Systems-Water Reactors, G.J.Theus and J.R. Weeks, Eds., The Metallurgical Society, 1988, pp. 121-131.

[69] Phythian, W.J.,"Microstructural Assessment of Belgian Weld Material," Report AEA-TRS-2062, 1991.

[70] Miller, M. K., and Burke, M. G.,"Fine-Scale Microstructural Characterization of Pressure Vessel Steels and Related Materials Using APFIM," Effects of Radiation on Materials: 14th International Symposium (Volume II), ASTM STP 1046, American Society for Testing and Materials, Philadelphia, 1990, pp. 107.

[71] Beaven, P.A., Frisius, F., Kampmann, R., Wagner, R. and Hawthorne, J.R., "SANS Investigation of Irradiated A533B Steels Doped with Phosphorus," Radiation Embrittlement of Nuclear Reactor Pressure Vessel Steels: An International Review (Third Volume), ASTM STP 1011, The American Society for Testing and Materials, Philadelphia, 1989, pp. 243.

[72] Fabry A., "Short-Range Irradiation-Induced Defects Under PWR Service Conditions," International Group on Radiation Damage Mechanisms, IGRDM-5, Santa Barbara, California, May 2-5, 1994. To be published.

[73] Foreman, A.J.E., and Makin, M.J., "Dislocation Movement through Random Arrays of Obstacles," Can. Journal of Physics, Vol. 45, 1967, pp. 511-517.

[74] Hawthorne J. R., "Radiation Effects Information Generated on the ASTM Reference Correlation-Monitor Steels," ASTM Data Series Publication, DS54, 1974.

[75] Hawthorne, J.R., Menke, B.H., and Hiser, A.L., "Notch Ductility and Fracture Toughness Degradation of A302-B and A533-B Reference Plates from PSF Simulated Surveillance and Through-Wall Irradiation Capsules," USNRC Report NUREG/CR-3295, U.S. Nuclear Regulatory Commission, Washington, D.C., USA, 1984.

[76] Hawthorne, J.R., and Hiser, A.L., "Influence of Fluence Rate on Radiation-Induced Mechanical Property Changes in Reactor Pressure Vessel Steels,, USNRC Report NUREG/CR-5493, U.S. Nuclear Regulatory Commission, Washington, D.C., USA, 1990.

[77] De Meester, P., Van Asbroeck, Ph., Van de Velde, J., Van Loon, C., and Laurent, L.,"Evaluation of the BR3 Third Core Vessel Steel Specimens," SCK-CEN Report BLG 459, SCK-CEN, Mol, Belgium, 1971.

[78] Mc Elroy, W.N., Editor, "LWR Pressure Vessel Surveillance Dosimetry Improvement Program: PCA Experiments, Blind Test and Physics-Dosimetry Support for the PSF Experiments," USNRC Report NUREG/CR-3318, U.S. Nuclear Regulatory Commission, Washington, D.C., USA, 1984.

[79] Simons, R.L., "Damage Rate and Spectrum Effects in Ferritic Steel ΔNDTT Data," Report NUREG/CR-4307, Table HEDL-16, U.S. Nuclear Regulatory Commission, Washington, D.C., USA, 1985, pp. HEDL-65.

[80] Vishkarev, O.M., Zvezdin, Y.I., Tulyakov, G.A., Pechorin, A.M., and Shamardin, V.K., "Pressurized Water Reactor (PWR) Vessel Material Irradiation Resistance," IAEA Specialist Meeting on Radiation Embrittlement of NRPV Steels, Balatonfüred, Hungary, September 25-28, 1990.

[81] Pachur, D., "Apparent Embrittlement Saturation and Radiation Mechanisms of Reactor Pressure Vessel Steels", Effects of Radiation on Materials:Tenth Conference, ASTM STP 725, D. Kramer, H. R. Brager and J. S. Perrin, Eds., American Society for Testing and Materials, 1981, pp. 5-19 and private communication.

[82] Mc Elroy, R.J., Williams, T.J., Boydon, F.M.D., and Hemsworth, B., "Low Temperature Embrittlement of LWR RPV Support Structures," OCDE, NEA/CSNI Workshop, Espoo, Finland, October 8-9, 1990.

[83] Grounes, M., " Review of SwedishWork on Irradiation Effects in Pressure Vessel Steels and on Significance of Obtained Data," ASTM STP 426, 1967, pp. 224-259.

[84] Fabry, A., et al.,"Improvement of LWR Pressure Vessel Steel Embrittlement Surveillance: 1984-1986 Progress Report on Belgian Activities in Cooperation with USNRC and Other R&D Programs," Proceedings of the ASTM-Euratom Symposium on Reactor Dosimetry, ASTM STP 1001, 1989, pp. 17-37.

[85] Ohnishi, K., Tsukada, H., Suzuki, K., Iwadate, T. and Tanaka, Y., "Prediction of Lower Bound Fracture Toughness for Lifetime Evaluation of Reactor Pressure Vessels," Nuclear Engineering and Design, Vol. 128, 1991, pp. 125-137.

[86] Tanaka, Y., Iwadate, T. and Suzuki, K., "Small Specimen Measurements of Dynamic Fracture Toughness of Heavy Section Steels for Nuclear Reactor Pressure Vessels," Int. J. Pres. Ves. & Piping, Vol. 31, 1988, pp. 221-236.

[87] Fabry, A., "The BR3 Vessel Anneal: Lessons and Perspective," Reactor Pressure Vessel Thermal Annealing Workshop Sponsored by USDOE, EPRI, SANDIA, Albuquerque, New Mexico, February 17-18, 1994.

[88] Stallmann, F. W., "The Pressure Vessel Steel Embrittlement Data Base (EDB)," NUREG/CR-4816, ORNL/TM-10328, U. S. Nuclear Regulatory Commission, Washington, D.C., USA.

[89] Hawthorne, J. R., and Hiser, A. L., "Investigations of Irradiation-Anneal-Reirradiation (IAR) Properties Trends of RPV Welds: Phase 2 Final Report," Report NUREG/CR-5492, U.S. Nuclear Regulatory Commission, Washington, D.C., USA, 1989.

[90] Gérard, R., and Fabry, A., "Integrity Assessment of Doel 1 and 2 Reactor Pressure Vessels," IAEA Specialist's Meeting on Integrity of Pressure Components of Reactor Systems, Paks, Hungary, May 25-29, 1992.

Microstructure Studies on RPV Steels

Timothy J Williams[1] and William J Phythian[2]

ELECTRON MICROSCOPY AND SMALL ANGLE NEUTRON SCATTERING STUDY OF PRECIPITATION IN LOW ALLOY STEEL SUBMERGED-ARC WELDS

REFERENCE: Williams, T. J. and Phythian, W. J., **"Electron Microscopy and Small Angle Neutron Scattering Study of Precipitation in Low Alloy Steel Submerged-Arc Welds,"** *Effects of Radiation on Materials: 17th International Symposium, ASTM STP 1270,* David S. Gelles, Randy K. Nanstad, Arvind S. Kumar, and Edward A. Little, Eds., American Society for Testing and Materials, 1996.

ABSTRACT: In previous studies, submerged-arc welds with a range of compositions were irradiated in test reactors over a range of dose and dose-rates. The effect of irradiation was measured by Charpy V-notch and hardness tests, and an irradiation response model was developed. In this paper we report the results of a combined electron m icroscopy and small angle neutron scattering (SANS) study on material from some of the Charpy specimens. The results have been interpreted in terms of the Russell and Brown modulus hardening model. In general they have confirmed the predictions of the irradiation response model, and shown that the copper precipitation contribution to the observed macroscopic hardening is strongly dependent on nickel, dose and dose-rate.

KEY WORDS: irradiation embrittlement, pressure vessel steels, weld metal, modelling, mechanisms, small angle neutron scattering, copper, modulus hardening.

1

Consultant - Fracture Technology, Rolls-Royce and Associates Limited, PO Box 31, Raynesway, Derby DE24 8BJ, United Kingdom.

2

Section Leader - Reactor Pressure Vessel Steels, Material Performance Department, AEA Reactor Services, Harwell Laboratory, Didcot, Oxfordshire, OX11 0RA, United Kingdom.

Copyright© 1996 by ASTM International www.astm.org

INTRODUCTION

The irradiation embrittlement of low alloy steels has been shown to be the result of two or more strengthening or embrittlement mechanisms [1, 2, 3, 4]. In many applications the dominant mechanism is the very fine-scale precipitation of copper-rich precipitates (CRPs). However, the magnitude of the effect of copper precipitation depends in a complex way on several other variables.

In previous work [5, 6], these and other interactions were studied by irradiating a large number of different materials under a range of irradiation conditions in test reactors, and developing an irradiation response model. In this paper we report the results of a combined TEM/FEGSTEM (transmission electron microscope/field emission gun scanning transmission electron microscope) and SANS (small angle neutron scattering) study on a material taken from a limited selection of the original specimens. The work was performed to validate certain features of the irradiation response model, in particular the dependence of copper precipitation on dose, dose-rate and nickel content.

EXPERIMENTAL DETAILS

Materials and Specimens

The four welds used for the experiment were selected from a range of materials previously irradiated, and reported in [5, 6]. For convenience, the key details are repeated here. The welds were single V-preparation submerged arc welds in 150 mm thick ASTM SA533-B plate. They were austenitized at 920 °C for six hours and water quenched, then tempered/stress relieved for 42 hours at 600 °C, followed by 6 hours at 650 °C. Furnace cooling was used in both instances. All welds had approximately 1.5% Mn, 0.5% Mo and 0.05% C, however they had different combinations of high and low nickel and high and low copper contents. Table 1 shows the nickel, sulphur, phosphorus and copper contents for the individual specimens. The copper contents in the high copper welds (SH and WV) were achieved by doping the welding flux. For convenience, the table also shows irradiation details and measurements of matrix copper; these are discussed below.

The specimens used for SANS were 10 x 10 x 2 mm tiles machined from unirradiated and irradiated Charpy specimens (undeformed, low absorbed impact energy, samples were chosen). The TEM/STEM samples were machined from the tiles after the SANS experiments.

Irradiation Conditions

The specimens had been irradiated (as Charpy samples) at 255 °C to the doses and at the dose rates shown in Table 1. The high dose rate irradiations were done in the Herald reactor at Aldermaston in a reflector position. The medium dose rate irradiations were in the same reactor but in the VT4 position, outside the reflector. The low dose rate

TABLE 1--Compositions and Irradiation Conditions

Specimen Identity	Nickel (%)	Sulphur (%)	Phos-phorus (%)	Total Copper (%)	Matrix Copper (Calc.) (%)	Matrix Copper (STEM) (%)	Irradiation Dose (dpa x 1E3)	Dose Rate (dpa/s x 1E12)
SH047	0.088	0.012	0.015	0.50	0.26	0.36	2.01	6900
SH052	0.088	0.012	0.015	0.50	0.26	0.36	8.16	5820
SH062	0.088	0.012	0.015	0.50	0.26	0.36	32.28	5770
SH604	0.075	0.012	0.015	0.57	0.22	0.36	3.48	640
SH514	0.065	0.012	0.015	0.59	0.22	0.36	12.17	630
SH515	0.065	0.012	0.015	0.59	0.22	0.36	1.48	90
SL151	0.089	0.013	0.017	0.12	0.07	0.11	13.88	5020
SL415	0.095	0.013	0.017	0.19	0.14	0.11	31.95	5770
WV216	1.620	0.010	0.013	0.52	0.48	0.48	1.50	5200
WV214	1.620	0.010	0.013	0.52	0.48	0.48	9.19	6490
WV012	1.720	0.010	0.013	0.63	0.59	0.48	30.11	6230
WV127	1.660	0.010	0.013	0.54	0.50	0.48	3.39	630
WV400	1.640	0.010	0.013	0.54	0.51	0.48	12.11	630
WV126	1.660	0.010	0.013	0.54	0.50	0.48	1.46	90
WL772	1.510	0.011	0.006	0.05	0.01	0.10	31.94	5770

irradiations were carried out in a special rig, at some distance from the core, in the CEA Osiris reactor at Saclay in France. Temperature uncertainties were about ± 3 °C (1 σ); dose and dose-rate uncertainties about ± 15% (1σ). Further details of the irradiations are given in [5, 6].

Mechanical Testing

Although the specimens were machined from Charpy specimens, the mechanical test data used in this paper are the hardness measurements made on these specimens individually. For each Charpy specimen, six 20 kg load Vickers diamond pyramid hardness impressions were made before irradiation, and four after irradiation. (For these welds the ratio between Charpy 41J shift and hardness change has been found [5] to be approximately 2.3 (°C/VPN).)

Electron Microscopy

Specimens were prepared in cell by spark erosion followed by twin-jet electropolishing. The preparation route developed by AEA Technology uses two types of electrolyte to ensure the surface is free from copper contamination [7]. The TEM

examinations were carried out on a Philips EM430 operating at 300 keV. The STEM was carried out on a dedicated ultra high vacuum machine at Harwell fitted with a field emission electron gun, enabling energy dispersive x-ray analysis on the nm scale.

Small Angle Neutron Scattering

The SANS measurements on welds SH and SL were carried out on the D11 spectrometer at the high flux beam reactor of the Institute Laue Langevin, Grenoble, France. This was, however, closed shortly afterwards and the measurements on the WV and WL welds were done using the PAXY Spectrometer at Laboratoire Leon Brillouin, CEN Saclay, France.

Measurements, in both facilities, were made in both a zero and a 1 Tesla magnetic field. The neutron wavelength was 6 Å, and measurements were made with sample to detector distances of 1.25 to 2.5 m. This allowed data to be accumulated in the range of scattering vectors ($Q=4\pi \sin q/l$) between 0.015 and 0.3 $Å^{-1}$. Background measurements and calibration runs with a thin wafer sample were also made for each spectrometer configuration.

Volume weighted particle size distributions were derived from the differential cross-sections measured for each sample using a Maximum Entropy Method [8], assuming spherical particles.

MODELS

RRA Irradiation Shift Model

The Rolls-Royce and Associates Limited irradiation shift model has been described in [5, 6]. It is a simple three component model, based on the models of Odette and Lucas [e.g. 1, 2] and Fisher and Buswell [e.g. 3, 4]. The mathematical formulation of the model is based on consideration of the physical mechanisms of damage. However, the model formulation is mitigated by observed data trends, and is empirically calibrated to a database. This consists of a large number of high dose rate (~6×10^{-9} dpa/s) test reactor data irradiated at temperatures between 225 and 315 °C. The high dose rate results shown in Table 1, but not the medium and low dose rate results, were included in the database fitted. Although the database consists of both Charpy and hardness measurements, the version of the model given below is calibrated to the hardness change data. This was considered to be a more direct measure of irradiation damage than Charpy shift. It is recognized that it might have been preferable to use yield stress data, but there were few such data in the database. The essential details of the model are as follows:

$$\Delta T = \Delta M + \Delta P + \Delta C \qquad (1)$$

$$\Delta M_{\text{Low Ni welds}} = 190 \times (d)^{0.5} \qquad (2a)$$

$$\Delta M_{\text{High Ni welds}} = 265 \times (d)^{0.5} \quad (2b)$$

$$\Delta P = 8.4x(0.1 \times \exp(-Cu_{mtx} \times 20)+1.0) \times P \times \Delta M \quad (3)$$

$$Cu_{mtx(\text{Low Ni welds})} = Cu_{eff} - Cu_{pdht} \quad (4)$$

$$Cu_{eff} = Cu_{total} - 3.57 \times S \quad (5)$$

$$Cu_{pdht(\text{Low Ni welds})} = 1.5 \times (Cu_{eff} - 0.32) \quad (6a)$$

$$Cu_{pdht(\text{High Ni welds})} = 0 \quad (6b)$$

$$\Delta C_{\text{Low Ni welds}} = \Delta C_{plat} \times \tanh(d/(0.0049-0.0039 \times Cu_{mtx})) \quad (7a)$$

$$\Delta C_{\text{High Ni welds}} = \Delta C_{plat} \times \tanh(d/(0.029-0.047 \times Cu_{mtx})) \quad (7b)$$

$$\Delta C_{plat} = 93 \times (Cu_{mtx} - 0.08456) \quad (8)$$

where: ΔT = total hardness change (VPN)
ΔM = hardness change due to matrix (radiation) damage (VPN)
ΔP = hardness change due to phosphorus precipitation (VPN)
ΔC = hardness change due to copper precipitation (VPN)
d = damage dose (dpa)
Cu_{mtx} = amount of copper (%) in solution in the ferrite matrix
Cu_{eff} = amount of copper (%) not combined in $Cu_{1.8}S$
Cu_{pdht} = amount of copper (%) precipitated during heat treatment
Cu_{total} = total copper content (%)
P = phosphorus (%)
S = sulphur (%)
ΔC_{plat} = plateau value of hardness change due to copper precipitation (VPN)

The above version of the model is valid for high dose-rate (~ 6×10^{-9} dpa/s) irradiations at 255 °C. As dose-rate is reduced the denominator in the tanh expression in Equation 7 reduces. This has the effect of causing ΔC_{plat} to be reached at lower doses. However, no attempt has yet been made to model this in detail or calibrate to the medium and low dose rate results. It should be noted that the phosphorus component (Eqn 3) was introduced for consistency with other models and is intended to represent a contribution from phosphorus precipitation (not segregation). The contribution from phosphorus is small and it is not now clear whether it is significant.

Russell and Brown Model of Barrier Hardening

The Russell and Brown model [9] has been used to predict the effects of CRPs. It is defined as follows:

$$\tau = 0.8 \times (Gb/L) \times (1-E_1^2/E_2^2)^{1/2} \text{ for } \sin^{-1} E_1/E_2 \leq 50° \quad (9a)$$

$$\tau = (Gb/L) \times (1-E_1^2/E_2^2)^{3/4} \text{ for } \sin^{-1} E_1/E_2 > 50° \quad (9b)$$

$$E_1/E_2 = (E_1^{\infty} \times \log(r/r_0))/(E_2^{\infty} \times \log(R/r_0)) + \log(R/r)/\log(R/r_0) \quad (10)$$

$$L^{-1} = V_f^{1/2}/1.77r \quad (11)$$

$$E_1^{\infty}/E_2^{\infty} = G_1/G_2 \text{ for a screw dislocation} \quad (12a)$$

$$E_1^{\infty}/E_2^{\infty} = G_1(1-\nu_2)/(G_2(1-\nu_1)) \text{ for an edge dislocation} \quad (12b)$$

where (values used in the analysis are shown in parentheses):

τ	= shear stress (MNm^{-2})
r	= precipitate radius (from SANS data) (nm)
b	= Burger's vector (0.248 nm)
L	= inter-particle spacing (nm)
V_f	= volume fraction of precipitates (from SANS data)
R	= outer cut-off radius of the dislocation (1000 x r_0) (nm)
r_0	= inner cut-off radius of the dislocation (2.5 x b) (nm)
G_1	= precipitate shear modulus (fitted, see below)
G_2	= matrix shear modulus (4.9×10^4 MNm^{-2})
E_1	= energy per unit length of dislocation in the precipitate
E_2	= energy per unit length of dislocation in the matrix
ν_1	= Poissons ratio for precipitate
ν_2	= Poissons ratio for the matrix

To convert from shear stress to hardness change the following relationships were used:

$$\sigma_y = 2.5 \times \tau \quad (13)$$

$$Hv = \sigma_y/2.72 \quad (14)$$

where: σ_y = yield stress (MNm^{-2})
Hv = hardness value (VPN)

The Schmidt Factor of 2.5 was used in this study to enable a comparison with previous work on simple Fe-Cu systems [7]. A value of 3.06 is recommended by Taylor [10] for polycrystalline material. This would, if used, affect the fitted parameters found, but not the overall trends observed.

RESULTS

Matrix copper content

Measurements of the amount of copper contained in solid solution in the matrix were made on one sample of each of the welds. This was done by focusing the STEM beam to a fine spot and taking a number of readings (>10) from precipitate-free regions. Values are shown in Table 1, where they may be compared with the total copper content (measured by bulk wet chemical analysis) and the matrix copper content predicted by the model (Eqns 4, 5,6). These equations predict that significant precipitation of copper should occur during heat treatment of the high copper low nickel weld (SH), but not in the others. This is seen to be the case, but the model appears to over-estimate the effect.

It is rather more difficult, from these results, to determine whether the model assumption about the effect of sulphur (Eqn 5) is correct. The STEM evidence for welds SL, and WV is quantitatively consistent with Eqn 5, however the effect of sulphur is relatively small (Cu_{total} - Cu_{eff} ≈ 0.04%) in these samples, relative to the uncertainties. It is suspected from other (unpublished) data, however, that Eqn 5 overestimates the sulphur effect.

TABLE 2--SANS Data

Specimen Identity	Irradiation Dose (dpa x 1E3)	Dose Rate (dpa/s x 1E12)	Average Small Feature Diameter (nm)	Magnetic A Ratio	Precipitate Volume Fraction (x 1E3)	Precipitate Number Density (x 1E-23/m³)	SANS Residual Matrix Copper (at %)	STEM Residual Matrix Copper (at %)	Uncertainty in STEM Residual Matrix Copper (1 SD at%)
SH047	2.01	6900	1.6	2.3	0.83	3.88	0.27	0.26	0.06
SH052	8.16	5820	1.9	5.0	1.63	4.54	0.20	0.15	0.05
SH062	32.28	5770	2.1	4.1	2.07	4.27	0.17	0.16	0.06
SH604	3.48	640	2.0	5.2	1.43	3.41	0.21	0.30	0.01
SH514	12.17	630	2.1	3.0	1.97	4.06	0.18	0.11	0.08
SH515	1.48	90	2.2		0.78	1.39	0.26	0.13	0.06
SL151	13.88	5020	1.4	2.4	0.32	2.19	0.04	0.15	0.03
SL415	31.95	5770	1.4	2.4	0.26	2.04	0.09	0.11	0.04
WV216	1.5	5200	1.3	2.3	1.07	9.30	0.39	0.32	0.05
WV214	9.19	6490	1.5	2.0	2.86	16.18	0.26	0.41	0.09
WV012	30.11	6230	1.9	2.2	5.09	15.35	0.11	0.35	0.06
WV127	3.39	630	1.6	2.0	2.81	13.10	0.27	0.37	0.03
WV400	12.11	630	1.9	2.4	5.07	15.29	0.11	0.28	0.08
WV126	1.46	90	1.8	2.0	2.46	8.06	0.29	0.34	0.07
WL772	31.94	5770	1.3	3.7	2.05	17.82	0.02	0.08	0.05

SANS data

The SANS results are shown in Table 2. The precipitate volume fractions (also the number densities and SANS residual matrix copper values) depend on assumptions about precipitate composition. STEM measurements on the irradiation-induced precipitates in the low nickel welds showed that these were approximately 70% Cu, 24% Mn and 6% Ni. This is in line with other reported composition values (eg [11, 12]). For each specimen, volume fractions were calculated for three or four plausible variants of this composition, with each variant constrained to be consistent with the magnetic A ratio. The high nickel welds tend to have smaller magnetic A ratios for the same precipitate size. This implies that they contain relatively higher manganese and nickel, and lower copper. The volume fraction values given in Table 2 are for the means of the compositional variants. The precipitate number densities and the SANS estimate of residual matrix copper follow from the precipitate sizes, compositions and mean volume fraction.

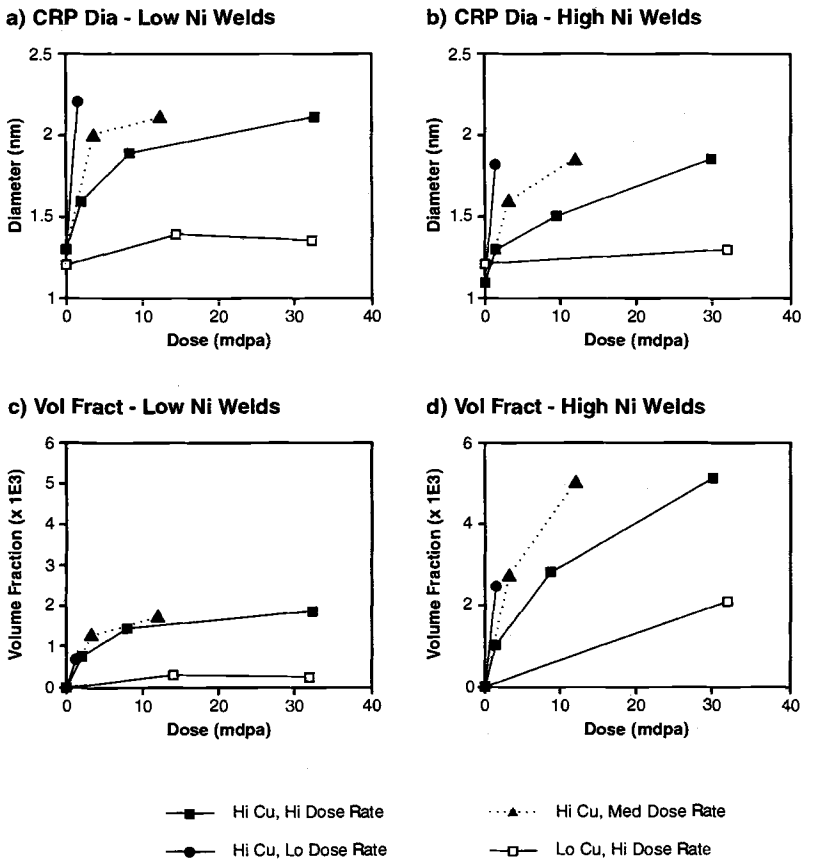


Fig 1 - Results of SANS Measurements

The SANS estimates of residual matrix copper may be compared in Table 2 with STEM measurements on each sample. In general the agreement is good, given the uncertainties in the measurements. This provides confidence in the assumed compositions and the SANS values. The STEM measurements also show that precipitation is not complete even at the highest doses.

Changes in precipitate diameter and volume fraction with dose are shown in Figure 1. The results clearly confirm the model prediction (Eqn 7) that precipitate growth in the high nickel welds is slower than in the low nickel welds, and show clearly that the effect of reducing dose rate is to reduce the dose at which a given level of precipitation has occurred.

It is also clear that the precipitates in the high nickel weld are smaller and have a higher number density than those in the low nickel weld. This is consistent with the TEM examination in which precipitates could only be seen in weld SH.

Fit to Russell and Brown Model

To interpret the SANS data in terms of mechanical property changes it is necessary to use a suitable hardening model. The Russell and Brown model has been widely used for this purpose. It cannot, however, be used directly since values of some of the important variables are not known with sufficient accuracy. It is therefore necessary to calibrate it to the data. There are a number of possible candidates for variables to be used as fitting parameters and a sensitivity study was done to assess which of these should be used. The variables examined and the values used were:

Burgers vector - 0.248 and 0.300 nm
Outer cut-off radius - 500, 1000, 5000 nm
Volume fraction - mean, mean ± 10%
Precipitate modulus - 4.9×10^{10} and 8.3×10^{10} N/m^2
Schmid factor (in Eqn 13) - 2.4, 2.5, 2.6
σ_y conversion factor (in Eqn 14) - 2.52, 2.72, 2.92.

In general these had little effect (less than about ± 10%) for precipitate diameters beyond about 2 nm (ie beyond the diameter for the peak strengthening effect). The model is sensitive to the precipitate modulus and it was considered reasonable to treat this as a fitting parameter, particularly as different values would be required for the low and high nickel welds. This could be rationalized on the basis of differences in composition noted earlier.

The precipitate modulus values were obtained by fitting to the hardness change results for the two high copper welds irradiated at the highest dose rate to the highest dose (ie specimens SH062 and WV012). These were chosen to ensure full copper precipitation. It was of course necessary to fit to the hardness contribution from copper precipitation alone. How the latter was estimated can be explained with reference to

Table 3. This shows hardness change values for each specimen. The first column of these gives the measured (total) change. The next column is an estimate using the RRA model of the amount of hardening caused by matrix damage and phosphorus precipitation (Eqns 2,3). The next three hardness value columns give estimates of the copper precipitation contribution to the total hardness change. The first is a model prediction based on the total copper content (Eqns 4 to 8). As noted earlier, the model can only be applied to low dose-rate irradiations if ΔCu_{plat} has been reached, hence not all predictions are available. The next column is a model prediction but using the STEM measured values of Cu_{mtx} (Table 2) in Eqns 7 and 8). The third is the total hardness change minus the model prediction of the contribution from matrix damage and phosphorus precipitation (ie Eqn 1 minus Eqns 2 and 3). In general the results are in reasonably good agreement with each other given the uncertainty in hardness change measurement (approximately ±4 VPN, 1σ). It was decided to use the STEM based results as the basis of fitting the Russell and Brown model to SH062 and WV012 (see Table 3). The values of precipitate modulus required to

TABLE 3--Hardness Data and Predictions

Specimen Identity	Dose (dpa x 1E3)	Dose Rate (dpa/s x 1E12)	Measured Hardness Change (VPN)	Calc'd Matrix Change (VPN)	Calc'd Copper Change (1) (VPN)	Calc'd Copper Change (2) (VPN)	Calc'd Copper Change (3) (VPN)	Calc'c Copper Change R&B Model (4) (VPN)	Comments
	0.000								
SH047	2.01	6900	32	10	19	25	22	24	
SH052	8.16	5820	57	19	38	48	38	41	
SH062	32.28	5770	73	38	39	49	35	49	Fitted
SH604	3.48	640	47	13	...	...	34	40	
SH514	12.17	630	67	24	33	49	43	48	
SH515	1.48	90	24	8	...	...	16	30	
SL151	13.88	5020	33	26	0	15	7	10	
SL415	31.95	5770	52	39	22	15	13	7	
WV216	1.50	5200	26	11	14	14	15	8	
WV214	9.19	6490	77	28	53	52	49	31	
WV012	30.11	6230	119	51	66	58	68	58	Fitted
WV127	3.39	630	73	17	...	...	56	36	
WV400	12.11	630	96	32	59	56	64	58	
WV126	1.46	90	55	11	...	...	44	40	
WL772	31.94	5770	80	50	0	10	30	11	

Copper change = hardness change due to copper precipitation
- (1) Based on model calculation
- (2) Based on model calculation but using matrix copper measured by STEM
- (3) Total hardness change minus model calculation of matrix damage
- (4) Russell & Brown Model using precipitate size and volume fraction from SANS data

achieve this fit were 1.6 and 2.4 x 10^4 MNm^{-2} respectively. These values are lower than those calculated by molecular dynamics for pure bcc Cu [7], but this may reflect the possibility that the addition of Mn and possibly vacancies, reduces the precipitate shear modulus. The other R&B model predictions shown in Table 3 were made using the fitted values of precipitate modulus. Figure 2 compares the predictions.

Figure 3 shows the hardness changes predicted by the Russell and Brown model from the SANS data versus dose. The effect of dose rate and nickel content, noted earlier in relation to the precipitate diameters and volume fractions, is again evident. Figure 4 compares the high dose rate results. It is of note that, although the copper level is higher in WV than in SH, the copper related shift in the latter is actually higher than in the former at low doses. However, the copper hardness change reaches its plateau at about 0.01 dpa in SH. The Russell and Brown model can be used to predict the further development of hardening. Figure 5 shows the Russell and Brown predictions (hardness change and hardness change divided by $V_f^{1/2}$) versus precipitate diameter for the highest dose, high dose rate irradiations. Examination of this, in conjunction with the residual matrix copper estimates (Table 2) suggests that significant further hardening may be expected in the high copper, high nickel, weld WV.

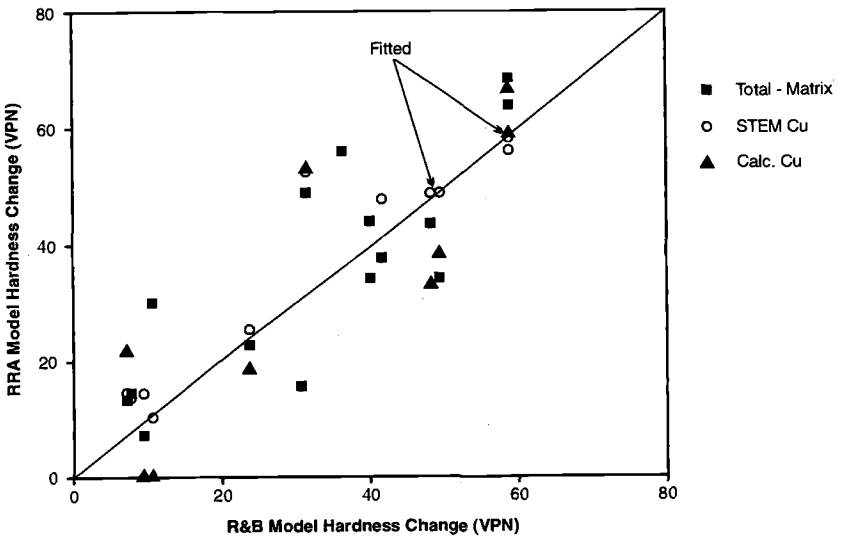


Fig 2--Comparison of SANS/Russell and Brown Model and RRA Model Predictions

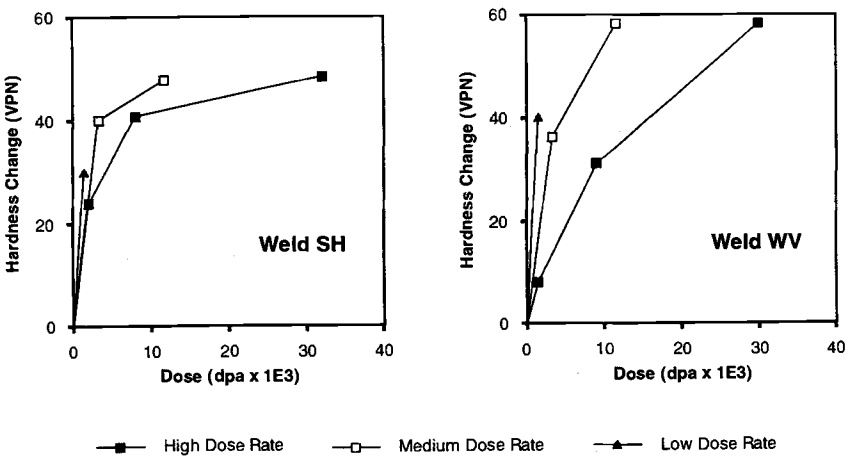


Fig 3--SANS/Russell and Brown Model Predictions of Hardness Change due to CRPs.

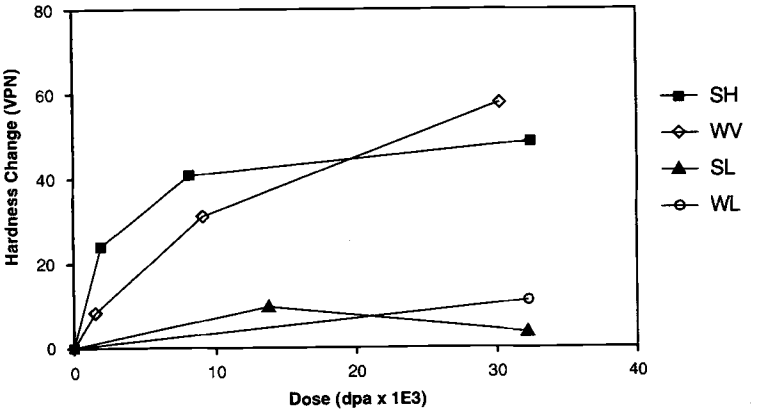


Fig 4--Comparison of Predictions for High Dose Rate Irradiations

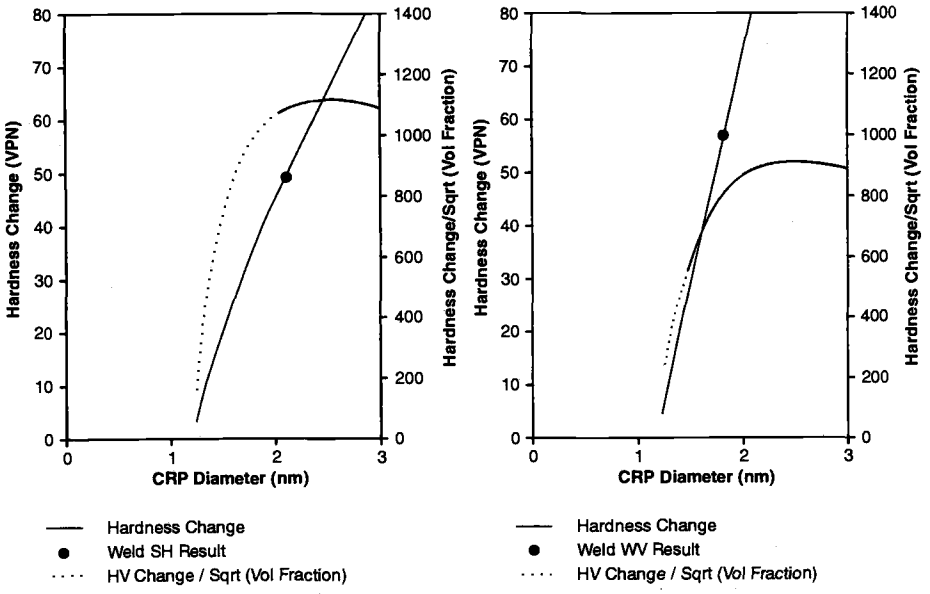


Fig 5--Examples of Individual Specimen Results Showing Potential for Further Hardening

DISCUSSION

As described above, this STEM/SANS study has provided a clear physical confirmation of many of the theoretically or empirically derived assumptions of the RRA model (and hence of the models on which it was based). Conversely, this provides confidence that the STEM/SANS observations are not particular to the limited samples of welds examined. (Further evidence for the validity of the observations may be found in [5, 6].)

The work has helped to elucidate the complex role of nickel in irradiation embrittlement. In high copper welds, nickel may affect sensitivity in various ways, most of which might be related (directly or indirectly) to an effect of nickel on diffusivity. First, in welds with copper contents at about the solubility limit at the heat treatment temperature, it appears to cause copper to be retained in supersaturated solid solution during heat treatment, increasing subsequent irradiation sensitivity. Second, it results in the formation of smaller, higher volume fraction, precipitates during irradiation; this can, depending on the precipitate size, increase the effectiveness of a given amount of copper. Third, the CRPs appear to have higher manganese and nickel contents and higher elastic modulus, which reduces their strengthening effect for a given radius and volume fraction. Fourth, nickel reduces the rate of precipitation during irradiation; this has no effect on ultimate strengthening, but may confound assessment of the differences between high and low nickel welds.

The above observations relate to the copper component of damage, however it has also been shown that, at a given irradiation temperature, there is more matrix damage in high nickel weld than low nickel welds [6].

CONCLUSIONS

In low nickel, high copper, welds, copper can be precipitated prior to irradiation, substantially reducing the amount available to cause strengthening and embrittlement during irradiation. The effect has not been observed in high nickel welds.

The CRPs (copper rich precipitates) formed during irradiation are alloyed with manganese and nickel; the copper content is higher in the low nickel weld than the high nickel weld.

The CRP's in high nickel welds are (at a given dose) smaller and have a higher volume fraction. CRP growth is substantially slower in high nickel welds. For both high and low nickel welds reducing dose rate produces higher CRP diameter and volume fraction at a given dose.

The hardness data have been successfully interpreted in terms of a precipitate volume fraction derived from SANS and STEM data using the Russell and Brown modulus hardening model with different (fitted) values of precipitate modulus for high and low nickel welds.

The work has shown that nickel can affect irradiation sensitivity in a number of ways: by retaining copper in solid solution during heat treatment; by affecting CRP size and number density; by affecting CRP growth rate and by affecting the precipitate elastic modulus.

The work has provided confirmatory evidence for a number of the features of the RRA, and similar, irradiation shift models, and has shown the value of co-ordinated studies in irradiation damage investigations.

ACKNOWLEDGEMENTS

The authors would like to acknowledge the contributions of S.N. Buckley, P. Brown, P.R. Burch, S. Dumbill, C. A. English, J. A. Mace, G. T. Newman, and R. N. Sinclair to the experimental work, the analysis and the assessment of the results.

REFERENCES

1. Odette, G. R., "On the Dominant Mechanism of Irradiation Embrittlement of Reactor Pressure Vessel Steels," Scripta Metallurgica, 17 (1983) pp 1183-1188.

2. Odette, G. R. and Lucas, G. E., "Irradiation Embrittlement of Reactor Pressure Vessel Steels: Mechanisms, Models and Data Correlations," Proceedings of the Second IAEA Specialists' Meeting on Irradiation Embrittlement, Vienna, Austria, October 1984, ASTM 1985.

3. Fisher, S. B., Harbottle, J. E. and Aldridge, N. B., "Radiation Hardening in Magnox Pressure Vessel Steels," Philosophical Transactions of the Royal Society of London, Vol. A315, 1985, p310.

4. Fisher, S. B. and Buswell, J. T., " A Model for PWR Pressure Vessel Embrittlement," International Journal of Pressure Vessels and Piping, Vol 27, 1987, p91.

5. Williams, T. J., Ellis, D., Swan, D. I., McGuire, J., Whalley, S. P., English, C. A., Venables, J. H., and de la cour Ray, P. H. N., "The Influence of Copper, Nickel and Irradiation Temperature on the Irradiation Shift of Low Alloy Steels.", Proceedings of the Second International Symposium on Environmental Degradation of Materials in Nuclear Power Systems - Water Reactors, TMS AIME/ANS/NACE, September 1985, ANS Illinois, 1986, pp 393-399.

6. Williams, T. J., Burch, P. R., English, C. A., and de la cour Ray, P. H. N., "The Effect of Irradiation Dose rate and Temperature, and Copper and Nickel Content, on the Irradiation Shift of Low Alloy Submerged Arc Welds", Proceedings of the Third International Symposium on Environmental Degradation of Materials in Nuclear Power Systems - Water Reactors,

7. Phythian, W. J., Foreman, A. J. E., English, C. A., Buswell, J. T., Hetherington, M., Roberts, K., Pizzini, S., Proceedings of the 15th International Symposium on Effects of Radiation on Materials, Nashville, TN, August 1992, ASTM STP 1125.

8. Potton, J. A., Daniell, D. J., and Rainford, B. D., "Particle Size Distributions from SANS Using the Maximim Entropy Method", J. Appl Cryst., 21 p891 (1988)

9. Russell, K. C., and Brown, L. M., Acta Metallurgica, 1972, 20, pp 969 -974.

10. Taylor, I., G., J. Inst. Met, 62, (1938), pp307-324.

11. Buswell, J. T., Bischler, P. J. E., Fenton, S. T., Ward, A., and Phythian, W. J., "Microstructural developments in neutron irradiated mild steel submerged-arc weld metal", J. Nucl. Mat., 205, 1993, pp198-205

12. Phythian, W. J., and English, C. A., "Microstructural evolution in reactor pressure vessel steels", J. Nucl. Mat., 205, 1993, pp162-177

Gianni Albertini[1] , Flavio Carsughi[2], Roberto Coppola[3], Franco Rustichelli[4], Mario Stefanon[5]

RADIATION DAMAGE STUDIES USING SMALL-ANGLE NEUTRON SCATTERING

REFERENCE: Albertini, G., Carsughi, F., Coppola, R., Rustichelli, F., and Stefanon, M., **"Radiation Damage Studies Using Small-Angle Neutron Scattering,"** *Effects of Radiation on Materials: 17th International Symposium, ASTM STP 1270,* David S. Gelles, Randy K. Nanstad, Arvind S. Kumar, and Edward A. Little, Eds., American Society for Testing and Materials, 1996.

ABSTRACT: This contribution reviews a number of small-angle neutron scattering (SANS) studies of irradiated metals and steels of relevance to fission and fusion technology. Information obtainable by SANS measurements is recalled with special reference to the determination of the size distribution function of the microstructural inhomogeneities. The selected examples concern studies of the main kinds of radiation defects: voids, precipitates, He-bubbles. Some recent results obtained on structural materials for the "first-wall" of fusion reactors are also presented.

KEYWORDS: small-angle neutron scattering, metallic materials, radiation damage, fusion reactors.

INTRODUCTION

Since its earliest applications small-angle neutron scattering (SANS) has turned out to be a powerful experimental tool to investigate the complex microstructural changes associated with radiation damage in metals and alloys. The general features of SANS, namely, its sensitivity to the presence of elements such as H or He

[1] INFM -Dipartimento di Scienze dei Materiali e della Terra, Università, 60129 Ancona, Italy.

[2] INFM -Istituto di Scienze Fisiche, Università, 60131 Ancona, Italy and Institut für Festkörperforschung, KFA, D-52425, Jülich, Germany.

[3] ENEA-Casaccia, C.P. 2400, 00100 Roma, Italy.

[4] INFM -Istituto di Scienze Fisiche, Università, 60131 Ancona, Italy.

[5] ENEA, Viale Ercolani 8, 40100 Bologna, Italy.

Copyright© 1996 by ASTM International www.astm.org

in metallic matrices or its selectivity between elements of close atomic number such as Fe and Cr, are in fact particularly useful to detect and characterize the different microdefects present in structural materials for fission reactors or for the future tokamak-based fusion reactors.

The reviews of ref.s [1 and 2] and the other more general papers of ref.s [3, 4, 5] show that in the last two decades a considerable amount of scientific work has been carried out by SANS to investigate problems such as microvoid formation, He-bubble growth, phase segregation phenomena under irradiation in model alloys as well as in technical steels. SANS applications to materials of interest for nuclear plants have also been reported in previous ASTM special technical publications [6-8] and are included in this publication [9].

Information obtainable by this technique ranges from physical quantities such as the gas pressure in He-bubbles to microstructural parameters, such as precipitate radius and volume fraction and can be useful in understanding microstructural phenomena depending on dose rate or irradiation temperature or alloy composition.

On the other side to fully exploit this technique measurements must be of high precision (especially in the case of complex steels, where different microdefects can be simultaneously present) and the data analysis method (namely the determination of the size distribution function) must be mathematically reliable and metallurgically sound. The aim of this contribution is to discuss this second aspect, which is the object of the next section where special emphasis on two-dimensional data analysis and size distribution function determination is presented. Some recent examples are then discussed. It is worth stressing that this paper is not to be intended as a general review, as those of ref. [1-5], but as a representative selection of SANS studies interesting the characterization of radiation damage microstructural effects.

SANS

It is well known that SANS is observed as the broadening of a collimated neutron beam when it passes through a material in which heterogeneities are present [3-5], having sizes typically between $\sim 10^{0}$ and 10^{+3} nm. SANS occurs when such inhomogeneities are characterized by a neutron scattering length density d_i different from that of metallic matrix d_m.

The layout of a typical SANS experiment is shown in Fig. 1, referring to a magnetic steel. In this case (quite frequent when studying alloys for nuclear applications) the measured intensity depends on the azimuthal angle, φ, between $\underline{Q}$ and $\underline{H}$

$$I_{total} = I_{nuclear} + I_{magnetic} \sin^2 \varphi \qquad (1)$$

In fact the neutron has a magnetic moment M and is scattered by the magnetic inhomogeneities of the sample. The magnetic interaction is such that only the component of magnetisation perpendicular to the scattering vector is effective.

If the momentum transfer $\underline{Q}$ is parallel to $\underline{H}$, then the sum of the different amplitudes of magnetic scattering is equal to zero (for symmetry reasons) and only the nuclear scattering amplitude can be not equal to zero. If $\underline{Q}$ is perpendicular to $\underline{H}$ both nuclear and magnetic contributions are present.

If an isotropic contribution is to be expected from the local magnetic fields inside a material, then the same average contribution to the scattering is expected in all the scattering

directions. On the other hand, if an external intense field is applied aligning the internal fields of the magnetic domains in the direction of the external one than a purely nuclear scattering is obtained for momentum transfer parallel to the external field ($I_{||} = I_{nuclear}$), and the maximum variation induced by magnetic scattering is in the perpendicular direction ($I_{\perp} = I_{nuclear} + I_{magnetic}$). A characteristic of the defect composition is the ratio

$$R(Q) = 1 + [I_{magnetic}(Q) / I_{nuclear}(Q)] = I_{\perp}(Q) / I_{||}(Q). \quad (2)$$

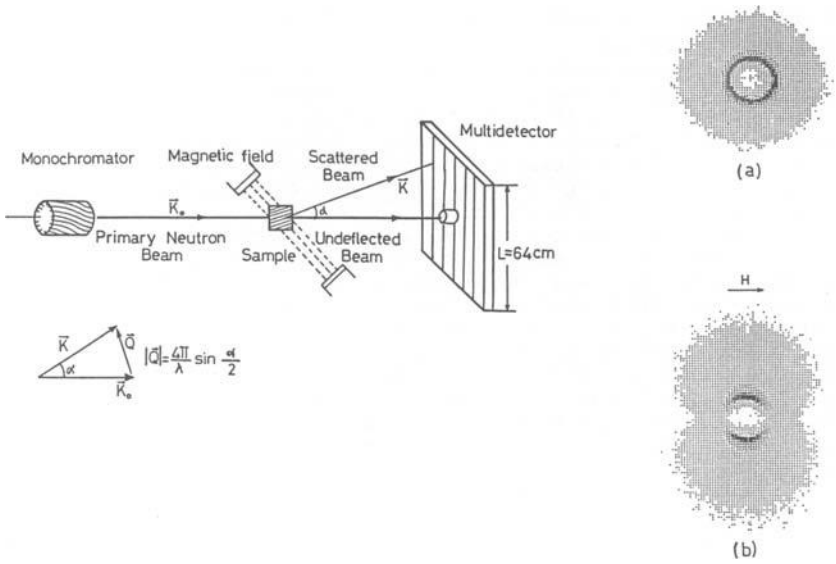


Fig. 1 Experimental layout of SANS measurements on MANET steel without (a) and with (b) a 1.4 T magnetic field [1].

(Figure 1 printed with permission from Elsevier Science Publishers B.V.)

The dependance of R on Q implies that defects of different composition contribute to different parts of the total SANS spectrum. Fig. 2 shows the results of a fit on the data of Fig. 1b to check whether eq. (1) is satisfied according to

$$I(\varphi) = \int_{Q_{min}}^{Q_{max}} I(Q,\varphi)\, dQ = I_M - I' \cos^2\varphi \quad (3)$$

(I_M and I' parameters are determined with the least square method).

The analysis of two-dimensional data is also fundamental in the case of non-spherical particles in single-crystal samples. In this regard, it is interesting to recall that one of the first SANS applications concerned the study of octahedral voids in neutron irradiated Al single crystals [10, 11].

Anisotropic SANS profiles were also measured for an aged single crystal of Al-Mg-Si alloy [12], a material originally considered in view of possible applications in fusion reactors [13]. The interpretation of these data was based on a model assuming the growth of rod-shaped Mg_2Si precipitates along preferential crystallographic axes. Simulations using this model give a series of

2-D patterns referring to a variety of conditions: different cylinder length to radius ratios, or, as in Fig. 3, different cylinder orientations with fixed length to radius ratio [14]. The reported example shows the sensitivity attainable with this method. Furthermore the "tails" of the SANS profile as those in Fig. 3 have well defined asymptotic behaviours so that also from high-Q measurements in principle it can be possible to identify the shape of oriented defects produced by irradiation in single crystals. As discussed in Ref. [14] the analysis of 2-D data also appears desirable in isotropic cases to improve the precision of the measurements and to correct the effect of asymmetries in beam-stop or sample positioning.

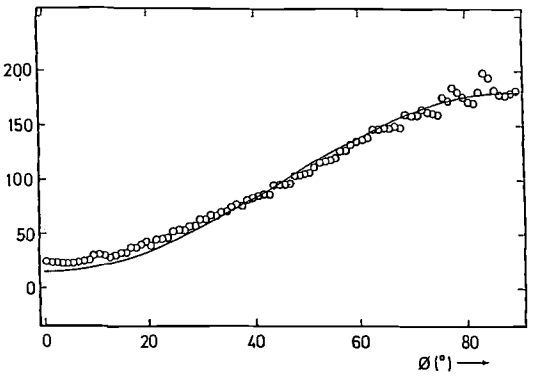


Fig. 2 Best fit of the data in Fig. 1b with eq. 1.

The experimental procedure to determine the coherent SANS macroscopic cross section from the scattering intensity is described for instance in ref. [4]. In a simple "two-phase model" [4-5] considering a matrix and N_i identical dispersed heterogeneities per unit volume, each having a volume V_i and a form factor F_i, this cross section is given by

$$\frac{d\Sigma}{d\Omega}(Q) = (d_m - d_i)^2 \, N_i \, V_i^2 \, |F_i(Q)|^2 = P(Q) \qquad (4)$$

where $| d_m - d_i |$ is the neutron "contrast" and $\hbar Q$ is the intensity of the exchanged momentum between neutron and material. The scattering angle α is connected with Q by

$$Q = \frac{4\pi}{\lambda} \sin(\alpha/2) \qquad (5)$$

where λ is the neutron wavelength. Microstructural information can be inferred from the behaviour of $d\Sigma/d\Omega$ as a function of the modulus of Q in the case of isotropic SANS. As a first approach the gyration radius R of the inhomogeneities can be obtained in the low-Q region (i.e. $Q \leq 1/R$), (Guinier approximation) [15].

$$|F_i(Q)|^2 \propto \exp(- Q^2R^2/3) \qquad (6)$$

In particular, for spherical heterogeneities with radius r

$$r^2 = 5 \, R^2 \, / \, 3.$$

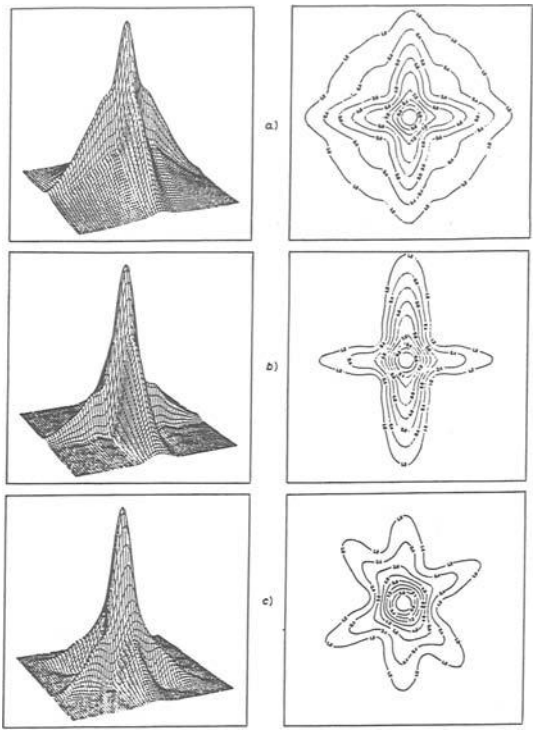


Fig. 3 Calculated SANS profiles for three orthogonal cylinders (length-to-size ratio = 5) with different orientations: a) cylindrical axis as x, y, z ((100) crystallographic directions), b) rotated 45°C around x-axis; c) further rotated around y-axis [14] SANS geometry as in Fig. 1.
(Figure 3 printed with permission from Elsevier Science Publishers B.V.)

In the high-Q range, an asymphotic behaviour is expected (Porod approximation) [4, 5]

$$\frac{d\Sigma}{d\Omega}(Q) = (d_m - d_i)^2 \, 2\pi S / Q^4 \qquad (7)$$

from which S, the total surface per unit volume, can be obtained.

The volume fraction C of heterogeneities can be evaluated, considering that

$$\int Q^2 \frac{d\Sigma}{d\Omega}(Q) \, dQ = 2\pi^2 (d_m - d_i)^2 \, C \, (1-C) \qquad (8)$$

In the case of non identical heterogeneities, the SANS curve is considered as the superposition of different curves, weighted by a size distribution function N(R) (number density of "particles" of size R, in unit volume)

$$\frac{d\Sigma}{d\Omega}(Q) = (d_m - d_i)^2 \int N(R) \, V_i^2(R) \, |F_i(Q,R)|^2 \, dR \qquad (9)$$

The determination, via the transformation of eq. (9), of the N(R) function is quite attractive from a metallurgical point of view, as it allows determination, in a more reliable way than Guinier or Porod plots, of the average size <R> and volume <V> and volume fraction of the scattering particles C, respectively,

$$\langle R \rangle = \frac{\int N(R)\ R\ dR}{\int N_{tot}} \qquad (10)$$

$$\langle V \rangle = \frac{\int N(R)\ V\ dR}{\int N_{tot}} \qquad (10\ bis)$$

$$C = N_{tot}\langle V \rangle \qquad (10\ ter)$$

as $N_{tot} = \int N(R)\ dR$.

Furthermore, the shape itself of N(R) contains relevant information and can be used to test the kinetic laws, as in the example of Fig. 4 [16] or in the work of ref. [17] on Al-Li.

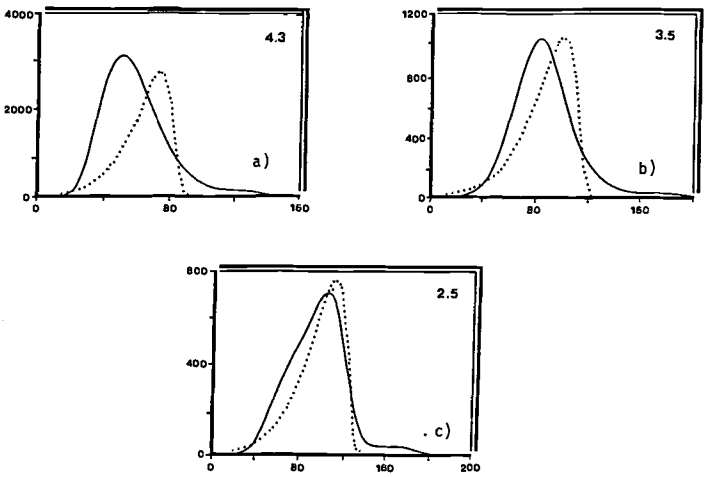


Fig. 4 Size distribution functions determined from SANS (continuous line) for γ'-precipitates in alloy 800 aged at 575°C a) 1000 h, b) 7800 h and c) 12000 h. The dotted line is the size distribution function predicted by the Lifshitz-Slyozov and Wagner theory; the agreement between the two is measured by the figure in the upper right corner (1 in case of coincidence) [16].

(Figure 4 printed with permission from Elsevier Science Publishers B.V.)

However, both the fact that $d\Sigma/d\Omega$ is known only over a limited Q interval and on a finite number of experimental points affected by an experimental error implies that the determination of N(R) is in practice quite complex and depends critically on the transformation

method. The one reported in Ref. [18] has given up to now interesting and reliable results. It is based on a cubic β spline combination to represent the N(R) (with no a-priori assumption on its shape) and operates with a generalized non-linear least-square procedure, including regularization and assisted convergence to cope with all-conditioned axes.

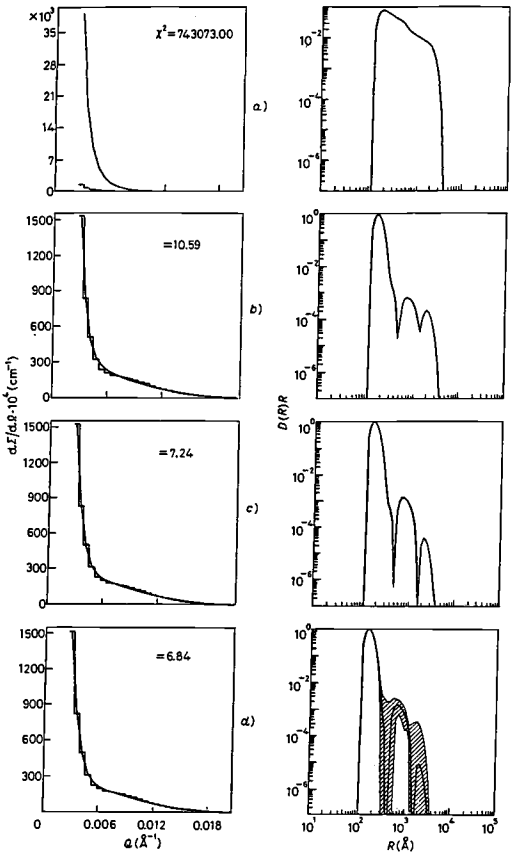


Fig. 5 Convergence of constrained least-square method. Left: SANS experiment and fit; right: size distribution a) first guess, b) 5th iteration, c) 20th iteration, d) final result (40 iterations) with statistical error band [18].

(Figure 5 printed with permission from Elsevier Science Publishers B.V.)

Figure 5 shows an example of how the non-linear constraint works. The final error band is determined by random simulation of experimental errors. It can be quite large as in the example reported below (Fig. 9) if the experimental error bars are high or if the experimental Q-window is not centered to the range corresponding to the particle size. In any case, this procedure has been shown to be quite efficient in avoiding those critical fluctuations and convergence failures that often discourage the use of fitting procedures in favor of simpler but questionable asymptotic methods.

If heterogeneities are not dilute, a correlation length L is

evaluated by

$$\int Q \frac{d\Sigma}{d\Omega} (Q)\ dQ = 2\pi (d_m - d_i)^2\ L\ C\ (1-C) \qquad (11)$$

In nondiluted systems, however, the interference between scattered waves gives a significant contribution to the SANS signal and an interference function S(Q) is considered in addition to the inhomogeneity scattering function P(Q).

$$\frac{d\Sigma}{d\Omega} (Q) = P(Q)\ S(Q) \qquad (12)$$

This is a frequent case of great technical importance which in case of polydisperse systems cannot be faced in a correct mathematical way. A semi empirical approach in which the scattering profile is supposed to factorize in a structure factor S(Q) and a size factor P(Q) gave encouraging results in the case of Al-Li alloy yielding to a precipitate volume fraction of 0.25 [17].

APPLICATIONS

One of the most recent and technologically relevant application fields for SANS regards the growth of He-bubbles in fusion reactor materials. It is well known in fact that the He generation rate in the structural materials for future tokamaks will be one order of magnitude larger than in fission reactors, with important consequences both on microstructure and on mechanical properties [19].

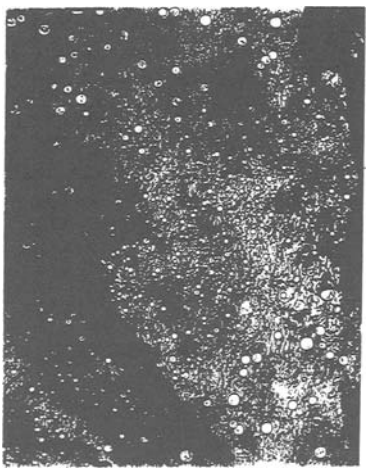


Fig. 6 TEM picture of He-bubbles in MANET steel.

In a first work [20] SANS was used to study the growth of He bubbles in a pure Ni sample implanted with 28 MeV α-particles at room-temperature, then annealed at different temperatures up to 850°C. The origin of the bimodal bubble size distribution function detected by SANS and in disagreement with TEM, was clarified in a subsequent experiment [21] showing a dense population of "large"

bubbles at the surface and grain boundaries of the specimen. Further studies [22] showed that this pressure is much higher than the value predicted by thermodynamic equilibrium, and this "over pressurization" phenomena has to be interpreted in the frame of the existing thesis. In these works the gas pressure in the bubbles was determined by using contrast variation methods.

The study of He-bubbles by SANS has also been carried out in technical steel, the modified martensitic steel DIN 1.4914 or "MANET" of interest because of its first-wall applications [23-25]. Since in this material precipitates can contribute to the total SANS pattern, preliminary work using TEM, was done to investigate the carbides in the tempered material and to identify the Q interval where the SANS contribution of He-bubbles is expected. Then MANET samples implanted at room temperature with α-particles and subsequently annealed at various temperature were investigated by SANS [24]. Fig. 6 shows a TEM picture of the He-bubbles. The results of the SANS experiment summarized in Fig. 7 show the increase of bubble average radius and the corresponding decrease in bubble surface with an increase of the annealing temperature. The SANS data were used to determine the gas pressure, related to the gas density. This density is reported in Fig. 8, together with the one obtained in pure Ni by contrast variation method [22] in a Ni-Cr-Fe alloy by analytical method [26] and with theoretical prediction based on thermodynamic equilibrium.

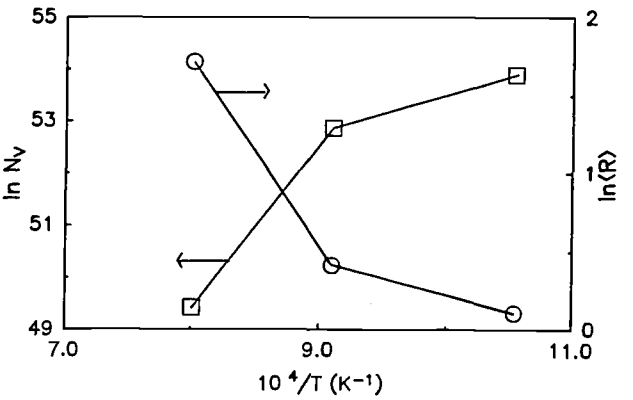


Fig. 7 Average radius (right) and bubble density (left) of He bubbles in MANET steel vs reciprocal annealing temperature after implantation [24].

(Figure 7 printed with permission from Elsevier Science Publishers B.V.)

SANS measurements were also carried out on MANET samples submitted to simultaneous proton and α-particles irradiation and to low cycle fatigue by means of the "dual-beam" facility in Kernförschungszentrum Karlsruhe [25]. The microstructural modifications produced by such treatment are obviously quite complicated (and also more representative of a tokamak environment), so that SANS measurements were only focussed on identifying the presence of He-bubbles by considering the difference between the irradiated part of the specimen and its non-irradiated "head". The result is reported in Fig. 9. The size distribution function is in agreement with the observation by TEM of bubbles having radius ~ 5 nm; there appears also a weak population of much larger defects which gives a strong contribution to the volume size distribution (Fig. 7c).

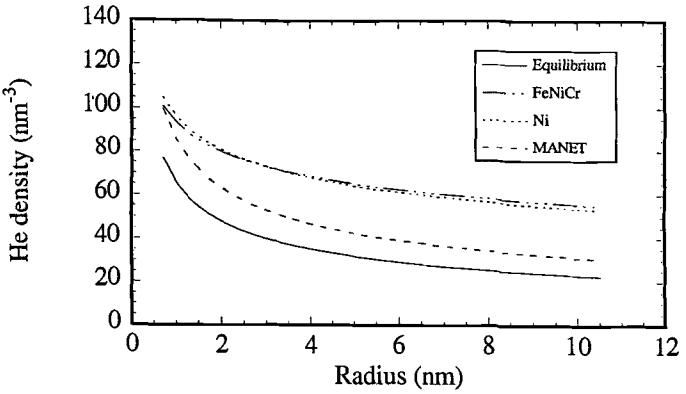


Fig. 8 He-pressure in the bubbles for different materials and at equilibrium ($p = 2\gamma/R$).

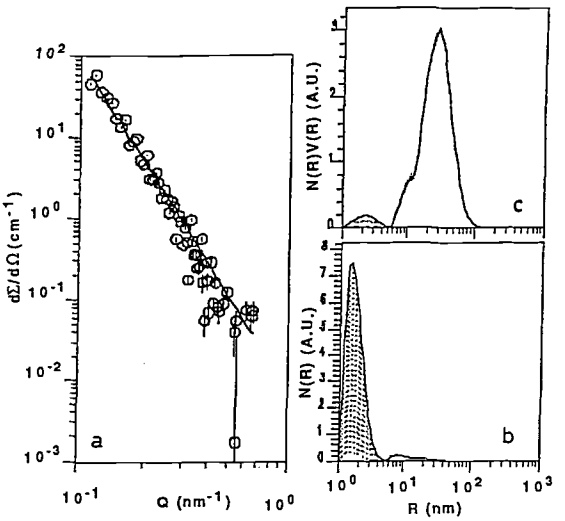


Fig. 9 MANET steel implanted with dual-beam: a) SANS data and best fit (continuous line), b) size distribution function and c) volume distribution function of the He-bubbles. The dashed area corresponds to the experimental uncertainty [25].

Phase segregation and precipitation phenomena under irradiation have also been extensively investigated by SANS both in model alloys and in technical steels for nuclear applications [1]. Concerning phase segregation, several works on Cu-Ni-Fe, Cu-Ni, Fe-Ni must be mentioned [1]. As it is well known, the growth of Cu-rich precipitates under irradiation or thermal ageing plays an important role in the embrittlement process of reactor pressure vessel steel [27], and the study of this phenomenon in a simplified material may yield useful information aiding in understanding this microstructural mechanism.

In this regard, a recent contribution is provided in Ref. [28] referring to Fe-Cu alloy (0.1-1.5 % Cu) irradiated with 2.5 MeV electron at temperatures from 170°C to 360°C. Reference aged samples

were also measured. Figure 10 shows as a function of fluence the variations of precipitated average size and density as determined by SANS and "monitored" by electrical resistivity and microhardness measurements. The similarity of the curves in Fig. 10 c-d shows that the irradiation accelerates the precipitation with respect to thermal ageing. Other interesting information is obtained from the analysis of the N(R) function with respect to theoretical models. The work of Ref. [29] must also be mentioned regarding the effect of Mn addition on the same kind of Fe-Cu alloy under electron irradiation.

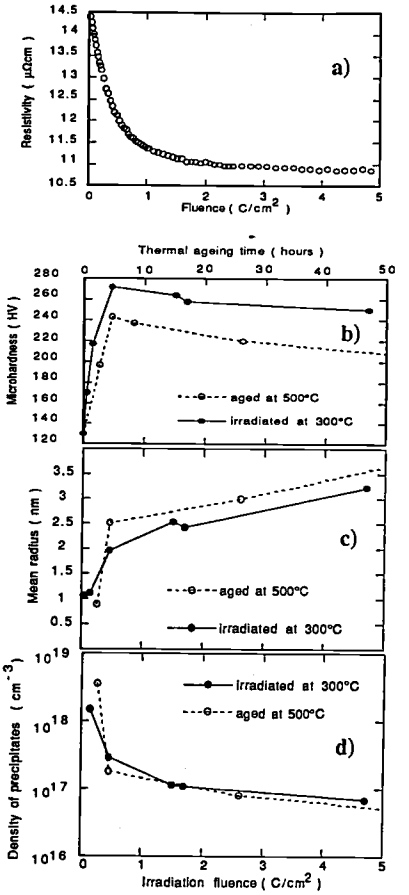


Fig. 10 Fe-Cu alloy aged and irradiated with 2.5 MeV electrons. Variations, vs fluence, of: a) electrical resistivity, b) microhardness, c) average size (nm) and d) number of precipitates [28].

As an example of the usefulness of SANS in the study of precipitation in complex alloys under irradiation, Fig. 11 from Ref. [30] shows the changes in the R(Q) ratio (see eq. 9) in a reactor pressure vessel steel, compared with pure Fe and with Fe-Cu: both Cu-rich precipitates and microvoids (of similar shape and size) are present in the steel. Other application have been mentioned in the

introduction. It is also worth mentioning another work concerning MANET and the occurrence of C-Cr elementary aggregates in this material. The presence of such particles, relating to some crystallographic features of the bcc lattice [31], has been shown by X-ray diffraction, internal friction and scanning electron microscopy and can be a key factor influencing the ductile-to-brittle transition [32]. The first SANS measurements (on non-irradiated material) are in agreement with this interpretation and with the results obtained by the other techniques.

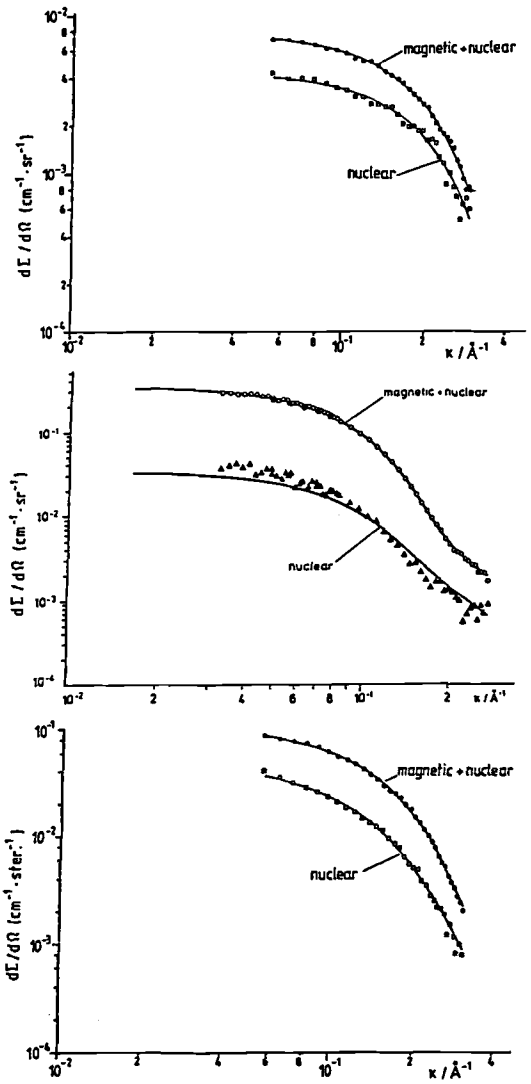


Fig. 11 SANS from irradiated a) Fe, b) Fe-0.3 at% Cu, c) KS12 steel; (o) $\vec{Q} \parallel \vec{H}$, (•) $\vec{Q} \perp \vec{H}$ [30].

(Figure 11 printed with permission from Springer-Verlag)

CONCLUSIONS

The usefulness of SANS in investigating radiation damage in structural materials is here reported. By using this technique important results have been obtained. In particular SANS was used in a large number of investigations in order to obtain quantitative results such as the mean radius, the mean volume, the volume fraction of the inhomogeneities.

Because of the non-destructive feature of the test, SANS is a suitable technique to follow directly "in situ" the kinetics of the evolution of microstructural defects.

The high sensitivity is another important peculiarity of the technique which was able in some cases, such as the large population of He bubbles in implanted materials, to give experimental indications not observed by other techniques, stimulating new investigations. This is related to the fact that even if SANS does not give any direct image of the material, the investigated volume is of the order of some cm^3, while transmission electron microscopy (TEM) gives a direct image of a very localized area; actually, according to some estimations, the total investigated volume by TEM world-wide since its introduction is of the order of the mm^3!

In conclusion, both SANS and TEM are powerful techniques and they have not to be considered competitors, but complementary.

REFERENCES

[1] Albertini, G., and Coppola, R., Nuclear Instruments and Methods, Vol. A314, 1992, p. 352.

[2] Albertini, G., Coppola, R., and Rustichelli, F., Physics Report, Vol. 233, No. 3, 1993, p. 137.

[3] Sinclair, R.N., and Windsor, C.G., Proceedings of the Workshop on Atomic Transport and Defects in Metals by Neutron Scattering, ed.s C. Janot et al., Springer, Berlin, 1986, p. 213.

[4] Hutchings, M.T., and Windsor, C.G., in "Neutron Scattering", ed.s K. Skold and L. Price, Academic Press, New York, 1989, p. 405.

[5] Kostorz, G., Journal of Applied Crystallography, Vol. 24, 1991, p. 444.

[6] Epperson, J.E., Lin, J.S., and Spoorer, S., ASTM STP, Vol. 955, 1987, p. 595.

[7] Solt, G., Frisius, F., and Woeber, W.B., ASTM STP, Vol. 1011, 1989, p. 229.

[8] Solt, G., Frisius, F., Woeber, W.B., Buhrer, W., ASTM STP, Vol. 1046, 1990, p. 154.

[9] Williams, T.J., and Phytian, W.J., this volume.

[10] Mook, H.A., Journal of Applied Physics, Vol. 45, 1974, p. 45.

[11] Hendricks, K.W., Scheltern, J., and Schnartz, W., Philosophical Magazine, Vol. 30, 1974, p. 819.

[12] Abis, S., Caciuffo, R., Coppola, R., Magnani, M., Rustichelli, F., and Stefanon, M., Physica B, Vol. 136, 1986, p. 469.

[13] Piath, G., and Schiller, P., Nucl. Ena. Des. / Fusion, Vol. 1, 1984, p. 137.

[14] Stefanon, M., Proceedings of the International School of Physics "Enrico Fermi" Course CXIV. Industrial and Technological Applications of Neutrons (Lerici, June 1990), ed.s M. Fontana, F. Rustichelli and R. Coppola, North Holland, Amsterdam, 1992, p. 113.

[15] Guinier, A., Fournet, G., in "Small Angle Scattering of X-rays", John Wiley, New York, 1955, p. 5.
[16] Coppola, R., and Re Fiorentin, S., Nuclear Instruments and Methods, Vol. B22, 1987, p. 564.
[17] Abis, S., Caciuffo, R., Carsughi, F., Coppola, R., Magnani, M., Rustichelli, F., and Stefanon, M., Physical Review B, Vol. 42 n. 4, 1990, p. 2275.
[18] Magnani, M., Puliti, P., and Stefanon, M., Nuclear Instruments and Methods, Vol. A271, 1988, p. 611.
[19] Ullmaier, H., Nuclear Fusion, Vol. 24, 1984, p. 1039.
[20] Schwahn, D., Ullmaier, H., Schelten, J., and Kesternich, W., Acta Metallurgica, Vol. 31, 1983, p. 2003.
[21] Kesternich, W., Schwahn, D., and Ullmaier, H., Scripta Metallurgica, Vol. 18, 1986, p. 1011.
[22] Qiang-Li, Kesternich, W., Schroeder, H., Schwahn, D., and Ullmaier, H., Acta Metallurgica et Materialia, Vol. 38, 1990, p. 2383.
[23] Albertini, G., Carsughi, F., Coppola, R., Rustichelli, F., Schwahn, D., and Mercurio, G., Nuclear Instruments and Methods, Vol. A321, 1992, p. 381.
[24] Albertini, G., Carsughi, F., Coppola, R., Kesternich, W., Mercurio, G., Rustichelli, F., Schwahn, D., and Ullmaier, H., Journal of Nuclear Materials, Vol. 191-194, 1992, p. 1327.
[25] Albertini, G., Carsughi, F., Ceretti, M., Coppola, R., Fiori, F., Möslang, A., and Rustichelli, F., Journal of Physics C8, Vol. J.P. III n. 12, 1993, p. 283.
[26] Carsughi, F., Kesternich, W., Schwahn, D., Ullmaier, H., and Schroeder, H., Journal of Nuclear Materials, Vol. 191-194, 1992, p. 1284.
[27] Odette, G.R., Scripta Metallurgica, Vol. 17, 1983, p. 969.
[28] Mathon, M. -H., Maury, F., Dunstetter, F., Lorenzelli, N., De Novion, C.-H., and Boue, F., Journal of Physics C8, Vol. J.P. III n. 12, 1993, p. 279.
[29] Barbu, A., Le, T.N., Lorenzelli, N., Maury, F., and De Novion, C. -H., Material Science Forum, Vol. 97-99, 1992, p. 351.
[30] Beaven, P.A., Frisius, F., Kampman, R., and Wagner, R., Proceedings of the Workshop on Atomic Transport and Defects in Metals by Neutron Scattering, eds. C. Janot et al., Springer, Berlin, 1986, p. 228.
[31] Gondi, P., Montanari, R., Physica Status Solidi, Vol . 131, 1992, p. 465.
[32] Gondi, P., Montanari, R., Sili, A., and Coppola, R., Journal of Nuclear Materials, Vol. 212-215, 1994, p. 564.

Akihiko Kimura,[1] Hiroshi Shibamoto,[2] Hideki Yuya,[2] Masayuki Hasegawa,[1] Sadae Yamaguchi,[1] and Hideki Matsui[1]

DAMAGE STRUCTURES OF PROTON IRRADIATED Fe-0.3wt.%Cu ALLOY

REFERENCE: Kimura, A., Shibamoto, H., Yuya, H., Hasegawa, M., Yamaguchi, S., and Matsui, H., **"Damage Structures of Proton Irradiated Fe-Cu Alloys,"** *Effects of Radiation on Materials: 17th International Symposium, ASTM STP 1270,* David S. Gelles, Randy K. Nanstad, Arvind S. Kumar, and Edward A. Little, Eds., American Society for Testing and Materials, 1996.

ABSTRACT: Microstructural observation was performed on an Fe-0.3wt.%Cu alloy using a cross-sectional method. The specimens were solution treated and aged at 893K for 22.5h, followed by proton irradiation up to a fluence of $3x10^{21}H^+/m^2$ (0.2 dpa at a peak position) at 353K. A band of structure, 0.8μm wide, was observed in a region 6.5 μm beneath the irradiated surface. The band consisted of a high density of black spot damage, which average size and number density at the center of the band was determined to be 2.3nm and $2.2x10^{26}/m^3$, respectively. Besides the black spot damage, a number of small structures (<3nm) were observed in the defect band at strong two beam condition, while precipitates having F.C.C structure with a lattice constant of 10.16A and large precipitates (> 6nm) causing halo rings corresponding to F.C.C. copper were observed at the region in and around both sides of the band. Taking in account results of micro vickers hardness and positron life-time measurements in Fe-Cu alloys, radiation hardening observed in Fe-0.3wt.%Cu alloy is attributed mainly to the radiation damage structures, such as dislocation loops and microvoids. However, It is pointed out that interaction between copper and carbon plays an important role on the microstructural evolution under irradiation and the resultant hardening in Fe-C-Cu alloys.

Keywords: damage structures, copper precipitates, carbides, Fe-0.3Cu alloy, proton irradiation, cross-sectional method, modeling irradiation hardening

[1]Associate professors and professors, respectively, Institute for Materials research, Tohoku University, 2-1-1 Katahira, Aoba-ku, Sendai 980-77, Japan

[2]Research scientists, Electrical Technology Research department, Chubu Electric Power Company, Inc., 20-1 Kitasekiyama, Odakacho, Midori-ku, Nagoya 459, Japan

Copyright© 1996 by ASTM International www.astm.org

INTRODUCTION

Great efforts have been made to understand the mechanism of irradiation hardening for the prediction of the life of reactor pressure vessel, since irradiation embrittlement was shown to be directly related to irradiation hardening. Irradiation induced hardening must be understood in terms of irradiation induced changes in microstructure. Although many empirical formulas to predict the end-of-life of the pressure vessel have been presented, more precise prediction can be achieved by modeling the hardening, taking account of changes in the microstructure with more precision. Moreover, understanding the hardening mechanism based on physical mechanisms will aid the development of a highly resistant steel to neutron irradiation embrittlement.

It has been recognized that copper precipitates play a significant role in embrittlement [1-7] as well as lattice defects such as dislocation loops and microvoids [8-10]. Several workers speculated that the effect of copper is to interact with and enhance the formation of small vacancy clusters [11,12]. Odette proposed a quantitative model of embrittlement through the hardening due to defect copper complexes based on a two- component model[1], involving contributions from a matrix damage component and a component due to radiation enhanced precipitation. He attributed the hardening to copper clusters that were expected to be left by annealing of lattice defects during the irradiation under long time-low flux conditions, typical of power reactors [13]. Buswell et al. reported, in their work on small clusters formed in a thermally aged and irradiated Fe-Cu model alloy, that a large number of black-white (BW) images were observed in both aged and irradiated specimens. These BW images were shown by energy dispersive X-ray analysis to be enriched with copper [14]. They also expected that the BW images stemmed from small spherical B.C.C. copper precipitates, which has a large potential for hardening [14]. In contrast, Stoller showed by using a kinetic model of point defect cluster formation that both Frank loops and microvoids can give rise to significant hardening and they may be responsible for greater hardening than the copper rich precipitates that occur under irradiation conditions [10]. Recently, Buswell and Jones showed that radiation embrittlement of submerged-arc welds could be interpreted in terms of a two component model [15]. Although these two irradiation induced microstructural components are thought to contribute to the hardening additively [11], there has been no direct experimental evidence of it. This stems from the difficulty of determining the characteristics of both the microstructures of lattice defects and copper precipitates simultaneously. In order to establish a methodology for more precise prediction of end-of-life for copper-bearing pressure vessel steels, the hardening potential of these two components should be evaluated separately, or their interactions, if any, should be considered and distinguished from each hardening contribution. Furthermore, recent studies indicate a role of secondary precipitates, such as nitride and carbides, on irradiation hardening [15-17].

In this study on microstructural evolution in Fe-0.3wt.%Cu model alloys under irradiation, we attempted to distinguish in the microstructures between point defect clusters and precipitates, such as copper and carbides, induced by proton irradiation. In regard to the results obtained together with hardness measurements and positron annihilation studies, the basic process forming the microstructures under the irradiation is discussed.

EXPERIMENTAL METHOD

Materials used were pure Fe, Fe-0.2, 0.35wt.%C and Fe-0.05, 0.15, 0.3wt.%Cu, which were prepared using an arc-melting method in an argon atmosphere from high purity iron (99.999 wt.%), copper (99.999 wt.%) and carbon. The alloy buttons were cold rolled to thin sheets (0.3mm thickness) and then cut into small sheet specimens (1.2mm x 5mm). They were solution treated in a vacuum of about 1.3×10^{-3} Pa at 1153K for 7.5h, followed by quenching into water and final aging in a vacuum at 893K for 22.5h. Although specimens were made from pure materials, 30wt ppm of carbon was included in the nominally carbon free alloys. The 1 MeV proton beam was injected into the sheets to a fluence of $3 \times 10^{21} H^+/m^2$ at 353K. Figure 1 shows the calculated depth-dependent displacement profile for 1 MeV H^+ ions incident on iron using the TRIM-1990 code (0.2 dpa at a peak position). Microvickers

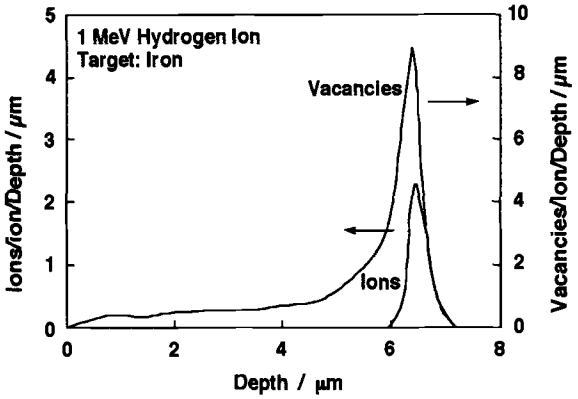


Fig.1; Calculated depth-dependent displacement profile for 1 MeV H^+ ions incident on iron.

hardness measurements were taken of both the specimen surfaces with a 25g load and the loading direction parallel to the incident beam. Since the depth of indentation was usually 2-3μm, the highly damaged area (6.5μm depth) was probably inside the plastic zone as a result of loading. Hardness was evaluated by averaging 21 measurements except for the minimum and maximum three values.

Observation of microstructure was done by the cross-sectional method, mainly on 0.3Cu alloy, and the procedure of specimen preparation is schematically shown in Fig.2. After irradiation, the sheets were plated first with iron and then with nickel in appropriate plating solutions. Specimens for

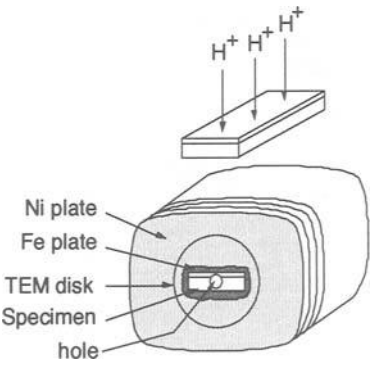


Fig.2; Schematic diagram of TEM specimen preparation.

transmission electron microscope (TEM) observation were produced by cutting the plated sheets in the direction parallel to the proton beam direction followed by punching the cut sheets into disks 3mm in diameter. Thinning was done by twin jet method in a solution of 95%CH_3COOH + 5%$HClO_4$ at 283K. Examinations were performed on JEOL JEM2010.

RESULTS AND DISCUSSION

Microstructure

Microstructures of unirradiated Fe-0.2C and Fe-0.3Cu are shown in Figs.3 and 4, respectively. The dark field image in Fig.3 indicates that there are many small particles in Fe-0.2C after annealing at 893K. Diffraction patterns correspond to M_6C type carbides that have an F.C.C. structure with a lattice constant of 10.16A. It is worthy of note that the same structures are also observed in pure Fe after annealing. Chemical analysis of the carbides is under way. As shown in Fig.4, particles of various sizes (larger than 6nm) are observed in Fe-0.3Cu, which causes the appearance of halo rings superimposed on the diffraction pattern of iron . Four rings, which consist of fine spots, correspond to F.C.C. copper, and the others stem from M_6C type carbides.

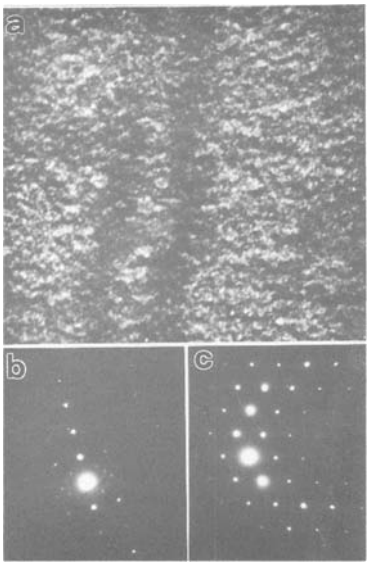


Fig. 3; Microstructure (a) and diffraction patterns (b) and (c) of unirradiated Fe-0.2C.

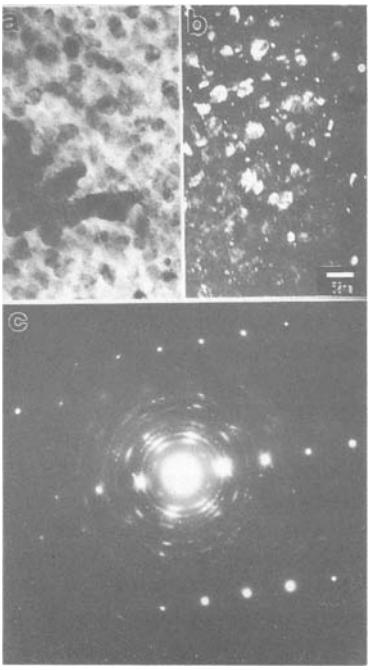


Fig. 4; Microstructure (a) and (b) and diffraction patterns (c) of Fe-0.3Cu.

Figure 5 shows bright (a) and dark (b) field images of the cross-sectional microstructure and its schematic drawing (c) of Fe-0.3Cu irradiated with 1 MeV H^+ ions at 353K. The direction of proton beam is as shown in Fig.5 (c). Images are obtained with $\boldsymbol{g} = 110$ at the two beam condition, $S_g = 0$. In Fig.5(a), a black band structure parallel to the specimen surface was observed at a depth of about 6.5μm from the specimen surface. Dark field imaging of the same area, Fig.5 (b), taken by using 220 diffraction spot, indicates that the image contrast of the band structure is similar to that of dislocations. This suggests that these black spots have a dilatation strain field similar to dislocations in iron. Figure 6 shows the band structure at

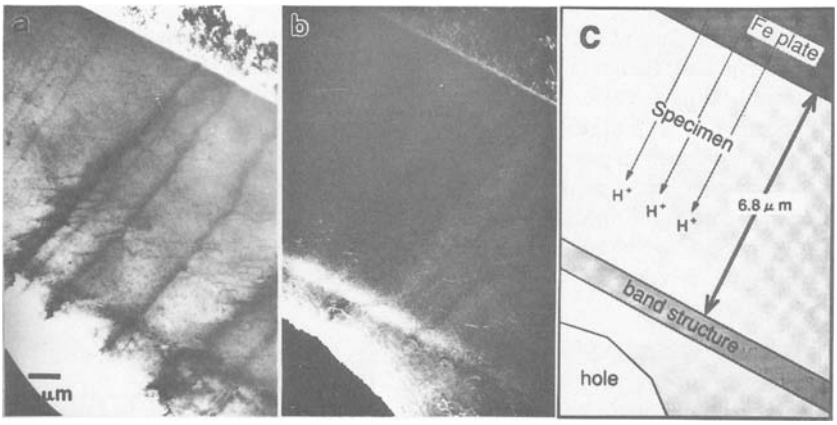


Fig. 5; Bright (a) and dark (b) field images of the cross-section microstructure and its schematic diagram (c) of Fe-0.3Cu irradiated with 1 MeV H^+ ions at 353K.

relatively high magnification taken with the diffraction condition near a two beam condition, which reveals that the band structure consists of a number of black spots (in the bright field image, $S_g > 0$). When they are imaged with a two beam diffraction condition, $S_g = 0$, a characteristic black-white contrast appears as shown in Fig. 7. Some of the vectors, $\boldsymbol{l}$, joining the center of the black lobe to the white lobe lie parallel to the diffraction vector $\boldsymbol{g}$, and the change in the direction of $\boldsymbol{g}$ vector from 110 to 112 results in a corresponding change in the $\boldsymbol{l}$ vector, suggesting that these images stem from spherical symmetry of the strain field that has been reported to be due to copper precipitates[5]. A dark field image, using the (220)M spot, which was used to estimate the number density and average size of the black spot structures, is shown in Fig.8, where a high density of black spot structures are observed over a 500nm wide range in the region 6.5μm from the irradiation surface, and some relatively larger black spots are observed in the area between the surface and the band. White spots in the dark field image (b), which was taken using a matrix reflection, may be dislocation loops induced by the irradiation. Dislocations, which could have been produced during preparation of TEM disks, are also observed. From this figure, the depth profile of the total number density and average size of the black spot structures are estimated for each area and plotted in Fig.9. Both the depth

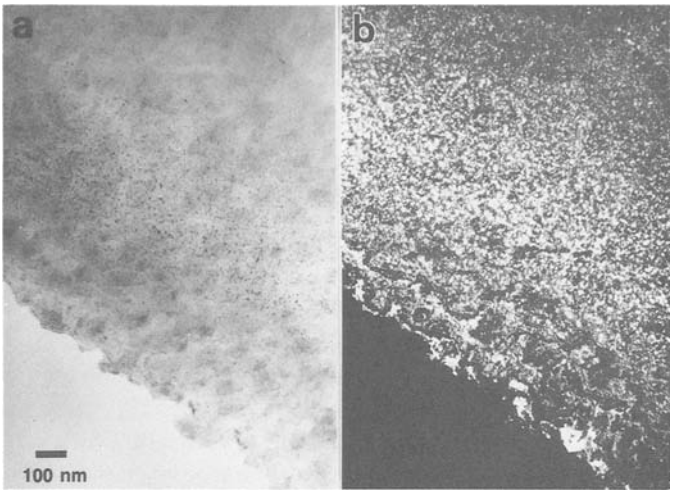


Fig. 6; Band structure at relatively high magnification taken with the diffraction condition near a two beam condition in Fe-0.3Cu (a) bright field image, $S_g > 0$ and (b) dark field image.

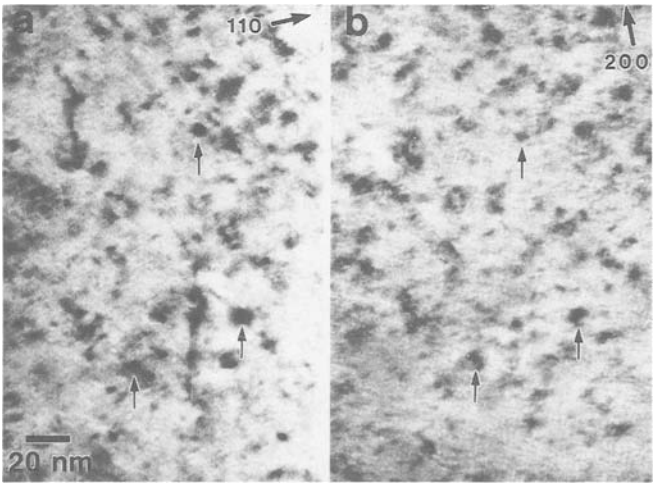


Fig. 7; Microstructure imaged with two beam diffraction condition, $S_g = 0$, a characteristic black-white contrasts appear in the band in the irradiated Fe-0.3Cu.

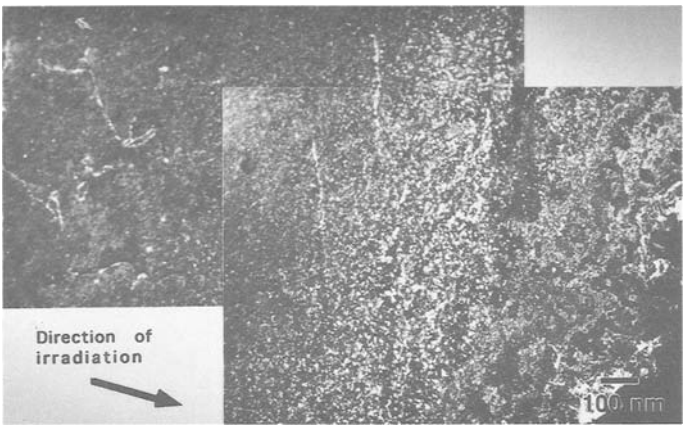


Fig. 8; A dark field image, using (220)M spot, which was used to estimate the number density and average size of the dot structures in the irradiated Fe-0.3Cu.

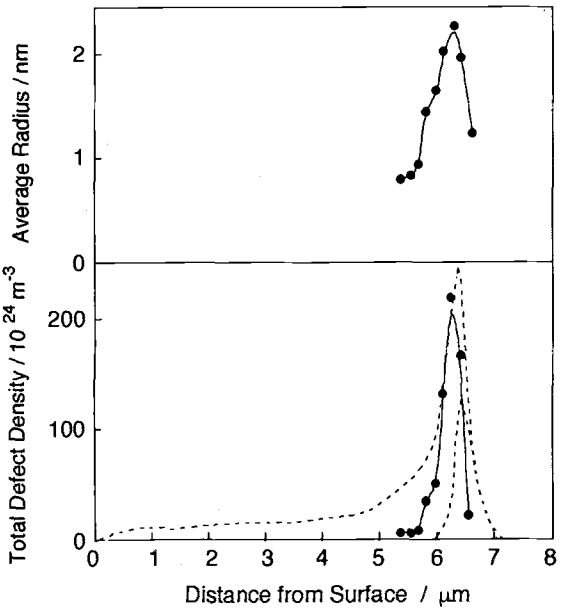


Fig. 9; The depth profile of the total number density and average size of black spot structures are estimated from Fig.8. Dotted lines represent the caliculated profile shown in Fig.1.

profile of the number density and average size are very similar to the dotted line, which shows the calculated depth profile of damage from Fig.1, indicating that irradiation to higher displacement level results in formation of larger spot structures at higher density. Figure 10(a) shows a diffraction pattern taken from the unirradiated area, which is deeper than the damage band, indicating that halo rings are superimposed on the diffraction pattern of the matrix. These halo rings observed in Fe-0.3Cu are the same to those shown in Fig. 4: F.C.C. copper precipitates and M_6C type carbides. A diffraction pattern of the damage band is shown in Fig.10(b), where the intensity of the F.C.C. copper halo rings seems to be reduced by the

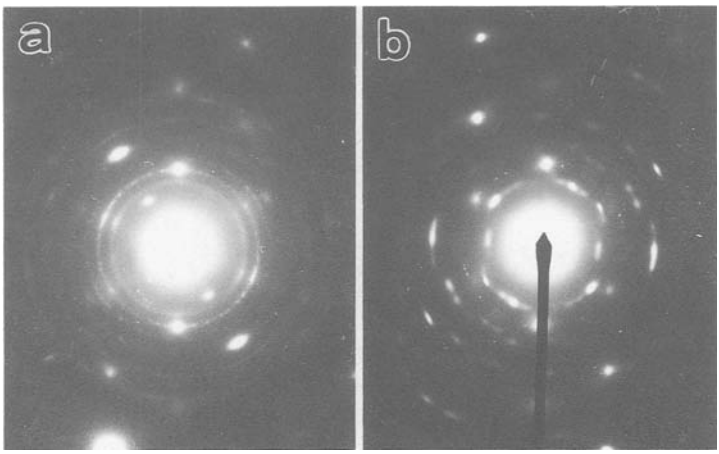


Fig. 10; Diffraction patterns of (a)unirradiated and (b)irradiated area of Fe-0.3Cu.

irradiation, while that of diffraction spots due to carbides appears to be unchanged. As is shown in another paper by authors in this issue [20], the positron irradiated Fe-0.3Cu alloys show more age hardening than pure Fe. Thus, the over-aged Fe-0.3Cu alloys irradiated by protons at 353K have a greater potential of age-hardening than pure Fe after the irradiation. Therefore, the reduction of the intensity of F.C.C. halo rings can be interpreted in terms of dissolution of F.C.C. copper precipitates and possibly formation of other structures by the irradiation. Figure 11 shows a bright field image (a), a dark field image using the (220)M spot (b), and a dark field image from an extra carbide spot (c) from the same damage band observed in the direction of <110>. The bright field image was taken under strong two beam conditions, resulting in a characteristic black-white contrast in addition to black spot damage. White dots in Fig.11(b) as well as small BW contrasts in Fig.11(a) were only observed within the band structure, while those in Fig.11(c) were observed in both the area irradiated and unirradiated, suggesting that the small carbides are not responsible for the irradiation hardening observed.

Two component analysis of positron life time measurements by the authors [20] suggest that the long life time components t_2 (300~360ps) in irradiated pure Fe and Fe-0.3Cu reflect the presence of vacancy type clusters consisting of about 10 vacancies, and it is possible that they may be responsible for the irradiation hardening as well as dislocation loops

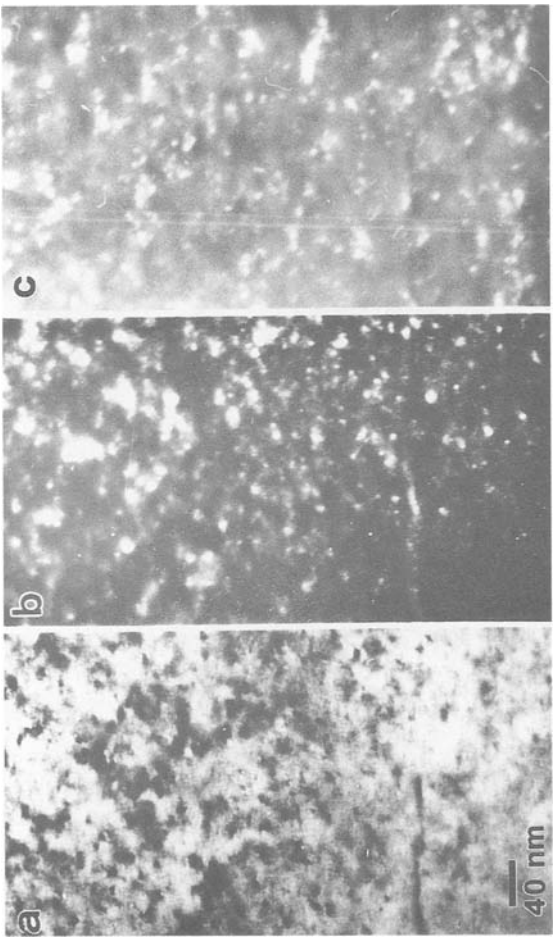


Fig. 11; Bright field image(a), dark field image(b) using (220)M spot and dark field image with extra spot of carbides(c) of the same band area observed in the direction of <110> (Fe-0.3Cu).

observed by TEM.

Micro-Vickers hardness

Figure 12 shows the increment to the hardness induced by the irradiation as a function of copper concentration, indicating that the increase in the radiation hardening with increasing copper concentration in Fe-Cu binary alloys is small, namely in Fe-0.3 alloy, ΔH_v(Fe-0.3Cu) - ΔH_v.(Fe) = 8, although radiation hardening of pure Fe is significant, namely $\Delta H_v = 25$. The increase in irradiation hardening due to the addition of 0.3Cu is considered to be due to the irradiation induced small (<3nm) structures that contain copper. Thus, the potential for irradiation hardening due to copper related structures in over-aged Fe-Cu alloys is not significant, and accordingly the major part of the irradiation hardening is considered to come from formation of defect clusters such as vacancy clusters, microvoids and dislocation loops. The role of carbon in pure Fe is to suppress the irradiation hardening, which is probably due to the retardation of clustering vacancies caused by trapping of vacancies by carbon atoms. It is noteworthy that the decrease in the irradiation hardening caused by an increase in carbon concentration becomes small by the addition of copper, and the effect becomes more significant in specimens with lower copper concentration. It is supposed that the interaction between vacancy and carbon may be reduced by copper, resulting in the formation of defect clusters. Therefore, in carbon bearing over-aged Fe-Cu alloys, the defect clustering that involves the role of both carbon and copper are probably responsible for the irradiation hardening.

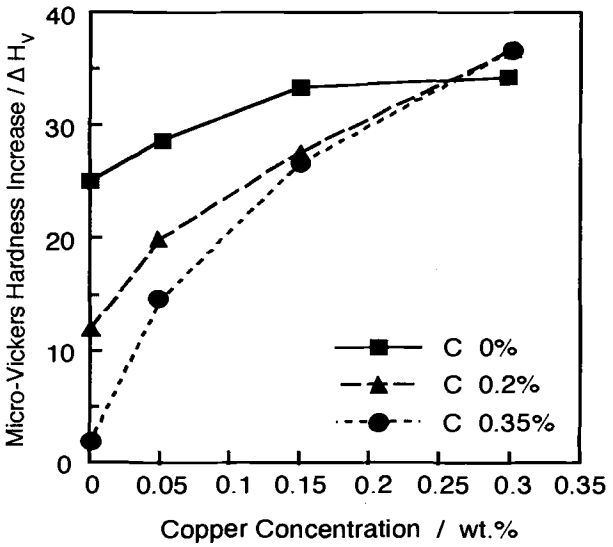


Fig. 12; Irradiation induced hardening as a function of copper and carbon concentrations.

CONCLUDING REMARKS

The microstructures of over-aged Fe-0.3wt.%Cu alloys consist of relatively large F.C.C. copper precipitates and small carbides. Proton irradiation up to a fluence of $3x10^{21}H^{+}/m^{2}$ at 353K induced formation of dislocation loops, microvoids, and small structures having a spherical symmetry of strain field dilatation. The depth of damage structures was very similar to the results of the calculated depth profile. Irradiation hardening due to the damage structures was greater than that due to the copper related structures in over-aged Fe-0.3wt.%Cu alloys. However, it is expected that in the Fe-C-Cu alloys, carbon together with copper plays a significant role in the hardening. Microstructural examination after post-irradiation annealing is under way.

REFERENCES

[1] Odette, G.R., "On the dominant Mechanism of Irradiation Embrittlement", Scripta Met., 11, 1983, p.1183.

[2] Odette, G.R. and Lucas, G.E., "Irradiation Embrittlement of Reactor Pressure vessel Steels: Mechanisms, Models, and data Correlations", Radiation Embrittlement of Nuclear Reactor Pressure Vessel Steels: An International Review - Volume II, ASTM STP 909, L.E. Steele, Ed., ASTM, Philadelphia, PA, 1986, p. 206.

[3] Beaven, P.A., Frisius, F.R.Kampmann, R.and Wagner, R., "SANS/TEM Studies of the Defect Microstructure Of Test Reactor Irradiation Fe-Cu Alloys and Cu-Containing RPV Steels", Proc. Second Int'l Symp. on Environmental Degradation of Materials in Nuclear Reactors - Water Reactors, J. T. A. Roberts, J. R. Weeks and G. J. Theus, Eds., ANS, LaGrange Park, I11, 1986, p.400.

[4] Beaven, P. A., Frisius, F.R.Kampmann, R., Wager, R. and Hawthorne, J.R.,"SANS Investigation of Irradiated A533-B Steels Doped With Phosphrous", Radiation Em brittlement of Nuclear Reactor Pressure Steels: An International Review ,Vol. III, ASTM STP 1011, L. E. Steels, Ed., ASTM, Philadelphia, PA, 1989, p.243.

[5] Phythian, W.J., Foremen, A.J.E., English, C.A., Buswell, J.T., Hetherington, M.Roberts, K. and Pizzini, S., "The Structure and Hardening Mechanisms In Thermally Aged or Irradiated Fe-Cu and Fe-Cu-Ni Model Alloys", The Effects of Radiation on Material: 15th International Symposium, ASTM STP 1125, R.Stoller, A.Kumer and H.Packen, Eds., ASTM STP 1125, ASTM, Philadelphia, PA, 1992, P.131.

[6] Kapmann, R., Frisius, F., Hackbarth, H., Beaven, P.A., Wagner, R. and Hawthorne, J.R., "SANS Analysis of Reactor Vessel Materials In Neutron Irradiated, Annealed and Re-Irradiated Conditions ", Proc. Fifth Int'l Symp. on Environmental Degradiation of Materials in Nuclear Reactors - Water Reactors, D.Cubicciotti, E.P. Simonen and R. Gold, Eds. ANS, LaGrange Park, Ill, 1992, p.679.

[7] Mader, E.V.,Lucas, G.E. and Odette, G.R., "The Effects of Metallurgical and Irradia tion Variables on the Kinetics of Post-Irradiation Annealing of Pressure Vessel Steels", The Effects of Radiation on Materials: 15th Int. Symp., ASTM STP 1125, R. Stoller, A. Kumar and H. Packan, Eds., Philadelphia, PA, 1992, p.151.

[8] Brailsford, A.D. and Bullough, R, Philosophical Transactions of the Royal Society of London 302 (1981) 87-137.

[9] Mansur, L.K., Nuclear Technology 40 (1978) 5-34.

[10] Stoller, R.E., "Modeling the Influence of Irradiation temperature and Displacement Rate on Hardening due to Point Defect Clusters in Ferritic Steels," Effects of Radiation on Materials: 16th Inter. Symp., ASTM ASP 1175, A.S. Kumar, D.S. Gelles, R.K. Nanstad, and E.A. Little, Eds, Philadelphia, 1994, 394-423.

[11] Fisher, S.B., Harbottle, J.E. and Aldridge, N., "Radiation Hardening in Magnox Pres sure Vessel Steels", Philosophical Transactions of the Royal Society of London, A315, 1985, p.301.

[12] Fisher, S.B. and Buswell, J.T., "A Model for PWR Pressure Vessel Embrittlement", Int. J. Pressure Vessels and Piping, 27, 1987, p.91.

[13] Odette, G.R., Mader, E.V., Lucas, G.E., Phythian, W.J. and English, C.E., "The Effect of Flux on the Irradiation Hardening of Pressure Vessel Steels", Effects of Radiation on Materials: 16th Inter. Symp., ASTM ASP 1175, A.S. Kumar, D.S. Gelles, R.K. Nanstad, and E.A. Little, Eds, Philadelphia, 1994, 373-393.

[14] Buswell, J.T., English, C.A., Hetherington, M.G., Phythian, W.J., Smith, G.D.W., and Worrall, G.M., "An Analysis of Small Clusters Formed in Thermally Aged and Irradi ated FeCu and FeCuNi Model Alloys", Effects of Radiation on Materials: 14th Inter. Symp., ASTM ASP 1175, H. Packan, R. Stoller and A. Kumar, Eds., Philadelphia, PA, 1990, 127-153.

[15] Buswell, J.T. and Jones, R.B., "The Modelling of Radiation Hardening and Embrittle ment in Magnox Mild Steel Submerged-Arc Welds", Effects of Radiation on Materi als: 16th Inter. Symp., ASTM ASP 1175, A.S. Kumar, D.S. Gelles, R.K. Nanstad, and E.A. Little, Eds, Philadelphia, 1994, 424-443.

[16] English, C.A., Phithian, W.J., Buswell, J.T., Hawthorne, J.R. and Ray, P.H.N., "Inves tigation of Gundremmingen RPV Archive Material Irradiated in Light Water and Heavy Water Reactors", Effects of Radiation on Materials: 15th Int. Symp. ASTM STP 1125, A.S. Kumar, D.S. Gelles, R.K. Nanstad, and E.A. Little, Eds, Philadelphia93-116.

[17] Miller, M.K. and Burke, M.G., "An APFIM Survey of Grain Boundary Segregation and Precipitation in Irradiated Pressure Vessel Steels", Effects of Radiation on Materials: 16th Inter. Symp., ASTM ASP 1175, A.S. Kumar, D.S. Gelles, R.K. Nanstad, and E.A. Little, Eds, Philadelphia, 1994, 492-502.

[18] Shirai, Y, Furukawa, K, Takamura, J, Yamada, W and Iwata, S, Appl. Phys. A37(1985)65.

[19] Hinode, K, Tanikawa,S, Kumakura, H, Doyama, M and Shiraishi, K, J. Phys. Soc. Jpn. 45(1978)1858.

[20] Shibamoto, H., Koyama, K., Yuya, H., Hasegawa, M., Kimura, A., Matsui, H., and Yamaguchi, S., "Effects of Proton Irradiation on Positron Annihilation and Micro-Vickers Hardness of Fe-C-Cu Model Alloys", Effects of Radiation on Materials: 17th Volume, ASTM STP 1270, David S. Gelles, Randy K. Nanstad, Arvind S. Kumar and Edward A. Little, Editors, American Society For Testing and Materials, Philadelphia, 1995, in this isuue.

Amir D. Amayev[1], Alexander M. Kryukov[1], Vladimir I. Levit[1], Pavel A. Platonov[1], and Mikhail A. Sokolov[2]

MITIGATION OF IRRADIATION EMBRITTLEMENT BY ANNEALING

REFERENCE: Amayev, A. D., Kryukov, A. M., Levit, V. I., Platonov, P. A., and Sokolov, M. A., **"Mitigation of Irradiation Embrittlement by Annealing,"** *Effects of Radiation on Materials: 17th International Symposium, ASTM STP 1270,* David S. Gelles, Randy K. Nanstad, Arvind S. Kumar, and Edward A. Little, Eds., American Society for Testing and Materials, 1996.

ABSTRACT: The main results of a complex investigation carried out in Russia of post irradiation annealing and reembrittlement of WWER-440 reactor pressure vessel materials are presented. The dependence of the Charpy transition temperature recovery on annealing temperature and fluence was established. Charpy specimens were reirradiated after annealing at 340, 380, 420, and 460°C. Experimental values of the Charpy transition temperature after reirradiation are compared to that predicted by three methods. At annealing temperatures equal to or above 420°C, results of the analysis indicate that, of the methods investigated, the "lateral shift" method gives the best result for estimating the transition temperature shift due to reirradiation.

KEYWORDS: pressure vessel steels, radiation embrittlement, radiation effects, neutron fluence, annealing, reembrittlement.

[1]Chief researcher, head of laboratory, lead researcher, and director of department, respectively, RNRC Kurchatov Institute, Kurchatov Square 1, 123182 Moscow, Russia.
[2] Former lead researcher, Kurchatov Institute, currently on assignment at Oak Ridge National Laboratory, P.O.Box 2008, Oak Ridge, TN 37831-6151.

Copyright© 1996 by ASTM International www.astm.org

Introduction

In the early 1980s in Russia and Eastern Europe the problem of safe operation of the first generation of the Soviet-built WWER-440 reactor pressure vessels (RPVs) became a critical issue due to accelerated embrittlement, resulting from elevated phosphorus and copper contents in RPV weld metal. Thermal annealing was considered the only technology capable of mitigating the irradiation embrittlement that had been already acquired in RPVs by that time. As a result, extensive studies were conducted to form the basis for the possibility of RPV base and weld metal properties' recovery by thermal annealing at a temperature exceeding the irradiation temperature. For the WWER RPV, irradiation embrittlement is characterized by an increase in the ductile-to-brittle transition temperature. According to current practice in Russia, the ductile-to-brittle transition temperature (T_k) is determined from the results of Charpy V-notch specimen tests and is evaluated at an impact toughness value of 59 J/cm^2 (47 J), see Ref. [1] for details. The dependence of recovery on annealing temperature (T_{ann}) and time, irradiation temperature (T_{irr}), and neutron fluence (F) has been established. Numerous investigations made it possible to substantiate conditions for conducting RPV thermal annealing and to successfully anneal 12 WWER-440 RPVs. To a certain extent, these results have been already published earlier [2-4]. Nevertheless, we shall briefly formulate the major outcomes in the light of results obtained recently.

Until recently, kinetics of the RPV reembrittlement after annealing has not been clarified sufficiently due to limited data. Therefore, a conservative dependence of reembrittlement rate has been used, which provided the maximum possible shift of transition temperature (T_k) at reirradiation after annealing. This dependence is described by the equation:

$$\Delta T_k^{reirr} = \Delta T_k^{res} + A_F \left(\frac{F_R}{F_o} \right)^{\frac{1}{3}} \quad (1)$$

where ΔT_k^{reirr} is the total shift of the transition temperature after reirradiation (difference between T_k in reirradiated and unirradiated conditions), ΔT_k^{res} is the residual shift of transition temperature after annealing (difference between T_k in annealed and unirradiated conditions), A_F is an irradiation embrittlement factor which depends on chemical composition and irradiation temperature, F_R is the neutron fluence incurred during reirradiation (E>0.5 MeV), and F_o is equal to 10^{18} neutron/cm^2 (E>0.5MeV). This conservative approach considerably decreases the lifetime of the RPV after annealing. In recent years investigations have been conducted aimed at developing a better understanding of the reembrittlement kinetics after annealing. The results of these studies are summarized in the present work.

Annealing

The major factors affecting the Charpy V-notch 47-J transition temperature recovery, underlying the justification of the annealing technology, are briefly considered below. Recovery of the transition temperature (T_k) takes place in the temperature range 350-500°C, and in this case the degree of recovery depends linearly on the difference between annealing (T_{ann}) and irradiation (T_{irr}) temperatures (Fig.1). The degree of transition temperature recovery (RD) was determined as followed:

$$RD = \frac{T_{kF} - T_k^{res}}{T_{kF} - T_{ko}} \times 100\% \qquad (2)$$

where T_{kF}, T_k^{res}, and T_{ko} are the transition temperatures in the irradiated (I), irradiated/annealed (IA), and unirradiated (U) conditions, respectively.

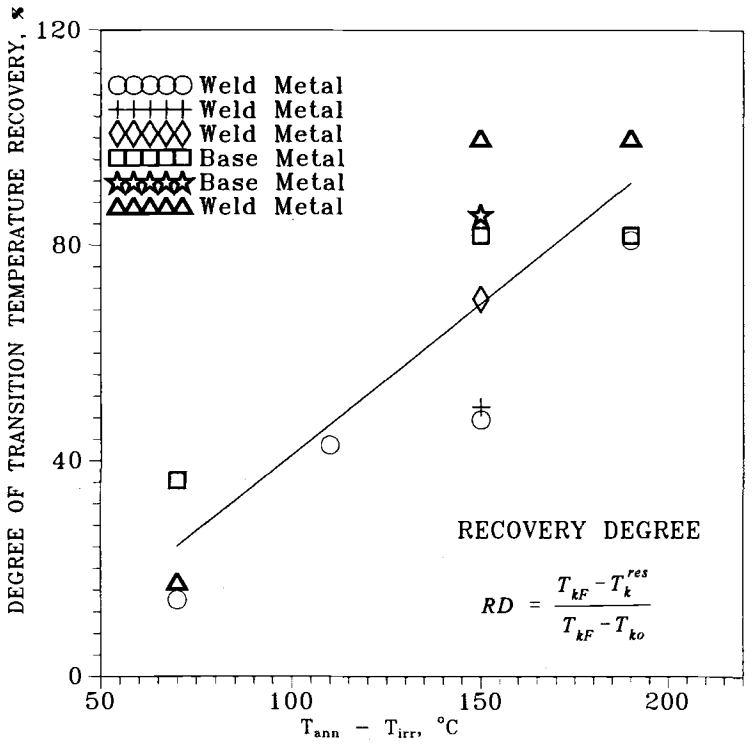


FIG. 1--Dependence of the Charpy V-notch transition temperature recovery on the difference between annealing (T_{ann}) and irradiation (T_{irr}) temperatures.

The residual shift of T_k, which is the difference between T_k in the irradiated/annealed and unirradiated conditions, depends on phosphorus content, if it exceeds 0.02% (Fig.2). The residual shift of T_k after annealing does not depend on neutron fluence (Fig.3). As the phosphorus content increases, a higher annealing temperature, T_{ann}, is necessary to obtain an equal level of property recovery (Fig.4).

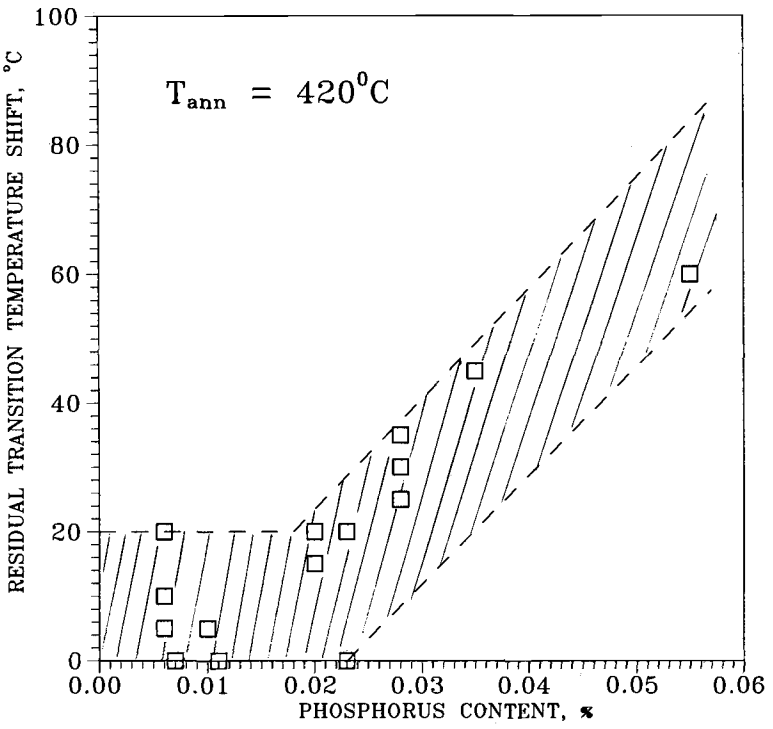


FIG. 2--Dependence of residual transition temperature shift after annealing at 420°C on phosphorus content in metal.

These data formed the basis for the justification of the annealing conditions. Predictions of the metal condition after annealing based on the annealing temperature and phosphorus content were verified by testing samples cut out from vessels before and after annealing [5].

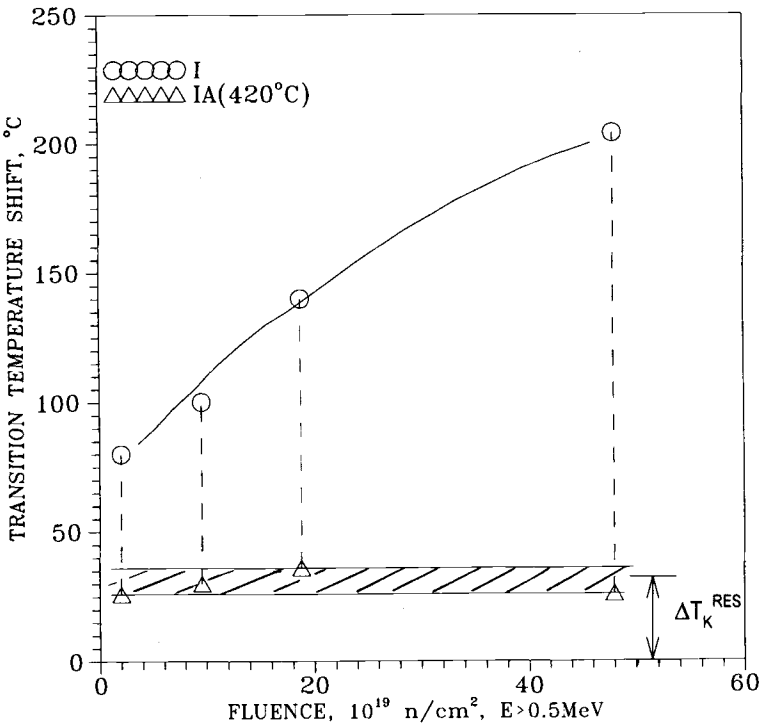


FIG. 3--Shift of Charpy V-notch transition temperature of weld metal due to irradiation and annealing at 420°C.

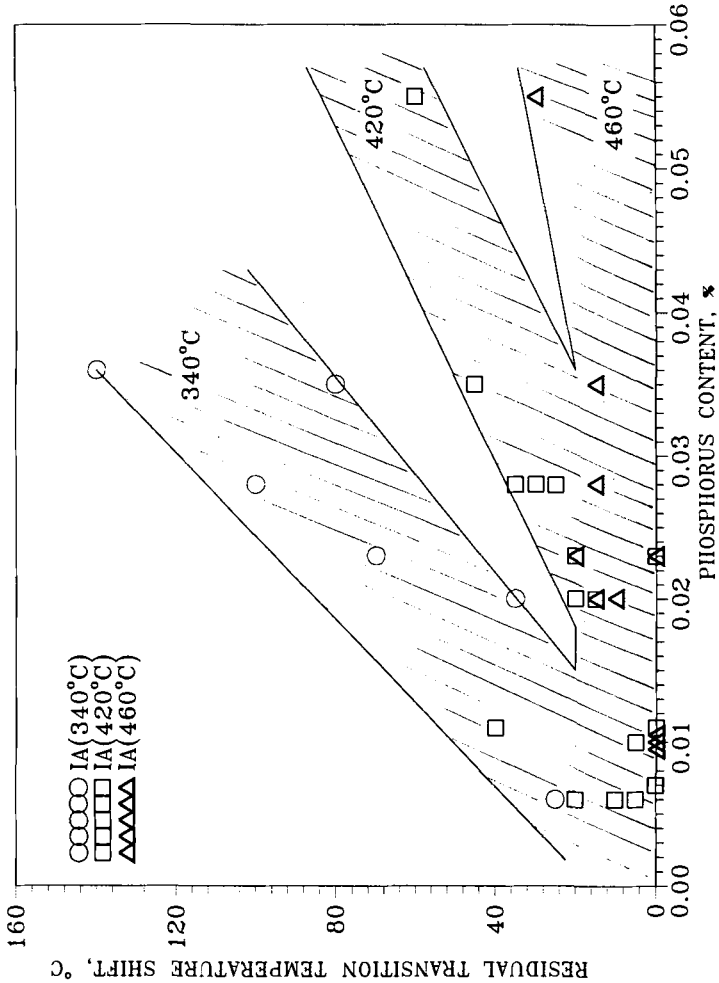


FIG. 4--Dependence of residual transition temperature shift on phosphorus content in metal for various annealing temperatures.

Reembrittlement After Annealing

When considering reembrittlement kinetics after annealing, it is usually assumed that the factors affecting the change of transition temperature are the same as those before annealing. Let us assume that the irradiation-induced shift of the Charpy transition temperature (ΔT_F) is described by some dependence:

$$\Delta T_F = f(A_F, F) \tag{3}$$

where A_F is an irradiation embrittlement factor and F is the neutron fluence. In this case three schemes for predicting T_k with reirradiation after annealing [6-9] may be considered, as shown in Fig.5. In the first scheme of prediction (Fig.5a), it is assumed that the transition temperature after annealing increases at a rate corresponding to the change of T_k in the primary cycle of irradiation. In other words, the primary curve of T_k change is transferred to the new origin of coordinates (point ΔT_k^{res}). This approach is now accepted in Russia for calculating embrittlement after annealing and has received the name "conservative shift". This model describes the shift of the transition temperature after reirradiation by the equation:

$$\Delta T_k^{reirr} = \Delta T_k^{res} + f(A_F, F_R) \tag{4}$$

where F_R is the neutron fluence after annealing. As mentioned above, taking into account the dependence of irradiation embrittlement accepted in Russia, equation (4) takes the form of equation (1).

Another approach (Fig.5b) assumes that an increase of the transition temperature due to reirradiation is represented by a horizontal transfer of the primary embrittlement dependence, starting at the ΔT_k^{res} level. This model received the name "lateral shift". In this case the reembrittlement curve is described by the relationship:

$$\Delta T_k^{reirr} = f(A_F, [F_{Eq} + F_R]) \tag{5}$$

where F_{Eq} is the neutron fluence evaluated from condition:

$$\Delta T_k^{res} = f(A_F, F_{Eq}) \tag{6}$$

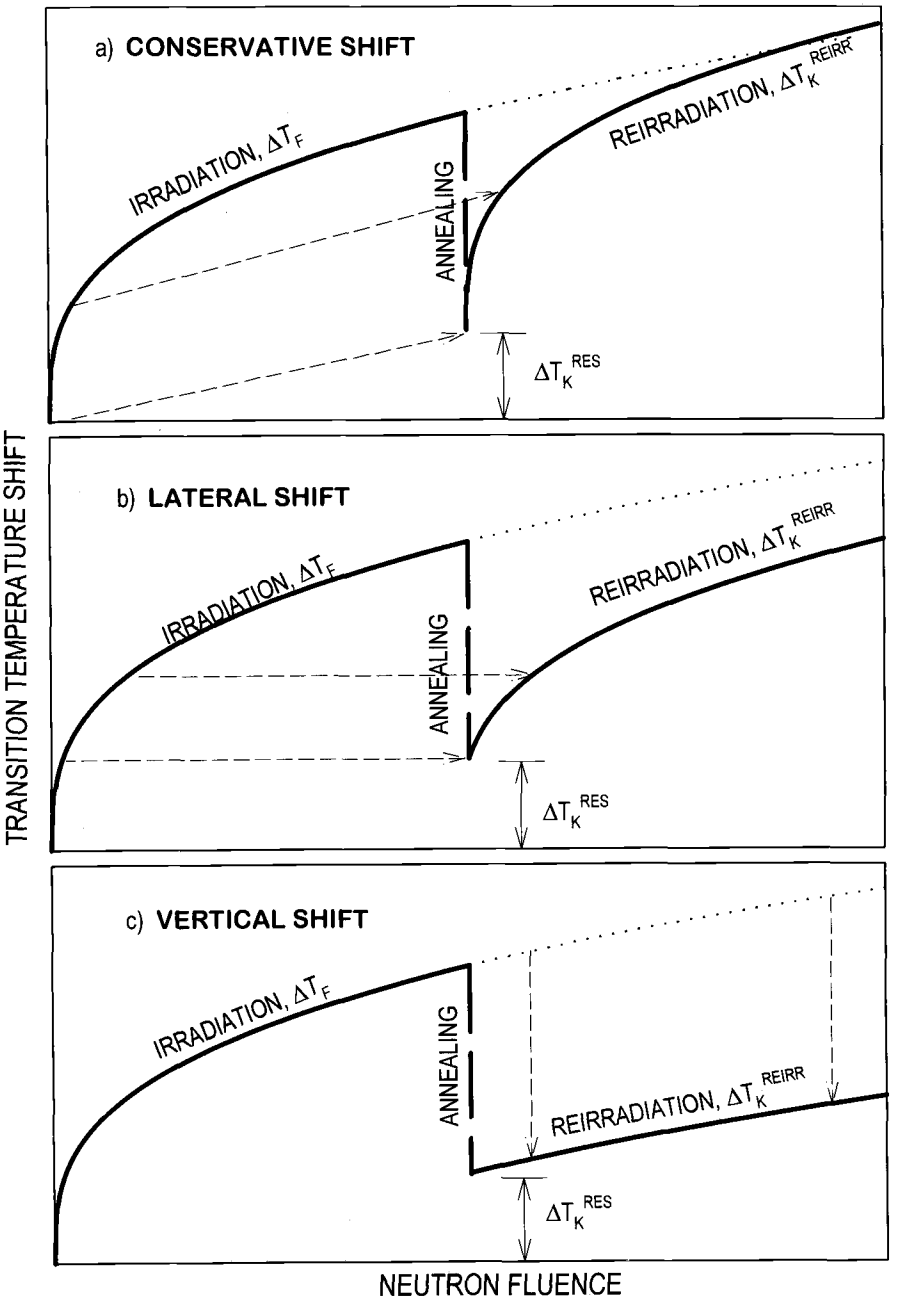


FIG. 5--Prediction of reembrittlement rate by different methods.

Finally, in the third case (Fig.5c), it is assumed that the reembrittlement rate is equal to the rate of the primary embrittlement at the point at which annealing was performed, corresponding to a vertical shift of the primary curve of embrittlement. In this case the reembrittlement curve is described by the equation:

$$\Delta T_k^{reirr} = \Delta T_k^{res} + f(A_F, F_R) - f(A_F, F_I) \quad (7)$$

where F_I is the neutron fluence before annealing.

In fact, as will be shown below, all these three models may be realized depending on the material and the structure formed in annealing, which will depend, in turn, on annealing temperature and time.

Results and Discussion

Irradiation of RPV materials was conducted in a neutron flux of 4×10^{12} n/cm²s (E>0.5 MeV) at 270°C. Annealing of Charpy specimens was performed at 340, 380, 420, and 460°C, then specimens were reirradiated together with specimens which had not been annealed.

As shown in Figs. 6-12, all three schemes of reembrittlement after annealing may be realized in practice. For example, Figs. 6, 9, and 11 show that after annealing at low temperature (343°C) the transition temperature shift is close to the vertical shift. At the same time, the transition temperature shift after annealing at high temperatures (420 and 460°C) is better described by the lateral shift, though taking into account that the residual shift is small in these cases, the "conservative" scheme is also appropriate. Data given in Figs. 7, 8, 10, and 12 show that the lateral shift provides a reasonable prediction of the transition temperature reembrittlement after annealing at 420°C.

A numerical analysis has been conducted in which the values of the transition temperature, calculated by each method, were compared to the experimental values. The vertical shift scheme provides the closest correspondence with measured transition temperature shifts after annealing at 340°C among the schemes analyzed. After annealing at 340°C all three schemes tended to overestimate the experimental values. The results of this analysis for annealing temperatures 420 and 460°C are given in Figs. 13-15. The values of the correlation coefficient (R_{xy}), dispersion (σ), and the determination coefficient (R2) are given in Table 1.

At annealing temperatures 420 and 460°C the results of the analysis indicate that, among the methods investigated, the lateral shift gives the best result for estimating the transition temperature shift due to reirradiation.

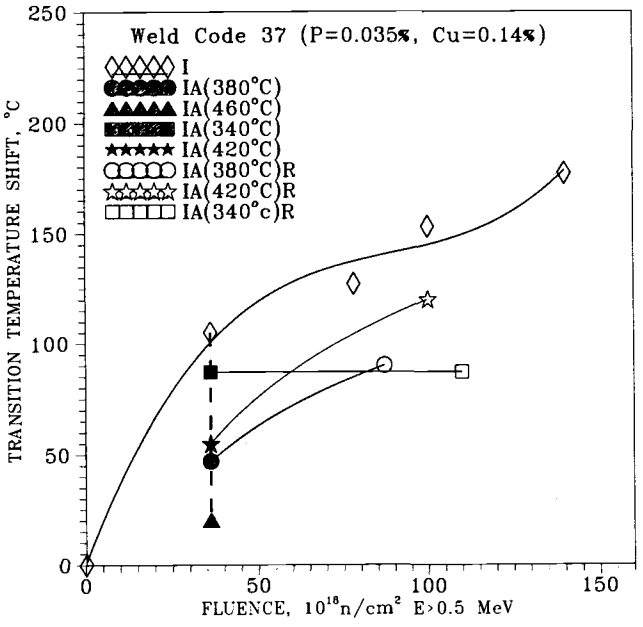


FIG. 6--Shift of the Charpy transition temperature due to irradiation (I), annealing (IA), and reirradiation (IAR) for weld code 37. Annealing temperatures are indicated in parentheses.

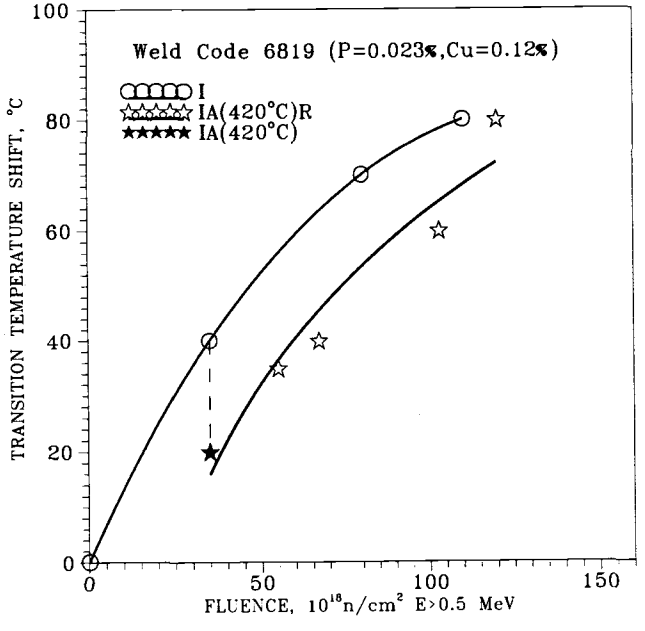


FIG. 7--Shift of the Charpy transition temperature due to irradiation (I), annealing (IA), and reirradiation (IAR) for weld code 6819. Annealing temperature is indicated in parentheses.

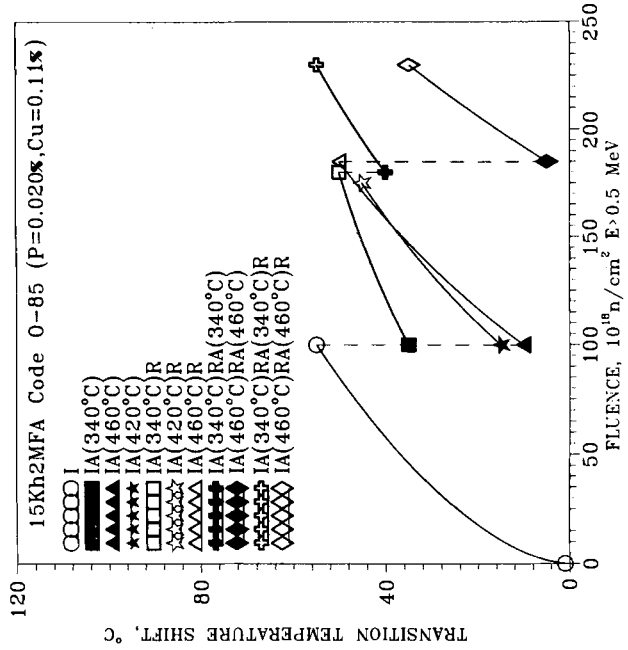


FIG. 9--Shift of the Charpy transition temperature due to irradiation (I), annealing (IA), and reirradiation (IAR) for forging 15Kh2MFA code O-85. Annealing temperatures are indicated in parentheses.

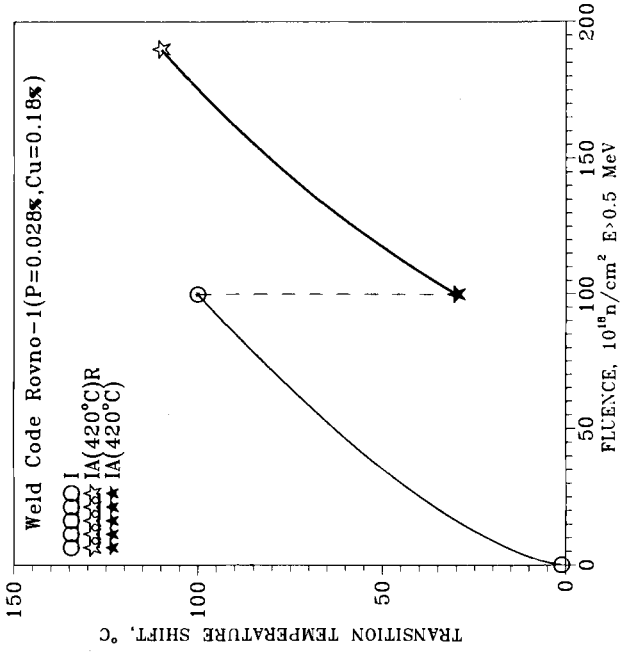


FIG. 8--Shift of the Charpy transition temperature due to irradiation (I), annealing (IA), and reirradiation (IAR) for weld code Rovno-1. Annealing temperature is indicated in parentheses.

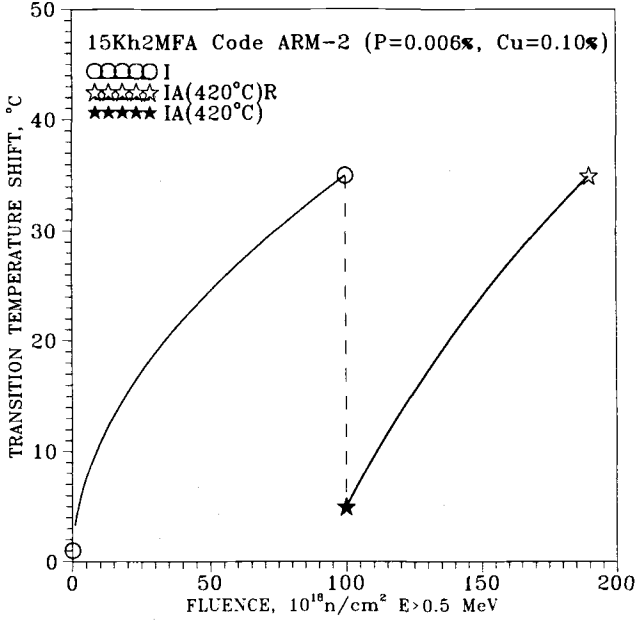


FIG. 10--Shift of the Charpy transition temperature due to irradiation (I), annealing (IA), and reirradiation (IAR) for forging 15Kh2MFA code ARM-2. Annealing temperature is indicated in parentheses.

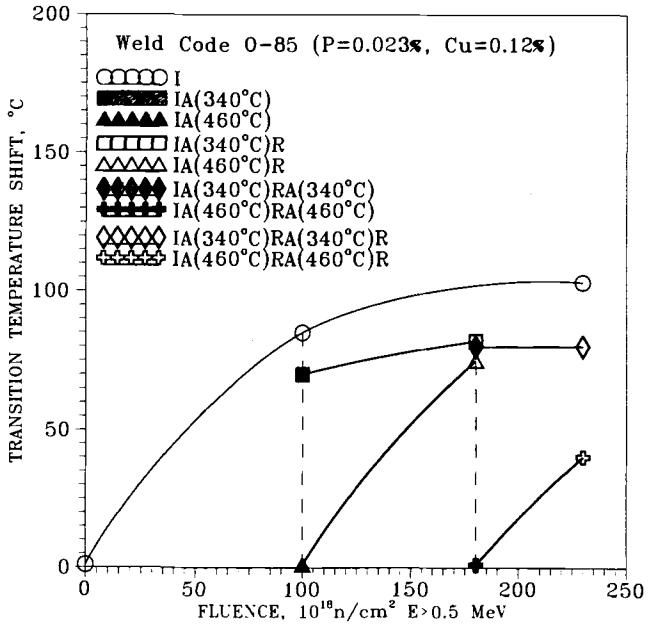


FIG. 11--Shift of the Charpy transition temperature due to irradiation (I), annealing (IA), and reirradiation (IAR) for weld code O-85. Annealing temperatures are indicated in parentheses.

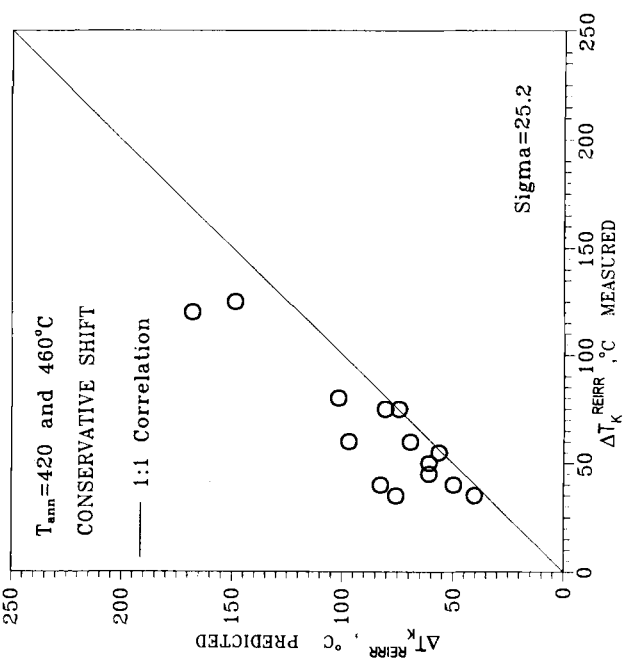


FIG. 13--Comparison of measured Charpy transition temperature shift after reirradiation with that predicted by conservative shift method.

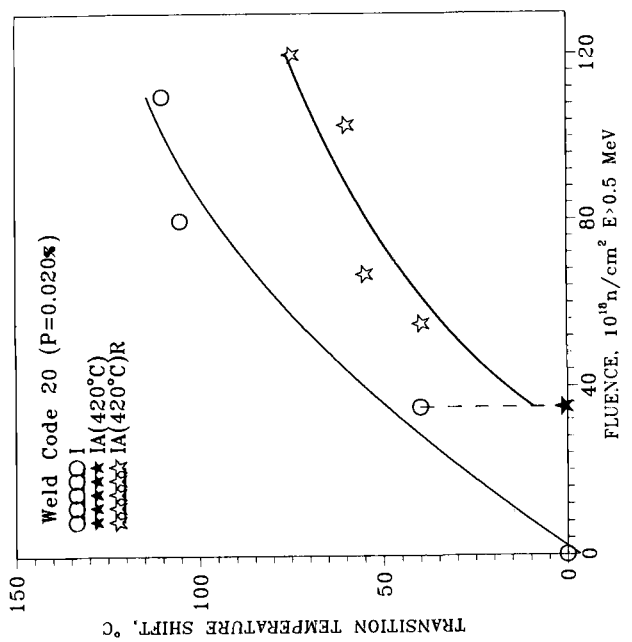


FIG. 12--Shift of the Charpy transition temperature due to irradiation (I), annealing (IA), and reirradiation (IAR) for weld code 20. Annealing temperature is indicated in parentheses.

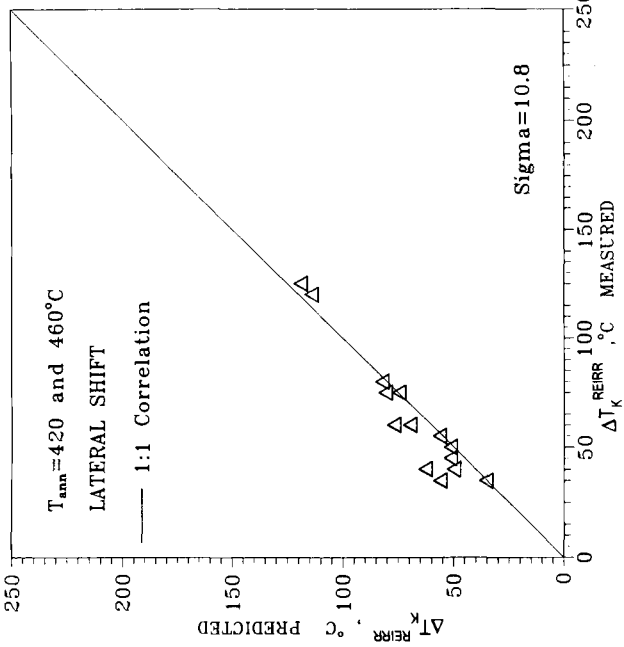


FIG. 15--Comparison of measured Charpy transition temperature shift after reirradiation with that predicted by lateral shift method.

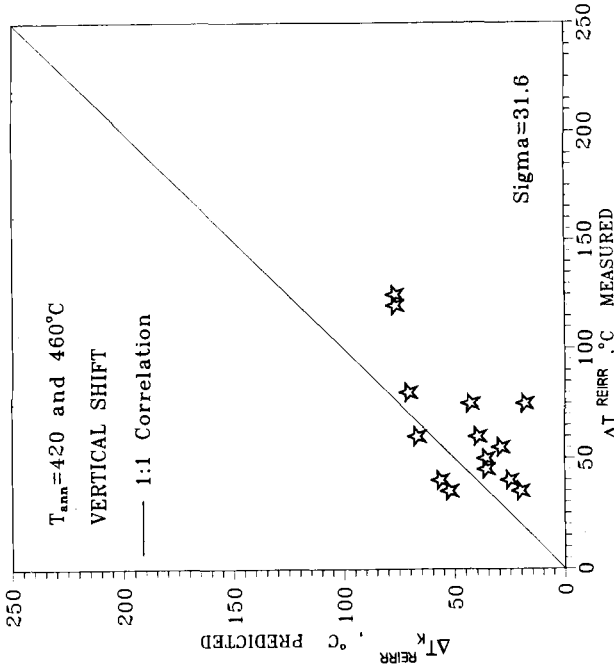


FIG. 14--Comparison of measured Charpy transition temperature shift after reirradiation with that predicted by vertical shift method.

TABLE 1--The numerical analysis results of comparison between the measured transition temperature shifts and those predicted by different methods after annealing at 420 and 460°C.

METHOD	R_{xy}	σ	R2
Conservative shift	0.89	25.2	0.48
Vertical shift	0.56	31.6	-1.25
Lateral shift	0.96	10.8	0.78

Acknowledgments

The authors would like to acknowledge David Alexander from Oak Ridge National Laboratory and ASTM reviewers for technical review.

REFERENCES

[1] A.D.Amayev, A.M.Kryukov, V.I.Levit, and M.A.Sokolov, "Radiation Stability of WWER-440 Vessel Materials," pp. 9-29 in *Radiation Embrittlement of Nuclear Reactor Pressure Vessel Steels: An International Review (Fourth Volume), ASTM STP 1170,* L.E.Steele, Ed., American Society for Testing and Materials, Philadelphia, 1993.
[2] A.D.Amayev, A.M.Kryukov, and M.A.Sokolov, "Recovery of the Transition Temperature of Irradiated WWER-440 Vessel Metal by Annealing," pp. 369-379 in *Radiation Embrittlement of Nuclear Reactor Pressure Vessel Steels: An International Review (Fourth Volume), ASTM STP 1170,* L.E.Steele, Ed., American Society for Testing and Materials, Philadelphia, 1993.
[3] A.D.Amayev, A.M.Kryukov, V.I.Levit, P.A.Platonov, and M.A.Sokolov, "Investigation of Irradiation Embrittlement and Recovery Properties of Pressure Vessel Steels of WWER Reactors in the USSR," pp. 77-97 In *Proceedings of a Technical Committee Meeting held in Plzen, Czechoslovakia, 14-17 May 1991, IAEA-TECDOC-665,* International Atomic Energy Agency, 1991.
[4] A.D.Amayev, A.M.Kryukov, V.I.Levit, P.A.Platonov, M.F.Rogov and M.A.Sokolov, "Radiation Damage and Recovery in VVER-440 Vessel Materials," in *Proceedings of International Conference PLEX-93, 29 Nov.-1 Dec., 1993,* Nuclear Engineering International, to be published.
[5] A.D.Amayev, V.I.Badanin, A.M.Kryukov, V.A.Nikolayev, M.F.Rogov, and M.A.Sokolov, "Use of Subsize Specimens for Determination of Radiation Embrittlement of Operating Reactor Pressure Vessels," pp.. 424-439 in *Small Specimen Techniques Applied to Nuclear Reactor Vessel Thermal Annealing and Plant Life Extension, ASTM STP 1204,* W.R.Corwin, F.M.Haggag, and W.L.Server, Eds., American Society for Testing and Materials, Philadelphia, 1993.

[6] V.A.Nikolayev, V.I.Badanin and A.M.Morozov, "Summing of Damages in Annealing and Reirradiation of Reactor Vessel Steel," pp.165-167 in *Atomnaya Energia,* Vol. 57, No. 3, 1984, (in Russian).
[7] A.M.Kryukov and M.A.Sokolov, "Investigation of Material Behavior Under Reirradiation after Annealing Using Subsize Specimens," pp.. 417-423 in *Small Specimen Techniques Applied to Nuclear Reactor Vessel Thermal Annealing and Plant Life Extension, ASTM STP 1204,* W.R.Corwin, F.M.Haggag, and W.L.Server, Eds., American Society for Testing and Materials, Philadelphia, 1993.
[8] W.L.Server and A.Taboada, "An Approach for Estimating Post-Anneal Reirradiation Embrittlement for Reactor Vessel Steels," pp. 361-368 in *Proceedings of the Second International Symposium on Environmental Degradation of Materials in Nuclear Power Systems-Water Reactors, American Nuclear Society*, La Grange Park, IL, 1986,
[9] Standard Guide for In-Service Annealing of Water-Cooled Nuclear Reactor Vessels, ASTM E 509-86, American Society for Testing and Materials, Philadelphia.

Igor V. Gorynin[1], Elena V. Nesterova[1], Vladimir A. Nikolaev[1] and Valery V. Rybin[1]

MICROSTRUCTURE AND MECHANICAL PROPERTIES OF WWER-440 REACTOR VESSEL METAL AFTER SERVICE LIFE EXPIRATION AND RECOVERY ANNEAL

REFERENCE: Gorynin, I. V., Nesterova, E. V., Nikolaev, V. A., and Rybin, V. V., **"Microstructure and Mechanical Properties of WWER-440 Reactor Vessel Metal after Service Life Expiration and Recovery Anneal,"** *Effects of Radiation on Materials: 17th International Symposium, ASTM STP 1270,* David S. Gelles, Randy K. Nanstad, Arvind S. Kumar, and Edward A. Little, Eds., American Society for Testing and Materials, 1996.

ABSTRACT: The microstructure of base and weld metals (st.15Kh2MFA) of Novovoronezh Nuclear Power Plant Units 1 and 4 reactor vessels was studied after service life expiration and recovery anneal by means of light metallography and transmission electron microscopy. The qualitative characteristics of flow structure were determined. The estimates were made for the contributions of different flows to the radiation hardening and its total value. The conclusion was made that the marked difference in the mechanical properties of irradiated weld and base metals can be caused either by different original structure conditions or by the difference of alloying and impurity elements content.

KEYWORDS: radiation, pressure vessel steel, hardening, embrittlement, microstructure.

An investigation of templets taken out of the Novovoronezh Nuclear Power Plant (NV NPP) Unit 1 reactor vessel showed an appreciable variation in irradiation embrittlement rate of a base metal and weld metal. As shown in Fig.1 the latter has been embrittled to a higher level. The irradiation hardening of both metals seems to be similar across the whole depth (h) of a reactor vessel wall, Fig.2. The annealing at 650° C for 2 h results in a recovery of properties of both materials. After this anneal, the yield strength values of the base metal and weld metal are approximately equal and remain the same across the wall depth. The similar changes of yield strength and hardness assume that under the neutron irradiation a similar radiation defect populations occur in both materials, but their influence on the radiation embrittlement is

[1] Director, senior research scientist, head of laboratory and division chief, respectively, Central research institute of structural materials "Prometey", St.Petersburg, 193167, Russia.

Copyright© 1996 by ASTM International www.astm.org

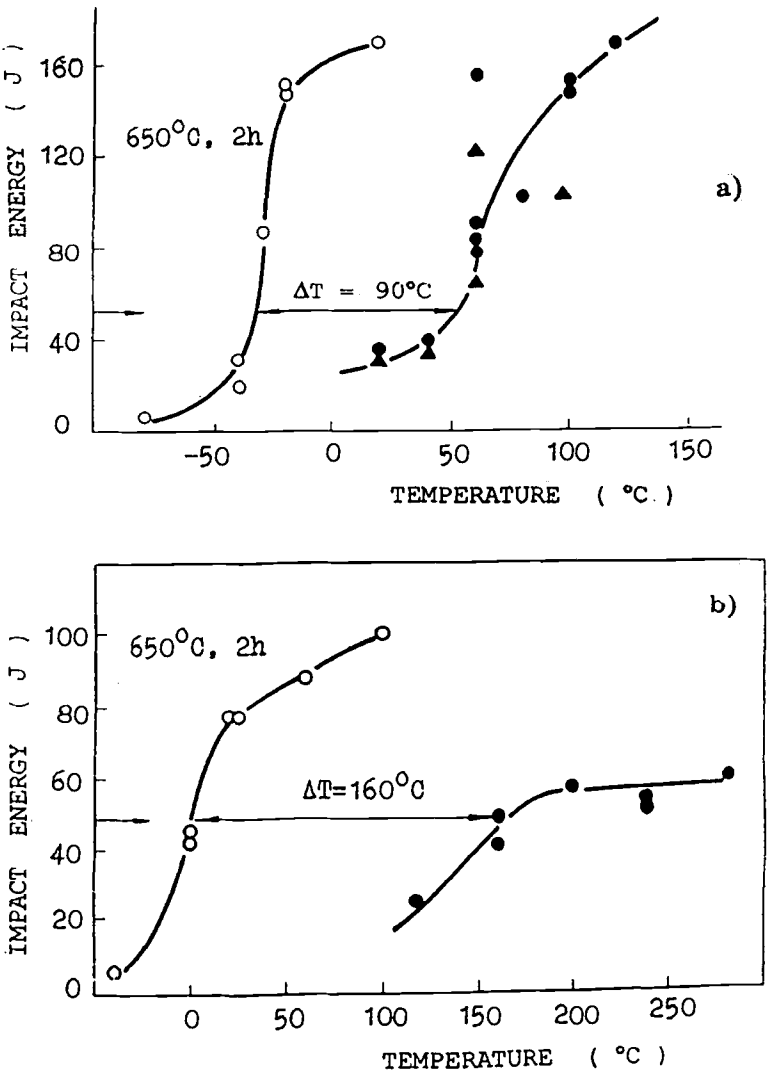


FIG.1 -- Radiation embrittlement and anneal of base (a) and weld (b) metals of NV NPP Unit 1 reactor vessel.

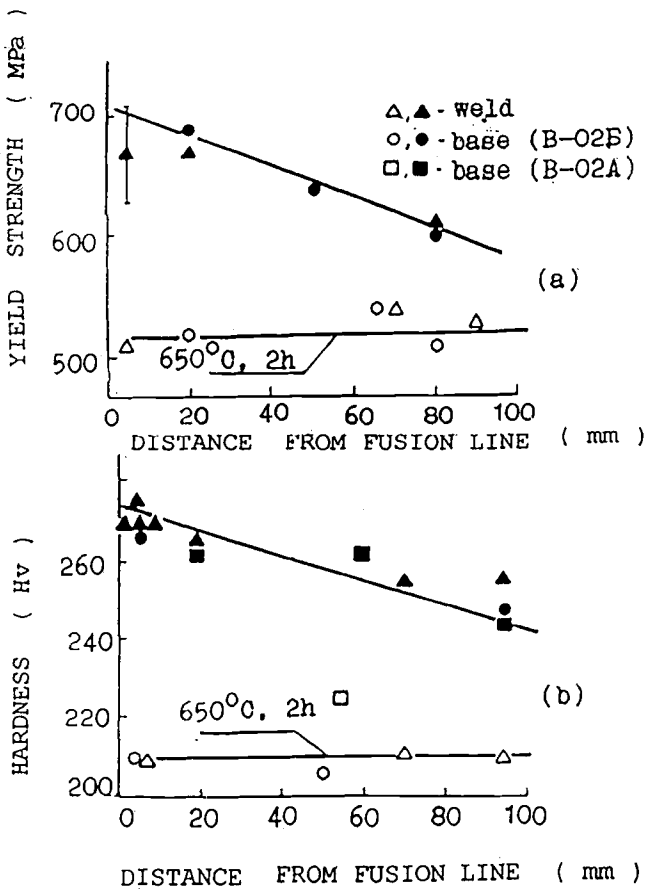


FIG.2 -- Distribution of yield strength and hardness on the depth of the wall of NV NPP Unit 1 reactor vessel.

different for the base and weld metal differing from each other by the initial microstructure and chemical composition.
To classify irradiation defects by type and importance, the microstructure of a base metal and a weld metal of NV NPP Unit 1 and 4 reactor vessels was investigated as irradiated and also after 470° C, 180 h and 650° C, 2 h annealing. The optical micrographs of base and weld metals are given Fig.3. The microstructures demonstrate the difference in the dispersitivity rate and ferrite content (the latter is higher in weld as compared to the base metal). But the morphological features of microstructure do not practically change under the annealing and this does not allow to establish the causes of mechanical property changes. Data on the irradiation damage were obtained by transmission electron microscopy methods.

EXPERIMENTAL PROCEDURE

The microstructure of base metal of Unit 1 NV NPP and weld metals of Units 1 and 4 NV NPP reactor vessels was investigated after the neutron irradiation at 250° C (Unit 1) and 270° C (Unit 4) up $3x10^{19}$ n/cm^2 and $6x10^{19}$ n/cm^2 for Unit 1 and Unit 4, respectively, as well as after the annealing 470° C, 180 h and 650° C, 2 h.
The chemical composition of the examined materials is given in Table 1. It is visible that they demonstrate some difference both in alloying elements and phosphorus content. The largest content of this impurity (0.036%) was observed in the weld metal of the Unit 4 . The smallest content of this impurity (0.015%) was demonstrated by the base metal of the Unit 1.

TABLE 1--Chemical composition of Novovoronezh Units 1 and 4 reactor pressure vessels

Material	Chemical composition, wt.%									
	C	Si	Mn	Cr	Ni	Mo	V	S	P	Cu
Base metal Unit 1	0.15	0.29	0.69	2.15	0.13	0.73	0.27	0.012	0.015	0.15
Weld metal Unit 1	0.06	0.41	1.06	1.47	0.12	0.48	0.20	0.014	0.033	0.12
Weld metal Unit 4	0.05	0.37	1.07	1.43	0.15	0.50	0.19	0.019	0.036	0.14

The TEM microstructure of irradiated materials was studied with EM-400T transmission electron microscope at an accelerating voltage of 120 kV. Thin foils were prepared in 20% $HClO_4$ + 80% C_2H_5OH electrolyte at 20...25 V. The chemical composition of inclusions 50 nm (and more) in size were determined by EDX methods. The single reflection method [3] was used for the identification of crystal lattice type and parameters of ultra fine precipitates.

RESULTS

The performed TEM investigations have shown that the microstructure of the irradiated base metal of Unit 1 NV NPP reactor vessel consists of

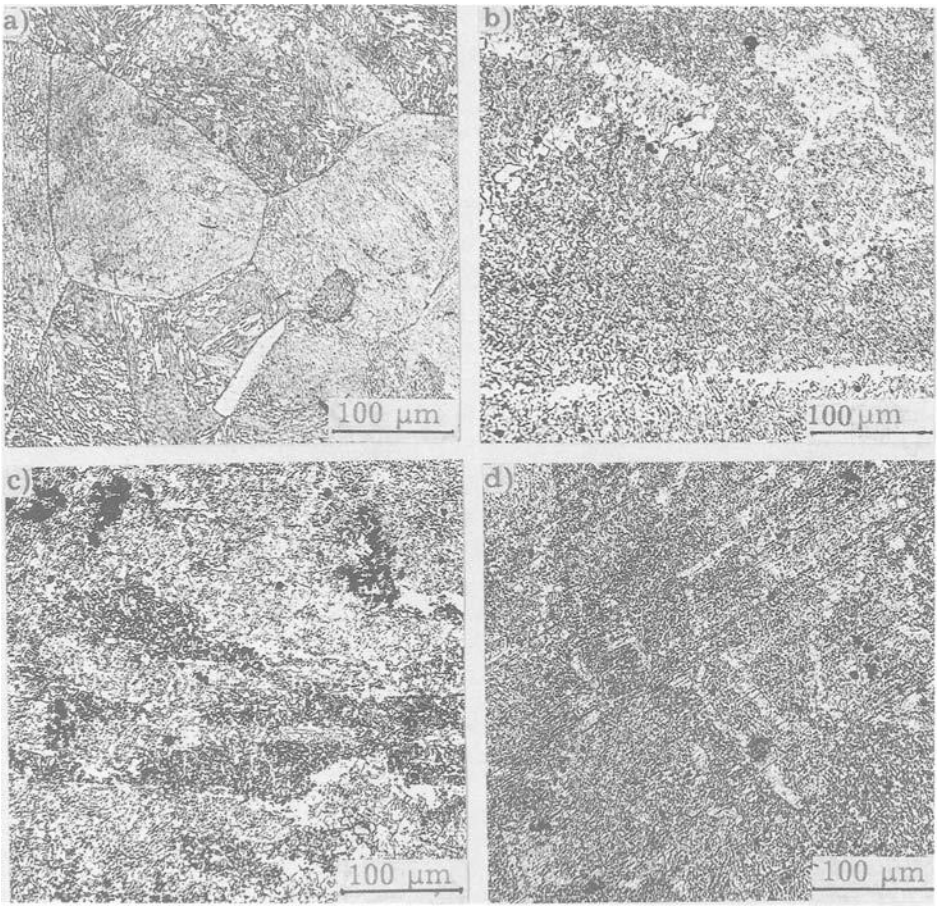


FIG.3-- Microstructure of irradiated base (a) and weld (b) metals of NV NPP Unit 1 and irradiated (c) and annealed at 650 C for 2 h (d) weld metal of NV NPP Unit 4.

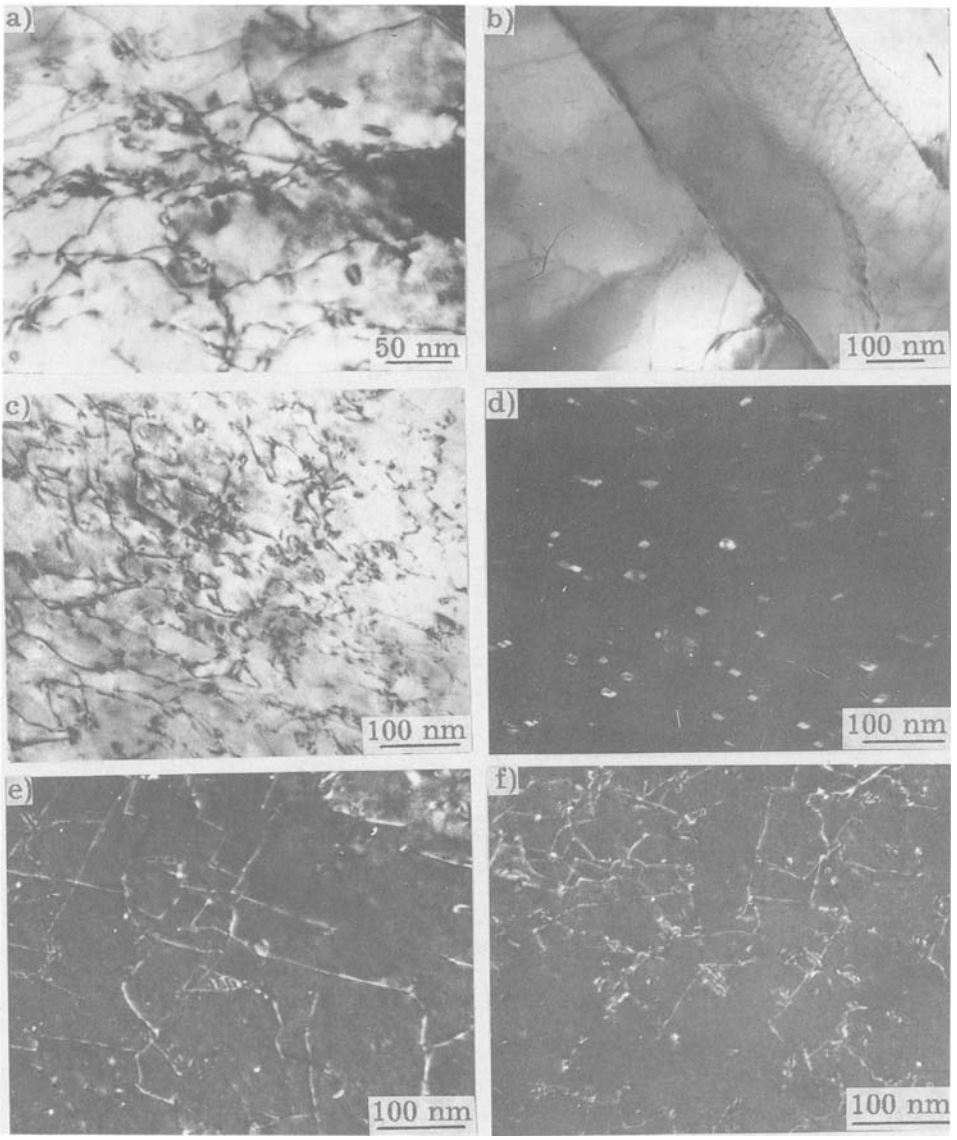


FIG.4--TEM microstructure of irradiated (a) and annealed at 470 °C for 180 hours (b) base metal and irradiated weld metals of NV NPP Unit 1 (c,d,f) and Unit 4 (e). d - dark field image of fine VC carbides, $g=(111)_{VC}$, e,f - dark field image of radiation defects, g=(110).

the lath 0.2...0.5 micron in width, which are combined in the 10...50 micron packets. The precipitates 0.1...0.5 micron in size were observed at the laths and packets boundaries. They were identified as M_7C_3 carbides. The mean value of dislocation density within the laths of irradiated base metal was determined equal to $2x10^{10}$ cm^{-2}. Besides that, the features observed in the irradiated base metal and which are affected by the anneal treatment, are as follows: a) "black dots" and small dislocation loops 5...10 nm size, b) the larger dislocation loops 20...40 nm in size, c) homogeneously distributed dispersed carbides 10...30 nm in size and d) carbide particles 30...40 nm in size on the lath boundaries (Fig.4a). The volume density of radiation defects and dispersed matrix carbides is given in Table 2.

TABLE 2--Microstructure parametrs of irradiated base and weld metal (st.15Kh2MFA)

Parameter	Base metal, NV NPP Unit 1	Weld metal, NV NPP Unit 1	Weld metal, NV NPP Unit 4
Dislocation density	$2x10^{10}$ cm^{-2}	$2x10^{10}$ cm^{-2}	$1.9x10^{10}$ cm^{-2}
Volume density of dispersed particles	$3x10^{14}$ cm^{-3}	$25x10^{14}$ cm^{-3}	$15x10^{14}$ cm^{-3}
Mean size of dispersed particles	20 nm	20 nm	15 nm
Volume density of "large" dislocation loops	$12x10^{14}$ cm^{-3}	$23x10^{14}$ cm^{-3}	$10x10^{14}$ cm^{-3}
Mean size of "large" dislocation loops	25 nm	30 nm	20 nm
Violume density of "black dots" and small dislocation loops	$40x10^{14}$ cm^{-3}	$24x10^{14}$ cm^{-3}	$35x10^{14}$ cm^{-3}
Irradiation temperature	250° C	250° C	270° C
Neutron fluence (>0.5 Mev)	$3x10^{19}$ n/cm^2	$3x10^{19}$ n/cm^2	$6x10^{19}$ n/cm^2

The annealing of base metal of NV NPP Unit 1 reactor vessel at 470° C, 180 h and at 650° C, 2 h does not change such microstructure parameters as the size of the laths and lath packets. It results in the reduction of dislocation density down to $5x10^9$ cm^{-2} as well as in the disappearance (annihilation) of the "black dots" and dislocation loops, in the disappearance of dispersed matrix carbides and some coarsening (from 30...40 up 50...70 nm) of dispersed precipitates located at the lath and packet boundaries (Fig.4b).
The microstructure of weld metals of NV NPP Unit 1 and 4 reactor vessels consists of microregions 2...10 micron in size fragmented sometimes by low angle dislocation boundaries. The precipitates of different shape and dispersion rate were observed in irradiated weld metal. There are

spherical (Mn,Si) inclusions 0.5...1.0 micron in size, elongated particles of V, Mo and Cr carbides 0.1...0.2 micron in size on the low angle and high angle boundaries and a lot of dispersed matrix carbides 10...40 nm in size (Fig.4d). The dispersed matrix carbides were identified by diffraction methods as VC carbides (or V(C,N) carbonitrides). The crystallographic analysis showed that the following orientation relationship is valid for VC precipitates with 1° of precision:

$$(100)_{VC} \parallel (100)_{\alpha\text{-Fe}} ; \ [011]_{VC} \parallel [010]_{\alpha\text{-Fe}} ; \ [011]_{VC} \parallel [001]_{\alpha\text{-Fe}}$$

The volume density of dispersed matrix carbides is determined as 2.5×10^{15} cm^{-3} and 1.5×10^{15} cm^{-3} for the weld metals of Unit 1 and Unit 4, respectively. It is to mention, that the individual dispersed particles in the weld metal of Unit 1 were identified as V_3P phosphides characterized by the tetragonal lattice with the parameters a=0.9387 nm, c=0.4756 nm. The dislocation density is determined as approximately 2×10^{10} cm^{-2} for both weld metals in irradiated condition. In addition, the "black dots" type defects and small dislocation loops 5...10 nm size as well as larger dislocation loops 20...40 nm decorated by MC precipitates or without precipitations were observed in the irradiated weld metals (Fig.4c, 4f). The volume density of dislocation loops is given in Table 2. At certain diffraction conditions the strip contrast was observed at the larger dislocation loops (Fig.4e, 4f). This indicates the existence of stacking faults in the loop plane and allows to identify them as partial dislocation loops.

The annealing of weld metal of NV NPP Unit 1 at 650° C, 2 h does not change microstructure parameters such as the size of misoriented microregions and the size and volume density of (Mn,Si) inclusions. It results in the annihilation of the "black dots" and dislocation loops of both types. Only a slight dislocation density decrease (from 2×10^{10} cm^{-2} to 1.6×10^{10} cm^{-2}) is observed. The fine MC carbides are present within the grains as before. However, their dimensions increase up to 30...40 nm, and the volume density is decreased (Table 3). These changes as a result of the thermal exposure allow to conclude that the matrix carbide coalescence, i.e. irradiation-induced precipitations formed at the time of operation, are thermally unstable at 650° C. The analysis of high and low angle boundaries shows the increase of intergrain precipitation density. Most of them were identified as M_7C_3 carbides.

The annealing of weld metal of NV NPP Unit 4 at 470° C for 180 h and 650° C for 2 h results in similar structure changes: slight decrease of dislocation density, decrease of matrix carbide density (up to 6×10^{14} cm^{-3} and 3×10^{14} cm^{-3} after the anneals at 470° C and 650° C, respectively), the annihilation of the "black dots" and small dislocation loops, the drastic decrease of volume density of "larger" dislocation loops (from 1×10^{15} cm^{-3} in as-irradiated condition to $1...2 \times 10^{14}$ and 5×10^{13} after the anneals at 470° C and 650° C, respectively).

TABLE 3--Microstructure parametrs of irradiated and annealed (650° C, 2h) base and weld metal (st.15Kh2MFA)

Parameter	Base metal, NV NPP Unit 1	Weld metal, NV NPP Unit 1	Weld metal, NV NPP Unit 4
Dislocation density	0.5×10^{10} cm^{-2}	1.6×10^{10} cm^{-2}	1.5×10^{10} cm^{-2}
Volume density of	-	4×10^{14} cm^{-3}	3.3×10^{14} cm^{-3}

dispersed particles			
Mean size of dispersed particles	-	35 nm	24 nm
Volume density of "large" dislocation loops	-	-	0.5×10^{14} cm^{-3}
Mean size of "large" dislocation loops	-	-	50 nm
Violume density of "black dots" and small dislocation loops	-	-	-

DISCUSSION

The results of microstructure investigation (Table 2,3) allow to evaluate the different flows contributions to radiation hardening and to calculate its total value. Let's consider an example of such a calculation for base and weld metals of NV NPP Unit 1 reactor vessel. In accordance with [4,5] the yield strength σ_{02} of ferritic steels can be written as

$$\sigma_{02} = \sigma_0 + \sum_{i=1}^{3} \sigma_i + \left(\sum_{i=4}^{5} \sigma_i^2\right)^{1/2} \quad (1)$$

where $\sigma 0$ is lattice friction, $\sigma 1$ - hardening by high angle and low angle boundaries, $\sigma 2$, $\sigma 3$ - solid solution hardening by interstitial and substitutional elements, $\sigma 4$ - dislocation hardening, $\sigma 5$ - hardening by dispersed particles.
In accordance with the microstructure investigation results let's supplement the root expression in the formula (1) with two additional terms σ_6 and σ_7 for the contributions to radiation hardening by "large" dislocation loops and "black dots" (or small dislocation loops), respectively, and let's write the yield strength of irradiated pressure vessel steels as

$$\sigma_{02} = \sigma_0 + \sum_{i=1}^{3} \sigma_i + \left(\sum_{i=4}^{7} \sigma_i^2\right)^{1/2} \quad (2)$$

As irradiation at 260...300° C does not change the dispersion rate of ferritic steels, related with the division of their microstructure into misoriented microcrystals, and as it does not practically affect solid solution hardening, the yield strength can be represented as a sum of two contributions

$$\sigma_{02} = \sigma^* + \Delta\sigma \quad (3)$$

where $\sigma^* = \sigma_0 + \sum_{i=1}^{3} \sigma_i$ is constant, in practice, and $\Delta\sigma = \left(\sum_{i=4}^{7} \sigma_i^2\right)^{1/2}$ is changed under the effect of irradiation.

We assume as initial microstructure state the condition which is generated in analyzed materials by the annealing at 650° C, 2 h. We evaluate σ_4 and σ_5 contributions by the equations

$$\sigma_4 = \alpha G b \rho^{1/2} \tag{4}$$

$$\sigma_5 = G b (\rho_p d_p)^{1/2} \tag{5}$$

where a = 0.4 [6], ρ - dislocation density, ρ_p, d_p - volume density and mean size of dispersed particles. We obtain on the base of experimental yield strength data the values $\sigma^* = 458$ MPa and 383 MPa for the base metal and weld metal, respectively (Table 4). The difference of unchangeable contribution values, σ^*, for the base and weld metal is in agreement with the observed variance of chemical composition and structure dispersion. Using the calculated σ^* values and data on the structure of irradiated materials, one can evaluate σ_{02} values of the base and weld metals irradiated in service condition.
The comparison of Tables 2 and 3 shows that in good agreement with previous results [7] the irradiation induced microstructure changes both in base and weld metal of NV NPP reactor vessels consist in some dislocation density change and in the appearance of: a) flaws of the "black dots" type (impurity clusters or small dislocation loops), b) dislocation loops 20...40 nm in size, c) dispersed particles.
Having evaluated, σ_5 by eq. (4,5) and σ_6, σ_7 contributions by

$$\sigma_i = 2\beta_i G b (\rho_i d_i)^{1/2} \tag{6}$$

and substituting the typical value $\beta_7 = 0.4$ for intermediate barriers of impurity clusters type and fine prismatic loops and $\beta_6 = 0.65$ for flow's loops [8], one determines the σ_{02} values for the irradiated base and weld metal equal to 668 MPa and 675 MPa, respectively. These values are in agreement with the experimental data (Table 4).
It should be noted that the same total values of radiation hardening of the base and weld metals of NV NPP Unit 1 determined both experimentally and by the analysis of real structural conditions, in practice, are the combinations of essentially differing contributions of similar flows. This can be the reason why despite similar hardening the irradiated base and weld metal demonstrate an essential difference in their embrittlement rates (Fig.1). Obviously, this effect is related both to the quantitative and qualitative changes of irradiation induced microstructure in the weld and base metal. Primarily a preferential formation in weld metal of fine MC carbides as well as partial dislocation loops can refer to them. This difference can be caused either by different original microstructure conditions of the base and weld metal or by different content of alloying elements (Cr,V) and dissolved impurity elements including interstitials (C,N) but primarily phosphorus. In accordance with [1] the latter can additionally stabilize radiation defect combinations and form intercrystalline segregations. Taking into account the information about the phosphorus enrichment of VC carbides, obtained by Burke and Miller using atom probe field ion microscopy methods [9], it is reasonable to assume that this impurity may influence the process of fine carbide formation as well as segregate on ferrite-carbide interfaces and cause therefore the cleavage strength reduction.

TABLE 4--Contributions of different flows to radiation hardening of base and weld metals of NV NPP Unit 1 reactor vessel

σ_i	Base metal		Weld metal	
MPa	$3x10^{19}$ n/cm^2	650° C, 2 h	$3x10^{19}$ n/cm^2	650° C, 2 h
σ_4	114	57	114	102
σ_5	49	-	143	76
σ_6	144	-	214	-
σ_7	102	-	79	-
$\Delta\sigma$	210	57	292	127
σ^*	458	458	383	383
σ_{02}	668	515	675	510
$\sigma_{02\ exp}$	690	515	675	510

CONCLUSIONS

The same values of radiation hardening of the base and weld metal of pressure vessel steel 15Kh2MFA type, as determined both experimentally and by the analysis of real microstructure conditions, is essentially the same, but it stems from the combination of considerably differing contributions of similar flows. This can cause essential differences in the embrittlement of these materials. In particular, the preferential formation in the weld metal of fine MC carbides may be considered as one of the reasons for the higher embrittlement rate of the weld as compared to the base metal.

REFERENCES

[1] Alekseenko, N.N., Amayev, A.D., Gorynin, I.V. and Nikolaev, V.A., "Radiation damage of water-water reactors vessel steel", Energoizdat, Moscow, 1981. (in Russian)
[2] Nikolaev, V.A., Rybin V.V. and Badanin V.I., "About the impurities role in the radiation embrittlement of low-alloyed steels, Atomnaya energiya, 1979, vol.47, pp.21-25. (in Russian)
[3] Rybin, V.V., Rubzov, A.S. and Nesterova, E.V., "The single reflection method and its using for electron microscopy analysis of dispersed phases", Zavodskaya laboratoriya, 1982, ' 5, pp.21-26. (in Russian).
[4] Kocks, Ju.F., The statistical theory of alloys hardening, Fizika prochnosti i plastichnosti, Moscow, Metallurgiya, 1972, p.111.
[5] Malyshevckiy, V.A., Rybin, V.V., et al., " Structural transformations by the secondary hardening of low-carbon alloyed steels, Fizika metallov, 1976, vol.41, pp.796-805. (in Russian)
[6] Key A.S. Direct observations of Imperfections in crystals. Newrick and Wernick, New-York, 1962.
[7] Keilova ,E. and Kocik, J., "Radiation damage structure of VVER type RPV steels, Journal of Nuclear Materials, vol.172, 1990, pp.26-129.

[8] Ibragimov, Sh.Sh. and Kirsanov, V.V., "Radiation hardening of metals", Radiation defects in metal crystals, Alma-Ata, 1978, pp.64-77. (in Russian).
[9] M.G.Burke and M.K.Miller. Solute clustering and precipitation in pressure vessel steels under low fluence irradiation condition. J. de Physique, 49-C6, 1988, pp.283-288.

Philip J.E. Bischler[1] and Robert K. Wild[2]

A MICROSTRUCTURAL STUDY OF PHOSPHORUS SEGREGATION AND INTERGRANULAR FRACTURE IN NEUTRON IRRADIATED SUBMERGED-ARC WELDS

REFERENCE: Bischler, P. J. E. and Wild, R. K., **"A Microstructural Study of Phosphorus Segregation and Intergranular Fracture in Neutron Irradiated Submerged-Arc Welds,"** *Effects of Radiation on Materials: 17th International Symposium, ASTM STP 1270,* David S. Gelles, Randy K. Nanstad, Arvind S. Kumar, and Edward A. Little, Eds., American Society for Testing and Materials, 1996.

ABSTRACT: Accelerated irradiation experiments have been carried out on submerged-arc welds to obtain validation of trend curves built up from surveillance results. This was done by withdrawing surveillance specimens and re-irradiating them in higher flux positions. One batch, from weld HS, showed a significantly higher increase in the Charpy ΔT_{40J} value than that for weld LS at a similar dose. Work done to explain this difference is described in this paper.

Selected Charpy specimens were examined using a shielded scanning electron microscope to determine the fracture modes present. Regions of mixed cleavage, micro-void coalescence (MVC) and intergranular failure (IGF) were found on HS weld specimens fractured in the transition region. The IGF was confined to certain regions within each weld bead. Significantly less IGF was found on LS weld specimens. Upper shelf specimens from both welds showed a fully ductile MVC fracture structure.

Sub-fracture surface 'matchstick' specimens were removed from embrittled regions and fractured within a scanning Auger microscope. IGF occurred in these specimens, and phosphorus was found to be the main grain boundary segregant. The levels of phosphorus increased with increasing neutron dose. No other embrittling element was consistently found at any significant level, but carbon was also found on grain boundary surfaces in some cases. The grain boundary coverage of phosphorus was determined for each weld at several neutron dose levels. These results have been compared with previous data obtained from surveillance dose specimens and some start-of-life data.

KEYWORDS: pressure vessels, irradiation, embrittlement, intergranular fracture

1 Nuclear Electric plc, Berkeley Technology Centre, Berkeley, Gloucestershire GL13 9PB, Great Britain

2 University of Bristol, Interface Analysis Centre, 121 St Michael's Hill, Bristol, BS2 8BS. Great Britain

Copyright© 1996 by ASTM International www.astm.org

In the UK, surveillance data on submerged-arc welds have from time to time been augmented by accelerated irradiation experiments, e.g. [1]. These experiments have involved either the irradiation of virgin materials, or the re-irradiation of previously exposed surveillance specimens. Re-irradiation experiments have the merits not only of providing results on welds previously tested in the surveillance programme, but also of using a starting material whose microstructural condition, especially in respect of pre-existing irradiation-induced copper precipitates, allows for a simplification in their interpretation [2].

In a recent set of re-irradiation experiments, specimens from a particular weld, HS, showed a significantly higher increase in Charpy ΔT_{40J} value than that for another weld, LS, irradiated to a similar dose. Preliminary work established that both irradiated HS and LS welds exhibited intergranular fracture features. This paper describes work done, using fractographic examinations and scanning Auger microscopy (SAM), to determine in detail why this difference in mechanical properties occurred.

MATERIALS AND TEST SPECIMENS EXAMINED

The materials examined were from surveillance specimens cut from weld HS and weld LS. Bulk chemical compositions are given in Table 1, in which the analysis given for LS is from a specimen cut from the same weld but about half an inch further from the surface.

Table 1 Bulk chemical analyses, wt%

Weld	C	Si	Mn	S	P	Ni	Cr	Mo	Cu
HS	0.067	0.55	1.52	0.019	0.040	0.09	0.09	0.02	0.28
LS	0.080	0.58	1.42	0.036	0.039	0.12	0.16	0.11	0.30
Combined Compositions of Surveillance and RPV Welds									
Mean	0.09	0.52	1.49	0.036	0.031	0.10	0.09	0.04	0.23
$\pm 1\sigma$	0.02	0.12	0.14	0.007	0.008	0.03	0.03	0.03	0.04

A comparison is made in the Table with the average composition of a large number of surveillance and RPV submerged-arc welds.

All the specimens were subjected to a surveillance exposure, with doses in the range 120-200 x 10^{-5} dpa, followed by accelerated re-irradiations to higher doses.

The total doses to which the specimens were exposed, along with the irradiation times, temperatures and measured Charpy T_{40J} temperature shifts, referenced to the unirradiated value, are shown in Table 2.

Table 2 - Accelerated irradiation data

Weld	Irr. Times (Days) 1st Irr.	2nd Irr.	Irr. Temp. (°C) 1st Irr.	2nd Irr.	Total Dose (dpa)	ΔT_{40J} (°C)
HS	6545	103	198	260	121.4×10^{-5}*	133
HS	7432	57	198	292	562.7×10^{-5}	191
HS	7432	21	198	311	1010.7×10^{-5}	258
LS	7689	-	198	-	995.6×10^{-5}	185

* Surveillance exposure only

EXAMINATION TECHNIQUES

Fractography

Selected Charpy specimens were examined using a JEOL 6100 shielded scanning electron microscope (SSEM). Each specimen, oriented so that the machined notch was located at the bottom of the image screen, was photographed at a magnification of about 12 times. This allowed the location of higher magnification images to be identified and provided a high resolution image with good depth of field for fibrosity measurements. The microscope was then used to identify the boundaries between regions of shear and brittle fracture mode. Within each fracture mode region any obvious macroscopic changes in fracture appearance were also identified, such as changes from one weld bead to another. The approximate grain size variation within the fracture was also noted as either fine (under 20μm in diameter), medium (20 to 60μm) or coarse (greater than 60μm).

The central region of the fracture surface was then examined at higher magnifications to identify different fracture mechanisms, e.g. ductile micro-void coalescence (MVC), integranular fracture (IGF) and cleavage. Typical images were taken of each fracture region at an appropriate magnification to show the dominant failure modes. Additional photographs were also taken of any unusual features.

A study was carried out to quantify the proportion of cleavage, IGF and ductile MVC present on the fracture surfaces. Due to the large grain size variation within each weld bead (this could vary between 10μm to 250μm) and the fact that more intergranular fracture was found in the fine grained material, only fine grained areas were measured. Thus the results indicate the worst situation.

The work was carried out using a motorised stage on the SSEM, capable of moving set distances in the X and Y directions. A region on the fracture surface measuring at least 0.5mm by 0.5mm was identified which contained grains no larger than 20μm in diameter. Within submerged-arc welds of this type the minimum grain size rarely falls below 8μm, so it may be taken that within such a region a good approximation for the variation was 10 to 20μm.

Once a suitable region was identified a high magnification image (at 4000 times) was obtained at the top left hand corner. A set of cross wires was called up on the TV screen to locate the centre point of the image. The region under this point was examined, at greater magnification if necessary, to classify the fracture mode. Four categories were used; cleavage, IGF, ductile MVC and unidentified. The fourth category included any points where no particular fracture mode could be positively identified, areas of dirt/oxide or deep fissures. When the fracture mode had been noted the SEM image was returned to the magnification of 4000x and the specimen stage was moved to the right by 20μm for examination of the next point. This process was repeated until 25 points had been examined. Then the specimen stage was moved down 20μm and the next 25 points examined stepping to the right. Thus by continuing this left-down-right-down sequence a square grid 500μm by 500μm was examined made up of 625 separate points. These data were subsequently analysed to give the mean coverage of each fracture mode.

After SEM examination the specimens were sectioned and mounted for optical metallographic examination. The samples were cut at right angles to the fracture face, to produce a section through the fracture, from the machined notch of the Charpy to the final part of fracture. The cut was made at the mid-section of the specimen thickness. This allowed a section of the fracture surface to be compared to the underlying grain structure.

Auger Examinations

Auger test material was obtained by cutting a 2mm thick slice from each fractured Charpy specimen, after removal of the fracture surface. These slices were then cut into matchstick specimens measuring 2 x 2 x 10mm containing a central notch to initiate fracture in the scanning Auger microscope (SAM). It should be noted that each matchstick specimen was cut across the width of the Charpy sample and notched to initiate fracture. Thus the orientation of the fracture plane in the matchstick specimen was at 90° to the Charpy fracture plane.

The matchstick specimen was ultrasonically cleaned in de-ionised water, followed by methanol and finally iso-propanol. It was then mounted in a holder for impact fracture, modified to fit the Perkin-Elmer 595 SAM located at the Interface Analysis Centre at Bristol University (Fig. 1). The two halves of the holder were connected by a length of copper wire 0.5mm in diameter to enable both halves of the sample to be removed following fracture. The holder was introduced to the SAM in the normal manner and was positioned in the jaws of the impact fracture stage. In order that a good vacuum could be achieved prior to testing, and contamination rates

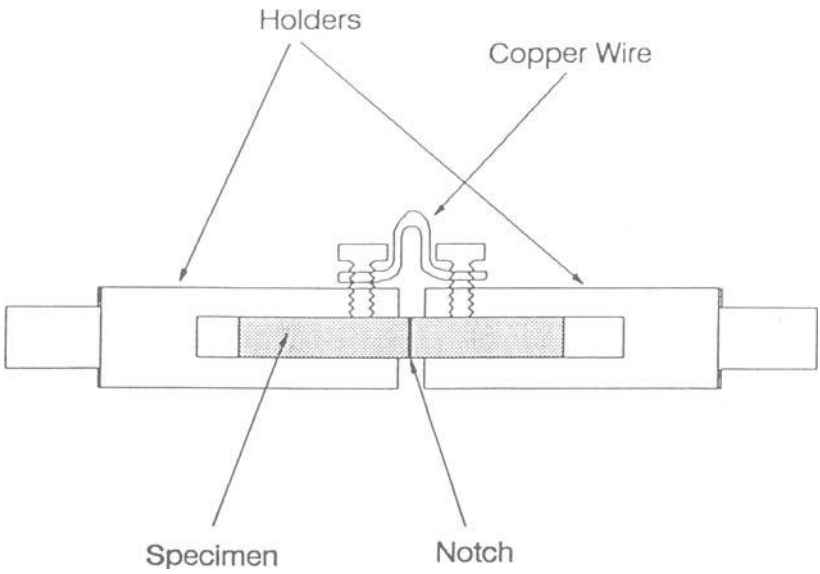


FIG. 1 Sample and Holder for Fracture of Active Specimens

reduced, the sample was left in the SAM for a minimum period of 16h. When the vacuum had achieved $< 10^{-8}$ Pa, the sample was cooled by passing liquid nitrogen through the fracture stage. To ensure that the sample temperature had equalised with that of the stage, cooling continued for one hour. The sample was then fractured by impact, the two halves separated, and the sample moved into position for analysis.

A freshly exposed fracture surface will contaminate due to the arrival of hydrocarbon, water and oxygen molecules in the chamber. At pressures $< 10^{-8}$ Pa, contamination does not seriously affect the results for 2-3 hours. However, it is important that all analytical measurements are obtained within this period. A standard procedure was adopted to obtain measurements from a minimum of 20 segregated points from three separate regions on each matchstick within the time period. As soon as the sample was positioned for analysis an area survey was recorded. This identified the elements present and was used to obtain settings for the phosphorus element maps. As will be seen later phosphorus was the only segregated element to be detected in any significant quantity. A phosphorus map of the region was then quickly obtained and used to identify 6 high phosphorus points for analysis. One point shown on the map to have no segregated phosphorus was also analysed as a control. After the spectra had been recorded a series of secondary electron images of the surface were obtained together with an image identifying the points which were analysed. This procedure was carried out on three regions per sample. Finally, a low magnification high resolution map was recorded from the surface to determine the extent of phosphorus segregation over a large proportion of the fracture surface.

Spectra obtained during the analysis were used to produce quantitative information concerning the segregation of phosphorus to interfaces within the bulk sample. In this instance the phosphorus (120 eV) to iron (703 eV) peak height ratio is used to gain a measure of phosphorus segregation expressed in monolayers.

Following the completion of the analysis, the sample was removed from the SAM, transferred to a conventional scanning electron microscope (SEM) and examined in greater detail. After examining the specimen at low magnification more detailed work concentrated on the actual sites analysed in the SAM. High resolution micrographs were obtained from a number of points, both those showing high phosphorus and those used as controls.

RESULTS

Fractography

At low magnification, the specimens showed the typical features of fractured Charpy samples. Specimens fractured in the ductile-to-brittle transition region showed a "crystalline" brittle centre area, surrounded by a ductile "picture frame", with shear lips on either side. All specimens, whatever the weld or the dose, when tested in the ductile upper shelf region, showed the usual 100% fibrous appearance.

Close examination at high magnifications of the brittle areas of transition region specimens of weld HS revealed that the fracture modes were a mixture of cleavage, ductile MVC and IGF. A typical fractograph from an area which failed mainly by cleavage, but with small ductile MVC regions, is shown in Fig. 2. Such fractographs

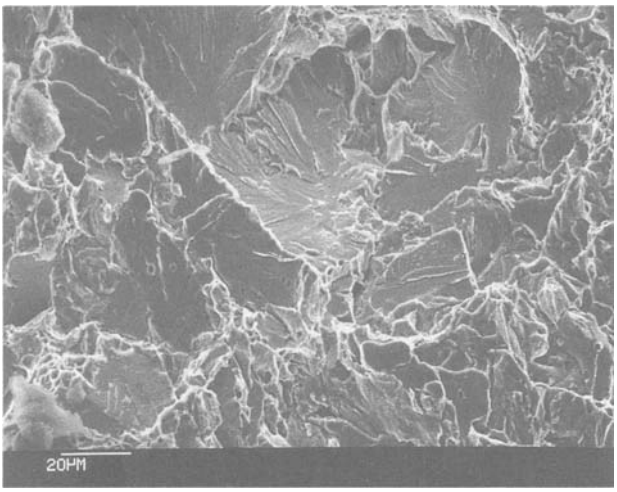


FIG. 2 Region of Weld HS. Cleavage fracture with small MVC areas

were obtained in all larger-grained regions of the specimens. In finer-grained regions of weld HS specimens, however, it was quite common to find (a) cleavage facets divided up by irregular, apparently intergranular cracks which extended into the specimen, along with small areas of fine ductile MVC, or (b) areas with a combination of cleavage, intergranular facets and small-scale MVC. Fig. 3 shows a fine-grained region containing intergranular facets. High magnification examination of specimens of weld HS which had been tested in the upper shelf region failed by a mixture of ductile shear (in the shear lip areas) and ductile MVC in the centre of the specimen. Fig. 4 shows an example of ductile MVC in a weld HS sample. In no case was any other fracture mode seen in upper shelf specimens.

Specimens of weld LS, which exhibited the lower Charpy shifts, were examined in the same way, and although the same pattern was found as depicted in Figs. 2 and 4 for weld HS, it was qualitatively clear that there was considerably less incidence of either intergranular cracking or intergranular fracture facets.

To examine the trends more quantitatively, the 625-point sampling method described earlier was adopted, and the results are given in Table 3.

Table 3 Quantitative fractography

Weld	Total Dose (dpa)	Cleavage (%)	IGF (%)	MVC (%)	Other (%)
HS	121.4×10^{-5}*	28.5	49.3	10.9	11.3
HS	562.7×10^{-5}	21.1	46.4	14.7	17.8
HS	1010.7×10^{-5}	17.0	49.4	16.0	17.6
LS	995.6×10^{-5}	30.9	29.4	23.0	16.7

* Surveillance exposure only

It is concluded from these results that HS weld specimens showed almost 50% of IGF in fine-grained regions, whilst LS weld showed about 30%.

The sections cut for optical microscopy showed an irregular fracture surface whose irregularities were on the scale of the grain size as illustrated by Fig. 5a. A number of secondary cracks and fissures extended into the metal from the surface. Some of these were straight cleavage cracks, while the majority were more angular, and characteristic of intergranular cracking. In the etched condition, it was possible to confirm this (Fig. 5b), and on sections examined in the SSEM a very clear picture could be obtained (Fig. 6).

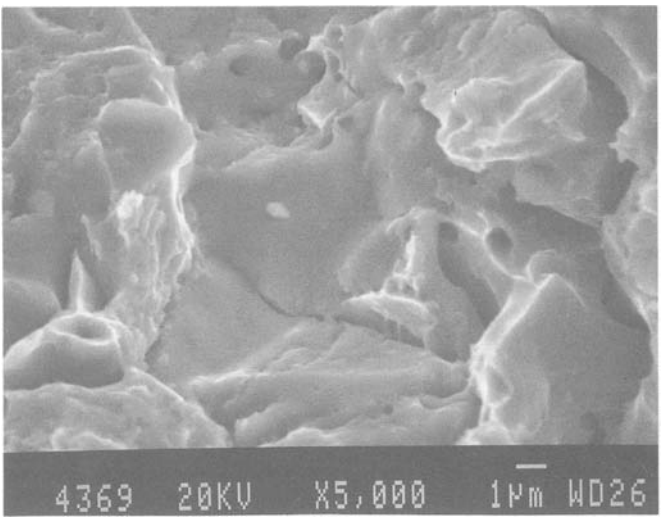


FIG. 3 Fine-grained Region of Weld HS; Intergranular Facets

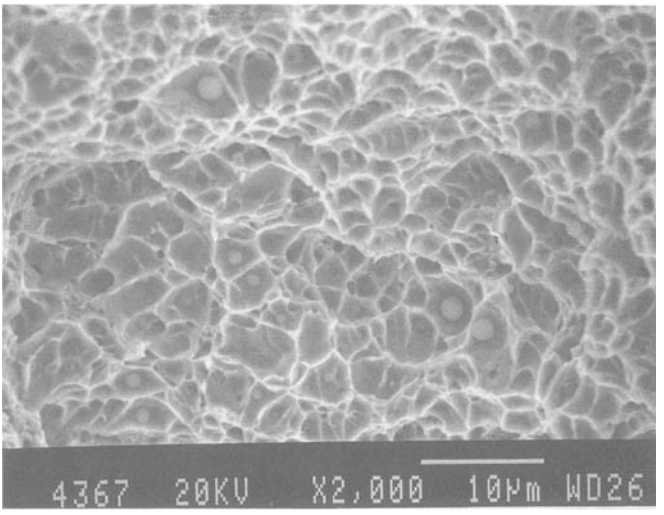


FIG. 4 Region of Weld HS; Ductile MVC

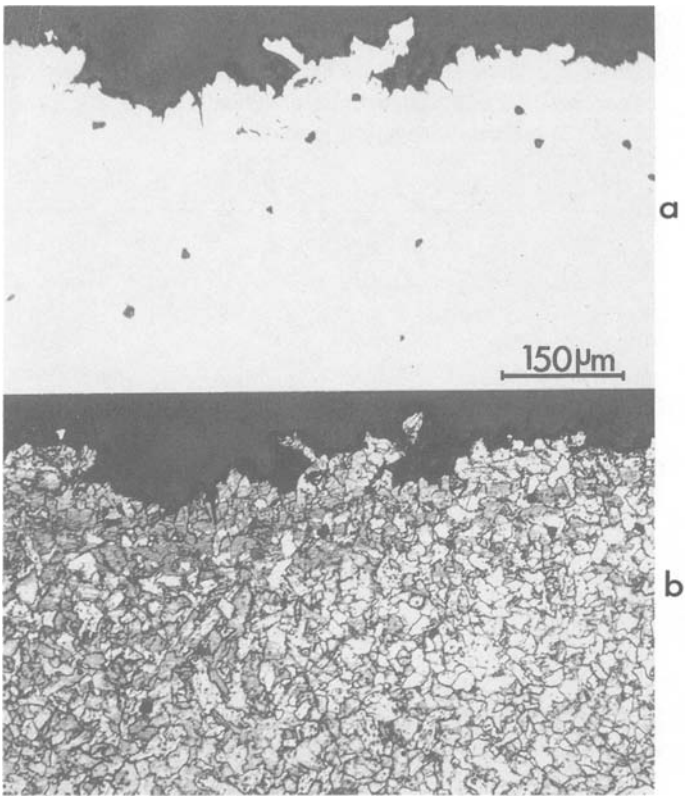


FIG.5 Optical Section of Weld HS Specimen. (a) Unetched (b) Etched

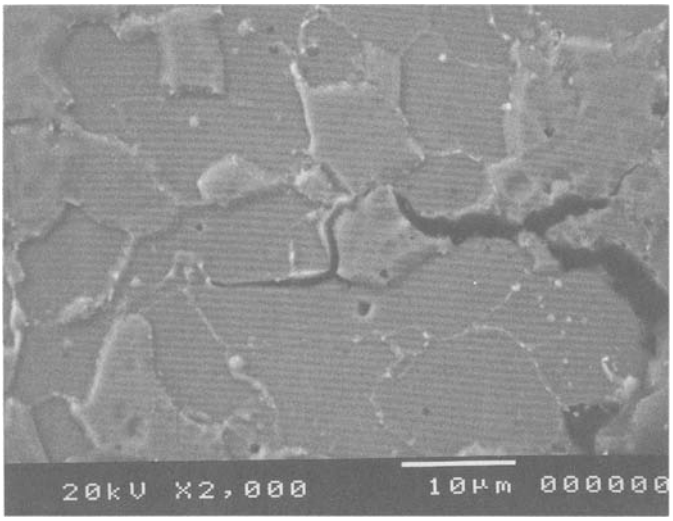


FIG.6 Section of Weld HS specimen examined in SEM

Auger Examinations

The most likely mechanism for inducing IGF is segregation of impurity or trace elements to grain boundaries, even though classical temper embrittlement is not usually thought of as occurring in carbon-manganese steels at these temperatures. For this reason, SAM examinations of matchstick specimens from welds HS and LS were undertaken using the method described earlier.

The only trace or impurity element present in significant proportions on the fracture surfaces of any of the specimens examined was phosphorus, and its distribution was patchy. Careful examination confirmed that the phosphorus-rich areas coincided with grain boundary facets, while phosphorus free areas coincided with cleavage facets and ductile MVC.

An Auger spectrum recorded from a phosphorus-rich region of fracture surface of a high-dose weld HS specimen is shown in Fig. 7, together with a spectrum from a low phosphorus region, Fig. 8. In addition to the phosphorus signal on Fig. 7, there is also a small carbon signal at 272 eV, whose shape may indicate the presence of a carbide. Fig. 8 also shows a small signal at 505 eV from the KLL transition in oxygen, and this signal frequently increased with time, indicating surface contamination. No other elements were found in significant proportions on the fracture surface.

A very similar picture was found in matchsticks taken from weld LS exposed to a similar dose. Here again the only trace or impurity element found in any significant proportion was phosphorus, but in the case the phosphorus peak and hence segregation levels were less than in weld HS.

By measuring the peak height of the phosphorus signal and the peak height of the iron signal, the surface coverage of phosphorus, expressed in monolayers, can be determined using the method and correction values published in [3]. This was done for all the specimens examined, and the results obtained are given in Table 4.

Table 4 Auger measurements of phosphorus segregation

Weld	Total Dose (dpa)	Phosphorus Coverage (Monolayers) (Mean of three 6-point areas)
HS	121.4×10^{-5}*	0.28
HS	562.7×10^{-5}	0.31
HS	1010.7×10^{-5}	0.42
LS	995.6×10^{-5}	0.29

* Surveillance exposure only

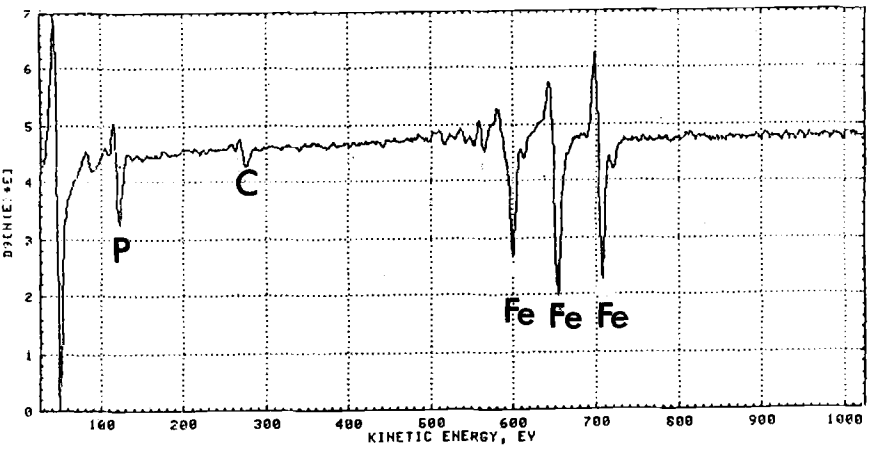


FIG. 7 Auger spectrum from phosphorus segregated region on Weld HS

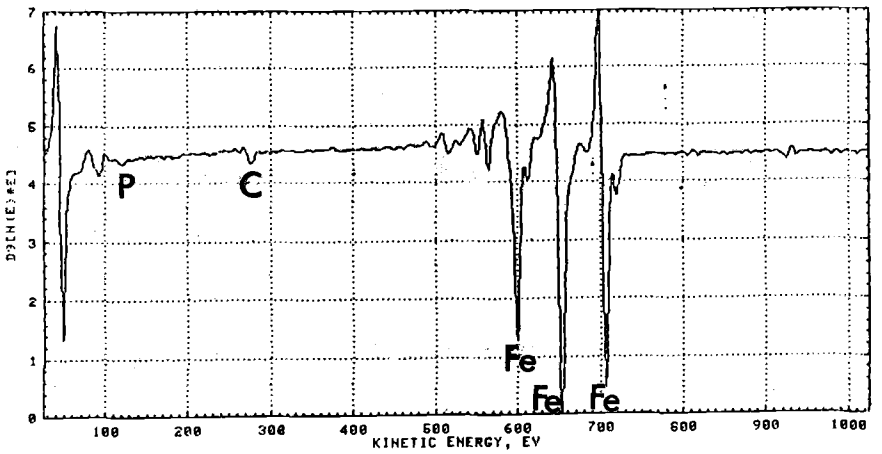


FIG. 8 Auger spectrum from region low in phosphorus on Weld HS

These results indicate once again a clear distinction between weld HS and weld LS, with the former showing significantly more segregation than the latter for almost identical doses of approximately 1000 x 10^{-5} dpa. In addition, the degree of segregation evident in the three HS specimens shows a systematic increase with dose.

DISCUSSION

Comparison with unirradiated welds

A number of comparable unirradiated submerged-arc welds have been examined both fractographically and in the SAM [4]. These showed IGF in the fine-grained regions ranging from 0.2.% to 1.3%, and phosphorus segregation levels of 0.06 to 0.13 monolayers. Thus, the quantitative measurements of IGF and phosphorus coverage reported here show consistently higher values than obtained in the unirradiated material, indicating that both IGF and segregation have been enhanced by irradiation exposure. This conclusion is consistent with the segregation data in Table 4, which show an increase with dose in weld HS in the SAM matchstick specimens. On the other hand, the % IGF data on the HS Charpy specimens in Table 3 do not show a systematic increase with dose. It is speculated that this may be due to differences in the average grain size of the weld area sampled - it being clear that in a given specimen the proportion of IGF increases as smaller grain sizes are sampled.

Irradiation Enhancement of Phosphorus Segregation

The work in this paper stimulated the development of theoretical models for the enhancement of phosphorus segregation by irradiation-enhanced concentrations of point defects [5]. These models clearly demonstrated the potential for the type of dependence of phosphorus segregation on dose exhibited in the present results, and also described quite well these and other experimental phosphorus segregation data derived from field emission gun scanning transmission electron microscopy (FEGSTEM) measurements [5]. Using the parametric dependence predicted by the modelling, for the variation of segregation with variables such as irradiation temperature, dose and dose-rate, it was possible to derive a trend curve to incorporate Charpy data from specimens in which IGF is influencing the shifts [2].

Differences Between Weld HS and Weld LS

It is of interest, finally, to consider the possible reasons for the difference between weld HS and weld LS. The segregation modelling [5] predicts that the degree of segregation is almost linearly proportional to the phosphorus content of the weld. Table 1 shows that, although weld HS has a phosphorus contents of 0.040 wt% considerably greater than 0.031 wt%, the mean of the large population, weld LS has a similar content, of 0.039 wt% phosphorus. Other elements are known to be important in influencing grain boundary phosphorus effects; in particular carbon atoms in the grain boundary may act in two ways to oppose the effect of phosphorus. Firstly, carbon atoms may occupy grain boundary sites so as to inhibit the occupation

of neighbouring sites by phosphorus; and secondly, carbon is known to be a grain boundary strengthener. Thus the difference between weld HS and weld LS is the latter's higher carbon content. This suggested explanation is consistent with the observation that the duct-cut weld, which is the subject of the experiment described in [1], has a high carbon content, and has been shown to be lacking in susceptibility to IGF.

CONCLUSIONS

(1) Submerged-arc welds which showed high Charpy shifts in accelerated re-irradiation experiments were examined fractographically, revealing intergranular fracture (IGF) in fine-grained regions of the welds.

(2) Specimens of welds HS and LS exposed to almost equal doses were examined quantitatively, and weld HS, which had higher Charpy shifts than weld LS, also showed significantly more IGF.

(3) Auger examination demonstrated that IGF was associated with the grain boundary segregation of phosphorus. No other embrittling elements were found to be segregated.

(4) Phosphorus segregation was greater, for a given dose, in weld HS than in weld LS. This may be due to differences in chemical composition, in particular the competition with carbon atoms at the fracture site.

(5) Phosphorus segregation was found to increase with dose.

(6) The degree of IGF and phosphorus segregation was greater in all the irradiated specimens than in unirradiated specimens of a number of different but comparable welds.

ACKNOWLEDGEMENT

This paper is published by permission of Nuclear Electric plc.

REFERENCES

[1] Buswell, J.T., Bolton, C.J., Wootton, M.R., Bischler, P.J.E., Jones, R.B., Jones., L.T., Phythian, W.J., and Sinclair, R.R., "The Radiation Hardening and Embrittlement of a Mild Steel Submerged-Arc Weld", Effects of Radiation on Materials: 16th International Symposium, ASTM STP 1175, American Society for Testing and Materials, Philadelphia, 1993, p.332.

[2] Bolton, C.J., Buswell, J.T., Jones, R.B., Moskovic, R., and Priest, R.H., "Modelling of Irradiation Embrittlement in Submerged-Arc Welds", Effects of Radiation on Materials: 17th Volume, ASTM STP 1270, American Society for Testing and Materials, Philadelphia, 1995, in this Publication.

[3] Briggs, D., and Seah, M.P., "Practical Surface Analysis by Auger and X-Ray Photoelectron Spectroscopy", Wiley, 1990.

[4] Abbott, K., Moskovic, R., Wild, R.K., and Flewitt, P.E.J., "Low Temperature Fracture of C-Mn Submerged-Arc Weld Metal", Materials Science and Technology, 11, 572, (1995).

[5] Druce, S.G., English, C.A., Foreman, A.J.E., McElroy, R.H., Vatter, I.A., Bolton, C.J., Buswell, J.T., and Jones, R.B., "Modelling of irradiation-Enhanced Phosphorus Segregation of Neutron-Irrated Submerged-Arc Welds", Effects of Radiation on Materials: 17th Volume, ASTM STP 1270, American Society for Testing and Materials, Philadelphia, 1995, in this publication.

Charpy Impact Response of RPV Steels

Shafik K. Iskander,[1] Mikhail A. Sokolov,[1] and Randy K. Nanstad[1]

EFFECTS OF ANNEALING TIME ON THE RECOVERY OF CHARPY V-NOTCH PROPERTIES OF IRRADIATED HIGH-COPPER WELD METAL

REFERENCE: Iskander, S. K., Sokolov, M. A., and Nanstad, R. K., **"Effects of Annealing Time on the Recovery of Charpy V-Notch Properties of Irradiated High-Copper Weld Metal,"** *Effects of Radiation on Materials: 17th International Symposium, ASTM STP 1270,* David S. Gelles, Randy K. Nanstad, Arvind S. Kumar, and Edward A. Little, Eds., American Society for Testing and Materials, 1996.

ABSTRACT: One of the options to mitigate the effects of irradiation on reactor pressure vessels is to thermally anneal them to restore the toughness properties that have been degraded by neutron irradiation. An important issue to be resolved is the effect on the toughness properties of reirradiating a vessel that has been annealed. This paper describes the annealing response of irradiated high-copper submerged-arc weld HSSI 73W. For this study, the weld has been annealed at 454°C (850°F) for lengths of time varying between 1 and 14 days. The Charpy V-notch 41-J (30-ft-lb) transition temperature (TT_{41J}) almost fully recovered for the longest period studied, but recovered to a lesser degree for the shorter periods. No significant recovery of the TT_{41J} was observed for a 7-day anneal at 343°C (650°F). At 454°C for the durations studied, the values of the upper-shelf impact energy of irradiated and annealed weld metal exceeded the values in the unirradiated condition. Similar behavior was observed after aging the *unirradiated* weld metal at 460 and 490°C for 1 week.

KEY WORDS: annealing, irradiation, recovery, Charpy V-notch, transition temperature, upper-shelf energy, copper, weld metal, toughness, reactor pressure vessel

INTRODUCTION

Some early nuclear power reactor pressure vessels (RPVs) fabricated from certain types of steels may not meet the pertinent regulatory requirements as they near end of life. These regulatory requirements are promulgated in Appendix G of Title 10 of the *Code of Federal Regulations*, Part 50, "Fracture Toughness Requirements." It is believed that in

[1]Metals and Ceramics Division, Oak Ridge National Laboratory, Oak Ridge, TN 37831-6151.

Copyright© 1996 by ASTM International www.astm.org

the next decade or so, several vessels may exceed the limits set by the pressurized thermal shock reference temperature. In that case, thermal annealing may be needed to mitigate effects of neutron embrittlement on fracture toughness. A dozen or so RPVs have already been thermally annealed in Eastern Europe [1].

Historically, the toughness of RPVs has been monitored through surveillance programs in which predominantly Charpy V-notch (CVN) specimens are placed in capsules that are withdrawn and tested periodically. The degradation of fracture toughness is estimated from both the radiation-induced shift of the CVN 41-J (30-ft-lb) transition temperature (ΔTT_{41J}) as well as the decrease in the upper-shelf energy (USE) level. The fracture toughness of irradiated RPV material is estimated from the American Society of Mechanical Engineers (ASME) *Boiler and Pressure Vessel Code* fracture toughness curves [2] by shifting them upward in temperature by ΔTT_{41J}. Recent advances in fracture mechanics allow the determination of the fracture toughness of the thick-section RPV steels from relatively small fracture toughness specimens, but for some of the earlier RPVs, the use of their CVN-based surveillance data and specimens will probably play a key role in the judgement of the efficacy of the anneal.

This paper discusses the effect of annealing on the CVN impact energy of irradiated high-copper welds. This research was performed within the Heavy Section Steel Irradiation (HSSI) Program sponsored by U.S. Nuclear Regulatory Commission at the Oak Ridge National Laboratory (ORNL). The long-term objectives of the HSSI Program annealing task are to determine the rates of fracture toughness degradation due to reembrittlement after annealing several critical irradiated materials and to relate them to the corresponding rates for unirradiated material upon irradiation, or to the recovery of the ΔTT_{41J} of irradiated and annealed material. The rate of reembrittlement is an important consideration since it will determine how long the plant may be safely operated after it is annealed. Most of the available data dealing with the recovery and reembrittlement response are based on the CVN impact energy, which must then be correlated with the fracture toughness.

DESCRIPTION OF MATERIAL USED

The commercially fabricated submerged arc-weld used for this study, designated HSSI weld 73W, has been very extensively characterized in other HSSI tasks [3–7]. Large variations in the copper content (from 0.22 to 0.46%) have been observed in welds fabricated using weld wire with copper coating [8]. To avoid these large variations, the 73W weld wire was fabricated with copper added to the melt, consequently, the variation in copper content is very small. The chemical composition and standard deviation of HSSI Weld 73W, obtained from a large number of analyses, is shown in Table 1.

The CVN specimens used in this study were slightly smaller in one cross-sectional dimension than the standard full-size CVN specimens. This slightly smaller dimension of the specimens was dictated by the space available in the HSSI Fifth Irradiation Series capsules [9]. A typical arrangement of these specimens is shown in Fig. 1. The dimension

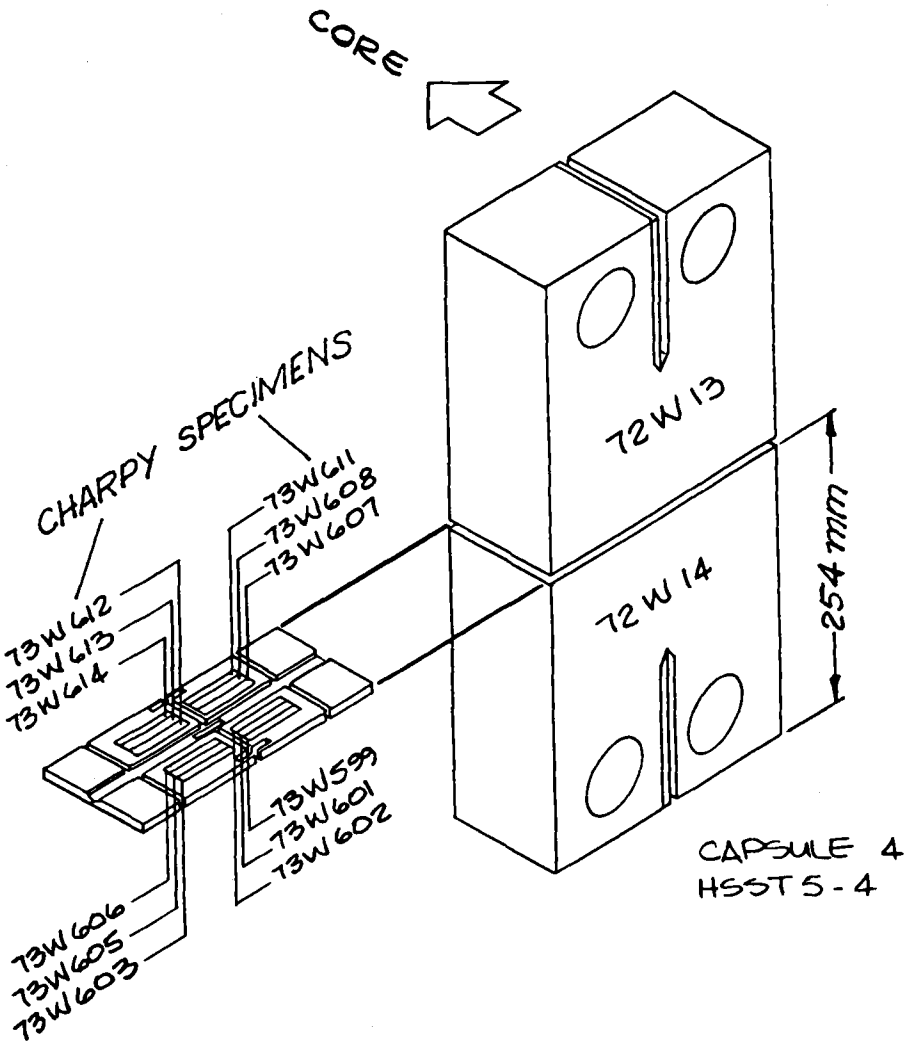


FIG. 1--The undersize Charpy V-notch specimens were irradiated in the available space of the Fifth Irradiation Series capsules.

normal to the notch of the "undersize" CVN specimens is 95% of full-size specimens, as shown in Fig. 2.

There were 120 undersized CVN specimens irradiated as part of the HSSI Fifth Irradiation Series, 12 in each of 10 capsules. They were irradiated at a nominal temperature of 288°C, and to average exposures of 1.8×10^{19} neutrons/cm^2 (> 1 MeV), 1.1×10^{20} neutrons/cm^2 (> 0.1 MeV), and 0.040 displacements per atom. The irradiation was performed in the Oak Ridge Research Reactor over a period of about 2 months, with an average flux of 3.4×10^{12} neutrons/(cm^2-s) (> 1 MeV); full details are presented elsewhere [9].

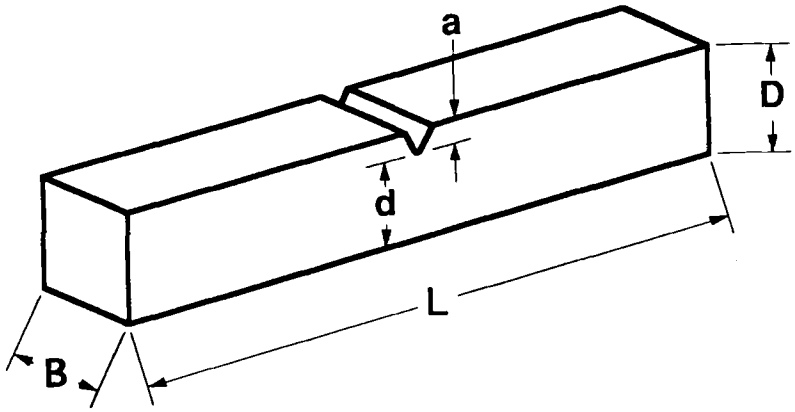
TABLE 1--Chemical composition and standard deviation of the various elements analyzed for HSSI weld 73W

Composition (wt % and standard deviation)									
C	Mn	P	S	Si	Cr	Ni	Mo	Cu	V
0.098 0.007	1.56 0.026	0.005 0.0004	0.005 0.0006	0.45 0.028	0.25 0.006	0.60 0.006	0.58 0.009	0.31 0.010	0.003 0.0001

The results of CVN impact testing of unirradiated undersize CVN specimens are compared to those of full-size specimens in Fig. 3. Each of the curves shown is a hyperbolic tangent fit by nonlinear regression to the experimental results of testing 55 and 85 specimens for the undersize and full-size specimens, respectively. Although the slope of the curves in the transition region for the undersize specimens is somewhat steeper than for the full-size specimens, the CVN 41-J transition temperatures (TT_{41J}) are approximately equal. As will be shown later, this difference in slope was not apparent in testing a smaller number of specimens (10 to 18) of either the irradiated or irradiated and annealed specimens of nominally the same geometry. Thus, this difference in slope may be due to the sensitivity of the undersize specimen to variations in the notch depth.

MATERIAL CONDITIONS INVESTIGATED

The irradiated CVN specimens were annealed at two temperatures, 343 and 454°C. These two temperatures have been often investigated as approximate lower and upper bounds of probable annealing temperatures [10]. The 343°C temperature could be used for a wet anneal. This is considerably simpler to perform than a dry anneal at 454°C since the reactor internals would not have to be removed. A 168-h annealing time was investigated for the lower temperature, and, since the recovery of the TT_{41J} was insignificant, no other annealing times were investigated. Four annealing times varying



	L (in) (mm)	B (in) (mm)	D (in) (mm)	d (in) (mm)	a (in) (mm)	a/D
Undersized specimens	2.165 55.00	0.394 10.00	0.375 9.52	0.303 7.71	0.072 1.82	0.191
Standard specimens	2.165 55.00	0.394 10.00	0.394 10.00	0.315 8.00	0.079 2.00	0.200

FIG. 2--Dimensions of the undersize Charpy V-notch specimens compared to the standard full-size specimens.

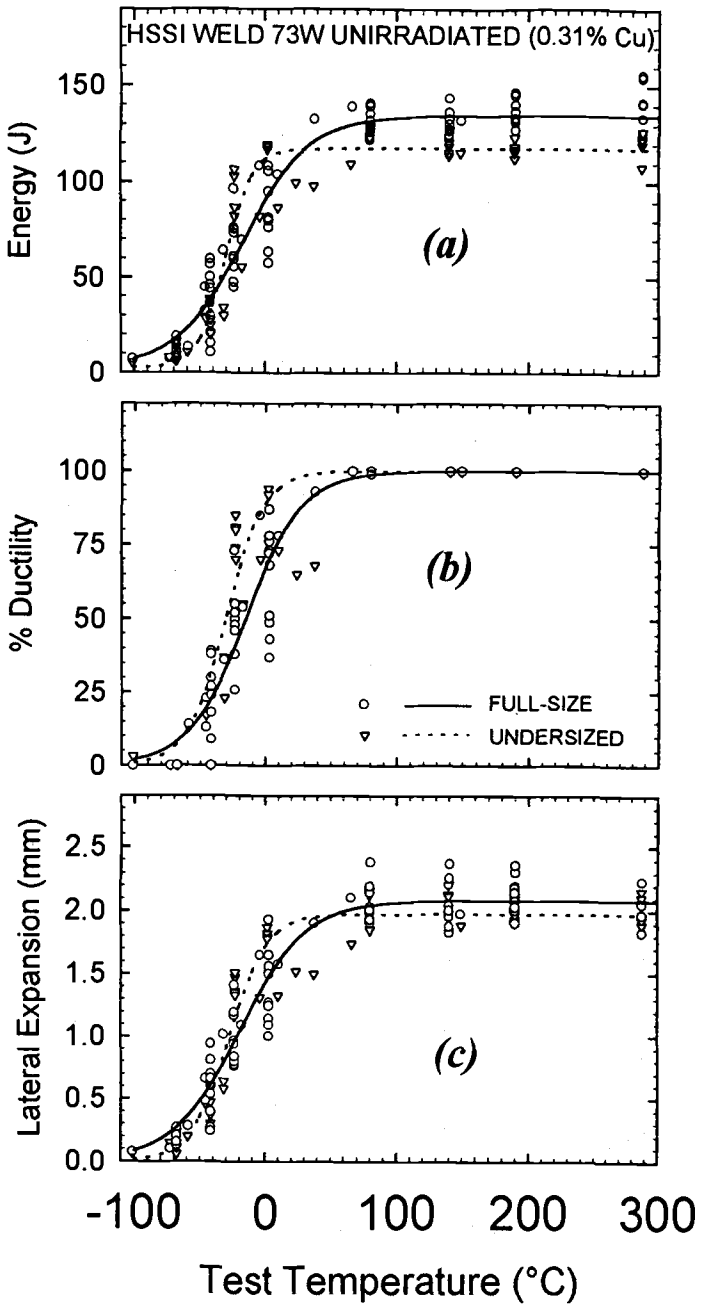


FIG. 3--Comparison of the Charpy V-notch impact energy of the unirradiated undersize HSSI weld 73W specimens to the full-size specimens: (a) energy, (b) ductile appearance, and (c) lateral expansion.

from 1 day to 2 weeks (336 h) were investigated at a temperature of 454°C. One of the results of this investigation is that annealing increased the USE to values greater than the unirradiated specimens. This was not unexpected since other investigators have also noted such an effect. Annealing, tempering and aging effects are diffusion processes where temperature is the dominant parameter and time is of secondary influence. As part of the original fabrication procedure, the 73W weld was postweld heat treated (PWHT) at a temperature of 607°C for 40 h, and thus exposure at the lower temperature of 454°C for 168 h would not be expected to have any effect. To determine whether this increase in USE was due to irradiation, unirradiated specimens were also aged at 460 and 490°C. The conditions investigated have been summarized in Table 2.

TABLE 2--Material conditions investigated

Material condition	Aging or annealing time (h)
Unirradiated	
Unirradiated and aged at 460°C (860°F)	168
Unirradiated and aged at 490°C (914°F)	168
Irradiated	
Irradiated and annealed 343°C(650°F)	168
Irradiated and annealed 454°C(850°F)	24, 96, 168, 336

TEST RESULTS

The results of CVN tests on 73W welds for the conditions investigated are shown in Figs. 4 through 8. The recovery of CVN impact properties is measured by the changes in values of the USE and TT_{41J} before and after annealing when compared to the unirradiated values. The values of the USE and TT_{41J} were calculated from a nonlinear regression fit of a hyperbolic tangent equation to the CVN impact energy results. The hyperbolic tangent equation was also fitted to the experimental values of percent ductile shear appearance and lateral expansion, and is of the form:

$$y = \frac{US + LS}{2} + \frac{US - LS}{2} \text{Tanh} \left(\frac{T - MTT}{TZW/2} \right), \quad (1)$$

where

y = energy, percent ductile shear appearance, or lateral expansion
US and LS = upper- and lower-shelf values, respectively,
T = test temperature,
MTT = mid-transition temperature, and,
TZW = transition zone width.

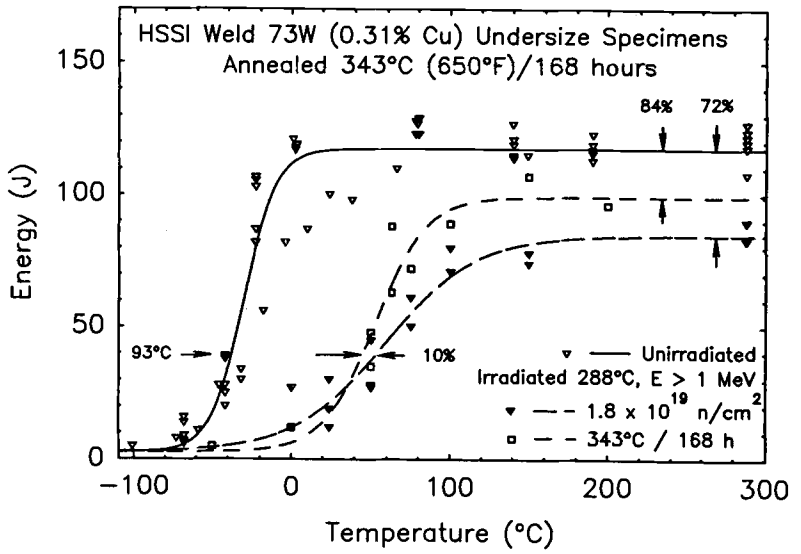


FIG. 4--Results of testing undersize irradiated Charpy V-notch specimens annealed at 343°C for 168 h compared to specimens in the unirradiated and irradiated conditions. The percent recovery is also indicated.

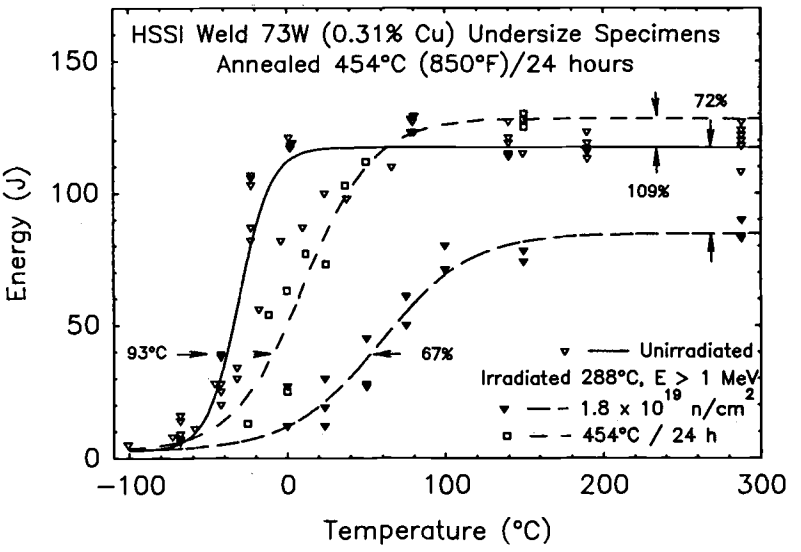


FIG. 5--Results of testing undersize irradiated Charpy V-notch specimens annealed at 454°C for 24 h compared to specimens in the unirradiated and irradiated conditions. The percent recovery is also indicated.

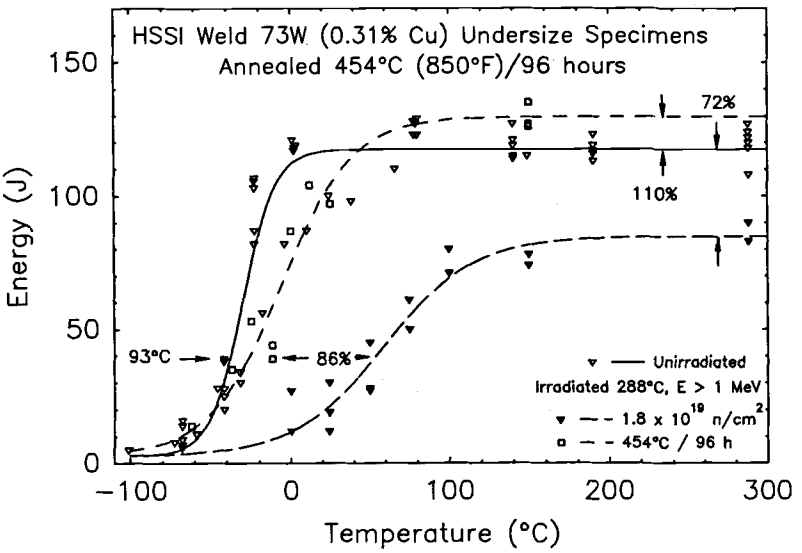


FIG. 6--Results of testing undersize irradiated Charpy V-notch specimens annealed at 454°C for 96 h compared to specimens in the unirradiated and irradiated conditions. The percent recovery is also indicated.

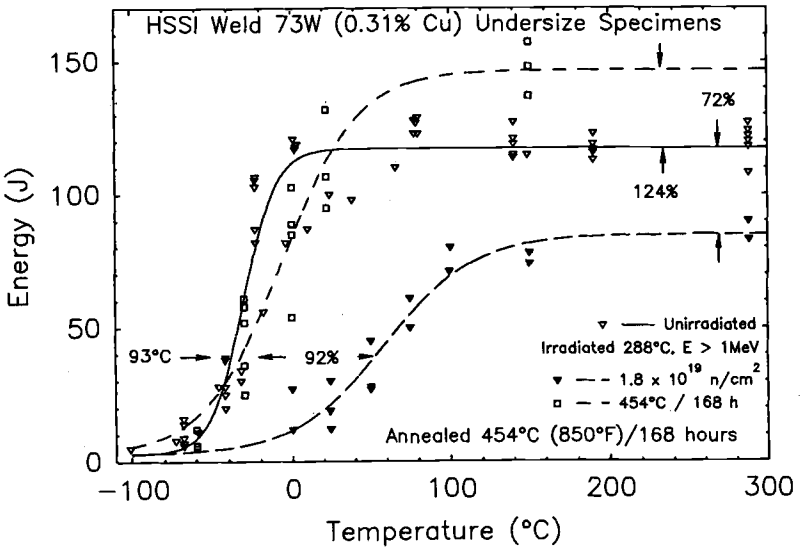


FIG. 7--Results of testing undersize irradiated Charpy V-notch specimens annealed at 454°C for 168 h compared to specimens in the unirradiated and irradiated conditions. The percent recovery is also indicated.

In the case of fitting energy values, the LS was prescribed to be 2.7 J, the average value obtained by testing five submerged-arc welds at liquid nitrogen temperature of −196°C [8]. For lateral expansion and percent ductile shear appearance, the value of LS was prescribed to be zero. The upper-shelf value, US, of ductile shear was prescribed to be 100%. Except for these prescribed values, US, MTT, and TZW were fitting parameters.

The percent recovery of the TT_{41J} is defined as the ratio of the residual transition temperature shift after annealing to the shift due to irradiation, ΔTT_{41J}, or:

$$\% \text{ Recovery } TT_{41J} = \frac{[TT_{41J}]_{irr} - [TT_{41J}]_{ann}}{[TT_{41J}]_{irr} - [TT_{41J}]_{unirr}} \cdot 100 , \tag{2}$$

where TT_{41J} is the transition temperature at the 41-J energy level for the condition indicated by the outer subscript. Thus, the percent recovery is related to the shift, ΔTT_{41J}, due to irradiation.

The percent recovery of the USE could also be defined in an analogous manner to Eq. (2):

$$\% \text{ USE Recovery} = \frac{USE_{ann} - USE_{irr}}{USE_{unirr} - USE_{irr}} \cdot 100 \tag{3}$$

On the other hand, changes in USE could be related to the unirradiated value, hence the percent recovery of the USE may also be defined as the ratio of the values of the USE in the irradiated and annealed (or aged) condition to the unirradiated condition:

$$\% \text{ USE Recovery} = \frac{USE_{ann}}{USE_{unirr}} \cdot 100 . \tag{4}$$

The disadvantage of Eq. (4) is that it makes no distinction in the case in which there is no recovery, indicating instead the loss of USE due to irradiation. Its main advantage is that, in cases of USE recovery (which is usually the case), the value relates to the unirradiated value. The disadvantage of Eq. (3) is that it cannot be applied to the case of unirradiated and aged material since there is no "irradiated" condition, while Eq. (4) allows comparisons between the changes of the USE in the unirradiated/aged and irradiated/annealed conditions. In this paper, both definitions of the percent recovery of USE have been used.

Except for the 343°C annealing temperature, which did not show any significant recovery in the TT_{41J} as mentioned previously, the degree of CVN impact energy recovery was dependent on the length of annealing time. The TT_{41J}, USE, change, and percentage

recovery for each of the conditions investigated has been summarized in Table 3. The percentage recovery of both the TT_{41J} and the USE have been plotted in Fig. 9 for annealing at 454°C.

DISCUSSION

Annealing the HSSI weld 73W at 454°C for various lengths of time from 24 to 336 h has "over-recovered" the USE to values that exceeded the unirradiated ones, which has been also been observed in other investigations. As mentioned above, this increase cannot be explained by a simple time-temperature diffusion process in which temperature is the dominant parameter, since the weld was already PWHT at the higher temperature of 607°C. Thus, the annealing at 454°C would not be expected to produce such changes in impact energy. Aging of unirradiated HSSI weld 73W at 460 and 490°C for 168 h also increased the value of USE, so this increase could not be explained solely by changes in the material caused by irradiation. The recovery by annealing of the neutron irradiation-induced transition temperature shift can be understood, to a large degree, in terms of coarsening or over aging and decrease in the number density of the copper-rich precipitates that are believed to be the primary cause of the transition temperature shift [11]. However, the reasons for the over-recovery of the USE in the unirradiated and irradiated conditions is still unknown, and the HSSI program will continue to investigate this phenomenon. It should be noted that the aging of unirradiated HSSI weld 73W did not cause any noticeable changes in the value of TT_{41J}.

Annealing HSSI weld 73W at 454°C for 24 h recovered about two-thirds of the transition temperature shift caused by the neutron irradiation. Annealing at this temperature for longer times increases the recovery, but at a decreasing rate, so that doubling the annealing time from 168 to 336 h increases the percent recovery from 92 to 96%, which may not be a reasonable return for the extra annealing time invested.

It is significant that in all the above cases of annealing of irradiated HSSI weld 73W at 454°C, the percentage recovery of the USE was greater than the percentage recovery of TT_{41J}. This was also observed in other investigations as can be shown by plotting the percent recovery of upper shelf versus the percent recovery of the TT_{41J} for RPV steels. The data in Fig. 10 of the % USE Recovery, Eq. (3), versus the % Recovery TT_{41J}, Eq. (2), show that the majority of the data lie above the straight line with a 1:1 slope. The data in Fig. 10 were extracted from the ORNL test reactor data base [12]. This confirms the results from this investigation, namely that (1) the USE recovers faster than the TT_{41J}, and (2) the percentage recovery of USE, as defined by either Eqs. (3) or (4), is greater than 100%. This result can be useful in cases where the number of specimens available is less than desired for an adequate determination of both TT_{41J} and USE. More specimens could be devoted to determine the TT_{41J}, and fewer specimens could be used to confirm the recovery of the USE.

TABLE 3--Values of the 41-J transition temperature and upper-shelf energy for all conditions investigated (blank values are unavailable or not applicable)

Condition	Annealing/aging		41-J transition temperature			Upper-shelf energy			
	Temperature (°C)	Time (h)	Value (°C)	Residual shift[a] (K)	Recovery[b] (%)	Value (J)	Change[c] (J)	Change[d] (%)	Change[e] (%)
Unnirradiated			−38			118			
Irradiated			55	93		85	−33		72
Irradiated and annealed	343	168	46	84	10	99	−19	42	84
Irradiated and annealed	454	24	−7	31	67	128	10	130	108
Irradiated and annealed	454	96	−25	13	86	130	12	136	110
Irradiated and annealed	454	168	−31	7	92	147	29	188	125
Irradiated and annealed	454	336	−34	4	96	154	36	209	131
Unirradiated and aged	460	168				138	20		117
Unirradiated and aged	490	168				138	20		117

[a]Change from unirradiated value, positive values indicated an increase in the transition temperature.
[b]Defined by Eq. (2).
[c]Change from unirradiated value, positive values indicate an increase in upper shelf.
[d]Defined by Eq. (3).
[e]Defined by Eq. (4).

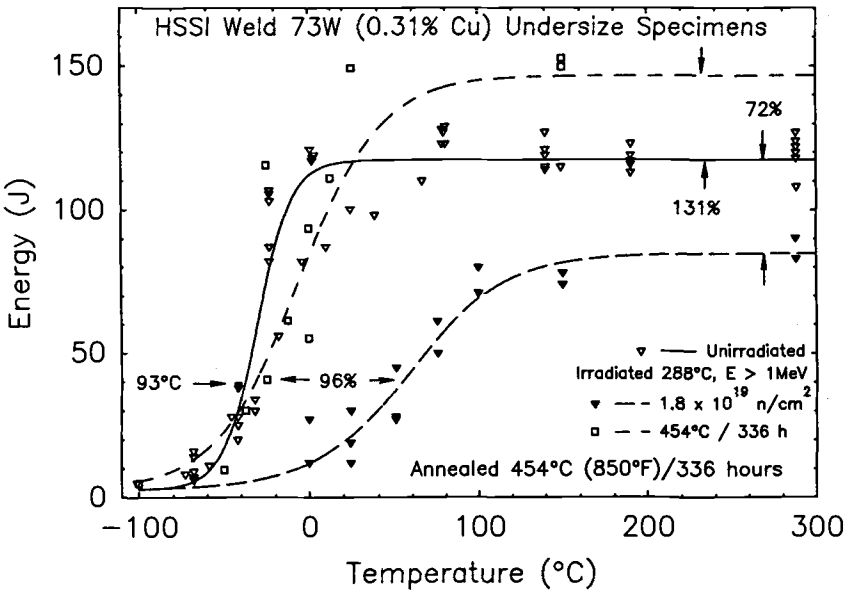


FIG. 8--Results of testing undersize irradiated Charpy V-notch specimens annealed at 454°C for 336 h compared to specimens in the unirradiated and irradiated conditions. The percent recovery is also indicated.

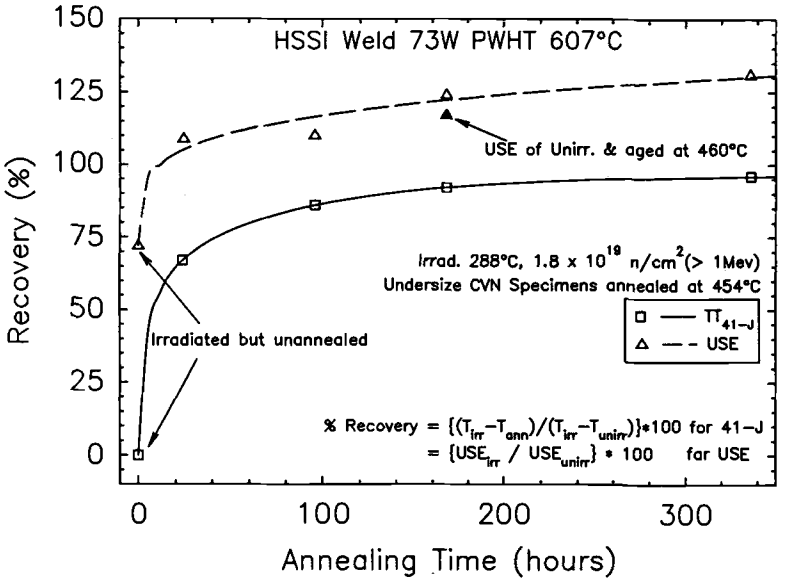


FIG. 9--Summary of percent recovery of the 41-J energy level transition temperature and the upper-shelf energy.

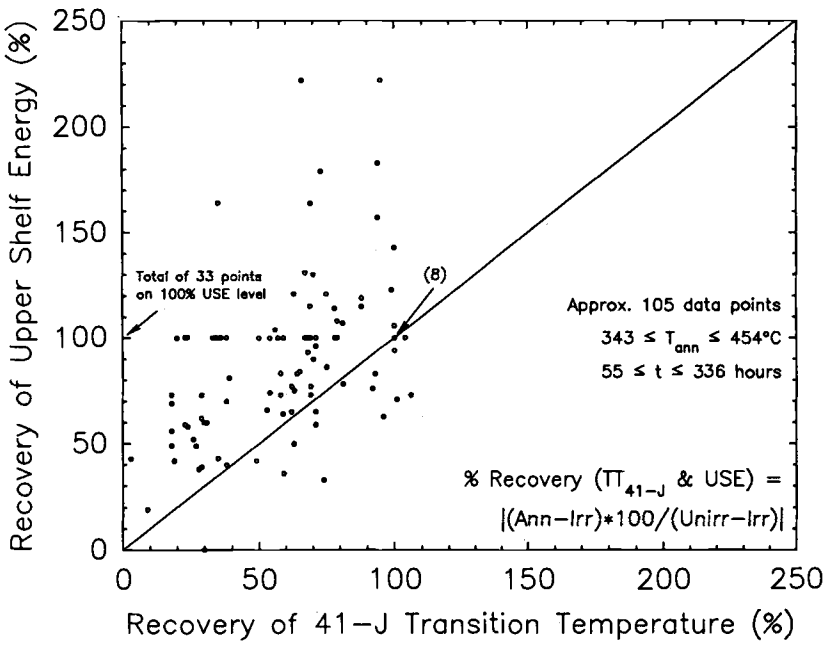


FIG. 10--Percent recovery of the upper-shelf energy versus percent recovery of the 41-J energy level transition temperature shift.

The rate of toughness degradation of irradiated and annealed RPV steels upon reirradiation is the present focus of investigations at ORNL. This is a major consideration in determining how long a RPV could be operated safely after it is annealed. It is possible that for some of the older RPVs for which annealing will be considered, no archival material is available, and the surveillance data from CVN specimens are the only data available that describe the rate of embrittlement. Thus, relating the rate of toughness degradation due to reirradiation to the rate of transition temperature shift of CVN specimens (the so-called "trend curve") from the unirradiated state becomes important.

CONCLUSIONS

HSSI weld 73W was annealed at two temperatures for various lengths of time. The following conclusions could be deduced from the results:

1. Annealing of HSSI weld 73W has resulted in various degrees of recovery of the transition temperature and USE that depend strongly upon the annealing temperature and to a somewhat lesser degree upon the annealing time.

2. Annealing at 454°C for 24 h recovered about two-thirds of the transition temperature shift caused by the neutron irradiation.

3. Annealing at 454°C for longer times increases the recovery, but at a decreasing rate, so that doubling the annealing time from 168 to 336 h increases the recovery from 92 to 96%, which may not be a reasonable return for the extra annealing time invested.

4. Annealing at 343°C has resulted in an insignificant recovery of the transition temperature and a relatively small recovery in the USE.

5. Annealing at 454°C for various lengths of time from 24 to 336 h has "over-recovered" the USE to values that exceeded the unirradiated values.

6. Over-recovery of the USE was also observed after aging the *unirradiated* weld at 460 and 490°C for 1 week, and thus over-recovery is not solely associated with recovery of irradiation-induced damage.

The reasons for the over-recovery of the USE in the unirradiated and irradiated conditions are still not understood, particularly since HSSI weld 73W has been postweld heat treated at 607°C for 40 h. The HSSI Program will continue to investigate this phenomenon.

ACKNOWLEDGMENTS

This research was sponsored by the Office of Nuclear Regulatory Research, Division of Engineering Technology, U.S. Nuclear Regulatory Commission, under Interagency Agreement DOE 1886-8109-8L with the U.S. Department of Energy under contract DE-AC05-84OR21400 with Lockheed Martin Energy Systems. The authors gratefully acknowledge the financial support and encouragement provided by the U.S. Nuclear Regulatory Commission, particularly A. Taboada and M. G. Vassilaros, the previous and present HSSI Program Monitors, respectively. The authors also wish to thank R. E. Stoller, and the ASTM reviewers for their helpful comments, and J. L. Bishop for preparation of the camera-ready manuscript.

REFERENCES

[1] A. M. Kryukov, and M. A. Sokolov, "Investigation of Material Behavior Under Reirradiation after Annealing Using Subsize Specimens," pp. 417-423 in *Small Specimen Test Techniques Applied to Nuclear Reactor Vessel Thermal Annealing and Plant Life Extension, ASTM STP 1204*, W. R. Corwin, F. M. Haggag, and W. L. Server, Editors, American Society for Testing and Materials, Philadelphia, 1993.

[2] *ASME Boiler and Pressure Code, An American National Standard*, 1992 Addenda, Section XI, Article A-4000, American Society of Mechanical Engineers, New York, December 31, 1992.

[3] R. K. Nanstad, F. M. Haggag, D. E. McCabe, S. K. Iskander, K. O. Bowman, and B. H. Menke, Martin Marietta Energy Systems, Inc., Oak Ridge Natl. Lab., *Irradiation Effects on Fracture Toughness of Two High-Copper Submerged-Arc Welds, HSSI Series 5,* USNRC Report NUREG/CR-5913, Vol. 1 (ORNL/TM-12156/V1), August 1992.

[4] R. K. Nanstad, D. E. McCabe, Blaine H. Menke, S. K. Iskander, and F. M. Haggag, "Effects of Irradiation on K_{Ic} Curves for High-Copper Welds," pp. 214-233 in *Effects of Radiation on Materials, 14th International Symposium, (Volume II), ASTM STP 1046,* N. H. Packan, R. E. Stoller, and A. S. Kumar, Editors, American Society for Testing and Materials, Philadelphia, 1990.

[5] S. K. Iskander, W. R. Corwin, and R. K. Nanstad, Martin Marietta Energy Systems, Inc., Oak Ridge Natl. Lab., *Results of Crack-Arrest Tests on Two Irradiated High-Copper Welds,* USNRC Report NUREG/CR-5584 (ORNL/TM-11575), December 1990.

[6] S. K. Iskander, W. R. Corwin, and R. K. Nanstad, "Effects of Irradiation on Crack-Arrest Toughness of Two High-Copper Welds," pp. 251-269 in *Effects of Radiation on Materials: 15th International Symposium, ASTM STP 1125,* R. E. Stoller, A. S. Kumar, and D. S. Gelles, Editors, American Society for Testing and Materials, Philadelphia, 1992,

[7] S. K. Iskander, W. R. Corwin, and R. K. Nanstad, Martin Marietta Energy Systems, Inc., Oak Ridge Natl. Lab., *Crack-Arrest Tests on Two Irradiated High-Copper Welds. Phase II: Results of Duplex-Type Specimens,* USNRC Report NUREG/CR-6139, (ORNL/TM-12513), March 1994.

[8] R. K. Nanstad, D. E. McCabe, R. L. Swain, and M. K. Miller, Martin Marietta Energy Systems, Inc., Oak Ridge Natl. Lab., *Chemical Composition and RT_{NDT} Determinations for Midland Weld WF-70,* USNRC Report NUREG/CR-5914 (ORNL-6740), December 1992.

[9] L. F. Miller, C. A. Baldwin, F. W. Stallmann, and F. B. K. Kam, Martin Marietta Energy Systems, Inc., Oak Ridge Natl. Lab., *Neutron Exposure Parameters for the Metallurgical Test Specimens in the Fifth Heavy-Section Steel Irradiation Series Capsules,* USNRC Report NUREG/CR-5019 (ORNL/TM-10582), March 1988.

[10] T. R. Major, and R. G. Lott, *Thermal Annealing of an Embrittled Reactor Pressure Vessel,* EPRI NP-6113-M, Electric Power Research Institute, Palo Alto, Calif., January 1989.

[11] G. R. Odette, "Radiation-Induced Microstructural Evolution in Reactor Pressure Vessel Steels," pp. 137-148 in *Microstructure of Irradiated Materials*, Materials Research Society Proceedings, Vol. 373, I. M. Robertson et al., Editors, Materials Research Society, Pittsburgh, 1995.

[12] F. W. Stallmann, J. A. Wang, F. B. K. Kam, Martin Marietta Energy Systems, Inc., Oak Ridge Natl. Lab., *TR-EDB: Test Reactor Embrittlement Data Base, Version 1*, USNRC Report NUREG/CR-6076 (ORNL/TM-12415), January 1994.

Robert Gérard[1], Albert Fabry[2], José Van de Velde[2], Jean-Louis Puzzolante[2], Alfons Verstrepen[2], Théo Van Ransbeeck[2], Eric van Walle[2]

IN-SERVICE EMBRITTLEMENT OF THE PRESSURE VESSEL WELDS AT THE DOEL I AND II NUCLEAR POWER PLANTS

REFERENCE: Gérard, R., Fabry, A., Van de Velde, J., Puzzolante, J. L., Verstrepen, A., Van Ransbeeck, T., and van Walle, E., **"In-Service Embrittlement of the Pressure Vessel Welds at the Doel I and II Nuclear Power Plants,"** *Effects of Radiation on Materials: 17th International Symposium, ASTM STP 1270,* David S. Gelles, Randy K. Nanstad, Arvind S. Kumar, and Edward A. Little, Eds., American Society for Testing and Materials, 1996.

ABSTRACT: In-service embrittlement of the welds at the Doel I and II pressure vessels displays an apparent "outlier" behaviour as compared to the predictions of US NRC Regulatory Guide 1.99 Rev.2. This issue is being addressed by a systematic R&D effort, supplementary to the mandatory surveillance programmes. The status of this effort is reviewed in this paper.

The anomalous trends can be outlined as follows. Extensive characterization of the chemical composition of representative test specimens reveals that these low nickel welds, although being nominally identical (same fabrication practice, heat treatment, microstructure,...), do feature an appreciable variability of their bulk copper content - covering a range of 0.13% to 0.35%. High copper Charpy-V weld specimens are however not available in the surveillance capsules. The variability could be identified only because the weld part of some HAZ (heat affected zone) Charpy-V specimens, as well as some tensile specimens, consist of the high copper melt. For the low copper contents, (0.13-0.18%), the 41 J Cv transition temperature shift, as obtained from seven capsules exposed in the neutron fluence range of 1 to 3.9 10^{19} n/cm^2 (>1 MeV), is rather constant, but significantly larger than predicted (by US NRC Regulatory Guide 1.99 rev.2).This has caused some concern on the upper bound shift to be adopted, given the possibility of higher copper content in the actual pressure vessel welds.

[1] Senior Engineer,TRACTEBEL ENERGY ENGINEERING, Avenue Ariane 7, B-1200, Brussels, Belgium

[2] Lead scientist, manager, senior engineer, engineer, senior engineer, senior research scientist, respectively, SCK/CEN, Boeretang 200, B-2400, Mol, Belgium

Copyright© 1996 by ASTM International www.astm.org

High copper samples were manufactured by applying the stud welding reconstitution technique to remnants of the HAZ specimens, and the results cannot be distinguished from the low copper data. Such insensitivity to copper,confirmed by tensile and hardness measurements, is at odds with current literature knowledge and with Regulatory guide-lines. A further anomaly observed for this type of weld metal is an appreciable sensitivity to thermal ageing.

The surveillance results will be evaluated in accordance with the USNRC Regulatory guide-lines, and the embrittlement trends described above will be thoroughly evaluated from a micromechanical perspective, in the light of a high resolution microstructural investigation.

KEYWORDS: Reactor pressure vessel weld, irradiation embrittlement, thermal ageing, microstructure, micromechanics.

INTRODUCTION

Doel I and II are two-loop PWR's of 390 MW electrical output, of Westinghouse design. They were the first commercial nuclear units to be commissioned in Belgium, in 1974 and 1975 respectively. As in many units of this vintage, the weld assembling the two core shells has a relatively high copper content, that is detrimental to irradiation embrittlement sensitivity.

The paper presents the main surveillance results obtained to date and their interpretation along the Regulatory guide-lines as well as from a micromechanical perspective backed by microstructural investigations.

DESCRIPTION OF THE REACTOR PRESSURE VESSELS

The reactor pressure vessels were manufactured in Belgium by Cockerill in 1970 - 1972, from forged rings of steel Soudotenax 56 (very similar to A508 Cl.3). They were welded by the submerged arc welding process using Unionmelt 40 wire and Unionmelt 89 flux from SAF (Soudure Autogène Française). The final post-weld heat treatment of the vessel was 8 hours at 600 °C.

The main characteristics of the vessels and the chemical composition of their materials are summarized in tables 1 and 2 hereafter.

TABLE 1: Characteristics of the pressure vessels

Inside diameter:		3327	mm
Thickness of the core shell:		178	mm
Thickness of the stainless steel cladding:		5	mm
Normal operating pressure:		15.7	MPa
Operating temperature:	inlet:	287.	°C
	outlet:	317.1	°C

TABLE 2: Chemical composition of the materials (weight %)

	C	Co	Cr	Mn	Ni	P	S	Si	Mo	Cu
Base:	0.147	0.012	0.58	0.96	0.79	0.01	0.01	0.25	0.35	0.085
SAW:	0.066	-	0.08	1.31	0.125	0.016	0.013	0.33	0.484	0.12-0.35

ASSESSMENT OF MATERIAL DEGRADATION UNDER SERVICE EXPOSURE

The representativeness of the weld material inserted in the surveillance capsules is questionable, since the wire and flux batches used for these welds might be different from those used for welding the pressure vessel shells.

The average copper content of the Charpy-V weld surveillance specimens is 0.13 % for Doel I, and 0.18 % for Doel II (these welds are designated hereafter as "low copper" welds). Some tensile and HAZ Charpy-V specimens from Doel II, however, come from another weld block with as much as 0.35% copper.

Surveillance Program Results

Besides the fact that all Charpy-V weld specimens come from "low copper" welds and are not necessarily representative of the real vessel welds, the surveillance results themselves are quite atypical. Previous results presented in [1] are summarized hereafter and updated to include the results of the fourth surveillance capsule from Doel II. This capsule received a fast neutron fluence of 3.9 10^{19} n/cm^2 (E>1 MeV), equivalent to approximately 27 years of operation .

A conventional evaluation of the results, using hyperbolic tangent fits of the Charpy curves and the shift of the curves at the 41 J level to determine the increase in RT_{NDT}, yields the results given on Figure 1 for the weld, where the measured shifts are compared to the estimations of the Regulatory Guide 1.99 rev.2 formula [2]. Separate baselines are used for Doel I and Doel II, although they are close to each other.

The curves given on the Figure 1 include 2σ margins (= 31°C), and should represent upper bounds for welds with these Cu and Ni contents. It is clear that the shift of the RT_{NDT} is higher than predicted for the first capsules. For the next capsules however, the shift remains approximately constant, except for the second capsule from Doel I for which the shift is much lower. It is also noticeable that the shift measured at the 50% shear fracture appearance (SFA) reference level is much lower than at the 41 J level, especially for Doel II.

The base material on the other hand behaves as expected, which rules out a generic problem with the surveillance program of these units.

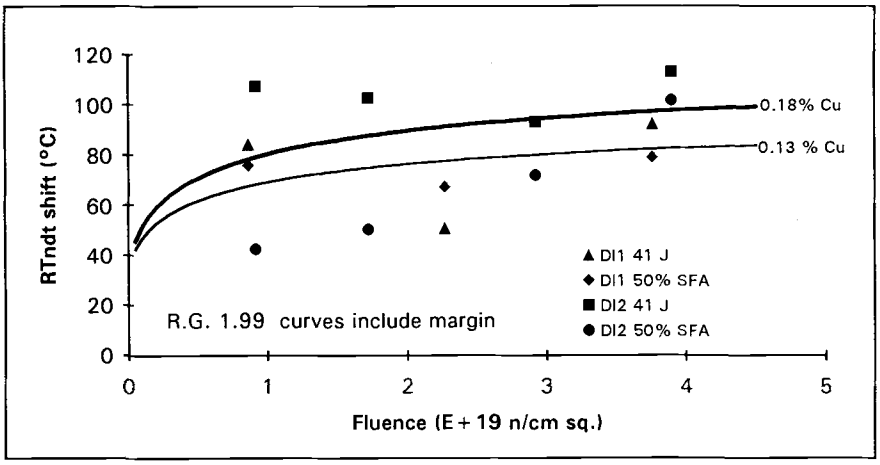


Figure 1: Doel I,II weld - surveillance results (41 J and 50% SFA shifts)

The tensile est results, which are confirmed by hardness measurements, yield two important piece of information:

- The test results of some tensile specimens coming from the high copper weld block, cannot be distinguished from those of the low copper specimens, which is contrary to the generally accepted influence of copper (Figures 2).

- The ration RTNDTshift/yield stress increase is higher than the generally accepted value of 0.63, and can be as high as 2 for some capsule, which means that the increase in yield stress is much lower than could be expected from the generally accepted correlations with RTNDT shifts (Figure 3). Since the tesile tests were performed at 300°C, the values were corrected by a factor 1.16 to estimate the values at 20°C before calculating the ratios on Figure 3. The factor 1.16 was estimated on a weld of the same specification for which tensile data are available at different temperatures.

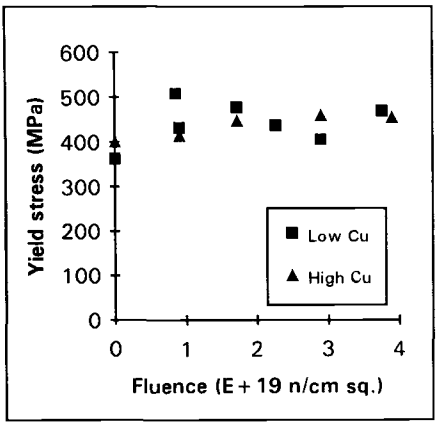


Figure 2: Yield stress at 300 °C

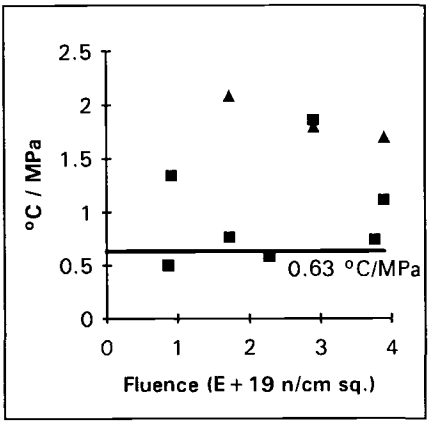


Figure 3: Ratio RTndt shift / Yield stress increase

The need to confirm this limited evidence of insensitivity to copper content encouraged the utility Electrabel to sponsor the development of a reconstitution technique for Charpy-V specimens at the Belgian Nuclear Research Center SCK-CEN. The necessary information on the transition temperature shift of the high copper weld was obtained by reconstituting broken Charpy-V HAZ specimens from Doel II, which come from the block with a high copper content. New specimens were obtained by welding end tabs to the part of the broken HAZ specimen taken out of the weld and machining. The detailed procedure and its qualification are described in several publications [3],[4] .

The technique was extensively qualified on various pressure vessel steels and welds, unirradiated and irradiated, and the reference Charpy curve obtained by testing as-received full-size Charpy specimens at different temperatures is generally well reproduced when testing reconstituted specimens [3],[4].

Here again, Doel I, II weld material behaved unexpectedly. Before reconstituting high copper specimens, the technique was applied to the low copper specimens from two capsules from Doel II, as a last validation on this particular material. A shift of about 20 C of the reconstituted curves with respect to the as-received ones was detected for both capsules. This effect is systematic in the transition region and is not simply due to the scatter of experimental results. The curves obtained for one of those capsules are illustrated on Figure 4. No explanation was found at that time, although it was suspected that this effect could be linked to the long storage time of the specimens before reconstitution (approx. 8 years)[1]. This is confirmed by the results obtained recently for the fourth capsule from Doel II (Figure 5). The reconstitution of the low copper specimens from this capsule, only a few months after the initial tests, shows that the shift between the as-received and reconstituted curves is strongly reduced, confirming that this material is influenced by a long storage time at ambient temperature.

The reasons for this behaviour are partly understood and will be presented in more details in a future publication. The responsible mechanism is thought to be the annealing at ambiant temperature of unstable defects created by the irradiation [14].

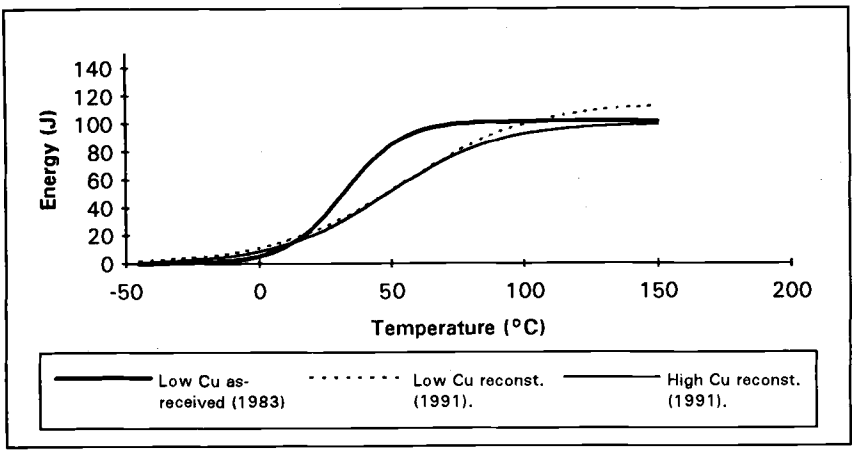


Figure 4: Doel II weld - Second capsule (1.7 10^{19} n/cm^2)

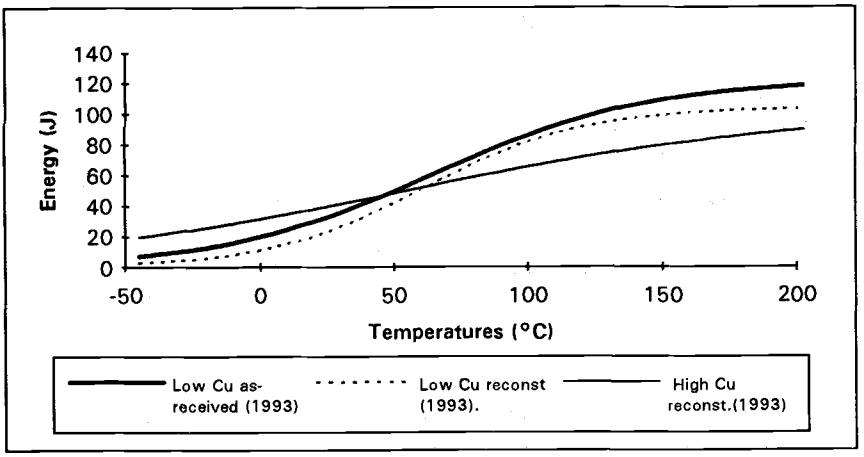


Figure 5: Doel II weld - Fourth capsule (3.9 10^{19} n/cm^2)

Another important result that is illustrated on Figures 4 and 5 is that the tests performed on reconstituted high copper specimens yielded results very close to those of the reconstituted low copper specimens from the same capsule, which demonstrates that the embrittlement of this material is only weakly influenced by its copper content.

Thermal Ageing

Another interesting result of the surveillance program is the behaviour of thermally aged specimens. Charpy specimens of base material, weld and HAZ, placed in a container fixed on the manhole cover on the cold leg side of a steam generator, were submitted to the operating temperature (287 °C), but not to irradiation.

They were withdrawn after 8 years of operation, or approximately 63000 hours. The test results show that there is indeed an effect of thermal ageing on the weld material, the shift of the Charpy curve measured at the 41 J level being approximately 30 °C, while the USE drop is 14 Joules (Figure 6). This thermal ageing effect interacts with the irradiation embrittlement and could explain why the RT_{NDT} shifts of the welds for the first capsules from both units are higher than expected, although it is not clear whether the thermal ageing effect is additive or competitive with the irradiation damage.

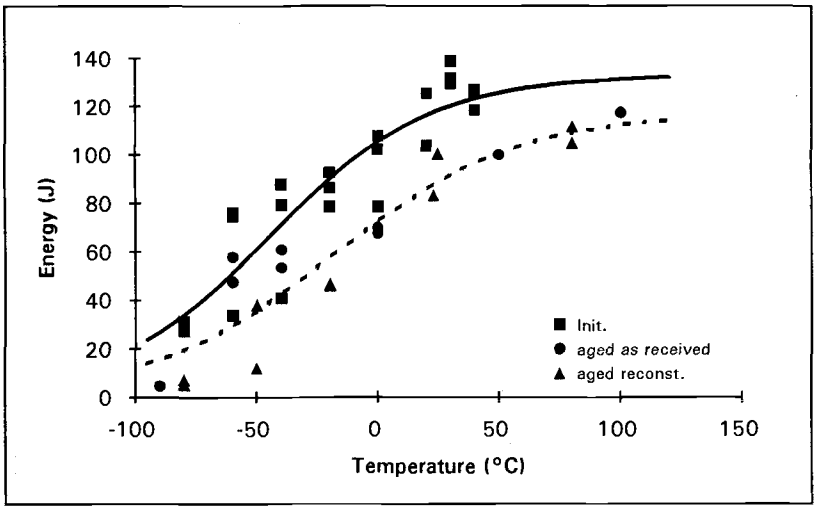


Figure 6: Doel I - uniradiated and thermally aged weld (63000 hours at 287°C)

REGULATORY EVALUATION

As mentioned above, the Charpy-V reconstitution technique allowed Charpy curves to be obtained for the high copper weld material for three fluences in the range 1.7 to 3.9 10^{19} n/cm^2. The Regulatory evaluation of these results yields the RT_{NDT} illustrated on Figure 7, where they are compared to the RT_{NDT} obtained for the low copper weld materials. The insensitivity of this weld material to the copper content is clearly evidenced.

The comparison of the experimental results obtained for the high copper weld with the predictions of Regulatory Guide 1.99 revision 2 for the Cu and Ni contents of interest (0.35% Cu, 0.125% Ni) shows that the Reg.Guide curve (which include 2σ margin) is conservative.

The Regulatory Position 2 of R.G.1.99 allows to make use of "credible" surveillance results to define a material-specific chemistry factor, by a least square fit of the measured RT_{NDT} shifts. The application of this procedure to the reconstituted high copper specimens yields a curve very close to the generic curve (Regulatory Position 1) for the material. The difference is in a large measure attributable to the smaller margin considered in Regulatory Position 2 (Figure 7).

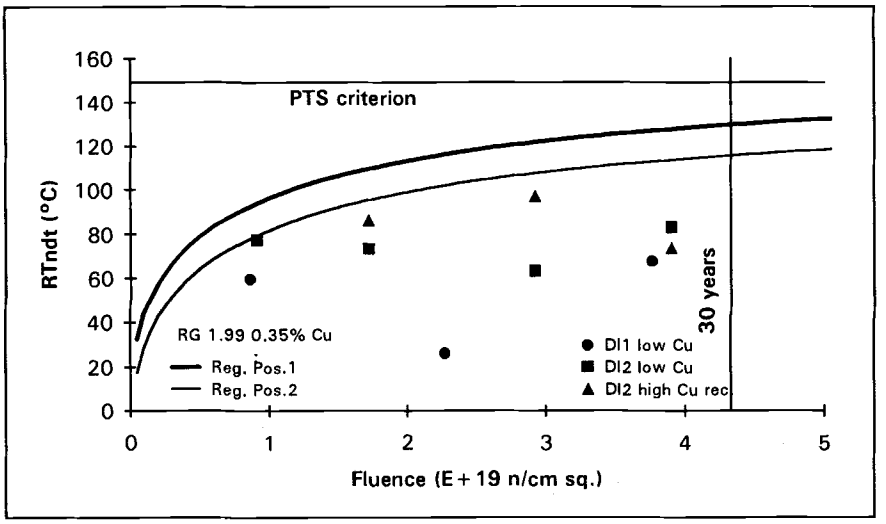


Figure 7: Doel II weld surveillance results - RTndt

On the basis of this plant specific curve, which is above all the experimental results for the copper contents of 0.13, 0.18 and 0.35% for the fluences of interest, the predicted RT_{NDT} shift is 141°C for a fluence of 4.3 10^{19} n/cm^2, corresponding to 30 years in operation.

Since the initial RT_{NDT}, measured by drop weight tests, is - 25 °C for Doel I and -30°C for Doel II, the RT_{NDT}, after 30 years of operation is 116 °C, which is well under the PTS criterion limit of 149°C for circumferential welds [5]. Extrapolation to 40 years of operation, for a fluence of the order of $5.6\ 10^{19}$ n/cm2, yields a RT_{NDT} of 120 °C, which is still acceptable.

Since the upper shelf energy remains largely above 68 Joules for the low and high copper welds, it may be concluded from the Regulatory point of view that the long-term embrittlement of these welds remains perfectly acceptable.

The uncertainty on the copper content of the vessel welds is without consequences, since the surveillance results cover both low and high copper weld materials in the range 0.12% to 0.35%.

MICROSTRUCTURAL INVESTIGATIONS

Microstructural investigations of the weld material (in the unirradiated, thermally aged and irradiated conditions) were performed by AEA Harwell [6], [7]. Both transmission and scanning transmission electron microscopy (TEM, STEM) were used in the examinations of these materials, the STEM being fitted with a field emission electron gun, allowing chemical information to be obtained by energy dispersive X-ray analysis (EDX) on the nanometer scale. Auger spectroscopy was used on the irradiated specimens only.

Unirradiated and Thermally Aged Materials [6]

The standard metallography showed that the microstructure was bainitic and contained a large number of precipitates and inclusions.

The precipitates/inclusions are mainly carbides or silicates and their size distribution peaks between 0 and 1 micrometer, but much larger inclusions were also identified.

The main purpose of the FEGSTEM examination was to determine the amount of copper in solution in the matrix ("effective, copper",i.e. the copper available for precipitation under irradiation). This matrix copper is lower than the bulk copper (which is measured by the chemical analyses) because some of it has precipitated during welding (copper sulphides) or during the post-weld heat treatment (fcc copper precipitates).

Some copper sulphide and fcc precipitates were identified, and the matrix copper for the high copper weld specimens is 0.25% (vs. 0.33 to 0.35% bulk copper), while it is 0.13% for the low copper weld specimens (equal to the bulk copper within the measuring accuracy). Although the matrix copper is significantly lower than the bulk copper in the high copper specimens, it is still two times higher than in the low copper specimens and this alone does not explain why their behaviour under irradiation is similar.

Within the errors of the technique, no difference in matrix copper levels between the as-received and aged materials was observed.

Grain boundary analysis by STEM showed that segregation of Mn, Mo and P to the boundary has occurred, but here again no significant differences between the as-received and aged samples can be seen.

Irradiated Specimens

Weld specimens of the high and low copper materials, irradiated to approximately 3.9 10^{19} n/cm^2 (E>1MeV), were also examined by Harwell. TEM and STEM examinations were performed in the fine grained (8-11 μm) and coarse grained zones (14-21 μm) of each weld specimen. Only minor differences were found between coarse and fine grained regions. The STEM examination provided information on the irradiation-induced precipitates, on the matrix composition and on the grain boundary composition, while the TEM analysis was carried out to provide dislocation density measurements and evidence of fine-scale copper precipitation, with estimates of number densities.

Spot measurements and small area measurements were performed in STEM. Small area measurements are thought to be representative of the matrix composition before irradiation (since they include fine scale precipitates), and comparison with spot measurements (which characterize the matrix composition after irradiation) indicate the elements that precipitate under irradiation.

The main results, which are still preliminary, are summarized hereafter [7]:

In the low copper material::

- Mn, Si and Cu are significantly lower in the spot measurements than in the small area measurements, indicating that these elements are precipitating.

- This is confirmed by the analysis of the precipitates themselves. 15 precipitates examined in the fine grained area (all of 2 nm diameter, except one which was 4 nm diameter) yield an average composition of 36Cu- 33Mn - 11P - 10Ni - 5Si - 5As (Figure 8), but with considerable variation about this composition (range of copper content from 10 to 60%). Precipitates in the coarse grained area seem to be comparable, although only 2 were analyzed. These precipitates having varying concentrations in Cu and Mn, even for a same size of precipitate, are rather atypical compared to small irradiation-induced precipitates identified in other studies

- Knowledge of the precipitate composition, combined with the depletion of copper in the matrix, allows predictions of the number densities of precipitates. The estimated densities range from 2.7 to 9.1 10^{23} m^{-3} (depending on an assumed precipitate diameter 3 or 2 nm respectively). The estimated sizes of precipitates range from 1.8 to 5 nm , which is larger than generally observed for irradiation-induced precipitates.

- Grain boundary analyses by STEM show enrichment of Mn, Ni, Mo , Si, Cu and P. The magnitude of the enrichment (particularly of copper) varies along the grain boundaries, indicating that very fine scale , unresolvable precipitation (<1 nm) occurs.

In the high copper material::

- Copious irradiation-induced precipitation is seen in this material, as indicated by differences in spot and small area measurements. The average composition of these precipitates, measured on 20 precipitates, is 72Cu - 16Mn -2P- 4Ni - 3Si - 3As (Figure 8). The difference in precipitate composition between the high and low copper specimens is contrary to the traditional view of copper precipitation in reactor pressure vessel steels.

- The number density of these precipitates ranges from 2 to 6.8 $10^{23}/m^3$ (for an assumed precipitate diameter 3 or 2 nm respectively) and is comparable to the number density measured in the low copper material. Although the number densities evaluated directly from the SEM or STEM images are lower, they are again comparable in the high and low copper materials, for a given evaluation technique.

- *Since the number densities and the sizes of the precipitates are also comparable in both materials, this can explain why their behaviour under irradiation is similar despite significant differences in bulk copper contents.*

- Just as in the low copper material, the grain boundaries are enriched to varying extents with Mn, Mo, Cu and P. Here again, fine scale precipitation is seen on the grain boundaries

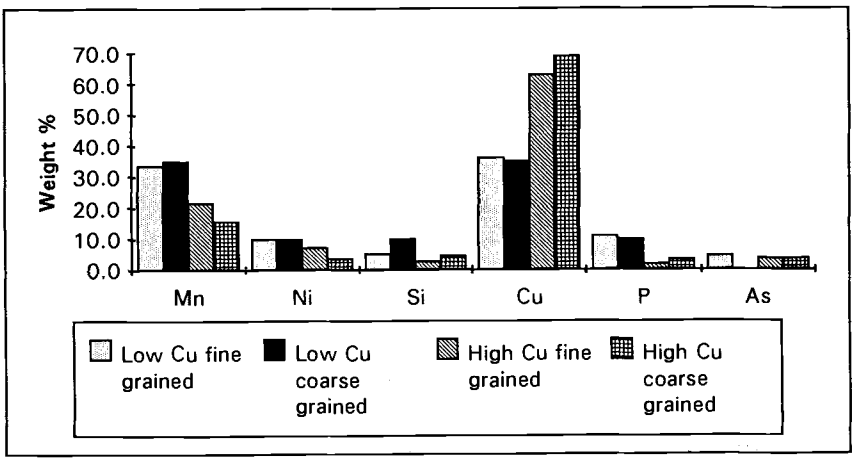


Figure 8 : Average irradiation-induced precipitates composition

- Auger spectroscopy was performed on both the low and high copper specimens . The specimens were cooled to -100 °C and fractured by impact. Despite extensive examination and analysis of fracture surfaces, no sign of intergranular fracture was found. The fracture surfaces were also examined in SEM, offering much better image quality than the Auger microscope, and the examination confirmed that the fracture was completely transgranular cleavage . This is consistent with previous SEM examinations of the fracture surfaces of numerous Charpy specimens, performed at the SCK-CEN on as-received, thermally aged and irradiated specimens, where intergranular fracture has never been observed.

  This very important finding allows us to rule out intergranular fracture of the specimens, despite the evidence of grain boundary segregation.

MICROMECHANICS-BASED EVALUATION

Damage modeling and micromechanics form the conceptual backbone of an "Enhanced Surveillance Strategy" being developed in Belgium [8]. This approach is aimed at the evaluation of plant-specific fracture toughness bounds, by combination of conventional Charpy-V and tensile test results with K_{Jc} measurements using reconstituted surveillance remnants. The major anticipated benefit is to achieve a less conservative, albeit safer definition of RPV steel embrittlement, leading to improved vessel life management.

A significant achievement at this stage of development entails the use of the load versus time (deflection) response of the Cv-notch impact test, as instrumented by strain gages mounted on the hammer tup. This allows a physically- grounded definition of ductile-brittle transition temperature (DBTT). This is most useful primarily in two respects:

1. To provide further damage modeling insights into the steel in-service behaviour.

2. For indexing of dynamic and crack arrest fracture toughness to the Cv test in more rigourous a manner than done in current Regulatory and engineering practice (i.e., 41 Joule index).

This methodology has been previously applied to the Doel I and II pressure vessel welds [1]; an update is presented herein on the basis of new experimental and analytical efforts.

Concepts, Definitions and Major Implications.

The following outline summarizes a more extensive presentation to be found in reference [8].

From a combined dislocation dynamics and fracture mechanics perspective, the most fundamental information contained in the Cv impact test is the load diagram, as derived from the instrumented load- time traces. An example of the evolution of such traces with test temperature for the Doel II weld (Capsule 3) is shown by Figure 9. The load diagram quantifies this evolution, as illustrated by Figure 10.

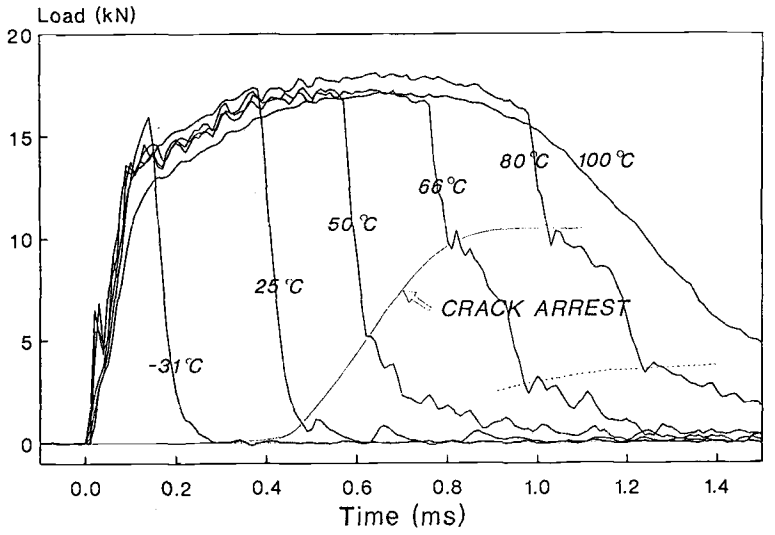


Figure 9: Instrumented Cv-impact load-time traces

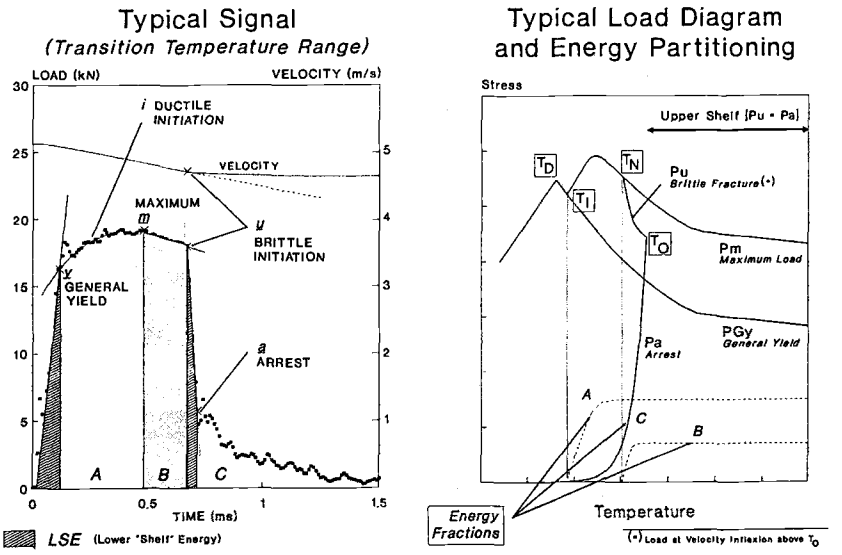


Figure 10: Typical load diagram and energy partitioning obtained from instrumented Cv-Impact traces

Considering a typical signal in the transition temperature range, the left-hand part of the Figure, it is well known - and acknowledged by testing standards in preparation [9] [10] - that at least four characteristic loads can be defined: Fy: General Yield Load; Fm: Maximum Load; Fu: Brittle Crack Initiation Load; Fa: Crack Arrest Load.

General Yield Load; a point at which yielding has spread to the entire area corresponding to the ligament under the notch (net area), while strain hardening is still negligible.

Maximum Load; a point at which a ductile crack initiated by void nucleation (on inclusions or second phase particles), growth and coalescence, at some distance under the notch (at time marked i on Figure 10, left), has extended into a crack front across the specimen width, collinearly to the notch;

Brittle Crack Initiation Load; in the transition temperature range, ductile stable crack growth is interrupted at this point by the competition of stress-controlled cleavage, initiated within "trigger" particles (such as grain boundary carbides or other "weak" spots) and propagated further (into the ferrite matrix, to the next grain, ...);

Arrest Load for fast (brittle) crack propagation and conversion back to ductile crack growth, but under plane stress conditions, with formation of shear lips along slant planes at ≈45° angle to the main fracture surface.

Some energy partitioning can be associated to the Cv load diagram, and if done according to the characteristic loads identified by the testing standards, this leads to four distinct fractions, labelled LSE, A, B and C. Their definition is illustrated by the left-hand side of Figure 10. The energy fraction LSE, Lower Shelf Energy, is composed of elastic energy and brittle crack propagation energy. It is largely insensitive to service exposure, and normally never exceeds 10 J. The energy fraction A correponds *very roughly* [8] to an "Initiation Energy" while B is *indicative* of the dynamic tearing resistance.

Concerning the transition temperature concept, the emphasis in this work lies on the characteristic temperatures marked T_I and T_0, right-hand side of Figure 10. The onset of Cv impact upper shelf regime begins at Characteristic Temperature T_0 , above which the load curves Fu(T) and Fa(T) coincide, i. e. there is no brittle crack initiation and the shear fracture appearance reaches 100%. By contrast, T_I, " Ductile Crack Initiation Temperature", corresponds to the onset of actual ductility, i.e. it is the temperature at which the shear fracture appearance begins to exceed 0%. As illustrated by Figure 11, the fracture appearance of Cv impact specimens can always be determined from the load diagram through the relationship:

$$SFA(\%) = \left[1 - \frac{Fu-Fa}{Fm + k(Fm-Fy)}\right] x100$$

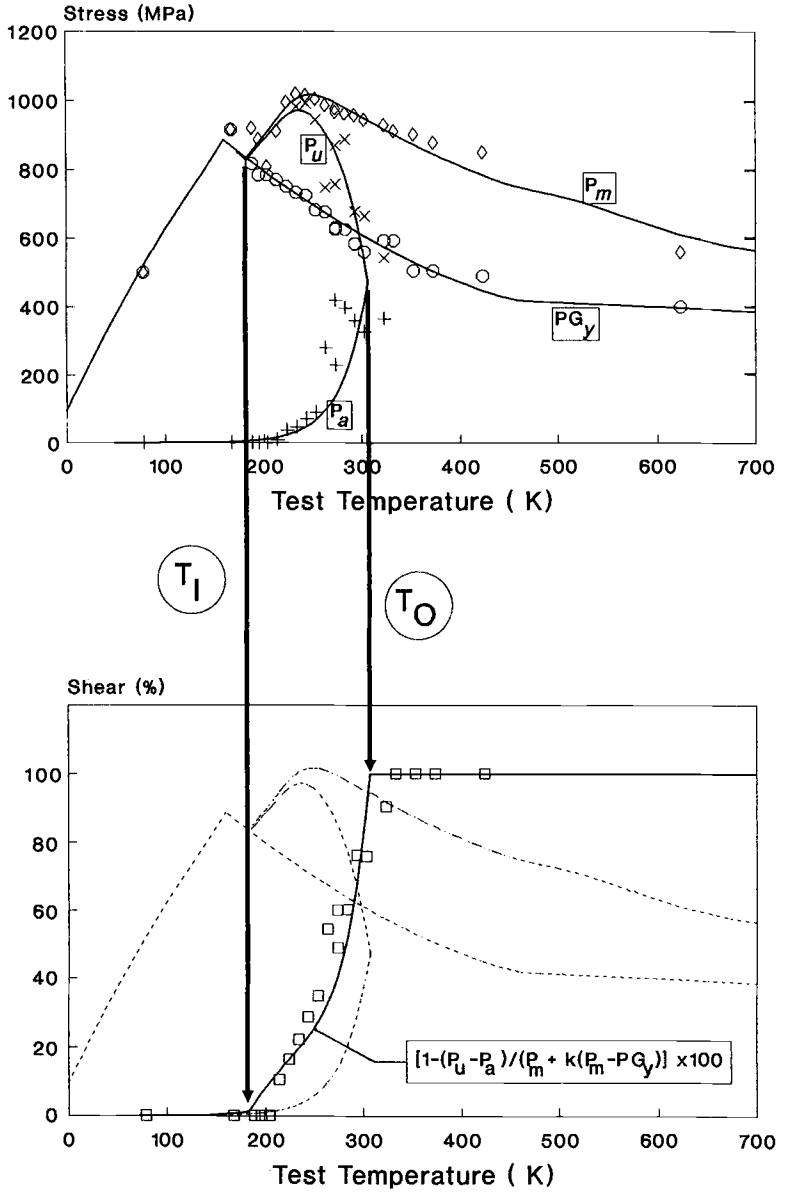


Figure 11: Correlation of fracture appearance to Cv-impact load diagram

where, generally, $k \approx 0.5$. The best value for k is most accurately defined, *on a case-by-case basis*, by means of simultaneous fit to both the load diagram and to planimetry measurements on the fracture surfaces.

The temperature T_I is rather insensitive to specimen thickness and notch angle, but it depends on notch acuity and strain rate. In any case, it is adequate for indexing fracture toughness. The increase of T_I under service conditions (thermal and strain ageing, irradiation) is a **good measure of the corresponding shift of the dynamic initiation fracture toughness K_{Id}** for the same strain rate - assuming the toughness-temperature dependency (shape) to be invariant, as also done in the Regulatory, ASME XI based framework.

It has been argued in [8] that T_0 is adequate for indexing K_{Ia}, this despite the near plane stress state for the specimen deflections at which this temperature is defined. Supportive experimental evidence has been provided (Cv miniaturization, Cv precracking). Very recently, Wallin [11] has considered an alternate K_{Ia} indexing method using the temperature at which the Cv crack arrest load reaches a level of 4 kN (a level aimed at providing a sufficient ligament for plane strain approximation); he has obtained a reasonably good correlation of this temperature with the temperature at which K_{Ia} reaches 100 MPa$\sqrt{m}$, and he has suggested that the same, exponential "master curve" can be used to represent the temperature dependence of K_{Ic} and K_{Ia}.

In our work, we also use an exponential master curve to fit the Cv crack arrest load in function of test temperature (Figure 12).

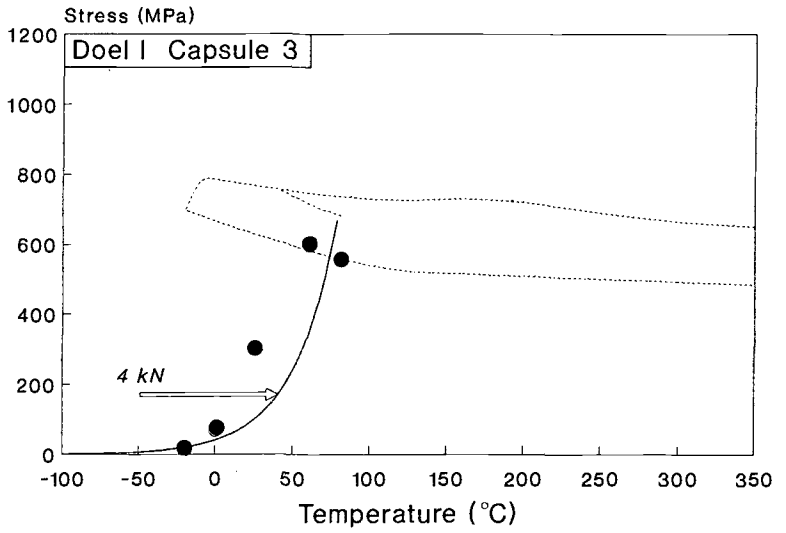


Figure 12: Crack arrest load

However, with increasing embrittlement, our T_0 intercept moves to higher loads (in relation to the decrease of "tearing energy" fraction B) and thus to higher temperatures; our index T_0 is more conservative, but quantitatively speaking, and especially in view of the metallurgical scatter, it differs little from Wallin's index; it can be estimated from fracture appearance data in the absence of load-time records.

Upon irradiation, one generally observes that the shifts of T_I and T_0 are roughly equal.

Yet, it may happen that the 41 J shift significantly exceeds the shifts of both T_I and T_0. In such case, the 41 J shift is inadequate for fracture toughness indexation. The physical reasons for such occurrence are explained elsewhere [1] [8] [12]; the Regulatory significance is reviewed in reference [12]. Such steels have been labelled "*Outliers*", in fracture mechanics terms. The present welds belong to such category. They also are outliers in damage modeling terms,as evident from the microstructural examination summarized in the preceding section.

In a statistical perspective, the characteristic temperatures defined above must be understood as best mean values; for instance, it may happen that a specimen broken at a temperature somewhat exceeding T_0, the mean upper shelf onset, does not display fully ductile, 100% shear response, and vice versa for T_I, 0% shear (Figure 11).

A final, most important feature of our approach entails an effort to bring together, into an engineering-oriented synthesis, the interrelated disciplines of irradiation damage modeling, dislocation dynamics and fracture mechanics. Of relevance here with respect to the previous paper on Doel I, II welds [1] is the combination of Cv and tensile test data at the light of dislocation theory [8]. In particular, this has led us to conclude, as shown below, that the microcleavage fracture stress for the Doel welds is not affected by in-service exposure corresponding to design life, despite suggestion to the contrary [1].

Results and Discussion.

The results of this evaluation are summarized by Figures 13 to 19. It is emphasized that the evaluation method *links consistently all features of the Cv- impact test:* not only energies (total and fractional), lateral expansion and fracture appearance, but also loads and deflections [13]. All these parameters are fitted *simultaneously*, and theoretical constraints are furthermore imposed whenever fully justified [8]. This allows identification of eventual experimental deficiencies or completion of missing information. For instance, the lack of instrumented data for the Doel I, II baseline originally developed at Cockerill many years ago, could be remedied unambiguously by just five new SCK-CEN tests. Here, reconstitution technology can also be put to optimized use. Of course, too many figures would be needed to illustrate here all details of such evaluation, and a selection had to be made.

Figures 13 , taken from [1], illustrates the effects of thermal ageing alone of the weld material (68000 hours at 287°C). The unusual aspect of the curves fitted through the data points is due to the fitting technique used, consisting of fitting separately the energy fractions A, B and C defined on Figure 10. Fractions A and B are fitted by the upper half of an hyperbolic tangent above the temperature corresponding to 50% of their respective shelf levels, and by a straight line below this temperature. Energy fraction C is fitted by an exponential. The three contributions are then added algebraically, to obtain the curves illustrated on Figure 13 and 14. This technique allows a finer interpretation of the effect of irradiation by showing how each energy fraction, associated with physical events (initiation, propagation and arrest), is affected.

It is shown on figure 13 that thermal ageing affects the "tearing energy" (fraction B): The shelf drop of this fraction is entirely due to time at temperature, the contribution of neutronic exposure being negligible. This appears clearly from a comparison with Figure 14 (taken from[1]), which illustrates the results obtained for the third surveillance capsule from Doel 1. A second ageing effect is a shift to higher temperature of the post-arrest energy fraction (C) and, by implication, an upwards shift of K_{Ia}.

Although Figure 13 might suggest two populations in the transition region for the baseline specimens from Doel I and Doel II respectively, a more detailed evaluation shows that the reference temperatures T_I and T_0 are identical. Furthermore, upper shelf energies cannot be statistically distinguished

The comparison of Figures 13 and 14 shows that neutronic exposure shifts all energy fractions to higher temperature, and decreases the shelf of the pre-maximum load energy fraction A. Most importantly, the 41 J shift is significantly larger than the physical shifts of T_I and T_0: This may be seen on Figure 14, where these shifts are estimated roughly by the shifts of the beginning of the transition region and of the upper shelf respectively. A better estimation is presented on Figure 15, where it can be seen that the shift measured at 50 % of shear fracture appearance constitutes a conservative approximation of the shifts of T_I and T_0.

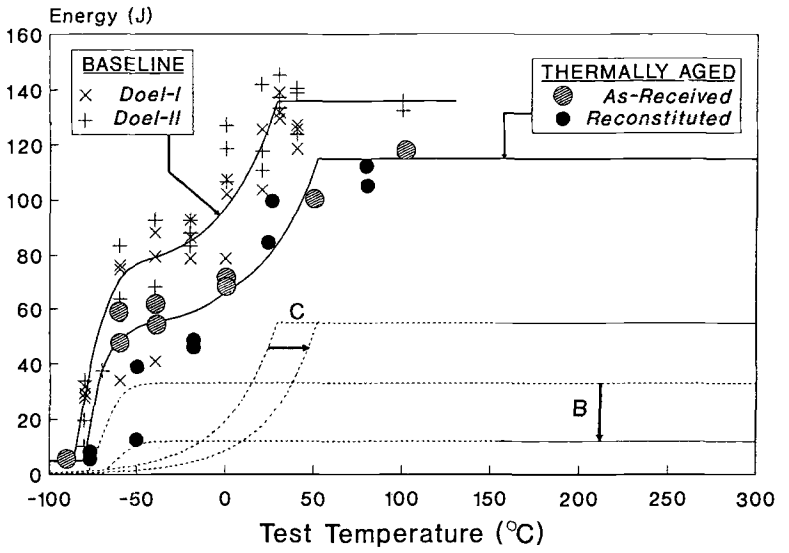


Figure 13: Thermally aged Doel I material (63000 h at 287°C)

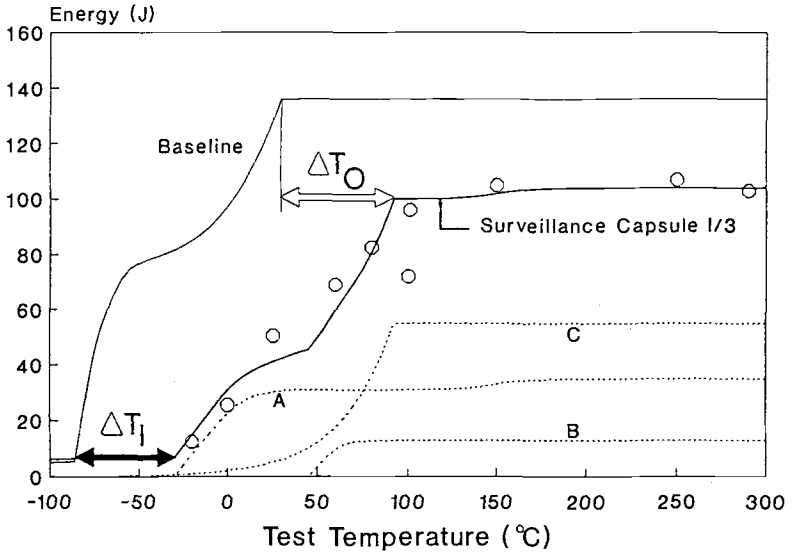


Figure 14: Irradiated Doel I material (3.7 10^{19} n/cm^2)

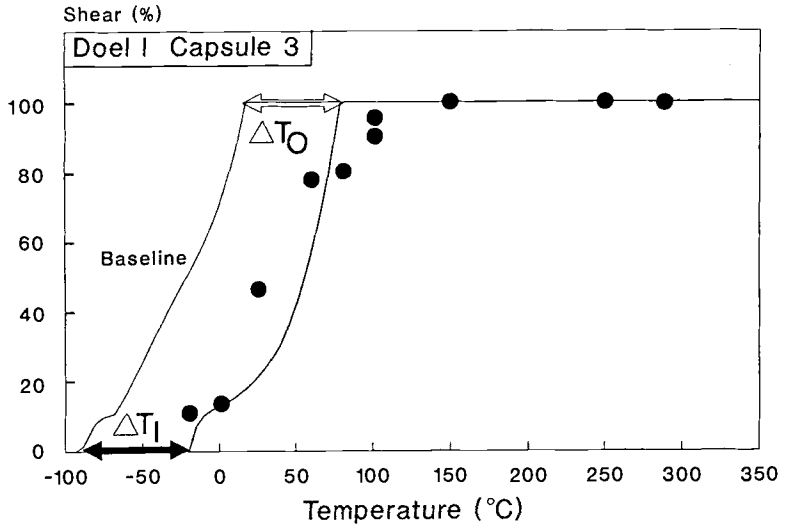


Figure 15: Irradiation effect on fracture appearance.

A more precise estimation of T_I is given on Figure 17 on the basis of the load diagram, where the shift is estimated to be 65°C between the thermally aged and the irradiated condition. It must be combined with a shift of 8°C between the baseline and thermally-aged condition (Figure 16), yielding a final value of 73°C.

This is the "Outlier" behaviour mentioned above; the difference is so large as to more than compensate for the strain rate effect on initiation fracture toughness, according to our current estimates.

The lack of copper influence is confirmed by the load diagrams of Figures 18 and 19 , where practically no difference can be seen between the low copper and high copper results.

The implication of Figures 16 to 19 is that the dynamic initiation fracture toughness shifts do not exceed about 73°C for both Doel I and II weld metals, irrespective of copper content. The static toughness shifts are estimated to be slightly larger, but this needs to be verified by actual measurements coupled to our micromechanical modeling capability [8], along our "Enhanced Surveillance Strategy".

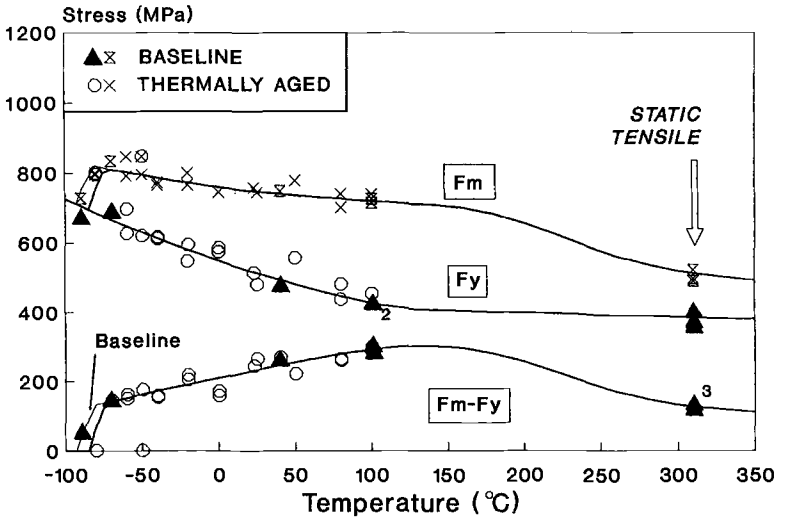


Figure 16: Combined Cv-impact and static tensile load diagram of unirradiated Doel I,II surveillance welds

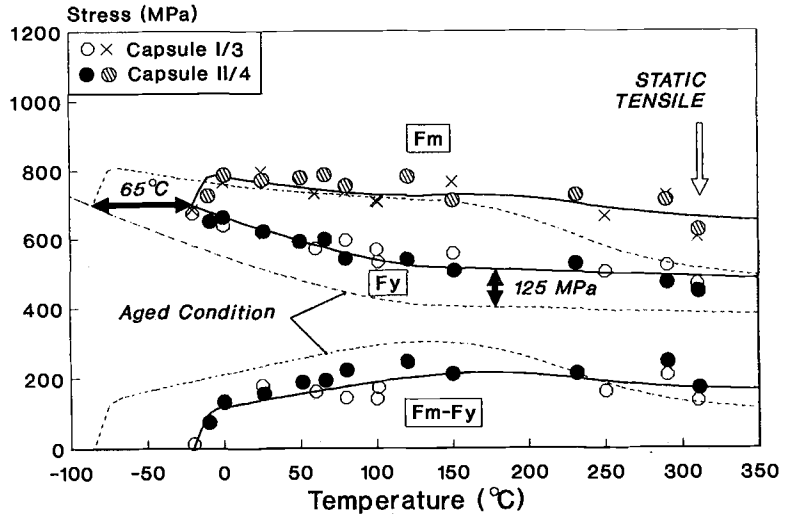


Figure 17: Irradiation embrittlement of Doel I, II surveillance weld.

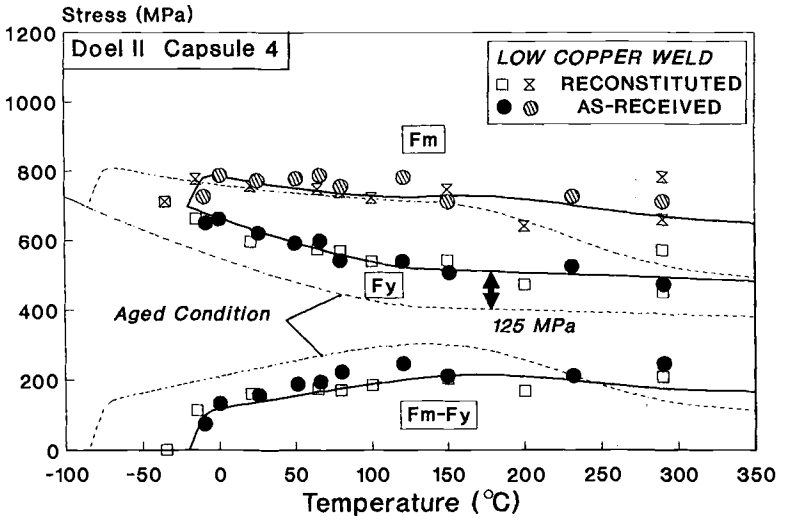


Figure 18: Cv-reconstitution of Doel II low copper weld.

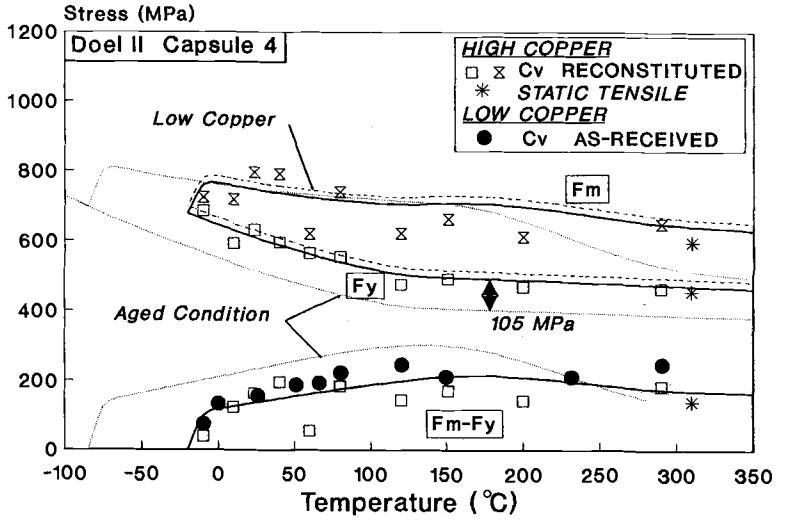


Figure 19: Cv- reconstitution of Doel II high copper weld and comparison to low copper weld.

The new analytical work [8] has imposed the conclusion that the microcleavage fracture stress is not affected by in-service exposure up to design life. This can be seen on Figures 16 to 19: the stress at T_I is constant. Previous suggestion of a reduction of this stress upon irradiation [1] was due to lack of the present theoretical insight and this was compounded by an experimental bias of the yield load for three specimens broken at low temperature: under such conditions, the usual hammer velocity of ≈5 m/s is too large; verification has been done by new tests at ≈2 m/s. The current conclusion is consistent with the absence of any evidence of intergranular fracture, as established by the intense scrutiny outlined in the previous section.

Other important learnings from Figures 16 to 19 are:

1. The irradiation-induced yield strength increase entails only the athermal component of the flow stress (i.e., long-range obstacles to dislocations); the static tensile yield data at 310°C are confirmed and considerably augmented by the related instrumented Cv results.

2. This yield increase of 105-125 MPa is consistent, to first order, with the precipitation features determined by FEG-STEM; here, further SANS characterization would allow to quantify this microstructure relationship to sufficient accuracy for the unravelling of the so-called "matrix damage" component of embrittlement (this is relevant for vessel management beyond design life).

3. The yield increase is consistent with the Davidenkoff diagram in terms of the shift of T_I but not in terms of the 41 J shift for the Doel II capsules (Figure 3). The reasons for this difference are partly understood [14] , and warrant further investigations

CONCLUSIONS

In-service embrittlement of Doel I, II RPV welds displays an apparent outlier behaviour when analyzed along current Regulatory guide-lines:

- apparent insensitivity to the copper content;
- a high RT_{NDT} shift for a low fluence, followed by apparent saturation;
- much lower yield stress or hardness increase than predicted by generally accepted correlations with RT_{NDT} shifts;
- sensitivity to thermal ageing at operating temperature.

The Regulatory evaluation of the surveillance results leads to the conclusion that the embrittlement remains acceptable by a large margin for the higher fluence reached by a surveillance capsule (corresponding approximately to 27 years of operation for the vessel).

Predictions for 40 years of operation also conclude to the acceptability of the embrittlement, the predicted RT_{NDT} being 120 °C, to be compared with the maximum value of 149 °C (for a circumferential weld) acceptable according to the PTS criterion. An additional safety margin is provided by the preheating of the safety injection water to 35°C. These predictions shall have to be confirmed by surveillance results, that shall be obtained in the coming years.

The microstructural investigations yielded two very important results:

- The sizes and number densities of precipitates are similar in the high and low copper materials, providing an acceptable explanation for the lack of influence of the copper content on the mechanical properties.
- No indication of intergranular fracture could be found.

The micromechanics evaluation has reached the following conclusions:

- The 41 J shift does not properly index the fracture toughness shift for this weld material: it is too conservative for what concerns dynamic cleavage initiation, and is believed conservative for static initiation toughness.
- The yield strength increases under service exposure are consistent, within uncertainties, with the FEG-STEM microstructural investigations
- The dynamic tearing resistance under upper shelf conditions seems quite sensitive to in-service temperature. This is primarily due to a thermal ageing effect.
- Actual fracture toughness tests are expected to confirm the current views that margins will remain adequate in the longer term, i.e. beyond the maximum fluence for which surveillance results are available.

In conclusion, there is essentially no doubt that the Doel I, II vessel welds will continue to feature excellent cleavage initiation fracture toughness throughout design life.

ACKNOWLEDGMENTS

The authors are grateful to Dr. Dumbill, Dr.Phythian and Dr.English, from AEA, for the constructive discussions of their excellent microstructural work. They are also indebted to the LHMA Technical Team, in particular P. Beckers, M. Eyckmans, Th. Noels and R. Vosch, for their careful and always diligent experimental support.

REFERENCES

[1] Gerard R. and Fabry A., "Integrity Assessment of Doel I and II Reactor Pressure Vessels", IAEA Specialist's Meeting on Integrity of Pressure Components of Reactor Systems, Paks, Hungary, May 25-29 (1992).

[2] US NRC Regulatory Guide 1.99 Revision 2 "Radiation Embrittlement of Reactor Vessels Materials" (May 1988)

[3] Chaouadi R.,Fabry A., Puzzolante J.L., Vandermeulen W., Van de Velde J., Van Ransbeeck T., van Walle E. (SCK-CEN), Klausnitzer E., Gerscha M. (Siemens KWU) "The reconstitution effort at SCK-CEN", ASTM E10.02, San Diego, January 1991

[4] van Walle E.,"The Reconstitution of Small Remnant Parts of Charpy-V Specimens: Influence of the Hammer Geometries, ASTM vs. ISO" , Smirt-11 Post-Conference Seminar "Assuring Structural Integrity of Steel Reactor Pressure Boundary Components", Taipei, August 26-26, 1991

[5] Code of Federal Regulations, Title 10, Part 50, paragraph 50.61:"Fracture Toughness Requirements for Protection Against Pressurized Thermal Shock Events" (November 1986)

[6] Phythian W.J.,AEA TRS-2062 "Microstructural Assessment of Belgian Weld Material" (March 1991)

[7] Dumbill S., Cattle G.C., Mace J.A., Phythian W.J., AEA Draft Report on Microstructural Analysis of Doel I,II Irradiated Weld Metal (June 1994).

[8] Fabry A., van Walle E., Chaouadi R., Wannijn J.P., Verstrepen A., Puzzolante J.L., Van Ransbeeck Th., Van de Velde J. (SCK-CEN), Petrova T., (INRNE, Sofia), "RPV Steel Embrittlement: Damage Modeling and Micromechanics in an Engineering Perspective", IAEA/OECD Specialists Meeting on Irradiation Embrittlement and Optimization on Annealing, Paris, September 20-23, 1993

[9] Proposed Standard Method for the Instrumented Charpy-V Impact Test on Metallic Materials", ESIS Instrumented Charpy-V Standard, Draft 9, (1993).

[10] "Standard Guide for Conducting Supplemental Surveillance Tests for Nuclear Power Reactor Vessels, E706(1H)", ASTM Committee E10, Revision of E0636-83, in Preparation.

[11] Wallin K. "Descriptive Potential of Charpy-V Fracture Arrest Parameter with Respect to Crack Arrest K_{Ia}", ESIS 2nd TCS Workshop, SCK-CEN, Mol, Belgium, April 28, 1994.

[12] Fabry A. et.al., "Research to Understand the Embrittlement Behaviour of Yankee/BR3 Surveillance Plate and Other Outlier RPV Steels", Effects of Radiation on Materials : 17th International Symposium, Sun Valley, USA, June 20-23, 1994.

[13] van Walle E. et.al., "Notch Reorientation of Charpy-V Specimens of the BWR Phillipsburg 1 through Reconstitution", Effects of Radiation on Materials : 17th International Symposium, Sun Valley, USA, June 20-23, 1994.

[14] Fabry A., "Short Range Irradiation-Induced defects under PWR Service conditions", (To be published).

Michel Bethmont,[1] Jean-Michel Frund,[2] Bernard Housin,[3] and Pierre Soulat[4]

THE TOUGHNESS OF IRRADIATED PRESSURE WATER REACTOR (PWR) VESSEL SHELL RINGS AND THE EFFECT OF SEGREGATION ZONES.

REFERENCE: Bethmont, M., Frund, J. M., Houssin, B., and Soulat, P., **"The Toughness of Irradiated PWR Vessel Shell Rings and the Effect of Segregation Zones,"** *Effects of Radiation on Materials: 17th International Symposium, ASTM STP 1270,* David S. Gelles, Randy K. Nanstad, Arvind S. Kumar, and Edward A. Little, Eds., American Society for Testing and Materials, 1996.

ABSTRACT: To establish the integrity of pressure water reactor (PWR) vessels it is necessary to determine the toughness of A508Cl.3 steel at the end of its life, that is after thermal ageing and irradiation embrittlement. In safety analyses the toughness can be deduced from a reference curve set forth in the code (ASME or RCC-M). The validity of the reference curve has been verified for several years for unirradiated French reactor vessels. Tests were performed on specimens taken from materials having heterogeneities in chemical composition. For most of the test results the reference curve is a lower bound. To solve the problem of determining the toughness of SA 508 Cl.3 steel after irradiation and in the presence of possible heterogeneities, the toughness results were gathered. The synthesis shows that the RCC-M code curve is conservative.

KEYWORDS: pressurized water reactor, pressure vessel steel, SA 508 CL.3, toughness, irradiation, chemical composition heterogeneities, Charpy-V tests

---

OBJECTIVE

Analyses of the brittle fracture resistance of pressure water reactor (PWR) power plant vessels make it necessary to determine the material toughness at the end of its life span ie, after irradiation embrittlement.

---

[1]Manager, Électricité de France, Research and Development Division, Materials Study Department, BP N°1, 77250 Moret-sur-Loing, France.

[2]Researcher, Électricité de France, Research and Development Division, Materials Study Department, BP N°1, 77250 Moret-sur-Loing, France.

[3]Senior Consulting Engineer, Framatome, Materials and Technology Department, Tour Fiat, Cedex 16, 92084 Paris La Défense, France.

[4]Manager, Commissariat à l'Énergie Atomique, DECM/SRMA, CE Saclay, 91191 Gif-sur-Yvette, France.

Copyright© 1996 by ASTM International www.astm.org

To evaluate the effect of irradiation upon steel A508Cl.3 the toughness in the unirradiated state must be known. A reference curve put forward by the RCC-M code[1] is generally used. The curve, which is the same than ASME one, presents the evolution of the minimum toughness of vessel steel in relation to temperature. The lower bound is defined from the tests results of the most brittle materials.

The presence of segregation zones in steel may question the toughness values used to evaluate the integrity of PWR power plant vessel shell rings produced from solid ingots. Segregation zones are enriched in alloying and residual elements. They are displayed during the solidification of the ingot used to manufacture vessel shell rings. The axial segregations are eliminated by piercing the ingot but some of them (A or inverted V) may still be seen near the inner surface of the shell ring (Fig. 1). The influence of segregation zones on mechanical properties of pressure vessel steel has been showed at the time of a previous study [1, 2]. So, this phenomenon has been studied and results are presented below.

SEGREGATION ZONES

Chemical Composition

We have studied twenty five segregation zones which were observed in nozzle support rings, tube plates, vessel nozzles (made up of solid ingots) and shell rings produced from hollow ingots with an electron probe microanalyser. The test results have shown that the segregation zones are very much enriched with alloying elements and impurities (Table 1). The levels are particularly high in the case of phosphorus, molybdenum, and carbon [3].

TABLE 1--Chemical composition of the segregation zones of forged parts made of steel SA 508 Cl.3 as deduced from microanalyses

$$\text{(Enrichment (\%)} = \frac{\text{maximal content in segregation zones - nominal content}}{\text{nominal content}} * 100)$$

	C	Mn	Ni	Cr	Mo	Si	Cu	P
Content by weight (%).	0,17 to 0,40	1,6 to 2,3	0,8 to 1	0,2 to 0,4	0,7 to 2	0,25 to 0,4	0,06 to 0,14	0,010 to 0,045
Enrichment (%)	15 to 110	20 to 70	10 to 50	30 to 80	40 to 300	15 to 75	15 to 75	25 to 500

Influence of Segregation Zones on Mechanical Characteristics

Hardness tests--Vickers Hardness tests have been performed under 0,1 Kgf on segregation zones. The hardness of these zones exceeds by 30 to 40 HV that of steel with nominal composition (hardness of that steel is about 225 HV).

---

[1] K_{IC} = Min [36,5 + 3,1 exp[0,036 (T - RTNDT + 55,5)] ; 220] [MPa $m^{1/2}$]

Charpy V tests : transition temperature shift before and after irradiation--A special experimental program has been carried out to check and quantify the influence of segregation zones on the ductile-brittle transition of the vessel steel.

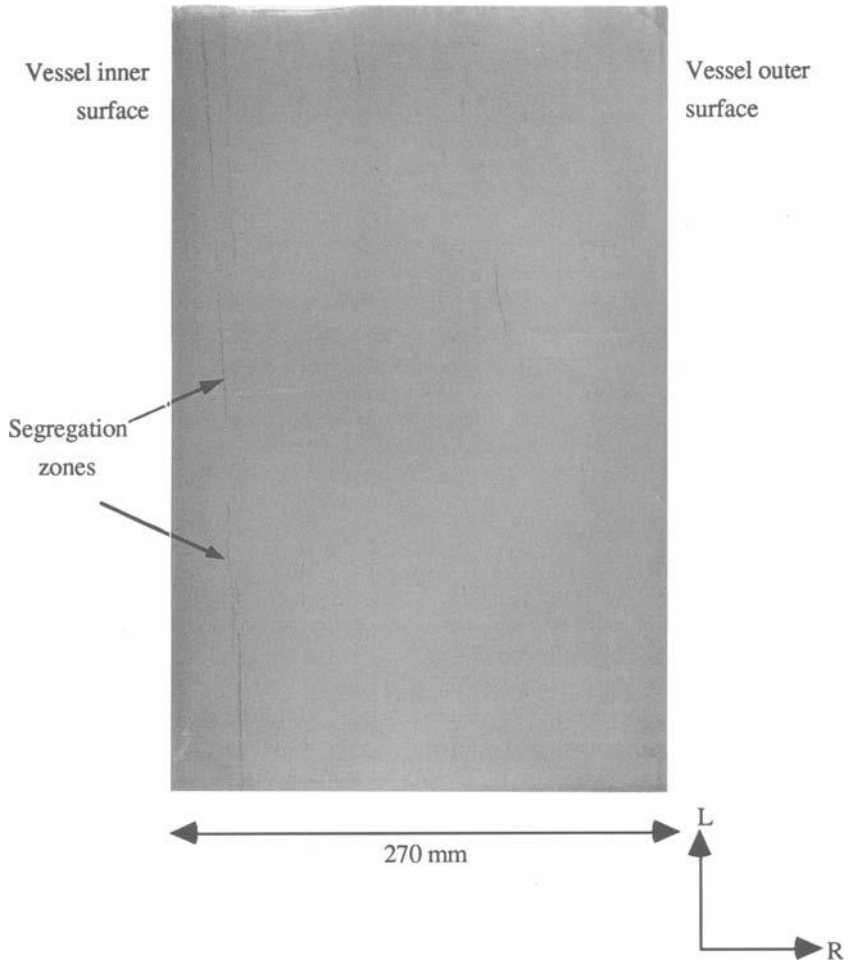


FIG. 1--Macrographic view of a section of a PWR shell ring.

Charpy-V notch specimens were taken - following the CR orientation - at a distance of 20 mm to 60 mm under the inner surface of the nozzle support ring. Two different types of specimens were machined. Two series are composed of specimens located with a segregation zone at the notch tip, and two other series are made of specimens which show no segregation zone in the notch plan. The specimens were irradiated in the experimental reactor OSIRIS, with neutrons at a 4.6 x 10^{19} n/cm^2 (E > 1 MeV) average fluence (irradiation temperature : 288 ± 5°C).

The resulting impact strength transition curves are presented in Fig. 2 (these curves have been determined from an hyperbolic tangent fit). With an unirradiated material, we notice a substantial difference between the results achieved from tests conducted on specimens showing a segregation zone at the notch tip and those obtained from specimens with no segregation zone. A shift of the transition temperature TK56 (temperature for a fracture energy of 56 J) of about 73°C is revealed. On the other hand, it seems that the upper shelf is not modified by the segregation zones.

For the most part these results are confirmed by the bibliography. Poitrault et al [4, 5], for example, have determined a shift of 70°C of the reference temperature TK68 (temperature for a fracture energy of 68 J) when segregation zones are present. The shift is 52°C for the same reference temperature in the study carried out by Cerjak et al [4, 6]. The few results available in the bibliography show that the upper shelf was reduced by about 25% to 55%, due to the presence of segregation zones [4, 6, 7]. The way specimens were taken could explain the different influence of the segregation zones over the upper shelf. When the segregation zone fills the whole of the notch ligament we notice a reduction of the upper shelf because the segregation zone affects both the start of the crack and its propagation. On the contrary, when the segregation zone only influences the notch tip, there is no drop of the upper shelf compared with the non-segregated material.

In the case of irradiated material, the shift of the transition curves reaches 108°C when no segregation zones are present, and 47°C when tests are performed on specimens with segregation zones at the notch tip (we have kept the maximum value of shifts exibited either by impact strength transition temperature or that of the lateral expansion transition curve). When using the FIS formula[1] (FIS is an empirical formula to evaluate the irradiation damage) the shift is predicted at 63°C. We can thus make the following remarks:

- the shift of the transition temperature for metal with no segregation zone exceeds by 45°C the one obtained with the FIS formula,
- the effect of irradiation is less important on steel that is already embrittled by segregation zones,
- when it comes to the upper shelf no significant difference has been noticed for the metal with no segregation zones.

However, the lack of experimental results make these results questionnable.

---

[1]FIS formula: $\Delta RTNDT\ (°C) = 8+[24+1537(\%P-0{,}008)+238(\%Cu-0{,}08)+191\ \%Ni^2\ \%Cu]\ [F/10^{19}]^{0{,}35}$

Where : F = neutrons fluence n/cm^2 (E > 1 MeV),
(%Cu-0,08) = 0 if Cu < 0,08%
(%P-0,08) = 0 if P < 0,08%

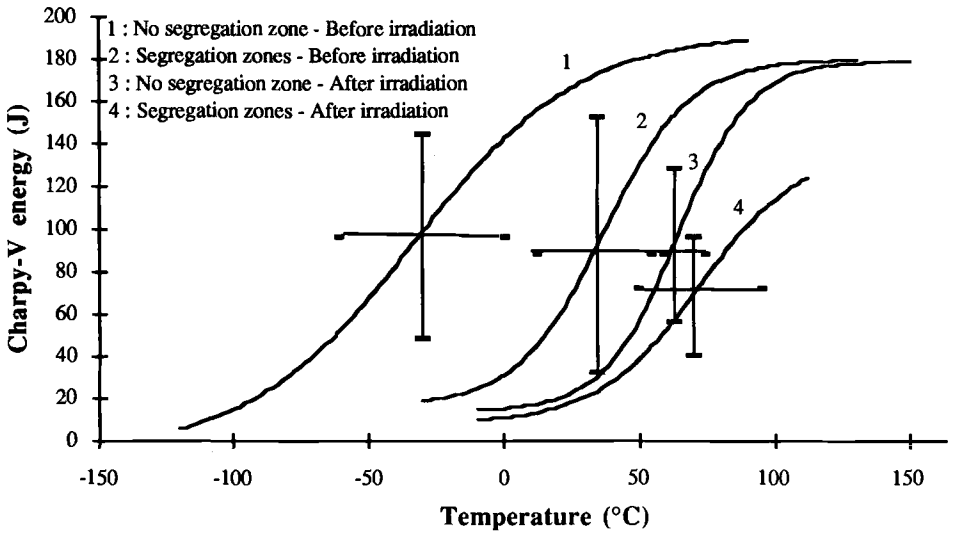


FIG. 2--Impact strength transition curves : comparison of the material with no segregation zones and that with segregation zones, before and after irradiation.

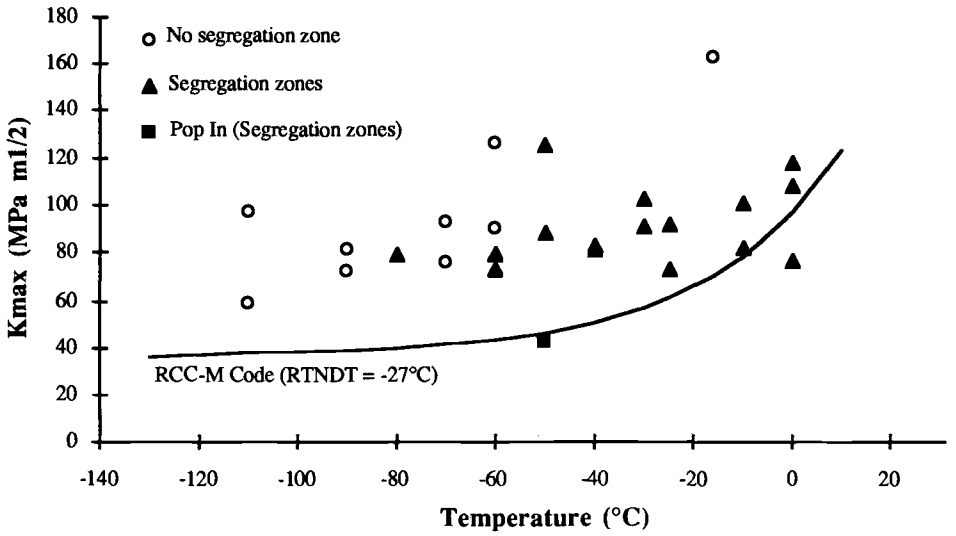


FIG. 3--Comparison of the toughness results obtained from tests conducted on 1T-CT specimens showing-or not- a segregation zone at the fatigue crack tip [2].

Study of Charpy-V tests : mode of fracture--Fractographic analyses carried out on some broken specimens with segregation zones have displayed near the notch the presence of intergranular rupture faces which end with a cleavage fracture. The maximum temperature at which this mode of fracture was noticed in the case of unirradiated specimens is 40°C.

Toughness tests--The following approaches have been adopted to study the influence of segregation zones over vessel steel toughness:

- comparison of the results of toughness tests conducted on CT type specimens of 25 mm thickness taken from a vessel shell ring. Some of these specimens show segregation zones located exactly at the fatigue crack tip.
- evaluation of the scatter band of toughness values resulting from the presence of segregation zones with tests on CT type specimens whose thicknesses range from 25 to 100 mm, with different orientations and taken out of two vessel shell rings.

Transition temperature shift due to the presence of segregation zones--The results obtained from tests carried out on CT 25 specimens are given in Fig. 3. We can see that the lower bound of the toughness transition curve for tests made on specimens showing a segregation zone at the fatigue crack tip is shifted by about 70°C, at the 80 MPa $m^{1/2}$ level when compared to the corresponding lower bound of specimens with no segregation zone. (Experimental results are numerous around the 80 MPa $m^{1/2}$ toughness level). The shift value for the toughness transition temperature in relation with the presence of segregation zones must be considered cautiously due to the wide experimental scatter, the very small quantity of valid test results, and a limited data base especially for segregation-free specimens.

In fact, it seems that the toughness transition temperature shift linked to the presence of segregation zones is similar to the one noticed with the impact strength tests results.

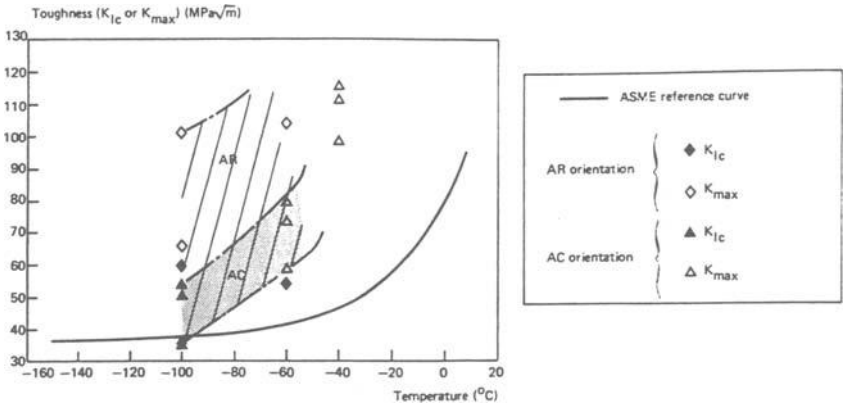
The static toughness reference curve as defined by the RCC-M code is also represented in Fig. 3, according to the RT_{NDT} temperature of the material.

Most of the toughness values including those obtained from tests made on samples showing segregation zones are higher than the reference values. This is true except for two toughness values. The first one at temperature of -50°C is lower than the reference value by 5 MPa $m^{1/2}$. The other one, determined at a temperature of 0°C shows a temperature shift of 10°C higher than that of the reference curve. The shift value of 10°C can be compared with the scatter band of the RT_{NDT} temperature within the vessel shell rings. A maximum variation of 17°C of the RT_{NDT} temperature has actually been measured (the RT_{NDT} temperature is generally equal to NDT).

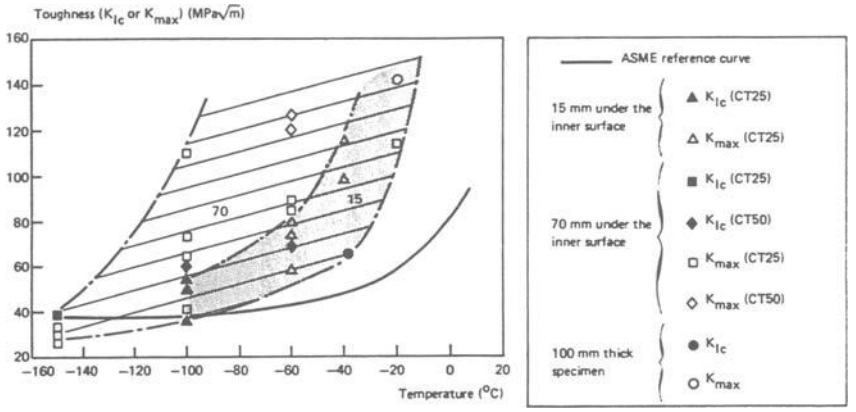
Study of the experimental scatter band--This study was carried out with tests on CT-type specimens (specimens thicknesses : 25, 50 or 100 mm). Two orientations (LC and LR) and two sampling levels (15 and 70 mm beneath the inner surface) have been studied from tests made on CT 25 specimens. Specimens of 50 and 100 mm thicknesses have been taken according to the LC orientation.The CT 50 specimens were located at the quarter of the thickness (equal to 270 mm) while CT 100 specimens had a face located on the inner surface of the nozzle support ring.

The resulting toughness transition curves are presented and compared with the reference curve of the RCC-M code in Fig. 4 [2].

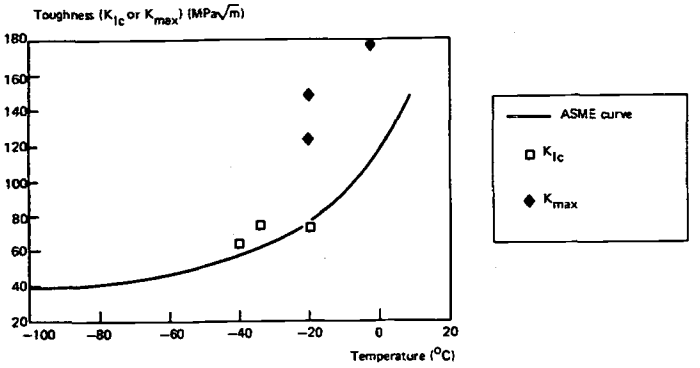
The toughness results obtained from tests on CT specimens taken according to the LC and LR orientations at a depth of 15 mm under the inner surface (Fig. 4a) show a common lower bound. On the contrary, the scatter is greater for the LR orientation. These results can be explained according to the position and configuration of the segregation zones in the vessel shell rings (Fig. 1). Taking specimens according to the



a – Comparison between AC and AR orientation (25 mm thick specimens located 15 mm under the inner surface of Q12 material).



b – Comparison between two locations (15 and 70 mm) under the inner surface (AC oriented specimen from Q12 material).



c – Result on Q3 material AC orientation 100 mm thick specimens.

FIG. 4 [2]

LC orientation introduces a greater probability to have a segregation at the fatigue crack tip than with specimens taken according to the LR orientation. This is why the scatter is greater with the LR orientation. On the other hand, the curves have identical lower bounds as they are representative of the presence of segregation zones at the fatigue crack tip.

Fig. 4b shows the toughness values obtained from tests conducted on specimens taken following the same orientation (LC) but at two different levels (15 and 70 mm under the inner surface). There again the results present identical lower bound for toughness transition curves. It is also clear that the scatter band seems wider for tests carried out on specimens taken at a depth of 70 mm under the inner surface. These results are consistent with a greater density of segregation zones between the quarter of the thickness (70 mm) and the inner surface.

Fig. 4 reveals a few toughness values below the reference curve given in the RCC-M code especially for a temperature of -150°C (Fig. 4b). Futhermore, a test at a temperature of -20°C resulted in a K_{IC} toughness value 3 MPa $m^{1/2}$ lower than the reference temperature (Fig. 4c).

Modes of fracture of CT specimens--Fractographic examinations have been conducted on two specimens with toughness values lower than the reference curve given in the RCC-M code. In the first case (specimen of 25 mm thickness), the analyses show that half of the fatigue crack lies within a segregation zone. We could see three intergranular fracture zones whose surface area was smaller than 5 mm^2. As for the second case (specimen of 100 mm thickness), we observed two intergranular fracture zones, whose maximum length was 50 μm in their main direction at the bottom of the fatigue crack tip. One of these zones has been identified as the zone where the brittle fracture started. These intergranular fracture zones are close to the inner surface of the shell ring, which is consistent with the way segregation zones are distributed in the thickness of shell rings.

EVALUATION OF THE REFERENCE CURVE CONSERVATISM

Before irradiation--In order to evaluate the conservatism of the RCC-M standard curve for non-irradiated vessel steel, we gathered on a same curve all the toughness values of steel A508Cl.3 as determined from tests on specimens taken from the scrap portions of vessel shell rings in the French PWR power plants (Fig. 5).

The reference curve of the RCC-M code indexed on the RT_{NDT} temperature is on the whole a bounding curve, nevertheless without margin. The few toughness values lower than the reference values in the transition zone show a 10°C shift from the code curve. The shift could be related to the variation of the RT_{NDT} temperature through out the shell ring thickness.

After irradiation--Similarly, all the toughness values determined from tests conducted on specimens taken from the French vessel irradiated steel have been brought together on a same curve (Fig. 6). This data base only includes 20 values, of which four were determined from tests made on specimens showing a segregation zone at the fatigue crack tip. All the specimens used to determine the toughness values were taken from the same vessel shell ring.

On Fig. 6 these results are compared with the reference curve given in the RCC-M code using the RT_{NDT} indexed temperature after irradiation. The irradiated RT_{NDT} was predicted on the basis of the FIS formula.

We can see that the code reference curve is a global envelope curve especially concerning the values determined on specimens taken from the segregation zones. Only two points are below the reference curve corresponding to a shift of about 17°C. The

difference could be related to the scatter of the RT_{NDT} temperature measured on the shell ring.

CONCLUSION

The presence in heavy forgings of segregation zones enriched in alloying elements and impurities may challenge the toughness values of the reference toughness curve that are used to analyse the integrity of PWR vessels in emergency conditions. A test program aimed at studying the influence of segregation zones on the toughness of forged shell rings made up of solid ingots before and after irradiation has been carried out. The main conclusions are as follows:

- Segregation zones affect the most part of the vessel between the inner surface and the mid-thickness. They show an important enrichment in phosphorus, carbon and molybdenum,

- The presence of segregations at the notch tip of unirradiated Charpy-V specimens induces a shift of about 73°C for the transition temperature (T_{K56}). With irradiated material, the transition curve shifts reach about 108°C with no segregation zone and 47°C for specimens showing segregation zones at the notch tip.

- Fractographic examinations of some broken Charpy-V specimens with segregation zones showed the presence close to the limited areas of intergranular fracture surfaces ending with a cleavage fracture.

- A maximum RT_{NDT} temperature variation of 17°C has been determined through the thickness of the forging.

- The presence of segregation zones at the fatigue crack tips in toughness specimens does not cause a transition temperature shift higher than the one measured in the case of impact strength tests. However, we noticed a high scatter band of the toughness results.

- The RCC-M code reference curve indexed on the RT_{NDT} temperature on the whole is an envelope curve, nethertheless without margin. The few toughness values which are lower than the reference values in the transition zone show a 10°C shift with the code curve. The difference could be related to the variation of the RT_{NDT} temperature through out the shell ring thickness.

- Fractographic studies carried out on specimens with toughness values lower than those given on the reference curve of the RCC-M code show intergranular fracture surfaces in the segregation zones at the bottom of fatigue crack. The toughness value corresponds to that of a local zone of material having high alloying element and impurity contents.

Acknowledgements

The authors wish to thank MM. C. BRILLAUD and D. BUISINE, of Électricité de France, M. A. PONSOT of Creusot Loire Industrie, for their participation in mechanical testing and for making useful comments.

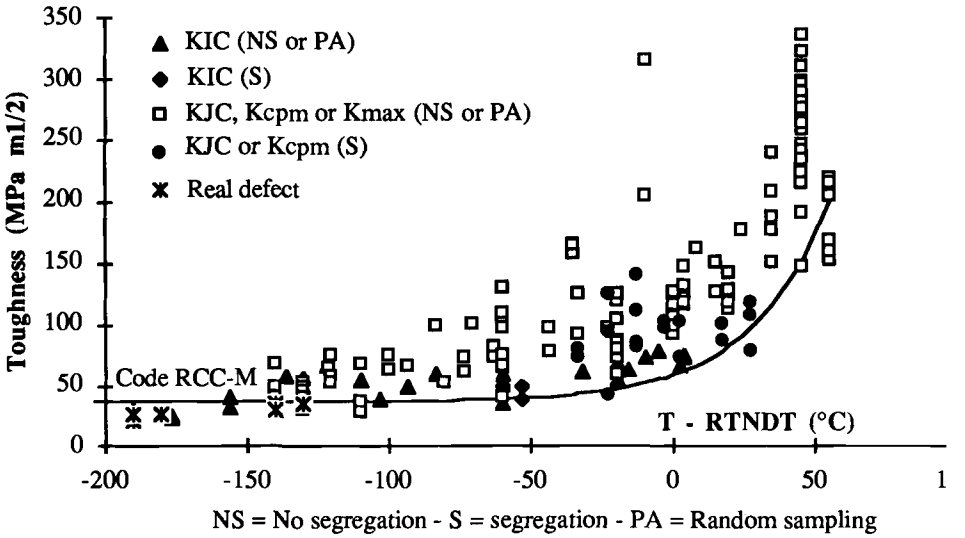


FIG. 5--Curve showing toughness values of A508 class 3 with no irradiation (pegged in accordance with the RTNDT reference temperature determined at the quater of the thickness).

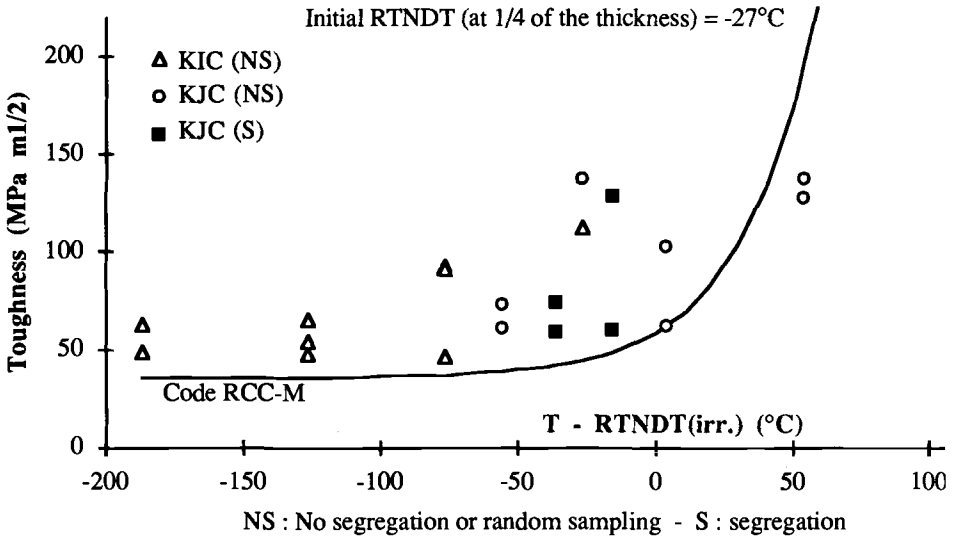


FIG. 6--Curve showing toughness values available after irradiation (pegged in accordance with the RTNDT temperature determined at the quater of the thickness. The shift of the RTNDT reference temperature is determined from the FIS formula).

REFERENCES

[1] - P. SOULAT - B. HOUSSIN - P. BOCQUET - M. BETHMONT - "Analysis of Radiation Embrittlement Results from a French Forging Examined in the Second Phase of an IAEA-Coordinated Research Program". Radiation Embrittlement of Nuclear Reactor Pressure Vessel Steels: An International Review (Fourth Volume), ASTM STP 1170, Lendell E. Steele, Ed., American Society for Testing and Materials, Philadelphia, 1993, pp.249-265.

[2] - D. BUISINE - M. BETHMONT - B. HOUSSIN - P. SOULAT - "Influence des zones de ségrégation et des inclusions non métalliques sur la ténacité des produits forgés en acier SA508cl3 pour cuve de réacteur à eau pressurisée". Note EDF/DER n° HT-A4/NTE 1362-A, march 1992.

[3] - D.BUISINE - M.BETHMONT - "Évaluation du risque de rupture brutale des cuves REP en situation accidentelle : des défauts dans les veines sombres à l'arrêt des fissures". Document EDF/DER/EMA n°HT-46/COM 1189-A, february1991.

[4] - G. FERGUSON - "The Effect of A-Type Segregation on the Toughness Properties of A508 Cl.3 Forgings". Document TWI n°620349/1/93, 1993.

[5] - I. POITRAULT - J. COET - R. DUMANT - P. BOCQUET - R. BLONDEAU - 32nd Mech. Working and Steel Processing Conf. Proc. Vol.XVIII, Cincinatti, october 1990.

[6] - H. CERJAK - J. SCHMIDT - E. BRECKWOLDT - F. PAPOUSCHEK - 6th MPA Seminar, october 1980.

[7] - S.G. DRUCE - UKAEA, Harwell Report AERE-R9581, 1979.

Franz M. D. Boydon[1], Ron J. M[c]Elroy[2], Gareth Gage[2] and Will J. Phythian[2]

Low Temperature Embrittlement of RPV Support Structure Steel

REFERENCE: Boydon, F. M. D., M[c]Elroy, R. J., Gage, G., and Phythian, W. J., **"Low Temperature Embrittlement of RPV Support Structure Steel,"** *Effects of Radiation on Materials: 17th International Symposium, ASTM STP 1270,* David S. Gelles, Randy K. Nanstad, Arvind S. Kumar, and Edward A. Little, Eds., American Society for Testing and Materials, 1996.

ABSTRACT: In recent years concerns have arisen regarding low temperature irradiation damage processes following the observation of an apparent tenfold increase in embrittlement in the HFIR reactor surveillance programme at Oak Ridge compared with accelerated material irradiation's in MTR's. The possible importance of this phenomenon to the integrity of LWR Support Structures was recognised by USNRC and it was formally designated Generic Safety Issue 15. This topic has also become an important UK regulatory issue in the context of the Sizewell PWR. Here the concern was that the high copper material used in the RPV Supports, when taken in light of the HFIR results of that time, highlighted the possibility that irradiation induced copper precipitation could occur at the low temperatures (50-60°C) and peak end-of-life dose of 2mdpa, ~$1x10^{18}$ $n.cm^{-2}$ (E>1MeV), encountered in RPV Supports, which contain significant levels (>0.20%) of copper.

This paper describes the results of an experiment set up to establish whether copper precipitation could occur at low temperatures in the Sizewell "B" RPV Support Structure steel. The irradiation was set up to achieve a target dose consistent with the full precipitation of copper, based on modelling data from conventional tests, at the lowest possible damage rate compatible with an irradiation of less than 1 year. The irradiation achieved a high dose of 49.6mdpa, $3.74x10^{19}$ $n.cm^{-2}$ (E>1MeV), at an average temperature of 71°C.

Mechanical properties measured by conventional hardness and Charpy test were performed. The data interpretation was aided by a combination of micro structural and post irradiation annealing experiments. In addition to the Support Structure material, two series of reference alloys with varying copper and nickel content were also irradiated. These alloys have been used in other programmes and offer the ability to cross check the effect of irradiation temperature.

The series of model steels previously studied after irradiation at 288°C in the IAEA CRP-3, under which conditions they exhibited a dependence of hardening on copper and nickel content, showed no clear evidence of copper precipitation under the low temperature irradiation conditions employed. Post irradiation annealing studies demonstrated that the irradiation embrittlement in the A588 support structure steel at low temperatures is due to matrix damage. Although the exact nature of the matrix defect/defects responsible for the embrittlement was not identified, the copper content is believed to be unimportant. There is, therefore, no reason to believe that the relatively high copper specification of A588 support structure steel will be detrimental to the steels toughness after low temperature/high dose irradiation as expected in the Sizewell B support structure.

KEYWORDS: neutron irradiation hardening, embrittlement, pressure vessel steels, support structures, mechanistic modelling, copper precipitation.

[1] Nuclear Safety Division, Health and Safety Executive, Bootle, UK
[2] AEA Technology, Harwell Laboratory, Didcot, Oxon., UK.

Copyright© 1996 by ASTM International www.astm.org

1. INTRODUCTION

Concerns have arisen regarding low temperature irradiation damage processes following the observation of an apparent tenfold increase in embrittlement in the HFIR reactor surveillance programme [1-4] at Oak Ridge compared with similar accelerated material irradiations in MTR's. The effect has been attributed to a dose rate effect occurring at the very low dose rates (10^{-13}-10^{-12} dpa.s^{-1}) experienced in the HFIR surveillance locations compared with MTR irradiation (10^{-9}-10^{-8} dpa.s^{-1}), although there has also been considerable speculation that the 'unique' HFIR neutron spectrum, with its potentially very high thermal-to-fast neutron flux ratio, might also be important. More recently, dosimetry has indicated lower thermal fluxes than originally estimated and attention has focused on the high γ-flux at the HFIR surveillance positions.

The possible importance of this phenomenon to the integrity of LWR RPV Support Structures was recognised by USNRC and it was formally designated a Generic Safety Issues (Generic Safety Issue 15). This latter topic also became an important UK regulatory issue in the context of the Sizewell PWR. The Nuclear Installations Inspectorate (NII) became concerned that high copper material has been used in the RPV supports, which have been designated as 'Incredibility of Failure' (IOF) items.

Druce[5], in an early analysis of the HFIR surveillance results, suggested that there was evidence, from the different response of the HFIR materials, for a copper effect. A recent detailed review of the low temperature embrittlement issues raised by the HFIR results was presented by McElroy et al [6] in 1990. The latter review highlighted the possibility that significant irradiation induced copper precipitation could occur at the lowest temperatures (50-60°C) and peak end-of-life (EOL) dose of 2mdpa, ~1x10^{18} n.cm^{-2} (E>1MeV), encountered in RPV Support Structure steels, some of which contain significant levels (>0.20%) of copper.

As stated, earlier the RPV supports in the Sizewell B PWR are designated as 'Incredibility of Failure' items and NII are concerned about the susceptibility to irradiation embrittlement of the high copper material used in their fabrication, such that it has become an important UK regulatory issue. As a result of this concern, NII initiated a high dose, low temperature irradiation specifically to establish whether copper precipitation could occur at low temperatures in the Sizewell "B" RPV Support Structure steel. The target dose chosen was 45 mdpa or 3x10^{19} n/cm^{2} (E>1MeV), i.e., an order of magnitude higher dose than that predicted to produce full copper precipitation using the Nuclear Electric Embrittlement Model [7] with input values similar to Druce [5] and McElroy et al [6] and also significantly higher than the doses predicted to be experienced by the support at end of life. This irradiation was to be conducted at the lowest possible damage rate compatible with an irradiation of less than 1 year.

The mechanical property, microstructural and post irradiation annealing (PIA) information are summarised in this report. In addition to Charpy specimens of Support Structure steel, two series of reference alloys with varying copper and nickel content were also irradiated in order to provide an indication of whether copper precipitation occurred. Interpretation of the latter effect was by a combination of hardness, microscopy and PIA analyses. Additionally, tensile test data has recently become available [8] on the Sizewell "B" material and some of the model alloys, employed as damage correlation monitors in the present experiment, were irradiated to similar maximum dose in the HFIR Hydraulic Tube facility at Oak Ridge.

2. EXPERIMENTAL DETAILS

2.1 Materials

The A588 steel used in this study was obtained from a 90mm thick offcut from one of the Sizewell "B" Support Structure Assemblies. This was procured by NII and held in store at The Welding Institute from whom a 150x280x90mm section was obtained. The piece supplied was flame-cut from the main plate with its rolling direction along the short (150mm) axis of the plate and was heat treated as follows:

Heating Rate	23°C/h (300-620°C)
Soak	620°C for 3h
Cooling Rate	15°C/h (620-300°C)

Note that the heating and cooling rates of the heat treatment used in this study were much slower than those in practice, although still within the allowed specification.

The chemical composition of the Sizewell "B" Support Structure steel employed in this work is summarised in TABLE 1. The specification of the Sizewell B support structure steel, also shown in TABLE 1, calls for a copper content in the range 0.2-0.4wt% and it is apparent that the material studied lies near the bottom of this range at 0.22wt%.

TABLE 1 --Chemical Specification (wt%) of A588B Sizewell "B" Support Structure Steel and ChemicalComposition (wt%) of Support Structure Steel (SS) Employed in the Present Study

Alloy	C	Si	Mn	P	S	Cu	Ni	Cr	Mo	Al
A588B Spec	0.20 max	0.15-0.35	0.75-1.35	0.012 max	0.010 max	0.20-0.40	0.50 max	0.40-0.70	-	-
SS	0.126	0.31	1.33	0.014	0.007	0.22	0.21	0.45	0.045	0.011
	±0.005	±0.01	±0.01	±0.007	±0.001	±0.01	±0.01	±0.01	±0.001	±0.005

2.2 Irradiation and Dosimetry

Specimens and three dosimetry packs were supplied to Saclay in April 1991 and the irradiation was complete in April 1992. Irradiated specimens and dosimetry packs were returned to Harwell in a flask and unloaded in July 1992. The loading pattern of the irradiation rig and its irradiation and temperature histories has been reported elsewhere [9]. The main parameters of the irradiation are summarised below.

The irradiation was planned to achieve a dose of 3×10^{19} n.cm^{-2} (E>1MeV), 45mdpa, at a temperature in the range 60-80°C. This was to be achieved by irradiation in the adjacent M10 and N9 positions in OSIRIS for 2 and 5 cycles respectively for a total period of 145 full-power days at a nominal reactor power of 65MW. In total, 27 Charpy specimens were loaded into the rig in pairs with the tile holder containing model iron alloy and steel hardness slices adjacent to the rig mid-plane. Three dosimetry capsules, supplied by Harwell, were positioned, one at the expected flux mid-plane and the others at approximately one quarter and three quarter axial positions. Copper and cobalt dosimeters supplied by Saclay, and used in their assessment of irradiation dose, were positioned at the rig mid-plane.

Specimen temperatures were monitored throughout the irradiation by six thermocouples spaced approximately evenly along the length of the irradiation volume. The average temperature during the irradiation was 71°C and the variation in average temperature was only about ± 2°C. Both the Saclay and Harwell dosimeters provided consistent results indicating that the irradiation dose of 49.6mdpa, 3.74×10^{19} n.cm^{-2} (E>1MeV), was achieved.

2.3 Mechanical Testing

Impact testing of both irradiated and unirradiated materials was carried out on a shielded Avery-Denison Charpy impact test machine specially adapted for remote operation to permit testing to the ASTM E23 specification, particularly in respect of the reproducibility of semi-automatic loading of correctly oriented specimens onto the anvil, from the temperature controlled bath, within 5 seconds to minimise specimen heating/cooling effects.

Lateral expansion and the percentage fibrosity was pre-measured after fracture in accordance with recommendations given in ASTM E23.

Hardness testing was carried out using the methods laid down in British Standard 427 : Part 1 : 1961. Both machines were verified at six monthly intervals by the manufacturers using the methods recommended in British Standard 427 : Part 2 : 1962 at a test load of 20kgf.

2.3.1 Charpy Curve fitting

A least squares minimisation routine has been used throughout to provide curve fits to the Charpy data using an equation of the form:

$$C_V = A + B \tanh\{ (T-T_0) / C \}.$$

where C_V is the dependant variable (i.e., Charpy impact energy, lateral expansion or fibrosity), T the test temperature and A, B, C and T_0 are constants.

In the case of Charpy absorbed energy, the combination of specimen inertia and anvil adhesion arising from the temperature control fluid, which coats the specimen, suggests that, in practice, the absorbed impact energy does not fall below 2.5 Joules, which seems to represent the minimum measured fracture energy of fully brittle material. Consequently a value of

$$B = A + 2.5$$

has been used in the analysis, unless otherwise specified.

2.4 Microstructural/Microchemical Analysis

2.4.1 Specimen Preparation

Specimens for microstructural examination by transmission electron microscopy (TEM) and microchemical examination by field emission gun scanning transmission electron microscopy (FEGSTEM) analysis were prepared from irradiated hardness tiles approximately 10x10x2mm. From each slice, three 3mm diameter discs were cut by spark erosion. After grinding to ~0.05mm, the samples were prepared by a two-stage electropolishing technique to ensure that the surface is free from deposited copper [10]. Storage of the samples in dry alcohol immediately after polishing and prior to examination reduced the surface oxidation to a minimum. In this report the microstructural examination has been limited to the model alloy 2D and the support structure steel.

2.4.2 TEM Examination

The initial objective of the high magnification TEM work was to confirm the presence of small copper rich precipitates or other matrix defects of diameter ~2 to 3 nm. Examination of the same area with dynamic contrast using different diffraction vectors, g, allows the spherically symmetrical or planar nature of defects to

be determined and therefore makes it possible to distinguish respectively between precipitates and dislocation loops. In addition to the black-white (B-W) contrast formed under dynamic diffraction conditions, both kinematic and weak beam imaging conditions were employed to distinguish between image contrast due to real lattice defects and artefacts due, for example, to any oxide on the surface of the thin foil.

2.4.3 FEGSTEM Precipitate Analysis

Previous reports [10,11] have shown the ability of the FEGSTEM, using energy dispersive X-ray analysis (EDX), to confirm the B-W images observed in the TEM as copper rich precipitates. By positioning the probe over a small feature and a few nm away, the difference in the composition can be attributed to the precipitate. This methodology can also be applied to parallel electron energy loss spectroscopy (PEELS), an added advantage of this technique is the ability to assess the manganese concentration in the irradiated steel [12], which is not possible by EDX due to the induced manganese signal observed as a result of the iron decay.

2.4.4 FEGSTEM *Matrix* copper determination

The latest techniques employed to determine the matrix copper levels involve the collection of approximately sixteen EDX spectra at standard tilt and microscope settings. The sample is held in a specially modified holder, which is of copper-free construction, thus eliminating any copper signal arising from beam/holder interactions. Calibration checks with an Fe sample have shown that the background copper level after a 300 second acquisition time spectrum is unresolvable and is therefore considered to be <0.05%. The quoted values have therefore not been adjusted for any background copper effects and were determined from the EDX spectra using standard commercial 'Link' software.

The approach adopted has been developed primarily for the examination of weld material, although the techniques are equally well suited to parent material. The method permits the initial distribution of embrittling species such as copper to be identified. Factors such as post weld heat treatment can greatly influence this, resulting in the copper concentration in the matrix to differ significantly from the bulk copper value through copper becoming incorporated in second phase particles:

In practice this reduces to

$$Cu_{Matrix} = Cu_{Bulk} - Cu_{S} - Cu_{HT\ ppt} - Cu_{Irrad\ ppt}$$

Cu_{Matrix}	=	Copper in solid solution and available for precipitation during irradiation
Cu_{Bulk}	=	Bulk copper content
Cu_{S}	=	Copper associated with sulphur in the form of copper sulphide
$Cu_{HT\ ppt}$	=	Copper in the form of large fcc copper precipitates formed during post-weld heat -treatment.
$Cu_{Irrad\ ppt}$	=	Copper in the form of small bcc precipitates formed under irradiation.

The ability of the STEM to produce nanometer diameter electron beams can be exploited to measure directly the Cu_{matrix} term in the above equation, when used in spot or point mode. Here the beam is placed between any visible precipitates when imaging under diffraction or absorption contrast. By scanning the beam over small areas between the dislocation networks, a measure of the matrix and small copper precipitates can be made. Such small precipitates, typically 1 to 2nm diameter, are usually associated with those induced by irradiation, or the onset of precipitation during, for example, cooling from heat treatment. Differencing the spot and small area scan results can therefore provide information on these small precipitates. In high copper materials, it is common to find large (~10nm diameter) copper precipitates associated with dislocations. By performing large area scans of the microstructure and differencing the results with those obtained by small area scans, the amount of copper associated with these large precipitates can be established.

FIG. 1 demonstrates the positioning of the electron beam by crosses for the spot mode and rectangles for the scan modes. The mean values from the spot, small area and large area scans for each sample can be interpreted to provide an indication of fine scale copper distribution which in turn can indicate whether fine copper precipitates are present.

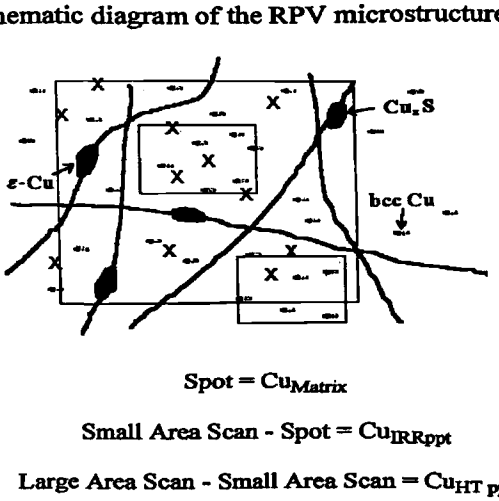


FIG. 1 Comparison of spot mode, small and large area scan measurements employed in FEGSTEM analysis; represented by X, small rectangle and large rectangle respectively.

2.5 Post Irradiation Annealing

The procedure adopted is based on isochronal annealing, which can be interpreted to provide an indication of whether copper precipitation has occurred and to assist in the characterisation of the matrix hardening component [13].

Samples in the form of 3mm diameter discs, ~2mm thick, of each material were cut from 10x10x2mm SANS or Hardness tiles by spark erosion. These discs were then mounted in a specially designed jig used in all the subsequent operations. Once mounted, the jig was used to grind and polish the samples down to a 1μm finish and base-line microhardness data obtained for each disc using a 300g load applied for 10 seconds. The jig was then placed into a preheated furnace at 50°C for 30 minutes, removed and air cooled before returning to the microhardness equipment for measurement. After hardness measurements, the tiles were annealed for 30 minutes at the next temperature in the sequence, i.e., 50°C above the previous annealing temperature. This process was repeated up to a temperature of 350°C such that the conditions examined in this study were as follows, 20°C baseline data plus 30 minutes at 50°C, 100°C, 150°C, 200°C, 250°C, 300°C and 350°C. When annealing was undertaken at temperatures above 150°C, samples were lapped prior to the measurement of microhardness to remove any oxide build up that may affect the measurements. At no time during the experiment was the sample removed from the jig.

Each individual hardness datum reported is the mean of two indentations each measured twice. Whilst more indentations would be desirable, any more would limit the total range of time/temperature data points investigated. Before each set of measurements, a standard hardness tile was tested as an equipment calibration. No non-conformity was found throughout the period of this investigation. It should also be noted

that a direct correspondence between these microhardness measurements and those obtained with conventional hardness as part of the other tasks in this programme is not appropriate. Microhardness values are an accurate means of defining a relative change in properties but, due to grain size effects, should not be compared directly with 20kg indentations. The microhardness values should not be used to correlate with transition temperature shift, etc., using conventional conversion factors. The purpose of the PIA data is to examine relative changes during the anneal and to correlate these changes with the microstructure.

3. RESULTS

3.1 Mechanical Testing

3.1.1 Charpy Testing

The Charpy energy data for unirradiated and irradiated cases are compared in FIG. 2, from which the large transition temperature shift due to irradiation is apparent. An interesting feature of the Charpy behaviour is the very sharp transition in the irradiated condition. This is apparent in energy, fracture appearance and lateral expansion, and is contrary to the behaviour after higher temperature (>150°C) irradiation in MAGNOX or Light Water Reactors and MTRs. In the latter cases, the slope of the transition region decreases with increasing irradiation dose, as the upper shelf drops. Hawthorne [14] has observed a similar effect after low temperature irradiation. It is possible that this is a phenomenon similar to yield point behaviour in strain ageing and may be associated with the evaporation of interstitial solute atoms from dislocations and point defect clusters or a similar process at a critical temperature. This could be a major influence on the transition shift which has not as yet been factored into the behaviour of low temperature irradiated materials.

The various transition temperatures derived from the Charpy data defined by the 41J, 68J, 50% fibrosity and 0.9mm lateral expansion temperatures, and the upper shelf energies and average hardnesses of unirradiated and irradiated material, are summarised in TABLE 2. The large irradiation induced shift in transition temperature is apparent in all cases as are the substantial reduction in upper shelf energy and increase in hardness. The correlation between Charpy shift and hardness change indicates a ratio of 2.04 which is broadly in line with correlations obtained in the IAEA CRP-3 [15].

TABLE 2 -- Comparison of Unirradiated and Irradiated Charpy Energy (T_{41J} and T_{68J}), 50% Fibrosity ($T_{50\%}$), 0.9mm Lateral Expansion ($T_{0.9mm}$) Transition Temperatures, Upper Shelf Energies (USE) and Hardnesses (HV) for Sizewell "B" Support Structure.

Condition	T_{41J} (C)	T_{68J} (C)	$T_{50\%}$ (C)	$T_{0.9mm}$ (C)	USE (J)	HV (VPN)
Unirradiated	-44	-24	2	-35	191	154
Irradiated	144	147	149	146	133	246
Difference	188	171	147	181	58	92

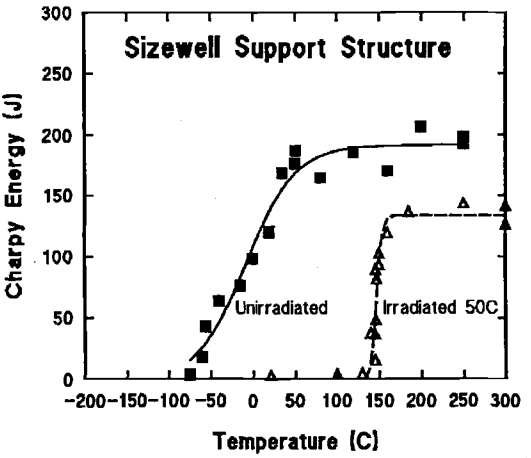


FIG. 2 Charpy energy transition curves for Sizewell "B" Support Structure steel in the unirradiated condition and irradiated to a dose of 49.6 mdpa, 3.74×10^{19} n.cm^{-2} (E>1MeV) at 71°C.

3.1.2 Hardness Testing

The hardness changes, due to irradiation of the model steel and Support Structure tiles and the Hawthorne model iron alloy tiles are summarised in TABLEs 3 and 4 respectively.

TABLE 3 compares the irradiation response of the IAEA CRP-3 model steels at 288°C (final column) with the response in the present irradiation (penultimate column). The steels JPA-H are a series of doped model A533B steels with varying copper and nickel contents irradiated in the IAEA CRP-3. JFL and JRQ are the reference steels from the latter programme. The former, JFL, was manufactured to modern steel making practice and nuclear specifications and the latter, JRQ, was manufactured to simulate steel making practice for RPVs of older (1960s and 1970s) reactors. BW is a high nickel weld, with a strong irradiation embrittlement response, supplied by RR&A for the IAEA CRP-3 and, finally, SS is the Sizewell "B" Support structure steel.

The model steels are split into several groups depending on their copper and nickel contents. JPB, JPC and JFL are all low (<0.03wt%) copper steels and have an intermediate (~0.75wt%) nickel content. The second group JPD-JPH have an intermediate (~0.15wt%) copper content and nickel content varying from 0.1-1.2wt%. JPA is the highest (0.3wt%) copper content studied and since it has the intermediate (0.8wt%) nickel content can be compared with JPB and JPG to test any systematic correlation of property change with copper content. Finally, JRQ, BW and JFL provide the opportunity to compare the response of several well characterised "commercial" steels with that of the Support Structure steel.

It is apparent from TABLE 3 that the response of all the above materials is quite different in the present irradiation compared to that at 288°C in the IAEA CRP-3, where clear correlations with copper and nickel content were evident. JFL and JRQ, which represent the difference between old and new steel manufacture and specification, appear to exhibit the same response in the present irradiation compared to their widely different response at 288°C, which is principally attributed to copper content. Similarly, JPB, JPG and JPA, which cover the widest range of copper content, appear to show no significant difference in their response in the present irradiation. Likewise, the series JPD-JPH shows no systematic correlation with nickel content, contrary to their behaviour at 288°C. Based on these observations it appears that there is no correlation between the response of these steels and copper or nickel content during low temperature irradiation.

TABLE 3 -- Comparison of Low Temperature Hardening in NII Saclay Irradiation with Results from IAEA CRP-3 Steels Irradiated at 288°C

ALLOY	COMPOSITION (wt%)				NII DH	IAEA DH
	Cu	Ni	P	N(ppm)	(VPN)	(VPN)
JPB	<0.01	0.78	0.017	5	78	19
JPC	0.03	0.78	0.007	29	71	13
JFL	<0.01	0.72	0.004	7	82	4
JPD	0.14	0.10	0.006	<2	73	18
JPE	0.15	0.40	0.006	18	85	21
JPF	0.14	0.59	0.020	9	77	34
JPG	0.16	0.79	0.017	6	79	33
JPH	0.15	1.17	0.006	<2	83	36
JPA	0.30	0.80	0.018	8	83	63
JRQ	0.14	0.82	0.017	<2	82	37
BW	0.23	1.59	0.007	?	90	40
SS	0.22	0.21	0.014	?	92	-

Interestingly, the high nickel weld, BW, and Support Structure, SS, appear to show a significantly greater response than the other steels discussed above, which all lie in the range 71-85VPN. Because of the lack of correlation, in the latter series, with either copper or nickel it is probable that the higher hardening of BW and SS arises from differences in interstitial (C, N or O) content which are known to influence the matrix hardening.

Hardness change results from the model binary, ternary and quaternary iron alloys are summarised in TABLE 4. In this case, the specimens have been separated into two series for comparison purposes. The first series, 1A-1D, indicate the effect of copper addition and the synergistic effect of copper and nickel additions in the absence of phosphorus, while the second series, 2A-2D, show the independent effect of nickel addition and the effect of adding phosphorus.

From the first series in TABLE 4, it is apparent that, in all cases, copper appears to produce a significant (>34VPN) increase in hardness and that this is enhanced by about 8VPN by the larger nickel addition of 0.7wt%. From the second series, nickel on its own also appears to increase the hardness by about 23VPN and this may be enhanced by a further 8VPN by phosphorus addition. Comparison of 1D and 2D suggests that the net effect of phosphorus, in the presence of both copper and nickel, appears to be negligible.

TABLE 4 -- Low Temperature Hardening in NII Saclay Irradiation of Model Alloys (ex Russ Hawthorne) Supplied by Nuclear Electric

ALLOY	COMPOSITION (wt%)			DH
	Cu	Ni	P	(VPN)
1A	0.01	0.0	0.0	61
1B	0.30	0.0	0.0	101
1C	0.30	0.40	0.0	100
1D	0.30	0.70	0.0	108
2A	0.0	0.0	0.0	65.5
2B	0.0	0.70	0.0	89
2C	0.0	0.70	0.025	97
2D	0.30	0.70	0.025	108

Based on the latter results on model iron alloys, an effect of copper and nickel can be inferred, in contrast to the apparent lack of such an effect in the model and commercial steels discussed earlier.

3.2 Microstructural data

3.2.1 TEM examination

FIG. 3 shows a typical micrograph taken under dynamic imaging conditions for the irradiated sample 2D. Indications of diffraction contrast consistent with small dislocation loops or precipitates, are arrowed in the irradiated sample 2D. Further examination of the same area of the sample under both kinematic and weak beam imaging conditions, confirmed that these images are not from a spherically symmetric precipitate, but are consistent with images formed by planar defects such as small dislocation loops. Further work is currently underway to confirm their geometry, as defined by the Burgers vector and habit plane, and nature, i.e. vacancy or interstitial. This interpretation of the observed defects being loops is further supported by FEGSTEM examination, as indicated below.

TEM examination revealed small black-white and slightly larger images in both the irradiated and unirradiated Support Structure steel, FIG. 4, shown here under kinematic conditions, also shows such dynamic contrast in the irradiated Support Structure steel. It seems probable that the larger images (A), which exhibit normal diffraction contrast, are copper precipitates formed during heat treatment. Small black-white images (B) may be irradiation induced precipitates or small loops, however, similar features were also observed in the unirradiated condition and may also be copper precipitates formed during heat treatment. It is not possible without extensive detailed quantitative analysis to determine whether the number density/size of these small features increased with irradiation although this could be readily obtained by SANS if required. The presence of such small precipitates is consistent with the wider distributions of copper matrix determinations by FEGSTEM in both the unirradiated and irradiated Support Structure steel when compared with the model alloy. It may also point to an inhomogeneous copper distribution in solution.

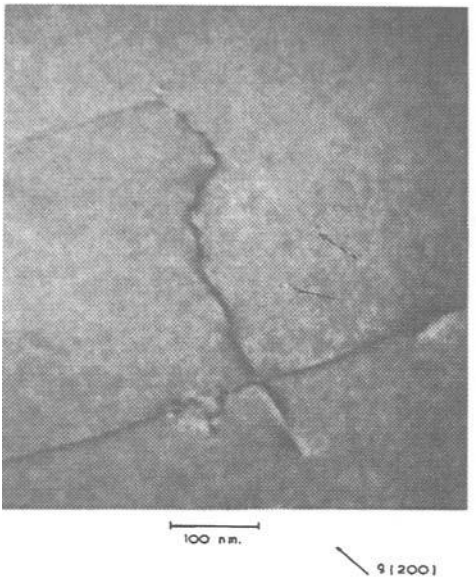


FIG. 3 Bright field TEM micrograph of irradiated model alloy 2D.

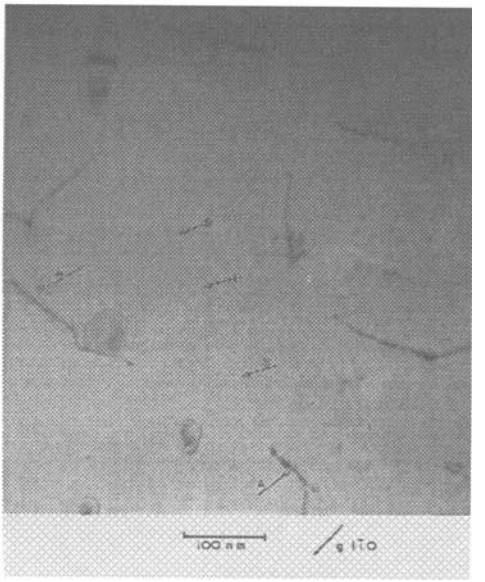


FIG. 4 Bright field TEM micrograph of irradiated Support Structure steel.

3.2.2 FEGSTEM Precipitate Analysis

While features exhibiting above background contrast were observed in the irradiated sample 2D, no difference between matrix and 'precipitate' spectra could be found. This would support the TEM observation that these defects are indeed dislocation loops. In the samples of SS, no difference in visible precipitation could be observed between the unirradiated and irradiated condition. This is confirmed by the similarity of the spot and small area scans in each case, described below.

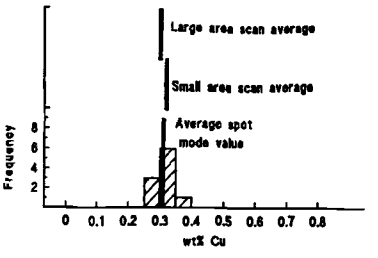
3.2.3 FEGSTEM Matrix Copper Determination

The individual and mean values from the spot and small area scans for each sample are presented graphically in FIG. 5 and 6.

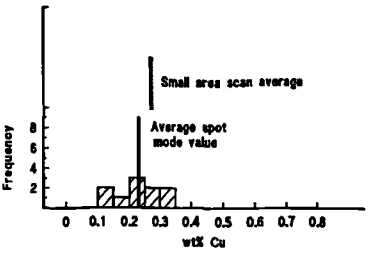
Considering first the 2D alloy, it can be seen from FIG. 5 that the distribution of values obtained in spot mode has an average and standard deviation of 0.31 ± 0.02 and 0.3 ± 0.05 in the unirradiated and irradiated conditions respectively. This spread in values is small and reflects the measuring error associated with the technique. The small area scans and the large area scans provided data suggesting that all have mean values that are identical within the measuring error. This suggests that the copper is distributed homogeneously in solid solution, and has not been affected by the irradiation. Alternatively, it is also possible that an extremely high density of very fine copper precipitates is present, which cannot be resolved by the technique. An extremely high number density ($\sim 10^{23}$ to 10^{24} ppt/m^3) would be required to produce such a result, i.e., the precipitate separation would not permit the electron beam to pass through the sample without significant

interaction with the precipitates. This latter option is considered to be highly improbable given the similarity of the data obtained from irradiated and unirradiated samples.

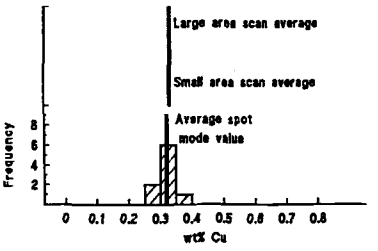
In the case of the Support Structure material, the range of spot mode values is larger than in the model alloy as can be seen by a comparison of FIG. 5 and 6. The observed variation in copper values is larger than the expected statistical measuring error, from 2D, and possibly represents the interaction of the beam with a high number density of small unresolvable precipitates in both unirradiated and irradiated conditions, or local inhomogeneous copper matrix levels as a result of the thermomechanical treatments given to the material. If the distribution arises from beam interaction with small precipitates, the true matrix level of copper is therefore thought to be at the lower end of the measured distribution. As is apparent from FIG. 6, the distribution is very similar in both the unirradiated and irradiated sample, except that in the irradiated case one very low (0.03wt%) spot mode value was obtained which lies well outside the expected measuring error. Examination of the spectra associated with this point revealed no measurement anomalies or specimen artefacts. It may therefore be concluded that the value is real and represents a high degree of copper depletion of the matrix in this area, the source of which is critical to the interpretation of the experiment. This observation therefore merits further detailed discussion.



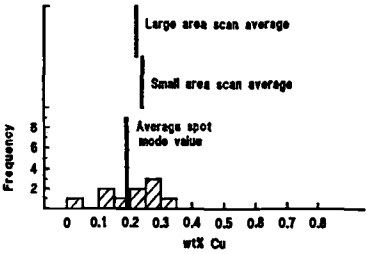
Comparison of Spot Mode, Small Area and Large Area Scan Data for Unirradiated Model Iron Alloy, 2D



Comparison of Spot Mode, Small Area and Large Area Scan Data for Unirradiated Sizewell "B" RPV Support Structure Steel



Comparison of Spot Mode, Small Area and Large Area Scan Data for Irradiated Mode Iron Alloy, 2D



Comparison of Spot Mode, Small Area and Large Area Scan Data for Irradiated Sizewell "B" RPV Support Structure Steel

FIG. 5 Comparison of Spot Mode and small and large area scan results obtained by FEGSTEM for the unirradiated and irradiated model alloy 2D.

FIG. 6 Comparison of Spot Mode and small and large area scan results obtained by FEGSTEM for the unirradiated and irradiated Support Structure steel

If, under irradiation, copper precipitation had occurred in the Support Structure material, this low copper value would have been confirmatory. However, TEM examination did not show any significant difference between the unirradiated and irradiated samples, particularly with regard to resolvable precipitates. This implies that, if copper precipitation had occurred under irradiation, the size of the precipitates would be below the visibility limit of ~1.5nm. If this is the case, it would be inconceivable to position the beam in a region of material for 300 sec without interaction with the small precipitates. It would, therefore, not be possible to produce a zero or very low copper value.

An alternative explanation is, however, available, which also supports the lack of a strong copper effect to the measured mechanical properties response of the Support Structure steel relative to the other model and commercial steels. The single low value could simply reflect the lower end of the spectrum of start of life matrix copper levels, and similar values might well be found in the unirradiated sample if sufficient areas were sampled.

3.3 Post Irradiation Annealing

The results obtained in the isochronal annealing programme are shown graphically in FIG. 7 to 10. In the low copper materials irradiated at approximately 71°C (JPB, JFL and JRQ), a recovery in hardness is evident at temperatures T ≥ 250°C; see FIG. 7. This is in contrast to the data for the high copper material JPA irradiated at approximately 288°C presented in FIG. 8, which show no such recovery but rather a slight trend of increasing hardness with increasing annealing temperature in both unirradiated and irradiated JPA. Data for the other materials, 2D and SS, presented in FIG. 9 and 10 respectively, show no change in hardness for the unirradiated condition, while that of the irradiated material show some recovery at T ≥ 250°C. The abnormally high value obtained in the unirradiated 2D at 150°C cannot be explained but is included for completeness. It is not thought to be significant in altering the overall trends observed and the conclusions drawn from this data.

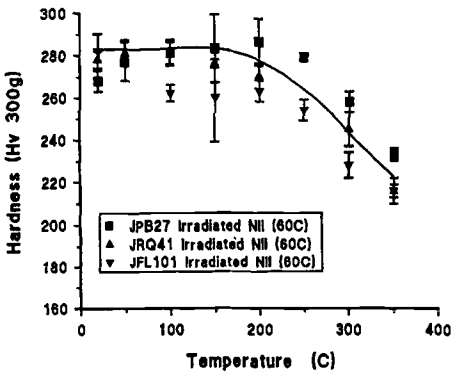


FIG. 7 Micro hardness versus annealing temperature obtained in the isochronal annealing study on low copper steels (JPB, JRQ and JFL) irradiated at 71°C.

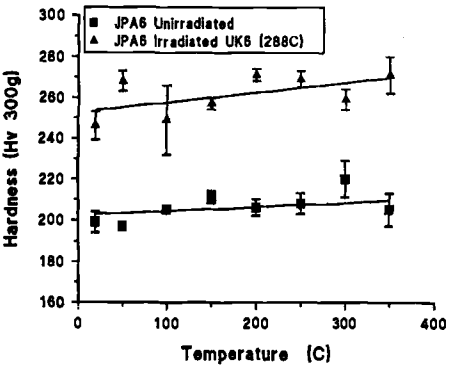


FIG. 8 Micro hardness versus annealing temperature obtained in the isochronal annealing study on high.

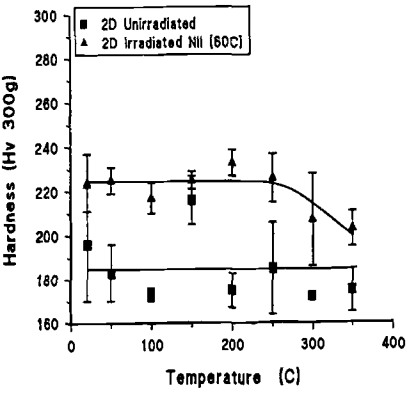


FIG. 9 Micro hardness versus annealing temperature obtained in the isochronal annealing study on high copper model alloy (2D) irradiated at 71°C.

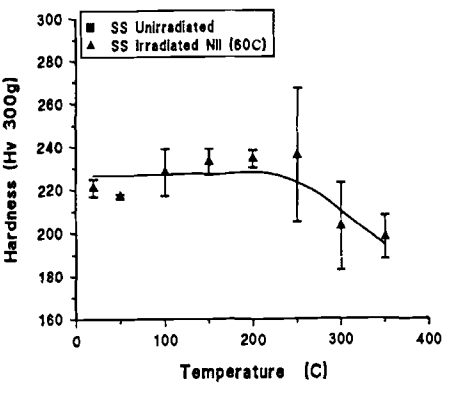


FIG. 10 Micro hardness versus annealing temperature obtained in the isochronal annealing study on Support Structure steel (SS) irradiated at 71°C.

The data reported here are extremely useful in clarifying some of the conclusions arrived at in the previous report on this low temperature irradiation. Namely, that the changes in materials properties induced by low temperature irradiation are dominated by a non copper precipitate component of hardening. This can be clearly seen by comparison of FIG. 7 and 8 for low temperature, low copper (JPB in NII rig) versus high copper high irradiation temperature (JPA in UK6 rig) respectively. The recovery in the low temperature irradiated low copper material can be understood in terms of an annealing out of a matrix component of irradiation damage, this being the dominant component of the measured hardness.

In contrast, the high copper, high temperature condition is dominated by copper precipitation (confirmed in this specimen of JPA by SANS and STEM as part of the IAEA CRP3 programme [16]. Hence the lack of any observed recovery at temperatures up to 350°C, as copper precipitates will remain stable (in these timescales) up to temperatures >450°C. After this some coarsening of the precipitates may be expected resulting in a decrease in hardness. Indeed the slight increase in hardness observed in JPA may be due to the extremely fine copper precipitates induced by irradiation approaching peak hardness due to the increase in thermal activation. This interpretation is in agreement with recent work undertaken as part of the IAEA CRP3 programme that indicates that peak copper precipitation has not been achieved by the dose attained in the UK6 rig for JPA.

For intermediate copper materials such as the A588 support structure steel (SS) and the high copper model alloy 2D, irradiation at low temperature is again dominated by the matrix damage component, as in both these conditions recovery of hardness is observed at temperatures above 250°C and complete or near complete recovery is accomplished by the end of the annealing run.

Interpretation of post irradiation annealing data can be extremely difficult and speculative because several different competing effects can occur at the same time in steels with complex microstructures. However, Mader et al [13] recently combined small angle neutron scattering (SANS) with isothermal annealing on a range of model steels and Phythian et al [12] have conducted isochronal annealing on quenched model alloys as a pre cursor to conducting studies on irradiated material. This latter study employed positron annihilation to monitor the recovery of the vacancy component of the microstructure. The current work has confirmed that, when used in conjunction with other microstructural techniques, post irradiation annealing can be

beneficial in identifying the relative contributions of stable (copper precipitates) and unstable (matrix defects) components of hardening. Furthermore, the data confirm the interpretation given earlier that no significant copper precipitation occurred during the high dose low temperature irradiation of the A588 support structure steel conducted at Saclay for the NII.

4. Discussion

The irradiation induced shift in transition temperature of 188°C for the Support Structure steel, which results from the present high dose, low temperature irradiation, is large by any standards, but provides no indication of whether copper precipitation has occurred. It was the purpose of the hardness studies on reference materials to give a clearer indication of any copper effect. At first sight, the results of the hardness studies are apparently in conflict, i.e. the results for model and commercial steels indicate no significant correlation with copper content, while the model iron alloys, on the other hand, appear to exhibit a significant copper hardening effect. Given the normal correlation between hardness change and Charpy shift, the latter hardness increase would correspond to a Charpy shift of about 80°C, which is comparable with the maximum shift expected from full precipitation of all the copper (0.3wt%) present in the model iron alloys.

If, as suggested by the IAEA CRP-3 steels, there is no contribution to hardening from copper precipitation, the whole of the observed hardening should be due to matrix hardening. The Nuclear Electric embrittlement model provides an evaluation of matrix hardening which is expressed by a square root dependence of transition temperature shift (ΔNDT) on dose (D) with the form

$$\Delta NDT = A(T)\ \sqrt{D}$$

where A(T) is the temperature dependent Barton coefficient and the dose D is expressed in units of 10^{-5}dpa. An extensive review of the literature revealed that the temperature dependence of the Barton coefficient is described by the relationship

$$A(T) = A\ .\ F(T)$$

where A is the Barton coefficient at the reference temperature (190°C) and F(T) is the temperature dependent term given by

$$F(T) = 1.869 - 4.57 \times 10^{-3}.T$$

such that F(T) is 1.00 at 190°C. Values of Barton coefficient lie in the range 3.08-3.44 for low nickel PWR steels. There is little doubt that the temperature dependence follows the above form at temperatures higher than about 200°C, but data for Charpy shift at lower temperatures suggests a saturation or even a decrease in Barton coefficient below 150°C. US data on typical RPV steels, reviewed by McElroy et al [6], suggests that embrittlement does not increase below about 220°C. To estimate the possible contribution of matrix hardening, upper and lower bounds may be set by assuming that the Barton coefficient, defined by the above relationships, is that corresponding to 50°C (no saturation) or that corresponding to 220°C (saturation). This provides upper and lower bound Charpy shifts of between ~350°C and ~180°C respectively. Other estimates based on the data of Grounes [17] for a number of US and Swedish RPV steels indicate upper and lower bounds between ~300°C and ~105°C respectively. It is apparent, therefore, that all or most of the observed embrittlement of the Support Structure steel in the present high dose irradiation could arise from matrix hardening alone. On this basis, at the peak dose experienced by the Support Boxes during service, 2mdpa, matrix hardening would produce upper and lower bound shifts in the range 20-70°C. Alternatively, if all the embrittlement (188°C) in the present irradiation of the Support Structure steel was due to matrix hardening

alone, a transition temperature shift of 40°C would be expected at the peak dose experienced by the Support Boxes.

The mechanical property variations in the commercial type steels in the present study did not show a strong copper dependence. The most probable interpretation of the results suggests that copper precipitation did not occur. For copper precipitation to account for a significant fraction of the observed increase in hardness it would require a very high number density of precipitates, as the size must be below the resolution of the TEM, smaller than that for peak hardening by the modulus hardening mechanism. Given such a requirement, it is not possible to explain the single low copper matrix level measured by FEGSTEM, as beam interaction with the requisite number of small precipitates would be significant, leading to spot mode values approaching those of the bulk copper concentration. The latter measurement therefore probably reflects the inhomogeneity of copper distribution in the Support Structure steel.

In the case of the model iron alloy studied, 2D, no clear TEM/FEGSTEM evidence for copper precipitation was obtained, though a copper dependant hardening response was observed. The TEM study did, however, reveal the existence of a high density of planar defects, which may be dislocation loops. This is currently under investigation and will be reported elsewhere. This appears to be the first observation of such defects at doses comparable with EOL RPV fluences, albeit at low temperature, and it is therefore of fundamental importance. This suggests that the observed dependence of hardening in the model alloys on copper content might not arise from copper precipitation, but from an effect of copper on the nucleation or stability of the latter planar defects. Such a synergy has been noted in positron annihilation studies of model alloys by Phythian et al [12] which indicate that copper vacancy complexes can be modified by interstitial impurities such as nitrogen. Such interstitial impurities are known to affect the microstructural development of the matrix component of damage, and therefore may offer an explanation in the present study for the discrepancy in behaviour for model iron alloys and commercial steels.

In the case of the Support Structure steel the important microstructural feature is the broader spot mode copper distribution compared with alloy 2D in both the unirradiated and irradiated conditions. This has been interpreted as evidence for local inhomogeneity in the start of life condition and the formation of pre-irradiation copper precipitates which would be consistent with the slow furnace cooling applied in the stress relief heat treatment, during which some precipitation would be expected to occur. Since this treatment was applied to simulate the post-weld heat treatment specified for the Sizewell "B" Support Structures it has important implications for the subsequent irradiation performance of the actual components. The original concern was that the A588B steel could have a copper content as high as 0.4wt%, which, depending on heat treatment, might be available for embrittlement. Subsequent chemical analysis of the material indicates that the copper content is near the lower bound of the specification, at 0.22wt%. Nuclear Electric chemical analysis of the Support Structure steel indicated a higher bulk copper content of about 0.26wt%.

As indicated in the review by M^{C}Elroy et al [6], the Charpy shift due to full copper precipitation would be about 80°C for 0.4wt% Cu, 60°C for 0.26wt% Cu and reduce to about 50°C for only 0.2wt% Cu. A reduction in matrix copper level as a result of the post-weld heat treatment would further reduce the potential for embrittlement. Such a reduction in the effective copper contribution could reduce the embrittlement from this source to levels which, given the apparently low fracture toughness transition temperature (-95°C), should not be of concern. It is noted that the heat treatment applied to the Support Structure steel in the present work employed a 50% slower cooling rate than the reported heat treatment of the Support Boxes, which might lower the potential for copper precipitation. However, the heating rate was also slower than in the case of the Support Boxes which, given the short soaking time, could have produced more dissolution of copper prior to cooling. The net effect of these differences in heat treatment is therefore likely to be small.

Returning to the embrittlement response of the Support Structure steel an assessment of the maximum shift in the Sizewell "B" RPV Support Structure steel can be made. If no copper precipitation occurs the embrittlement is likely to scale with dose according to the familiar $\sqrt{\text{Dose}}$ relationship, producing an EOL Charpy shift of 40°C, as indicated earlier.

Though contrary to the general trend in behaviour of the IAEA CRP-3 steels and the interpretation of the TEM/FEGSTEM information, it is possible that copper precipitation could have occurred, producing the additional hardening indicated in TABLE 3. This being the case, it is possible that the hardening contribution could be as high as 20VPN, which would correspond to a shift of about 40°C. Based on the copper embrittlement estimated [6], such a shift would correspond to a precipitated copper content of about 0.15wt%. This would be consistent with the measured copper content of the steel, allowing for some copper precipitation during post-weld heat treatment. To avoid double accounting, the above EOL matrix shift would in turn be slightly lower, at 31°C, since the matrix shift in the OSIRIS irradiation would be about 148°C instead of 188°C. The maximum EOL transition temperature shift in the Sizewell "B" Support Structure steel would therefore be about 71°C given the copper content of the present material. Factoring in the possibility that the copper content of the Support Boxes might be as high as 0.26wt% and assuming a similar reduction in effective copper level due to heat treatment, the maximum shift could be about 85°C.

It is therefore concluded that the EOL (2mdpa) transition temperature shift of the Sizewell "B" Support Structure steel is likely to lie in the range 40-85°C, the upper bound depending on copper precipitation. Based on the present results the possibility that copper precipitation could occur has not been completely ruled out but, on balance, it is thought to be unlikely. The post-irradiation annealing experiment supports the argument that copper precipitation in this material in service is extremely unlikely.

5. Conclusions

Irradiation hardening studies of a range of model iron alloys and model steels from the IAEA CRP-3 and Charpy tests of Sizewell "B" RPV Support Structure steel have been performed in association with a high dose, low temperature irradiation in OSIRIS at Saclay. The purpose of the irradiation was to establish if copper precipitation could occur during low temperature irradiation of this material. Based on modelling considerations, it was judged that full copper precipitation should occur at a dose of less than 4mdpa, $3x10^{18}$ $n.cm^{-2}$ (E>1MeV) during irradiation at about 60°C. It was therefore decided to irradiate to a dose of 45mdpa, $3x10^{19}$ $n.cm^{-2}$ (E>1MeV), at the lowest possible damage rate compatible with an irradiation of less than 1 year. These experiments have been supplemented by TEM/FEGSTEM measurements to determine the role of copper precipitation in low temperature embrittlement. The main observations and conclusions are summarised below:

1. Irradiation to a dose of 49.6mdpa, $3.74x10^{19}$ $n.cm^{-2}$ (E>1MeV) at an average temperature of 71°C in OSIRIS at Saclay produced a Charpy transition temperature shift of 188°C and a corresponding hardness increase of 92VPN;

2. A series of model steels previously studied after irradiation at 288°C in the IAEA CRP-3, under which conditions they exhibited a dependence of hardening on copper and nickel content, showed no clear evidence of such correlations in the present low temperature irradiation. This is in contrast to the results obtained from a series of model iron alloys with varying copper and nickel contents that showed a strong correlation between hardening and copper content and a weaker correlation with nickel;

3. TEM/FEGSTEM studies on the 2D model iron alloy failed to resolve copper precipitates even though a clear copper dependence of hardening was established; visible planar matrix defects, which may be dislocation loops, were observed by TEM; this observation is important since it is believed to be the first identification of such defects at EOL PWR doses, albeit at a low temperature; the copper dependence of hardening may reflect a secondary effect of copper on the stability of point defect clusters rather than copper precipitation;

4. FEGSTEM studies of the Support Structure steel indicate the presence of fine copper precipitates in both unirradiated and irradiated conditions; this may be due to precipitation during the slow cooling phase of the post-weld heat treatment; the single low spot mode copper measurement in irradiated material is thought to reflect inhomogeneity in the unirradiated material rather than significant depletion of the matrix copper as a result of precipitation during irradiation

5. Post irradiation annealing studies have demonstrated that irradiation embrittlement in the A588 support structure steel at low temperatures is due to matrix damage. Although the exact nature of the matrix defect/defects responsible for the embrittlement has not been identified, the copper content is believed to be unimportant. There is, therefore, no reason to believe that the relatively high copper specification of the A588 support structure steel will be detrimental to the steel's toughness after low temperature/high dose irradiation as expected in the Sizewell B support structure.

6. Acknowledgement

The views expressed in this paper are those of the authors and do not necessarily represent the views of the organisations involved, AEA and NII. Part of this work was supported under the corporate research programme of AEA under grant CIRE/93-1049.

5. References

1. Cheverton, R.D., Merkle, J.G. and Nanstad, R.K., Eds., "Evaluation of HFIR Pressure-Vessel Integrity Considering Radiation Embrittlement", Oak Ridge National Laboratory Report ORNL/TM-104, 1987.

2. Cheverton, R.D., Kam, F.B., Nanstad, R.K. and Robinson, G.C., "An Embrittlement Rate Effect Deduced from HFIR that may Impact LWR Vessel Support Life Expectancy", Nuclear Engineering and Design, 1989, Vol.117, pp.349-355.

3. Nanstad, R.K., Farrell, K, Braski, D.N. and Corwin, W.R., "Accelerated Neutron Embrittlement of Ferritic Steels at Low Fluence: Flux and Spectrum Effects", J. Nucl. Mat., 1988, Vol.158, pp.1-6.

4. Nanstad, R.K., Iskander, S.K., Rowcliffe, A.F., Corwin, W.R. and Odette, G.R., "Effects of 50C Surveillance and Test Reactor Irradiations on Ferritic Pressure Vessel Embrittlement", Effects of Radiation on Materials: 14th International Symposium, (Vol.II), ASTM STP 1046, 1990, pp.5-29.

5. Druce, S.G., "Application of a United Kingdom Magnox Steel Irradiation Model to the HFIR Pressure Vessel", ibid, p.30-44.

6. McElroy, R.J., Williams, T.J., Boydon, F.M.D. and Hemsworth, B., "Low Temperature Embrittlement of LWR RPV Support Structures", Proceedings of NEA/CSNI Workshop on Safety of Reactor Pressure Vessels - Ability to Provide Reliable Safety Assessment of Long-Term Component Integrity Using Available Data and Methods, Espoo, Finland, October 1990, pp. 311-364.

7. S.B. Fisher, J.E. Harbottle and N. Aldridge, "Radiation Hardening in MAGNOX Pressure Vessel Steels", Phil. Trans. Roy. Soc. Lond., Vol. A 315, 1983, p.301.

8. Mamhood, S.T., and Farrell,K., "Low temperature irradiation of RPV steels and model alloys in the HFIR hydraulic tube". These proceedings.

9. Toussaint, P., "SIAT H.S.E. - Compte-rendu d'irradiation des cycles F97 a F103", Rapport D.M.T./93-069 (SETIC/LERI/93-0066), January 1993.

10. Phythian, W.J., Foreman, A.J.E., English, C.A., Buswell, J.T., Hetherington, M., Roberts, K. and Pizzini, S., "The structure and hardening mechanism of copper precipitation in thermally aged or irradiated FeCu and FeCuNi model alloys", Proc. 15th ASTM International Symposium on Effects of Radiation on Materials, Nashville, Tennessee, June 1990, ASTM-STP-1125 Aug. 1992: Also as AEA-TRS-2004 May 1990.

11. Phythian, W.J. and English, C.A., "Microstructural changes in ferritic pressure vessel steels subjected to irradiation", Proc. Int. Conf. "Evolution of Microstructure in Metals During Irradiation", Muskoka, Canada, Sept. 1992, J. Nuclear Materials, Vol. 205, 1993, pp.162-177.

12. Phythian, W.J., de Diego, N., Mace, J. and McElroy, R.J., "Characterisation of Model Fe-Cu-Mn-N Alloys by Electron Microscopy and Positron Annihilation", Effects of Radiation on Materials: 16th International Symposium, ASTM STP 1175, Denver Colorado, June 1992, Arvind S. Kumar, David S. Gelles, and Randy K. Nanstad, Editors, American Society for Testing and Materials, Philadelphia, 1993, in press.

13. Mader, E., Lucas, G.E. and Odette. G.R., "The effects of metallurgical and irradiation variables on the kinetics of post irradiation annealing of pressure vessel steels", Proc. 15th ASTM International Symposium on Effects of Radiation on Materials. Nashville, Tennessee, June 1990, ASTM-STP-1125, Aug. 1992.

14. Hawthorne, J.R., private communication, Nov. 1992.

15. McElroy, R.J., Foreman, A.J.E., Gage, G., Phythian, W.J., Ray, P.H.N. and Vatter, I.A., Final report on the UK Contribution to the IAEA Phase 3 Coordinated Research Programme on "Optimisation of Reactor Pressure Vessel Surveillance Programmes and their Analysis", March 1994, AEA-RS-2426; also to be published by IAEA.

16. Buswell, J.T., Phythian, W.J., McElroy, R.J., Dumbill, S., Ray, P.H.N., Mace, J. and Sinclair, R.N., "Irradiation induced microstructural changes and hardening mechanisms in model PWR reactor vessel steels", these proceedings

17. Grounes, M., "Effects of Radiation on Structural Metals", ASTM STP 426, 1967, p.224.

Masahide Suzuki,[1] Kunio Onizawa,[2] and Minoru Kizaki[3]

EFFECTS OF NEUTRON FLUX AND IRRADIATION TEMPERATURE ON IRRADIATION EMBRITTLEMENT OF A533B STEELS

REFERENCE: Suzuki, M., Onizawa, K., and Kizaki, M., **"Effects of Neutron Flux and Irradiation Temperature on Irradiation Embrittlement of A533B Steels,"** *Effects of Radiation on Materials: 17th International Symposium, ASTM STP 1270,* David S. Gelles, Randy K. Nanstad, Arvind S. Kumar, and Edward A. Little, Eds., American Society for Testing and Materials, 1996.

ABSTRACT: Irradiation embrittlement of A533B steels with low copper contents were investigated from the point of dose rate and irradiation temperature effects. Change of neutron flux in the range from $\sim 10^{12}$ to $\sim 10^{13}$ n/cm^2/s (E>1MeV) did not have a significant effect on the embrittlement. Irradiation temperature change of 1°C resulted in the transition temperature shift (ΔT_{41J}) of about 1°C and yield stress change ($\Delta\sigma_y$) of about 0.8MPa. Factors that might affect the embrittlement of low copper steels are also discussed.

KEYWORDS: irradiation embrittlement, pressure vessel steels, dose rate effect, Charpy shift, hardening

INTRODUCTION

Irradiation embrittlement of pressure vessel steels is governed by various factors, such as chemical composition, heat treatment, irradiation temperature and neutron flux. Moreover, some of these factors are interactive. When a steel contains high impurity copper (Cu), embrittlement behavior is strongly dependent on the irradiation induced Cu-rich precipitates[1-3], a process which is dependent on dose rate. Japanese modern pressure vessel steels contain very low concentrations of Cu and other detrimental impurity atoms such as phosphorus (P), and hence have very low susceptibility to irradiation embrittlement. In materials with very low Cu content, effects of other metallurgical factors or irradiation variables should become discernible[4]. However,

[1]Principal engineer, [2]research engineer, respectively, Department of nuclear safety research,
3Chief, Department of Hot Laboratory,
Japan Atomic Energy Research Institute, Tokai-mura, Ibaraki-ken, 319-11 Japan

Copyright© 1996 by ASTM International www.astm.org

irradiation characteristics of low Cu steels (or highly purified materials in a level of industrial product) is not well established.

In the present experiment, embrittlement characteristics of two low Cu A533B steels with different phosphorus (P) and sulfur (S) contents were evaluated in terms of the effects of dose, dose rate and irradiation temperature.

EXPERIMENTAL PROCEDURE

Materials

Two kinds of MnMoNi steels (A533B) were used in the present irradiation experiments. These are hereinafter referred to as L and M. Both materials were produced as thick plates (thickness: 200 mm). Alloy L is a very low impurity material for an industrial product (P:0.003,Cu:0.02, S:0.003 in wt%). Alloy M is a slightly higher impurity material (P:0.006, Cu:0.03, S:0.014). In particular, M contains higher manganese (Mn) to adjust to increased S level, and hence contains a larger amount of MnS inclusions. Chemical compositions and heat treatment conditions are shown in Tables 1 and 2, respectively. Microstructure of these materials was bainitic.

Table 1 --Chemical composition of the materials used. (wt%)

Alloy	C	Si	Mn	P	S	Ni	Cr	Cu	Co	Mo	V	N
L	0.17	0.24	1.39	0.003	0.003	0.60	0.07	0.02	0.009	0.46	<0.01	0.0082
M	0.21	0.29	1.44	0.006	0.014	0.65	0.03	0.03	0.009	0.51	<0.01	0.0096

Table 2 --Material specification used for the irradiation experiment.

1) Material
A533 Gr.B cl.1, Production form: plate 200 mm^t

2) Heat treatment

Alloy L:		Alloy M:	
Normalizing	970℃ @ 7.0h (AC)	Normalizing	920℃ @ 7.0h (AC)
Tempering	660℃ @ 7.0h (AC)	Tempering	660℃ @ 7.0h (AC)
Quenching	900℃ @ 7.0h (WQ)	Quenching	900℃ @ 7.0h (WQ)
Tempering	660℃ @ 5.0h (AC)	Tempering	660℃ @ 5.0h (AC)
SR	600℃ @ 25h (*)	SR	600℃ @ 25h (*)

(*) Heating and cooling rate 50℃/h max.

3) Microstructure
bainite

Irradiation

Neutron irradiations were conducted in the Japan Materials Testing Reactor (JMTR) to fluences of ~2×10^{18} and ~2×10^{19} n/cm^2 (E>1MeV) at temperatures of 260, 275 and 290°C. Two different dose rates were adopted for irradiations at 290°C: the first at ~1×10^{12} n/cm^2/s (E>1MeV) was carried out at a second aluminum reflector region, and the other at ~$0.5\text{-}1\times10^{13}$ n/cm^2/s (E>1MeV) at a second beryllium reflector region of the JMTR core. Irradiations at positions of different neutron flux will inevitably be associated with different neutron spectra. However, it is considered that the difference between the spectra for positions A and B will not have a significant effect. The neutron spectra in these positions are shown in Fig.1. Parameters relating to the neutron energy spectra are as follows:

parameter	Position A (higher flux)	Position B (lower flux)
thermal/fast neutron flux ratio	~8	~18
dpa/fast fluence ratio, cm^2	2.16×10^{-21}	2.46×10^{-21}

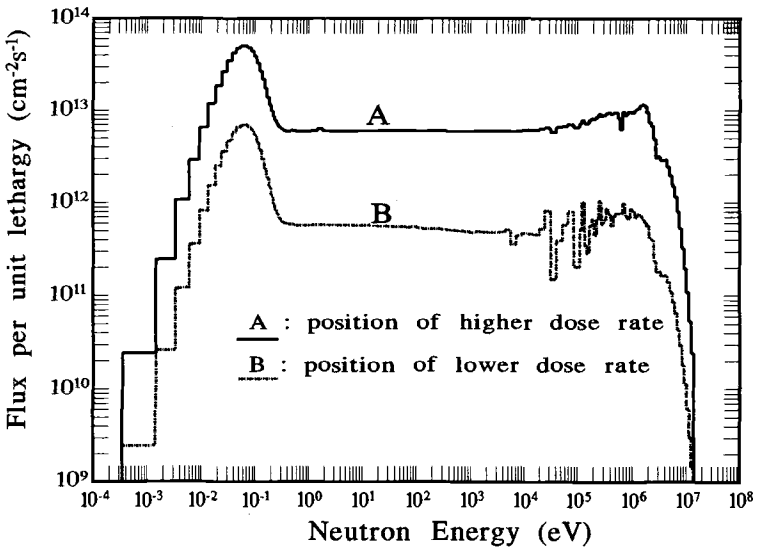


FIG.1 --Neutron energy spectra for positions A (higher dose rate) and B (lower dose rate).

Mechanical property tests

After irradiation, Charpy impact, tensile and hardness tests were performed. Specimens were machined from the quarter thickness portion (1/4T) of the plate. The notch orientation of Charpy specimens was T-L in the ASTM designation. Procedures for Charpy test and specimen preparation were in accordance with the Japanese Industrial Standards (JIS) B7722 and JIS Z2202 (standard 10x10x55 mm^3 size), respectively. Tensile specimens had dimensions of 4 mm in diameter and 22 mm in gauge length. Vickers hardness (DPH) measurements were conducted at the applied load of 10kgf using the brittle fractured Charpy specimens.

RESULTS AND DISCUSSION

Dose and dose rate effects on Charpy impact properties

Alloys L and M are both low copper steels and contain low levels of these impurity atoms which are known to be important for irradiation embrittlement. Therefore, irradiation embrittlement was expected to be very small. For example, predicted transition temperature (ΔT_{41J}) shifts for the two alloys after irradiation to $2x10^{19}n/cm^2$ (E>1MeV) by prediction equations [5,6] are as follows:

	Predicted shift	
	US R.G.1.99 Rev.2 [5]	JEAC 4201[6]
Alloy L:	13.2°C	14.2°C
Alloy M:	13.2°C	20.7°C

In the upper shelf region, alloy M shows lower toughness owing to the increased number density of MnS.

Fig.2 shows the absorbed energy transition curves after irradiation to ~$1x10^{18}$ and ~$2x10^{19}n/cm^2$ (E>1MeV) at 290°C. Fig.3 shows the Charpy shift (ΔT_{41J}) as a function of dpa (displacements per atom). At lower dose, alloy M showed a larger shift than L. However, the shift of L became larger after irradiation to ~$2x10^{19}n/cm^2$ (E>1MeV). The shift itself was much larger than expected.

Alloy L showed almost no dose rate dependence of embrittlement, whereas alloy M seemed to be more embrittled by lower dose rate irradiation (by about 12°C shift by one order change of dose rate).

Hardness test results were consistent with the Charpy impact results, i.e. only alloy M showed a slight difference of irradiation induced hardening by changing the dose rate (see Fig.4). However, the difference is small when compared with the magnitude of scatter band. So, one can conclude

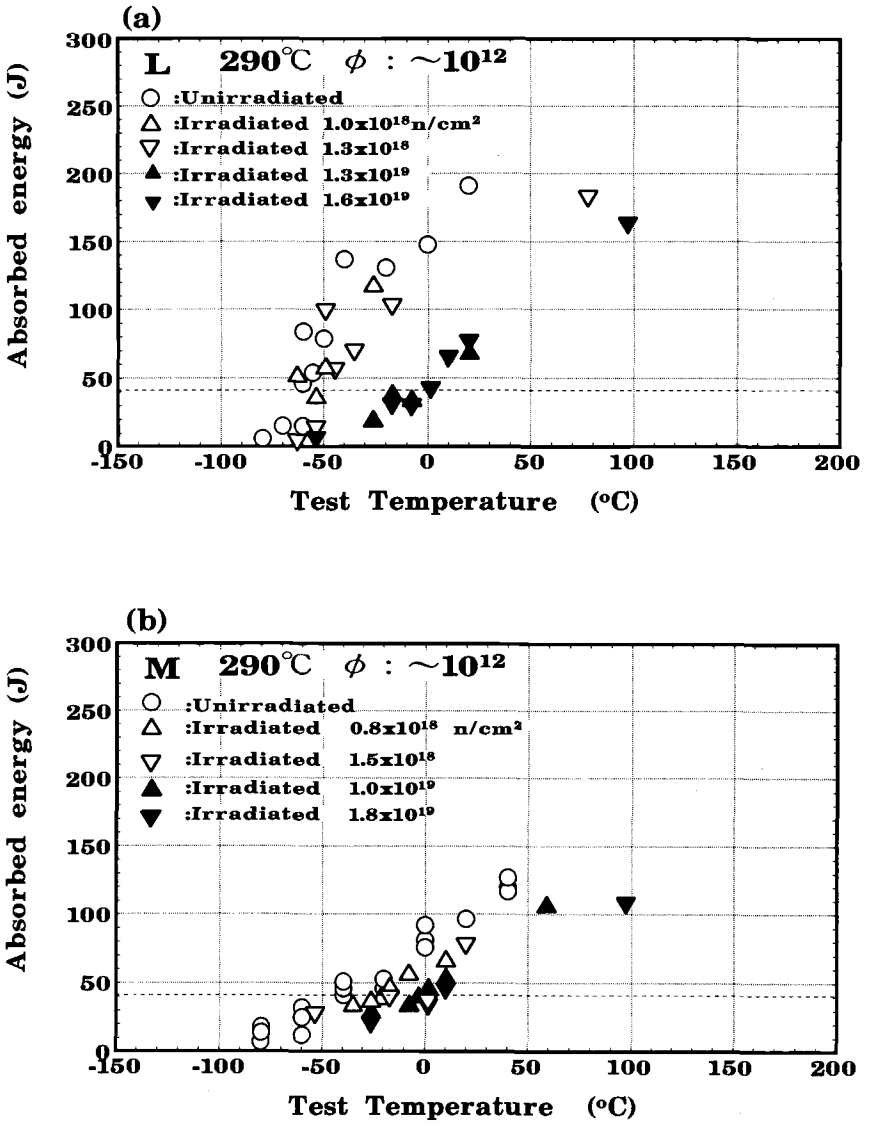


FIG.2 --Absorbed energy transition curves before and after irradiation to $1x10^{18}$ and $2x10^{19}n/cm^2$ (E>1MeV) at 290°C for (a) alloy L and (b) alloy M. All data are of dose rate of $\sim10^{12}n/cm^2/s$.

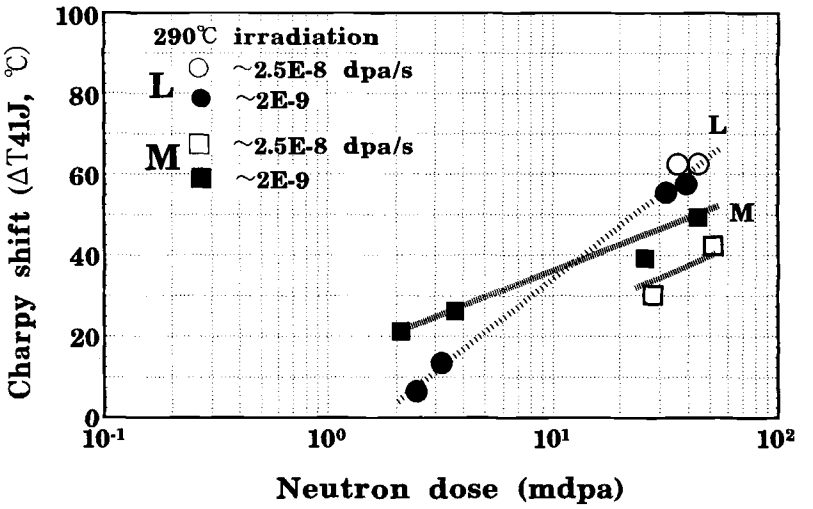


FIG.3 --Charpy shift (ΔT_{41J}) as a function of dose (dpa).

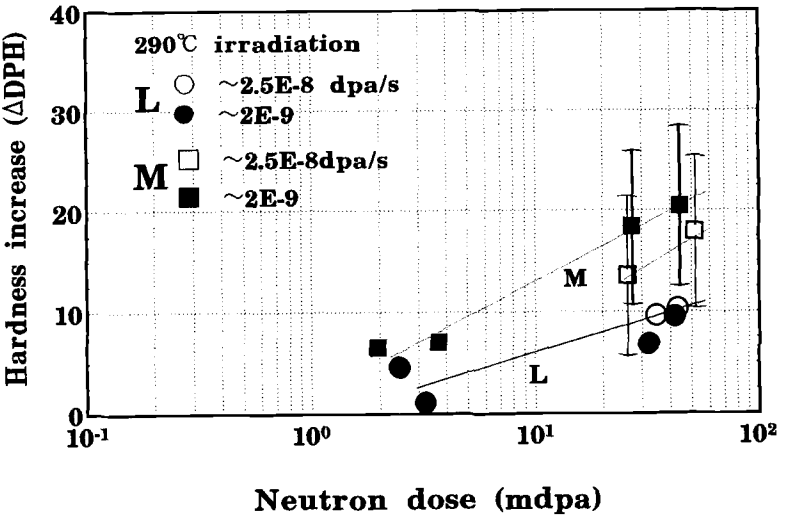


FIG.4 --Hardness increase (ΔDPH) as a function of dose (dpa).

from the hardness measurements that dose rate dependence is weak in the dose rate range and irradiation temperature tested for both materials.

Irradiation temperature dependence

Fig.5 (a) and (b) shows the temperature dependence of irradiation effects. Fig.5(a) shows the transition temperature shift caused by irradiation to ~$2x10^{19}$ n/cm^2 (E>1MeV) as a function of irradiation temperature. In the temperature range from 260°C to 290°C, as the irradiation temperature decreased by 1°C, the transition temperature shift increased by 1°C for both alloys L and M.

Fig.5(b) shows the irradiation induced yield stress increase as a function of irradiation temperature. An irradiation temperature change of 1°C resulted in a yield stress

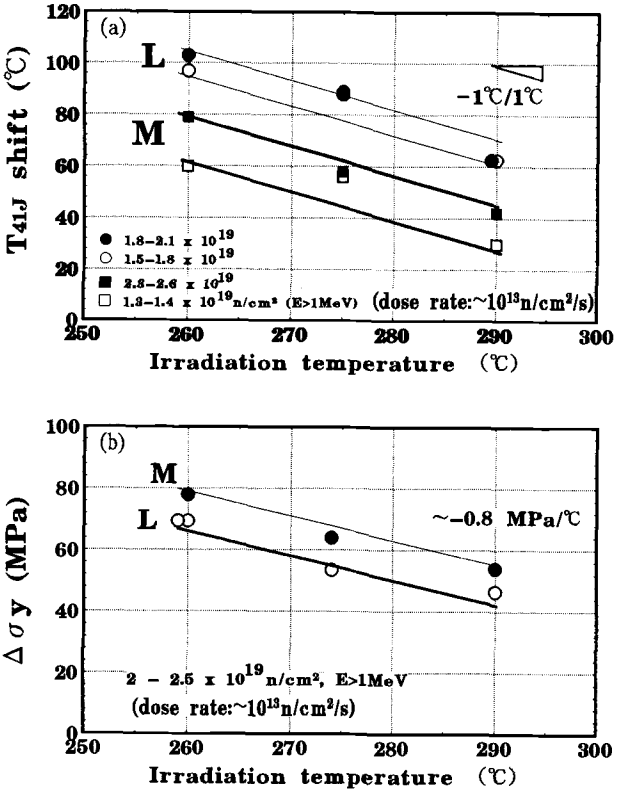


FIG.5 --Effects of irradiation temperature on (a) transition temperature shift and (b) yield stress increase, after irradiation to ~$2x10^{19}$ n/cm^2 (E>1MeV).

change of about 0.8MPa. Almost the same temperature dependence was observed for both alloys.

Anomalousness of embrittlement characteristics

The present experiment showed alloy L to have an anomalous embrittlement characteristic, despite its low impurity content. The key observation for this anomalous behavior may be the very high ratio of transition temperature shift versus irradiation hardening. Usually the shift in

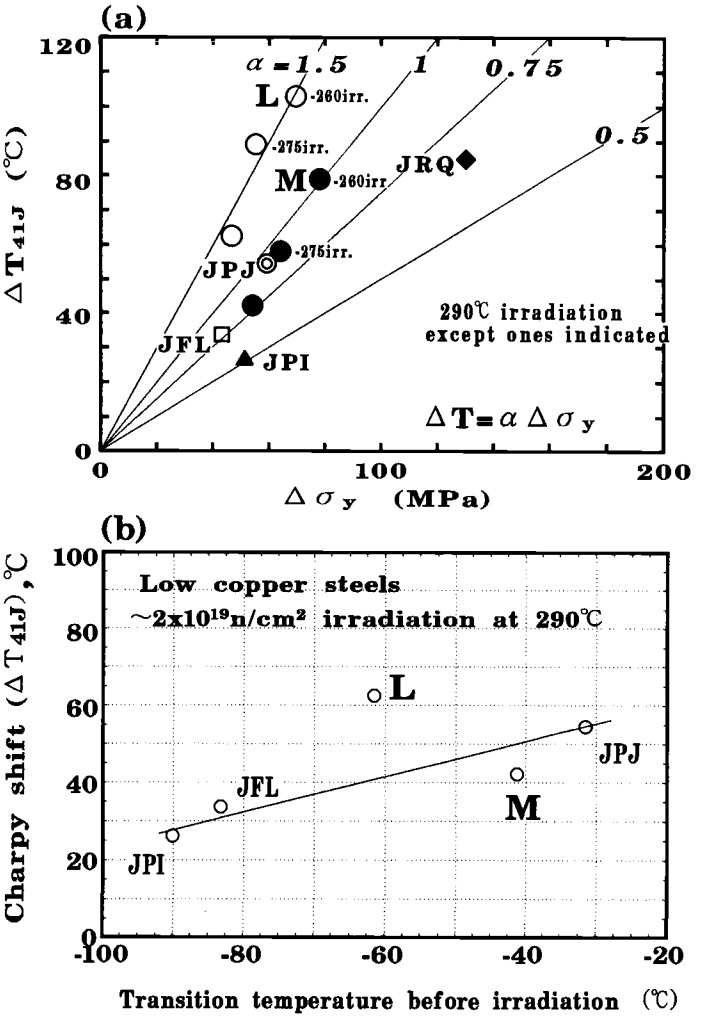


FIG.6 --(a)Relation between ΔT_{41J} and $\Delta\sigma_y$ and (b)relation between ΔT_{41J} and transition temperature before irradiation for alloys L,M and the IAEA heavy section steels.

transition temperature is proportional to the change in yield strength:

$$\Delta T_{41J} = \alpha * \Delta\sigma_y .$$

Here, the coefficient α lies in the range from ~0.45 to ~0.85 °C/MPa[7].

Fig.6(a) shows the ratio of $\Delta T_{41J}/\Delta\sigma_y$ (=α) for alloys L and M together with data for various IAEA steels (IAEA coordinated research program Phase III, JAERI contribution [8]). Most of the steels have α value of less than 1.0, while that of L was about 1.5. Because transition temperature shift would depend on the initial (unirradiated) value of the 41J transition temperature[7], Charpy transition temperatures of low copper steels after similar irradiations (~2×10^{19} n/cm^2 at 290°C) were plotted as a function of initial values in Fig.6(b). From these observations, it is clear that large transition temperature shift for L gave rise to the high α value. In addition, the enhanced embrittlement sometimes observed for high purity steels (JPJ, besides L) seems to be correlated to high α value. Fig.7 compares the measured shift (ΔT_{41J}) with the predicted value by JEAC 4201 for the IAEA low copper materials. Although the chemical compositions of these materials were similar, measured shifts were widely scattered. The microstructures were also almost identical, i.e., bainitic structure with carbides of M_3C and M_2C. The reason for differences in irradiation characteristics is not clear, but should be related to the fine scale microstructural difference. For example, the morphology and density of M_2C

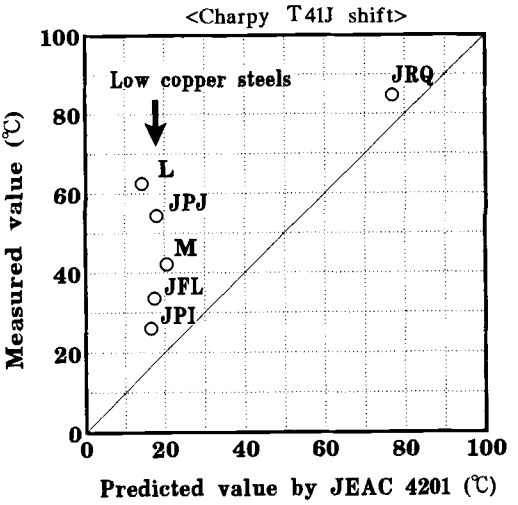


FIG.7 --Comparison of measured and predicted Charpy T_{41J} shift.

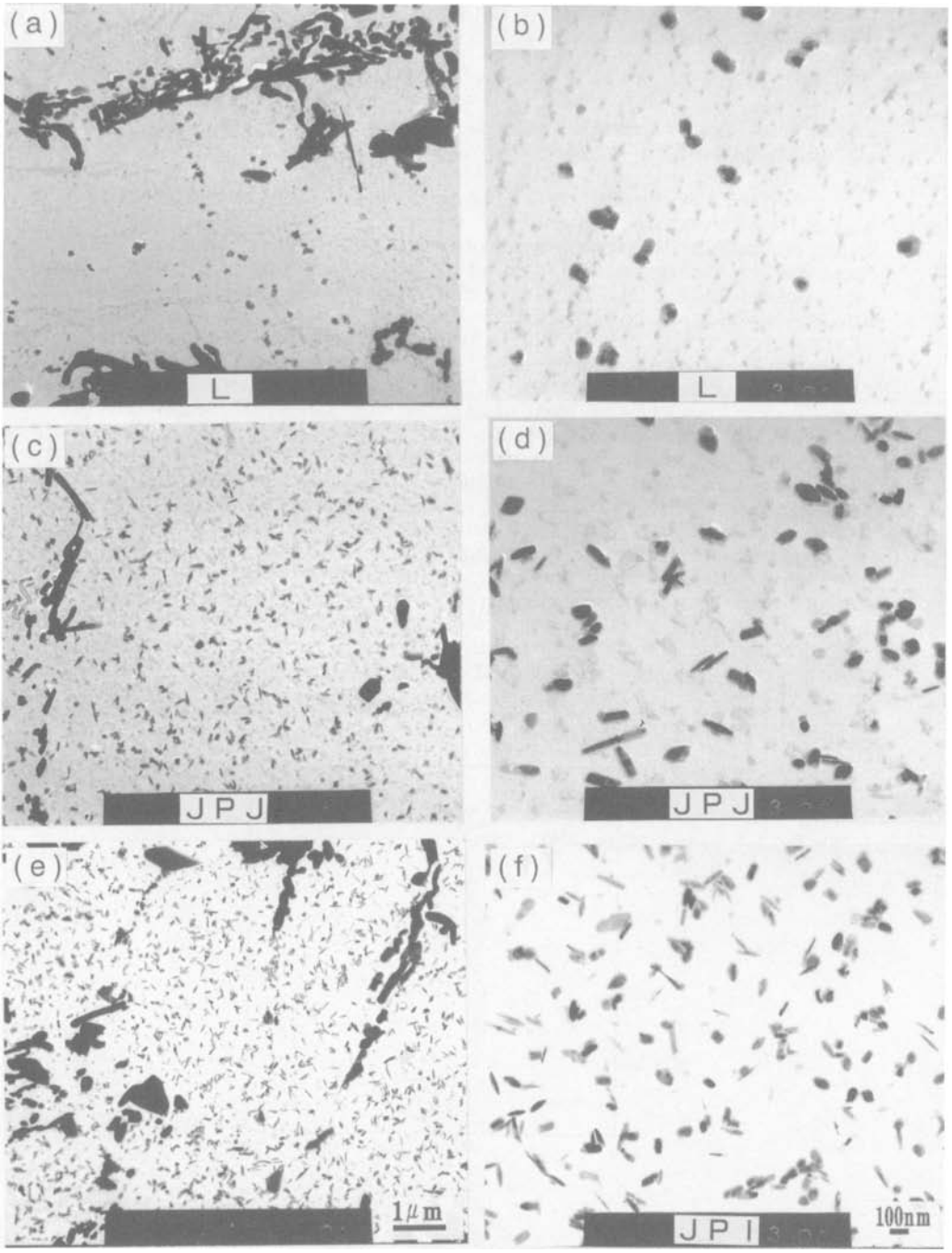


FIG.8 --Carbide distribution for the alloy L (a,b), JPJ (c,d) and JPI (e,f) observed by TEM for carbon extraction replicas. Large ones are M_3C and others M_2C.

carbides are different among these materials. Fig.8 shows the carbides extracted onto the carbon replica films. Fine needle-like particles of M_2C were observed in high density for the alloy JPI. By contrast, high α materials (L and JPJ) contain larger M_2C in less density. This tendency is more distinct for the alloy L. The reason for producing a high α value is unknown. At the present stage, we can say at least that this embrittlement is not related to intergranular embrittlement, nor with some strain rate dependent phenomena. The former was confirmed by SEM observation of fracture surface, and the latter was examined by the analysis of instrumented Charpy test data. It may be related to the nano-scale microstructural change which is related with the strengthening mechanism of low alloy steels like "interaction solid solution hardening" [9]. Re-distribution of portions of various strengthening factors during irradiation may have caused the anomalous mechanical property correlations of the alloys L and JPJ. Microstructural characterization will be needed for the purified low cooper steels for the accurate embrittlement prediction.

CONCLUSIONS

Irradiation embrittlement of A533B steels with low copper contents were investigated from the point of dose rate and irradiation temperature effects. Conclusions obtained were:

1. A change of neutron flux in the range from $\sim 10^{12}$ to $\sim 10^{13}$ n/cm^2/s (E>1MeV) did not have a significant effect on the embrittlement at 290°C.
2. An irradiation temperature change of 1°C resulted in a transition temperature shift (ΔT_{41J}) of about 1°C and a yield stress change ($\Delta\sigma_Y$) of about 0.8MPa.
3. A high ratio of transition temperature shift to irradiation hardening was observed for alloy L. Microstructural data will be needed to give an accurate prediction of irradiation embrittlement for low Cu steels.

ACKNOWLEDGEMENTS

The authors would like to thank Mr.T.Takeda and other staffs of the department of JMTR Project for performing material irradiations and dose calculations. Thanks are also due to many people of the department of Research Hot Laboratory for doing post irradiation tests, and Mr.N.Nakajima of Reactor Component Reliability Laboratory for giving us helpful advice.

REFERENCES

[1] Phythian,W.J. and English,C.A., Journal of Nuclear Materials, Vol.205,1993,pp.162.
[2] Williams,T.J., Burch,P.R., English,C.A. and de la cour Ray,P.H.N., Proceeding of Environmental Degradation of Materials in Nuclear Power Systems-Water Reactors,1988,pp.121-131.
[3] Odette,G.R., Mader,E.V., Lucas,G.E., Phythian W.J. and English,C.A., ASTM STP 1175,1993,pp.373-393.
[4] Odette,G.R., Scripta metallurgica, Vol.17,1983,pp.1183-1188.
[5] Revision 2 of U.S.NRC Regulatory Guide 1.99, "Radiation Damage to Reactor Vessel Materials,",U.S. Nuclear regulatory Commission,1988.
[6] Japanese Electric Association Codes (JEAC) 4201-1991, "Surveillance Tests of Structural Materials for Nuclear Reactors", Japanese Electric Associations, 1991 (in Japanese).
[7] Odette,G.R., Lombrozo,P.M., and Wullaert,R.A., ASTM STP870, 1985,pp.840-860.
[8] Onizawa,K.,Suzuki,M. and Ueda,S.,JAERI-M 93-201,October 1993.
[9] Baird,J.D. and Jamieson,A, Journal of Iron and Steel Institute, Vol.210, 1972, pp.841-846.

John L. Helm[1]

THE INTERPRETATION OF CHARPY IMPACT TEST DATA USING HYPER-LOGISTIC FITTING FUNCTIONS

REFERENCE: Helm, J. L., **"The Interpretation of Charpy Impact Test Data Using Hyper-Logistic Fitting Functions,** *Effects of Radiation on Materials: 17th International Symposium, ASTM STP 1270,* David S. Gelles, Randy K. Nanstad, Arvind S. Kumar, and Edward A. Little, Eds., American Society for Testing and Materials, 1996.

ABSTRACT: The hyperbolic tangent function is used almost exclusively for computer assisted curve fitting of Charpy impact test data. Unfortunately, there is no physical basis to justify the use of this function and it cannot be generalized to test data that exhibits asymmetry. Using simple physical arguments, a semi-empirical model is derived and identified as a special case of the so called hyper-logistic equation. Although one solution of this equation is the hyperbolic tangent, other more physically interpretable solutions are provided. From the mathematics of the family of functions derived from the hyper-logistic equation, several useful generalizations are made such that asymmetric and wavy Charpy data can be physically interpreted.

KEYWORDS: charpy data, curve fitting, logistic and hyperlogistic functions

Charpy impact test data are collected at several temperatures in order to obtain the nil ductility transition temperature (RT_{NDT}) or the upper shelf energy (USE) of pressure vessel (PV) steels. Although other desirable material tests are available, for historical and practical reasons, RT_{NDT} and USE are employed for the PV materials assessment required by many nuclear regulatory agencies worldwide.

Because Charpy data are collected only at discrete temperatures, an interpolation method is required to obtain the RT_{NDT} and USE. Standards exist for conducting the Charpy impact test [1]; however, little guidance is available for fitting the interpolation function. In the past, both manual and computerized curve fitting have been performed and neither approach is completely satisfactory: manual fitting is vulnerable to bias unconsciously introduced by the analyst, and computerized fitting often requires the use of *ad hoc* measures to avoid unphysical results.

The most prevalent methods for computerized curve-fitting employ least-squares to estimate the parameters of an appropriately formed tanh function. This function provides a poor representation for many sets of Charpy data and a more realistic fitting function is needed. In the next section the problems of current methods are examined more closely. Following that, a semi-empirical function is derived, generalized, and explored.

[1]Assistant Professor, Department of Applied Physics, School of Engineering and Applied Science, Columbia University, New York, N.Y., 10027; helm@columbia.edu

Copyright© 1996 by ASTM International www.astm.org

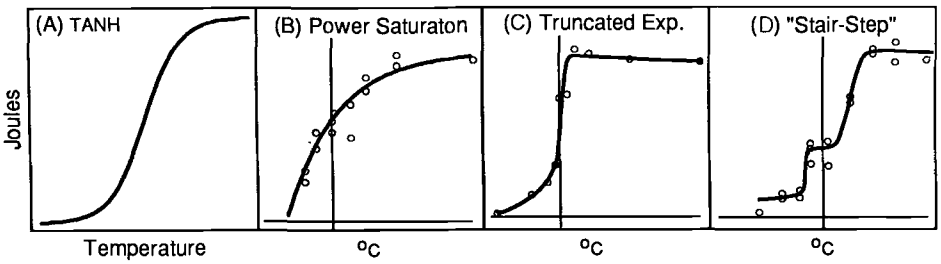


Figure 1: The tanh function and examples of "rogue" (i.e. non-tanh) Charpy curves.

CHARPY DATA EVALUATION

Over the years two schools of thought have developed among analysts of Charpy data. One school advocates computer based least-squares curve fitting of interpolation functions to assure that bias by human subjectivity is avoided and to support uncertainty analysis. The other school advocates manual interpolation because the programmed fitting functions have no physical basis [2], often fail to possess the same functional dependence exhibited by the data, and sometimes yield unphysical parameters such as negative lower shelf energies. Evidence abounds to support both points of view.

To illustrate the view of manual interpreters, some "rogue" Charpy curves are shown in Figure 1; for reference a tanh curve is given in panel (1A); panel (1B) [3] presents a fairly common shape resembling power saturation; panel (1C) [4] shows asymmetric data suggesting a truncated exponential function; and panel (1D) [5] contains "stair-step" Charpy data. Computer fitting the tanh function when the Charpy data resembles one of the other forms can produce significantly biased estimates or unphysical parameters. Manual interpreters note that the practice of introducing fictitious data points or artificially setting the lower shelf energy to a fixed value gives further evidence for the inadequacy of computerized fitting procedures.

Advocates of computer based data fitting object to manual methods because of the inherent difficulty in performing consistently unbiased visual judgments and because of concern over the opportunity for an interpreter to introduce bias. Concerns about graphical perception are well supported by a large body of literature which addresses the visual display and interpretation of data [6, 7, 8, 9]. Figure 2 illustrates a classic example; our task is to compare the values of two functions $y = f(x)$ over a given range of x using the plots in the left panel. Casual inspection of the curves suggests that they are further apart in the middle region than at the extremes. In fact, the two curves are separated by *exactly* the same vertical distance over the entire range. We perceive that they are farther apart in the center region because our visual systems tend to extract *minimum* distances, which, in this case are given by lines perpendicular to the curves. A subtler version of this same phenomenon is given in the right panel, where one curve is shown with several associated data points. Of the 25 points plotted, six are exactly on the curve and the rest are exactly the same vertical distance from it. Again, because of our tendency to judge minimum distances, the fit looks much better in the regions of high slope when, in fact, it is the same.

In theory one could guard against perceptual biases in manual interpretation by appropriate procedures and discipline; however, consistent application of such procedures on a large scale would be difficult. Furthermore, it is not possible to perform an uncertainty analysis with manual methods. Given these limitations, let us consider ways to improve computer based fitting of Charpy data.

Current Fitting Functions Over the years, several functions have been considered for fitting to Charpy data. By far the most frequently used function has been:

$$E_{cv}(T) = \frac{\text{USE} + \text{LSE}}{2} + \frac{\text{USE} - \text{LSE}}{2} \tanh\left(\frac{T - T_m}{C}\right) \quad (1)$$

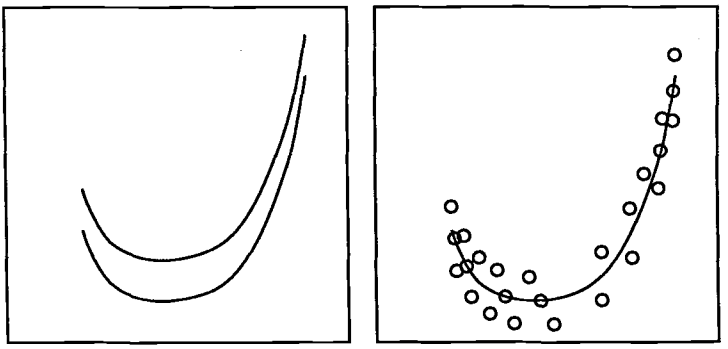


Figure 2: Examples of the opportunity for bias in graphical perception.

where T is temperature, $E_{cv}(T)$ is the temperature dependent Charpy impact energy, LSE and USE are the lower and upper shelf energies, respectively, T_m locates the curve center point, and C is the slope of the tangent at T_m. Equation 1 was introduced by Chun in 1972 [10], but he used a Bayesian fitting procedure which may have discouraged its use. Three years later Oldfield presented a minimum variance algorithm for fitting Equation 1 [11], but this also proved cumbersome and was replaced by a regression method using a Taylor series linearization [12]. Several other approaches for tanh fitting have been developed [13, 14, 15]; and, a variety of other fitting functions have been tried in addition to Equation 1. These include models based on arctan [16], erfc [17, 18], Fourier expansions [19], power series [11, 20], temperature dependent Weibull distributions [21, 22], exponential saturation functions [23], and Gompertz[2] functions [26, 27]. Given that all of the previously mentioned functions are without physical basis or require more complicated fitting procedures, in conjunction with the fact that they do not yield unambiguously superior curve fits, have prevented any of these from replacing Equation 1.

MECHANISMS OF FRACTURE

In this discussion, we restrict ourselves to metals that exhibit a pronounced ductile-brittle transition (DBT). Three temperature-dependent fracture mechanisms can be important during impact loading: transgranular cleavage, intergranular failure, and ductile rupture.

Cleavage and intergranular failure involve the rupture of atomic bonds, either across grain boundaries weakened by the segregation of impurities (intergranular failure), or within grains by stress concentration at point defects or in front of cracks (transgranular cleavage). Although surface active phenomena are operative in PV steels, impact specimens almost always fail by transgranular fracture; impurity segregation mainly appears to reduce the USE [28] although exceptions are noted [29].

Some plastic deformation always occurs at a crack tip before forces accumulate to exceed the atomic bond strength and extend the crack; and extensive plastic flow is required for ductile rupture to occur[30]. Thus strength is synonymous with resistance to plastic flow, which, in turn is related to the strain rate and temperature dependence of dislocation mobility.

Models of the Ductile-Brittle Transition The model of the DBT used most often in irradiation effects work is based on the Ludwik-Davidenkov criterion [31, 32], which can be traced back to ideas originally due to Orowan [33]. A fundamental distinction is made between the cleavage stress σ_f and flow stress σ_y. If σ_f is reached before σ_y (i.e. $\sigma_y > \sigma_f$), brittle failure occurs. If instead $\sigma_y < \sigma_f$, plastic flow, void formation and growth, and strain

[2]The Gompertz function used for $E_{cv}(T)$ modeling is $E_{cv}(T) = \text{USE}-(\text{USE}-\text{LSE})\exp[-L_m \exp[-U_m T]]$, where L_m and U_m are unknown activation energies. The first known use of this function was by Benjamin Gompertz in 1825 [24, 25].

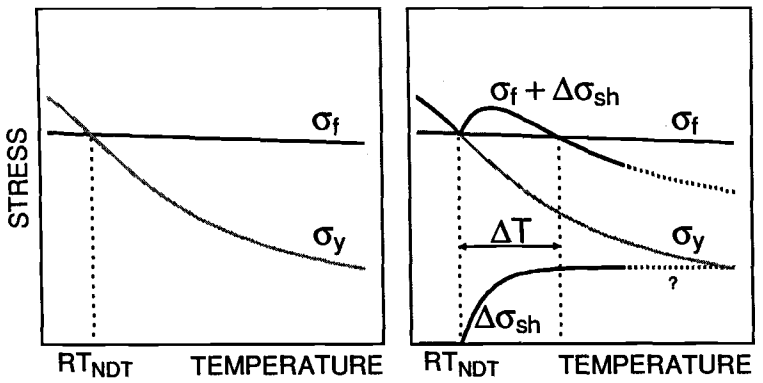


Figure 3: The Ludwig-Davidenkov criterion for RT_{NDT}. The left panel shows its traditional application, feedback by $\Delta\sigma_{sh}$ is shown in the right panel.

hardening commence. If strain hardening strengthens the material to the point of cleavage, then a mixed mode fracture is said to have occurred, otherwise the material fails by ductile rupture. In this model the RT_{NDT} is defined as the point where $\sigma_y = \sigma_f$.

In the Ludwik-Davidenkov model the temperature dependence of the DBT follows from the assumption that σ_f is mostly insensitive to temperature, whereas σ_y decreases with increasing temperature. This is shown in the left panel of Figure 3. Models of this type have been derived by Cottrell & Bilby [34, 35], Petch [36], and Louat [37] among others. We also note that these ideas have been applied to model the irradiation induced shift of RT_{NDT} by Hawthorne [38] and Odette [39]. To the best of our knowledge none of these models have been used successfully to describe the shape of Charpy curves.

To apply the Ludwig-Davidenkov approach in the mixed mode regime above RT_{NDT}, some accounting for the temperature dependence of strain hardening and dislocation emission must be proposed. The current assumption is that the yielding ligaments undergo local strain hardening during flow [39]; this is schematically illustrated in the right panel of Figure 3. The curve labeled $\Delta\sigma_{sh}$ is a stylized representation of the increase in σ_y that occurs at T due to a hypothetical hardening process operative during plastic flow. The key features of the processes depicted here are: (1) $\Delta\sigma_{sh} = 0$ prior to the onset of plasticity, and (2) only a finite amount of hardening is possible for any given temperature. As indicated on the figure, we assume that the DBT is complete when $\Delta\sigma_{sh} = \sigma_f - \sigma_y$ and failure occurs by ductile rupture. According to this model the transition begins at the temperature defined by Ludwig-Davidenkov criterion for RT_{NDT}, and ends when $\Delta\sigma_{sh}$ is no longer sufficient to elevate σ_y up to σ_f.

The Temperature Dependence of Dislocation Emission and Motion Since dislocation mobility underlies σ_y, we now consider the mechanisms of dislocation emission and locking. A variety of complex phenomena can be involved and their temperature dependence is not fully understood. For impact testing the most important locking mechanisms are [30, 40]: pinning by either hard or shearable particles that can exist over a range of sizes, interactions at grain boundaries, and the segregation of impurities to form "Cottrell atmospheres". A review of these and their functional dependence on temperature is given elsewhere [41]. The main conclusion of this review is that under the conditions of Charpy impact testing:

1. For any given Charpy specimen, regardless of thermal-mechanical treatment and irradiation history, its impurity content and microstructure are fixed with regard to the time and temperature existent during impact testing.

2. A general class of phenomena called temperature-dependent strain field driven rearrangement (TDSFDR) of interstitial impurities must be operative over the temperature range and timescale of impact testing. Familiar examples of TDSFDR are

Cottrell Atmospheres and grain boundary segregation. However, the concept is quite general and can be applied to any lattice structure characterized by a set of strain-field altered sites.

By assuming a finite number of identical lattice sites, each of which is characterized by discrete strain energy, one can derive the McLean-Langmuir isotherm [42, 43] which give the temperature dependent fraction of sites, θ, occupied by a "compatible agent" (e.g. solute atoms at grain boundaries) in low concentration:

$$\theta = \frac{Ce^{\frac{\Delta U}{kT}}}{1 + Ce^{\frac{\Delta U}{kT}}} \tag{2}$$

where $\Delta U = U_0 - U_1$ is the difference in configuration energy between the strain field sites U_1 and the sites present in the bulk of the grain U_0, k is Boltzmann's constant, T is temperature, and C is a constant.

3. The kinetics of certain TDSFDRs are adequately fast so that the equilibrium described by Equation 2 is valid for the times and temperatures existant during of impact testing. Studies of grain boundary and dislocation line segregation of carbon (and nitrogen) show that the kinetics can be very fast [42]. Larger solutes such as phosphorous, sulfur, and oxygen diffuse more slowly and therefore should not have a direct effect on the temperature dependence of Charpy data.

Although escape from Cottrell atmospheres is likely in high purity materials, dense atmospheres can form at low solute concentrations[44, 46].[3] For commercial alloys, the dislocation lines are usually so heavily locked that unpinned dislocations are created by some mechanism other than breaking away from atmospheres. Several types of dislocation source exist and many are insensitive to temperature (e.g. grain boundary sources). However, there are reasons to propose that the temperature dependence for some important sources originates from TDSFDR. For example, in the case of Frank-Read sources, TDSFDR would affect the stress needed for bowing. On dislocation lines, fluctuation of the atmosphere density around more heavily locked sections can create relatively flexible segments [45, 35]. Since they are fixed at each end, under high stress these arrangements could operate in a manner similar to that of a Frank-Read source.

Finally, the temperature dependence of the resistance to glide can also have a significant TDSFDR component, especially at low strain rates. Since all but the smallest point defects possess a strain field, TDSFDR of solute serves to change the effective size of the defects (and, possibly, the effective modulus of those that are shearable). Moreover, it is plausible that many of these structures possess include *labile* interstitial elemets such as C or N, for which the ΔU which is of the order kT or less in the transition temperature range. Using these arguments, we assume that generalized TDSFDR about dislocation lines and other structures is the mechanism for the temperature dependence of yielding under impact testing conditions.

A SEMI-EMPIRICAL MODEL OF IMPACT TEST RESULTS

Assumption 1 – We assume that the region that will be divided by an impact failure can be subdivided into an array of very small, identical volumes, perhaps on the order of those envisioned in the meshlength theory of work hardening [47]. Each mesh-volume possesses a dislocation source capacity defined by both temperature dependent and independent sources as discussed above.

Assumption 2 – Under impact loading, strain hardening is independent of temperature. This implies that the temperature dependence of σ_y is governed by the temperature dependence of dislocation sources or dislocation unlocking via TDSFDR-type mechanisms [45, 35].

The standard model for strain or work hardening is that it arises from unpinned dislocations interfering with each other or interacting with other lattice defects as they glide

[3] For example, in a pure metal with 10^8 cm^{-2} of dislocation line, only about 5×10^{-5} atomic percent of solute is required to supply one solute atom to each atom plane of every dislocation.

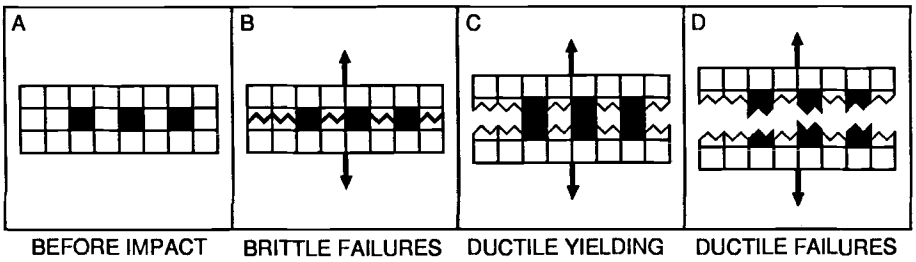


Figure 4: Mixed mode failure in a finite element model—see text for discussion.

across the lattice. At low strain rates, dislocations interact elastically and attempt to form 3-D meshes (Taylor lattices). In this situation, temperature dependent thermal activation is important since the applied stresses are insufficient to overcome obstacles. In contrast to this low strain rate situation, little is known about temperature dependence under high strain rate (impact loading) conditions.

At very high strain rates we would expect the accompanying large stresses to effect copious dislocation emission, or "avalanches". Moreover, high strain rates imply very rapid line movement, which implies there is no time to attempt any relaxation into a network. Indeed, the picture that emerges is one of a "tangled tumble" traversing the lattice. Since the role of thermal activation is to assist with relaxation, and since the force acting to move the tangle of lines is very large relative to those produced by thermal motions, it is reasonable to assume that, at most, there is only a weak dependence of strain hardening on temperature under impact conditions.

Assumption 3 – A critical unpinned dislocation density is required for a mesh volume to fail in a ductile manner. Since, by Assumption 2, the yield stress is proportional to active dislocation density, volumes with less than the critical density are assumed to be completely brittle while those exceeding this density are completely ductile for the duration of the impact fracture event. Clearly this is an oversimplified picture since it ignores the possibility of crack formation due to dislocation pile-up and the possibility that work hardening really can raise local stresses to exceed σ_y. At this point, we simply assume that these volumes will be unimportant either because of their rarity, or because they will be sufficiently monomodal to be regarded as pure.

Assumption 4 – At the moment of impact, all the brittle mesh-volumes fail with little energy absorption and only the ductile volumes, if any, remain. As the impact event continues, the energy absorbed is consumed by the work necessary to strain the ductile zones to failure; this is illustrated in Figure 4. Panel (4A) shows a side view of an idealized fracture plane meshed as described in Assumption 1. Although, three rows are shown; we assume that the fracture will propagate through the middle one because, for example, a notch has intensified the local stress there. The shaded volumes are completely ductile and the rest are completely brittle (according to Assumptions 2 and 3). The failure of all the brittle volumes at impact is illustrated in panel (4B). The ductile volumes are shown yielding in panel (4C) and have strained to failure as indicated in panel (4D).

The Absorbed Energy For the moment it will be convenient to assume that the energy absorbed by the failure of the brittle volumes is so small that we can neglect it; it will be a simple matter to add it back later. Assuming that each ductile mesh-volume is the same implies that each consumes a "quantum" ϵ_d of energy. Consequently, the total energy absorbed will be $E_{cv}(T) = N_d(T)\epsilon_d$, where $N_d(T)$ is the temperature dependent number of ductile volumes. Thus the key to constructing an $E_{cv}(T)$ model is in the definition of how $N_d(T)$ grows with T. For brevity as we explore this matter, let us simply denote $N_d(T)$ as N, let $T = 0$ correspond to the temperature at which the transition begins (e.g. the T at which $\sigma_y = \sigma_f$ in Figure 3), let T_m be a midpoint or inflection temperature, and β, ξ, κ, and C denote arbitrary constants.

Since there is a large but finite number of volumes N_t, any realistic growth model must converge to N_t as T gets large. Perhaps the simplest model for the rate of increase per increase in T is to assume that dN/dT increases in proportion to the number of brittle volumes:

$$\frac{dN}{dT} = \beta(N_t - N) \tag{3}$$

This implies that each volume is unaffected by its neighbors. The solution to this familiar equation for N(0) = 0 is the power saturation function $N(T) = N_t(1-e^{-\beta t})$. Since $E_{cv}(T) = \epsilon_d N$, we obtain:

$$E_{cv}(T) = USE(1 - e^{-\beta t}) \tag{4}$$

In reality, there is some interaction between regions. For example, if the mesh-volumes are on the order of grains, we know that dislocation pile-up at a grain boundary can generate a dislocation source in the adjacent grain. Therefore, we seek a reasonable way to extend Equation 3 to account for a neighbor effect. If we assume a proportional effect, then the rate of ductile volume growth jointly depends on the number of ductile volumes and the number of brittle volumes remaining:

$$\frac{dN}{dT} = \beta N(N_t - N) \tag{5}$$

This is the so-called "Logistic" equation. If we compare Equation 3 with Equation 5, the former could be interpreted as the linear decline with increasing ductility of the instantaneous rate of ductility increase with temperature, and the latter represents the case where the rate of ductility increase *relative* to the number of ductile volumes, declines linearly with increasing ductility; in either case β is an intrinsic transition rate parameter. The solution of Equation 5 is of the form:

$$N = \frac{N_t}{1 + Ce^{-\beta T}} \tag{6}$$

where C is a constant of integration. This solution has an inflection point of $N_t/2$, which occurs at $T_m = (\ln C)/\beta$. We define $u = T - T_m$ and substitute this into Equation 6 to obtain:

$$N = \frac{N_t}{1 + e^{-\beta(T-T_m)}} \tag{7}$$

Now write $N(T_m)$ as N_m and consider $N(T)$ relative to the inflection point:

$$N - N_m = \frac{N_t}{2}\left\{\frac{1 - e^{-\beta u}}{1 + e^{-\beta u}}\right\} \tag{8}$$

Multiplying Equation 8 by $\epsilon_d e^{\beta u/2}/e^{\beta u/2}$, after rearrangement, gives:

$$E_{cv}(T) = \frac{USE}{2} + \frac{USE}{2}\tanh\left[\frac{T - T_m}{2/\beta}\right] \tag{9}$$

Thus we have obtained Equation 1 for the case LSE = 0. Repeating this exercise with a non-zero lower shelf energy results in:

$$E_{cv}(T) = LSE + \frac{USE - LSE}{1 + e^{-\beta(T-T_m)}} \tag{10}$$

Straightforward manipulation can be used to transform Equation 10 into Equation 1.

By the above assumptions and the simple model of Equation 5, we have obtained the familiar tanh Charpy fitting function. By inspection we see the tanh slope parameter is $C = 2/\beta$. Although we could interpret tanh fits in terms of Equation 1, fitting Equation 10 is more direct and physically more meaningful; therefore we prefer it. However, our task is not complete because we have yet to obtain a model that can explain all the panels of Figure 1.

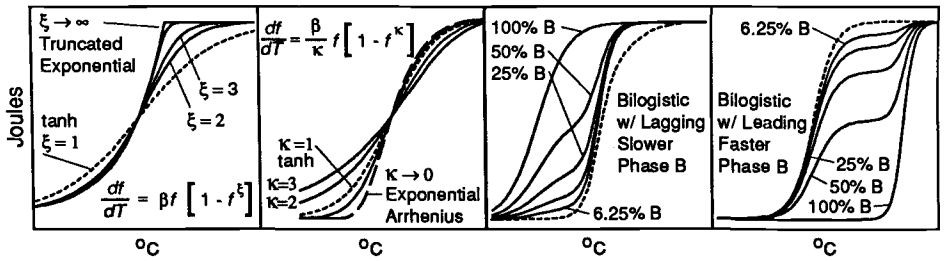


Figure 5: Charpy curves generated by generalized logistic models.

Generalizations of The Logistic Differential Equation We begin by noting that Equation 10 is the result of our first generalization, i.e. a non-zero lower shelf energy. However, given the large number of Charpy curves that are asymmetric, it is necessary to examine our model more carefully.

Since complex interaction among proximate mesh-volumes is possible during plastic flow, we shall first examine neighborhood effects for opportunities to increase the realism of our model. Let us regard the inventory of non-ductile volumes as a measure of the potential increase in ductility relative to the current number of brittle volumes. The algebra is simpler if we constrain the range of this function between zero and one and write $(1 - f^{\xi})$ where $f = N/N_t$; this quantity can be thought of as the transition potential. Equation 5 then becomes:

$$\frac{df}{dT} = \beta f \left(1 - f^{\xi}\right) \tag{11}$$

For $\xi = 1$ this equation is the logistic. Large ξ represents an enhancement of the rate of conversion; physically this would correspond to the case where brittle volumes convert more easily to ductile ones as the number of ductile neighbors increases. The opposite case is represented by $\xi \to 0$. The solution of this equation is of the form:

$$f = \frac{1}{[1 + e^{-\beta\xi T}]^{\frac{1}{\xi}}} \tag{12}$$

The family of curves obtained is shown in the left panel of Figure 5.

Consideration of Equation 11 with $\beta = 1$ reveals that early in the transition the rate of volume conversion increases as e^{T} and, as the end of the transition is approached, saturates as $e^{-\xi T}$. If instead we have reason to believe that saturation should behave as e^{-T}, then Equation 11 can be modified by substituting $dT = \xi dT'$. Because this substitution changes the interpretation of ξ, we replace it with κ and write:

$$\frac{df}{dT} = \frac{\beta}{\kappa} f(1 - f^{\kappa}) \tag{13}$$

which has solutions of the form:

$$f = \frac{1}{[1 + e^{-\beta T}]^{\frac{1}{\kappa}}} \tag{14}$$

The family of curves generated by Equation 14 appears in the second panel of Figure 5. An interesting feature of Equation 14 occurs as $\kappa \to 0$ in that it converges to $f(T) = \exp[-\exp[-T]]$; i.e., the Gompertz function. Recall that this function was introduced empirically by Pachur[26, 49]. One physical context that gives rise to the Gompertz function is a system that has first order interaction kinetics and an Arrhenius law dependence for activation (e.g. of dislocation sources). For this reason we have labeled its curve "exponential-Arrhenius" in the figure.

Finally, we propose that stair-step logistics result from materials with sufficient heterogeneity so that there are two independent mesh-volume systems a and b, each with its own temperature center point and intrinsic transition parameter. For a binary system with each component obeying Equation 5, we have:

$$N = N_t \left[\frac{1 - c_b}{1 + e^{-\beta_a (T - T_{m,a})}} + \frac{c_b}{1 + e^{-\beta_b (T - T_{m,b})}} \right] \tag{15}$$

where c_b is the fraction of type b volumes. We call Equation 15 the "bilogistic", and several plots of it appear in the two right panels of Figure 5. Clearly, with more terms and/or different term types a very large variety of curves can be modeled, including those with sloping shelves.

DISCUSSION and CONCLUSIONS

The fitting functions presented above offer much promise in advancing the interpretation of Charpy data. For example, work is underway to determine whether materials can be classified by fitting equation (Equation 12, Equation 14, or bilogistic); and within these classifications, whether subclasses exist according to β, ξ, or κ values. Furthermore, for those data that clearly exhibit stair-stepping, work must be done to find a plausible physical explanation. Several traps and subtilities must be negotiated in order to obtain defensible results. Although a full exposition of these is beyond the scope of this discussion and appears elsewhere, we offer the following remarks.

Curve Fitting Logistic Functions is Difficult – Many of the functions described above are strongly non-linear and some of the parameters, especially exponents in the potential term, are very sensitive to error. Although linearizations are often possible, fitting to linear forms frequently results in biased parameter estimates, especially with "noisy" data or sparse datasets. Special care must be taken with regard to error models, choice of norm, and regression method. The author recommends either the GaussFit or GENLS programs as a starting point, see Reference [50] for more information. Also, analysis of residuals is critical; an especially helpful tool for this task is LOESS regression [6, 51].

Charpy Data Are Messy – Large amounts of Charpy data have been contaminated by extraneous effects. The two most common problems are incomplete coverage of the transition temperature range and significant biases in some older datasets due to machine flexibility. Older data may also suffer from an unusual *one-sided* error function due to notch misalignment on some older machines. The effect of misalignment, whether to the left or right of the striker, is to raise the energy required to fracture the specimen; tests performed in compliance with ASTM Standard E-23 are not vulnerable to this problem.

Logistic Charpy Models Remain Substantially Empirical – The model presented here depends on assumptions that need further verification. Even if the simple logistic model can be placed on firmer ground, the generalizations are likely to remain fairly empirical. Furthermore, all of the functions presented thusfar are monotonically increasing. Although downward sloping features can be introduced by appropriate forms of the bilogistic, doing so is *ad hoc* and increases the empirical content of the model. Indeed, the cost of each generalization to the logistic is an additional increment in empiricism, and it is not clear *a priori* which generalizations make the most physical sense for a given material. The most flexible model, the bilogistic (or even multilogistic), can be easily abused by virtue of its large number of parameters. With a sufficiently casual approach, the bilogistic can be fit to almost any single valued functional dependence. More physical insight is needed before a high degree of confidence can be placed in logistic model fitting.

Conclusion Our goal was to devise a framework of interpretation for Charpy impact test data that was free of the *adhocery* and limitations that critics of tanh fitting find objectionable. The functions derived here represent useful progress towards this goal.

Acknowledgment: This work was supported by the Empire State Electric Energy Research Corporation, New York, N.Y. Their support is gratefully acknowledged. The author would like to thank D.N. Beshers, M.P. Manahan, R.K. Nanstad, R. Stoller for their helpful discussions; and the late Ed Schmidt for introducing me to the wonderful world of logistic functions. Of course, any errors or omissions are the sole responsibility of the author.

References

[1] ASTM E 23-88. Test methods for notched bar impact testing of metallic materials. In *Annual Book of ASTM Standards*, volume 3.1. American Society for Testing and Materials, Philadelphia, Pennsylvania, 1992.

[2] Lowe, Jr., A.L. Factors influencing accuracy of Charpy impact test data. In *Charpy Impact Test: Factors and Variables, ASTM STP 1072*, pages 54–66. American Society for Testing and Materials, 1990.

[3] Hawthorne J.R. and Hiser, A.L. Influence of fluence rate on radiation-induced mechanical property changes in reactor pressure vessel steels. Technical Report NUREG/CR-5493, MEA-2379, Materials Engineering Associates, 1990. Data taken for Unirradiated Weld W8A, page D-7.

[4] Soulat, P.E., Houssin, B., Bocquet, P., and Bethmont, M. Analysis of radiation embrittlement results from a French forging examined in the second phase of an IAEA-coordinated research program. In L.E. Steele, editor, *Radiation Embrittlement of Nuclear Reactor Pressure Vessel Steels: An International Review (Fourth Volume), ASTM STP 1170*, pages 249–265. ASTM, 1993. Unirradiated data FF material, Fig. 6.

[5] Hawthorne, J.R., Koziol,J.J., and Byrne, S.T. Evaluation of commercial production A533B steel plates and weld deposits with extra-low copper content for radiation resistance. In J.A. Sprague and D.Kramer, editors, *Effects of Radiation on Structural Materials, ASTM STP 683*, pages 235–251. American Society for Testing and Materials, 1979. Unirradiated data taken from Experiment 2 of Plate 5, also see Fig. 1.

[6] Cleveland, W.S. *The Elements of Graphing Data.* Wadsworth, 1985.

[7] Cleveland, W.S. and McGill, R. Graphical perception and graphical methods for analyzing scientific data. *Science*, 229:828–833, 1985.

[8] Tufte, E.R. *The Visual Display of Quantitaive Information.* Graphics Press, Cheshire, CT., 1983.

[9] Tufte, E.R. *Envisioning Information.* Graphics Press, Cheshire, CT, 1990.

[10] Chun, D. Alternate criteria for notch toughness behavior characterization of certain metals and associated design of experiments. *Journal of Materials*, 7(2):257–262, 1972.

[11] Oldfield, W. Curve fitting impact test data: A statistical procedure. *ASTM Standardisation News*, 3(11):24–29, Nov. 1975.

[12] Oldfield, W. Fitting curves to toughness data. *Journal of Testing and Evaluation*, 7(6):326–333, Nov. 1979.

[13] Stallmann, F.W. Curve fitting and uncertainty analysis of Charpy impact data. Technical Report NUREG/CR-2408, Oak Ridge National Laboratory, National Technical Information Center, January 1982.

[14] Urwank, P. Unambiguous curve fitting and error estimation for Charpy impact test data of reactor pressure vessel steels, suitable for a small number of samples. *Journal of Nuclear Materials*, 161:24–29, 1989.

[15] Mager, T.A. Steady-state radiation embrittlement of reactor pressure vessels. Technical Report NP-4224, Volume 2, Electric Power Research Institute, 1985.

[16] Siefer, W. and Orthus, K. Neus Verfahren zur Formulierung von Ablösefunktionen, dargestelt am Beispiel der Temperaturabhängigkeit der Schlagzähigkeit. *Giessereiforschung*, 296:1–13, 1977.

[17] Hofer, G., Hung, C.C. and Günes, U. Eine mathematische Funktion für die Beschreibung der ergemnisse aus Kerbschlagbiegeversuchen. *Z. Werkstogfftech*, 8:109–111, 1977.

[18] Hofer, G. and Hung, C.C. Experimental evidence for the use of the Gauss function in the functional description of the ductile-brittle transition of ferritic steels. *Nuclear Technology*, 49:492–497, Aug. 1980.

[19] Urwank, P. *Nuclear Instruments and Methods*, 203:329, 1982.

[20] Blumenauer, H., *et. al. Neue Hütte*, 10:389, 1984.

[21] Bishop, T.A., Markworth, A.J. and Rosenfield, A.R. *Metallurgical Transactions*, 14A:687, 1983.

[22] Manahan, M.P., Quayle, S, Rosenfield, A.R. and Shetty, D.K. Statistical analysis of cleavage-fracture data. In *Proceedings of the International Conference and Exhibition on Fatigue, Corrosion Cracking, Fracture Mechanics, and Failure Analysis*, 1985.

[23] Berggren, R.G., Hawthorne, J.R. and Nanstad, R.K. Analysis of Charpy v-notch impact toughness of irradiated A533B class 1 plate and four submerged-arc welds. In *Effects of Radiation on Materials: Twelfth International Symposium, ASTM STP 870*, pages 1094–1110. American Society for Testing and Materials, 1985.

[24] Gompertz, B. On the nature of the function expressive of the law of human mortality, and on a new method of determining the value of life contingencies. *Philosophical Transactions of the Royal Society*, 36:513–585, 1825.

[25] Montroll, E.W. and Badger, W.W. *Introduction to Quantitative Aspects of Social Phenomena*. Gordon and Breach, 1974.

[26] Pachur, D. Influence of radiation damage mechanisms on the load signal and on the transition curve of instrumented impact testing. *J. of Nuclear Materials*, 160:24–33, 1988.

[27] Stallmann, F.W. Analysis of the A302B and A533B standard reference materials in surveillance capsules of commercial power reactors. Technical Report NUREG/CR-4947, Oak Ridge National Laboratory, National Technical Information Center, Januarary 1988.

[28] Ebrahimi, F., Hoelzer, D.T., Venables, D. and Krishnamoorthy, V. Development of a mechanistic understanding of radiation embrittlement in reactor pressure vessel steels. Technical Report NUREG/CR-5063, MEA-2268, U.S. NRC, 1988. available from NTIS, Springfield, VA.

[29] Soulat, P.E., Miannay, D. and Horowitz, H. Influence of phosphorous on thermal and neutron embrittlement of pressure vessel steels. In *Radiation Embrittlement of Nucelar Reactor Pressure Vessel Steels: An International Review (Fourth Volume), ASTM STP 1170*, pages 283–299. American Society for Testing and Materials, 1993.

[30] Reidel, H. Fracture mechanisms. In H. Mughrabi, editor, *Materials Science and Technology: A Comprehensive Treatment*, volume 6, chapter 12, pages 566–633. VCH, 1991.

[31] Wechsler, M.S. Radiation embrittlement of metals and alloys. In M.T. Robinson and Jr. F.W. Young, editors, *Fundamental Aspects of Radiation Damage in Metals, (Volume 2), Proceedings of an International Conference, Gatlinburg, TN, 6–10 October 1975*, pages 991–1009. CONF-75-1006-P2, NTIS, Springfield, Virginia, 1976.

[32] Tetelman, A.S. and McEvily, A.J. *Fracture of Structural Materials*. Wiley, 1967.

[33] Orowan, E. Classical and dislocation theories of brittle fracture. In *Fracture*, pages 147–160. Wiley, 1959.

[34] Cottrell, A.H. and Bilby, B.A. *Proceedings of the Royal Physical Society (London), A*, 62A:49, 1949.

[35] Cottrell, A.H. Theoretical aspects of fracture. In B.L. Averback, D.K. Felbeck, G.T. Hahn, and D.A. Thomas, editors, *Fracture: Proceedings of An International Conference on the Atomic Mechanisms of Fracture*, chapter 2, pages 20–53. M.I.T Press, 1959.

[36] Petch, N.J. The ductile-cleavage transition in alpha-iron. In B.L. Averback, D.K. Felbeck, G.T. Hahn, and D.A. Thomas, editors, *Fracture: Proceedings of An International Conference on the Atomic Mechanisms of Fracture*, chapter 3, pages 54–67. M.I.T Press, 1959.

[37] Louat, N. The effect of temperature on Cottrell atmospheres. *Proceedings of the Physical Society (London), B*, 69:459–467, 1956.

[38] Hawthorne, J.R. Irradiation embrittlement. In C.L. Briant and S.K. Banerji, editors, *Embrittlement of Engineering Alloys*, volume 25 of *Treatise on Materials Science and Technology Materials Science and Technology*, chapter 10, pages 461–524. Academic Press, 1993.

[39] Odette, G.R., Lombrozo, P.M. and Wullaert, R.A. Relationship between irradiation hardening and embrittlement of pressure vessel steels. In F.A. Garner and J.S. Perrin, editors, *Effects of Radiation on Materials: Twelfth International Symposium, ASTM STP 870*, pages 840–860. American Society for Testing and Materials, Philadelphia, Pennsylvania, 1985.

[40] Hahn, G.T. and Flanagan, W.F. Relations between dislocation mechanisms and fracture toughness. In M.F. Ashby, R. Bullough, C.S. Hartley, and J.P. Hirth, editors, *Dislocation Modeling of Physical Systems*, pages 1–17. Pergamon, NY, NY, 1984.

[41] Helm, J.L. Reactor vessel irradiation damage: The interpretation of charpy impact data. Technical Report EP89-21-*, Empire State Electric Energy Research Coproration, 1996. To be released in 1996.

[42] McLean, D. *Grain Boundaries in Metals.* Oxford, 1957.

[43] Guttmann, M. and McLean, D. Grain boundary segregation in multicomponent systems. In W.C. Johnson and J.M. Blakely, editors, *Interfacial Segregation.* American Society for Metals, 1979.

[44] Johnson, W.C. and Blakely, J.M., editors. *Interfacial Segregation.* American Society for Metals, 1979.

[45] Cottrell, A.H. Theory of brittle fracture in steel and similar metals. *Transaction of the Metallurgical Society*, 211:192–203, 1958.

[46] Smallman, R.E. *Modern Physical Metallurgy.* Butterworth, 1985.

[47] Kuhlmann-Wilsdorf, D. Theory of work hardening 1934–1984. *Metallurgical Transactions A*, 16A:2091–2108, 1985.

[48] Kingsland, S. The refractory model: The logistic curve and the history of population ecology. *The Quarterly Review of Biology*, 57:29–52, 1982.

[49] Pachur, D. Radiation annealing mechanisms of low-alloy reactor pressure vessel steels dependent on irradiation temperature and neutron fluence. *Nuclear Technology*, 59:463–475, 1981.

[50] Macdonald J.R. and Thompson, W.J. Least-squares fitting when both variables contain errors: Pitfalls and possibilities. *American Journal of Physics*, 60(1):66–73, 1992.

[51] Cleveland, W.S. Robust locally weighted regression and smoothing scatterplots. *Journal of the American Statistical Association*, 74(368):892–836, 1979.

Christian BRILLAUD[1], Hervé AUGENDRE[2] and Michel BETHMONT[3]

UNCERTAINTY EVALUATION IN TRANSITION TEMPERATURE MEASUREMENTS

REFERENCE: Brillaud, C., Augendre, H., and Bethmont, M., **"Uncertainty Evaluation in Transition Temperature Measurements,"** *Effects of Radiation on Materials: 17th International Symposium, ASTM STP 1270,* David S. Gelles, Randy K. Nanstad, Arvind S. Kumar, and Edward A. Little, Eds., American Society for Testing and Materials, 1996.

ABSTRACT: The pressure vessel surveillance program is mainly based on the transition temperature change assessment, a change which is induced by neutron irradiation. Uncertainties in Charpy test measurements are well known; however, we are less familiar with uncertainties due to general procedures governing experiments, which can be significant and therefore must be taken into account. In fact, procedures specify neither the number of specimens needed to obtain a transition curve, nor the choice of test temperatures, nor the fitting method for the transition curve.

A study has been conducted to determine the influence of the experimental procedure on the accuracy of transition temperature determination, and the initial results are presented in this paper. Two EDF laboratories performed Charpy tests on the surveillance program reference metal, using 8, 16, 24, 32 and 64 specimens to evaluate how the number of specimens affects the transition temperature. The influence of the scatter of mechanical properties has also been studied at two levels of irradiation. We have evaluated the effect of different sampling strategies and investigated a new fitting method, which is based on a simultaneous fitting of all curves with common constraints on parameters.

KEY WORDS: transition, temperature, uncertainty, charpy impact, irradiation

Surveillance of steel embrittlement in reactor pressure vessels is one of the major factors in ensuring safety; it allows us to justify the margins established in relation to the risk of a fast fracture of this element. In France, as in a number of other countries, embrittlement is assessed by determining the transition temperature of materials, and how this temperature changes as a function of irradiation. Whether considering experimental results or calculations, one fact is inescapable: these results are incomplete because the

[1] Electricité de France - Groupe des laboratoires - Service Contrôle des Matériaux Irradiés - B.P. 23 - 37420 AVOINE - FRANCE
[2] Electricité de France - DER-TIEM - 1 Avenue du Général de Gaulle
92141 CLAMART - FRANCE
[3] Electricité de France - DER-EMA - Les Renardières
77250 ECUELLES - FRANCE

Copyright© 1996 by ASTM International www.astm.org

associated uncertainties are almost never noted. In consequence, we have an optimum estimate of the quantities measured, without knowing the confidence interval. EDF is currently analysing this subject, to meet a fourfold objective:

identify sources of uncertainty,
estimate uncertainties
take these uncertainties into account within the scope of a probabilistic approach for the safety margins assessment,
reduce these uncertainties.

This paper presents the initial work carried out within the scope of the pressure vessel surveillance program, in particular the work concerning the impact tests used to assess material embrittlement. In the previous paper, uncertainties in the current standard practice used to define RT_{ndt} for indexing the fracture toughness reference curve of irradiation materials by adding the shift in transition temperature was presented [*1*].

Main sources of uncertainty

Two families of uncertainties have already been identified: those on an experimental level, directly related to the accuracy of measurements (energy, temperature, etc.); and those inherent to the procedures and methods used to determine the ductile-brittle transition temperature of the materials.

In the first case, the actual Charpy impact tests, it is easy to quantify the uncertainties, since the applicable standards set out specifications governing test facilities, their precision and conditions for verification. We therefore focused on methods which are in no way covered by recommended standards. The main sources of uncertainty affecting transition temperature measurements are:

the number of tests performed,
the testing schedule, that selects tests according to temperature,
the metallurgic heterogeneities of the material in relation to the representativeness of the samples.

Study program

A program was therefore conducted to analyse the sensitivity of transition temperature measurements to each identified source of uncertainty.

Influence of the number of tests on the transition temperature

This study was designed to specify the influence of the number of tests carried out on the mean transition temperature value. A single testing program was carried out independently by two EDF laboratories (GDL-SCMI and DER-EMA), using

homogenous batches of Charpy specimens taken from a low-alloy steel plate corresponding to the ASME grade SA 533 grade B Class 1.

Prior to the testing program, the two laboratory facilities were calibrated using standard specimens supplied by the Laboratoire National d'Essais (LNE). For each laboratory, two batches of 8 specimens and one of 16 specimens were machined in LT orientation at quarter-thickness depth of the steel plate. Tests were carried out as shown below to generate four series of results for each laboratory:

Series 1: Batch No. 1 of 8 specimens
Series 2: Batch No. 2 of 16 specimens
Series 3: Results of series 2 completed with Batch No. 3 (8 specimens)
Series 4: all of batches 1, 2 and 3.

Series 5 was obtained by grouping the 64 results from the two laboratories. For each series of results, the transition temperatures corresponding to 56J of fracture energy (T_{56}) and to 0.9 mm of lateral expansion ($T_{0.9}$), were recorded after fitting the transition curves. For this fitting, the two laboratories use the hyperbolic tangent function, which is the most commonly used [*2*]. Table 1 below shows the results.

TABLE 1—*CHARPY test results*

Series	Lab. ref.	Transition temperature (°C)				USE
		T_{56}	σ_{T56}	$T_{0.9}$	$\sigma_{T0.9}$	(J)
1	1	-86	12	-83	16	190
	2	-69	4	-68	5	189
2	1	-68	13	-67	15	196
	2	-66	9	-65	9	192
3	1	-66	11	-63	13	195
	2	-68	8	-67	7	189
4	1	-71	13	-70	16	193
	2	-69	7	-68	7	190
5	1 & 2	-70	10	-68	11	194

There is no significant difference between the energy values obtained at the upper shelf: the largest difference is 7J. For a given curve, the transition temperatures T_{56} and $T_{0.9}$ seem well correlated, with a discrepancy that does not exceed 3°C. If we assume that the transition temperature obtained with 64 tests (series 5) represents the material under study, we note that with 8 specimens (series 1), the maximum difference is 16°C, and that this difference is only 4°C with 16 or 24 specimens (series 2 and 3). With 32 tests (series 4), the results obtained by the two laboratories are very similar, with the difference not exceeding 2°C. A wider scatter of results obtained by laboratory 1 was

attributed to small variations of temperature at the specimen surface during their transfer for testing. These variations obviously depend on the time and the value of the test temperature (e.g., at -80°C, variations have been evaluated at 5°C on surface and 0.5°C at specimen center).

For a given laboratory, the largest recorded discrepancy between two evaluations of a given characteristic (T_{56} or $T_{0.9}$) is 20°C. Figure 1 shows the absolute value of the maximum error $|\varepsilon|$ recorded for the transition temperature as a function of the number of tests. Based on this analysis, we can conclude that for the case under study, the best compromise between the number of specimens and the accuracy needed is obtained with 16 tests.

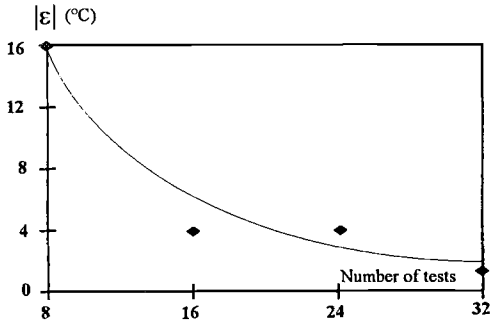


FIG. 1—*Influence of the number of tests on the accuracy of the transition temperature.*

Influence of test choice as a function of temperature

Having set the number of tests at 16, we can now focus on the best temperature distribution for the tests. Is it better to spread the tests over the whole temperature range, group the tests in series of 2 or 4, or group all tests near the transition temperature (e.g., T_{56}) ?

If we only consider the transition temperature, the third option is the best, assuming that we have a preliminary idea of the transition temperature value. If instead, we would rather accurately determine the transition curve parameters (hyperbolic tangent), then we should use one of the first two options. This is the situation that we have studied in detail.

We have designated these strategies "U" for the uniformly distributed points, and "G" for the grouped points. To compare them, we have used a two-pronged approach: on one hand, running simulations, and on the other, random selections (bootstrap) from two series of 60 actual measurements from the same material before and after irradiation. These data are different from the ones used for simulation but are the same that will be used in the following study. The simulations involved generating a set of 16 values based on a transition curve equation, with a Gaussian noise to simulate the random aspect. This operation was repeated 321 times. For the random selection, 151 sets of 16 values were analysed. We studied three different situations to analyse the grouped points strategy:

8 groups of 2 points (G2)
4 groups of 4 points (G4)
4 groups of 4 points at selected temperatures (GS)

For the strategies U, G2 and G4, the temperatures are chosen at random, after first dividing the temperature range into 16, 8 or 4 intervals. For the GS strategy, involving selected temperatures, we rely on the intrinsic qualities of the transition curve fitting model to determine the four optimum temperature values: upper shelf, lower shelf, center and one of the edges of the transition zone. It is of course only possible to choose these four temperatures if we know beforehand the shape of the curve. This simulation was carried out to reproduce what we could consider as the ideal experimental case. The table below summarises these results; for each situation, we can see the parameter T_{56} mean and its standard deviation.

TABLE 2—*Mean $\overline{T}_{56}$ values and standard deviation for each strategy studied (°C).*

	Simulation		Bootstrap results			
	$\overline{T}_{56}$	$\sigma_{\overline{T}_{56}}$	$\overline{T}_{56}$	$\sigma_{\overline{T}_{56}}$	$\overline{T}_{56}$	$\sigma_{\overline{T}_{56}}$
U	28	6	-44	7	-26	6
G2	28	5	-42	6	-26	5
G4	27	6	-53	7	-26	5
GS	28	5	NA	NA	NA	NA
reference	28		-46		-27	

No matter what method is used, the standard deviation values are between 5 and 7°C inclusive. Given these results, it would therefore be difficult to say if one strategy is better than another. We can nonetheless conclude that the strategy based on tests carried out at temperatures closest to those intrinsic to the fitting model should offer the best guarantee of results with minimum uncertainty. On the other hand, our experience has shown that the fitting can be improved by using general non-linear regression programs (e.g., the NLIN procedure in the SAS system).

Influence of metallurgical heterogeneities in relation to sampling

To precisely determine and reduce the degree of uncertainty, several measurements are routinely made and then averaged. The accuracy of the results obtained in this way increases with the number of measurements in relation to the observed scatter.

Reactor pressure vessels are made of forged steel that contain metallurgical heterogeneities, which lead to imprecision in evaluating transition temperatures when the

number of tests is not sufficient. A sensitivity test was carried out to specify the extent of this source of uncertainty in the case of transition curves obtained with a constant number of specimens, set at 16 on the basis of previous results. Impact tests were carried out on specimens taken from a low-alloy steel plate chosen for its heterogeneous mechanical properties.

Three populations of 60 specimens each are used as a reference. Two of these populations are made of irradiated material, one at a fluence of 1.5 10^{19} n.cm^{-2}, and the other at 3 10^{19} n.cm^{-2} (E>1MeV). The temperature interval covered by the different transition curves obtained for these three populations was split into five ranges, each about 20°C, which correspond to:

* upper shelf
* lower shelf
* the transition zone, split into three equal parts.

Within these five ranges, random drawings without replacement were made of experimental results, with two drawings at the upper shelf, two drawings at the lower shelf and four in each of the other ranges. This gave us a secondary population of 16 values; the operation was repeated six times on each reference population. Transition curves were then fitted with the different secondary populations thus generated, and the T_{56} values recorded. Table 3 below shows the results obtained for each population, compared with the corresponding reference population.

TABLE 3—*Transition temperature results (°C)*

Population	Unirradiated		Irradiated 1.5 10^{19} n.cm^{-2}		Irradiated 3 10^{19} n.cm^{-2}	
	T_{56}	σ_{T56}	T_{56}	σ_{T56}	T_{56}	σ_{T56}
reference	-46	18	-27	9	-23	11
1	-60	20	-31	11	-30	12
2	-50	20	-29	9	-29	12
3	-50	12	-29	6	-25	11
4	-46	19	-26	7	-24	8
5	-45	19	-21	6	-22	9
6	-42	12	-21	6	-17	10
mean 1 to 6	-48.8	17	-26	7.5	-24.5	10
$\lvert\varepsilon_1\rvert$	18		10		13	
$\lvert\varepsilon_2\rvert$	14		6		7	

$\lvert\varepsilon_1\rvert$ = absolute value of the maximum difference between secondary populations
$\lvert\varepsilon_2\rvert$ = absolute value of the maximum difference in relation to the reference population.

The standard deviation obtained after fitting the transition curves according to the experimental values of the different populations takes into account the scatter of results. For the three cases studied (irradiated and non-irradiated), the mean transition temperatures of the secondary populations are very close to the transition temperatures for the reference populations. As expected, there is a relation between the scatter of results and the recorded discrepancies $|\varepsilon_1|$ and $|\varepsilon_2|$, as shown in Figure 2 below.

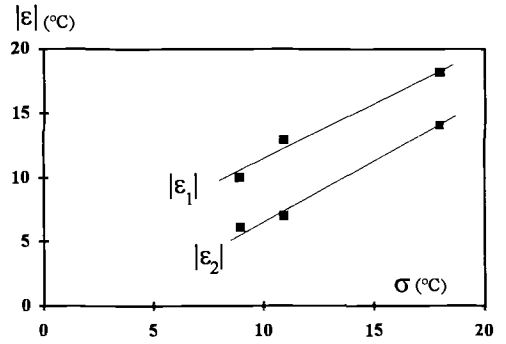


FIG. 2—*Influence of scatter on the accuracy of the transition temperature.*

The largest difference (14°C in relation to the reference value) is observed for the non-irradiated state, which shows the largest scatter. If we compare these results with those of the previous experiment (16 tests), at the same level of scatter (σ = 10°C), transition temperature error is the same order of magnitude.

DISCUSSION OF RESULTS

Based on the results presented above, with 16 specimens, the greatest source of uncertainty is due to the scatter caused by metallurgical heterogeneities. This scatter is greatest for the unirradiated populations. After irradiation this scatter seems to be less. Although we cannot automatically conclude that irradiation has an effect, we nonetheless note that irradiation does not seem to be a source of significant additional scatter. Within the scope of the pressure vessel surveillance program, the transition temperature for materials is determined independently at different stages of irradiation. In terms of the change in transition temperature after irradiation, the maximum recorded error is 20°C, no matter what is the value of neutron fluence.

A method for improving results is based on the idea that if we cannot increase the number of specimens for a given transition curve, we can nonetheless try to use the results from previous characterizations of the same material.

We have therefore developed a program that is capable of simultaneously integrating the results of tests at different stages of irradiation. In fact, for each new series of tests, we will fit again all the results, using all data available for the material.

The first consequence is to determine a fitting error, and thus a margin of uncertainty on T_{56} which is more certain. If we impose no other constraint, this margin is simply the weighted average of the margins obtained for each series of results. However, this simultaneous fitting enables us to impose physical trends to the irradiation embrittlement, such as the progressive lowering of the upper shelf, or simply the fact that the lower shelf is positive and stable. Expressed as constraints, these physical trends enables us to obtain more consistent transition temperature results. On the other hand, the results are called into question when we fit again after a new series of tests. Moreover, the uncertainty margins can increase for certain series where there is less observed variability. We will therefore continue our work based on the following model:

$$Y = \left(\frac{u_h + l}{2}\right) + \left(\frac{u_h - l}{2}\right) * \tanh\left(s_h * \frac{T - i_h}{\frac{u_h - l}{2}}\right)$$

where h is the series of tests with constraints involving :
the decrease in u_h (upper shelf) and S_h (slope),
the growth of i_h,
a constant positive value for l (lower shelf).

Finally, it is possible to obtain directly shifts in the transition temperature (ΔT_{56}) and there error margins by introducing this shift as a variable in the model in place of i. This method offers a significant gain compared to current practices, which independently fits the transition curves. On the other hand, it is based on the fundamental idea that the mathematical model used (hyperbolic tangent) accurately represents the physical reality, since the added constraints no longer allow us to check this hypothesis.

CONCLUSION

In the studies described in this paper, we examined the sensitivity of the transition temperature to different sources of uncertainty. The main conclusions we have drawn are as follows:

The best compromise between the number of tests and the degree of accuracy needed in determining the transition temperature is obtained with 16 specimens.

The method used to distribute the tests in the temperature interval of the transition curve does not constitute a significant source of uncertainty.

The largest source of uncertainty is the scatter of test results caused by metallurgical heterogeneities. In terms of the shift in transition temperature, the maximum recorded error is 20°C.

We have proposed a method that, for a given material, enables integrating all information available concerning several curves to make the fitting. This method

allows obtaining a margin of uncertainty on the transition temperature which is more sure, and a margin of error on the shift after irradiation.

References

[*1*] Houssin, B., Meyzaud, Y., Hedin, F., and Brillaud, C., "An alternative approach for the use of surveillance program results," *Effects of radiation on materials: 15th International Symposium, ASTM STP 1125,pp.216-237.*

[*2*] Oldfield, W., "Curve Fitting Impact Test Data : A Statistical Procedure," *ASTM Standardization News, Vol. 3, No. 11, November 1975.*

Mikhail A. Sokolov[1] and Randy K. Nanstad[1]

ON IMPACT TESTING OF SUBSIZE CHARPY V-NOTCH TYPE SPECIMENS

REFERENCE: Sokolov, M. A. and Nanstad, R. K., **"On Impact Testing of Subsize Charpy V-Notch Type Specimens,"** *Effects of Radiation on Materials: 17th International Symposium, ASTM STP 1270,* David S. Gelles, Randy K. Nanstad, Arvind S. Kumar, and Edward A. Little, Eds., American Society for Testing and Materials, 1996.

ABSTRACT: The potential for using subsize specimens to determine the actual properties of reactor pressure vessel steels is receiving increasing attention for improved vessel condition monitoring that could be beneficial for light-water reactor plant-life extension. This potential is made conditional upon, on the one hand, by the possibility of cutting samples of small volume from the internal surface of the pressure vessel for determination of actual properties of the operating pressure vessel. On the other hand, the plant-life extension will require supplemental surveillance data that cannot be provided by the existing surveillance programs. Testing of subsize specimens manufactured from broken halves of previously tested surveillance Charpy V-notch (CVN) specimens offers an attractive means of extending existing surveillance programs. Using subsize CVN type specimens requires the establishment of a specimen geometry that is adequate to obtain a ductile-to-brittle transition curve similar to that obtained from full-size specimens. This requires the development of a correlation of transition temperature and upper-shelf toughness between subsize and full-size specimens. The present study was conducted under the Heavy-Section Steel Irradiation Program. Different published approaches to the use of subsize specimens were analyzed and five different geometries of subsize specimens were selected for testing and evaluation. The specimens were made from several types of pressure vessel steels with a wide range of yield strengths, transition temperatures, and upper-shelf energies (USEs). The effects of specimen dimensions, including depth, angle, and radius of notch have been studied. The correlation of transition temperature determined from different types of subsize specimens and the full-size specimen is presented. A new procedure for transforming data from subsize specimens was developed and is presented. The transformed data are in good agreement with data from full-size specimens for materials that have USE levels < 200 J.

[1]Metals and Ceramics Division, Oak Ridge National Laboratory, Oak Ridge, TN 37831-6151.

Copyright© 1996 by ASTM International www.astm.org

KEYWORDS: ductile-to-brittle transition temperature, subsize specimens, Charpy V-notch, correlation, normalization

INTRODUCTION

The potential for using subsize specimens to determine the actual properties of reactor pressure vessel (RPV) steels is receiving increasing attention for improved vessel condition monitoring that could be beneficial to light-water reactor (LWR) plant-life extension. This potential is made conditional upon several reasons. It is well known that annealing of Soviet-built reactors [1-2] led to significant recovery of irradiation embrittlement and to extension of plant life. This suggests that annealing of RPVs might be a very attractive way to extend plant life for some U.S. LWRs [3,4]. However, practical implementation of annealing includes some regulatory aspects. One of those is extension of the surveillance program so that properties of the RPV can be monitored after annealing. Machining of subsize specimens from the broken halves of previously tested Charpy surveillance specimens as well as use of sample reconstitution techniques are the most feasible ways to resolve this problem. Additionally, subsize specimens could be used in performance experiments to study the general behavior of RPV steels after reirradiation. Such experiments usually require simultaneous irradiation of a large number of specimens under the same conditions, as well as intermediate annealing of a portion of them after the first cycle of irradiation and after the second reirradiation. Another application for subsize specimens is also associated with annealing. The subsize specimens can be used to confirm the beneficial effects of vessel annealing by cutting pieces of small volume from the inside surface of the vessel before and after annealing [5,6] as well as periodically during reoperation of the annealed vessel. In the last case, it could be an alternative to the standard surveillance program.

The main issue for the feasibility of using subsize Charpy V-notch (CVN) specimens to determine properties of RPV steels is a correlation of transition temperature and upper-shelf energy (USE) between subsize and full-size specimens. The present study, conducted under the Heavy-Section Steel Irradiation (HSSI) Program, analyzed different published approaches to the use of subsize CVN specimens. Five different geometries of subsize specimens from 11 material conditions were selected for testing and evaluation. The effects of specimen size and notch dimensions, including depth, angle, and root radius, on the correlation with data from full-size specimens have been studied.

MATERIALS

Four types of RPV steels were studied: (1) American Society for Testing and Materials (ASTM) A 533 grade B class 1 plates (one of them after quenching and tempering at 950°C), (2) specially heat-treated steel with A 508 class 2 chemical composition, (3) a Russian forging, designated 15Kh2MFA, and (4) a submerged-arc weld. All of these RPV steels were studied previously at Oak Ridge National Laboratory

(ORNL) using standard specimens under different tasks of the Heavy-Section Steel Technology (HSST) and HSSI programs, sponsored by the U.S. Nuclear Regulatory Commission (NRC). The materials were selected to have a relatively wide range of transition temperatures and USEs as measured with standard full-size Charpy specimens as well as a range of yield strengths. Typically the properties of many RPV steels in the as-produced state are quite similar. To increase the range of properties, some steels were studied in the quenched-only or quenched-and-tempered condition. As a result, the USEs varied from 73 to 330 J, the transition temperatures varied from −46 to 58°C, and the yield strengths varied from 410 to 940 MPa. Table 1 lists the types and properties of the different materials.

SPECIMEN DESIGN

The ASTM Method for Notched Bar Impact Testing of Metallic Materials (E 23-93a) [7] allows the use of subsize specimens when the amount of material available does not permit making the standard impact test specimens, but the "results obtained on different sizes of specimens cannot be compared directly." Therefore, the use of subsize specimens recommended by ASTM E 23 requires correlating the results with standard specimens. According to ASTM E 23, the length, notch angle, and notch root radius for subsize specimens are the same as for full-size specimens, which restricts the range of possible subsize specimen dimensions. A key feature of subsize specimens for RPV applications is based on the ability to use halves of broken full-size surveillance specimens. As a result, several attempts have been made to develop subsize impact specimens with geometries acceptable for nuclear application, for example, refs. [6,8–15]. Specimens were varied by all dimensions and are as small as 1 × 1 × 20 mm [14,15]. However, there are some limitations on the dimensions of subsize specimens for RPV materials.

First, they should be large enough to be tested on commercially produced equipment in hot cell conditions. For example, the USE of 1 × 1 × 20 mm specimens could be as low as 0.16 J [15] for steel with a standard specimen USE equal to 200 J. It would be even smaller for so-called low upper-shelf welds, where the USE of standard specimens could decrease to ~ 70 J due to irradiation. For 1- by 1-mm cross-section specimens, the USE might be < 0.1 J, and in the transition region it would be much less than 0.1 J.

ASTM E 23 requires that the specimen be broken within 5 s after removal from the conditioning medium. A reduction of size resulting in a significant increase in the surface area to volume ratio may lead to excessive temperature losses prior to impact.

Another important limitation in decreasing specimen size is the extent of the microstructural inhomogeneities. For example, a study of a special heat of A 508 forging steel [16,17] indicated that carbon segregates in slender bands about 0.25 mm wide. Investigation of the Midland RPV weld metal [18] showed that the cross sections of individual weld passes could be several millimeters. Testing of full-size CVN specimens

TABLE 1--Test matrix and mechanical properties of materials for subsize Charpy specimen evaluation

Material and condition	Upper-shelf energy[a] (J)	$DBTT_{41}$[a] (°C)	Yield strength (MPa)	5 × 5 Type 1[b]	3.3 × 3.3 Type 2[b]	5 × 5 Type 3[b]	3 × 4 Type 4[b]	5 × 5 Type 5[b]
A 533 wide plate, LT orientation	330	–43	422	X	X	X	X	
A 533 wide plate, TL orientation	244	–46	410	X	X	X	X	
A 508, as-quenched	115	58	634	X	X	X	X	
A 508, quenched and tempered at 599°C	102	40	697	X	X	X	X	
A 508, quenched and tempered at 677°C	116	18	605	X	X	X	X	
A 508, quenched and tempered at 704°C	164	–32	500	X	X	X	X	
HSST Plate 02, TL orientation, quarter thickness	141	3	432	X	X	X	X	
HSST Plate 02, TL orientation, half thickness	114	15				X		X
HSST Plate 014, quenched and tempered at 950°C	73	–34	940	X	X	X	X	
15Kh2MFA, melt 103672	181	–40	630	X	X	X	X	
HSST weld 72W	136	–28	500	X	X	X	X	X

[a]Determined with standard full-size Charpy specimens.
[b]X = 12 to 15 specimens.

tends to give average properties of the material, but test results from very small subsize specimens may be dependent on the location of the specimens within the material.

Thus, the practical lower bound for the cross-sectional dimensions of subsize specimens for irradiated RPV steels may be limited to about 3 mm. As far as the length of a subsize specimen, it should be no longer than one-half of the standard CVN specimen (to allow for machining from a broken specimen). Taking into account all these considerations, five designs of subsize specimens were selected for this study (see Fig. 1). The type 1 specimen is 25.4 mm long with a 5- by 5-mm cross section, a 0.8-mm-deep 30° notch, and a root radius of 0.1 mm. Two type 1 specimens could be machined from one broken full-size CVN specimen. The type 2 specimen has a length of 25.4 mm, a 3.3- by 3.3-mm cross section, a 0.5-mm-deep 30°notch, and a radius of 0.08 mm. Eight type 2 specimens could be machined from one broken full-size CVN specimen. One advantage of choosing types 1 and 2 specimens is the accumulated experience of using these subsize specimens in the United States [12,19–23] and Japan [14,15–24] for studies of fusion reactor materials. The type 3 specimen has a length of 27 mm, a 5- by 5-mm cross section, a 1-mm-deep 45°notch, and a notch root radius of 0.25 mm. This type of specimen has exactly the same geometry as the smallest ASTM E 23 subsize specimen, but is one-half as long. Two type 3 specimens could be machined from one broken full-size CVN specimens. Experience with this type of subsize specimen has been accrued in Russia [2,6] for RPV steels. The type 4 specimen has a length of 26 mm, a 3- by 4-mm cross section, a 1-mm-deep 60° notch, and a root radius of 0.1 mm. Up to 12 type 4 specimens could be machined from one broken full-size CVN specimen. Experience with this type of subsize specimen has accrued in Europe [5,11,25] and Russia [6] for different low-alloy steels, including RPV steels. The type 5 specimen has a length of 55 mm, a 5- by 5-mm cross section, a 1-mm-deep 45° notch, and a root radius of 0.25 mm. This is the smallest subsize specimen recommended by ASTM E 23. A major disadvantage of this design is that it is not possible to make this type of subsize specimen from a broken full-size CVN specimen without reconstitution. Nevertheless, specimens of this design were studied for two materials.

TESTING PROCEDURE

All subsize specimens were tested on a specially modified pendulum-type instrumented impact machine [12]. The modified anvils supported the types 1 and 3 subsize specimens so that their relative position with respect to the pendulum was the same as for the full-size specimen; that is, the center of percussion of the pendulum was maintained at the center of the point of impact, with the specimen just touching the striker with the pendulum hanging free. The types 2 and 4 subsize specimens were tested using the same anvils, resulting in the center of the point of impact being slightly lower and further ahead than the center of percussion of the pendulum when hanging free. Similarly, the offset was 2.5 mm for the type 5 subsize specimens tested using the full-size anvils. The span (minimum distance between the radii of the anvils) was 20 mm for types 1, 2, and 3 and 22 mm for type 4. The thickness of the ASTM E 23 striker was reduced to 4 mm to allow

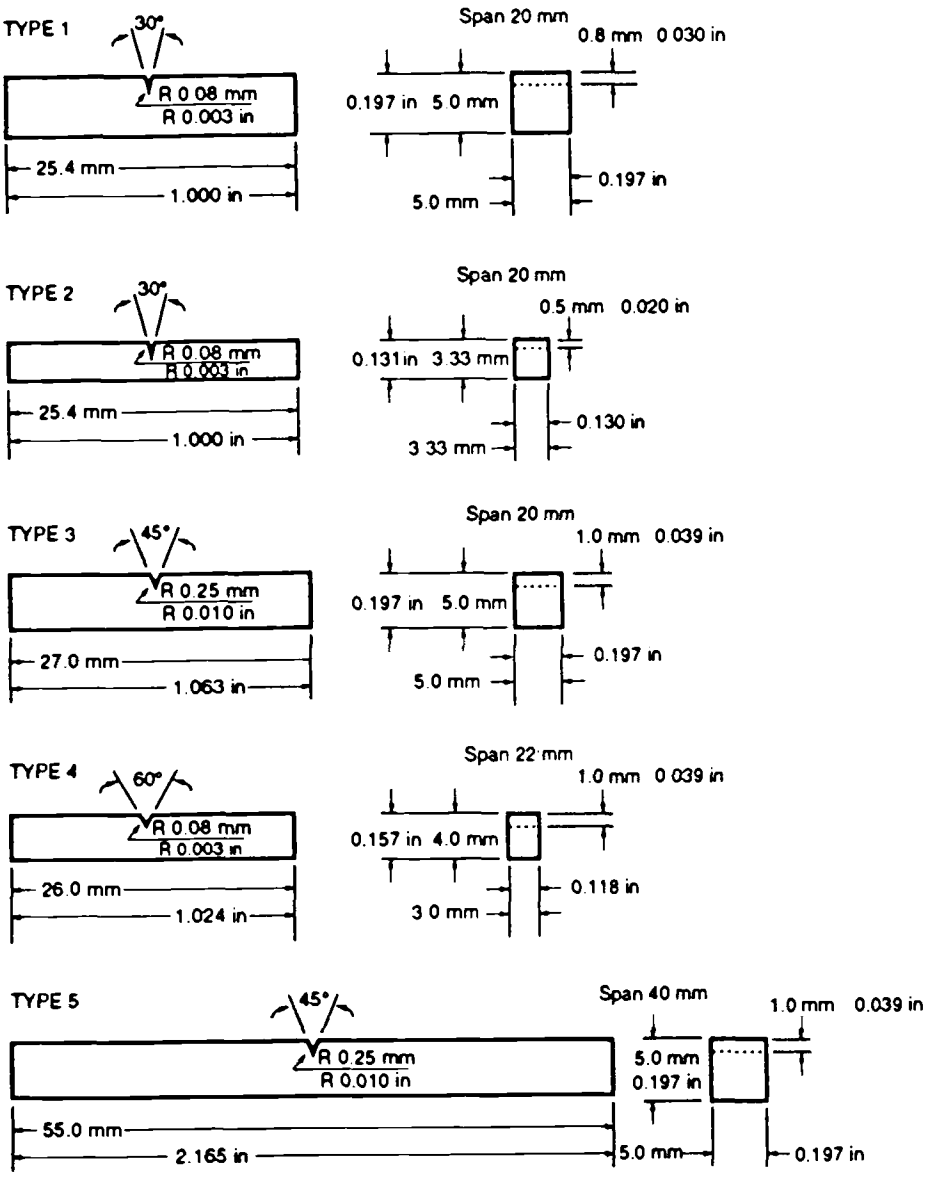


FIG. 1--Dimensions of subsize specimens used in this study.

clearance of the specimen halves between the anvils. The radii of the striker and the anvils, however, were maintained in accordance with ASTM E 23. The type 5 specimens were tested at full capacity of the machine [407 J (300 ft-lb)] and an impact velocity of 5.5 m/s (18 ft/s). All other subsize specimens were tested at a lower potential energy [69 J (51 ft-lb)], with a corresponding reduction of the impact velocity to 2.24 m/s (7.4 ft/s).

The impact data for each material condition and specimen type were fitted with a hyperbolic tangent function to obtain transition temperatures and upper-shelf energies:

$$Y = \frac{US + LS}{2} + \frac{US - LS}{2} \cdot \tanh\left[\frac{T - T_{MT}}{C}\right], \quad (1)$$

where T is test temperature and US, LS, T_{MT}, and C are fitting parameters. Parameters US and LS can be upper- and lower-shelf values of energy, lateral expansion, or percent shear; T_{MT} is the temperature at the middle of the transition range, and C is one-half of the transition zone width. All hyperbolic tangent analyses for full-size specimens were conducted with the lower shelves fixed at 2.7 J and 0.061 mm for energy and lateral expansion, respectively. All hyperbolic tangent analyses for subsize specimens were conducted with the lower shelves fixed at 0.1 J and 0.0 mm for energy and lateral expansion, respectively. Upper and lower shelves of percent shear fracture were always fixed at 100 and 0%, respectively.

EFFECT OF SPECIMEN DIMENSIONS

One objective of this study was to determine the effects of specimen dimensions on the Charpy impact results. Analyses of these effects will be used in the development of a methodology for determination of the ductile-to-brittle transition temperature (DBTT) and USE of full-size specimens using the test data from subsize specimens.

More obvious is the effect of the notch depth (a) on the USE. The sensitivity of the USE to the V-notch depth was studied on type 3 specimens of HSST Plate 02 (Fig. 2). One set of specimens was made with a 1.7-mm-notch (0.065 in.) and a second set was made with a 0.8-mm-deep (0.030-in.) notch. The results were compared with results for the common 1.0-mm-deep (0.039-in.) notch. Increasing the depth significantly reduced the USE from 31 J for a = 0.8 mm to 13 J for a = 1.7 mm. The temperatures at the middle of the transition region, T_{MT}, were -31, -6, and -19°C for specimens with notch depths 0.8, 1.0, and 1.7 mm, respectively. These changes in transition temperature are mainly due to changes in the USE rather than the effect of the notch depth on the transition behavior.

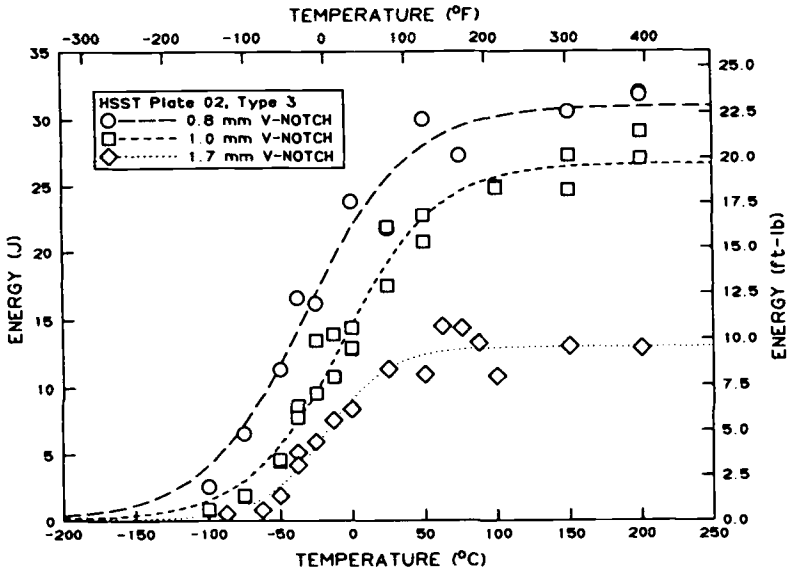


FIG. 2--Impact curve for type 3 specimens from HSST Plate 02, quarter-thickness location, with 0.8-, 1.0-, and 1.7-mm V-notch depths.

The effect of the notch root radius can be seen by comparing CVN curves of HSST Plate 02 type 3 specimens with 0.25- and 0.10-mm radii (Fig. 3). For this particular experiment, specimens with a 0.8-mm-deep notch were used. Sharpening of the notch led to an increase in transition temperature of ~ 20°C and a decrease of the USE of ~ 5 J. The data agree with other observations of notch dimension effects on impact data [15,26].

The effect of notch angle was studied on two sets of HSST Plate 02 type 1 specimens with 45 and 30° angles (Fig. 4). This change in the notch angle did not result in any significant effect on transition temperature or USE.

Another parameter is the distance between the anvil supports (span). Figure 5 shows CVN curves of HSST Plate 02 type 4 specimens tested with spans of 22 and 20 mm. No difference was observed in the transition region. Data from specimens with shorter span possibly indicate a slightly higher USE, but this difference could be due to scatter in the data. However, there is a mechanism that may explain higher energies for specimens tested with the shorter span (20 mm). The 3- by 4-mm subsize specimens tested on the upper shelf usually do not fracture completely, but bend around the tup until they are forced out past the anvils. With a shorter span, the specimens must be bent further and scraped against the anvils for a longer time until they can be pushed out. This will result in a longer tail on the end of the load-deflection curve, which will be reflected in slightly higher absorbed energies, as the data tend to show. In the transition region, the specimens do break completely, so no extra force is required to push the specimen through the anvils.

In this case no effect of span would be expected, and no effect is observed (Fig. 5). Another example of the effect of span on impact properties is given by a comparison on data from types 3 and 5 subsize specimens. The only difference between these specimens is that type 3 specimens have one-half the span of type 5. The impact curves of types 3 and 5 weld 72W specimens are presented in Fig. 6. Figure 7 presents the impact curves of types 3 and 5 specimens of HSST Plate 02. The type 5 specimens were cut from the half-thickness region in the plate. The type 3 specimens of this plate were cut from the broken halves of tested type 5 specimens. In Figs. 6 and 7, these results did not show any difference between types 3 and 5. The 5- by 5-mm specimens break even on the upper shelf, so no effect of span is observed.

One set of HSST Plate 02 type 3 specimens was tested at an impact velocity of 5.5 m/s (18 ft/s), while another set was tested at 2.25 m/s (7.4 ft/s) (the common impact velocity for subsize specimens in this study). The results show no sensitivity of impact properties to the increase of impact velocity from 2.25 to 5.5 m/s (Fig. 8).

CORRELATION OF ABSORBED ENERGY BETWEEN FULL-SIZE AND SUBSIZE SPECIMENS

The absence of standardization for subsize specimen results in various correlations of data between subsize and standard specimens. Generally, the existing correlations of USE between full-size and subsize specimens can be divided into two categories. One method widely used in Europe [5–7,11,25] consists of establishing an empirical ratio between USE of full-size ($USE_{full\text{-}size}$) and USE of subsize ($USE_{subsize}$) specimens based on large numbers of tests. The second approach, primarily used by North American [12,13,19–23,27] and Japanese [14,15,24] researchers, consists of correlation of the ratio between USE of full-size and subsize specimens with the ratio of different geometrical parameters of full-size and subsize specimens:

$$\frac{USE_{full\ size}}{USE_{subsize}} = \frac{f(\text{geometric parameters})_{full\ size}}{f(\text{geometric parameters})_{subsize}} . \quad (2)$$

In other words, the ratio of geometrical parameters can be used as a normalization factor (NF) to determine USE of full-size specimens based on the results of testing subsize specimens :

$$USE_{full\ size} = NF \times USE_{subsize} . \quad (3)$$

Published ratios of geometric parameters of full-size to subsize specimens or normalization factors are shown in Table 2 and described below.

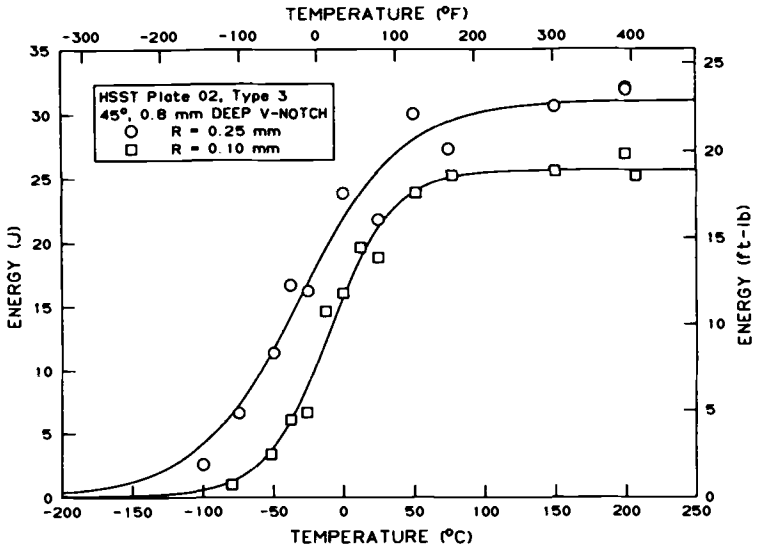


FIG. 3--Impact curve for type 3 specimens from HSST Plate 02, quarter-thickness location, with 0.25- and 0.10-mm V-notch root radii.

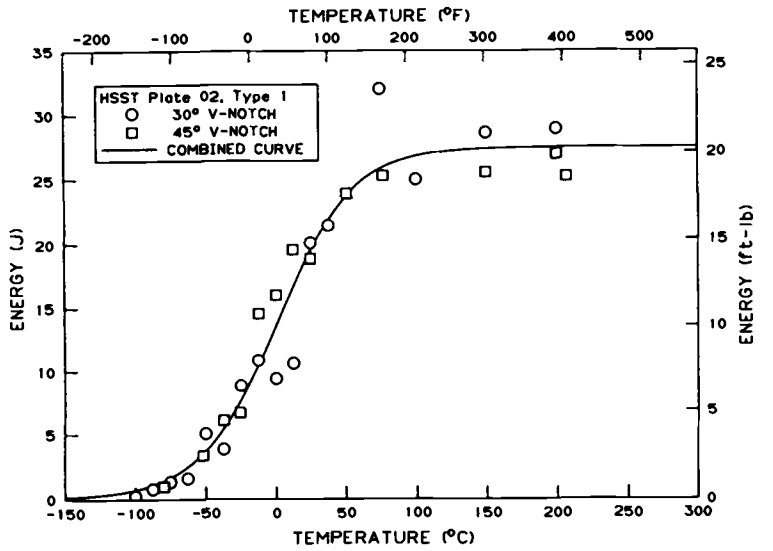


FIG. 4--Impact curve for type 1 subsize specimens from HSST Plate 02, quarter-thickness location, with 30 and 45° V-notch angles.

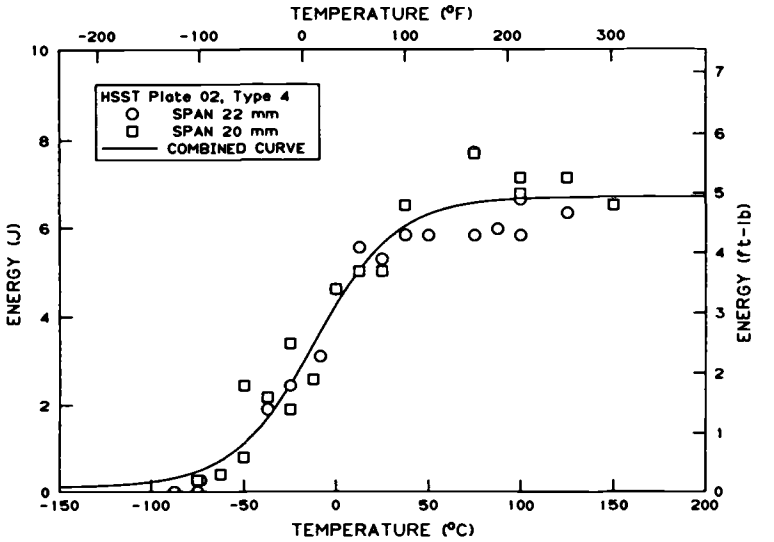


FIG. 5--Impact curve for type 4 specimens from HSST Plate 02, quarter-thickness location, tested at 22- and 20-mm span.

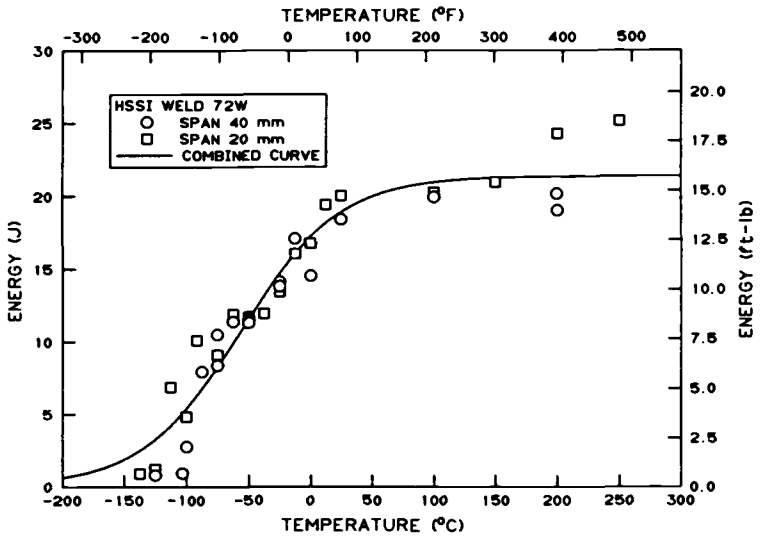


FIG. 6--Impact curve for type 3 and type 5 specimens of weld 72W tested at 40- and 20-mm span.

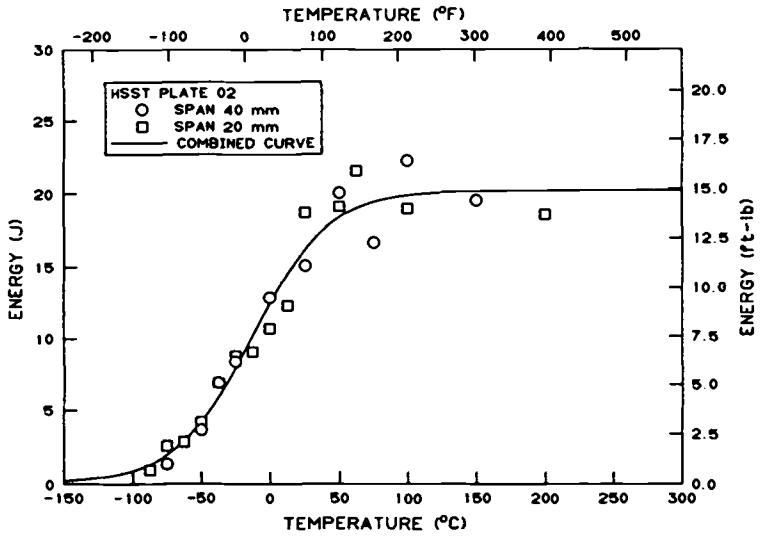


FIG. 7--Impact curve for type 3 and type 5 specimens from HSST Plate 02, half-thickness location, tested at 20- and 40-mm span.

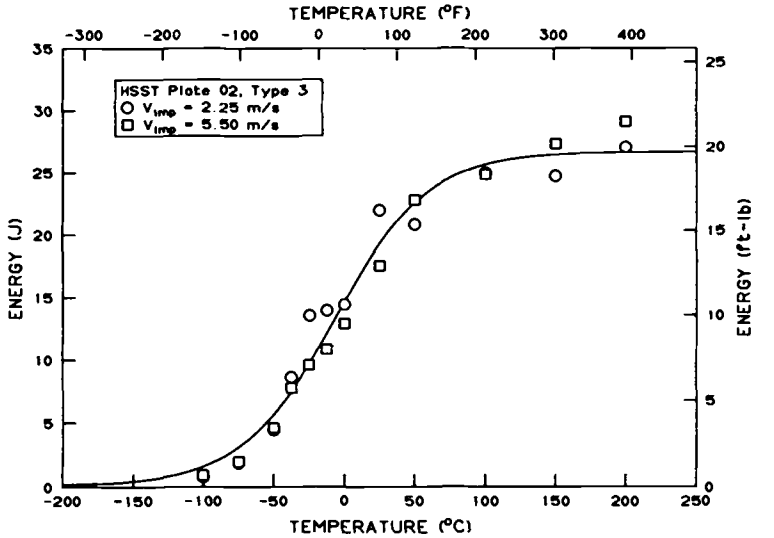


FIG. 8--Absorbed energy versus test temperature for type 3 specimens of HSST Plate 02, quarter-thickness location, test at impact velocities of 5.5 and 2.25 m/s.

Corwin et al. [12,23] compared two normalization factors. The first factor was equal to the ratio of the fracture area (Bb) of the full-size specimen to that of the subsize specimen, where B is the width and b is the depth of the ligament below the notch of the specimen (see Fig. 9). The second was the ratio of the nominal fracture volume $[(Bb)^{3/2}]$ of the full-size to the subsize specimen. It was shown that use of the normalization factor $(Bb)^{3/2}$ gave good correspondence. Normalization by Bb gave poor agreement for USE data.

Lucas et al. [13,27] also used a normalization factor equal to the ratio of the fracture volume of full-size to subsize specimens, but expressed the nominal fracture volume as Bb^2.

Louden et al. [21] suggested a normalization factor equal to the ratio of Bb^2/LK_t of full-size to subsize specimens, where L is the span and K_t is the elastic stress concentration factor [29], which is dependent on ligament size b and notch radius R. The present study has shown (see Fig. 7) that Charpy data, including USE, of specimens tested at spans that differed by a factor of 2 (20 and 40 mm) did not depend on span. However, the USE depends on ligament size b (see Fig. 2) and notch radius R (see Fig. 3), which might support using K_t. Nevertheless, it is not clear how an elastic stress concentration factor can be related to behavior on the upper shelf, where fracture is taking place in a ductile manner dominated by plastic strain.

Kumar et al. [20,22,28] have developed an interesting approach to predict the USE of full-size specimens by using both notched and precracked subsize specimens. They suggest that this allows a separation of the USE into energies for crack initiation and crack propagation. This approach is based on the assumption that the energy for crack initiation normalized by fracture volume of the specimen (F.V.) is equal for full-size and subsize specimens. Energy for crack initiation can be determined from the difference between the USE of notched specimens (USE) and precracked specimens (USE_p), that is:

$$\left[\frac{USE - USE_p}{F.V.}\right]_{full\ size} = \left[\frac{USE - USE_p}{F.V.}\right]_{subsize}, \quad (4)$$

where fracture volume, F.V., is equal to Bb^2. Additionally, it was found that the ratio of the USE of notched specimens to the USE of precracked specimens (USE_p) did not depend on specimen size, namely:

$$\left[\frac{USE}{USE_p}\right]_{full\ size} = \left[\frac{USE}{USE_p}\right]_{subsize}. \quad (5)$$

Thus, Kumar et al. claimed that knowledge of USE and USE_p of subsize specimens allows the use of Eqs. (4) and (5) to determine the USE of full-size specimens. Examination shows, however, that Eqs. (4) and (5) are interdependent and can be transformed into one equation:

$$\left[\frac{\text{USE}}{\text{F.V.}}\right]_{\text{full size}} = \left[\frac{\text{USE}}{\text{F.V.}}\right]_{\text{subsize}}, \tag{6}$$

which is the same as Lucas et al. [13,27] proposed previously for a nominal fracture volume of Bb^2 and does not require testing of precracked specimens.

Kayano et al. [14] have proposed a normalization factor that incorporates not only fracture volume but elastic (K_t) and plastic (Q) stress concentration factors as well. For the plastic stress concentration factor, the following expression based on slip-line field theory for a notched specimen [30] was used:

$$Q = 1 + \frac{\pi - \theta}{2}, \tag{7}$$

where θ is the notch angle in radians. Some uncertainty remains as to the exact value of Q in CVN testing. Slip-line field theory also assumes elastic-perfectly plastic behavior, and neglects work hardening, which is clearly not a valid assumption for most materials. Additionally, slip-line field theory can only be used when fracture occurs exactly at the point of general yielding. This will apply only at one specific temperature for a given material, not over the whole transition regime. In any case, implementation of Q as in Eq. (7) includes the effect of notch angle on USE. However, the results of the present study did not show such a dependence over the limited range of notch angles examined.

In the present work, different normalization factors described above as well as modifications by the authors were implemented in the analysis of the data (see Table 2). Table 3 summarizes the results of measured USE values for full-size and subsize specimens of the steels investigated in the present study. For all types of subsize specimens, a linear dependence between the USE of full-size and subsize specimens is observed except for two points with USEs of full-size specimens higher than 200 J. Values of USE higher than 200 J for full-size specimens require special consideration. Specimens tested in the upper-shelf region show large amounts of plastic deformation at the support points and at the contact area with a striker. These features are associated with the specimen "wrapping around" the striking edge and squeezing through the anvils. All interactions between the specimen, striker, and the anvils will require additional energy as reflected by the absorbed energy value [31,32]. Specimens with high USE values will have significant amounts of energy associated with such interactions in addition to the fracture process at the notch.

TABLE 2--Comparison of different normalization factors for USE as ratios of different specimen dimensions

Geometric parameter, G.P.	Bb	Bb^2/LK_t	$(Bb)^{3/2}/LK_t$	Bb^2	$(Bb)^{3/2}$	Bb^2/Q	$(Bb)^{3/2}/Q$	Bb^2/QK_t	$(Bb)^{3/2}/QK_t$
$G.P._{\cdot fullsize}/G.P._{\cdot type\ 1}$	3.77	5.63	5.8	7.12	7.33	7.54	7.76	11.9	12.3
$G.P._{\cdot fullsize}/G.P._{\cdot type\ 2}$	8.52	15.6	16	24.2	24.8	25.6	26.3	33.1	33.9
$G.P._{\cdot fullsize}/G.P._{\cdot type\ 3}$	4	2.8	2.8	8	8	8	8	5.7	5.7
$G.P._{\cdot fullsize}/G.P._{\cdot type\ 4}$	8.9	13	14.6	23.7	26.5	22.3	24.9	22.3	24.9
Note: L = span, K_t = elastic stress concentration factor, Q = plastic stress concentration factor.									

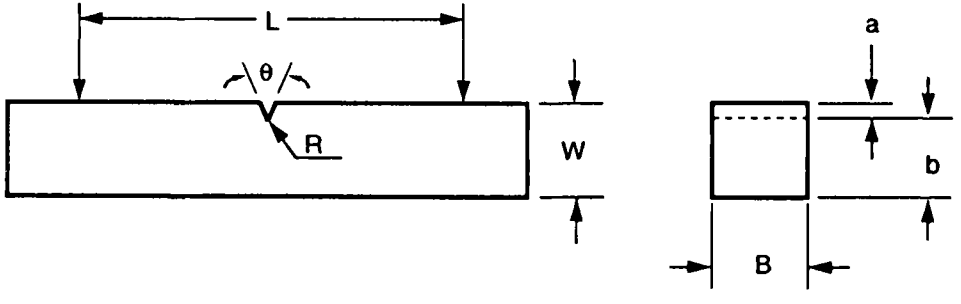


FIG.9--Definition of specimen dimensions.

TABLE 3--Upper-shelf energies

Material	$USE_{full\ size}$ (J)	$USE_{type\ 1}$ (J)	$\frac{USE_{full\ size}}{USE_{type\ 1}}$	$USE_{type\ 2}$ (J)	$\frac{USE_{full\ size}}{USE_{type\ 2}}$	$USE_{type\ 3}$ (J)	$\frac{USE_{full\ size}}{USE_{type\ 3}}$	$USE_{type\ 4}$ (J)	$\frac{USE_{full\ size}}{USE_{type\ 4}}$
A 533 wide plate, LT orientation	330	34.6	9.5	8.6	38.4	28.4	11.6	7.7	42.9
A 533 wide plate, TL orientation	244	34.3	7.1	8.9	27.4	35.9	6.8	7.2	33.9
A 508, as quenched	115	21.6	5.3	6.1	18.9	17.6	6.5	5.5	20.9
A 508, quenced and tempered at 599°C	102	21.1	4.8	5.3	19.2	15.0	6.8	5.1	20.0
A 508, quenced and tempered at 677°C	116	26.2	4.4	6.8	17.1	17.2	6.7	6.5	17.8
A 508, quenched and tempered at 704°C	164	37.3	4.4	9.3	17.6	24.6	6.7	7.5	21.9
HSST Plate 02, TL orientation, quarter thickness	141	29.3	4.8	6.7	21.0	26.7	5.3	6.3	29.4
HSST Plate 02, TL orientation, half thickness	114					20.3	5.6		
HSST Plate 014, quenched and tempered at 950°C	73	15.1	4.8	5.6	13.0	13.9	5.3	4.5	16.2
15Kh2MFA, melt 103672	181	29.2	6.2	8.3	21.8	24.5	7.4	7.8	23.2
HSSI weld 72W	136	23.7	5.7	7.7	17.7	22.5	6.0	5.9	23.1

Further investigations need to be performed to analyze these data. For the purposes of this study, analysis of USE data was limited to data below 200 J for full-size specimens.

Figures 10 through 13 present the correlation observed for the USE from full-size specimens to the USE from subsize specimen types 1 through 4 as well as ratios of $USE_{full\ size}$ to $USE_{subsize}$ for each type of subsize specimen. Comparison of the ratios obtained with the normalization factors in Table 2 shows that no single factor can be considered as universal for any specimen geometry, although a normalization factor based on the fracture volume of specimens, namely $(Bb^2)_{full\ size}/(Bb^2)_{subsize}$, gives the closest estimation for each geometry, but these estimations are slightly higher than empirical ratios for each specimen geometry. An implementation of elastic or plastic stress concentration factors did not improve the correspondence. The results of this study indicate that it is preferable to use the obtained empirical ratios (see Figs. 10–13) as USE normalization factors for each specific geometry. The data do not show an obvious effect of the yield strength on the empirical ratios of USEs.

Since no single known existing correlation procedure would work for data from different subsize specimens, a new correlation was developed. It was assumed that the fracture process could be partitioned into low-energy brittle and high-energy ductile modes, and that different correlation procedures should be applied to each component of the fracture process. On the lower shelf, where fracture occurs by a low-energy cleavage mechanism, it is reasonable to assume a constant value of absorbed energy per unit of fracture surface area or:

$$\left[\frac{LSE}{Bb}\right]_{full\ size} = \left[\frac{LSE}{Bb}\right]_{subsize}, \tag{8}$$

and thus

$$LSE_{full\ size} = NF_{brittle} \times LSE_{subsize}, \tag{9}$$

where

$$NF_{brittle} = \frac{(Bb)_{full\ size}}{(Bb)_{subsize}}. \tag{10}$$

In the transition region there is a competition between brittle and ductile fracture. It is assumed that the percent of shear on the fracture surface can be used as a measure of the amount of ductile fracture in the transition region. Based on these considerations, the following expression is proposed for normalizing the absorbed energy (E) of subsize specimens:

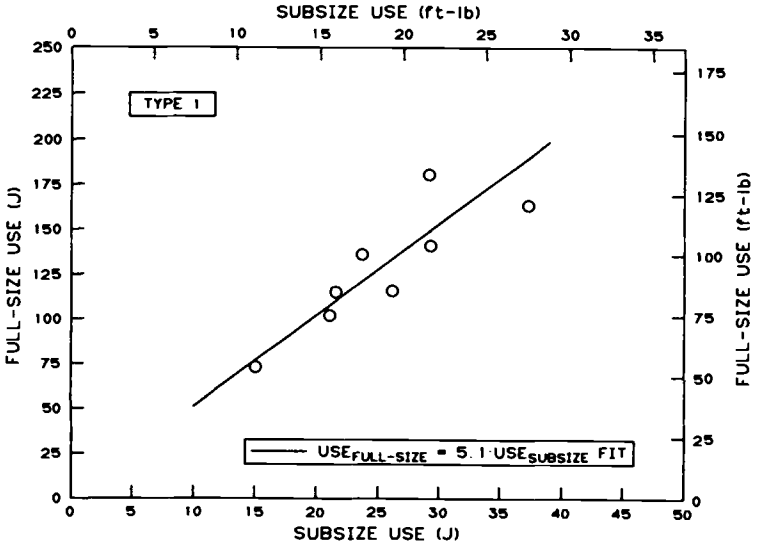


FIG. 10--Correlation of upper-shelf energies of full-size and type 1 subsize specimens.

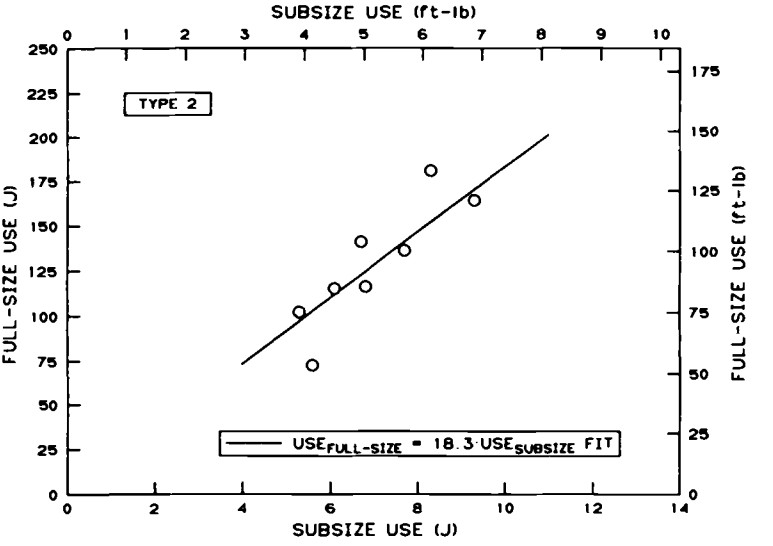


FIG. 11--Correlation of upper-shelf energies of full-size and type 2 subsize specimens.

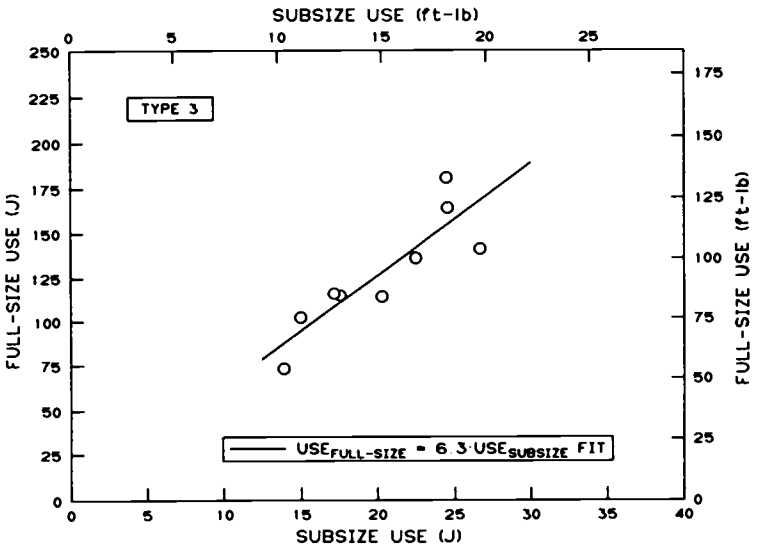


FIG. 12--Correlation of upper-shelf energies of full-size and type 3 subsize specimens.

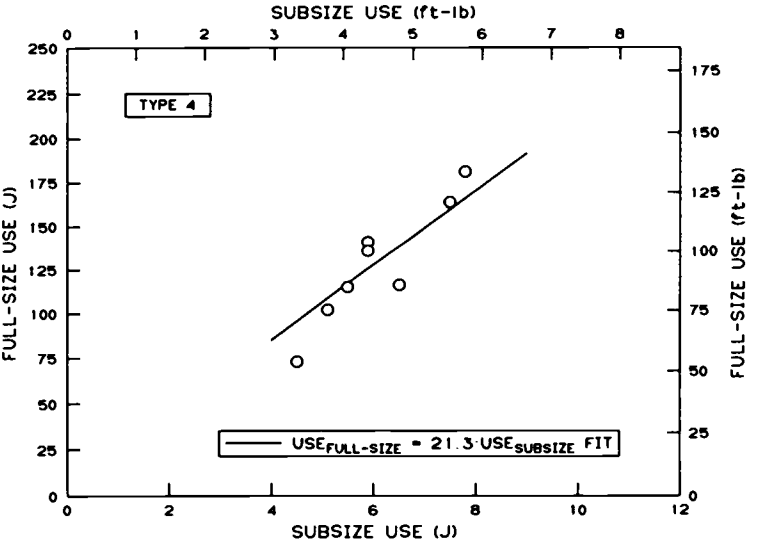


FIG. 13--Correlation of upper-shelf energies of full-size and type 4 subsize specimens.

$$E = E_{subsize} \times \left[NF_{brittle} \frac{100 - SHEAR}{100} + NF_{ductile} \frac{SHEAR}{100} \right], \quad (11)$$

where $NF_{brittle}$ is a normalization factor for the brittle mode of fracture [Eq. (10)] and is equal to 3.77, 8.52, 4.00, and 8.90 for types 1, 2, 3, and 4 subsize specimens, respectively. $NF_{ductile}$ is a normalization factor for the ductile mode and is equal to 5.1, 18.3, 6.3, and 21.3 for types 1, 2, 3, and 4 subsize specimens, respectively (see Figs. 10 through 13). SHEAR is the percent of shear fracture on the fracture surface measured, in general, visually. Visual determination of the percent of shear fracture requires an interpretation of the appearance of the fracture surface, a process that is subjective and may vary from person to person. This variability may lead to some uncertainty in values of the transition temperature determined with the normalization process in Eq. (11). To estimate how serious a problem this might be, data from HSST Plate 02 type 3 specimens were examined. The original data were normalized and analyzed to determine the transition temperatures at energy levels of 41 and 68 J (T_{41J} and T_{68J}, respectively). Then the percent shear data were modified, first by adding 10% to each data point, and then by subtracting 10% from each data point. The lower- and upper-shelf levels were kept at 0 and 100%, respectively, in both cases. The energy levels from the subsize specimens were then normalized with the altered shear values, in both cases. The results of these changes in the shear values are shown in Table 4. Changing of the shear values by $\pm 10\%$ results in very small changes in the transition temperatures, showing that the normalization procedure is not overly sensitive to changes in the measured value of percent shear.

CORRELATION OF TRANSITION TEMPERATURE OF FULL-SIZE AND SUBSIZE SPECIMENS

The effect of specimen size on the DBTT can be explained as suggested by Davidenkov [33]. The yield stress (σ_y) depends on temperature, increasing as the temperature decreases, while the cleavage fracture stress (σ_f) is assumed to be temperature independent (see Fig. 14). The intersection of these curves determines the ductile-to-brittle transition. The size effect can be explained by a statistical theory of strength, whose mathematical interpretation was given by Weibull [34]. It is based on the assumption that brittle failure is determined by the value of the local stress in the piece at the point where the most critical structural defect is located. Using the theory of probability, Weibull established the dependence of the brittle strength on the volume of the specimen. For the same states of stress but various dimensions of the specimens, the brittle fracture stress changes as $V^{-1/m}$, where V is the volume of the specimen and m is a constant of the material. The scatter obtained will be larger for smaller specimens. The dependence of brittle fracture on the volume of specimens for different types of tests has been experimentally confirmed [35,36].

TABLE 4--Effects of changes in percent shear on values of transition temperatures at 41 and 68 J for normalized data from type 3 specimens of HSST Plate 02

	Transition temperature (°C)		
	As-measured shear[a]	As-measured + 10%[b]	As-measured − 10%[c]
T_{41J}	−28	−30	−26
T_{68J}	−2	−5	1

[a]Normalization performed with as-measured percent shear.
[b]Normalization performed with percent shear +10%.
[c]Normalization performed with percent shear −10%.

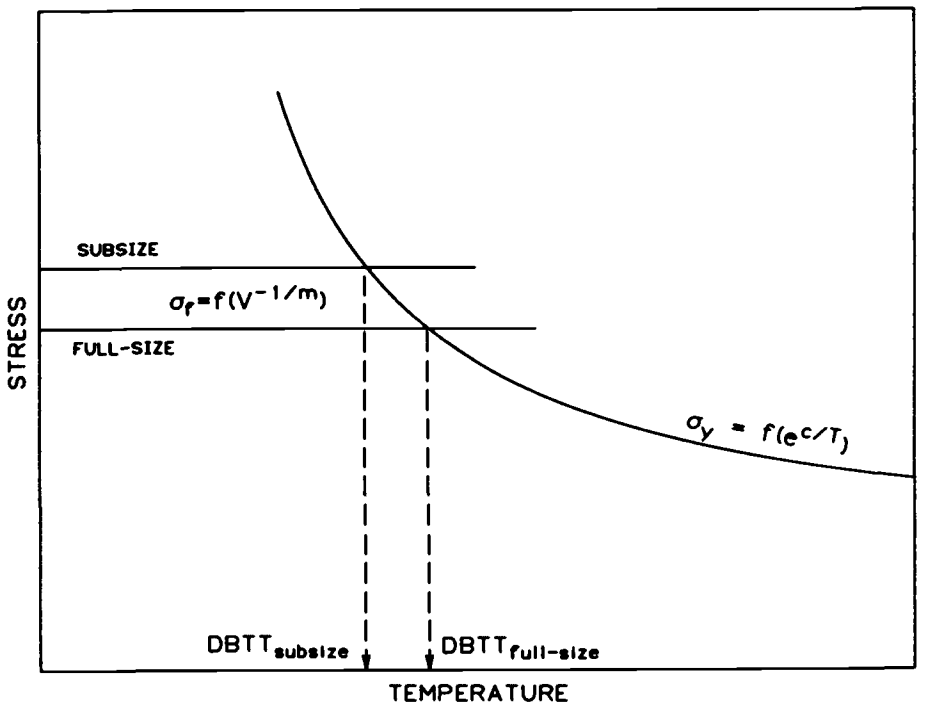


FIG. 14--Stress-temperature diagram showing the effect of specimen size on transition temperature.

The above discussion is illustrated in Fig. 14. The dependence of yield stress on temperature can be expressed as:

$$\sigma_y = Ae^{c/T} , \tag{12}$$

where A and c are constants and T is temperature in K. According to Weibull, the dependence of the brittle fracture stress on volume is:

$$\sigma_f = ZV^{-1/m} , \tag{13}$$

where Z and m are constants. If we define the DBTT as the temperature at which σ_y is raised so that it equals σ_f (see Fig. 14), then:

$$Ae^{\frac{c}{DBTT}} = ZV^{-1/m} . \tag{14}$$

Taking the natural logarithm of Eq. (14) results in:

$$DBTT = \frac{1}{R - S \ln V} , \tag{15}$$

where R and S are constants.

Thus, Eq. (15) describes, in general, the shift of DBTT to lower temperatures due to a reduction in size. However, different notch geometries result in different stress distributions under the notch for different subsize specimens, which does not allow the use of Eq. (16) for a quantitative account of size effects in notched impact tests. Nevertheless, it suggests the establishment of an empirical correlation:

$$DBTT_{fullsize} = DBTT_{subsize} + M , \tag{16}$$

where $DBTT_{full\ size}$ and $DBTT_{subsize}$ are transition temperatures for full-size and subsize specimens, respectively, and M is a shift of DBTT due to specimen size. A similar approach has been used in Refs. [6,11,19].

The following procedure was used to determine the temperature correction M. Absorbed energy values from subsize specimens were normalized by Eq. (11). These data

were then fit with a hyperbolic tangent function [Eq. (1)] to determine temperatures at 41 J (T_{41J}), 68 J (T_{68J}), and at the middle of the transition zone (T_{MT}). Figures 15 through 18 summarize the comparison of transition temperatures for full-size and different subsize specimens. Transition temperatures at 50% shear ($T_{50\%}$) were also included in the analysis. The data show a linear correspondence of transition temperatures. The following equations were obtained for the different subsize specimens:

$$DBTT_{full\ size} = DBTT_{type\ 1} + 30\ (\pm 28)\ °C; \quad \textbf{(17)}$$

$$DBTT_{full\ size} = DBTT_{type\ 2} + 53\ (\pm 24)\ °C; \quad \textbf{(18)}$$

$$DBTT_{full\ size} = DBTT_{type\ 3} + 34\ (\pm 20)\ °C; \quad \textbf{(19)}$$

$$DBTT_{full\ size} = DBTT_{type\ 4} + 38\ (\pm 30)\ °C; \quad \textbf{(20)}$$

where the numbers in parentheses are $\pm\ 2\sigma$ intervals.

Figure 19 shows the dependence of the temperature-size correction, M, taken from Eqs. (17) through (20), on the nominal fracture volume, Bb^2, for the subsize specimens used in this work. The solid line is a fit to the data:

$$M = 98 - 15.1 \times \ln (Bb^2)\ . \quad \textbf{(21)}$$

The form of this fit is suggested by Eq. (15), and the equation was forced to give a correction factor of 0 for the full-size specimen. The trend agrees, in general, with the scheme for the effects of specimen size on the DBTT based on the statistical theory of strength (Fig. 14). Deviations from this dependence reflect the constraint effects of different notch dimensions, but the form of the dependence may be used as guidance to estimate size corrections for subsize specimens. Other investigators, i.e., [16], are considering the use of side-grooving to improve the DBTT shift correlations.

Figure 20 illustrates the normalization procedure described above with the data from HSSI weld 72W. The absorbed energies for subsize specimens were normalized by Eq. (11). Test temperatures were then shifted forward to size adjustment values from Eq. (17) through (20) for the corresponding subsize specimens. Data from subsize specimens normalized by this procedure correspond very well with the mean and 95% confidence intervals from full-size specimens, as Fig. 20 shows.

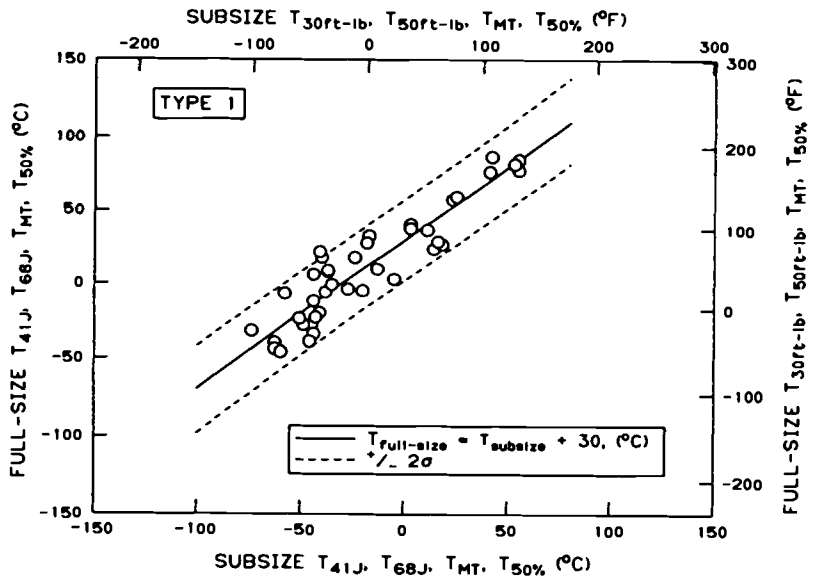


FIG. 15--Correlation of transition temperatures determined from data from full-size specimens and normalized data for type 1 subsize specimens.

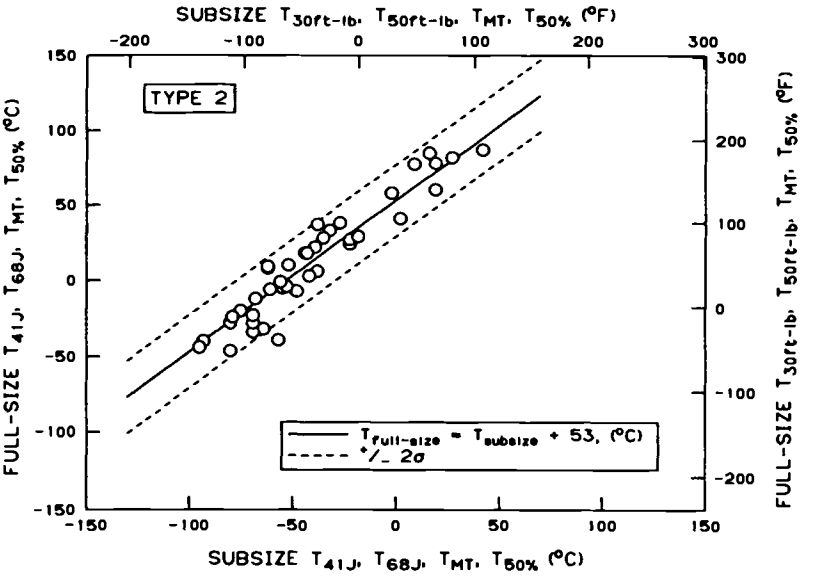


FIG. 16--Correlation of transition temperatures determined from data from full-size specimens and normalized data for type 2 subsize specimens.

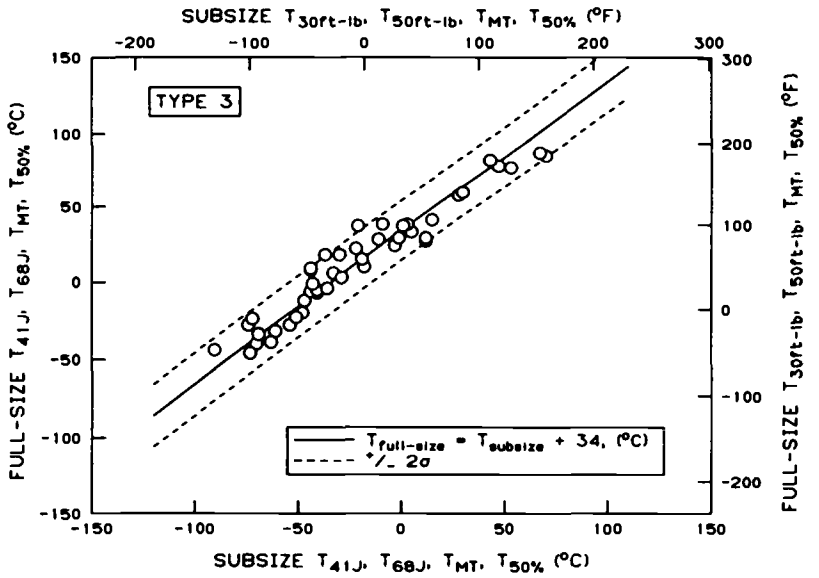


FIG. 17--Correlation of transition temperatures determined from data from full-size specimens and normalized data for type 3 subsize specimens.

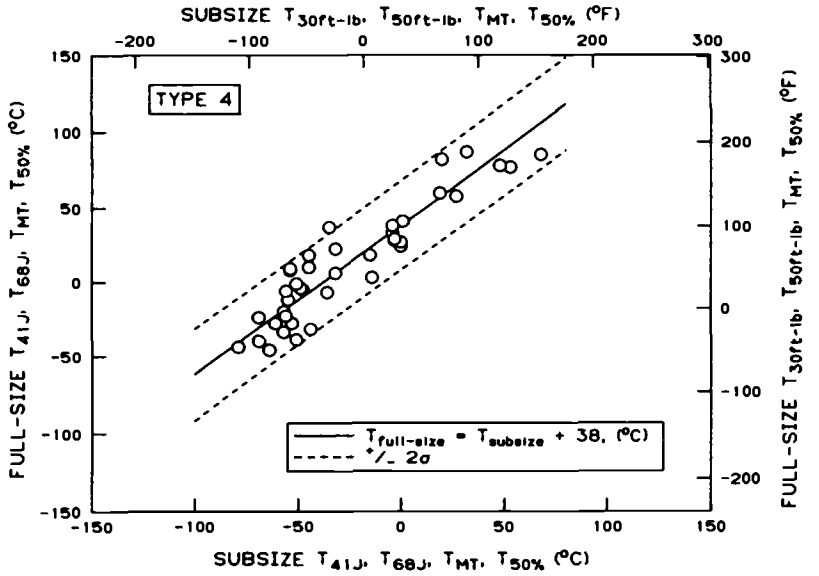


FIG. 18--Correlation of transition temperatures determined from data from full-size specimens and normalized data for type 4 subsize specimens.

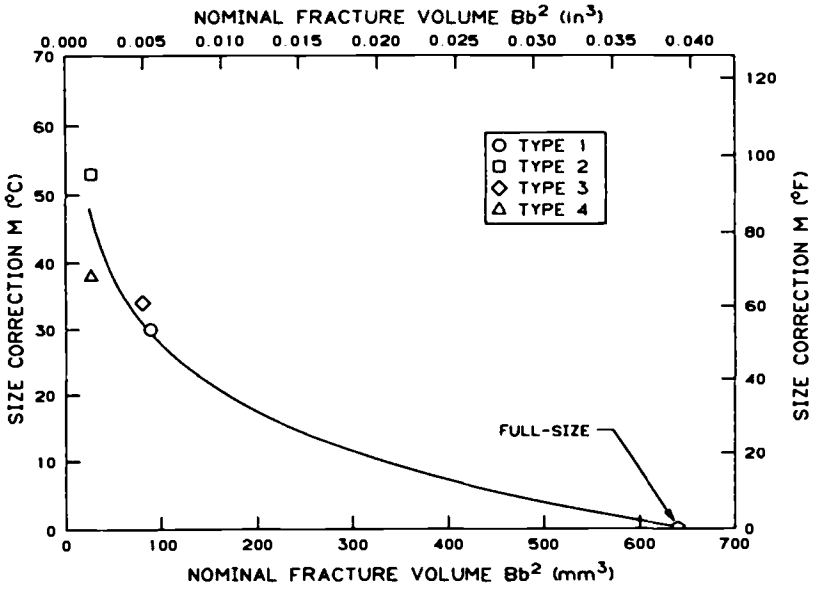


FIG. 19--Temperature correlation for subsize specimens as a function of nominal fracture volume.

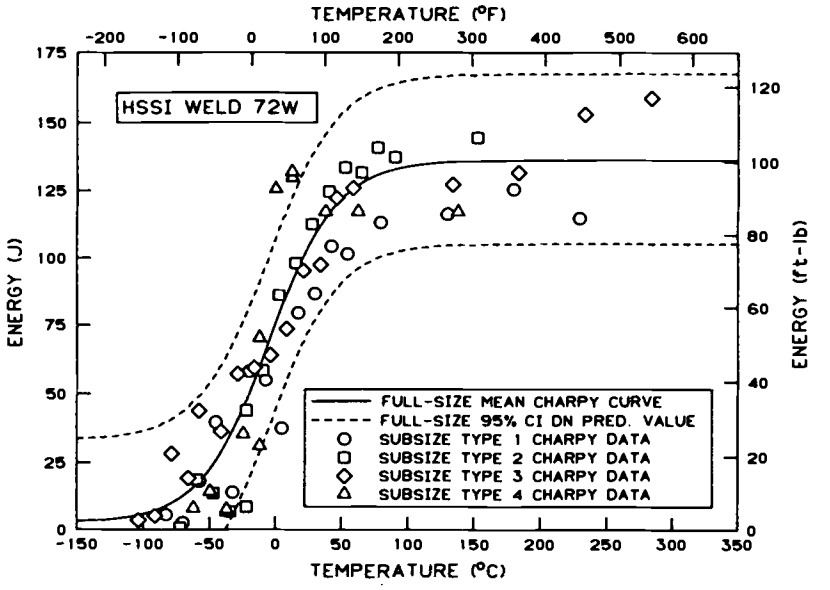


FIG. 20--Comparison of Charpy curve for full-size specimens of HSSI weld 72W with data from subsize Charpy specimens normalized by the proposed procedure.

Examination of the standard deviations reported for Eqs. (17) through (20) shows that the type 3 specimen has the smallest value, suggesting that this specimen is the best of the four types examined for determining the DBTT, since it results in the smallest error. It was also noted that this specimen was more likely to fracture completely when tested in the upper-shelf regime, whereas the other subsize specimens tended to wrap around the tup rather than fracture in this regime. This failure to fracture on the upper shelf is exacerbated with high upper-shelf materials, and accounts for the poor agreement found for materials with upper-shelf levels over 200 J, as measured with full-size specimens. The type 1 and 2 subsize specimens have relatively short notch depth to specimen width ratios (a/W) of 0.16 and 0.15, respectively. The type 3 specimen has a relatively deeper notch, with a/W = 0.2. This relatively deeper notch will encourage fracture on the upper shelf. The type 4 specimen has a value of a/W of 0.25, but the specimen thickness is only 3 mm as compared to 5 mm for type 3. The greater thickness of the type 3 specimen will increase the transverse constraint developed in this specimen as compared to the thinner type 4 specimen, and again encourage fracture. Thus, of all the specimens tested, the type 3 specimen seems to be the best, although it is the largest of the subsize specimens.

SUMMARY AND CONCLUSIONS

Five types of subsize specimens from ten materials were studied in the present work. The main results are as follows:

1. Subsize Charpy specimens may be useful for studies when material availability is limited. The broken halves of surveillance specimens can be remachined into subsize specimens to extend current surveillance programs and monitor annealing response. The smallest specimen recommended by ASTM E 23 (5 × 5 × 55 mm) is too long for such an application without resorting to reconstitution techniques.

2. It was found that (a) an increase in the notch depth decreases the USE, but has little effect on the DBTT; (b) a decrease of the notch root radius reduces the USE and increases the DBTT; (c) variation of notch angle from 30 to 45° while keeping the remaining dimensions identical does not result in any effect on transition temperature or USE, and (d) span and impact velocity (in the ranges studied) do not affect the USE and DBTT.

3. The following equation is proposed for normalizing impact energy values from subsize Charpy specimens:

$$E = E_{subsize} \times \left[NF_{brittle} \frac{100 - SHEAR}{100} + NF_{ductile} \frac{SHEAR}{100} \right],$$

where $NF_{brittle}$ is a normalization factor equal to the ratio of the fracture surface of the full-size specimen to the fracture surface of the corresponding subsize specimen; $NF_{ductile}$ is an empirical normalization factor equal to 5.1, 18.3, 6.3, and 21.3 for types 1, 2, 3, and 4 subsize specimens, respectively, and SHEAR is the percent of shear fracture on the fracture surface.

4. The empirical correlations between the DBTT of full-size and the different subsize specimens were determined as follows:

$$DBTT_{full\ size} = DBTT_{type\ 1} + 30\ (\pm 28)\ °C;$$

$$DBTT_{full\ size} = DBTT_{type\ 2} + 53\ (\pm 24)\ °C;$$

$$DBTT_{full\ size} = DBTT_{type\ 3} + 34\ (\pm 20)\ °C;$$

$$DBTT_{full\ size} = DBTT_{type\ 4} + 38\ (\pm 30)\ °C;$$

where the numbers in parentheses are $\pm\ 2\sigma$ intervals. Further understanding of the shift in the DBTT as a function of specimen size needs to be pursued.

5. Results obtained from the subsize specimens as well as the empirical correlations can be used for development of an ASTM standard practice for impact testing of subsize specimens for supplementary surveillance data in nuclear applications.

ACKNOWLEDGMENTS

This research was sponsored by the Office of Nuclear Regulatory Research, U.S. Nuclear Regulatory Commission under Interagency Agreement DOE 1886-8109-8L with the U.S. Department of Energy under contract DE-AC05-84OR21400 with Lockheed Martin Energy Systems. The authors would like to acknowledge the programmatic support of the Heavy-Section Steel Irradiation Program at ORNL. We appreciate the useful discussions of results and the helpful review of the manuscript by David J. Alexander. The impact tests were conducted by Eric T. Manneschmidt and the technical manuscript was prepared by Julia L. Bishop. This research was also supported in part by an appointment to the ORNL Postdoctoral Research Program administered by the Oak Ridge Institute for Science and Education.

REFERENCES

[1] A. D. Amayev, A. M. Kryukov, and M. A. Sokolov, "Recovery of the Transition Temperature of Irradiated WWER-440 Vessel Metal by Annealing," pp. 369-79 in *Radiation Embrittlement of Nuclear Reactor Pressure Vessel Steels: An International Review (Fourth Volume), ASTM STP 1170*, L. E. Steele, Ed., American Society for Testing and Materials, Philadelphia, 1993.

[2] A. M. Kryukov and M. A. Sokolov, "Investigation of Material Behavior Under Reirradiation after Annealing Using Subsize Specimens," pp. 417-23 in *Small Specimen Test Techniques Applied to Nuclear Reactor Vessel Thermal Annealing and Plant Life Extension, ASTM STP 1204*, W. R.Corwin, F. M.Haggag, and W. L.Server, Eds., American Society for Testing and Materials, Philadelphia, 1993.

[3] W. L. Server, "Review of In-Service Thermal Annealing of Nuclear Reactor Pressure Vessels,"pp. 979-1008 in *Effects of Radiation on Materials: Twelfth International Symposium, ASTM STP 870*, F. A. Garner and J. S. Perrin, Eds., American Society for Testing and Materials, Philadelphia, 1985.

[4] *Proceedings of the DOE/SNL/EPRI-Sponsored Reactor Pressure Vessel Thermal Annealing Workshop, February 17-18, 1994, Albuquerque, New Mexico*, SAND 94-1515, 1994.

[5] R. Ahlstrand, E. N. Klausnitzer, D. Lange, C. Leitz, D. Pastor, and M. Valo, "Evaluation of the Recovery Annealing of the Reactor Pressure Vessel of NPP Nord (Greifswald) Units 1 and 2 by Means of Subsize Impact Specimens," pp. 312-43 in *Radiation Embrittlement of Nuclear Reactor Pressure Vessel Steels: An International Review (Fourth Volume), ASTM STP 1170*, L. E. Steele, Ed., American Society for Testing and Materials, Philadelphia, 1993.

[6] A. D. Amayev, V. I. Badanin, A. M. Kryukov, V. A. Nikolayev, M. F. Rogov, and M. A. Sokolov, "Use of Subsize Specimens for Determination of Radiation Embrittlement of Operating Reactor Pressure Vessels," pp. 424-39 in *Small Specimen Test Techniques Applied to Nuclear Reactor Vessel Thermal Annealing and Plant Life Extension, ASTM STP 1204*, W. R. Corwin, F. M. Haggag, and W. L. Server, Eds., American Society for Testing and Materials, Philadelphia, 1993.

[7] Standard Test Method for Notched Bar Impact Testing of Metallic Materials, ASTM E 23-93a, American Society for Testing and Materials, Philadelphia, 1993.

[8] M. Grounes, "Review of Swedish Work on Irradiation Effects in Pressure Vessel Steels and on Significance of Data Obtained," pp. 224-59 in *Effects of Radiation on Structural Metals, ASTM STP 426*, American Society for Testing and Materials, Philadelphia, 1967.

[9] C. Curll, "Subsize Charpy Correlation with Standard Charpy," *Materials Research & Standards*, 91-94 (February 1961).

[10] R. C. McNicol, "Correlation of Charpy Test Results for Standard and Nonstandard Size Specimens," *Welding Research Supplement*, 385-93 (September 1965).

[11] E. Klausnitzer, H. Kristof, and R. Leistner, "Assessment of Toughness Behavior of Low Alloy Steels by Subsize Impact Specimens," pp. 3-37 in *Transactions of the 8th International Conference on Structural Mechanics in Reactor Technology, Brussels,*

August 1985, Vol G, International Association for Structural Mechanics in Reactor Technology, 1986.

[12] W. R. Corwin and A. M. Hougland, "Effect of Specimen Size and Material Condition on the Charpy Impact Properties of 9Cr-1Mo-V-Nb Steel," pp. 325-38 in *The Use of Small-Scale Specimens for Testing Irradiated Material, ASTM STP 888*, W. R. Corwin and G. E. Lucas, Eds., American Society for Testing and Materials, Philadelphia, 1986.

[13] G. E. Lucas, G. R. Odette, J. W. Sheckherd, P. McConnell, and J. Perrin, "Subsized Bend and Charpy V-Notch Specimens for Irradiated Testing," pp. 304-24 in *The Use of Small-Scale Specimens for Testing Irradiated Material, ASTM STP 888*, W. R. Corwin and G. E. Lucas, Eds., American Society for Testing and Materials, Philadelphia, 1986.

[14] H. Kayano, H. Kurishita, A. Kimura, M. Narui, M. Yamazaki, and Y. Suzuki, "Charpy Impact Testing Using Miniature Specimens and Its Application to the Study of Irradiation Behavior of Low-Activation Ferritic Steels," *J. Nucl. Mater.* 179-181, 425-88 (1991).

[15] H. Kurishita, H. Kayano, M. Narui, M. Yamazaki, Y. Kano, and I. Shibahara, "Effects of V-Notch Dimensions on Charpy Impact Test Results for Differently Sized Miniature Specimens of Ferritic Steel," *Mater. Trans., JIM*, 34(11), 1042-52 (1993).

[16] M. P. Manahan and C. Charles, "A Generalized Methodology for Obtaining Quantitative Charpy Data from Test Specimens of Nonstandard Dimensions," *Nucl. Technol.* 90, 245-59 (May 1990).

[17] M. P. Manahan, "Determination of Charpy Transition Temperature of Ferritic Steels Using Miniaturized Specimens," *J. Mater. Sci.* 25, 3429-38 (1990).

[18] R. K. Nanstad, D. E. McCabe, R. L. Swain, and M. K. Miller, Martin Marietta Energy Systems, Inc., Oak Ridge Natl. Lab., *Chemical Composition and RT_{NDT} Determinations for Midland Weld WF-70*, USNRC Report NUREG/CR-5914 (ORNL-6740), December 1992.

[19] D. J. Alexander and R. L. Klueh, "Specimen Size Effects in Charpy Impact Testing," pp. 179-91 in *Charpy Impact Test: Factors and Variables, ASTM STP 1072*, J. M. Holt, Ed., American Society for Testing and Materials, Philadelphia, 1990.

[20] A. S. Kumar, F. A. Garner, and M. L. Hamilton, "Effect of Specimen Size on the Upper Shelf Energy of Ferritic Steels," pp. 487-95 in *Effects of Radiation on Materials: 14th International Symposium (Volume II), ASTM STP 1046*, N. H. Packan, R. E. Stoller, and A. S. Kumar, Eds., American Society for Testing and Materials, Philadelphia, 1990.

[21] B. S. Louden, A. S. Kumar, F. A. Garner, M. L. Hamilton, and W. L. Hu, "The Influence of Specimen Size on Charpy Impact Testing of Unirradiated HT-9," *J. Nucl. Mater.* 155-157. 662-67 (1988).

[22] A. S. Kumar, B. S. Louden, F. A. Garner, and M. L. Hamilton, "Recent Improvements in Size Effects Correlations for DBTT and Upper Shelf Energy of Ferritic Steels," pp. 47-61 in *Small Specimen Test Techniques Applied to Nuclear Reactor Vessel Thermal Annealing and Plant Life Extension, ASTM STP 1204*, W. R. Corwin, F. M. Haggag, and W. L. Server, Eds., American Society for Testing and Materials, Philadelphia, 1993.

[23] W. R. Corwin, R. L. Klueh, and J. M. Vitek, "Effect of Specimen Size and Nickel Content on the Impact Properties of 12 Cr-1 MoVW Ferritic Steel," *J. Nucl. Mater.* 22-123, 343-48 (1984).

[24] F. Abe, T. Noda, H. Araki, M. Okada, M. Narui, and H. Kayano, "Effect of Specimen Size on the Ductile-Brittle Transition Behavior and the Fracture Sequence of 9Cr-W Steels," *J. Nucl. Mater.* 150, 292-301 (1987).*

[25] E. N. Klausnitzer and G. Hofmann, "Reconstituted Impact Specimens with Small Inserts," pp. 76-90 in *Effects of Radiation on Materials: 15th International Symposium, ASTM STP 1125*, R. E. Stoller, A. S. Kumar, and D. S. Gelles, Eds., American Society for Testing and Materials, Philadelphia, 1992.

[26] N. H. Fahey, "Effects of Variables in Charpy Impact Testing," *Materials Research & Standards* 1, 872-76 (November 1961).

[27] G. E. Lucas, G. R. Odette, J. W. Sheckherd, and M. R. Krishnadev, "Recent Progress in Subsized Charpy Impact Specimen Testing for Fusion Reactor Materials Development," pp. 728-33 in *Fusion Technology*, Vol. 10, November 1986.

[28] A. S. Kumar, S. T. Rosinski, N. S. Cannon, and M. L. Hamilton, "Subsize Specimen Testing of a Nuclear Reactor Pressure Vessel Material," pp. 147-55 in *Effects of Radiation on Materials: 16th International Symposium, ASTM STP 1175*, A. S. Kumar, D. S. Gelles, R. K. Nanstad, and E. A. Little, Eds., American Society for Testing and Materials, Philadelphia, 1993.

[29] H. Neuber, *Theory of Notch Stresses*, Springer, Berlin, 1958.

[30] R. Sandstrom and Y. Bergstrom, "Relationship Between Charpy V Transition Temperature in Mild Steel and Various Material Parameters," *Mat. Sci.* 18, 177-86 (1984).

[31] T. Naniwa, M. Shibaike, M. Tanaki, H. Tani, H. N. Shiota, and T. Shiraishi, Effects of the Striking Edge Radius on the Charpy Impact Test,"pp. 67-80 in *Charpy Impact Test: Factors and Variables, ASTM STP 1072*, J. M. Holt, Ed., American Society for Testing and Materials, Philadelphia, 1990.

[32] R. K. Nanstad and M. A. Sokolov, "Charpy Impact Test Results on Five Materials and NIST Verification Specimens using Instrumented 2-mm and 8-mm Strikers," pp. 111-39 in *Pendulum Impact Machines: Procedures and Specimens for Verification. ASTM STP 1248*, T. A. Siewert and A. K. Schmieder, Eds., American Society for Testing and Materials, Philadelphia, 1995.

[33] N. N. Davidenkov, *The Problems of Impact in Material Science*, Academy of Science of U.S.S.R., 1938 (in Russian).

[34] W. Weibull, "A Statistical Theory of the Strength of Materials," p. 151 in *Proceedings of the Royal Swedish Institute for Engineering Research*, 1939.

[35] W. Weibull, "A Survey of 'Statistical Effects' in the Field of Material Failure," *Appl. Mech. Rev.* 5(11), 449-51 (1952).

[36] N. Davidenkov, E. Shevandin, and F. Wittmann, "The Influence of Size on the Brittle Strength of Steel," *J. Appl. Mech.* 63-67 (March 1947).

Eric van Walle[1]

RECONSTITUTION: WHERE DO WE STAND?

REFERENCE: van Walle, E., **"Reconstitution: Where Do We Stand?,"** *Effects of Radiation on Materials: 17th International Symposium, ASTM STP 1270,* David S. Gelles, Randy K. Nanstad, Arvind S. Kumar, and Edward A. Little, Eds., American Society for Testing and Materials, 1996.

ABSTRACT: A comprehensive review of the status of the reconstitution technique, as applied to reactor pressure vessel steel, is given. The reconstruction techniques in use at this moment on different small-size specimen geometries are highlighted, and the reconstitution methodology is evaluated. The advantages and limitations of reconstituted specimens are discussed, in relation to preparation and material conditions and in view of the test techniques to be used. For plant life management issues, the importance of finding an indexing parameter independent of the reconstitution process will be indicated.

KEYWORDS: reconstitution, welding techniques, reactor pressure vessel steel, Charpy-V, instrumented Charpy-V test, fracture toughness, pressure vessel surveillance, plant life management, orientation

The original impetus to construct compound specimens from a limited volume of material of interest, lay in the available material stock and the restricted space in irradiation capsules. Nowadays, the evolution in vessel integrity evaluation and the reflection that the vessel fracture toughness at the actually projected end-of-life date of many older plants might still be sufficient for further plant operation, provides the need to obtain more surveillance data for the nuclear vessel structure. The fact that for older plants practically no coupons of original surveillance material remain unused, is supplemented with large quantities of broken specimens and untested geometries of surveillance material. In some situations one only has small quantities of reactor pressure vessel steel (RPVS) of an operating plant or a plant under decommissioning [1, 2]. The general purpose is then, of course, to use this material as efficiently as possible.

[1]Senior research scientist, SCK•CEN, RMR Department, Fracture Mechanics and Modeling, Boeretang 200, B-2400 Mol, Belgium

Copyright© 1996 by ASTM International www.astm.org

The technique to construct specimens from small quantities of material is commonly called 'reconstitution'. The potential of such a technique can only be accepted if it can be guaranteed that the - unirradiated or irradiated - material of interest, solicited during a particular test, has not been altered by the reconstitution process. The first condition is therefore that the temperature within the test volume of the RPVS should remain low enough not to induce effects of annealing or metallurgical changes. Moreover, ideally, the test results on reconstituted specimens should be identical to those of full-size one-material samples, or deviations should be understood to allow for correction. Latter arguments put stringent conditions on the technical qualification process of the reconstitution methodology and on the evaluation procedure of the information extracted from the fracture tests.
This paper will describe and discuss the different reconstitution techniques that are actually in use, such as electron-beam welding, arc stud welding, laser welding, projection and upset butt welding. The aim is to include Charpy-V (C_V) type and size geometries for which reconstitution has been used, as the interest of the nuclear pressure vessel community clearly goes in this direction. From the methodological point of view, recommendations that are at the basis for the procedure for the ASTM Round-Robin on Reconstitution [3] and that might end-up in standards such as the ASTM Standard Guide for Reconstitution of Irradiated Charpy Specimens (E1253) [4], will be discussed. The actual knowledge on variables within the reconstitution process, such as material condition, insert geometry, and test geometries and compatible test procedures, will be enunciated. The known influences on the fracture test results will be summarised and a procedure to avoid some of the inadequacies, encountered in the classical Charpy-V impact test evaluation, will be discussed. Key experiences with reconstitution as a central issue will be indicated.

RECONSTITUTION: GENERAL PRINCIPLE

The technique of reconstitution, or construction of compound specimens, consists of attaching additional material around a material of interest - the insert material - to prepare a test specimen of standard dimensions. An example is the standard 10x10x55mm Charpy-V specimen reconstituted from a broken Charpy-V half by adding two end pieces. Here the interface can be obtained with rather simple welding techniques, whereas for more complicated shapes - like Compact Tension (CT) specimens - only sophisticated weld techniques have been successfully applied. Some examples derived from broken C_V-samples are shown in Figure 1 [5].

RECONSTITUTION TECHNIQUES

More than 20 years ago, the electron-beam welding technique was used at Siemens/KWU to prepare fracture toughness compact tension specimens from small amounts of 'insert' material [6, 7, 8]. Gradually, the amount of insert material was reduced and the technique was adapted to reconstruct C_V-specimens from broken standard Charpy-V samples [9]. Alternative preparation techniques for Charpy-V reconstituted specimens were evaluated. This led in the early 1980s to the application of arc stud welding on broken

Charpy-V halves at Batelle Columbus Laboratories [10, 11]. The latter technique was adopted and improved by several research institutes [12-15]. Moreover, it was applied to other geometries, e.g. Charpy-size tensile specimens [16, 17] and mini Charpy-V samples (dimensions 3x4x27mm) [1]. Parallel developments led to application of projection welding, a resistance welding technique, to reconstitute C_V-specimens [18]. The upset butt

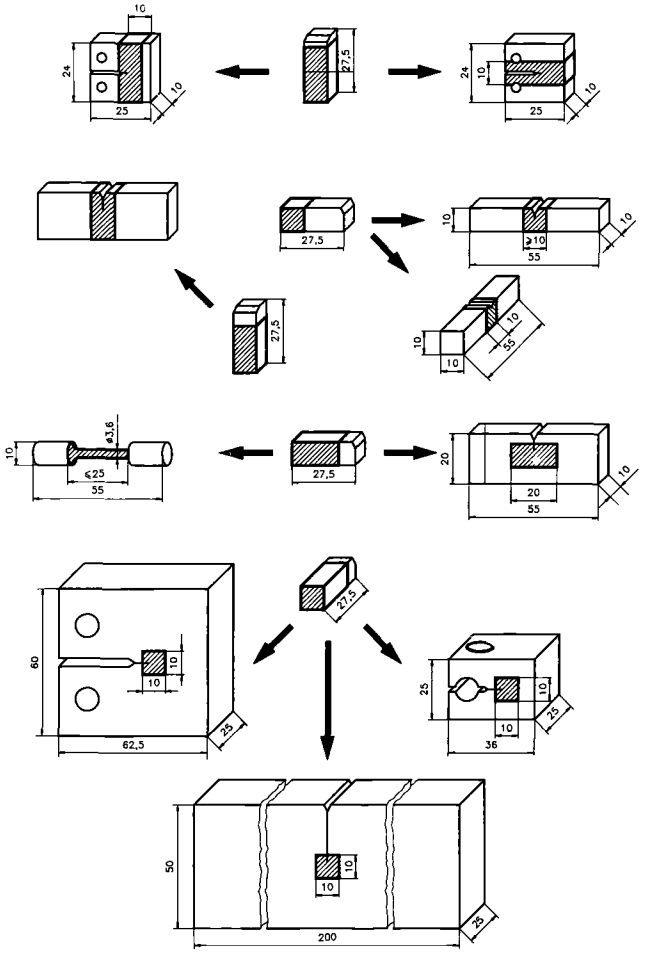


FIG. 1--Specimen geometries reconstituted from broken Charpy-V halves. Stud welding, projection and upset butt welding are limited to C_V-type reconstituted specimens. Electron beam welding and, in principle, laser welding are suited for all geometries (figure partly taken from reference [5]).

welding technique for Charpy-V reconstitution - a variation of projection welding - was introduced in 1991 [19, 20] and more recently the first results of laser welding on broken C_V-halves were reported [21]. Some preparation techniques were less successful: for instance, the gluing of end tabs to insert material remains limited to the precracked Charpy-V impact specimen geometry [22] and to relatively low test temperatures.
An excellent overview of the welding techniques that can or cannot be used to reconstitute Charpy-V type specimens (and in some cases also other geometries) can be found in reference [10]; here, the discussion will be limited to the advantages and limitations of those techniques that have been successfully applied in hot-cells.

Electron beam welding

Electron beam welding (EBW) is the most versatile reconstitution technique, but along with laser welding the most expensive. Electron-beam welding can be applied to all geometries (see Figure 1), from CT to Charpy-V specimens: the electron beam with energy densities up to 10^8 W/cm^2 allows deep penetration and creates homogeneous narrow V-shaped welds (for Charpy-V specimens the weld width varies between .3 and 1mm, the heat affected zone (HAZ) has similar dimensions on either side of the weld) [23, 24]. Small weld widths and HAZs are important in small insert applications. In most situations the components are welded together without additional finishing requirements. However, by preference, the specimens should be welded from two sides - each time to half the thickness of the material - to avoid bending of the specimen. Since EBW is performed in a vacuum chamber, hot-cell application is tedious and needs a lot of space. Precautions, also due to the vacuum conditions, must be taken to keep the insert temperature low enough during and after the welding: a cooled sample clamping system and a time gap between the two reconstitution welds are necessities [24].

Laser welding

Laser welding (LW) should be equivalent to EBW with the advantage that no vacuum is needed for this technique. This provides for easy adaptation to hot-cell environments. The technique has not been widely applied due to the large equipment costs. First results have been reported [21].

Arc stud-welding

The stud-welding (SW) technique can be applied for simple geometries like C_V-specimens or tensile specimens. Application to CT-type specimens appears to be difficult and has not been performed. The equipment is based on a commercial stud gun, is moderately priced and can easily be installed in a hot-cell [13, 15, 25]. An arc is initiated between the end tab (stud) and the insert piece, melting the surfaces of both pieces. Subsequently, the stud is projected onto the insert and both materials fuse. This process takes place in an argon atmosphere to avoid oxidation of the weld. Since the input energy is a few kJ in about 100 msec, additional cooling of the insert piece is required. To insure proper alignment and square sectional welds, the stud is slightly oversized; therefore, the reconsti-

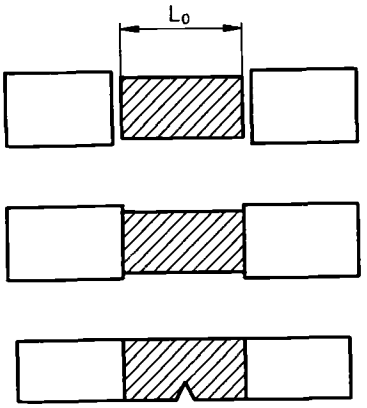


FIG. 2--The C_V reconstitution procedure [2]

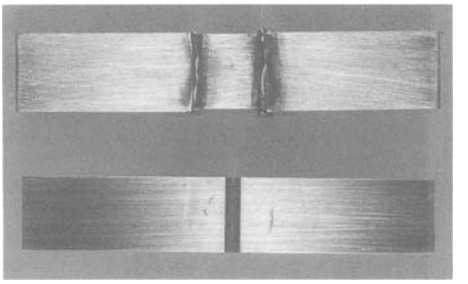


FIG. 3--C_V reconstituted samples [28] The upper picture shows the sample before finishing, the lower after finishing

tuted specimen needs mechanical finishing - a schematics is shown in Figure 2 [2]. Another example of stud-insert arrangement can be found in reference [26]. The welds are symmetric, have a maximum width of approximately 2mm and may contain small gas bubbles. However, they do not influence the fracture behaviour of the reconstituted specimen. The HAZ extends about 1mm to either side of the weld.

Projection and upset butt-welding

With projection welding, the welding machine is a spot/projection welder, with typically a 50 kVA transformer and a projection load of some 450 kg/cm^2 [18, 27]. A welding cycle consists of several phases: a load and 'squeeze' period, a current flow for a preset time, a force hold period and a release of force stage. The insert pieces are chilled during the welding and show a temperature behaviour similar to the other welding techniques. The fusing is nearly 100% with porosity-free welds. Oversized end tabs are needed to assure alignment and allow final machining to ASTM dimensions. No exact information on welding time is reported [27]. The total width of the weld and HAZ zone is between 2 and 3mm, primarily positioned in the end tab material. The reported results [18, 27] are similar to those of arc stud-welding. The welding equipment can easily be installed in hot-cell.

A modified upset butt-welding technique - very similar to the projection welding technique - has been used for the reconstitution of C_V-specimens [19, 20]. The results are again similar to those of arc stud-welding. A welding cycle consists of three steps, that can be adjusted in time: preloading (~ 350 kg/cm^2), preheating and fusing. The total energy input

for preheating and fusing is some 30kJ in about 400 msec (75kVA transformer) [20]. Cooling is assured by liquid nitrogen cooled copper clamps. Oversized end tabs are used to assure final alignment of the reconstituted C_V-specimen. The weld quality and final specimen quality are very good, as can be seen on Figure 3 [28]. The welds are very homogeneous, as was demonstrated with X-ray photography. Although the energy input seems very high, the temperature distribution within the insert is similar to those of the other welding techniques. The installation can readily be realized in a hot-cell.

THE RECONSTITUTION PROCEDURE FOR C_V-TYPE SPECIMENS

The 'Standard Guide for the Reconstitution of Irradiated Charpy Specimens', ASTM E1253-88 [4], stipulates a number of guidelines to reconstitute irradiated broken C_V-material. This guide was written with limited experience on reconstitution, impact testing of reconstituted specimens and analysis of the test results. In 1992, an ASTM Round-Robin effort on reconstitution was initiated on un-irradiated base and weld material to get documented data on variables including: the reconstitution technique, insert length, impact tup geometry. A detailed procedure, partly based on ASTM E1253-88, has been written [3]; the reconstitutions have been performed by 10 international organisations and the first results on instrumented impact testing of the reconstituted specimens have been reported [29]. The results will contribute to review ASTM E1253-88, that already now sets important principles, some of which will be discussed below.

Qualification of the reconstitution technique according to ASTM E1253-88 [4]

The ASTM E1253-88 guide states in paragraph 4.2.5. that '*the length of the specimen insert shall be sufficient to provide a minimum of 7mm of such material (where 'such' refers to material that underwent no plastic deformation during previous testing), between the notch root and the (closest) heat affected zones of the reconstituted specimen*'. This statement is based on micro hardness testing, metallography and optical comparator measurements of the plastic deformation zone of broken full-size specimens tested on the upper shelf [30]. Not mentioned in the guide is that in practice, considering the loss in insert length L_0 (Figure 2) due to melt off during reconstitution (<1mm) and the typical 1mm width of the HAZ [15, 24, 28], this puts the insert length before reconstitution to 17mm. On the other hand, many experiments have been carried out with reconstituted specimens with insert lengths down to 10mm (before welding). Here substantial losses, due to the constraint of plastic deformation at the weld interfaces - see below, have been detected [15, 20, 23, 31]. However, the resulting transition curves from these reconstituted specimens are, from regulatory viewpoint, always conservative [26]. Moreover, these constraint effects are rather well understood now and as will be seen, there exists a methodology to account for these losses [32, 33]. Latter arguments were not known when the guide, that states in paragraph 5.1.4 that '*the reconstitution technique shall yield impact properties (absorbed energy, lateral expansion and fracture appearance) equivalent to those of original testing*', was issued. Since the development of the standard guide, it has been established that the shear fracture appearance is, at least for inserts greater or equal to 10

mm, independent of the reconstitution and that other properties of the instrumented impact test spectrum may also remain invariant [34, 35].

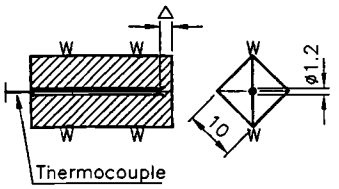
On dimensional control the guide stipulates in 5.1.2 that '*the reconstitution process shall produce specimens conforming to the dimensional requirements of ASTM E23*'. In practice this means that with any welding technique oversized end tabs are needed in order to assure proper alignment. However, the welds (except for EBW and LW) are 'never' 100% cross-sectional; an element out of the scope of ASTM E23.

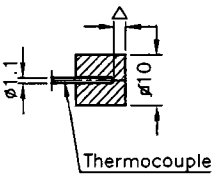
Important but incomplete guidelines are given for the heat input into the insert piece. The guide says, respectively, in 4.4.1 and 4.4.2 that '*to preclude irradiation damage annealing, heat input during the welding shall be controlled such that the temperature of the central 10 mm portion of the reconstituted Charpy-V specimen does not exceed the prior metal irradiation temperature any time during welding*' and '*... temperature records shall be made, using thermocouples, during welding on the first and last specimens of each set of Charpy specimens or on dummy specimens preceding and following welding of the set*'.

The first statement says that one has to measure the temperature at 5mm from the future notch, but it does not state how to measure the temperature. Different techniques are in use: thermocouples spot-welded on the surface of the insert, sheathed and grounded thermocouples tightly stuck into a drilled hole in the insert or brased into the insert, uninsulated thermocouple wires pressed between two spot welded diagonally-split halves of a dummy insert. Of importance are the correct highest temperature measurements and, correlated with it, the reaction time of thermocouple-measurement chain. It is clear that the temperature has to be measured in the centre of the dummy specimen. Given that the measurement chain reacts fast enough, thermocouples pressed into a drilled hole can result in non-conservative temperature measurements [12], whereas sheathed thermocouples carefully brased into the insert can give - due to the thermal insulation - systematically low temperature measurements (approximately 50°C in the range of interest) [36]. The fragile instrumented split bar system [2] - depicted in Figure 4 - is very sensitive, has a fast reaction time and gives good temperature measurements. The temperature measurements plotted in Figure 4 - taken from reference [2] - demonstrate that the temperature requirement, being below the reactor operating temperature of some 300°C, is fulfilled with this stud-gun welding set up at some 3mm from the welding surface. This number has also been confirmed for EBW of Charpy-V specimens by the Siemens/KWU measurements (spot-welded thermocouples on insert) [23]. The grounded thermocouple, carefully brased into the dummy insert, gives comparable results. The design and some measured temperatures are shown in Figure 5 [17]. This configuration has been used in the ASTM Round Robin for Reconstitution.

The other dimension is the length of time during which the 'high' temperatures are reached in the central piece: with EBW, stud-gun and upset butt welding with proper cooling these times are in the 1 to 3 second range [2, 17, 20, 24]. The question is whether some irradiation damage can be annealed in this short time. Hardness measurements on the irradiated insert material before and after reconstitution can be an indicative parameter for damage re-

covery and or metallurgical changes. Experiments on reconstituted 10mm size un-irradiated [23, 24, 26] and irradiated [26] insert pieces - that can only fulfil the ASTM temperature requirement in the central 4 to 5mm of the insert - do not show any change in hardness between the notch and the HAZ. The impact tests do also not show substantial changes in the fracture energy or lateral expansion that cannot be explained by plastic constraint due to the reconstitution welds [26]. Therefore it appears that the statement of





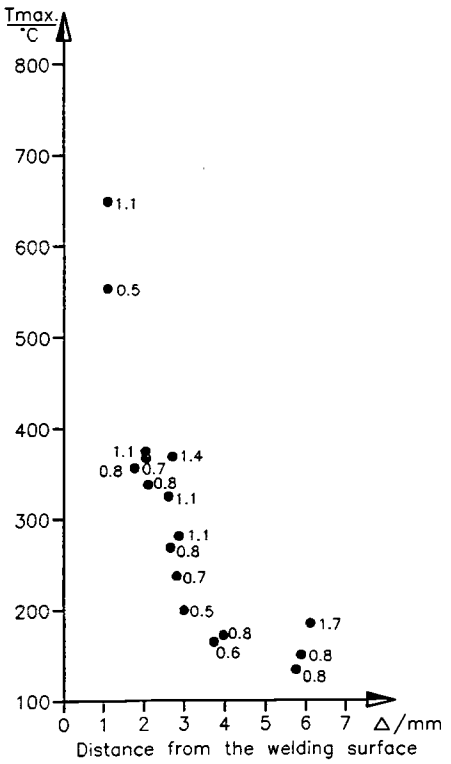


FIG. 4--Temperature measurements with the split bar system [2]. The input energy is indicated (in kJ) next to the data points.

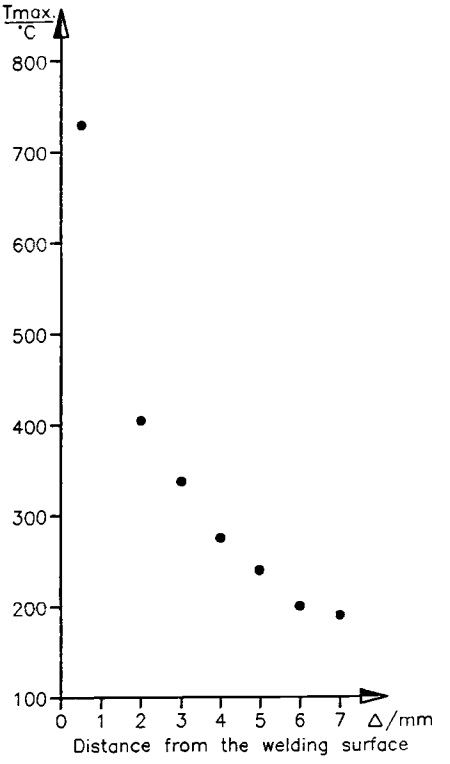


FIG. 5--Temperature measurements with the brased grounded thermocouple. The input power is about 5kJ.

paragraph 4.4.1 of ASTM E1253-88 could be relaxed. This argument is also supported by fracture toughness measurements on respectively unirradiated and irradiated C_V-specimens with insert lengths as small as 6 and 5mm [2].

The statement of paragraph 4.4.2 introduces a basic principle in the reconstitution procedure, that is respected by the reconstitution groups: all give preference to use dummy specimens that can in fact be prepared in series.

Some recommendations for the reconstitution procedure of C_V-type specimens

Material preparation -- *Insert:* if already tested material is used, remove the plastic deformed zone but keep in mind that 2mm of material is 'lost' in the welding process (weld + HAZ). If inserts become smaller than 15mm and the reconstituted specimens will be *impact* tested according to ASTM, use the same insert length for all inserts. This condition can be relaxed for the ISO *impact* test configuration (see later). The notch is added after reconstitution. Make hardness measurements over the full length of the inserts. *End tabs:* well-aligned specimens need oversized end tabs to be used. Except for EBW, a better cross-sectional weld is obtained when oversized tabs are used. If possible, make hardness tests.

Temperature control -- Make temperature records, before and after a reconstitution campaign, on dummy inserts. Use fast electronics (transient recorder). The dummy inserts should be centrally loaded, 5mm from the future notch, with a calibrated thermocouple - or grounded and brased into the insert, or clamped with open end wiring. If insert lengths smaller than 12mm are used, the thermocouple should be positioned at 3mm from the welding surface.

Reconstitution -- The narrowest welds, and therefore the smallest loss of insert material, are achieved with EBW. This can have importance if small insert lengths are used. With the other welding techniques, at least one more millimetre of virgin material is lost.
Maximum chilling of the insert should be foreseen and a minimum power input to obtain a proper reconstitution weld (more power is needed when larger end tabs are used; however, due to the larger end tab volume, larger power does not automatically mean higher insert temperature).
For the mechanical finishing use an electric discharge or a milling machine. Especially for small insert lengths, it can be helpful to etch the reconstituted specimen, before cutting it to length, to determine the

notch position. Make hardness tests on the reconstituted specimens to look for deviations from the original insert hardness.

Fracture test -- The optimisation of insert length depends on the kind of test. It has been demonstrated that for fracture toughness measurements on un-irradiated precracked side-grooved C_V-size specimens, the insert length can be reduced down to below 10mm [2, 37]; when irradiated material is used it is conservative to go not smaller than 10mm to avoid temperature effects from the reconstitution [2].
For Charpy-V impact testing, it is sometimes necessary to use 10mm inserts. The effects on the impact fracture properties of the reconstituted specimens are - as explained below - fairly well understood and are primarily not a consequence of material changes. Moreover, when instrumented impact testing is adopted, invariant properties of the load diagram can be recorded [34].
Hardness testing should reveal the extent of the plastic zone after the test.
For C_V-size tensile specimens, the insert length should be long enough to assure that the reconstitution welds lie in the gripping area of the specimens [17].

RECONSTITUTION: CURRENT UNDERSTANDING OF INFLUENCES ON TEST BEHAVIOUR

The technique of reconstitution is recognised as a cornerstone for future plant life management. The prerequisite is to optimise and qualify the technique extensively for un-irradiated and irradiated pressure vessel steels by varying different material and experimental parameters, in order to guarantee continuity with the extensive surveillance data base on pressure vessel steels obtained from non-reconstituted specimens. Guided by material-saving arguments, typical reconstitution experiments and a desire to understand the test behaviour of reconstituted specimens, several research labs have contributed to the knowledge presented below.

Standard size 10x10x55mm Charpy-V impact specimens

The most frequent application of the reconstitution technique is the reconstitution of broken standard-size Charpy-V specimens. Several impact-test qualification studies have been carried out on reconstituted specimens made of unirradiated and irradiated plate and weld inserts with lengths of approximately 20mm [9, 13, 15, 20, 31]; in general no deviations from the standard impact quantities - dial energy, lateral expansion and shear fracture appearance (SFA) - as determined from full-size specimens, have been detected. The obvious parameter to vary is the insert length and to look for influences on the fracture behaviour. The main reason for doing this is to maximise the statistics on the material [24], but in a number of situations like, Charpy notch reorientation [26, 32], in situ sampling of

material [1, 2], or simply because not enough material is available (typically: broken C_V weld specimens), one is forced to use smaller inserts. By gradually changing the insert length, one can detect influences of the material and test conditions on two of the properties that are normally recorded: the fracture energy and the lateral expansion. A useful insert size is 10x10x10mm since it allows one to reorient a Charpy sample, as can be seen from Figure 1.

Reconstitution and insert length-- When reducing the insert length L_0 of Figure 2, the reconstitution welds are closer to the notch, and the plastic deformation that occurs during the impact test, can be constrained by the reconstitution welds. This constraint of plastic deformation can be determined by taking hardness measurements on broken Charpy samples. Figure 6 illustrates the deformation pattern for impact tests performed at upper shelf temperature to obtain the maximum plastic deformation [23, 24]. The left part shows a map of hardness measurements marked on a broken Charpy half. With the reference hardness value taken at the undeformed region near the notch, the extent of the plastic region within

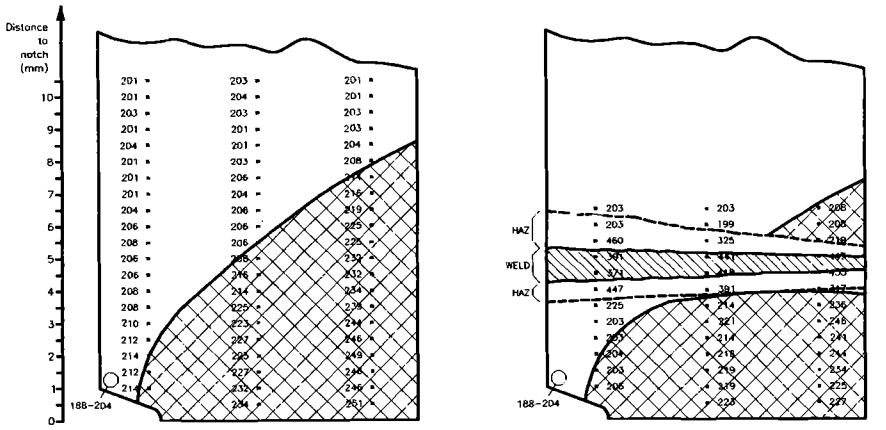


FIG. 6--Deformation pattern of broken Charpy-V specimens, tested at upper shelf temperatures, derived from Vickers hardness measurements. The left figure shows the plastic deformation of an as-received specimen, the right shows an electron-beam welded specimen with 10mm insert length (concept adopted from reference [23]).

the Charpy specimen can be determined from higher hardness values. The plastic zone extends 9mm from the notch, showing that - as indicated before - the plastic zone in reconstituted specimens with 20mm inserts will not be influenced by the reconstitution welds. The right part of Figure 6 shows the hardness values for an electron-beam reconstituted sample, with insert length 10mm, tested under identical conditions as the as-received specimen. Here the contour demonstrates that the plastic zone is reduced by the reconstitution weld: the weld and HAZ region remain undeformed and the plastic zone in the stud re-

gion is reduced. As no energy needs to be spent to deform these zones, the net effect on the impact properties of the Charpy specimen will be a reduction of its fracture energy. This reduction can clearly be seen in several figures of reference [26, 32], and in Figure 9 of the next paragraph. The lowering in energy creates an apparent shift in temperature after reconstitution. The energy reduction disappears gradually as the length of the insert is increased [15, 20]. The reduction also occurs for the lateral expansion, but no influence is detected on the SFA behaviour - see figures of reference [26, 32].
For small insert lengths, the width of the welds, or the welding technique, becomes important: it is clear that with electron-beam welding the remaining length of the insert after welding is longer than with the other welding techniques. Hence, the loss in fracture energy and lateral expansion will be less when going to very small insert lengths; a nice example is given in reference [23, 24]: C_V-specimens made with electron-beam welded inserts of 11mm length and tested under ISO conditions show no deviation between as-received and reconstituted specimens: this led to the proposal by [23] to take 12mm as a minimum insert length for C_V-specimens. This 12mm insert length does, in general, as will be explained below, not work for other welding techniques and/or tests under ASTM E 23 conditions [15].

Reconstitution and tup geometry-- Another source for energy differences with small inserts comes from the impact hammer geometry - ISO or ASTM - used for breaking the reconstituted samples [15, 23, 38, 39]. These geometries are compared in Figure 7. The edge of the ASTM tup can introduce Brinell deformation on the impact side of as-received samples.

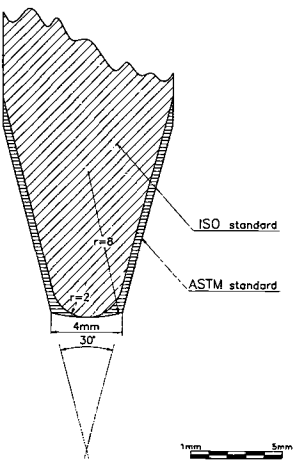


FIG. 7--The ASTM versus ISO tup geometry

This is shown for 22NiMoCr37 specimens in Figure 8. In going from reconstituted inserts of length 18mm to reconstituted samples made of 10mm inserts, there will come a moment

(~14mm) when the hard weld zones will interact with the ASTM-tup and the Brinell deformation will gradually disappear. Accordingly, not only the growing loss due to constraint of plastic deformation is present, but an additional reduction in the fracture energy is detected due to the tup-weld interaction. The smooth ISO-tup does not suffer from this effect as the Brinell deformation is not introduced on as-received nor on reconstituted samples - as is depicted in Figure 8. This combined effect of plastic flow constraint (ISO and ASTM) and hammer influence (only ASTM) on the Charpy energy of 22NiMoCr37 steel is shown in Figure 9 for 10mm inserts (most data come from the excellent thesis work of reference [38]). The as-received upper shelf energy for tests with

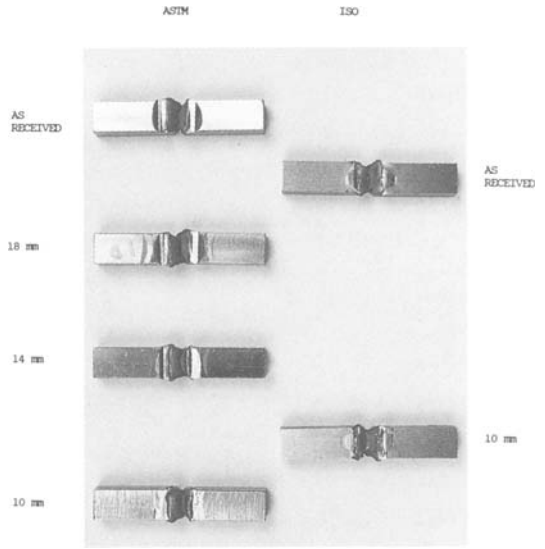


FIG. 8--The influence of the impact tup geometry on the impact side of the Charpy samples. Various insert lengths are depicted for ASTM and ISO tups. Remark the gradual disappearance of the 'lips' produced by the ASTM tup with decreasing insert length. The ISO-tup does, at any stage, not induce such Brinell type of deformation.

an ASTM tup is higher than for a ISO tup: this well-known effect [40, 41, 42] is mainly due to the hammer-anvil geometry, but also because the ISO tup usually pulls the Charpy-V sample through the anvils without fully breaking it. The energy curves of the reconstituted samples with 10mm inserts coincide for the two tup geometries, as the plastic flow is constrained equally for both hammer geometries and as the hammer-sample interaction becomes similar. This demonstrates the advantage of using a ISO tup: the only effect that is

detected, when varying the insert length (typically below 12mm), is the constraint of plastic deformation (unless test temperatures equal to or above 300°C are used).
The tup effect is material dependent: it is less apparent for HSST-03, where losses mainly come from plastic constraint. In fact, the shape of the instrumented Charpy-V load-time curve and the inspection of the broken Charpy halves reveal whether the hammer effect is present [25].
The SFA for the ASTM and ISO tests on 22NiMoCr37 - illustrated in Figure 10 - is, however, again independent of the impact hammer. The shear fracture appearance gives information on a localised region, i.e. the fracture plane under the notch. The lateral expansion and fracture energy depend on the volume surrounding the notch, a volume restrained by the weldments.

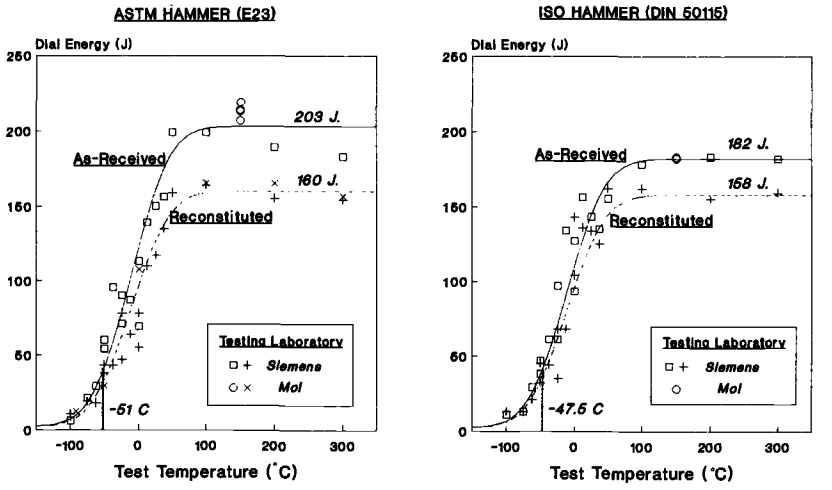


FIG. 9--The combined influence of confined plastic deformation and impact tup geometry on the transition curves of reconstituted 22NiMoCr37-material (10mm insert length). The loss in energy after reconstitution is limited to restraint of plastic deformation for the ISO impact configuration, whereas an additional reduction due to the disappearance of Brinell-type of deformation on the impact side of the C_V-specimen occurs for the ASTM-tup. The tup effect is material dependent.

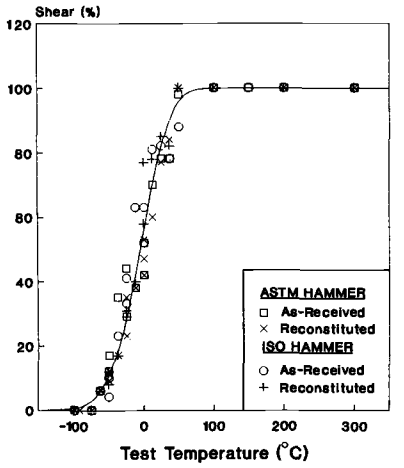


FIG. 10--The SFA-behaviour (here shown for 22NiMoCr37 material) is independent of the confined plastic deformation and the tup geometry.

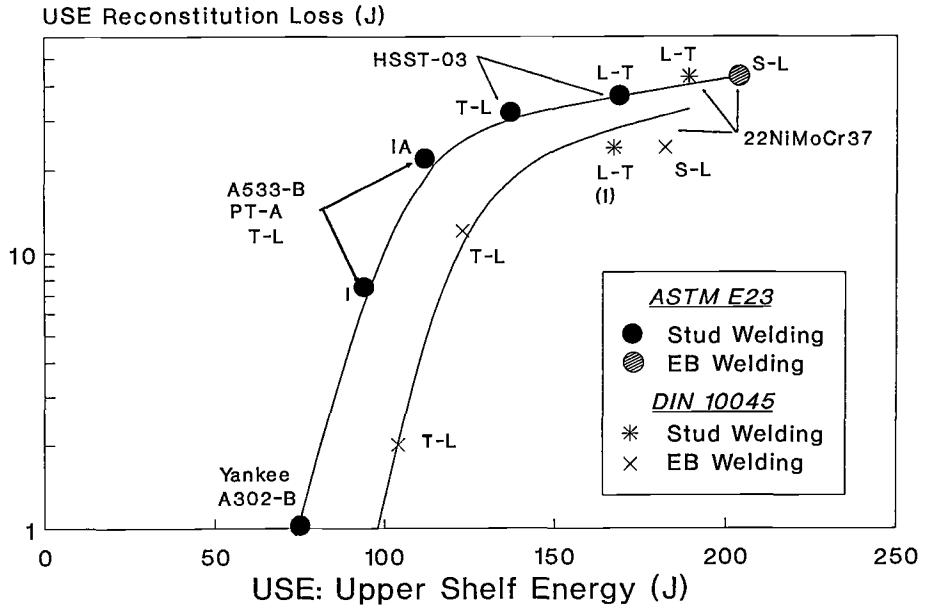


FIG. 11--The drop in USE due to reconstitution as a function of USE for 10mm insert length.

Reconstitution and loss of C_V-impact upper shelf level-- The application of the reconstitution technique on 10mm long inserts of materials with different upper shelf energy reveals that the maximum energy loss due to reconstitution, recorded after testing at upper shelf temperatures, depends on the upper shelf energy of the samples [33]. This is illustrated in Figure 11, where the spline fits through the experimental unirradiated, as well as, irradiated data indicate two other effects: energy losses can depend on the hammer geometry (and material) and there is a threshold USE below which no losses occur, due to the reconstitution of 10mm inserts, (an example is given in Figure 20 of reference [43]). An important application of the reconstitution technique is the possibility to re-orient C_V-specimens from the strong, longitudinal L-T direction to the weak, transverse T-L orientation. Many older plants have data on L-T oriented surveillance specimens, but current regulations require the knowledge of the T-L transition properties of the material. Reconstitution of 10x10x55mm blocks (machined from L-T (broken) surveillance material) allows one to obtain T-L reconstituted values. A qualification study on HSST-03, L-T and T-L as-received material [32] first determines the reconstitution energy loss as function of temperature in the L-T direction and adds this information to the reconstituted T-L data to obtain the projected T-L transition curves. These are in good agreement with the test results on the original T-L material. This methodology works well when the original L-T and T-L upper shelf energies are similar. However, if the L-T and T-L upper shelves are in the steep region of Figure 11, the loss depends strongly on the orientation of the material and the procedure to determine T-L properties of C_V-specimens becomes more complicated. The reconstituted T-L transition curve represents conservative lower bound of the actual T-L properties of the material. An extensive application of the re-orientation technique as applied to un-irradiated and irradiated C_V-material is presented in another paper of this conference [26].

Reconstitution and the instrumented impact test [32, 34]--The instrumented Charpy impact curve can contain several characteristic load points: F_{GY}, the general yield load; F_m, the maximum load; F_u, the brittle crack initiation load; F_a, the crack arrest load. The change of these values with test temperature constitutes the load diagram of the material. A schematic and more information can be found in Figure 10 of reference [44], but an application for un-irradiated HSST-03 is shown in Figure 12. Two characteristic temperatures, T_I and T_0, corresponding respectively to the onset of ductile crack growth (SFA≠0) and the onset of the C_V upper shelf (SFA reaching 100%), can be determined from the load diagram. Moreover, a one-to-one correlation between the C_V-impact load diagram and the SFA exists, bound by the two characteristic temperatures T_I and T_0. An excellent fit of the experimental SFA-data can be derived from the load diagram with the formula indicated on the SFA plot on Figure 12.
An interesting feature of the load diagram - automatically reflected in the SFA - is the insensitivity to reconstitution and to the hammer geometry. These effects are also illustrated in Figure 12 for the reconstitution of 10mm long inserts of HSST-03 material [34] and examples on 22NiMoCr37 can be found in references [24, 35]. The T_I and T_0 temperatures do not vary after reconstitution but, as seen before, in energy terms the reconstitution can induce an apparent temperature shift. Within a proposed enhanced embrittlement surveillance methodology, where T_I and T_0 are taken as physically-justified

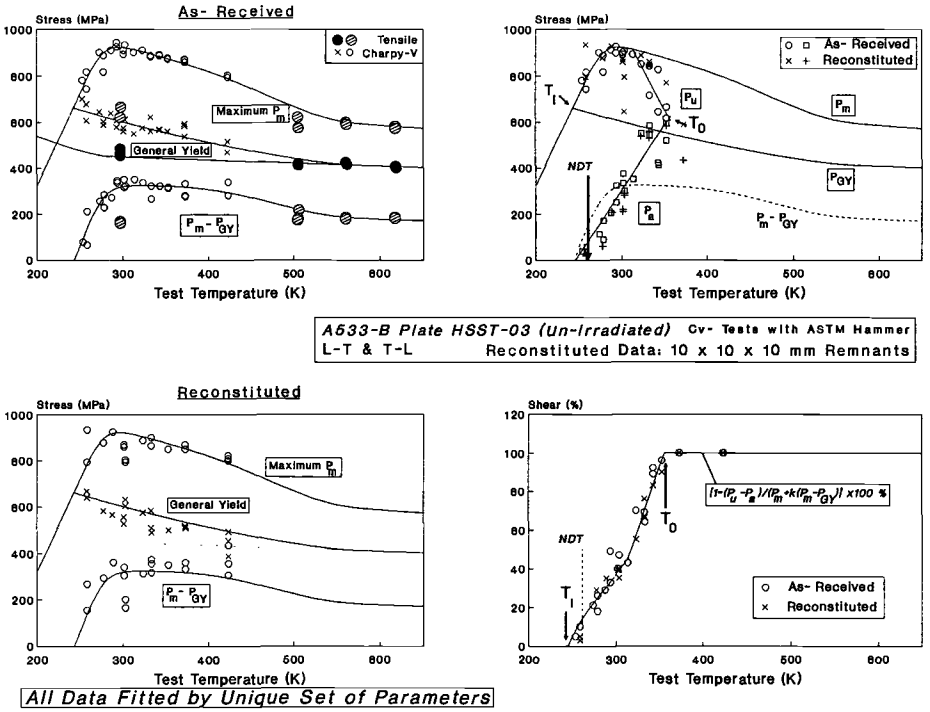


FIG. 12--Invariance to reconstitution of the C_V load diagram and the fracture appearance (the scale and fits need updating, but do not alter the conclusions).

index parameters (instead of the arbitrary 41J level), this invariance due to reconstitution allows a comparison between full-size and reconstituted of different material conditions data (or a mixture of both) [44]. The invariance due to insert length and test geometry conditions allows one to make maximum use of the amount of available material.

Reconstitution and irradiated C_V impact specimens--Until now no distinction has been made between un-irradiated and irradiated materials. The ASTM E 1253-88 guideline was written for irradiated material without experience on irradiated materials, leading to paragraph 4.4.1 of the guide that requires a 10mm insert zone to be less than reactor operating temperatures. This condition can easily be realised with inserts of 14mm or greater and for these situations several studies have confirmed no differences between reconstituted and as-received irradiated specimens [2, 31]. Although the 10mm-below-operating-temperature principle is good, no effects of recovery of irradiation-induced embrittlement on the normally-detected fracture parameters - energy, lateral expansion and SFA - have been detected, even for standard specimens reconstituted with irradiated insert lengths as small as 10mm [26, 43] and mini specimens made from irradiated inserts as small as 8mm [45]. In either case this is confirmed by hardness measurements. The insert

length in effect restricts the plastic flow due to the weldments. The extent of the plastic zone should, however, be reduced for irradiated material as compared with unirradiated steel; consequently, the effect should be less.

In one situation, very different transition curves have been recorded before and after reconstitution of irradiated broken C_V-halves (insert length minimum 20 mm). Doel I and II irradiated broken C_V surveillance specimens, that had been stored at SCK•CEN for about 15 years, were reconstituted and tested. The transition curves of the reconstituted irradiated base and weld material had clearly increased in temperature in comparison to the as-received irradiated condition [46]. The base-metal energy-transition curve is shown in Figure 13: no lowering of the USE (long insert), but a clear temperature shift of about 30°C after reconstitution. To eliminate the reconstitution technique as a contributing factor two actions were taken: the base metal C_V-specimens of the next surveillance capsule were tested and immediately reconstituted, and some of the freshly broken samples were sent to VTT for reconstitution. All reconstituted specimens were then impact tested. As can be seen from Figure 13, there is no difference between the as-received irradiated and reconsti-

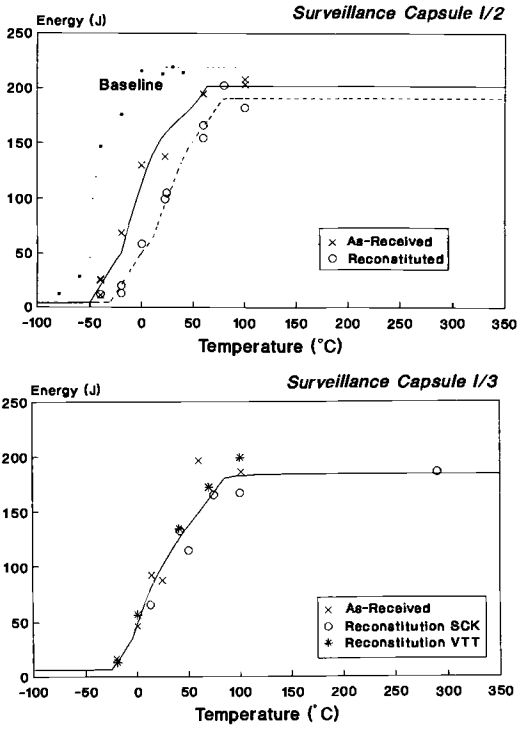


FIG. 13--The data of reconstituted surveillance base metal (reconstituted from half-size broken C_V-specimens) of the Belgian Doel I power plant. The upper part shows the anomaly on the transition curve detected after reconstitution of broken C_V-specimens that were stored for some 10 years at ambient temperature. The lower curve show the as-received and reconstituted results of a recent surveillance capsule. Here the reconstitutions were done by two laboratories and immediately after breaking the as-received specimens.

tuted irradiated specimens, eliminating any bias due to the reconstitution technique. The observed initial temperature shift, is attributed to the long storage time of the broken Doel I & II specimens at ambient temperature [35] and is under further investigation.
Another surprising effect was found with the reconstitution of irradiated 10mm long inserts from the KKP1 power plant; as can be seen on the load diagrams on Figure 22 of reference [26]. Reconstituted C_V-specimens with 10mm irradiated inserts were impact tested with instrumented equipment. The load diagram shows that the work hardening of the irradiated material after reconstitution has been restored (no temperature shift is induced). Here, modelling arguments exist, based on experimental data, that relate the phenomenon to the thermal activation of an irradiation-induced defect in the irradiated material after long storage time at ambient temperature [35]. However, the consequences on the fracture energy of the irradiated reconstituted material are only a few Joules [26]. Again, the effect is not believed to be a consequence of the reconstitution procedure.
Currently, plans exist to look at the sensitivity of the reconstitution technique to thermal annealing of irradiation induced defects. Here, irradiated highly-irradiation-sensitive material will be reconstituted and compared to the original irradiated C_V-data.

Reconstitution and other Charpy type specimens

Three Point Bend (3PB) fracture mechanics specimens--Current assessments of toughness of RPV material is directed toward measurement of static fracture toughness properties using C_V-type specimens. The C_V-specimens used for these purposes are pre-cracked and side-grooved, in order to, respectively, promote stable crack growth and parallel development of the crack front. Side-grooving of Charpy-V specimens leads essentially to plane strain conditions in the notch plane. Three point bend tests on these samples act on the material concentrated in the notch plane. Consequently, the volume that undergoes plastic deformation during the toughness test will be smaller than in the C_V-impact test. Reconstitution should therefore be possible with small insert lengths without influencing the results of the fracture toughness measurements. This knowledge has led several investigators to look at the potential of the reconstitution technique to obtain fracture toughness values using small amounts of material [2, 37, 47].
Limited testing, at upper shelf temperatures, on un-irradiated HSST-03 material revealed that there was no difference between the fracture toughness value of 'as-received' C_V-specimens and reconstituted specimens with 10mm inserts [47]. A far more advanced qualification study [2] was performed on JRQ-material, an irradiation-sensitive A533B-type Japanese forging prepared for the IAEA Coordinated Research Program for 'Optimizing of Reactor Pressure Vessel Surveillance Programmes and Their Analysis', phase 3. Figure 14 and 15 show fracture resistance curves for C_V-specimens of JRQ-material, 3PB tested in, respectively, un-irradiated and irradiated condition. The variable in both plots is the insert length L_0 used in the reconstitution process. The figures show that the 'as-received' ductile tearing curves can be reproduced from reconstituted specimens with very short insert length: for un-irradiated material about 6 mm, for irradiated material 5mm. As irradiated material is harder than unirradiated material, the plastic deformation zone is smaller and shorter inserts can be used. In order to prevent a thermal annealing from the reconstitution technique on the irradiated material, inserts of 10mm length are

recommended for this condition [2]. The same authors validated the reconstitution technique for brittle fracture initiation K_{Jc} on un-irradiated and irradiated JRQ-inserts of 10 and 12mm. The results fall within the scatter band for the as-received data. This qualification study was the basis for the characterisation of the fracture toughness properties of a base metal trepan taken from the Novovoronesh Unit-1 PWR [2]. Dimensional limitations of the trepan and material efficiency necessitated the application of the reconstitution technique. An independent study of the fracture toughness of Charpy-size reconstituted specimens was reported in reference [37]. Here different materials and material conditions were investigated for different insert lengths: using both a baseline condition and a heat-treated condition representative of an embrittled RPVS. The conclusions are that 5mm insert lengths of baseline material and 3mm lengths for the heat-treated give identical J-values as for full-size specimens condition (although the latter has more scatter). These results are even better than the Finnish results on JRQ [2]; the reason might be the high density welding technique used (no specifications were given [37]). The authors also investigated the dependence of the fracture toughness results of the insert material on the flow properties of the end tabs used. Their conclusion is that it does not influence the J-values.

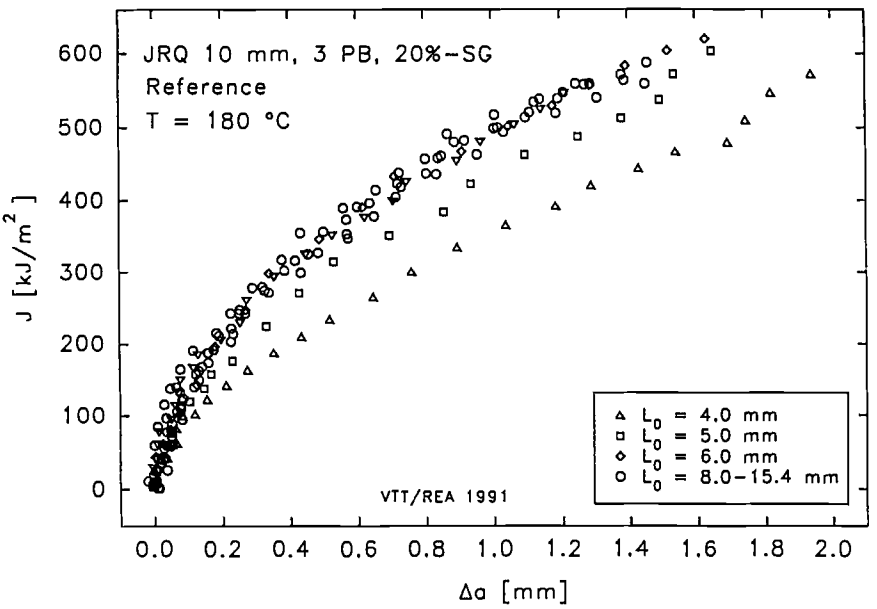


FIG. 14--Fracture toughness testing on un-irradiated reconstituted C_V-specimens [2]

C_V-size tensile specimens--Small tensile specimens have been constructed with EBW [48] and SW [16, 17] for different applications. The mini EBW-specimens (insert length between 10 and 30mm) were used in creep and low cycle fatigue testing, and give similar re

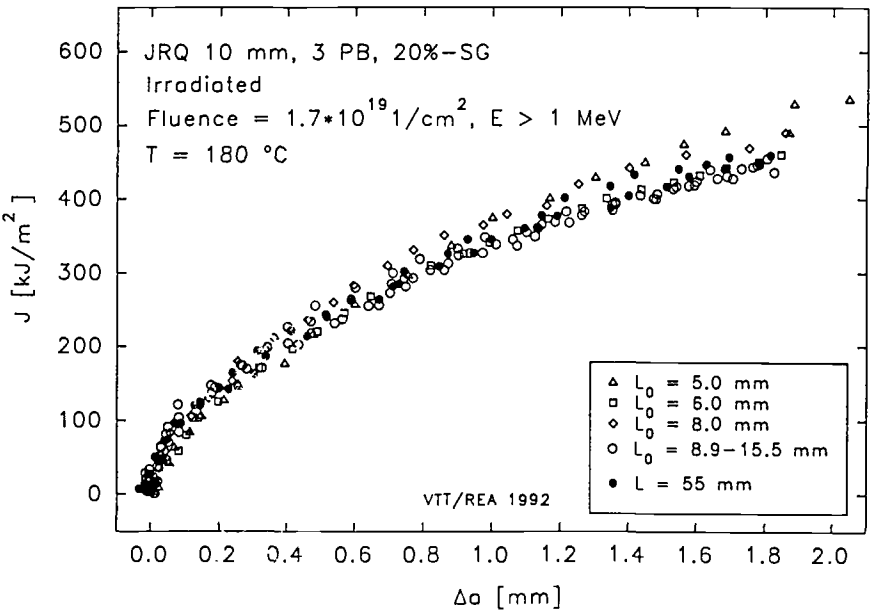


FIG. 15--Fracture toughness testing on irradiated reconstituted C_V-specimens [2]

sults as subsize standard specimens[48]. The C_V-size tensile specimen was stud-welded starting from broken C_V-halves and has been qualified against the ASTM E8 defined Pin-Loaded Tension Test Specimen with 2 inch gage length; a specimen commonly present in surveillance capsules. After qualification, the reconstituted specimen size was used to determine baseline tensile properties of un-irradiated base and weld surveillance material of Nuclear Power Plants (NPP) [16, 17].

Mini C_V-specimens--Reconstituted mini C_V-specimens of 3x4x27mm (ISO 50115) have been made from trepans taken from the Nord Greifswald Unit 1 and Unit 2 NPP's, to check the recovery after annealing of the NPP's [1, 24]. A qualification program on stud-welded un-irradiated base and weld metal inserts with a length of 8mm was carried out. Figure 16 shows the flat hardness measurements on the insert and the peaked regions for the reconstitution welds of the base metal reconstituted specimen. The temperature profile showed that 350°C was reached at 2mm from the notch. Charpy-V impact testing with a ISO tup configuration revealed no difference in the impact properties from as-received specimens [24]. Reconstituted mini C_V-specimens were prepared from the Greifswald Unit 1 irradiated weld material; the insert length varied between 12 and 19mm. The impact tests showed that the transition curve parameters, deduced from testing these small-size reconstituted speci mens and converted to standard C_V transition curve parameters, can lead to valuable conclusions regarding the annealed vessel [1].

The reconstitution of mini C_V-specimens was, more recently, also applied on irradiated inserts of the Loviisa NPP. The results on reconstituted samples of 8, 10 and 12 mm inserts show no difference with original (non-reconstituted) specimens [45].

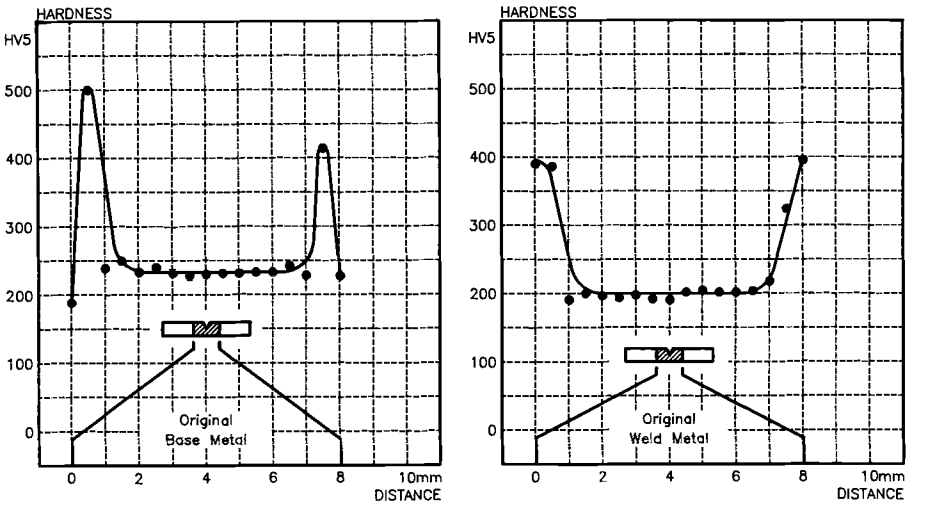


FIG. 16-- Hardness measurements on reconstituted mini C_V-specimens [24]

CONCLUSION

An overview of the status of the reconstitution technique and its assessment for C_V-type specimens is given. This information provides confidence that the reconstitution technique is a technique that will play a major role in future plant life management.

Five reconstitution techniques are being used. All give satisfactory weld quality, weld and HAZ thickness, as indicated by hardness measurements on the reconstituted samples. The technique of electron-beam welding gives the smallest weld widths and thus the largest remaining undisturbed section of the insert material; this can be of importance when small insert lengths are used.

A discussion of the ASTM E 1253-88 guideline leads to the conclusion that some items have to be changed and that others have to be included: the 14mm insert limitation does not take the weld and HAZ widths into account; assessment of small insert lengths should be included into the guide; proper guidelines should be given regarding how to measure the temperature distribution within the insert piece; no evidence has been found that requires the temperature of the insert piece not to exceed the reactor operating temperature (say, up to 450°C) for a few seconds.

The reconstitution and its assessment depends on a number of parameters:

1. *the insert length:* small insert lengths give rise to constraint of the plastic deformation at the reconstitution welds during the impact test. This results in reduced fracture energy and lateral expansion of the sample; the SFA is invariant to insert length.
2. *the impact tup configuration:* the ASTM tup geometry can introduce Brinell deformation on the impact side of an as-received C_V-specimen. With reconstituted specimens, the proximity of the reconstitution welds can prevent this type of energy consumption and thereby reduce the measured impact energy. This effect is material dependent and can occur when the insert length is smaller than 15mm. The ISO-tup does not suffer from this effect. This tup effect also influences the lateral expansion, but not the SFA.
3. *the C_V impact upper shelf:* for a fixed small insert length, the loss in energy (and lateral expansion) - due to constraint of plastic deformation - depends on the upper shelf values of the material.
4. *the instrumented C_V impact test:* the characteristic forces recorded during the instrumented impact test are invariant to reconstitution. The behaviour of the load diagram is reflected in the SFA behaviour. This invariance of the load diagram has its application in a broader surveillance approach.
5. *un-irradiated versus irradiated material:* in general, no different behaviour after reconstitution has been detected for un-irradiated or irradiated C_V-specimens. If differences occur - whether from reconstitution or due to other reasons - the load diagram will sense them. More experience is needed with irradiated materials.
6. *other C_V-type geometries:* the reconstitution technique has been applied to construct 3PB fracture toughness specimens, mini tensile specimens and mini C_V impact specimens. All geometries, except the mini tensile, have been validated for un-irradiated and irradiated material. It has been shown that for side-grooved and pre-cracked 3PB specimens, the insert length can be reduced as low as 6mm.

ACKNOWLEDGEMENTS

The author is indebted to those who contributed information for making this paper, in particular: M. Valo from VTT, Finland; E. Klausnitzer (retired) and C. Leitz from Siemens/KWU; Roang-Ching Kuo from INER, Taiwan; X.P. Zhang and Y.W. Shi from Xi'an Jiaotong University, P.R. of China; A. Fabry, SCK•CEN, Belgium. He also wishes to thank all the people of the reconstitution group of SCK•CEN for their technical efforts and valuable discussions. In Belgium, this reconstitution work is supported by Tractebel Energy Engineering.

REFERENCES

[1] Ahlstrand, R., Klausnitzer, E. N., Lange, D., Leitz, C., Pastor, D., and Valo, M., "Evaluation of the Recovery Annealing of the Reactor Pressure Vessel of NPP Nord (Greifswald) Units 1 and 2 by Means of Subsize Impact Specimens," Radiation Embrittlement of Nuclear Reactor Pressure Vessel Steels: An International Review (Fourth Volume) , ASTM STP 1070, Lendell E. Steele, Ed., American Society for Testing and Materials, Philadelphia, 1993, pp. 321-343.

[2] Valo, M., and Ahlstrand, R., "Application of Reconstitution Welding Technique for Studying Base Metal of a Novovoronesh Unit-1 Trepan Sample," Small Specimen Test Techniques Applied to Nuclear Vessel Thermal Annealing and Plant Life Extension, ASTM STP 1204, W. R. Corwin, F. M. Haggag, and W. L. Server, Eds., American Society for Testing and Materials, Philadelphia, 1993, pp. 62-76.

[3] van Walle, E., Pavinich, W., Van Ransbeeck, T., and Van de Velde, J., "Procedure for the ASTM Round-Robin on Reconstitution," available upon request.

[4] "Standard Guide for Reconstitution of Irradiated Charpy Specimens, " ASTM E 1253-88, ASTM, 1988.

[5] Klausnitzer, E., Aβmann, H.-D., Gerscha, A., Hofmann, G. and Leitz, C., "The Use of Micro and Compound Specimens for Investigations at Operating Nuclear Pressure Vessels,", presented at the SMiRT11, PCS 2, Taipei, Taiwan, 1991.

[6] Klausnitzer, E., "Messung der Bruchzähigkeit (KIc) metallischer Werkstoffe mittels Verbundproben," Atomwirtschaft-Atomtechnik, 1971, pp. 190.

[7] Gerscha, A., and Klausnitzer E., "Development of Electron-Beam Welded CT-Specimens for Fracture Toughness Measurements with a Small Amount of Original Material," 6th Annual Information Meeting of the HSST Program, ORNL, Oak Ridge, TN, USA, April 1972.

[8] Klausnitzer, E., "Development of Large Compound-Material Fracture Toughness Specimens," 3th Water-Reactor Safety-Research Information Meeting, Washington DC, USA, October 1975.

[9] Klausnitzer, E., "Elektronenstrahlgeschweißte Verbundproben für die mechanische Werkstoffprüfung," Journal of Materials Technology 7, 1976, pp. 357-364.

[10] Perrin, J. S., Wullaert, R. A., McConnell, P., Server, W. L., and Fromm, E. O., "Reconstituted Charpy Impact Specimens," Report NP-2759, EPRI, Palo Alto, CA, USA, 1982.

[11] Perrin, J. S., Fromm, E. O., Server, W. L., and Wullaert, R. A., "Preparation of Reconstituted Charpy V-Notch Impact Specimens for Generating Pressure Vessel Steel Fracture Toughness Data," Effects of Radiation on Structural Materials: 11th Conference, ASTM STP 782, American Society for Testing and Materials, 1982, pp. 582-593.

[12] Langouche, F., Chaouadi, R., Puzzolante, J. L., Vandermeulen, W., Van de Velde, J., and Van Ransbeeck, T., "Qualification of Charpy Specimen Reconstitution Procedure for Un-Irradiated Specimens," Report R2756, SCK•CEN, Mol, Belgium, 1989.

[13] Valo, M., "Reconstitution of Charpy Specimens," presented at the Workshop on Experience with Testing Reconstituted Charpy Specimens, San Diego, CA, USA, January 1991.

[14] Ahlstrand, J. R., "Neutron Irradiation Embrittlement of the Reactor Pressure Vessel at Loviisa NPS and Measures to Ensure Safe Operation of the Plant," presented at the 4th Nuclear Energy Symposium on The Operation and Maintenance Experiences of Power Plant Units, Paks, Hungary, August 1988.

[15] van Walle, E., Chaouadi, R., Fabry, A., Puzzolante, J.-L., Vandermeulen, W., Van de Velde, J., Van Ransbeeck, T., Klausnitzer, E., and Gerscha, A., "The Reconstitution Effort at SCK•CEN," presented at the Workshop on Experience with Testing Reconstituted Charpy Specimens, San Diego, CA, USA, January 1991.

[16] van Walle, E., Van Ransbeeck, T., Fabry, A., Puzzolante, J.-L., Vandermeulen, W., and Van de Velde, J., "Qualification of Reduced Reconstituted Tensile Specimens," Report R2883, SCK•CEN, Mol, Belgium, 1991.

[17] Van Ransbeeck, T., van Walle, E., Fabry, A., Puzzolante, J. L., and Van de Velde, J., "The Reconstitution of Charpy-size Tensile Specimens," contribution to this conference.

[18] Shogan, R. P., Yanichko, S., E., and Galloway, W., S., "The Use of Reconstituted Charpy Specimens to Extend RE Ginna Reactor Pressure Surveillance Data," Nuclear Technology **72**, 1986, pp. 345.

[19] Kuo, R. C., private communication.

[20] Kuo, R. C., Chu, H. C., and Chen, C. Y., "Reconstitution of Charpy Specimens by Upset Butt Welding," presented at the ASTM E10.02 Subcommittee Meeting in New Orleans, Louisiana, USA, 1992.

[21] Manahan, M. P., Williams, J., and Martukanitz, R. P., "Laser Weld Reconstitution of Conventional Charpy and Miniaturised Notch Test (MNT) Specimens," Small Specimen Test Techniques Applied to Nuclear Vessel Thermal Annealing and Plant Life Extension, ASTM STP 1204, W. R. Corwin, F. M. Haggag, and W. L. Server, Eds., American Society for Testing and Materials, Philadelphia, 1993, pp. 62-76.

[22] Ghomein, M. M., Hammad, F. H., Pachur, D., and Britz, L., "Compound Charpy specimens by adhesive joining," Journal of Nuclear Materials **187**, 1992, pp. 80-88.

[23] Klausnitzer, E., "Detailed Investigations on Reconstituted Charpy Specimens with Insert Lengths down to 10mm," presented at the Workshop on Experience with Testing Reconstituted Charpy Specimens, San Diego, CA, USA, January 1991.

[24] Klausnitzer, E. N., and Hofmann, G., "Reconstituted Impact Specimens with Small Inserts," Effects of Radiation on Materials: 15th International Symposium, ASTM STP 1225, R. E. Stoller, A. S. Kumar, D. S. Gelles, Eds., American Society for Testing and Materials, Philadelphia, 1992, pp. 76-90.

[25] van Walle, E., Fabry, A., Van Ransbeeck, T., Puzzolante J.L., Vandermeulen, W., Van de Velde, J., Klausnitzer, E., and Gerscha, M., "The Reconstitution of Small Remnant Parts of Charpy-V Specimens," presented at SMIRT11, PCS 2, Taipei, Taiwan, 1991.

[26] van Walle E., Fabry A., Van Ransbeeck T., Puzzolante J.-L., Van de Velde J., Tulke K., and Backfisch W., "Notch Reorientation of Charpy-V specimens of the BWR Philippsburg 1 through reconstitution," contribution to this conference.

[27] Williams, J. F., Shogan, R. P. and Albertin, L., "The Optimisation of Insert Size for Reconstituting Previously Tested Charpy Specimens," Pendulum Impact Machine: Procedures and Specimens for Verification, ASTM STP 1248, Thomas A. Siewert and A. Karl Schmeider, Eds., American Society for Testing and Materials, Philadelphia, 1995.

[28] Chu, H. C., Kuo, R. C., and You, W. S., "Reconstitution of RPV Charpy Impact Specimens," presented at the 4th International Topical Meeting on Nuclear Thermal Hydrolics, Operations and Safety," Taipei, Taiwan, 1994.

[29] Nanstad, R, "Preliminary Results on The Round-Robin for Reconstitution," reported at the ASTM E10.02 Meeting, Sun Valley, Idaho, 1994.

[30] Pavinich, W. A., "Basis of the Size Requirements for the Central Test Section in ASTM E-1253-88," presented at the Workshop on Experience with Testing Reconstituted Charpy Specimens, San Diego, CA, USA, January 1991.

[31] Vandermeulen, W., Fabry, A., Puzzolante, J.L., Van de Velde, J., Van Ransbeeck, Th., and van Walle, E., "Charpy Specimen Reconstitution as a Means of Providing Data for Plex Licensing Purposes," Int. Journ. Pres. Ves. & Piping **54**, 1993, pp 89-98.

[32] Fabry, A., Puzzolante, J. L., van Walle, E., Vandermeulen, W., Van de Velde, J. and Van Ransbeeck, T., "Changing the Notch Orientation of Charpy-V Specimens by Stud Welding of Broken Remnants," Report for the Yankee Atomic Electric Company, September 1990.

[33] van Walle, E., Fabry, A., Aït Abderrahim, H., Chaouadi, R., D'hondt, P., Puzzolante, J.L., Van de Velde, J., Van Ransbeeck, Th., and Gerard, R., "Pressure Vessel Steel Research: Belgian Activities," Proceedings of the IAEA Specialists Meeting on Advanced Structural Integrity Assessment Procedures, IWG-LMNPP-94/4, San Carlos de Bariloche, Argentina, 1994.

[34] Fabry, A., van Walle, E., Chaouadi, R., Wannijn, J.P., Verstrepen, A., Puzzolante, J.L., Van Ransbeeck, Th., Van de Velde, J., and Petrova, T., "RPV Steel Embrittlement: Damage Modeling and Micromechanics in an Engineering Perspective," Proceedings of the IAEA/OECD Specialists Meeting on Irradiation Embrittlement and Optimization of Annealing, Paris, France, 1993.

[35] Fabry, A., van Walle, E., Van de Velde, J., Chaouadi, R., Puzzolante, J.L., Van Ransbeeck, Th., and Verstrepen, A., "On the Use of the Instrumented Charpy-V Impact Signal for Assessment of RPVS Embrittlement," presented at the 2nd ESIS/TC5 Workshop, Mol, Belgium, and Report BLG 650, SCK•CEN, Mol, Belgium, 1994

[36] Valo, M., private communication

[37] Zhang, X. P., and Shi, Y. W., "Fracture toughness of Charpy-size compound specimens and its application in engineering," Int. J. Pres. Ves. & Piping **57**, 1994, pp. 91-98.

[38] Berthold, J., and Stübner, F., "Qualifizierung von Kerbschlagbiege-Verbundproben im Vergleich zwischen DIN- und ASTM-Normen," Ingenieur Abschlussarbeit, Siemens/KWU, Erlangen, Germany, 1991.

[39] Klausnitzer, E., Berthold, J., and Stübner, F., "Qualifizierung von Kerbschlagbiege-Verbundproben im Vergleich zwischen DIN- und ASTM-Normen," presented at the 17th MPA-Seminar, October 1991.

[40] Roux, J. H., and Cheviet, A., "Homogeneity of Heavy Section Plates for Reactor Vessels," 3rd MPA-Seminar, Stuttgart, September 1977.

[41] Siewert, T. A., and Vigliotti, D. P., " The effect of Charpy V-notch Striker Radii on the Absorbed Energy," Pendulum Impact Machines: Procedures and Specimens for Verification, ASTM STP1248, Thomas A. Siewert and A. Karl Schmieder, Eds., American Society for Testing of Materials, Philadelphia, 1995.

[42] Tanaka, M., Ohno, Y., Horigome, H., Tani, H., Shiota, K., and Misawa, A., "Effects of the Striking Edge Radius in the Charpy-V Test," Pendulum Impact Machines: Procedures and Specimens for Verification, ASTM STP1248, Thomas A. Siewert and A. Karl Schmieder, Eds., American Society for Testing of Materials, Philadelphia, 1995.

[43] Fabry, A., Van de Velde, J., Biemiller, E.C., Carter, R.G., and Petrova, T., "Research to Understand the Embrittlement Behavior of the Yankee Surveillance Plate and Other Outlier Steels," contribution to this conference.

[44] Gérard, R., Fabry, A., Van de Velde, J., Puzzolante, J.-L., Verstrepen, A., Van Ransbeeck, T., and van Walle, E., "In-Service Embrittlement of The Pressure Vessel Welds at the Doel I and II Nuclear Power Plants," contribution to this conference.

[45] Valo, M., "Verification of Specimen Reconstitution Technique," contribution to IG-RDM5, Sant Barbara, CA, May 1994.

[46] Gérard, R., and Fabry, A., "Integrity Assessment of Doel I and II Reactor Pressure Vessels," IAEA Specialist's Meeting on Integrity of Pressure Components of Reactor Systems, Paks, Hungary, May 1992 (to be published in the Journal of Theoretical and Applied Fracture Mechanics).

[47] Bolton C., private communication.

[48] Lucon, E., Bicego, V., D'Angelo, D., and Fossati, C., "Evaluating a Service-Exposed Component's Mechanical Properties by Means of Subsized and Miniature Specimens," Small Specimen Test Techniques Applied to Nuclear Vessel Thermal Annealing and Plant Life Extension, ASTM STP 1204, W. R. Corwin, F. M. Haggag, and W. L. Server, Eds., American Society for Testing and Materials, Philadelphia, 1993, pp. 311-323.

T. Van Ransbeeck[1] , E. Van Walle[2], A. Fabry[3], J.L.Puzzolante[1], J. Van de Velde[4]

THE RECONSTITUTION OF CHARPY-SIZE TENSILE SPECIMENS

REFERENCE: Van Ransbeeck, T. M. J., Van Walle, E., Fabry, A., Puzzolante, J. L., and Van de Velde, J., **"The Reconstitution of Charpy-Size Tensile Specimens,"** *Effects of Radiation on Materials: 17th International Symposium, ASTM STP 1270,* David S. Gelles, Randy K. Nanstad, Arvind S. Kumar, and Edward A. Little, Eds., American Society for Testing and Materials, 1996.

ABSTRACT: Charpy-size tensile specimens have been reconstituted starting from broken Charpy specimens. Precautions have been taken to prevent fracture in the weld regions of the reconstituted specimens.
Careful qualification of the tensile properties of the reconstituted tensile bars has been established and is in agreement with test results on ASTM/E8-size tensile specimens.
The tensile properties of the unirradiated weld material of the Belgian PWR Doel 2 and of the unirradiated base metal of the German BWR Philippsburg 1 have been determined using this methodology. Both the resulting yield and maximum loads are in agreement with the actual expectations.
Qualification to apply the technique on irradiated specimens is in preparation.

KEYWORDS: reconstitution, Charpy-size specimens, tensile specimens, weld material, stud gun welding.

---

[1]Senior engineer, [2]Senior research scientist, [3]lead scientist, [4]manager, respectively, SCK•CEN, Reactor Materials Department,Boeretang 200, B-2400 Mol, Belgium.

Copyright© 1996 by ASTM International www.astm.org

1. Introduction

The reconstitution technique permits material properties to be determined from a limited amount of material.
Here, the aim is to determine the tensile properties of pressure vessel steel through reconstitution of broken Charpy specimens, The qualification has been done on the French forging steel, 18MND5, in the form of Charpy-size tensile specimens.

2. Test Procedure:

1. Testing of "full-size " tensile specimens, of dimensions prepared according to the drawing shown in Fig.1.
2. Reconstitution of remnant parts (10*10*22 mm) of a 10*10*55 mm Charpy-size specimen.
3. Preparation of a tensile specimen from this reconstituted Charpy specimen, according to the drawing given in Fig.2.
4. Tensile testing of the reconstituted tensile specimens.
5. Comparision of the data obtained from full-size and reconstituted specimens.

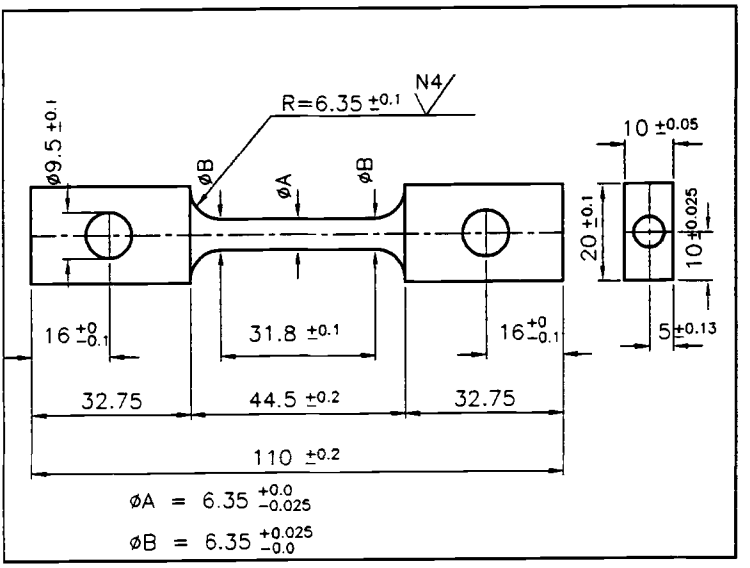


FIG. 1 - - Full size tensile specimen

3. Specimen preparation techniques

Specimens have been prepared with the reconstitution technique.The finishing work, in order to obtain the final tensile specimen shape, has been executed on a milling machine and on a lathe.

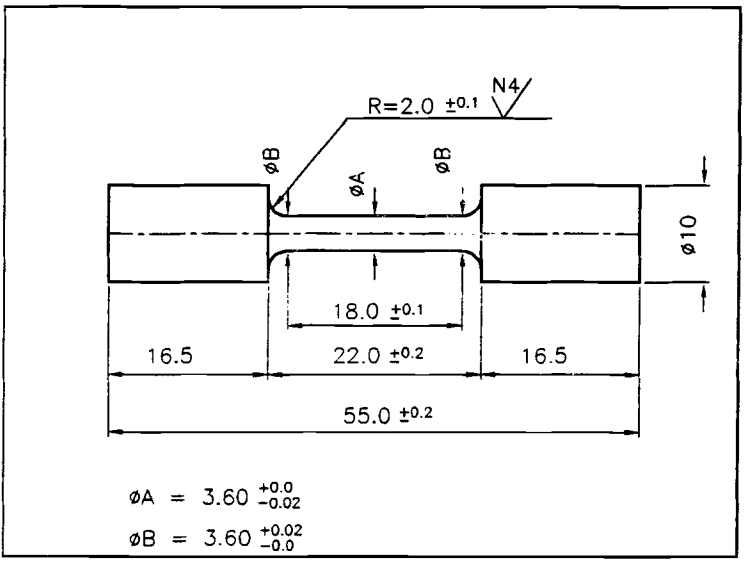


FIG. 2 - - Charpy size tensile specimen

3.1 Reconstitution.

Reconstitution of the inserts is executed with stud-gun welding equipment.
The welding procedure for reconstituting half-size Charpy specimens has been initially qualified for 18MND5 steel.[1].
Basically, the same technique is used since it has proven to be very effective and to give good results for impact testing. The schematic procedure for the reconstitution of tensile specimens is given in Fig.3.

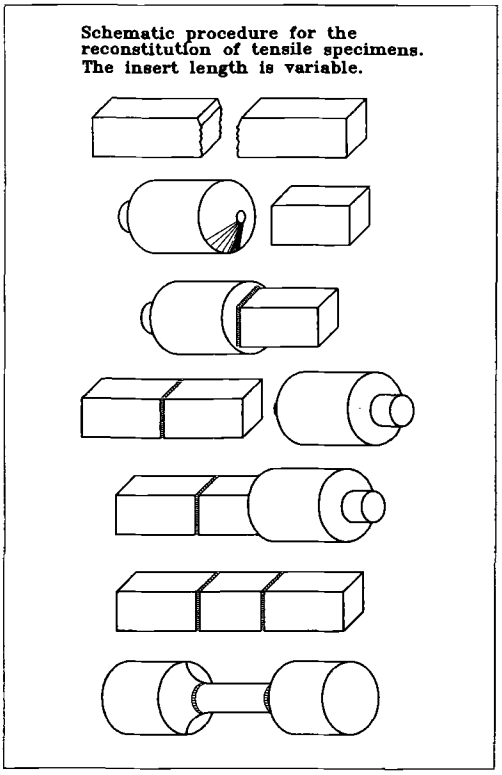


FIG. 3 - - Schematic procedure

3.1.1 The main components of the reconstitution equipment. (Fig. 4)

Figure 4 shows the reconstitution equipment with a number of components specifically identified , as follows,
(i). The stud gun assembly which consists of:
(a) the stud gun, fixed on the alignment frame
(b) a quick clamping chuck to hold the cylindrical stud
(c) a magnetic solenoid system in the gun, that lifts the chuck, loaded with the stud, from the working table that contains the insert .
(ii). The alignment frame that has:
(d) a ball-bushing guided alignment, allowing the stud gun support to move vertically;
(e) a table with a clamping system for the inserts, moving vertically on a ball bushing guided alignment, that allows modification of the working distance for inserts of different length;

(f) a removable shroud unit, that creates an argon atmosphere, around the welding area
(iii). Power supply and control unit (not illustrated)
This comprises , KSM 2000, microprocessor controlled, stud gun welding system, which acts as the power supply and control unit for the welding procedure. The system has precise regulation and digital verification of the welding parameters, as well as the necessary signalisation of welding and system deviations during operation.

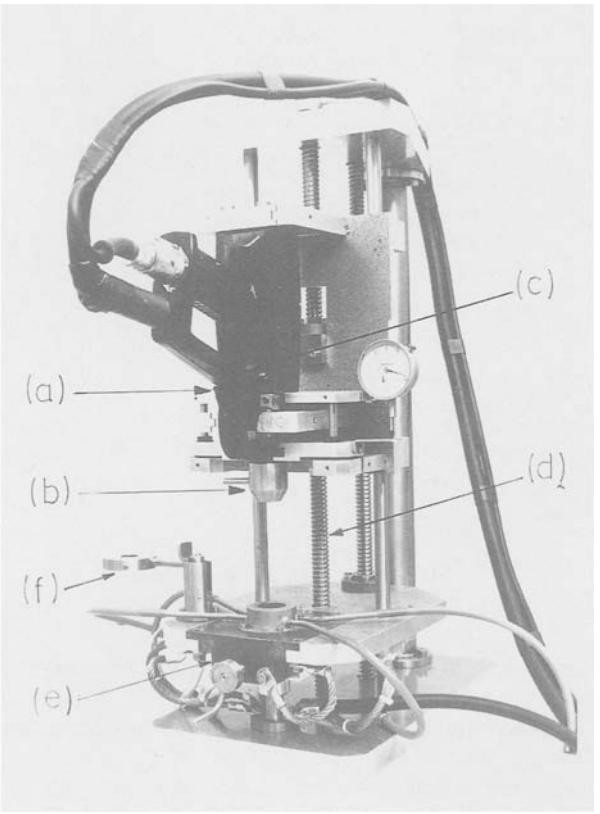


FIG. 4 - - The reconstitution equipment

3.1.2 The stud shape.

A cylindrical stud with a diameter of 16 mm is used. One end is conically shaped to guide the arc and to allow for the lateral ejection of melted material. A small aluminium ball is

pressed in the tip of the stud to promote the arc initiation and to avoid oxidation of the weld metal.

3.1.3 Reconstitution parameters

When executed in the classical way, it often happens that, small gas bubbles are observed in the welding region throughout the welded cross section. These impurities do not play a major role in the case of impact testing, but for a tensile test, where the force is acting perpendicular on a small section, they become a major problem. Initial tensile tests on reconstituted samples resulted in rupture at the weld.

In order to overcome this problem, the original reconstitution procedure has been changed, by using additional Argon shielding gas in the weld area.
Keeping the weld current constant at 1000A, the arc voltage drops from about 40V to 23 V by introducing Argon shielding gas due to the improved conductivity of the arc zone. The overall effect, apart from the improved weld quality, is a major reduction of the power input by about 40% , i.e. an energy input reduction from 8 kJ to 5kJ (12 cycles at 50 Hz). Consequently, one expects that the power reduction should lower the temperature induced in the insert. Reconstitution tests with temperature monitoring revealed that temperature reduction is only small compared to that formerly detected using dummy inserts (see below), it is concluded that the temperature within the insert does not change significantly. This could be due to an improved thermal conduction between the insert and the stud, caused by the absence of the gas bubbles.
The reconstitution parameters are recorded, for each reconstituted insert, on an " Individual reconstitution record sheet", that contains all the detailed information of the reconstitution process.

3.2. Temperature control measurement

To prevent overheating of the insert material and to check weld parameters, temperature measurements are carried out before and after each series of reconstituted inserts. The temperature variation in the insert lasts only a few seconds. The temperature control method gives confidence that the reconstitution technique gives no biases with the original material, as has been proven by multiple tests in the past. A typical temperature/time curve is shown in fig.5.
The temperature measurement has been performed using thermocouples brazed with Ni-Cr filler in dummy insert pieces 10x10x 10 mm . In the 10 mm inserts, the calibrated thermocouple is positioned at the distance of 4 mm from the welding surface. The thermocouple is a Chromel-Alumel K type with a diameter of 1 mm, and a grounded hot-junction. (Fig.6). Recording of the results was made on a penplotter with paper displacement at 10mm/sec and a temperature scale of 20mV/°C.
The precision of the temperature control set-up is +/- 7°C and the response time of the plotter is 0.3 sec.

Fig. 7 shows the temperature/distance to weld curve that results from multiple testing at SCK●CEN. The square (temperature at 4mm of the weld surface) and the triangular (at 2 mm of the weld surface) dots give some temperatures measured during the temperature

control weldings for this work. In a number of separate experiments it was found that a reduction of the weld energy only gave a small lowering in temperature in the insert. A preliminary curve (Fig.8), shows the experimentally determined quasi-linear relation between temperature and weld energy, to illustrate this behaviour.

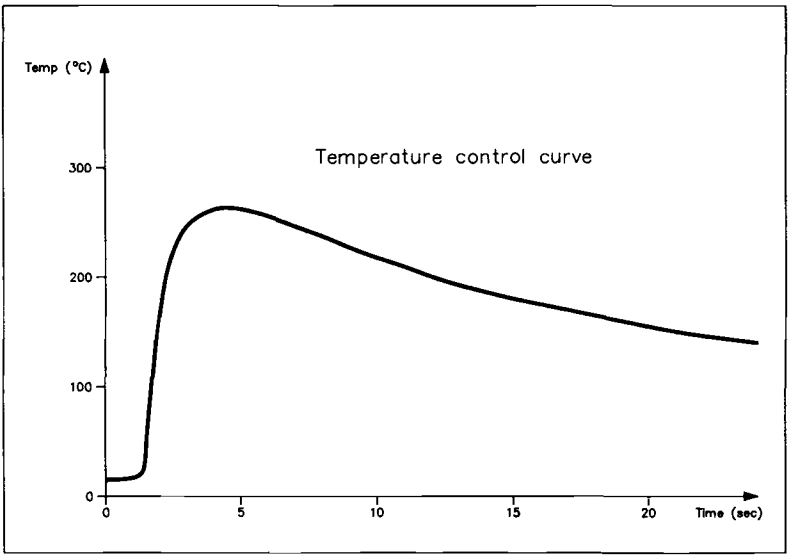


FIG. 5 - - Temperature control curve

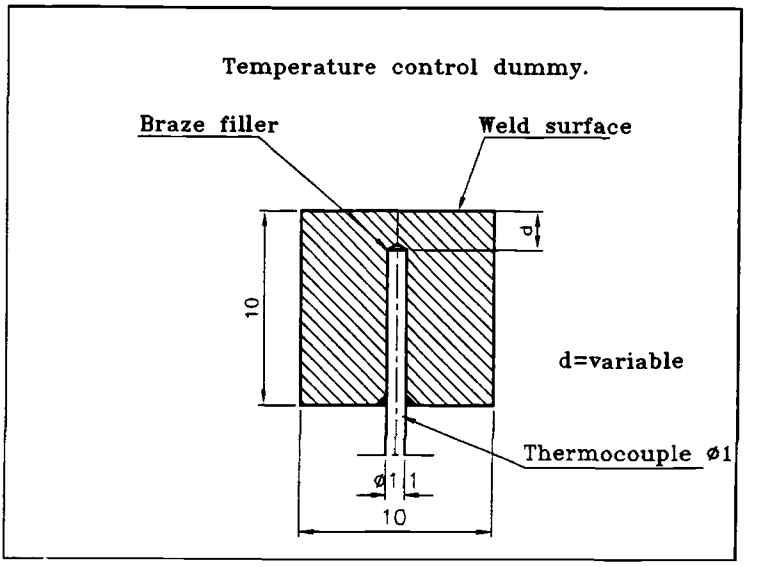


FIG. 6 - - Temperature control dummy

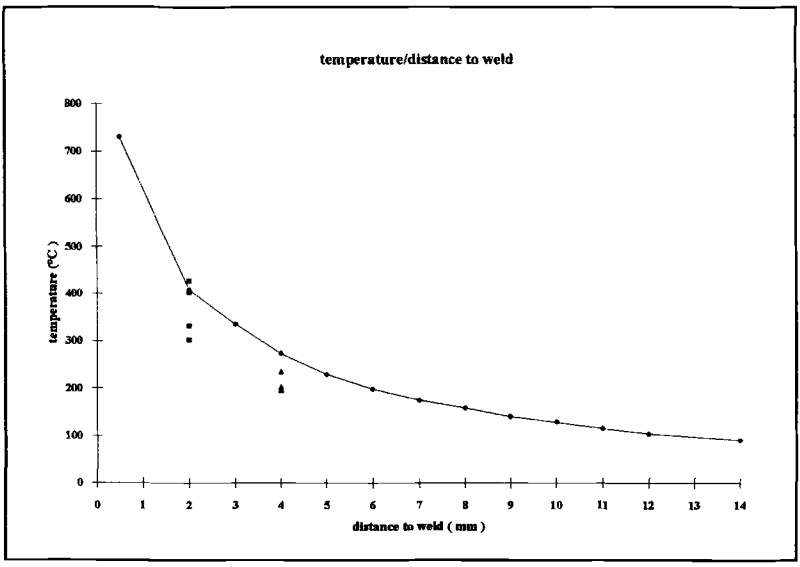


FIG. 7 - - Temperature/distance to weld curve

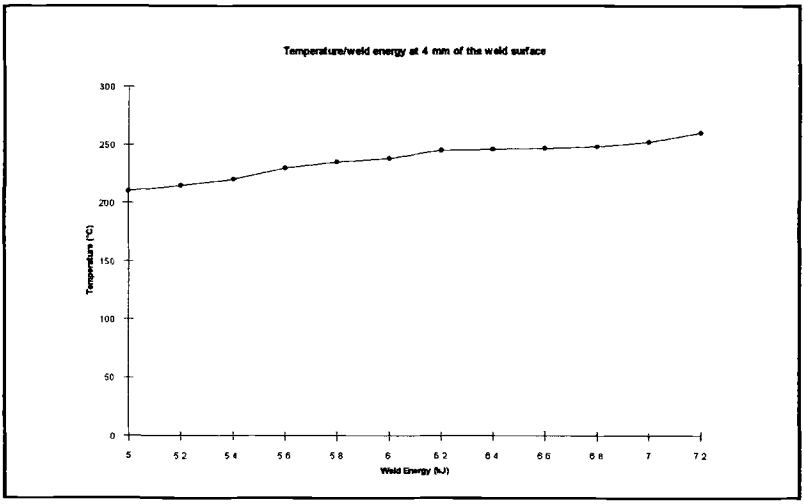


FIG.8 - -Temperature/weldenergy

3.3. Qualification

The qualification of the reconstitution procedure for tensile specimens has until now only been performed on unirradiated 18MND5 material. The qualification for irradiated material is under preparation. Care has been taken that the ratio of the length to diameter of the reduced region of the Charpy-size tensile test specimen (Fig.2) is identical to the full-size ratio (Fig.1). The ratio of the reduced length to the crosshead speed of the tensile machine was kept approximately constant. The tests were performed at 310° C (± 1 °C) on an Instron machine.
The upper picture shows two reconstituted tensile specimens tested at 310°C. The sample at the left side was welded under Argon atmosphere while the sample on the right side was welded under air. The influence of welding under Argon shielding gas can be seen in Fig. 9. The left hand sample clearly shows a fracture in the weld area, whereas the sample welded under argon gas shows a normal fracture behaviour in the reduced section. Fracture in the weld is associated with gas bubbles.

Tensile tests were performed on non-reconstituted specimens of Charpy-V size (Fig.2), reconstituted C_v tensile specimens and full-size (Fig.1) specimens. All the test results and the mean values for the qualification are summarized in Table 1.

TABLE 1 - - Qualification Tensile test results

Specimen	Insert size (mm)	Test Temp (°C)	Crosshead speed (mm/min)	$\sigma_{0.2}$ (MPa)	U.T.S. (MPa)	ϵ_{tot} (%)	ϵ_u (%)	Red. Area (%)
Full-size tensile specimen	-	310	0.2	484	666	20	8.3	58
	-	310	0.2	542	659	27	8.2	48
	-	310	0.2	477	650	30	8.8	47
MEAN				501(36)	658(8)	26(5)	8.4(3)	51(6)
Small-size as received specimen	-	310	1.0	516	670	28	9.5	46
	-	310	0.1	501	659	22	7.8	46
	-	310	0.1	497	648	22	8.2	56
MEAN				505(10)	659(11)	24(3)	8.5(9)	49(6)
Small-size reconstit. specimen	22	310	0.1	502	662	23	8.2	47
	22	310	0.1	494	638	25	8.9	52
	22	310	0.1	495	640	28	9.0	53
	22	310	0.1	495	640	28	8.5	46
MEAN				497(4)	645(11)	26(2)	8.4(5)	50(4)

The yield values of Table 1 indicate an excellent correspondance of the data for the three specimen types.

4. Test results.

4.1 Testing of weld material from the Belgian Power plant DOEL 2.

The purpose of these tests was to determine baseline tensile data for Doel 2 weld material using econstituted Charpy-V size specimens since such data for the full-size tensile specimens were not available

The region of interest, the weld region of the Charpy sample, was first detected by means of chemical etching. From this region 22 mm was cut to be reconstituted according to the procedure described in paragraph 1. The welding was performed using an argon shielding gas and temperature control weldings were performed after welding , the samples were machined to the final dimensions of Fig. 2 .All the reconstitution parameters (also for the temperature monitors) are summarized in Table 2.

In the Table 2. the temperature monitors are nominated as Temp.1 and Temp.2 for the control weldings executed before and after welding the first stud, and respectively Temp.3 and Temp. 4 for the temperature control weldings before and after welding the second stud.

TABLE 2.- -Reconstitution parameters

Specimen	Current (A)	Arc Voltage (V)	Time (s)	Weld energy (kJ)	Temperature (°C)
Temp.1	996	22	0.24	5.2	293
2Z1	995	23	0.24	5.4	
1Z9	995	22	0.24	5.2	
4Y6	996	22	0.24	5.2	
Temp.2	23	23	0.24	5.4	261
Temp.3	998	21	0.24	5.0	243
2Z1	998	20	0.24	4.7	
1Z9	998	21	0.24	5.0	
4Y6	991	23	0.24	5.4	
Temp.4	996	20	0.24	4.7	254

The tensile tests were performed at (310°C ± 2)°C on an Instron 1195 machine at a crosshead speed of 0.1 mm/min. The results of these tests are compiled in Table 3. Fig. 10 to 12 show the specimens after testing.

TABLE 3- -Test results for Doel 2 weld material

Specimen	Insert size (mm)	T (°C)	Crosshead Speed (mm/min)	$\sigma_{0.2}$ (MPa)	U.T.S. (MPa)	ϵ_{tot} (%)	ϵ_u (%)	Reduced Area (%)
2Z1 REW	22	310±2	0.1	368	498	22	8.2	66
1Z9 REW	22	310±2	0.1	356	490	20	8.4	60
4Y6 REW	22	310±2	0.1	402	523	20	7.8	65

4.2. Testing of base metal surveillance steel specimens from the German KKP1 power plant

Two unirradiated reconstituted Charpy-size tensile specimens of 22NiMoCr 37 material have been tested at 22°C and at 300°C respectively. The original remnants were broken Charpy-V notch specimens from the BWR "Kernkraftwerk" Philippsburg 1, reactor in Germany. After removing the plastic deformation reconstitution in Argon was executed on 22 mm long inserts using the 22NiMoCr 37 stud material. The test results are given in Table 4.

TABLE 4- -Test results for KKP1 base material

Specimen	Insert size (mm)	T (°C)	Crosshead Speed (mm/min)	$\sigma_{0.2}$ (MPa)	U.T.S. (MPa)	ϵ_{tot} (%)	ϵ_u (%)	Reduced Area (%)
78UL	22	22	0.1	448	605	22.7	8.8	-
78UR	22	300	0.1	421	594	22.3	9.3	-

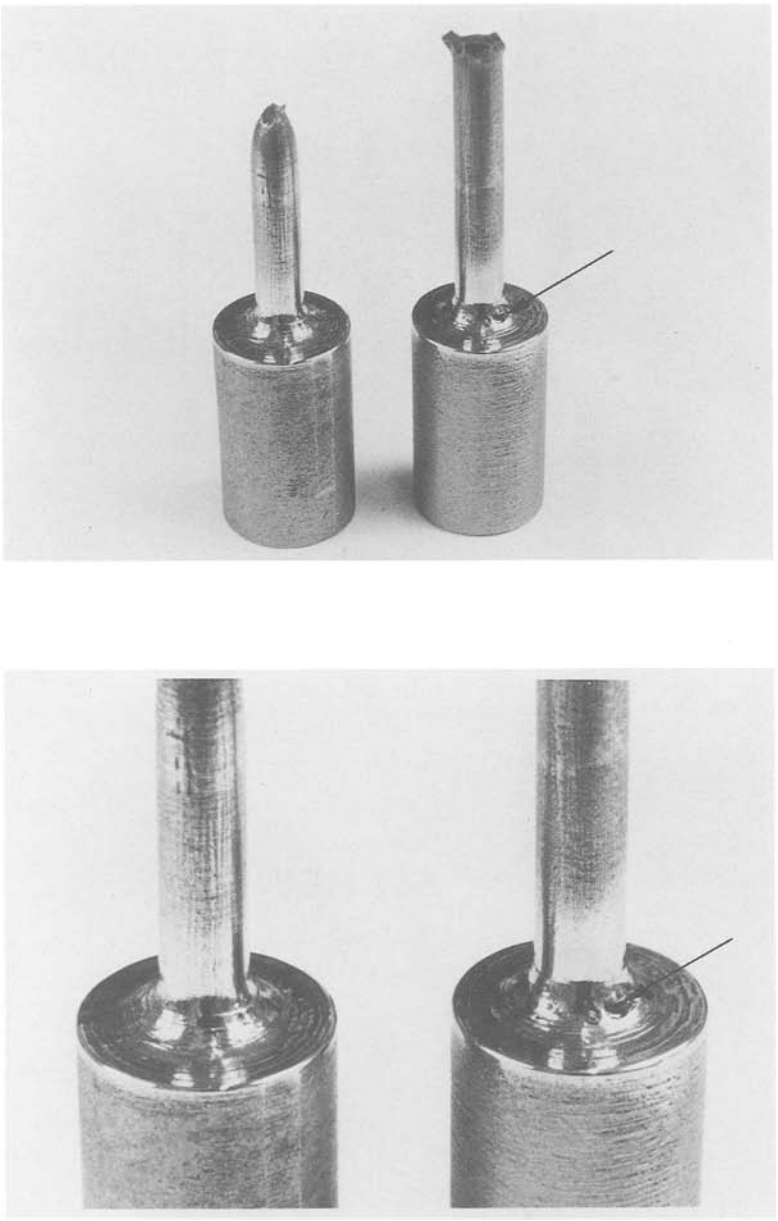


FIG. 9 - - Gas bubbles in the weld



FIG. 10 - - The 1Z9 REW specimen after testing



FIG. 11 - - The 2Z1 REW specimen after testing



FIG. 12 - - The 4Y6 REW specimen after testing

5. Comparison with existing data.

Table 5. compiles the existing tensile test results on the Doel 2 unirradiated and irradiated weld surveillance material and repeats the KKP1 test results.

For the Doel weld material, the yield values for the un-irradiated weld surveillance material complete the existing irradiated data set. These data allow the irradiation hardening that occured for this material to be determined.

The KKP1 un-irradiated base metal results are in agreement with a recent study performed by TÜV Südwest Mannheim on representative material for KKP1.

TABLE 5 - - Tensile results of the Doel weld material and the KKP1 base material

Source	Sample	Dose (10^{19} n/cm^2)	Test temp. (°C)	$\sigma_{0.2}$ (MPa)	UTS (MPa)	Remarks
	4Y6 REW	0	310	402	523	Reconstituted
DOEL	10A4Y17	0.91	310	417	562	
	8V4Y18	1.72	310	450	581	
	2Z1 REW	0	310	368	498	Reconstituted
	1Z9 REW	0	310	356	490	Reconstituted
	6A4Y10	0.86	310	510	681	
DOEL	10F4Y3	0.91	310	431	576	
	10V4Y8	0.91	310	688	873	
	8A4Y47	1.72	310	479	611	
	3F4Y2	2.27	310	437	577	
	9V4Y11	2.9	310	406	615	
KKP	78UL	0	22	448	605	Reconstituted
	78UR	0	300	421	594	Reconstituted

6. Conclusions.

It has been demonstated that the reconstitution technique permits Charpy-V size tensile specimens to be made, starting from broken Cv remnants. These specimens yield equivalent results to non-reconstituted Cv tensile specimens and to the larger size ASTM-E8-recommendet tensile specimens.
The technique was applied succesfully to base and weld surveillance material of two actual power plants.

7. Acknowledgements.

The authors are indebted to the technical staff of SCK●CEN. They also thank K. Tulke from KKW Philippsburg and W. Backfisch from TUV Südwest Mannheim for supplying the data from the German vessel steel.

8. References.

[1] Langouche, F., Chaouadi, R., Puzzolante, J.L., Vandermeulen, W., Van de Velde, J., Van Ransbeeck,T., in "Qualification of Charpy specimen reconstitution procedure for unirradiated specimens," SCK report R2756, Mol, 1989

[2] Backfisch, W. TUV Südwest Mannheim, and Tulke, K. KKW Philippsburg, private communication.

Eric van Walle,[1] Albert Fabry,[1] Theo Van Ransbeeck,[1] Jean-Louis Puzzolante,[1] José Van de Velde,[1] Klaus Tulke,[2] and Willi Backfisch[3]

NOTCH REORIENTATION OF CHARPY-V SPECIMENS OF THE BWR PHILIPPSBURG 1 THROUGH RECONSTITUTION

REFERENCE: van Walle, E., Fabry, A., Van Ransbeeck, T., Puzzolante, J.-L., Van de Velde, J., Tulke, K., and Backfisch, W., "**Notch Reorientation of Charpy-V Specimens of the BWR Philippsburg 1 Through Reconstitution,**" *Effects of Radiation on Materials: 17th International Symposium, ASTM STP 1270,* David S. Gelles, Randy K. Nanstad, Arvind S. Kumar, and Edward A. Little, Eds., American Society for Testing and Materials, 1996.

ABSTRACT: 10x10x10mm cubes, made from broken halves of un-irradiated and irradiated L-T oriented Charpy-V surveillance specimens of the Boiling Water Reactor (BWR) Philippsburg 1, were reconstituted to L-T and T-L oriented Charpy-V bars using the stud-gun welding technique of the Belgian Nuclear Research Centre SCK•CEN. Instrumented Charpy-V (C_V) impact testing, according to the European Standard EN10045, was performed in order to determine the T-L transition curves of the reconstituted surveillance material. Losses of fracture energy and lateral expansion, mainly as a consequence of constraint of plastic flow due to the reconstitution welds, were detected. No change in shear fracture appearance was observed. The transition curves of the tested T-L reconstituted specimens represent conservative lower bounds that fulfil the C_V upper shelf energy requirements of the Regulator. A correction curve allows estimation of the T-L transition curves of non-reconstituted T-L specimens.
The data were consistently analysed with hyperbolic tangent functions, while the load diagram recorded during the instrumented impact tests was used for guidance in the analysis. The quality assurance (QA) was ensured by the 'Technischer Überwachungs-Verein Südwestdeutchland' (TÜV-Südwest), 'Staatliche Materialprüfungsanstalt Universität Stuttgart' (MPA-Stuttgart) and 'Kernkraftwerk Philippsburg' (KKP).

[1]Senior research scientist, lead scientist, senior engineer, senior engineer, manager, respectively, SCK•CEN, RMR Department, Boeretang 200, B-2400 Mol, Belgium

[2]Senior engineer, Division Nuclear Technology, Kernkraftwerk Philippsburg Gmbh, Postfach 1140, 76652 Philippsburg, Germany

[3]Senior engineer, Division Nuclear Technology and Radiation Protection, TÜV Südwest e.V., Postfach 103262, 68032 Mannheim, Germany

Copyright© 1996 by ASTM International www.astm.org

KEYWORDS: reactor pressure vessel steel, fracture toughness indexation, Charpy-V, reconstitution, instrumented Charpy-V test, pressure vessel surveillance, plant life management

The Philippsburg Nuclear Power Plant near Mannheim, Germany, consists of two Units: Kernkraftwerk Philippsburg 1 (KKP1), a 900MWe BWR, began operation in 1979 and KKP2, a Pressurized Water Reactor (PWR) of 1300MWe that became critical in 1984. In 1993, these reactors delivered some 16 million MWh of electrical power to the grid in Germany.

The Reactor Pressure Vessel (RPV) of KKP1 is fabricated of rolled plates of 22NiMoCr37, an A508Cl.2 steel, with the rolling direction parallel to the circumference of the vessel. The surveillance programme of KKP1 contains C_V-specimens selected in the longitudinal orientation, i.e. the L-T direction of highest stress within the cylindrical shell. Current regulatory guidelines for nuclear power plants, i.e. KTA3203 in Germany, require however that the Charpy-V surveillance base metal of the RPV be impact tested in the weak, i.e. transverse T-L direction. This code requirement led to the decision to evaluate the C_V-properties of the core beltline region of the KKP1 RPV in the T-L orientation for the un-irradiated, or 'baseline', and irradiated conditions.

The baseline condition of the KKP1 base material was determined in 1976 through non-instrumented impact tests on 24 L-T oriented specimens. The surveillance programme of KKP1 consists of 2 capsules with scheduled retrieval in 1986 and 2002 in order to guarantee the vessel integrity up to a stipulated end-of-life fluence of 1.1 10^{18}n/cm^2 (E>1 MeV). The first capsule which received a fluence of 5.6 10^{17}n/cm^2 contained, among others, 18 L-T oriented base metal Charpy-V specimens that were evaluated with instrumented impact testing in 1987. These 84 broken Charpy-V samples - 48 un-irradiated, 36 irradiated - make up the stock, partly available to obtain the T-L properties of the material.

German regulation stipulates that the impact testing has to be performed according to the European Standard EN10045, where the DIN shaped impact tup is used and where there is also a requirement to perform instrumented C_V impact testing.

The only solution to prepare T-L oriented specimens from L-T oriented (broken) Charpy-V samples is to reconstruct, or 'reconstitute', 10x10x10mm cubes made of the L-T oriented broken C_V halves as shown in Figure 1. The welding technique used by SCK•CEN to reconstitute specimens is stud-gun welding.

It will be demonstrated that the Charpy-V impact tests, performed on L-T→L-T and L-T→T-L reconstituted KKP1 specimens, in both the un-irradiated and irradiated condition, lead to transition curves that represent conservative bounds for the T-L material conditions and that fulfil the Regulatory requirements. Accordingly, the data will be analysed using the hyperbolic tangent function. This analysis was supported with a consistent evaluation of the load diagrams recorded during the instrumented Charpy-tests of all the KKP1 specimens. It will be shown that this load diagram approach can reveal additional information on the material under investigation.

As reconstitution of small cubes of irradiated material is a fairly new methodology, the importance of QA, especially when used in a regulatory context, should be stressed. Therefore, the QA was ensured by TÜV-Südwest, MPA-Stuttgart and KKP.

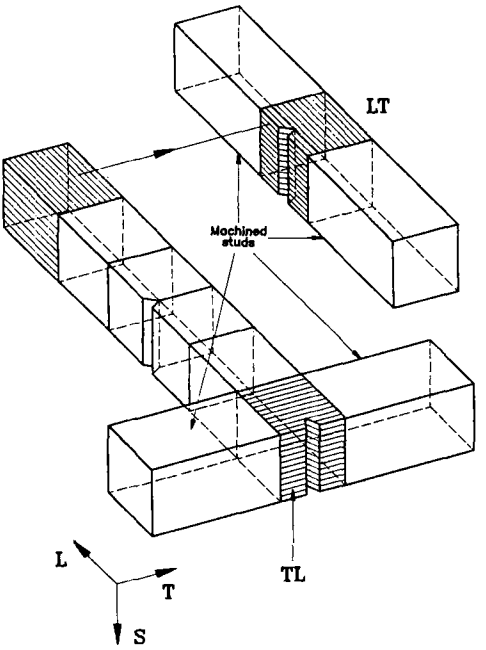


FIG. 1--C_V-reorientation philosophy

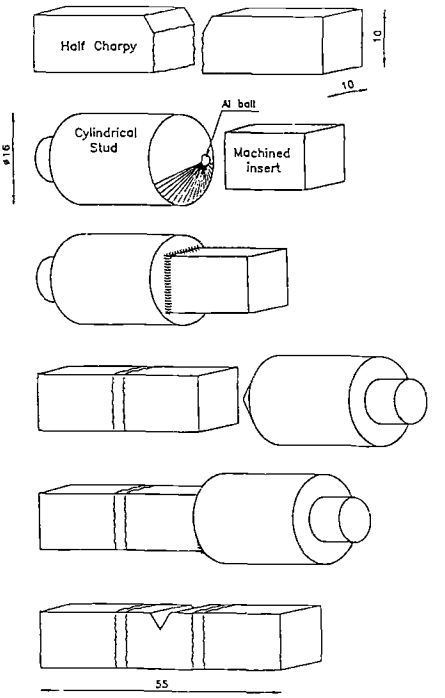


FIG. 2--The SCK•CEN methodology

THE RECONSTITUTION TECHNIQUE: AN OUTLINE OF CURRENT ASSESSMENT

Reconstitution Methodology: Stud-Welding

SCK•CEN has developed a stud welding technique to reconstitute broken Charpy specimens [1, 2, 3]. The impetus for the development was the need to investigate the weld part of heat-affected-zone specimens of the Doel I & II Belgian nuclear power plants. More generally, the technique offers a solution to obtain more information from the limited stock of vintage material for older nuclear plants.

The method, as adopted at SCK•CEN and schematically illustrated by Figure 2, has been qualified extensively on various pressure vessel materials in non-irradiated and irradiated conditions, leading to acceptance for application to the Belgian power plants. The method consists of welding two end pieces (studs) to a central piece (insert) made of pressure vessel material, with subsequent re-machining into a 'new' Charpy-V specimen with dimensions 10x10x55mm. In order to assure good square cross-sectional welds and perfect

alignment of the final Charpy-V specimen, oversized and conical-shaped cylindrical studs are used. An aluminium ball is pressed into a cavity on the conical end of the stud to act as an arc initiator and an anti-oxidant. The welding is executed under an argon atmosphere to prevent oxidation of the weld surfaces and to promote the homogeneity of the weld. Typical welding parameters are 1000A at 25V for 0.24s, or an energy input of some 5kJ. After pulling the arc, a large amount of melt material is ejected during the pressing between stud and insert, thereby reducing the heat input into the insert. Moreover, the specimen is clamped into a cooled copper brace to reduce the heat input to the insert.
To prevent overheating and to check the welding equipment, reconstitution weldments are carried out on dummy specimens, before and after a welding project on inserts of interest. These dummy specimens contain a calibrated Cr-Al thermocouple - brazed with Ni-Cr filler - measuring the temperature at a fixed distance from the future notch position. The temperature within the volume of the insert material, that will be solicited during the to-be-executed C_V-test, should remain below the normal operating temperature of the plant, i.e. 300°C, in order to be in agreement with the 'Standard Guide for the Reconstitution of Irradiated Charpy Specimens', ASTM E1253 and to guarantee no changes of material properties. For 10mm insert pieces, the central volume below the plant operating temperature is 6mm long [4]. Moreover, the duration of temperature variation (increase and decrease) takes only a few seconds. Hardness measurements do not show any variation over the central insert length of 7 to 8 mm before or after reconstitution. Together with the extensive tests and evaluations done on various materials in various conditions, the temperature control method gives confidence that the reconstitution technique, as used for this work, is properly designed to avoid any biases with respect to the original specimens.

Experience with Reconstitution: Effects on Transition Curves

The original qualification tests for the reconstitution technique were executed on inserts, made of RPV material, with a length of 20mm. No deviation in energy (upper shelf energy (USE)), lateral expansion (LE) and shear fracture appearance (SFA) between as-received and reconstituted Charpy-V impact tests was observed. However, when the insert length is reduced to 10mm to allow for reorientation of a Charpy sample, the impact test reveals that at higher test temperatures the plastic flow is constrained by the welds. These welds are situated at less than 5mm from the sample notch, whereas hardness testing on broken as-received specimens shows that, at upper shelf test temperatures, the plastic flow can extend to 10mm from the notch [5]. Consequently, the loss in plastic deformation energy causes the recorded fracture energy to be less than for an as-received sample. Preliminary two-dimensional finite element calculations at SCK•CEN confirm this behaviour.
Figure 3 shows the energy reduction for un-irradiated HSST-03 material in the L-T and T-L orientation (the shape of the transition curves in explained in the next paragraph) [1, 2]. The 'apparent' shift in temperature (for Regulatory requirements the temperature shift is to be indexed at 41J) after reconstitution is - on Figure 3 - a direct consequence of the lower energy of the C_V-tests for the reconstituted specimens. Similar losses occur on the lateral expansion (indexed at 0.89mm) of the reconstituted 10mm inserts after testing. As can be seen on Figure 4, the SFA is independent of the reconstitution and, in the HSST-03 case, of the sample orientation. The SFA gives information on a more localised region, i.e. mainly the

fracture plane under the notch, whereas the lateral expansion and fracture energy depend on the volume surrounding the notch.

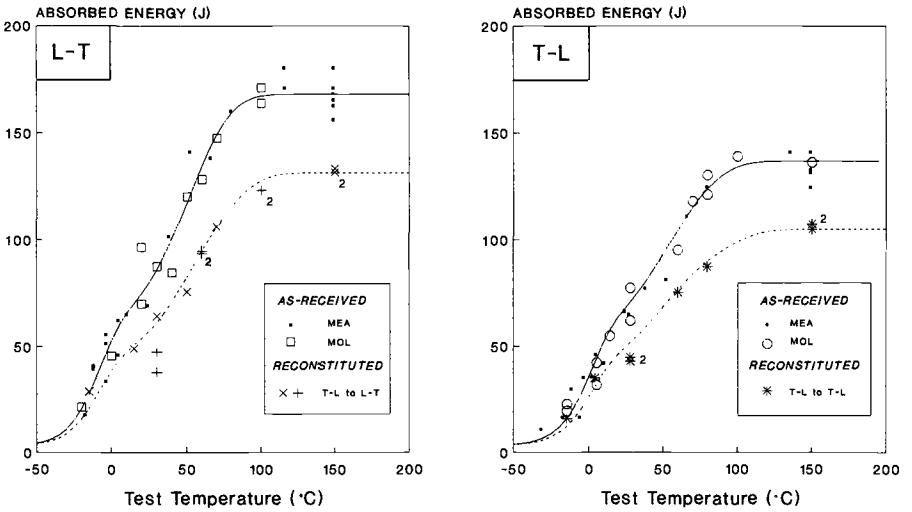


FIG. 3--Fracture energy loss due to plastic deformation constraint by the hard welded zones in the reconstituted C_V-specimen with 10mm insert length. The material is un-irradiated plate HSST-03 in the L-T and T-L orientation.

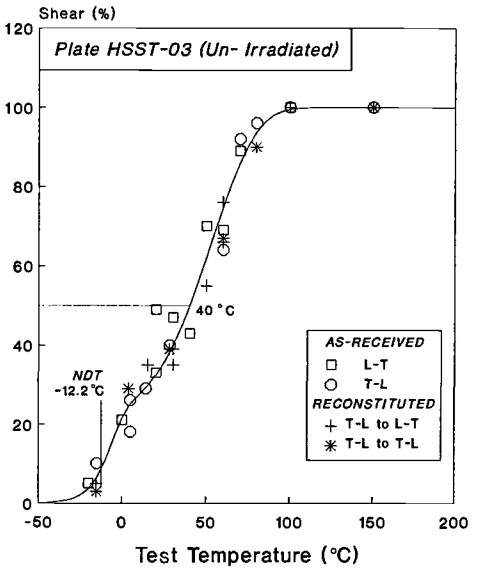


FIG. 4--Invariance of C_V shear fracture appearance to reconstitution. Plate HSST-03 also shows invariance to notch orientation.

As will be shown, the KKP1, 22NiMoCr37 nuclear grade material has a lateral shift in temperature between the L-T and T-L transition curves, for both the unirradiated and irradiated conditions. This temperature shift, that depends on material properties, is reflected after reconstitution.

In order to estimate the T-L properties of the KKP1 baseline material, the idea was to follow the strategy that had proven successful on un-irradiated HSST-03 steel [1]. Having L-T and T-L as-received specimens of HSST-03 available, the concept is illustrated by Figure 5. This experiment demonstrates that the difference in energy between the L-T as-received and the L-T reconstituted curves - being the loss due to reconstitution welds- can be added to the experimentally determined T-L reconstituted curve, leading to a predicted T-L 'as-received' curve. The latter curve is in excellent agreement with the experimentally determined T-L as-received curve. It is assumed that, to first approximation, the loss in USE

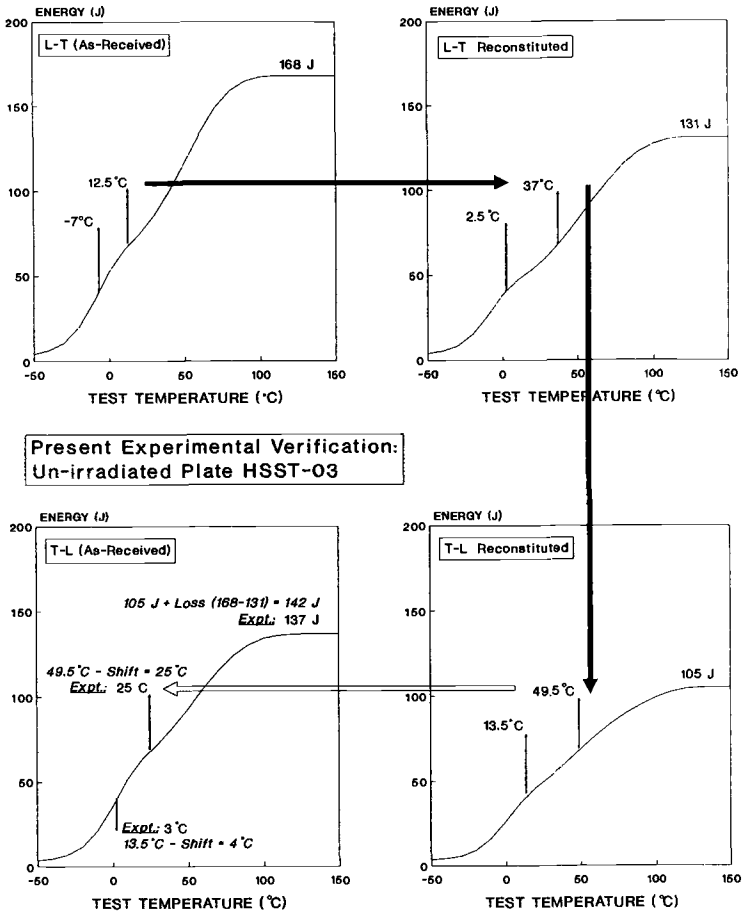


FIG. 5--Correction scheme for notch re-orientation as applied to HSST-03.

due to reconstitution is independent of the sample orientation.
Similarly, the methodology implemented for the KKP1 material was to first determine the energy losses due to the reconstitution of 10mm inserts in the L-T geometry (un-irradiated and irradiated material), followed by the reconstitution of reoriented L-T inserts into T-L specimens. If the correction method as used for HSST-03 material is valid, then the T-L corrected (the constructed T-L 'as-received') curve for KKP1 material will simply follow by adding the energy loss, detected from L-T → L-T reconstitutions, to the energy curve of the reconstituted T-L specimens.

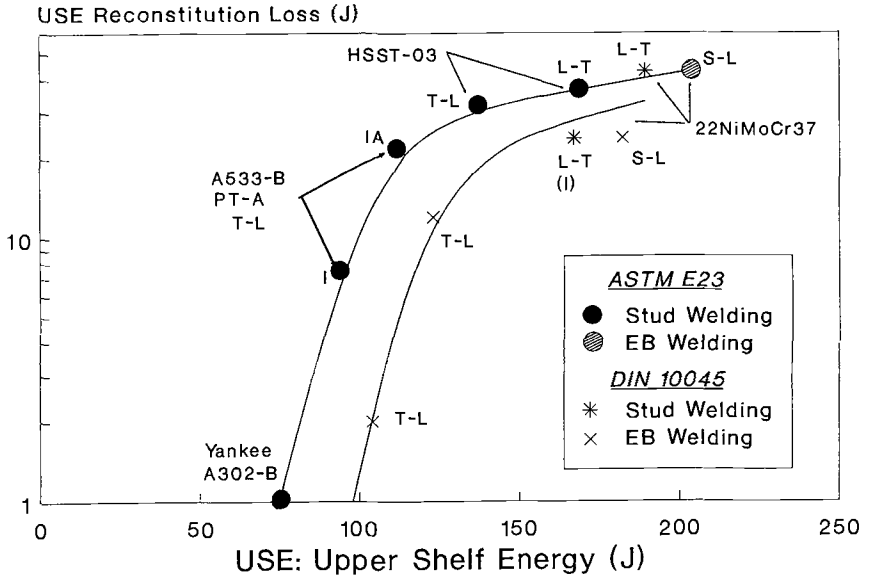


FIG. 6--Upper shelf energy losses for C_V-reconstituted 10x10x55mm inserts

However, the SCK•CEN research program on the application of the reconstitution technique on 10mm long inserts of materials with different USE had also revealed that the maximum losses, recorded after testing at upper shelf temperatures, depend on the USE of the samples. This is illustrated in Figure 6, where the spline fits through the experimental data- non-irradiated, as well as, irradiated - identify the data trends. Three further effects are seen: i) energy losses depend on the hammer tup geometry - ASTM or DIN - used for testing; ii) there is a threshold USE below which no losses, due to the reconstitution of 10mm inserts, occur [3]; iii) the losses seem to be less when the electron-beam (EB) welding technique is used instead of stud-welding: this can be related to the remaining length of the insert after welding [4]. The curves of Figure 6 prove that the losses depend on the condition of the material, complicating the application of the simple correction method used for the initial HSST-03 work. Since, in general, the fracture behaviour of T-L oriented (as-received) samples results in a lower USE than for the L-T orientation, the correction will be

different for each orientation; the difference being more pronounced when the upper shelf energies are located in the steep part of Figure 6, as is the case for KKP1 material. It is therefore difficult to come up with accurate correction values. However, if the upper shelf energy obtained from reconstituted specimens lies above the Regulatory lower limits, the uncorrected transition curves are lower bounds of the 'corrected' curves.

In conclusion, it can be stated that the C_V-reconstitution of small insert lengths does influence the fracture energy and lateral expansion behaviour, but does not affect the SFA. The reduction in USE and the induced apparent shift in temperature at 41J are conservative from the safety viewpoint. The invariance of the SFA is advantageous in the frame of a new analysis and fracture toughness indexation methodology, highlighted in the next paragraph.

Reconstitution and The Instrumented Charpy-V Impact Signal [6, 7, 8]

The Charpy-V impact machines, used for testing the KKP1 material, are instrumented with strain gages, that measure - as a function of time t - the load F exerted by the impacting tup on the Charpy sample. The (F,t) Charpy impact curve can contain, depending upon the test parameters, several characteristic load points: F_{GY}, the general yield load; F_m, the maximum load; F_u, the brittle crack initiation load; F_a, the crack arrest load. Moreover, the instrumented signal can be subdivided in several parts A, B and C; this is also illustrated on the left side of Figure 7. The various load points as a function of test temperature are depicted in the right plot of Figure 7. Several critical temperatures and a related energy partitioning can experimentally be determined to reasonable accuracy from the impact traces. Of primary importance are two characteristic temperatures: T_I, the ductile crack initiation tem-

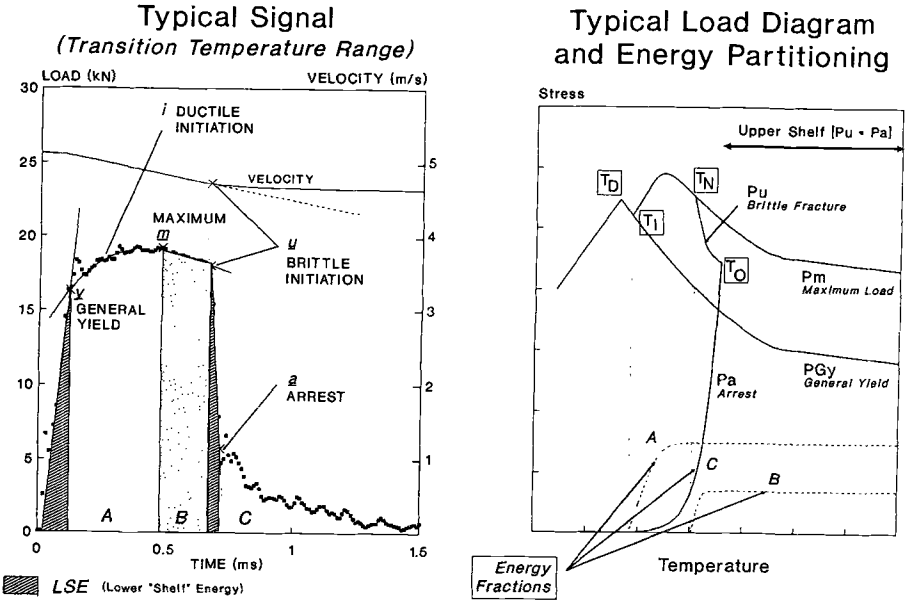


FIG. 7--The load diagram: the use of instrumented C_V load time traces.

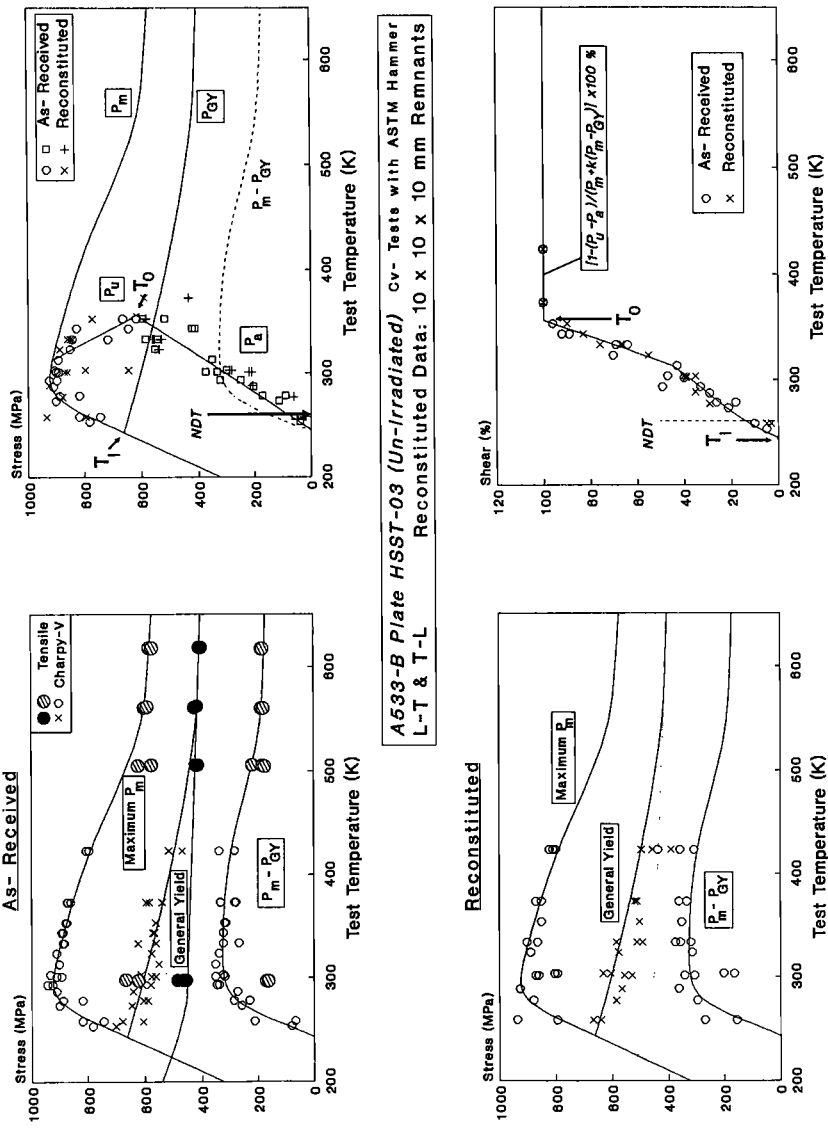


FIG. 8--Invariance to reconstitution of the C_V load diagram and the fracture appearance (the scale and fits need to be updated, but do not alter the conclusions).

perature, i.e. the temperature at which the SFA starts to exceed 0%; and T_0, the onset of the C_V upper shelf, i.e. the temperature at which brittle crack initiation and crack arrest loads coincide and the fracture reaches 100% ductility. Detailed information on the other characteristic temperature points can be found in reference 6. The energy (and lateral expansion) transition curves, like Figure 3 and others, are a superposition of the individual fits of the fractions A, B and C of the instrumented signals of the specimens. These fractions relate to different physical processes that occur during a Charpy-V test. The functional dependence of these fractions with changing temperature is shown on the right side of Figure 7 (for more information we refer to reference 6). This subdivision in energy fractions gives rise to the 'unusual' shapes of the transition curves, as for instance shown in Figure 3.

A basic ingredient for the analysis according to the load diagram approach is the correlation that exists between the C_V-impact load diagram and the shear fracture appearance: an excellent fit of the experimental SFA-data can be derived from the load diagram [6] as

$$SFA\ (\%) = [1 - (F_u - F_a)/(F_m + (F_m - F_{GY})/2)] \times 100\%.$$

Another interesting feature of the load diagram - automatically reflected in the SFA - is the independence to reconstitution. This is because the load diagram reflects the steel flow properties and the stress-controlled nature of brittle fracture. This is illustrated by Figure 8 for the reconstitution of 10mm long inserts of HSST-03 material. The T_I and T_0 temperatures, in contrast to the 41J-level temperature, do not vary after reconstitution.

The load diagram approach is part of an enhanced surveillance methodology under development at SCK•CEN [6, 7]; here, its application was limited to guide us systematically through the analysis according to the KTA 3203 rules, with a preference for hyperbolic tangent fits.

THE RECONSTITUTION OF KKP1 BROKEN SPECIMENS

Quality Assurance

The execution of the KKP1 program was outlined in a quality plan agreed upon by KKP, MPA Stuttgart, TÜV Südwest and SCK•CEN. This plan provides the details of the program and the testing requirements.

Equipment, Calibration, Qualification and General Technical Procedure

The reconstitutions were carried out with two equivalent reconstitution set-ups: one outside the reconstitution hot-cell and one inside the cell. Both stud guns use the same power supply. Every insert was accompanied with an 'Individual Reconstitution Record Sheet', that contains all details on the reconstitution. Every phase within the reconstitution procedure of each insert was documented with photographs. The stud material was made from 22NiMoCr37 material with very similar flow properties as the un-irradiated KKP1 material. The inserts were carefully prepared and identified. All temperature control measurements were below 300°C. The mechanical finishing of the reconstituted specimens to

EN10045 standards was done on milling machines; the V-notch was in all cases prepared with a V-shaped broaching tool. All reconstituted specimens were subjected to dimensional control measurements according to EN10045; these measurements were done with high performance profile projectors.

The Charpy-V impact tests were executed on two instrumented pendulum machines. The experiments were conducted, as a function of temperature, according to EN10045. The information extracted from the test is the dial energy, supplemented with the LE and SFA data, as defined in DIN50115 (equivalent to ASTM E-23). The LE information is deduced from profile projector measurements, while the SFA is planimetrically measured from enlarged surfaces of the broken specimens. Moreover, the load-time traces were obtained from the instrumentation added to the machines. Here, in general, the approach outlined in the proposed European Structural Integrity Society (ESIS) Instrumented Charpy-V Standard was followed [9]: characteristic loads and partial energies were determined. The instrumented Toni-MFL machine - positioned outside of the hot-cell - fulfils the suggested band width condition (>100 kHz), while the Tinius-Olsen machine (20 kHz) - positioned inside - does not. To our experience, 20 kHz is sufficient provided the instrumented data are carefully analysed.

The calibration of the two instrumented impact machines, was checked with Watertown and Community Bureau of Reference (BCR) reference specimens. The force calibration of the tup instrumentation was originally done in a static manner in a tensile bench. Good correspondence has been found between the integrated energy value, obtained from the load-time traces, and the dial energy.

The reconstitution procedure and the impact testing was qualified on un-irradiated 22NiMoCr37 material, which is similar to the KKP1 material. The weld quality was checked with metallography and Vickers hardness profiles were taken along the full length of the longitudinal mid plane of a specimen. These profiles showed no changes in hardness of the stud and insert material, before and after the reconstitution.

After the qualification tests, four groups of 10x10x10mm inserts were reconstituted:

a) non-irradiated L-T to L-T;
b) non-irradiated L-T to T-L;
c) irradiated L-T to L-T;
d) irradiated L-T to T-L.

Each group of reconstituted specimens was limited to 12 in order to preserve some of the broken KKP1 surveillance material for future purposes. As will be seen, there is significant scatter of the impact data that is not easily quantified given the limited amount of reconstituted samples.

Analysis Procedure

The SCK•CEN analysis procedure makes extensive use of the load diagram of the instrumented Charpy test. The loads and deflections are fitted simultaneously with the shear fracture appearance data. This process allows the determination of characteristic temperatures for the condition of the steel under consideration. In combination with the load diagram, the different energy fractions that sum up to the experimentally determined energy

transition curve are plotted. The same parameters are used to fit the lateral expansion data. Taking the total set of KKP1 data into account, this provides a consistent set of parameters for the different conditions of the steel, even when the statistics for a certain condition is rather poor. More details can be found in reference 10. A typical illustration of the analysis procedure, as applied to the KKP1 material, is given on Figure 9.

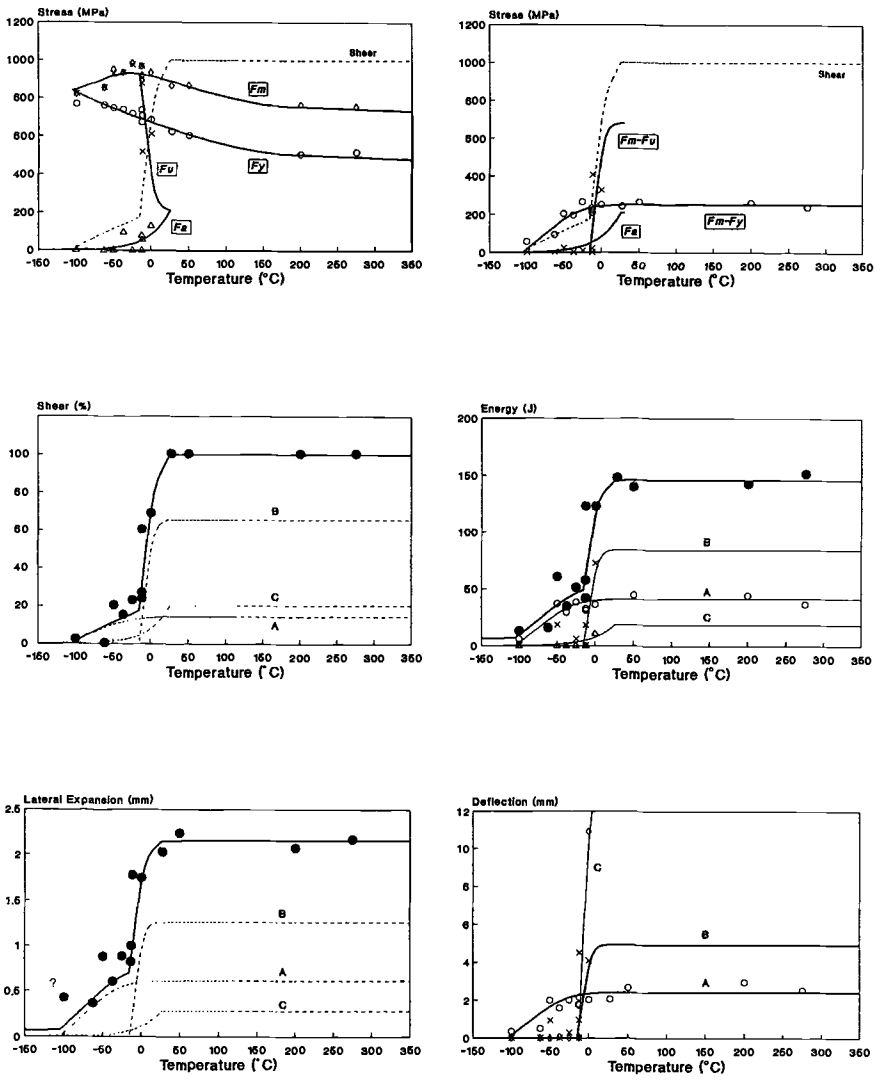


FIG. 9--The load diagram approach for the analysis of C_V-notch impact data

All KKP1 data were initially analysed according to the load diagram approach [10]. This analysis then served as guidance to hyperbolic tangent fitting of the KKP1 data [11]. These fits are presented in this work; we emphasise that they are **consistent** fits, i.e. they take the overall KKP1 data set into account. Emphasis on the physically-based requirements for overall consistency may sometimes result in a fit for a specific parameter (say, lateral expansion) to be less ideal than if the parameter was evaluated in isolation; departures exceeding uncertainties are treated as clues, either to improve the evaluation, or to detect experimental biases. The resulting set of parameters is further bound by the need to quantify properly the loss in upper shelf energy for reconstituted specimens (non-irradiated and irradiated condition).

The dial energy values, lateral expansion and shear fracture appearance data of the Charpy tests are as such plotted as a function of test temperature T and fitted with the familiar tanh function

$$y = A + B \times \tanh\left[(T - T_T)/C\right],$$

where

(A+B)/2 = Upper Shelf Energy (USE),

(A–B)/2 = Lower Shelf Energy (LSE),

T_T = Transition Temperature, C = Slope,

y = Energy, LE, SFA.

The upper shelf data points correspond to those specimens that show 100% SFA. The mean value of the energies and lateral expansions of those upper shelf specimens determine, respectively, the USE and upper shelf lateral expansion of the specimens under investigation. The fitting parameters, characteristic transition temperatures and mutual shifts are summarised for all the KKP1 tests in Tables 1, 2 and 3. Table 1 gives information for the un-irradiated conditions, Table 2 contains the irradiated data and Table 3 gives the irradiation-induced shifts.

RESULTS AND DISCUSSION OF THE REGULATORY APPROACH [11]

Reference Data of KKP1 L-T oriented Material

The non-instrumented baseline C_V data of the un-irradiated L-T oriented KKP1 specimens and the instrumented C_V data of the L-T specimens from the first KKP1 surveillance capsule were provided by Siemens AG / Power Generation Group KWU (Siemens/KWU). The energy transition curves are plotted in Figure 10; the LE and SFA data are shown in Figure 11. Two effects can be seen on Figure 10: irradiation shifts the baseline condition by 10 °C at 41 Joule and irradiation lowers the mean upper shelf by 20 Joule. The non-irradiated baseline data show a large scatter in the upper shelf region, raising the uncertainty on this value. The LE data in Figure 11 display the same shift of about 10°C.

TABLE 1--KKP1 un-irradiated condition.

		L-T As-Received		L-T Reconstituted		T-L Reconstituted	
Tanh Fit Parameters		Energy	LE	Energy	LE	Energy	LE
T_T	(°C)	-32	-40	-41	-43	-20	-23
Slope C	(°C)	27	20	27	27	37	37
LSE	(J) or (mm)	10	0.168	10	0.168	10	0.168
USE	(J) or (mm)	188	2.414	148	1.949	116	1.919
Transition Temperature							
TT41	(°C)	-53.3		-58.0		-36.7	
TT68	(°C)	-42.0		-45.4		-16.7	
TT .89mm	(°C)	-47.6		-48.2		-29.6	
SFA 50%	(°C)	-30.0		-30.0		-15.0	
Shifts Relative to "As-Received" Condition							
STT41	(°C)			-4.7		16.6	
STT68	(°C)			-3.4		25.3	
STT .89mm	(°C)			-0.6		18.0	
SSFA 50%	(°C)			0.0		15.0	
L-T to T-L Orientation Shift							
QTT41	(°C)					21.3	
QTT68	(°C)					28.7	
QTT .89mm	(°C)					18.6	
QSFA 50%	(°C)					15.0	

TABLE 2--KKP1 irradiated condition.

		L-T As-Received		L-T Reconstituted		T-L Reconstituted	
Tanh Fit Parameters		Energy	LE	Energy	LE	Energy	LE
T_T	(°C)	-24	-30	-19	-21	-2	-4
Slope C	(°C)	27	27	27	27	37	37
LSE	(J) or (mm)	10	0.182	10	0.182	10	0.182
USE	(J) or (mm)	168	2.506	146	2.122	117	1.935
Transition Temperature							
TT41	(°C)	-43.3		-35.7		-18.9	
TT68	(°C)	-31.4		-23.1		1.0	
TT .89mm	(°C)	-41.2		-28.6		-11.3	
SFA 50%	(°C)	-15.0		-15.0		0.0	
Shifts Relative to "As-Received" Condition							
STT41	(°C)			7.6		24.4	
STT68	(°C)			8.3		32.4	
STT .89mm	(°C)			12.6		29.9	
SSFA 50%	(°C)			0.0		15.0	
L-T to T-L Orientation Shift							
OTT41	(°C)					16.8	
OTT68	(°C)					24.1	
OTT .89mm	(°C)					17.3	
OSFA 50%	(°C)					15.0	

TABLE 3--KKP1 irradiation-induced shifts.

		L-T As-Received	L-T Reconstituted	T-L Reconstituted
Irradiation-induced shift				
ITT41	(°C)	10	22	18
ITT68	(°C)	11	22	18
ITT .89mm	(°C)	6	20	18
ISFA 50%	(°C)	15	15	15

For ductile upper shelf conditions the LE appears to slightly increase after irradiation. As expected, the SFA data reflect the shift of the baseline data induced by irradiation.

Un-irradiated L-T specimens: effect of reconstitution

Figure 12 shows 35 Joules loss of energy for the reconstituted un-irradiated L-T specimens (the reconstituted results in the upper shelf area are based on the low energy as-received upper shelf specimens). From Tables 1, 2 and 3, it can be seen that at the 41J and 68J energy levels, no real shift occurs within the experimental uncertainties of a few degrees, although one would expect a small shift due to the lowering of the upper shelf. Pau

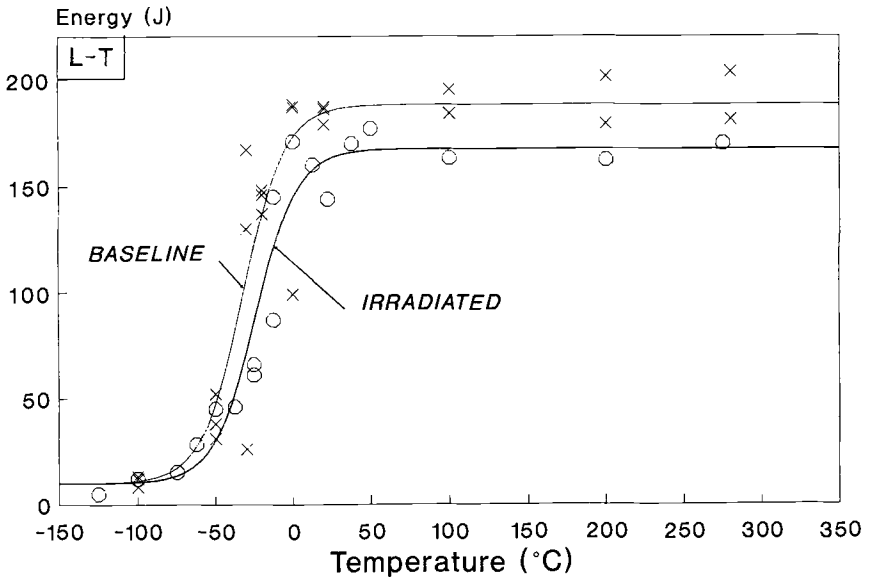


FIG. 10--The effect of irradiation on as-received energy data.

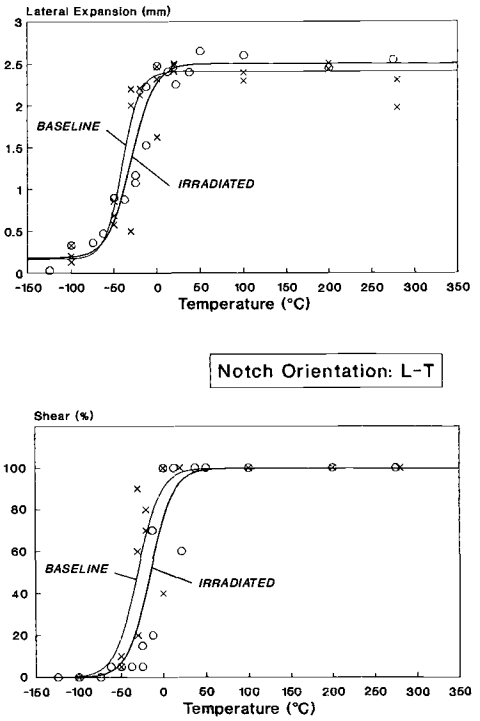


FIG. 11--The effect of irradiation on as-received LE and SFA data.

city of data in the transition region and lower shelf probably causes this observation. From Table 1, there is an expected loss in LE after reconstitution in the upper shelf region; the consequence of plastic constraint. The SFA data of the as-received and reconstituted samples coincide. This is in agreement with the work on HSST-03, where it was shown that within the same orientation, no change in the SFA occurs before or after reconstitution: *the SFA is not influenced by the reconstitution.*

Irradiated L-T Specimens: Effect of Reconstitution

Figure 13 shows the loss of energy for the reconstituted irradiated L-T specimens: the reconstitution loss is 22 Joule, essentially due to plastic constraint. The temperature shift between the irradiated as-received and reconstituted curve is 8°C at 41J and 68J, with an experimental uncertainty of 5 to 10°C. There is a loss in LE after reconstitution and a temperature 'shift' of 13°C (± 5-10°C) at the 0.89 mm index level. The SFA data of the irradiated as-received and reconstituted samples coincide as expected.

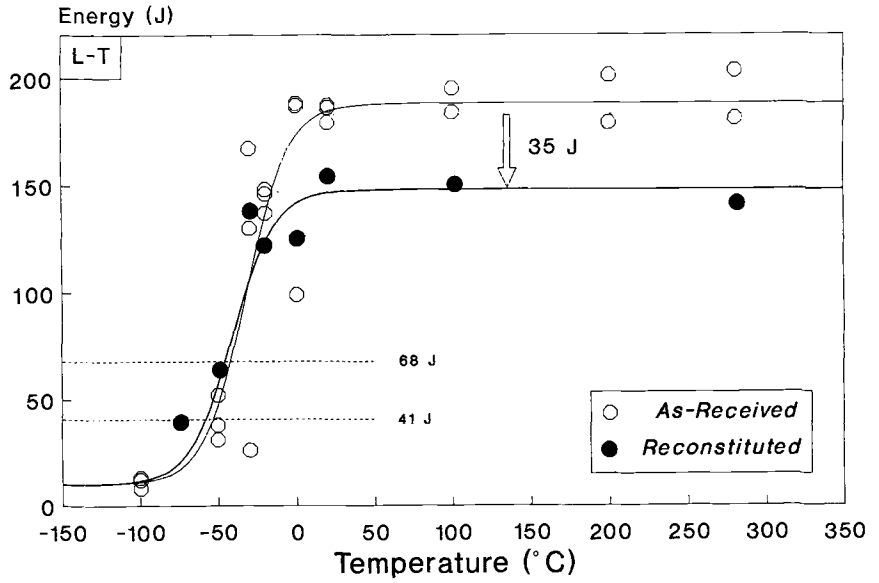


FIG. 12--The effect of reconstitution on fracture energy in the un-irradiated L-T condition.

Conclusion for L-T Reconstituted Specimens

The USE of reconstituted un-irradiated and irradiated L-T specimens are equivalent, as seen in Figure 14. This is because the loss of energy due to the reconstitution is larger for the un-irradiated material than for the irradiated material: indeed, the baseline un-irradiated material has a larger mean upper shelf (and there was quite some scatter on these data) than the irradiated one. The reconstitution energy loss curve, Figure 6, explains the observed pattern. Within the statistical uncertainty on the upper shelf, it is not possible to see an effect of irradiation (here one should remember that the decrease in upper shelf energy due to irradiation on the as-received data was 20J with a large error bar).
Another explanation for the equivalent USE of the un-irradiated and irradiated transition curves was that the reconstitution might have induced annealing effects of irradiation damage, thereby raising the upper shelf of the reconstituted irradiated material. It must be acknowledged that the load diagram approach indicates a slight systematic increase of the energy fraction A (3 Joules) after reconstitution. This effect is a small annealing effect correlated to a change in work hardening capability, but - as will be explained further - we do not believe it to be a consequence of the reconstitution. If annealing due to reconstitution would occur, one would expect a negative temperature shift of the reconstituted irradiated curve of Figure 14 towards the baseline curve. This is not the case and the reconstituted L-T data reflect the irradiation-induced shift of the Siemens/KWU data. This can also be seen in Figure 15, where the effect of irradiation on the LE and SFA data is shown. Here another argument in support of the present views does surface: irradiation does slightly increase the lateral expansion at ductile upper shelf temperatures, much in the same way as observed for

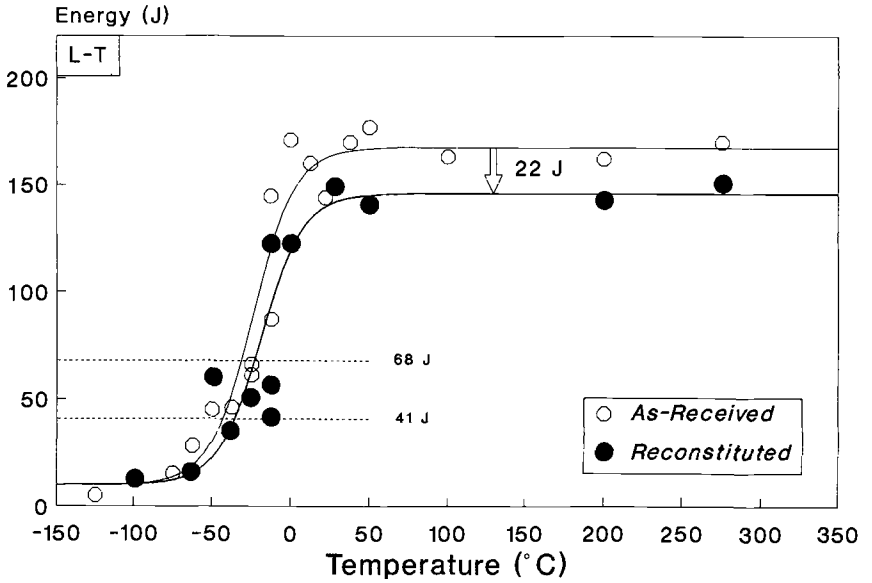


FIG. 13--The effect of reconstitution on fracture energy in the irradiated L-T condition.

the as-received irradiated specimens (Figure 11). This promotes strong confidence in the reconstitution procedure and reinforces our interpretation of the absorbed-energy trends (because lateral expansion is much less sensitive to flow blockage by the welded zones). The observed energy and LE shifts are the sum of the irradiation-induced shift with the

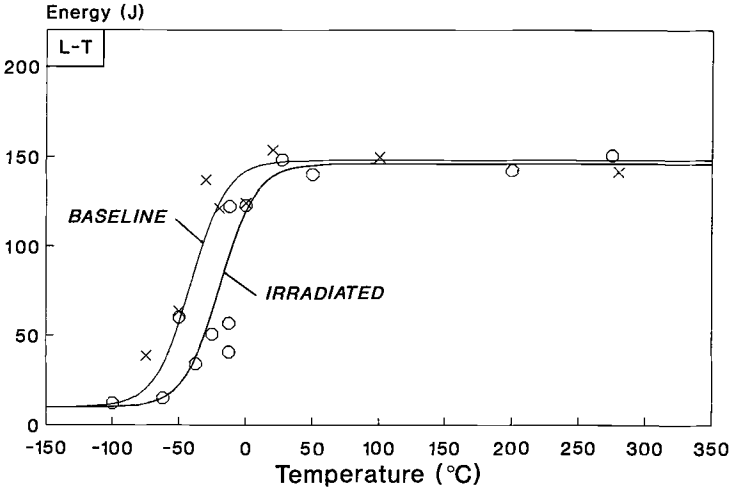


FIG. 14--The effect of irradiation on L-T reconstituted energy data.

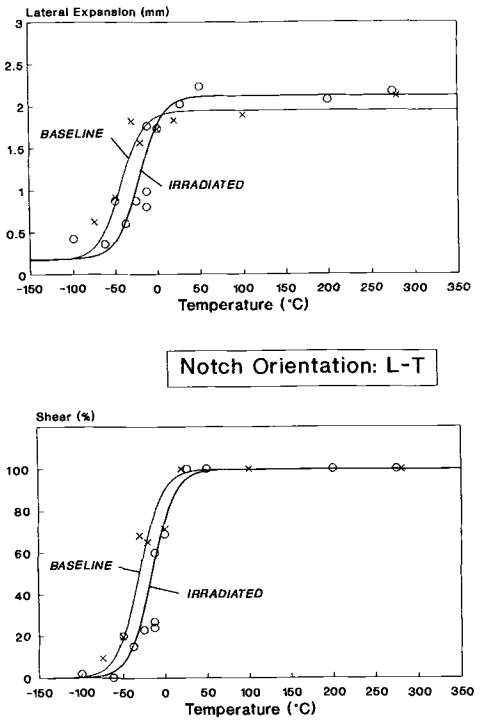


FIG. 15--The effect of irradiation on reconstituted LE and SFA data.

shifts due to the lowering of the upper shelf (plastic constraint). As the SFA-data in Figure 15 are not subjected to this artificial increase of the shift, the SFA-shift shows the real irradiation-induced shift previously observed on the Siemens/KWU data of Figure 11.

Un-Irradiated L-T versus T-L Reconstituted Specimens: Effect of Notch Orientation

Figure 16 demonstrates the notch orientation effect on the Charpy energy for the un-irradiated reconstituted samples. The mean upper shelf energy difference is 32 Joules and, as can be seen, the scatter on the un-irradiated reconstituted T-L data is rather high. As we can not state that the L-T reconstitution loss will be the same as the T-L reconstitution loss, we cannot derive the T-L as-received energy curve accurately. *The reconstituted T-L energy curve must be seen as a lower bound energy curve for un-irradiated T-L oriented samples. This conservative upper shelf is well above the Regulatory KTA 3203 limit of 100 Joules in the un-irradiated condition.*

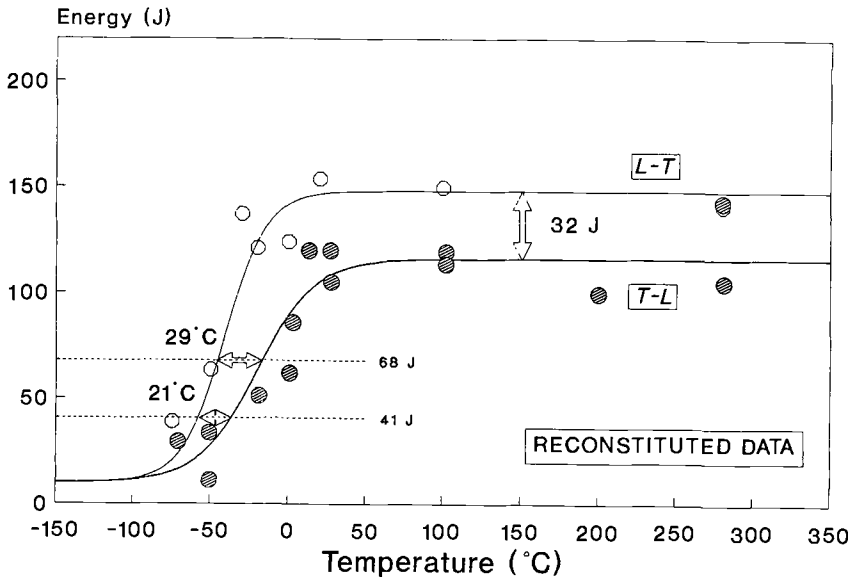


FIG. 16--The effect of notch orientation on fracture energy in the un-irradiated condition.

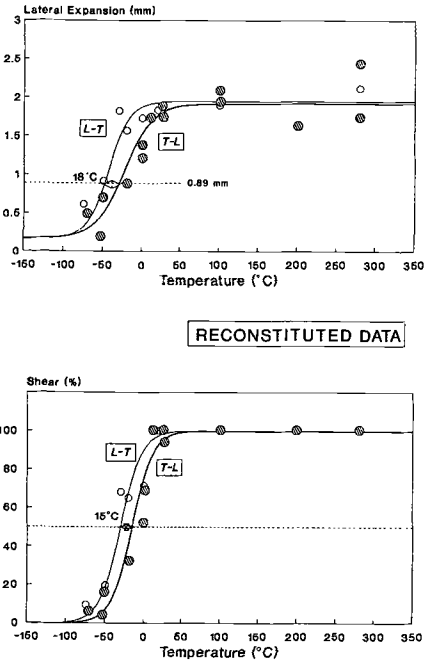


FIG. 17--The effect of notch orientation on LE and SFA in the un-irradiated condition.

Transition temperature shifts are 21°C at the 41 Joule level and 29°C at the 68 Joule Regulatory level. These shifts are a combination of the effect of upper shelf lowering (of both L-T and T-L data) and of a real temperature shift due to the difference in orientation of the specimens. Latter shift component of 15°C can be found from the SFA-fits of Figure 17. The LE data show equal shelf for un-irradiated L-T and T-L reconstituted specimens; the shift at 0.89 mm reflects therefore the difference in material properties between the two orientations, and is thus, within uncertainties, the same as the SFA shift.

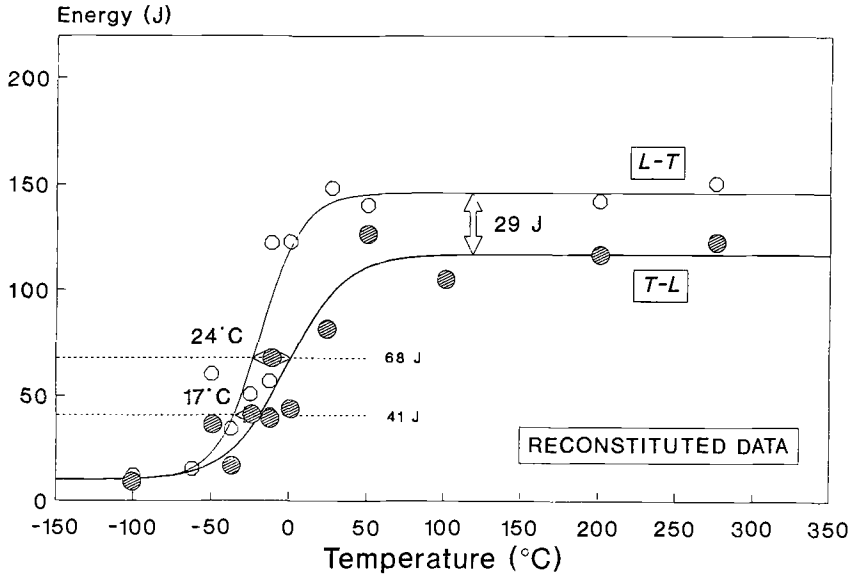


FIG. 18--The effect of notch orientation on fracture energy in the irradiated condition.

Irradiated L-T versus T-L Reconstituted Specimens: Effect of Notch Orientation

Figure 18 demonstrates the notch orientation effect on the Charpy energy for the irradiated reconstituted samples. The conclusions are similar to the ones for the un-irradiated situation from the previous paragraph. The USE difference is 29 Joule. *The reconstituted T-L energy curve must again be seen as a lower bound energy curve for irradiated T-L oriented samples. This conservative upper shelf is well above the limiting 68 Joule level for irradiated beltline material.*

From Table 2, the conclusions for the LE and SFA behaviour are similar to those for the un-irradiated situation.

Conclusion for T-L Reconstituted Specimens

Statistically the upper shelf energy of reconstituted non-irradiated and irradiated T-L specimens coincides, as can be seen in Figure 19. The same reasoning as for the L-T orientation holds and Figure 6 explains the observed patterns. Again, it is important to acknowl

edge the large amount of scatter on the data, so that a small effect of irradiation can be hidden. Figure 20 shows the effect of irradiation on the LE and SFA reconstituted T-L data. The conclusions are the same as for the L-T reconstituted data.

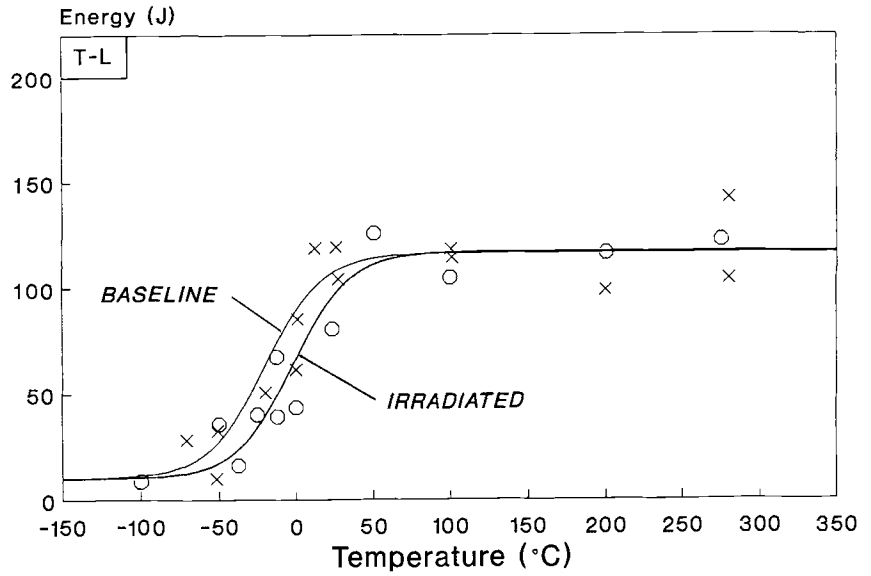


FIG. 19--The effect of irradiation on T-L reconstituted energy data.

Conclusions for the T-L Upper Shelf Behaviour

The corrected USE for the un-irradiated and irradiated T-L orientation of the KKP1 material cannot be derived accurately because the reconstitution energy loss is a function of the upper shelf energy of the different KKP1 material conditions. The reconstituted energy curves do, however, represent a conservative lower bound for the real USE. These USE-values for the reconstituted un-irradiated and irradiated T-L transition curves, respectively 116J and 117J (given in Tables 1 and 2), are well above the limiting 100J (un-irradiated) and 68J (irradiated) value specified in KTA 3203, paragraph 9.2 e, for beltline materials. Using the correction curve, Figure 6, an estimation of the real energy transition curves can be made by evaluating the energy loss needed to come to the measured reconstituted energy values. The estimated loss is about 10 J; discrimination between the non-irradiated and irradiated data is not relevant in views of the statistical uncertainties. The corrected energy curves are presented in Figure 21 and the characteristic parameters are given in Table 4. The USE values of the 'corrected' T-L transition curves are in good correspondence with the values found in reference 12.

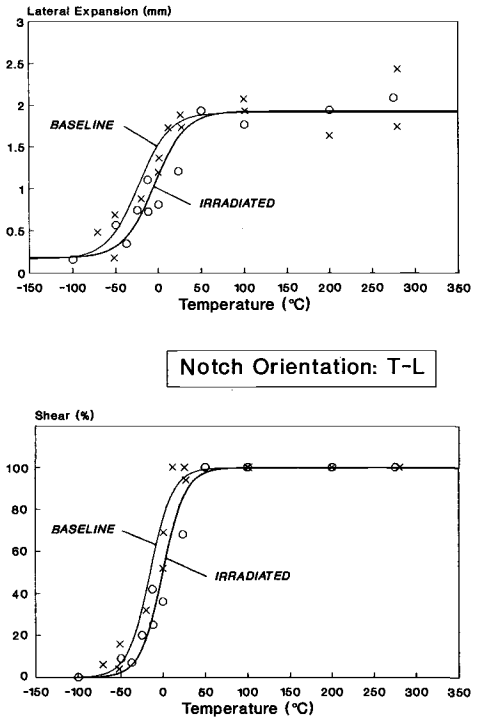


FIG. 20--The effect of irradiation on reconstituted LE and SFA data.

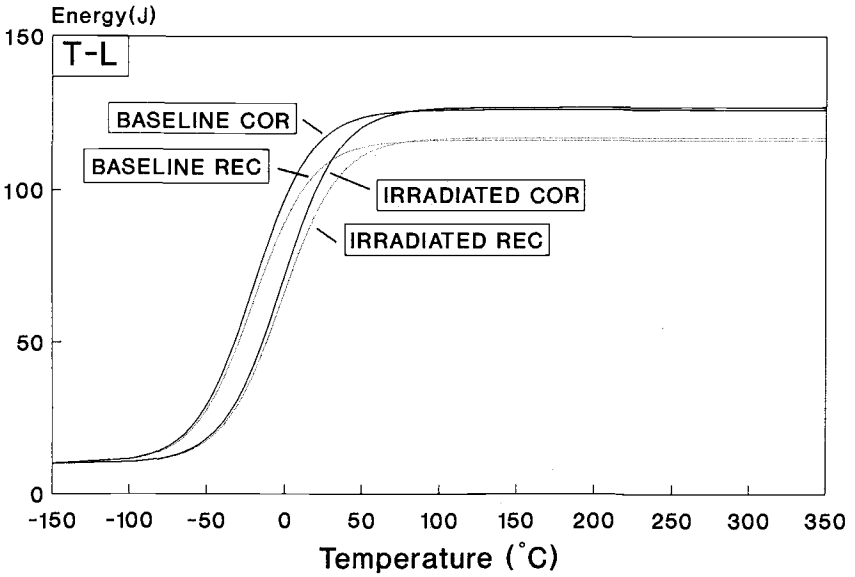


FIG. 21--KKP1 T-L curves 'corrected' for reconstitution losses.

TABLE 4--Corrected T-L energy parameters.

		T-L Reconstituted Baseline	T-L Corrected Baseline	T-L Reconstituted Irradiated	T-L Corrected Irradiated
Tanh Fit Parameters		Energy	Energy	Energy	Energy
T_T	(°C)	-20	-20	-2	-2
Slope C	(°C)	37	37	37	37
LSE	(J) or (mm)	10	10	10	10
USE	(J) or (mm)	116	126	117	127
Transition Temperature					
TT41	(°C)	-36	-39	-19	-21

Conclusions for the Temperature Shifts

Tables 1, 2 and 3 give the characteristic parameters for the fits. Besides the classical engineering parameters - according to KTA 3203 - the different temperature shifts, already mentioned before, are indicated. The important facts to note are:

1. There is no SFA shift, relative to the as-received condition, for un-irradiated and irradiated reconstituted KKP1 L-T material. The energy and lateral expansion shifts, in the engineering hyperbolic tangent formulation, are a consequence of the change in upper shelf due to plastic constraint.

2. There exists a true 15°C SFA temperature shift between L-T and T-L material (in the un-irradiated and as well as in the irradiated condition). This shift is not affected by the reconstitution. Some additional, small effects can be seen on the energy and lateral expansion data, again a consequence of plastic flow constraint.

3. Irradiation induces a 15°C SFA temperature shift between the baseline and the irradiated data, independently of reconstitution and notch orientation. The uncertainty of this shift is due to the scatter of the experimental data and is of the order of 5 - 10°C.

4. The methodology to reconstruct the corrected T-L curves does not alter the conclusions 1 through 3 of this paragraph.

THE LOAD DIAGRAM APPROACH [6, 7, 10]

This analysis encompasses all tests performed on the KKP1 base material in the unirradiated and irradiated, as-received and reconstituted conditions. All instrumented tests taken by SCK•CEN were carefully analysed and the non-instrumented and instrumented Siemens/KWU data were revisited. The fit methodology, shown in Figure 9, disentangles for each condition of the KKP1 material the different energy fractions of the instrumented test spectrum. Most losses after reconstitution come from fraction B and represent a loss of tearing-related energy. For the irradiated L-T reconstitutions a slight increase of 3 Joules of fraction A is found. This effect is clearly related to a change in work hardening of the material as discussed below.

As mentioned before, the load diagram analysis serves here as a guide to pattern the hyperbolic tangent analysis. The fit results from the load diagram approach are therefore, in general, in accordance with the tanh approach. The discussion will as such be limited to some supplementary findings that can be seen on the load diagrams of the KKP1 material.

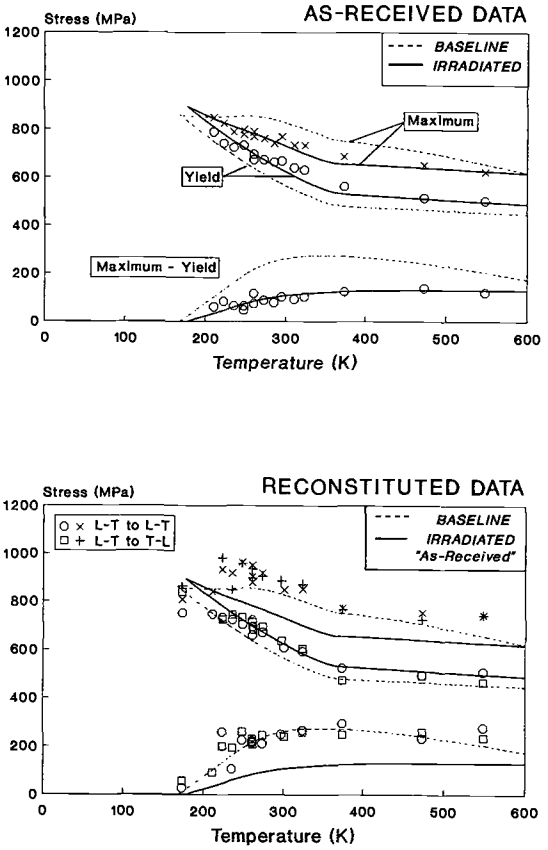


FIG. 22--Restoration of work hardening of the KKP1 irradiated surveillance material.

The top part of Figure 22 shows the usual irradiation-induced increase of yield stress, but also a decrease of work hardening for the irradiated as-received L-T oriented KKP1 specimens. The baseline data are not the actual KKP1 loads - as no instrumented data are available - but the indicated work hardening is representative for the un-irradiated KKP1 22NiMoCr37 material [6]. The lower part of Figure 22 contains, besides the indicative yield and maximum load evolution from the top part of the figure, the experimental yield and maximum load points from the reconstituted broken irradiated KKP1 specimens. It is obvious that the work hardening of the reconstituted irradiated specimens has been restored. At this time, we are convinced - given our extensive experience with reconstitution - that this effect is not due to the reconstitution of the broken irradiated KKP1 material. Modelling arguments, based on experimental data, exist that relate the phenomenon to the thermal activation of an irradiation-induced defect in the irradiated material after long storage time at ambient temperature [7]. Small temperature shifts can be induced by this phenomenon as well, but are not in the present case.
The consequences on the fracture energy of the irradiated KKP1 material have been evaluated from the load diagram. The effect of the restoration of the work hardening corresponds to a maximum increase of the C_V-absorbed energy of 3 Joules. It therefore does not alter any of the conclusions made in the Regulatory context.

GENERAL CONCLUSION

Broken Charpy-V specimens with L-T orientation in un-irradiated and irradiated condition have been reconstituted into T-L oriented specimens using stud-gun welding. The reconstituted specimens have been tested according to EN10045 to determine the Charpy-V transition temperature and the upper shelf energy of the transverse oriented material, as required by KTA 3203. The data have been analysed according to the Regulatory rules and according to the load diagram approach.
Although the analysed C_V-test results show excellent overall consistency of the expected reconstitution energy loss patterns due to constraint by the hard welded zones, it is not straightforward to quantitatively account for these losses. The energy loss due to reconstitution is a function of the USE of the material and depends therefore on its orientation and irradiation condition. The mean USE values of the un-irradiated and irradiated reconstituted T-L material are 116J and 117J, respectively. The fact of having two identical upper shelf levels is coincidental and a consequence of having different losses for different USE for the un-irradiated and irradiated material in the full-size condition. The scatter of the results of the reconstituted T-L specimens might, however, mask a small irradiation effect.
A ***correction*** curve, based on a limited amount of tested material, allows for the adjustment of the transition curves of reconstituted specimens for these energy losses. As indicated, the gain in USE is only small (~ 10 Joules) and the transition temperature hardly changes. It is important to stress the fact that the energy loss curve needs more experimental verification. **The experimentally-observed T-L reconstituted curves are the lower bounds of the actual full-size curves.** These conservative bounds are well above the limiting 100J value for the un-irradiated baseline condition and 68J value for the irradiated condition, as specified by the Regulator in KTA 3203, paragraph 9.2 e, for beltline material.

The consistent analysis of the instrumented KKP1 data, according to the load diagram procedure, has guided the hyperbolic tangent analysis and given supplementary information on the fracture behaviour of the material. The load diagram of the irradiated KKP1 material revealed that the strain hardening capability of the reconstituted material is superior. This behaviour is believed to stem from the presence of unstable irradiation-induced defects, thermally activated during long storage time at ambient temperature; the consequences of such possibility are under further investigation.

The quality assurance of this KKP1 program was followed up by TÜV Südwest, MPA-Stuttgart and KKP.

ACKNOWLEDGEMENTS

The authors are indebted to the technical staff of SCK•CEN. They also wish to thank T. Weissenberg and J. Föhl from MPA Stuttgart, for the fruitful discussions that contributed to this work and this report. The SCK•CEN authors thank KKP for the encouragement to extend this work beyond the normal surveillance practice; they also are indebted to TÜV and MPA for the valuable contributions to the QA of the reconstitution technique at SCK•CEN.

REFERENCES

[1] Vandermeulen, W., Fabry, A., Puzzolante, J.L., Van de Velde, J., Van Ransbeeck, Th., and van Walle, E., "Charpy Specimen Reconstitution as a Means of Providing Data for Plex Licensing Purposes," Int. Journ. Pres. Ves. & Piping, Vol. 54, 1993, pp 89-98.

[2] van Walle, E., Fabry, A., Van Ransbeeck, T., Puzzolante J.L., Vandermeulen, W., Van de Velde, J., Klausnitzer, E., and Gerscha, M., "The Reconstitution of Small Remnant Parts of Charpy-V Specimens," presented at SMIRT11, PCS 2, Taipei, Taiwan, 1991.

[3] van Walle, E., Fabry, A., Aït Abderrahim, H., Chaouadi, R., D'hondt, P., Puzzolante, J.L., Van de Velde, J., Van Ransbeeck, Th., and Gerard, R., "Pressure Vessel Steel Research: Belgian Activities," Proceedings of the IAEA Specialists Meeting on Advanced Structural Integrity Assessment Procedures, IWG-LMNPP-94/4, San Carlos de Bariloche, Argentina, 1994.

[4] van Walle, E., "Reconstitution: where do we stand?" and references therein, contribution to this conference.

[5] Klausnitzer, E., contribution to the 'ASTM Workshop on Reconstitution', San Diego, CA, 1991.

[6] Fabry, A., van Walle, E., Chaouadi, R., Wannijn, J.P., Verstrepen, A., Puzzolante, J.L., Van Ransbeeck, Th., Van de Velde, J., and Petrova, T., "RPV Steel Embrittlement: Damage Modeling and Micromechanics in an Engineering Perspective," Proceedings of the IAEA/OECD Specialists Meeting on Irradiation Embrittlement and Optimization of Annealing, Paris, France, 1993.

[7] Fabry, A., van Walle, E., Van de Velde, J., Chaouadi, R., Puzzolante, J.L., Van Ransbeeck, Th., and Verstrepen, A., "On the Use of the Instrumented Charpy-V Impact Signal for Assessment of RPVS Embrittlement," presented at the 2nd ESIS/TC5 Workshop, Mol, Belgium, and Report BLG 650, SCK•CEN, Mol, Belgium, 1994.

[8] Fabry, A., Van de Velde, J., Biemiller, E.C., Carter, R.G., and Petrova, T., "Research to Understand the Embrittlement Behavior of the Yankee Surveillance Plate and Other Outlier Steels," contribution to this conference.

[9] ESIS/TC5 Technical Sub-Committee on Dynamic Testing at Intermediate Srain Rates, "Proposed Standard Method for the Instrumented Charpy-V Impact Test on Metallic Materials," Draft 7, June 1992.

[10] Fabry, A., van Walle, E., and Verstrepen, A., "Analysis of the RPVS of KKP1 on basis of instrumented Charpy traces," Report R2989, SCK•CEN, Mol, Belgium, 1993.

[11] van Walle, E., Fabry, A., Van Ransbeeck, Th., and Van de Velde, J., ,"Ergänzende Untersuchungen zum Bestrahlungsprogramm des Reaktordruckbehälteers Kernkraftwerk Philippsburg (KKP1), Final Report TEC94/39/EvW, SCK•CEN, Mol, Belgium, 1994.

[12] TÜV Südwest, 'Report of the RPV of KKP1', KS (M)-127/91, Kap. 8, June 1991.

Arthur L. Lowe, Jr., P.E.[1]

VARIATIONS IN CHARPY IMPACT DATA EVALUATED BY A ROUND-ROBIN TESTING PROGRAM - A SUMMARY

REFERENCE: Lowe, A. L., Jr., **"Variations in Charpy Impact Data Evaluated by a Round-Robin Testing Program—A Summary,"** *Effects of Radiation on Materials: 17th International Symposium, ASTM STP 1270,* David S. Gelles, Randy K. Nanstad, Arvind S. Kumar, and Edward A. Little, Eds., American Society for Testing and Materials, 1996.

ABSTRACT: A round-robin type test program was designed to quantify some of the variables associated with Charpy impact test data. Each participant tested pre-machined specimens at each of six designated test temperatures. The data were evaluated using several techniques normally used to determine transition region temperatures and upper-shelf energies. These data were interpreted statistically to determine mean values and standard deviations. Variations in data appear to be more a factor of the specimen location within the material than related to test temperature. The variations in the data between the different testing participants were within the limits commonly observed. The expected erosion determining the 30 and 50 ft-lb transition temperatures and the upper-shelf energies were found to be independent of the evaluation technique used.

KEYWORDS: Charpy impact data, Charpy data, error analysis, controlling parameters, transition temperature shift, upper-shelf energy

The idea for this program resulted from a review of the papers presented at the ASTM Symposium on Charpy Impact Test: Factors and Variables[1]. The papers primarily address the small differences in the physical components of the testing process[2-8]. These provided an insight and justification as to why the test procedure must be followed without any deviations. However, a question still exists which has to do with the comparability of data developed by different testing facilities[9]. It was reasoned that this could be resolved by conducting a round-robin test program in which all parameters are controlled except for the actual testing and recording of the

[1]Mr. Lowe is with Lowe Associates, P. O. Box 11964, Lynchburg, VA 24506-1964.

Copyright© 1996 by ASTM International www.astm.org

test data. It was with this purpose in mind that this study was planned and conducted. Another question related to this problem is the variability in the interpretation of results, but that has to be another program.

PROGRAM DESIGN

A total of ten laboratories agreed to participate in the round-robin testing. It was agreed that the identify of the participants would not be published. The program was designed such that all testing would be performed in accordance with each participant's established procedures. The only requirement was that all testing be performed in accordance with ASTM E-23[10]. All specimens were machined by the same machine shop to minimize as far as practical variations in specimen geometry. The specimens were designated as to the temperature at which they were to be tested with each participant testing three specimens at each test temperature. The test temperatures were 10F(-12.2C), 40F(4.4C), 70F(21.1C), 100F(37.8C), 170F(115.5C) and 240F(115.5C). The temperatures were selected based on previously obtained data for the weld metal and designed to provide three test temperatures in the transition region and three test temperatures on the upper-shelf region. This information was provided on a form that listed the specimen number and test temperature and provided spaces to record the impact energy, lateral expansion and shear fracture data. (Only the impact energy data is presented and evaluated in this paper.) The participant completed the form by providing the test results after impact testing. No analysis of the data by the participants was required because all the analyses would be performed at one time. This was designed to eliminate variations in interpretation of the data. This is not to imply that only one source was qualified to evaluate the data, but was done to minimize another potential variable that could be a factor in the later interpretation and evaluation of the data.

MATERIAL

The material selected was a Mn-Mo-Ni/Linde 80 submerged-arc weld metal. A weld metal was selected because of the relative uniform through thickness toughness properties, especially as compared to a piece of forging or plate material. In addition, the selected material had been tested in several test programs and the basic Charpy impact properties were known. This minimized the opportunity of selecting test temperatures which would not provide the data in the transition region and on the upper-shelf needed to perform the evaluation.

Three blocks of weld metal cut from the same weldment were selected to provide the best consistency in material impact properties. The cutting diagrams and specimen numbering sequence of each of the three blocks are shown in Figure 1. The number of specimens in each block permitted the selection of one specimen per temperature per block. This permitted an evaluation of the toughness properties within each block, as well as a block to block averaging and comparison.

Test Temp, F	**Bold Figures** = Charpy Impact Energy, ft-lbs Light Figures = Specimen Designation												
10 / 40	**25.0** 001	**27.5** 002	**20.0** 003	**22.0** 004	**28.0** 005	**23.0** 006	**27.0** 007	**23.0** 008	**24.9** 009	**24.0** 010		**27.5** 012	**31.5** 013
40 / 70	**30.0** 014	**38.0** 015	**30.0** 016	**23.0** 017	**25.0** 018	**29.0** 019	**26.7** 020	**33.5** 021		**39.0** 023	**35.0** 024	**35.5** 025	**41.9** 026
70 / 100	**42.0** 027	* 028	**41.0** 029	**35.0** 030	**41.2** 031	**38.5** 032		**51.0** 034	**48.0** 035	**49.0** 036	**48.0** 037	**47.0** 038	* 039
100 / 170	**58.0** 040	**55.0** 041	**52.3** 042	**46.0** 043		**57.5** 045	**58.0** 046	**63.0** 047	**63.0** 048	**60.0** 049	* 050	**63.0** 051	**60.0** 052
170 / 240	**65.2** 053	**66.5** 054		**63.0** 056	**61.5** 057	**69.0** 058	**66.0** 059	**69.0** 060	* 061	**66.0** 062	**64.0** 063	**69.0** 064	**67.0** 065

Block "A"

Test Temp, F	**Bold Figures** = Charpy Impact Energy, ft-lbs Light Figures = Specimen Designation												
10 / 40	**30.0** 066	**32.5** 067	**29.0** 068	**23.4** 069	**28.0** 070	**25.0** 071	**29.0** 072	**32.0** 073	**35.0** 074	**23.5** 075		**37.0** 077	**36.0** 078
40 / 70	**36.0** 080	**35.0** 081	**31.0** 082	**26.5** 083	**28.0** 084	**31.0** 085	**30.0** 086	**31.5** 087		**47.0** 089	**45.0** 090	**45.0** 091	**46.7** 092
70 / 100	**41.0** 094	* 095	**36.0** 096	**40.0** 097	**36.6** 098	**39.5** 099		**50.0** 101	**48.0** 102	**58.0** 013	**56.8** 104	**53.0** 105	* 106
100 / 170	**49.0** 108	**51.0** 109	**50.5** 110	**54.0** 111		**59.5** 113	**56.5** 114	**66.0** 115	**64.2** 116	**68.0** 117	* 118	**69.0** 119	**62.0** 120
170 / 240	**61.0** 122	**55.0** 123		**58.0** 125	**56.0** 126	**65.0** 127	**62.8** 128	**63.0** 129	* 130	**64.0** 131	**62.0** 132	**66.5** 133	**63.0** 134

Block "B"

Test Temp, F	**Bold Figures** = Charpy Impact Energy, ft-lbs Light Figures = Specimen Designation												
10 / 40	**14.0** 136	**18.0** 137	**20.0** 138	**21.9** 139	**19.0** 140	**16.5** 141	**17.0** 142	**22.0** 143	**19.3** 144	**25.0** 145		**35.0** 147	**30.0** 148
40 / 70	**24.0** 151	**24.4** 152	**23.0** 153	**23.5** 154	**21.0** 155	**23.0** 156	**25.5** 157	**32.0** 158		**29.0** 160	**26.0** 161	**34.0** 162	**40.0** 163
70 / 100	**45.0** 166	* 167	**53.0** 168	**53.0** 169	**54.8** 170	**54.5** 171		**61.0** 173	**60.0** 174	**62.5** 175	**65.0** 176	**64.0** 177	* 178
100 / 170	**53.0** 181	**53.0** 182	**51.0** 183	**49.5** 184		**55.0** 186	**51.0** 187	**60.0** 188	**60.8** 189	**60.0** 190	* 191	**61.0** 192	**53.0** 193
170 / 240	**70.5** 196	**65.0** 197		**69.0** 199	**65.0** 200	**74.0** 201	**74.0** 202	**73.0** 203	* 204	**75.0** 205	**67.0** 206	**78.4** 207	**71.0** 208

Block "C"

FIGURE 1 -- Identification of Individual Charpy Specimens and Their Corresponding Tested Impact Energy. The Test Temperature for Each Group of Specimens is Shown at the Left. (Specimen marked * tested at a different temperature.)

RESULTS

The Charpy impact energy data for each specimen is presented in Figure 1 along with the specimen identification. The top number on each specimen is the measured Charpy impact energy. The lower number is the specimen identifier. The first ten specimens in each block were tested at 10F(-12.2C) and the second ten specimens were tested at 40F(4.4C). This is repeated through the specimens of each block with the "X" block indicating the change in test temperature. These data were evaluated to determine the statistical variations in the individual specimen data sets within each block. These data are represented in Table 1 which shows the mean value and standard deviation for each test temperature group of specimens. These groups contained between 2 and 10 specimens per test temperature. It is recognized that any data obtained from a group of less than three specimens should be ignored but is included for completeness.

The Charpy impact energy data for each participant in the program are presented in Figures 3 through 7 and shows a comparison of all participants data at a test temperature compared to the mean and one standard deviation of all the data at the comparison temperature. Each participant's data is designated by the mean value and the one standard deviation data values. In addition, standard deviations of each participants individual temperature data sets are summarized in Figure 8 and are compared to the mean value for each participants data.

The individual Charpy energy curves are not presented because of space limitations. Each set of data for each participant was evaluated by developing Charpy curves using three different techniques. These were, the normal empirical curve fit which has been common practice for years, the linear average data fit which is nothing more than the statistical average of the data in the transition region and in the upper-shelf region, and finally the tanh curve fit method[11] which is a computer statistical technique that uses a hyperbolic tangent curve fit mechanism for fitting a curve to Charpy data. These data curves were used to determine the 30 ft-lb(40.7J) and 50 ft-lb(67.8J) transition temperatures and the upper-shelf energies. All these data are summarized in Table 2 along with an evaluation of the mean and standard deviations of each transition temperature and the upper-shelf energy.

DISCUSSION

Analysis of the measured Charpy energy data grouped by test temperature within each material block are presented in Table 1. This provides an opportunity to determine the relative characteristics of the individual blocks of weld metal. A comparison of the energy data obtained at 10F(-12.2C) and at 240F(115.5C) show similar values for Blocks A and B while Block C has a lower 10F(-12.2C) value and a higher value at 240F(115.5C). This is not inconsistent with the variations that may be expected within a weldment. The relative closeness of the two energy values in

TABLE 1 -- Evaluation of Charpy Energy Data Within Each Material Block Grouped by Test Temperature

Specimen Row	Specimen Numbers	Number of Specimens	Test Temp. F(C)	Charpy Energy, ft-lbs(J) Mean	Standard Deviation
Block A					
1	001-010	10	10(-12.2)	24.4(33.1)	2.56(3.4)
1	012-013	2	40(4.4)	29.5(40.0)	2.83(3.8)*
2	014-021	8	40(4.4)	29.4(39.9)	4.77(6.5)
2	023-026	4	70(21.1)	37.8(43.1)	3.15(4.3)
3	027-032	5	70(21.1)	39.4(53.4)	2.86(3.9)
3	034-038	5	100(37.8)	48.6(65.9)	1.52(2.1)
4	040-043	4	100(37.8)	52.8(71.6)	5.11(6.9)
4	045-052	7	170(76.7)	60.6(82.2)	2.39(3.2)
5	053-054	2	170(76.7)	65.8(89.2)	0.92(1.2)*
5	056-065	9	240(115.5)	66.0(89.5)	2.77(3.7)
Block B					
1	066-075	10	10(-12.2)	23.7(32.1)	3.89(5.3)
1	077-078	2	40(4.4)	36.5(49.5)	0.71(1.0)*
2	080-087	8	40(4.4)	31.1(41.2)	3.19(4.3)
2	089-092	4	70(21.1)	45.9(62.2)	1.08(1.5)
3	094-099	5	70(21.1)	38.6(52.3)	2.19(3.0)
3	101-105	5	100(37.8)	53.1(72.0)	4.28(5.8)
4	108-111	4	100(37.8)	51.1(69.3)	2.10(2.8)
4	113-120	7	170(76.7)	63.6(86.2)	4.55(6.2)
5	120-123	2	170(76.7)	58.0(78.6)	4.24(5.7)
5	125-134	9	240(115.5)	62.2(84.3)	3.30(4.5)
Block C					
1	136-145	10	10(-12.2)	19.2(26.0)	3.16(4.3)
1	147-148	2	40(4.4)	32.5(44.1)	3.53(4.8)*
2	151-158	8	40(4.4)	24.5(33.2)	3.28(4.4)
2	160-163	4	70(21.1)	32.2(43.7)	6.13(8.3)
3	166-171	5	70(21.1)	52.0(70.5)	4.03(5.5)
3	173-177	5	100(37.8)	62.5(84.7)	2.06(2.8)
4	181-184	4	100(37.8)	51.6(70.0)	1.70(2.3)
4	186-193	7	170(76.7)	57.2(77.5)	4.16(5.6)
5	196-197	2	170(76.7)	67.7(91.8)	3.89(5.3)*
5	199-208	9	240(115.5)	71.8(97.3)	4.22(5.7)

*Statistically not correct because only two specimens in test temperature block.

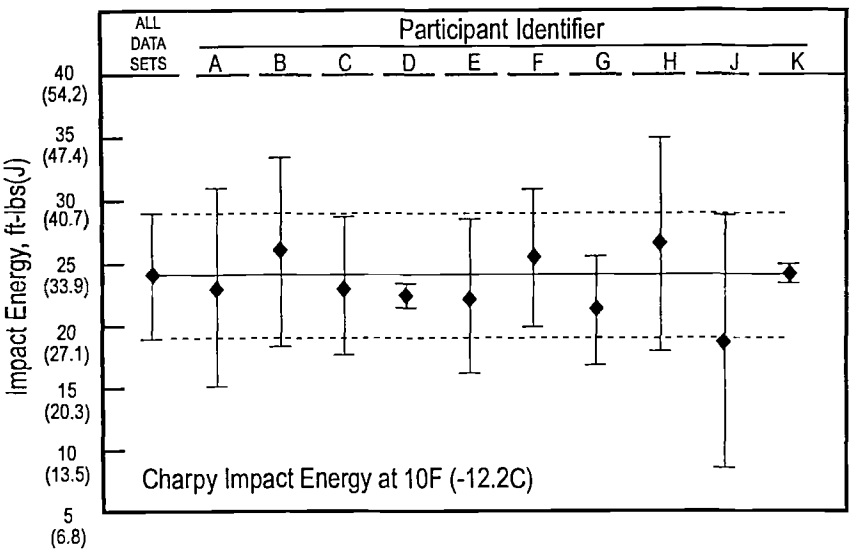


FIGURE 2 -- Comparison of Each Participant's Charpy Energy Data Mean Value and One Standard Deviation to the Total Data Set Mean Value and One Standard Deviation at 10F(-12.2C)

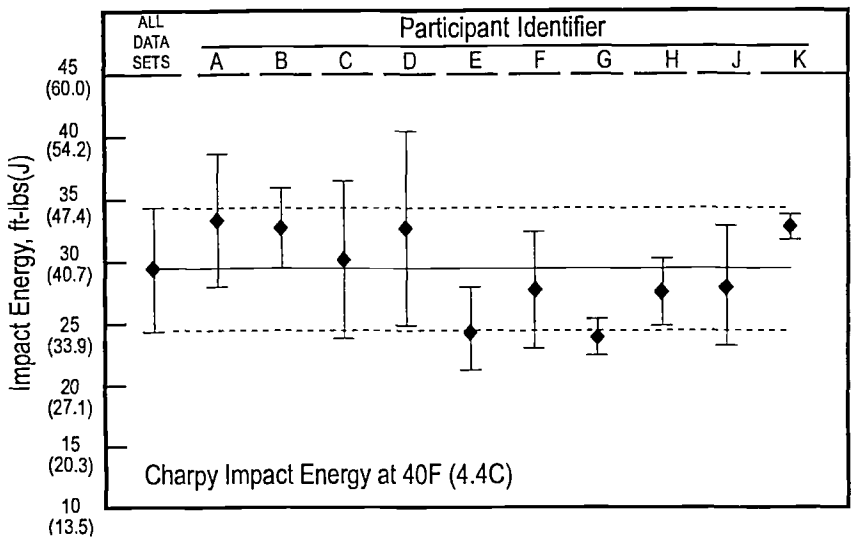


FIGURE 3 -- Comparison of Each Participant's Charpy Energy Data Mean Value and One Standard Deviation to the Total Data Set Mean Value and One Standard Deviation at 40F(4.4C)

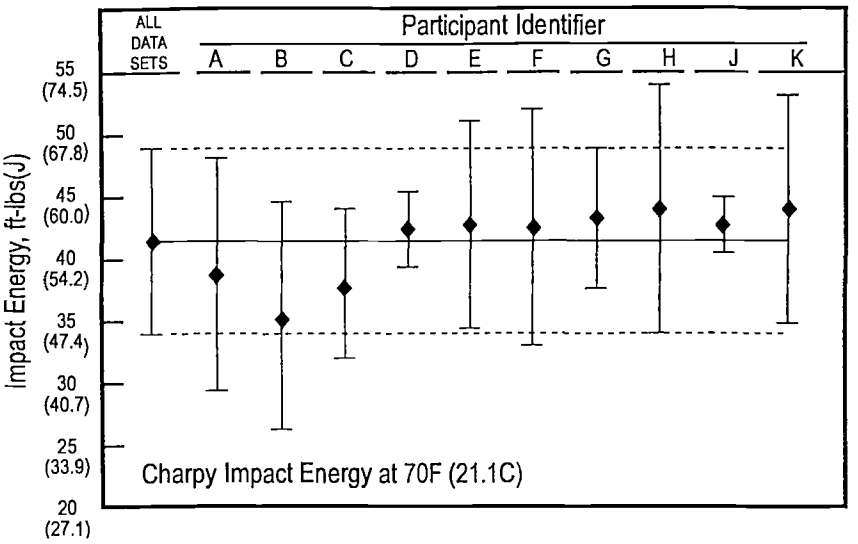


FIGURE 4 -- Comparison of Each Participant's Charpy Energy Data Mean Value and One Standard Deviation to the Total Data Set Mean Value and One Standard Deviation at 70F(21.1C)

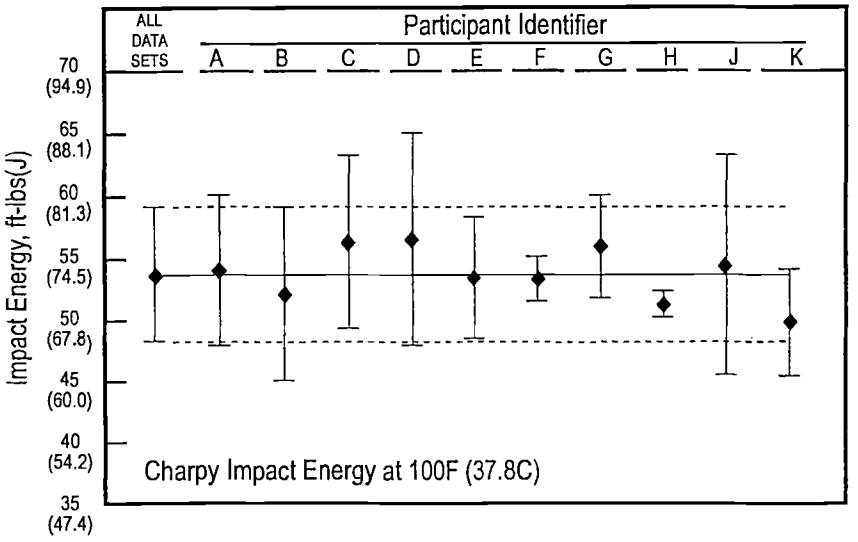


FIGURE 5 -- Comparison of Each Participant's Charpy Energy Data Mean Value and One Standard Deviation to the Total Data Set Mean Value and One Standard Deviation at 100F(37.8C)

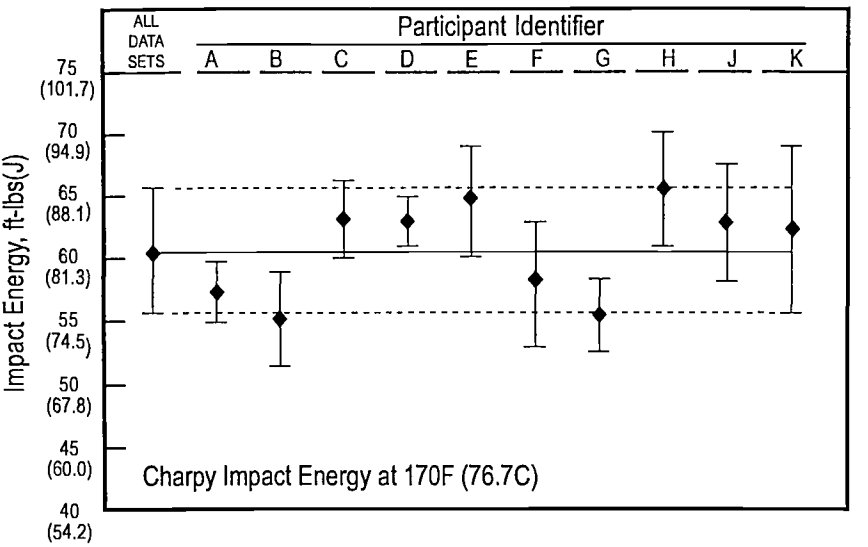


FIGURE 6 -- Comparison of Each Participant's Charpy Energy Data Mean Value and One Standard Deviation to the Total Data Set Mean Value and One Standard Deviation at 170F(76.7C)

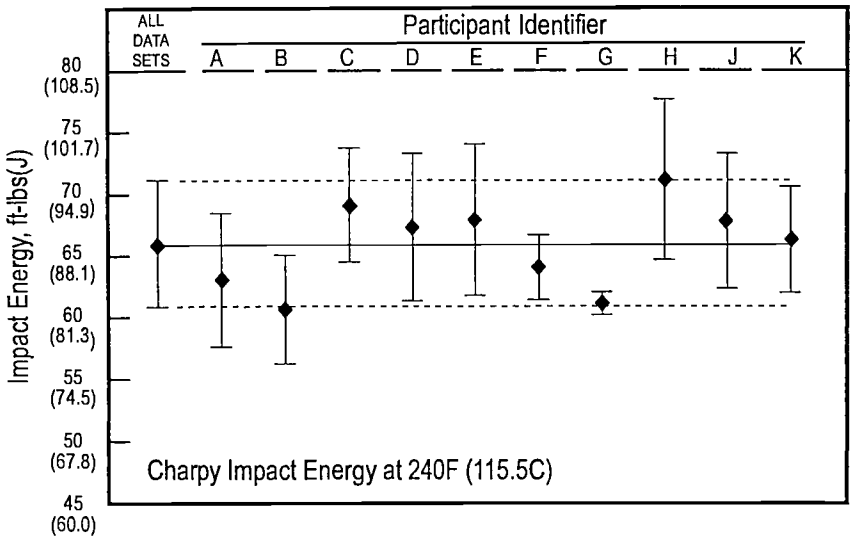


FIGURE 7 -- Comparison of Each Participant's Charpy Energy Data Mean Value and One Standard Deviation to the Total Data Set Mean Value and One Standard Deviation at 240F(115.5C)

TABLE 2 -- Comparison of Charpy Energy Test Results Based on Different Methods of Data Evaluation

	Empirical Curve Fit			Linear Average Fit			Tanh Curve Fit		
Participant	30 ft-lb (40.7J) Temp,F(C)	50 ft-lb (67.8J) Temp,F(C)	USE* ft-lbs (J)	30 ft-lb (40.7J) Temp,F(C)	50 ft-lb (67.8J) Temp,F(C)	USE** ft-lbs (J)	30 ft-lb (40.7J) Temp,F(C)	50 ft-lb (67.8J) Temp,F(C)	USE ft-lbs (J)
A	38(3.3)	94(34.4)	63(85.4)	31(-0.5)	92(27.8)	60(81.3)	36(2.2)	97(36.1)	62(84.1)
B	39(3.9)	102(38.9)	61(82.7)	28(-2.2)	96(35.5)	58(78.6)	46(7.8)	98(36.7)	58(78.6)
C	44(6.7)	90(32.2)	69(93.6)	40(4.4)	89(31.7)	66(89.5)	47(8.3)	89(31.7)	68(92.2)
D	36(2.2)	84(28.9)	68(92.2)	33(0.5)	86(30.0)	65(88.1)	35(1.7)	85(29.4)	66(89.5)
E	55(12.8)	86(30.0)	68(92.2)	49(9.4)	90(32.2)	66(89.5)	46(7.8)	88(31.1)	68(92.2)
F	46(7.8)	84(28.9)	64(86.8)	45(7.2)	91(32.8)	61(82.7)	42(5.5)	89(31.7)	61(82.7)
G	52(11.1)	77(25.0)	62(84.1)	49(9.4)	86(30.0)	59(80.0)	52(11.1)	81(27.2)	59(80.0)
H	46(7.8)	92(33.3)	71(96.3)	45(7.2)	95(35.0)	68(92.2)	34(1.1)	94(34.4)	71(96.3)
J	44(6.7)	82(27.8)	68(92.2)	44(6.7)	88(31.1)	66(89.5)	41(5.0)	88(31.1)	66(89.5)
K	32(0.0)	100(37.8)	67(90.8)	31(-0.5)	100(37.8)	65(88.1)	29(-1.7)	98(36.7)	69(93.6)
Mean	43.2(6.2)	89.1(31.7)	66.1(89.6)	39.5(4.2)	91.3(32.9)	63.4(85.9)	40.8(4.9)	90.7(32.6)	64.8(87.8)
Std. Dev.	6.7(3.7)	8.0(4.4)	3.3(4.5)	8.0(4.4)	4.5(2.5)	3.5(4.7)	7.2(4.0)	5.8(3.2)	4.5(6.1)

*Highest average data set after 100 percent shear reached.
**Average of all data after 100 percent sheer reached.

Blocks A and B would indicate that they were removed from the same region of the weldment and Block C removed from another region of the weldment. This is not an unusual occurrence where large weldments were fabricated to provide material for reactor vessel surveillance programs. It is interesting to note that the average standard deviation for the individual blocks are 3.14 ± 1.21; 3.11 ± 1.25; and 3.59 ± 1.39 ft-lbs (4.26 ± 1.64; 4.22 ± 1.69; 4.87 ± 1.88J) for Blocks A, B, and C respectively. These data implies that there is little overall differences in the characteristics of the blocks, but again Block C is slightly different. This does not create any problems for the program because only one specimen from Block C was included in each test temperature set.

A review of the variations of the standard deviations of the individual test temperatures in Figures 3 through 7 showed no patterns in the data behavior. Participants may have low average value at one temperature and a high average value at another temperature. Likewise, the variations in the average standard deviations varied over a wide range of values. It was anticipated that the results would exhibit a more consistent standard deviation for each energy range tested. This would support the idea that the Charpy energy data were reproducible. The variability of the data is illustrated in Figure 8 where the comparison is made of each participant's Charpy energy standard deviation for each test temperature to the mean standard deviation for each individual data set. The range of the mean standard deviations are similar but the variations in the standard deviations extend over a wide range which demonstrate that there are significant variables influencing the individual data.

Since the real value in Charpy energy data is the determination of the key energy level temperatures required to meet standards and regulatory requirements, the data was evaluated using three commonly accepted techniques. These evaluations show some interesting relationships in the data. At the 30 ft-lb(40.7J) level the range in temperatures using the three evaluation techniques was 3 to 18F (1.9 to 11.3C) with an average value for all the data of 6.9 ± 4.8F (4.3 ± 3.0C). At the 50 ft-lb(67.8J) level the range in temperatures using the same evaluation techniques was 2 to 9F (1.3 to 5.6C) with an average value for all the data of 4.5 ± 2.6F (2.8 ± 1.6C). These results indicate that the definition of the 50 ft-lb (67.8J) energy level is easier and more reliably performed than the 30 ft-lb (40.7J) energy level.

The upper-shelf energy was determined using the same three techniques and these resulted in a range of value between 2 and 4 ft-lbs (2.7 and 5.4J) with an average value for all the data of 3 ± 0.7 ft-lbs (4.1 ± 0.9J). These data demonstrate a consistent evaluation of upper-shelf energy.

CONCLUSIONS

These round-robin test results demonstrate that there is a significant variation in Charpy energy test results, however, when the results are evaluated in a consistent

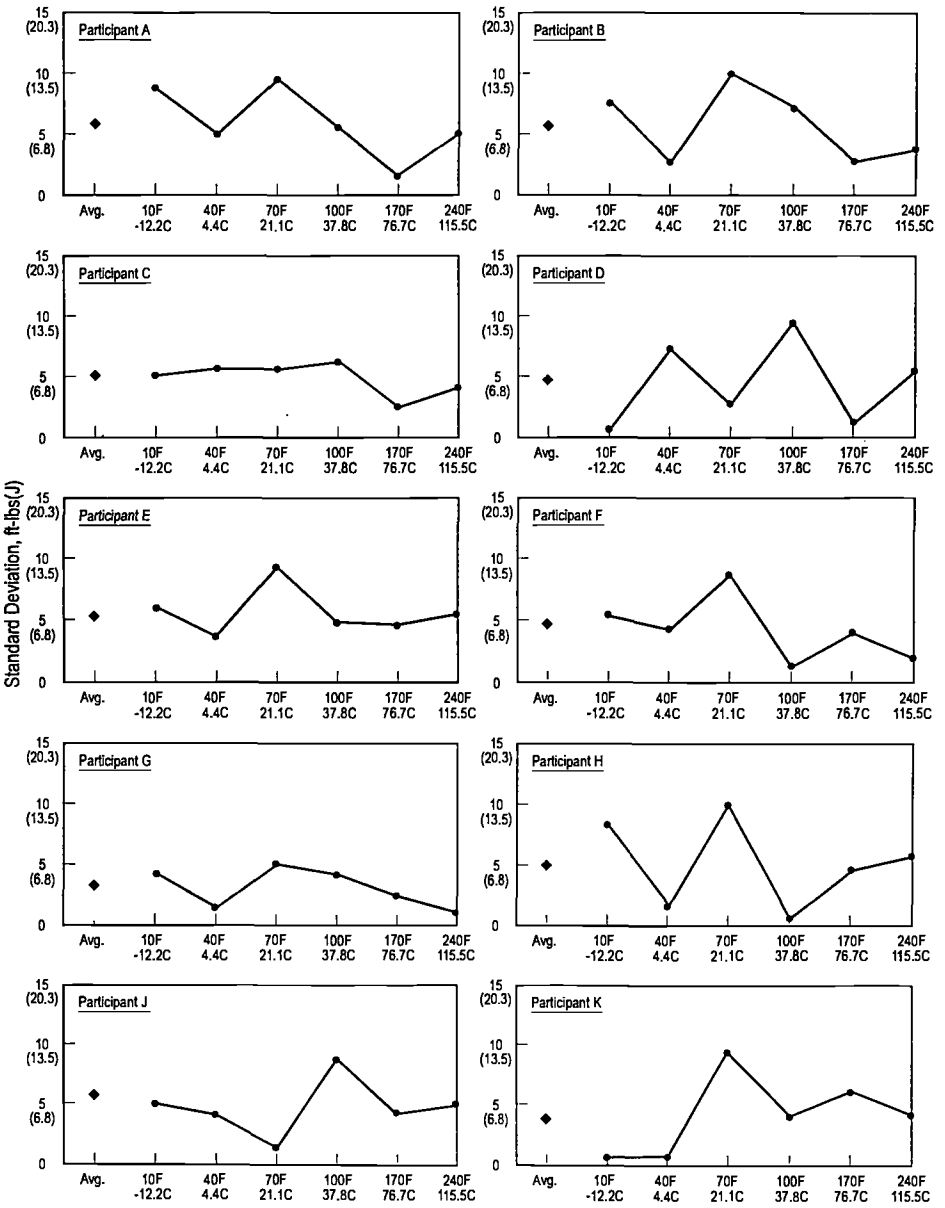


FIGURE 8 -- Comparison of Each Participant's Charpy Energy Standard Deviation for Each Test Temperature to the Mean Standard Deviation for Each Individual Data Set

manner using accepted methods the errors are reduced to a small value. These values, although small statistically, may be significant when applied in the application of standards and regulatory requirements and, therefore, efforts are needed to further improve testing techniques to reduce the error in the valuation of material properties.

ACKNOWLEDGEMENTS

The author expresses appreciation to the B&W Owners Group Reactor Vessel Integrity Program for the weld metal used in the program. The author acknowledges B&W Nuclear Technologies for providing the resources needed to conduct the program.

REFERENCES

[1] Charpy Impact Test: Factors and Variables, ASTM STP 1072, John M. Holt, Editor, American Society for Testing and Materials, Philadelphia, 1990.

[2] Porro, F., Trippodo, R., Bertozzi, R., Garagnani, G., "Impact Tester Compliance: Significance, Sensitivity and Evaluation," Charpy Impact Test: Factors and Variables, ASTM STP 1072, John M. Holt, Editor, American Society for Testing and Materials, Philadelphia, 1990.

[3] Schmieder, A. K., "Comparison of Metrological Techniques for Charpy Impact Machine Verification," Charpy Impact Test - Factors and Variables: ASTM STP 1072, J. M. Holt, Ed., American Society for Testing and Materials, Philadelphia, 1990.

[4] Revise, G., "Influence of Dimensional Parameter of an Impact Test Machine on the Results of a Test," Charpy Impact Test: Factors and Variables, ASTM STP 1072, John M. Holt, Editor, American Society for Testing and Materials, Philadelphia, 1990.

[5] Naniwa, T., Shibaike, M., Tanaka, M., Tani, H., Shiota, K., Hanawa, N., and Shiraishi, T., "Effects of the Striking Edge Radius on the Charpy Impact Test," Charpy Impact Test: Factors and Variables, ASTM STP 1072, John M. Holt, Editor, American Society for Testing and Materials, Philadelphia, 1990.

[6] Koester, R. D., and Barcus, S. E., "Evaluation of Fabrication Methods for Making Notches for Charpy V-Notch Impact Specimens," Charpy Impact Test: Factors and Variables, ASTM STP 1072, John M. Holt, Editor, American Society for Testing and Materials, Philadelphia, 1990.

[7] Fink, D. A., "Quantitative Comparison and Evaluation of Various Notch Machining Methods and How They Affect ASTM E23 and ISO R442 Testing

Equipment Results," Charpy Impact Test: Factors and Variables, ASTM STP 1072, John M. Holt, Editor, American Society for Testing and Materials, Philadelphia, 1990.

[8] Nanstad, R. K., Swain, R. L., and Berggren, R. G., "Influence of Thermal Conditioning Media on Charpy Specimen Test Temperature," Charpy Impact Test: Factors and Variables, ASTM STP 1072, John M. Holt, Editor, American Society for Testing and Materials, Philadelphia, 1990.

[9] Lowe, A. L. Jr., "Factors Influencing Accuracy of Charpy Impact Test Data," Charpy Impact Test: Factors and Variables, ASTM STP 1072, John M. Holt, Editor, American Society for Testing and Materials, Philadelphia, 1990.

[10] Designation E23-86, "Standard Method for Notched Impact Testing of Metallic Materials," Annual Book of ASTM Standards, American Society for Testing and Materials, Philadelphia.

[11] Oldfield, W. Journal of Testing and Materials, Vol. 7, No. 6, November 1979, pp. 326-333.

J. A. Wang,[1] F. B. K. Kam,[1] and F. W. Stallmann[2]

THE EMBRITTLEMENT DATA BASE (EDB) AND ITS APPLICATIONS

REFERENCE: Wang, J. A., Kam, F. B. K., and Stallmann, F. W., **"The Embrittlement Data Base (EDB) and Its Applications,"** *Effects of Radiation on Materials: 17th International Symposium, ASTM STP 1270,* David S. Gelles, Randy K. Nanstad, Arvind S. Kumar, and Edward A. Little, Eds., American Society for Testing and Materials, 1996.

ABSTRACT: Investigations of regulatory issues, such as vessel integrity over plant life, vessel failure, and plant license renewal, can be greatly expedited by the use of a well-designed computerized data base. Also, such a data base is essential for the validation of embrittlement prediction models by researchers. The EDB is this comprehensive collection of data resulting from the merging of the Power Reactor Embrittlement Data Base (PR-EDB) and the Test Reactor Embrittlement Data Base (TR-EDB). The current version of the PR-EDB lists the test results of 98 heat-affected-zone (HAZ) materials, 105 weld materials, and 136 base materials that were irradiated in 252 capsules from 96 power reactors. The current data collection of the TR-EDB contains 1230 different irradiated sets, 797 of which are from base materials, 378 from welds materials, and 55 from HAZ materials. The data files are given in dBASE format and can be accessed with any personal computer using the DOS operating system. The different types of data that are implemented or planned for EDB are discussed. "User-friendly" utility programs have been written to investigate a variety of problems using this data base. The results of several studies, which include the parameter study of the chemistry composition effect on radiation embrittlement, the irradiation temperature effect on radiation embrittlement, vendor-specific embrittlement model, etc., are presented in this paper.

KEYWORDS: radiation embrittlement, power reactor, test reactor, data base, LWR

EDB BACKGROUND

It is well known that the fluxes of energetic neutrons can displace significant numbers of atoms and thus alter physical and mechanical properties of reactor pressure vessel (RPV) steels. Property changes in materials due to neutron-induced displacement damage are a function of neutron energy, neutron flux, and temperature, as well as the material variables that determine

[1]Research scientist, Oak Ridge National Laboratory, P.O.Box 2008, Oak Ridge, TN 37831

[2]Research scientist, retired, 140 Sunrise Drive, Knoxville, TN 37919.

Copyright© 1996 by ASTM International www.astm.org

how neutrons interact with atoms and how defects interact within the material [1,2]. The success of reactor technology depends critically on the choice of material with satisfactory material properties to resist the radiation damage. Presently, interest focuses on the radiation damage and its effect on reactor pressure vessel materials. It is generally accepted that radiation hardening and embrittlement in metals are primarily caused by clusters of vacancies, interstitial, and solute atoms that impede the motion of slip dislocations. The degree of embrittlement is conventionally correlated with fast neutrons or with total displacements per atom (dpa).

The aging and degradation of light-water-reactor (LWR) pressure vessels is of particular concern because of their relevance to plant safety and the magnitude of the expected irradiation embrittlement. The failure of an RPV due to embrittlement by neutron irradiation could lead to a rapid core meltdown generating high pressure and temperature loading, possibly above those for which containments are designed. The radiation embrittlement of RPV materials depends on many different factors such as neutron flux, fluence, fluence spectrum, irradiation temperature, pre-irradiation material history and its chemical compositions [3,4]. These factors must be considered in order to reliably predict the pressure vessel embrittlement and to ensure the safe operation of the reactor. Based on embrittlement predictions, decisions must be made concerning operating parameters, low-leakage-fuel management, possible life extension, and the need for annealing of the pressure vessel [5]. Large amounts of data obtained from surveillance capsules and test reactor experiments are needed, comprising many different materials and different irradiation conditions, to develop generally applicable damage prediction models that can be used for industry standards and regulatory guides. The EDB is this comprehensive collection of data for ferritic alloys resulting from the merging of the PR-EDB and the TR-EDB.

Three major categories of data are included in the EDB, namely, pre-irradiation material history, irradiation environments, and mechanical test results, containing the following types of data (Fig. 1):

1. fluence ($E > 1.0$ MeV, $E > 0.1$ MeV, and dpa), irradiation time, and irradiation temperature for each irradiated capsule;
2. Charpy test results before and after irradiation, both for individual specimen and evaluation of transition temperature and upper-shelf energies;
3. tensile test results before and after irradiation;
4. chemistry data for each material;
5. pre-irradiation heat treatment;
6. data concerning the fabrication of weld material; and
7. data related to the determination of the pressure-temperature (P-T) limits.

The current version of the PR-EDB lists the test results of 98 HAZ materials, 105 weld materials, and 136 base materials that were irradiated in 252 capsules from 96 power reactors [6]. The current data collection of the TR-EDB contains 1230 different irradiated sets, 797 of which are from base materials, 378 from welds materials, and 55 from HAZ materials [7]. The EDB has been used in many radiation embrittlement studies of reactor vessels. This computerized data base for base material and weldments was collected, as reported mainly from surveillance reports of operating power reactors and available technical reports. All data are traceable to the source of references, including page numbers. Most of the surveillance data have been verified by the reactor vendors responsible for the insertion of the material into surveillance capsules, and any changes and corrections have been documented in special files for future reference. The data files are given in dBASE format, which allows the use of dBASE III PLUS and higher versions, as well as any compatible Xbase software (e.g., CLIPPER and FOXPRO). The architecture of

the data base is characteristic of a relational data base that makes it relatively simple to maintain and perform quality control.

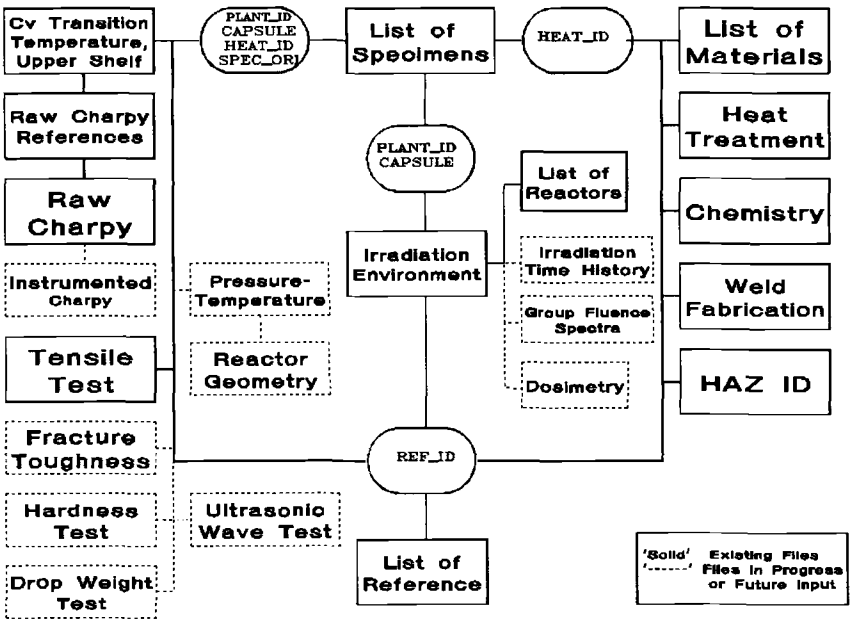


FIG. 1--Architecture of the embrittlement data base EDB.

Software utility routines have been written to update and manipulate the data for easy maintenance by a computer technician and to select, combine, and process the data for tables, model fitting, and graphs. Special software routines have been written to perform the different studies, such as determination of P-T limits for commercial power reactors.

PROPOSED DATA INPUT

The transition temperature approach, mainly relying on the Charpy impact test, is simple and has been used successfully. However, it has the limitation of being a temperature criterion rather than a more familiar stress criterion, such as fracture toughness. Therefore, it cannot be used directly in the design. This shortcoming can be mended by the creation of a parallel fracture toughness data base to the existing EDB, which can offer a direct linkage to stress analysis and verify the relationships between the Charpy test data and fracture toughness test data for common materials. This project has already been initiated, and there are three categories of the fracture toughness data available from the reports: static fracture toughness, K_{IC} or K_{JC};

dynamics fracture toughness, K_{ID}; and crack-arrest fracture toughness, K_{Ia} data.

Another important category of material test data for future EDB data input is the nondestructive test data, including the hardness test and ultrasonic wave test. This proposed nondestructive data base is essential for the calibration and construction of the correlation between the existing mechanical test data and the nondestructive test results. This task of analytical nondestructive technique has its potential area in the near future, especially for those older plants that will be on the verge of exhausting all the available mechanical test specimens loaded in the surveillance capsules of RPV.

The proposed data input for the irradiation environment are power-time history, history of the reactor core configurations, the calculated neutron energy spectra, and dosimetry data, which are essential for the detailed study of the rate effect, spectrum effect, and further investigation of the damage efficiency and residual defects. The degree of embrittlement is conventionally correlated with fast neutron fluence or with dpa, which are measures of the production rate of point defects. However, radiation effects are driven not by the total atoms displaced but by the small fraction of point defects that avoid annihilation by mutual recombination and are made available to form clusters or to be absorbed at sinks [8-11]. Therefore, radiation effects are determined by the survival rate of point defects, not by their production rate. The survival rate of point defects (or defect availability) depends on several factors: (1) the temperature of the material, (2) the rate at which the fluence is accumulated, and (3) the energy of the neutrons causing the displacements. Thus the development of radiation embrittlement under different irradiation environments will not necessarily scale with fast fluence or with dpa unless the survival rate of point defects for each different irradiation also scale with the total defect production rate. Therefore, the above-mentioned proposed radiation environment data are crucial for obtaining a better correlation parameter for the prediction of the radiation embrittlement of RPV steels.

APPLICATION OF EDB IN RADIATION EMBRITTLEMENT STUDY

The EDB can be used in the following embrittlement studies:

- Validation of the embrittlement prediction models, such as those of the Regulatory Guide, French FIM, Babcock & Wilcox (B&W), Odette, Fisher, and Pachur's models.
- Parameter study of the effect of chemistry compositions on radiation embrittlement.
- Irradiation temperature effect on radiation embrittlement.
- Reactor pressure vessel thermal annealing study.
- Investigation of the spectrum effect and rate effect; and residual defects modeling.
- Characterization of heat treatment on radiation embrittlement.
- Correlation between Charpy test data versus tensile test data, and Charpy test data versus fracture toughness data.
- Comparison and unification of Charpy data fitting procedures.
- Statistical characterization of radiation embrittlement.

The EDB has been used in many radiation embrittlement studies. Research has been done on the following issues:

- Analysis of the correlation monitor materials, A302B and A533B, in the surveillance capsule of commercial power reactors.

- Differences between the measured ΔRT_{NDT} in PR-EDB with the values predicted by the Regulatory Guide for base and weld materials.
- Re-evaluation of the two standard deviation values for the base and weld materials.
- The phosphorus effect in low-copper materials.
- Sensitivity of specimen orientation to radiation embrittlement.
- Check if test results from LT specimens reduced to 65% of their value provided conservative estimates of the expected value from TL specimens.
- Raw Charpy data curve-fitting procedures and comparison of the TANH fitting program at Oak Ridge National Laboratory (ORNL) with one from the Electric Power Research Institute (EPRI).
- Comparison of Reg. Guide 1.99, Rev. 2, model with French FIM model.
- Metallurgical and irradiation effects study for the Yankee Rowe reactor-related events.
- Data analysis for evaluation of irradiation temperature effects.
- Evaluation of initial RT_{NDT} and ART per ASME Code and Reg. Guide 1.99, Rev. 2.
- Determination of P-T limit curves for commercial power reactors.
- Residual study on the impact of improvement of fluence evaluation to Reg. Guide 1.99, Rev. 2.
- Background study for Reg. Guide 1.99, Rev. 2 [12].
- HFIR accelerated embrittlement study [13].
- Vendor-specific radiation embrittlement models study.

The results of items 1 through 8 were published in the Proceedings of the Aging Research Conference, 1992 [14]. The results of several studies are presented in the following.

Residual Study of PR-EDB Surveillance Weld and Base Materials per Reg. Guide 1.99, Rev. 2

The residual is defined as the reported transitional temperature shift value minus the predicted shift of Reg. Guide 1.99, Rev. 2. The mean residual and its corresponding 2-sigma uncertainty, not taking into account the absolute residual value greater than 100°F (there are 11 such observations, which are from Yankee Rowe and Garigliano), were -4.51°F and 58°F for the base materials, respectively; and -3.04°F and 68°F for the weld materials, respectively. (see Figs. 2 and 3). Detailed residual studies were done for each individual vendor: Westinghouse, General Electric (GE), B&W, CE, and Allis-Chalmers. The mean residual and the corresponding 2-sigma uncertainty of base and weld for each individual vendor are listed in Table 1.

TABLE 1--The mean residual and 2-sigma uncertainty of plates and welds per vendor data.

Vendor	Base Residaul °F			Weld Residaul °F		
	mean	2-sigma	points	mean	2-sigma	points
Westinghouse	-2.43	51°F	253	-0.85	61°F	93
B&W	-23.40	59°F	55	-23.43	64°F	23
GE	-0.04	77°F	50	-2.10	76°F	42
CE	-2.33	34°F	30	4.57	84°F	14
Allis-Chalmers	33.00	56°F	6	11.75	20°F	4
Overall	-4.51	58°F	394	-3.04	68°F	176

A clear bias was shown in the B&W data, and it indicated that Rev. 2 of Reg. Guide 1.99 overestimated the shift. The reasonable explanation is that B&W's reactors are operated at a higher temperature (the nominal capsule temperature of B&W is about 608°F per melt wires) than reactors of other vendors. Therefore, a meaningful comparison of mechanical property

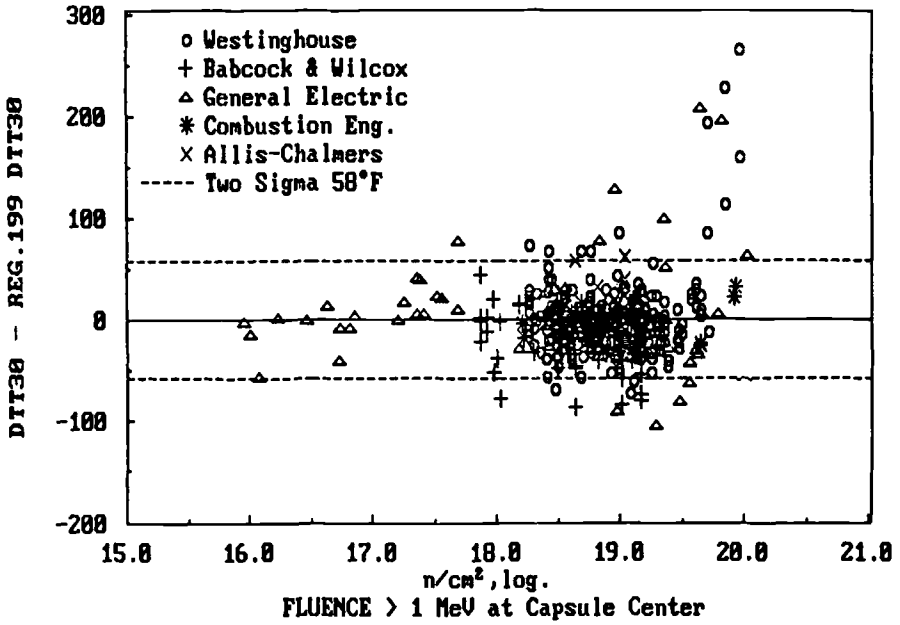


FIG. 2--Residual vs fluence for base materials of PR-EDB, per Reg. Guide 1.99, Rev. 2, where the fluence greater than 1E+20 n/cm² are from Big Rock and Dresden Unit 1.

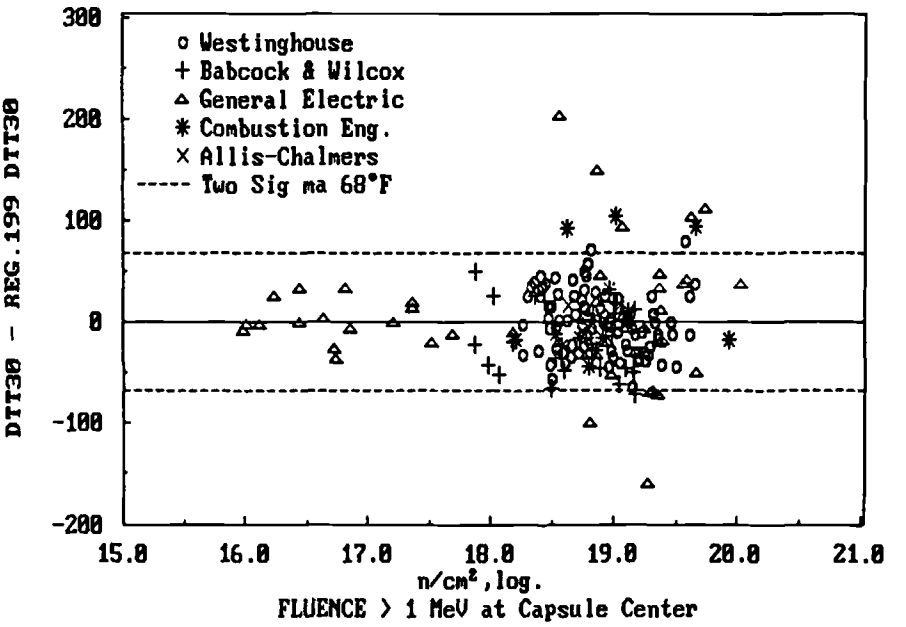


FIG. 3--Residual vs fluence for weld materials of PR-EDB, per Reg. Guide 1.99, Rev. 2.

change of materials irradiated in different neutron environments requires a physical based model that accounts for all the irradiation variables and material parameters.

Combustion Engineering's reactors are generally operated at a lower temperature than other vendors, but no systematic bias can be observed, except in having a very large scatter band for the weld materials, which has 84°F of 2-sigma uncertainty. Also, there existed a fluence-dependent effect for weld materials, which indicates that the Regulatory Guide underpredicts the shift at high fluences but overestimates the shift at low fluences. An additional study was done on the copper distribution of the residual data, which indicates that the Regulatory Guide underestimates the shift at high-copper content but overestimates at low-copper content. The copper and nickel contents for Palisades base material are 0.25 wt% and 0.53 wt%, respectively. The residuals of the base materials are in the reasonable range. The copper and nickel contents for the Palisades welds are range from 0.22 to 0.26 wt %, and 0.63 to 1.27 wt%, respectively. Due to the variation of the copper and nickel contents in the weldment, the measured shift of the weld material is either greater or less than the Regulatory Guide predicted value depending on what chemistries were used. This may imply that the Palisades base materials may not be sensitive to the irradiation temperature per Reg. Guide 1.99, Rev. 2. However, the inhomogeneity of the weld material of Palisades may deserve special attention.

Metallurgical and Irradiation Effects for the Yankee Rowe Materials

This study was carried out due to the concern over the issue of "Does Reg. Guide 1.99, Rev. 2, overpredict the Charpy shift for the Yankee Rowe reactor vessel?" The approach was to plot the residuals versus fluence.

In order to characterize the plates used in the Yankee Rowe related events (such as Yankee's upper shell, lower shell, and two Yankee Rowe vessel surrogates YA1 and YA9), five ranges of copper and nickel contents, Cu $<=$ 0.2 Ni $<=$ 0.5 wt%, Cu $<=$ 0.2 Ni $>$ 0.5 wt%, Cu $>$ 0.2 Ni $>$ 0.5 wt%, Cu $<=$ 0.2 Ni $<=$ 0.4 wt% and Cu $<=$ 0.2 Ni $<=$ 0.2 wt%, for the base metals were investigated. The plot of residuals versus fluence for high nickel content, Ni $>$ 0.5 wt%, and low copper content, Cu $<=$ 0.2 wt%, indicated that there may be a fluence-dependence effect per Regulatory Guide's prediction (see Fig. 4). At relatively low fluence (e.g., 10^{18} n/cm^2), the Regulatory Guide's value underpredicts the shifts, and at relatively high fluence (e.g., 4.0×10^{19} n/cm^2), the Regulatory Guide's values also underpredict the shifts. However, the data between fluences of 10^{18} and 4×10^{19} n/cm^2 have more residual data below the zero axis than data above, therefore, this bias can be interpreted as the Regulatory Guide overpredicts the shifts.

As for the high copper and high nickel content, Cu $>$ 0.2% Ni $>$ 0.5 wt%, a bias indicated that the Regulatory Guide's values overpredicted the shift (see Fig. 5). For the low copper and low nickel content, Cu $<=$ 0.2% Ni $<=$ 0.5%, the Regulatory Guide underpredicts the shift (see Fig. 6). This indicated that the Regulatory Guide could underpredict the shift for low nickel but overpredict for high nickel content for Yankee Rowe related materials.

The Impact of Irradiation Temperature on Reg. Guide 1.99, Rev. 2

Irradiation temperature undoubtedly exerts a strong influence on embrittlement by controlling the migration rate of vacancies, the bulk recombination rate and the annealing rate of clusters. Therefore, without proper consideration of irradiation temperature effect, bias will result in the embrittlement model. The main objective of this task was to determine the

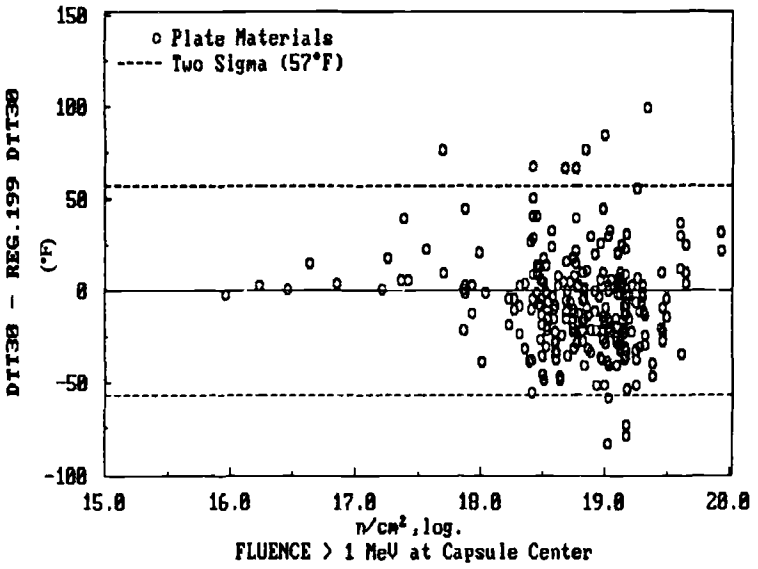


Fig. 4. Plot of Residaul vs. Fluence for Base Materials with Cu≤0.2wt%, Ni>0.5wt%.

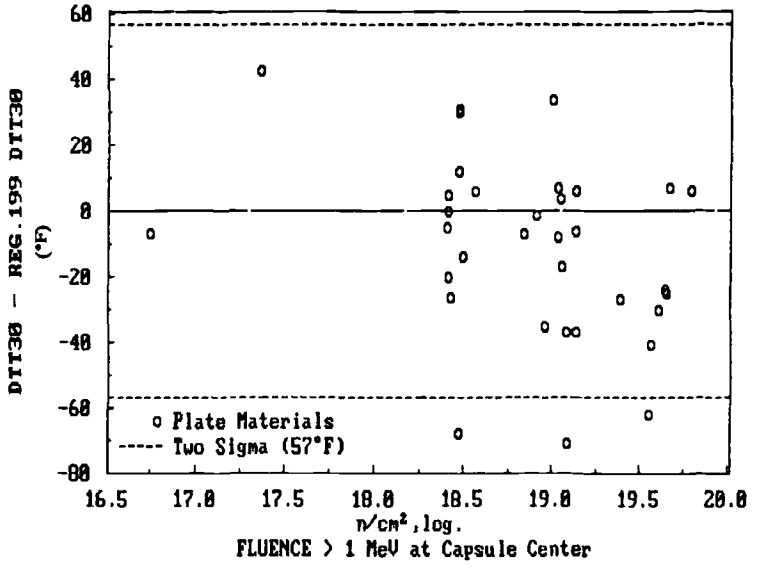


Fig. 5. Plot of Residual vs. Fluence for Base Materials with Cu>0.2wt%, Ni>0.5wt%.

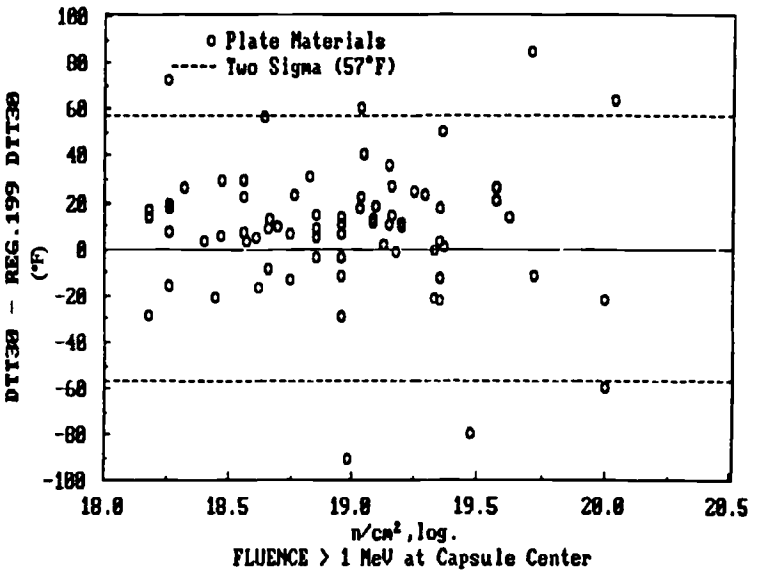


FIG. 6--Plot of residual vs fluence for base materials with Cu ≤ 0.2 wt%, Ni ≤ 0.5 wt%.

correction factor for Reg. Guide 1.99, Rev. 2, due to the irradiation temperature effect. The linear regression scheme was used in the analysis, and an assumption was made that the residuals were primarily due to the irradiation temperature effect in order to have a conservative estimate of the correction factor. The first phase was to investigate "What is the major trend of the irradiation temperature for Regulatory Guide 177 data points." Due to the uncertainty of the irradiation temperature from the surveillance reports, the index irradiation temperature was determined and defined as, "If both maximum and minimum capsule temperature were given, the average is taken as the index irradiation temperature. Otherwise, use whatever is available." The mean temperature of the index irradiation temperature of the 177 data points is 578°F, which was estimated from melt wires, and the corresponding 2-sigma is 25°F. The average irradiation temperatures of the individual vendors are listed in Table 2. The second phase was to determine the mean irradiation temperature from the current PR-EDB. The mean temperature of the average irradiation temperature of the 589 residual data of PR-EDB is 577°F, which is based on melt wires, and the corresponding 2-sigma is 42°F. The average irradiation temperature of each individual vendor is listed in Table 3.

The third phase was to determine the correction factor by a linear-regression scheme. A linear equation, Y = A*X + B, is fitted through the residual data, and the X-axis is defined as the difference between the irradiation temperature and the mean irradiation temperature of the Regulatory Guide 177 data points. Here, A and B are fitting parameters. A can be defined as a correction factor (i.e., degrees change in transition temperature per degree deviation of irradiation temperature from the mean irradiation temperature of the Regulatory Guide). Severe inconsistencies exist in the major trend of the residual data which are mainly caused by the boiling-water-reactor (BWR) data of GE. Moreover, there are only 6 BWR data in the Regulatory Guide 177 data points; therefore, Reg. Guide 1.99, Rev. 2, seems suitable for characterizing pressurized-water-reactor (PWR) data but not BWR data. Due to the above

TABLE 2--The mean irradiation temperature of the 177 data points per vendor.

Vendor	Mean irradiation temperature	2-sigma	Data point
Westinghouse	580°F	10°F	135
B&W	595°F	13°F	17
CE	553°F	3°F	19
GE	550°F	0°F	6

TABLE 3--The mean irradiation temperature of PR-EDB per vendor.

Vendor	Mean irradiation temperature	2-sigma	Data point
Westinghouse	578°F	30°F	353
B&W	608°F	22°F	80
CE	554°F	10°F	45
GE	554°F	24°F	101

finding, the BWR data were not included in the linear regression study .

The best fit line is Y = -1.14*X - 1.2 (see Fig. 7). The data on the very upper left of the plot are Yankee Rowe data. These data have large residuals and are far away from the mean irradiation temperature, 578°F; therefore, they give a much larger weight than other residual data in the least-squares fitting procedure. Additional fitting was done without Yankee Rowe data, which gives the best fit line as Y = -0.61*X - 1.10 (see Fig. 8). The correction factor, A, was reduced by almost 50%. From the above observation, two issues need to be mentioned about Yankee Rowe data. First, the residual data imply that the linear fit may not be appropriate to characterize the temperature effect for the higher irradiation temperature shift, and a higher-order curve fit may be needed. Second, due to the nature of the data, which are at lower irradiation temperatures than other vendors and also exposed to a higher flux than other PWRs (about a order magnitude higher than others), there is a possibility of a synergistic effect of a lower irradiation temperature and higher flux on radiation embrittlement. The correction factor for the base (without Yankee Rowe data) and weld are -0.48°F/°F and -0.78°F/°F, respectively. This may be because the weld materials are more sensitive to the irradiation temperature than the base materials. Additional studies were carried out on the A533B, A302B, and forging materials, respectively. The correction factor for the A533B materials is -0.65°F/°F. The correction factors for A302B materials with Yankee Rowe and without Yankee Rowe data are -1.75 and -0.67°F/°F, respectively. The correction factor for forging materials is -0.26°F/°F. For irradiation temperatures greater than 550°F, both A302B and A533B reveal the same major trend (i.e., their behavior is more or less the same toward the sensitivity of the irradiation temperature shift). Among the different materials, forging materials seem to be less sensitive to the irradiation temperature than other materials. Based on this study, the correction factor per Reg. Guide 1.99, Rev. 2, was recommended as 0.61°F/°F.

Impact of Improvement of Fluence Evaluation on Reg. Guide 1.99, Rev. 2

This study concerns the issue, "What is the impact on the reduction of margin of Reg. Guide 1.99, Rev. 2, by improved fluence evaluation?" The approach was to study the residuals

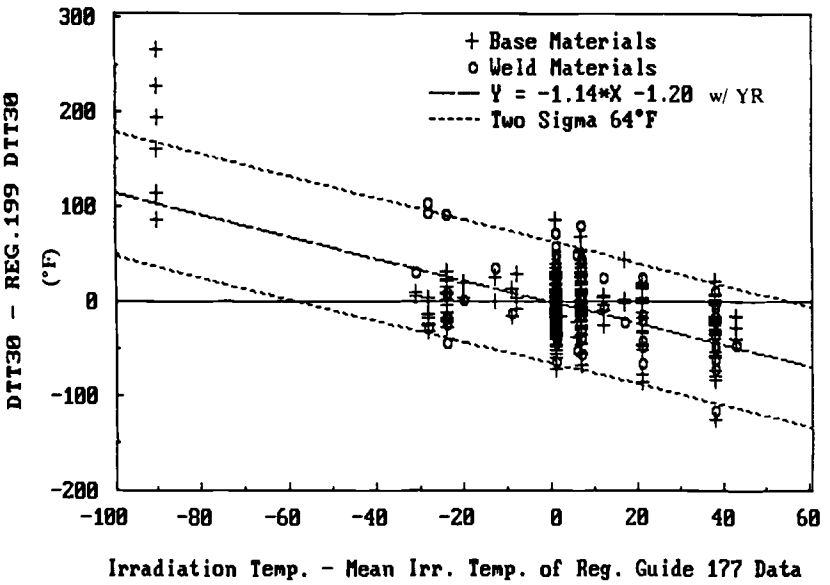


Fig. 7. Residual vs. Irradiation Temperature Shift, Fitting Model with Yankee Rowe's Data.

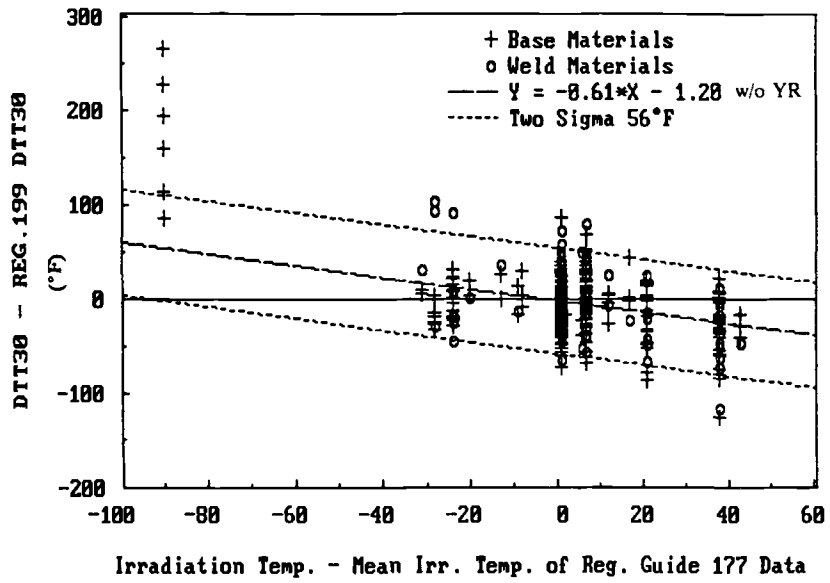


Fig. 8. Residual vs. Irradiation Temperature Shift, Fitting Model w/o Yankee Rowe's Data.

generated by different fluence sets. Here, the residual is defined as the reported transition temperature shift minus the value calculated by Reg. Guide 1.99, Rev. 2. In order to have some quantitative measurement of the improvement of the 2-sigma bounds of Reg. Guide 1.99, Rev. 2, due to the increasing accuracy of the fluence evaluation, the CF and FF are assumed to be two independent factors. The 177 data points are used as the main data source for the current study. Two fluence data sets, Simon's fluence data of 177 data points and the corresponding surveillance fluence data of the PR-EDB, are used in the comparison of improvement of the 2-sigma bounds. The 1 standard deviations of the residual of Simon's fluence set for plate and weld materials are 18.10°F and 27.21°F, respectively. The standard deviations of residual of surveillance fluence set for plate and weld materials are 18.36°F and 29.62°F, respectively. Here, one assumes that 177 data fluences are improved data compared with PR-EDB's surveillance fluences. There are about 130 fluence data that were updated in the 177 data points; the rest of the fluence data of 177 data points are surveillance fluence data, except for two test reactors' fluences. The percentage of improvement for the 2-sigma bounds for plate and weld are 1.4% and 8%, respectively. The overall average improvement of the 130 fluence data is 32%. A preliminary conclusion can be drawn from the above study, that is "the 32% improvement of fluence evaluation can only result in an 8% reduction in the safety margin of Reg. Guide 1.99, Rev. 2, for the weld materials, and 1.4% reduction for the base materials." An additional study was done for the updated fluence data set of Westinghouse's data, supplied by E. P. Lippincott of Westinghouse Hanford Company. A total of 123 fluences of 177 data points were updated per Westinghouse's updated fluences. The overall average improvement of the 123 fluence data is 13.3%. The resulting 1 standard deviations of plate and weld materials are 17.92°F and 27.82°F, respectively. The percentage of the improvement for the 2-sigma margins for plate and weld are 1 and -2.2%, respectively. Comparing the residual generated by updated fluence and the fluence of the 177 data points, the major trends of the data scatter remained the same (see Figs. 9 and 10).

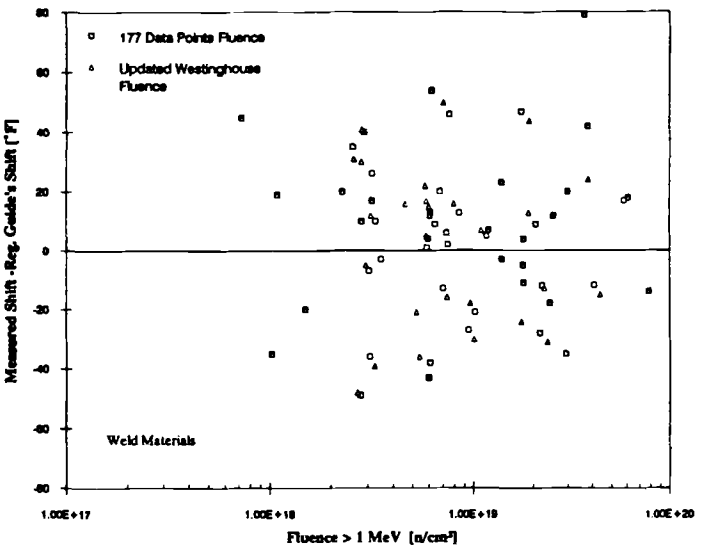


FIG. 9--Plot of residual vs fluence for weld materials, per 177 data points.

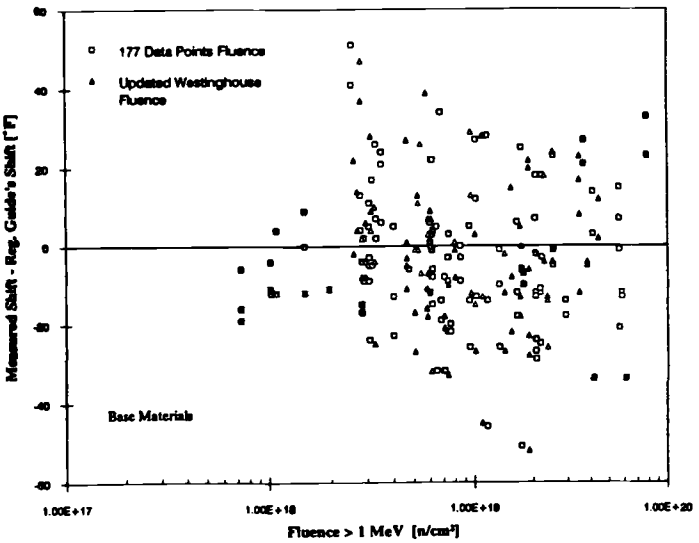


FIG. 10--Plot of residual vs fluence for base materials, per 177 data points.

Major contributions on the margin of the embrittlement model come from the mechanical test result, fluence calculation, irradiation environment, chemical analysis, and inhomogeneous material properties. Thus insufficient consideration of all the error sources in the determination of the correlation procedure will not result in substantial improvement of the margin of the embrittlement model; in fact it may even result in misleading correlation and thus incorrect prediction of material state and material behavior as well as incorrect end-of-life determinations.

HFIR Accelerated Embrittlement Phenomena

The main sources for this study are the High Flux Isotope Reactor (HFIR) surveillance program and the test reactor data listed in TR-EDB. Accelerated radiation-induced embrittlement of the HFIR surveillance materials has been investigated since its discovery in 1986 [15,16]. Recent comprehensive dosimetry experiments revealed the presence of an intense gamma field at the HFIR surveillance locations near the pressure vessel. Gamma-induced reactions were found to dominate the response of several dosimeters and were crucial for the explanation of dosimetry results [17]. This finding precipitated the assessment of the gamma-induced dpa rate, which was found to exceed the neutron-induced dpa rate at all locations analyzed. When the sum of neutron and gamma dpa is used for the interpretation of the HFIR surveillance results, the HFIR data are consistent with data from the Oak Ridge Research Reactor (ORR) and other test reactors [13], as noted in Fig. 11. However, experimental verification that gamma-induced displacements cause material embrittlement is necessary. Applying the annealing heat treatments and hardness test on the irradiated specimens will be a straightforward procedure to identify the characteristics of the different defect mechanisms, which was first pointed out by Pachur [18]. The annealing specimens can be made from the broken Charpy specimens of HFIR surveillance material, which were irradiated in HFIR and ORR and experienced with similar fast neutron fluence, and irradiation temperature. The broken Charpy specimens from key 6 and key 7 positions of HFIR surveillance, which have the highest gamma dpa to neutron dpa ratio (about 5 to 1), will be the best candidate for this study.

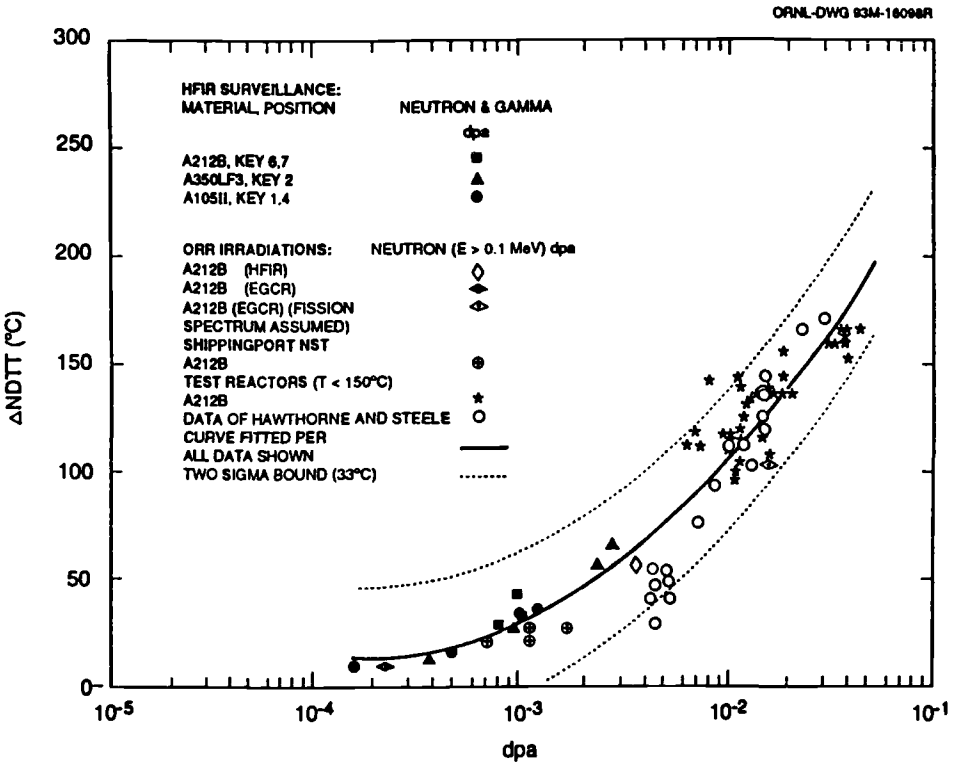


FIG. 11--HFIR Charpy shift vs neutron plus gamma-induced dpa and ORR, Shippingport, and test reactor data vs neutron (E > 0.1 MeV) dpa [13].

Background Study for Reg. Guide 1.99, Rev. 2

The objective of this study is to trace the origin of Reg. Guide 1.99, Rev. 2. Three major data bases and two embrittlement models were involved in the modeling of Reg. Guide 1.99, Rev. 2 [19]. The three data bases are Reg. Guide's 177 data points, EPRI's data base [20], and French test reactor data [21,22]. A detailed data comparison was carried out by using PR-EDB to identify the data base. The content of the data base and the impact of its related model to Reg. Guide 1.99, Rev. 2, are stated below:

George Guthrie's model, 177 data points: A total of 51 weld and 126 base metal data points were taken from surveillance reports by Neil Randall and rechecked by George Guthrie. These data were used in George Guthrie's embrittlement model [23]. Of the 177 data points, 128 fluences can be identified as Simons' data, which are registered in NUREG/CR-3319. The 95% copper and 85% nickel data are consistent with PR-EDB. Twenty-five shifts can be identified as 50-ft-lb shifts, and 146 shifts can be identified as 30-ft-lb shifts. The fluence factor (FF) of Reg. Guide 1.99, Rev. 2, is mainly determined by Guthrie's FF with slight modifications. For base metal, Guthrie's chemistry factor (CF) is used with two exceptions. First, when Guthrie's

CF for base metal exceeded those for welds predicted by Odette, the latter were used. Second, at very low copper levels, the CF is assigned as 20°F. The 2-sigma margin of Reg. Guide 1.99, Rev. 2, is based on the residual study of the 177 data points.

Odette's model, EPRI data base: The EPRI data base used in Odette's modeling [24], which contains 65 weld and 151 base metal data, is collected directly from surveillance reports, except for the shift value which is determined by EPRI's tangent fitting procedure. EPRI's data base overlapped the 177 data points almost completely. The 97% of fluence data are consistent with the surveillance's fluence data. The 99% copper and 85% nickel data are consistent with PR-EDB. For weld materials, Odette's CF is used as the main guidelines for Reg. Guide 1.99, Rev. 2, except at very low copper that is leveled to 20°F.

French test reactor data: The French test reactor data contain 56 base and 21 weld data which are collected from refs. 21 and 22. For very low copper content, there are insufficient surveillance data. Therefore, for low copper content judgment was made by the French test reactor data. For both bases with copper less than 0.03% and weld with copper less than 0.01%, the CF was assigned as 20°F.

Vendor-Specific Embrittlement Prediction Models

The margins and model evolution of the current Reg. Guide 1.99, Rev. 2, was based on Neil Randall's 177 data points and EPRI's data base, where 76% of 177 data points and 60% of EPRI's data base were from the Westinghouse data; therefore, the other vendor's radiation environment may not be properly characterized in the Regulatory Guide's prediction model. There are factors that participated in the radiation embrittlement that were still not well characterized, such as irradiation temperature effect, spectrum effect, and rate effect. In order to eliminate or minimize the influence of these parameters on the embrittlement models, developing embrittlement models based on group data that have similar radiation environments (e.g., data from same vendor) is one option which may reduce the margin and have a better characterization for the vendor-specific case.

A total of 734 shift data points of current PR-EDB, including 434 Westinghouse data, 94 B&W data, 57 CE data, and 149 GE data, were used in the current embrittlement model development. A nonlinear-least-squares fitting FORTRAN program, incorporated with a Monte Carlo procedure with 35% and 10% uncertainty assigned to the fluence and shift data, respectively, was written for this study. This program has the ability to duplicate the Guthrie model based on the 177 data points and generate similar results for the 11 fitting parameters and safety margins for base and weld materials. In order to have the same adjusted fluence value for the weld and plate material in the same capsule, the Monte Carlo least-squares fitting procedure has the capability of adjusting the fluence values while running the weld and plate formula simultaneously.

Guthrie embrittlement model: The formula for Guthrie's embrittlement model is

$$\begin{aligned} Shift(Weld) &= [\,C(1)\cdot Cu + C(2)\cdot\sqrt{Cu\cdot Ni} + C(3)\cdot Ni\,][f^{C(4)+C(5)\cdot \ln f}] \\ Shift(Base) &= [\,C(6) + C(7)\cdot Cu + C(8)\cdot \tanh C(9)\cdot\frac{Ni}{Cu}\,][f^{C(10)+C(11)\cdot \ln f}] \end{aligned} \quad (1)$$

where fluence, f, is in units of 10^{19} n/cm² (E > 1 MeV), and Cu and Ni are in wt%. Constant coefficients C(I), I = 1 to 11, are fitting parameters, and are listed in Table 4.

TABLE 4--Fitting parameters per Guthrie's model

Vendor	C1	C2	C3	C4	C5	C6	C7	C8	C9	C10	C11
B&W	501	-620	461	0.22	-.057	5.31	390	55.8	110	.1763	-.0729
CE	23.2	449	13.1	0.067	.033	-47.89	396	2265	.0794	.409	-.0843
GE	539	-334	284	0.368	-.017	2.08	307	21900	.00573	.301	-.00963
West.	109	509	-71	0.227	.0004	-20.0	552	306	.380	.282	-.040

The regression analyses were done on Eq. (1) for each individual vendor. The resulting 2-sigma margins for each individual vendor, not taking into account the residual value greater than 100°F, were compared with that of Reg. Guide 1.99, Rev. 2, 2-sigma margins and listed in Table 5. The Guthrie model, per B&W and CE data, showed consistent improvement on 2-sigma margins for base and weld materials, whereas, per Westinghouse and GE data, there was a slight improvement on 2-sigma margins for plate materials only. The explanation for these inconsistencies is that the CF of the Regulatory Guide predicted shift for the weldments was based on Odette's embrittlement model, and furthermore, the Guthrie model was developed on 177 data points, which has only 6 GE data; therefore, the applicability of the Guthrie model to GE data is questionable.

TABLE 5--Comparison of 1 standard deviation of residual for plate and weldments*.

	Reg. Guide		Guthrie		New Model	
Vendor	weld	plate	weld	plate	weld	plate
B&W	39.15	36.04	24.69	19.77	21.34	17.98
CE	37.15	16.74	19.37	15.42	16.36	14.06
GE	36.09	38.12	39.75	32.92	27.86	27.59
Westinghouse	28.32	24.68	29.29	23.87	27.66	22.29
Overall	32.45	28.61	30.65	24.83	25.88	22.34

(*Comparison was made based on PR-EDB data)

New embrittlement prediction equations: The development of new prediction equations results from a series of studies on radiation embrittlement models, such as Guthrie's model [23], Odette's model [24], Fisher's model [25], B&W Lowe's model [26], French's FIM model [27], etc, and several other parameters studies. Although the copper-precipitation model has been extremely successful in explaining many aspects of irradiation embrittlement, it is becoming increasingly evident that there are other important mechanisms contributing to the embrittlement of the RPV steel, such as Ni, P, Mn, Mo, and S. Theoretically, all the impurities in the low alloy steel are candidates to be included in the modeling. For example, C, Si, etc., were investigated in the test run, but including or excluding these elements did not affect the overall outcome of the statistical parameters, therefore, these parameters (or elements) were not incorporated into final governing equations. Also due to the lack of the completeness for the available chemistry data from EDB, the Cu, Ni, P, Mn, Mo, and S were tentatively selected as key chemistries, and were incorporated into the formula of the new prediction equations. Furthermore, the reason of separating weld and base metals, is because the weld presents a

possible region of physical and metallurgical discontinuity. The welding process offers added chances for the introduction of defects and undesirable components or stresses, and the radiation environment may accentuate the other negative aspects of the weld through differential radiation damage. The selected equations for each individual vendor are listed below:
Westinghouse:

$$\begin{aligned} Shift(Weld) &= [\,C(1)\cdot Cu + C(2)\cdot\sqrt{Cu\cdot Ni}\cdot Mo + C(3)\cdot\frac{P}{Cu}\,][f^{C(4)+C(5)\cdot \ln f}] \\ Shift(Base) &= [\,\frac{C(6)}{Mn} + C(7)\cdot Cu + C(8)\cdot\sqrt{Cu\cdot Ni} + C(9)\cdot P\,][f^{C(10)+C(11)\cdot \ln f}] \end{aligned} \tag{2}$$

Babcock & Wilcox:

$$\begin{aligned} Shift(Weld) &= [\,C(1)\cdot\frac{Cu}{Mn} + C(2)\cdot\sqrt{Cu\cdot Ni} + C(3)\cdot Ni\cdot Mo\,][f^{C(4)+C(5)\cdot \ln f}] \\ Shift(Base) &= [\,\frac{C(6)}{Mn} + C(7)\cdot Cu + C(8)\cdot\sqrt{\frac{Cu\cdot Ni}{Mn}} + C(9)\cdot S\,][f^{C(10)+C(11)\cdot \ln f}] \end{aligned} \tag{3}$$

Combustion Engineering:

$$\begin{aligned} Shift(Weld) &= [\,C(1)\cdot Cu + C(2)\cdot\sqrt{Cu\cdot Ni} + C(3)\cdot P\,][f^{C(4)+C(5)\cdot \ln f}] \\ Shift(Base) &= [\,\frac{C(6)}{Mn} + C(7)\cdot Cu + C(8)\cdot\sqrt{Cu\cdot Ni} + C(9)\cdot S\,][f^{C(10)+C(11)\cdot \ln f}] \end{aligned} \tag{4}$$

General Electric:

$$\begin{aligned} Shift(Weld) &= [\,C(1)\cdot Cu + C(2)\cdot\sqrt{Cu\cdot Ni}\cdot Mo + C(3)\cdot P\,][f^{C(4)+C(5)\cdot \ln f}] \\ Shift(Base) &= [\,C(6) + C(7)\cdot Cu + C(8)\frac{Ni\cdot Mo}{Mn} + C(9)\cdot S\,][f^{C(10)+C(11)\cdot \ln f}] \end{aligned} \tag{5}$$

TABLE 6--Fitting parameters per new embrittlement equations

Vendor	C1	C2	C3	C4	C5	C6	C7	C8	C9	C10	C11
B&W	1082	-1034	1655	.212	-.062	52.28	1116	-544	140	.1869	-.06265
CE	112.5	460	-1475	.086	.0206	-83.63	-242.	672	645	.3865	-.0642
GE	200	816	-148	.321	-.0144	78.5	223	81.6	-1538	.303	-.00301
West.	320	602	-67	.224	-.0054	-34.5	482	145	1397	.272	-.0511

The resulting 1 standard deviation of residuals for each individual vendor have not taken into account the residual values greater than 100°F, which were compared with that of Reg. Guide 1.99, Rev. 2, and listed in Table 5. All 2-sigma margins of new equations have significant improvement compared with that of the Reg. Guide's margin. The overall safety margin for the weld and base materials of the new model are 51.76°F and 44.68°F, respectively. The safety margin for the weld and base materials of Reg. Guide 1.99, Rev. 2, are 64.9°F and 57.22°F, respectively. The percentage of improvement of safety margins for weld and base materials are

20.25% and 21.92%, respectively. The data trends per the Regulatory Guide model and new models are demonstrated in the residual plots; less data scatters were revealed in the plots of the new model than in the plots of the Regulatory Guide model (see Figs. 12 through 15).

A great improvement in the safety margin can be achieved simply by taking into account the vendor-specific data and the proper chemistry compositions in the fitting formula. From the residual defects point, only the point defects that survive from the bulk recombination and in cascade recombination can contribute to the final mechanical property changes; the residual defects strongly depend on the material properties and irradiation environments, such as chemistry composition, heat treatment, irradiation temperature, and neutron spectrum. More chemical compositions of the vendor-specific data are being properly considered in the embrittlement model, thus a more correct correlation to the residual defects will be obtained. The result will be a more accurate prediction of the material property change, which was demonstrated in the new embrittlement models.

From a microstructure point, vacancy clusters are thought to be responsible for more strengthening than are interstitial clusters at a given temperature and damage rate [28,29]. Vacancy clusters, such as dislocation loops, voids, and stacking fault tetrahedra, are strong obstacles to the movement of dislocations and, therefore, may determine the material hardening [30]. Copper and other fcc metals compositions are believed to stabilize vacancy-type defects in irradiation material [31-35]. From a mechanics point, the overall material properties depend on the property of individual material component. If the volume or the property of the component undergo a large transformation, this component will definitely play a dominant role in the final overall material property change. The formation of the vacancy-type defect is such a candidate due to the dramatic change of material property in the matrix by forming a new phase with zero mass. On the microstructure defect evolution, all the residual defects created through the radiation events will contribute to the final macroscopic material property changes. And the residual defects in materials due to neutron induced displacement damage are a function of neutron energy, neutron flux, and exposure temperature, as well as the material properties that determine how neutrons interact with atoms and how defects interact within the material. Vacancy clusters is a major contributor to the material hardening at higher temperatures and lower displacement rates, for example, at a commercial power reactor environment [29]. Thus, from microstructure and mechanics points, vacancy-type defects not only can be considered as a major contributor to the material hardening, but also indicate the co-existence of other precipitates, such as copper. Furthermore, the total volume change of the vacancy-type defects may serve as a direct index to the final residual defects by taking into account the spectral effect, rate effect, and temperature effect, in addition to the material properties, implicitly. Therefore, the total volume change of the vacancy-type defects contained in the irradiated material may serve as a direct correlation index to the embrittlement model than that of the chemical compositions.

Currently, dpa is used as a measure of the potential to create point defects. It is not necessarily equal to, or even proportional to, the actual number of residual point defects. Clearly, a complete and accurate description of microstructural development during irradiation has not been attempted and seems to be beyond the present state of art. However, a better correlation parameter for radiation embrittlement can be expected through the upgraded dpa that incorporated the concepts of residual defects. A continued need exists to develop data bases on materials typical of current practice and from various sources of supply. In order to do this, there is a requirement for the continued development and standardization of test methods and techniques for both surveillance and post-irradiation testing procedures.

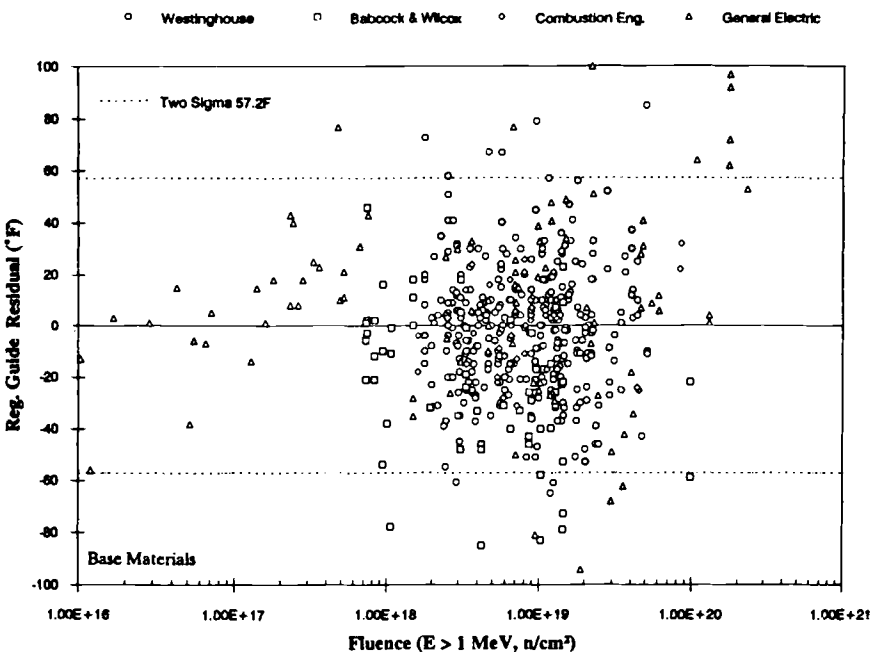


FIG. 12--Plot of residual vs fluence for base materials, per Reg. Guide 1.99, Rev. 2.

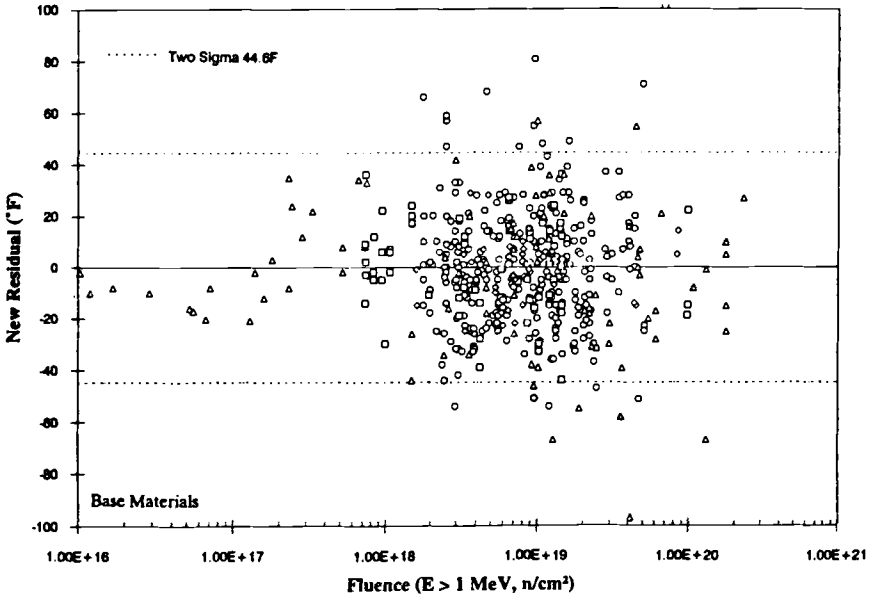


FIG. 13--Residual vs fluence for base materials, per new embrittlement models.

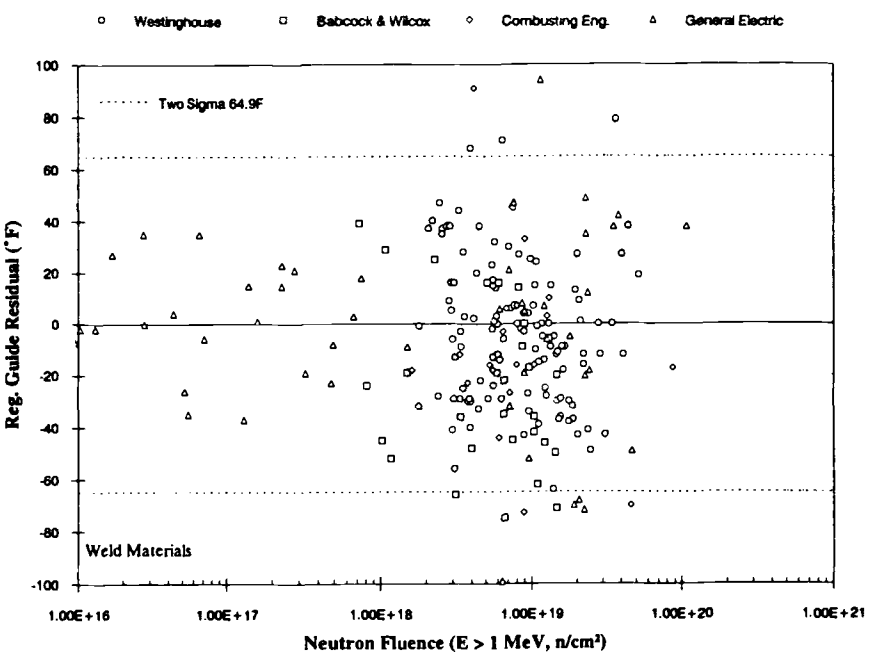


FIG. 14--Plot of residual vs fluence for weld materials, per Reg. Guide 1.99, Rev. 2.

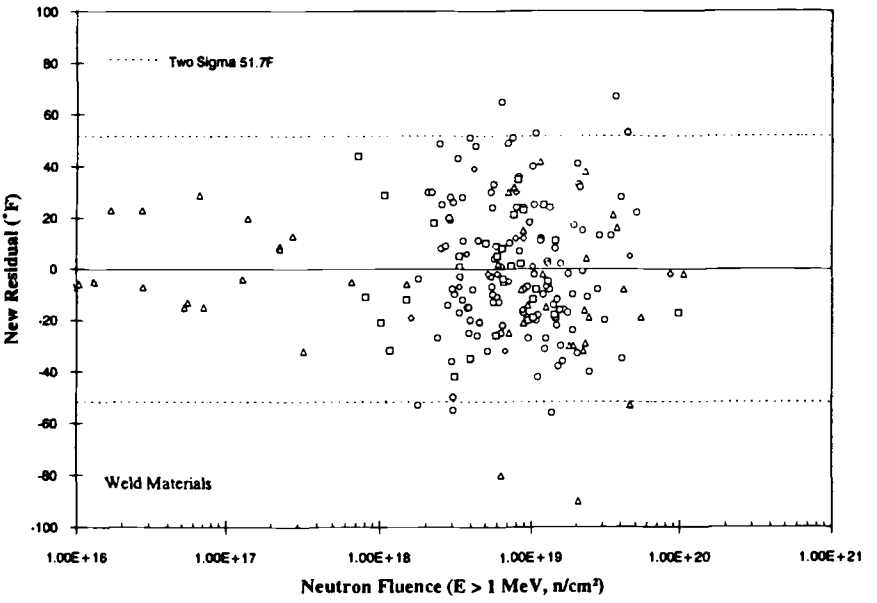


FIG. 15--Plot of residual vs fluence for weld materials, per new embrittlement models.

REFERENCES

[1] Mansur, L. K., "Mechanisms and Kinetics of Radiation Effects in Metals and Alloys," Kinetics of Nonhomogeneous Processes, ed. by Gordon R. Freeman, 1987.

[2] Russell, K. C., "Phase Stability Under Irradiation," Progress in Materials Science, ed. by B. Chalmers, J. Christian, T. B. Massalski, Pergamon Press, Oxford, 1982.

[3] Odette, G. R., Lombrozo, P. M., and Wullaert, R. A., "Relationship Between Irradiation Hardening and Embrittlement of Pressure Vessel Steels," Effects of Radiation on Materials, Twelfth International Symposium, ASTM STP 870, eds. Garner, F. A. and Perrin, J.S., American Society for Testing and Materials, Philadelphia, 1985, pp.840-860.

[4] Lucas, G. E., Odette, G. R., Lombrozo, P. M., and Sheckherd, J. W., "Effects of Composition, Microstructure, and Temperature on Irradiation Hardening of Pressure Vessel Steels," Effects of Radiation on Materials, Twelfth International Symposium, ASTM STP 870, eds. Garner, A. and Perrin, J., American Society for Testing and Materials, Philadelphia, 1985, pp. 900-930.

[5] Shah, V. N., Server, W. L., Odette, G. R., and Amar, A. S., "Residual Life Assessment of Light Water Reactor Pressure Vessels," Effects of Radiation on Materials, ASTM STP 1011, 1989, pp. 161-175.

[6] Stallmann, F. W., Wang, J. A., Kam, F. B. K. and B. J. Taylor, "PR-EDB: Power Reactor Embrittlement Data Base, Version 2," NUREG/CR-4816, U.S. Nuclear Regulatory Commission, 1994.

[7] Stallmann, F. W., Wang, J. A., and Kam, F. B. K., "TR-EDB: Test Reactor Embrittlement Data Base, Version 1," NUREG/CR-6076, U.S. Nuclear Regulatory Commission, 1994.

[8] Wiedersich, H., "Effects of The Primary Recoil Spectrum on long-Range Migration of Defects," Radiation Effects and Defects in Solids, 1990, Vol 113, pp 97-107.

[9] Rehn, L. E., Okamoto, P. R., and Averback, R. S., "Relative Efficiencies of Different Ions for Producing Freely Migrating Defects," Physical Review B, 30 (1984) 3073

[10] Mansur, L. K. and Farrell, K., "On Mechanisms By Which a Soft Neutron May Induce Accelerated Embrittlement," J. Nuclear Mater., 170 (1990) 236-245.

[11] Heinsich, H. L., "Correlation of Mechanical Property Changes in Neutron Irradiated Pressure Vessel Steels on The Basis of Spectral Effects," Fusion Reactor Quarterly Progress Report, DOE/ERD-0313/6, 1990.

[12] U.S. NRC Regulatory Guide 1.99, "Radiation Embrittlement of Reactor Vessel Materials, Revision 2," May 1988.

[13] Remec, I., Wang, J. A., Kam, F. B. K., and Farrell, K., "Effects of Gamma-Induced Displacements on HFIR Pressure Vessel Materials," J. Nuclear Mater, 217 (1994) 258-268.

[14] Kam, F. B. K., Stallmann, F. W., and Wang, J. A., "Power Reactor Embrittlement Data Base(PR-EDB): Uses in Evaluating Radiation Embrittlement of Reactor Vessels," Proceedings of Aging Research Conference, 1992.

[15] Cheverton, R. D., Merkle, J. G., and Nanstad, R. K., eds., "Evaluation of HFIR Pressure-Vessel Integrity Considering Radiation Embrittlement," ORNL/TM-10444, Oak Ridge National Laboratory, 1988.

[16] Nanstad, R. K., Iskander, S. K., Rowcliffe, A. F., Corwin, W. R., and Odette, G. R., "Effect of 50°C Surveillance and Test Reactor Irradiations on Ferritic Pressure Vessel Steel Embrittlement," Effects of Radiation on Materials: 14th International Symposium (Vol. II), ASTM STP 1046, N. H. Packan, R. E. Stoller, and A. S. Kumar, Eds., 1990, pp. 5-29.

[17] Remec, I. and Kam, F. B. K., "Neutron Spectra at Different HFIR Pressure Vessel Surveillance Locations", NUREG/CR-6117, ORNL/TM-12484, U.S. NRC, 1993.

[18] Pachur, D., "Radiation Annealing Mechanisms of Low-Alloy Reactor Pressure Vessel Steels Dpecndent on Irradiation Temperature and Neutron Fluence," Nuclear Technology, Vol.

59, 1982, pp. 463-475.

[19] Randall, P. R., "Basis for Revision 2 of the U.S. Nuclear Regulatory Commission's Regulatory Guide 1.99," ASTM STP 909, ed. Steele, L. E., American Society for Testing and Materials, Philadelphia, 1986, pp. 149-162.

[20] Oldfield, W., McConnell, P., Sever, W., and Oldfield, E., "Irradiated Nuclear Pressure Vessel Steel Data Base," EPRI NP-2428, Electric Power Research Institute, June 1982.

[21] Pierre Petrequin, "Irradiation Embrittlement of Pressure Vessel Steels: A Review of Activities in France," Radiation Embrittlement and Surveillance of Nuclear Reactor Pressure Vessels, ASTM STP 819, ed. Steele, L. E., ASTM 1983, pp. 29-52,

[22] Guionnet, C., Houssin, D.,Brasseur, A., Lefort, D., Gros, and Perdreau, "Radiation Embrittlement of PWR Reactor Vessel Weld Metals: Nickel and Copper Synergism Effects," Effects of Radiation on Materials, ASTM STP 782, eds. Brager, H. R. and Perrin, J. B., American Society for Testing and Materials, 1982, pp. 392-411.

[23] Guthrie, G. L., "Charpy Trend Curves Based on 177 PWR Data Points," NUREG/CR-3391, U.S. Nuclear Regulatory Commission, 1983.

[24] Odette, G. R., Lombrozo, P. M.,Perrin, J, F., and Wullaert, R. A., "Physically Based Regression Correlations of Embrittlement Data From Reactor Pressure Vessel Surveillance Programs," EPRI NP-3319, Electric Power Research Institute, 1984.

[25] Fisher, S. B., and Buswell, J. T., "A Model for PWR Pressure Vessel Embrittlement," Berkeley Nuclear Laboratories, Central Electric Generating Board, GL139PB, 1986.

[26] Lowe, A. L., Jr., and Pegram, J. W., "Correlations for Predicting the Effects of Neutron Radiation on Linde 80 Submerged-Arc Welds," BAW-1803, Rev. 1, May 1991.

[27] Brillaud, C., Hedin, F., and Houssin, B., "A Comparison Between French Surveillance Program Results and Predictions of Irradiation Embritllement," Influence of Radiation on Material Properties, ASTM STP 956, eds. F. A. Garner, C. H. Henager, Jr., and N. Igata, American Society for Testing and Materials, 1987, pp. 420-447.

[28] Spitznagel, J. A., and Venskytis, F. J., "The Annealing of Copper Vacancy Aggregates in Neutron Irradiated Ferritic Pressure Vessel Steels, TRANS ANS 1975, p.161.

[29] Stoller, R. E., "Modeling The Influence of Irradiation Temperature and Displacement Rate on hardening Due to Point Defect Clusters in Ferritic Steels,"Effects of Radiation on Materials: 16th International Symposium, ASTM STP 1175, Arvind S. Kumar, David S. Gelles, Randy K. Nanstad, and Edward A. Little, Editors, ASTM, 1993, pp.394-423.

[30] Jung, P., "Relevance of the Displacement Damage Concept for the Evaluation of Radiation Effects in Metals," Radiation Effects and Defects in Solids, Vol. 113, 1990, pp. 109-118.

[31] Brenner, S. S., Wagner, R. and Spitznagel, J.A. "Field Ion Microscope Detection of Ultra-Fine Defects in Neutron-Irradiated Fe-34% Cu Alloy", Metallurgical Transactions, Vol. 9A, 1978, pp. 1761.

[32] Smitd, F.A. and Sprague, J.A. "Property Changes Resulting from Impurity-Defect Interactions in Iromn and Pressure Vessel Steel Alloys," Effects of Radiation on Substructure and Mechanical Properties of Metals and Alloys, ASTM STP 529, 78, (1973).

[33] English, C. A., "Recoil Effects in Radiation Damage," Radiation Effects and Defects in Solids, Vol. 113, 1990, pp. 15-28.

[34] Simons, R. L., "Damage Rate and Spectrun Effects in Ferritic Steel NDTT Data," Influence of Radiation on Material Properties: 13th International Symposium (Part II), ASTM STP 956, F.A. Garner, C. H. Henager, Jr., and N. Igata, Eds., American Society for testing and Materials, Philadelphia, 1987, pp. 535-551.

[351 Odette, G. R., and Sheeks, C. K. ,"A model for Displacement Casade-Induced Microvoid and Precipitator Formation in Dilute Iron-Copper Alloys," Phase Stability During Irradiation, J. R. Holland, L. K. Mansur, and D. I. Potter, Eds., Metallurgical Society of the American Institute of Mining, Metallurgical and Petroleum Engineers, (1982), p. 415.

M. Brumovský[1], P. Novosad[1], J. Ždárek[1]

SURVEILLANCE PROGRAMME FOR WWER-440/TYPE 213 REACTOR PRESSURE VESSELS- STANDARD PROGRAMME, RE-EVALUATION OF RESULTS, SUPPLEMENTARY PROGRAMME

REFERENCE: Brumovský, M., Novosad, P., Žd'árek, J., **"Surveillance Programme for WWER-440/Type 213 Reactor Pressure Vessels—Standard Programme, Re-evaluation of Results, Supplementary Programme,"** *Effects of Radiation on Materials: 17th International Symposium, ASTM STP 1270,* David S. Gelles, Randy K. Nanstad, Arvind S. Kumar, and Edward A. Little, Eds., American Society for Testing and Materials, 1996.

ABSTRACT: Irradiation embrittlement of the reactor pressure vessel beltline materials of WWER-440/Type 213 reactors is monitored by a material irradiation surveillance programme. Due to the high lead factor, the duration of the standard surveillance programme is only five years, after which no further surveillance samples remain in the reactor. The large variation and uncertaintity in neutron flux over the irradiated materials produce significant scatter in mechanical properties and necessitate a re-evaluation of results using gamma scanning, specimen reconstitution and recalculation. In order to provide information on the impact of changes in plant operation during later years a supplementary surveillance programme has been devised.

KEYWORDS: reactor pressure vessel, surveillance programme, irradiation embrittlement, gamma scanning, reconstitution, supplementary surveillance programme

Irradiation damage affects reactor pressure materials by increasing the ductile-to-brittle transition temperature , yield stress and ultimate tensile stress and by decreasing the ductility, Charpy upper shelf energy and upper shelf fracture toughness. The effect on the material properties of the reactor beltline materials is potentially the most important life limiting factor for most reactors. Consequently, the irradiation induced changes in these materials properties are monitored by a surveillance programme.

[1]Managers and research scientists, Nuclear Research Institute Řež plc, 250 68 Řež, Czech Republic

Copyright© 1996 by ASTM International www.astm.org

The surveillance programme for WWER-440 reactors was instituted after construction of the reactors and it was not possible to locate surveillance specimens closer to the inner wall of the pressure vessel. Specimens were located in channels at a distance of approximately 156 mm from the pressure vessel inner surface which resulted in a high lead factor of about 13 for specimens from base metal and about 17 for specimens from weld metal.

STANDARD SURVEILLANCE PROGRAM

Because of the high lead factor, the duration of a typical surveillance programme was only five years, with specimen withdrawals after 1, 2, 3 and 5 years of reactor operation.

Specimens were loaded into small capsules, connected together to form a chain, which extended well beyond the flat portion of the flux profile close to the reactor centreline, as indicated in Fig.1. This resulted in a severe gradient in flux over some groups of capsules, particularly those containing precracked Charpy (COD) specimens. Additionally, problems were encountered in determining fluences for individual specimens since their position in the capsules (Fig.2) relative to the core could not be determined since the orientation of the capsules was not constrained.

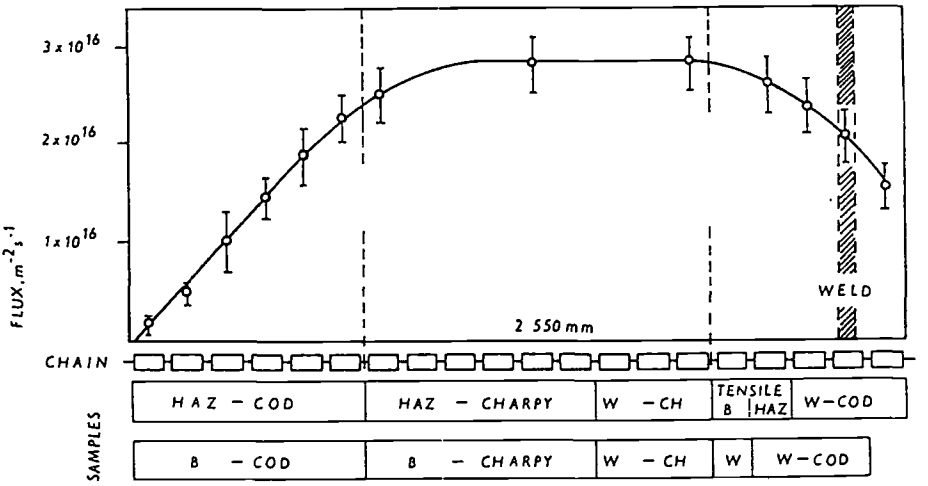


Fig.1 - Flux distribution in surveillance channel of WWER-440/Type 213 Reactor
B - base metal W - weld metal
HAZ - heat affected zone
CH - impact Charpy specimens
COD - pre-cracked Charpy specimens

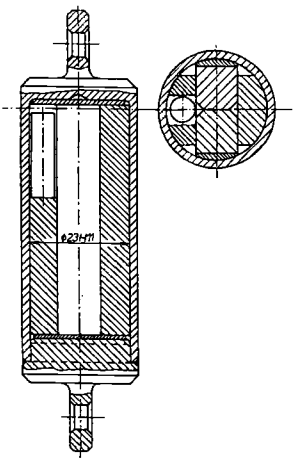


Fig. 2 - Capsule for standard surveillance programme

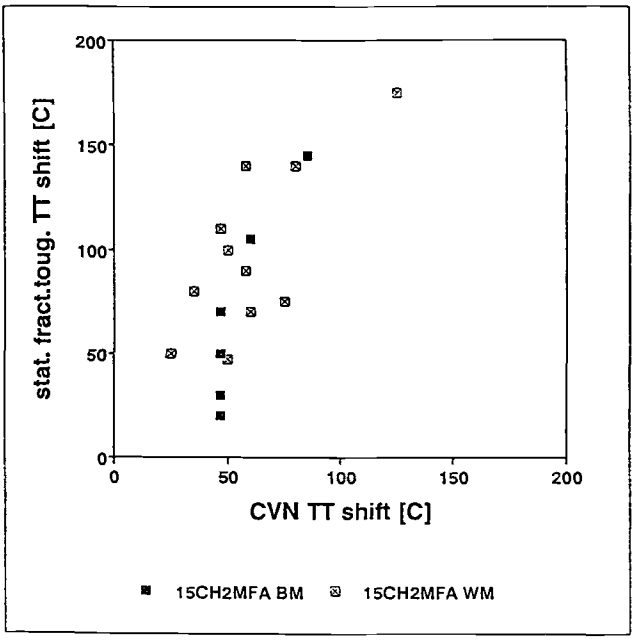


Fig.3 - Typical results of mechanical properties testing, comparison of impact (CVN TT) and static fracture toughness shifts
BM - base metal WM - weld metal

Diamond powder was chosen as a temperature monitor - its lattice parameters are used as a measure of an irradiation temperature. Unfortunately, it was shown that changes in these lattice parameters depend not only on irradiation temperature and neutron fluence but on neutron flux, too. Moreover, these dependencies are connected with high uncertaintities. Thus, this temperature monitor was found as an unsuitable and irradiation temperature is determined by calculations, only.

The main disadvantage of the standard surveillance program is its short-time duration and use - pressure vessel is no more monitored after five years of operation.

To improve this situation, the following steps have been chosen and step by step are realized:
- re-evaluation of the standard surveillance programme,
- implementation of measuring chains - passive and active ones,
- design of a supplementary surveillance programme.

RE-EVALUATION OF STANDARD SURVEILLANCE PROGRAM

Aim of this activity is to obtain as many results as it is possible from the irradiated and tested specimens.

Neutron fluences are re-evaluated by use of single specimens gamma scanning and re-calculation of neutron fluences and fluxes using new more advanced codes as well as cross sections.

Newly establishment of surveillance specimens irradiation temperature is practically impossible.

One of the disadvantages of the standard surveillance programme is seen in Fig.1 - specimens for impact notch toughness testing (Charpy type) are receiving much higher neutron fluence than specimens for static fracture toughness tests (pre-cracked of COD type). Thus, any comparison of results from both type of tests is very difficult, as neutron fluxes differ substantially in their irradiation places, too. Comparison of results from these tests is of the highest importance, as calculation of pressure vessel resistance against non-ductile failure is based on fracture mechanics, but according to Codes, only Charpy transition temperature shifts are taken into account. Fig.3 shows results from the standard surveillance programmes of WWER-440 type reactors - it is clearly seen that transition temperature shifts determined from static fracture toughness tests are mostly higher than those from notch impact tests. If this fact would be generally proved the calculations according to Codes would be nonconservative.

To solve this problem, at least partially for given conditions, new data are receiving using a reconstitution method - halves of broken Charpy specimens are taken as inserts for reconstitution of new Charpy-size specimens using electron beam welding technique. These new specimens are prepared for static as well as dynamic fracture toughness testing.

Finally, a detailed analysis of all surveillance test results together with results from reconstituted specimens are under way to establish new trend curves for transition temperature shifts to be applied in pressure vessel lifetime calculations.

MEASURING CHAINS

Even the re-evaluation of all results from the standard surveillance programme is unable to answer to all important questions on irradiation conditions of these specimens. Two experiments were chosen and designed in such a way to improve substantially our knowledge on neutron fluences and irradiation temperature and to give necessary background for future supplementary surveillance programme.

Two passive measuring chains were loaded into surveillance position during 1993 refueling period and irradiated for one year. These chains contained standard type of capsules (see Fig.2) as well as new type of capsules prepared for the supplementary programme (see Fig.4). All these capsules are supplied by an enormous quantity of different neutron monitors - different elements in the form of foils or wires were put in every capsule in such a way to monitor neutron flux along the capsule length as well as in its azimuthal direction. Activation as well as fission monitors were chosen for improving our knowledge of neutron fluxes and neutron spectra, too.

Additionally, ex-vessel neutron fluence measurement was realized using similar type of monitors. More precise 3-D calculations of neutron fluxes and spectra in surveillance, pressure vessel as well as in ex-vessel positions are carried out.

Melting wire monitors were also inserted into these capsules is to obtain some information on upper limits of the irradiation temperature.

Even though the main purpose of these chains is in the improvement of neutron dosimetry, mechanical tests play an important role, too. Specimens for different type of tests (Charpy impact, static and dynamic fracture toughness) from an archive base material as well as from austenitic cladding and from the IAEA reference material of JRQ type were inserted into capsules. Some of specimens will serve as inserts (10x10x14 mm) for further reconstitution into standard size specimens.

These chains were withdrawn during refueling in 1994 and their tests are now under progress.

Another *active measuring chains* are designed and their manufacturing is prepared. Their main purpose is seen in a possibility of a direct measurement of the irradiation temperature using thermocouples in different irradiation capsules.

SUPPLEMENTARY SURVEILLANCE PROGRAM

There are some strong reasons for such a programme, as the Czech Regulatory body strongly required to monitor the pressure vessels behaviour during their full residual lifetime. At the same time, the following requirements have been defined :

- only real archive reactor pressure vessel materials can be used,
- capsules with specimens must be located in places with a low lead factor, not larger than three,
- neutron fluence must be much more correctly measured and determined for each specimen,
- irradiation temperature must be correctly measured,
- specimens for notch impact tests as well as for static and dynamic fracture toughness tests should be used.

For all mechanical properties (except tensile) tests will be used samples made by reconstitution technique, using the electron beam welding technique.

Irradiation capsules have a new design (Fig. 4) - each of them contains twelve inserts which are sufficient to obtain one temperature dependance of a tested property. Design of the chains has been also changed to ensure a constant and defined position with respect to the reactor active core. Thus, neutron fluences on individual specimens could be better determined. These capsules will be located in places with a low lead factor, not larger than three, i.e. instead the upper three capsules from the standard programme.

Activation and fission monitors are put into each of capsules in the form of foils as well as of wires, located along the capsule. Ex-vessel neutron fluence measurements has been defined as a mandatory for the whole remaining residual lifetime of the vessels - monitors are located in the same radial positions as chains which will be withdrawn at the same time. Ex-vessel monitoring has one year period of their withdrawal.

A low temperature melting alloys are used as temperature monitors, placed in special positions in every capsule.

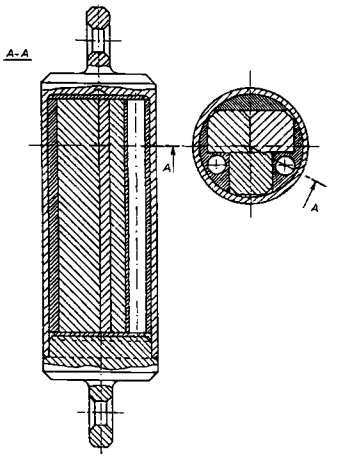


FIG. 4--Capsule for supplementary surveillance programme

The following tests are planned to monitor a material degradation trends :

- Tensile tests
- Instrumented Charpy-V notch tests
- Static fracture toughness tests
- Dynamic fracture toughness tests

Realization of this supplementary surveillance programme in nuclear power plant in Dukovany will start in the end of 1995.

CONCLUSIONS

Results and experience obtained from the standard surveillance programme of WWER-440 reactor pressure vessels showed to some

disadvantages, mainly in neutron fluence and irradiation temperature correct determination. High lead factor is also an another disturbing parameter for correct application of the results into pressure vessel lifetime calculation.

A new, supplementary surveillance programme was designed to improve these disadvantages as well to obtain some additional important data. This programme is based on reconstitution technique of archive material inserts irradiated in positions with a low lead factor. More complex set of neutron monitors as well of melting monitors for irradiation temperature determination will be placed into every capsule. Neutron fluence measurement in capsules is directly connected with ex-vessel neutron monitoring.

This supplementary surveillance programme will monitor the pressure vessel behaviour during the whole remaining lifetime.

Strength and Toughness Issues in RPV Steels

Rachid Chaouadi[1], Paul De Meester[2], Eric van Walle[1], Albert Fabry[1] and José Van de Velde[1]

APPLICATION OF MICROMECHANICAL MODELS OF DUCTILE FRACTURE INITIATION TO REACTOR PRESSURE VESSEL MATERIALS

REFERENCE: Chaouadi, R., De Meester, P., van Walle, E., Fabry, A., and Van de Velde, J., **"Application of Micromechanical Models of Ductile Fracture Initiation to Reactor Pressure Vessel Materials,"** *Effects of Radiation on Materials: 17th International Symposium, ASTM STP 1270,* David S. Gelles, Randy K. Nanstad, Arvind S. Kumar, and Edward A. Little, Eds., American Society for Testing and Materials, 1996.

ABSTRACT: The aim of the current study is the application of local micromechanical models to predict crack initiation in ductile materials. Two reactor pressure vessel materials have been selected for this study: JRQ IAEA monitor base metal (A533B Cl.1) and Doel-IV weld material. Charpy impact tests have been performed in both un-irradiated and irradiated conditions. In addition to standard tensile tests, notched tensile specimens have been tested.
The upper shelf energy of the weld material remains almost un-affected by irradiation, whereas a decrease of 20% is detected for the base metal. Accordingly, the tensile properties of the weld material do not reveal a clear irradiation effect on the yield and ultimate stresses, this in contrast to the base material flow properties. The tensile tests have been analyzed in terms of micromechanical models. A good correlation is found between the standard tests and the micromechanical models, that are able to predict the ductile damage evolution in these materials. Additional information on the ductility behaviour of these materials is revealed by this micromechanical analysis.

KEY WORDS: ductile fracture, cavity growth, damage work, reactor pressure vessel steel, irradiation effect, upper shelf, tensile test, finite element

[1] Research scientist, senior research scientist, lead scientist and manager, respectively, SCK•CEN, Boeretang 200, 2400 Mol, Belgium.

[2] Professor, KUL, Metals and Materials Science Department, de Croylaan 2, 3001 Heverlee, Belgium.

Copyright© 1996 by ASTM International www.astm.org

Generally, a basic consequence of irradiating reactor pressure vessel steels is to shift the C_v-impact transition curve to higher temperatures and to lower its upper shelf energy. The tensile properties are normally also affected: the yield stress increases reflecting the hardening of the material.
The upper shelf has received less attention than the transition regime, despite the fact that the latter experiences both cleavage and ductile fracture processes.
In order to better understand the physical phenomena that govern the competition between cleavage and ductile processes in the transition region and at the upper shelf, particular attention should be given to the ductile fracture process.

The present work aims to apply micromechanical models of ductile fracture to the upper shelf and attempts to correlate them to the standard tensile and Charpy impact properties. In this context, various notched tensile specimens were tested at room temperature as well as at 310°C, in both un-irradiated and irradiated conditions. Subsequently, some micromechanical models were applied to predict the onset of ductile fracture. These models combine the micro-mechanisms of fracture with stress/strain history.

DUCTILE DAMAGE MODELLING

It is known that the ductile fracture phenomenon is a cavitation process that consists of three phases. First, one has the nucleation phase, when voids are initiated around second phase particles (inclusions and precipitates). This initial phase is primarily a consequence of the deformation incompatibility between the matrix and the inclusion. The second phase is the void growth which is mainly affected by the hydrostatic stress. Finally, the coalescence phase leads to a macroscopic crack. However, the ductile fracture process is essentially dominated by the enlargement of cavities until their final coalescence and macroscopic crack initiation.

Bridgman [1] was the first to point out the important role of the hydrostatic stress in ductile fracture. McClintock [2] and Rice and Tracey [3] suggested void growth models, respectively, in a non-linear elastic material with a cylindrical void and in a perfectly plastic material containing a spherical cavity. Both models emphasize the influence of stress triaxiality. Beremin [4] suggested the use of the kinetics of void growth, as developed by Rice and Tracey, to model the ductile fracture process. This cavitation kinetics is given by:

$$\frac{dR}{R} = \alpha \exp\left(\frac{3\sigma_h}{2\sigma_e}\right) d\epsilon_p$$

where:
- R is the cavity (void) radius
- σ_h is the hydrostatic stress ($\sigma_{ii}/3$)
- σ_e is the equivalent (von Mises) stress
- $d\epsilon_p$ is the equivalent plastic strain
- α is a proportionality factor

The factor α is a constant (α=0.283 in the Rice and Tracey model). Huang [5] has shown that α underestimates the void growth and suggests a value of 0.428. However, this factor turns out to be not so critical and can be adjusted to fit the experimental data. Furthermore, Marini [6] has shown that α is material dependent and that it is related to the volume fraction of inclusions: the larger the volume fraction, the higher becomes α.

Generally, the decohesion phase of inclusions can be neglected. We, therefore, assume that cavities initiate as soon as plastic deformation occurs. Accepting that crack initiation occurs when the cavity size reaches its critical value, Beremin [4] has introduced the critical cavity ratio that corresponds to void coalescence. This critical cavity growth rate is then given by:

$$\left(\frac{R_c}{R_0}\right) = \exp\left[\int_0^{\epsilon_c} \alpha \exp\left(\frac{3\sigma_h}{2\sigma_e}\right) d\epsilon_p\right]$$

where R_0 is the initial cavity radius (inclusion radius)
R_c is the cavity radius at fracture initiation
ε_c is the local plastic strain at fracture initiation, obtained from the knowledge of the original diameter (D_0) and the diameter at crack initiation (D_c), namely:

$$\epsilon_c = 2\ln\left(\frac{D_0}{D_c}\right)$$

So, when the strain - stress history during the whole deformation process and the onset of ductile crack initiation are known, a critical value of the damage can be derived. This model has been successfully used by many authors [4,6-9].

Historically, many attempts have been made to extract a fracture criterion from the tensile test [10-12]. Critical strain, critical stress and semi-empirical strain-stress relations have been proposed. However, these relations are geometry dependent. Recently, it has been shown that when the plastic strain work incorporates the hydrostatic components to include the volume variation due to void enlargement, the so-called damage work becomes geometry independent. This allows the damage work to be used as a ductile fracture criterion [9], and its kinetics is given by:

$$\delta W_d = \left[1 + 3\alpha\xi \exp\left(\frac{3}{2}\xi\right)\right] \sigma_e d\epsilon_p$$

where: ξ is the triaxiality ratio ($\xi = \sigma_h / \sigma_e$)
α is as before a material dependent constant or, in other words, a microstructural parameter.
δW_d is the increment of damage work

The total energy density involved in the ductile crack initiation process is then given by:

$$W_{dc} = \int_0^{\epsilon_c} [1 + 3\alpha\xi \exp(\frac{3}{2}\xi)]\,\sigma_e d\epsilon_p$$

As can be seen, the model encompasses the material flow properties and geometry dependence (σ_e, ϵ_p, ξ) and the microstructural parameters (α, ϵ_c). The factor α is related to the volume fraction of non-metallic second phase particles, whereas the strain at crack initiation ϵ_c is related to the coalescence phase.

Other similar models have been proposed by Gurson [13] and Rousselier [14] taking the cavitation process directly into account in the constitutive equations. However, these models need to be implemented into the finite element package.

MATERIAL CONDITIONS

In the framework of the IAEA Phase 3 Co-ordinated Research Programme on "Optimisation of Reactor Pressure Vessel Surveillance Programmes and Their Analysis", two materials have been irradiated in the Doel-IV power plant: the IAEA correlation monitor material, a A533B Cl.1 plate, identified as JRQ and a Belgian A508 Cl.3 weld identified as D4W. The chemical compositions are given in Table 1.

TABLE 1- Chemical Composition

Material	C	Cr	Cu	Mn	Mo	Ni
JRQ	0.18	0.13	0.14	1.37	0.50	0.82
D4W	0.07	0.14	0.05	1.57	0.48	0.78

Tensile specimens, Charpy-V samples, half-size Compact Tension and axisymmetrically notched tensile bars of both materials have been irradiated up to a fluence of 1.19 10^{19}n/cm^2 (E>1MeV) at a designed temperature of 290°C in a Doel-IV surveillance position [15]. In parallel, Charpy specimens of both materials have been thermally aged for the same period as the irradiation in the nuclear power station, i.e. 3 years at 290°C.

The mechanical properties of the un-irradiated and irradiated conditions are given in Table 2. The yield stress and ultimate strength changes due to irradiation are also indicated. The yield stress and the ultimate stress of the JRQ plate are more affected by irradiation than the D4W weld properties.

A series of Charpy specimens have been tested at different temperatures. The details of these tests have been reported elsewhere [15]. The main results are summarized in Table 3, where the upper shelf energy (USE), the 41J-transition temperature (T41J), the 68J-transition temperature (T68J), and the temperature corresponding to 50%-shear

fracture appearance (T50%) are given. In addition, the temperature shift at 41J-energy (ΔTT_{41J}) and the drop of the upper shelf energy (ΔUSE), due to irradiation, are also indicated.

TABLE 2- Mechanical Properties (static)

	Condition	temp (°C)	YS (MPa)	UTS (MPa)	δ (%)	RA (%)	ΔYS (MPa)	ΔUTS (MPa)
JRQ								
	Un-ir	RT	446	671	21.1	69.4		
	Un-ir	310	446	606	19.9	72.6		
	Irrad	310	521	728	19.2	66.8	75	122
D4W								
	Un-ir	RT	565	693	19.0	72.0		
	Un-ir	310	500	687	22.3	63.0		
	Irrad	RT	577	729	24.5	70.7	12	36
	Irrad	310	508	663	18.6	61.5	8	-30

TABLE 3- Charpy Results (dynamic)

Material	Condition	USE (J)	T41J (°C)	T68J (°C)	T50% (°C)	ΔTT_{41J} (°C)	ΔUSE (J)
JRQ							
	Un-ir	217	-21	-5	22		
	Irrad	173	+73	93	99	94	44
D4W							
	Un-ir	199	-63	-49	-43		
	Irrad	196	-51	-34	-27	12	3

As is clear from Table 3, and in accordance with the tensile data, the JRQ material is more radiation sensitive than D4W weld material. The 41J-shift of the transition temperature is 94°C for JRQ in comparison to 12°C for D4W. In addition, the loss of upper shelf energy is 44J for JRQ, whereas D4W is almost un-affected by irradiation. The transition curves of both materials are shown in Figure 1.
The thermally-aged Charpy specimens have not revealed any embrittlement in comparison with the un-irradiated condition

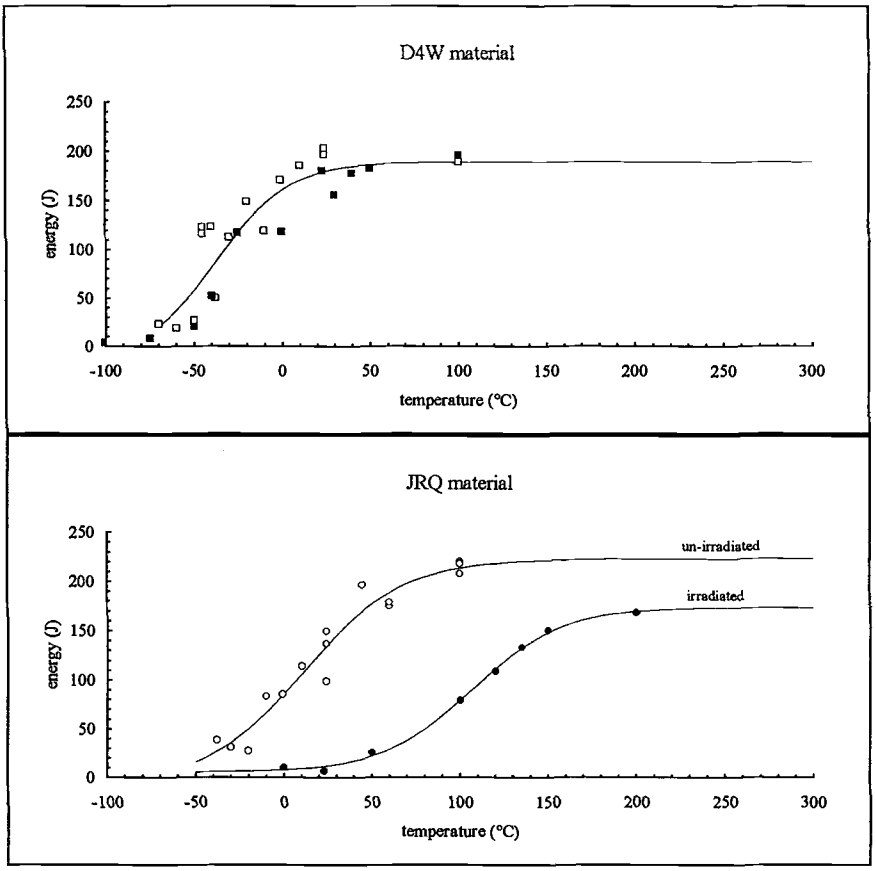


Figure 1: Charpy transition curve for D4W (weld) and JRQ (base) materials. Open symbols for un-irradiated material and filled symbols for irradiated materials.

To perform the finite element calculations, the uniaxial material response should be introduced. Therefore, the stress-strain flow curves of the different material conditions were derived from the tensile tests and modified by the Bridgman correction for specimen necking. This is done by transforming the axial elongation into diameter reduction and by calculating the true stress and true strain up to the ultimate point. At fracture, the load, diameter and the curvature radius of the necked specimen are used to calculate approximately the true stress and true strain at fracture. These measurements need to be as accurate as possible in order to avoid discrepancies in the results. Indeed, any small variation causes changes in the flow curve. The resulting flow curve consists of two parts: the first one relates the yield stress to the ultimate true stress while the remaining part is a linear or power fit up to the fracture stress. This procedure has been applied to selected tensile data where both elongation and

diameter reduction measurements were available. Very good agreement was found [16]. The application of this procedure has allowed derivation of the flow curve of every material condition; these curves are shown in Figure 2.

EXPERIMENTAL

Notched tensile specimens in both un-irradiated and irradiated conditions have been tested at room temperature and at 310°C. This temperature is slightly higher than the irradiation temperature because historically, tensile test were usually performed at this temperature. This test temperature was also adopted here to allow comparison with data generated from other capsules of Belgian reactors.

The specimens are cylindrical bars that have been axisymmetrically notched with different notch radii to vary the stress triaxiality. Three different geometries have been used: NTS1.2, NTS2.4 and NTS8.7 having respectively a 1.2, 2.4 and 8.7mm notch radius. The diameter at the minimum section of all specimens is equal to 6mm.

The tensile tests were carried out at a constant crosshead speed of 0.2mm/min and the load versus displacement was recorded. After fracture, the minimum diameter is measured to derive the fracture strain (ε_f). Some room temperature tests were instrumented to allow for continuous measurement of diameter reduction. This allows derivation of the strain at crack initiation which is lower than the strain measured after complete fracture.

FINITE ELEMENT SIMULATION

Due to the axial symmetry of the specimens, only a quarter of the specimen is simulated, using two-dimensional isoparametric 8-node elements with reduced Gauss integration. Plasticity was modeled using incremental theory with a von Mises yield surface, associated flow rule and isotropic hardening. Because of the large displacements and strains, the updated Lagrangian procedure is employed. The quasi-Newton method (BFGS algorithm) is used to solve the constitutive equations. The stress - strain history at the centre element is obtained by averaging the stresses and strains of the four Gauss points.

As indicated before, some of the notched tensile tests have been instrumented with an LVDT to register continuously the diameter variation as a function of applied load. This enables comparison of the finite element results with the experimental data. It is done by plotting the mean strain (ε) versus mean stress (σ), defined as:

$$\sigma = \frac{4F}{\pi D^2}$$

$$\epsilon = 2\ln\left(\frac{D_0}{D}\right)$$

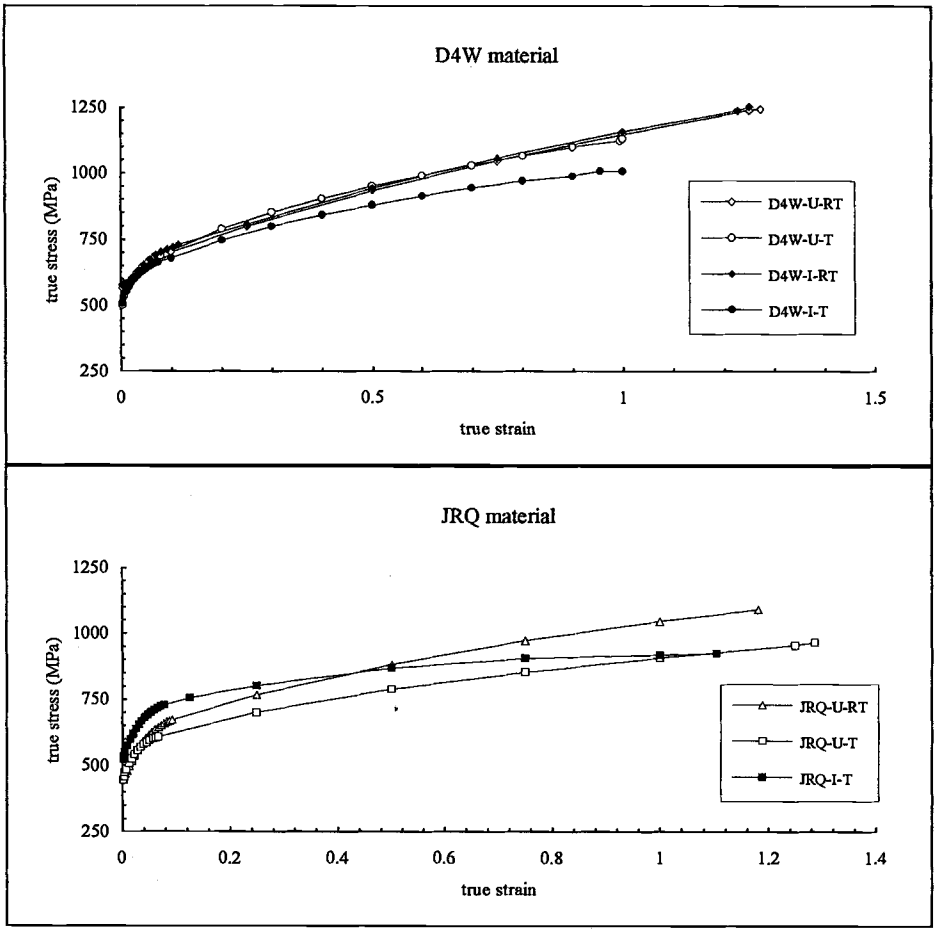


Figure 2: True stress - true strain flow curves for various material conditions. Open symbols for un-irradiated material and filled symbols for irradiated materials.

The comparison between the finite element calculations and the experimental results for the JRQ material in the un-irradiated condition and measured at room temperature is shown in Figure 3. A quite reasonable agreement is obtained.

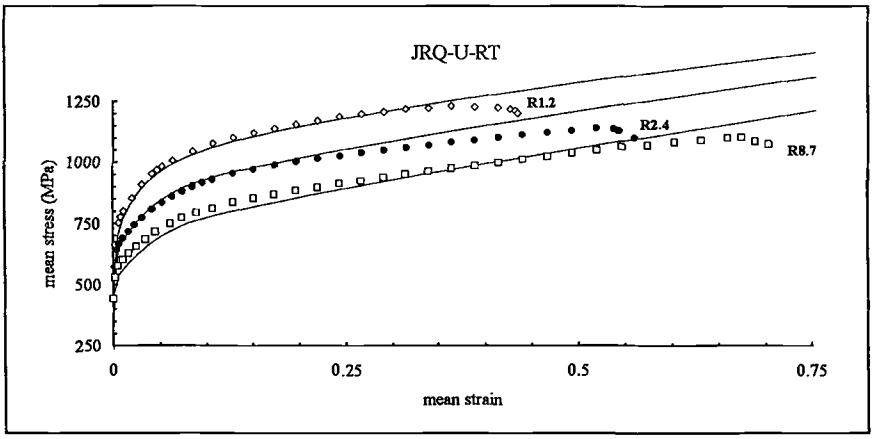


Figure 3: Finite element calculations (full curves) versus experimental data show reasonable agreement.

RESULTS AND DISCUSSION

The main results are reported in Table 4, where F_u is the ultimate load, F_f the load at fracture, D_0 the initial diameter, D_f the diameter at fracture, ε_f the mean fracture strain and σ_f the mean stress at fracture. For comparison, the maximum load, derived from the finite element calculations F_U^{FEM}, has also been added.

The evolution of the damage is plotted against the mean strain for different specimen geometries and conditions; an example of such a plot is shown in Figure 4.

Subsequently, for each specimen, the critical values of the cavity growth rate $(R/R_0)_c$ and damage work W_{dc} were then derived from these damage evolution curves, by taking the damage values that correspond to the experimental mean fracture strains. These critical values are given in Table 5. As expected, the stress triaxiality does not seem to have any obvious influence on these critical values. However, the scatter is large. Previous tests on another reactor pressure vessel steel indicated less than 5% deviation [9]. Figure 5 shows the critical damage for each material condition. For each material condition, a mean value of the critical damage at fracture is determined irrespective of the notch geometry. These results are gathered in Table 6, where n represents the number of specimens tested, the standard deviation is given when appropriate.

From Table 6, it can be seen that the damage work exhibits much more scatter than the cavity growth model: 12.5 to 24% versus 7 to 12.5%. This is expected because the evolution of the damage work evolution has a much steeper slope than the cavity growth model.

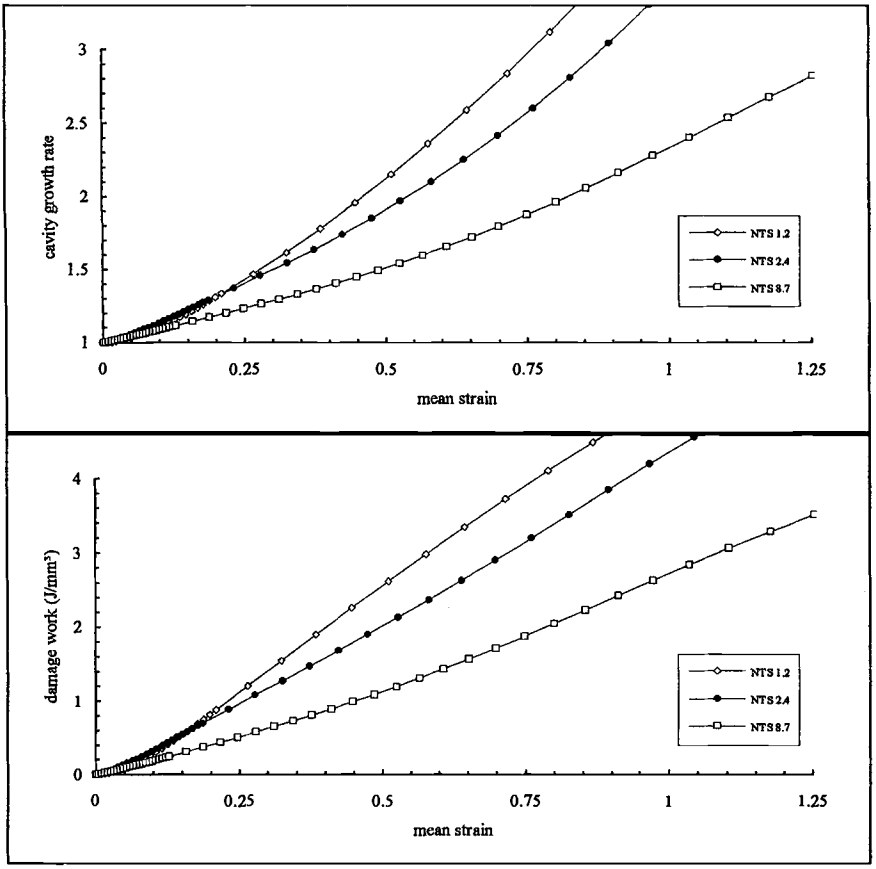


Figure 4: Damage evolution with the change in mean strain.

Two interesting features can be seen from these results. First, the Doel-IV weld material exhibits a lower critical damage at 310°C than at room temperature. This ductility degradation with temperature is more sensitive than the irradiation effect on the JRQ material. Soulat et al. [17] have performed fracture toughness tests on similar steels, i.e. A533 B Cl.1 and A508 Cl.3 in both un-irradiated and irradiated conditions. Their conclusions on the effects of temperature and irradiation on fracture toughness are completely consistent with our evaluation. For the A508 steel in the un-irradiated condition, J_{IC} decreases from 429 to 250 kJ/m² when tested at 25 and 290°C, respectively. On the other hand, J_{IC} does not vary for the irradiated material.
At 290°C, the irradiation decreases the crack initiation toughness by 4% in the A508 steel and by 27% in the A533 B steel.

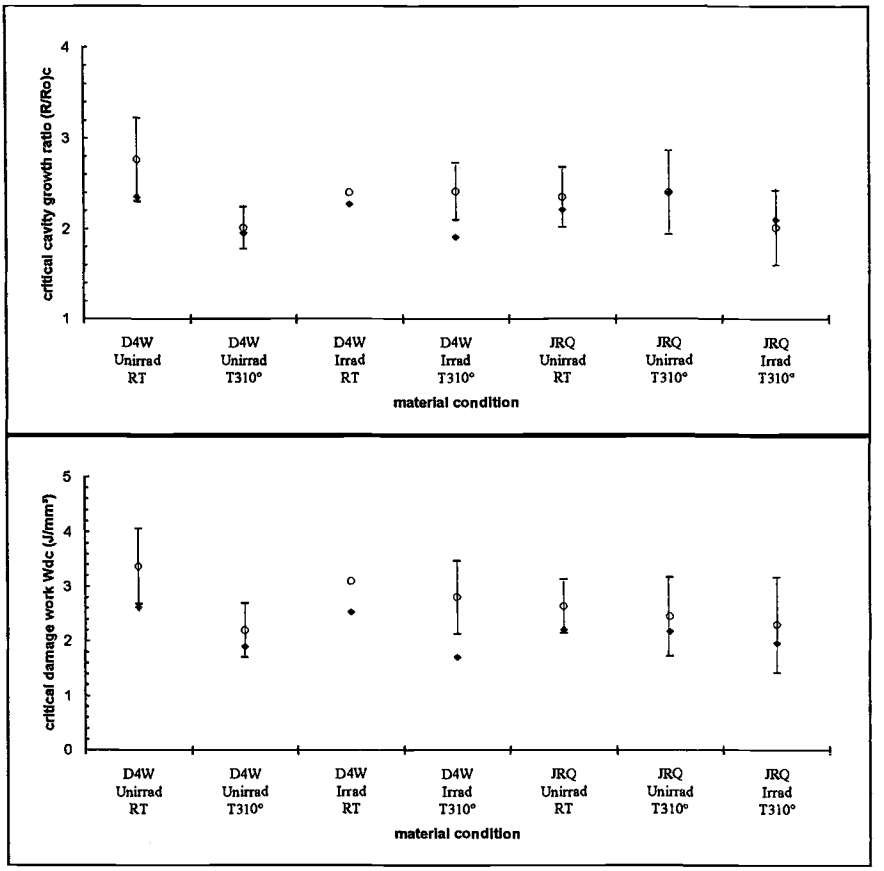


Figure 5: Critical damage values and their 90%-confidence interval for various material conditions. Results obtained from the smooth tensile specimens are also displayed for comparison (symbol: ◆).

Second, these values, in particular for un-irradiated material at room temperature, are rather high, when compared to similar material tested in a previous work [9]. This is due to the fact that strain at fracture is measured after the specimen is completely broken. In fact, the strain at crack initiation should be taken at the onset of ductile fracture (see Figure 6).

When damage is evaluated at crack initiation rather than fracture, the critical values are much lower: $(R/R_0)_c$=1.99 and W_{dc}=2.03 J/mm³ rather than 2.59 and 2.98 J/mm³ respectively. The higher the triaxiality ratio, the higher these differences, as shown from the shape of damage evolution (see figure 4).

TABLE 4- Experimental Results on NTS specimens

Mat	Spec	Cond	Temp (°C)	F_u (kN)	F_u^{FEM} (kN)	F_f (kN)	D_0 (mm)	D_f (mm)	ε_f	σ_f (MPa)
JRQ										
	R1.2	Un-ir	RT	27.8	27.0	24.3	6.05	4.60	0.548	1462
		Un-ir	RT	27.3	27.0	23.4	6.05	4.59	0.553	1414
		Un-ir	310	26.8	25.7	25.3	6.05	4.75	0.481	1428
		Irrad	310	29.1	30.2	27.1	6.04	4.97	0.392	1397
		Irrad	310	28.9	30.2	28.0	6.00	4.99	0.367	1432
	R2.4	Un-ir	RT	24.3	23.9	19.4	6.05	4.21	0.725	1394
		Un-ir	RT	23.7	23.9	16.4	6.05	4.16	0.748	1206
		Un-ir	310	23.2	22.4	20.0	5.99	4.39	0.622	1321
		Un-ir	310	24.4	22.4	18.9	5.94	4.23	0.683	1345
		Un-ir	310	23.4	22.4	21.8	6.05	4.54	0.575	1347
		Un-ir	310	23.1	22.4	19.5	5.96	4.21	0.697	1401
		Un-ir	310	22.6	22.4	18.2	6.00	4.29	0.670	1252
		Irrad	310	25.6	26.5	22.1	6.04	4.67	0.516	1290
	R8.7	Un-ir	RT	19.9	19.9	11.2	5.99	3.54	1.053	1138
		Un-ir	RT	20.8	19.9	14.6	6.02	3.92	0.859	1213
		Un-ir	310	20.2	18.6	15.3	6.01	4.16	0.735	1126
		Un-ir	310	20.1	18.6	14.9	6.01	4.13	0.752	1112
		Un-ir	310	19.4	18.6	13.5	5.95	3.37	0.932	1235
		Irrad	310	21.4	22.0	16.9	6.05	4.59	0.551	1027
D4W										
	R1.2	Un-ir	RT	27.3	28.7	24.6	6.00	4.53	0.567	1526
		Un-ir	RT	27.5	28.7	25.8	6.01	4.64	0.515	1520
		Un-ir	310	27.1	28.8	25.9	6.00	4.78	0.454	1443
		Irrad	RT	28.9	29.4	26.5	6.00	4.72	0.478	1515
		Irrad	310	26.5	28.0	23.1	5.95	4.62	0.504	1384
	R2.4	Un-ir	RT	23.8	25.0	18.5	6.00	4.02	0.801	1458
		Un-ir	RT	25.2	25.0	23.0	5.98	4.43	0.601	1494
		Un-ir	310	24.1	25.2	21.1	5.98	4.38	0.624	1400
		Irrad	310	25.1	26.0	21.1	6.00	4.47	0.591	1347
	R8.7	Un-ir	RT	19.8	20.7	13.3	5.95	3.46	1.084	1415
		Un-ir	310	19.8	21.0	15.2	5.93	4.07	0.751	1168
		Un-ir	310	20.0	21.0	16.0	5.96	4.00	0.797	1273
		Irrad	310	20.1	21.6	15.2	6.00	4.07	0.778	1170

TABLE 5- Critical damage at crack initiation of the NTS specimens

Mat	Spec	Cond	Temp (°C)	$(R/R_0)_c$	W_{dc} (J/mm³)
JRQ					
	R1.2	Un-ir	RT	2.23	2.59
		Un-ir	RT	2.25	2.61
		Un-ir	310	2.34	2.60
		Irrad	310	2.05	2.55
		Irrad	310	1.94	2.32
	R2.4	Un-ir	RT	2.52	2.87
		Un-ir	RT	2.59	2.98
		Un-ir	310	2.48	2.59
		Un-ir	310	2.70	2.87
		Un-ir	310	2.33	2.39
		Un-ir	310	2.75	2.93
		Un-ir	310	2.65	2.81
		Irrad	310	2.33	2.77
	R8.7	Un-ir	RT	2.45	2.71
		Un-ir	RT	2.08	2.11
		Un-ir	310	1.97	1.74
		Un-ir	310	2.00	1.79
		Un-ir	310	2.38	2.33
		Irrad	310	1.74	1.55
D4W					
	R1.2	Un-ir	RT	2.99	3.87
		Un-ir	RT	2.74	3.54
		Un-ir	310	1.98	2.30
		Irrad	RT	2.40	3.10
		Irrad	310	2.38	2.91
	R2.4	Un-ir	RT	3.07	3.70
		Un-ir	RT	2.44	2.82
		Un-ir	310	2.21	2.56
		Irrad	310	2.62	3.14
	R8.7	Un-ir	RT	2.55	2.91
		Un-ir	310	1.88	1.89
		Un-ir	310	1.96	2.04
		Irrad	310	2.24	2.35

TABLE 6- Critical Damage for different material conditions

Mat	Cond.	Temp (°C)	n	(R_c/R_0)	W_{dc} (J/mm³)	(R_c/R_0) (from smooth tensile tests)	W_{dc} (J/mm³) (from smooth tensile tests)
D4W	Un-ir	RT	5	2.76 ±0.28	3.37 ±0.42	2.35	2.62
D4W	Un-ir	310°C	4	2.01 ±0.14	2.20 ±0.30	1.95	1.91
JRQ	Un-ir	RT	6	2.35 ±0.20	2.64 ±0.30	2.21	2.21
JRQ	Un-ir	310°C	9	2.40 ±0.28	2.45 ±0.44	2.39	2.18
D4W	Irrad	RT	1	2.40	3.10	2.27	2.54
D4W	Irrad	310°C	3	2.41 ±0.19	2.80 ±0.41	1.90	1.70
JRQ	Irrad	310°C	4	2.01 ±0.25	2.30 ±0.53	2.10	1.96

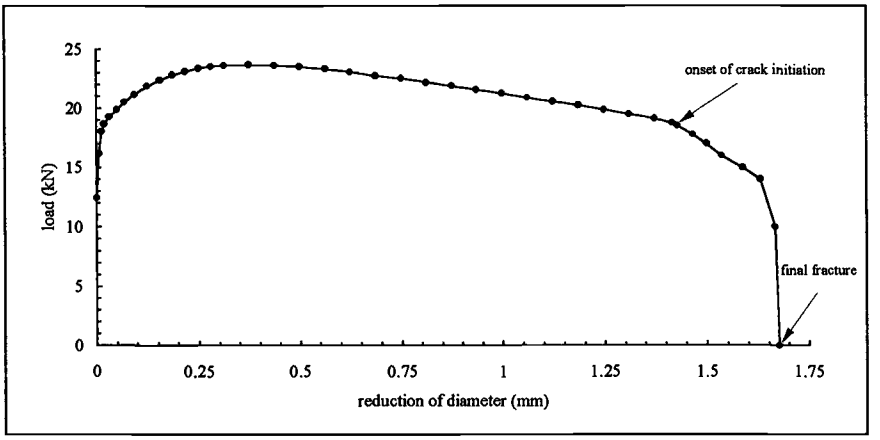


Figure 6. Tensile recording showing the loci of crack initiation and the fracture.

Analytical damage calculations [16], based on the tensile tests performed on smooth bars to extract the flow curves, allow one to derive the critical damage at fracture. The results are also given in Table 6 and included in Figure 5.

As can be seen, the trend of the damage parameters, as derived from the smooth tensile specimens, follows the notched bar data. However, the critical damage values obtained from the smooth tensile specimens are slightly lower than those obtained from the notched tensile samples. It should be mentioned that these results overestimate the actual crack initiation energy because the strain at fracture has been taken instead of the strain at crack initiation in the integration of the damage model. Some tensile tests performed at room temperature with continuous diameter measurement have shown quite a large difference between the strain at crack initiation and the strain at fracture. The strain at crack initiation corresponds to the sudden loss of load whereas stain at fracture is measured from the broken specimen (Figure 6).

CONCLUSION

The influence of irradiation on the Charpy transition curves, established for JRQ and D4W materials in un-irradiated and irradiated conditions is almost nil for the D4W weld material but reveals a shift and a drop of the upper shelf energy for the JRQ material. In accordance, the tensile properties of the weld material remain almost unchanged, whereas an increase in the yield and ultimate stresses is observed for the JRQ material. No thermal ageing induced embrittlement was revealed for either materials.

The application of micromechanical models to these materials, in un-irradiated and irradiated conditions, confirms the previous observations. Additional interesting features, not detected from the tensile and Charpy impact data have been found: the degradation of ductility as a consequence of the test temperature (room temperature versus 310°C) of the weld material in the un-irradiated condition is larger than reduction induced by the irradiation embrittlement of the JRQ base material. This is in agreement with fracture toughness data obtained on similar materials.

Both models - the cavity growth rate and the damage work - gave reasonable results. The first model is simpler and needs only two parameters: the stress triaxiality and the strain at crack initiation; the material flow properties intervene indirectly in the triaxiality ratio. The damage work model, on the other hand explicitly includes the flow properties of the material.

In radiation damage modelling, these models could be very helpful as they contain the main ingredients susceptible to the influence of neutron irradiation: the flow properties (yield stress, ultimate stress, strain hardening) and microstructural properties (volume fraction of second phase particles like inclusions and precipitates and strain at crack initiation).

ACKNOWLEDGEMENTS

The authors are very grateful to Mr. R. Gérard, from Electrabel Engineering who supported this research. We would like to express our acknowledgements to R. Mertens, T. Noels, R. Sneyers, J-L. Puzzolante, T. Van Houdt and R. Vosh for their assistance in performing the experimental tests, and J.P. Wannijn for his very helpful computer-macros.

REFERENCES

[1] Bridgman, P.W.,"Studies in large plastic flow and fracture", McGraw-Hill (1952).

[2] McClintock, F.A.,"A criterion for ductile fracture by growth of holes", Transactions of the ASME, Journal of Applied Mechanics, June 1968, pp. 363-371.

[3] Rice, J.R. and Tracey, D.M.,"On the ductile enlargement of voids in triaxial stress fields," Journal of the Mechanics and Physics of Solids, 1969, Vol. 17, pp. 201-217.

[4] Beremin, F.M.,"Cavity formation from inclusions in ductile fracture of A508 steel," Metallurgical Transactions, 12A, 1981, pp.723-731.

[5] Huang, Y., "Accurate dilatation rates for spherical voids in triaxial stress fields,"Transactions of the ASME, Journal of Applied Mechanics, Vol. 58, 1991, pp. 1084-1086.

[6] Marini, B., "Croissance des cavités en plasticité: Rupture sous chargements non radiaux mixtes", PhD thesis, Ecole des Mines de Paris, 1984.

[7] Mackenzie, A.C., Hancock, J.W. and Brown, D.K.,"On the influence of state of stress on ductile failure initiation in high strength steels," Engineering Fracture Mechanics,, Vol. 9, 1977, pp. 167-188.

[8] Mudry, F., "Etude de la rupture ductile et de la rupture par clivage d'aciers faiblement alliés", PhD thesis, Ecole des Mines de Paris, 1982.

[9] Chaouadi, R., De Meester, P. and Vandermeulen, W.,"Damage work as ductile fracture criterion," International Journal of Fracture, 66, 1994, pp.155-164.

[10] Gillemot, L.F., "Criterion of crack initiation and spreading", Engineering Fracture Mechanics, 1976, Vol. 8, pp. 239-253.

[11] Helms, R. and Naseband, K., "A ductile fracture criterion for metals", Proceedings of the 4th International Conference on Fracture, Vol. 2, ICF4, Waterloo, Canada, 1977, pp. 503-512.

[12] Ray S.K., Bhaduri A.K. and Rodriguez P., "New toughness parameters from the tensile test - A first report", Journal of Nuclear Materials, 200, 1993, pp.70-77.

[13] Gurson, A.L.,"Continuum theory of ductile rupture by void nucleation and growth: Part 1- Yield criteria and flow rules for porous ductile media," Transactions of the ASME, Journal of Engineering Materials and Technology, Jan. 1977, pp. 2-15.

[14] Rousselier, G.,"Finite deformation Constitutive relations including ductile fracture damage," in Three-Dimensional Constitutive Relations and Ductile Fracture, S. Nemat-Nasser, Ed., North-Holland Pub. Co., 1981, pp. 331-355.

[15] van Walle, E., Fabry, A., Puzzolante, J.L., Pouleur, Y., Verstrepen, A., Wannijn, J.P. and Vandevelde, J., "Optimisation of reactor pressure vessel surveillance programmes and their analysis", Belgian contribution to the IAEA Phase 3 coordinated research programme, presented at Vienna, November 22-23, 1993.

[16] Chaouadi, R., "Micromechanically-based damage modeling of fracture initiation in reactor materials", PhD thesis, 1995.

[17] Soulat P., Petrequin P. and Houssin B., "Effect of irradiation on elastic-plastic toughness of pressure vessel steels", Radiation Embrittlement on Elastic-Plastic Toughness of Pressure Vessel Steels, ASTM STP 819, L.E. Steele, Ed., American Society for Testing and Materials, Philadelphia, 1983, pp. 64-85.

G. R. Odette[1], G. E. Lucas[1], R. D. Klingensmith[1] and R. E. Stoller[2]

ON THE EFFECT OF FLUX AND COMPOSITION ON IRRADIATION HARDENING AT 60°C

REFERENCE: Odette, G. R., Lucas, G. E., Klingensmith, R. D., and Stoller, R. E., **"On the Effect of Flux and Composition on Irradiation at 60°C,"** *Effects of Radiation on Materials: 17th International Symposium, ASTM STP 1270,* David S. Gelles, Randy K. Nanstad, Arvind S. Kumar, and Edward A. Little, Eds., American Society for Testing and Materials, 1996.

ABSTRACT: A large matrix of simple alloys and complex commercial type steels was irradiated over a range of fluxes at 60°C up to a fast fluence of about $3x10^{22}$ n/m^2. Combined with data in the literature, these results show a negligible effect of flux on irradiation hardening in the range of $2x10^{13}$ to $5x10^{18}$ n/m^2-s. This observation lends indirect support to the proposal that the accelerated embrittlement in the High Flux Isotope Reactor surveillance steels was due to an anomalously high level of damage from gamma rays. A weak dependence of hardening on a number of elements, including copper, nickel, phosphorous, molybdenum and manganese, can be described by a simple empirical chemistry factor. Particular combinations of elements resulted in hardening differences of up to about 60% in the complex commercial type steels and up to about 100% in simple model alloys. Direct effects of microstructure appear to be minimal. Hardening varies with the square root of fluence above a threshold around $4x10^{20}$ n/m^2. The results suggest that low temperature hardening is dominated by local intracascade processes leading to the formation of small defect-solute clusters/complexes. The observed hardening corresponds to nominal maximum end-of-life transition temperature shifts in support structure steels of about 120°C.

KEYWORDS: pressure vessel steels, irradiation hardening, irradiation embrittlement, composition effects, irradiation temperature

The individual and combined effects of irradiation and metallurgical variables on the embrittlement of pressure vessel steels at around 300°C has been reasonably well characterized [1,2]. In contrast, both experimental characterization and theoretical understanding of hardening and embrittlement relevant to the low operating temperature range of reactor support structures -- about 50 to 150°C -- is much more limited. Considerable concern about the potential for significant embrittlement of support structures emerged

[1] Department of Mechanical Engineering, University of California Santa Barabara, Santa Barbara, CA 93106-5070

[2] Metals and Ceramics Divison, Oak Ridge National Laboratory, Oak Ridge, TN 37831-6151

Copyright© 1996 by ASTM International www.astm.org

from the High Flux Isotope Reactor (HFIR) surveillance program [3,4], where the rates of hardening and transition temperature shifts were found to be about a factor of ten greater than for high flux test reactor irradiations. The accelerated embrittlement in HFIR has been variously ascribed to the effect of: a) low flux [4]; b) a high thermal-to-fast flux ratio (note, the preliminary belief that this ratio was very large turned out to be incorrect) [5]; and c) most recently, gamma-ray induced damage [6,7]. Theoretical considerations suggest that, at these temperatures, transient effects may be dominant and that the primary damage processes may be fundamentally different from those at higher temperatures [7]. Further, only a very limited data base exists on the effect of key metallurgical variables such as copper, nickel, phosphorous and microstructure. Recent low fluence ($< 10^{22}$ n/m^2) studies have suggested that while there may be considerable metallurgically mediated variations in hardening, differences in commercial type steels are not primarily due to copper; the low copper sensitivity was attributed to a cut-off in precipitation below about 160°C [8]. Unlike, commercial type steels, however, significant effects of copper have been reported for simple model steels [7].

This paper describes results of a systematic study of the effects of metallurgical variables, flux and fluence on irradiation hardening at 60°C. The overall program involves: a) mechanical property measurements using microhardness and tensile tests; b) microstructural characterization based on small angle neutron scattering (SANS), transmission electron microscopy (TEM) and field ion microscope/atom probe (FIM/AP) measurements; c) post irradiation annealing/re-irradiation; and d) modeling. However, the focus in this paper will be on the effects of metallurgical variables on hardening, as measured by changes in yield stress ($\Delta\sigma_y$).

EXPERIMENT

Alloys and Specimens

A large set of alloys was investigated in this study; the alloys are classified in four general categories:

1) The compositions and heat treatment for a set of twenty simple split melt model iron and steel alloys (VX-series) with systematic variations in Cu, C, Mn, Ti and N are shown in Table 1. The microstructures of these alloys are generally characterized by a wide distribution of ferrite grain sizes (in some cases duplex and/or with processing texture). Rapid quenching was carried out to maintain copper in solution. The low temperature tempers were intended to precipitate carbon in the form of dispersed but reasonably stable Fe_3C or M_3C intergranular carbides. Yield stresses averaged about 190±40 MPa. The VX-series steels fall into four subgroups.

   a) VF -- Iron with average ferrite grain sizes from 17 to 138 μm (average ≈ 73 μm) containing 0.0, 0.5 and 0.9Cu at both high (100±20 ppm) and low (15±10 ppm) N levels and variants with 0.25Ti at high N at both 0.0 and 0.9Cu.

   b) VM -- Fe-1Mn alloys with average ferrite grain sizes from 17 to 138 μm (average ≈ 54 μm) containing 0.0 and 0.9Cu, with high (105±5 ppm) and low (25±15 ppm) N and a 0.9Cu high N variant with 0.25Ti.

   c) VC -- Fe-0.15C steels with average ferrite grain sizes of 13 to 244 μm (average ≈ 112 μm) containing 0.0, 0.5 and 0.9Cu at low N (10 ppm) and a 0.9Cu melt with high N (110 ppm).

TABLE 1 -- VX-Series Alloy Compositions

Alloy Group/Code		Composition (weight per cent)*				
		Cu	Mn	C	Ti	N(appm)
VF	VA	–	–	–	–	5
VM	VB	–	1.0	–	–	40
VA	VC	–	1.0	0.15	–	30
VM	VD	0.9	1.0	–	–	10
VA	VE	0.9	1.0	0.15	–	20
VF	VG	0.5	–	–	–	20
VF	VH	0.9	–	–	–	20
VC	VI	0.5	–	0.15	–	10
VC	VJ	0.9	–	0.15	–	10
VF	VK	–	–	–	–	100
VF	VL	–	–	–	0.25	100
VF	VM	0.5	–	–	–	120
VF	VN	0.9	–	–	–	110
VC	VO	0.9	–	0.15	–	110
VF	VP	0.9	–	–	0.25	110
VM	VR	–	1.0	–	–	100
VM	VS	0.9	1.0	–	–	110
VM	VT	0.9	1.0	–	0.25	90

* solution treat 775°C, 17h; quench in salt bath at 450°C, 3 minutes; air cool

d) VA -- Fe-0.15C-1Mn steels with average ferrite grain sizes of 50 to 85 μm (average ≈ 68 μm) containing 0.0 and 0.9Cu at low N (35±5 ppm).

2) The compositions and heat treatments of 41 complex A533B-type split melt steels (CM-series) are shown in Table 2. A total of 31 variants around a base composition were used to evaluate the effects of both: a) *combinations* of Cu (0.0 to 0.8)[3] , Ni (0.0 to 1.6), Mn (0 to 1.6) and P (0.005 to 0.040) contents; and b) *single* variable modifications of Mo, N, C, B, Al and As/Sn/Sb contents. All 31 alloys contained 0.005Al and 0.25Si and received the base heat treatment (c1 - Table 2), yielding prior austenite grain sizes of about 50±10 μm and microstructures ranging from tempered bainite (most CM alloys) to mixed tempered ferrite-bainite. The yield stresses for alloys with 0.5Mo averaged about 475 MPa (only 2 of the 31 base heat treated steels had yield stresses below 440 and only 2 above 520 MPa). The alloy without this secondary hardening element had a much lower unirradiated yield stress of 315 MPa. Eleven alloys received alternate heat treatments involving: a) variations in the salt bath temperature (400 or 500 versus 450°C); b) a higher (1100°C versus 900°C) austenitizing temperature; c) additional stress relief anneals at 600°C (at times of 8, 40 and 80 h); and d) a simulated temper embrittling aging treatment (480°C/100h). The higher austenitizing temperature resulted in substantially larger prior austenitic grain sizes (75-100μm) and lower yield stresses (by about 80 MPa). Other alternate heat treatments had little systematic effects on the unirradiated yield stress or microstructures observed optically.

[3] Unless otherwise indicated compositions are in weight percent.

TABLE 2 -- CM-Series Alloy Compositions and Heat Treatments

Code	COMPOSITION (weight per cent) Cu	Ni	Mn	Cr	Mo	P	N	Sn/As/Sn	B	C	HT†
CM1	0.0	0.0	1.4	0.0	0.5	0.005	<50	<0.005	<1	0.15	c1
CM2	0.0	0.0	1.4	0.0	0.5	0.040	<50	<0.005	<1	0.15	c1
CM3	0.0	0.8	1.4	0.0	0.5	0.005	<50	<0.005	<1	0.15	c1
CM4	0.0	0.8	1.4	0.0	0.5	0.025	<50	<0.005	<1	0.15	c1
CM5, 5a	0.0	0.8	1.4	0.0	0.5	0.040	<50	<0.005	<1	0.15	c1, 5
CM6	0.0	1.6	1.4	0.0	0.5	0.005	<50	<0.005	<1	0.15	c1
CM7	0.0	1.6	1.4	0.0	0.5	0.040	<50	<0.005	<1	0.15	c1
CM8, 8a	0.0	0.8	0.0	0.0	0.5	0.005	<50	<0.005	<1	0.15	c1, 3
CM9	0.0	0.8	0.7	0.0	0.5	0.005	<50	<0.005	<1	0.15	c1
CM10	0.05	0.8	1.4	0.0	0.5	0.005	<50	<0.005	<1	0.15	c1
CM11	0.3	0.8	1.4	0.0	0.5	0.005	<50	<0.005	<1	0.15	c1
CM12, 12a	0.8	0.8	1.4	0.0	0.5	0.005	<50	<0.005	<1	0.15	c1, 6
CM13	0.1	0.8	1.4	0.0	0.5	0.005	<50	<0.005	<1	0.15	c1
CM14	0.1	0.8	1.4	0.0	0.5	0.040	<50	<0.005	<1	0.15	c1
CM15, 15a	0.2	0.0	1.4	0.0	0.5	0.005	<50	<0.005	<1	0.15	c1, 4
CM16, 16a	0.2	0.8	1.4	0.0	0.5	0.005	<50	<0.005	<1	0.15	c1, 4
CM17, 17a	0.2	1.6	1.4	0.0	0.5	0.005	<50	<0.005	<1	0.15	c1, 4
CM18, 18a	0.4	0.0	1.4	0.0	0.5	0.005	<50	<0.005	<1	0.15	c1, 7
CM19, 19a, 19b	0.4	0.8	1.4	0.0	0.5	0.005	<50	<0.005	<1	0.15	c1, 2, 4
CM19c,19d, 19e	0.4	0.8	1.4	0.0	0.5	0.005	<50	<0.005	<1	0.15	c6, 7, 8
CM20, 20a, 20b	0.4	1.6	1.4	0.0	0.5	0.005	<50	<0.005	<1	0.15	c1, 2, 7
CM21	0.4	0.8	0.0	0.0	0.5	0.005	<50	<0.005	<1	0.15	c1
CM22	0.4	0.8	0.7	0.0	0.5	0.005	<50	<0.005	<1	0.15	c1
CM23, 23a	0.0	0.8	1.4	0.0	0.5	0.005	<50	<0.005	<1	0.05	c1, 3
CM24	0.0	0.8	1.4	0.0	0.5	0.005	<50	<0.005	<1	0.30	c1
CM25	0.0	0.8	1.4	0.0	0.5	0.005	200	<0.005	<1	0.15	c1
CM26, 26a	0.0	0.8	1.4	0.0	0.5	0.005	<50	0.020	<1	0.15	c1, 5
CM27	0.0	0.8	1.4	0.0	0.5	0.005	<50	<0.005	10	0.15	c1
CM28	0.4	0.8	1.4	0.0	0.5	0.005	<50	<0.005	10	0.15	c1
CM29	0.2	0.0	1.4	0.0	0.0	0.005	<50	<0.005	<1	0.15	c1
CM30	0.2	0.8	1.4	0.4	0.5	0.005	<50	<0.005	<1	0.15	c1
CM31	0.0	0.8	1.4	0.0	0.5	0.005	<50	<0.005	<1	0.15	c1

† HT	Purpose	Heat Treatment
c1	Base treatment	Austenitize 900°C/0.5h; salt bath quench 450°C/10min; air cool; temper 660°C/4h: air cool
c2	Vary structure/properties	Same as c1, except salt bath quench 500°C/10min
c3	" " "	Same as c1, except salt bath quench 400°C/10min
c4	Vary grain size/carbides	Same as c1, except austenitize 1100°C/1.0h
c5	Temper embrittlement	c1 plus 480°C/100h
c6	Stress relief	c1 plus 600°C/8h, air cool
c7	Stress relief	c1 plus 600°C/40h, air cool
c8	Stress relief	c1 plus 600°C/80h, air cool

TABLE 3 -- L-Series Alloy Compositions and Heat Treatments

Code	Composition (weight percent)†† C	Cu	Ni	Mn	Si
LA	0.14	0.40	0.00	1.37	0.22
LB	0.14	0.40	0.18	1.35	0.22
LD	0.19	0.38	1.25	1.38	0.23
LG	0.16	0.00	0.74	1.37	0.22
LH	0.16	0.11	0.74	1.39	0.24
LI	0.16	0.20	0.74	1.37	0.24
LJ	0.16	0.42	0.81	1.34	0.13
LK	0.13	0.80	0.81	1.13	0.13

†† Alloys contained P < 0.005, S ≤ 0.015, Cr ≤ 0.085, Mo ≈ 0.55; they were austenitized 900°C/1h; air cooled; tempered 664°C/4h; air cooled; stress relieved 600°C/40h; furnace cooled to 300°C; air cooled.

3) The compositions and heat treatment for a set of eight complex commercial type bainitic model steels (L-series) with systematic variations in copper and nickel are shown in Table 3. These steels have been irradiated in previous programs at a variety of conditions, primarily around 300°C. They have microstructures and unirradiated properties very similar to those in the CM-series.

4) The compositions and heat treatments for a set of four commercial CC-series steels are shown in Table 4. The CC-series consists of two Mn-C mild steels from the HFIR surveillance program and the Shippingport shield tank; and an A588 and a medium carbon A36 structural steel. The CC-alloys permit the irradiations in this program to be tied to other data, including low flux surveillance/service conditions (e.g., the HFIR and Shippingport steels).

Sheet tensile specimens with a gage section 9 mm x 2 mm x 0.5 mm were prepared by precision die punching heat treated coupons lapped to 0.5±0.005 mm thick. The quality of the die was monitored by punching and tensile testing a variety of calibration metals after about every 500 specimens had been punched. Specimens were loaded into aluminum capsules for irradiation. The capsules were evacuated, back-filled with helium and welded shut.

Irradiations

The results reported here are for four completed capsules out of a total of 12 capsules in the program. These capsules were irradiated in three out-of-core positions at the University of Michigan Ford Reactor (UMFR). The overall program irradiation matrix is shown in Table 5 and also includes the four UMFR capsules that are still in-reactor or yet to be tested, three capsules irradiated in high flux locations in HFIR and the High Flux Beam Reactor (HFBR) and one capsule with a high thermal-to-fast flux

TABLE 4 -- CC-Series Alloy Compositions and Heat Treatments

Alloy Code	Description	Composition, % by weight C	Cu	Ni	Mn	Si	P	S	Cr	Mo	V	PIA§
OH	A588B	0.126	0.22	0.21	1.33	0.31	0.014	0.007	0.45	0.045	0.056	---
OC	HFIR A212B Archive	0.26	0.15	<0.20	0.85	0.29	0.006	0.04	0.075	0.02	0.005	cc1
ODa,b	HFIR A212B Surveillance	0.26	0.15	<0.20	0.85	0.29	0.006	0.04	0.075	0.02	0.005	cc2-4
OG	HFIR A350 Archive	0.18	0.11	3.3	0.55	0.29	0.01	0.02	0.09	0.03	0.001	cc1
OEa,b	HFIR A350 Surveillance	0.18	0.11	3.3	0.55	0.29	0.01	0.02	0.09	0.03	0.001	cc2-4
OA	Shippingport outer NST	0.23	0.05	0.04	0.76	0.27	0.02	0.03	0.04	<0.01	---	cc1
OIa,b	Shippingport inner NST	0.23	0.05	0.04	0.76	0.27	0.02	0.03	0.04	<0.01	---	cc2-4
OB	ORNL A36	0.21	0.05	0.07	1.10	0.03	0.009	0.026	0.04	0.03	0.001	cc1

§ Post-Irradiation Anneals Before Reirradiation:
cc1 -- with and without post-irradiation anneal at 450°C, 50h
cc2 -- post-irradiation annealed 450°C, 50h
cc3 -- post-irradiation annealed 343°C, 290h
cc4 -- post-irradiation annealed 600°C, 5h

TABLE 5 -- The Irradiation Matrix

Flux ($n/m^2/s$)	Fluence (n/m^2)				Reactor
	$2x10^{21}$	$5x10^{21}$	$3x10^{22}$	$7x10^{22}$	
1.4×10^{14}	F1§	F4	---	---	UMFR
1.8×10^{15}	R2§	R5§	F7	---	UMFR
7.3×10^{15}	---	R6	F8§	R9	UMFR
4.5×10^{17}	---	---	R10	---	HFBR
5.0×10^{18}	---	---	R12	R13	HFIR
3.8×10^{15}	---	R11§§	---	---	HFBR

§ tested and reported in this paper;
§§ thermal/fast flux ratio ~370

ratio irradiated in the HFBR. Only selected UMFR irradiations, designated by the F in Table 5, contained a full set of alloys; the other smaller capsules, designated as R, generally only contained a reduced subset of the CM-series. As noted above, another ongoing element of the program involves annealing and re-irradiation studies of the HFIR and Shippingport steels, but it will not be discussed here.

The UMFR capsules were moved to remote locations during periods of reactor startups, shutdowns and variable power operation to minimize transient effects. Measurements on dummy capsules and gamma heating/heat transfer calculations indicated specimen temperatures of 60±5°C. The estimated flux and fluence (E > 1 MeV) matrix is shown in Table 5. All capsules contained nickel activation wires and, generally, the large capsules contained more complete dosimeter sets including on a selected basis Al-0.1 Co, Nb, Ni, Fe, Ti, Cu, ^{238}U and ^{237}Np. Detailed capsule dosimetry is underway, but is not yet available. The preliminary fluence estimates used here are based on the reactor full power hours combined with flux maps for these locations. Existing flux maps were supplemented and corrected using removable nickel dosimeter wires inserted at the beginning of the experiment. The relative fluence estimates are believed to be precise within about ±20% and the effects of spectral variation should be minor, with a corresponding estimate for the displacement cross section (E > 1 MeV) of about 1500±150 b .

Post Irradiation Mechanical Testing

Static tensile tests were carried out at room temperature (20±2°C) at a strain rate of 10^{-3} s^{-1} on an automated tensile tester. Testing involves loading twenty-nine specimens, including the calibration samples, in a precision alignment cartridge, which is positioned under pneumatically-activated, hydraulic grips by a linear stage in an Instron 1122 load frame. The cartridge/stage also serves as the lower grip. A computer actuates the specimen positioning, gripping and loading sequence and records, plots and analyzes the load-displacement record. Displacements are monitored by an LVDT which measures the movement of the upper grip relative to the lower grip. A minimum redundancy of 2

tests was used in all cases. Although there are steel-to-steel variations, the average precision of the yield stress measurements was less than about ± 15 MPa.

RESULTS

Flux and Fluence

The results of data from the four capsules tested in this program cover a range of flux from about 0.014×10^{16} to 0.73×10^{16} n/m^2/s and fluences from about 0.2 to 3×10^{22} n/m^2. Figure 1a plots the average yield stress change versus the square root of the fluence for the base set of CM-series alloys contained in all four capsules.[4] Note the bars on the data are not 'errors', but indicate the standard deviation of the individual $\Delta\sigma_y$ values around the average. The data closely follow a flux independent relation

$$\Delta\sigma_y \text{ (MPa)} = 92.1\sqrt{\phi t(10^{22} \text{ n/m}^2)} - 17.7 \qquad (1)$$

Figure 1b shows a similar plot for the VX, CC and L-series steels where the solid line is the fit to the CM-series data in Figure 1a. While only two data points are not sufficient to reliably establish flux-fluence dependence, the data trends are similar and consistent with hardening that is independent of flux and depends on the square root of fluence. Again, the large bars on the VX data do not indicate errors, but rather a larger variation (shown later to be due to copper differences) in the $\Delta\sigma_y$ values in the simple model steels. Given the similarity of the alloys, it is not surprising that the results for the L-series alloys are almost exactly the same as for the CM-series alloys. Figure 1c extends the flux range by comparing the CM-series data from this study with the results from the literature. The solid circles are data from Farrell et. al. for irradiations of 5 alloys (including the HFIR and Shippingport A212 B and the A36 steels irradiated in this program) in HFIR at very high fluxes of about 2 to 5×10^{18} n/m^2-s [7]. The filled diamond is from samples taken from the Shippingport shield tank itself at a flux of about 2×10^{13} n/m^2-s and a fluence of about 6×10^{21} n/m^2 [9]. Clearly all of the data follow a nearly identical trend, indicating independence of low temperature hardening over a flux range of more than 10^5. Note comparisons of the individual steels are equally consistent; however, one exception (not shown) is data for the HFIR A212B steel irradiated in the Oak Ridge Research Reactor which falls considerably below data for all other irradiations [4].

Compositional Variables - Complex Steels

The effects of compositional variables for the high fluence/high flux F8 capsule irradiated to 3×10^{22} n/m^2 are shown in Figure 2. Table 6 summarizes these results in terms of: a) the element studied; b) the figure showing the data; c) the range of copper and or nickel in the alloys studied; d) the observed effect -- negligible (N), weak (W), moderate (M) or strong (S); and d) qualifying comments, if any. In general the influence of individual elements is negligible to moderate. The strongest effects appear to be a decrease in $\Delta\sigma_y$ by an average of about 35 MPa between both 0.040 and 0.005P (Fig. 2e) and between 0.0 and 0.5 Mo (Fig. 2f). The phosphorous effect is strongest in the high nickel alloy, with a 60 MPa difference between the high and low levels; this may indicate nickel-phosphorous interaction. The $\Delta\sigma_y$ in low nickel steel without molybdenum is consistent with that observed in similar alloys in the CC-series (Fig. 2f). The effects of several other variables appear to be weak (Mn, Figure 2g) or negligible (C - Figure 2h, Sn/Sb/As, N and B for the 0.4Cu alloy - not shown). While copper effects at high nickel

[4] CM: 1,3,5,6,11,12,13,16,18,19,20,22

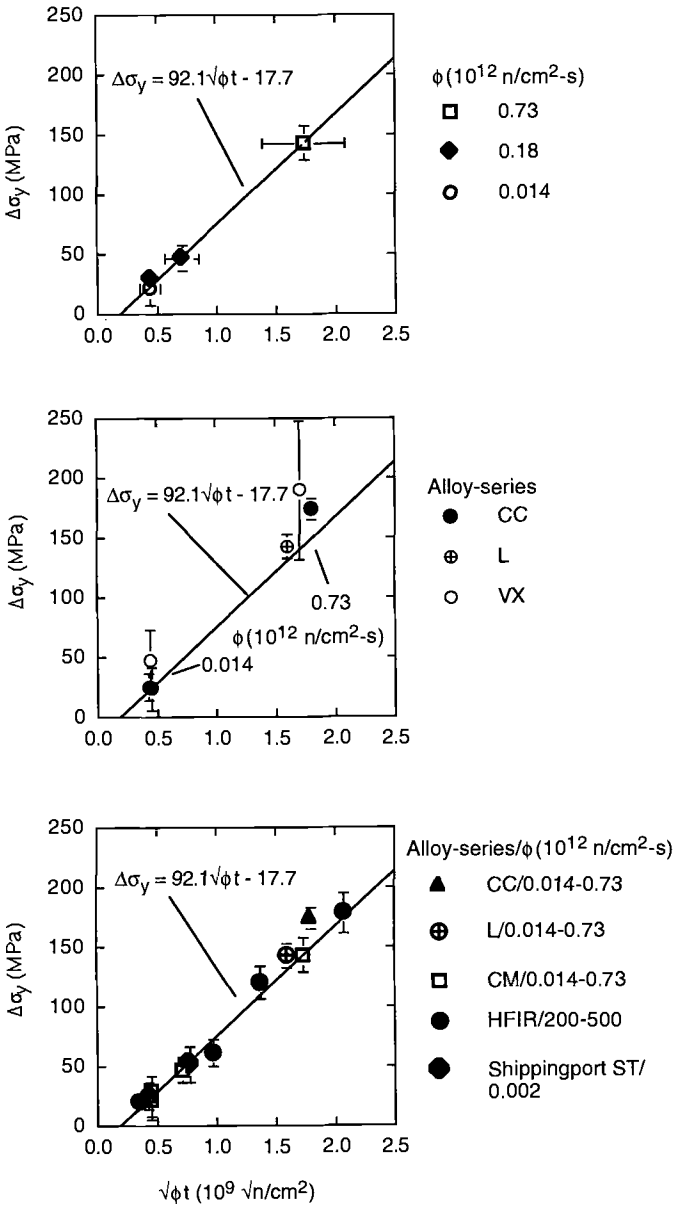


FIG. 1-- Variation of the change in yield stress with square root of fluence: a) average values of yield stress change for the CM-series alloys b) yield stress changes for the VX, CC and L-series alloys; c) comparison to results in the literature.

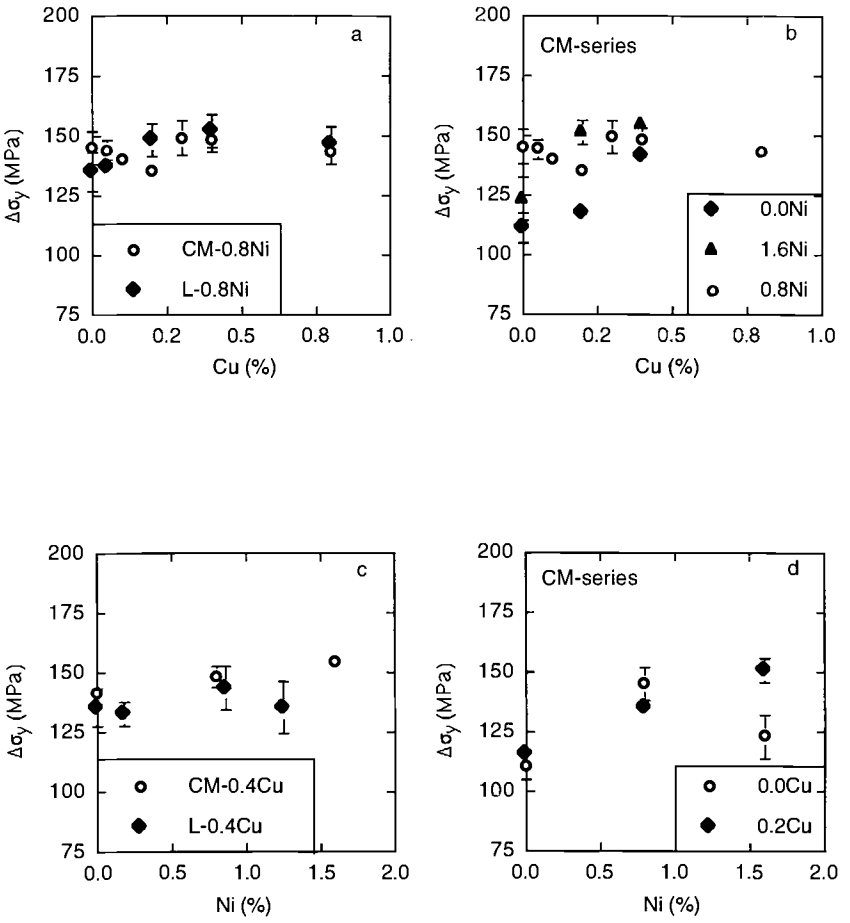


FIG. 2-- Variation of yield stress change in the complex steels at $3x10^{18}$ n/cm^2 with a) Cu at 0.8 Ni; b) Cu at various Ni contents; c) Ni at 0.4 Cu; d) Ni at two Cu levels; e) P; f) Mn at two Cu levels; g) Mo; h) C at low Cu.(Continued next page)

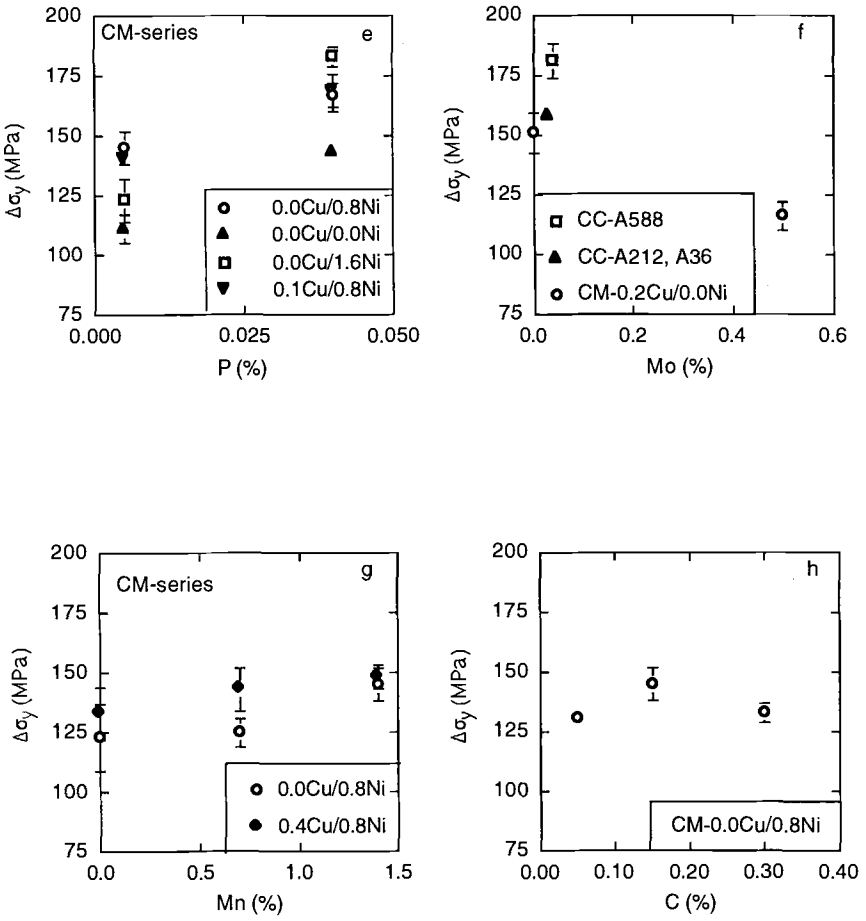


FIG. 2 -- Continued

TABLE 6 -- Summary of Effect of Composition in Complex Alloys

Element	Figure 2	Cu/Ni Range	Effect*	Comment
Cu	a,b	0.8	N	
Cu	b	0.0 & 1.6Ni	M	1.6Ni/0.0Cu lower
Ni	c	0.4Cu	W	
Ni	d	0.0&0.2Cu	M	
P	e	0.0Cu/0.0, 0.8 & 1.6Ni; 0.1Cu/0.8Ni	S	Ni interaction?
Mo	g	0.2Cu/0.0Ni	S	
Mn	f	0.0&0.4Cu/	W	
C	h	0.0Cu/0.8Ni	N	
B	not shown	0.4Cu/0.8Ni	N	+B @0.0Cu/0.8Ni lower
**	not shown	0.0Cu/0.8Ni	N	

* N-negligible; W-weak; M-moderate; S-strong
** Cr, Sn, Sb, As, N

and nickel effects at high copper are negligible to weak (Figures 2a and c), there is some evidence of moderate copper effects at low nickel and nickel effects at low copper (Figure 2b and d).

While the individual effects of the various elements are generally modest, in combination, composition variations result in a substantial spread in the $\Delta\sigma_y$ values ranging from about 110 to 180 MPa. Figure 3a shows that while there is some scatter in the data, $\Delta\sigma_y$ for the base (Mn, Mo, B, N, C, ..) steels increases roughly linearly with the square root of the effective copper plus nickel content and is greater for high (circles) versus low (diamonds) phosphorous steels. The square root function was chosen to reflect the possible interactive effects of copper and nickel described above. The effective dissolved copper (Cu') for the 0.4 and 0.8Cu commercial alloys has been taken as 0.3 to account for pre-precipitation during tempering [2]. The effects of phosphorous, as well as manganese and nickel, were treated as linear terms in a least squares fit of the yield stress change at a fluence of 3 x 10^{22} n/m^2 [$\Delta\sigma_y(3)$] to a chemistry term shown in Figure 3b and given by

$$\Delta\sigma_y(3) \approx 137 + 26\sqrt{Cu' + Ni} + 790P + 15Mn - 70Mo \quad (MPa) \qquad (2)$$

The two data points labeled in Figure 3b fall somewhat below the trend band. However, in these cases the errors (shown) are relatively large and, hence, these data may not be inconsistent with the general trend. Even if these data are included, however, the standard error in the predicted $\Delta\sigma_y$ is only about 8 MPa. The results at $3x10^{22}$ n/m^2 can be extrapolated to other fluences by combining the square root dependence of $\Delta\sigma_y$ on fluence above a threshold (Equations 1) and with the chemistry dependence at $3x10^{22}$ n/m^2 (Equation 2) to obtain

$$\Delta\sigma_y \text{ (MPa)} \approx CF\left(\sqrt{\phi t\,(10^{22} n/m^2)} - 0.2\right) \qquad (3a)$$

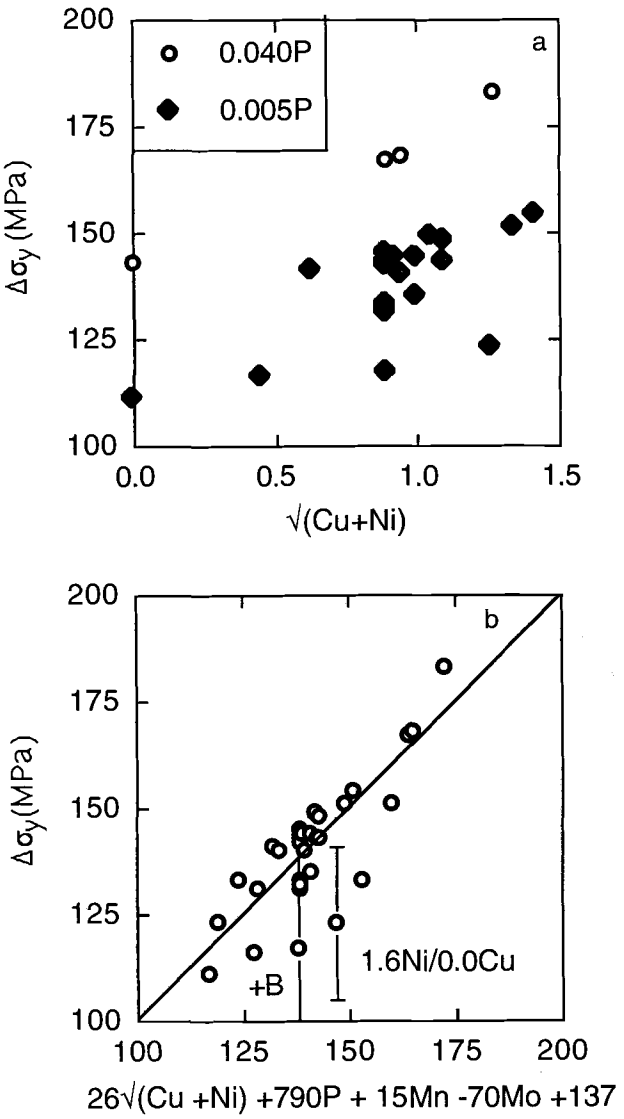


FIG. 3-- Variation of yield stress change with: a) square root of Cu plus Ni b) a chemistry factor defined by Equation (2).

where

$$CF = 89.4 + 16.9\sqrt{Cu + Ni} + 516P + 9.7\,Mn - 45.7\,Mo \quad (3b)$$

It is important to emphasize that this simple formulation is neither a unique best fit nor a physically-based model. Hence, Equation 3 cannot be reliably extrapolated or even interpolated. However, the empirical correlation does reflect the cumulative and combined effects of the most important compositional effects and clearly illustrates that composition can influence low temperature hardening.

Figure 4 plots the differences in the values of $\Delta\sigma_y$ for the materials with the base and the alternative heat treatments for the CM-series. There is a slight tendency towards less hardening in the higher normalizing temperature (differences averaging 20 MPa) and following the temper embrittlement aging (differences averaging 11 MPa). No consistent pattern is observed for various salt quench temperatures (differences averaging 0 MPa). However, in general the effects of heat treatment on hardening are relatively small and within or close to the estimated error limits.

Compositional Variables - Simple Steels

The results for the simple VX-series model alloys for the high fluence/high flux F8 capsule are shown in Figure 5. Figure 5a plots $\Delta\sigma_y$ versus copper for the nitrogen and titanium variants in the simple iron based VF-series. Note, the nominal copper content is

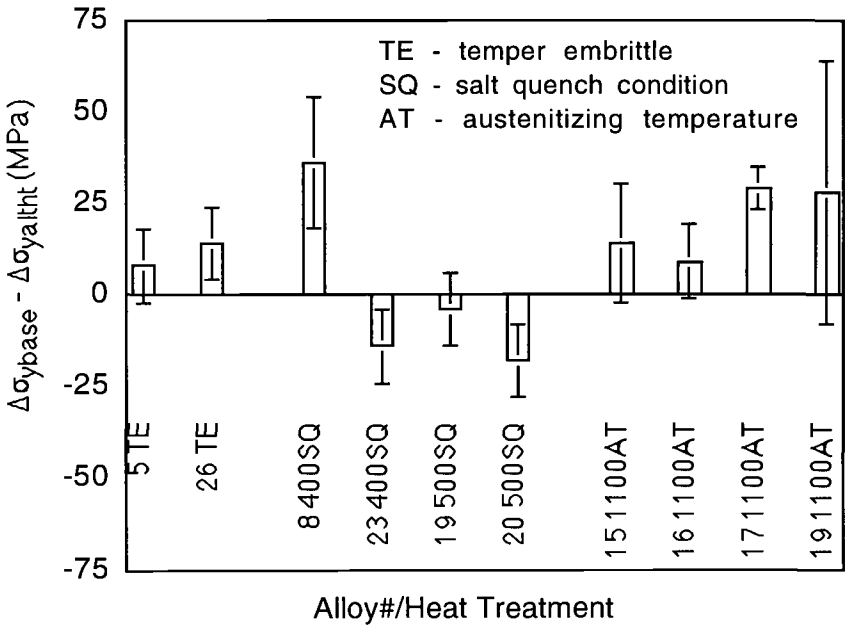


FIG. 4 -- Comparison of the difference between yield stress change in materials given the base heat treatment and materials given an alternative heat treatment.

used for the model alloys since the heat treatment is expected to retain most of this element in solution. Within scatter in the data (±15 MPa), there is little apparent effect of nitrogen or titanium. It may be notable that the iron-titanium-high nitrogen alloy had somewhat lower hardening (83 MPa) compared to either the iron-low nitrogen (127 MPa) or the iron-high nitrogen alloy (112 MPa). However, the effect of nitrogen-titanium interactions, if any, is weaker than the systematic increases in hardening with increasing copper. Similar copper trends are observed in Figure 5b for the VM alloys containing manganese and low nitrogen; however, the 0.0Cu-1.0Mn-high N alloy has a much higher $\Delta\sigma_y$ than the corresponding VF (without manganese)-high nitrogen alloy. The apparent Mn-N interaction is not observed in the VM-alloy with 0.9Cu. Figure 5c compares the $\Delta\sigma_y$ versus copper for the VC and VA steels with the simple VF-iron alloy series. No significant differences are observed. It is noted that similar trends are observed in the low flux, low fluence specimens, including the manganese-nitrogen interaction at low copper content.

The relatively strong copper effect in the simple iron alloys and steels appears to be inconsistent with the generally weaker trend in the complex steels. However, as discussed below, this is probably due to higher matrix copper concentrations and the absence of nickel in the VX-series (see below). The effect of nitrogen variations is generally minimal in both the simple model VX-series alloys without manganese and the complex CM-series steels. However, this element has been found previously to be an important factor in hardening of low copper mild steels, consistent with our observation of a strong manganese-nitrogen interaction in the simple VM alloy without copper. Further, the smaller $\Delta\sigma_y$ observed in the 0.25Ti/0.0Cu alloy may be due to a more complete gettering of nitrogen than in the nominally low nitrogen alloys without titanium. The apparent copper-manganese-nitrogen-molybdenum-titanium interaction is not understood, but may be due to a combination of: a) gettering of nitrogen in alloys with high concentrations of copper and molybdenum; and/or b) suppression of strengthening contributions from nitrogen related features due to hardening by Mo_2C and copper rich precipitate phases; and/or c) a plateau in nitrogen effects above about 10-15 ppm.

Microstructural Variables

As noted previously, alloys studied in this program cover a very wide range of microstructures and unirradiated properties, including: a) simple VX-series iron alloys and ferritic steels ($\sigma_{yu} \approx 190$ MPa); b) mild steels without secondary hardening elements ($\sigma_{yu} \approx 310$ MPa); and c) bainitic A533B pressure vessel type steels with secondary hardening phases (Mo_2C, $\sigma_{yu} \approx 475$ MPa). The effects of microstructure/unirradiated property variations are shown in Figure 6a which plots $\Delta\sigma_y$ versus σ_{yu} for the data at $3x10^{22}$ n/m^2. The circles are for the CM and L-series, with the open symbols the base heat treatment and the triangles the alternate CM-series heat treatments. The diamonds represent the CC-series with low molybdenum and lower σ_{yu} (note the CM-steel without molybdenum also falls into this grouping). The squares represent the simple VX-series iron alloys and steels with varying amounts of copper.

The CC and CM data suggests that the lower strength steels without molybdenum (and Mo_2C phases) experience a slightly higher $\Delta\sigma_y$. However, the comparisons of the CM and VX-series to assess microstructural and yield stress effects are confounded by dissolved copper variations. Direct application of the chemistry factor in Equation 2 does not predict the high yield stress values observed in the VX-series steels. However, this is not surprising given the significant microstructural and unirradiated property differences and the fact that the empirical treatment for the complex steels is restricted to a much lower range of copper in solution. A more direct comparison is given in Figure 6b, which plots $\Delta\sigma_y$ versus copper for the 0.0Ni CM-series alloys (circles) and other CM-series

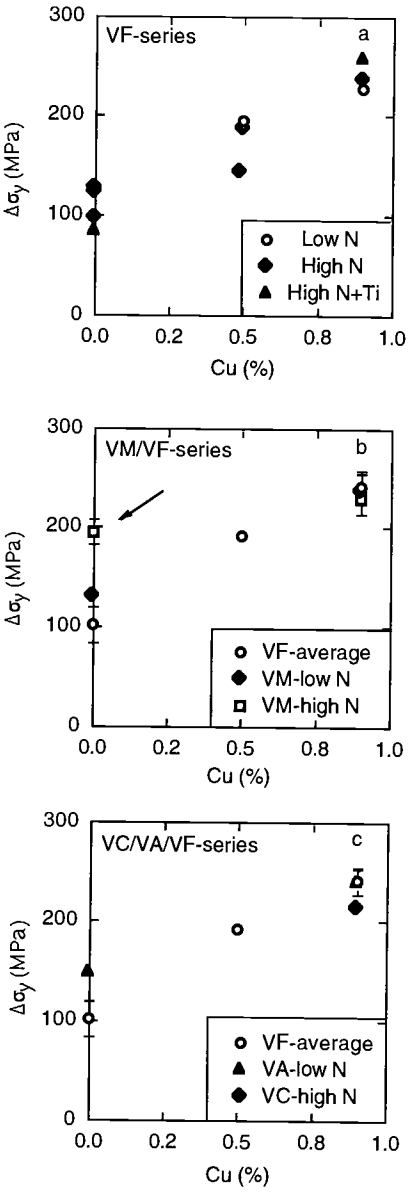


FIG. 5 -- Variation of yield stress change in the VX-series alloys at $3x10^{18}$ n/cm^2 with: copper for the a) VF-series, b) VM-series and c) VF and VA series.

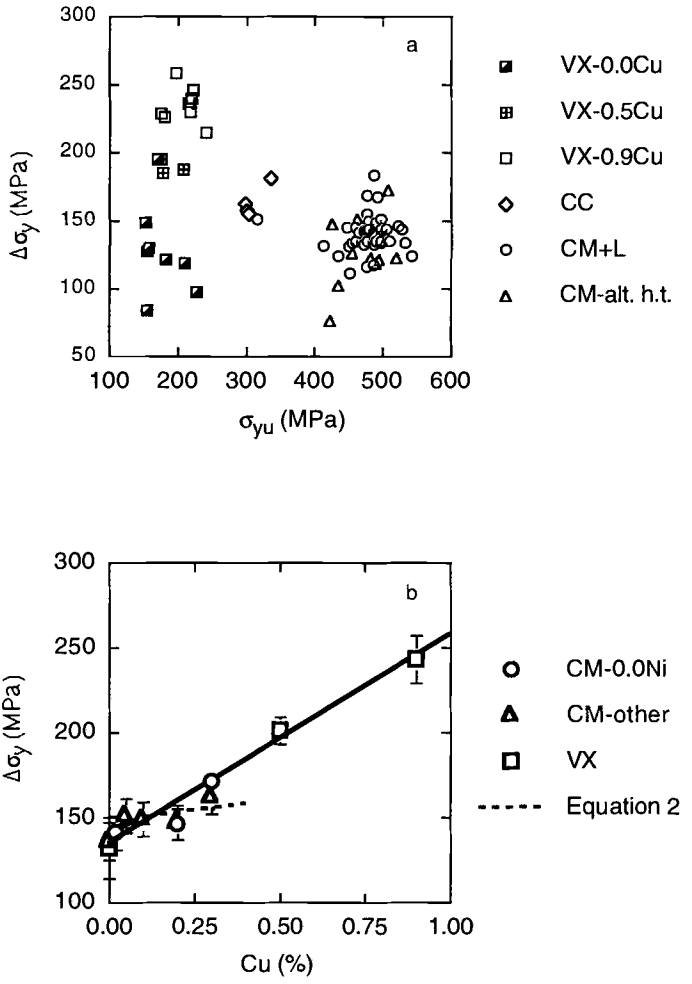


FIG. 6 -- Variation of yield stress change with a) unirradiated yield stress and b) copper, correcting for differences in compositional variables using Equation 2.

steels (triangles) along with the corresponding averages for the VX-series (squares), excluding the 0Cu-1Mn-high N alloy. Here the data have been corrected to a common manganese (1.0), molybdenum, phosphorous and nickel content (0.0) using Equation 2. Recall the maximum copper content of the CM alloys was taken as 0.3 to account for pre-precipitation. The predictions of Equation 2, shown as the dashed line in Figure 6b, under-predict $\Delta\sigma_y$ for the simple VX-series model steels at higher copper contents. However, both data sets fall along the least squares fit to the VX-series data shown as the solid line.

Equation 2 is not unique and, indeed, alternate formulations (e.g. terms that are linear in copper and nickel) may fit a wider range of data. More importantly, however, cumulative and particular combinations of compositional factors influence hardening over a wide range of microstructures and unirradiated properties. In contrast, the microstructure does not appear to play a significant role, per-se, in low temperature hardening.

COMPARISON WITH OTHER DATA

While it is certainly not possible to review the entire literature, it is useful to briefly note similarities and differences between this work and the results of other studies. With regard to the effect of flux at low irradiation temperatures, long ago Barton et. al. reported a negligible effect of flux on mild steels irradiated down to 100°C in the range of about $3x10^{15}$ to $3x10^{17}$ n/m^2-s for fluences up to about $5x10^{21}$ n/m^2 [10]. A similar result was found by Hinkle et. al for low temperature irradiations of high purity (ferrovac) iron at higher fluence [11]. Based on these and other data, Buswell et. al. have proposed a temperature dependent-flux independent matrix hardening model, which is presumably applicable down to the low temperatures in this study [12]. Yield stress data reported on the Shippingport steels by Chopra et al. [9] versus Hawthorne and Rosinski [13] could be interpreted to indicate a moderate flux effect (e.g. 51 MPa versus 28 MPa elevations for low and high flux irradiations, respectively). However, the more extended range of data for this steel in this work did not reveal a significant flux effect (note, based on transition temperature shifts, these workers also concluded that there was no flux effect).

With regard to composition effects, a large body of 60°C hardening data reported by Nikolayev et. al on both simple model alloys and complex Cr-V-Mo Russian VVER steels is qualitatively consistent with the effects of copper, nickel and manganese we have observed [14]. However, these irradiations were at a much higher fluence (>10^{19} n/cm^2) and, in general, Nikolayev et. al. found the relative effects of individual elements to be larger than observed in this study. Further, these workers did not observe a hardening effect of phosphorous or molybdenum found in this work. Barton et. al observed a metallurgical sensitivity in mild steels which they attributed to the free nitrogen content [10]. With the exception of the 0.0Cu-1Mn-high N model alloy, nitrogen effects were not seen in this study. More recent studies by Farrell and coworkers have observed effects of copper and nickel in simple model steels which increased with increasing fluence [7]. However, contrary to our results, these workers suggested that composition did not influence the corresponding low temperature hardening in complex alloys. A similar conclusion concerning both simple and complex steels was reached by Boydon et. al. for 70°C irradiations to high fluence (note, however, they also find a phosphorous effect in low copper model steels) [15]. Hawthorne also reports a lack of compositional sensitivity for low fluence, low temperature irradiations of complex steels [16]; he had also previously reported a lack of sensitivity for low temperature irradiations to phosphorous but not copper [17, 18]. The data of both Farrell and Hawthorne on complex steels may be confounded by uncontrolled variables and a detailed analysis of the type presented here has not yet been carried out on the data reported by Boydon et. al.

In summary, within experimental error and considering possible confounding factors, the present results are generally consistent with most data in the literature. However, in contrast to some conclusions of other workers, the systematic, single variable experimental matrix employed here reveals subtle but significant effects of composition. This compositional sensitivity is different than that observed at higher temperatures and suggests dominance of a different type of hardening feature, viz., a matrix type defect due to a cut-off of precipitation resulting from long range copper diffusion below about 150°C (this matrix type defect is also observed at the higher temperatures in conjunction with copper precipitates in steels with significant trace quantities of this element).

DISCUSSION -- SOME POSSIBLE HARDENING MECHANISMS

The observations in the previous section can be summarized as follows. Irradiation hardening at 60°C varies with the square root of fluence above an extrapolated threshold around $4x10^{20}$ n/m^2 up to the maximum fluence in this study of about $3x10^{22}$ n/m^2. The hardening is remarkably independent of flux over a range from about $2x10^{13}$ to $5x10^{18}$ n/m^2-s. However, hardening is dependent on compositional factors including phosphorous, molybdenum, manganese, copper, nickel and nitrogen (the latter only in simple model alloys containing manganese). While not unique, the compositional effects in the data base can be represented by a simple empirical chemistry factor that reflects hardening behavior over a wide range of alloy types and conditions. This suggests the operation of a common mechanism.

The dominant mechanism must be consistent with: a) the observed dependence on flux, fluence, composition and irradiation temperature [8]; b) the magnitude of hardening; c) limited microstructural data; and d) the annealing response. It is clear that the hardening is due to very small features since they have not been imaged by TEM in this fluence range and result in very weak SANS signals (see below). The insensitivity to coarser scale microstructures is consistent with highly localized damage production. The square root fluence dependence is also consistent with the number of dispersed barrier dislocation obstacles increasing in proportion to fluence. Together these observations suggest that the hardening features are formed in displacement cascades. Assuming a rate of one for every two cascades, a fluence of $3x10^{22}$ n/m^2 would produce about 4 $x10^{23}$/m^3 obstacles (N) with an estimated diameter (d) of about 1.5 nm. The obstacle hardening efficiency (β) can be approximated as $\beta \approx \Delta\sigma_y/3Gb\sqrt{Nd}$. For a typical $\Delta\sigma_y$ = 150 MPa, $\beta \approx 0.1$. This value is consistent with previous estimates for very small defect clusters or cluster complexes [19]. Significant hardening recovery following a short 4 h post irradiation anneal is observed at 300°C and approaches 100% at 400°C[5]. Small vacancy clusters would anneal in this temperature range also resulting in the dispersion of complexed solutes.

Preliminary SANS measurements reveal very weak scattering in the complex L-series steels[5]. The failure to observe copper rich precipitates (CRP) is consistent with the previously proposed cut-off in precipitation by long range copper diffusion at low temperatures [8]. Notably, the SANS signal decreases with increasing copper and nickel content: the magnetic scattering is independent of nickel but decreases with increasing copper; nuclear scattering decreases with increasing nickel but is independent of copper. Annealing at 400°C for 4h coarsens the scattering centers. In contrast to the commercial type steels, scattering in simple iron-copper alloys increases with increasing copper. The scattering magnitudes and ratios of nuclear-to-magnetic scattering are consistent with vacancies complexed with dilute atmospheres of copper.

---

[5] This discussion cites preliminary data generated in our program that will be presented in detail elswhere.

Taken together, these observations are broadly consistent with low temperature hardening features formed in isolated displacement cascades composed of relatively dilute atmospheres of solutes (manganese-nickel-copper-...) surrounding a very small vacancy cluster (a looser sponge-like arrangement may also be possible but is thermodynamically less likely). The co-clustering of vacancies and copper at the core of cascades has been previously modeled [20]. Significant copper segregation occurs due to a small binding energy with both vacancies and free surfaces. The segregated copper lowers the free surface energy, thermally stabilizing the small clusters. Even in relative small concentrations, the complexed solutes may also increase the hardening efficiency of the cascade features. Dilute solute clusters following elevated temperature irradiations have been observed in FIM/AP studies [21]. Co-clustering may also be the mechanism for CRP nucleation at low copper concentrations [20, 21].

In spite of this general consistency, other possible mechanisms should be considered. For example, small interstitial clusters produced directly in displacement cascades would act as dislocation obstacles. Interstitial clusters may also be complexed with solutes. While interstitial clusters have high binding energies and would not be expected to recover quickly by normal self-diffusion controlled processes at 400°C, immobile interstitial clusters could co-anneal with vacancy clusters. More significantly, however, it is now known that small interstitial clusters are highly mobile in perfect iron lattices; thus recovery might be due to thermally activated release of interstitial clusters from trapping sites [22].

Compositional effects may also be mediated by other mechanisms. For example the effect of molybdenum is probably related to the presence (or absence) of Mo_2C secondary hardening phases. Post-irradiation annealing studies and computer simulations have suggested that superposition of a significant hardening contribution from such strong dislocation obstacles may decrease the effective hardening efficiency of weaker radiation induced barriers [23].

HARDENING FROM GAMMA-RAYS AND ELECTRONS -- A CONUNDRUM

The most significant residual question relates to the accelerated embrittlement in HFIR which now seems unlikely to be due to flux effects. Recent suggestions that displacement damage from very high fluxes of high energy gamma rays appears to be the most plausible explanation [6,7]. However, gamma-rays, along with electrons and thermal neutrons produce low energy primary recoil atoms, yielding isolated defects rather than cascades. Similar hardening in electron versus neutron irradiations at the same dpa have also been reported for both commercial steels and simple Fe-Cu alloys [23]. Some recent preliminary data in this program (capsule R11) shows extra hardening apparently due to thermal neutrons in mixed spectrum irradiations, consistent with enhanced residual defect production relative to fast neutrons by a factor of about two. Hence, while a near-dpa equivalence provides some level of rationalization of the HFIR data, the gamma ray, electron and thermal neutron results seem to be inconsistent with the proposed cascade mechanism. An alternative explanation is that the irradiations yielding low energy primary recoil atoms harden by an entirely different mechanism. Hardening depends on a combination of factors including: a) the type and fate of the defects (i.e. migrating free defects, immobile clusters, diffusional clustering, recombination or loss to sinks); b) the defect production efficiency; and c) respective hardening efficiencies of the induced features. This conundrum can only be resolved by additional research on the mechanisms and microstructures of hardening.

CLOSING REMARKS -- IMPLICATIONS TO SUPPORT STRUCTURE EMBRITTLEMENT

A major motivation for this study was the concern about the potential for accelerated embrittlement of support structures irradiated at low temperatures and fluxes to exposures in the range of 4 to 6 mdpa (equivalent to about 2.5 to $4x10^{22}$ n/m^2 $E > 1$ MeV). The remarkable insensitivity of hardening to flux that was observed in this work should largely resolve this issue, although the data at very low fluxes are limited. However, while accelerated embrittlement is unlikely, substantial shifts may still occur under support structure irradiation conditions. At the highest fluence, molybdenum free steels with high phosphorous would be predicted to have a $\Delta\sigma_y$ of about 200 MPa or more depending on the nickel content. Based on a typical shift/hardening coefficient of 0.6°C/MPa [2, 4, 22], the corresponding transition temperature elevations would be 120°C. The significance of such shifts to the integrity of support structures should be evaluated.

ACKNOWLEDGMENTS

The authors thank D. Gragg and J. W. Sheckherd for their contributions to specimen preparation and to post-irradiation testing and W. Phythian for collaboration in acquiring many of the alloys used in this study. We also thank Phil Simpson and the staff at the University of Michigan Ford Reactor for cooperation in carrying out the irradiations. The work was supported by the US Department of Energy, Office of Energy Research, grant numbers FE--FG07-89ER 12895 and 93ER 75902 under the Nuclear Engineering Research Initiatives Program.

REFERENCES

[1] United States Nuclear Regulatory Commission, Regulatory Guide 1.99: Radiation Embrittlement to Reactor Vessel Materials, U.S. Government Printing Office, Washington, D.C., 1988.

[2] Odette, G. R., and Lucas, G. E., An Experimental Investigation of Kinetic Aspects of Neutron Irradiation Embrittlement of Light Water Reactor Pressure Vessel Steels, EPRI Report NP 6114, Electric Power Research Institute, 1989.

[3] Nanstad, R. K., Iskander, S. K., Rowcliffe, A., Corwin, W. R. and Odette, G. R., Effects of Radiation on Materials: 14th International Symposium,. 2, ASTM-STP-1046, N. H. Packan, R. E. Stoller and A. S. Kumar, Eds., American Society for Testing and Materials, Philadelphia, 1990, p5.

[4] Rowcliffe, A. F. and Odette, G. R., Evaluation of HFIR Pressure Vessel Integrity Considering Radiation Embrittlement - Section 6, ORNL/TM-10444, R. D. Cheverton, J. G. Merkle and R. K. Nanstad, Eds., 1987, p152.

[5] Mansur, L. K. and Farrell, K., Journal of Nuclear Materials, 170, 1990, p236.

[6] Rehn L. E. and Bircher, R. C., Journal of Nuclear Materials, 205, 1993, p31.

[7] Farrell, K., Mahmood, S. T., Stoller, R. E. and Mansur, L. K., Journal of Nuclear Materials, 210, 1994, p268.

[8] Lucas, G. E., Odette, G. R., Mader, E., Haggag, F., and Nanstad, R., Proceedings of the Fifth International Symposium on Environmental Degradation of Materials in Nuclear Power Systems - Water Reactors, D. Cubicciotti, E. Simonen and R. Gold, Eds. ANS, La Grange Park, Ill., 1992, p696.

[9] Chopra, O. K., Rosinski, S. T., and Shack, W. J., "Radiation Embrittlement of the Neutron Shield Tank from the Shippingport Reactor," NUREG/CR-5748, US Nuclear Regulatory Commission, 1991.

[10] Barton, P. J., Harries, D.R. and Mogford, I. L., Journal of the Iron and Steel Institute, 203, 1965, p507.
[11] Hinkle, N. E., Ohr, S. M. and Weschler, M. S., Effects of Radiation on Structural Materials: 3rd International Symposium, ASTM-STP 426, W. R. Rice Ed., American Society for Testing and Materials, Philadelphia, 1967, p573.
[12] Buswell, J. T., and Jones, R. B., Effects of Radiation on Materials: 16th International Symposium, ASTM STP 1175, A. S. Kumar, D. S., Gelles, R. K., Nanstad and E. A. Little, Eds., American Society for Testing and Materials, Philadelphia, 1992, p424.
[13] Hawthorne, J. R. and Rosinski, S.T., Accelerated 54°C Irradiated Test of Shippingport Neutron Shield Tank and HFIR Vessel Materials, SAND92-2420.UC-523/MEA-2494, 1993.
[14] Nikolayev, V. A. and Rybin, V. V., Radiation Embrittlement of Vessel and Support Structures and Vessel Annealing, NRC Translation 2132, 1989.
[15] Boydon, F. M. D., McElroy, R. J., Gage, G. and Phythian, W. J., "Low Temperature Irradiation Embrittlement of RPV Support Structure Steel", Effects of Radiation on Materials: 17th International Symposium, ASTM STP 1270, R. K. Nanstad, D. S. Gelles, A. S. Kumar and E. A. Little, Eds., American Society for Testing and Materials, Philadelphia, 1996,
[16] Hawthorne, J. R., Effects of Radiation on Materials: 16th International Symposium, ASTM STP 1175, A. S. Kumar, D. S. Gelles, R. K., Nanstad and E. A. Little, Eds., American Society for Testing and Materials, Philadelphia, 1992, p306.
[17] Hawthorne, J. R., Transactions of the ANS, 14-1, 1966, p165.
[18] Hawthorne, J. R., Transactions of the ANS, 15-2, 1966, p756.
[19] Odette, G. R. , "Modeling of Irradiation Embrittlement in Reactor Pressure Vessel Steels", Neutron Irradiation Effects in Reactor Pressure Vessel Steels and Weldments, IAEA Technical Report Series, M. Davies, Ed., International Atomic Energy Agency, Vienna (in press).
[20] Odette, G. R. and Sheeks, C. K., Phase Stability During Irradiation, J. R. Holland, L. K. Mansur and D. I. Potter, Eds., TMS, Warrendale, Pa, 1982, p415.
[21] Akamatsu, M., Van Duysen, J. C., Pariege, P and Auger, P., "Microstructural and Mechanical Characterization of Radiation Damage in Model and Industrial Ferritic Alloys", Effects of Radiation on Materials: 17th International Symposium, ASTM STP 1270, R. K. Nanstad, D. S. Gelles, A. S. Kumar and E. A. Little, Eds., American Society for Testing and Materials, Philadelphia, 1996,
[22] Odette, G. R., Microstructure of Irradiated Materials, Materials Research Society Symposium Proceedings 373, I. Robertson, L. Rehn, S. Zinkle and W. Phythian, Eds., 1995, p137.
[23] Mader, E., Lucas, G. E. and Odette, G. R., Effects of Radiation on Materials: 15th International Symposium, ASTM STP 1125, R. E. Stoller, A. S. Kumar and D. S. Gelles, Eds., American Society for Testing and Materials, Philadelphia, 1992, p151.
[24] Alexander, D. E., Rehn, L. E., Farrell, K and Stoller, R. E., Gamma-ray (electron) Effects on Tensile properties in Ferritic Alloys, Journal of Nuclear Materials (in press).

R. Barry Jones (1) and Timothy J. Williams (2)

THE DEPENDENCE OF RADIATION HARDENING AND EMBRITTLEMENT ON IRRADIATION TEMPERATURE

REFERENCE: Jones, R. B. and Williams, T. J., **"The Dependence of Radiation Hardening and Embrittlement on Irradiation Temperature,"** *Effects of Radiation on Materials: 17th International Symposium, ASTM STP 1270,* David S. Gelles, Randy K. Nanstad, Arvind S. Kumar, and Edward A. Little, Eds., American Society for Testing and Materials, 1996.

ABSTRACT: Assessments of the hardening and embrittlement of pressure vessel steels and welds as a function of neutron dose use trend curves derived from surveillance programmes and accelerated irradiation data. A temperature dependent factor is incorporated for assessing vessel locations operating at different temperatures. As hardening and embrittlement arise from the sum of matrix damage and copper impurity precipitation, the influence of irradiation temperature on each process needs to be established. For irradiations performed below ~300°C recent data shows that the dose-dependent growth of copper precipitates ceases at a mean diameter of about 2 nm that also corresponds to peak hardening and embrittlement by copper. For doses beyond this peak copper dose the property-dependence on irradiation temperature can be identified with that of matrix damage alone. An analysis of several experiments on plate steels, performed at differing irradiation temperatures, has permitted the temperature dependence of matrix hardening to be defined by the simple empirical factor

$$F_T = 1.869 - 4.57 \times 10^{-3} T$$

where T is the irradiation temperature. When a linear correlation between irradiation hardening and embrittlement is observed, then F_T can be used to analyse the temperature dependence of matrix embrittlement. The validity of using F_T in successfully correlating irradiation results has been demonstrated for several plate steels and welds with differing copper contents.

KEYWORDS: Irradiation temperature, pressure vessel steels, hardening, embrittlement, copper precipitation

(1) Principal Engineer, Nuclear Electric plc, Berkeley Technology Centre, Berkeley, Glos. GL13 9PB, United Kingdom.

(2) Consultant, Fracture Technology, Rolls-Royce and Associates Limited, P O Box 31, Raynesway, Derby, DE24 8BJ, United Kingdom

Copyright© 1996 by ASTM International www.astm.org

In the United Kingdom the assessment of the integrity of the ferritic steel pressure vessels in the Magnox and PWR systems involves the use of trend curves. These trend curves are equations that describe the changes in mechanical properties (yield stress, Charpy transition temperature, hardness, etc) as a function of neutron dose. The equations are derived from the results of reactor surveillance programmes and accelerated irradiation experiments performed at a number of differing irradiation temperatures on representative samples of vessel plate, forging and weld materials. In order to derive the trend curves initially, and to apply them in practice to vessel locations at differing exposure temperatures, the trend equations incorporate a temperature-dependent factor.

The irradiation temperature range covered by this factor is quite wide. In the Magnox system the pressure vessels experience irradiation temperatures ranging from 150°C to 360°C determined by the coolant gas inlet and outlet temperatures and by the individual vessel design. The operating temperature range for PWR vessels is narrower than for Magnox vessels; for the Sizewell "B" power station the temperature range is 292°C to 325°C.

In the literature, the reduction in irradiation hardening and embrittlement in ferritic steel at higher irradiation temperatures has been well documented. For example, in Revision 1 of the USNRC Regulatory Guide (RG 1.99) [1] the guidance given is that the embrittlement found after irradiation at 288°C in typical LWR steels with 0.15% Cu would be doubled, or halved respectively, if the steel had been similarly irradiated at 232°C, or 343°C. To take account of such effects a number of irradiation temperature correction factors have been derived [2 - 6]. These factors may be either empirical in nature, being derived from some analysis of experimental data, or based on a modelling approach in which the opposing effects of damage accumulation and temperature-dependent damage annealing are considered. The factors may often be used as simple multipliers of the irradiation-induced shifts, i.e. all processes contributing to the shifts are corrected with the same factor.

The purpose of the current paper is to describe the derivation of an irradiation temperature factor that is based on metallurgical considerations and on an assessment of the relative temperature-dependence of the various processes contributing to the irradiation hardening and embrittlement shifts.

BASIC EQUATIONS USED IN MODELLING

Dose Dependence of Hardening and Embrittlement

It is now accepted that the irradiation hardening and embrittlement of steel plates, forgings and welds can be accentuated by the irradiation-induced precipitation of nanometre-size Cu-rich particles in the grains. Apart from such visible Cu-rich particles, the steel matrix itself will be subject to atom displacement damage. Matrix damage gives observable hardening which is postulated to arise from defect clusters, dislocation loops or micro-voids. These defects are nearly always on too fine a scale to be visible by electron microscopy. The separate contributions to the increase in

yield stress of a steel ($\Delta\sigma$) may be added together linearly

$$\Delta\sigma = \Delta\sigma_m + \Delta\sigma_{Cu} \quad (1)$$

where the suffixes m and Cu refer to the irradiation hardening effects arising from matrix displacement damage and Cu particle precipitation respectively. In general, each of these terms depends on irradiation temperature and dose.

Irradiation embrittlement is directly related to the magnitude of irradiation hardening under conditions where other embrittling processes, like temper embrittlement, are absent. Hence, multiplying the total calculated hardening value by a factor (Z) of about 0.5 (for plates) and about 0.65 (for submerged-arc welds in PWR steels) enables an estimate to be derived for the shift in the Charpy transition temperature due to irradiation [7, 8, 9, 10]. The calculational route outlined above is the basis of a number of other irradiation embrittlement modelling procedures now in use world-wide [6, 10].

From analysis of a wide range of experimental data [6, 7, 8] the matrix displacement damage term may be written

$$\Delta\sigma_m = A'_T (\phi t)^{0.5} \quad (2)$$

where A'_T is dependent on temperature, ϕ is the neutron damage flux and t is the irradiation time. The form of this equation can be supported from theoretical analysis [11].

The Cu particle precipitation hardening is a complicated function of the neutron flux, dose, irradiation temperature, material dislocation density and the formation and diffusion activation energies for vacancies. In the earlier models [7, 8, 10] these parameters played a role during the Cu nucleation stage and during the anticipated Cu particle growth to and beyond peak hardening. However the assumption that the Cu particles will continue to grow and overage under irradiation seems increasingly questionable, for reasons given below.

A recent analysis of UK, US and European Small Angle Neutron Scattering (SANS) determinations of the diameters of irradiation-induced Cu particles in steels and iron alloys has been undertaken by Jones [12]. It was noted that the particles did not coarsen significantly during continued irradiation exposure. Figure 1 shows the evidence for this invariance of Cu particle size with irradiation at, or below, 300°C for both accelerated and surveillance irradiation conditions. Subsequently this observation has been confirmed by Buswell et al [9, 13, 14] using new SANS experimental irradiation results covering a wide dose range in the post-peak Cu particle size regime. Figure 2 illustrates the dose-invariant Cu particle diameter observed by Buswell et al [13] in Magnox pressure vessel submerged-arc welds during surveillance and extended irradiation exposures at temperatures in the range 190 - 290°C.

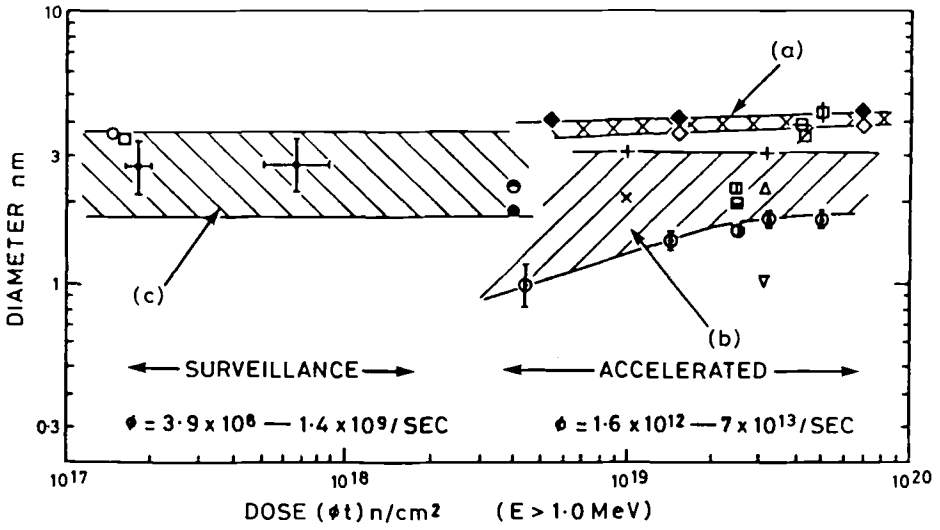


FIG.1 Absence of irradiation-induced growth of Cu precipitates, from SANS measurements on ferritic steels and model alloys with 0.09-1.30wt.% Cu.
(a)Fe-Cu and Fe-Cu-Ni model alloys in accelerated irradiations at 280-300°C
(b)Accelerated irradiation data on PWR steels at 280-300°C
(c)Surveillance and accelerated irradiation data on UK Magnox C-Mn plate and welds at 180-225°C

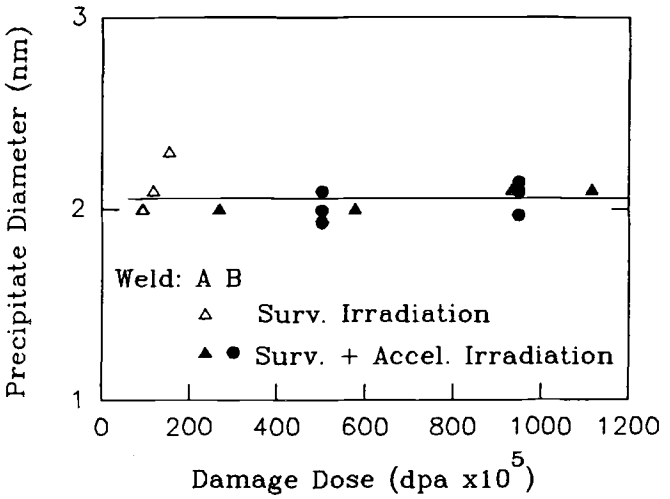


FIG.2 The Dose Dependence of the Mean Diameter of Cu-Rich Precipitates in Magnox Submerged-Arc Welds, as determined by SANS experiments [13]

The absence of particle coarsening was considered in one of the earlier modelling studies of irradiated steel behaviour [10]; other studies assumed coarsening [7,8]. Particle growth to a limiting size is incorporated in recent modelling studies of submerged-arc welds [6, 9]. The mechanism by which the coarsening is prevented has not yet been identified. Nevertheless, there are considerable practical implications arising from the inhibition of particle coarsening on the embrittlement modelling procedures. First, it results in a simplification of the calculation of hardening and embrittlement once the maximum contribution from Cu precipitation has been developed. Secondly, it has an influence in modifying the methodology used to estimate the influence of irradiation temperature on hardening and embrittlement.

Since the overaging of Cu particles is suppressed under irradiation, and this occurs at a particle diameter that approximates to that of peak Cu hardening, then for a given irradiation temperature and for all doses in excess of that for Cu peak hardening, eq (1) may be rewritten

$$\Delta\sigma = A'_T (\phi t)^{0.5} + \Delta\sigma_{Cu(peak)} \quad (3)$$

Eq (3) indicates that a plot of experimental post-peak $\Delta\sigma$ values versus $(\phi t)^{0.5}$ should exhibit a slope of A'_T and a zero dose intercept of $\Delta\sigma_{Cu(peak)}$. In eq (3) the temperature dependence of the total yield stress increment ($\Delta\sigma$) will be determined only from that of the matrix displacement damage term ($A'_T (\phi t)^{0.5}$). As the dose is independent of the irradiation temperature then it follows from eq (2) that the temperature dependence of $\Delta\sigma$ will be determined by that of the constant A'_T

$$d(\Delta\sigma)/dT = d(A'(\phi t)^{0.5})/dT = (\text{constant})\ dA'_T/dT \quad (4)$$

This derivation will now be tested against experimental observation in a variety of ways.

ANALYSIS OF THE TEMPERATURE DEPENDENCE OF MATRIX HARDENING

Methodology

In steels and welds with a low Cu content ($\leq 0.05\%$) the magnitude of $\Delta\sigma_{Cu}$ is small and the dependence of A'_T on irradiation temperature may be directly evaluated from the measured irradiation-induced increase in yield stress. A'_T may also be determined in steels containing moderate Cu levels ($Cu \sim 0.10\%$) under conditions of high flux, low dose irradiation where the Cu precipitates have not been nucleated, as has been justified by Fisher et al [7]. Finally the temperature dependence of A'_T may be determined from the post-peak properties of high Cu steels ($Cu \geq 0.20\%$).

The selection of data for the present analysis has been based on sources where use was made of temperature controlled irradiation rigs; here the accuracy of the temperatures is known to be better than $\pm 3°C$. The various experimental

investigations have been performed under differing neutron flux levels to a variety of doses in reactors with dissimilar neutron spectra. In order to combine these data sets appropriately it is useful to examine the relative change in materials response as a function of irradiation temperature. Each iso-dose data set is examined individually as a function of irradiation temperature and a "best estimate" empirical linear relation is fitted by the method of least squares, using temperature as the independent variable. For Magnox applications the irradiation temperature range has been restricted between 100 and 350°C. The derived equations are each normalised to give a value of the irradiation temperature dependence parameter (F_T) equal to unity at a preselected temperature. In this instance each equation has been normalised using the predicted yield stress increment or A'_T value for a temperature of 190°C, which is an irradiation temperature identical to that of Duct 1 in the Trawsfynydd Magnox reactor surveillance scheme [9], so that

$$F_{T(\Delta\sigma)} = \frac{A'_T}{A'_{190°C}} \qquad (5)$$

The normalised F_T values for each data set are then combined onto a single plot of F_T as a function of irradiation temperature; the best estimate equation is then determined by the least squares method.

Data Analysis

Results of Barton, Harries and Mogford

These authors [15] reported the irradiation temperature and the dose-rate dependence of the yield stress increase following irradiation in the PLUTO materials testing reactor for C-Mn steels comprising EN2, a Si-killed mild steel and an Al-killed grain-size controlled mild steel. The Cu contents of the steels were 0.14%, 0.18% and 0.13% respectively, by weight (see Table 1). Irradiation temperatures were reported to have been controlled to ± 1°C [16] and the fast neutron doses were restricted to a maximum of $2.5 * 10^{17}$ n.cm^{-2} (as measured by Ni monitors). The doses were too small for Cu particles to have nucleated [7]. For each steel the hardening parameter (A'_T in eq 2) for the differing dose rates and irradiation temperatures was evaluated. Barton et al reported that A'_T was independent of dose rate but was affected by irradiation temperature. Accordingly, the A'_T values as listed in reference [17], for the three differing dose rates, have been averaged for each combination of steel and irradiation temperature investigated. These averaged results are shown in Table 2 in units of MPa/$(\phi t_{Ni})^{0.5}$, where ϕt_{Ni} is the fast neutron dose evaluated from Ni monitors assuming a fission spectrum.

The results between 100 and 350°C have been analysed as a simple linear function of irradiation temperature; the equations are listed at the foot of Table 2. $F_{T(\Delta\sigma)}$ values have been obtained by normalising the results to $F_{T(\Delta\sigma)} = 1.0$ at 190°C and the derived values are also recorded in Table 2. All $F_{T(\Delta\sigma)}$ data are plotted against irradiation temperature in Figure 3.

Table 1
Chemical Composition of the Steels Examined

Steel	C	Si	Mn	S	P	Ni	Mo	Al	Cu	Cr	Other	Ref
EN2	0.10	0.04	0.66	0.043	0.012	0.12	0.05	-	0.14	0.02	0 0.026 N 0.004 Co 0.013 B 0.6ppm	15
Al grain size controlled mild steel	0.13	0.14	1.22	0.027	0.017	0.06	<0.05	0.021	0.13	0.05	V <0.03 O 0.002 N 0.008 Co 0.008 B 0.8ppm	15
Si-killed mild steel	0.12	0.10	1.26	0.027	0.014	0.06	<0.05	0.006	0.18	<0.05	V <0.03 O 0.03 N 0.004 Co 0.011 B 0.5ppm	15
2103/R3 Al-killed	0.15	0.41	1.59	0.012	0.014	0.01	0.05	0.034	0.05	-	-	18
Plate	-	-	1.18	-	0.018	0.62	0.38	-	0.08	0.11	-	21
Fabrication test ring	0.16	0.30	1.33	0.009	0.019	0.58	0.44	-	0.075	0.16	-	21
SH	0.047	0.38	1.51	0.0120	0.0155	0.077	0.48	0.006	0.56	-	-	3
1W	0.056	0.50	1.57	0.0225	0.016	0.107	0.50	0.006	0.171	-	-	3
SL	0.063	0.45	1.66	0.0130	0.017	0.088	0.48	0.006	0.118	-	-	3
SP	N/A	N/A	N/A	0.015	0.024	0.047	N/A	N/A	0.069	-	-	23
Magnox*	0.088	0.52	1.49	0.037	0.031	0.096	0.037	0.010	0.233	-	-	14

* Average of many welds

Results of Grounes

Grounes [18] conducted experiments on the irradiation hardening of an Al-killed mild steel (code 2103R3) containing a low Cu content of 0.05% (see Table 1). Tests were undertaken between 40 and 335°C; only those results between 110 and 335°C have been used here because these were all performed in electrically heated rigs (with an accuracy ± 3°C) in the heavy water reactor DR3 in similar neutron spectra. Yield stress increments have been obtained for a dose of $1.0 * 10^{19}$ n.cm^{-2} ($E > 1.0$ MeV) by analysis of the published graphs (from Figure 12 in Reference [18]). The yield stress increments ($\Delta\sigma$) and derived values of A'_T are listed in Table 2 together with the equation for the linear regression of A'_T against irradiation temperature. $F_{T(\Delta\sigma)}$ values obtained by normalising the data to $F_{T(\Delta\sigma)} = 1.0$ at 190°C are also recorded in Table 2 and are plotted against irradiation temperature in Figure 3.

TABLE 2

Irradiation Temperature Dependence of $F_T(\Delta\sigma)$ Calculated for Four Mild Steels. Data from Barton, Harries and Mogford [15, 17] and Grounes [18]

Steel	Irradiation	A′ equation (2) MPa/$(\phi t_{Ni}/10^{16})^{0.5}$	$F_{T(\Delta\sigma)}$ (normalised to unity at 190°C)
EN2	100	10.93	1.342
0.14% Cu	150	10.19	1.251
	200	8.57	1.052
	250	5.82	0.714
	300	2.95	0.362
	350	2.28	0.280
Si-killed	100	9.22	1.282
mild steel	150	8.49	1.180
0.18%	200	7.83	1.088
	250	5.55	0.771
	300	3.68	0.511
	350	2.14	0.297
Al-killed	100	6.53	1.390
mild steel	150	5.80	1.235
0.13% Cu	200	4.25	0.905
	250	3.23	0.688
	300	2.51	0.534
	350	1.59	0.338
2103/R3	110	247* **7.81	1.457
Al-killed	125	232 7.34	1.368
mild steel	160	181.5 5.74	1.070
0.05% Cu	195	153 4.84	0.901
	230	138 4.36	0.812
	265	113 3.57	0.667
	300	72 2.28	0.423
	335	49 1.55	0.289

* $\Delta\sigma$ (MPa) at 1.0 x 10^{19} n cm^{-2} (E > 1MeV)

** A′ derived in n/cm^2 (E>1 MeV) units.

Correlation equations:

A′ = 15.497 - 3.87 x 10^{-2}T for EN2

A′ = 12.851 - 2.98 x 10^{-2} T for Si-killed steel

A′ = 8.561 - 2.03 x 10^{-2}T for Al-killed steel, and

A′ = 10.505 - 2.71 x 10^{-2}T for 2103/R3

Irradiation temperature dependence of $F_{T(\Delta\sigma)}$

The $F_{T(\Delta\sigma)}$ results from the four data sets from Table 2 are all plotted in Figure 3 as a function of irradiation temperature (T in °C). The points from the differing materials and irradiation environments form a homogeneous data set with relatively little variability. The least squares regression equation is

$$F_{T(\Delta\sigma)} = 1.869 - 4.57\times10^{-3}T \qquad (6)$$

The appropriate $F_{T(\Delta\sigma)}$ value can then be used to adjust matrix yield stress increments ($\Delta\sigma$) obtained within the irradiation temperature range 100 to 350°C.

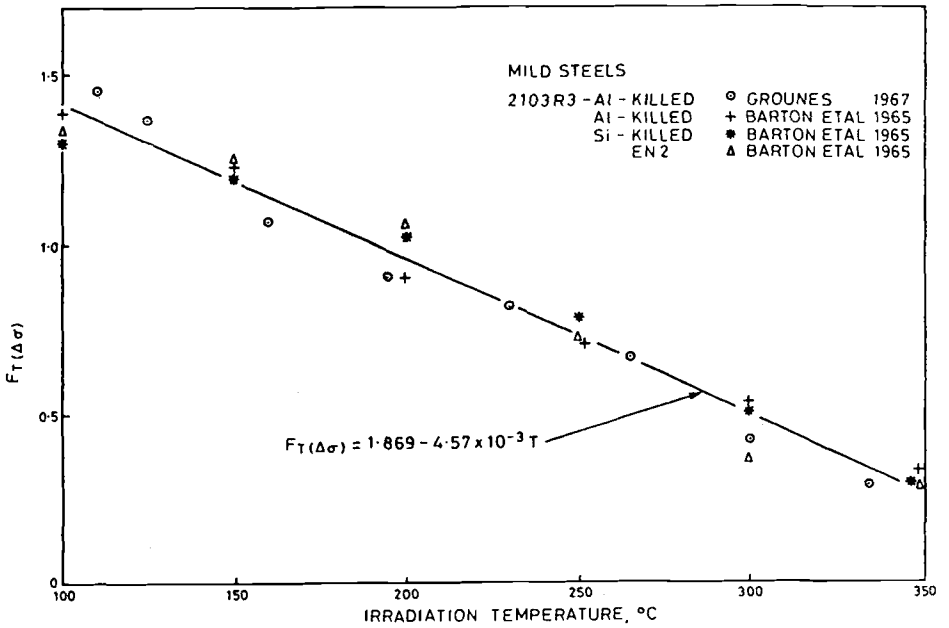


FIG.3 $F_{T(\Delta\sigma)}$ versus irradiation temperature for Si-killed and Al-killed mild steels. Data from yield stress changes normalised to $F_{T(\Delta\sigma)} = 1$ at 190°C

Irradiation temperature dependence of $F_{T(\Delta T)}$

If the transition temperature shift (ΔT) is to be adjusted for differing irradiation temperatures, it is necessary to redefine equation (6) in terms of the parameter $F_{T(\Delta T)}$. This may be done if there is constant value for the ratio between $\Delta\sigma$ and ΔT. For Magnox surveillance submerged-arc weld samples irradiated at temperatures up to 225°C, a linear relationship between ΔT_{40J} and $\Delta\sigma$ may be derived but the range of ΔT and $\Delta\sigma$ covered is restricted. A similar relationship has been

derived for accelerated irradiation results on submerged-arc welds using the data of Cowan and Fearnehough [19] for an irradiation temperature range of 150-275°C. Recently, results from accelerated irradiation tests on one particular submerged-arc weld composition were obtained over wide ranges of $\Delta\sigma$ and ΔT [14] to give a relation

$$\Delta T_{40J} = 0.765\ \Delta\sigma \tag{7}$$

where ΔT_{40J} is in °C and $\Delta\sigma$ is in MPa.

Similar forms of equation apply to other C-Mn steel product forms (plates, forgings, manual weld metals) or to other (alloyed) types of ferritic steel. Using eq (7) as an illustration

$$F_{T(\Delta T)} = \Delta T/\Delta T_{(190)} = 0.765\Delta\sigma/0.765\Delta\sigma_{(190)} = F_{T(\Delta\sigma)} \tag{8}$$

Hence the parameter $F_{T(\Delta T)}$ is identical to $F_{T(\Delta\sigma)}$ for all conditions where a constant proportionality between $\Delta\sigma$ and ΔT can be demonstrated.

Consequently the dose and temperature dependence of the Charpy transition shift, for post-peak conditions, can be written

$$\Delta T = AF_T(\phi t)^{0.5} + \Delta T_{Cu(peak)} \tag{9}$$

Validation of F_T using Published Data

Three comparisons with published data have been made in order to illustrate the validity of the derived irradiation temperature dependence factor (F_T).

Results of Grounes

This comparison makes use of the embrittlement data of Grounes [18] obtained using sub-size Charpy samples of the same Al-killed mild steel (2103/R3) used in the derivation of $F_{T(\Delta T)}$ above. In this steel the embrittlement contribution from Cu is negligible since the Cu content is only 0.05%. Figure 4 shows the modified matrix embrittlement coefficient, $A_{\Delta T}=\Delta T/0.53[\phi t(E>1MeV)/10^{18}]^{0.5}$ as evaluated by McElroy et al [20], as a function of irradiation temperature from 50°C to 335°C . The results for irradiations at and above 160°C show a consistent decrease with increasing temperature and were analysed using linear regression to give an estimate at 190°C of $A_{\Delta T} = 61.9$. This value was then multiplied by the appropriate value of F_T, from equation (6), to give the F_T trend line drawn on Figure 4. It is concluded that F_T is a good description of the effect of irradiation temperature on this steel.

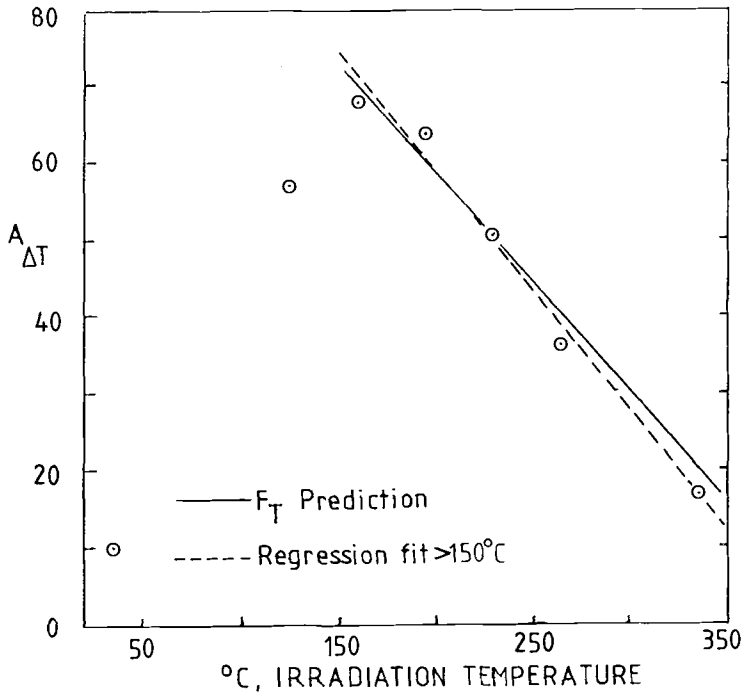


FIG.4 Irradiation temperature dependence of embrittlement parameter $A_{\Delta T}$ [18,20] compared with trend predicted by F_T

Results of Dufour, Lijbrink and Zijp

Dufour et al [21] studied the irradiation shifts obtained in Charpy tests on two similar steels of low Cu content made to the 1.2MD07 specification (derived from A302B). The chemical analyses are given in Table 1 and indicate that any influence of Cu precipitation will be small. The steels were irradiated at various temperatures from 150°C to 350°C under accelerated conditions in a loop in the HFR reactor at Petten. From the irradiation temperatures, shifts and dpa doses listed in a subsequent publication [22] the irradiation temperature dependence of the Charpy shift was obtained for a mean dose of 5.6 $\pm$ 1.2 mdpa (actual dose range 4.1 -7.9 mdpa), see Figure 5. Linear regression of these results gave an estimated Charpy shift at 190°C of $\Delta T = 86.6$°C. This value was then multiplied by the appropriate value of F_T, from equation (6), to give the F_T trend line drawn on Figure 5. Bearing in mind the dose variability between the data points, it is concluded that F_T is a reasonable description of the effect of irradiation temperature on these steels.

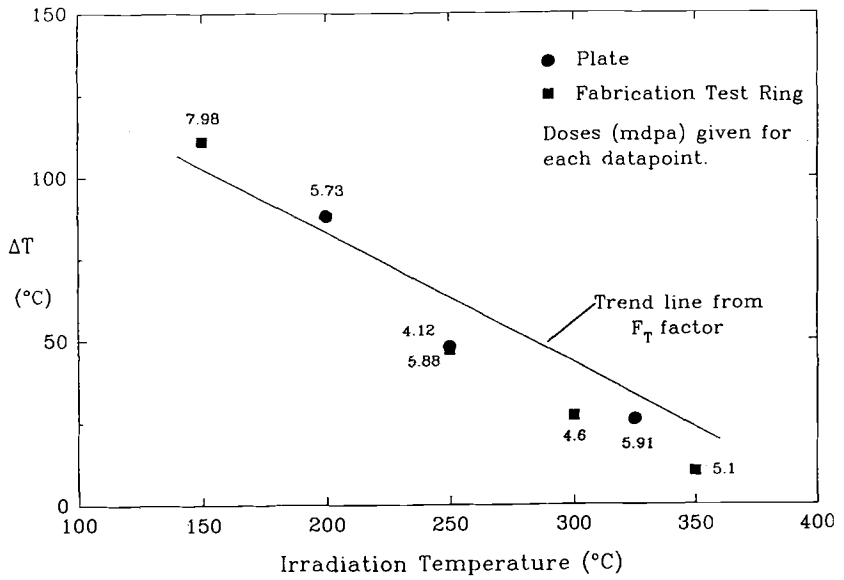


FIG.5 Irradiation temperature dependence of transition temperature shifts in 1.2MD07 steel in accelerated irradiations [21,22] compared with F_T prediction

Validation from low alloy steel weld data

An alternative method of testing the validity of F_T is to examine the post-peak properties of Cu-containing steels and to apply eq (9) to the irradiation embrittlement behaviour. An equation of similar form to (9) can be used to assess the irradiation hardening behaviour. Such tests would be particularly appropriate to the behaviour of submerged-arc weld metals which may have relatively high copper contents.

A suitable source of irradiation data on ferritic low alloy submerged-arc welds comes from the experiments of Williams et al [6]. Here numerous accelerated irradiations were performed at different temperatures on a series of low alloy steel submerged-arc reproduction welds. Although a fraction of the welds contained significant quantities of Ni, an element known to affect irradiation embrittlement and its temperature dependence [6], it was possible to identify welds with Ni < 0.15% in the database. Although these low Ni welds contained about 0.5% Mo, in all other respects the compositions were similar to Magnox vessel welds [9, 14]. The chemical analyses of the selected welds (Cu contents 0.07 - 0.56%) are shown in Table 1 [4, 23] together with a typical composition of a Magnox submerged-arc weld [14].

The pre-irradiation heat treatment for the low Ni welds involved weld austenitisation for 6 hours at 920°C, quenching, and then temper/stress relief cycles for 42 hours at 600°C and 6 hours at 650°C respectively [4]. Table 3 lists the data and exposure conditions together with the F_T factors derived from the irradiation temperatures using eq (6) [3, 4, 6, 23].

TABLE 3

Irradiation-Hardening (ΔH_v) and Embrittlement (ΔT_{41J}) for Low Alloy Submerged-Arc Reproduction Welds [4, 6, 23]

Irradiation	F_T	Dose (ϕt) dpa x 10^5	$F_T (\phi t)^{0.5}$ $(dpa \times 10^5)^{0.5}$	ΔH_v	ΔT_{41J} °C	Comment
Weld SH						
225	0.841	183	11.37	30.0	-	Pre-peak
225	0.841	1442	31.92	63.0	-	
225	0.841	2588	42.77	81.4	193.9	
255	0.704	201	9.97	30.7	57.3	Pre-peak
255	0.704	223	10.51	41.0	-	Pre-peak
255	0.704	816	20.10	56.3	120.6	
255	0.704	1924	30.86	65.4	153.8	
255	0.704	2318	33.87	70.7	178.0	
255	0.704	3228	39.97	74.8	174.8	
295	0.521	197	7.31	21.0	-	Pre-peak
295	0.521	986	16.35	47.5	105.6	
295	0.521	2524	26.16	51.6	125.5	
295	0.521	3130	29.14	52.0	-	
315	0.429	212	6.25	23.0	-	Pre-peak
315	0.429	875	12.70	45.2	86.2	
315	0.429	1232	15.07	43.1	97.4	
315	0.429	2532	21.61	47.0	-	
Weld 1W						
225	0.841	183	11.37	14.0	-	Pre-peak
225	0.841	1442	31.92	39.0	-	
225	0.841	2444	41.56	39.0	-	
255	0.704	127	7.93	-	27.4	Pre-peak
255	0.704	443*	14.81	23.5	50.9	
255	0.704	1587	28.03	-	97.0	
255	0.704	1645	28.54	38.4	113.2	
255	0.704	1790	29.77	31.0	-	
255	0.704	4178	45.48	55.6	146.7	
295	0.521	197	7.31	3.0	-	Pre-peak
295	0.521	906	15.68	15.0	-	
295	0.521	3130	29.14	32.0	-	
315	0.429	212	6.25	0	-	Pre-peak
315	0.429	826	12.34	17.0	-	
315	0.429	1149	14.56	17.0	-	
315	0.429	2532	21.61	51.0	-	
Weld SL						
225	0.841	211	12.21	8.7	42.5	
225	0.841	1442	31.92	31.0	-	
225	0.841	2588	42.77	42.7	121.4	
255	0.704	151	8.65	9.5	33.9	
255	0.704	919	21.33	25.0	75.0	
255	0.704	1388	26.21	33.7	86.4	
255	0.704	1790	29.77	23.0	-	
255	0.704	3195	39.77	51.9	112.6	
295	0.521	197	7.31	-	-	
295	0.521	906	15.68	3.0	-	
295	0.521	1426	19.67	20.8	55.8	
295	0.521	3130	29.14	26.0	-	
315	0.429	224	6.43	3.1	20.3	
315	0.429	826	12.34	9.0	-	
315	0.429	1149	14.56	7.0	-	
315	0.429	1734	17.88	15.4	41.4	
315	0.429	2663	22.16	17.9	57.0	
Weld SP						
255	0.704	78	6.21	4.8	33.0	
255	0.704	80	6.29	3.2	27.0	
255	0.704	319	12.57	10.0	46.0	
255	0.704	327	12.72	14.5	40.0	
255	0.704	1281	25.18	23.0	75.0	
255	0.704	1316	25.52	27.9	116.0	
255	0.704	3695	42.77	34.0	89.0	
255	0.704	3816	43.46	42.3	83.0	

In order to evaluate the matrix embrittlement from these results it is necessary to know the magnitude of the embrittlement due to Cu. This was done by subtracting the embrittlement exhibited by welds with a low Cu content from the embrittlement observed with a high Cu weld. Figure 6, reproduced from reference 4, shows the resulting embrittlement. The Cu contribution to embrittlement can be seen to be independent of irradiation temperature over the range 225°C to 315°C and independent of irradiation dose for doses exceeding about 0.008 dpa. In addition it can be concluded that there will only be a Cu contribution to embrittlement for welds with gross Cu contents exceeding 0.118%, the Cu content of weld SL.

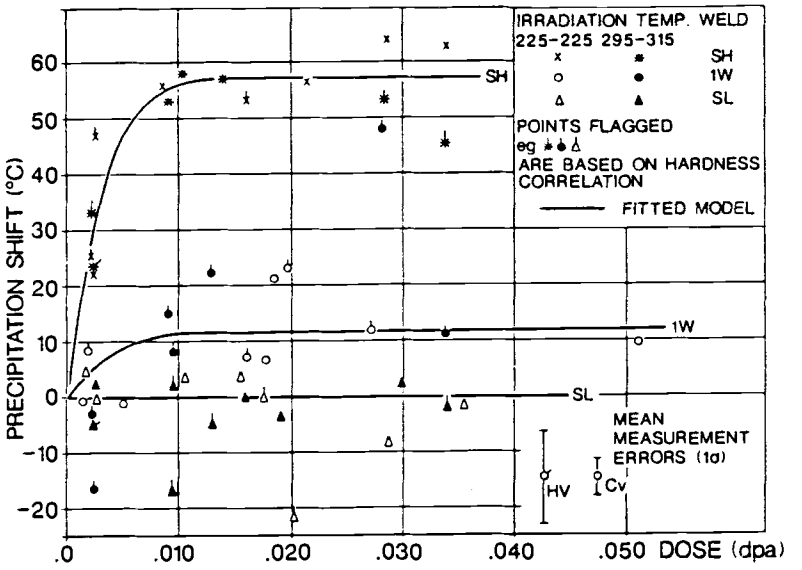


FIG.6 Precipitation shifts for low alloy submerged-arc reproduction welds SH, 1W and SL deduced by subtracting fitted model predictions for the matrix shift from the total measured shift (reproduced from Ref 6)

It follows that the magnitude and dose dependence of weld matrix embrittlement can be determined by examining, first, the results at doses exceeding 0.008 dpa for the welds with Cu > 0.118% (e.g. SH), and, second, the results at all dose levels for those welds where the Cu content is ineffective in enhancing embrittlement (e.g. SL and SP). Figure 7 shows examples of the dose dependence of the transition shift at various irradiation temperatures for welds SH and SL where the behaviour is defined by at least three shift results. The shifts have been plotted as a function of the square root of the dpa dose. This dose relation produces a reasonable representation of the data, as was found by Williams et al [4]. The matrix embrittlement values for weld SL varied with irradiation temperature in the expected manner.

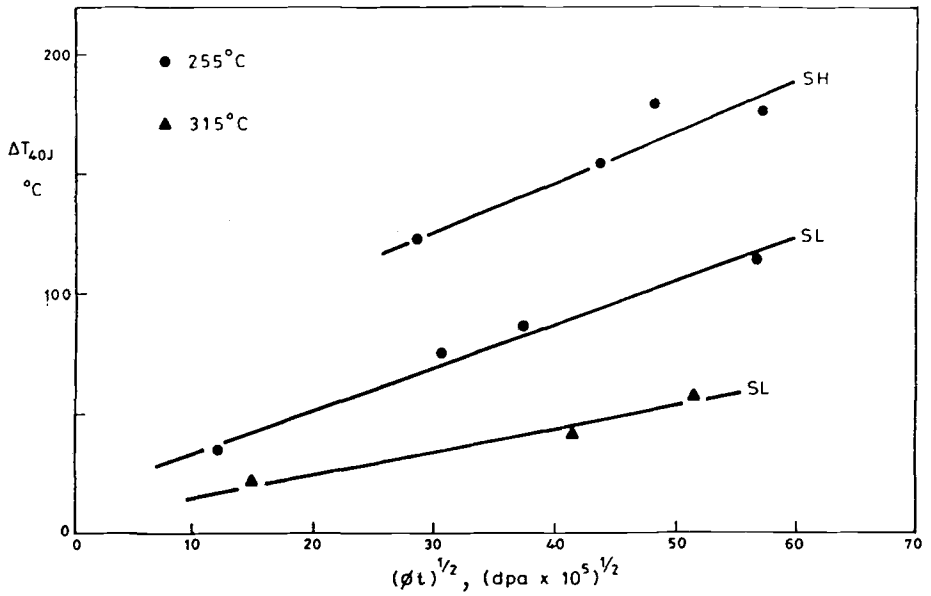


FIG.7 Transition temperature shifts for low alloy submerged-arc reproduction welds SL and SH as a function of $(\phi t)^{0.5}$, Cu content and irradiation temperature [3, 4, 6, 23]

All the data for SL and SP and the post-peak data for SH and 1W are plotted as a function of $F_T(\phi t)^{0.5}$ in Figure 8. For each weld the results of different temperatures are brought together, thus confirming eq (9). For welds SH and 1W, the Cu content affects the magnitude of ΔT_{Cu} whereas in welds SL and SP the value of ΔT_{Cu} is effectively zero. For welds SL and SP, but not for welds SH and 1W, there is evidence of a saturation in the matrix embrittlement behaviour at higher doses, as noted previously by Williams et al [4]. In terms of the temperature compensated dose parameter, saturation starts at a value of $F_T(\Phi t)^{0.5} > 30$.

The actual values of the weld matrix embrittlement parameter (A), obtained by least squares regression analysis, lie between 3.08 and 3.44 °C/(dpa * $10^5)^{0.5}$ and are relatively independent of weld composition.

Although no tensile hardening data are available to test eq (3), a similar analysis may be performed using the hardness changes (ΔH_v) listed in Table 3 as a function of irradiation dose and temperature in the equation

$$\Delta H_v = (A(\Delta H_v)\ F_T\ (\phi t)^{0.5} + \Delta H_{vCu} \qquad (10)$$

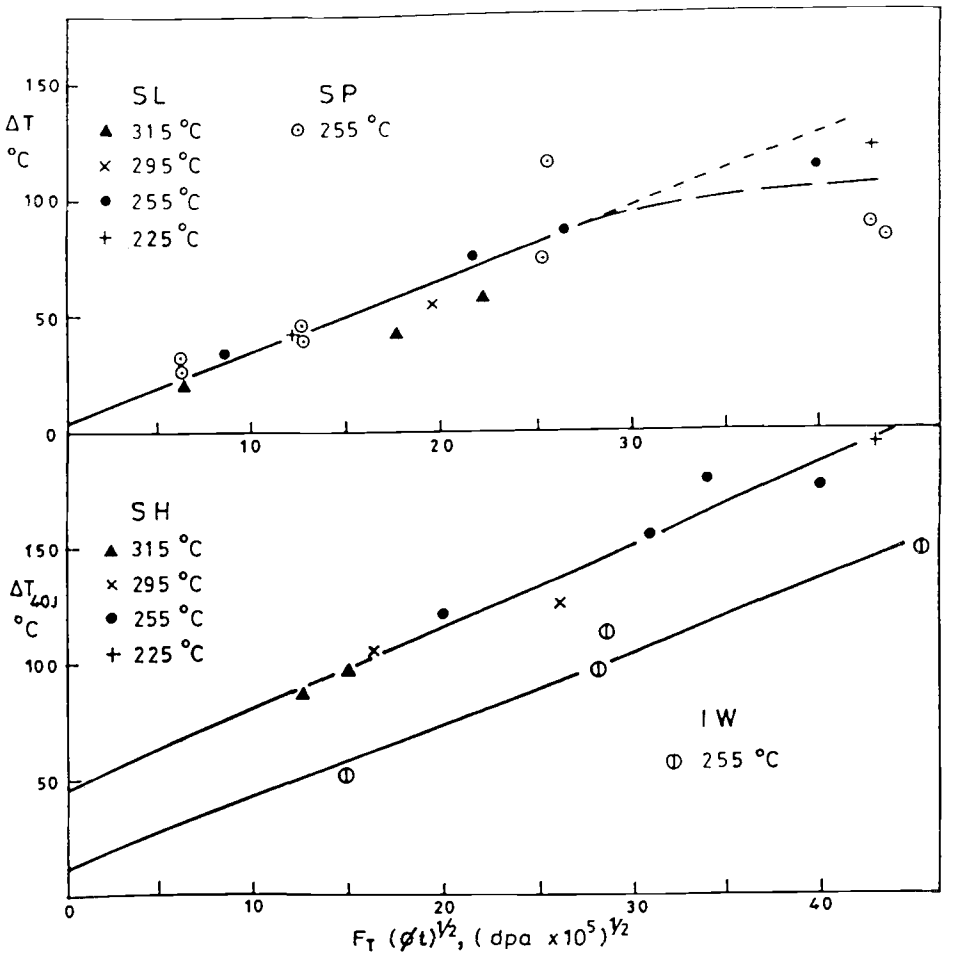


FIG.8 Transition temperature shifts for low alloy submerged-arc reproduction welds as a function of $F_T(\phi T)^{0.5}$ and Cu content [3, 4, 6, 23]. Data for welds SH, 1W, SL and SP

In Figure 9, ΔH_v is shown as a function of F_T $(\Phi t)^{0.5}$ for welds SH and 1W respectively at doses above 0.008dpa. Figure 9 includes a similar plot for the combined data of welds SL and SP without applying any dose restriction. In contrast to Figure 8 there is no sign of any saturation of the hardening in welds SL and SP. The value of ΔH_{vCu}increases with Cu content from a zero value for the combined data of SL and SP to about 20 ΔH_v for weld SH. The matrix hardening values $A(\Delta H_v)$ are relatively independent of composition and range from 1.03 to 1.21 $\Delta H_v/(dpa * 10^5)^{0.5}$.

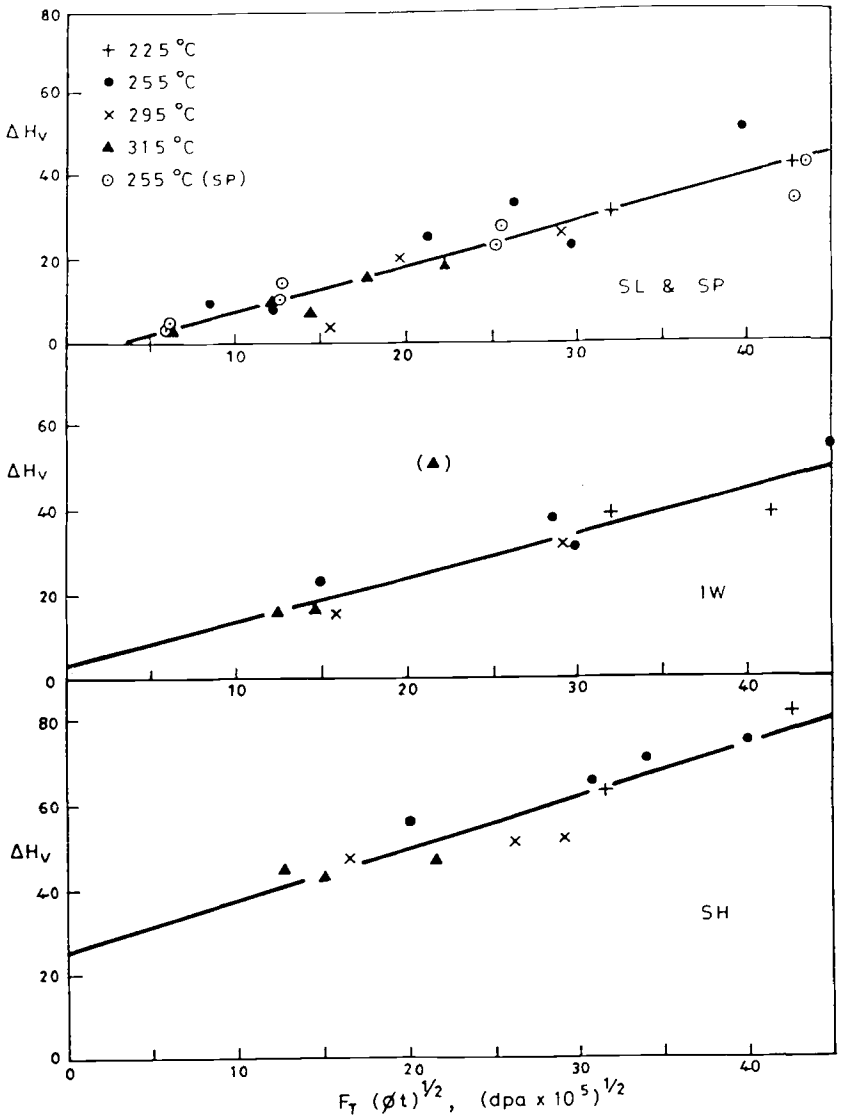


FIG.9 Vickers hardness shifts for low alloy submerged-arc reproduction welds as a function of $F_T(\phi t)^{0.5}$ and Cu content [3, 4, 6, 23]. Data for welds welds SH, 1W, SL and SP

It is concluded that embrittlement and hardening results for the low alloy submerged-arc welds provide convincing independent support for the form of trend curves described by eqs (9) and (10), and the temperature correction factor F_T (eq (6)), over the temperature range 225°C to 315°C.

COMPARISON OF F_T WITH OTHER TEMPERATURE DEPENDENCE FACTORS

Figure 10 compares the temperature dependence of F_T with the temperature factor described by Williams et al [6] and fitted to data over the range from 225°C to 315°C. Although there is reasonable correspondence between the factors over the irradiation temperature range from 200°C to 270°C, the F_T values are larger for all temperatures above and below this range. Consequently F_T gives more conservative estimates of embrittlement and hardening.

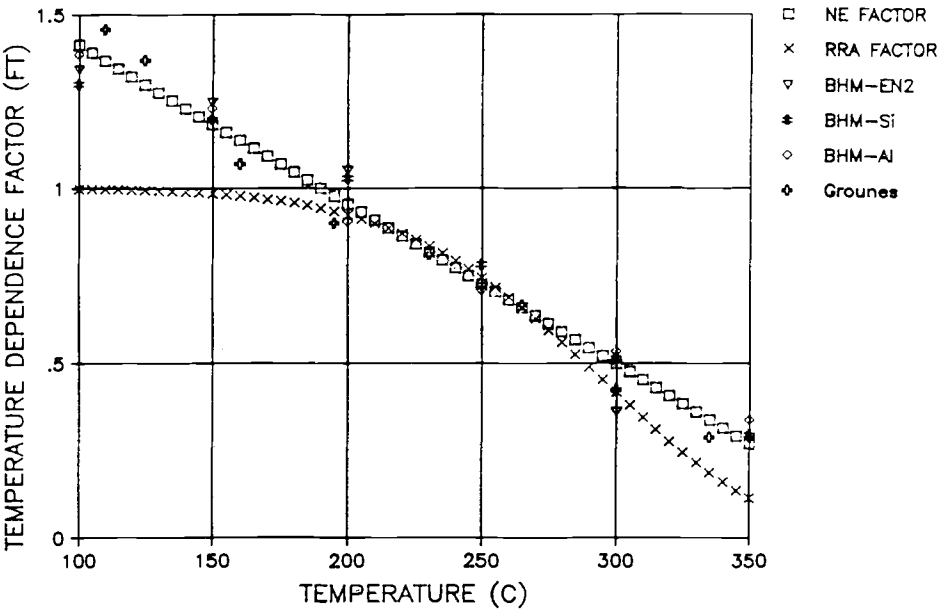


FIG.10 Comparison of Temperature Dependence Factors

CONCLUSIONS

(1) In steels and welds containing significant amounts of copper impurity, the experimentally observed invariance of the Cu particle size following full precipitation during irradiation at temperatures below 300°C has enabled simplified equations to be derived for the dose dependence of hardening and embrittlement. For irradiation embrittlement the equation is

$$\Delta T_T = A_T(\phi t)^{0.5} + \Delta T_{Cu(peak)}$$

For irradiation hardening ($\Delta\sigma_y$ or ΔH_v) the equations have a similar parametric form.

(2) The irradiation temperature dependence of the total hardening (and embrittlement) is due to the irradiation temperature dependence of the matrix hardening (and embrittlement), provided Cu precipitation is complete; the hardening (and embrittlement) contribution from fully precipitated Cu is independent of irradiation temperature below 300°C.

(3) The irradiation temperature dependence of matrix hardening ($F_{T(\Delta\sigma)}$), determined from published results on four different mild steels irradiated in experiments from 100 to 350°C using electrically heated and controlled rigs, is

$$F_{T(\Delta\sigma)} = 1.869 - 4.57 \times 10^{-3} T$$

(4) The irradiation temperature dependence of matrix embrittlement is the same as that for matrix hardening over the range of irradiation temperatures for which a constant proportionality between embrittlement and hardening can be demonstrated.

(5) The irradiation temperature dependence of embrittlement in several low Cu plate steels can be satisfactorily described by F_T over the temperature range from 150°C to 350°C.

(6) Accelerated irradiation data on low alloy steel submerged-arc welds provide strong support for F_T and the simplified embrittlement (and hardening) equations shown in conclusion (1).

(7) The use of the F_T factor reduces the differing values of matrix embrittlement observed at various irradiation temperatures for low alloy steel welds to a common value. A similar conclusion applies to matrix hardening behaviour.

(8) Embrittlement at irradiation temperatures between 150 and 300°C should be evaluated from submerged-arc weld data at doses exceeding that for peak copper precipitation using the equation

$$\Delta T_T = (1.869 - 4.57 \times 10^{-3} T)\, A\, (\Phi t)^{0.5} + \Delta T_{Cu(peak)}$$

where A is the matrix embrittlement parameter and $\Delta T_{Cu(peak)}$ is a constant. For irradiation hardening an analagous equation is applicable.

ACKNOWLEDGMENT

This paper is published by permission of Nuclear Electric plc and Rolls-Royce and Associates Limited.

REFERENCES

[1] "Effects of Residual Elements on Predicted Radiation Damage to Pressure Vessel Materials", Regulatory Guide RG 1.99 Revision 1, USNRC, 1977.

[2] Odette, G.R., "Recent Advances in Predicting Embrittlement of Reactor Pressure Vessel Steels", Proceedings of the Second International Symposium on the Environmental Degradation of Materials in Nuclear Power Systems - Water Reactors, Monterey, USA, 1985, J.T.A. Roberts, J.R. Weeks, and G.J. Theus, Eds, ANS, pp. 121-130.

[3] Williams, T.J., Thomas, A.F., Berrisford, R.A., Austin, M., Squires, R.L., and Venables, J.H., 1982, "The Influence of Neutron Exposure, Chemical Composition and Metallurgical Condition on the Irradiation Shift of Reactor Pressure Vessel Steels", ASTM STP 782, 343.

[4] Williams, T.H., Ellis, D., Swan, D.I., McGuire, J., and Whalley, S.P., "The Influence of Copper, Nickel and Irradiation Temperature on the Irradiation Shift of Low Alloy Steels", Proceedings of the Second International Symposium on the Environmental Degradation of Materials in Nuclear Power Systems - Water Reactors, Monterey, USA, 1985, J.T.A. Roberts, J.R. Weeks, and G.J. Theus, Eds, ANS, pp.393-399.

[5] Vishkarev, O.M., Zvezdin, Yu. I., Shamardin, V.K., and Tulyarkov, G.A., "Radiation Embrittlement of Soviet 1000-MW Pressurised Water Reactor Vessel Steel 15KH2NMFAA", Radiation Embrittlement of Nuclear Reactor Pressure Vessel Steels: An International Review (Fourth Volume), ASTM STP 1170, Lendell F. Steel, Ed. ASTM, Philadelphia, 1993 pp. 218-226.

[6] Williams, T. J., Burch, P. R., English, C. A., and Ray, P. H. N., "The Effect of Irradiation Dose Rate and Temperature, and Copper and Nickel Content, on the Irradiation Shift of Low Alloy Steel Submerged Arc Welds", Proceedings of the Third International Symposium on Environmental Degradation of Materials in Nuclear Power Systems - Water Reactors, Traverse City, 1987. The Metallurgical Society, 1988, p 121.

[7] Fisher, S. B., Harbottle, J. E., and Aldridge, N., "Radiation Hardening in Magnox Pressure Vessel Steels", Philosophical Transactions of the Royal Society of London, Vol.A315, 1985, p 301.

[8] Fisher, S. B., and Buswell, J. T., "A Model for PWR Pressure Vessel Embrittlement", International Journal of Pressure Vessels and Piping, Vol. 27, 1987, p 91.

[9] Buswell, J.T., and Jones, R.B., "The Modelling of Radiation Hardening and Embrittlement in Magnox Mild Steel Submerged-Arc Welds", Effects of Radiation on Materials: 16th International Symposium, ASTM STP 1175, American Society for Testing and Materials, Philadelphia, 1993, p 424.

[10] Odette, G.R., and Lucas, G., "Irradiation Embrittlement of Reactor Pressure Vessel Steels: Mechanisms, Models, and Data Correlations", Radiation Embrittlement of Nuclear Reactor Pressure Vessel Steels: An International Review (Second Volume), ASTM STP 909, American Society for Testing and Materials, Philadelphia, 1986, p.206.

[11] Makin, M.J., and Minter, F.J., Irradiation Hardening in Copper and Nickel, 1960, Acta Met., 8, 691.

[12] Jones, R.B., 1989, Presentation at International Working Group on Irradiation Damage Mechanisms, Helsinki, Finland.

[13] Buswell, J.T., Bischler, P.J.E., Fenton, S.T., Ward, A.E., and Phythian, W.J., "Microstructural Developments in Neutron Irradiated Mild Steel Submerged-Arc Weld Metal", Proceedings of Conference on the Evolution of Microstructure in Metals During Irradiation", Minett, Muskoka, Canada, Sept/Oct. 1992.

[14] Buswell, J.T., Bolton, C.J., Wootton, M.R., Bischler, P.J.E., Jones, R.B., Jones, L.T., Phythian, W.J., and Sinclair, R.N., "The Radiation Hardening and Embrittlement of a Mild Steel Submerged-Arc Weld", Effects of Radiation on Materials: Sixteenth International Symposium, ASTM STP 1175, American Society for Testing and Materials, Philadelphia, 1993.

[15] Barton, P.J., Harries, D.R., and Mogford, I.L., "Effects of Neutron Dose Rate and Irradiation Temperature on Radiation Hardening in Mild Steels", Journal of The Iron and Steel Institute, Vol. 203, 1965, p.507.

[16] Harries, D.R., and Eyre, B.L., "Effects of Irradiation on Steels", Flow and Fracture in Nuclear Environment, ASTM STP 380, 1965, pp.105-119.

[17] Barton, P.J., Harries, D.R., and Mogford, I.L., "Effects of Neutron Dose Rate and Irradiation Temperature on Radiation Hardening in Mild Steels", UKAEA Report, AERE-R4489, 1963.

[18] Grounes, M., "Review of Swedish Work on Irradiation Effects in Pressure Vessel Steels and Significance of Data Obtained", ASTM STP 426, 1967, pp.224.

[19] Cowan, A., and Fearnehough, G.D., "Progress Report on Irradiation Experiments on Ferritic Steels", UKAEA Memo TRG 2679(C), 1965.

[20] McElroy, R.J., Williams, T.J., Boydon, F.M.D., and Hemsworth, B., 1990, "Low Temperature Embrittlement of LWR RPV Support Structures", NEA/CSNI Workshop Proceedings, 1990 pp.311-364.

[21] Dufour, L.B., Ljbrink, E., and Zijp, W.L., "Results of the Steel Surveillance Programme for the Pressure Vessel of the Dutch 50 Dodewaard BWR", Proceedings of the IAEA Specialists Meeting on Irradiation Embrittlement, Thermal Annealing and Surveillance of RPVs, Vienna 1979, pp 97-111.

[22] Zijp, W.L., and Aaldijk, J.K., "Results of a Netherlands Experience in Pressure Vessel Surveillance", Proceedings of the Third ASTM-Euratom Symposium on Reactor Dosimetry, Ispra, Italy, EUR 6813(1), 1980, pp.510-517.

[23] Williams, T.J., 1991, unpublished work.

Igor Remec,[1] Jy-An Wang,[1] and Frank B. K. Kam[2]

HFIR STEELS EMBRITTLEMENT: THE POSSIBLE EFFECT OF GAMMA FIELD CONTRIBUTION

REFERENCE: Remec, I., Wang, J. A., and Kam, F. B. K., **"HFIR Steels Embrittlement: The Possible Effect of Gamma Field Contribution,"** *Effects of Radiation on Materials: 17th International Symposium, ASTM STP 1270,* David S. Gelles, Randy K. Nanstad, Arvind S. Kumar, and Edward A. Little, Eds., American Society for Testing and Materials, 1996.

ABSTRACT: Recent comprehensive dosimetry experiments revealed the presence of an intense gamma field at the High Flux Isotope Reactor (HFIR) surveillance locations near the pressure vessel. Measured responses of fission dosimeters ^{238}U and ^{237}Np, as well as ^{9}Be helium accumulation fluence monitors were placed in accordance with responses of threshold and thermal neutron activation dosimeters only when photofission and photo-neutron reactions, respectively, were taken into account. Gamma-flux (E > 1MeV)-to-neutron-flux (E > 1MeV) ratios as high as 10^4 were observed.

It has been generally accepted that neutron interactions with materials are the main cause of changes in mechanical properties of ferritic steels in nuclear reactor environments. However, gamma rays can also create displaced atoms that can in turn contribute to material embrittlement. Gamma-induced displacements may be quite negligible when compared with neutron-induced displacements in most irradiations, and need not be taken into account. However, at the HFIR surveillance position the gamma-induced atom displacement rate dominates or at least equals the neutron-induced atom displacement rate. When the sum of neutron- and gamma-induced displacements per atom is used as an irradiation exposure parameter the HFIR surveillance results are in agreement with other test reactor results. The "accelerated embrittlement" phenomenon, therefore, appears to be caused by the previously unaccounted atomic displacements induced by gamma rays. However, independent verification that gamma-induced displacements can cause material embrittlement is necessary.

KEYWORDS: High Flux Isotope Reactor, steel embrittlement, neutron field, gamma field, displacements per atom

[1]Research scientist, Oak Ridge National Laboratory, P.O.Box 2008, Oak Ridge, TN 37831-8250.
[2]Research scientist and leader of Radiation Effects, Shielding & Dosimetry Group, Oak Ridge National Laboratory, P.O.Box 2008, Oak Ridge, TN 37831-8250.

Copyright© 1996 by ASTM International www.astm.org

The High Flux Isotope Reactor (HFIR) is a high-flux light-water-cooled, low-temperature (50°-70°C) research reactor at the Oak Ridge National Laboratory that began operation in 1965 [1]. The compact cylindrical core (50-L) with a high-power density (2 MW/L) is surrounded by a 0.3-m-thick cylindrical reflector of beryllium and contained in a large (approximately 2.44-m-diameter) pressure vessel (PV). An approximately 0.6-m-wide annulus between the beryllium reflector and the PV is filled with light water. A horizontal cross section of HFIR is shown in Fig. 1. The cylindrical part of the PV was rolled from a single 73-mm-thick plate of A212 grade B (A212B) carbon steel plate. It contains a single longitudinal seam weld and is clad with stainless steel. A hemispherical bottom head is welded to the shell. The beam tube nozzles were forged of either A105 grade II (A105II) or A350 grade LF3 (A350LF3) steels, chosen for their relatively low nil-ductility transition temperature (NDTT). The pressure vessel was designed for 20 effective full-power years of operation at the reactor power of 100 MW.

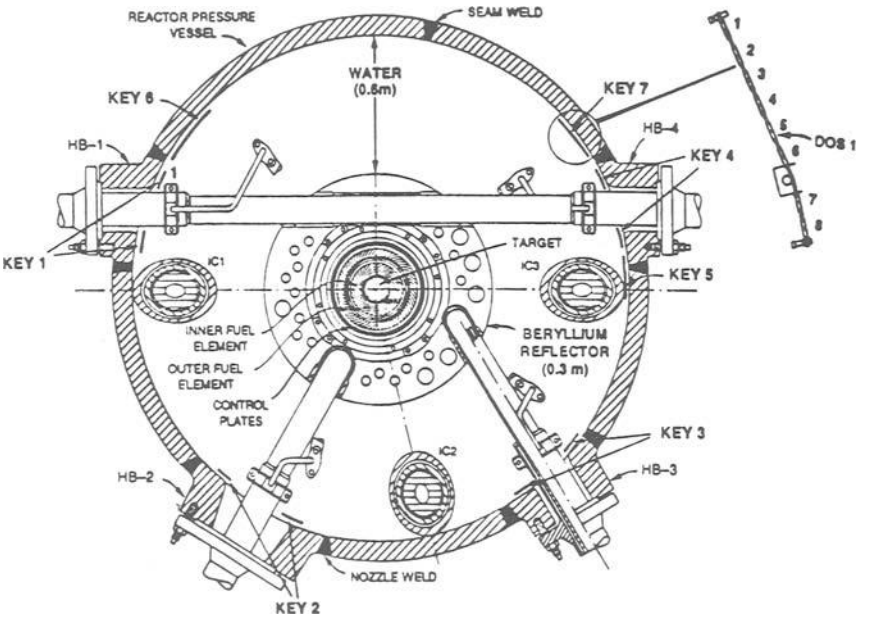


FIG. 1--Horizontal cross section of HFIR showing locations of surveillance capsules identified by "key" numbers.

The HFIR pressure vessel surveillance program is based on measurements of ductile-to-brittle transition temperature obtained from Charpy V-notch (CVN) specimens [2]. Surveillance capsules, each containing three CVN specimens, are irradiated at locations, referred to as keys, shown in Fig. 1. All capsules are positioned near the inner surface of the vessel. Shell specimens (material A212B) are placed along an azimuthal line at the core mid-plane (keys 6 and 7) and just below mid-plane (key 5). Specimens of nozzle materials (forging steels A350LF3 and A105II) are mounted in a ring around each beam tube (keys 1 to 4). In late 1986, surveillance program results indicated that the radiation-

induced embrittlement was significantly greater than had been anticipated on the basis of data from materials testing reactors (MTRs) [3]. The phenomenon is illustrated in Fig. 2 and is known as "accelerated embrittlement." HFIR, which was temporarily shut down because the original criterion for safe PV operation was exceeded, was allowed to resume operation in 1989, after thorough PV safety analysis had demonstrated that it could be operated safely [3]. During the planned 10-year extension of operation the core power level was reduced to 85 MW, a hydrostatic proof test of the vessel was instituted, and the surveillance program was augmented.

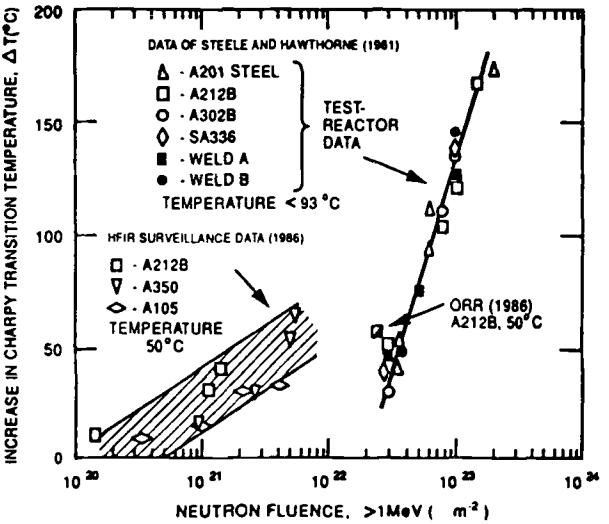


FIG.2--Comparison of HFIR surveillance and ORR data with test reactor irradiations of similar materials at temperatures < 93°C.

Investigations into the causes of the accelerated embrittlement, which started soon after it was discovered, were of interest for the future of HFIR, for understanding the mechanisms of radiation-induced embrittlement and, perhaps most important, for assessing the life expectancy for supports of some light-water commercial power reactor vessels, which are exposed to fast-neutron fluxes and irradiation temperatures that are about the same as for HFIR surveillance specimens [4]. The search for the causes of the accelerated embrittlement has centered on the effects of low flux (low atomic displacement rate), softened neutron spectrum, and boron and copper impurities in steel [4-7]. Each of these suspects has been carefully examined, using a combination of experiments and modeling, and none of them has been found to offer a satisfactory explanation of the accelerated embrittlement [7].

NEW DOSIMETRY EXPERIMENTS AND ANALYSIS

In 1992 a neutron dosimetry experiment (DOS 1) of a HFIR surveillance site was performed, with the primary goal of providing reliable thermal flux values [8]. For DOS 1 key 7, position 5, was chosen, because most of the specimens of the material A212B, which has the highest NDTT and the highest adjusted reference temperature, were

irradiated at this location. In the DOS 1 experiment, the thermal flux values were derived from cobalt and silver dosimeters and from lithium and boron helium accumulation fluence monitors (HAFMs). Values obtained from different dosimeters were consistent and in fair agreement with the thermal flux from new transport calculations [9].The fast neutron monitors used were nickel (Ni), neptunium (^{237}Np) and beryllium helium accumulation fluence monitors (Be HAFMs). Fast-neutron flux determined from the Ni dosimeters was consistent with the values obtained earlier from the stainless steel monitors used in the surveillance program and with the fast-flux value from transport calculations. But the ^{237}Np dosimeter and Be HAFMs gave fast fluxes that were 17 and 15 times higher, respectively. Measurements were carefully checked, and experimental error was ruled out.

In order to clarify the situation, further comprehensive dosimetry experiments, named DOS 2 and DOS 3, were performed in 1993. Each experiment consisted of 4 capsules, which were irradiated at key 7, position 5; key 2, position 9; and key 4, position 2 and 10 [10]. Each capsule contained threshold activation monitors of nickel, aluminum, titanium, copper, and iron and thermal monitors of scandium, cobalt, and gold. In addition, in the DOS 3 experiment the fission monitors ^{235}U, ^{238}U and ^{237}Np were used as radiometric monitors and as solid-state track recorders. Be HAFMs were used in the DOS 2 experiment and in one location of the DOS 3 experiment. In the DOS 2 experiment dosimeters were "bare," and in the DOS 3 experiment a 0.10-mm gadolinium cover was used to shield thermal neutrons.

The DOS 2 and DOS 3 results confirmed the findings of the DOS 1 experiment. The reaction product concentrations of fission monitors ^{238}U, ^{237}Np, and Be HAFMs were reproducible, but were again inconsistent with the responses of other fast- and thermal-neutron dosimeters. A comparison of measured and calculated reaction rates for these monitors are given in Table 1. The measured-to-calculated (M/C) reaction-rate ratios for ^{238}U, ^{237}Np, and Be HAFMs are much higher than M/C for Ni dosimeters or other threshold dosimeters not shown in Table 1. Complete dosimetry results are given in ref. 10.

Because of the large number of measured responses and different monitors used (e.g., for key 7, position 5, more than 65 measured reaction rates were available), it was believed that the neutron spectrum could be reliably determined when the measurements were combined with calculated neutron spectrum through the adjustment procedure. However, as expected, in the adjustment calculations, for which the LSL-M2 computer code [11] was used, the responses of ^{238}U, ^{237}Np, and Be HAFMs, were found to be inconsistent with other measurements and were consequently rejected. Therefore, reproducible and accurately measured responses of ^{238}U, ^{237}Np, and Be HAFMs remained incompatible with adjusted neutron spectrum, which was also accurately and reliably determined.

It is well known that fission monitors are sensitive not only to neutrons but also to gamma rays with sufficiently high energy. Measured fission product activities contain the contributions from both neutron- and gamma-induced fissions. Similarly, helium accumulated in the Be HAFMs can be generated by neutron-induced reactions [^{9}Be (n,α) ^{6}He --> ^{6}Li; ^{9}Be (n,2n) ^{8}Be (2α) and ^{9}Be(n,d)^{8}Li --> ^{8}Be(2α)] and photo-neutron reaction [^{9}Be (γ,n) ^{8}Be (2α)]. However, findings in the literature [12, 13] indicated that contributions of the gamma-induced reactions in fission monitors remain relatively low, typically of the order of a few percent of the total activity, and may eventually reach up to approximately 20%, and would therefore not be sufficient to explain HFIR dosimetry results.

TABLE 1--Comparison of measured and calculated reaction rates for fission and Be monitors.

	Measured[a]	Calculated[b]	M/C[c]	M/C for Ni monitor
Key 7.5				
Be (n,x) He (DOS 1)	$1.46\ 10^{-15}$	$7.60\ 10^{-17}$	19.2	1.35 Top[d]
Be (n,x) He (DOS 2)	$1.44\ 10^{-15}$	$7.60\ 10^{-17}$	18.9	1.42 Bot.[e]
Be (n,x) He (DOS 2)	$1.42\ 10^{-15}$	$7.60\ 10^{-17}$	18.7	
Be (n,x) He (DOS 3)	$1.46\ 10^{-15}$	$7.60\ 10^{-17}$	19.3	
$^{238}U(n,f)$	$1.60\ 10^{-15}$	$6.24\ 10^{-17}$	25.6	
$^{237}Np(n,f)$	$4.59\ 10^{-15}$	$2.25\ 10^{-16}$	20.4	
$^{238}U(n,f)$ SSTR[f]	$1.36\ 10^{-15}$	$6.24\ 10^{-17}$	21.8	
$^{237}Np(n,f)$SSTR	$4.75\ 10^{-15}$	$2.25\ 10^{-16}$	21.1	
$^{235}U(n,f)$	$7.75\ 10^{-15}$	$8.13\ 10^{-15}$	1.0	
$^{235}U(n,f)$ SSTR	$1.50\ 10^{-14}$	$8.13\ 10^{-15}$	1.8	
Key 2.9				
Be (n,x) He	$1.82\ 10^{-15}$	$2.84\ 10^{-16}$	6.4	1.47 Top
Be (n,x) He	$2.19\ 10^{-15}$	$2.84\ 10^{-16}$	7.7	2.90 Bot.
$^{238}U(n,f)$	$2.74\ 10^{-15}$	$2.69\ 10^{-16}$	10.2	
$^{237}Np(n,f)$	$9.57\ 10^{-15}$	$1.15\ 10^{-15}$	8.4	
$^{238}U(n,f)$ SSTR	$2.01\ 10^{-15}$	$2.69\ 10^{-16}$	7.5	
$^{237}Np(n,f)$SSTR	$8.62\ 10^{-15}$	$1.15\ 10^{-15}$	7.5	
$^{235}U(n,f)$	$2.85\ 10^{-13}$	$2.05\ 10^{-13}$	1.4	
Key 4.2				
Be (n,x) He	$1.38\ 10^{-15}$	$1.12\ 10^{-16}$	12.3	0.91 Top
$^{238}U(n,f)$	$1.48\ 10^{-15}$	$1.11\ 10^{-16}$	13.3	1.60 Bot.
$^{237}Np(n,f)$	$6.84\ 10^{-15}$	$5.41\ 10^{-16}$	12.6	
$^{238}U(n,f)$ SSTR	$1.65\ 10^{-15}$	$1.11\ 10^{-16}$	14.9	
$^{237}Np(n,f)$SSTR	$6.08\ 10^{-15}$	$5.41\ 10^{-16}$	11.2	
$^{235}U(n,f)$	$5.46\ 10^{-13}$	$3.48\ 10^{-13}$	1.6	
$^{235}U(n,f)$ SSTR	$5.97\ 10^{-13}$	$3.48\ 10^{-13}$	1.7	
Key 4.10				
Be (n,x) He	$7.96\ 10^{-16}$	$2.08\ 10^{-16}$	3.8	0.69 Top
$^{238}U(n,f)$	$1.62\ 10^{-15}$	$1.90\ 10^{-16}$	8.5	1.37 Bot.
$^{237}Np(n,f)$	$6.52\ 10^{-15}$	$8.51\ 10^{-16}$	7.7	
$^{238}U(n,f)$ SSTR	$1.29\ 10^{-15}$	$1.90\ 10^{-16}$	6.8	
$^{237}Np(n,f)$SSTR	$5.66\ 10^{-15}$	$8.51\ 10^{-16}$	6.7	
$^{235}U(n,f)$	$5.45\ 10^{-13}$	$3.89\ 10^{-13}$	1.4	
$^{235}U(n,f)$ SSTR	$6.98\ 10^{-13}$	$3.89\ 10^{-13}$	1.8	

[a]Reaction rate per atom per second, including neutron and gamma reactions.
[b]Reaction rate per atom per second, for neutron reactions only.
[c]Measured-to-calculated reaction rate ratio.
[d]Measured-to-calculated reaction rate ratio, for Ni monitor close to the top of the capsule.
[e]Measured-to-calculated reaction rate ratio, for Ni monitor close to the bottom of the capsule.
[f]Solid State Track Recorder.

Nevertheless, the results from one- dimensional coupled neutron-gamma transport calculation, which were available, were used to calculate the gamma-induced and neutron-induced reaction rates for the above-mentioned dosimeters. Figure 3 shows the calculated neutron-induced and gamma-induced fission reaction rates for ^{237}Np. Similar radial distributions were observed for ^{238}U and Be HAFM. In or near the reactor core the neutron-induced reaction rate is much higher than the gamma-induced reaction rate in Np; therefore, the latter can be neglected. This holds for most, if not all, reactors. Going outwards from the core towards the pressure vessel, in thick layers of low-Z materials (e.g., ordinary or heavy water, beryllium), the neutron flux is attenuated more rapidly than the flux of energetic gamma rays. Gamma-induced reaction rates become increasingly important and can exceed neutron-induced reaction rates. At HFIR surveillance locations gamma- induced reactions strongly dominate the responses of ^{238}U, ^{237}Np, and Be HAFMs. For these dosimeters, the ratio of neutron-induced reaction rates to the total, that is, neutron- and gamma-induced reaction rates, as obtained from one-dimensional coupled neutron-gamma calculation, for key 7, position 5, is given in Table 2. It can be seen that for Be HAFMs, ^{238}U, and ^{237}Np the neutron-induced reactions contribute only 4.5% to 6.1% of the total reaction rate, while the remaining 94% to 96% is due to the gamma-induced reactions.

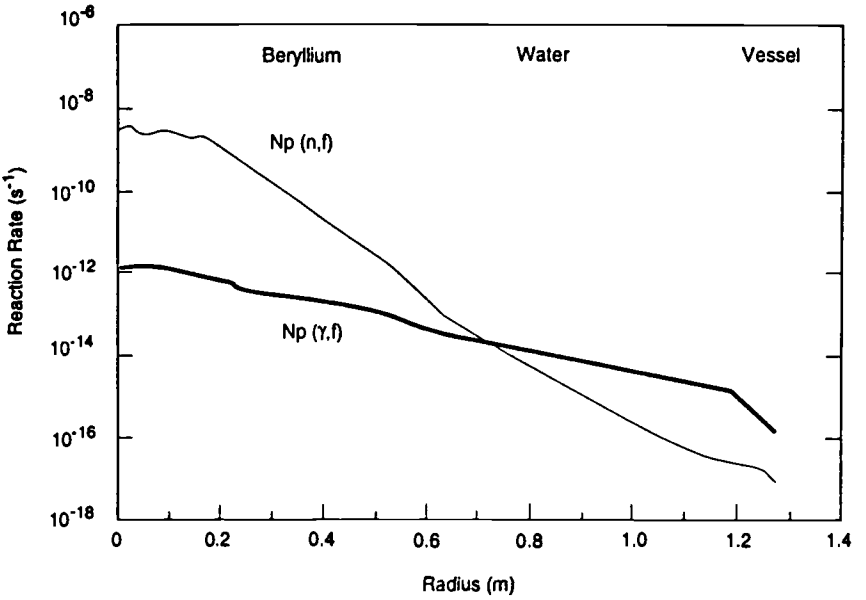


FIG.3--The neutron- and gamma-induced fission rate in ^{237}Np, as obtained from one dimensional coupled neutron-gamma transport calculation, plotted versus radial distance from the vertical axis of the HFIR core.

The gamma-to-neutron reaction rate ratios found were much higher than have ever been reported before in reactor pressure vessel dosimetry experiments, and thus necessitated additional verification. An experiment, called DOS 4, was performed at key 7, position 5, to measure the gamma field. Several sets of polychlorostyrene film were irradiated and based on the optical densities measured, the absorbed dose (silicon

dose) was determined [10]. The measured absorbed gamma dose rate was found to be consistent with the gamma field used to calculate the above-mentioned photo-fission and photo-neutron reaction rates. However, most of the absorbed dose in silicon is due to gamma rays below the threshold for photo-induced reactions in ^{238}U, ^{237}Np, and ^{9}Be. No correction was made for the polychlorostyrene drop in sensitivity (approximately 20%) caused by the irradiation temperature.

TABLE 2 --Ratio of neutron-induced reaction rate to the sum of neutron- and gamma-induced reaction rate (R_n/ (R_n + R_γ)) for key 7, position 5, obtained from one-dimensional coupled neutron-gamma transport calculation. Measured and calculated reaction rates are given also.

	Measured, $s^{-1}atom^{-1}$	Calculated[a], $s^{-1}atom^{-1}$	M/C[b]	$R_n/(R_n+R_\gamma)$	Corrected M/C
Be (n,x) He DOS 1	$1.46\ 10^{-15}$	$7.60\ 10^{-17}$	19.2	0.045	0.9
Be (n,x) He DOS 2	$1.44\ 10^{-15}$	$7.60\ 10^{-17}$	18.9	0.045	0.9
Be (n,x) He DOS 2	$1.42\ 10^{-15}$	$7.60\ 10^{-17}$	18.7	0.045	0.8
Be (n,x) He DOS 3	$1.46\ 10^{-15}$	$7.60\ 10^{-17}$	19.3	0.045	0.9
^{238}U (n,f)	$1.60\ 10^{-15}$	$6.24\ 10^{-17}$	25.6	0.055	1.4
^{237}Np (n,f)	$4.59\ 10^{-15}$	$2.25\ 10^{-16}$	20.4	0.061	1.3
^{238}U (n,f) SSTR[c]	$1.36\ 10^{-15}$	$6.24\ 10^{-17}$	21.8	0.055	1.2
^{237}Np (n,f)SSTR	$4.75\ 10^{-15}$	$2.25\ 10^{-16}$	21.1	0.061	1.3
^{235}U (n,f)	$7.75\ 10^{-15}$	$8.13\ 10^{-15}$	1.0	0.822	0.8
^{235}U (n,f) SSTR	$1.50\ 10^{-14}$	$8.13\ 10^{-15}$	1.8	0.822	1.5

[a]Calculated neutron-induced reaction rate.
[b]Ratio of measured to neutron-induced calculated reaction rate.
[c]Solid State Track Recorder.

Knowing that measured responses of the ^{238}U, ^{237}Np, and Be HAFMs are dominated by photo-reactions, the options for the determination of the neutron irradiation exposure parameters through the adjustment procedure are
A. to perform adjustment with all the dosimeters without corrections for photo-reactions,
B. to apply calculated photo-reaction corrections and to use all the dosimeters in the adjustment, and
C. to perform the simultaneous adjustment of neutron and gamma spectrum with all the dosimeters.

In approach **A** the ^{238}U, ^{237}Np, and Be HAFMs (not corrected) were found to be inconsistent with responses of other dosimeters and were rejected. Adjustment was done with the remaining dosimeters. Approach **B** has the disadvantage that large photo-reaction corrections are applied to the ^{238}U, ^{237}Np, and Be HAFMs. Such large corrections to a few monitors may be hard to accept and may be suspected to distort the results, but the consistency of the corrected reaction rates with the other dosimeters can be assessed, and, if verified, can support the procedure used to obtain the corrections.

Approach **C** represents modification and improvement of the current adjustment methodology. In short, the equation used to calculate the neutron-induced reaction rates is exactly the same as the equation to calculate the photo-induced reaction rates. Therefore, by adding the gamma spectrum and cross-section set to the neutron set, the two can be adjusted simultaneously. This approach has several advantages: no

corrections for gamma contribution to the measured reaction rates are necessary; gamma monitors (e.g., polychlorostyrene film) responses can be added to the neutron monitors measurements; and both neutron and gamma irradiation parameters are determined (e.g., neutron and gamma fluxes, and displacement per atom rates). The disadvantages are that more input data are necessary, namely calculated gamma spectrum and cross sections for gamma reactions. Also, some assumptions need to be made regarding the gamma spectrum covariance matrix.

In Table 3, adjusted irradiation parameters for the reactor core power of 85 MW, at key 7 position 5, obtained following the approaches A, B and C described above, are given in columns labeled A, B and C respectively. Values of any neutron irradiation parameter obtained by the three different adjustment runs agree within the standard deviations. This agreement shows that the large set of dosimeters, which does not need photo-reaction corrections, anchors the adjusted neutron flux values (approach A). Adding a few measured reaction rates corrected for gamma-induced contributions does not alter significantly the results (column B), but since the corrected reaction rates are consistent with the others, this indicates that the corrections applied are appropriate. Finally, simultaneous neutron and gamma adjustment (column C) gives neutron irradiation parameters that agree well with the values from the other two runs, thus showing the feasibility of this new adjustment technique. Besides, gamma fluxes and the gamma-induced dpa rate are also provided. The gamma flux (E > 1 MeV) is more than four orders of magnitude higher than the neutron flux (E > 1 MeV), and the gamma flux (E > 3 MeV) is still more than 3000 times higher than the fast neutron flux. Consequently, the gamma-induced dpa rate is approximately five times higher than the neutron-induced dpa rate. The neutron-induced dpa rate was calculated by folding adjusted neutron multigroup spectra with the ASTM dpa cross section for iron [14] and the gamma-induced dpa rate was calculated by folding adjusted gamma fluxes by Baumann's [15] gamma dpa cross section for iron.

TABLE 3--Irradiation parameters at key 7, position 5, obtained from different adjustment runs.

	A		B		C	
	Value, $m^{-2}s^{-1}$	σ, %	Value, $m^{-2}s^{-1}$	σ, %	Value, $m^{-2}s^{-1}$	σ, %
NEUTRON						
$\phi_{E > 1\ MeV}$	$1.58\ 10^{12}$	± 8	$1.49\ 10^{12}$	± 6	$1.58\ 10^{12}$	± 8
$\phi_{E > 0.1\ MeV}$	$2.34\ 10^{12}$	± 11	$2.24\ 10^{12}$	± 9	$2.37\ 10^{12}$	± 11
$\phi_{E \leq 0.4\ MeV}$	$2.71\ 10^{12}$	± 19	$3.09\ 10^{12}$	± 19	$3.11\ 10^{12}$	± 19
dpa^a	$2.47\ 10^{-13}$	± 7	$2.36\ 10^{-13}$	± 5	$2.50\ 10^{-13}$	± 7
GAMMA						
$\phi_{E > 5\ MeV}$					$1.99\ 10^{15}$	± 9
$\phi_{E > 3\ MeV}$					$4.91\ 10^{15}$	± 12
$\phi_{E \geq 1\ MeV}$					$1.71\ 10^{16}$	± 9
dpa^a					$1.22\ 10^{-12}$	± 7

[a]Displacement per atom rate; units are s^{-1}.

Similar analyses, as presented for the key 7 above, were done for all the locations analyzed, and it was found that the gamma-induced dpa rate is equal to or exceeds the neutron-induced dpa rate at all locations. Ratios of gamma-to-neutron induced dpa rates of 5.2, 1.2, 1.9 and 1.0 were found for key 7, position 5, key 2, position 9, key 4 position 2, and key 4 position 10, respectively. A summary of the

irradiation exposure parameters and Charpy-impact test results for HFIR surveillance, as used in the interpretation of HFIR results below, is given in Table 4 [16].

TABLE 4--Summary of irradiation exposure parameters and Charpy impact test results for HFIR surveillance.

Material (Position)	EFPY[a] year	ΔNDTT[b] °C	Neutron flux (E>1MeV) $m^{-2}s^{-1}$	Neutron fluence (E>1MeV) m^{-2}	Neutron dpa	Gamma dpa	Total dpa
A212B	15.01	29	$1.75\ 10^{12}$	$8.30\ 10^{20}$	$1.32\ 10^{-4}$	$6.79\ 10^{-4}$	$8.11\ 10^{-4}$
(Key 6,7)	17.53	42	$1.75\ 10^{12}$	$9.70\ 10^{20}$	$1.53\ 10^{-4}$	$7.93\ 10^{-4}$	$9.47\ 10^{-4}$
	19.20	32[c]	$1.75\ 10^{12}$	$1.06\ 10^{21}$	$1.68\ 10^{-4}$	$8.69\ 10^{-4}$	$1.04\ 10^{-3}$
A350LF3	2.34	14	$1.42\ 10^{13}$	$1.05\ 10^{21}$	$1.64\ 10^{-4}$	$1.88\ 10^{-4}$	$3.53\ 10^{-4}$
(Key 2)	6.45	29	$1.42\ 10^{13}$	$2.89\ 10^{21}$	$4.52\ 10^{-4}$	$5.20\ 10^{-4}$	$9.72\ 10^{-4}$
	15.01	56	$1.42\ 10^{13}$	$6.74\ 10^{21}$	$1.05\ 10^{-3}$	$1.21\ 10^{-3}$	$2.26\ 10^{-3}$
	17.53	66	$1.42\ 10^{13}$	$7.87\ 10^{21}$	$1.23\ 10^{-3}$	$1.41\ 10^{-3}$	$2.64\ 10^{-3}$
A105II	2.34	10	$4.23\ 10^{12}$	$3.12\ 10^{20}$	$6.63\ 10^{-5}$	$9.27\ 10^{-5}$	$1.59\ 10^{-4}$
(Key 1,4)	6.45	17	$4.23\ 10^{12}$	$8.60\ 10^{20}$	$1.83\ 10^{-4}$	$2.55\ 10^{-4}$	$4.38\ 10^{-4}$
	15.01	33	$4.23\ 10^{12}$	$2.00\ 10^{21}$	$4.25\ 10^{-4}$	$5.94\ 10^{-4}$	$1.02\ 10^{-3}$
	17.53	35	$4.23\ 10^{12}$	$2.34\ 10^{21}$	$4.97\ 10^{-4}$	$6.94\ 10^{-4}$	$1.19\ 10^{-3}$

[a]Effective full-power years (100 MW).
[b]Nil-ductility transition temperature shift.
[c]Personal communication [17].

EFFECTS ON HFIR SURVEILLANCE RESULTS INTERPRETATION

It has generally been accepted that radiation-induced changes in the mechanical properties of ferritic steels irradiated in nuclear reactors are caused by neutron interactions with material. This is reflected in current NRC Regulatory Guide 1.99 [18], as well as in ASTM Standard Practices and Guides [19], where the fast neutron flux or neutron-induced displacements per atom (dpa) are used to characterize irradiation conditions and correlate material embrittlement to irradiation parameters. However, interaction of gamma rays with matter can also create displaced atoms [15,20], mostly through a two-step processes. Energetic gamma rays create Compton electrons and electron-positron pairs, which in turn displace atoms. If these displaced atoms also contribute to material embrittlement, than gamma-induced displacements must be taken into account in the analysis of irradiation-induced material embrittlement. Gamma-induced displacements may be quite negligible when compared with neutron-induced displacements in most irradiations, and consequently in such cases neglecting the gamma-induced dpa will not affect the embrittlement trend curves. However, at HFIR surveillance positions analyzed, gamma-induced dpa dominates or at least equals neutron dpa and alters completely the HFIR surveillance results. This finding is illustrated in the following examples:

Figure 4 shows measured NDTT shifts (ΔNDTT) plotted versus neutron-induced dpa. Charpy-impact test results for HFIR surveillance and ORR accelerated irradiation data were taken from ref. 3 and ref. 21. HFIR surveillance results are given also versus neutron-induced dpa from older analyses [3,21]. The differences between the two neutronics analyses are discussed in ref. 16; however, the differences between the

"old" and "new" neutron induced dpa are relatively small and do not affect significantly HFIR-to-ORR comparisons. All three materials: A212B, A350LF3, and A105II irradiated in HFIR, show higher NDTT shifts than A212B material irradiated in the Oak Ridge Research Reactor (ORR). In other words: materials irradiated in HFIR show "accelerated embrittlement." Materials A212B and A350LF3 were expected to behave similarly, because they showed similar trend curves of yield stress versus fast fluence [3] for ORR irradiations. But the A350LF3 material irradiated at HFIR key 2 shows accelerated embrittlement with respect to ORR-irradiated A212B and less embrittlement than HFIR-irradiated A212B material.

In Fig. 5, the HFIR ΔNDTTs are plotted versus the sum of gamma-induced and neutron-induced dpa. HFIR results fall close to the curve fitted through the ORR-irradiated specimens data. Therefore, taking into account the gamma-induced displacements explains the higher than expected embrittlement of materials irradiated in HFIR. Also, results for materials A212B and A350LF3, which were irradiated at different positions in HFIR, are brought together due to considerable differences in the gamma-to-neutron-induced dpa rates between different keys.

The ORR results are plotted against dpa (E > 0.1 MeV) [3,21]. Therefore, it can be argued that the contributions from neutrons below 0.1 MeV and from gamma-induced displacements would increase the total dpa and hence move the ORR curve farther to the right. However, the two data points from the ORR (the one with the lowest dpa value and the next higher), that cover the dpa range of the HFIR surveillance data, were obtained from samples irradiated at an in-core location. Dosimetry measurements performed there [3] showed only small differences in fast fluxes derived from ^{237}Np, ^{238}U, ^{58}Ni, ^{54}Fe and other threshold dosimeters. These results indicate that at in-core locations of the ORR, the gamma-induced reactions contribute very little to the total reaction rates and hence to the total dpa. Based on experience, it also appears reasonable (and probably conservative) to estimate that neutrons with energies below 0.1 MeV do not contribute more than 10% to the total dpa at in-core locations. The third ORR data point, with the highest dpa value, was obtained from irradiations in the ORR poolside facility [21,22], where conditions may differ from that in the core. However, this point has a dpa value almost an order of magnitude greater than the largest dpa for HFIR surveillance data and hence does not affect significantly the HFIR-ORR comparison (see Fig. 5). Therefore, a second thin-line ORR curve, parallel to but shifted to 10% higher values of dpa, was drawn to illustrate the estimated effect of ORR total dpa, which is expected to be appropriate at least for the in-core locations. As seen, the effect of this shift is not significant, and the agreement between the ORR ΔNDTT versus dpa trend curve and HFIR data remains very good.

In Fig. 6 data for A212B material from Shippingport [23] and the test reactors data [24] are added to the picture. The data points of Steele and Hawthorne [25], which were shown on Fig. 2, are also given. Data from test reactors and Steele and Hawthorne's data were converted from ΔNDTT versus fast fluence to ΔNDTT versus dpa using the dpa-to-fast-fluence ratio from the ORR in-core irradiation location (dpa-to-fast-fluence ratio of $1.39\ 10^{-25}\ m^2$). The least-squares-fit curve of all the data points is given, and the "2-sigma" ($\pm 33^{o}C$) scattering band of the fit is shown. Steele and Hawthorne's data set includes materials other than A212B (see Fig. 2). Nevertheless, the consistency of HFIR and other data remains very good when the sum of neutron-induced and gamma-induced dpa is used to characterize HFIR irradiations.

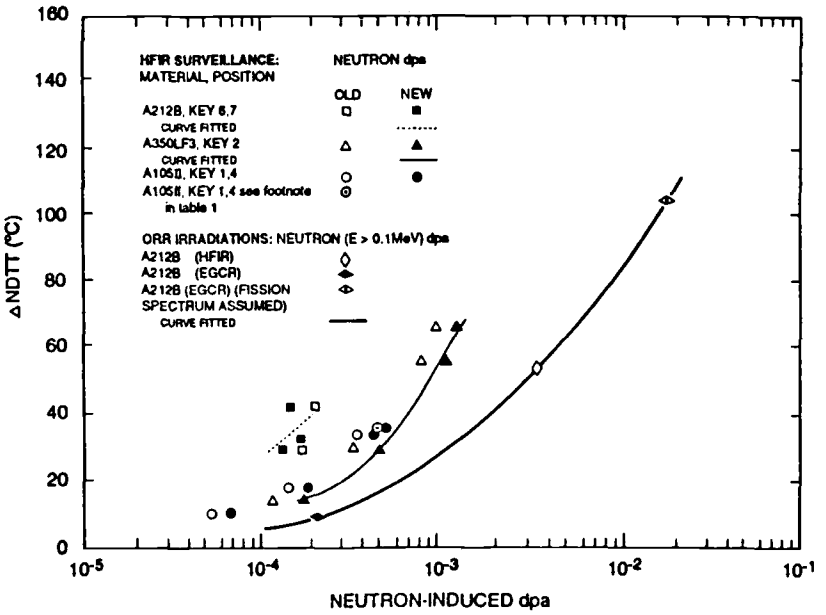


FIG. 4--Charpy NDTT shifts versus neutron-induced dpa for HFIR surveillance materials in (a) HFIR (all energies) and (b) ORR (>0.1 MeV).

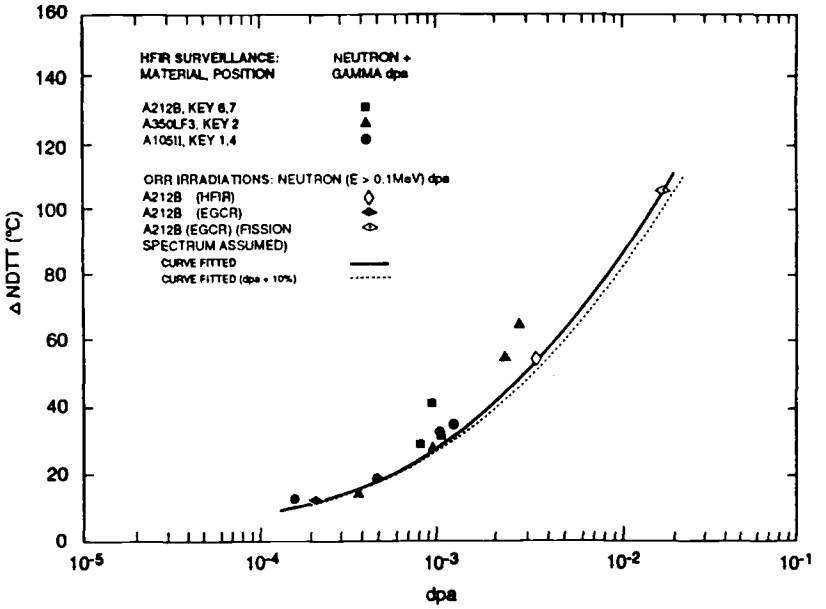


FIG. 5--Charpy NDTT shifts versus dpa for HFIR surveillance materials in (a) HFIR for neutron-induced and gamma-induced displacements (all energies) and (b) ORR for neutron-induced displacements (>0.1 MeV).

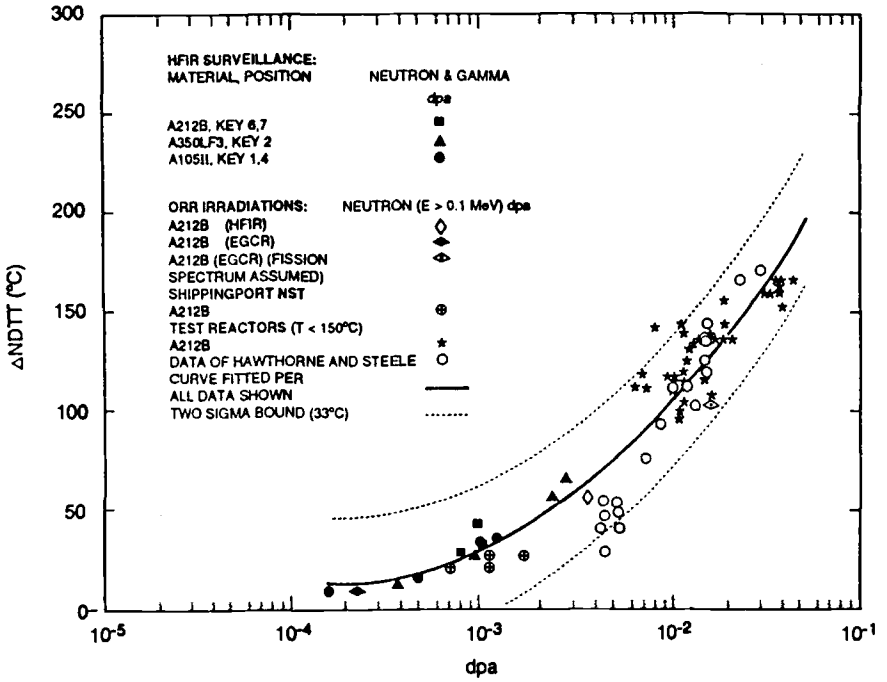


FIG. 6--Comparison of Charpy NDTT shifts versus dpa for HFIR surveillance materials in (a) HFIR for neutron-induced and gamma-induced displacements (all energies) and (b) the data points of Steele and Hawthorne, other test reactors and Shippingport NST for neutron-induced displacements (>0.1 MeV).

FINDINGS AND CONCLUSIONS

Comprehensive dosimetry experiments at several HFIR surveillance positions revealed the presence of an intense gamma field. The responses of ^{238}U and ^{237}Np fission monitors and ^{9}Be HAFMs were explained through the contribution of photo-induced reactions. At one of the HFIR surveillance locations analyzed the photo-induced reactions accounted for approximately 95% of the responses of ^{238}U, ^{237}Np and ^{9}Be monitors.

A commonly used neutron spectrum adjustment technique was extended to allow the simultaneous adjustment of neutron and gamma fields. Feasibility of adjusting the gamma and neutron fluxes simultaneously was demonstrated, probably for the first time. Simultaneous adjustment provided adjusted irradiation parameters for the neutron and also gamma fields. This allowed an assessment of HFIR surveillance results based on neutron- and gamma-irradiation parameters.

At all locations analyzed gamma-induced dpa were found to be higher than neutron-induced dpa, and ratios greater than 5 were observed at certain locations. The sum of neutron-induced and gamma-induced dpa was used as a correlation parameter for HFIR surveillance data. No efficiency factors were used for either neutron- or gamma-induced dpa rate.

When the sum of neutron- and gamma-induced dpa was used to analyze the HFIR surveillance Charpy test results, they were found to be in accordance with results for ORR-irradiated specimens, Shippingport NST data and test reactors data for A212B material, as well as with data of Steele and Hawthorne, which include different materials. Materials expected to behave similarly, which were irradiated at different positions in HFIR, indeed show consistent behavior, due to considerable differences in gamma-to-neutron-induced dpa rates between different keys. Though not addressed in this paper, it was also found [16] that the total dpa values bring the results from tensile specimens irradiated in the HFIR in agreement with the curve for the ORR irradiated samples. Therefore, evidence exists that gamma-induced atomic displacements, which were not taken into account in previous analyses, are the cause of the higher-than-expected embrittlement observed in HFIR surveillance.

To verify that gamma-induced atomic displacements cause radiation embrittlement, additional experiments are necessary. Preferably, the irradiations of material specimens should be done in a strong gamma field with accompanying neutron flux as low as possible. In order to keep the neutron-induced dpa rate below about 10% of the total dpa, the ratio of gamma flux (E > 1 MeV) to neutron flux (E > 1 MeV) should be around 2×10^4, and the neutron flux below 1 MeV should not be excessive either. Because an intensive gamma field is necessary to accumulate the needed gamma fluence in a reasonable time, this requirement is very demanding.

If this interpretation of HFIR surveillance results through gamma-induced displacements, as proposed here, is verified, this will probably circumvent the issue of accelerated embrittlement of support structures of commercial light-water power reactor vessels. It is expected that in the reactor cavity, on the outer side of the relatively thick steel pressure vessel wall, ratios of high-energy-gamma flux to neutron flux will not be large enough to make gamma-induced displacements significant. The Babcock & Wilcox cavity dosimetry results [26] indirectly support this opinion.

REFERENCES

[1] R. D. Cheverton and T. M. Sims, *HFIR Core Nuclear Design*, Oak Ridge National Laboratory Report ORNL-4621, July 1971.

[2] J. R. McWherter, R. E. Schappel, and J. R. McGuffey, *HFIR Pressure Vessel and Structural Components Material Surveillance Program*, Oak Ridge National Laboratory Report ORNL/TM-1372, January 1966.

[3] R. D. Cheverton, J. G. Merkle, and R. K. Nanstad, eds., *Evaluation of HFIR Pressure-vessel Integrity Considering Radiation Embrittlement*, Oak Ridge National Laboratory Report ORNL TM/10444, April 1988.

[4] R. D. Cheverton, F. B. K. Kam, R. K. Nanstad, and G. C. Robinson, *Nuc. Eng. Des.* 117 (1989) 349-355.

[5] R. K. Nanstad, K. Farrell, D. N. Braski and W. R. Corwin, *J. Nucl. Mater.* 158 (1988) 1-6.

[6] L. K. Mansur and K. Farrell, *J. Nucl. Mater.* 170 (1990), 236-245.

[7] K. Farrell, S. T. Mahmood, R. E. Stoller, and L. K.Mansur, *J. Nucl. Mater.*210 (1994) 268-281.

[8] K. Farrell et al., *The DOS 1 Neutron Dosimetry Experiment at the HB-4-A Key 7 Surveillance Site on the HFIR Pressure Vessel*, Oak Ridge National Laboratory Report ORNL/TM-12511, Jan. 1994.

[9] J. V. Pace III, C. O. Slater, and M. S. Smith, "Three-Dimensional Discrete Ordinates Radiation Transport Calculations of Neutron Fluxes for Beginning-of-Cycle at Several Pressure Vessel Surveillance Positions in the High Flux Isotope Reactor," *Reactor Dosimetry, ASTM STP 1228*, Herry Farrar IV, E. Parvin Lippincott, John G. Williams, and D. W. Vehar eds., American Society for Testing and Materials, Philadelphia, 1994, pp. 140-146.

[10] I. Remec and F. B. K. Kam, *Neutron Spectra at Different HFIR Pressure Vessel Surveillance Locations*, NUREG/CR-6117, ORNL/TM-12484, Nov. 1993.

[11] F. W. Stallmann, *LSL-M2: A Computer Program for Least-Squares Logarithmic Adjustment of Neutron Spectra*, NUREG/CR-4349, ORNL/TM-9933, March 1986.

[12] V. V. Verbinski et al., *Nucl. Sci. and Eng.* 75 (1980), 159-166.

[13] L. Petrusha, "Photofission Effects in B&W 177-Fa Reactor Vessel Surveillance Capsule Dosimeters," *Proc. of the Seventh ASTM-EURATOM Symposium on Reactor Dosimetry*, Strasbourg, France, August 1990, pp. 537-545.

[14] E 693-79, Practice for Characterizing Neutron Exposures in Ferritic Steels in Terms of Displacements Per Atom (DPA), E 706 (ID), Annual Book of ASTM Standards, Section 12.

[15] N. P. Baumann, "Gamma-ray Induced Displacements in D_2O Reactors," *Proc. of the Seventh ASTM-EURATOM Symposium on Reactor Dosimetry*, Strasbourg, France, August 1990, pp. 689-697.

[16] I. Remec, J. A. Wang, F. B. K. Kam, and K. Farrell, *J. Nucl. Mater.* 217 (1994) 258-268.

[17] R. K. Nanstad, Oak Ridge National Laboratory, "Charpy Impact Test Results for HFIR Surveillance Program," personal communication to R. D. Cheverton, Oak Ridge National Laboratory, October 1993.

[18] U.S. NRC Regulatory Guide 1.99: Radiation Embrittlement of Reactor Vessel Materials, Revision 2, May 1988.

[19] Annual Book of ASTM Standards, Section 12, Standard Practices and Guides E 185, E 462, E 560, E 693, E 844, 1992.

[20] R. Gold, J. H. Roberts, and D. G. Doran, "Determination of Gamma-Ray-Induced Displacement Rates," *Proc. Reactor Dosimetry: Methods, Applications, and Standardization*, ASTM STP 1001, Henry Farrar IV and E. P. Lippincott, Eds., American Society for Testing and Materials, Philadelphia, 1989.

[21] R. K. Nanstad et al., "Effects of 50°C Surveillance and Test Reactor Irradiations on Ferritic Pressure Vessel Steel Embrittlement," *Effects of Radiation on Materials: 14th International Symposium*, ASTM STP 1046, N. H. Packan, R. E. Stoller and A. S. Kumar, Eds., American Society for Testing and Materials, Philadelphia, 1990, pp. 5-29.

[22] M. S. Wechsler, R. G. Berggren, N. E. Hinkle, and W. J. Stelzman, "Radiation Hardening and Embrittlement in a Reactor Pressure Vessel

Steel," *Irradiation Effects in Structural Alloys for Thermal and Fast Reactors*, ASTM STP 457, 1969, pp. 242-260.

[23] O. K. Chopra, W. J. Shack, S. T. Rosinski, *Radiation Embrittlement of the Neutron Shield Tank from the Shippingport Reactor*, NUREG/CR-5748, ANL-91/23, October 1991.

[24] J. R. Hawthorne, "Radiation Effects Information Generated on the ASTM Reference Correlation Monitor Steel," ASTM DS54-62, July 1974.

[25] L. E. Steele and J. R. Hawthorne, *Effect of Irradiation Temperature on the Neutron-Induced Changes in Notch Ductility of Pressure-Vessel Steels*, U.S. Naval Research Laboratory Report NRL 5629, Washington, D.C., June 28, 1961.

[26] S. Q. King and D. M. Gilliam, "Characterization of the Gamma Field in the B&W Owners Group Cavity Dosimetry Benchmark Experiment," *Reactor Dosimetry, ASTM STP 1228*, Herry Farrar IV, E. Parvin Lippincott, John G. Williams, and D. W. Vehar eds., American Society for Testing and Materials, Philadelphia, 1994, pp. 447-455.

G. R. Odette[1], G. E. Lucas[1] and R. D. Klingensmith[1]

THE INFLUENCE OF METALLURGICAL VARIABLES ON THE TEMPERATURE DEPENDENCE OF IRRADIATION HARDENING IN PRESSURE VESSEL STEELS

REFERENCE: Odette, G. R., Lucas, G. E. and Klingensmith, R. D., **"The Influence of Metallurgical Variables on the Temperature Dependence of Irradiation Hardening in Pressure Vessel Steels,"** *Effects of Radiation on Materials: 17th International Symposium, ASTM STP 1270,* David S. Gelles, Randy K. Nanstad, Arvind S. Kumar, and Edward A. Little, Eds., American Society for Testing and Materials, 1996.

ABSTRACT: Yield stress elevations ($\Delta\sigma_y$) in pressure vessel steels irradiated at intermediate flux and fluence systematically decreased with increasing temperature and decreasing copper and nickel content. Lower stress relief temperature also decreased $\Delta\sigma_y$ at bulk copper concentrations greater than about 0.3%. The dependence of $\Delta\sigma_y$ on irradiation temperature between 260 and 316°C increased with copper and nickel content and decreased with phosphorous content. When normalized by the average $\Delta\sigma_y$, the fractional temperature dependence correlates with a simple empirical chemistry factor of copper and phosphorous. The correlation predicts data on the irradiation temperature dependence of $\Delta\sigma_y$ found in the literature within a standard error of about 0.3 MPa/°C and is consistent with current understanding of hardening mechanisms. However, questions remain about the effects at very low flux and finer scale variations over smaller temperature intervals.

KEYWORDS: pressure vessel steels, irradiation hardening, irradiation embrittlement, composition effects, heat treatment effects, irradiation temperature dependence

There is a relatively large body of materials test reactor (MTR) data on the effects of irradiation temperature on hardening and embrittlement[2] of Mn-Mo-Ni steels irradiated at about 300°C [1-16]. As a rule of thumb, the shift and yield stress elevation sensitivities are on-the-order of 1±0.6°/° and 1.7±1.0 MPa/°C, respectively [7]. However, useful predictions of temperature effects require extrapolation of accelerated MTR data to low flux service conditions over a wide range of fluences and metallurgical conditions. Hardening and embrittlement are known to be mediated by complex interactions between a number of irradiation and metallurgical variables [3,7,8,10,17,18]. For example, both theory and experiment indicate that the effect of neutron flux is influenced by copper content, fluence

[1] Department of Mechanical Engineering, University of California Santa Barabara, Santa Barbara, CA 93106-5070

[2] As used in this paper, the terms embrittlement and shift specifically refer to changes in the transition temperature measured in standard Charpy V-notch tests indexed at 41 J. Note, we suppress the negative sign on $\Delta P/\Delta T$ with the implicit assumption of decreasing property changes with increasing temperature

Copyright© 1996 by ASTM International www.astm.org

and temperature [18]. In view of such "complexity," it is clear that reliable extrapolations require physical models calibrated by relevant controlled single variable experiments.

Hardening and corresponding embrittlement can be understood and modeled in terms of an evolution of at least three classes of ultrafine scale features [17]. The dominant role of copper is known to be due to the accelerated formation of nanoscale, copper rich precipitates (CRP) from supersaturated solution as a consequence of radiation enhanced diffusion [19,20]. A variety of other even smaller defect clusters/complexes and precipitate phases may also contribute to hardening. These so-called matrix defects (MD) can be divided into thermally unstable (UMD) and stable (SMD) classes (MD = UMD + SMD); the former undergo recovery under irradiation, while the latter are stable up to much higher temperatures in post-irradiation annealing experiments [17,18,21,22]. Each of these classes (and, indeed, various subclasses) of features respond to the metallurgical and irradiation variables in both independent and interdependent ways. For example, the UMD are dependent on flux, temperature and nickel, but appear to be insensitive to copper content. However, the presence of a large population of UMD features retards the formation of the CRP phases [18].

The objective of this study was to characterize the effects of alloy composition on the temperature dependence of yield stress (σ_y) elevations ($\Delta\sigma_y$) for an irradiation at intermediate flux and fluence. The intermediate flux is significant since previous studies have suggested a copper-temperature-flux-fluence interaction. Most notably, flux effects were observed at higher copper contents and lower fluence; and the temperature sensitivity appeared to be reduced at intermediate versus high flux. A secondary objective of the study was to evaluate the effect of stress relief temperature on hardening over a range of irradiation temperatures and compositions; this also follows previous studies indicating that low temperature stress relief reduces the amount of dissolved copper available to form CRP. While not the focus of this paper, small angle neutron scattering (SANS) and post irradiation annealing measurements have been carried out to evaluate the microstructural basis of the mechanical property trends, and are briefly summarized.

EXPERIMENT

Alloys and Specimens

The compositions and heat treatments for a set of 22 L-series alloy conditions are given in Table 1. Twelve A533B-type split melts with systematic variations in copper (0.0 to 0.8 at 0.8Ni)[3] and nickel (0 to 1.25 at 0.4Cu and 0.7 and 1.1 at 0.2Cu) were heat treated at both low (HTL: 600°C/40 h) and high (HTH: 660°C/4 h) stress relief temperatures in order to examine the effect of copper pre-precipitation. Two other A533B split melts contained phosphorous (0.025 versus 0.005) and silicon (0.75 versus 0.25) additions to the base composition. Three commercial CW-series welds had from 0.19 to 0.24Cu and 0.07 to 1.02Ni. All of these steels have been irradiated in previous programs at a variety of conditions [7].

The steels were irradiated in selected combinations of 0.5 mm thick x 3 mm diameter discs, 18.3 x 20 x 2 mm SANS coupons and subsized tensile specimens. Sheet tensile specimens with a gage section 9 mm x 2 mm x 0.5 mm were prepared by precision die punching heat treated coupons lapped to 0.5±0.005 mm thick. The quality of the die was monitored by punching and tensile testing a variety of calibration metals after about every 500 specimens had been punched.

---

[3] The compositions cited in the text are nominal values of weight percent. The actual values, given in Table 1, are within ±0.03Cu, ±0.06Ni and ±0.03Si of the nominal values.

TABLE 1 -- Alloy Compositions and Heat Treatments

	Composition (weight percent)[a]									
Alloy	C	Cu	Ni	Mn	Si	P	S	Cr	Mo	HT[c]
LA	0.14	0.40	0.00	1.37	0.22	0.005	0.005	0.06	0.54	31
LB	0.16	0.40	0.18	1.35	0.22	0.005	0.005	0.06	0.53	31
LC	0.14	0.41	0.86	1.44	0.23	0.005	0.008	0.06	0.55	31
LD	0.19	0.38	1.25	1.38	0.23	0.005	0.015	0.07[b]	0.55	31
LF	0.16	0.42	0.81	1.47	0.73	0.005	0.015	0.06	0.56	31
LG	0.16	0.00	0.74	1.37	0.22	0.005[b]	0.005[b]	0.05	0.55	31
LH	0.16	0.11	0.74	1.39	0.24	0.005[b]	0.005[b]	0.05	0.55	31
LI	0.16	0.20	0.74	1.37	0.24	0.005[b]	0.005[b]	0.05	0.55	31
LJ	0.14	0.42	0.81	1.34	0.13	0.005[b]	0.005[b]	0.09	0.54	31
LK	0.13	0.80	0.81	1.13	0.13	0.005[b]	0.005[b]	0.09	0.56	31
LL	0.15	0.21	1.10	1.37	0.23	0.005[b]	0.005[b]	0.05	0.55	31
LM	0.14	0.40	0.00	1.37	0.22	0.005	0.005	0.06	0.54	32
LN	0.16	0.40	0.18	1.35	0.22	0.005	0.005	0.06	0.53	32
LO	0.14	0.41	0.86	1.44	0.23	0.005	0.008	0.06	0.55	32
LP	0.19	0.38	1.25	1.38	0.23	0.005	0.015	0.07[b]	0.53	32
LR	0.16	0.42	0.81	1.47	0.73	0.005	0.015	0.06	0.56	32
LS	0.16	0.01	0.74	1.37	0.22	0.005[b]	0.005[b]	0.05	0.55	32
LT	0.16	0.11	0.74	1.39	0.22	0.005[b]	0.005[b]	0.05	0.55	32
LU	0.16	0.20	0.74	1.37	0.24	0.005[b]	0.005[b]	0.05	0.54	32
LV	0.14	0.42	0.81	1.34	0.13	0.005[b]	0.005[b]	0.09	0.54	32
LW	0.13	0.80	0.81	1.30	0.13	0.005[b]	0.005[b]	0.09	0.56	32
LX	0.15	0.21	1.10	1.37	0.24	0.005[b]	0.005[b]	0.05	0.55	32
CW	0.09	0.24	0.56	1.68	0.55	0.014	0.016	0.07	0.40	21
CW	0.13	0.22	0.07	1.37	0.29	0.014	0.016	0.16	0.46	22
CW	0.11	0.19	1.02	1.30	0.18	0.017	0.015	0.05	0.51	22

[a] Al < 0.015 and Sn/Sb/As < 0.004 (not available for CW-series)

[b] Maximum values

[c] Heat Treatments:
21. Submerged arc welded; post heat treated 607°C, 30-50h; slow cooled
22. Submerged arc welded; post heat treated 621°C, 30-50h; slow cooled
31. Austenitize 900°C, 1h; air cool; temper 664°C, 4h; air cool; stress relieve 600°C, 40h; furnace cool to 300°C; air cool
32. Austenitize 900°C, 1h; air cool; temper 664°C, 4h; air cool

Irradiations

Irradiations of small subcapsules, piggybacked in Materials Engineering Associates (MEA) capsules, were carried out in a core face position at the University of Michigan Ford Reactor (UMFR). The irradiation temperatures were 260 and 316±5°C. The neutron flux and fluence (for neutron energies E > 1 MeV) were 0.76×10^{16} n/m^2-s and 7.1×10^{22} n/m^2, respectively, with uncertainties on the order of ±10%. The corresponding displacement cross section (E > 1 MeV) was about $1.5 \pm 0.2 \times 10^{-25}$ m^2 [4].

Post Irradiation Testing

Static tensile tests were carried out at room temperature (20±2°C) at a strain rate of 10^{-3} s^{-1} on an automated tensile tester. Testing involves loading twenty-nine specimens, including calibration samples, in a precision alignment cartridge. This is positioned under pneumatically-actuated, hydraulic grips by a linear stage in an Instron 1122 load frame, and it serves as the lower grip. A computer actuates the specimen positioning, gripping and loading sequence and records, plots and analyses the load-displacement record. Displacements are monitored by an LVDT which measures the movement of the upper grip relative to the lower grip. The irradiated and unirradiated yield stresses (σ_{yi} and σ_{yu}, respectively) were determined using a 0.2% off-set procedure and represent the average of at least two and five tests, respectively. Although there are steel-to-steel variations, the average standard error in σ_y is estimated to be about ± 10 MPa with a similar accuracy indicated by comparisons with conventional specimens. Thus the standard error in $\Delta\sigma_y$ is estimated to be about ±15 MPa.

Small angle neutron scattering studies measurements have been carried out on a subset of these alloys to provide information on size, number density, volume fraction and composition of the CRP. Further, extensive annealing studies at temperatures in the range of 290 to 350°C have been carried out to discriminate hardening contributions from the various MD features. A detailed description of these experiments will be presented elsewhere [23], but some salient results are summarized here to help interpret the mechanical property data.

RESULTS AND ANALYSIS

The $\Delta\sigma_y$ data are shown in Figure 1. Figure 1a plots the $\Delta\sigma_y$ versus copper at both 260 (solid lines, open symbols) and 316°C (dashed lines, filled symbols) for 0.8Ni alloys given low (HTL - circles)) and high (HTH - diamonds) temperature heat treatments. In all cases a sigmoidal-type dependence is observed with lower $\Delta\sigma_y$ at the higher irradiation temperature. Further, $\Delta\sigma_y$ is lower for the HTL at 0.4Cu and above, presumably as a consequence of pre-precipitation. (Note, the $\Delta\sigma_y$ is even lower for the 0.8 versus 0.4Cu for the HTL; this is probably due to enhanced nucleation driven by higher copper supersaturations during pre-precipitation). Figures 1b and c show increasing $\Delta\sigma_y$ with higher nickel for the L-series alloys with about 0.4 and 0.2Cu, respectively. However, this trend is not observed in the CW-series (potentially confounded) welds with 0.19 to 0.22Cu also shown in Figure 1c. Figure 1d shows that $\Delta\sigma_y$ slightly increases at higher phosphorous at 316°C for the HTH, but is independent of this element for the HTL. In contrast, $\Delta\sigma_y$ decreases at higher phosphorous in both heat treatment conditions for the irradiations at 260°C. A minimal effect of silicon variations was also observed (not shown).

Figure 2 plots the temperature sensitivity (S') of $\Delta\sigma_y$ between 260 and 316°C, where $S' = [\Delta\sigma_y(260°C) - \Delta\sigma_y(316°C)]/56°C$. Figure 2a shows that for alloys with about 0.8Ni and 0.005P and 0.025P, S' increases significantly with increasing copper and

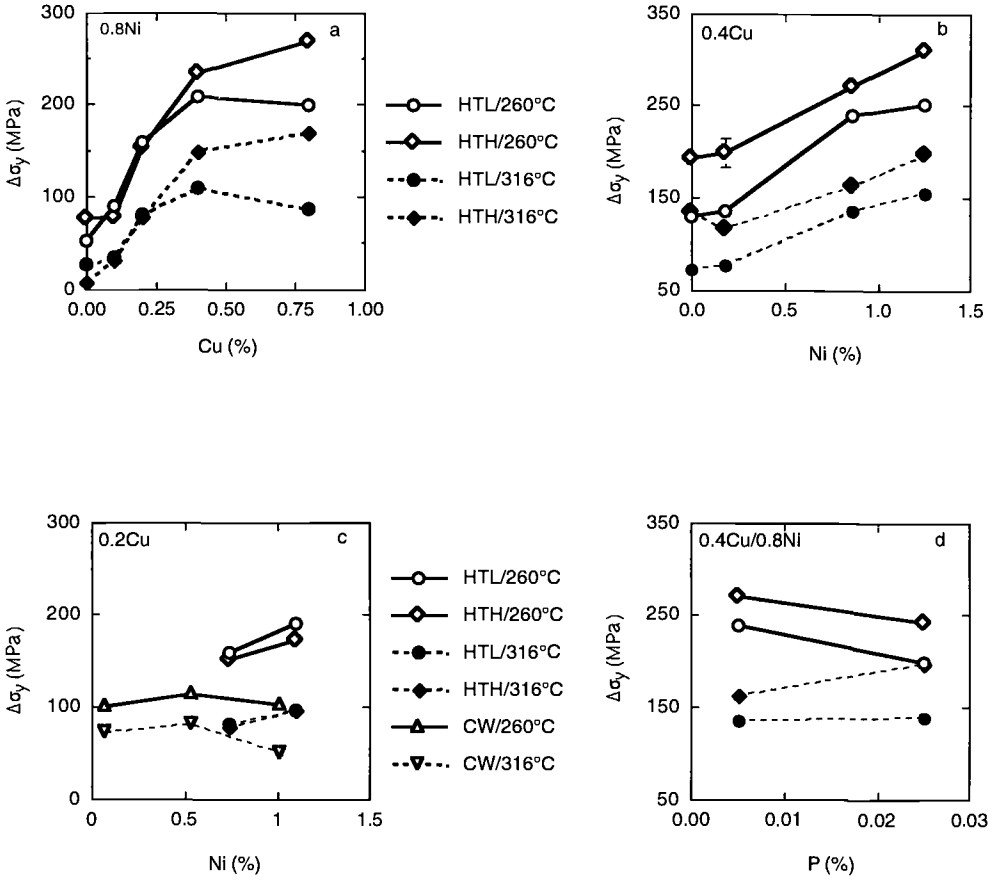


FIG. 1 -- Variation of $\Delta\sigma_y$ after irradiation at 260 and 316°C for two heat treatment conditions with: a) copper for alloys with 0.8% nickel; b) nickel for L-series alloys with 0.4% copper; c) nickel for L-series and CW alloys with 0.2% copper; d) phosphorous for L-series alloys with 0.4% copper.

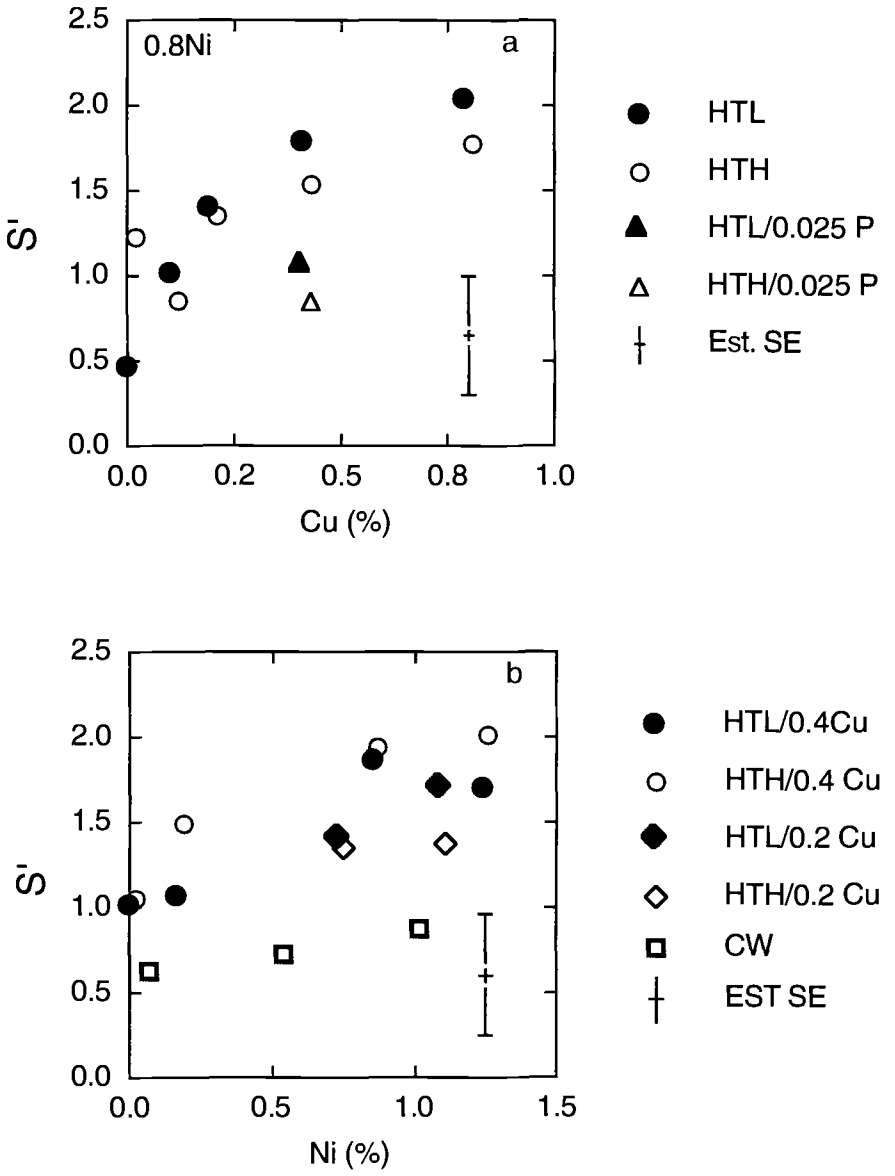


FIG. 2 -- Variation of the temperature sensitivity (S') of yield stress change with: a) copper and b) nickel content.

appears to be lower for higher phosphorous. A similar plot in Figure 2b for alloys with 0.4 and 0.2Cu shows S' increases with nickel in both the L and CW-series alloys, although the absolute values are lower in the latter case. The average S' for the 0.8Ni/0.005P/0.2 to 0.4Cu L-series alloys is about 1.6 MPa/°C. The nominal ratio of $\Delta\sigma_y$ to the 41J transition temperature shift, $\Delta T_{41}/\Delta\sigma_y$, is about 0.6 [24]. These values combine to yield a nominal shift sensitivity of about 1°/°, consistent with conventional understanding. However, the lower copper and nickel, higher phosphorous alloys and commercial welds all have considerably smaller temperature sensitivity.

Various approaches to correlating the data were tried. The simplest and most successful method was based on the relative (or fractional) temperature sensitivity, $f_T = S'/\langle\Delta\sigma_y\rangle$, where $\langle\Delta\sigma_y\rangle$ is simply the average $\Delta\sigma_y$ for the 260 and 316°C irradiations, $[\Delta\sigma_y(260°C) + \Delta\sigma_y(316°C)]/2$; assuming f_T is linear, this is equivalent to a normalization of the temperature sensitivity at 288°C. Plots of f_T versus nickel show no systematic trend. In contrast, f_T was found to decrease systematically with higher copper content. However, it is important to consider the actual dissolved copper available for precipitation under irradiation. This effective maximum copper (Cu_{max}) is limited by pre-precipitation to a level that depends on the heat treatment time and temperature. Thus, $Cu_{eff} = Cu$ for $Cu < Cu_{max}$, and $Cu_{eff} = Cu_{max}$ for $Cu > Cu_{max}$. The Cu_{max} is not precisely known, but was estimated from the mechanical property data through the following logic and assumptions:

Cu_{eff} controls the CRP component of $\Delta\sigma_y$.

The $\Delta\sigma_y$ due to the CRP ($\Delta\sigma_{ycu}$) can be estimated as $\Delta\sigma_{ycu}(Cu) = \Delta\sigma_y(Cu) - \Delta\sigma_y(0)$.

To a first approximation, $\Delta\sigma_{ycu}$ linearly scales with the $\sqrt{Cu_{eff}}$ above a minimum threshold and below Cu_{max}.

Cu_{max} depends on the final heat treatment, but exceeds 0.2Cu for the heat treatment times and temperatures used in this study.

There is roughly the same amount of dissolved copper in the 0.4 to 0.8Cu alloys.

Thus the location of the 0.4 and 0.8Cu $\Delta\sigma_{ycu}$ versus $\sqrt{Cu_{eff}}$ data on the extrapolated line through the lower copper data provides a crude estimate of Cu_{max}. As shown in Figure 3 this procedure yields Cu_{max} estimates of about 0.28% and 0.40% for the HTL and HTH heat treatments, respectively. These estimates are in reasonable agreement with direct experimental measurements [23] and are about and 50% and 25% above the corresponding solubility limits, respectively, consistent with slower kinetics at the lower heat treatment temperature.

The CRP contribution to hardening is much less sensitive to irradiation temperature than the corresponding contribution from MD. Therefore, f_T is expected to decrease with increasing $\sqrt{Cu_{eff}}$. This trend is confirmed by the data in Figure 4a for the L and CW-series alloys along with results from the same irradiation experiment reported by Hawthorne [4]. However, phosphorpous also appears to play a role since in all three data sets alloys with more than 0.005P consistently fall on the low side of the scatter band. The separate effects of copper and phosphorous were evaluated by first least squares fitting the 0.005P L-series alloys data (open circles), yielding

$$f_T(Cu_{eff}, 0.005P) = 0.023(1 - \sqrt{Cu_{eff}}) \quad (1)$$

The dashed lines are the estimated uncertainties in f_T associated with a standard error in the $\Delta\sigma_y$ and $\langle\Delta\sigma_y\rangle$ measurements of ±15MPa. The effect of phosphorous in copper bearing steels was evaluated in Figure 4b by plotting the f_T data, normalized to a $Cu_{eff} = 0.3$ using Equation 1, versus phosphorous. The solid line is a least square fit to the L-series data as

$$f_T(Cu_{eff} = 0.3, P) = 0.012 - 0.27P \quad (2)$$

Phosphorous increases hardening and embrittlement only at low copper levels. At higher copper, the effects of phosphorous are minimal. This is believed to be primarily due to the fact that the CRP getter phosphorous, thereby preventing the formation of phosphides. This phosphorous-copper interaction could also influence f_T. Indeed, Hawthorne's data for 0.002Cu and 0.025P fall precisely on the L-series fit line for 0.005P, suggesting that f_T is independent of phosphorous at low copper. Such behavior can be crudely modeled by defining low and high copper regimes of less than 0.1Cu and greater than 0.2Cu, respectively. In the high copper regime, f_T is simply found by combining Equations 1 and 2 as

$$f_T(Cu_{eff}, P) = 0.024 - 0.023\sqrt{Cu_{eff}} - 0.27P \qquad Cu \geq 0.2 \quad (3a)$$

At low copper levels f_T is independent of phosphorous, thus

$$f_T(Cu_{eff}, P) = 0.023 - 0.023\sqrt{Cu_{eff}} \qquad Cu \leq 0.1 \quad (3b)$$

In the intermediate copper regime a simple linear interpolation yields

$$f_T = 0.024 - 0.023\sqrt{Cu_{eff}} - 2.7(Cu - 0.1)P \qquad 0.1 < Cu < 0.2 \quad (3c)$$

As shown in Figure 4c, data adjusted to a common level of 0.005P using Equation 2 approximately falls within the ±15 MPa error limits cited above.

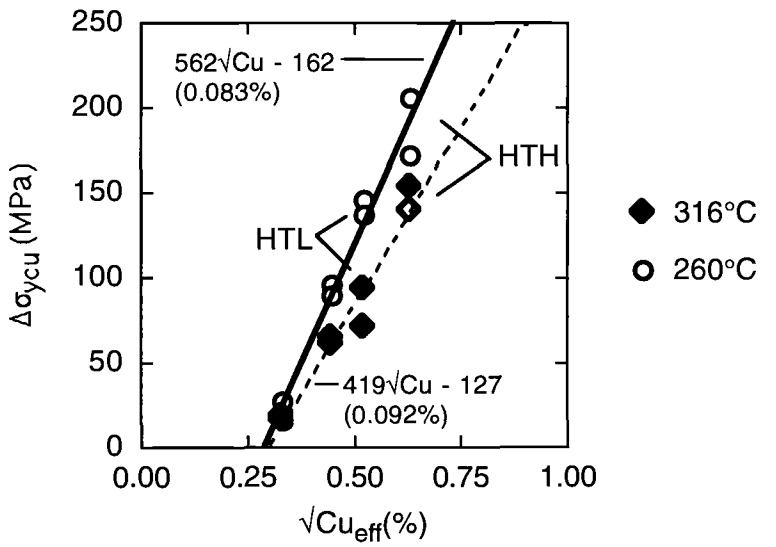


FIG. 3 -- The difference between the yield stress change for a copper-bearing alloy $\Delta\sigma_y(Cu)$ and a corresponding alloy with no copper $\Delta\sigma_y(0)$ versus the square root of Cu_{eff} for alloys irradiated at 260 and 316°C.

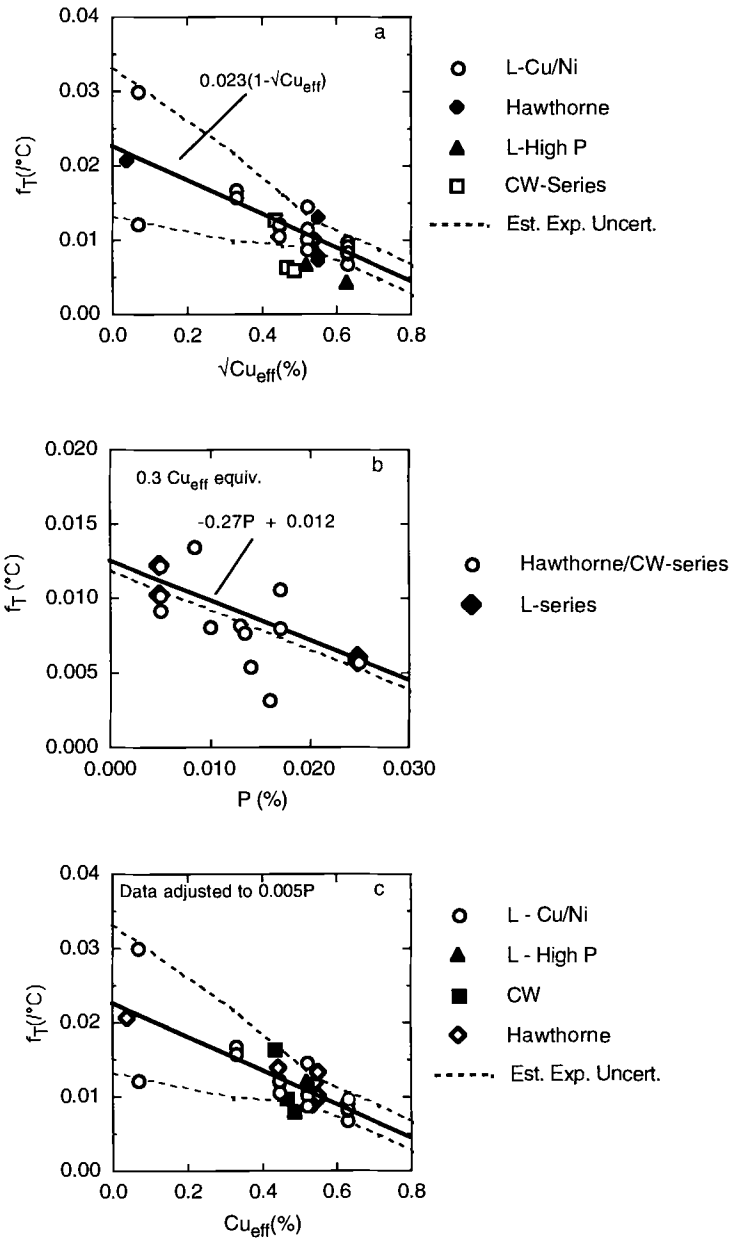


Figure 4 Variation of f_T with: a) the square root of Cu_{eff}; b) phosphorous, with data adjusted to Cu_{eff}=0.3 using Equation 1; c) the square root of Cu_{eff} with the data corrected to 0.005P using Equation 2.

Figure 5 tests the validity of Equation 3 by comparing predicted versus measured differences in the $\Delta\sigma_y$ at 260 versus 316°C, $\delta = \Delta\sigma_y(260°C) - \Delta\sigma_y(316°C)$. The circles and triangles represent the Hawthorne and CW-data, respectively; recall that these data were generated in the same experiment, but they were not used in deriving Equation 3. The squares are taken from data in the literature on a variety of plates and welds. The latter included Charpy shift (mostly) and hardness change data which have been converted to equivalent δ values using nominal conversion factors of 0.6°C/MPa and 3.6 MPa/kg/mm^2, respectively. In many cases these data required additional (linear) extrapolation to the 260 to 316°C temperature range. In spite of the various approximate extrapolations in estimating the equivalent "experimental" values of δ and the wide range of materials and irradiation conditions, the overall agreement is reasonable, and is certainly supportive of the trends predicted by Equation 3. The major discrepancy appears to be that Equation 3 systematically underpredicts the temperature sensitivity at very high values of δ. Neglecting these data, the standard error of the procedure proposed in this study is ± 15 MPa (with a small underprediction bias of 4 MPa). This is equivalent to a relatively small error in the temperature sensitivity of about 0.16°/°. Clearly using more simplified approaches, such as a fixed value of 1.7 MPa/°C (≈1°/° equivalent) shown as the large cross in Figure 5, would yield much larger errors.

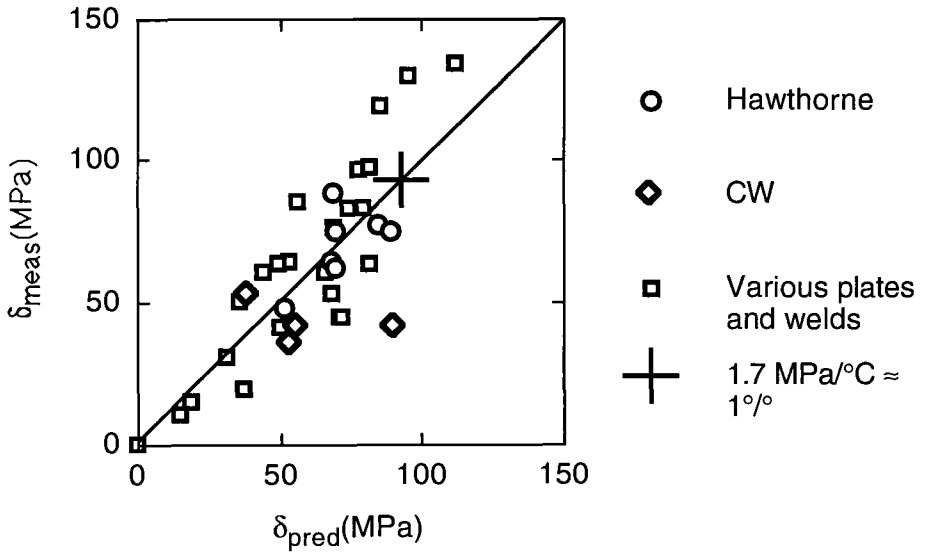


FIG. 5 -- Comparison of predicted versus measured δ [= $\Delta\sigma_y(260°C) - \Delta\sigma_y(316°C)$].

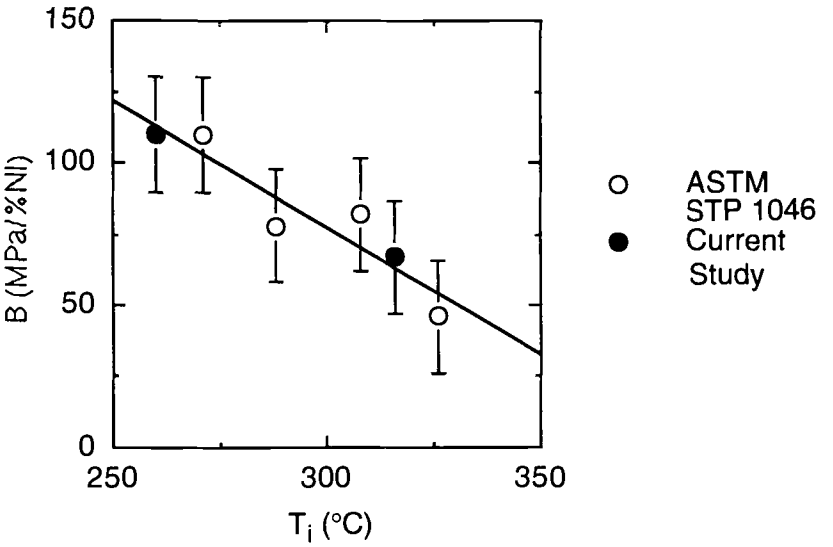


FIG. 6 -- Variation of the nickel coefficient (B) with the irradiation temperature.

Before closing this section it is useful to evaluate the data from another perspective: namely, the effect of irradiation temperature on the sensitivity of $\Delta\sigma_y$ to nickel. The nickel sensitivity can be expressed in terms of a coefficient, B, derived by least squares fitting the data to an expression of the form: $\Delta\sigma_y = A + BNi$. We have previously shown that B depends on both the fluence and irradiation temperature, but is relatively insensitive to copper at contents greater than 0.2 [25]. Figure 6 plots B versus irradiation temperature for the L-series alloys (see Figure 1b) with 0.4Cu (filled symbols) along with the previous results (open symbols); all the data have been adjusted slightly to a common exposure of 10^{23} n/m^2 based on the fluence dependence derived previously. The data consistently show that B increases with decreasing irradiation temperature down to the minimum in the current experiment of 260°C.

DISCUSSION

The correlation derived in the previous section is empirical. While it is beyond the scope of this paper to provide a detailed fundamental analysis, it is nevertheless useful to discuss these results in the context of current mechanistic microstructural understanding -- viz. the compositional and temperature sensitivity of the balance of hardening contributions from the CRP, UMD and SMD features.

A great deal of insight is provided by small angle neutron scattering studies of the L-series alloys illustrated in Figure 7. An interpretation of these data (and other results not shown) can be summarized as follows [23]:

The size and volume fraction of CRP increases with copper above a threshold in the range of 0.05 to 0.1. The CRP number density is relatively insensitive to copper in the range of 0.2 to 0.4. The CRP are alloyed with manganese and a smaller amount of nickel.

Higher irradiation temperatures increase the size and decrease the number density and volume fraction of the CRP. The volume fraction decreases about 30% between 260 and 316°C. For a Cu_{eff} at 260°C of 0.3% and assuming $\Delta\sigma_{ycu} \propto \sqrt{Cu_{eff}} - \sqrt{0.083}$, a reduction in the CRP hardening by about 20% at 316°C is predicted, which is reasonably consistent with previous estimate (illustrated in Figure 3). The reduced volume fraction is primarily associated with lower manganese and nickel concentrations of the CRP.

Higher nickel content increases the number density and volume fraction and decreases the size of the CRP. Volume fraction differences are about the same at both 260 and 316°C.

High phosphorous increases the number density and decreases the size of the CRP but has little effect on their volume fraction.

Low temperature (343°C) anneals show a small amount of recovery (a volume fraction of about 0.05%) of an unidentified feature in alloys irradiated at 260°C. Presumably, this primarily represents a partial recovery of the MD features. There is some evidence that this feature is a small vacancy cluster or cluster complex. Very limited data also suggest that the corresponding recovery for the 316°C irradiations is less.

The UMD and SMD components of hardening have proven to be extremely difficult to directly characterize by any technique, including SANS. Recently, however, we have carried out extensive post irradiation annealing (PIA) studies at low temperatures between about 290 and 350°C to try to identify and characterize the metallurgical and irradiation variable sensitivity of the various MD features by discriminating their thermal (stability) signatures. These results can be summarized as follows [22-24]:

At intermediate fluences the UMD were found to increase with increasing flux and nickel content and decreasing irradiation temperature. Copper appears to have little effect on the UMD features. However, for the conditions in this study the UMD would be expected to make relatively modest contributions and can be lumped with the SMD.

The SMD were found to have a range of thermal stability. The SMD hardening increases roughly with the square root of fluence times the nickel and temperature dependent coefficient. However, the SMD hardening appears to be relatively independent of flux and copper. The overall MD would be expected to contribute about 40 MPa hardening at 0.7×10^{23} n/m^2 and 288°C. The data suggest an approximately 80% decrease in the MD contribution between 260 and 316°C.

The CRP contribution increases with fluence up to an approximate saturation level in the range of 1 to 4×10^{23} n/m^2. The fluence required to achieve a specified level of CRP hardening increases with increasing flux. However, the effect of damage rate dies out below about 0.5 to 1×10^{16} n/m^2-s at 288°C and is expected to be modest for the flux in this study even at 260°C. The CRP would be expected to contribute about 125 MPa to

the hardening at 0.7 x10^{23} n/m^2 and 288°C. The nominal temperature dependence of CRP hardening evaluated between 285 and 305°C extrapolates to an approximately 35% decrease between 260 and 316°C.

These observations can be used to rationalize the observed trends in the temperature sensitivity represented in terms of f_T:

The effect of copper is due to the differences in the irradiation temperature dependence of CRP versus MD hardening contributions. Based on Figure 3, CRP hardening

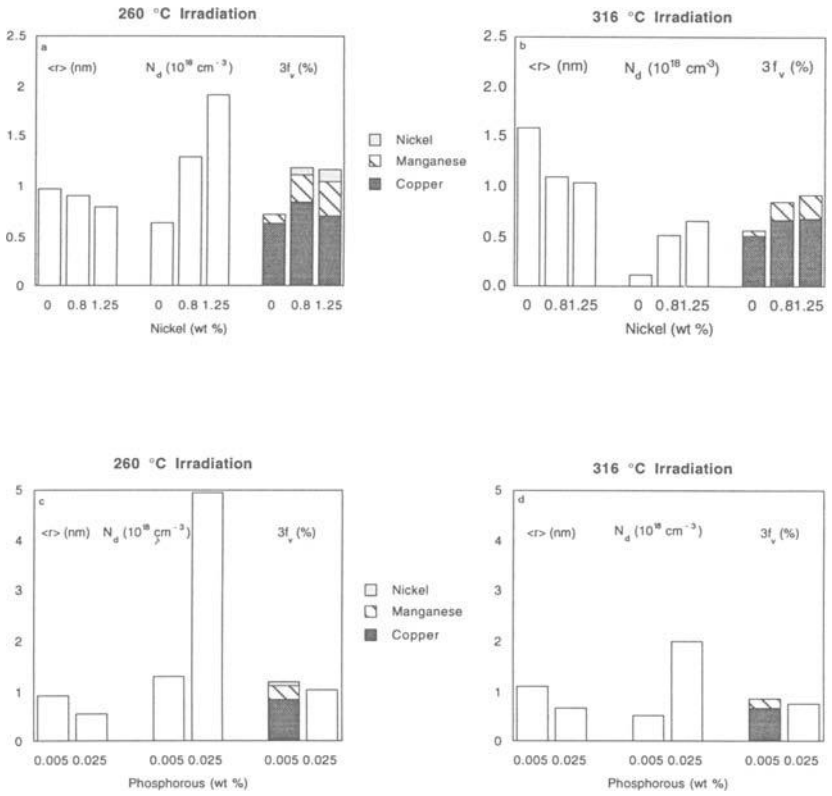


FIG. 7 -- Representative SANS results showing the variation of CRP radius, number density, volume fraction and composition with : a) nickel variation at 260 °C; b) nickel variation at 316 °C; c) phosphorous variation at 260 °C; d) phosphorous variation at 316°C.

decreases about 28±8% from 260°C to 316°C for 0.2 to 0.4Cu, 0.8Ni steels. The MD hardening in copper steels decreases by about 78±5%. These trends, consistently derived from both the PIA and irradiation temperature dependence data, are illustrated in Figure 8.

The f_T is roughly independent of nickel. Since both S' and $<\Delta\sigma_y>$ increase with higher concentrations of this element, these trends offset one another.

Higher phosphorous increases the number densities but does not affect the volume fraction of the CRP. Higher densities decrease hardening at low irradiation temperatures when the precipitates are smaller than the peak hardening size (≈1 nm). The opposite is true at high irradiation temperatures when the CRP are larger than the peak hardening size. Hence, $<\Delta\sigma_y>$ (with offsetting $-\Delta\sigma_y$ at 260 and $+\Delta\sigma_y$ at 316°C) is much less sensitive to phosphorus than S'. Thus, f_T decreases with increasing phosphorous in copper bearing steels.

While these mechanistic/microstructural interpretations add some additional confidence to the empirical expression given in Equation 3, some caveats are warranted. First, a simple linear interpolation of σ_y between the experimental endpoints at 260 and 316°C may not be valid for smaller intermediate temperature intervals. This point is illustrated in Figure 9 which compares the results of this study for the low temperature heat treatment (HTL) condition of the L-series steels with 0.4% copper and 0.8% Ni (LC and LJ) with data from a previous study on a 0.4 Cu - 0.6Ni weld (D) which received

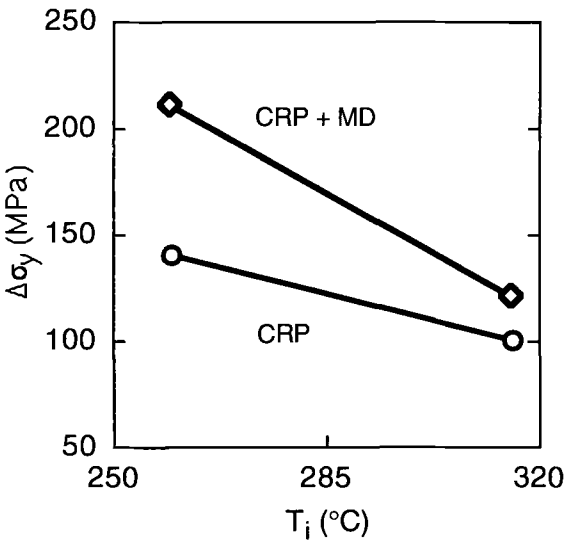


FIG. 8 -- Contributions of CRP and MD hardening as a function of irradiation temperature self-consistently estimated from the yield stress data in this study, PIA studies and SANS data.

essentially the same heat treatment. The fluxes are roughly the same for both irradiations (0.5±0.2 versus 0.76×10^{16} n/m^2-s for D weld and the L-series, respectively), and the data have been adjusted to a common fluence of 0.7×10^{23} n/m^2 and nickel content of 0.6%. Over a wide range of temperature, the data can be reasonably fit with a common sensitivity of about 1.4 MPa/°C. However, closer examination of the data suggests that the sensitivity may be significantly lower for intermediate temperatures between about 275 and 305°C. There are a number of other examples in the literature which show that the hardening and embrittlement do not vary linearly over a wide range of irradiation temperatures.

Other uncertainties are associated with the effects of flux, fluence and compositional factors which were not explored in the current experiment. For example, the structure in the $\Delta\sigma_y$ versus irradiation temperature curve shown in Figure 9 for irradiations at intermediate flux of less than about 0.7×10^{16} n/m^2-s was not observed at higher fluxes in the range of 3 to 5×10^{16} n/m^2-s. However, since flux effects are expected to diminish below about 0.5×10^{16} n/m^2 [18], we believe that the present results are representative of behavior at lower flux levels in surveillance locations [6,26]. Extrapolation to even lower flux levels, characteristic of pressure vessel operation, is more problematic. However, limited data from surveillance programs support this conclusion. The effect of much higher fluences is more difficult to address. Assuming a saturation and increase with the square root of fluence for the CRP and MD contributions, respectively, f_T would be expected to be

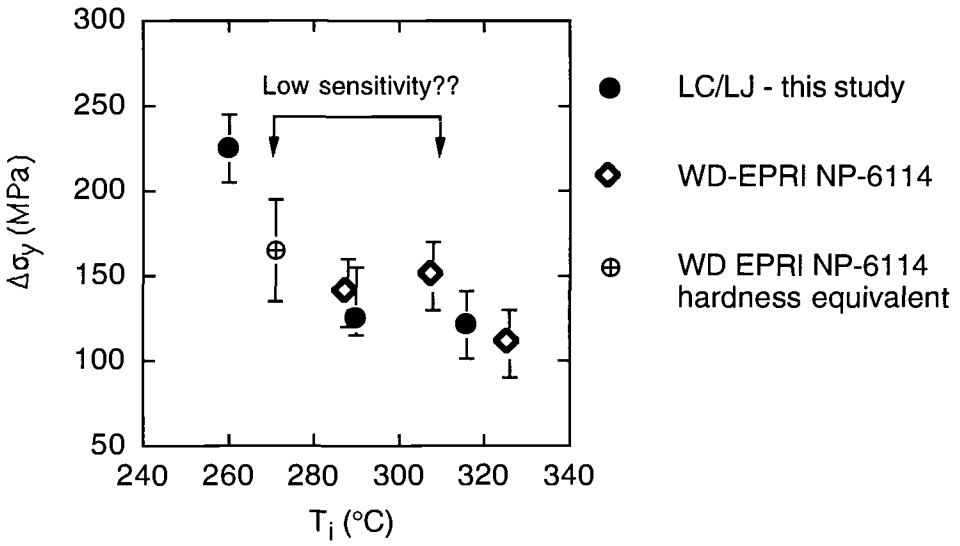


FIG. 9 -- Comparisons of the irradiation data from this study with previous results indicating possible "structure" in the $\Delta\sigma_y$ versus T_i curve.

roughly independent of fluence for low copper steels and increase only slightly with increasing fluence for intermediate to high copper steels. In the latter case, typical increments in f_T of less than about 0.003 could be expected.

SUMMARY AND CONCLUSIONS

A new empirical correlation of the effect of irradiation temperature on $\Delta\sigma_y$ in the range of 260 to 316°C has been developed. The temperature sensitivity is best expressed as a ratio, f_T, of the difference in $\Delta\sigma_y$ between 260 and 316°C normalized by the average yield stress increase ($<\Delta\sigma_y>$, nominally $\Delta\sigma_y$ at 288°C). The dependence of f_T on copper and phosphorous described in Equation 3 can be rationalized by fundamental mechanistic and microstructural observations. These observations are also consistent with a minimal effect of nickel and can be used to postulate a modest effect of a somewhat lower flux and higher fluence. However, some caution must be exercised in applying these results. For example, there are indications that f_T is not constant and, indeed, may be lower at intermediate temperatures between 275 and 305°C. Further, the temperature dependence at very low fluxes is not known. These issues should be addressed in future studies.

ACKNOWLEDGMENTS

The authors thank D. Gragg and J. W. Sheckherd for their contributions to specimen preparation and to post-irradiation testing. We also thank Russ Hawthorne for providing irradiation space. The work was supported by the US Nuclear Regulatory Commission, contract number NRC 04-90-046. The encouragement and support of our contract monitor, A. Taboada, is gratefully acknowledged.

REFERENCES

[1] Jones, R. B., and Williams, T. J., "The Dependence of Irradiation Hardening and Embrittlement on Irradiation Temperature", Effects of Radiation on Materials: 17th International Symposium, ASTM STP 1270, R. K. Nanstad, D. S. Gelles, A. S. Kumar, and E. A. Little, Eds., American Society for Testing and materials, Phildelphia, 1996.

[2] Lucas, G. E., Odette, G. R., Mader, E., Haggag, F., and Nanstad, R., Proceedings of the Fifth International Symposium on Environmental Degradation in Nuclear Power Systems - Water Reactors, Cubicciotti, D., Simonen, E., and Gold, R., Eds. ANS, La Grange Park, Ill., 1992, p696.

[3] Buswell, J. T., and Jones, R. B., Effects of Radiation on Materials:16th International Symposium, ASTM STP 1175, A. S. Kumar, D. S. Gelles, R. K. Nanstad and E. A. Little, eds., ASTM, Philadelphia, Pa., 1992, p424.

[4] Hawthorne, J. R., ibid p306.

[5] Nanstad, R. K. and Berggren, R. G., ibid p.424.

[6] Brillaud, C., and Hedin, F., Effects of Radiation on Materials: 15th International Symposium, ASTM STP 1125, Stoller, R. E., Kumar, A. S. and Gelles, D. S., eds., ASTM, Philadelphia, Pa., 1990, p23.

[7] Odette, G. R., and Lucas, G. E., An Experimental Investigation of Kinetic Aspects of Neutron Irradiation Embrittlement of Light Water Reactor Pressure Vessel Steels, EPRI Report NP 6114, Electric Power Research Institute , 1989.

[8] Williams, T. J., Burch, P. R., English, C. A. and de la cour Ray, P. H. N., Proc. Third Int'l Symp. on Env. Degradation of Matls. in Nucl. Power Systems - Water

Reactors; Theus, G. J., and Weeks, J. R., eds., TMS, Warrendale, PA, 1988, p121.

[9] Brumovsky, M., Comparison of Radiation Embrittlement of Western and Conecom Type Reactor Pressure Vessel Steels, International Course on Implications of Radiation Induced Embrittlement for the Integrity of Pressure Vessels, IAEA-CNEA Mar del Plata, Argentina, 1987.

[10] Odette, G. R., and Lucas, G. E., "Irradiation Embrittlement of Reactor Pressure Vessel Steels: Mechanisms, Models, and Data Correlations", Radiation Embrittlement of Nuclear Reactor Pressure Vessel Steels: An International Review - Volume II, ASTM STP 909, L. E. Steele, Ed., ASTM, Philadelphia, PA, 1986, p206.

[11] Pachur, D., Evaluation of BR3 Materials Metallurgical Trend Curves, 1985.

[12] Ahlf, J. Nuc. Eng. and Des., 81, 1984, p231.

[13] Hawthorne, J. R., Radiation Effects Information Generated on the ASTM Reference Correlation-Monitor Steels, ASTM Data Series Publication DS 54, ASTM Philadelphia, PA, 1974.

[14] Steele, L. E., Atomic Energy Review - Neutron Embrittlement of Reactor Pressure Vessel Steels, Int. Atomic Energy Agency, Vienna, 1969.

[15] Grounes, M., Effects of Radiation on Structural Metals, ASTM STP 426, ASTM, Philadelphia, PA, 1967, p224.

[16] Barton, P.J., Harries, D.R. and Mogford, I.L., J. Iron and Steel Inst. 203, 1965, p507.

[17] Odette, G. R., "Modeling Irradiation Embrittlement of Reactor Pressure Vessel Steels", IAEA Technical Report Series, Davies, M. ed. (to be published)

[18] Odette, G. R., Lucas, G. E., Mader, E., Phythian, W., and English, C., Effects of Irradiation on Materials:16th International Symposium, ASTM STP 1175, A.S. Kumar, D.S. Gelles and R., Nanstad Eds, ASTM, Philadelphia, PA, 1994, p373.

[19] Odette, G. R., "On the Dominant Mechanism of Irradiation Embrittlement", Scripta Met., 11, 1983, p1183.

[20] Fisher ,S.B., and Buswell J.T., "A Model For PWR Pressure Vessel Embrittlement", Int. J. Pres. Ves.&Piping, 27, 1987, p91.

[21] Mader, E., Lucas, G. E., and Odette, G. R., Effects of Radiation on Materials: 15th International Symposium, ASTM STP 1125, Stoller, R. E., Kumar, A. S. and Gelles, D. S., eds., ASTM, Philadelphia, Pa., 1992, p151.

[22] Mader, E., Lucas, G. E., and Odette, Proceedings of the Sixth International Symposium on Environmental Degradation in Nuclear Power Systems - Water Reactors, Gold, R. E and Simonen,eds. TMS, Warrendale, PA., 1993, p739.

[23] Odette, G. R., et. al., to be published

[24] Odette, G. R., Lombrozo, P. M., and Wullaert, R. A., Effects of Radiation on Materials: 12th International Symposium, ASTM STP 870, F. A. Garner and J. S. Perrin, Eds., ASTM, Philadelphia, PA, 1985, p840.

[25] Odette, G. R., and Lucas, G. E., Effects of Radiation on Materials: 14th International Symposium, Vol. 2, ASTM-STP-1046, N. H. Packan, R. E. Stoller, and A. S. Kumar, Eds., American Society for Testing and Materials, 1990, p323.

[26] McElroy, R. J. and Lowe, A. L., "Irradiation Embrittlement Modeling of Linde 80 Weld Metals" ASTM STP 1270, R. K. Nanstad, D. S. Gelles, A. S. Kumar, and E. A. Little, Eds., American Society for Testing and materials, Phildelphia, 1996.

Hiroshi Shibamoto,[1] Kunio Koyama,[1] Hideki Yuya,[1], Masayuki Hasegawa,[2] Akihiko Kimura,[2], Hideki Matsui,[2] and Sadae Yamaguchi [2]

EFFECTS OF PROTON IRRADIATION ON POSITRON ANNIHILATION AND MICRO-VICKERS HARDNESS OF Fe-C-Cu MODEL ALLOYS

REFERENCE: Shibamoto, H., Koyama, K., Yuya, H., Hasegawa, M., Kimura, A., Matsui, H., and Yamaguchi, S., **"Effects of Proton Irradiation on Positron Annihilation and Micro-Vickers Hardness of Fe-C-Cu Model Alloys,"** *Effects of Radiation on Materials: 17th International Symposium, ASTM STP 1270,* David S. Gelles, Randy K. Nanstad, Arvind S. Kumar, and Edward A. Little, Eds., American Society for Testing and Materials, 1996.

ABSTRACT: Positron lifetime and micro-Vickers hardness were measured on well annealed model alloys, Fe-C(0%, 0.2%, 0.35%)-Cu(0%, 0.15%, 0.3%), after 1MeV proton irradiation with a dose of $3x10^{17}$ /cm^2 below 80°C. Longer lifetime, ranging from 310 to 360 ps, component appears and gives evidence of formation of microvoids containing about 10 vacancies. The longer lifetime decreases with increasing copper content and suggests smaller microvoids for Fe-Cu alloys. The longer lifetime increases with annealing temperature up to 400°C in pure Fe, but exhibits decrease around 300°C in Fe-C-Cu alloys. This decrease indicates reduction in effective size of microvoid around 350°C. Irradiation hardening is accelerated by copper but retarded by carbon. Post-irradiation anneal hardening is revealed at about 150°C and 350°C in Fe-C and Fe-C-Cu alloys. In Fe-Cu alloys, however, a single narrow hardening peak is observed around 350°C. The irradiation hardening in Fe-C alloy anneals out around 550°C, while that in alloys containing Cu makes complete recovery at about 650°C.

KEYWORDS: proton irradiation, positron annihilation, irradiation hardening, Fe-C-Cu model alloys

INTRODUCTION

An accurate understanding of the mechanism of irradiation embrittlement of pressure vessel steels is very necessary for design and endurance assessment. It has been widely known for many years that copper impurity plays a significant role in the embrittlement process [1-2]. It has been suggested that irradiation-induced hardening and embrittlement are caused by copper precipitation and microvoids [3-6]. Therefore experimental confirmation of these hypothesis is indispensable for the studies of the irradiation effects.

The positron annihilation technique is widely used in studies of irradiation-induced voids in metals, especially for investigating the initial stage of void nucleation [7-11]. Positron annihilation studies have been reported on reactor pressure vessel (RPV) steels after neutron irradiation [12-15] and Fe model alloys after electron irradiation [16,17].

[1]Research Engineers, Electric Power Research and Development Center, Chubu Electric Power Company, Inc., 20-1 Kita-Sekiyama, Odaka-Cho, Midori-ku, Nagoya 459, Japan
[2]Associate Professors and Professors, respectively, Institute for Materials Research, Tohoku University, Sendai 980-77, Japan

Copyright© 1996 by ASTM International www.astm.org

Longer positron lifetime (300 – 500 ps) components, being due to positrons trapped at microvoids, and their annealing behavior were studied [14–15]. Then it is very important to carry out systematic studies with the use of various experimental tools such as positron annihilation, mechanical testing, small angle neutron scattering (SANS) which are expected to provide useful information about irradiation–induced defects. In the present study, positron lifetime, micro–Vickers hardness and TEM are employed to investigate possible microvoid formation, copper precipitates and their influence on simple model alloys of RPV steels, namely Fe–C–Cu alloys. Detailed TEM observation will be presented in a separate paper in these proceedings [18].

EXPERIMENTAL

Model alloy samples were prepared as follows. First, mother alloys of Fe–4wt.%C and Fe–5wt.% Cu were made from pure iron (ATOMIRON 5N, Showa Denko Co.) , Specure–Copper (99.999%, Johnson Matthey Chem. Ltd.) and high–purity graphite (IG–110U, Toyo Tanso Co.,) by arc melting in Ar gas atmosphere. They were diluted with appropriate amounts of iron by arc–melting. The resulting alloys were cold–rolled to about 0.3 mm (positron annihilation and micro–Vickers hardness) or 0.15 mm (transmission electron microscope, TEM) in thickness and subsequently punched to disks of 3mm or 5 mm in diameter, mechanically polished and then electropolished. The contents of copper and carbon were determined by chemical analysis as listed in Table 1.

The disk samples were wrapped with zirconium foils and sealed in evacuated quartz tubes and heat–treated: solution heat treated at 880°C for 8 h, tempered at 670°C, stress–relieved at 620°C for 22 h and finally furnace–cooled to room temperature. Then the sample were electropolished to remove surface contamination introduced during the heat treatment.

To observe microstructure these samples were examined with optical, scanning electron and transmission electron microscopes. Grain sizes were 10 to 100 μm in the Fe–Cu alloys and 1 to 20 μm in the carbon–doped alloys as seen in Fig. 1 (optical microscopic observation) and in Fig.2 (SEM observation). In Fe–Cu alloys fine copper precipitates were seen in the grains as shown in Fig. 2(b) (SEM) and Fig. 3(b)(TEM). Large precipitates were identified as fcc copper, while fine precipitates are possibly bcc–copper or twinned 9R close–packed structure [19]. No precipitation of copper at the grain boundaries were observed. In the carbon–doped alloys coarse cementite precipitates were seen at grain boundaries as shown in Fig. 2(c) and (d) and very fine cementites were observed in grains as seen in TEM picture (Fig. 3(c) and (d)).

These samples were bombarded with 1 MeV protons to a dose of 3×10^{17} /cm^2 below 80°C in the Tohoku University Tandetron Accelerator. After irradiation, the samples were isochronally step–annealed from 100 to 650°C for 30 min. Positron lifetime and micro–Vickers hardness were measured on the as–irradiated state and after annealing.

Table 1. Chemical composition of Fe–Cu–C alloys.

Sample	Cu (wt%)	C (wt%)	Sample	Cu (wt%)	C (wt%)
Pure Fe		0.0028	0.15 Cu - 0.2 C	0.157	0.21
0.05 Cu	0.054	0.0031	0.3 Cu - 0.2 C	0.339	0.20
0.15 Cu	0.157	0.0041	0.35 C	0.001	0.36
0.3 Cu	0.314	0.0035	0.05 Cu - 0.35 C	0.053	0.35
0.2 C		0.20	0.15 Cu - 0.35 C	0.157	0.35
0.05 Cu - 0.2 C	0.057	0.20	0.3 Cu - 0.35 C	0.339	0.35

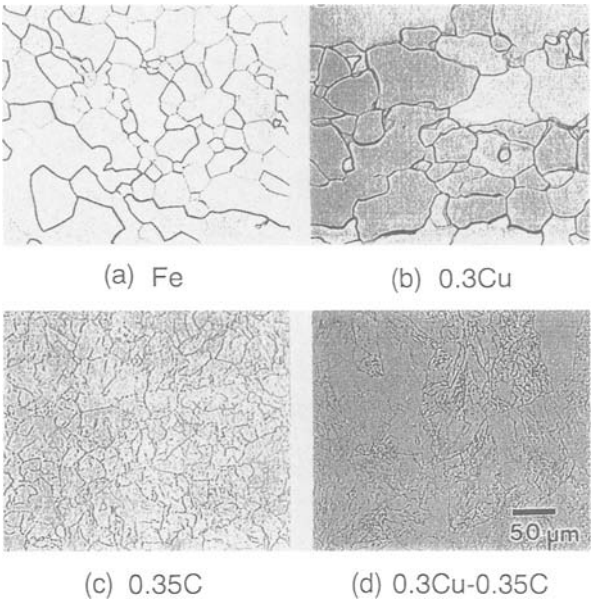


Fig. 1. Photomicrographs showing grain sizes of the alloys: (a) pure Fe, (b) 0.3Cu, (c) 0.35C, and (d) 0.3Cu–0.35C.

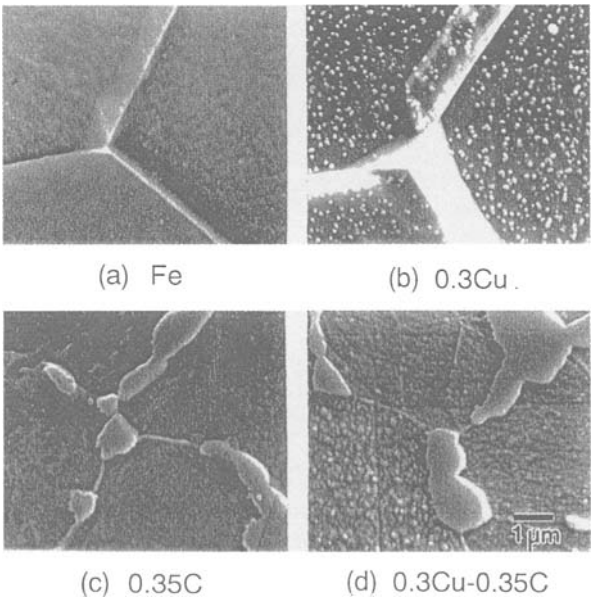


Fig. 2. Scanning electron micrographs showing copper and carbide precipitation at grain boundaries and in grains.

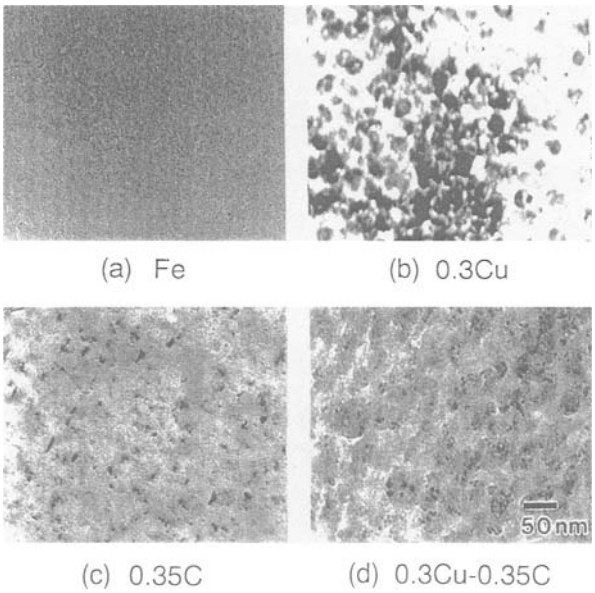


Fig. 3. Transmission electron micrographs showing the copper and carbide precipitates.

Positron lifetime measurements were carried out with use of a usual time-spectrometer with time resolution of about 180 ps (FWHM) and positron source of ^{22}Na (0.7MBq) sealed with Mylar film (5 μm in thickness). The lifetime spectra were analyzed with the PATFIT-88 program [20]. Micro-Vickers hardness was determined as the average of at least 20 indentations on each state of the samples using a conventional apparatus with a load of 25 g. The hardness measurements were made both on the irradiated and unirradiated (rear) faces of the samples to correct for slight increase in the hardness, presumably due to surface contamination, during step-annealing. TEM observation was made with a JEOL JEM2010 electron microscope. Experimental details and observation of TEM experiments after irradiation will be presented in these proceedings [18].

RESULTS AND DISCUSSION

Depth Profile of Irradiation-Induced Defects

Figure 4(b) shows depth profiles of displacement damage (vacancies) and implanted hydrogen calculated with TRIM program [21] under the usual assumption of threshold energy of 40eV. It can be seen that the projected range of the protons is 6.6 μm and the damage peak is at 6.4 μm; displacement-per-atom (dpa) ratio at the peak is about 0.2 and its average across the whole of the penetrated region, including the peak damage, is about 0.06. A preliminary cross-sectional TEM observation revealed a damaged band around the damage peak. In the damaged band black dots, presumably interstitial-type dislocation loops, were observed. The averaged radius and number density, obtained with TEM observation, are plotted against depth in Fig. 4(c). In the copper-doped samples very small copper precipitates have been found to form after the irradiation [18].

Positrons emitted from ^{22}Na have an energy distribution ranging from zero to 0.54

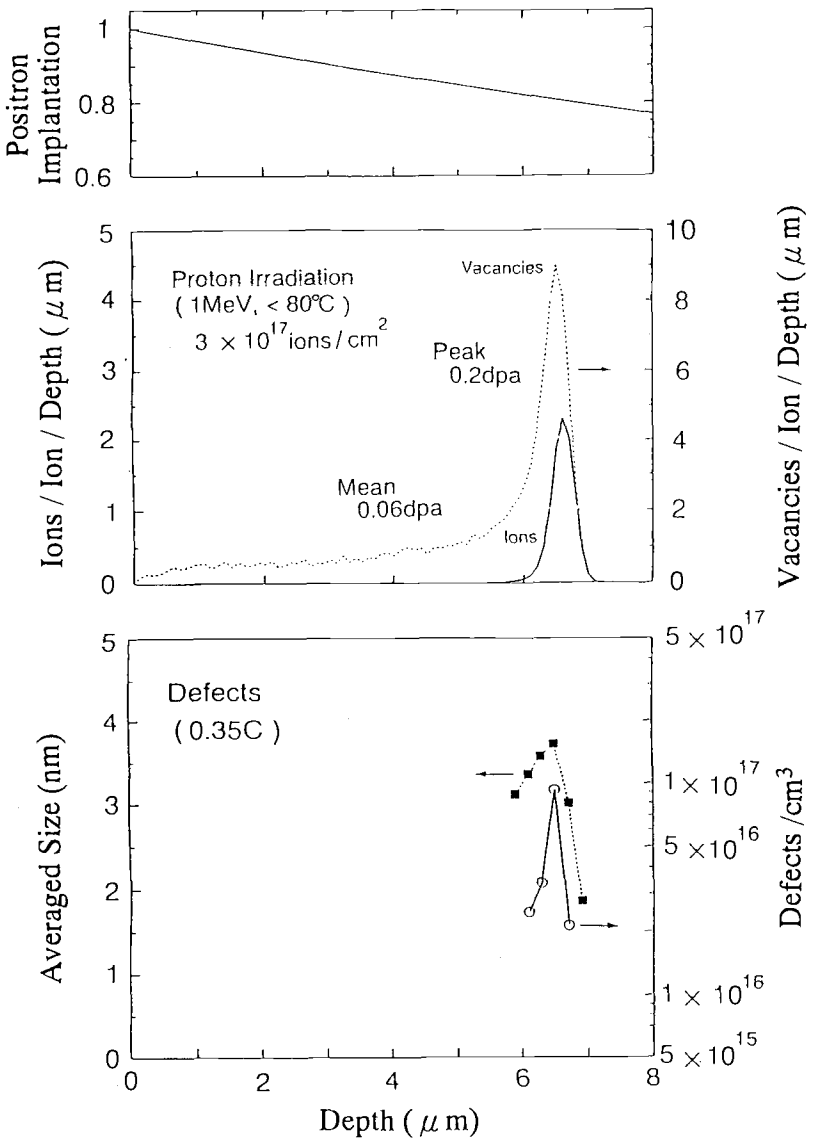


Fig. 4. Implantation profiles of positrons from ^{22}Na source (a), and 1 MeV protons (b). Depth profile of displacement of atoms (b), and those of averaged size and number density of the black dots revealed by TEM observation (c) are shown.

MeV and have a maximum at 0.19 MeV. The implantation profile of positrons is given by $\exp(-\alpha x)$, where α is an attenuation length (α=33 mm^{-1}) and x is the depth [21], and shown in Fig.4(a). It is demonstrated that about 25% of the positrons are implanted within the damaged region. Positron diffusion length in iron is estimated to be 0.5 to 1 μm. Then we can say that about 25 % of positrons annihilate from the damaged region while the remaining positrons penetrate further into undamaged region and annihilate there.

Positron Lifetime

Figure 5 shows typical lifetime spectra for the unirradiated and irradiated samples. After irradiation the lifetime spectrum shows a characteristic longer lifetime component due to microvoids which gives about 300ps. The lifetime spectra for the irradiated samples are well decomposed into two lifetime components with the time constants τ_i and the relative intensities I_i (i=1,2) ($I_1 + I_2 = 1$). The longer lifetime (τ_2) component and its intensity (I_2) is shown against copper content in Fig.6. For the alloys doped with 0.35wt%C, τ_2 slightly decreases with copper content. Previous theoretical calculations for the lifetime of positrons trapped at microvoids are shown against the number of vacancies contained in the microvoids (Fig.7)[10,23]. The slight decrease with copper content strongly suggests the smaller microvoids for the higher content of Cu. It is consistent with previous observation with TEM and SANS by Smidt et al. [24] and Frisius et al. [25] that copper impurities refine voids induced by neutron irradiation at higher temperatures. From positron annihilation experiments, however, Akamatsu et al. noticed in Fe model alloys after 3-MeV electron irradiation that the clustering of vacancies is favored by carbon but not affected by copper. This observation makes quite contrast with the above results after neutron irradiation or proton irradiation. Further Hori et al. suggested that copper atoms restrict the vacancy migration and aggregation in electron-

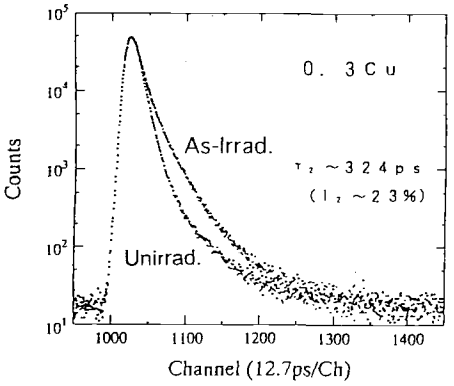


Fig. 5. Typical positron lifetime spectrum before and after irradiation (0.3Cu).

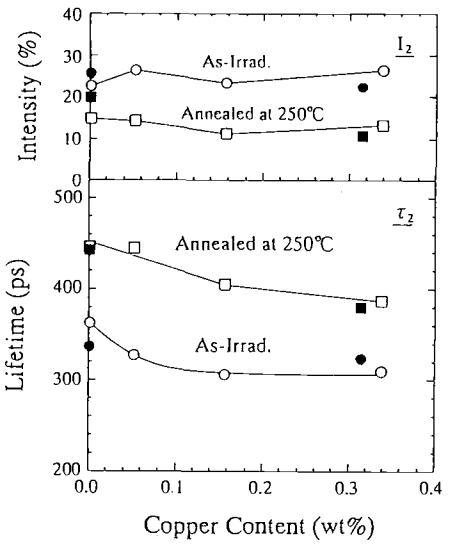


Fig. 6. The long lifetime (τ_2) and its intensity (I_2) for pure Fe and Fe-0.3Cu with no carbon (● ■), and Fe-0.3Cu alloys with 0.35C (○ □).

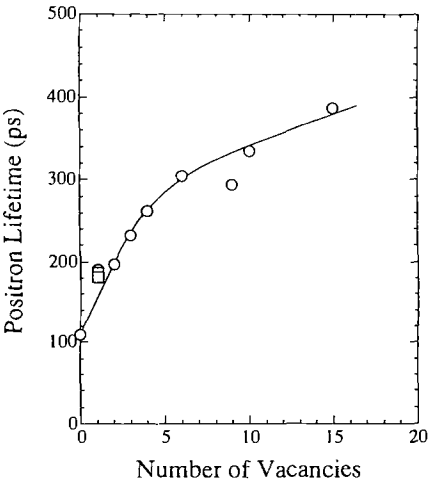


Fig. 7. Theoretical calculations for positron lifetimes at microvoids in Fe by Puska and Nieminen (O)[10], and by Kamimura et al (□) [23]. The solid line is only to guide the eye.

irradiated Fe–Cu model alloys below 280K. Possible reasons for the discrepancy are the irradiation particles and their irradiation conditions such as the dpa rate and irradiation temperature. At this stage it is tempting to suggest that very small vacancy clusters were formed by electron irradiation and are not stable because the dpa rate of the electron irradiation (dpa = 0.004), is more than one order of magnitude smaller than that of the neutron or proton irradiation. Definite answer for this discrepancy, however, must wait future studies.

Irradiation induced vacancies in the samples with higher Cu content presumably tend to trapped at copper precipitates and consequently give smaller microvoids. The calculation shown in Fig. 7 suggests that the number of vacancies is about 12 for 0.3Cu and about 6 in 0.3Cu–0.35C.

The observed short lifetime (τ_1) is an average between the short lifetime in the damaged region and the bulk lifetime of undamaged region (110ps) and then mostly due to positrons in the undamaged region. The I_2 intensities for the as–irradiated states are very close to the positron implantation fraction for damaged region of about 25% (Fig.6). This means that almost all the positrons in the damaged region are trapped at the microvoids and strongly suggests a high density of microvoid formed throughout the proton range. In general positrons in a sample containing microvoids are subjected to competition between annihilation in the free state and trapping into localized states at the microvoids; the higher concentration of microvoids will cause the larger trapping rate and resulting annihilation at the microvoids. In Fe the free annihilation rate of positrons ($\lambda_f = 1/\tau_f$, τ_f =110ps) is $9ns^{-1}$. Then the above result indicates that the trapping rate at the microvoids is much larger than 9 ns^{-1}. Unfortunately, no calculation on specific trapping rate, trapping rate per unit defect concentration, at microvoids has been reported. A calculation for microvoids of 10 vacancies in Al gives about $3x10^{-8}$ cm^3/s [26]. This specific trapping rate is close to that deduced by a simple propagation model [22]. Assuming the same specific trapping rate for Fe as that in Al, we can estimate the microvoid density to

be of the order of $10^{18}/cm^3$.

Isochronal annealing behavior of the lifetime parameters are shown in Fig.8. In pure Fe the longer lifetime progressively increases with annealing temperature and reaches about 500 ps, while its intensity (I_2) decreases with temperature and recovers to zero at 450°C. This means that the microvoids anneal out around 450°C. This temperature agrees very well with that observed for neutron-irradiated Fe alloys by Valo et al[15]. This result suggests that the microvoids are unlikely to be stabilized by implanted hydrogen impurities at least at higher temperatures. It should be mentioned here that all the electron damage in the model alloys, however, is reported by Akamatsu et al.[16] and Hori et al. [17] to annealed out below 300°C. The electron damage is supposed to be unstable as compared with that of neutron or proton irradiation, as suggested above.

In the alloy samples the longer lifetime increases with temperature up to about 250°C, but shows a decrease around 300-350°C and then increases again with temperature. It should be noted that no decrease in τ_2 is seen in pure Fe after annealing around 300°C. The decrease means a reduction in average size of the microvoids.

The progressive increase in τ_2 accompanying the decrease in I_2 suggests growth of the microvoids by a process of Ostwald ripening. Possible explanation of the temporal decrease in τ_2 around 300°C is nucleation of smaller microvoids from vacancies trapped at multiple carbon-vacancy complexes or copper-vacancy complexes. Takaki et al [27]. suggested from a resistivity study on carbon-doped iron after electron irradiation that multiple carbon-vacancy complexes break up around 300°C. These vacancies released from the complexes would agglomerate into small microvoids and give shortening in τ_2 accompanying small increase in I_2 as seen in the some alloys such as 0.3Cu and 0.3Cu-0.35C. The other possible interpretation will be migration of carbon or copper atoms released from irradiation-induced defects to the microvoids which give shrinkage of the microvoids. It should be noted that τ_2 after annealing at 250°C also decreases with increasing copper content, in a similar way for the as-irradiated state (fig.6). Exact clarification of physical process for annealing behavior of the microvoids must wait future studies.

Micro-Vickers Hardness

Figure 9 shows the dependence of micro-Vickers hardness on copper content in the unirradiated (a) and the as-irradiated states (b). It is seen in the unirradiated samples that the hardness markedly increases with carbon content, which is the usual hardening in carbon-doped iron due to carbide precipitates and very small grain sizes. The hardness increases only slowly with copper content as seen in Fig. 9(a). It should be noted that the slope for the increase per copper content is nearly independent of carbon content, as seen in the parallel solid lines in Fig.9(a). After irradiation, however, in the carbon-doped samples the hardness increases more rapidly with copper content than in the samples without carbon. This clearly indicates that interactive effect between copper and carbon is operative in the irradiation hardening mechanism in Fe-Cu-C alloys.

Figure 10 presents the isochronal annealing behavior of the irradiation-induced increase (ΔH) in the micro-Vickers hardness. For the unirradiated faces of the irradiated samples, small and progressive hardening, which reached increases of 10 to 20 micro-Vickers hardness after the final step-annealing at 700 °C, was observed during the successive step-annealing. It is very likely that this hardening is caused by slight surface contamination during the annealing. Thus the irradiation hardening was obtained as the difference of the micro-Vickers hardness between those of the irradiated and unirradiated (rear) face. It should be noted that all the bumps and valleys seen in Fig.10 are due to the recovery changes in the irradiated faces but not to those in the unirradiated faces. In pure Fe (Fig. 10(a)) the hardening decreases gradually with annealing temperature up to about 400°C and recovers completely around 500°C. In 0.35 C alloy , Fig.10(c), the

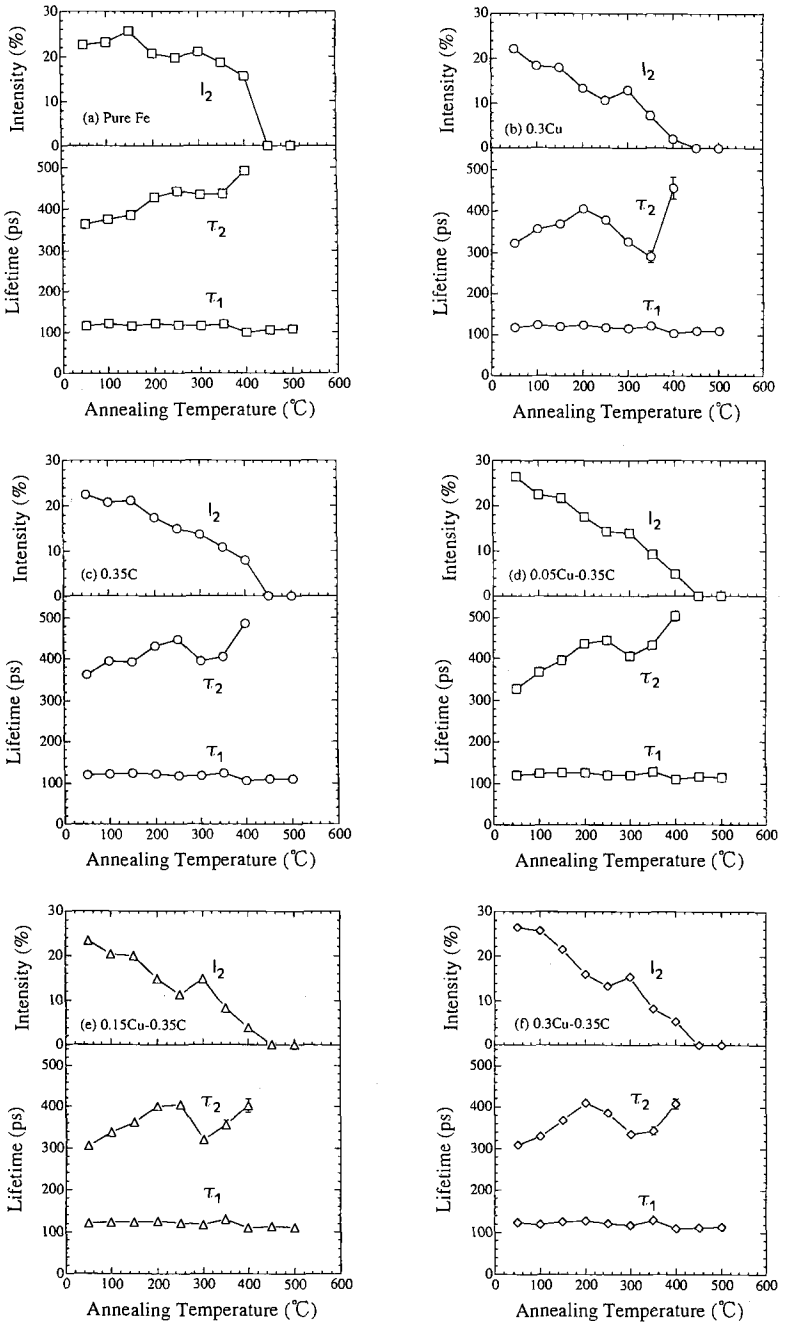


Fig. 8. Isochronal annealing behavior of positron lifetime parameters.

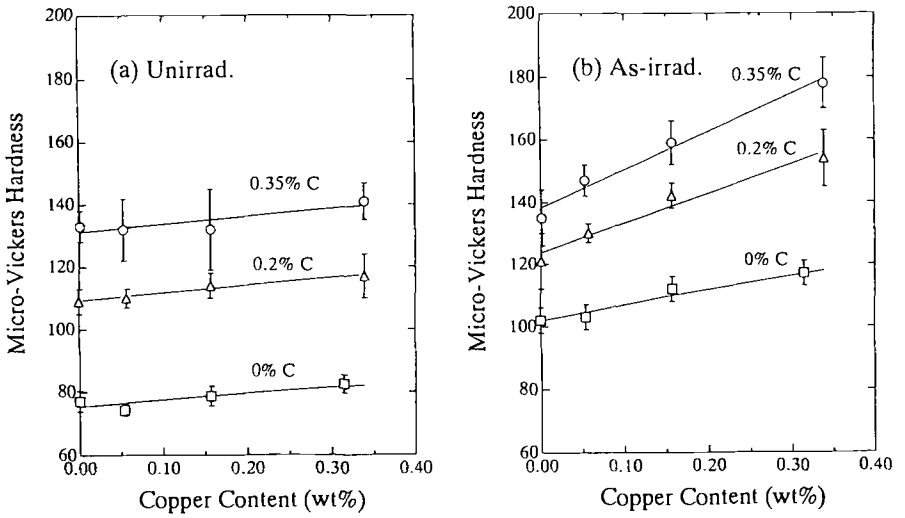


Fig. 9. Dependence of micro-Vickers hardness on copper content: (a) unirradiated, and (b) as-irradiated state.

recovery of the hardening show two humps centered at 150°C and 350°C. The hardening peak around 150°C is likely to be caused by metastable ε phase formation. The second peak around 350°C is considered to have different origin. It coincides with a minimum around 350°C in the longer positron lifetime (τ_2), and therefore implies a connection with small microvoids.

In 0.3Cu alloy, there is only one hardness peak at 350°C, but much narrower than that observed in 0.35C alloys. Anneal hardening after neutron irradiation was observed in Fe-Cu alloy by Takaku et al [28]; they interpreted it as formation of irradiation-induced defect complex containing Cu and C or N impurities. It is tempting to consider that the rather sharp peak centered at 350°C is due to copper precipitation. In quenched samples [29], it has been shown that copper precipitation takes place at a temperature only above 500°C. The presence of the hardening peak around 350°C implies that vacancies are available for copper diffusion to take place.As stated above, the I_2 intensity is decreasing in this temperature range. Many vacancies in the as-irradiated state are in the form of the microvoids while some of the single vacancies are likely to be trapped by copper (atoms or precipitates). Then around 350°C copper-complexes of vacancies might be formed and give the anneal hardening in Fe-Cu alloy. In the Fe-0.35C alloys containing Cu (Fig. 10 (d)-(f)) two hardening peaks are seen and ascribed to the hardening due to carbon and copper. It should be noted that the hardening anneals out at about 550°C in pure Fe and Fe-0.35C alloy while at about 600°C in the Cu-doped alloys such as Fe-0.3Cu and Fe-0.15Cu-0.35C. This means some irradiation-induced vacancies associated with copper are stable up to about 600°C.

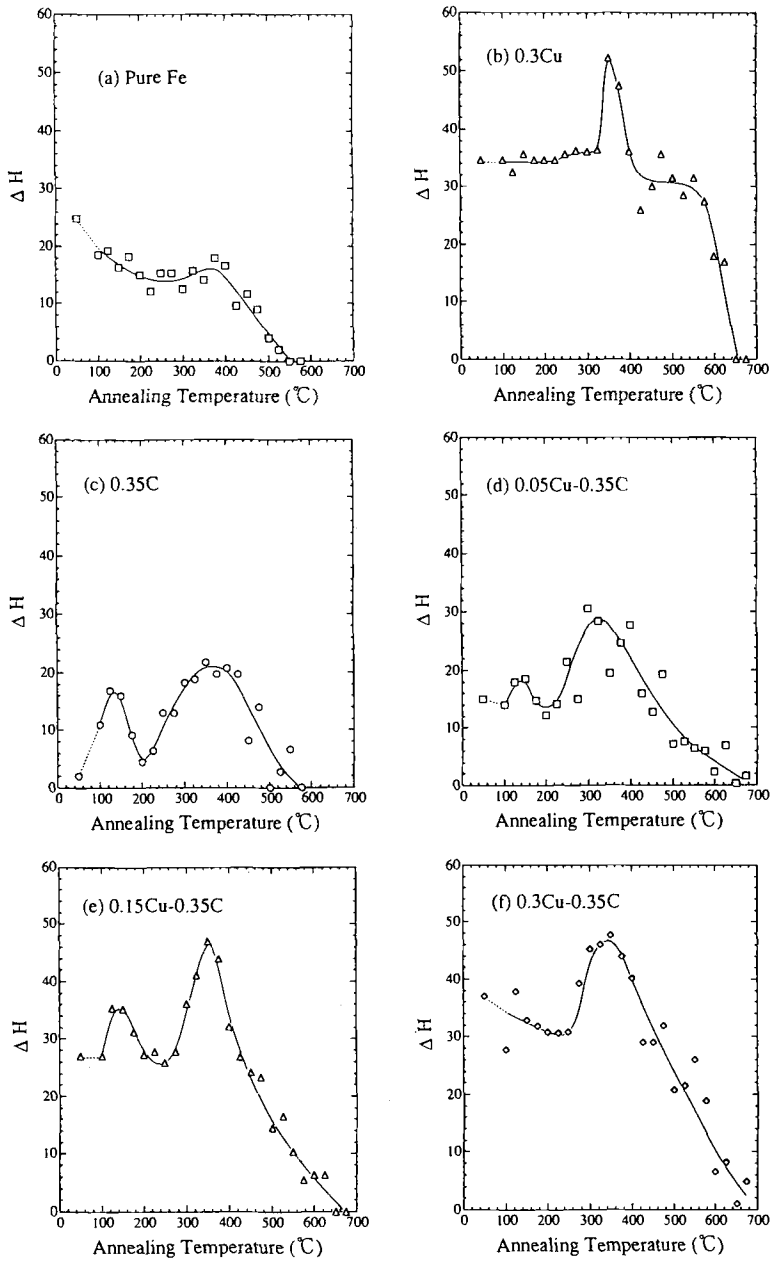


Fig. 10. Recovery of irradiation-induced increase in micro-Vickers hardness after isochronal annealing.

SUMMARY

Positron lifetime and micro-Vickers hardness measurements were carried out on well annealed Fe-Cu-C model alloys irradiated with 1 MeV protons to a dose of $3x10^{17}$ /cm^2 below 80°C. Positron lifetime spectra showed longer lifetime components due to irradiation induced microvoids consisting of about 10 vacancies. The longer lifetime decreased with increasing copper content, which suggests smaller microvoids for the higher content of copper. In pure Fe the longer lifetime increases progressively with post-irradiation annealing temperature up to 400°C, which shows thermal growth of the microvoids. In Fe-Cu-C alloys temporal shortening in the longer lifetime was observed after annealing around 300°C which indicated smaller microvoids.

Before irradiation, micro-Vickers hardness increases markedly with carbon content but slowly with copper content. Irradiation hardening, however, is enhanced by Cu doping but dehanced by carbon doping. This observation strongly demonstrate the importance of interactive effects between various impurities in irradiation hardening and embrittlement in Fe model alloys. Post-irradiation anneal hardening was seen around 150°C and around 350°C in Fe-C and Fe-Cu-C alloys. The hardening around 350°C is likely to be correlated with the temporal shortening in the longer positron lifetime. A narrow peak hardening was detected at 350°C in Fe-0.3Cu alloy. Irradiation hardening in Fe-Cu alloys remained up to 650°C which was about 100°C higher than Fe-C alloys.

Acknowledgements

We would like to thank Drs. Nagata and K. Takahiro for their proton-irradiation, and Mr. T. Miyamoto for his help in positron experiments, and Mr. T. Takahashi for his arc-melting of the samples.

References

[1] Phythian, W.J., Foreman, A.J.E., English, C.A., Buswell, J.T., Hetherington, M., Roberts, K., and Pizzini, S., "The Structue and Hardening Mechanism of Copper Precipitation in Thermally Aged or Irradiated Fe-Cu and Fe-Cu-Ni Model Alloys," Effects of Radiation on Materials: 15th International Symposium, ASTM STP 1125, R.E. Stoller, A. S. Kumar, and D. S. Gelles, Eds., American Society for Testing and Materials, Philadelphia, 1992, pp. 131-150.

[2] Buswell, J.T., and Jones, R.B., "The Modeling of Radiation Hardening and Embrittlement in Magnox Mild Steel Submerged-Arc Welds," Effects of Radiation on Materials: 16th International Symposium, ASTM STP 1175, A. S. Kumar, D. S. Gelles, R. K. Nanstad, and E. A. Little, Eds., American Society for Testing and Materials, Philadelphia, 1993, pp.424-443.

[3] Odette, G. R., "On the Dominant Mechanism of Irradiation Embrittlement of Reactor Pressure Vessel Steels," Scripta Metallurgica, Vol. 17, 1983, pp. 1183-1188.

[4] Lucas, G. E., Odette, G. R., Lombrozo, P. M., and Sheckherd, J. W., "Effects of Composition, Microstructure, and Temperature on Irradiation Hardening of Pressure Vessel Steels," Effects of Radiation on Materials: Twelfth International Symposium, ASTM STP 870, F. A. Garner, and J. S. Perrin, Eds., American Society for Testing and Materials, Philadelphia, 1985, pp. 900-930.

[5] Stoller, R. E., "Modeling th Influence of Irradiation Temperature and Displacement Rate on Radiation-Induced Hardening in Ferritic Steels," Effects of Radiation on Materials: 16th International Symposium, ASTM STP 1175, A. S. Kumar, D. S. Gelles, R. K. Nanstad, and

E. A. Little, Eds., American Society for Testing and Materials, Philadelphia, 1993, pp394–423.

[6] Phytian, W. J. and English, C. A., "Microstructural evolution in reactor pressure vessel steels," Journal of Nuclear Materials, Vol. 205, 1993, pp.162–177.

[7] Triftshäuser, W., "Positron Annihilation," Topics in Current Physics, Vol.40, "Microscopic Methods in Metals", U. Gonser, Ed., Springer, 1986, pp. 249–295.

[8] Eldrup, M., "Application of the Positron Annihilation Technique in Studies of Defects in Solids," Defects in Solids, A. V. Chadwick, and M. Terenzi, Eds., Plenum, New York, 1986, pp. 145–178.

[9] Hautojärvi, P., "Vacancies and Vacancy–Impurity Interactions in Metals Studied by Positrons," Materials Science Forum, Vol. 15–18, 1987, pp. 81–98.

[10] Puska, M. J., Nieminen, R. M., "Defect spectroscopy with positrons: a general calculation methods," Journal of Physics F: Metal Physics, Vol. 13, 1983, pp. 333–346.

[11] Yoshiie, T., Hasegawa, M., Kojima, S., Sato, K., Saitoh, Y., and Yamaguchi, S., and Kiritani, M., "Positron Lifetime Measurement and Latent Vacancy Clusters in 14 MeV Neutron Irradiated Nickel," Journal of Nuclear Materials, Vol. 179–181, 1991, pp. 931–934.

[12] Viswanathan, B.S., Pachur, D., and Nandedkar, R. V., "Investigation of Neutron Irradiated Reactor Vessel Steel by Positron Annihilation and Electron Microscopy", Influence of Radiation on Material Properties: 13th International Symposium (part II) ASTM STP 956, F. A. Garner, C. H. Henager, Jr., and N. Igata, Eds., American Society for Testing and Materials, Philadelphia, 1987, pp. 369–378.

[13] Popp, K., Brauer, G., Leonhardt, W.–D., and Viehrig, H–W., "Evaluation of Thermal Annealing Behavior of Neutron–Irradiated Reactor Vessel Steels Using Nondestructive Test Methods," Radiation Embrittlement of Nuclear Reactor Pressure Vessel Steels: An International Review (Third Volume), ASTM STP 1011, L. E. Steele, Ed., American Society for Testing and Materials, Philadelphia, 1989, pp. 188–205.

[14] Brauer, G., Liszkay, L., Molnar, B., and Krause R., "Microstructural aspects of neutron embrittlement of reactor pressure vessel steels – A view from positron annihilation spectroscopy," Nuclear Engineering and Design, Vol. 127, 1991, pp. 47–68.

[15] Valo, M., Krause, R., Saarinen, K., Hautojarvi, P., and Hawthrone, J. R., "Irradiation Response and Annealing Behavior of Pressure Vessel Model Steels and Iron Ternary Alloys Measured with Positron Techniques," Effects of Radiation on Materials: 15th International Symposium, ASTM STP 1125, R. E. Stoller, A. S. Kumar, and D. S. Gelles, Eds., American Society for Testing Materials, Philadelphia, 1992, pp. 172–185.

[16] Akamatsu, M., Dai, G., Li, X., Moser, P., Van Duysen, J.C., and Zacharie, G., "Influence of Some Alloying Elements on the Formation of Vacancy Defects in Ferritic Steels during Irradiation at 288 C", Effects of Radiation on Materials: 16th International Symposium, ASTM STP 1175, A.S. Kumar, D.S. Gells, R.K. Nanstad and E.A. Little, Eds., American Society for Testing and Materials, Philadelphia, 1993, pp.516–527.

[17] Hori, f, Aono, Y., Takenaka, M., and Kuramoto, E., "Positron Annihilation Study of Electron–Irradiated FeCu and FeCuC Alloys", Scripta Metallurgica, Vol.29, 1993, pp.243–248.

[18] Kimura, A., Shibamoto, H., Yuya, H., Hasegawa, M., Yamaguchi, S., and Matsui, H., "Damage Structures of Proton Irradiated Fe–Cu Alloy", in the present proceedings.

[19] Othen, P. J., Jenkins, M. L., Smith, G. D. W., and Phythian, W. J., "Transmission electron microscope investigations of the structure of copper precipitations in thermally–aged Fe–Cu and Fe–Cu–Ni", Philosophical Magazine Letters, Vol. 64, 1991, pp. 383–391.

[20] Kirkegaad, P., Pedersen, N. J., and Eldrup, M., "PATFIT–88: A Data–Processing System for Positron Annihilation Spectra on Mainframe and Personal Computers", Risø M–2740,

Risφ, 1989, pp. 1–132.
[21] Ziegler, J. F., "Ion Implantation Physics," Handbook of Ion Implantation Technology, J. F. Ziegler, Ed., North–Holland, Amsterdam, 1992, pp. 1–68.
[22] Brandt, W., "Positron Dynamics in Solids", Applied Physics, Vol. 5, 1974, pp. 1–23.
[23] Kamimura, Y., Hori, F., Tsutsumi, T., and Kuramoto, E., "Positron Annihilation Lifetime Calculation at Vacancy Sites in Fe and Au in Consideration of Lattice Relaxation," Materials Science Forum, 1995, in press.
[24] Smidt, Jr., F.A., and Sprague, J.A., "Property Changes Resulting from Impurity–Defect Interactions in Iron and Pressure Vessel Steel Alloys", Effects of Radiation on Substructure and Mechanical Properties of Metals and Alloys, ASTM STP 529, American Society for Testing and Materials, 1973, pp.78–91.
[25] Frisius, F., Kampmann, R., Beaven, P.A. and Wagner, R., "Influence of copper on the defect microstructure and radiation strengthening of iron", Proc. Conf. on Dimensional Stability and Mechanical Behavior of Irradiated Metals and Alloys, Vol.1, British Nuclear Energy Society, London, 1984, pp.171–174.
[26] Nieminen, R. M., and Laakkonen, J., "Positron Trapping Rate into Vacancy Clusters," Applied Physics, Vol. 20, 1979, pp. 181–184.
[27] Takaki, S., Fuss, J., Kugler, H., Dedek, U., and Schultz, H., "The Resistivity Recovery of High Purity and Carbon Doped Iron Following Low Temperature Electron radiation," Radiation Effects, Vol. 79, 1983, pp. 87–122.
[28] Takaku, H., Tokiwai, M., Kayano, H., Higashiguchi, Y., Narui, M., Suzuki, Y., and Matsuyama, K., "The Improvement of Irradiation–Enhanced Copper Embrittlement in Fe–Cu Alloys," Journal of Nuclear Materials, Vol. 80, 1979, pp. 57–68.
[29] Worrall, G. M., Buswell, J. T., English, C. A., Hetherington, M. G., and Smith, G. D. W., "A Study of the Precipitation of Copper Particles in a Ferrite Matrix," Journal of Nuclear Materials, Vol. 148, 1987, pp. 107–114.

L.J. Cuddy[1], M.P. Manahan[2], G. Brauer[3], J. Martinko[4]

DUCTILE FRACTURE MECHANISMS IN AN A302B MODIFIED REACTOR PRESSURE VESSEL STEEL

REFERENCE: Cuddy, L. J., Manahan, M. P., Brauer, G., and Martinko, J., **"Ductile Fracture Mechanisms in an A302B Modified Reactor Pressure Vessel Steel,"** *Effects of Radiation on Materials: 17th International Symposium, ASTM STP 1270,* David S. Gelles, Randy K. Nanstad, Arvind S. Kumar, and Edward A. Little, Eds., American Society for Testing and Materials, 1996.

ABSTRACT: It has been demonstrated that thermal cycling of a previously quenched and tempered reactor pressure vessel (RPV) steel induces a hardness increase equivalent to an increase in flow stress of about 70 MPa. Single cycle heat treatments produce no such changes in hardness, flow stress, ductility or upper shelf energy (USE). Equivalent cycles will occur during reactor operation and may thus contribute to the observed changes during service of the properties of RPV steels. Preliminary microstructural examination offered no clear explanation for these effects, although it was observed that thermal cycling induced decomposition of retained austenite. It is demonstrated that, should the defects involved be shearable defects similar to those introduced by irradiation, they would promote ductile fracture by enhancing the growth and linking of microvoids and thus contribute to a drop in USE.

An analysis was performed which demonstrates that, of the several defects of the shearable type produced during irradiation of steels, vacancy clusters (or voids) are unstable with respect to both individual vacancies and collapsed vacancy loops. Thus, the latter defect and depleted zones would be the predominant vacancy hardening defects. Since irradiation produces both shearable (Cu/Ni/Mn rich precipitates, depleted zones, and loops) and non-shearable (Mo_2C) hardening defects, it is important to resolve whether the shearable or non-shearable contribution is greater in order to be able to adequately model the effect on ductile fracture. For this purpose, a study of light water reactor (LWR) surveillance tensile

[1]Consultant, Metallurgical Consultants, Boalsburg, PA

[2]President, MPM Research & Consulting, Lemont, PA 16851

[3]Professor, Research Centre Rossendorf, Inc., Dresden, Germany

[4]Student, Pennsylvania State University, University Park, PA 16801

Copyright© 1996 by ASTM International www.astm.org

data trends was performed and the results show negligible copper dependence of the yield strength change on fluence for fluences less than the boiling water reactor (BWR) end-of-license (EOL) fluence. These trends also show that the change in strain hardening behavior for U.S. steels is also negligible which indicates that shearable particles are the primary defect responsible for hardening. In addition to the Charpy curve shift, the shearable obstacles also cause a shelf drop during the strain controlled ductile fracture process. Rather than diffusing strain by slip plane hardening, as with non-deformable particles, shearable obstacles cause localization of strain in the unhardened slip plane. Strain localization in ligaments between voids leads to premature ligament failure in the irradiated material by the flow localization mechanism of void linkage.

KEYWORDS:ductile fracture, upper shelf energy, pressure vessel embrittlement, microstructural evolution under neutron irradiation

INTRODUCTION

Radiation induced Charpy shift indexed at 30 ft-lbs (41J) (ΔT_{30}) and elevation in tensile yield strength (ΔYS) are associated with the formation during irradiation of Mn/Ni/Si/Cu-rich precipitates and matrix defects (depleted zones, loops). These radiation-induced defects increase YS by inhibiting dislocation motion along the slip plane. The ΔT_{30} reflects an increased propensity for brittle failure with increase in strength which is a common observation in steels independent of the strengthening mechanism [1]. Thus, it is not surprising that there is a correlation between ΔYS and ΔT_{30} as noted by Ebrahimi and others [2].

There is also an apparent correlation between ΔYS and ΔUSE [2], from which one might conclude that there exists a causal relation. However, this relation is not as straightforward as that for $\Delta YS/\Delta T_{30}$ since ΔYS deals with inhibition of dislocation motion as indicated above, whereas ΔUSE deals with premature ductile fracture through the enhanced formation, growth, and/or linking of microvoids. The question then is how radiation induced defects enhance the microvoid linking processes. There are two possibilities. The first is that irradiation increases the propensity to nucleate voids at particle/matrix interfaces (i.e., at the surfaces of carbides, oxides, and sulfides which are the normal void-nucleation sites) leading to a higher void number density which allows them to link at lower strains. This could occur for example if surface active elements such as P segregate during irradiation to these internal interfaces thereby weakening the interfacial bond to promote delamination and void formation. The other possibility is that irradiation has no effect on microvoid nucleation, which is already profuse in carbide and sulfide bearing RPV steels, but instead accelerates the growth and linking of voids, again leading to failure at lower macro strain. This latter mechanism may result from the presence in the ligaments between void nuclei of radiation-induced shearable clusters and loops. As will be discussed below, such defects tend to concentrate the strain in coarse slip bands which accelerates linking and ultimate ductile failure, a process termed void sheeting [3,4].

These changes may be observable as changes in stress-strain behavior and fracture mode, i.e., the number density or the distribution of ductile dimples. Accordingly, experiments are underway to investigate the changes in stress-strain behavior and fracture mode in RPV steels in three conditions: as heat treated prior to service; after thermal aging; and after irradiation. The rationale is as follows. RPV plates are put into service in the quenched, tempered, and stress relieved condition. Cu is present as an impurity at levels of 0.1 to 0.3 wt.%; at such low levels, most of the Cu remains in solution at the tempering and stress relief temperatures (600-650°C), and at these levels, most of the Cu also remains in solution during the extremely slow cooling of the stress relief anneal [5,6]. Thus Cu is unlikely to precipitate during subsequent thermal aging treatments and will therefore not have a strong influence on property changes observed in thermal aging studies. Cu (and other solutes such as Mn, Ni, and Si) does however cluster and precipitate during neutron irradiation as a result of the presence of radiation-induced nucleation sites and excess vacancies which enhance solute transport [2]. In radiation studies therefore, Cu does contribute to property changes.

However, two other diffusional processes, carbide precipitation and P segregation, behave differently. These reactions are rarely completed during industrial processing and thus may contribute to property changes during both thermal aging and irradiation. Their effects can therefore be separated from those of Cu by a combination of thermal aging and irradiation studies. Specifically, Cu in the range $0.05<Cu<0.3$ wt.%, will have little effect on property changes during thermal aging, but will participate in radiation-induced property changes; residual carbide precipitation will affect strength and hardness during both thermal aging and irradiation; and residual P segregation will affect ductility and toughness during both thermal aging and irradiation.

This paper presents the first part of a two-part program focused on characterizing changes in the ductile fracture of RPV steels induced by irradiation and thermal treatment. The present paper covers the effects on the microstructure, fracture behavior, and mechanical properties of defects introduced by thermal aging of two types, single heat treatments, and thermal cycles. Thermal cycles are of interest because of observations by Hawthorne and Steele [7], who demonstrated that changes in flow stress (about 10 ksi (69MPa)), changes in USE (about 10 ft. lb (13.6J).), and Charpy transition shifts can be induced in quenched and tempered RPV steels (A302B) by thermal cycling between 25 and 600°C. No explanation for these observations was offered, and no further investigations were performed. Because these property changes are significant fractions of the changes seen in RPV plates in service where they are subjected to both thermal and neutron-flux cycles, these thermal effects warrant further study. In addition, analyses of the effect of defect type on ductile fracture, and of the relative stabilities of various vacancy-type defects are presented.

EXPERIMENTAL

The experimental portion of this study involved thermal aging studies of a modified A302B RPV steel (designated G-8-3) with the following composition in weight percent.

C	Mn	P	S	Si	Cu	Ni	Mo
.23	1.13	.023	.018	.16	.17	.59	.48

This material was hot rolled to 200 mm thick plate, re-austenitized at 815-870°C for four hours, and then water quenched, tempered at 650-680°C for four hours, and subsequently air cooled. After the welding assembly of the vessel, it was stress relieved at 610-640°C for 30 hours and furnace cooled over a period of several days. This treatment produced a mixture of ferrite and tempered upper bainite (Fig. 1). It should be noted, that with its relatively high Mn and S contents, this material has a high number density of MnS stringers oriented in the rolling direction (Fig. 2). These inclusions contribute to the initially low USE level of this steel.

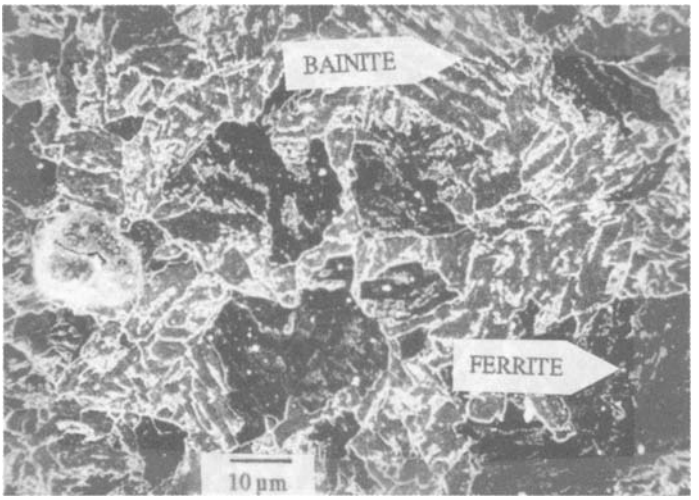


Figure 1: Microstructure of G-8-3 as Processed Before Service Showing Tempered Ferrite Plus Upper Bainite



Figure 2: MnS Stringers in G-8-3

Hardness (Vickers hardness using 300 grain load) and positron annihilation coupons, tensile, and Charpy specimens were prepared at the quarter thickness of this plate. The tensile and Charpy specimens were cut in the TL orientation to maximize the effect of inclusion orientation on ductile fracture. After various aging treatments, tensile specimens were tested at room temperature, and Charpy specimens were tested at two temperatures on the upper shelf, 71 and 100°C. Specimens for scanning electron microscopy (SEM) examination of fracture faces and for SEM and transmission electron microscopy (TEM) examination of microstructure were prepared from the hardness, tensile, and Charpy specimens.

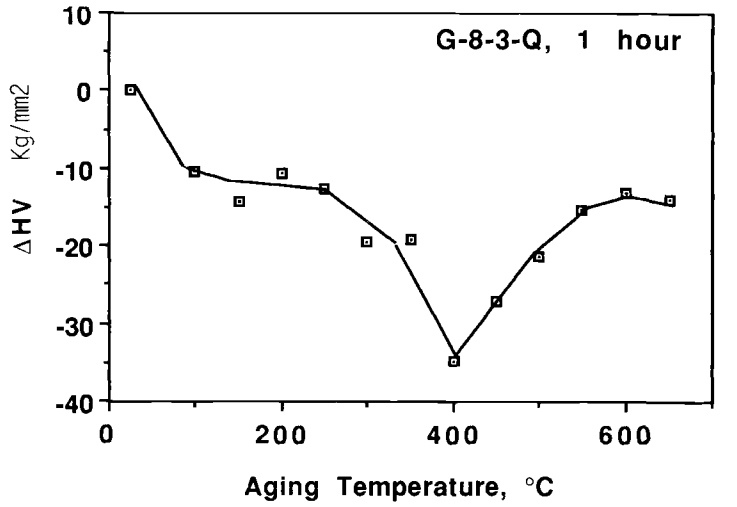
RESULTS AND DISCUSSION

Property Changes Caused by Thermal Cycling

The response to thermal aging of G-8-3 was first examined by means of hardness changes. Despite extensive tempering and stress-relief anneals during prior processing of this plate, hardness responses were observed in isochronal and, under certain conditions, in isothermal aging treatments of this steel. One hour isochronal anneals were first employed to determine the temperature ranges in which hardness changes occurred. It was found that these anneals caused first a drop in hardness between 25°C and 400°C, then a hardness rise

that peaked at ~600°C (Fig. 3a). This hardness response is the classic tempering response for an alloy steel which demonstrates secondary hardening [8]. The initial hardness drop results from the dissolution of excess carbon that is trapped in the bainite, and its precipitation as coarse Fe_3C. The higher temperature hardness peak is caused by the formation of a fine dispersion of the more stable alloy carbide (in this case Mo_2C) from a part of the less stable Fe_3C. However, there are problems with this interpretation as will be discussed later.

A corresponding isochronal (20 minute hold times) study using positron annihilation spectrometry (PAS) shows considerably more structure than the hardness data (Fig. 3b). The normalized parameter, S, is accurate to +/- 0.15% or +/- 6 units The additional peaks may reflect the greater sensitivity of PAS to carbon vacancy interactions or to the sequential formation and dissolution of the transient eta and epsilon carbides [1].



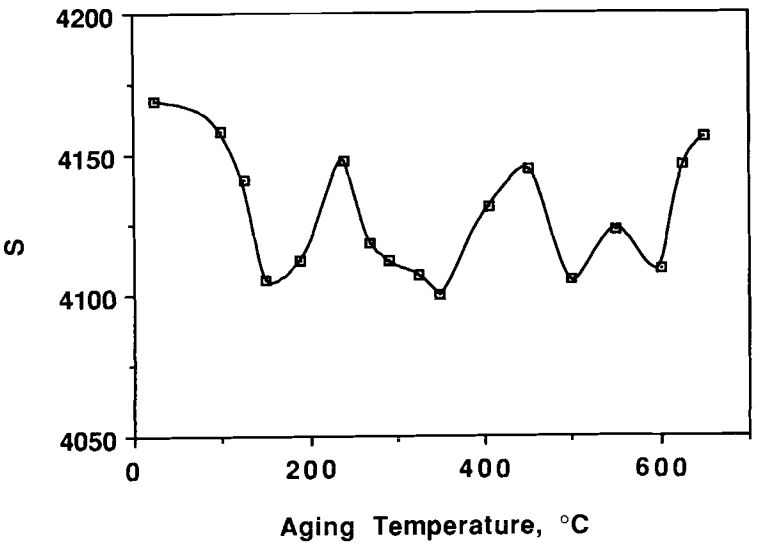


Figure 3: a. Response of Hardness of G-8-3 Aged One Hour at Temperatures Between 25 and 650°

b. Positron Annihilation Spectrum of G-8-3 Aged 20 Minutes at Temperatures Between 25 and 650°C. Error In normalized response Δ sx +/- 6

Two series of specimens were prepared for isothermal aging studies of the hardness peak. These specimens were first pre-aged for eight hours at 300°C to eliminate the initial hardness drop, and then aged by two different procedures. In the first set of hardness tests, duplicate coupons were cycled repeatedly through a heat/hold/quench treatment, and after each cycle the hardness was determined. This procedure was repeated for a number of cycles until the samples achieved peak hardness and finally overaging. The results of these anneals at 400, 450, 500 and 550°C are plotted in Fig. 4 as hardness vs. accumulated time for the cyclic aging. For example, at 500°C peak hardness occurred after four cycles with an accumulated time of four hours, and overaging occurred after five cycles totalling eight hours. These curves (for all temperatures) demonstrate hardness peaks of about the same magnitude, ΔHV~20-25, and also show that the aging time to peak hardness decreases with increasing aging temperature as would be expected for a thermally activated (e.g., diffusion controlled) process. An analysis of the temperature dependence of the peak times yielded an apparent activation energy Q=76.2 kJ/mole, which is approximately the activation energy for the diffusion of C in alpha iron (80.2 kJ/mole) [9]. However, if the hardening mechanism were the formation of Mo_2C, the activation energy for the process would be that for the slower diffusing element, in this case Mo in Fe, for which Q=250 kJ/mole [9].

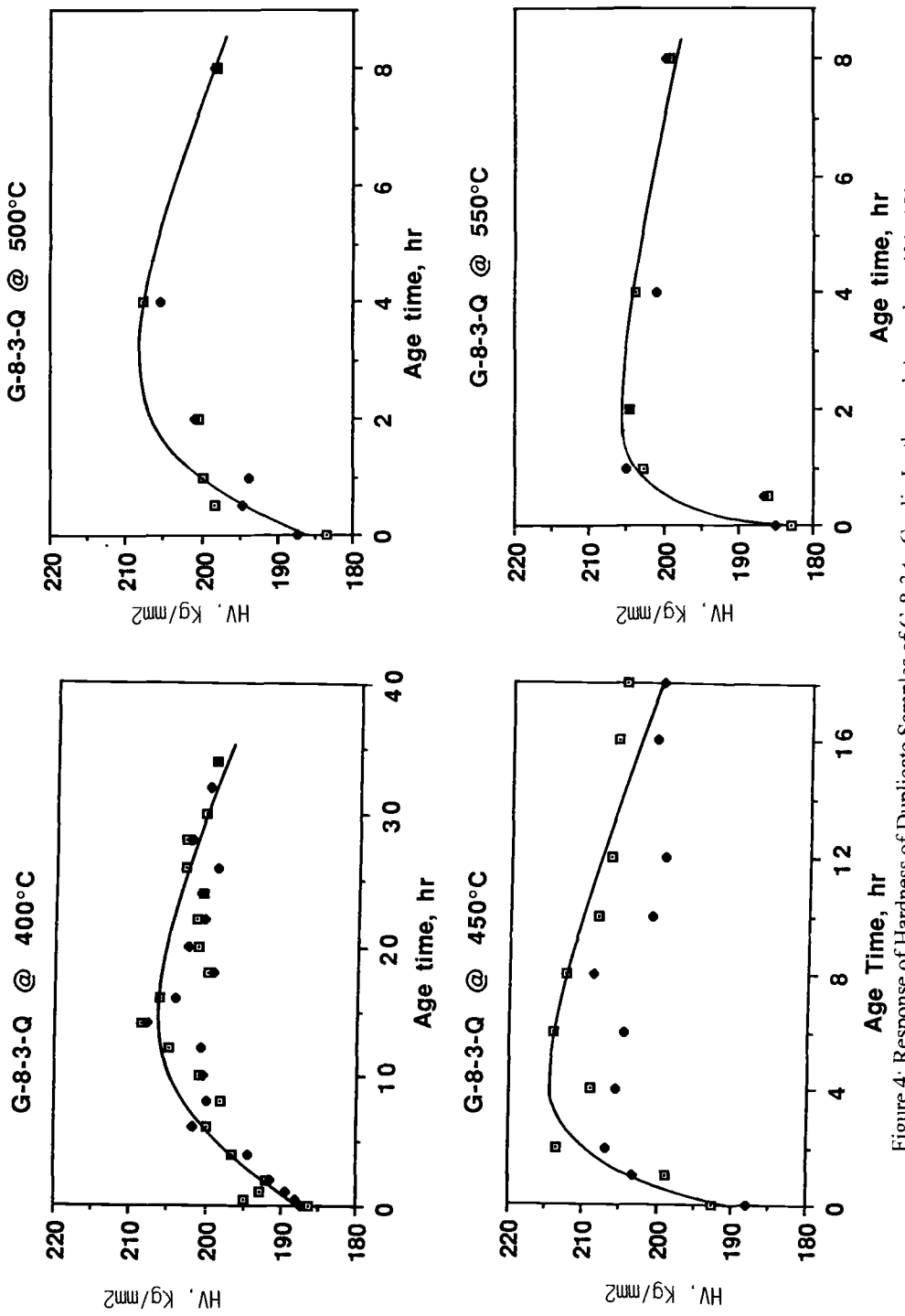


Figure 4: Response of Hardness of Duplicate Samples of G-8-3 to Cyclic Isothermal Anneals at 400, 450, 500, and 550°C

The second set of samples were broken tensile and Charpy specimens which had been pre-aged at 300°C for eight hours and then aged at 500°C to the peakaged and overaged conditions. The results in Fig. 4 were used as a guide for the time to peak hardness, (four hours) and the time for overaging, (eight hours). These specimens did not exhibit the same response to aging as did the cyclicly aged specimens. As shown in Fig. 5, there was no change in the hardness of these specimens as a result of these aging treatments. In addition, no changes in tensile strength, ductility, or in Charpy USE were observed. Fractures in all cases were entirely ductile-dimple with no indication that any embrittlement as a result of P segregation had been induced by aging.

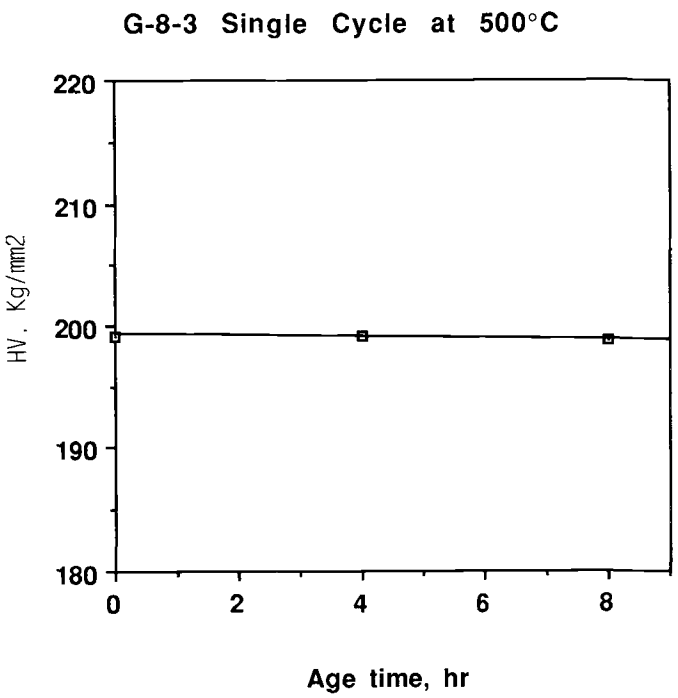


Figure 5: Response of Hardness of G-8-3 to Single Anneals of 0, 4, and 8 Hours at 500°C

To confirm the effects of cyclic aging, the broken tensile specimen which had shown no response when previously aged in a single treatment at 500°C, was cyclicly aged at that same temperature. The results of these experiments are shown in Fig. 6 and indicate a hardness rise to a peak which is identical to that of the corresponding cyclicly aged hardness coupon, (also shown) but quite different from the specimen given a single four hour aging treatment at 500°C (Fig. 5). The study of the effect of such cyclic treatment on tensile and Charpy properties is yet to be completed.

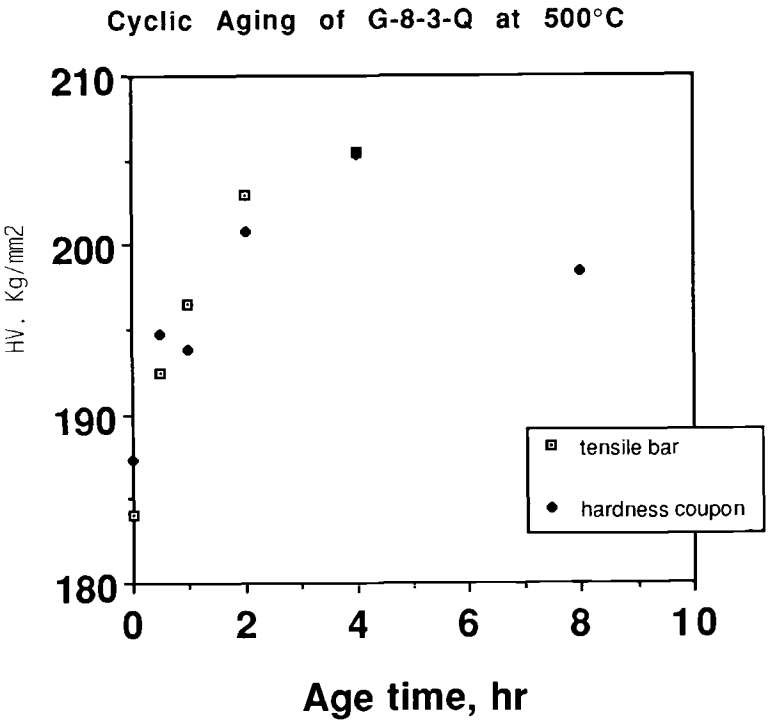


Figure 6: Responses of Hardness of a Previously-Aged Tensile Specimen And a Hardness Coupon to Cyclic Aging at 500°C

Obviously, single aging treatments do not produce the same response as do the cyclic treatments. The cyclic treatments induce a hardness response in this steel that is not developed by a single heating treatment of the same duration. Thus it appears that the number of cycles between room temperature and the aging temperature may be more important than the time at the aging temperature. This observation may explain the unusual value that was obtained for the apparent activation energy for aging.

In an attempt to determine the mechanism responsible for the hardness response in the cyclicly aged hardness coupons, pre-aged and cyclicly overaged samples were examined by transmission electron microscopy. Preliminary results show no marked differences in precipitate structure as a result of aging. However, higher resolution studies are needed to substantiate this conclusion. The outstanding difference in the two samples is the amount of retained austenite. The interlath precipitates in the upper bainite structure of the pre-aged sample (Fig. 7a) were in many cases retained austenite as can be seen from the stacking faults in the dark field image of Fig. 7b, and from their fcc diffraction pattern (Fig. 7c). After cyclic overaging (five cycles for a total of eight hours at 500°C), no traces of retained austenite could be found in interlath precipitates, which appear to be entirely Fe_3C (Fig. 8). X-ray diffraction measurements of retained austenite were also performed on these samples. Results revealed that neither sample contained more than 2% by volume (the limit of resolution) of retained austenite. It is difficult to see how the transformation of such a small fraction of retained austenite would result in the observed 10% increase in hardness. Furthermore, the transformation of retained austenite to ferrite plus Fe_3C is not a hardening mechanism.

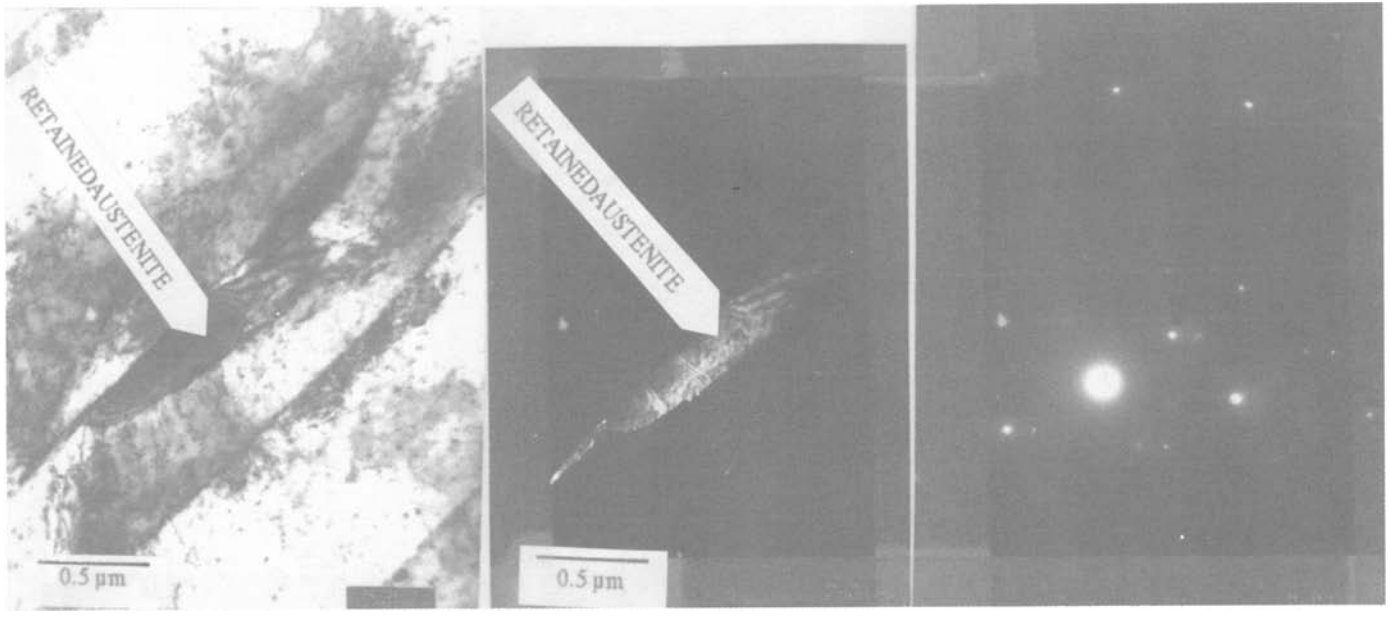


Figure 7: a&b. Bright Field, and Dark Field Images of Interlath Retained Austenite in Upper Bainite Of Quenched, Tempered and Stress Relieved G-8-3.
c. Diffraction Pattern of Interlath Retained Austenite in Upper Bainite

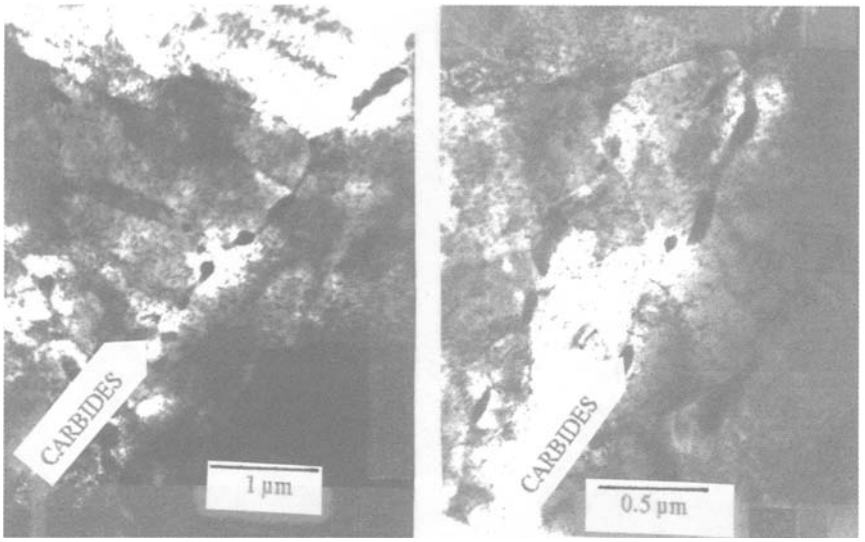


Figure 8: Interlath Carbides in Upper Bainite of G-8-3 After Cyclic Aging; Five Cycles Totaling Eight Hours at 500°C.

At present, we have no completely satisfactory explanation for the mechanism that induces hardening as a result of thermal cycling between room temperature and temperatures in the range 400 to 550°C. There are objections to all proposals: cycling may induce precipitation of Mo_2C, however, there should be very little Mo or C in solution after the tempering and stress relief anneal given this material during processing; thermal cycling might induce clustering or precipitation of other solutes such as Cu, but at this low level, that is not likely; thermal cycling does induce transformation of some residual retained austenite, but in very small quantities; and finally, thermal cycling might induce residual stresses which would increase the dislocation density, but that seems unlikely in these small, simple-shaped specimens.

Independent of the mechanism involved, a temperature-independent hardening of RPV steels equivalent to ~70 MPa which is induced by thermal cycling to temperatures as low as 400°C is of interest to plants whose reactors are subject to periodic shutdowns. Such operating cycles even though to lower temperatures (300-340°C) may make a significant contribution to the property changes observed during service of reactors, over and above changes induced by radiation damage. Still, the nature of the strengthening defects introduced by irradiation and thermal cycling will be important in predicting changes in ductile fracture behavior and in the magnitude of Charpy upper shelf energy drop (ΔUSE).

Effects of Strengthening on Ductile Fracture and USE

Analysis of the data base for RPV steels [10] shows that with irradiation strengthening, the flow stress increase is relatively constant for all strains, that is, the flow curve for the irradiation-hardened steel is raised above but is parallel to the flow curve for unirradiated material. This means that the average work hardening rate, or the average slope of the stress-strain curve $[(UTS-YS)/\epsilon_u]$, is relatively unchanged as a result of irradiation (Fig. 9). Such behavior suggests that the strengthening results mainly from shearable defects (solute or vacancy clusters, vacancy or interstitial loops, voids, coherent or semi-coherent precipitates, dislocation tangles) lying on the slip plane, which are the type of defects introduced by irradiation and possibly by thermal cycling. Such defects act as obstacles to dislocation motion that are ultimately cut through by deforming the obstacle rather than requiring the dislocation to loop around (Orowan hardening). As such, they do not cause a buildup of dislocation debris on the slip plane, and thus do not increase the resistance to slip in that plane. On the contrary, such defects tend to concentrate the slip into previously slipped planes because the resisting area of the sheared obstacle is now reduced and is therefore more easily sheared. Thus a plane once slipped becomes easier to reslip [3,4]. On the other hand, non-coherent particles that require dislocation looping, work harden the slipped plane and tend to spread the slip to other unhardened planes thus producing uniform, fine slip lines. This difference in slip-plane hardening is important in the ductile fracture process.

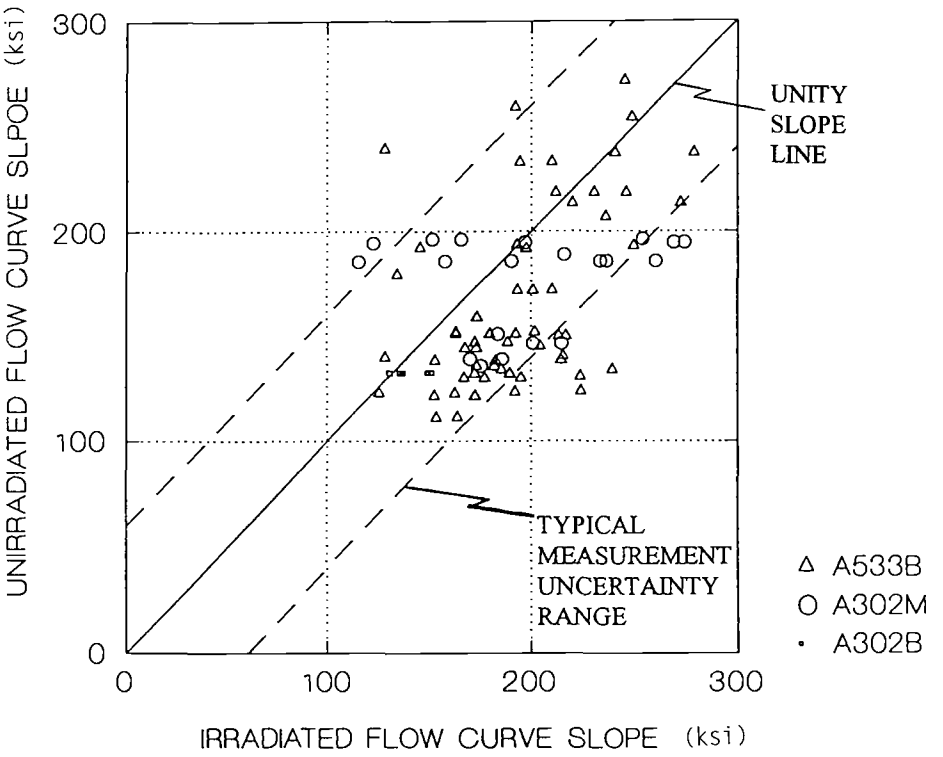


Figure 9: Plot Showing the Similarity of the Average Slope of the Flow Curves [(UTS-YS)/ϵ_u] of RPV Steels Before and After Irradiation

Ductile fracture is a process that occurs by the nucleation, growth and linking of deformation-induced microvoids. Microvoid nuclei generally form at the interfaces between non-metallic phases or inclusions (carbides, oxides, or sulfides) and the metal matrix. In quenched and tempered RPV steels, such nucleation sites are numerous, so that nucleation occurs readily. The controlling stages in ductile fracture of RPV steels are thus the growth and linking of the microvoids. The concentration of slip in coarse bands, when it occurs in the ligaments between microvoid nuclei, promotes the growth and linking of voids by a process known as void sheeting [3,4]. Thus the presence of irradiation or thermally induced shearable defects in RPV steels leads to premature ductile failure which accounts for the drop in USE. Two of the shearable defects cited in the literature are microvoids created from clustered vacancies, and loops created from collapsed voids. It was of interest therefore to examine the relative stabilities of these defects.

Relative Stabilities of Radiation-Induced Microvoids and Loops

Many existing RPV material models postulate the formation of a nearly spherical small void (microvoid) which forms as the primary knock-on atom (PKA) comes to rest in the lattice. Originally, the depleted zone, or displacement spike, was simply defined as the dense cluster of point defects which results from the displacement cascade when a neutron collides with a lattice atom. The question concerning the configuration of displaced atoms and vacancies in the cascade region was originally investigated by Brinkman [11] before detailed computer simulations were possible. Brinkman's analysis led to the unstable configuration which he called a displacement spike. Later, Seeger [12] modified Brinkman's concept of the displacement spike to account for long range transport of struck atoms (focusing and channeling). Seeger called the nearly empty hole at the end of the PKA's path a depleted zone. Computer simulated cascades [13] have confirmed the qualitative concepts of Brinkman and Seeger. Interstitials form a shell around a vacancy rich core. Focused collision chains and channelling are responsible for removing interstitials from the vacancy rich core.

While the current view of the cascade geometry has been enhanced over recent years with molecular dynamics advancements, the basic picture of Seeger remains unchanged. However, there is still the question as to whether the vacancy rich region is roughly spherical (microvoid), or simply a loosely connected collection of vacancy clusters (depleted zone), or possibly a collapsed loop. A substantial amount of field ion microscopy (FIM) has been performed on RPV steels over the past 5 years. To the best of our knowledge, there have been no reports of microvoids or discernable depleted zones. Therefore, in order to gain further understanding concerning the cascade core morphology, a simple internal energy model has been developed and applied to RPV steels.

Vacancy vs. Microvoid

We first examine the stability of a microvoid against the vacancy supersaturation. The focus of these calculations is to estimate the critical radius at which the microvoid is stable. The internal energy of the system can be written as:

$$E_{Vm} = 4\pi r^2\gamma - n\,(\mu-\mu_o)$$

where,

E_{Vm}	=	vacancy/microvoid system energy
γ	=	surface energy
r	=	microvoid radius
n	=	number of vacancies
	=	$\frac{4\pi}{3\Omega} r^3$
Ω	=	atomic volume
$\mu-\mu_o$	=	chemical potential of the matrix/vacancy system
	=	kT ln (S_v)
S_v	=	vacancy supersaturation = C_v / C_v^e
C_v	=	vacancy concentration under irradiation
C_v^e	=	thermal equilibrium vacancy concentration
T	=	temperature
k	=	Boltzmann constant

The first term represents the energy increase associated with the creation of surface as the microvoid forms. The second term represents the energy decrease within the crystal as n vacancies are clustered. The vacancy supersaturation can be calculated using a rate theory formulation. Calculations yield S_v (BWR) = 142 for a typical BWR and S_v (PWR) = 8340 for a typical pressurized water reactor (PWR).

Microvoid vs. Loop

We next developed the equation to calculate the critical radius at which the microvoid is stable against collapse to a vacancy loop. The internal energy of the system is written as:

$$E_{ML} = E_L\, 2\pi r - 4\pi r^2 \gamma$$

where,

E_{ML}	=	microvoid/loop system energy
E_L	=	dislocation line energy

The first term represents the energy required to form the loop and the second represents the microvoid surface energy loss as the microvoid collapses.

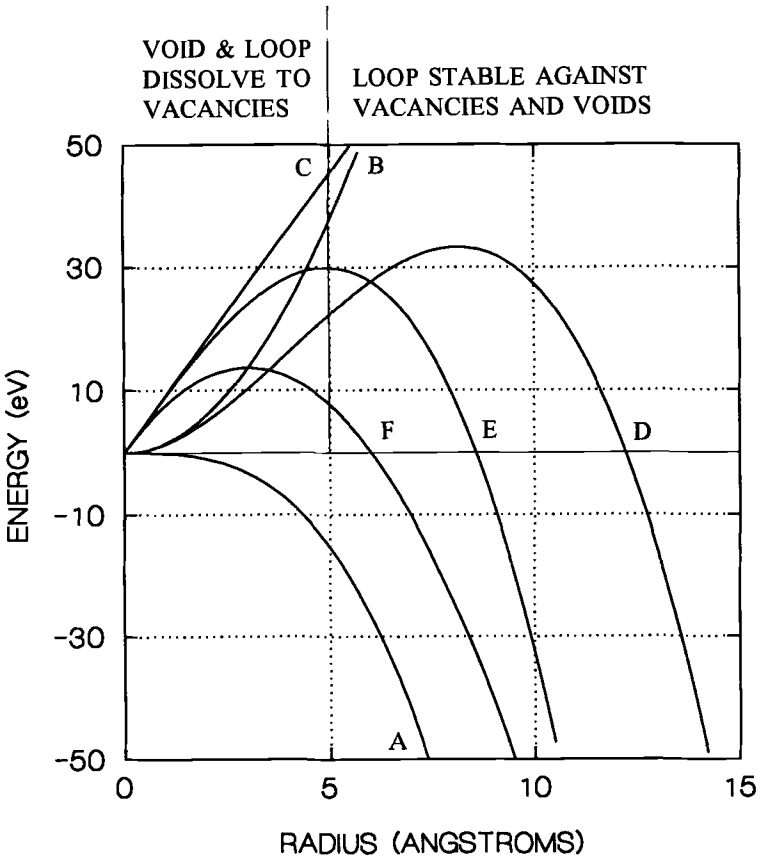
Loop vs. Vacancy

Finally, we develop the equation to calculate the critical radius at which the loop is stable against the vacancy supersaturation. The internal energy of the system is written as:

$$E_{LV} = E_L 2\pi r - n (\mu - \mu_o)$$

Internal Energy Model Results

The results of the critical radius calculations are shown in Figure 10. The calculations show that the microvoid is unstable for all radii. The loop is stable against dissolution to individual vacancies for radii greater than ~5Å. Computer simulations show that the high end of the vacancy concentration in a cascade is in the range of 10 to 30 vacancies. Therefore, if vacancy clusters were to form from the core of the cascade, the radii would be in the range of about 2.6Å<r<3.9Å. Based on the internal energy model, we would expect the clusters with radii greater than ~5Å to collapse to stable loops. However, for those clusters with r<~5Å, neither the microvoid nor the loop would be expected to be stable against the vacancy supersaturation.



A) vacancy chemical potential
B) microvoid surface energy
C) dislocation loop line energy
D) void vs. vacancy
E) loop vs. vacancy
F) loop vs. void

Figure 10: Relative Stabilities of Individual Vacancies, Vacancy Clusters or Voids, and Collapsed Vacancy Loops.

The internal energy formulation used to model microvoid stability in iron lattices strongly suggests that microvoids do not form. Rather, the larger clusters formed at the core of the cascade volume are expected to collapse to loops or dissolve into separate vacancies. The smaller vacancy clusters are expected to anneal or remain as a loosely connected depleted zone as originally proposed by Seeger. These observations are consistent with the large number of FIM studies conducted over the past five years. The FIM studies have not shown any evidence supporting the existence of a roughly spherical microvoid.

SUMMARY

It has been demonstrated that thermal cycling of a previously quenched and tempered RPV steel between room temperature and 400-550°C induces a temperature-independent hardness increase equivalent to an increase in flow stress of about 70 MPa; this is not observed in single cyle heat treatments. Similar, lower-temperature cycles (to 300-340°C) cycles occur during reactor operation and may also contribute to observed changes in the properties of RPV steels. Preliminary microstructural examination offered no clear explanation for these effects, although it was observed that thermal cycling induced decomposition of retained austenite.

It has been demonstrated that in RPV steels, microvoids are unstable with respect to both individual vacancies and collapsed vacancy loops. Thus, the latter defect and depleted zones would be the predominant vacancy hardening defect. Atom probe studies by other researchers have shown that shearable solute clusters (Mn, Si, Ni, and Cu) also form in irradiated steels as a result of the enhanced diffusivity. Our recent study has also shown that secondary carbide (Mo_2C) hardening may play a role in embrittlement. However, analysis of the tensile data trends reveals that the strain hardening change is small which shows that shearable defects are primarily responsible for the flow stress elevation.

The question concerning the physical mechanism of shelf drop has not been adequately addressed in earlier studies. Our analysis indicates that after irradiation, the strain induced void nucleation process which occurs at sulfides, oxides, and carbides remains essentially unchanged. Since the work hardening after irradiation changes little, it is believed that mainly shearable defects contribute to the shelf drop. Rather than diffusing strain by slip plane hardening, as with non-deformable particles, shearable obstacles cause localization of strain in the unhardened slip plane. Strain localization in ligaments between voids is expected to lead to premature ligament failure in the irradiated material by the flow localization mechanism of void linkage.

REFERENCES

1. W.C. Leslie, The Physical Metallurgy of Steels, McGraw-Hill, 1981, pp. 164-167.

2. F. Ebrahimi, et al., Development of a Mechanistic Understanding of Radiation Embrittlement in RPV Steels, NUREG/CR-5058, January, 1988.

3. J.W. Martin, Micromechanisms in Particle Hardened Alloys, Cambridge Press, 1980, p. 99ff.

4. P.F. Thomason, Ductile Fracture of Metals, Pergamon, 1990, pp. 19, 61, 103.

5. M.K. Miller and M.G. Burke, "Microstructural Characterization of Irradiated PWR Steels Using the Atom Probe Field-Ion Microscope in Environmental Degradiation of Materials in Nuclear Power Systems", Theus and Weeks, eds., TMS, 1988, p. 141.

6. M.K. Miller et al., ibid, p. 133.

7. J.R. Hawthorne and L.E. Steele, "Metallurgical Variables as Possible Factors Controlling Irradiation Response of Structural Steels", in Effects of Radiation on Structural Steels, ASTMSTP 426, ASTM, 1967, p. 534.

8. R.W.K. Honeycombe, Steels, Microstructure and Properties, Edward Arnold, 1981, p. 154.

9. Smithells Metals Reference Book, seventh ed., Butterworth-Heinemann, 1992, pp.

10. Nuclear Regulatory Commission, Power Reactor Embrittlement Data Base (PR-EDB), 1994.

11. J.A. Brinkman, Journal of Applied Physics, 25:961 (1954).

12. A. Seeger, "On the Theory of Radiation Damage and Radiation Hardening", in Proceedings of the Second United Nations International Conference on the Peaceful Uses of Atomic Energy, Geneva, 1958, Vol. 6, p. 260, United Nations, NY, 1958.

13. D.R. Olander, "Fundamental Aspects of Nuclear Reactor Fuel Elements", Prepared for the Division of Reactor Development and Demonstration, Energy Research and Development Administration, 1976.

Matthew J. DeVan,[1] Arthur L. Lowe, Jr.,[2] and J. Brian Hall[3]

FRACTURE TOUGHNESS TEST RESULTS OF THERMAL AGED REACTOR VESSEL MATERIALS

REFERENCE: DeVan, M. J., Lowe, Jr., A. L., and Hall, J. B., **"Fracture Toughness Test Results of Thermal Aged Reactor Vessel Materials,"** *Effects of Radiation on Materials: 17th International Symposium, ASTM STP 1270,* David S. Gelles, Randy K. Nanstad, Arvind S. Kumar, and Edward A. Little, Eds., American Society for Testing and Materials, 1996.

ABSTRACT: Thermal-aged surveillance materials consisting of SA-533, Grade B, Class 1 plate material; SA-508, Class 2 forging material; and 2 Mn-Mo-Ni/Linde 80 weld metals were removed from two commercial reactor pressure vessels. The material from the first reactor vessel received a thermal exposure of approximately 103,000 hours at 282°C (540°F), while the material from the second reactor vessel received a thermal exposure of approximately 93,000 hours at 282°C (540°F). Tensile and ½T compact fracture toughness specimens were fabricated from these materials and tested. In addition, to examine the effects of annealing, selected thermal-aged and unaged specimens were annealed at 454°C (850°F) and tested. Varying responses in the fracture toughness properties were observed for all materials after exposure to the thermal-aging temperature. The base metal plate had an observed decrease in J-values after its respective aging exposure, while no significant difference in the J-values were observed for the Linde 80 weld metals. No significant difference was seen in the J-data for the aged/annealed materials, but because of the small number of test specimens available, no conclusion could be determined for the response to annealing.

KEYWORDS: thermal aging, reactor vessel materials, SA-533 Gr. B1 plate, SA-508, Class 2 forging, submerged-arc weld

[1]Engineer, Nuclear Engineering Department, B&W Nuclear Technologies Inc., Lynchburg, VA 24506.

[2]Retired Advisory Engineer, Nuclear Engineering Department, B&W Nuclear Technologies Inc., Lynchburg, VA 24506.

[3]Research Engineer, Materials Performance, The Babcock & Wilcox Company, Alliance, OH 44601.

Copyright© 1996 by ASTM International www.astm.org

Introduction

Thermal degradation of the mechanical properties of materials used in the construction of power systems is apparent when the materials operate at relatively high temperatures (> 371°C). However, the degradation in properties as the result of long-term exposure at lower temperatures is not well understood. In fact, failure of materials as a result of these conditions is often attributed to other causes. In most power generation plants, this approach to material behavior is manageable; however, in nuclear power plants, long-term gradual degradation is not acceptable. Therefore, if it can be avoided, or otherwise anticipated, the necessary corrective actions must be instituted.

The first-generation nuclear reactor pressure vessels were designed and fabricated in accordance with ASME Boiler and Pressure Vessel Code Section VIII[1] with materials that were commonly used in low-temperature, unfired pressure vessels. The second generation of nuclear reactor vessels used relatively new materials for their construction, i.e., SA-533, Grade B, Class 1 plates and SA-508, Class 2 forgings. Little was known about the long-term stability of these materials, but the assumption was made, based on the then-current knowledge from similar steels, that the materials would perform satisfactorily.

Reactor vessel service temperatures, 260-302°C (500-575°F), are equal to or less than 0.3 times the absolute melting temperature of the steels used in fabrication, and therefore, creep, or other self-diffusion-controlled embrittlement mechanisms are believed to be of no concern. Furthermore, inservice temperatures are approximately 316°C (600°F) below those incurred during final tempering, or post-weld heat treatment (PWHT). Therefore, long-term microstructural stability would be anticipated, although small changes in properties may occur as the result of the differences in solute solubilities between final heat treatment and inservice temperatures. In addition, the reactor vessel service temperatures are below the 371-593°C (700-1100°F) temperature range normally associated with temper embrittlement in alloy steels. However, no studies have investigated aging durations up to 32 years. Strain-aging is generally considered to be important in steels with high concentrations of interstitial solutes, such as carbon and nitrogen, when aged at temperatures in the range 52-177°C (125-350°F), conditions that may be relevant to reactor vessel materials. Minor strain-aging effects are reported to result from complex dislocation interactions with substitutional solutes, a reaction that is normally expected to occur at higher temperatures. Such a mechanism may be of importance although it is unlikely to produce significant embrittlement.

This paper describes the results of the tensile and compact fracture toughness thermal-aged material removed from two reactor vessels. The thermal-aged materials were removed after long-term exposure to temperatures exceeding 282°C (540°F). Charpy V-notch test results of these same thermal-aged materials are reported in a separate publication.[2] The compact fracture toughness specimens were tested using an automated single specimen J-test procedure.

Materials Aging History

The aging specimen boxes are located on the service structure support of reactor vessel heads. The boxes are located under the head insulation to help maintain the aging temperature. Because of the location of these boxes, the surveillance material was considered to have zero neutron fluence exposure during the aging time. The surveillance material removed from the first reactor vessel had been aged for approximately 103,000 hours at 282°C (540°F), and the surveillance material from the second reactor vessel had been aged for approximately 93,000 hours at 280°C (540°F). The exact exposure time for each set of materials was difficult to determine because of the time allowance for reactor heatup, cooldown and hot standby. To account for the exposure time at reactor heatup, cooldown, and hot standby, the aging times specified above reflect a 10% increase of the actual effective full power times when the surveillance materials were removed.

Material Description

Base metal and weld metal blocks were removed from thermal aging surveillance boxes. These materials are representative of the materials used to fabricate the beltline region of reactor pressure vessels. Blocks of material rather than machined specimens were included because it allowed a greater flexibility in fabricating specimens to meet current specifications. The base metal materials were SA-533 Grade B, Class 1 plate steel and SA-508 Class 2 forging steel. The two weld metals were typical Mn-Mo-Ni weld wire/Linde 80 flux submerged arc welds. The chemical composition and heat treatment for these materials are described in Tables 1 and 2.

Table 1 -- Composition of Thermal-Aged Surveillance Materials

Material (Heat No.)	Chemical Compositions, wt%								
	C	Mn	P	S	Si	Ni	Cr	Mo	Cu
Plate A	0.21	1.32	0.010	0.016	0.20	0.52	0.19	0.57	0.15
Forging A	0.24	0.72	0.014	0.012	0.21	0.76	0.34	0.62	0.02
Weld A	0.09	1.49	0.016	0.016	0.51	0.59	0.06	0.39	0.28
Weld B	0.08	1.63	0.017	0.012	0.61	0.58	0.10	0.39	0.30

Table 2 -- Heat Treatment of Thermal-Aged Surveillance Materials

Material Type	Heat Treatment*
Plate A	Austenitized 899-927°C (1650-1700°F) for 1 hr/in, WQ Tempered 649°C (1200°F) for 1 hr/in, AC Stress-relieved 593-621°C (1100-1150°F) for 29 hrs, FC
Forging A	Austenitized 829-913°C (1525-1675°F) for 4 hr, WQ Tempered 649-677°C (1200-1250°F) for 4 hr, FC Stress-relieved 593-621°C (1100-1150°F) for 40 hrs, FC
Weld Metal A	Stress-relieved 593-621°C (1100-1150°F) for 29 hrs, FC
Weld Metal B	Stress-relieved 593-621°C (1100-1150°F) for 30 hrs, FC

* WQ = water quenched
AC = air cooled
FC = furnace cooled

Test Specimens

From the surveillance block material, subsize tensile specimens and ½T compact fracture specimens were machined. To investigate the effects of annealing after aging, a number of specimens from each material were subjected to a thermal anneal heat treatment at 454°C (850°F) for 168 hours. The 454°C (850°F) annealing temperature was selected to investigate possible 100% recovery of the Charpy upper-shelf energy and transition temperature based on experimental research[3].

A total of 59 subsize tensile specimens were fabricated in accordance with the requirements of ASTM E 8-79a.[4] The subsize specimens were 55 mm (2.165 in.) long with a reduced section 24 mm (0.945 in.) long by 5.33 mm (0.210 in.) in diameter. A total of 13 specimens received the 454°C (850°F) anneal.

A total of 34 ½T compact fracture specimens were fabricated. The geometry of the specimens satisfied the proportionality requirements of ASTM E 813-87.[5] All of the compact fracture specimens were precracked prior to any thermal anneal heat treatment. After precracking, the specimens were side-grooved 10% of thickness per side (20% total reduction). Nine fracture toughness specimens received the 454°C (850°F) anneal after precracking and side-grooving had been completed. As specified in ASTM E 813, specimens must be precracked in their final test condition. Therefore, these nine specimens were precracked to obtain additional crack extensions of approximately 1.27 mm (0.05 in.) after the 454°C (850°F) anneal.

Test Procedure

The tensile tests were conducted following the guidelines provided in ASTM E 21-79.[6] The specimens were loaded with a clevis and pin arrangement. The tensile tests were performed at 121°C (250°F) and 288°C (550°F) in air. The temperature was monitored at two positions on the specimen.

A fully automated digital system was used to control the test, collect data, and perform an analysis. Load was indicated by a certified cell placed in series with the specimen in the load train. A cross head speed of 0.102 mm/min. (0.004 in./min.)was used through yield, where it switched to a rate of 1.27 mm/min.(0.05 in/min.). A 12.7 mm (0.5 in.) gage length extensometer was used to measure elongation of the specimen.

The fracture toughness tests were conducted using the single specimen, unloading compliance technique defined in ASTM E 813-87 and ASTM E 1152-87[7]. However, the crack extension imposed during testing was not limited to 10% of the initial ligament as required by ASTM E 1152-87. Crack extensions of 20 to 30% of the initial ligament were imposed during testing to better define the J-R curves. Fracture toughness tests were performed at 121°C (250°F) and 288°C (550°F) in air.

All J-integrated fracture toughness tests were completed in a fully automated, closed loop, servohydraulic load frame. The load frame was controlled using crack mouth opening displacement as the feedback signal. Applied specimen loads were indicated by a certified load cell. Load line displacement was indicated by a standardized clip gage mounted on integral knife edges machined into the crack mouth of the specimen. Test control, data acquisition, and data conversion were performed using the certified software. The tensile data required by the J-integral analysis procedures were taken from the accompanying tensile tests.

After testing was completed, the specimens were heat tinted, cooled and broken. The optical crack length was measured using the nine-point method described in ASTM E 813-87. The J-R curves were determined following the ASTM E 1152-87 guidelines and the J_{Ic} or J_Q values were obtained from J-R curves according to the method defined in ASTM E 813-87.

Results

The fracture toughness test results for the unaged specimens, thermal-aged specimens, and thermal-aged/annealed specimens are shown in Table 3. Attempting to validate J_Q as J_{Ic} as defined in paragraph 9.4 of ASTM E 813-87, the two most common violations are related to final crack straightness and final crack extension. These criteria are difficult to satisfy when large crack extensions are imposed.[8] Since these criteria relate to the final crack length, it is unclear if the violations are significant with regard to the initiation toughness measured in the first part of the test.

Two specimens violated the initial crack front straightness requirement. These specimens violated the initial crack front straightness because the final precrack was grown after the specimen was side-grooved. Precracks grown in side-grooved

Table 3 -- Fracture Toughness Test Results

Material Type	Material Condition	Test Temp., °C (°F)	J_{Ic} or J_Q, KJ/m^2 (in-lb/in^2)	ASTM E 813-87 Violations
Base Metal Plate A	Unaged	121 (250)	154.5 (882)	1
	Unaged	121 (250)	154.1 (880)	None
	Unaged	288 (550)	139.4 (796)	2
	Unaged	288 (550)	148.9 (850)	1, 2
	Aged	121 (250)	126.4 (722)	None
	Aged	288 (550)	128.0 (731)	1
	Aged	288 (550)	117.0 (668)	1
	Aged/Annealed	288 (550)	121.4 (693)	2, 7
Base Metal Forging	Unaged	121 (250)	131.9 (753)	1, 3
	Unaged	121 (250)	158.8 (907)	3
	Unaged	288 (550)	190.9 (1,090)	1, 2, 3
	Unaged	288 (550)	231.2 (1,320)	1, 3, 4
	Aged	121 (250)	220.7 (1,260)	1, 3, 4
	Aged	121 (250)	224.2 (1,280)	1, 3, 4, 6
	Aged	288 (550)	220.7 (1,260)	1, 2, 3, 4
	Aged	288 (550)	182.1 (1,040)	1, 3
	Aged/Annealed	121 (250)	280.2 (1,600)	1, 3, 4, 5
	Aged/Annealed	288 (550)	236.4 (1,350)	1, 3, 4
Weld Metal A	Aged	121 (250)	104.9 (599)	1
	Aged	288 (550)	78.6 (449)	1
	Aged	288 (550)	66.0 (377)	None
	Aged/Annealed	288 (550)	82.3 (470)	1
Weld Metal B	Unaged	121 (250)	96.1 (549)	1
	Unaged	121 (250)	103.0 (588)	None
	Unaged	288 (550)	70.0 (400)	1
	Unaged	288 (550)	78.8 (450)	None
	Aged	121 (250)	81.8 (467)	1
	Aged	288 (550)	69.0 (394)	1, 2
	Aged	288 (550)	66.9 (382)	1
	Aged/Annealed	288 (550)	81.8 (467)	1, 7

ASTM E 813-87 Violations:

1	9.4.1.6	final crack front straightness
2	9.4.1.7	final crack extension
3	9.2.2	data specing - zone B
4	9.4.1	specimen size
5	9.3.2	insufficinet points in exclusion lines
6	9.4.1.3	too steep tearing modulus
7	9.4.1.5	initial crack front straightness

specimens typically grow faster at the specimen edges, as was the case here. This preferential crack growth resulted in the violations of crack front straightness.

Ten specimens violated the data spacing in zone B as defined in paragraph 9.2.2 of ASTM E 813-87. This paragraph defines requirements for data spacing between the 0.1524 mm (0.006 in.) and 1.524 mm (0.060 in.) exclusion lines. The data spacing was violated by the specimens which had a high J_Q, because the measurement of J within the exclusion lines exceeded the measuring capacity of the specimen. The measuring capacity is a function of the material yield strength and specimen size. A consequence of tests that have high J_Q values is that they typically have very steep J-R curves. When a J-R curve is steep, any slight error in the placement of the blunting line (a_o) results in a significant error in the value of J_Q.

Six specimens violated the specimen size requirement as defined in paragraph 9.4.1 of ASTM E 813-87, which specifies a minimum specimen size based on J_Q. The specimens that violated this requirement are the aged and unaged forging base metal. These violations are attributed to the specimen size for the tough (high J_Q values) forging base metal's being too small. Another indication of an under-sized specimen is the plastic deformation of the metal in the region of the plastic zone beyond the side-grooves on the surface of the specimens. This is what was observed in the forging base metal specimens.

Violation of the specimen size requirement is a significant violation. The J_Q data reported for the forging base metal specimens, which violated this requirement, should not be used. The violations reported from the remaining fracture toughness tests (i.e., initial and final crack front staightness and final crack extensions) are not considered to be as serious.

Discussion

To investigate the effects of aging and aging/annealing, the J_Q or J_{Ic} values were plotted for each of the conditions. A general review of the fracture toughness data indicates virtually no significant change in the J_Q or J_{Ic} value after aging. Because of the small number of specimens available for testing, only the fracture toughness trends with respect to aging could be evaluated.

Figure 1 presents the J_Q or J_{Ic} data for the base metal plate material which received 93,000 hours of thermal exposure. The test data for the unaged material condition at both test temperatures, 121 and 288°C (250 and 550°F), fall within the same scatter. This phenomenon is also seen in the J_Q or J_{Ic} data for the aged material condition; however, there appears to be a 15% drop in the J_Q or J_{Ic} data. The 454°C (550°F) anneal after aging appears not to have had any effect on the fracture toughness of the material.

The test data for the Linde 80 weld metals represent the typical behavior for these materials and are shown in Figures 2 and 3. The unaged J_Q or J_{Ic} data for Weld Metal B indicates a 25% difference between the 121 and 288°C (250 and 550°F) test temperatures, which is expected for Linde 80 weld metals. This difference is also seen in the test data for both weld metals in the aged condition although the difference is not as great for Weld Metal B. Comparing the J_Q or J_{Ic} data for Weld Metal A and

Figure 1 -- Comparison of Fracture Toughness (J_{Ic}) Data For Base Metal Plate A

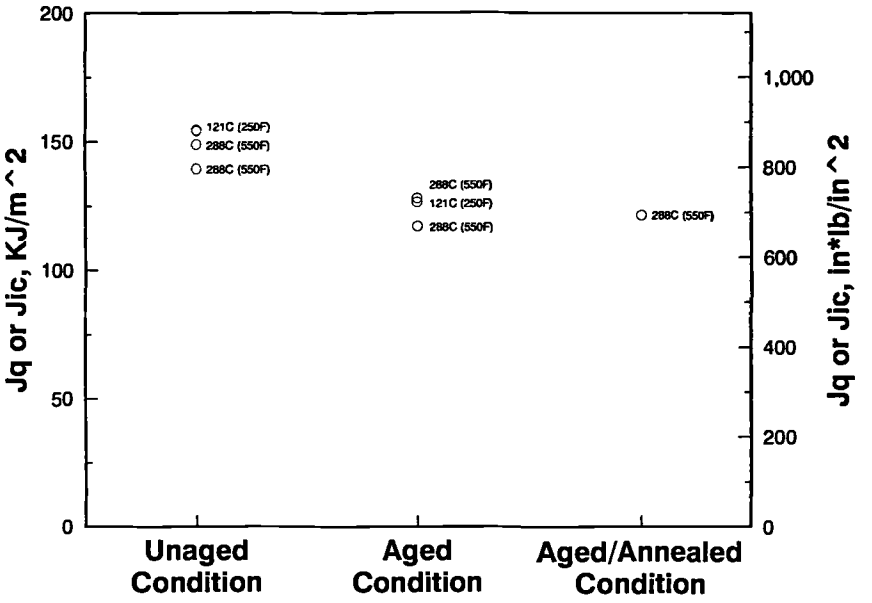


Figure 2 -- Comparison of Fracture Toughness (J_{Ic}) Data For Weld Metal A

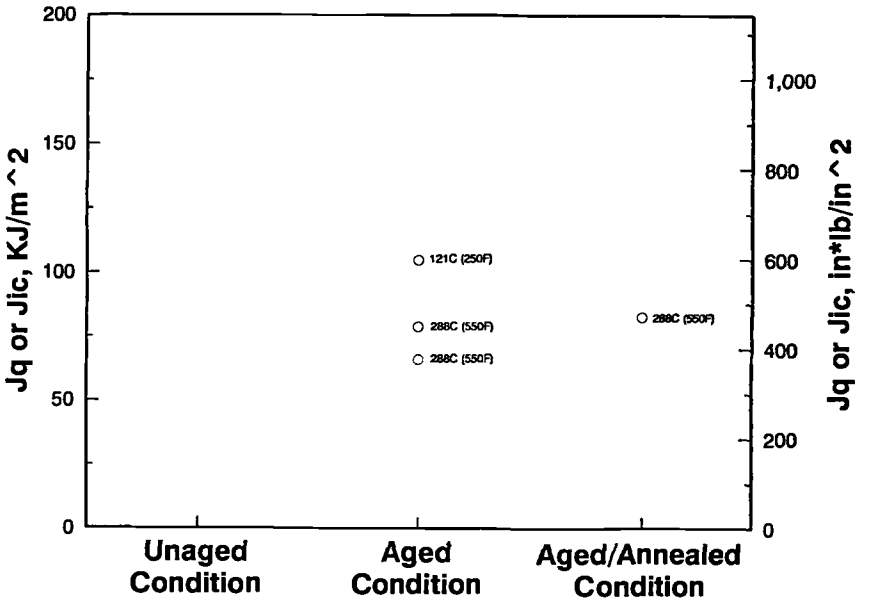
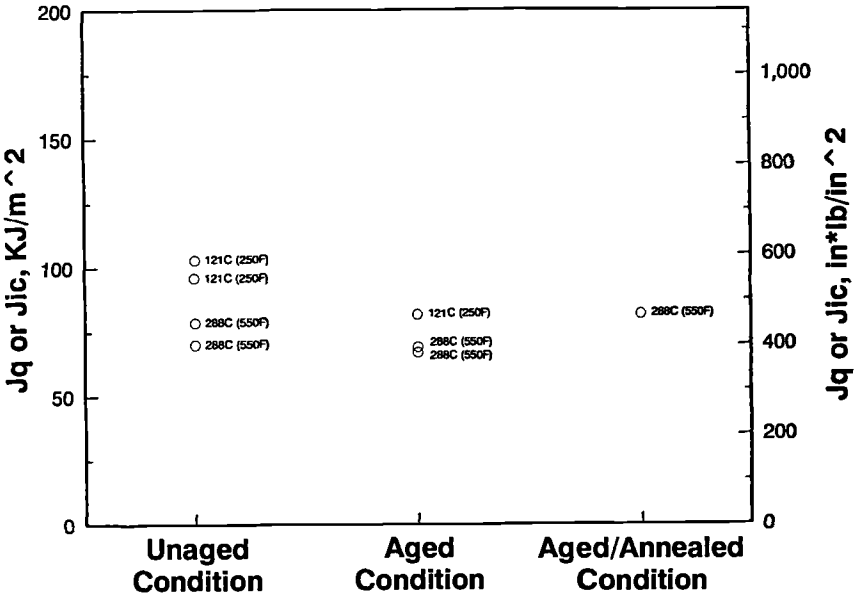


Figure 3 -- Comparison of Fracture Toughness (J_{Ic}) Data For Weld Metal B



Weld Metal B with 93,000 and 103,000 hours of thermal exposure, respectively, it appears that the fracture toughness in the aged and aged/annealed conditions are similar. The only difference is the aged J_Q or J_{Ic} data at the 121°C (250°F) test temperature.

Comparing the unaged and aged data for Weld Metal B, a drop (~15%) in the J_Q or J_{Ic} data is only seen at the 121°C (250°F) test temperature. The J_Q or J_{Ic} data at the 288°C (550°F) test temperature lie within the scatter of the data. The test data for the aged/annealed condition for both weld metals indicates a small increase (~10 KJ/m^2) in the J_Q or J_{Ic} value; however, these values lie within the scatter of the data; therefore, the material response to annealing could not be determined.

Conclusion

A 15% drop in the J_Q or J_{Ic} data between the unaged and aged material condition was observed in the base metal plate; however, the J_Q or J_{Ic} values still indicate a very tough material. No significant difference in the J_Q or J_{Ic} data is seen between the aged material and the aged/annealed material; thus the fracture toughness is not affected.

The J_Q or J_{Ic} data for the Linde 80 weld metals represent typical behavior that is seen for this class of weld metal. Comparing the unaged and aged J_Q or J_{Ic} data, no significant difference was observed for these materials. Therefore, long-term thermal exposure at ~288°C (~550°F) had no effect on the fracture toughness of these weld

metals. Both aged weld metals showed increases in the J_Q or J_{Ic} values after annealing at 454°C (850°F), however, because of the lack of aged/annealed specimens available for testing, the effect of the annealing process cannot be determined.

These materials are continuing to be aged in surveillance boxes as part of the on-going B&W Owners Group Program. As part of this program, further evaluations on the effects of thermal-aging on reactor vessel materials are continuing. Additional evaluations will include mechanical testing and microstructural examinations.

Acknowledgements

This study was sponsored by the B&W Owners Group as a part of their Reactor Vessel Integrity Program. The authors acknowledge and express appreciation for their support and permission to report this work.

References

[1] American Society of Mechanical Engineers Boiler and Pressure Vessel Code, Section VIII, Pressure Vessels.

[2] DeVan, M. J., Lowe, A. L. Jr., Wade, C. S., "Evaluation of Thermal-Aged Plates, Forgings, and Submerged-Arc Weld Materials," Effects of Radiation on Materials: 16th. International Symposium STP 1175, Arvind S. Kumar, David S. Gelles, Randy K. Nanstad, and Edward A. Little, Editors, American Society for Testing and Materials, Philadelphia, 1993.

[3] Mager, T. R., "Feasibility of and Methodology for Thermal Annealing an Embrittled Reactor Vessel," EPRI NP-2712, Vol. 1 and 2, Electric Power Research Institute, November 1982.

[4] American Society for Testing and Materials, "Standard Methods of Tension Testing of Metallic Materials," E 8-79a.

[5] American Society for Testing and Materials, "Standard Test Method for J_{IC}, A Measure of Fracture Toughness," E 813-87.

[6] American Society for Testing and Materials, "Standard Recommended Practice for Elevated Temperature Tension Tests of Metallic Materials," E 21-79.

[7] American Society for Testing and Materials, "Standard Test Method for Determining J-R Curves," E 1152-87.

[8] Van Der Sluys, W. A. and Wade C. S., "Experience with the Use of the New ASTM E 813-87," Elastic-Plastic Fracture Test Methods: The User's Experience, ASTM STP 1114, J. A. Joyce, Ed., pp. 2-18.

Kurt Edsinger[1] , G. Robert Odette[2,3] , Glenn E. Lucas[1,2] and Brian Wirth[2]

The Effect of Constraint on Toughness of a Pressure Vessel Steel

REFERENCE: Edsinger, K., Odette, G. R., Lucas, G. E., and Wirth, B., **"The Effect of Constraint on Toughness of a Pressure Vessel Steel,"** *Effects of Radiation on Materials: 17th International Symposium, ASTM STP 1270,* David S. Gelles, Randy K. Nanstad, Arvind S. Kumar, and Edward A. Little, Eds., American Society for Testing and Materials, 1996.

ABSTRACT: One-third-sized pre-cracked Charpy bars (MPCC, a/W ~ 0.5) were tested over a range of temperatures. Initiation by unstable fracture or extensive pop-in/arrest events took place in the low and intermediate temperature/toughness regime; at higher temperatures/toughness levels, crack growth was limited to blunting/local damage. The small specimen toughness curve is shifted down in temperature and has steeper transition slopes compared with data for larger compact tension (CT) specimens from the literature. Full size pre-cracked Charpy (PCC) specimens with a/W ratios of nominally 0.1 and 0.5 were tested at -73°C. The toughness for PCCs with a/W = 0.1 was higher by factors of 2 to 4. Confocal microscopy (CM), fracture reconstruction (FR) and finite element method (FEM) simulations were used to evaluate the local conditions at cleavage fracture. For a/W = 0.5 (PCC and MPCC), initiation took place at a single critical stress-critical area criteria independent of size and temperature. However, for the a/W = 0.1 specimens, the critical stress was lower with a correspondingly larger critical area. This is consistent with the reduced stress field present in shallow cracks. Failure by cleavage initiation at a lower critical stress is tentatively attributed to the effects of higher local strains modifying cleavage conditions.

KEYWORDS: pressure vessel steels, constraint, fracture reconstruction, finite element modeling

The fundamental, albeit often unstated, assumption of linear elastic (LE) and elastic plastic (EP) fracture mechanics (FM) is that unique stress-strain fields develop in the vicinity of any crack and thus, are the same in full sized structures as in test specimens [1-3]. Indeed, under specified conditions -- plane strain, bending, deep cracks and small scale yielding (SSY) -- well defined local stress and strain fields, dominated by the nearby crack tip, are unique and self-similar when distances (e.g., x, the distance ahead of the crack in the crack plane) are normalized by the crack tip opening displacement (δ). The crack tip opening displacement is directly related to the energy release rate integral J (or stress

[1-3] Departments of (1) Chemical Engineering, (2) Mechanical Engineering and (3) Materials, University of California Santa Barbara, Santa Barbara, CA 93106.

Copyright© 1996 by ASTM International www.astm.org

intensity factor, K, in the linear elastic regime) by the constitutive law. The principal tensile stresses (σ_{22}) in the plastic zone surrounding a blunting crack tip are elevated above the uniaxial yield stress (σ_y) by the multiaxial stresses (σ_{11} and σ_{33}). For elastic-perfectly plastic constitutive laws, the maximum σ_{22} reaches $3\sigma_y$ at a distance a few δ ahead of the blunted crack. Even greater σ_{22} elevations occur in materials that strain harden. The effect of multiaxial stresses on elevating σ_{22} is known as *constraint.* Thus for a given constitutive law, constraint is also assumed to be unique and self-similar. The second basic assumption of FM is that the processes around the crack tip leading to fracture are controlled solely by the crack tip fields. If both assumptions are true, the critical δ_{Ic} (or, J_{Ic} or K_{Ic}) at fracture is the same in a test specimen as in a structure.

In reality, such conditions are the exception rather than the rule. For example, loss of constraint, and corresponding reductions of σ_{22}, occur beyond general yielding when the plastic zone of the crack is no longer small compared to the crack or ligament dimension [4]. Assuming that locally elevated fields must envelop some microstructurally-mediated minimum region to induce fracture at a critical δ_{Ic} or (J_{Ic}), the effects of loss of constraint on fracture increase with decreasing specimen size. Another source of deviation from SSY fields is associated with second order, non-singular stress fields parallel to the crack plane and the direction of crack propagation. For linear elastic conditions, this is the effect of so-called T-stresses [5]. Compressive T-fields also reduce the peak stresses and increase with a) decreasing crack depth; b) tensile versus bending loads; and c) specimen size. In contrast, tensile T-stresses and biaxial applied stresses may slightly increase constraint and decrease toughness.

Whatever the source of constraint loss, σ_{22} stress reductions tend to increase cleavage toughness (δ_{Ic} or J_{Ic}). Corresponding reductions in constraint also reduce microvoid growth rates per unit strain, increasing ductile toughness. Within the validity of the constitutive laws and assumptions of homogeneity, it is now possible to accurately simulate crack tip stress-strain fields using finite element methods (FEM) for arbitrary geometries. In combination with *local* measures of the field conditions leading to fracture[2], the simulations can be used to calculate critical δ_{Ic} or J_{Ic}. Such models have frequently adopted a simple but plausible cleavage criteria that a critical σ_{22} stress contour envelop a critical area ahead of the crack tip [6]. While trends towards higher toughness with shallow cracks and smaller specimens have been observed, the quantitative predictions based on *continuum* models have not always been fully consistent with experiment [7]. Improvements will require more rigorous criteria derived from physically-based micromechanical understanding reflecting the underlying *microstructural* elements of local fracture. Advanced micromechanical models, and corresponding local fracture criteria, can be developed to account for factors such as distributions of initiation sites, multiple event/instability versus single event criteria, interactions between stress and strain, history effects and the like.

Thus, the objective of this work was to evaluate the micromechanisms and characterize local conditions for cleavage initiation in a prototypic pressure vessel steel.

---

[2] For cases not involving extensive large scale yielding an alternate/complementary more empirical approach is to use J and T (or equivalent) criteria to characterize fracture conditions. Loci of critical J/T combinations can be determined from tests on different specimen geometries and, in principle, applied to the conditions appropriate to a structure.

The effects of irradiation on micromechanisms and local criteria for cleavage fracture are examined in a companion paper [8].

EXPERIMENT

The composition of the A533B HSST Plate 02 reference steel characterized in this study is given in Table 1 [9]. The microstructure and mechanical properties of this steel have been extensively characterized in a number of studies [10,11].

One-third-sized Charpy (MPCC) specimens (3.33x3.33x16.67 mm) were pre-cracked to a crack depth to specimen width ratio of a/W $\approx$ 0.5 at $\Delta K \leq 20$ MPa•m$^{1/2}$ and tested in three point bending over a range of temperatures from the lower shelf to the upper transition regime to provide a $K_{Jc}(T)$ curve. It is important to emphasize that we are not claiming to be measuring "valid" toughness using such tiny specimens. However, the tests provide an effective toughness for cleavage initiation in this geometry. On the lower shelf the MPCC specimens experienced elastic-plastic unstable fracture or large pop-ins ($\geq$ 50% load drops) (type A). In the lower transition regime, fracture events were defined on the basis of significant load shedding pop-ins, which signaled the end of the test (type B). At higher temperature/toughness levels, the pop-ins were very small and/or crack growth was defined in terms of damage localized to the blunting zone (type C). While not a real fracture event per se, we believe that these quasi-fracture events can be used to estimate toughness. At still higher temperatures, the limited capacity of these very small specimens and the displacement range of the test fixture resulted in only crack blunting, without any sign of incipient fracture. In these cases, we can only record the maximum applied J (or K_J) at the end of the test (type D). Additionally, in some of the tests carried out to larger deflections, blunting combined with small amounts of ductile tearing was observed (type E) [8]. Following testing, the specimens were heat tinted and broken in liquid nitrogen to provide a second reference surface for confocal microscopy/fracture reconstruction (CM/FR) studies.

TABLE 1--Composition of HSST-02 (wt%)

C	Mn	P	S	Si	Cr	Ni	Mo	Cu	V
0.23	1.55	0.009	0.014	0.20	0.04	0.67	0.53	0.140	0.003

Full size pre-cracked Charpy (PCC) bars (W = 10 mm) with two a/W ratios of about 0.1 and 0.5 (i.e. 0.1PCC and 0.5PCC, respectively) were also tested at -73°C. Five specimens were tested at each a/W. Two of the five were side notched 20% to increase lateral constraint. All of the PCC specimens failed by elastic-plastic cleavage initiation, but two of the five a/W = 0.1 specimens exhibited some ductile tearing prior to cleavage fracture.

The fracture surfaces were characterized with CM, which can provide digitized topographic images of three dimensional conjugate fracture surfaces with a resolution down to less than 1 μm (depending on the magnification used and other experimental variables). Individual digitized images were assembled into montages to cover larger regions of the

fracture surface and aligned with the conjugate set using specially designed algorithms. Extending the pioneering work of Kobayashi and co-workers [12-16], the FR method is based on the concept that the deformed conjugate surfaces contain an approximate record of the sequence-of-events leading to material separation. The topographic maps were first overlapped, referenced by the position of the fatigue precrack and cold-fracture surfaces at the beginning and end of the test, and subsequently separated in a series of small ($\approx$ 1 μm) steps using a combination of FEM calculations of material flows and load-point displacement data from the mechanical test record. Most of the reconstructions reported here are lower resolution, aimed at characterizing large regions of the fracture surfaces; higher resolution studies, needed to establish details such as the precise location of initiation sites, will be the topic of future publications. In addition to providing the temporal and spatial sequence of events in the process zone leading to macroscopic crack initiation and growth, CM/FR directly measures the critical initiation crack tip opening displacement, δ_{Ic}, and subsequent increments of opening during stable crack growth (if any). A gray-scale displacement map is used to plot the crack opening δ for each point in the FR (with black representing a $\delta = 0$ and white δ = maximum). The δ_{Ic} can be related to fracture toughness, K_{Jc}, through the relation $K_{J\delta} \approx (2\sigma_y \delta_{Ic} E')^{1/2}$ [17], where E' is the plane strain elastic modulus and σ_y is the temperature-dependent yield stress.

Scanning electron microscopy (SEM) studies (using a JEOL-840) were conducted to evaluate both the general characteristics of the fracture surfaces and, in some cases using the CM/FR visualizations as a guide, to closely examine locations of "interesting" events (e.g., apparent sites of cleavage facet initiation). Essentially one-to-one correspondence between individual features in the SEM micrographs and grey scale CM images were consistently observed. The SEM micrographs clearly demonstrate the fidelity of the CM technique and are needed in various steps of the FR process.

EXPERIMENTAL RESULTS

Fracture Toughness

Figure 1 compares K_{Jc} data from the literature based primarily on larger 1T compact tension (CT) specimens (a/W $\approx$ 0.5 and W = 51 mm) [10,11] with a) MPCC and b) PCC results. Data for the 0.5PCCs generally fall within the scatter band of the CT trend, although the average is slightly higher ($\approx$ 75 versus 65 MPa$\bullet$m$^{1/2}$), broadly consistent with statistical effects of specimen thickness. The K_{Jc}(T) curve for the 0.5MPCC specimen is shifted down in temperature and has a steeper slope in the transition region compared to the corresponding CT curve. At 100 MPa$\bullet$m$^{1/2}$, the shift is about -55°C. The 0.1PCCs fall into two groups: a cluster of 3 data points failed by cleavage initiation at an average K_{Jc} of 162$\pm$ 10 MPa$\bullet$m$^{1/2}$ while two exhibited some ductile tearing prior to cleavage initiation and failed at much higher average toughness of about 270 MPa$\bullet$m$^{1/2}$.

Confocal Microscopy/Fracture Reconstruction

Figure 2 summarizes results of the CM/FR studies for tests at -73°C. The sequences shown are CM topographic maps, displacement maps, SEM images and corresponding FR

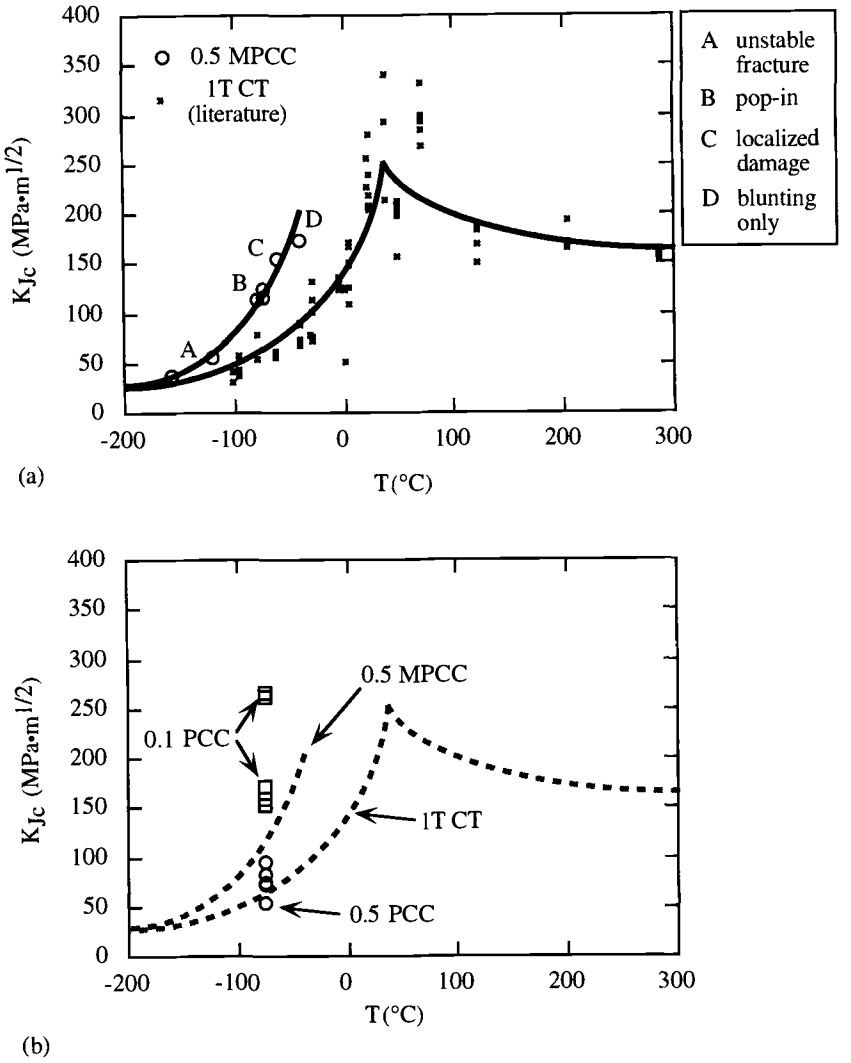


FIG. 1—Comparison of 1TCT data from literature with (a) 0.5 MPCC and (b) 0.1 and 0.5 PCC data

snapshots at a given δ. In this figure, the crack runs from left to right and broken material is represented as black, while intact material is shown in white. The first δ is taken slightly below the point of damage initiation. In this case, the black regions in the process zone represent noise and/or unreconstructable damage (such as a microcrack perpendicular to the primary crack plane). Figure 2a shows a reconstruction of a pop-in event in the MPCC specimen. A load drop of about 30% occurred at a K_{Jc} level of 115 MPa•m$^{1/2}$. The MPCC fracture sequence involves the nucleation of a cluster of several microcrack facets at a $\delta \approx$ 80 to 84 μm ahead of the peak stress region (~200 μm) near one side and toward the center of the crack front. Over an additional $\Delta\delta$ increment of 2-4 μm, additional isolated microcracks form and link to form a half penny pop-in crack penetrating to a maximum depth of 400 μm and covering about 60% of the crack front at a δ_{Ic} of 86 ± 2 μm.The arrested pop-in itself contains areas of unbroken ligaments. Note in this case, there is a fairly large difference between toughness estimates based on δ_{Ic} (146 MPa•m$^{1/2}$) versus the standard K_{Jc}. Figure 2b shows the CM/FR sequence at the center of a 0.5PCC specimen with a K_{Jc} of 94 MPa•m$^{1/2}$. In this case, regions of cleavage appear at δ = 32-34 μm and the next several μm of $\Delta\delta$, additional isolated microcracks form and link to form an unstable macroscopic cleavage crack at δ_{Ic} = 39 ± 2 μm. The CM/FR sequence for an a/W = 0.1 PCC with a K_{Jc} of 129 MPa•m$^{1/2}$ is shown in Figure 2c. Microcracking initiates at about $\delta \approx$ 70 to 72 μm in areas roughly 100 to 600 μm ahead of the crack. At a δ = 72-74 μm, many quasi-cleavage facets are seen to be completely isolated by ductile ridges. Macroscopic instability occurs at about δ_{Ic} = 76 ± 2 μm. Hence, the MPCC and PCC specimens with both deep and shallow cracks appear to experience a similar sequence-of-events prior to cleavage initiation. One possible difference, however, is that the PCC specimens with a shallow a/W = 0.1 crack appear to exhibit microcrack initiation at somewhat larger distances from the crack tip. As shown later, this is consistent with the difference in peak stress location. The fracture surfaces of both types of PCC specimens also contain areas of unbroken ligaments following unstable macroscopic cleavage crack propagation. There is good agreement between the toughness estimates based on δ_{Ic} versus the standard K_{Jc} for both a/W in the PCC specimens.

The CM/FR method can also be used to evaluate the blunting and initiation process in other ways. For example, Figure 3a shows the crack tip opening (δ_{rem}) at a fixed location of roughly one final δ_{Ic} behind the original crack tip as a function of distance ahead of the crack tip (x). Profiles, averaged over 100 μm of lateral distances (parallel to the crack front), are used to monitor blunting and the onset of fracture. Figure 3a illustrates these opening profiles for the MPCC specimens tested over a range of temperatures. In the lower shelf/lower knee regime with increasing temperature (-120, -80 and -73°C) increasing amounts of blunting precede fast fracture. At -40°C, there appears to be some blunting zone damage and a small amount of extension by a combination of tearing and blunting. At higher temperatures (not shown) only blunting is observed. Figure 3b shows a similar plot for a 0.5 and 0.1 PCC specimen which fail by cleavage initiation. The shallow crack specimen is seen to have a δ_{Ic} of nearly twice that of the deep crack. As shown in Figure 4, overall, the estimates of $K_{J\delta}$ derived from CM/FR estimates of δ_{Ic} compare favorably with standard mechanical test estimates of K_{Jc}.

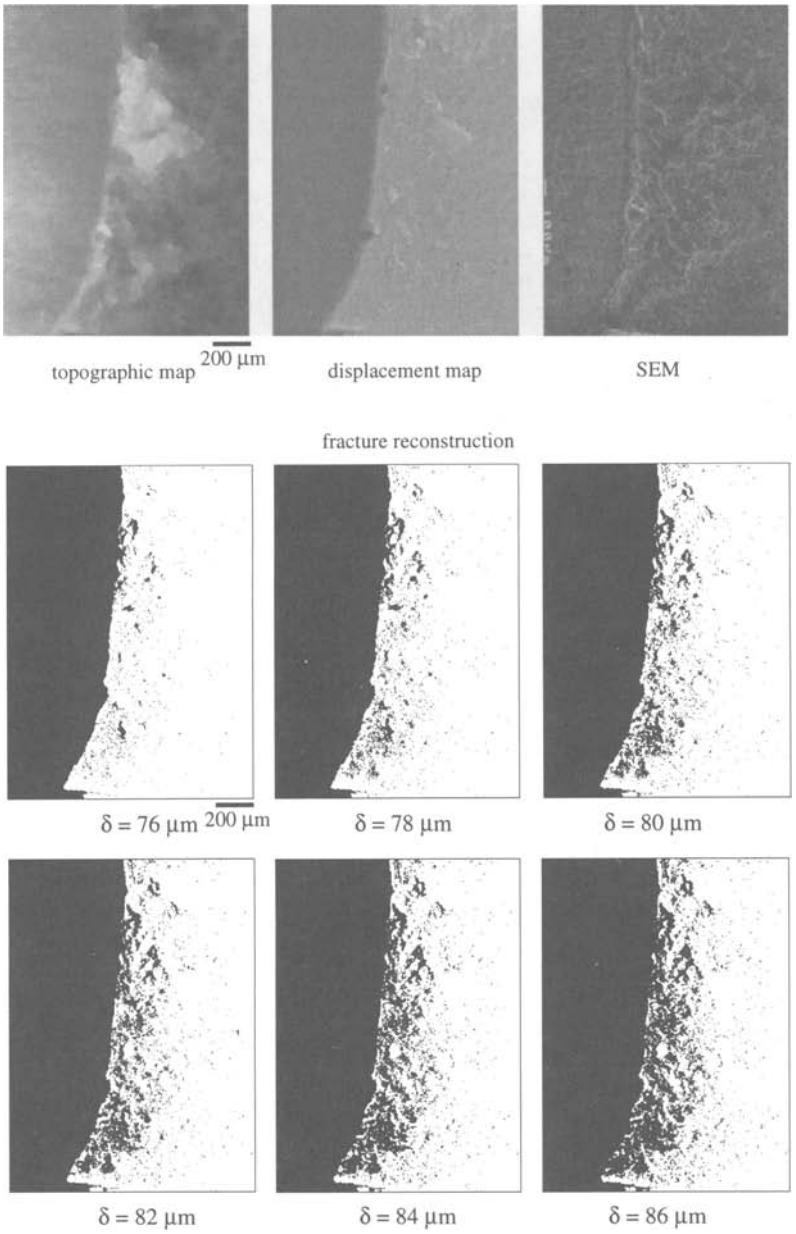


FIG. 2a—CM/FR results for the test temperature of -73°C for a 0.5 MPCC specimen exhibiting pop-in behavior.

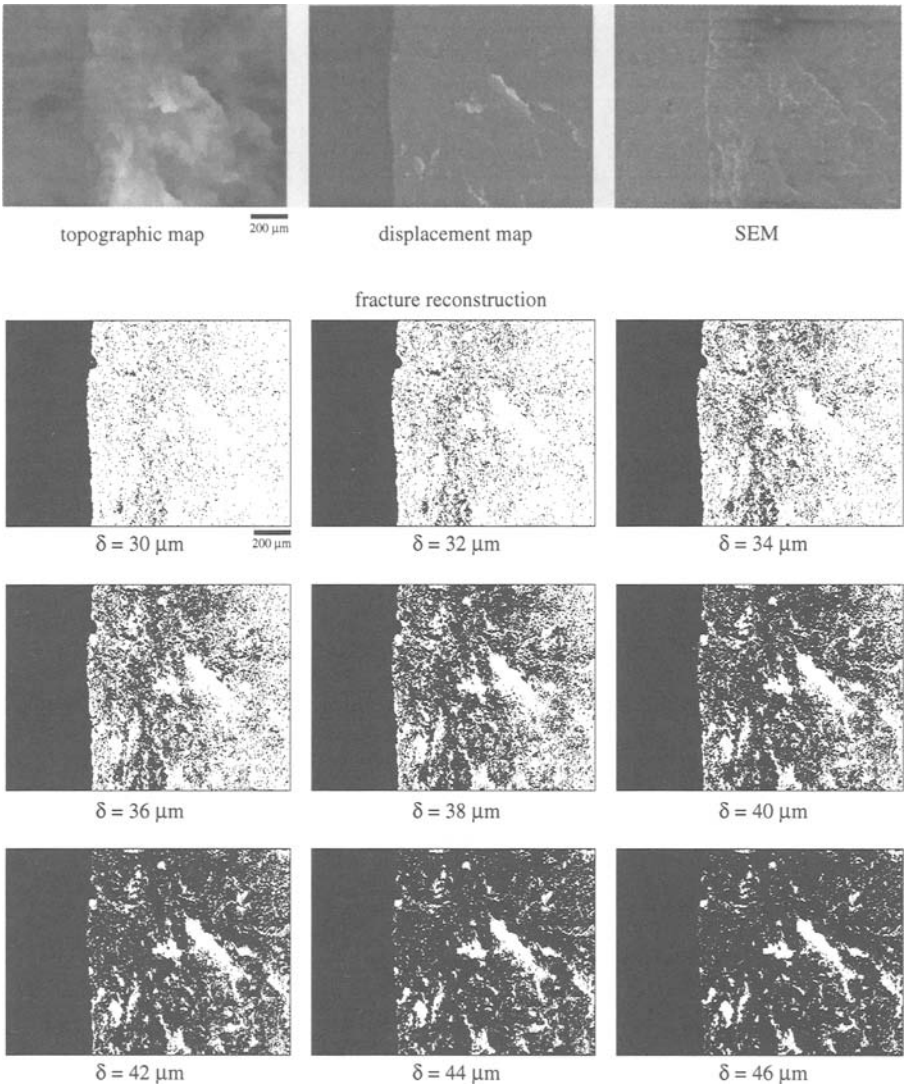


FIG. 2b—CM/FR results for the test temperature of -73°C for a 0.5 PCC specimen.

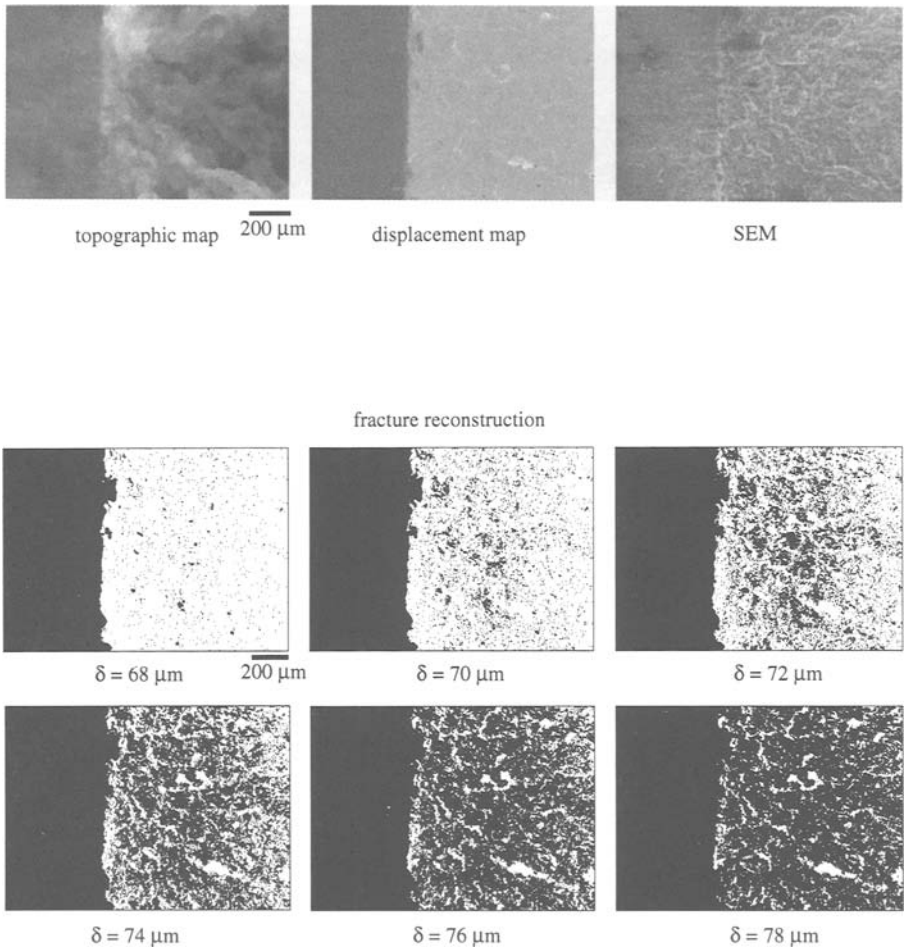


FIG. 2c—CM/FR results for the test temperature of -73°C of a 0.1 PCC specimen.

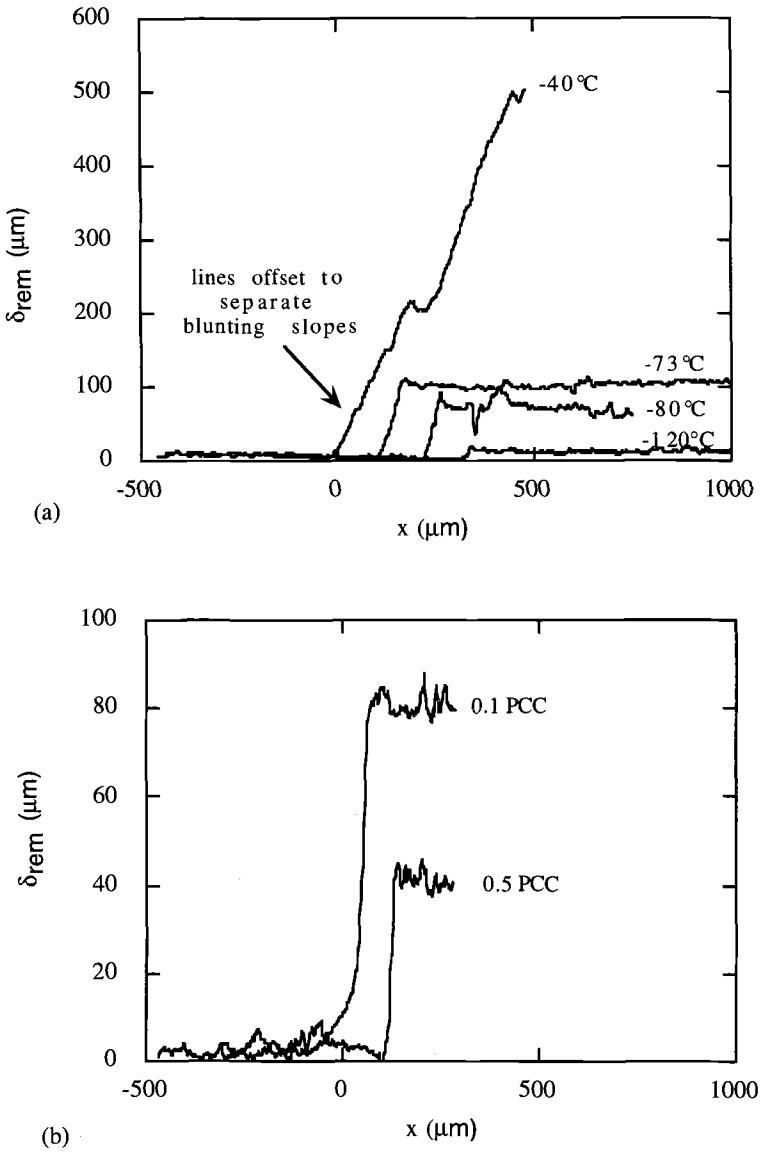


FIG. 3—Crack tip opening displacement as a function of distance ahead of the crack tip for (a) MPCC specimens and (b) 0.1 and 0.5 PCC specimens.

ANALYSIS

Two dimensional, large scale deformation FEM simulations were carried out using the ABAQUS code [18]. Meshes were generated using half symmetry about the crack plane for geometries of a/W=0.1 and 0.5 and 3PB loading. A typical mesh, as shown in Figure 5, consists of 606 eight-noded plane strain elements. Of these elements, 92 are used to refine the crack tip along ten percent of W. All calculations were carried out in non-dimensional form, with an initial crack root radius ranging from W/10000 to W/4000 to represent a sharp precrack.

The constitutive behavior as a function of temperature was fit from tensile stress-strain data [9,19,20] to a Ramberg-Osgood relationship

$$\frac{\varepsilon}{\varepsilon_0} = \frac{\sigma}{\sigma_0} + \left(\frac{\sigma}{\sigma_0}\right)^N, \tag{1}$$

where ε is the total strain at stress σ, σ_0 and ε_0 ($=\sigma_0/E$) are the reference stress and strain, and N is a constant (taken as the inverse of the strain hardening exponent, N = 1/n). The temperature variation of σ_0 was assumed to scale with the uniaxial yield stress. The static yield stress data was corrected for crack tip strain rates ($\dot{\varepsilon}_t$) using a rate compensated effective temperature ($T_e = T_{0.02}[1 + 0.023\ln(0.02/\dot{\varepsilon}_t)]$). The strain hardening exponent was found to approximately fit the relation $n \approx 57/\sigma_y$ (MPa).

Non-dimensional σ_{22}/σ_y versus x/δ fields are shown in Figure 6 for the two crack depths and two δ/W ratios corresponding to δ = 20 μm. The stresses are lower and the peak closer to the crack tip for the shallow crack, and fall off more rapidly for the larger δ/W (viz., smaller specimen).

The appropriate local fracture criteria are not known, but previous work suggests a criteria based on a critical area (A_c) enveloped by a critical stress (σ_c) contour [6,7]. Note this is also roughly equivalent to the classical critical stress/critical distance criteria proposed by Ritchie, Knott and Rice [21] which has been applied to modeling toughness of pressure vessel steels [22]. More complex multi-parameter statistical models differ in quantitative detail, but derive from the same concept that cleavage is controlled by local principal stresses [23-25].

Figure 7 shows the area A_c stressed at or above various specified levels σ_c from the FEM calculations as a function of the applied J for a PCC with a/W = 0.5 at -75 °C. Similar plots can be constructed for other specimen dimensions (simply adjusting the A and J) and a/W to fit the K_{Jc} curves for different specimen sizes and crack depths. The A_c initially varies approximately as J^2, but tends toward linear and saturation behavior at higher J, which is associated with the loss of constraint.

Figure 8a shows that the predicted K_{Jc} values are in reasonable agreement with both the MPCC and 1TCT data trends up to above 100 MPa•$m^{1/2}$ for $A_c = 0.5 \times 10^{-8}$ m^2 and σ_c = 1800 MPa. Figure 8b shows that cleavage initiation in the a/W = 0.1 PCC specimens can be fit by a lower σ_c = 1650 MPa and correspondingly larger A_c of about 0.8×10^{-8} m^2. It should be emphasized that these are not unique fits. For example, different combinations of critical stress and critical area also provide reasonable, albeit generally somewhat less perfect fits. For example a common set of 1725 ± 75 MPa and $0.65 \pm 0.15 \times 10^{-8}$ m^2 may be a reasonable compromise. Further, alternate models may also give comparable results.

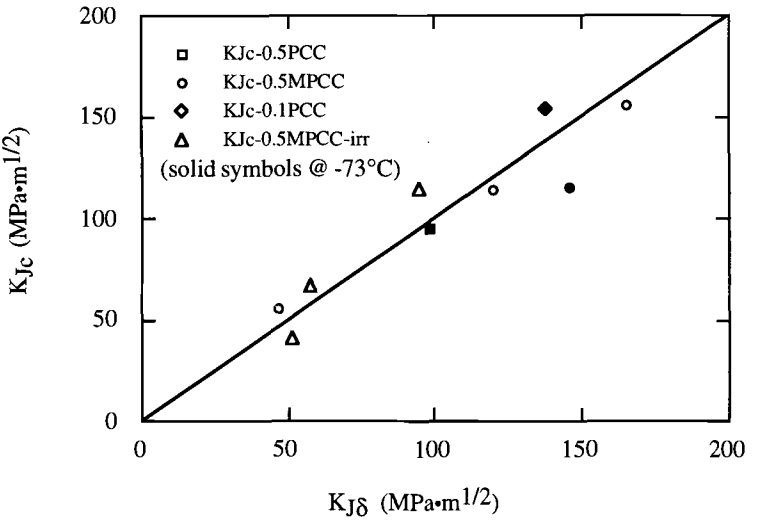


FIG. 4—Comparison of local measures of toughness with standard methods.

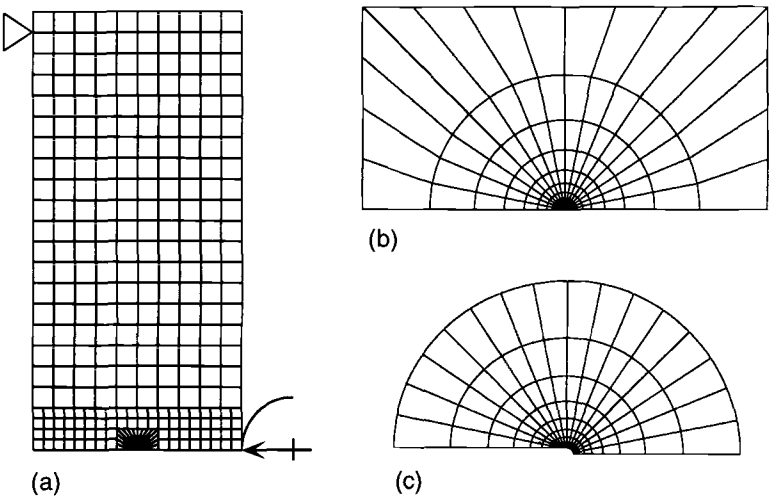


FIG. 5—Typical FEM mesh (a/w = 0.5) with increased detail in (b) and (c).

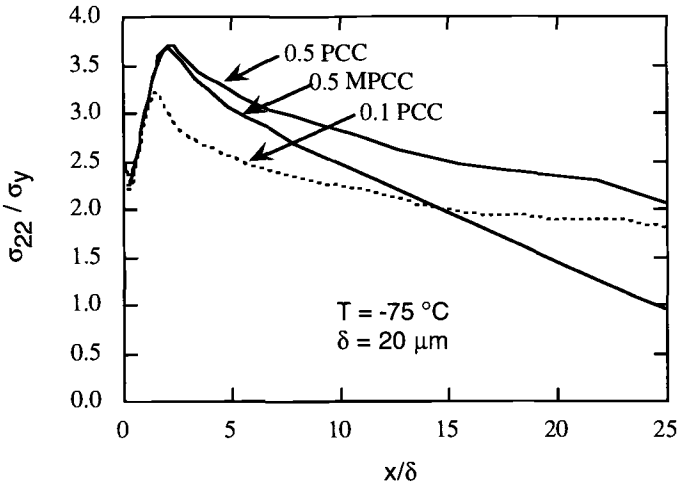


FIG. 6—Stress fields for MPCC specimen and PCC specimen with a/w = 0.1 and 0.5.

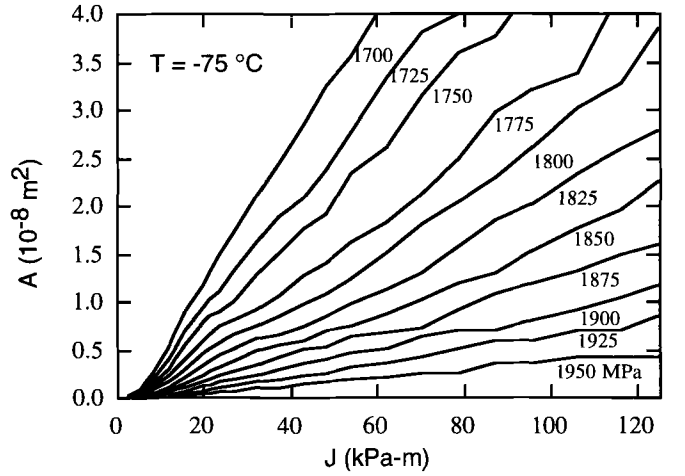
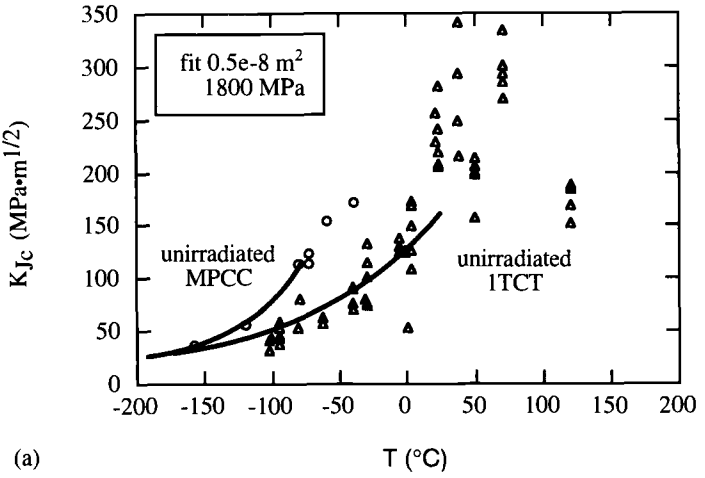


FIG. 7—Area stressed above a given critical stress as a function of J.



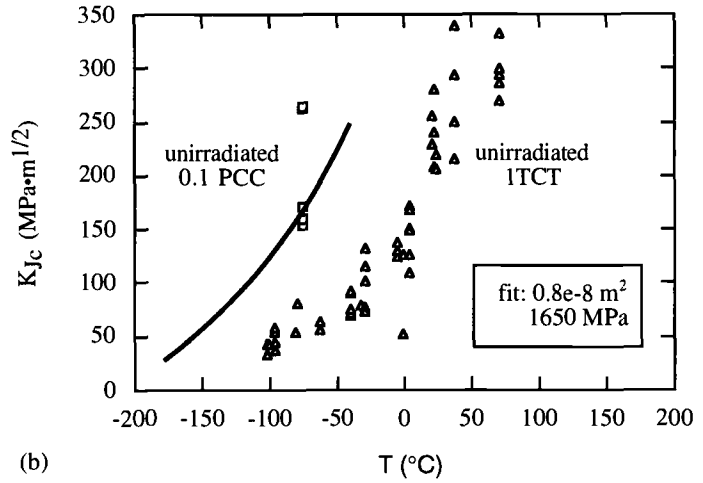


FIG. 8—Critical stress-critical area model predictions for (a) a/w=0.5 PCC and MPCC specimens, and (b) 0.1 PCC specimens.

However, a single critical stress/critical area criteria alone is not sufficient to precisely describe cleavage initiation conditions. Further, we have not attempted to fit the high toughness data points in Figure 8b which failed by cleavage following ductile tearing. The bifurcation of the failure mechanism involves the operation of a ductile fracture mechanism generally associated with stress-modified, strain-controlled microvoid growth. Note the jump in the toughness for the shallow crack PCC tests also resembles the region of rapid upswing or jump in the 1TCT data at higher temperatures.

Assuming cleavage initiation takes place at a lower stress in the a/W = 0.1 specimen suggests that strain may play a role. Figures 9a and 9b show σ_{22} and ε_{22} plots as a function of x at the average cleavage initiation K_{Jc} for the -73°C tests. Note, this toughness rationalization does not exactly represent a common A_c, σ_c criteria. As expected, the magnitude and position of the peak stresses are similar for the MPCC and PCC with a/W = 0.5. The peak stress in the 0.1PCC does not even quite reach 1800 MPa. In contrast to the stresses, however, strains in the region of the crack tip are much larger in the case of the shallow crack compared to the PCC and MPCC cleavage conditions. Note the larger strains are primarily a result of the larger δ_{Ic}. These results indicate that, for deep cracks with similar peak stresses, a common critical stress-critical area criteria provides a reasonable local measure of cleavage fracture resistance. However, for shallow cracks with lower peak stresses and higher strains, the critical stress-area criteria may be modified. We believe that this may be associated with the nucleation and growth of localized secondary damage in the process zone associated with various heterogeneities (inclusions, microvoids, microcracks). The presence of such process zone damage is also indicated by the imminence of the transition to ductile tearing, involving a combination of distributed cleavage facet and particle nucleated microvoids.

The stress and strain fields (σ_{22} and ε_{22}) calculated with FEM are integrated with the FR in Figure 10. Figures 10a-c show the FR from Figures 2a-c at the specified δ near δ_{Ic}. In Figure 10a for the MPCC specimen, the peak stress is near the region of cleavage initiation. In Figure 10b and c, the peak stress is slightly closer to the crack tip than the damage initiation sites. In the latter case the damage initiation takes place at lower strains and over a larger region in front of the crack tip. Figure 10d shows two displacements from a FR sequence of an oversized PCC specimen (a/W=0.5, B=10, W=13 mm) tested at 20 °C. The specimen started out with a sharp precrack which blunted until $\delta \approx 180$ μm, where material separation initiated approximately 200-300 μm ahead of the crack tip. The location of initiation is also seen to correspond to the peak stress region. As δ is increased further, the damage grows and tears back to the tip to propagate the crack. At $\delta \approx 350$ μm, new damage initiates slightly closer to the crack tip and the fracture sequence repeats. This behavior in Figure 10d is in contrast to that shown in Figure 10e for a MPCC specimen tested at -40°C. As demonstrated in Figure 3a, this specimen exhibited only blunting and small amounts of ductile tearing with all of the damage directly in the vicinity of the crack tip and within the region of very high strain.

SUMMARY

We have examined the effects of constraint on the elastic-plastic cleavage toughness of an A533B pressure vessel steel. Sub-sized specimens with an a/W ~ 0.5 were tested over a

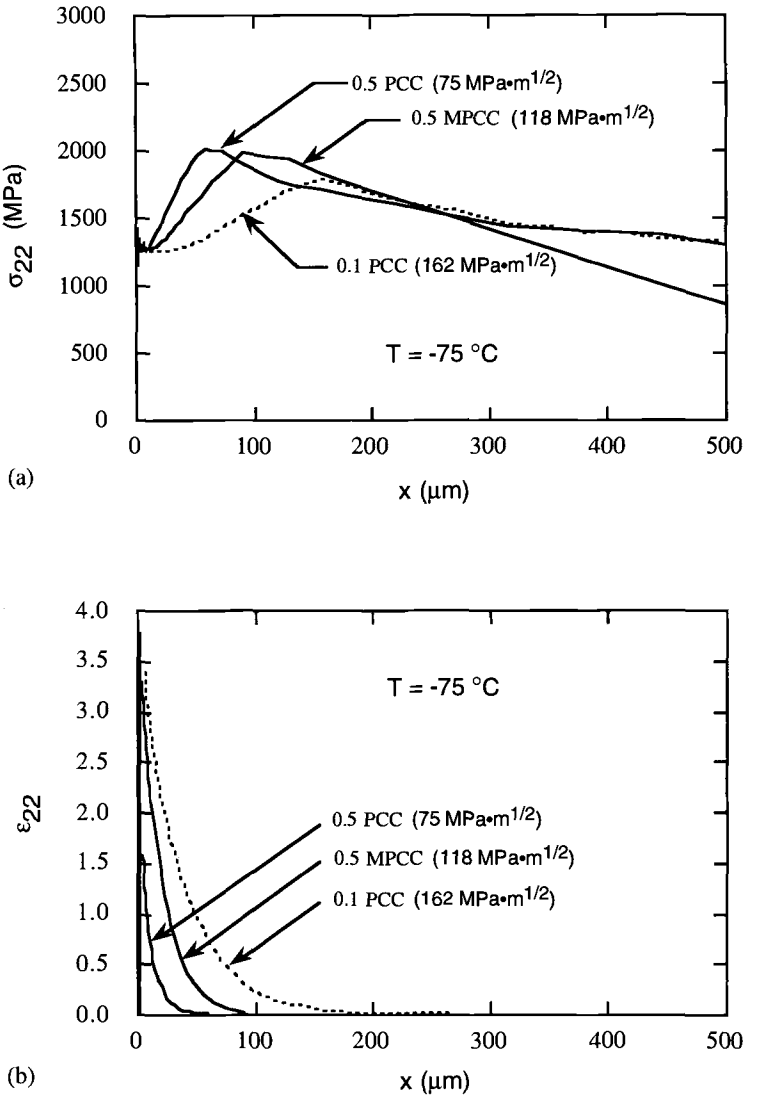


FIG. 9—Principle stress (a) and strain (b) ahead of a blunting crack tip for PCC and MPCC geometries.

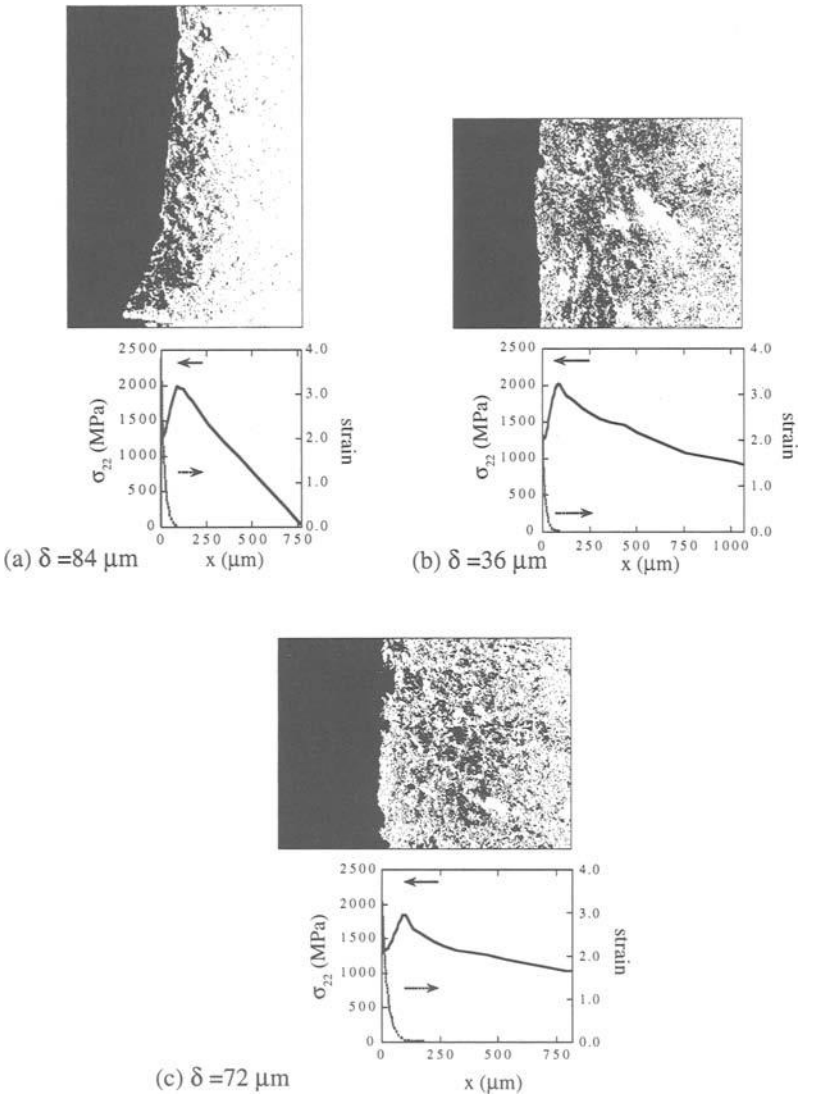
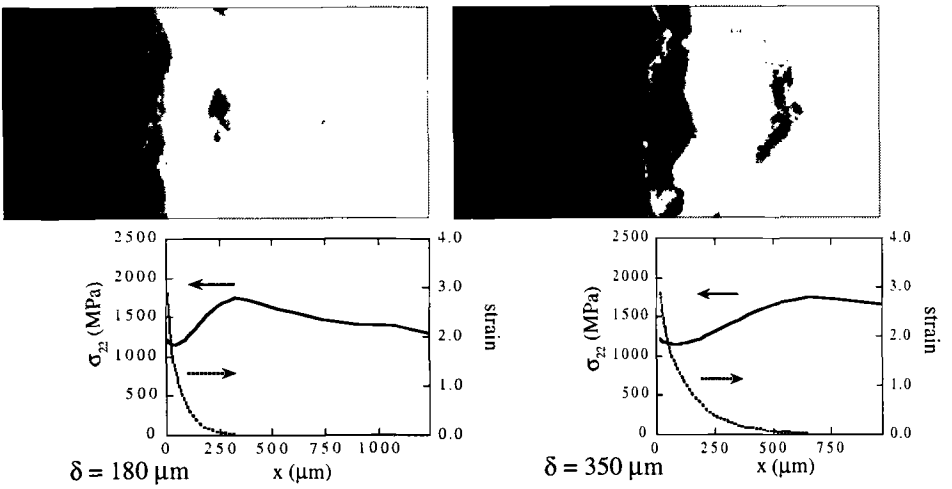
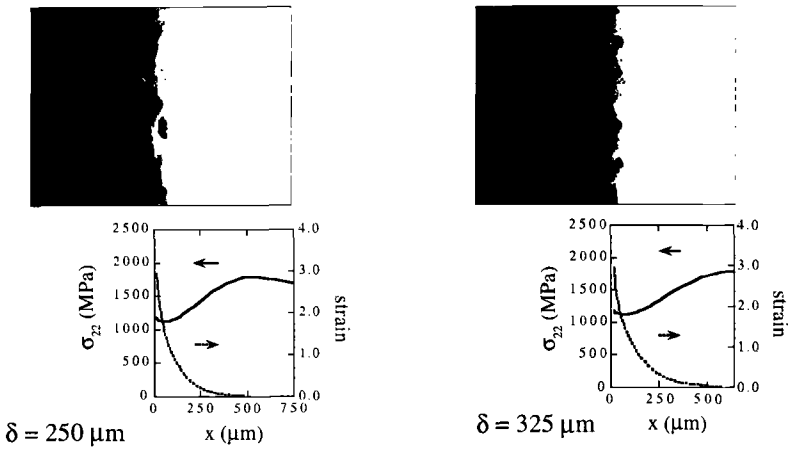


FIG. 10—FEM and CM/FR results for (a) 0.5 MPCC specimen at -73°C, (b) 0.5 PCC specimen at -73°C and (c) 0.1 PCC specimen at -73°C.



(d)



(e)

FIG. 10 —FEM and CM/FR results for (d) oversized 0.5 PCC specimen at 20°C and (e) 0.5 MPCC specimen at -40°C.

range of temperatures, and pre-cracked Charpy specimens were tested at -73°C with two a/W ratios (0.1 and 0.5). The fracture surfaces were analyzed by confocal microscopy and fracture reconstruction techniques.

Decreasing specimen size at constant a/W shifted the $K_{Jc}(T)$ curve down in temperature, and steepened the transition regime, while decreasing a/W increased the K_{Jc} at the same temperature. Selected CM/FR showed that in the cleavage initiation regime, microcracks nucleate near the peak stress region ahead of the crack tip and coalesce over a fairly narrow increment of displacement. This process could be modeled by a critical stress/critical area criteria, but may be modified by the local strain (and hence specimen size/geometry) sufficient to develop secondary damage.

ACKNOWLEDGEMENTS

The authors gratefully acknowledge the work of J.W. Sheckherd and D. Gragg in mechanical testing and B.L. Chao in FEM. This research was supported by the U.S. NRC under contract number NRC 04-90-046 and U.S. DOE Office of Fusion Energy under grant number DE-FG03-87ER-52143.

REFERENCES

[1] Ritchie, R.O. and Thompson, A.W., "On Macroscopic and Microscopic Analysis for Crack Initiation and Crack Growth Toughness in Ductile Alloys," Met Trans, 16A (1985) 233.

[2] Parks, D.M., "Defect Assessment in Components--Fundamentals and Applications", J.G. Blauel, K.H. Schwalbe (eds), Mech. Eng Publ., (1991) 205.

[3] McMeeking, "Finite Deformation Analysis of Crack Tip Opening in Elastic-plastic Materials and Implication fro Fracture," R., J. Mech Phys Solids, 25 (1977) 357.

[4] Anderson, T.L. and Dodds, R.H., "Specimen Size Requirements for Fracture Toughness Testing in the Transition Regime," J Test and Eval 192 (1991) 123.

[5] Hancock, J.W. and Betegon, R.H., "Two Parameter Characterization of Elastic-Plastic Crack Tip Fields," J App Mech, 58 (1991) 104.

[6] Odette, G.R., "On the Ductile to Brittle Transition in Martensitic Stainless Steels - Mechanisms, Models and Structural Implications", J. Nucl Mater 212-215 (1994) 45.

[7] Odette, G.R., Chao, B.L., and Lucas, G.E., "On Size and Geometry Effects on the Brittle Fracture of Ferritic and Tempered Martensitic Steels," J. Nucl Mater 191-194, (1992) p. 821.

[8] Wirth, B, Edsinger, K., Odette, G.R., and Lucas, G.E., and "Evaluation of Embrittlement in Pressure Vessel Steels by Fracture Reconstruction", Effects of Radiation on Materials: 17th Int'l Symposium, ASTM STP 1270, D. S. Gelles, R. K. Nanstad, A. S. Kumar, and E. A. Little (eds), Philadelphia, PA, ASTM STP 1270 (1996).

[9]. McGowan, J. J., Nanstad, R. K., and Thoms, K. R., "Characterization of Irradiated Current-Practice Welds and A533 Grade B Class 1 Plate for Nuclear Pressure Vessel Service", NRC NUREG/CR-4880, Vol. 1 (ORNL-6484/V1) (July 1988).

[10] Mager, T.R., et. al., "Feasibility and Methodology for Thermal Annealing an Embrittled Reactor Vessel," EPRI NP-2712-2 (1982).
[11] Hawthorne, J.R., Menke, B.H., and Hiser, A.C., "Light Water Reactor Pressure Vessel Dosimetry Program, Post Irradiation Notch Ductility and Tensile Strength Determination for PSF Simulated Through-Wall Specimen Capsules," NRC NUREG/CR-3457 (1984).
[12]. Kobayashi, T. and Shockey, D. A., "A Fractographic Investigation of Thermal Embrittlement in Cast Duplex Stainless Steel", Met. Trans. 18A (1987) 1941.
[13]. Ogawa, K., Zhang, X. J., Kobayashi, T., Armstrong, R. W., and Irwin, G. R., "Microstructural Aspects of the Fracture Toughness Cleavage-Fibrous Transition for Reactor-Grade Steel", Fracture Mechanics: Fifteenth Symposium, ASTM STP 833 (1984) 393.
[14]. Kobayashi, T. and Shockey, D. A., "FRASTA: A New Way to Analyze Fracture Surfaces -- Part 1: Reconstructing Crack Histories", Advanced Materials & Processes 140-5 (1991) 28.
[15]. Kobayashi, T. and Shockey, D. A., "FRASTA: A New Way to Analyze Fracture Surfaces -- Part 2: Determining Fracture Mechanisms and Parameters", Advanced Materials & Processes 140-6 (1991) 24.
[16]. Edsinger, K., Wirth, B., Odette, G. R., and Lucas, G. E., "Characterization of the Local Fracture Process in Martensitic Stainless Steels" (submitted to J. Nucl. Mater).
[17] Shih, C.F., "Relationships between J-Integral and the Crack Opening Displacement for Stationary and Extending Cracks, J. Mech Phys Solids 29 (1981) 305-326.
[18] Hibbit, Karlsson and Sorensen, Inc, ABAQUS Users Manual, Version 5.4 (1994).
[19] G.R. Odette and G.E. Lucas, "An Experimental Investigation of Kinetic Aspects of Neutron Irradiation Embrittlement of Light Water Reactor Pressure Vessel Steels", EPRI Report NP 6114 (1989).
[20] Server, W.L., and Oldfield, W., "Nuclear Pressure Vessel Steel Data Base," EPRI NP-933 (1978).
[21] Ritchie, R.O., Knott, J.F., and Rice, J.R., "On the Relationship between Critical Tensile Stress and Fracture Toughness in Mild Steel," J Mech Phys Solids, 21 (1973) 395.
[22] Ritchie, R.O., Server, W.L., and Wullart, R.A., "Critical Fracture Stress and Fracture Strain Models for the Prediction of Lower and Upper Shelf Toughness in Nuclear Pressure Vessel Steels," Met Trans, 10A (1979) 1557.
[23] Lin, T., Evans, A.G., and Ritchie, R.O., Stochastic Modeling of the Independent Role of Particle Size and Grain Size in Transgranular Cleavage Fracture," J Mech Phys Solids (1986).
[24] Beremin, "A Local Criterion for Cleavage Fracture of a Nuclear Pressure Vessel Steel," F. Met Trans 14A (1983) 2277.
[25] Wallin, K., Saavio, T, and Torronen, K. "Statistical Model for Carbide Induced Brittle Fracture in Steel," Met Trans, 18 (1984) 13.

Mikhail A. Sokolov,[1] Randy K. Nanstad,[1] and Shafik K. Iskander[1]

THE EFFECTS OF THERMAL ANNEALING ON FRACTURE TOUGHNESS OF LOW UPPER-SHELF WELDS

REFERENCE: Sokolov, M. A., Nanstad, R. K., and Iskander, S. K., **"The Effects of Thermal Annealing on Fracture Toughness of Low Upper-Shelf Welds,"** *Effects of Radiation on Materials: 17th International Symposium, ASTM STP 1270,* David S. Gelles, Randy K. Nanstad, Arvind S. Kumar, and Edward A. Little, Eds., American Society for Testing and Materials, 1996.

ABSTRACT: Experimental results are presented from a study of the effects of thermal annealing on recovery of fracture toughness of low upper-shelf submerged-arc welds (weld designations 61W through 67W) from the Heavy-Section Steel Irradiation (HSSI) Program Second and Third Irradiation Series. Most of the study was conducted to evaluate the effects of annealing on the J-R curves of the submerged-arc welds. The recovery of fracture toughness in the transition range as the result of annealing was studied for welds 63W, 64, and 65W only. Compact specimens of 12.7- and 20.3-mm-thick (0.5T and 0.8T, respectively) were tested in this study. The specimens had been previously irradiated at the Oak Ridge National Laboratory (ORNL) Bulk Shielding Reactor. Each weld was irradiated to a certain value of neutron fluence in the range from 0.4 to 1.3×10^{19} neutrons/cm^2 (> 1 MeV) in the average temperature range of 275 to 300°C. Annealing of the irradiated specimens was done at 454°C for 168 h. Fracture toughness tests were performed at temperatures selected to match those of the previously conducted unirradiated and irradiated tests.

KEYWORDS: fracture toughness, annealing, low upper-shelf weld

INTRODUCTION

Prevention of reactor pressure vessel (RPV) failure in light-water moderated nuclear power reactors depends primarily on maintaining the RPV material fracture toughness at levels that will resist fracture, either brittle or ductile, during plant operation, including normal and emergency conditions. A number of reactor vessels in commercial

[1]Metals and Ceramics Division, Oak Ridge National Laboratory, Oak Ridge, TN 37831-6151.

Copyright© 1996 by ASTM International www.astm.org

pressurized-water reactor (PWR) plants include welds with both relatively low initial Charpy V-notch (CVN) upper-shelf energies and high copper concentrations that make them highly sensitive to neutron irradiation. Accordingly, the fracture toughness requirements of *Title 10, Code of Federal Regulations, Part 50* (10CFR50), Appendix G [1], may not be met by some beltline weld materials as the RPV approaches the end of design life. The regulations require, as an option, that a fracture mechanics analysis be performed that conservatively demonstrates adequate safety margins for continued operation. Otherwise, thermal annealing may need to be performed to recover the fracture toughness of the embrittled materials.

The object of this present study is the effect of thermal annealing on recovery of fracture toughness of low upper-shelf submerged-arc welds (weld designations 61W through 67W) from the HSSI Program Second and Third Irradiation Series and the behavior of annealed welds upon reirradiation. This paper describes the first stage of this study, which is associated with creation of a database of fracture toughness recovery of high-copper, low upper-shelf submerged-arc welds after thermal annealing. In the second stage, this database will be used to study the degradation of fracture toughness properties upon reirradiation.

The HSSI Program Second and Third Irradiation Series were conducted in the late 1970s and early 1980s to examine irradiation effects on the tearing resistance of these welds by means of J-R curve testing. The J-R curve characterization of the welds studied [2,3] concluded that (1) irradiation significantly decreased the critical values of J-integral near onset of slow stable crack growth (J_{Ic}) and the tearing modulus (T_{avg}) from the preirradiation values, and (2) T_{avg} was a more discriminating indicator of the degradation in fracture toughness than J_{Ic}. Fracture toughness tests were not conducted at temperatures where cleavage would occur. More detailed presentations are given in Refs. [2,4,5], while Ref. [6] provides a summary of all of the irradiation series conducted under the HSSI Program.

MATERIALS AND IRRADIATION HISTORY

As previously described [2,4], the seven submerged-arc welds, identified as HSSI welds 61W through 67W, were fabricated with materials and procedures used in early PWRs. These welds had average copper levels ranging from 0.21 to 0.42% with nickel levels of around 0.6% and, thus, were considered "sensitive" to neutron irradiation embrittlement and typical of some early pressure vessel welds. The use of Linde 80 flux produced welds with large contents of very small inclusions, leading to relatively low CVN upper-shelf energies. Chemical compositions and postweld stress-relief heat treatments of the welds are presented in Table 1.

TABLE 1--Chemical compositions and postweld stress-relief heat treatments of HSSI welds 61W through 67W

Weld	Content of chemical elements[a] (wt %)						Postweld heat treatment
	C	Mn	Mo	P	Ni	Cu	
61W	0.09 0.07 0.10	1.48 1.45 1.52	0.37 0.36 0.38	0.020 0.018 0.021	0.63 0.62 0.64	0.28 0.26 0.31	25 h at 593 to 621°C (1100–1150°F)
62WA[b]	0.083 0.078 0.088	1.51 1.41 1.61	0.377 0.365 0.390	0.013 0.012 0.014	0.51 0.48 0.54	0.20 0.14 0.27	8 cycles of 6 h at 593 to 621°C (1100–1150°F)
62WB[b]	0.083 0.078 0.088	1.51 1.41 1.61	0.377 0.365 0.390	0.018 0.016 0.020	0.55 0.54 0.60	0.177 0.160 0.230	
63W	0.098 0.088 0.109	1.65 1.62 1.67	0.427 0.415 0.440	0.016 0.015 0.017	0.685 0.663 0.707	0.299 0.272 0.326	48 h at 593 to 621°C (1100–1150°F)
64W	0.085 0.070 0.100	1.59 1.54 1.64	0.420 0.410 0.430	0.014 0.012 0.017	0.66 0.60 0.72	0.35 0.31 0.39	48 h at 593 to 621°C (1100–1150°F)
65W	0.080 0.070 0.090	1.45 1.42 1.49	0.385 0.370 0.400	0.015 0.014 0.017	0.597 0.585 0.610	0.215 0.180 0.250	80 h at 593 to 621°C (1100–1150°F)
66W	0.092 0.075 0.110	1.63 1.59 1.67	0.400 0.380 0.420	0.018 0.017 0.020	0.595 0.580 0.610	0.42 0.35 0.49	48 h at 593 to 621°C (1100–1150°F)
67W	0.082 0.070 0.095	1.44 1.40 1.48	0.390 0.370 0.410	0.011 0.010 0.013	0.59 0.58 0.60	0.265 0.220 0.310	Not available

[a]Top entry is the average value, while numbers shown below each entry indicate the range of composition measurements.

[b]Weld 62W is a duplex weld designated 62WA and 62WB.

The design of the irradiation capsules was based on the irradiation of two 101.6-mm-thick compact specimens [4TC (T)] in one capsule. In addition to the 4TC (T) fracture toughness specimens, 0.5T, 0.8T, and 1.6TC (T) (12.7, 20.3, and 40.6 mm thick, respectively), CVN, and tensile specimens were included in the irradiation capsules. The first capsule was loaded for irradiation into the Bulk Shielding Reactor in November 1976, while the last capsule was removed from the reactor in March 1978 [6]. A total of six capsules were irradiated under the Second and Third Irradiation Series.

Because of neutron flux gradients through the 101.6-mm (4-in.) thickness of the largest specimens, the capsule design provided for 180° rotation of the capsules during the irradiations. These rotations were scheduled to average total neutron fluence through the thickness of the 4TC (T) specimens. The neutron flux for the specimens varied, depending on location in the capsule, but averaged about 1×10^{12} neutrons/(cm^2 · s) (> 1 MeV) [7]. Each weld was irradiated to a certain value of neutron fluence in the range from 0.4 to 1.3×10^{19} neutrons/cm^2 (> 1 MeV).

The primary temperature control was at the fatigue crack front of the 4TC (T) specimens with a target irradiation temperature of 288°C (550°F). Since there was no independent control of temperatures for the small specimens, they were irradiated over a temperature range about 288°C, depending on their location in the capsules and the degree of thermal contact between them and the 4TC (T) specimens. These temperatures were also different in the forward and reverse position. Thus, the irradiation temperature for each specimen is an average of the temperatures experienced in the forward and reverse positions. Additional details of capsule design and operation conditions are contained in Ref. [4].

The specimens for the present annealing/reirradiation study were chosen to be as comparable as possible with the irradiation conditions (temperature and neutron fluence) of specimens tested in the previous irradiation study [2]. Moreover, due to uncertainties in copper content, as well as variations in irradiation conditions and toughness properties after irradiation [2,4], weld 62W was not included in this study.

TEST MATRIX

Annealing of all specimens was performed at 454°C for 168 h. The annealing furnace in the hot cell was set to heat specimens at the rate of 20°C/h up to 454°C, then keep the specimens at this temperature for 168 h. After annealing for 168 h, the furnace was turned off automatically and specimens were cooled in the furnace.

Two 0.5T compact specimens of each weld were assigned for the tearing resistance characterization in each annealed and reirradiated conditions. Additionally, all available 0.8TC (T) specimens were tested after annealing. J-R curve tests in the ductile range were performed at temperatures selected to match those of the unirradiated and irradiated tests [2].

Six 0.5TC (T) specimens of welds 63W, 64W, and 65W were selected for fracture toughness tests in the transition range after thermal annealing and reirradiation. Transition fracture toughness of these three welds in the unirradiated condition has been determined by testing of 12 precracked CVN (PCVN) specimens of each weld. For weld 63W, only three Charpy specimens were available initially. The rest of the specimens for that weld were obtained by weld reconstitution of broken 63W Charpy halves at the Kurchatov Institute, Moscow, using inserts no shorter than 17 mm that consisted of 63W weld metal only. After reconstitution, the specimens were notched and fatigue precracked.

All specimens were tested with a single-specimen unloading compliance procedure. PCVN specimens were tested in three-point slow bending while measuring load versus load-line displacement. Unfortunately, the design of the already irradiated compact specimens did not allow for placement of the clip gage on the load line. To overcome this problem, razor blades were spot-welded to the front face of the specimens (crack mouth) and the clip gage was attached to the razor blades. The front face displacements were converted to load line displacements using a geometric correction factor that accounted for the specimen center of rotation [8].

Table 2 provides the irradiation conditions, test temperatures, and the fracture toughness properties (discussed in the next section) after annealing at 454°C for 168 h.

RESULTS AND DISCUSSION

Fracture Toughness in the Transition Region

With testing of the PCVN and 0.5T compact specimens of 10 and 12.7 mm thickness, respectively, some amount of local crack tip plasticity was present and fracture toughness up to cleavage instability was calculated in terms of the J-integral, J_c. Then the J_c is converted to its equivalent in terms of the elastic-plastic stress intensity factor, K_{Jc}. The K_{Jc} values are size-dependent and distinguished by a broad scattering in the transition region. To characterize the elastic-plastic fracture toughness of welds studied, the K_{Jc} data were analyzed by a procedure based on the earlier work by Wallin [9] and developed in an American Society for Testing and Materials (ASTM) draft standard on test method for fracture toughness in the transition range.[1] The procedure uses weakest-link theory to adjust for specimen size effects so that data equivalent to that for a 1T specimen size $[K_{Jc(1T)}]$ can be calculated from data measured with specimens of different sizes $[K_{Jc(xT)}]$ as follows:

---

[1]"Determination of Reference Temperature, T_o, for Ferritic Steels in the Transition Range," Draft 11, Task Group E08.08.03 on Ductile-Brittle Transition, American Society for Testing and Materials, Philadelphia, 1995.

TABLE 2--Irradiation conditions and test data of the specimens studied

Specimen	Specimen Type[a]	T_{irr}[b] (°C)	Neutron fluence[c] (10^{18} n/cm^2)	T_{test} (°C)	J_{Ic}[d] (kJ/m^2)	T_{avg}[e]	K_{Jc}[f] (MPa$\sqrt{m}$)
61W-043	0.8T(10)	303(278/328)	12.0(3.2/8.8)	121	187(181)	77(90)	N/A
61W-101	0.5T(20)	281(274/288)	15.9(3.2/12.7)	121	111(105)	60(73)	N/A
61W-130	0.5T(20)	309(285/334)	13.3(2.2/11.1)	121	129(126)	63(76)	N/A
63W-043	0.8T(20)	297(267/328)	14.1(2.7/11.4)	171	136(133)	91(100)	N/A
63W-120	0.5T(20)	293(328/259)	12.6(10.9/1.7)	171	105(101)	83(100)	N/A
63W-117	0.5T(0)	282(285/278)	6.2(5.1/1.1)	–46	N/A	N/A	138(119)
63W-128	0.5T(0)	293(328/259)	12.0(10.4/1.6)	–46	N/A	N/A	132(114)
63W-129	0.5T(0)	299(320/278)	8.9(5.4/3.5)	–46	N/A	N/A	55(49)
63W-130	0.5T(0)	299(320/278)	8.4(5.2/3.2)	–46	N/A	N/A	116(101)
63W-131	0.5T(0)	299(320/278)	7.7(4.7/3.0)	–46	N/A	N/A	137(118)
63W-138	0.5T(0)	298(298/299)	8.5(6.0/2.5)	–46	N/A	N/A	61(54)
64W-040	0.8T(20)	284(298/271)	7.7(5.2/2.5)	177	203(201)	124(139)	N/A
64W-107	0.5T(20)	286(298/279)	5.7(3.1/2.6)	177	113(109)	67(79)	N/A
64W-148	0.5T(20)	281(277/285)	5.6(0.8/4.8)	177	129(126)	68(84)	N/A
64W-136	0.5T(0)	283(279/288)	4.5(3.5/1.0)	–50	N/A	N/A	47(43)
64W-138	0.5T(0)	283(279/288)	4.8(3.7/1.1)	–15	N/A	N/A	212(181)
64W-139	0.5T(0)	283(279/288)	4.1(3.2/0.9)	–40	N/A	N/A	97(85)
64W-141	0.5T(0)	284(292/277)	5.4(4.5/0.9)	–40	N/A	N/A	91(80)
64W-142	0.5T(0)	284(292/277)	5.0(4.2/0.8)	–40	N/A	N/A	76(67)
64W-143	0.5T(0)	284(292/277)	4.4(3.7/0.7)	–40	N/A	N/A	88(77)
64W-144	0.5T(0)	282(290/275)	4.7(0.9/3.8)	–40	N/A	N/A	44(40)
65W-101	0.5T(20)	286(289/283)	6.5(3.5/3.0)	200	128(123)	64(80)	N/A
65W-137	0.5T(20)	279(253/304)	5.6(0.8/4.8)	200	107(105)	70(84)	N/A
65W-105	0.5T(0)	287(286/287)	5.4(2.9/2.5)	–60	N/A	N/A	54(49)
65W-133	0.5T(0)	282(269/296)	4.8(2.0/2.8)	–50	N/A	N/A	72(64)
65W-140	0.5T(0)	289(320/259)	5.6(4.8/0.8)	–50	N/A	N/A	100(87)
65W-142	0.5T(0)	289(319/258)	4.7(4.0/0.7)	–50	N/A	N/A	83(73)
65W-157	0.5T(0)	278(265/292)	5.1(0.7/4.4)	–50	N/A	N/A	100(87)
65W-160	0.5T(0)	284(293/276)	4.5(3.8/0.7)	–50	N/A	N/A	113(98)
66W-117	0.5T(20)	288(294/283)	7.6(4.1/3.5)	200	89(87)	16(20)	N/A
66W-120	0.5T(20)	279(287/271)	8.0(6.3/1.7)	200	106(98)	43(53)	N/A
67W-140	0.5T(20)	278(269/286)	3.8(2.8/1.0)	200	130(127)	67(83)	N/A
67W-141	0.5T(20)	278(266/289)	7.6(0.9/6.7)	200	117(112)	62(76)	N/A

[a]Number in parentheses indicates the percent of side grooves.
[b]First entry is the average value, while numbers in parentheses indicate irradiation temperature in forward and reverse position, respectively.
[c]First entry in the total neutron fluence (> 1 MeV), while number in parentheses indicate neutron fluence accumulated in forward and reverse position, respectively.
[d,e]First entry is the value determined according to ASTM E-1152-87, while number in parentheses is the value determined from the modified version of the J-integral.
[f]Number in parentheses indicates the value of K_{Jc} adjusted to 1T size.

$$K_{Jc(1T)} = 20 + (K_{Jc(xT)} - 20)\left(\frac{B_{xT}}{B_{1T}}\right)^{1/4}, \quad (1)$$

where $B_{(xT)}$ and $B_{(1T)}$ are the test specimen and 1T compact specimen thicknesses, respectively.

The scatter of fracture toughness is described by applying the statistical distribution developed by Weibull. The procedure also employs the maximum likelihood concept [10] regarded as the most accurate method of obtaining median value of fracture toughness [$K_{Jc(med)}$] at a given test temperature:

$$K_{Jc(med)} = \left[\frac{\sum_{i=1}^{N}(K_{Jc(i)} - 20)^4}{N - 1 + \ln 2}\ln 2\right]^{1/4} + 20, \quad (2)$$

where N is the number of fracture toughness tests at the test temperature. Finally, the master curve approach for 1T size specimens is applied to the median K_{Jc} to define the temperature dependence of fracture toughness in the transition region as follows:

$$K_{Jc(med)} = 30 + 70 \exp[0.019(T - T_o)], \quad (3)$$

where T_o is the reference temperature at $K_{Jc(med)} = 100$ MPa$\sqrt{m}$. Thus, the T_o can be used to measure the radiation-induced shift of the transition fracture toughness and the recovery due to annealing.

In this study, attempts were made to test six specimens at the given test temperature to perform statistical analysis by Eqs. (1) through (3). In those cases where only one K_{Jc} was obtained, the datum was not used in positioning of the master curve. The T_o values obtained from PCVN data sets at two temperatures tended to be the same and were averaged.

Table 3 summarizes the T_o values of welds studied in the unirradiated [T_o(U)], irradiated [T_o(I)], and irradiated/annealed [T_o(IA)] conditions. The T_o values in irradiated condition were estimated by the following expression:

$$T_o(I) = T_o(U) + \Delta RT_{NDT}, \quad (4)$$

where ΔRT_{NDT} is the radiation-induced shift in reference temperature (assumed equal to ΔT_o for this study) calculated according to *Regulatory Guide 1.99* (RG 1.99) [11]. According to Refs. [4,5], the RG 1.99 predictions of the radiation-induced shifts were comparable to Charpy 41-J transition temperature shifts observed for these welds following adjustment to an irradiation temperature of 288°C. Thus, to eliminate the need for fluence adjustments in this study, it was assumed that RG 1.99 could provide reasonable estimates of radiation-induced shifts of fracture toughness. In this study, the ΔRT_{NDT} predictions by RG 1.99 were made based on the average copper and nickel content (see Table 1) and the average value of neutron fluence for specimens tested in the irradiated/annealed condition.

TABLE 3--Fracture toughness transition temperatures, T_o, in the unirradiated (U), irradiated (I), and irradiated and annealed (IA) conditions

Weld	Neutron fluence (avg. ± SD) $\times 10^{18}$ neutrons/cm^2	T_o (U) (°C)	ΔRT_{NDT} (RG 1.99) (°C)	T_o (I) (°C)	T_o (IA) (°C)	T_o(IA)-T_o(U) (°C)
63W	8.6 ± 1.9	–90	110	20	–44	46
64W	4.7 ± 0.4	–59	98	39	–12	47
65W	5.0 ± 0.4	–80	74	–6	–33	47

Figures 1, 2, and 3 show the K_{Jc} values adjusted to 1T size and transition master curves obtained for the welds studied in the unirradiated and annealed conditions and estimated by RG 1.99 for the irradiated condition. Each weld exhibits a broad spread of fracture toughness data in both the unirradiated and irradiated and annealed conditions. Significant scatter of the transition fracture toughness data was also reported for two other Linde 80 welds from the unirradiated Midland pressure vessel [12]. Together, these data illustrate the necessity of using a statistically based analysis procedure to characterize the fracture toughness in the transition region. The procedure used in the present work proves to be the unique tool in performance of such analysis.

Residual transition temperature shift, or difference between T_o(IA) and T_o(U), is used to describe the recovery of fracture toughness due to thermal annealing. In the case of welds 63W, 64W, and 65W, the values of residual shift were 46, 47, and 47°C, respectively. Such residual shifts indicate only partial recovery of fracture toughness in the transition temperature regime. It is interesting to note that the residual transition temperature shifts are the same despite the fact that the copper content is different for the welds studied; namely, the average copper contents are 0.30, 0.35, and 0.22% in welds 63W, 64W, and 65W, respectively. These data will be used to evaluate the fracture toughness behavior after reirradiation, because the rate of reembrittlement is the proper attribute to evaluate the advantage of thermal annealing.

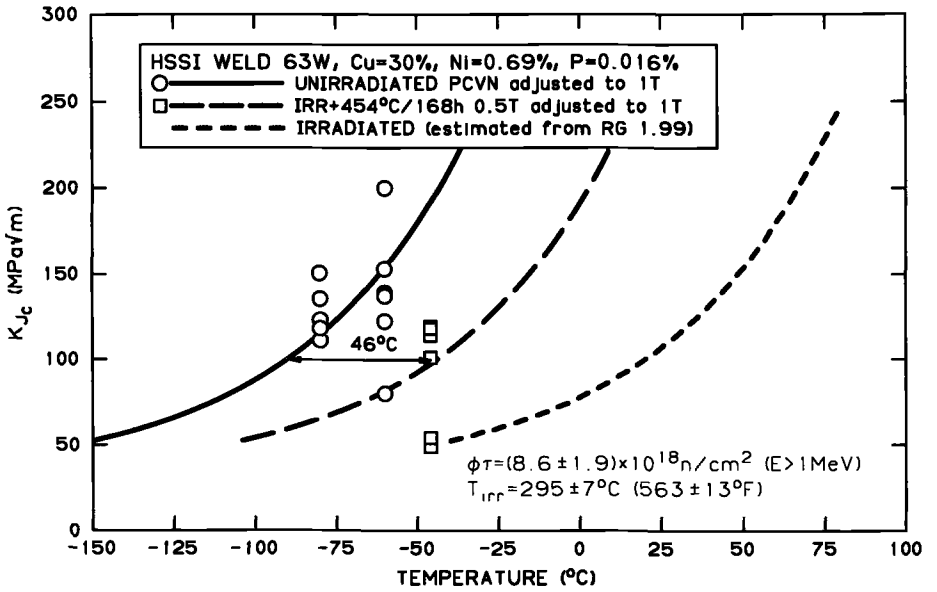


FIG. 1--Fracture toughness data and master curves of weld 63W in the unirradiated, irradiated, and irradiated and annealed conditions.

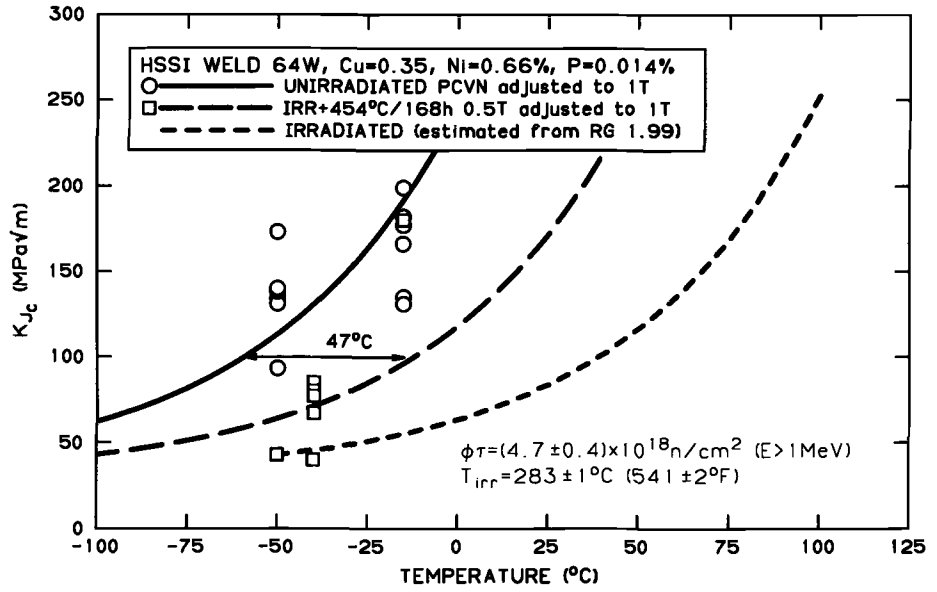


FIG. 2--Fracture toughness data and master curves of weld 64W in the unirradiated, irradiated, and irradiated and annealed conditions.

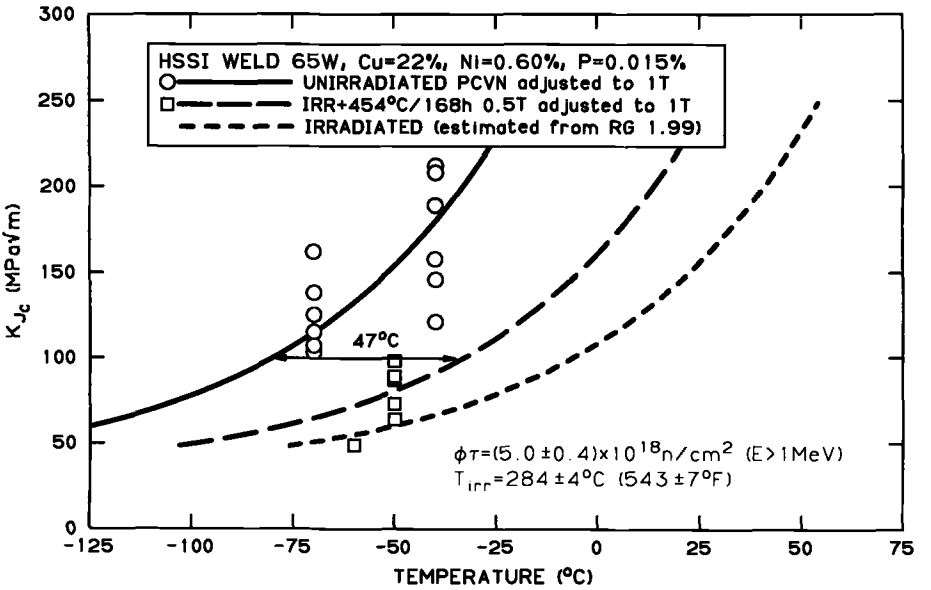


FIG. 3--Fracture toughness data and master curves of weld 65W in the unirradiated, irradiated, and irradiated and annealed conditions.

Tearing Resistance Characterization

The values of the J-integral were determined using both the procedure specified in the ASTM Standard Test Method for Determining J-R Curves (E 1152-87) and a modified version of the J-integral as proposed by Ernst [13]. Modified J is used here because this version of the J-integral was chosen and reported in the previous study for the unirradiated and irradiated conditions [2]. The values of tearing modulus were determined as:

$$T_{avg} = \frac{E}{\sigma_f^2}\frac{dJ}{da}, \tag{5}$$

where E is the modulus of elasticity; σ_f is the flow stress (the average of the yield and ultimate strength); and dJ/da is the average slope of the J-R curve between the exclusion lines. The test temperatures of annealed specimens were also chosen to provide direct comparisons with the previous results in the unirradiated and irradiated conditions.

From analysis of data in Table 2, it can be seen that calculation of the J-integral by the modified version results in slightly lower values of J_{Ic} compared to those calculated according to E 1152-87. The differences are less than 5 %. Primarily, use of modified

J-integral manifests in an increase of the J-R curve slope and, consequently, the tearing modulus.

Figure 4 presents J-R curves of welds studied after annealing at 454°C for 168 h. J-R curves of these welds in the unirradiated and irradiated conditions were digitized from the previous study [2] and they are also plotted in Fig. 4 for comparison. Table 2 provides the individual specimen results while Table 4 lists the averaged values of modified J_{Ic} and T_{avg} of welds studied in the unirradiated, irradiated, and irradiated/annealed conditions. The data show that in all cases annealing at 454°C produces a very positive effect on recovery of J-R curves of irradiated high-copper, low upper-shelf welds. The J_{Ic} data tend to indicate some "over recovery" after annealing, when the property of irradiated and annealed material becomes even better than the unirradiated material. The tearing modulus recovery also appears to be complete; the deviations from unirradiated values are varied from one weld to another but all are within the interval of ± 9.

TABLE 4--Modified J_{Ic} and T_{avg} of welds 61W through 67W in the unirradiated (U), irradiated (I) and irradiated and annealed (IA) conditions

Weld	Temperature (°C/°F)	J_{Ic} (kJ/m^2)			T_{avg}		
		U	I	IA	U	I	IA
61W	121/250	129	88	137	80	37	80
63W	171/340	121	83	117	89	34	100
64W	177/350	126	104	145	99	36	101
65W	200/392	107	91	114	89	50	82
66W	200/392	84	68	93	46	25	37
67W	200/392	104	75	120	89	43	80

SUMMARY

Fracture toughness characterization of irradiated high-copper, low upper-shelf welds 61W, 63W, 64W, 65W, 66W, and 67W after annealing at 454°C for 168 h was performed. Recovery of welds 63W, 64W, and 65W was studied in the transition region and on the ductile shelf. Welds 61W, 66W, and 67W were characterized on the ductile shelf only. The fracture toughness properties of the welds studied show the following responses to annealing at 454°C for 168 h: (1) partial recovery of the fracture toughness in the transition region (K_{Jc}); (2) complete recovery of the tearing modulus; and (3) complete or even over-recovery of the J_{Ic}.

The data obtained for the fracture toughness properties of irradiated and annealed high-copper, low upper-shelf welds will be used to study the effects of reirradiation on the degradation of fracture toughness properties of the same welds.

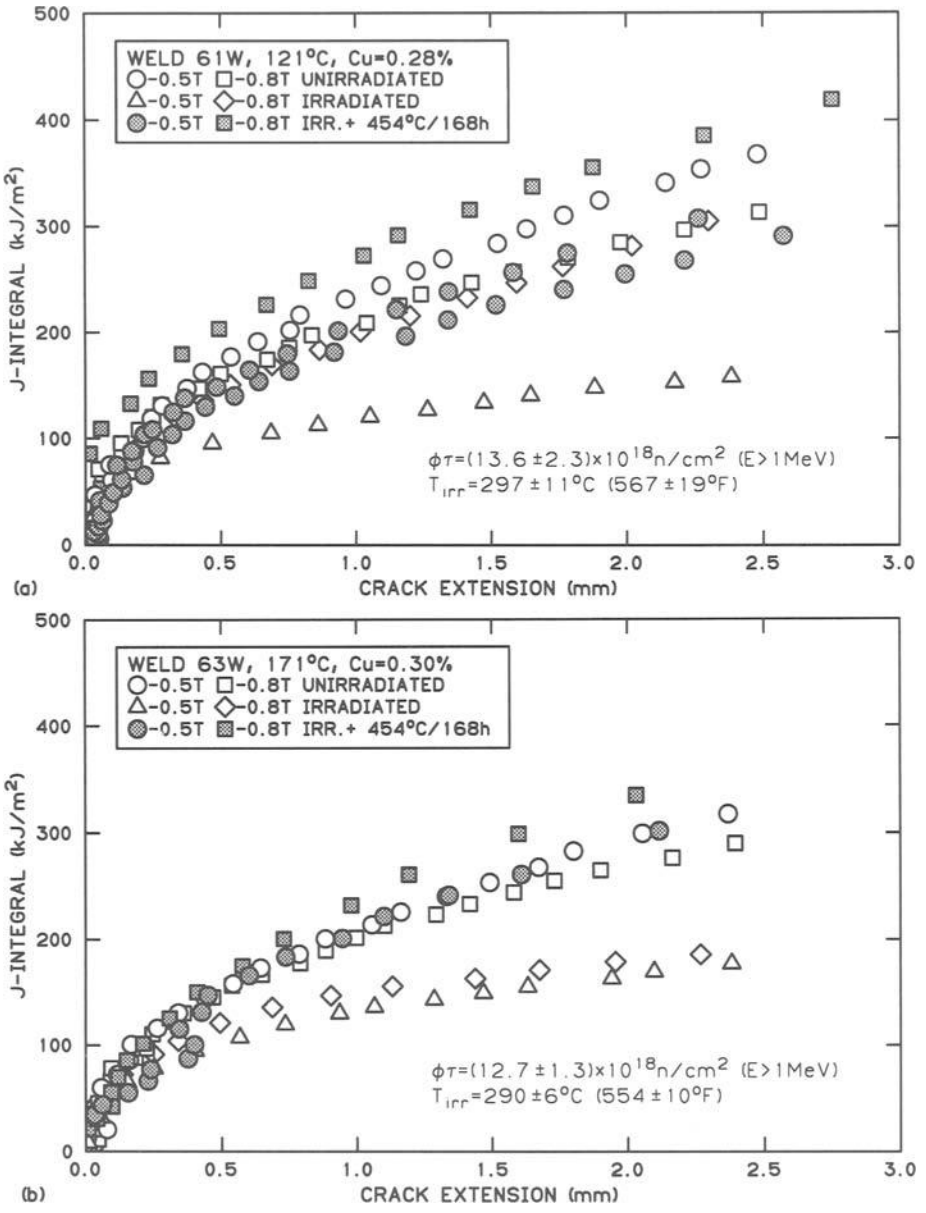


FIG. 4--J-R curves of welds (a) 61W, (b) 63W, (c) 64W, (d) 65W, (e) 66W, and (f) 67W in the unirradiated, irradiated, and irradiated and annealed conditions. The unirradiated and irradiated data were digitized from A. L. Hiser, F. J. Loss, and B. H. Menke, Materials Engineering Associates, *J-R Curve Characterization of Irradiated Low Upper Shelf Welds*, USNRC Report NUREG/CR-3506 (MEA-2028), April 1984.

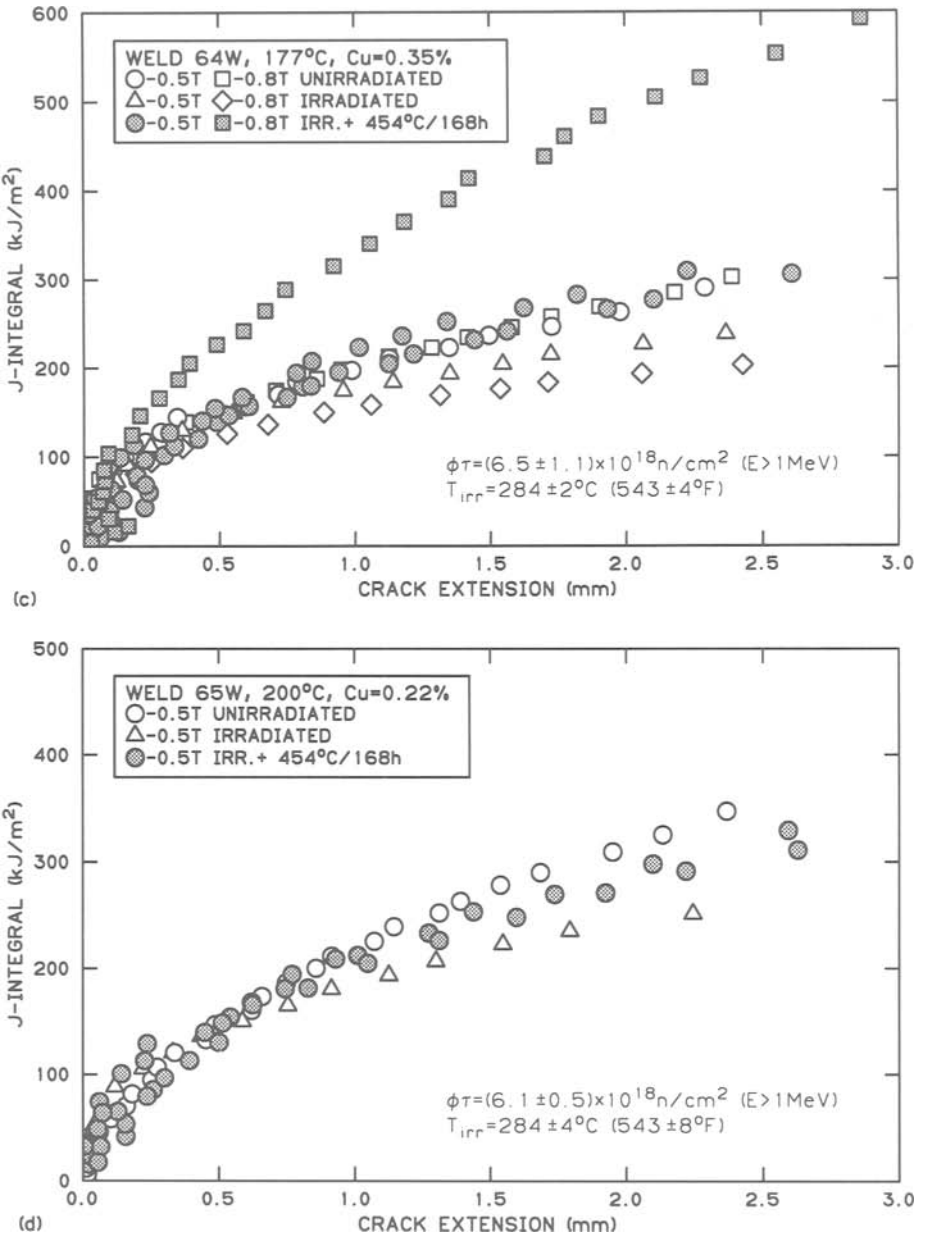


FIG. 4--(Continued)

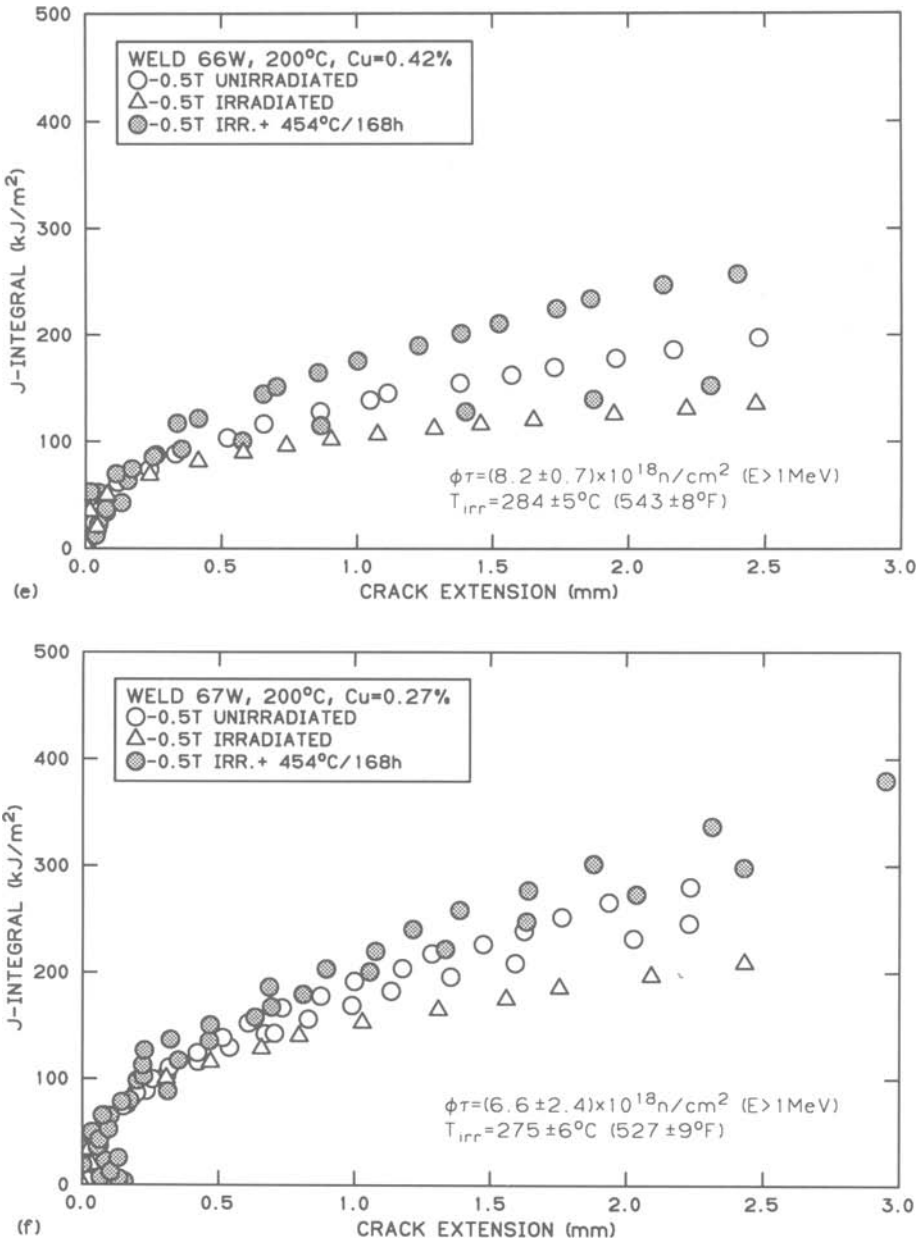


FIG. 4--(Continued)

ACKNOWLEDGMENTS

The authors acknowledge the programmatic support of the Heavy-Section Steel Irradiation Program at ORNL by the Office of Nuclear Regulatory Research, U.S. Nuclear Regulatory Commission, under Interagency Agreement DOE 1886-8109-8L with the U.S. Department of Energy under contract DE-AC05-84OR21400 with Lockheed Martin Energy Systems. The fracture toughness tests were conducted by Ronald L. Swain. Julia L. Bishop prepared the final manuscript. Dr. Ya. I. Shtrombakh, Kurchatov Institute, Moscow, is acknowledged for assistance with reconstitution of Charpy specimens. This research was supported in part by an appointment to the ORNL Postdoctoral Research Program administered by the Oak Ridge Institute for Science and Education.

REFERENCES

[1] *Title 10, Code of Federal Regulations*, Parts 0 to 199, U.S. Government Printing Office, January 1987.

[2] A. L. Hiser, F. J. Loss, and B. H. Menke, Materials Engineering Associates, *J-R Curve Characterization of Irradiated Low Upper Shelf Welds*, USNRC Report NUREG/CR-3506 (MEA-2028), April 1984.

[3] A. L. Hiser, F. J. Loss, and B. H. Menke, "Fracture Toughness Characterization of Irradiated Low Upper-Shelf Welds," pp. 1131-1149 in *Effects of Radiation on Materials: Twelfth International Symposium, ASTM STP 870*, F. A. Garner and J. S. Perrin, Eds., American Society for Testing and Materials, Philadelphia, 1985.

[4] R. K. Nanstad and R. G. Berggren, Martin Marietta Energy Systems, Inc. Oak Ridge Natl. Lab., *Irradiation Effects on Charpy and Tensile Properties of Low Upper-Shelf Welds, HSSI Series 2 and 3*, USNRC Report NUREG/CR-5696 (ORNL/TM-11804), August 1991.

[5] R. K. Nanstad and R. G. Berggren, "Effects of Irradiation Temperature on Charpy Impact and Tensile Properties of High-Copper, Low Upper-Shelf, Submerged-Arc Welds," pp. 239-267 in *Effects of Radiation on Materials: 16th International Symposium, ASTM STP 1175*, A. S. Kumar, D. S. Gelles, R. K. Nanstad, and E. A. Little, Eds., American Society for Testing and Materials, Philadelphia, 1993.

[6] R. K. Nanstad, W. R. Corwin, D. J. Alexander, F. M. Haggag, S. K. Iskander, D. E. McCabe, and R. E. Stoller, "Heavy-Section Steel Irradiation Program on Irradiation Effects in Light-Water Reactor Pressure Vessel Materials," pp. 297-310 in *Fatigue and Crack Growth: Environmental Effects, Modeling Studies, and Design Considerations*, PVP-Vol. 306, S. Yukawa, Ed., American Society of Mechanical Engineers, New York, 1995.

[7] F. W. Stallman and F. B. K. Kam, Union Carbide Nucl. Div., Oak Ridge Natl. Lab., *Neutron Spectral Characterization of the Second Nuclear Regulatory Commission Heavy Section Steel Technology 4T-CT Irradiation Experiment*, USNRC Report NUREG/CR-0505 (ORNL/TM-285), December 1978.

[8] J. D. Landes, "A Calculation from Front Face Displacement Measurement on a Compact Specimen," *Int. J. Fracture*, 16, 93-100 (1980).

[9] K. Wallin, "Scatter in K_{Ic}-Results," *Eng. Fracture Mech.*, 19(6) 1085-1093 (1984).

[10] K. Wallin, "Validity of Small Specimens Fracture Toughness Estimates Neglecting Constraint Corrections," in *Constraint Effects in Fracture: Theory and Applications, ASTM STP 1244*, M. Kirk and A. Bakker, Eds., American Society for Testing and Materials, Philadelphia, 1995.

[11] U.S. Nuclear Regulatory Commission, *Regulatory Guide 1.99, Revision 2*, "Radiation Embrittlement of Reactor Vessel Materials," May 1988.

[12] D. E. McCabe, R. K. Nanstad, S. K. Iskander, and R. L. Swain, Martin Marietta Energy Systems, Inc., Oak Ridge Natl. Lab., *Unirradiated Material Properties of Midland Weld WF-70*, USNRC Report NUREG/CR-6249 (ORNL/TM-12777), 1994.

[13] H. A. Ernst, "Materials Resistance and Instability Beyond J-Controlled Crack Growth," pp. 191-213 in *Elastic-Plastic Fracture, ASTM STP 803*, Vol. 1, C. F. Shih and J. P. Gudas, Eds., American Society for Testing and Materials, Philadelphia, 1983.

Brian Wirth[1], Kurt Edsinger[1], G. Robert Odette[2] and Glenn E. Lucas[2]

EVALUATION OF EMBRITTLEMENT IN A PRESSURE VESSEL STEEL BY FRACTURE RECONSTRUCTION

REFERENCE: Wirth, B., Edsinger, K., Odette, G. R., and Lucas, G. E., **"Evaluation of Embrittlement in Pressure Vessel Steels by Fracture Reconstruction,"** *Effects of Radiation on Materials: 17th International Symposium, ASTM STP 1270,* David S. Gelles, Randy K. Nanstad, Arvind S. Kumar, and Edward A. Little, Eds., American Society for Testing and Materials, 1996.

ABSTRACT: Confocal microscopy (CM) and fracture reconstruction (FR), along with mechanical tests and scanning electron microscopy, were used to characterize irradiation embrittlement of a reference A533B pressure vessel steel. Toughness-temperature [K(T)] curves from tests on one-third size, pre-cracked Charpy specimens resemble the results from full sized specimens; however, the small specimen curves are shifted down in temperature and have steeper transition slopes. Cleavage fracture generally occurred by load-shedding pop-ins, arresting at distances which decreased with increasing temperature. The CM/FR measurements showed nucleation of multiple cleavage facets in high-stress regions in front of the crack tip, followed by coalescence into unstable fracture over a small increment of crack opening. At higher temperature and toughness values the damage was confined to the region around the blunting zone due to the limited specimen capacity. In this regime microvoids were also nucleated on inclusion particles. Irradiation shifted the K(T) curve about 95°C at 75 $MPa\cdot m^{1/2}$. However, no major differences in the basic cleavage fracture mechanisms were observed. Indeed at low toughness, shifts in the K(T) curve closely reflected temperature differences at a common yield stress in the irradiated versus unirradiated material. Finally, the toughness values estimated from CM/FR measurements of the critical crack tip opening displacement were in good agreement with the results of the mechanical tests.

KEY WORDS: pressure vessel steels, embrittlement, confocal microscopy, fracture reconstruction, fracture toughness

The most useful measures of irradiation embrittlement of reactor pressure vessel steels are shifts and possible shape changes for various measures of fracture toughness

[1] Graduate students in Mechanical Engineering and Chemical Engineering, University of California, Santa Barbara, Santa Barbara, CA 93106

[2] Professors of Mechanical Engineering and Materials, University of California, Santa Barbara, Santa Barbara, CA 93106

Copyright© 1996 by ASTM International www.astm.org

versus temperature [K(T)] curves. One of several[3] relevant measures of fracture toughness is cleavage initiation in the elastic-plastic transition regime [$K_{Jc}(T)$]. A number of studies have suggested that the shape of the $K_{Jc}(T)$ curve is unaffected by irradiation; hence, measurement of temperature at a reference toughness in the transition region (e.g., around the 100 MPa•$m^{1/2}$) can not only be used to index the reference $K_{Jc}(T)$ shapes, but also to establish statistical effects (lower bound toughness) and to correct (within constraint limits) for specimen size[1-3]. However, the fundamental basis for a constant shape $K_{Jc}(T)$ and the detailed mechanisms by which radiation-induced microstructures effect toughness shifts are not fully understood.

In the case of blunt notched Charpy specimens, shifts in the maximum temperature of linear-elastic fracture in manganese-molybdenum pressure vessel steels are known to be due to increases in yield strength caused by a population of ultrafine, irradiation-induced features[4-6]. The yield stress based models are also generally consistent with the observed trends in the toughness shifts[7]. However, these models also predict that for large elevations of yield stress: i) the Charpy shifts could be much smaller than those indexed by toughness; and ii) there may be a large reduction in the slope of the transition region. Neither of these predictions is fully consistent with current observations.

Another important unresolved issue is related to establishing relevant measures of toughness under conditions deviating from classical deep crack, small-scale yielding conditions. Typically, these circumstances lead to a loss of crack tip constraint resulting in increased effective toughness. One approach to deal with such complexities is to define appropriate local measures of fracture resistance. Such local measures can be combined with constitutive laws and simulations of crack tip fields to predict fracture initiation for arbitrary geometries. However, rigorous local approaches must be based on realistic treatments of the detailed microscopic mechanisms leading to fracture.

The work reported in this paper is part of a broader effort to develop a better fundamental understanding of the micromechanisms of fracture and embrittlement. The particular questions addressed include:

What are the sequence-of-events and micromechanisms leading to cleavage fracture in a prototypic pressure vessel steel?

How does this sequence-of-events relate to the underlying microstructure?

Does irradiation change these micromechanisms and microstructural relations?

The first two items are addressed in more detail in a companion paper [21]. The third item is the focus of the results reported here.

EXPERIMENT

Composition and Irradiation

The composition of the A533B HSST Plate 02 reference steel characterized in this study is given in Table 1 [8]. The unirradiated microstructure and mechanical properties of this heat have been extensively characterized in a number of studies and it has also been included in a large number of test reactor and surveillance irradiation programs [9-13]. This steel was also irradiated in previous programs in a variety of forms, including one-third-

[3] Other measures include those applicable to a variety of types of static conditions [linear elastic (K_{Ic})], elastic-plastic cleavage following limited ductile tearing (K_{Jc} >> 100 MPa•$m^{1/2}$) and upper shelf J_R-Δa resistance curves, dynamic loading (K_{Id}) and crack arrest (K_{Ia}).

sized Charpy bars and miniature tensile specimens [14]. The neutron irradiations performed in the current study were at 305°C with a flux of 3.6×10^{16} n/m^2-s (E> 1MeV) and fluences to 2.6×10^{23} n/m^2.

TABLE 1—Composition of HSST-02 (wt%)

C	Mn	P	S	Si	Cr	Ni	Mo	Cu	V
0.23	1.55	0.009	0.014	0.20	0.04	0.67	0.53	0.140	0.003

Post Irradiation Mechanical Testing

The one-third-sized Charpy specimens (3.33x3.33x16.67 mm) were pre-cracked to a crack depth (a) to specimen width (W) ratio of $a/W \approx 0.5$ at a final stress intensity range of $\Delta K \leq 20$ MPa•m$^{1/2}$ and tested in three point bending over a range of temperatures from the lower shelf to the upper-transition regime. The tests produced behavior ranging from cleavage initiation to pure blunting as shown in Figure 1 discussed below. On the lower shelf the specimens experienced elastic-plastic unstable fracture or large pop-ins (≥ 50% maximum load) (type A). In the lower transition regime, fracture events were defined on the basis of significant load shedding 'pop-ins' which signaled the end of the test (type B). The specimens were subsequently heat tinted and broken in liquid nitrogen to provide a second reference surface for confocal microscopy (CM) and fracture reconstruction (FR) studies. At higher temperature/toughness levels the pop-ins were very small and/or crack growth was defined in terms of damage localized to the blunting zone (type C). While not a real fracture *per se*, we believe that these quasi-fracture events can be used to estimate toughness since fracture would be more likely at higher constraint levels. At still higher temperatures the limited capacity of these very small specimens and displacement range of the test fixture resulted in only crack blunting without any sign of incipient fracture. In these cases we can only record the maximum applied J (J_m or K_{Jm}) at the end of the test (type D). Finally, the irradiated specimen tested at the highest temperature exhibited ductile tearing, in the form of a tunnel crack, that was not detected during the test by unloading compliance (Type E).

Post Irradiation CM/FR

The CM measurements provide digitized images of three-dimensional topographic conjugate fracture surfaces with a resolution down to less than 1 μm. Individual digitized images are assembled into montages and aligned across the conjugate fracture plane using specially designed algorithms. Extending the pioneering work of Kobayashi and co-workers [15-18], the FR method [19] is based on the concept that the deformed conjugate surfaces contain an approximate record of the sequence-of-events leading to material separation. The fractured surface images are first overlapped -- based on the position of the fatigue precrack and cold-fracture reference surfaces at the beginning and end of the test -- and subsequently separated in a series of small steps (typically 1 μm). The displacement trajectories are determined from a combination of finite element method calculations of material flows and load-point displacement data from the mechanical test record. Most of the reconstructions reported here are fairly low resolution aimed at characterizing the general patterns of microscopic fracture over large regions of the macroscopic fracture surface (the entire pre-crack front for irradiated specimens and the center third of the pre-crack front for unirradiated specimens). Higher resolution studies will be needed to establish details like the location and identity of initiation sites.

In addition to providing the temporal and spatial sequence of events in the process zone leading to macroscopic crack initiation and growth, CM/FR directly measures the critical initiation crack tip opening displacement, δ_c, and subsequent increments of opening during stable crack growth (if any). The δ_c can be related to fracture toughness, K_{Jc}, through the relation $K_{J\delta} \approx (2\sigma_y \delta_c E')^{1/2}$ [20], where E' is the plane strain modulus and σ_y is the temperature dependent yield stress.

Scanning electron microscopy (SEM) studies (using a JEOL-840) were conducted to evaluate both the general characteristics of the fracture surfaces and, using the CM/FR visualizations as a guide, to closely examine locations of "interesting" events (e.g., cleavage facet and microvoid initiation). Essentially one-to-one correspondence between individual features in the SEM micrographs and grey scale CM images were consistently observed. The SEM micrographs clearly demonstrate the fidelity of the CM technique and are needed in various steps of the FR process.

RESULTS

K(T) Curves and Irradiation-Induced Shifts

Toughness versus temperature K(T) curves are plotted in Figure 1. The points are labeled by the type of event, as defined previously. Note the data are very limited, particularly for the irradiated condition. However, based on these preliminary results, the irradiated curve appears to be shifted by an approximately constant increment of temperature. The shift is estimated to be about 95 °C at the 75 MPa•m$^{1/2}$ index. The only redundant tests, for the unirradiated condition at -73°C, show surprisingly little scatter.

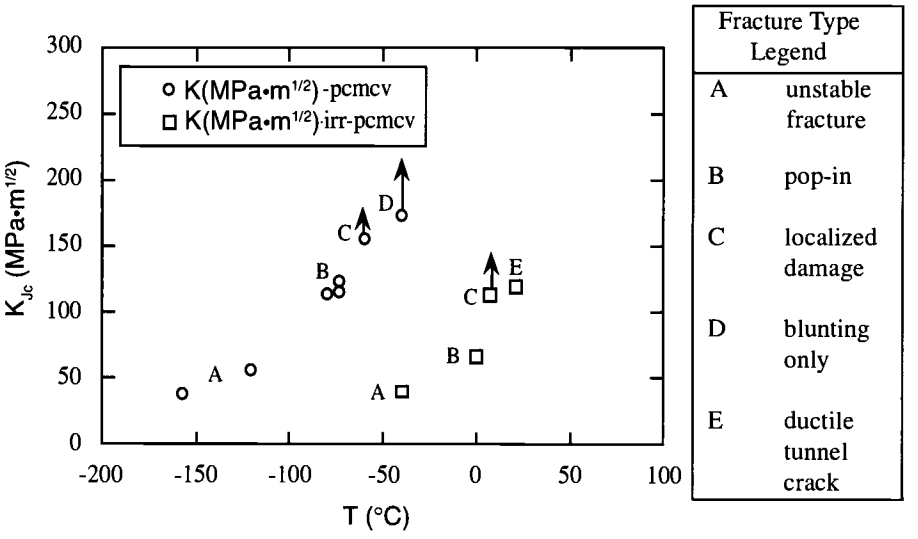


FIG. 1 -- Toughness-temperature [$K_{Jc}(t)$] curves for unirradiated and irradiated one-third-size pre-cracked Charpy specimens.

CM/FR

In Figures 2 through 4, CM/FR and SEM comparisons of irradiated and unirradiated specimens are made for similar toughness levels from the lower knee to the upper transition region. The CM/FR examples are shown as a top view looking down onto the crack plane for a sequence of crack opening displacements (δ) measured at the crack tip. The black and white regions represent separated and intact material, respectively. The first δ is taken slightly below the point of damage initiation. In this case, the black regions in the process zone represent noise and/or unreconstructable damage (such as a microcrack perpendicular to the primary crack plane).

Lower Shelf/Knee -- Figure 2a shows the CM/FR along with the corresponding SEM and CM topograph for the unirradiated specimen tested at -120°C with a K_{Jc} of 55 MPa•m$^{1/2}$ (type A). Multiple microcracks form a few hundred μm ahead of the crack tip at crack tip opening displacements (δ) from about 5 to 6 μm. This is followed by unstable macroscopic crack propagation for δ between 8 and 10 μm. The critical COD at initiation was taken as about 9±1 μm. A corresponding CM/FR for the irradiated specimen tested at -40 °C with a K_{Jc} of about 40 MPa•m$^{1/2}$ (type A/B) is shown in Figure 2b. Essentially the same sequence-of-events is observed with damage initiating at 6 to 8 μm and unstable initiation at a δ of 10 to 12 μm. The SEM fractographs are also qualitatively similar. CM/FR of the irradiated specimen tested at 0°C with a K_{Jc} of about 67 MPa•m$^{1/2}$ (type B) in Figure 2c revealed an extensive cleavage pop-in corresponding to an unloading of approximately 20% at a δ_c of about 16±2 μm. Note the reconstruction stops at δ = 16 μm since the specimen was fast fractured in liquid nitrogen following the pop-in. The sequence-of-events leading to this initiation is also qualitatively similar to those observed at lower temperatures as well as other pop-in events (Type B) in unirradiated specimens at higher toughness (see Figure 3 discussed below). Once again, the SEM fractography did not reveal any obvious effects of irradiation.

Transition Region -- Figure 3a shows the SEM, CM topograph and CM/FR sequence for an unirradiated specimen tested at -73°C with a K_{Jc} of 115 MPa•m$^{1/2}$ (type B). Following the initiation of microcracking at a δ of 80 to 84 μm, a significant pop-in corresponding to an approximately 30% unloading is observed by a δ of 86 μm. The test on an irradiated specimen at 8°C was stopped following a load drop of only a few percent in order to detect any incipient damage. The corresponding K_{Jc} is 114 MPa•m$^{1/2}$. Indeed, as shown in Figure 3b, localized damage regions are observed along the crack front initiating as early as δ=20 μm and developing through 40 μm. The appearance of this damage signals that cleavage initiation is imminent.

Only blunting and highly localized damage near the crack tip are observed in the unirradiated specimen tested at -40°C (as shown in a companion paper [21]). In contrast, the CM/FR in Figure 4 on the irradiated specimen tested at 21°C ($K_{Jc} \approx$ 120 MPa•m$^{1/2}$) shows a significant amount of ductile tearing reaching a depth of about 300 μm in the middle of the specimen. The crack is pinned at the edges, but penetrates relatively uniformly over about 70% of the middle of the specimen by a process of repeated nucleation, growth and coalescence of damage. The SEM fractography of the damaged region revealed a mixture of microvoids and small cleavage regions connected by ductile tearing. The contrast between cleavage initiation in the unirradiated specimen (-73°C) and damage and ductile tearing in the irradiated specimens (-8 and 21°C) at similar toughness levels may indicate a substantial reduction in the upper shelf toughness following irradiation.

Damage Sites and Bridging Ligaments -- The relatively low resolution CM/FR used in this work does not permit precise identification of initiation sites. However, guided by CM/FR, SEM studies have been used to image a number of interesting features. For example, Figure 5 shows cleavage facets that have formed near the blunting zone of an

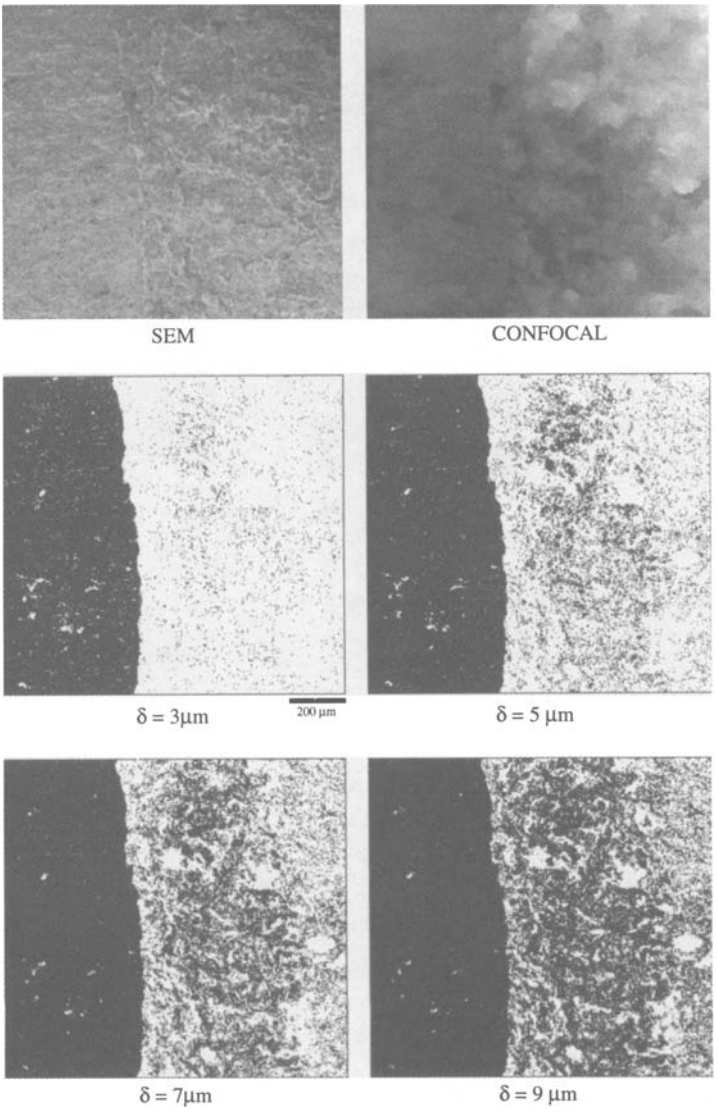


FIG. 2 a) -- SEM micrograph, CM topographical map, and FR sequence for the unirradiated specimen tested at -120°C.

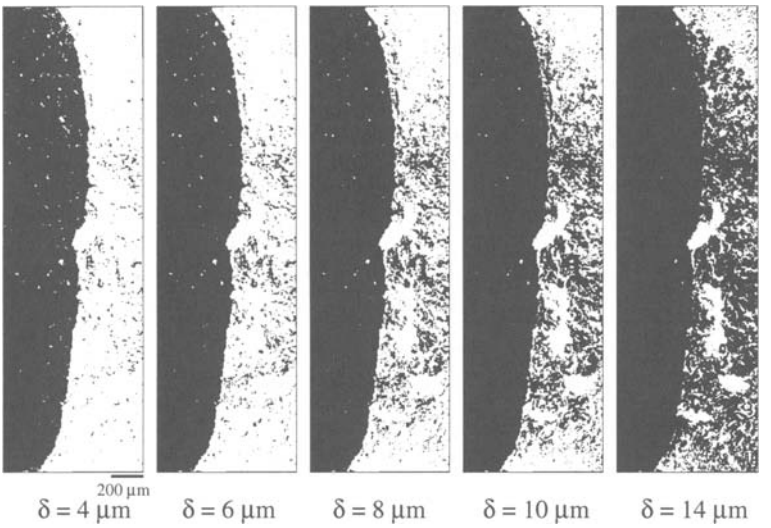


FIG. 2 b) — FR of the irradiated specimen tested at -40°C.

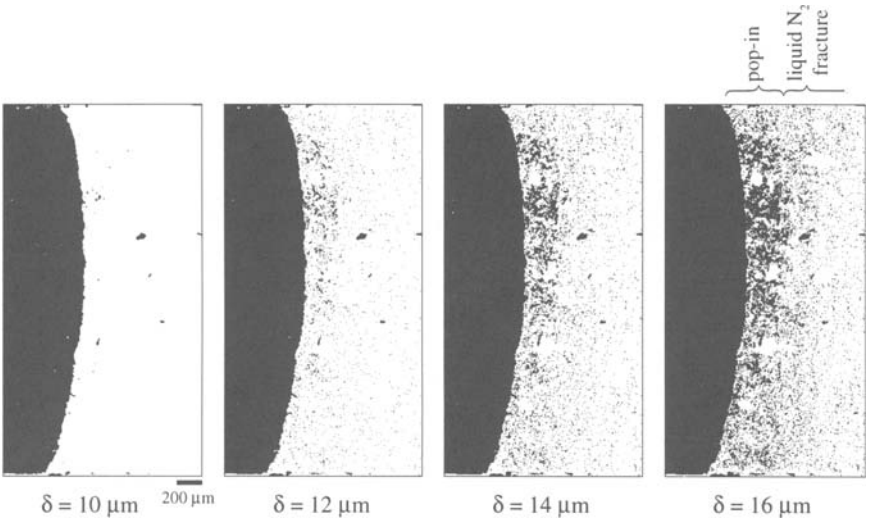


FIG. 2 c) — FR of the irradiated specimen tested at 0°C.

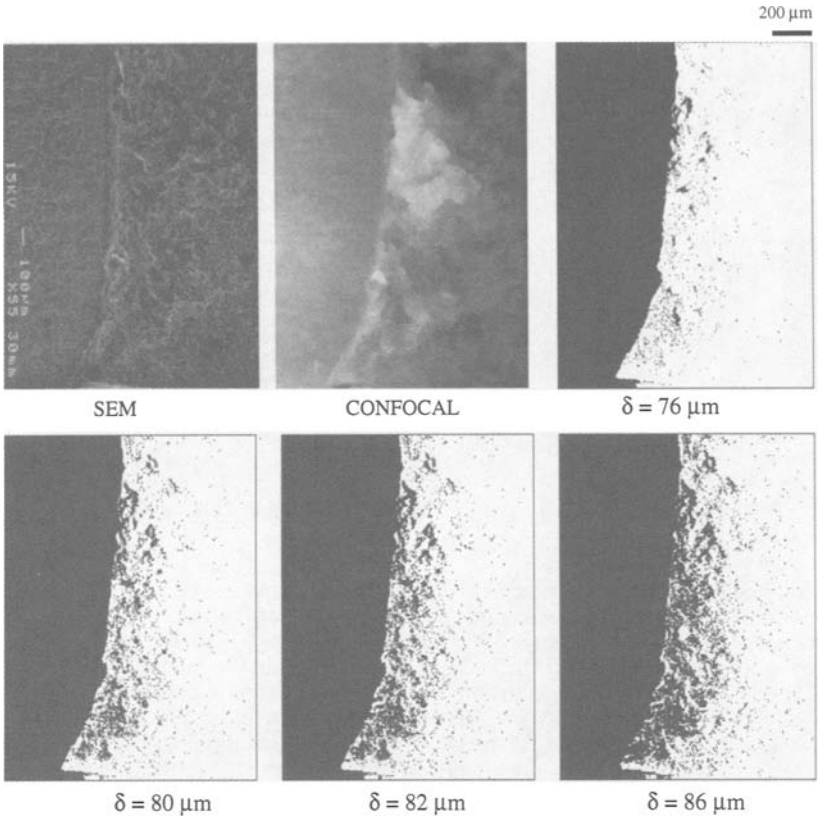


FIG. 3 a) — SEM micrograph, CM topographical map, and FR of an unirradiated specimen at -73°C.

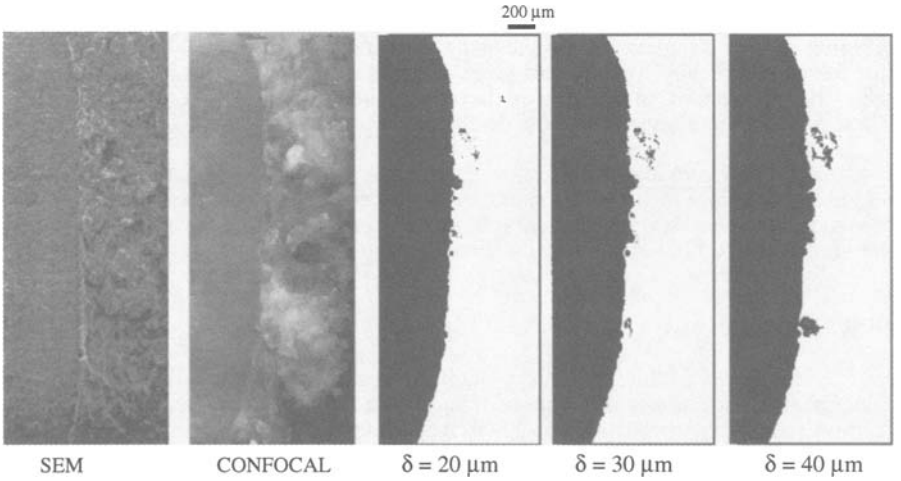


FIG. 3 b) — SEM, CM, and FR of the irradiated specimen tested at 8°C.

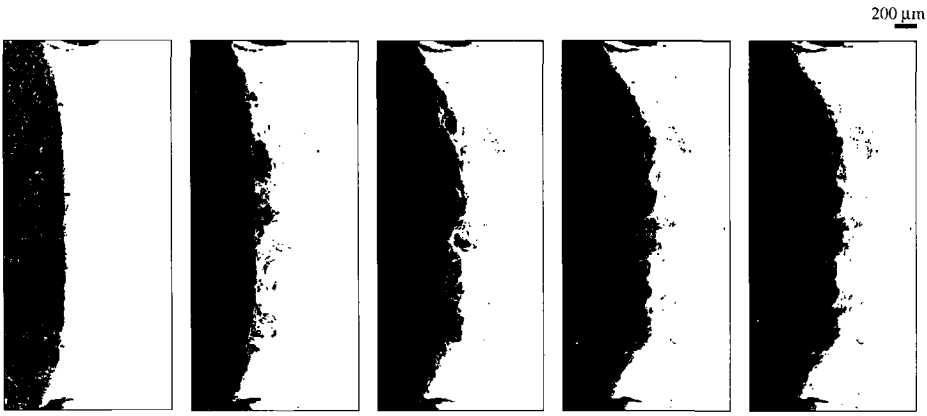


FIG. 4 — FR sequence of an irradiated specimen tested at 21°C.

unirradiated specimen tested at -73°C in low magnification (Figure 5a) and at higher magnification at sites labeled A and B (Figure 5b and 5c). The facets in Figure 5b may be associated with a cluster of boundary particles (see arrows). Figure 5c shows two adjoining facets that seem to emanate from the same site that can also be faintly seen to be a particle, separated by a narrow tear ridge. In both cases, however the microcracks are arrested; indeed these features are essentially cleavage-initiated microvoids. Figure 5d shows a more classical particle-nucleated microvoid surrounded by a region of smaller dimples. As is often observed, the inclusion is fractured. Figure 6a (low magnification) and Figure 6b (high magnification of the region indicated by the arrow in Figure 6a) shows a similar microvoid nucleated by a fractured particle in the irradiated specimen tested at 8°C. Figures 6c and 6d show low and high magnifications of isolated clusters of cleavage facets surrounded by regions of ductile failure.

The CM/FR also shows that even after macroscopic crack instability, a number of bridging ligaments remain in the wake of the main crack front. The SEM observations show that these are typically composed of hinge-like features that are partially pulled out of the main fracture surface. In other cases they are regions of ductile microvoid coalescence. These features are discussed in more detail in the companion paper [21].

K_{Jc}-$K_{J\delta}$ Correlations -- As shown previously [19], the δ_c obtained from the fracture reconstruction provides a good measure of the initiation toughness of the material, consistent with standard mechanical testing measures. Figure 7 shows that the results of this study show similar agreement for irradiated and unirradiated specimens.

DISCUSSION

The results of this preliminary study suggest that irradiation does not change the fundamental mechanisms of cleavage fracture. Rather the main effect of the fine scale features induced by irradiation appears to be manifested in the corresponding increase in the yield stress. The local critical stress/area criteria for cleavage do not appear to be influenced by irradiation and is, within limits, independent of temperature. This behavior

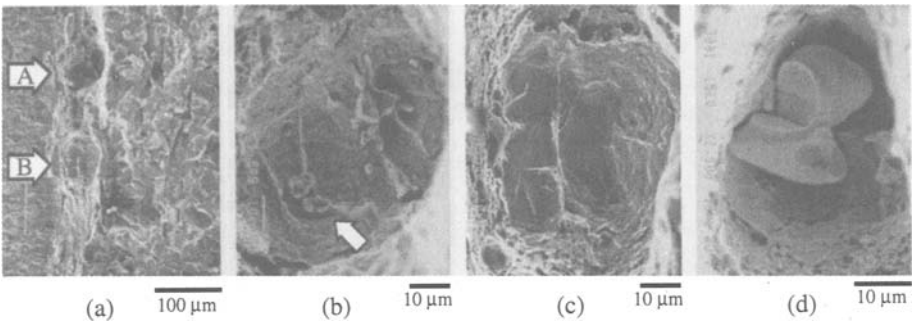


FIG. 5 — SEM micrographs of damage sites in the unirradiated specimen at -73°C. a) Cleavage facets formed near the blunting zone (low magnification). b) High magnification view of facet A. c) High magnification view of facet B. d) High magnification of a typical particle-nucleated microvoid.

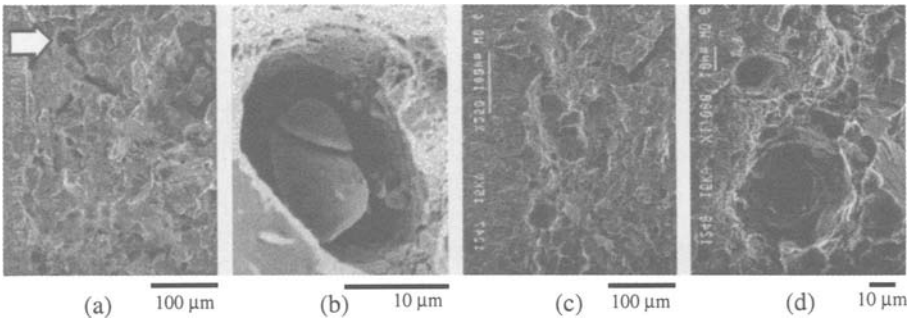


FIG. 6 — SEM micrographs of damage sites in the unirradiated specimen at 8°C. a) Low magnification view of damaged region showing a particle nucleated microvoid. b) High magnification view of the fractured inclusion of Fig. 6 a). c) Low magnification of cleavage facets surrounded by regions of ductile failure. d) High magnification view of the region in Fig 6 c).

is consistent with control of local cleavage processes by coarse scale microstructures. This conclusion is also in agreement with previous results on toughness shifts [7] and, more generally, on elastic transition temperature shifts in blunt notch Charpy specimens, which are directly related to increases in yield stress [5].

The mechanisms of cleavage fracture are discussed and modeled in a companion paper [21]. However, a much simpler approach is proposed here. If the local critical conditions are unchanged, then cleavage should occur at different temperatures in irradiated versus unirradiated specimens which have the same (or similar) constitutive properties. Of course exactly the same constitutive behavior in irradiated and unirradiated specimens cannot be achieved by a temperature adjustment. However, to a good approximation the strain hardening exponent varies inversely with yield stress. Hence, to first order fracture conditions can be mapped simply on the basis of yield stress (σ_y).

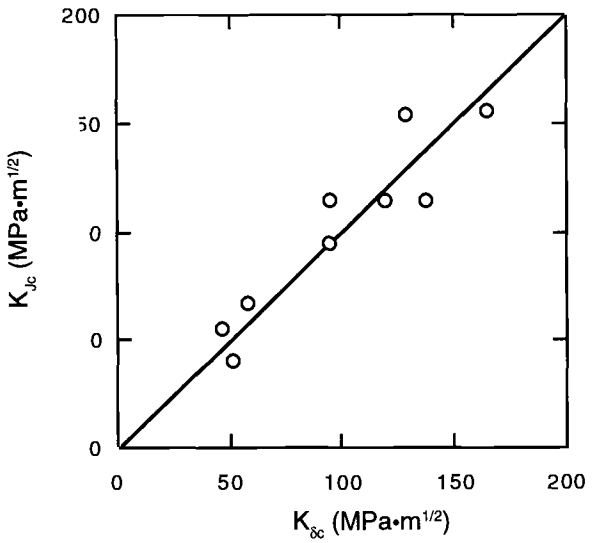


FIG. 7 — Comparison of standard measures of toughness (K_{Jc}) with local CM/FR measures ($K_{\delta c}$).

With appropriate corrections for strain rate, the measured shift in yield stress of 155 MPa [14] is consistent with a corresponding shift of about 95°C leading to the condition that $\sigma_y(T_{K75irr}) \approx \sigma_y(T_{K75unirr})$.

SUMMARY AND CONCLUSIONS

We have examined the irradiation embrittlement of an A533B pressure vessel steel using a combination of mechanical tests on subsized, pre-cracked Charpy specimens and confocal microscopy/fracture reconstruction. Toughness-temperature K (T) curves were shifted up by about 95°C at 75 MPa•m$^{1/2}$ in the irradiated material. CM/FR measurements of the critical crack tip opening displacements were in good agreement with the standard measures of elastic-plastic K_{Jc}. CM/FR showed that cleavage fracture occurred by nucleation of multiple microcracks coalescing into unstable fracture over a small increment δ, generally corresponding to load-shedding pop-ins. No obvious differences in cleavage mechanisms were observed in the unirradiated versus irradiated material and the shift in K(T) with irradiation was consistent with the irradiation-induced yield stress elevations. However, there are indications that irradiation (or the higher temperatures) promoted the transition from brittle to ductile fracture at equivalent toughness levels.

ACKNOWLEDGMENTS

The authors gratefully acknowledge the contributions of J. W. Sheckherd. This research was supported by the U.S. NRC under contract number NRC 04-90-046. The work of BW was performed under appointment of the Nuclear Engineering/Health Physics Fellowship Program administered by Oak Ridge Institute for Science and Education for the U.S. Department of Energy.

REFERENCES

[1] Wallin, K., "Validity of Small Specimen Fracture Toughness Estimates Neglecting Constraint Corrections," Constraint Effects in Fracture: Theory and Applications, ASTM STP 1244, M. Kirk and A. Bakker, Eds., ASTM, Philadelphia, PA 1994, in press.

[2] Anderson, T.L., Vanaparthy, N.M.R., and Dodds, R. H., Jr., "Predictions of Specimen Size Dependence on Fracture Toughness for Cleavage and Ductile Tearing," Constraint Effects in Fracture, ASTM STP 1171, E. M. Hackett, K.-H. Schwalbe, and R. H. Dodds, Eds., ASTM, Philadelphia, PA, 1993, p. 473.

[3] McCabe, D.E., Nanstad, R.K., Rosenfield, A.R., Marschall, C.W. and Irwin, G.R., "Investigation of the Basis for use of the KIc Curve," Pressure Vessel Integrity, ASME PVP-Vol. 32, 1991, p. 141.

[4] Odette, G.R. and Lucas, G.E., "Irradiation Embrittlement of Pressure Vessel Steels: Mechanisms, Models and Data Correlations," Radiation Embrittlement of Nuclear Reactor Pressure Vessel Steels: An International Review - Volume II, ASTM STP 909, L. E. Steele, Ed., ASTM, Philadelphia, PA, 1986, p. 206.

[5] Odette, G.R., Lombrozo, P.M. and Wullaert, R.A., "Relationship Between Irradiation Hardening and Embrittlement of Pressure Vessel Steels" , Effects of Radiation on Materials: 12th International Symposium, ASTM STP 870, F. A. Garner and J. S. Perrin, Eds., ASTM, Philadelphia, PA, 1995, p. 840.

[6] Odette, G.R.,in Neutron Irradiation Effects in Reactor Pressure Vessel Steels and Weldments, IAEA Technical Report Series, Vienna, in press.

[7] Odette, G.R. , "Recent Advances in Predicting Embrittlement of Reactor Pressure Vessel Steels," Proc. Second Int'l Symposium on Environmental Degradation of Materials in Nuclear Power Systems — Water Reactors, J. T. A. Roberts, J. R. Weeks and G. J. Theus, Eds., ANS-NACE-TMS/ASME, LaGrange, Ill, 1986, p. 121.

[8] McGowan, J. J., Nanstad, R. K., and Thoms, K. R., "Characterization of Irradiated Current-Practice Welds and A533 Grade B Class 1 Plate for Nuclear Pressure Vessel Service", NRC NUREG/CR-4880, Vol. 1 (ORNL-6484/V1), July 1988.

[9] Mager, T.R., et. al., "Feasibility and Methodology for Thermal Annealing an Embrittled Reactor Vessel," EPRI Report NP-2712-2, Electric Power Research Institute, 1982.

[10] Server, W.L., and Oldfield, W., "Nuclear Pressure Vessel Steel Data Base," Electric Power Research Institute, NP-933, 1978.

[11] Hawthorne, J.R., Menke, B.H., and Hiser, A.C., "Light Water Reactor Pressure Vessel Dosimetry Program, Post Irradiation Notch Ductility and Tensile Strength Determination for PSF Simulated Through-Wall Specimen Capsules," NRC NUREG/CR-3457, 1984.

[12] Streichen, J.M.,and Williams, J.A., "Effect of Strain Rate and Temperature on the Tensile Properties of Irradiated ASTM A533-B Steel", *J. of Nucl Mater.* 57, 1975, p. 303.

[13] McGowan, J. J., "Tensile Properties of Irradiated Nuclear Grade Pressure Vessel Plate and Welds for the Fourth HSST Irradiation Series", NRC NUREG/CR-3978 (ORNL/TM-9516), January 1985.

[14] Odette, G. R. and Lucas, G. E., "An Experimental Investigation of Kinetic Aspects of Neutron Irradiation Embrittlement of LWR Pressure Vessel Steels", EPRI Report NP 6114, Electric Power Research Institute, 1989.

[15] Kobayashi, T. and Shockey, D. A., "A Fractographic Investigation of Thermal Embrittlement in Cast Duplex Stainless Steel", *Met. Trans.*, 18A, 1987, p. 1941.

[16] Ogawa, K., Zhang, X. J., Kobayashi, T., Armstrong, R. W., and Irwin, G. R., "Microstructural Aspects of the Fracture Toughness Cleavage-Fibrous Transition for Reactor-Grade Steel", Fracture Mechanics: Fifteenth Symposium, ASTM STP 833, R. J. Sanford, ed., ASTM, Philadelphia, PA, 1984, p. 393.

[17] Kobayashi, T. and Shockey, D. A., "FRASTA: A New Way to Analyze Fracture Surfaces — Part 1: Reconstructing Crack Histories", *Advanced Materials & Processes,* 140-5, 1991, p. 28.

[18] Kobayashi, T. and Shockey, D. A., "FRASTA: A New Way to Analyze Fracture Surfaces — Part 2: Determining Fracture Mechanisms and Parameters", *Advanced Materials & Processes*, 140-6, 1991, p. 24.
[19] Edsinger, K., Wirth, B., Odette, G. R., and Lucas, G. E., "Characterization of the Local Fracture Process in Martensitic Stainless Steels", submitted to *J. Nucl. Mater.*
[20] Shih, C.F., "Relationships between J-Integral and the Crack Opening Displacement for Stationary and Extending Cracks," *J. Mech Phys Solids,* 29, 1981, p. 305.
[21] Edsinger, K., Odette, G.R., Lucas, G.E., and Wirth, B., "Evaluation of Embrittlement in Pressure Vessel Steels by Fracture Reconstruction", Effects of Radiation on Materials: 17th Volume, ASTM STP 1270, D. S. Gelles, R. K. Nanstad, A. S. Kumar, and E. A. Little, Eds., ASTM, Philadelphia, PA, 1995, this publication.

Ferritic and Martensitic Steels

M. Victoria[1], E. Batawi[2] , Ch. Briguet[3] , D.Gavillet[4] , P. Marmy,[1] J.Peters[2] , F. Rézai-Aria[3]

THE MICROSTRUCTURAL STABILITY AND MECHANICAL PROPERTIES OF TWO LOW ACTIVATION MARTENSITIC STEELS

REFERENCE: Victoria, M., Batawi, E., Briguet, Ch., Gavillet, D., Marmy, P., Peters, J., and RézaiAria, F., **"The Microstructural Stability and Mechanical Properties of Two Low Activation Martensitic Steels,"** *Effects of Radiation on Materials: 17th International Symposium, ASTM STP 1270,* David S. Gelles, Randy K. Nanstad, Arvind S. Kumar, and Edward A. Little, Eds., American Society for Testing and Materials, 1996.

ABSTRACT: A low activation composition of a martensitic 9 % Cr steel has been studied, based on the DIN (Deutsches Institüt für Normung) 1.4914 composition (MANET) but replacing Ni, Mo and Nb by the low activation elements W, V and Ta. Two casts were produced from high purity components, in which the effects of controlled additions of Mn (0.58 and 0.055 wt. %) and N (7 and 290 wt. ppm) were studied, so that the final compositions resulted in one cast with high Mn and low N (steel A) and the other with the opposite conditions (steel B). The two steels were evaluated in terms of structural stability and mechanical properties under tensile, fatigue and fracture toughness tests.
It has been found that both alloys have a DBTT below room temperature, which in the case of the steel A is 70 K below that of MANET. Although the tensile strength is somewhat below that of the parent steel, both steels have longer fatigue life.

KEYWORDS: martensitic steels, low activation materials, mechanical properties

A desirable feature of future magnetically confined fusion reactors is the prospect of producing low level radioactive waste. In order to minimise the volume of radioactive material, in particular from the first wall and blanket structures, reduced long term activation alloys are being developed. Simplified criteria based on safety, maintenance waste disposal and recycling scenarios have been put forward for these low activation materials (LAM) [1,2]

[1] CRPP-Fusion Technology Materials, École Polytechnique Fédérale de Lausanne,5232 Villigen PSI, Switzerland.
[2] Materials and Surface Engineering, Sulzer Innotec, P.O. Box 65, 8404 Winterthur, Switzerland.
[3] Department of Materials, École Polytechnique Fédérale de Lausanne, 1015 Lausanne.
[4] Laboratory for Materials Behaviour, Paul Scherrer Institut, 5232 Villigen PSI, Switzerland.

Copyright© 1996 by ASTM International www.astm.org

The 9-12 % Cr steels have been extensively investigated for fast and fusion reactor applications [3-5]. In particular, within the European Fusion Technology Program, two casts of a 10 Cr Ni Mo V Nb martensitic steel, designated MANET I and II, have been studied as a blanket reference material. More recently, a series of low activation steel (LAS) variations of this composition, in which Ni is eliminated and Mo and Nb are replaced by W and Ta, have been developed at Kernforschungszentrum Karlsruhe [5], based on the 9Cr W V Ti Ta composition. The overall mechanical properties of these LAS variations are as good as those of the MANET cast. There is though, room for improving some characteristics, such as the ductile-brittle transition temperature (DBTT). Some previous studies [6] have shown that controlling the amounts of N can lead to a decrease in the DBTT in 12% Cr steels.

In the present report the results of an investigation on the effects of (i) clean steel practices in small, laboratory size casts and (ii) the N content on the overall mechanical properties of a 9 Cr W V Ta steel are presented.

EXPERIMENTAL METHOD

Material preparation

The material was prepared from high purity stock by Sulzer Inotec in Switzerland. Two alloys were prepared and named alloy A for the one containing a low concentration of N and a high concentration of Mn and B for the one with a slightly higher concentration of N and a low concentration of Mn.

An ingot of about 40 Kg was produced of each alloy. They were hot rolled at 1223 K to a thickness of 10 to 15 mm. The rolling was performed in successive passes of ~ 10 % deformation, resulting in a total reduction of thickness of approximately 80 %. After this treatment, the average grain size is 10 μm and about 30 % of δ-ferrite is observed.

Detailed chemical analysis , down to ppm levels, were performed on the casts after the thermomechanical treatment. The final composition of the materials is presented on Table 1.

Material Characterisation

The variation of the grain size and of the material hardness (Vickers - 10 Kg) have been determined as a function of the austenization temperature for both alloys, see Fig. 1. Steel B is fully austenized after 30 minutes at1203 K, while alloy A has to be heated for the same time to 1223 K to reach the same state. The grain size increased rapidly in alloy A for austenization temperatures higher than1263 K. It increases also, but at a slower rate, in steel B. In order to obtain a fully martensitic steel, with small prior austenite grain size, the austenizing temperature was chosen to be 1233 K for alloy A and 1253 K for alloy B.

The variation of the hardness as a function of the tempering temperature is shown in Fig. 2. Secondary hardening is visible in alloy B but not in alloy A. The tempering temperature has been chosen at 1023 K in both alloys, comparable to that used as standard treatment in the MANET steels.

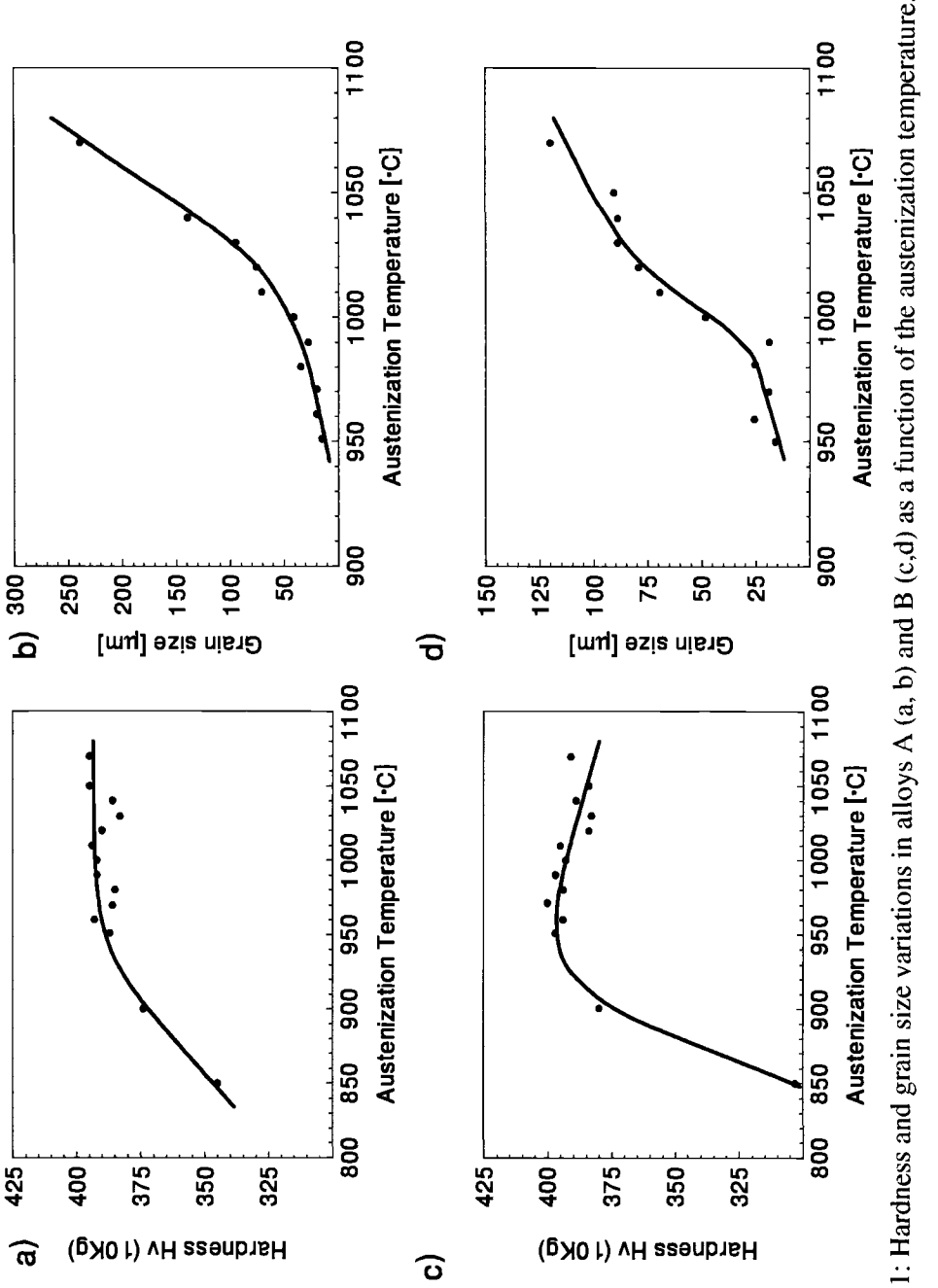


FIG. 1: Hardness and grain size variations in alloys A (a, b) and B (c,d) as a function of the austenization temperature.

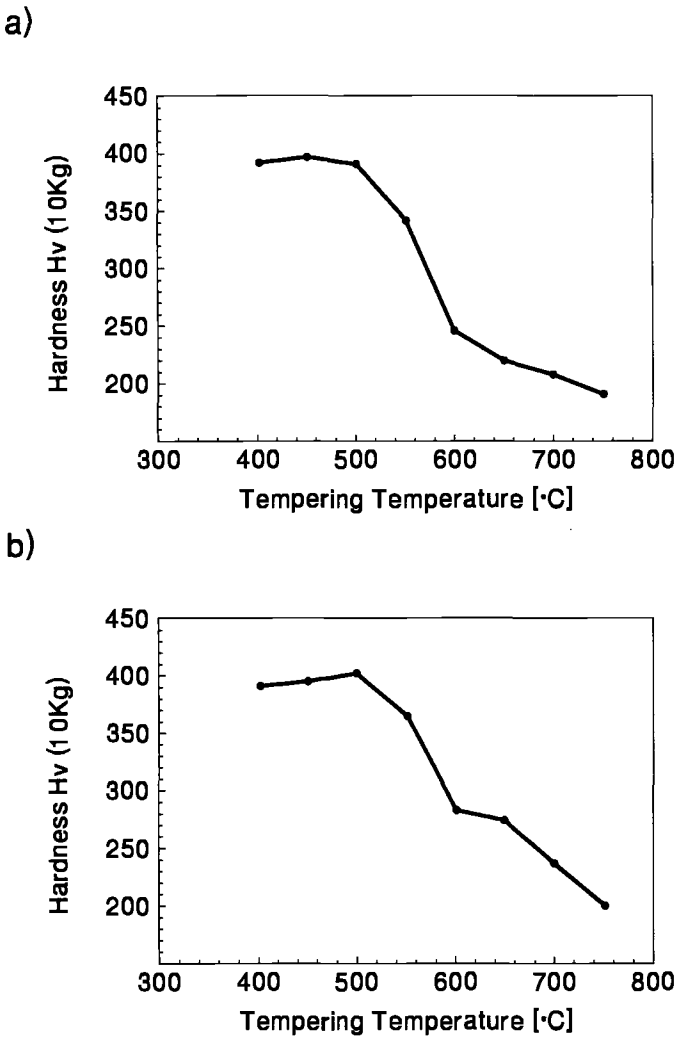


FIG. 2: Hardness variation (Vickers-10 Kg) in alloys A and B versus tempering temperture (2 hours)

TABLE 1: Alloy composition after thermo-mechanical treatments.

	A	B		A	B		A	B
Al	< 0.02	< 0.02	**Mn**	0.56	0.037	**Si**	< 0.02	< 0.02
As	< 0.005	< 0.005	**Mo**	0.093	0.048	**Sn**	< 0.003	< 0.003
B	0.0061*	0.0061*	**N**	0.0007	0.029	**Ta**	0.08*	0.08*
Bi	0.005	0.005	**Nb**	< 0.005	< 0.005	**Te**	< 0.005	< 0.005
C	0.094	0.09	**Ni**	< 0.01	< 0.01	**Ti**	< 0.005	< 0.005
Ce	0.036	0.033	**O**	0.0021	0.0024	**V**	0.24	0.23
Co	< 0.01	< 0.1	**P**	0.007	0.008	**W**	0.96	0.97
Cr	9.24	9.42	**Pb**	< 0.005	< 0.005	**Zn**	< 0.005	< 0.005
Cu	<0.01	< 0.01	**S**	0.0002	0.0005	**Zr**	< 0.003	< 0.003
Fe	Basis	Basis	**Sb**	< 0.003	< 0.003			
Mg	< 0.01	< 0.01	**Se**	< 0.003	< 0.003			

* : Value from the table A (Not measured after heat treatment).

The grain size has been checked after all thermal treatments on both material and is about 18 μm in alloy A and 16 μm in alloy B. No δ-ferrite has been observed in the material after the heat treatment was completed.

Carbide size and density

Carbide extractions have been performed on both steels in order to determine the size distribution, the composition and the type of the carbides present. The carbides where extracted on a carbon foil and examined with a transmission electron microscope at 200 KV. Typical images of the extractions at low magnification are presented in Figs. 3 (a) and (b). Aspects of the carbide distribution in steel B at a higher magnification are shown in Fig. 4.

Carbide extractions have been made both on austenized but not tempered and on austenized and tempered materials. Prior to tempering a lower density of carbide is observed. Their size ranges from 10 to 200 nm and their shape is spherical or slightly elongated.

On the tempered materials, the maximum size (length), the minimum size (width) and the area of about 1500 carbides in alloy A and 3100 carbides in alloy B where determined with an image analyser (IBAS 2000). A form factor, FF, (length divided by width) has been calculated, as well as an equivalent diameter (ED) which corresponds to the diameter of a circle having the same area as the carbide contrast. The distribution of the length and width being very similar that for ED, this last value was used for comparison between the two alloys.

The size distribution is presented in Fig. 5 for steel A and in Fig. 6 for alloy B. In alloy A a bimodal size distribution is clearly visible, with small carbides of about 10 to 20 nm diameter and a near spherical shape (form factor between 1 and 1.4), and a wide distribution of larger carbides with a size between 20 and 250 nm and a larger form factor (about 1.5 to 1.8). This bimodal distribution is not so clearly visible in alloy B, because the distribution of small carbide is larger. They are clearly visible in the higher magnification observation shown in Fig. 4.

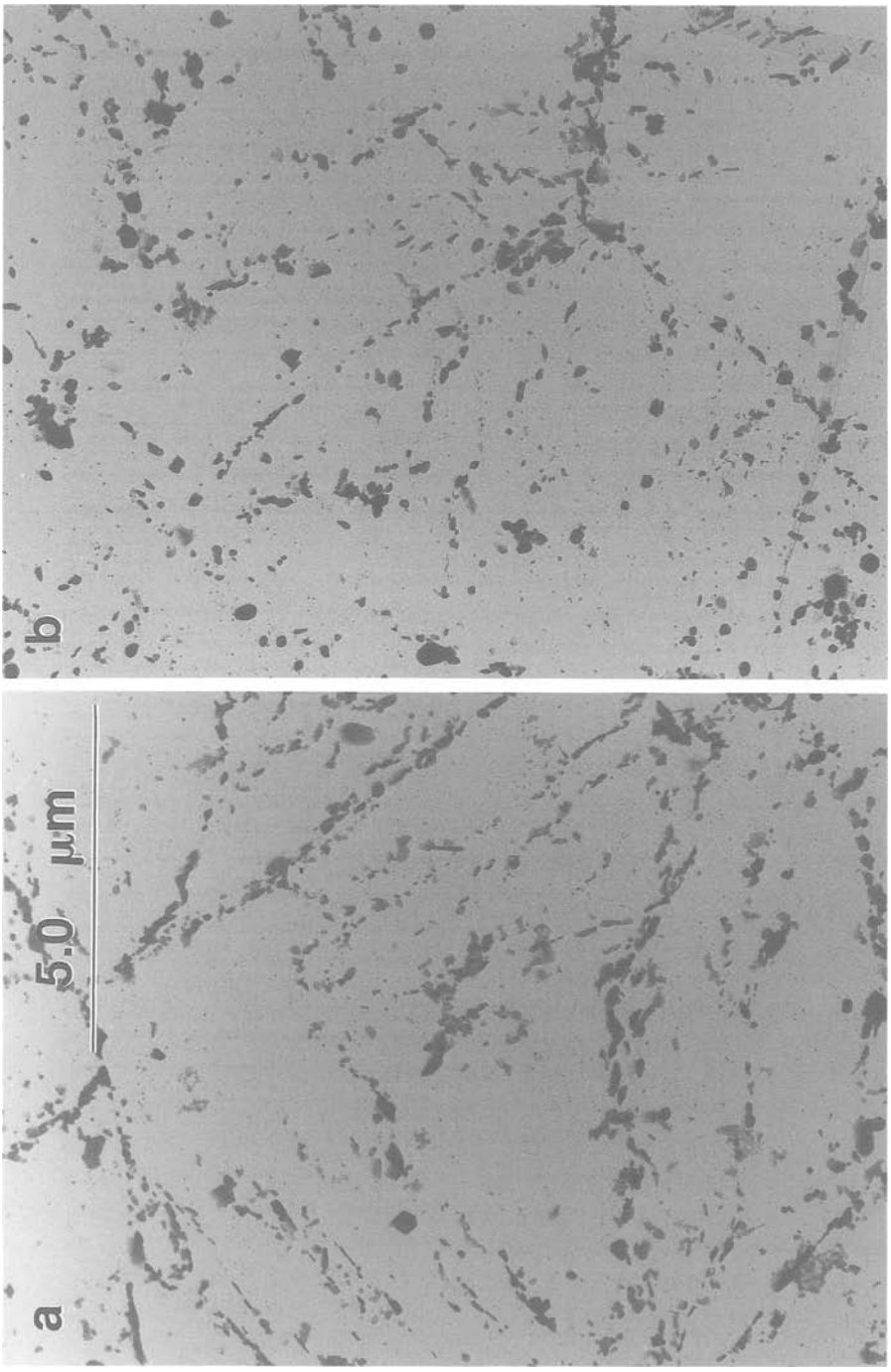


FIG. 3: Carbide extraction at low magnification. (a) alloy A, (b) alloy B

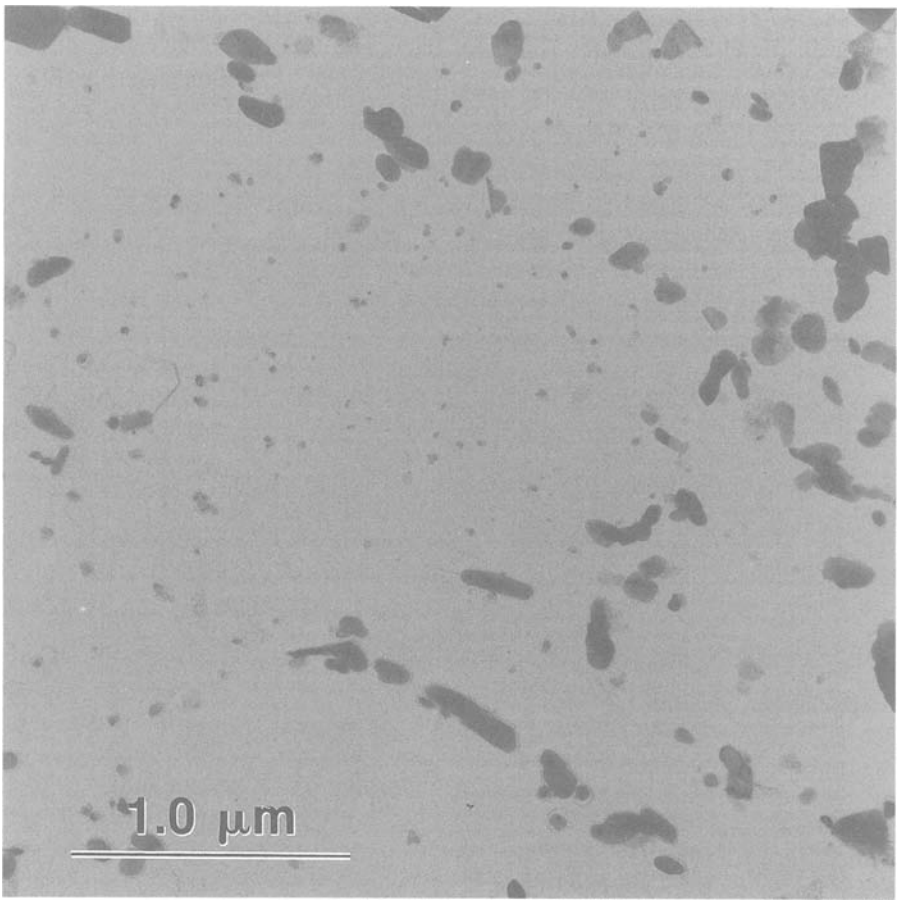


FIG. 4: Carbide extraction of alloy B at high magnification

A surface density has been determined for the carbides, as the average number of carbides per surface unit on the extraction foil. The density of small carbides (< 40 nm) and large carbides (> 40 nm) have also been estimated and the results are presented in table 2. The small carbides represent about 53 % of the total carbide in alloy A, and about 64 % in alloy B. The carbide density in alloy B is almost a factor two higher than in alloy A, and the larger difference is observed in the density of the small carbides. In fact, if the limit for small/large carbide is set at 65 nm, the density of large carbides in alloy B is only 1.15 times higher than in steel A (1.28 for the limit at 40 nm) which confirms that the density difference observed between alloy A and B is mostly due to the presence of a higher density of small carbides in alloy B.

An estimation of the volume density has been made by considering an extraction depth of 150 nm (which corresponds to the average radius of the carbides). A volume fraction has also been estimated with the same assumption. Both are presented in Table 2.

TABLE 2 : Carbide density and volume fraction in alloy A and B austenized and tempered.

	Alloy A	**Alloy B**
Surface density [m^{-2}]	$1.78\ 10^{13}$	$3.01\ 10^{13}$
Surface density of small carbides [m^{-2}] [a]	$9.42\ 10^{12}$	$1.94\ 10^{13}$
Surface density of big carbide [m^{-2}] [b]	$8.35\ 10^{12}$	$1.07\ 10^{13}$
Volume density [m^{-3}] [c]	$1.1\ 10^{20}$	$2.0\ 10^{20}$
Volume fraction [%] [c]	4.0	4.1

[a] : Small carbide = < 40 nm
[b] : Big carbide = > 40 nm
[c] : Extraction depth estimated at 150 nm

Carbide composition

The composition of the carbides has been determined by EDX measurements on the extraction specimens. The system used was a high purity Germanium (HP-GE) detector with a carbon thin window linked to a VOYAGER analysing system.

Two type of carbides have been observed in both steels before and after tempering: Cr-Fe-W-V based carbides and Ta-V-Fe based carbides. The Cr-Fe-W-V based carbide are mostly relatively large carbides (30 to 300 nm), although some smaller ones (10-15 nm) have also been observed, with an elliptical shape much more pronounced after tempering. Before tempering no particular localization of these carbides can be determined on the extraction foil, but after tempering they are often located on what appear to be prior austenite grain boundaries or martensitic lath boundaries on the extraction replicas. After tempering, an enrichment in Cr is observed and their composition varies from 50-70 at % Cr, 25-35 at%Fe, about 3 at% W and 1 at% V in both alloys. Typical results are presented in Table 3. Selected Area Diffraction (SAD) obtained on these carbide shows a fcc structure with a lattice parameter near 10 Å. All these observations are typical for $M_{23}C_6$ carbides.

The Ta-based carbide are mostly small, spherical carbides. They are also observed before tempering but in lower densities. Their composition varies widely, with a range from 25% Ta up to 80%Ta observed in alloy B, but most of the carbide

of this type have a composition of the order of 65-70 % Ta, 14-18 % V and 2-6 % Fe. Due to the small size of these carbide we have not been able to characterize their crystallographic structure by SAD or convergent beam diffraction.

Table 3: EDX analysis of carbides in LAS A and B

Alloy	Equ. Diameter. [nm]	Form Factor	Composition in Weight %				
			Cr	Fe	W	Ta	V
A-a	166	1.3	46.7	48.0	3.3		1.7
A-a	37	1.0	44.3	49.9	4.6		1.1
A-a	16	1.2		15.6	75.5	8.9	
A-a	11	1.0		24.0		62.5	13.5
B-a	160	1.0	54.8	40.1	3.2		1.9
B-a	142	1.0	53.6	41.3	3.2		1.9
B-a	19	1.3		6.0		67.4	26.6
B-a	29	1.2		3.1		72.3	24.6
A-at	235	1.0	55.5	38.8	3.8		1.9
A-at	81	1.4	67.4	27.8	3.8		1.0
A-at	24	1.4		7.4		77.8	14.8
A-at	29	1.1		4.8		78.6	16.6
B-at	164	1,7	68.0	27.2	3.7		1.1
B-at	135	2.5	67.7	27.5	3.7		1.0
B-at	26	1.1		6.6		79.5	14.0
B-at	15	1.1		3.4		25.6	71.0

A-a : Austenized 30 min-1233 K, **A-at** : Austenized 30 min-1233 K and tempered 2h 1023 K

B-a : Austenized 30 min-1253 K, **B-at** : Austenized 30 min-1253 and tempered 2h 1023 K

Due to the absorption of the C window, the nitrogen spectrum can not be detected with the instrument used. So it was not possible to determine the N content in the precipitates and, in particular, if nitrides are present. Some measurement have been performed with a HP-GE detector equipped with a very thin Al window, which were unsuccessful. Measurements by Parallel Electron Energy Loss Spectroscopy (PEELS) realised with the help of Dr. P. Stadelman (I2M - EPFL Lausanne) have shown that N is present in most of the small Ta based carbides, but are not detectable in the large Cr-Fe-W V based carbide. These measurements were not conclusive due to the very large C pick-up coming from the carbon foil on which the carbide are deposited, which overlaps the N edge. Even then, as the main compositional difference in alloy B is the higher N content, these fine particles can be assumed to be carbonitrides.

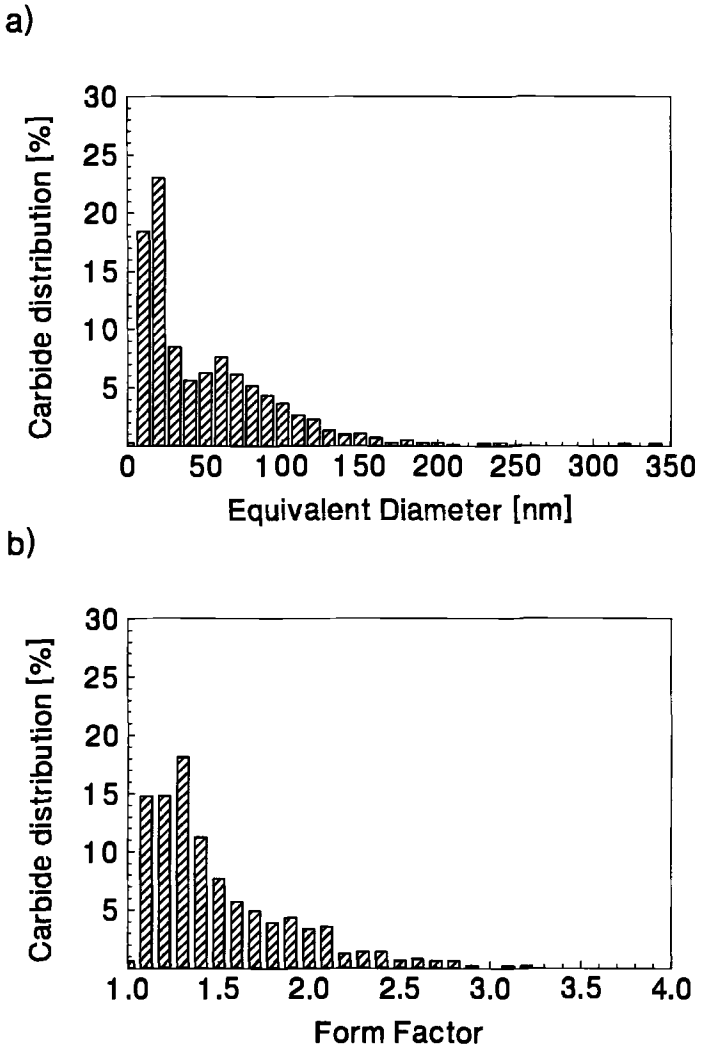


FIG. 5: Equivalent diameter (a) and form factor (b) distribution in alloy A

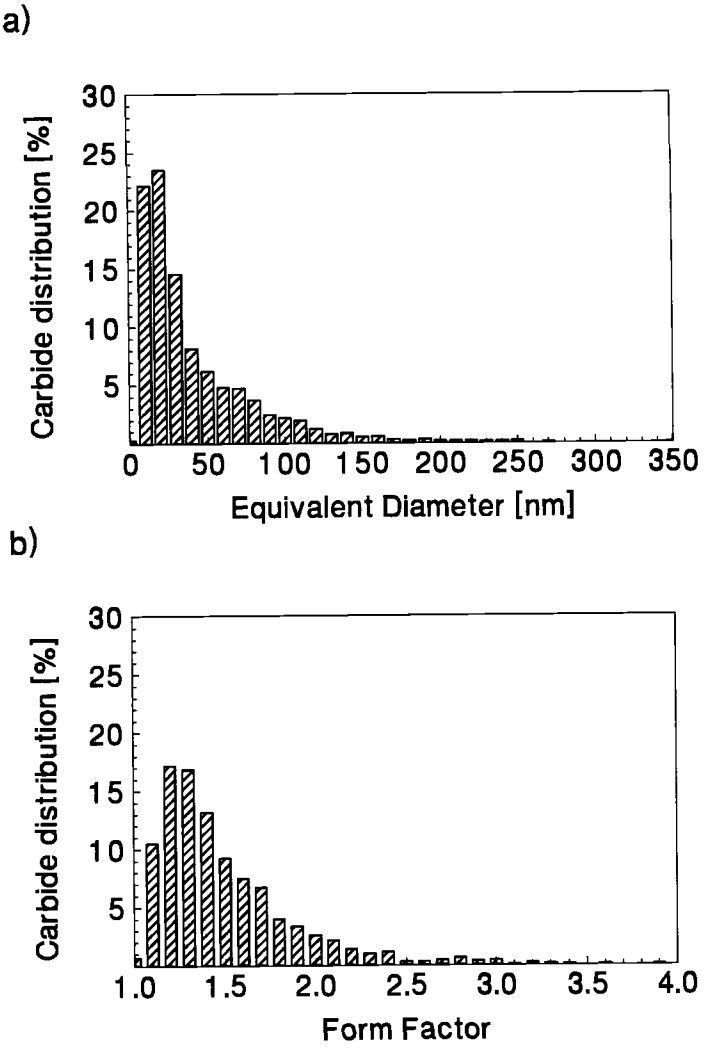


FIG. 6: Equivalent diameter (a) and form factor (b) distribution in alloy B

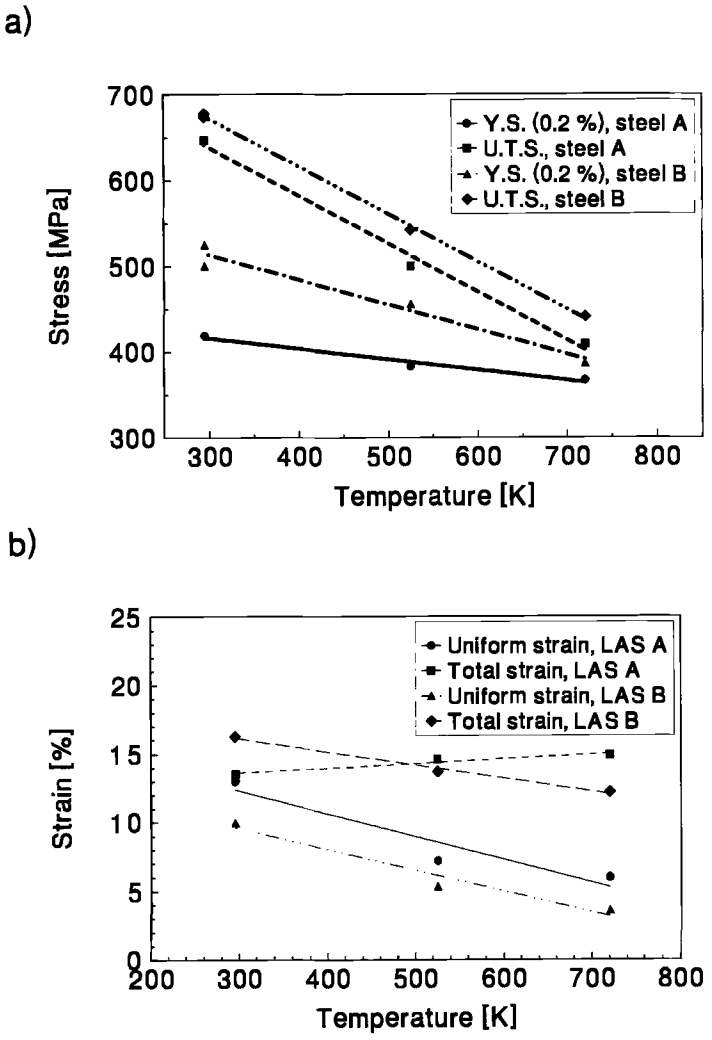


FIG. 7: Tensile results in LAS A and B: (a) Yield Stress (Y.S.) and Ultimate Tensile Stress (U.T.S.) versus temperature, (b) Uniform and Total Strain versus temperature

MECHANICAL TESTING

Tensile tests

Tensile tests were performed on subsize 3 mm diameter specimens, with a nominal gauge length of 19 mm. The tests were done under vacuum at three temperatures: 295, 525 and 720 K. The results are plotted in Fig. 7 (a) and (b). The overall levels of stress are higher for the B steel, the difference in the yield strength $\sigma_{0.2}$ decreasing from 93 MPa at room temperature to 20 MPa at 720 K, while an average difference of approximately 90 MPa in the U.T.S. is observed at all testing temperatures. Uniform elongations of the order of 10-12 % are obtained at room temperature, which decrease to 4-6 % at 720 K. On the other hand, the total strain values remain between 14-16 % at all temperatures, showing a tendency to increase with temperature in steel A.

Charpy tests

Charpy tests were performed in an instrumented machine on subsize specimens 8 mm width by 7.5 mm high, with the notch machined on the width.

The results are presented in Fig. 8, together with the MANET II results on identical specimen geometry. The two steels show a lower transition temperature than that of MANET II and a higher upper shelf energy. The upper shelf values are 200, 100 and 90 J for steels A, B and MANET II respectively. If the transition temperature is taken at one half the range between upper and lower shelves, the values obtained for it are, in the same order as above: 190, 230 and 260 K. In the scanning electron microscope observations of the fracture surfaces, also shown in Fig. 9, a brittle transgranular-cleavage type fracture is found over the total section of the specimen at the lower shelf.

Low Cycle Fatigue tests

Strain controlled fatigue tests have been performed on both steels in air at room temperature. Cylindrical specimens of 6 mm diameter and 10.2 mm gage length (between extensometer edges) were used.

As in other martensitic steels, a softening is observed during fatigue life. In Fig. 10 (a), (b) and (c), the number of cycles to failure has been plotted as a function of the total strain $\Delta\varepsilon_t$, the total plastic strain $\Delta\varepsilon_p$ and the total stress $\Delta\sigma$. Results from tests on the MANET II steel are shown in the same figure. The stress behaviour is consistent with the higher stress levels found in MANET under monotonical loading. On the other hand, for the same total deformation, both steels A and B have a longer fatigue life than MANET. From the regression lines indicated, the exponential α and constant C of the Coffin-Manson equation $\Delta\varepsilon_p N_f^{\alpha} = C$ can be calculated. They are 0.62 and 4.94 for the A alloy and 0.49 and 3.57 for the B steel. The corresponding parameters for the MANET steel are 0.51 and 3.27.

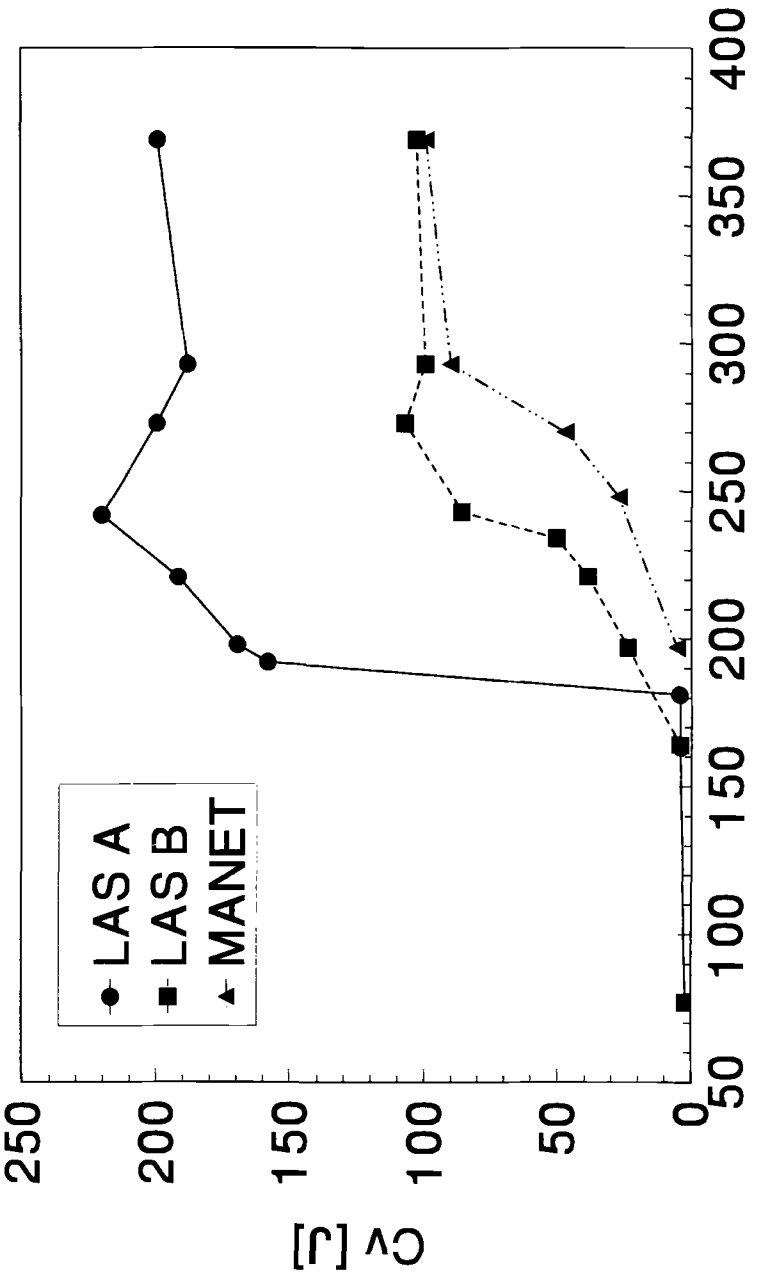


FIG 8: Instrumented Charpy test results on LAS A, LAS B and MANET steels

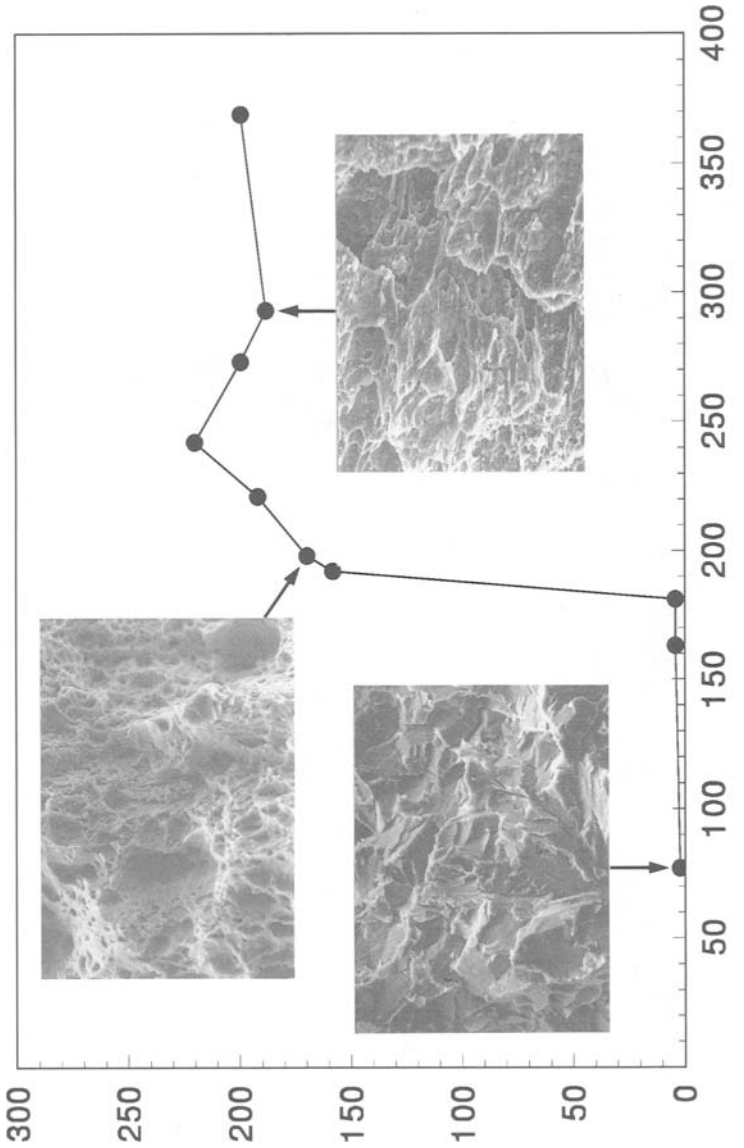


FIG. 9: Charpy test results on LAS A with corresponding fractography SEM pictures.

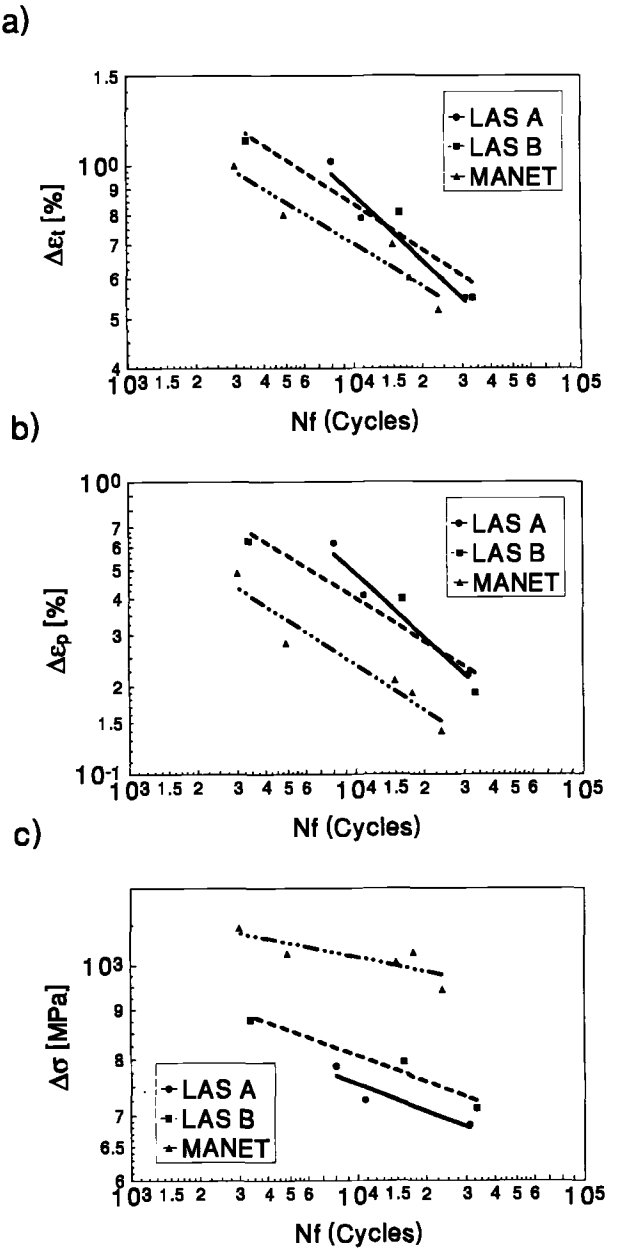


FIG: 10: Low Cycle Fatigue test results in LAS A, LAS B and MANET steels: (a) Total strain $\Delta\varepsilon_t$ versus the number of cycles at rupture N_f, (b) Plastic strain $\Delta\varepsilon_p$ versus N_f, (c) Stress $\Delta\sigma$ versus N_f.

DISCUSSION

The level of nitrogen attained in the A steel is low. The main microstructural variation observed is the presence of a finer carbide distribution in alloy B. Although from the present observations only those performed with PEELS have given an indication that there is nitrogen in the composition of the small particles, it can be expected that at the higher nitrogen level, these particles are nitrates or carbonitrates. The strength difference between the two alloys can then be explained on the basis of the effect of the nitrogen level on the particle distribution, which leads to a higher particle density with a finer distribution in alloy B. As a comparison, the strength attained in alloy B is similar to that obtained in a LAS with a total comparable C + N content, alloy LA12TaLC in [8], after tempering at 1023 K.

Furthermore, in spite of differences in composition, the level of strength measured in alloy B is comparable to that obtained for the MANET I steel [7], the overall microstructural characteristics being similar [9] and the carbide distribution in MANET I being comparable to that of alloy B, see Table 2

A substantial lowering of the ductile-brittle transition temperature has been obtained, together with a strong increase in the upper shelf energy in the case of alloy A. A factor that plays a role in this case is clean steel practices. In particular, low values of S and P have been obtained. Furthermore, Faulkner et al. [10] have shown that Si segregation to lath boundaries in a 12CrMoVNb, enhancing the interfacial cohesive energy. The Si level is below 0.02 wt. % in both casts. Nitrogen content has also been singled out as a factor determining the transition temperature [7]. But no evidence for any strong effects of nitrogen levels was found when comparing different LAS compositions in [8]. On the other hand, nitrogen could have an indirect effect by rising the strength level. The different behaviour of the transition temperature and upper shelf values in steels A and B could be explained on this basis.

Finally, the fatigue behaviour of both alloys is similar. Although their strength level is below that of MANET II, both alloys have a stronger strain hardening rate. This fact can explain the differences in fatigue response with MANET II steel.

Further measurements are in progress to better define the composition of the particles observed, together with creep and long term ageing experiments.

CONCLUSIONS

The microstructure and mechanical properties of two LAS martensitic steels based on the 9 Cr W V Ta composition have been investigated, in which variations in N content have been made.

The two modified steel compositions show a substantial decrease in DBTT, while other mechanical properties are comparable to those of the parent steel. The main differences can be ascribed to clean steel practices, i.e. the absence of Si and to the different amounts of nitrogen, that modify the precipitate size and distribution.

ACKNOWLEDGEMENTS

This investigation has been partially financed with a grant from the Swiss Priority Materials Program. The authors would also like to thank Prof. K. Ehrlich and Dr. M. Schirra from KfK as well as Dr. D.R. Harries for very helpful discussions.

REFERENCES

[1] K. Ehrlich, S.W. Cierjacks, S. Kelzenberg and A. Möslang; "The development of materials of reduced long-term activation", Effects of Radiation on Materials: 17th international Symposium, ASTM STP 1270, D.S. Gelles, R.K. Nanstad, A.S. Kumar and E.A. Little, Eds. ASTM, Philadelphia, 1995.

[2] M. Zucchetti and M. Merola; "Low-activation properties of novel Cr-based materials for fusion reactors", To be published, J. Nucl. Mater. (1995).

[3] Harries D.R.; Proc. Topical Conference on Ferritic Alloys for Use in Nuclear Energy Technologies, The Metallurgical Society of the AIME (1984) p.141.

[4] Bagley K.Q., Little E.A., Levy V., Alamo A, Ehrlich K., Anderko K., Calza Bini A.; Nucl. Energy 27 (1988) 295.

[5] Klueh R.L., Ehrlich K and Abe F.; J. Nucl. Mater. 191-194 (1992) 116.

[6] Cierjacks S., Erhlich K., Materna-Morris E., Schäfer L., Schirra M. and Wassilew C.; Proc of the IEA Workshop on Ferritic/Martensitic Steels, JAERI, Tokyo, Japan, (1992) p.125.

[7] Anderko K., David K., Ohly W., Schirra M.and Wassilew C., Proc. Topical Conference on Ferritic Alloys for Use in Nuclear Energy Technologies, The Metallurgical Society of the AIME (1984) p. 299.

[8] Tupholme K.W., Dulieu D.and Butterworth G.J.; J. Nucl. Mater. 155-157 (1988) 650.

[7] Marmy P., Ruan Yuzhen and Victoria M.; J. Nucl. Mater. 179-181 (1991) 697.

[9] Gavillet D., Marmy P. and Victoria M.; J. Nucl. Mater. 191-194 (1992) 890.

[10] Faulkner R.G., Schäfer L., Adetunji G.J. and Little E.A.; J. Nucl. Mater. 155-157 (1988) 612.

Edward A. Little[1]

INFLUENCE OF THERMOMECHANICAL TREATMENT ON IRRADIATION MICROSTRUCTURES IN AN ODS FERRITIC STEEL

REFERENCE: Little, E. A., **"Influence of Thermomechanical Treatment on Irradiation Microstructures in an ODS Ferritic Steel,"** *Effects of Radiation on Materials: 17th International Symposium, ASTM STP 1270*, David S. Gelles, Randy K. Nanstad, Arvind S. Kumar, and Edward A. Little, Eds., American Society for Testing and Materials, 1996.

ABSTRACT: The effects of thermomechanical treatment on microstructural changes and void swelling in a DT2203YO5-grade 13%Cr oxide-dispersion-strengthened (ODS) ferritic alloy have been studied following ion irradiations to a damage level of 50 dpa at 475°C with 600 appm helium gas implantation. Swelling in a solution treated and aged (STA) condition ranges from 0.07 to 0.24% due to cast-to-cast variations, whilst in a solution treated, cold-worked and aged (STCWA) condition the swelling decreases to 0.025%. Cavities are in general irregularly shaped, non-uniformly distributed and frequently attached to small yttria dispersoid particles.

The results confirm that this ODS ferritic steel exhibits low irradiation-induced swelling in the presence of high gas concentrations, as required for advanced fast and fusion reactor applications. The observed sensitivity of irradiation-induced swelling to compositional or processing variables implies that ODS ferritic alloys can be further optimized for high radiation resistance.

KEYWORDS: ODS ferritic steel, thermomechanical treatment, void swelling, ion irradiations, fast and fusion reactors

Increasing attention is now directed towards the development of oxide-dispersion-strengthened (ODS) ferritic steels for advanced reactor systems. These alloys offer improved elevated temperature strength properties above ~525°C compared to the 10-13%Cr ferritic-martensitic grades currently specified or under consideration for fast and

[1] Department of Materials Engineering, University College, Swansea SA2 8PP, United Kingdom.

Copyright© 1996 by ASTM International www.astm.org

fusion reactor components and should also possess good resistance to both void swelling and high temperature helium embrittlement, as noted generally for ferritic grades. The use of ODS ferritic steels therefore offers the attractive possibility of extending the temperature capability of the ferritic alloy system into the range presently served principally by austenitic stainless steels.

The current generation of nuclear-grade ODS ferritic steels is based on a fully ferritic non-transformable high-chromium (13-14 wt.%) matrix containing a dispersion of yttria particles, together with molybdenum and titanium matrix alloying additions [1-3]. At present two ODS grades are commercially available; these are the DT2203YO5 alloy (nominal composition: Fe-13Cr-2.2Ti-1.5Mo-0.5Y_2O_3 wt.%) developed by CEN/SCK of Belgium [1,2] and MA957 (nominal composition: Fe-14Cr-1Ti-0.3Mo-0.3Y_2O_3 wt.%) manufactured by Inco [3]. The alloys are produced by a powder metallurgy route of mechanical alloying, viz. ball milling, compaction and extrusion. The compositions are generally specified with low carbon additions to inhibit the formation of titanium carbide, and, for the case of the DT2203YO5 alloy, the levels of titanium plus molybdenum additions permit the precipitation of a stable bcc FeCrTiMo intermetallic (chi-phase) by application of an ageing heat treatment at 800°C, and which can impart an additional strengthening component [4,5]. Most recently, new experimental compositions have been investigated in Japanese studies [6-8]. On-going development programmes now focus mainly on fabrication technology, and in particular on the prototype production and testing of thin-walled tubing for future fast reactor fuel cladding [2,9].

A significantly enlarged data base will clearly be required before the selection of ODS ferritic steels can be fully endorsed for advanced nuclear applications. Whilst it is well established that ferritic steels as a class appear to exhibit generic high resistance to radiation-induced void swelling, these conclusions need to be reaffirmed for the rather special microstructures of the ODS steels and particularly at high gas concentrations typical of fusion reactors and high burn-up fast reactors. The present paper therefore details initial results of studies on void swelling response and the effects of starting microstructure.

A complete appraisal of the void swelling response and associated microstructural changes in irradiated ODS ferritic steels would require an extensive experimental programme covering a range of heat treatments, starting microstructures and irradiation parameters such as displacement dose and irradiation temperature. In the present investigation, a limited and more closely focussed programme was devised with the objective of addressing the following specific aspects: (1) to provide information on the role of the yttria dispersoids on radiation damage evolution. These particles are incoherent and weakly bonded to the matrix as a consequence of the unique method of manufacture of the ODS alloys, viz. the powder metallurgy route. Such particles may therefore act as traps for gas atoms and/or provide sites for easy void nucleation. (2) to evaluate the role of matrix microstructure; the ODS ferritic steels are generally characterized by variable and relatively high dislocation densities due to the fabrication method and the limited recovery induced by the standard heat treatments. (3) to gain an insight into phase

stability, in particular, the stability of the yttria particles under irradiation and the possibility of formation of additional radiation-induced phases.

EXPERIMENTAL PROCEDURE

The ODS alloy used in the present investigations was the DT2203YO5 grade as described above. The material was supplied in the form of thin-walled prototype reactor tubing. Four separately manufactured batches of tubing were selected for the irradiation programme, to provide a range of compositions for this product type and a variation in thermomechanical condition, as listed in Table 1.

TABLE 1 --Chemical compositions of DT2203YO5 casts (wt.%)

Designation	Condition	Cr	Ti	Mo	Y	O_2	Fe*
Batch A	STA	12.95	2.22	1.50	0.44	0.34	bal
Batch B	STA	13.00	2.22	1.48	0.44	0.32	bal
Batch C	STA	13.01	2.22	1.60	0.44	0.31	bal
Batch D	STCWA	.....as for Batch A.....					

*Typically N < 0.050, C < 0.030 (wt.%), with cast to cast variations

The tubing was examined in two thermomechanical conditions: (i) solution treated and aged (STA), consisting of a short induction anneal of 3 min at 1050°C followed by ageing 24 h/800°C; and (ii) solution treated, cold-worked and aged (STCWA), based on an induction anneal of 3 min at 1050°C, followed by 9% cold-work (cold drawing) then ageing 24 h/800°C.

Disc samples 3 mm in diameter and 0.25 mm thick were spark machined from the tubing and fabricated into a single composite ion irradiation target measuring 30 x 15 x 1.1 mm using a copper plating technique [10], thereby ensuring good heat transfer and temperature control (better than +/- 7°C).

The samples were irradiated at 475°C under scanned beam conditions with 52 MeV Cr^{6+} ions and 4 MeV α particles in the Harwell Variable Energy Cyclotron (VEC) to a total displacement dose of 50 dpa at a dose rate of ~1 dpa/ hour and a helium content of 600 appm, i.e. a high He/dpa ratio of 12. Radiation damage and gas implantation were carried out in consecutive 10 dpa and 120 appm intervals, respectively, to reach these aggregates. The irradiation temperature of 475°C was selected to correspond with the peak void swelling temperature for complex ferritic alloys under ion bombardment, as deduced from other recent VEC studies on ferritic-martensitic steels [10,11] and the

results of a literature survey [12]. A rocked-target assembly [13] giving a controlled oscillation to the target was used to give a uniform damage plateau extending from ~2 μm down to the range end of ~4.5 μm for 52 MeV Cr^{6+} ions in steel, together with a uniform helium concentration over the range 0.5-10 μm.

After irradiation, samples were mechanically polished using a vibratory technique [14] to remove a 2 μm surface layer and expose the region of uniform displacement damage. The irradiated surface was then masked off and electropolished in a 10% perchloric acid-methanol solution at a temperature of -10°C using a back-thinning procedure, to produce thin foils suitable for transmission electron microscopy. These were then examined in a Philips EM 430 instrument operating at 300 keV for improved resolution of ferromagnetic materials. Where necessary, elemental analyses were made using an energy dispersive X-ray (EDX) unit attached to the microscope.

Standard quantitative metallographic procedures were used to determine histograms of cavity distributions from which their mean diameter and concentration, and hence the % swelling, were evaluated. Estimated errors in swelling values are about +/- 25-30%, based on examinations of a large number of foil areas so as to encompass upper and lower bound swelling parameters. Dislocation densities were measured using the linear intercept method from high magnification micrographs taken under two beam conditions. No allowance was made for dislocations out of contrast, and hence the errors in values are around +/- 50%.

RESULTS

Unirradiated Microstructures

All samples of tubing exhibit a highly elongated grain structure when examined at low magnification, with grain length to width ratios of > 5 in the extrusion direction, as previously reported for ODS steels [15-18]. ODS ferritic steels are also known to be highly resistant to recrystallization, with bulk secondary recrystallization (i.e. significant grain growth) taking place only at high temperatures, typically exceeding ~1300°C [17,18]. It was therefore anticipated that the standard solution treatment (i.e. annealing at 1050°C) applied to the DT2203YO5 alloy would result in only limited recovery of the high dislocation density network introduced by the fabrication route. This is confirmed in all samples, and a typical microstructure for the STA condition shown in Fig. 1(a) indicates the retention of a relatively high dislocation density, which appears to be pinned on an array of small particles, deduced to be the yttria addition. The STCWA condition, as illustrated in Fig. 1(b), is characterized by an increased dislocation density, consistent with the application of 9% cold-work. A further feature of the microstructure, apparent from the examination of a wide range of samples, is that the dislocation density is spatially heterogeneous both within grains, and also between grains, indicating non-uniform recovery throughout the material.

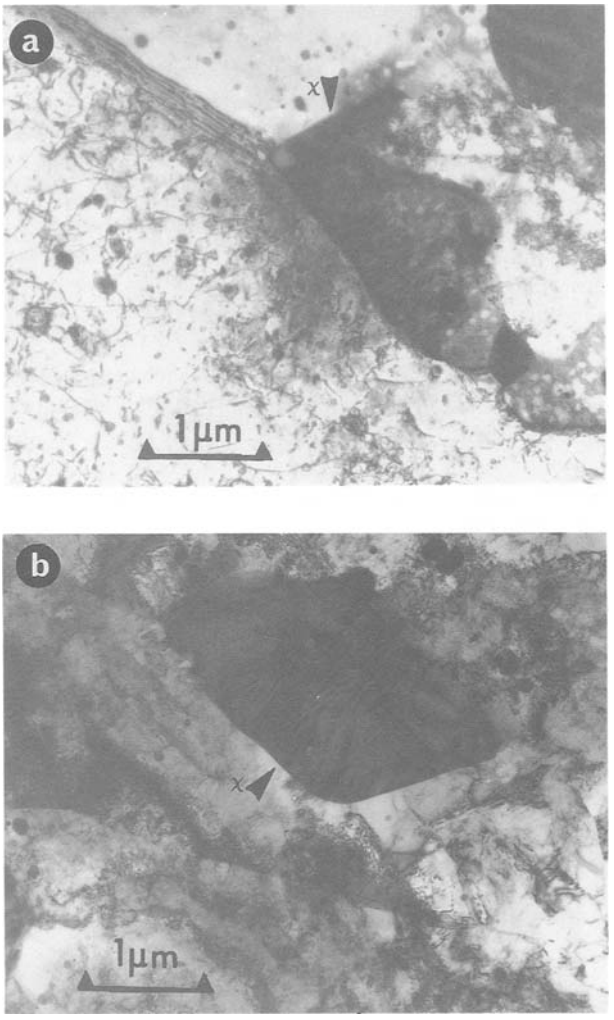


FIG. 1--Transmission electron micrographs of the unirradiated microstructures of alloy DT2203YO5. (a) Solution treated and aged (STA) condition; (b) Solution treated, cold-worked and aged (STCWA) condition; Particles arrowed are typical chi-phase.

An examination of the second phases for both STA and STCWA conditions indicates a relatively uniform intragranular distribution of Y_2O_3 particles as introduced by the mechanical alloying process, with an average dispersoid diameter of ~30-50 nm but with occasional oxides up to 200 nm across. Coarse (up to 500 nm across) Ti_2O_3 particles are also present and it is suggested that these form by oxygen gettering during manufacture; however, TiN phase is not detected. Also present are massive (up to 2 μm across) chi-phase particles - as identified by electron diffraction - formed by the 800°C ageing treatment and which nucleate principally at grain boundary sites. An interesting aspect of these precipitates is the presence of narrow ribbon-like defects which exhibit contrast consistent with antiphase boundaries, as shown in Fig. 1(b). Particle distributions in both the STA and the STCWA conditions are broadly similar.

Complex oxides containing yttrium and titanium have been reported in the literature in prototype experimental ODS ferritic steels [19], but are not detected in the present alloy.

A summary of the phases present in the DT2203YO5 alloy after fabrication and heat treatment is given in Table 2.

TABLE 2--Phases present in DT2203YO5 alloy

Phase	Remarks
Y_2O_3 bcc, a = 1.06 nm	Approx. 0.5 wt.% (~0.8 vol.%) added; particles typically 30-50 nm in dia.,but observed down to resolution limit (~2 nm)
Ti_2O_3 rhombohedral (α-Al_2O_3 structure) a = 0.543 nm	Approx. 0.9 wt.% (~1.6 vol.%) of coarse particles up to 500 nm dia. formed by gettering of oxygen during fabrication
chi-phase bcc (Mn structure), a = ~0.92 nm; partially coherent in Fe-13%Cr matrix; intermetallic, close to $Fe_{36}Cr_{12}Ti_7Mo_3$	Precipitates during ageing heat treatment (24h/800°C) giving ~8 wt.% as 1-2 μm particles; quantity depends on Ti left in solution after oxygen gettering
$Y_2Ti_2O_7$, Y_2TiO_5, TiN	Not detected

Irradiated Microstructures

Small cavities are observed in all samples, with a variation in cavity size and concentration between batches, as detailed in Table 3; also given in the table are data on overall levels of swelling and dislocation densities.

TABLE 3--Irradiated microstructure parameters

Alloy and Condition	Cavity Concentration (N) x 10^{21} (m^{-3})	Cavity Diameter (d) (nm)	Swelling (%)	Dislocation Density x 10^{14} (m^{-2})
Batch A, STA	4.3	8.8	0.16	5.5
Batch B, STA	9.5	5.2	0.07	7.6
Batch C, STA	8.0	8.3	0.24	9.7
Batch D, STCWA	4.3	4.8	0.025	5.8

The essential features evident from this tabulated data are as follows:
(a) Swelling is very low in all batches, and this is consistent with the expected high swelling resistance behaviour of irradiated ferritic steels;
(b) The swelling in the three STA samples indicates cast-to-cast variations over the range 0.07-0.24%, i.e. a threefold variation - which is large;
(c) The swelling is significantly reduced (0.025%) in the STCWA samples, i.e. to approximately one third of the swelling in the lowest swelling STA cast.

The detailed metallographic observations provide further insight into the nature of the swelling in this ODS ferritic alloy. Typical electron micrographs of cavity distributions in the STA and STCWA conditions are illustrated in Fig. 2(a)-(c), whilst a high magnification micrograph is presented in Fig. 3. It is seen that:
(a) the cavity distributions are rather non-uniform and this may reflect the heterogeneous pre-irradiation dislocation structures characteristic of these alloys;
(b) many of the cavities are extremely irregular in shape (Fig.3) and are often associated with small yttria particles or nucleate at the matrix interfaces of larger particles; and
(c) the average diameter of the cavities (~5-8 nm) suggests they are probably near-equilibrium helium bubbles.

The irregular shape of the cavities is in marked contrast to the voids which form in ferritic-martensitic steels and ferritic binary iron-chromium alloys, which are usually facetted with a regular polyhedral shape, e.g. see Gelles [20]. This could indicate a dominant influence of a surface-active element such as oxygen, or even yttrium, on the surface energy of cavities in the ferritic ODS system.

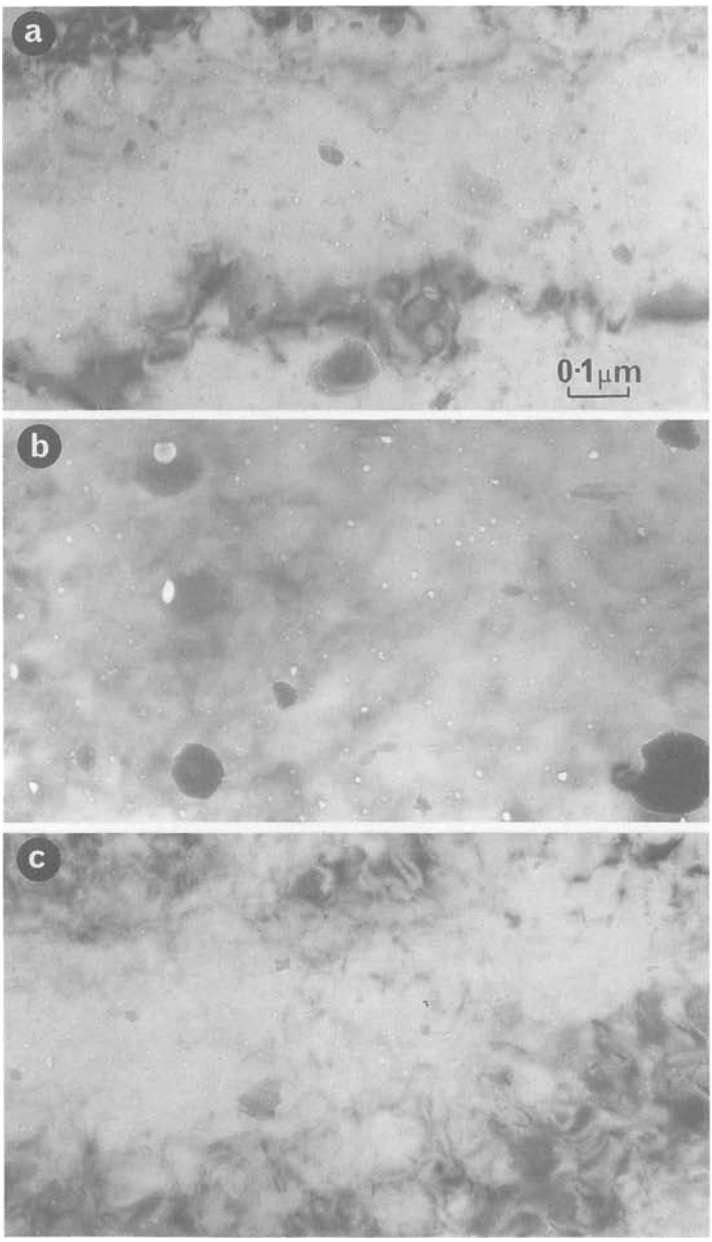


FIG. 2--Transmission electron micrographs illustrating typical void distributions in alloy DT2203YO5 after ion irradiation at 475°C to 50 dpa with 600 appm injected helium. (a) STA condition, batch B (swelling 0.07%); (b) STA condition, batch C (swelling 0.24%); (c) STCWA condition, batch D (swelling 0.025%).

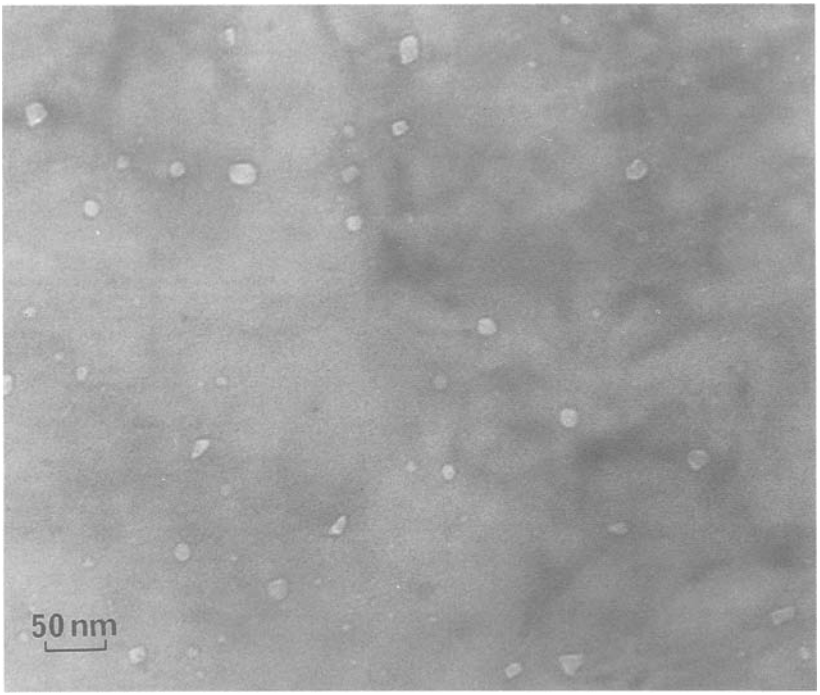


FIG. 3--High magnification electron micrograph illustrating irregular void profiles in alloy DT2203YO5 after ion irradiation at 475°C to 50 dpa (batch A, swelling 0.16%).

The dislocation substructures in the irradiated conditions are again heterogeneous and are comprised of line dislocations and loops resulting from the ion irradiation damage together with pre-existing dislocation networks; the measured dislocation densities quoted in Table 3 are quite high for irradiated ferritic steels but clearly do not result solely from irradiation. It is noted that the dislocation density in the STCWA condition is lower than for some of the STA casts implying that there is significant evolution of the dislocation network involving the starting substructure for this condition.

An additional factor contributing to microstructural stability and therefore to acceptable mechanical properties of candidate reactor alloys under irradiation is the formation of new phases by radiation-induced non-equilibrium segregation of solutes to sinks and/or the modification of existing precipitate types in terms of both composition and distribution by this and other mechanisms, e.g. see Nolfi [21]. In 9-12%Cr martensitic steels significant irradiation-induced precipitation of Si- and Ni-rich eta phase (M_6X) and also chi and sigma phases incorporating these elements is noted. The starting bulk silicon

and nickel contents in these steels are low and in the range 0.2-0.7 wt.%, but local enrichment occurs at sinks by coupling of point defect and solute fluxes as a consequence of binding interactions [22]. Also noted in 12%Cr martensitic steels [23], but most prominent in 17%Cr fully ferritic steels and binary Fe-Cr alloys containing 10-18%Cr [20,24] is the irradiation-enhanced formation of α' (Cr-rich ferrite), often associated with severe radiation embrittlement [25]. It is noted that this phase is well known to form after long-term thermal ageing at 475°C in fully ferritic steels with Cr contents > ~14%.

Consideration of the matrix composition of the DT2203YO5 alloy (viz. 13%Cr + 1.5%Mo) suggests the possible formation of only two additional phases by irradiation-induced segregation, namely, α' and Laves phase of the Fe_2Mo type. In particular, the absence of Ni and Si precludes the formation of eta phase.

Detailed examinations of the irradiation microstructures failed to positively detect either of these phases; however, small areas are observed in which the characteristic images of spherical precipitates of α' are seen in bend contours of the thin foils, but the total volume fraction is clearly small. The possibility of irradiation-induced changes to existing precipitates (i.e. Y_2O_3, Ti_2O_3 and chi-phase) was considered but the studies demonstrate that the distribution of these phases remains essentially unchanged. However, all precipitate types contain irradiation defects typically in the form of loops and dislocation tangles; cavities are also found inside the larger Y_2O_3 particles.

DISCUSSION

The generic high void swelling resistance of ferritic steels under irradiation is now well documented, e.g. see Little [12] and references cited there. However, the experimental observations relate principally to studies at low helium contents (< ~50 appm) and have not generally been reaffirmed at high gas concentrations. Furthermore, the overall data base on the irradiation response of ODS ferritic steels is relatively limited [26-30]. The present studies were therefore devised to address these aspects, and the data demonstrate - in an ion-beam simulation experiment - that the DT2203YO5-grade ODS ferritic steel exhibits measurable but low swelling levels at 475°C - the peak swelling temperature for ferritics - after irradiation to 50 dpa in the presence of 600 appm helium. Evidence is also presented which shows that cold-work followed by ageing applied to the steel results in reduced swelling.

A key feature of the data is the observation of significant variability in swelling, even at low absolute swelling levels, in different casts of the alloy, indicating a dependence on some aspect of the manufacturing route. The three batches examined in the STA condition possess only minor variations in bulk composition (Table 1) which probably would not account for the differences in swelling, - although detailed C, N and O contents are not available, and these elements in solution have been postulated to influence swelling in ferritic alloys [31]. More important may be minor differences in the yttria particle distribution in terms of size and number density and also the possibility of gas entrainment

in the alloy and/or occlusion of gas on the surface of the yttria, arising from the argon gas environment present during the milling phase of the fabrication procedure.

The cast-to-cast variations cannot be explained in terms of systematic trends in either mean cavity diameter or cavity density; however, the lowest swelling STA batch (0.07%) is certainly due to a significantly reduced mean cavity size (5.2 nm) compared with that in the highest swelling batch (8.3 nm). In contrast, in the intermediate swelling batch (0.16%) the cavity concentration (4.3×10^{21} m^{-3}) is markedly reduced compared to that in the high swelling batch (8.0×10^{21} m^{-3}). The data thus imply that reductions in both cavity nucleation and cavity growth contribute to the observed variations in swelling. A combination of several of the metallurgical factors given above may therefore be operative.

A further significant observation specific to the ODS alloy is that the locations of the cavities are principally at small oxide particles and also at the matrix-precipitate interfaces of larger such particles. This suggests that the yttria dispersoids may act as efficient trapping sites for helium gas; furthermore, the size range of many of the cavities (i.e. with mean diameters below ~5 nm) is consistent with their being near-equilibrium gas bubbles.

A feature which distinguishes the cavities in this ODS ferritic alloy from voids observed in many irradiated alloys is their irregular shape. This suggests non-uniform growth after the cavity has nucleated at the oxide particle. One explanation that can be advanced is that a surface-active element - specifically oxygen - present either as a residual impurity or created by dynamic displacement from the contiguous oxide particle may change the surface energy locally such that uniform facetting of the low-index planes to produce an equiaxed polyhedral cavity is inhibited. There is certainly evidence in the literature to show that oxygen in metals tends to enhance void stability by decreasing the surface energy of the void, based on a mechanism of chemisorption [32].

Overall the studies demonstrate that the 13%Cr ODS ferritic alloy type DT2203YO5 can accomodate high levels of helium up to 600 appm with only minimal swelling (< 0.24%) at doses of 50 dpa. The alloy thus performs better than most conventional low swelling ferritic grades considered for fast and fusion reactor applications.

CONCLUSIONS

Ion-beam irradiations have been carried out on a 13%Cr ODS ferritic steel designated DT2203YO5, as part of a programme devised to examine the role of thermomechanical treatment on the microstructural response to radiation damage in the presence of a high matrix concentration of inert gas (600 appm helium). The principal conclusions emerging from the investigations are as follows:

(1) Irradiations at 475°C demonstrate that alloy DT2203YO5 exhibits high swelling resistance at 50 dpa and at a He/dpa ratio of 12, and this is combined with good microstructural stability in terms of an absence of obvious irradiation-induced phase transformations.

(2) The mechanically alloyed yttria particles appear to be beneficial in acting as preferred sites for cavity nucleation and may exert a role as efficient traps for helium gas.

(3) Pre-irradiation microstructures are markedly heterogeneous and the irradiation behaviour is characterized by a significant cast-to-cast variation in swelling level (0.07-0.24%).

(4) The magnitude of the swelling in a solution treated, cold-worked and aged condition is significantly lower than in a solution treated and aged condition.

ACKNOWLEDGEMENTS

The research was carried out whilst the author was with AEA Technology (Harwell Laboratory) and formed part of the Corporate Research Programme of the U.K. Atomic Energy Authority. The author is indebted to Mr. W. Hanks and Mr. B. C. Sowden for experimental assistance and to Dr. D. J. Mazey for helpful discussions.

REFERENCES

[1] Huet, J.J., Met. Powder Report, Vol. 40, 1985, p. 155.

[2] Huet, J.J., Coheur, L., De Bremaecker, A., De Wilde, L., Gedopt, J., Hendrix, W., and Vandermeulen, W., Nuclear Technology, Vol. 70, 1985, p. 215.

[3] Fischer, J.J. and Weber, J.H., Advanced Materials and Processes, Vol. 10, 1990, p. 43.

[4] Okafor, I.C.I. and Carlson, O.N., Metallurgical Transactions, Vol. 9A, 1978, p. 1651.

[5] Snykers, M. and Huet, J.J., in Proceedings, Conference on Creep Strength in Steel and High Temperature Alloys, The Metals Society, London, 1974, p 237.

[6] Tokiwai, M., Horie, M., Kako, K. and Fujiwara, M., Journal of Nuclear Materials, Vol. 204, 1993, p. 56.

[7] Ukai, S. et al., Journal of Nuclear Materials, Vol. 204, 1993, p. 65.

[8] Ukai, S. et al., Journal of Nuclear Materials, Vol. 204, 1993, p. 74.

[9] De Wilde, L., Gedopt, J., De Burbure, S., Delbrassine, A., Driesen, C. and Kazimierzak, B., in Proceedings, International Conference on Materials for Nuclear Reactor Core Applications, BNES, London, Vol. 1, 1987, p. 271.

[10] Mazey, D.J. et al., Euratom/UKAEA Fusion Technology Task MAT-12, Unclassified Harwell Report AERE-R11710, 1985.

[11] Mazey, D.J., Hanks, W. and Williams, T.M., Journal of Nuclear Materials, Vol. 168, 1989, p. 228.

[12] Little, E.A., in Proceedings, International Conference on Materials for Nuclear Reactor Core Applications, BNES, London, Vol. 2, 1988, p. 47.

[13] Hudson, J.H., Francis, S., Mazey, D.J. and Nelson, R.S., in Effects of Radiation on Substructure and Mechanical Properties of Metals and Alloys, ASTM STP 539, American Society for Testing and Materials, Philadelphia, 1973, p. 326.

[14] Mazey, D.J., Hudson, J.H., Francis, S. and Whitton, J.L., Journal of Microscopy, Vol. 96, 1972, p. 326.

[15] Whittenberger, J.D., Metallurgical Transactions, Vol. 9A, 1978, p. 101.

[16] Evans, R.W., Preston, J., Wilshire, B. and Little, E.A., Journal of Nuclear Materials, Vol. 195, 1992, p. 24.

[17] Evens, P.J., Martin, J.W. and Little, E.A., Materials Science and Technology, Vol. 8, 1992, p. 531.

[18] Miodownik, M.A., Martin, J.W. and Little, E.A., Materials Science and Technology, Vol. 10, 1994, p. 102.

[19] Okuda, T. et al., in Proceedings, Solid State Powder Processing, The Minerals, Metals and Materials Society, TMS, USA, 1990, p. 203.

[20] Gelles, D.S., in Effects of Radiation on Materials: 14th International Symposium, Vol. I, ASTM STP 1046, American Society for Testing and Materials, Philadelphia, 1989, p. 73.

[21] Nolfi, F.V., (Ed.), Phase Transformations during Irradiation, Applied Science Publishers Ltd., London, 1983.

[22] Faulkner, R.G., Waite, N.C., Little, E.A. and Morgan, T.S., Materials Science and Engineering, Vol. A171, 1993, p. 241.

[23] Little, E.A. and Stoter, L.P., in Effects of Radiation on Materials: Eleventh Conference, ASTM STP 782, American Society for Testing and Materials, Philadelphia, 1982, p. 207.

[24] Little, E.A. and Stow, D.S., Metal Science, Vol. 14, 1980, p. 89.

[25] Gilbon, D. et al., in Effects of Radiation on Materials: 14th International Symposium, Vol. I, ASTM STP 1046, American Society for Testing and Materials, Philadelphia, 1989, p. 5.

[26] Snykers, M., Journal of Nuclear Materials, Vol. 89, 1980, p. 80.

[27] Snykers, M. and Vandermeulen, W., in Proceedings, International Conference on Dimensional Stability and Mechanical Behaviour of Irradiated Metals and Alloys, BNES, London, 1983, p.91.

[28] Asano, K. et al., Journal of Nuclear Materials, Vol. 155-157, 1988, p. 928.

[29] Hide, K. et al., in Effects of Radiation on Materials: 14th International Symposium, Vol.I, ASTM STP 1046, American Society for Testing and Materials, Philadelphia, 1989, p. 61.

[30] Kinoshita, H. et al., Journal of Nuclear Materials, Vol. 179-181, 1991, p. 722.

[31] Little, E.A., Journal of Nuclear Materials, Vol. 87, 1979, p. 11.

[32] Zinkle, S.J., Wolfer, W. G., Kulcinski, G.L. and Seitzman, L.E., Philosophical Magazine, Vol. A55, 1987, p. 127.

Kiyoyuki Shiba[1], Masahide Suzuki[1], Akimichi Hishinuma[1] and Janet E. Pawel[2]

EFFECT OF BORON ON POST IRRADIATION TENSILE PROPERTIES OF REDUCED ACTIVATION FERRITIC STEEL (F-82H) IRRADIATED IN HFIR

REFERENCE: Shiba, K., Suzuki, M., Hishinuma, A., and Pawel, J. E., **"Effect of Boron on Post Irradiation Tensile Properties of Reduced Activation Ferritic Steel (F-82H) Irradiated in HFIR,"** *Effects of Radiation on Materials: 17th International Symposium, ASTM STP 1270,* David S. Gelles, Randy K. Nanstad, Arvind S. Kumar, and Edward A. Little, Eds., American Society for Testing and Materials, 1996.

ABSTRACT: Reduced activation ferritic / martensitic steel, F-82H (Fe-8Cr-2W-V-Ta), was irradiated in the High Flux Isotope Reactor (HFIR) to doses between 11 and 34 dpa at 400 and 500 °C. Post irradiation tensile tests were performed at the nominal irradiation temperature in vacuum. Some specimens included ^{10}B or natural boron (nB) to estimate the helium effect on tensile properties.

Tensile properties including the 0.2% offset yield stress, the ultimate tensile strength, the uniform elongation and the total elongation were measured. The tensile properties were not depend on helium content in specimens irradiated to 34 dpa; however ^{10}B-doped specimens with the highset levels of hilium showed slightly higher yield strength and less ductility than boron-free specimens. Strength appears to go through a peak, and ductility through a trough at about 11 dpa. The irradiation to more than 21 dpa reduced the strength and increased the elongation to the unirradiated levels.

KEYWORDS: Reduced Activation, Ferritic / martensitic steel, HFIR irradiation, Tensile properties, Boron-10 dope, helium effect

[1] Engineer, principal research engineer and group leader, respectively, Department of Materials Science and Engineering, Japan Atomic Energy Research Institute, Tokai-mura Ibaraki-ken 319-11.

[2] Research staff member, Metals and Ceramics Division, Oak Ridge National Laboratory, P.O. Box 2008, Oak Ridge, TN 37831-6376, USA.

Copyright© 1996 by ASTM International www.astm.org

INTRODUCTION

Ferritic steels are one of the candidate alloys for nuclear fusion reactors because of their good thermophisical and mechanical properties, their superior swelling resistance, and the low corrosion rate in contact with potential breeder and coolant materials. Another attractive point of ferritic steels is the possibility of low activation. Several kinds of ferritic steels are now under investigation. The typical alloy compositions of ferritic / martensitic steels are 2.25 Cr, 7-9 Cr and 12 Cr.

Alloy F-82H was developed as a reduced activation ferritic steel by Japan Atomic Energy Research Institute (JAERI) and Nippon Kokan KK (NKK) [1]. Some characteristics have been researched in the unirradiated conditions [2-4]; however the study of the behavior under irradiation has just started [5]. The effect of helium on mechanical properties of irradiated ferritic steels has been reported [6,7]. Several techniques can be applied to generate helium during irradiation in fission reactor. The addition of ^{10}B to steel can generate helium according to the ^{10}B (n, α) ^{7}Li reaction [8]. This technique was used in this investigation to study the effect of helium on tensile properties.

EXPERIMENTAL PROCEDURE

The alloy investigated was an 8Cr-1W-V-Ta ferritic / martensitic steel (F-82H). The same composition with boron additions was also prepared for this experiment to investigate the helium effect on tensile properties. The three alloys are standard F-82H, ^{10}B-doped F-82H and natural-boron doped F-82H; hereafter they are called as STD F-82H, ^{10}B F-82H and nB F-82H, respectively. The ^{10}B was added for the production of helium during irradiation, and nB F-82H specimens were prepared in order to study the effect of boron itself. The chemical compositions of these alloys are given in TABLE 1. The amounts of ^{10}B or nB were both about 300 appm. Pure ^{10}B was used for ^{10}B F-82H, while natural boron includes about 20 % of ^{10}B. All three alloys were cast into 25 kg ingots individually, then hot rolled to 10 mm plates at 1200 °C. The normalizing treatment for these alloys was 0.5 h at 1040 °C (air cooled), and then they were tempered for 1.5 h at 720 °C (air cooled). The structure after tempering was a tempered lath martensitic structure for all steels.

The steels were fabricated into SS-3 type sheet tensile specimens which are 25.4 mm in length, 4.95 mm in width and 0.76 mm in thickness. The gage section of this specimen was 7.62 mm in length and 1.52 mm in width.

These tensile specimens were irradiated in the High Flux Isotope Reactor (HFIR) target position capsules HFIR-MFE-JP-13, -16 and -14. The details of irradiation are given elsewhere [9]. The peak fluence of fast neutrons (E > 1 MeV) and thermal neutrons were about 2.0 x 10^{26} neutrons/m^2 and 3.0 x 10^{26} neutrons/m^2 for JP-13 and -16, respectively and about 3.8 x 10^{26} neutrons/m^2 and 5.6 x 10^{26} neutrons/m^2 for JP-14. These fluences correspond to 18 and 34 dpa in atom displacement damage. The neutron flux varies in the axial direction of the capsule, so that the displacement damage of each specimen varied, depending on its position. The analyses of the flux monitors are not

completed yet, therefore the irradiation information used in this paper is approximate. The high cross section of ^{10}B (n, α) ^{7}Li (4000 barns) and the high thermal flux cause complete burn up of ^{10}B in the early stage of irradiation [8]. Damage by the recoiled alphas is negligible compared to the nuetron damage level investigated in this experiment . About 20% of ^{10}B is included in natural B and pure ^{10}B is used for the ^{10}B F82H. Therefore, the amount of helium in ^{10}B F-82H is about 300 appm and that in natural B F-82H is about 60 appm after irradiation.

Tensile testing was carried out in an Instron universal testing machine at the nominal irradiation temperature in vacuum for each specimen. The strain rate was $1x10^{-3}$ /s. The 0.2% proof stress (YS), ultimate tensile stress (UTS), uniform elongation (Eu) and total elongation (Et) were calculated from the load-displacement chart.

TABLE 1--Chemical composition of alloys (wt%)

	Fe	Cr	W	V	Ta	Total B	^{10}B
F82H	bal.	7.44	2.0	0.20	0.04	...	...
F82H+nB	bal.	7.49	2.1	0.20	0.04	0.0060	0.0012
F82H+^{10}B	bal.	7.23	2.1	0.22	0.04	0.0058	0.0058

	C	Si	Mn	P	S	Al	N
F82H	0.100	0.14	0.49	0.001	0.001	0.019	0.002
F82H+nB	0.099	0.15	0.50	0.001	0.001	0.021	0.001
F82H+^{10}B	0.098	0.17	0.50	0.001	0.001	0.021	0.002

RESULTS AND DISCUSSIONS

Dose dependence

The tensile results before and after irradiation are listed in TABLE 2. FIG. 1 shows the yield stress and total elongation of STD F-82H irradiated at 400 and 500 °C as a function of neutron damage.

As shown in FIG. 1, all three types of alloys had some irradiation hardening after irradiation to the dose of 34 dpa at 400 °C. Data at the dose of 11 dpa at 400 °C was obtained only for ^{10}B F-82H and this showed the maximum strength and minimum elongation in this experiment. The irradiation to 21 dpa reduced the change in yield strength and recovered the elongation. There was no change in yield stress between 21 dpa and 34 dpa, but there was a slight increase in elongation. STD F-82H showed the same dose dependence as ^{10}B F-82H at more than 21 dpa. However, the reduction of yield stress of ^{10}B from 11 dpa to 21 dpa seems very large, compared to the other results [6,10-12]. FIG. 2 illustrates the stress - strain curves of F82H irradiated in several irradiation conditions from this experiment and others. The stress - strain curve of ^{10}B F-82H irradiated to 11 dpa at 400 °C deformed in the same manner as the specimens irradiated at lower temperatures. These specimens (3 dpa and 11 dpa) exhibited necking just after yielding, so that they did not show any work hardening. These results

TABLE 2--The tensile test results of F-82H irradiated in HFIR target position

Alloy	Irradiation			Test	Strength		Elongation		Increase			
	Temp.	Damage	Helium	Temp.	YS	UTS	Uniform	Total	YS	UTS	Uniform	Total
	°C	dpa	appm He	°C	MPa	MPa	%	%	MPa	MPa	%	%
STD F-82H	...	0	0	250	507	578	3.2	13.3	...	...	...	...
	250	3	1	250	853	856	0.3	7.8	346	278	-2.9	-5.5
	...	0	0	400	460	534	2.5	11.5	...	...	...	...
	400	21	6	400	524	570	2.1	11.3	64	36	-0.4	-0.2
	400	32	9	400	513	580	3.0	13.3	53	46	0.5	1.8
	...	0	0	500	455	503	2.0	11.6	...	...	...	...
	500	32	9	500	437	478	1.8	12.4	-18	-25	-0.2	0.8
	500	34	9	500	411	494	2.6	13.3	-44	-9	0.6	1.7
F-82H + ^{10}B	...	0	0	400	515	600	3.3	13.4	...	...	...	...
	400	12	303	400	764	783	1.0	8.3	249	183	-2.3	-5.1
	400	21	306	400	604	642	2.0	10.1	89	42	-1.3	-3.3
	400	32	309	400	593	655	3.3	12.1	78	55	0	-1.3
	400	32	309	400	578	636	3.3	11.0	63	36	0	-2.4
	...	0	0	500	467	514	1.9	11.9	...	...	...	...
	500	34	309	500	510	543	2.3	12.2	43	29	0.4	0.3
	500	34	309	500	512	557	2.8	12.3	45	43	0.9	0.4
F-82H + nB	...	0	0	400	467	539	3.5	13.8	...	...	...	...
	400	32	69	400	451	555	2.7	12.3	-16	16	-0.8	-1.5
	...	0	0	500	432	509	3.7	15.0	...	...	...	...
	500	32	69	500	457	520	2.9	14.4	25	11	-0.8	-0.6
	500	34	69	500	453	504	2.7	14.0	21	-5	-1.0	-1.0

demonstrate much irradiation hardening occurs at lower irradiation temperatures, and it appears in the relatively early stages of irradiation at 250 °C. Since ^{10}B F-82H irradiated to 11 dpa at 400 °C deformed similarly, the same levels of irradiation hardening occurred in these specimens.

Only results for irradiations to more than 30 dpa were obtained at 500 °C. Both of boron doped specimens and STD F-82H showed the same strength and elongation as unirradiated value at this temperature. The stress - strain curves of STD F-82H irradiated to 34 dpa at 400 and 500 °C shown in FIG. 2 demonstrate the specimens irradiated at 400 and 500 °C deformed in the same manner and they are apparently different from the results at lower irradiation doses and temperature. The specimens irradiated to 34 dpa at 400 and 500 °C have some work hardening capacity. This means that recovery of the lath structure occurred at the higher irradiation temperatures; however some degradation of ductility occurred at 500 °C. One possible reason for this result is the coarsening of carbides or an aging effect, since helium production during irradiation in STD F-82H specimens is small. The irradiation time for both 21 and 34 dpa specimens (which were irradiated in the same irradiation capsule) was about 45 Ms, while it was 25 Ms for 11 dpa specimens. This is sufficient to cause the coarsening of carbides even in the unirradiated condition [2]. Microstructural observation for the same F-82H irradiated in the Fast Flux Test Facility (FFTF) by Kohno et. al [5] showed partial recovery of lath martesite at both 400 and 500 °C. This FFTF irradiation time was 29 Ms. It is likely that the longer irradiation time of the present HFIR specimens caused much more recovery of the lath structure.

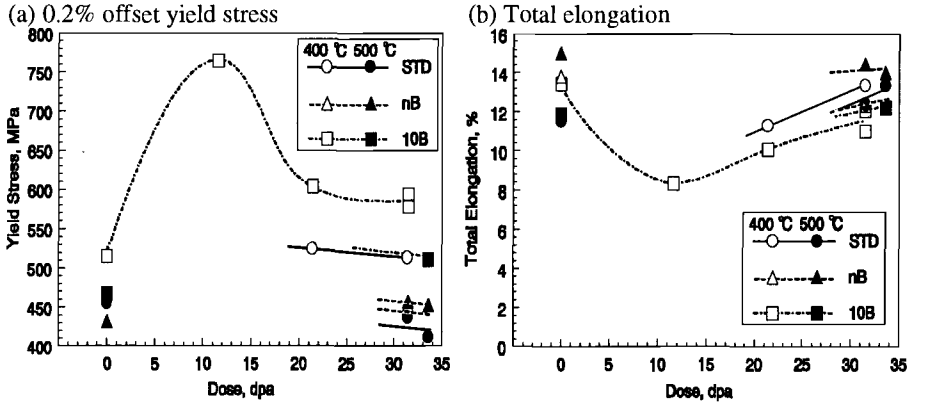


FIG. 1--0.2% offset yield stress (a) and total elongation (b) of F82H (STD, natural B doped and ^{10}B doped) irradiated in HFIR target position at 400 and 500 °C.

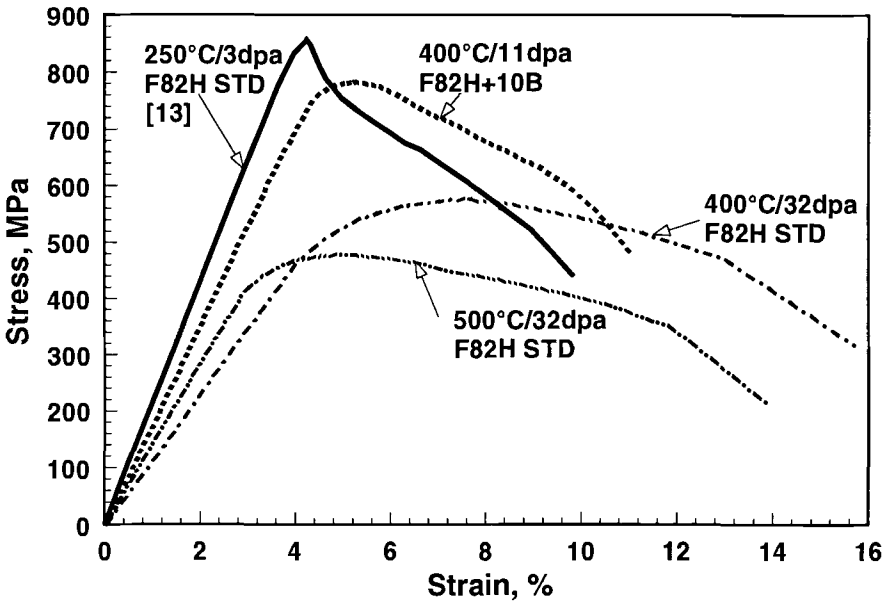


FIG. 2--Stress - strain diagram of F-82H irradiated in HFIR target position [13].

The effect of boron addition

Three types of steels were irradiated to investigate the helium effect on tensile properties. The differences between these three steels were small in all irradiation conditions in this experiment. FIG. 3 shows the yield strength and total elongation of boron-free and boron-doped F-82H irradiated to 34 dpa at 400 and 500 °C with changes of these properties. ^{10}B F-82H had slightly higher strength than STD F-82H in all conditions, and the increase of yield strength due to irradiation was also larger. The strength of nB F-82H was lower than ^{10}B F-82H, but the differences between nB and STD were not consistent in helium content even though the nB specimens have more helium than STD F-82H at 34 dpa. The helium can affect the strength as small helium bubbles. Kimura et al. found tiny voids which caused higher swelling in boron-doped 9Cr ferritic steels irradiated in FFTF at 420 °C [14]. Thier boron-doped steels contained 30 wppm of natural boron. The slightly higher strength of ^{10}B specimens might be caused by this helium cavities, but the helium produced from nB was not sufficient to make a difference in strength. Lithium is also produced with helium, according to the ^{10}B (n, α) ^{7}Li reaction. This lithium could affect the tensile properties, however no useful evidence has been obtained yet. The effect of aging accelerated by irradiation overshadowed the helium effect of nB. ^{10}B F-82H had a peak of irradiation hardening at the dose of 11 dpa at 400 °C. The irradiation temperatures of 400 and 500 °C are too high to sustain the irradiation -induced dislocation loop structure. Helium cavities produced in boron-doped

F-82H and the irradiation-accelerated aging effect could cause a transient hardening peak at 11 dpa.

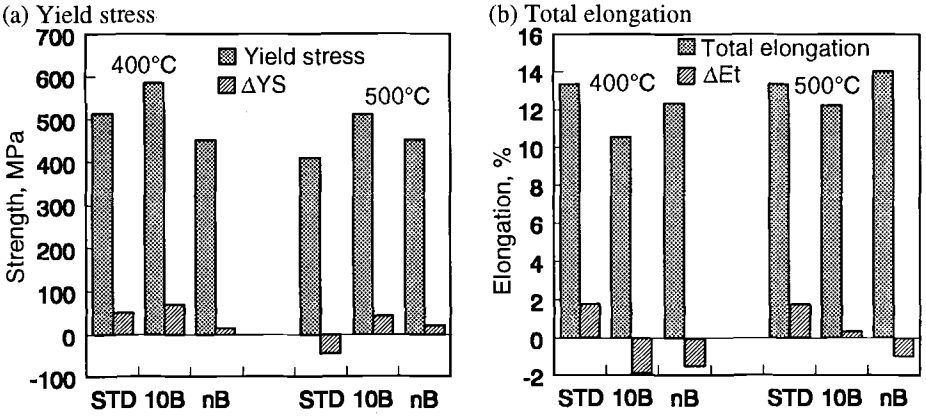


FIG. 3-- Comparison of tensile properties between F-82H (STD) and boron doped (^{10}B and nB) specimens irradiated to 32 dpa at 400 °C and 34 dpa at 500 °C in HFIR target position. (a) yield stress and (b) total elongation. The changes of yield stress and total elongation due to irradiation are also displayed in these graphs.

SUMMARY

The tensile properties of 8Cr-1W-V-Ta ferritic / martensitic steel (F-82H) irradiated in the HFIR up to 34 dpa at irradiation and test temperatures of 400 and 500 °C, were studied. Some of the steels investigated had ^{10}B or natural B added to the material to investigate the helium effect on the tensile properties. The following summarize the obserbations:

1. In ^{10}B F-82H alloy irradiated and tested at 400 °C, more hardening occurred at a dose of 11 dpa than at doses of 21 nad 32 dpa.

2. Any helium effects due to ^{10}B or natural B were small . ^{10}B F-82H, which had the most helium, had slightly higher strength than STD, but the differences between nB and STD were not consistent with helium content.

3. Thermal recovery of the lath structure may have masked the effects of boron.

ACKNOWLEDGMENTS

Research sponsored by the Japan Atomic Energy Research Institute and the Office of Fusion Energy, U.S. Department of Energy, under contract DE-AC05-84OR21400 with Martin Marietta Energy Systems, Inc. The authors are grateful to L.T. Gibson, W.S. Eatherly, and R.L. Martin for tensile testing, and to Drs. R.L. Klueh and K. Farrell for critical reviews of the manuscript.

REFERENCES

[1] M. Tamura, H. Hayakawa, M. Tanimura, A. Hishinuma and T. Kondo, J. Nucl. Mater. 141-143 (1986) 1067-1073.
[2] M. Tamura, H. Hayakawa, A. Yoshitake, A, Hishinuma and T. Kondo, J. Nucl. Mater .155-157 (1988) 620-625.
[3] H. Hayakawa, A. Yoshitake, M. Tamura, S. Natsume, A. Gotoh and A. Hishinuma, J. Nucl. Mater. 189-181 (1991) 693-696.
[4] N. Yamanouchi, M. Tamura, H. Hayakawa, A. Hishinuma and T. Kondo, J. Nucl. Mater. 191-194 (1992) 822-826.
[5] K. Kohno, D.S. Gelles, A. Kohyama, M. Tamura and A. Hishinuma, J. Nucl. Mater. 191-194 (1992) 868-873.
[6] R.L. Klueh and P.J. Maziasz, J. Nucl. Mater. 187 (1992) 43-54.
[7] R.L. Klueh and D.J. Alexander, J. Nucl. Mater. 187 (1992) 60-69.
[8] L.K. Mansur and K. Farrell, J. Nucl. Mater. 170 (1990) 236-245.
[9] J.E. Pawel and R.L. Senn, Fusion Reactor Material Semiannual Progress Report, DOE/ER-0313/12, Office of Fusion Energy (1992) 15-23.
[10] R.L. Klueh and J.M. Vitek, J. Nucl. Mater. 132 (1985) 27-31.
[11] R.L. Klueh and J.M. Vitek, J. Nucl. Mater. 150 (1987) 272-280.
[12] H. Kurishita, H. Kayano, M. Narui, A. Kimura, M.L. Hamilton and D.S. Gelles, J. Nucl. Mater. 212-215 (1994) 730-735.
[13] D.J. Alexander, Effects of Radiation on Materials: 17th Volume, ASTM STP 1270, David S. Gelles, Randy K. Nanstad, Arvind S. Kumar and Edward A. Little, Editors, American Society For Testing and Materials, Philadelphia, 1995.
[14] A. Kimura, M. Narui and H. Kayano, J. Nucl. Mater. 191-194 (1992) 879-884.

A. Alamo [1], J. L. Séran [1], O. Rabouille [2], J. C. Brachet [1], A. Maillard [1], H. Touron [1], J. Royer [2].

IRRADIATION EFFECTS ON BASE METAL AND WELDS OF 9Cr-1Mo (EM10) MARTENSITIC STEEL.

REFERENCE: Alamo, A., Séran, J. L., Rabouille, O., Brachet, J. C., Maillard, A., Touron, H., and Royer, J., **"Irradiation Effects on Base Metal and Welds of 9Cr-1Mo (EM10) Martensitic Steel,"** *Effects of Radiation on Materials: 17th International Symposium, ASTM STP 1270,* David S. Gelles, Randy K. Nanstad, Arvind S. Kumar, and Edward A. Little, Eds., American Society for Testing and Materials, 1996.

ABSTRACT: The effects of fast neutron irradiation on the mechanical behaviour of base metal and welds of 9Cr-1Mo (EM10) martensitic steel have been studied. Two types of weldments have been produced by TIG and electron beam techniques. Half of samples have been post-weld heat treated to produce a stress-relieved structure. The irradiation has been conducted in the Phénix reactor to doses of 63 - 65 dpa in the temperature range 450 - 459 °C. The characterization of the welds, before and after irradiation, includes metallographic observations, hardness measurements, tensile and Charpy tests. It is shown that the mechanical properties of the welds after irradiation are in general similar to the characteristics obtained on the base metal, which is little affected by neutron irradiation.

KEYWORDS: 9Cr-1Mo martensitic steel, TIG welds, EB welds, tensile tests, Charpy tests, hardness, mechanical behaviour after irradiation.

9Cr martensitic steels are being developed for core components (wrapper tubes) of fast breeder reactors as well as for fusion reactor structures. These fully martensitic materials are very promising candidates because of the high stability of physical and mechanical properties under irradiation as well as under thermal ageing. In particular, the unstabilized EM10 alloy (9Cr-1Mo-0.1C) has been studied after high neutron exposure ($\leq 2.10^{23}$ n/cm^2, E>0.1 MeV) in the Phénix reactor as samples or as wrappers in the temperature range from 390 to 550°C [1, 2, 3]. Post-irradiation tests have shown only a slight increase in the ductile-brittle transition temperature (DBTT), which always remains below room temperature with a small irradiation-induced hardening for T_{irrad} < 450°C. The minor changes in mechanical properties are associated with a very stable microstructure where only an irradiation-induced evolution of the dislocation network can be invoked [4].

Commissariat à l'Energie Atomique,
[1] CEREM/DECM/SRMA, [2] DRN/DMT/SETIC,
CEA Saclay, 91191 Gif-sur-Yvette Cédex, France.

Copyright© 1996 by ASTM International www.astm.org

For technological applications it is also necessary to characterise the behaviour of welds under irradiation. For this purpose, samples of EM10 base metal and two types of welds, tungsten inert gas (TIG) and electron beam (EB) welds have been produced. Both kinds of welds are studied in the as-welded condition and after a post-weld heat treatment to obtain a stress-relieved state. The irradiation has been conducted in Phénix reactor in the temperature range 450-459°C and to doses of 63-65 NRT dpa. In this paper, hardness values, tensile and impact properties of irradiated specimens are reported and compared with values obtained for the initial condition and thermally aged samples.

MATERIAL AND WELDS

The chemical composition of the EM10 alloy (base metal) is given in table 1. All samples (base metal and welds) have been obtained from the same sheet of 3.5 mm thickness in the normalized and tempered condition (N & T). Normalization and tempering heat treatments of the EM10 steel have been performed respectively at 1000°C/30 minutes and 750°C/30 minutes.

TABLE 1 -- Chemical composition of the EM10 martensitic steel (wt.%).

C	Cr	Mn	Si	P	S	Ni	Mo	Fe
0.105	8.76	0.48	0.37	0.016	0.003	0.18	1.05	bal

Weldments have been produced perpendicularly to the rolling direction of the sheets. TIG welds have been performed by pulsed automatic welding, in one pass, without filler material under an argon atmosphere. The parameters used to produce EB welds were: beam voltage 50 KV, beam current 60 mA and welding speed 1 m/min. After welding, half of specimens have been annealed in air at 750°C for 30 minutes to relieve stresses mainly induced during cooling by the martensitic transformation in the weld metal (WM) and in the heat-affected zone (HAZ).

EXPERIMENTAL PROCEDURE

Hardness profiles, tensile and impact properties have been determined for irradiated samples of the base metal (BM), the TIG and EB welds in the as-welded condition and after a post-weld anneal (TIG-PWA and EB-PWA).

All specimens, base metal and different welds, have been irradiated in two close levels of the irradiation capsule. For metallography, hardness and tensile samples the total dose was 65 dpa and the irradiation temperature (T_{irrad}) was 459°C. For Charpy specimens, the dose was 63 dpa and T_{irrad} = 450°C. The irradiation time was about 12 000 hours. To obtain a better understanding of the irradiation effects, properties of the irradiated specimens were compared with samples in the initial condition and with thermal controls aged for 13 000 hours at 475°C.

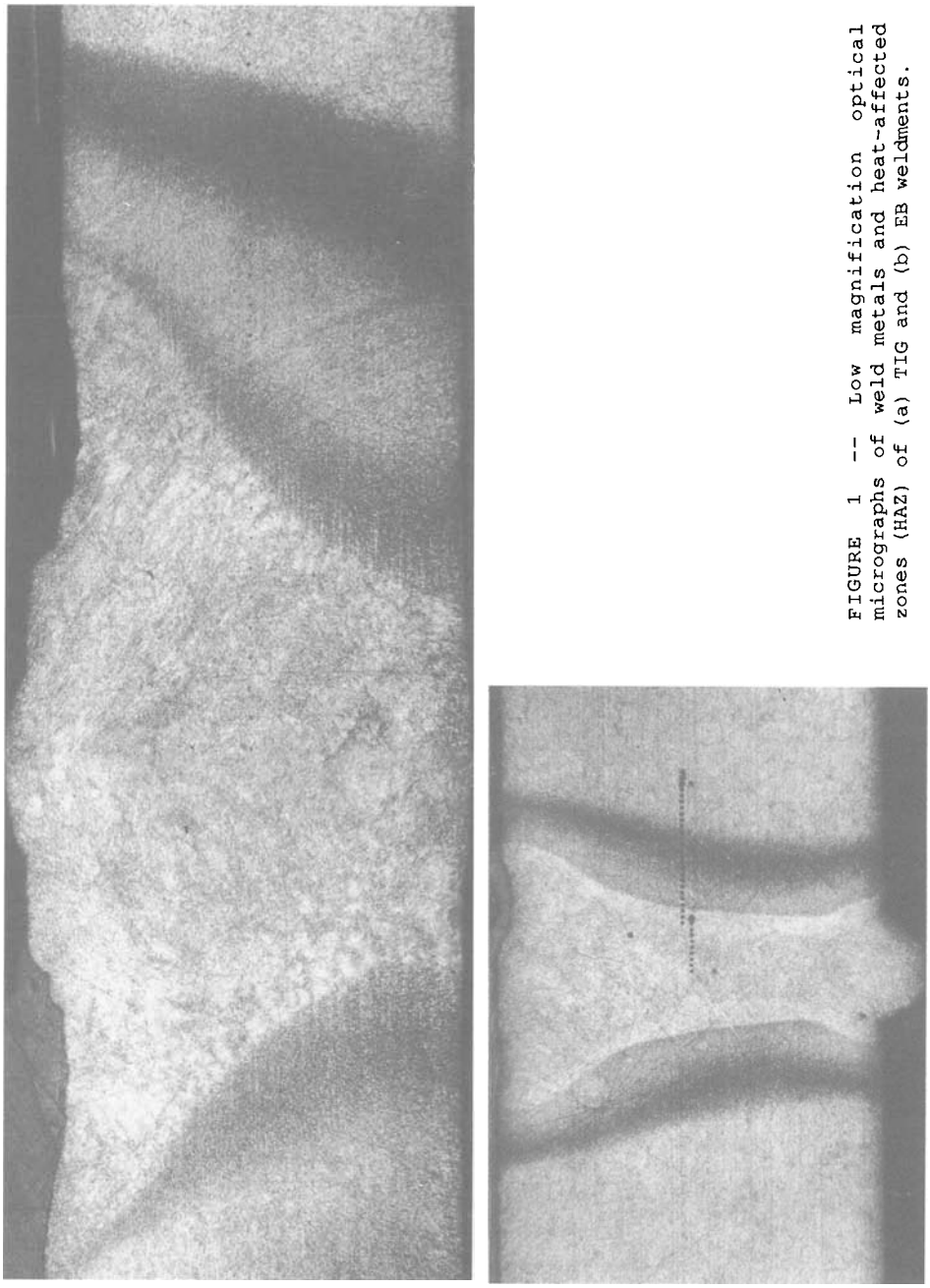


FIGURE 1 -- Low magnification optical micrographs of weld metals and heat-affected zones (HAZ) of (a) TIG and (b) EB weldments.

Vickers hardness measurements have been performed with a 100 g load on the cross-section of different welds. Cylindrical tensile specimens of 2 mm in diameter and 12 mm gage length, were machined so that the weld joint was located in the center of the gage length, with interfaces between the WM and the BM perpendicular to the tensile axis. The strain rate used was 3.10^{-4}/s and the test temperature ranged from 20 to 450°C. Impact specimens, also machined perpendicular to the weld, were quasi-standard Charpy V-notch samples (55 mm long, 10 mm wide) except for the thickness, which was 2.5 mm instead of 10 mm. In all the cases, the notch was located in the weld metal. Charpy tests were conducted over the temperature range -120 to +180°C, in order to produce full transition curves for each welding process (after irradiation) and the base metal.

Unfortunately, partial data on tensile and impact properties were available for unirradiated welds in the initial condition as well as thermally aged specimens. Charpy tests were only performed at 20, 180 and 400°C, which allow estimating the upper shelf energy (absorbed energy was nearly the same for these test temperatures). But, the absence of full transition curves prevent determination of DBTT values.

RESULTS

Metallographic Structure

The unirradiated BM exhibits a typical tempered martensitic structure, where the prior austenitic grains reached an average size of about 80 µm. Figure 1 shows optical micrographs of tranverse sections of TIG and EB weldments. The WM widths are about 5 mm and 1 mm and the lengths of the HAZ are 3.5 mm and 0.7 mm respectively for TIG and EB welds, measured at mid-thickness.

In the as-welded condition, the microstructure of both weldments is qualitatively the same, except for the extension of each typical zone. A small fraction of δ-ferrite (< 2%) is observed in the fusion zone (WM) as well as in a narrow band along the fusion boundary in the HAZ. The latter one shows a quenched martensitic structure, where the prior austenitic grain size decreases with the increasing distances from the interface WM/HAZ as shown in the schematic representation given in figure 2. The distribution of austenite grain size in the HAZ is not modified by tempering, ageing and irradiation.

Hardness Profiles

Hardness measurements were performed under 100 g load along a line located at mid-thickness in the cross-section of welds. Indentations were spaced at 250 µm in the case of the TIG welds and 50 µm for the EB welds. Figures 3 and 4, show the hardness profiles determined for both types of weldments, in the as-welded and post-weld annealed (PWA) initial conditions, and are compared to curves obtained after thermal ageing and irradiation at 459°C. Typical hardness of the BM is about 240 HV and it does not seem to be modified by ageing and/or irradiation.

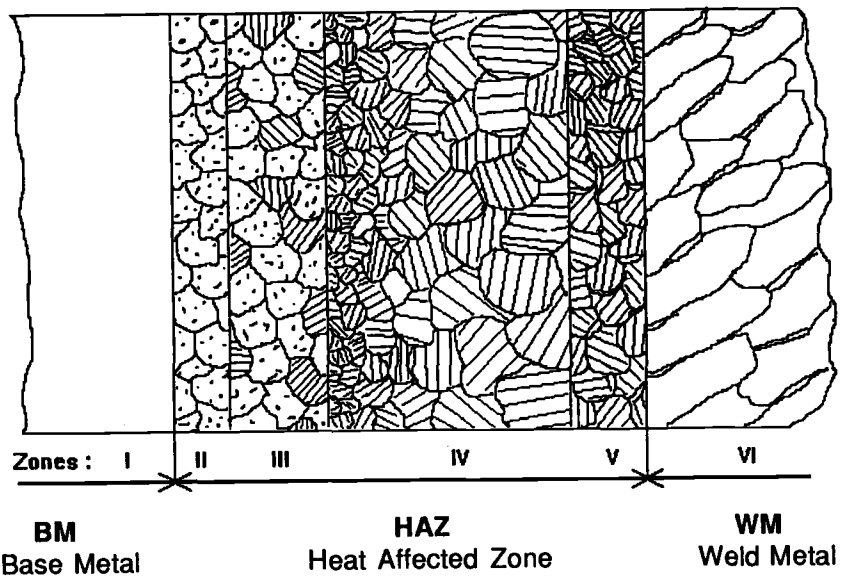


FIGURE 2 -- Schematic representation of the variation of prior austenitic grain structure according to the austenitization temperature reached in the heat-affected zone during TIG and EB welding.

Zone I: Base metal, tempered martensite at 750°C.

Zone II: HAZ, overtempered martensite, $750°C < T < Ac_1$.

Zone III: HAZ, tempered and quenched martensite, $Ac_1 < T < Ac_3$.

Zone IV: HAZ, quenched martensite, $Ac_3 < T < A\delta$ ($A\delta$: boundary for δ-ferrite occurrence).

Zone V: HAZ, quenched martensite and δ-ferrite, $T_{melting} > T > A\delta$.

Zone VI: Weld metal, quenched martensite and δ-ferrite, $T > T_{melting}$.

As expected, as-welded TIG and EB specimens display high initial values of hardness (~440 HV) due to the quenched martensite produced during cooling in the WM and HAZ. Nevertheless, these regions are recovered after thermal ageing and also under irradiation. Hardness of WM and HAZ decreases to a final level of 300 HV. In the case of post-weld heat treated samples, the initial hardness level of the WM and the HAZ is about 250 HV for both weldments and no sensitive modification is induced by the irradiation. However, it is interesting to note that a higher strength level is obtained after irradiation in the as-welded condition compared to the PWA welds.

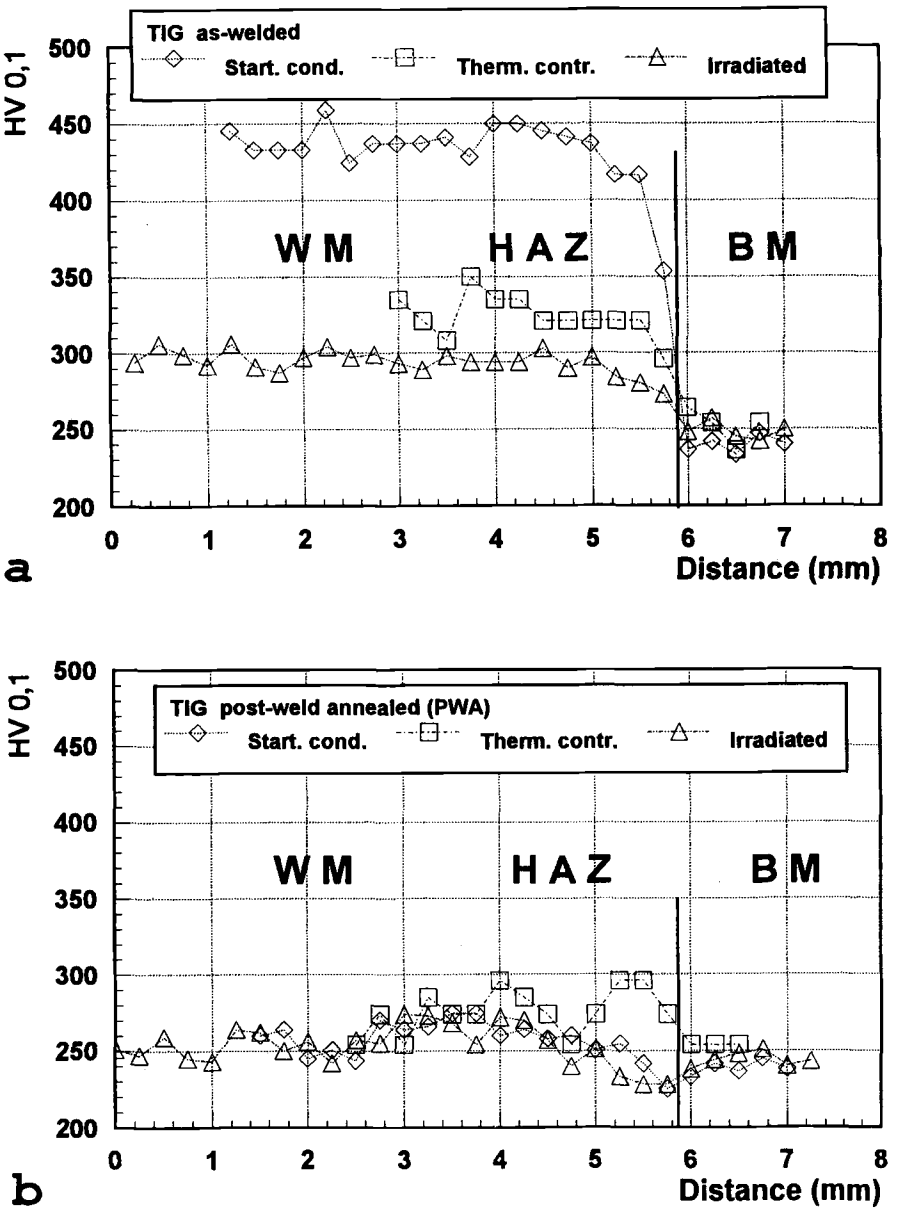


FIGURE 3 -- Hardness values after thermal ageing and irradiation for two initial conditions of TIG joints: (a) as-welded and (b) post-weld annealed states. Hardness profiles obtained on the weld metal (WM), heat affected zone (HAZ) and the base metal (BM).

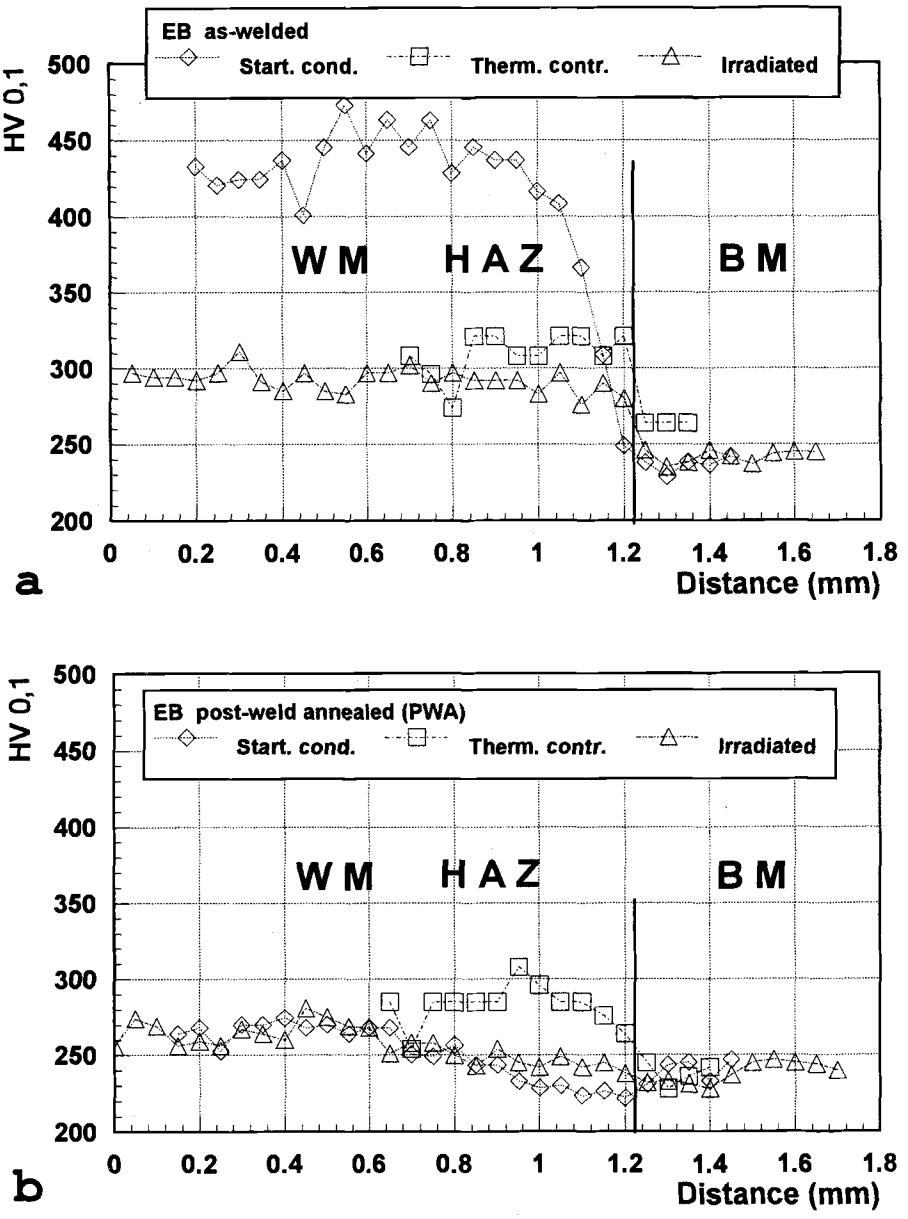


FIGURE 4 -- Hardness values after thermal ageing and irradiation for two initial conditions of EB joints: (a) as-welded and (b) post-weld annealed states. Hardness profiles obtained on the weld metal (WM), heat affected zone (HAZ) and the base metal (BM).

Tensile Properties

The total width of the TIG welds, including the fusion zone and the heat-affected regions, is about 12 mm which is comparable to the gage length of tensile specimens. Thus, the tensile tests really characterise properties of TIG welds, which occupy the whole gage length. In the case of EB welds, where the extension (2.5 mm) is about 20% of the gage length, a preponderant contribution of the base metal is obtained.

Tensile properties of irradiated specimens have been measured at 20, 180, 275 and 450°C. Figure 5 illustrates the 0.2% proof stress and total elongation values as a function of test temperatures. The higher values of tensile strength are found for TIG welds, in the as-welded state, over the whole range of test temperature. In contrast, EB joints as-welded and PWA present strength values very close to those of the base metal. Total elongation data range from 13 to 18% at 20°C (10-15% at 450°C) and uniform elongation values between 5 and 8% at 20°C (2 and 4% at 450°C) for all specimens; the base metal shows the higher values. The lower ductility is found for TIG weldments, especially at 450°C. Fracture occurs mainly in the WM in the case of TIG samples, but for EB joints (as-welded and PWA) it is always occurs in the base metal. So, no brittle regions seem to be developed in welds, even in the as-welded condition.

Figure 6 permits a comparison of the tensile properties measured at 450°C of specimens in the initial condition, after thermal ageing and after neutron irradiation. In general, the irradiation as well as ageing induces a decrease of the tensile strength of the welds, specially for TIG joints, compared to initial conditions. No sensitive hardening is observed for the base metal at this irradiation temperature in agreement with previous results on the same material [1, 4]. Even elongation data of unirradiated welds (initial and thermal aged conditions) are not available, these results showed that no detrimental irradiation induced effects are detected on ductility values. At 450°C, all irradiated specimens, including welds and the base metal, display nearly the same values of the total elongation (10-15%) and reduction in area RA ~ 70%.

Consequently, for TIG and EB as-welded joints the main effect of the irradiation at 459°C is to recover the quenched martensitic structure in such a way that the final strength is higher and the ductility comparable to the equivalent properties of the base metal. This point can be explained by the equivalence relation between the time and the temperature of anneals derived by Hollomon-Jaffe, i.e. HJ = T(22.3 + log t)/1000, where T is the temperature (expressed in °K) and t the time (expressed in seconds) of heat treatments. Evaluation of the HJ parameter for the post-weld annealing (30 minutes at 750°C) and the thermal contribution during irradiation (11952 hours at 459°C) gives HJ = 26.4 and HJ = 21.9 respectively. Increasing values of this parameter indicate a higher recovery and so a decreasing strength. Thus, these figures indicate that the degree of recovery of the quenched martensite reached during the post-weld annealing is much higher than that obtained after the in-pile ageing and so we can expect a higher strength in the last case as is observed in tensile tests as well as in hardness measurements.

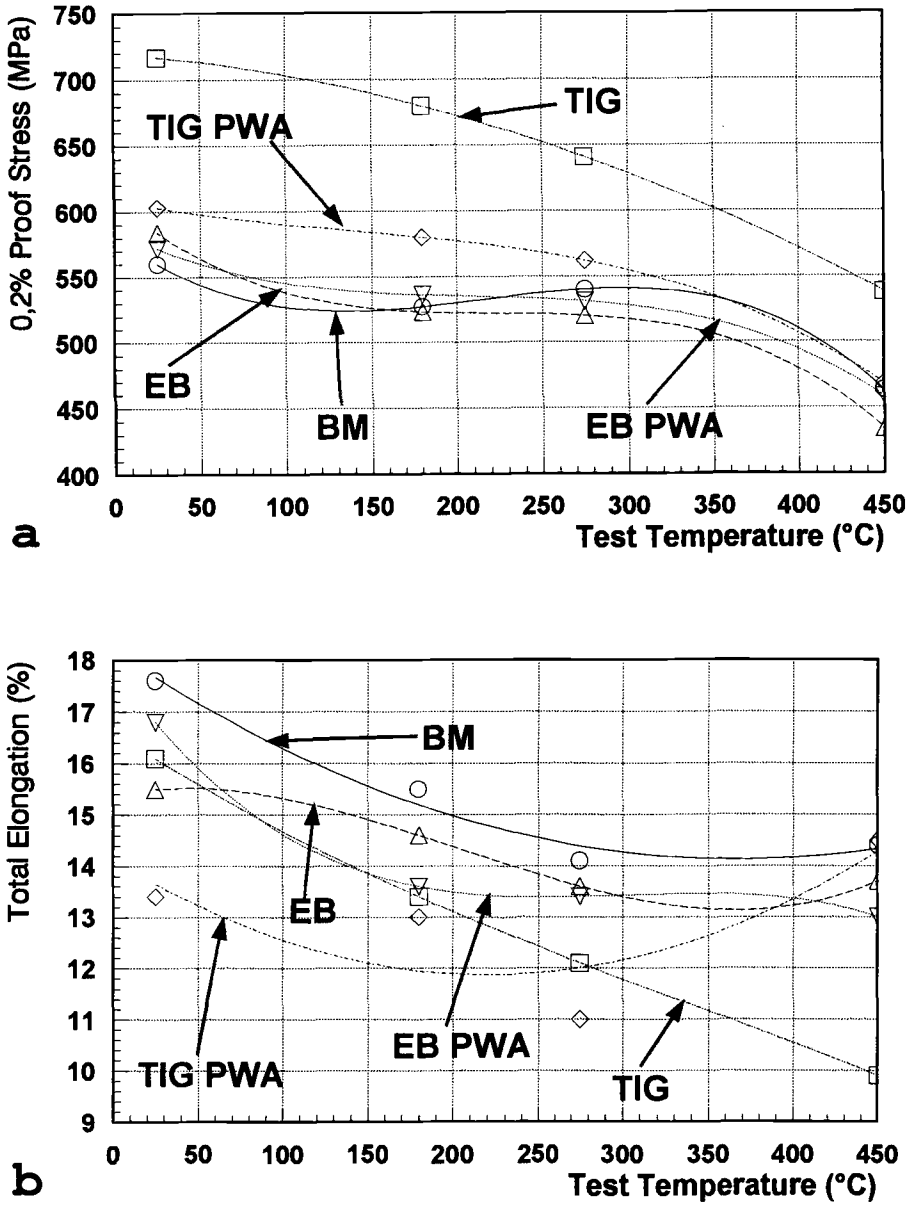


FIGURE 5 -- Tensile properties of irradiated samples (T_{irrad} = 459°C, dose 65 dpa) as a function of test temperature. (a) 0.2% proof stress. (b) total elongation.

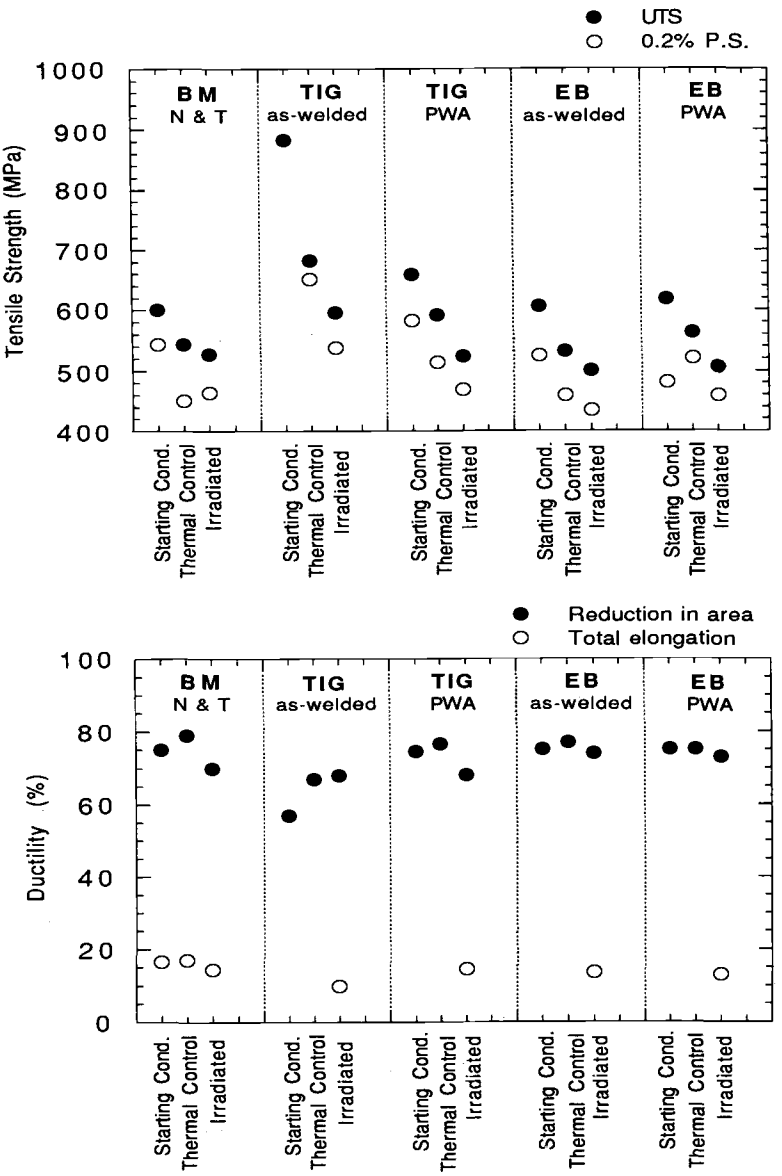


FIGURE 6 -- Comparison of tensile properties (tensile strength, total elongation and reduction in area values) of specimens in the initial condition, after thermal ageing and irradiation, measured at 450°C.

Impact Properties

Impact transition curves have been determined for the base metal and the different irradiated welds. The ductile-brittle transition temperature (DBTT) is defined as being midway between the upper and lower shelves of the transition curves; the determination accuracy is about ± 10°C. Energy values are normalized to the initial cross-section area (8 x 2.5 mm^2) of Charpy specimens. Data obtained for irradiated specimens, are presented in figure 7.
Transition curves were fitted with the usual relation:

$$E = (E_{us}) + E_{ls})(1 + \tanh((T-T_o)/\Delta T))/2$$

where E_{us} and E_{ls} are the upper and lower shelf energies respectively, T_o = DBTT and ΔT is the temperature range over which the transition occurs. In the present work, it is assumed that $E_{ls} = 0$.

Table 2 summarizes the parameters obtained after fitting of experimental curves. The higher upper shelf energy (USE) of about 160-170 J/cm^2 is obtained for EB welds, which display the lower DBTT values. The base metal, TIG and EB-PWA joints show nearly the same impact energy curves. The lower USE and the higher DBTT values are found for the TIG-PWA welds.

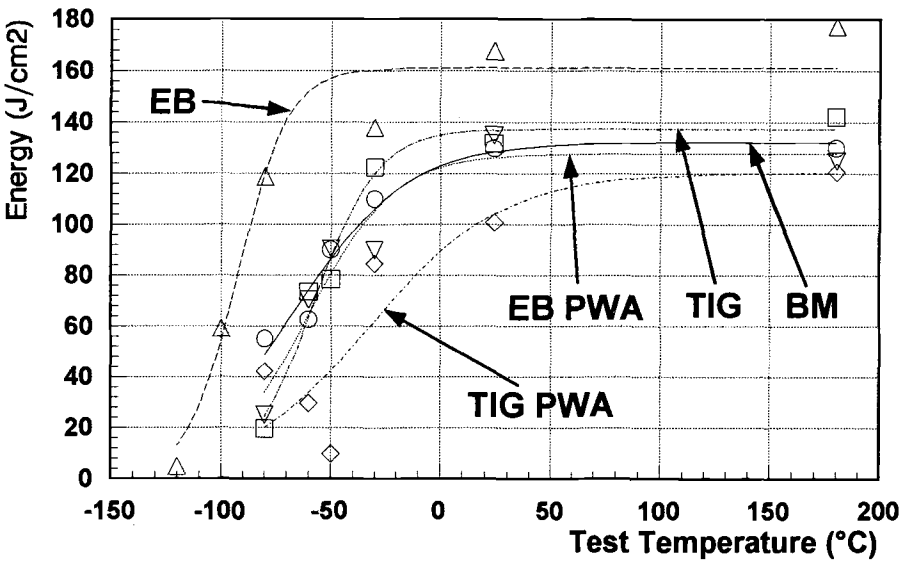


FIGURE 7 -- Impact transition curves determined for irradiated samples of the EM10 base metal and welds (T_{irrad} = 450°C, dose 63 dpa).

TABLE 2 -- Parameters used to fit the experimental impact transition curves of irradiated specimens.

Sample	DBTT (T_O) °C	ΔT °C	USE (E_{US}) J/cm^2
Base Metal	-66	51	132
TIG	-58	29	**137**
TIG - PWA	-32	60	120
EB	-92	23	**161**
EB - PWA	-60	39	129

DBTT and USE values are summarized in figure 8 and compared with the available data determined on the starting state and thermally aged specimens. DBTT ranges from -92°C to -32°C for all irradiated samples. The slight change in these parameters for the base metal, from -75°C to -66°C, corresponding to the initial and irradiated conditions respectively, confirm the high stability of EM10 alloy under irradiation according to previous determinations [1, 4]. The effect of irradiation on USE weld values depends on the starting condition of samples. For post-weld heat treated TIG and EB joints, the irradiation decreases the initial upper shelf energy, while an increase of USE is observed for the as-welded TIG and EB related to the irradiation-induced recovery of these specimens. Nevertheless, all weld samples display USE values ranging from 120 to 160 J/cm^2, which must be compared to the base metal level of 130 J/cm^2. In particular, the final properties of irradiated as-welded TIG joints are very similar to those of the base metal.

It is worthwhile to point out that visual observations of broken specimens sometimes provided evidence of a deviated fracture propagation, especially for the EB welds, where the weld metal region is narrow (~2.5mm), and for high test temperatures. The actual rupture surface area is difficult to evaluate and consequently the values of USE could be overestimated in this case. Also, the thickness of Charpy specimens, used in this experiment (2.5 mm), prevent comparison of USE values with previous results obtained on irradiated samples of 3.5 mm, because the effect of geometry could be important for thin Charpy specimens. But, even though the USE magnitude is not comparable, the DBTT value determined for the base metal agrees with previous results on EM10 samples of 3.5 mm thick irradiated at the same temperature and dose.

In the case of as-welded TIG joints, the increase of the upper shelf energy after irradiation, compared to the initial condition, can not be attributed to a deviated fracture propagation, but to thermal and irradiation-induced recovery. In fact, as-welded joints behave in a similar way to cold-worked martensitic steels (EM10 and T91), which exhibit a higher stability under thermal ageing compared to tempered materials. Cold-work seems to slow down ageing hardening, and consequently the increase of DBTT. Simultaneously the enhancement of

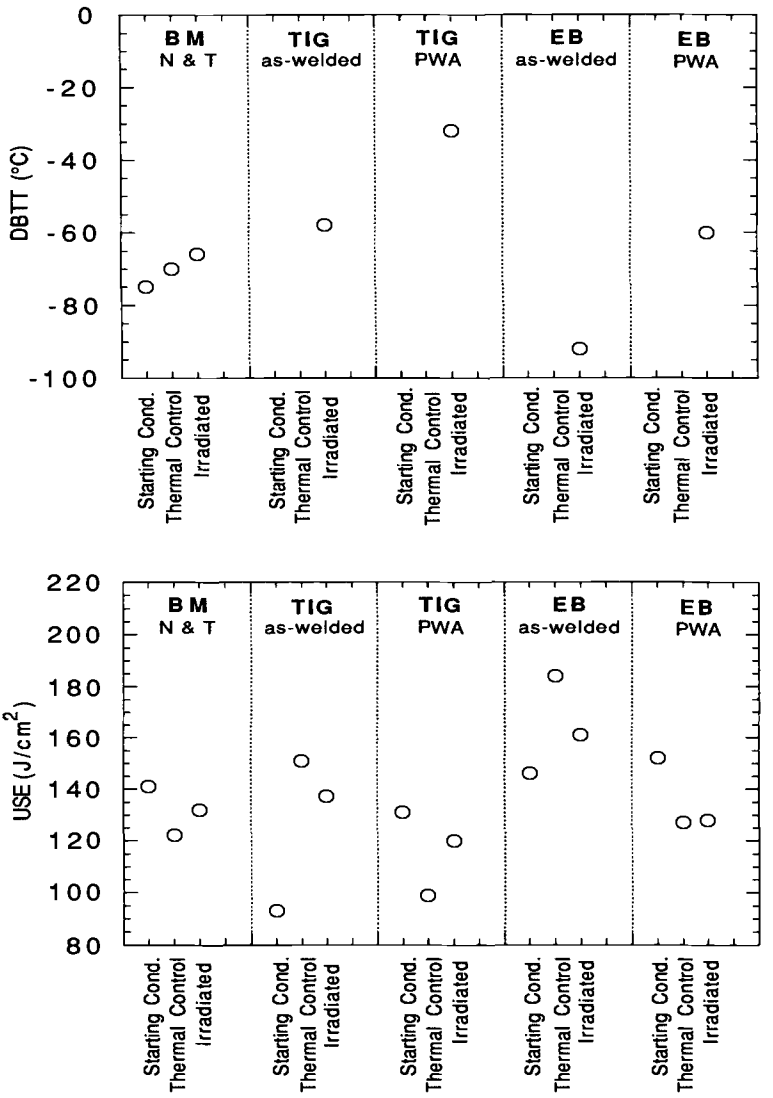


FIGURE 8 -- Comparison of impact properties, DBTT and USE values, of specimens in the initial condition, after thermal ageing and irradiation. .

ductility by thermal recovery is detected, whilst at the same time maintaining a relatively high strength level in the material [5].

In the present work, the effect of residual stress due to the welding process was not evaluated. This effect should be important, especially for heavy thickness specimens, and further experiments should be needed to estimate this contribution.

CONCLUSIONS

Neutron irradiation at 450-459°C up to 63-69 dpa has shown no deleterious effects on mechanical properties of TIG and EB welds of EM10 9Cr-1Mo martensitic steel.

The ductile-brittle transition temperatures after irradiation range from -92°C to -32°C, the base metal DBTT is about -66°C. No irradiation-induced hardening is detected in the base metal nor in welds.

In general, tensile strength decreases after irradiation. For as-welded specimens a thermal recovery occurs during irradiation at 450-459°C, resulting in a higher strength and nearly the same ductility as that of the base metal.

The technological implications of the last point are interesting. The absence of post-weld heat treatments has no detrimental effect under irradiation, at least for the dimensions of specimens examined here. So, if the post-weld anneal is not actually needed, the direct consequences are a shortened fabrication route and an advantage in the case of replacement or repairing of in-service structures.

REFERENCES

[1] Séran J. L., Lévy V., Dubuisson P., Gilbon D., Maillard A., Fissolo A., Touron H., Cauvin R., Chalony A., Le Boulbin E., Proc.of the 15th Intern. Conf. on Effects of Radiation on Materials, (Nashville, June 1990). ASTM STP 1125 (1992), p. 1209.

[2] Séran J.L., Lévy V., Maillard A., Alamo A., Dubuisson P.,Proc. of the Workshop on Ferritic/Martensitic Steels, (Tokyo, October 1992), Ed. JAERI, vol. 2, p. 287.

[3] Séran J.L., Alamo A., Maillard A. , Touron H., Brachet J. C., Dubuisson P. , Rabouille O., "Pre- and post- irradiation mechanical properties of ferritic-martensitic steels for fusion applications: EM10 base metal and EM10/EM10 welds", Journal of Nuclear Materials, vol. 212-215 (1994), p.588.

[4] Dubuisson P., Gilbon D., Séran J.L.,"Microstructural evolution of ferritic-martensitic steels irradiated in the Fast breeder reactor Phénix", Journal of Nuclear Materials, vol. 205 (1993), p. 178.

[5] Alamo A., Brachet, J.C., Castaing A., Foucher C., to be published in the Proc. of the Second International Conference on Microstructures and Mechanical Properties of Aging Materials, (Las Vegas, February 1995), Ed. P.K. Liaw, TMS, 1995.

Hiroaki Kurishita,[1] Itaru Shibahara,[2] Minoru Narui,[1] Syunji Mizuta,[2] and Hideo Kayano[1]

EVALUATION OF THE UPPER SHELF ENERGY FOR FERRITIC STEELS FROM MINIATURIZED CHARPY SPECIMEN DATA

REFERENCE: Kurishita, H., Shibahara, I., Narui, M., Mizuta, S., and Kayano, H., **"Evaluation of the Upper Shelf Energy for Ferritic Steels from Miniaturized Charpy Specimen Data,"** *Effects of Radiation on Materials: 17th International Symposium, ASTM STP 1270,* David S. Gelles, Randy K. Nanstad, Arvind S. Kumar, and Edward A. Little, Eds., American Society for Testing and Materials, 1996.

ABSTRACT: In order to develop the methodology to evaluate the upper shelf energy (USE) for full size Charpy specimens of ferritic steels from miniaturized specimen data, the effects of specimen size and notch dimensions (notch root radius and notch depth) on the USE were studied for high strength ferritic steels with relatively low USE values of 135 and 107 J. The USE for miniaturized specimens, normalized by Bb^2 or $(Bb)^{3/2}$ (B is the specimen thickness, b is the ligament size), was essentially independent of specimen size and tended to decrease with increasing the elastic stress concentration factor, K_t, but the K_t dependence was not significant. The normalized USE for full size specimens was considerably lower than that for miniaturized specimens. A general relationship was found that allows to determine the USE of full size specimens of ferritic steels directly from miniaturized specimen data.

KEYWORDS: small specimen technology, Charpy impact test, notch root radius, notch depth, USE, elastic stress concentration factor, miniaturized specimen, full size specimen

The small specimen technology is required in mechanical testing of irradiated materials because of very limited irradiation volume in currently available high flux reactors and future accelerator-based high energy neutron sources. The technology also contributes to the

[1]Associate professor, research associate and professor, respectively, the Oarai Branch, Institute for Materials Research, Tohoku University, Oarai, Ibaraki-ken 311-13, Japan.

[2]Manager and research scientist, respectively, Materials Monitoring Section, Fuels and Materials Division, Oarai Engineering Center, Power Reactor and Nuclear Fuel Development Corporation, Oarai, Ibaraki-ken 311-13, Japan.

Copyright© 1996 by ASTM International www.astm.org

minimization of radioactive wastes after post irradiation examination (PIE) as well as the minimization of inhomogeneity in flux and temperature distributions during irradiation. For Charpy impact testing, which has most widely been used for evaluating irradiation embrittlement of ferritic steels, it is well known that specimen miniaturization causes a downward shift in both the ductile-to-brittle transition temperature (DBTT) and upper shelf energy (USE). Many attempts have been made to determine the USE and DBTT of full size specimens by using one third sized [1-9] or more miniaturized specimens [10-13]. However, our current knowledge is still far from the final goal.

Some of the present authors developed an instrumented Charpy impact machine that permits to obtain reproducible load-displacement curves for miniaturized specimens as small as 1 by 1 by 20 mm as well as full size specimens [10, 14]. By using the machine they studied the effects of specimen size and notch dimensions on impact test results for differently sized miniature specimens. The specimens used were of the dimensions 3.3 by 3.3 by 23.6 mm, 2.0 by 2.0 by 20 mm, 1.5 by 1.5 by 20 mm and 1.0 by 1.0 by 20 mm of JFMS (Japanese ferrite/martensite dual phase steel) unirradiated and irradiated to 3×10^{22} n/m^2 ($E > 0.1$ MeV) in JMTR (Japan Materials Testing Reactor) in JAERI [11, 12]. It was shown that the DBTT of the miniaturized specimens was significantly affected by notch root radius and notch depth, some of the DBTTs exceeding that of full size specimens, whereas the USE was dependent only on notch depth, or ligament size. These unirradiated and irradiated JFMS have relatively high USE and low DBTT values and therefore it is necessary to examine the effects of specimen size and notch dimensions for ferritic steels with relatively low USE and high DBTT.

The objective of the present paper is to study the USE of such ferritic steels as functions of specimen size and notch dimensions and show a relationship that allows the determination of the USE of full size specimens from the miniaturized specimens data.

EXPERIMENTAL

The materials used in this study are unaged and aged high-strength ferritic steels, which are designated 2WFK-U and 2WFK-A, respectively, and have higher DBTT and lower USE than unirradiated and irradiated JFMS. The chemical composition of 2WFK is specifically 11Cr-0.5Mo-2.0W-0.2V (weight percent). The heat treatment for aging was made at 973K for 2000 h. From these materials full size and miniaturized Charpy specimens were prepared in which the axis of the specimen lay in the rolling direction (LT orientation). The miniaturized specimens were of four different sizes, 3.3 by 3.3 by 23.6 mm, 2.0 by 2.0 by 20 mm, 1.5 by 1.5 by 20 mm and 1.0 by 1.0 by 20 mm. They are here called 3.3 mm, 2 mm, 1.5 mm and 1 mm specimen, respectively. Each of them had three variations in notch dimensions; the nominal and measured values are tabulated in Table 1. The measured value corresponds to the average. In this study the value of notch angle was made constant because our previous study on unirradiated JFMS [11] showed that the effect of notch angle on Charpy impact test results is not significant. A notch root radius of approximately 0.02 mm is the minimum value that can be achieved by machining. A very large notch root radius of 0.25 mm for 1 mm specimens is specially introduced to examine the effect of less sharp notch on the impact test results.

All of the full size and miniaturized specimens were subjected to instrumented Charpy impact tests at temperatures from 81 to 450 K using a specially designed electrically controlled hydraulic machine. The details of the machine and the procedures developed for testing were described earlier [14]. The span was set at 40 mm for full size specimens, 15 mm for 3.3 mm specimens, 12.5 mm for the other miniaturized specimens. The values of USE and DBTT were determined from total absorbed energy vs temperature curves of all specimens tested.

TABLE 1--Dimensions of V-notch in differently sized Charpy specimens of unaged 2WFK (U-1~13) and aged 2WFK (A-1~7).

Specimen type	Size	Notch root radius ρ (mm)		Notch depth a (mm)		Notch angle θ (degree)	
		Nominal	Measured	Nominal	Measured	Nominal	Measured
U-1	Full Size	0.25	0.240	2.00	2.00	45	45.2
U-2		0.08	0.080	0.51	0.501	30	30.6
U-3	3.3 mm	0.02	0.019	0.51	0.502	30	29.3
U-4		0.02	0.022	0.66	0.651	30	29.1
U-5		0.08	0.082	0.40	0.396	30	31.0
U-6	2.0 mm	0.02	0.021	0.40	0.396	30	29.0
U-7		0.02	0.024	0.60	0.604	30	29.3
U-8		0.08	0.080	0.30	0.303	30	31.4
U-9	1.5 mm	0.02	0.021	0.30	0.304	30	30.1
U-10		0.02	0.020	0.45	0.447	30	30.2
U-11		0.25	0.250	0.20	0.192	---	---
U-12	1.0 mm	0.05	0.045	0.20	0.203	30	31.3
U-13		0.02	0.023	0.30	0.292	30	29.4
A-1	Full Size	0.25	0.234	2.00	1.993	45	45.1
A-2	3.3 mm	0.08	0.079	0.51	0.509	30	29.2
A-3	2.0 mm	0.02	0.022	0.60	0.606	30	29.5
A-4	1.5 mm	0.08	0.082	0.30	0.299	30	29.8
A-5		0.02	0.021	0.45	0.453	30	29.6
A-6	1.0 mm	0.25	0.234	0.20	0.201	---	---
A-7		0.02	0.020	0.30	0.304	30	29.8

RESULTS AND DISCUSSION

Figure 1 gives the comparison of impact properties for full size specimens of 2WFK-U, 2WFK-A, and the unirradiated and irradiated JFMS. It is seen that 2WFK-U and 2WFK-A exhibit considerably lower USE and higher DBTT than JFMS.

Figures 2 to 4 are examples of total absorbed energy vs test temperature curves for full size and miniaturized specimens of 2WFK-U and 2WFK-A. Notch dimensions in the figures are the nominal values shown in Table 1. It is obvious from the figures that the impact properties of miniaturized specimens depend on notch dimensions, i. e., the ductile-to-brittle transition behavior, thus the DBTT, changes depending on notch depth and notch root radius. On the other hand, the USE is dependent on notch depth, but not on notch root radius, except for the case of extremely large notch root radius of 0.25 mm in Figs. 3(b) and

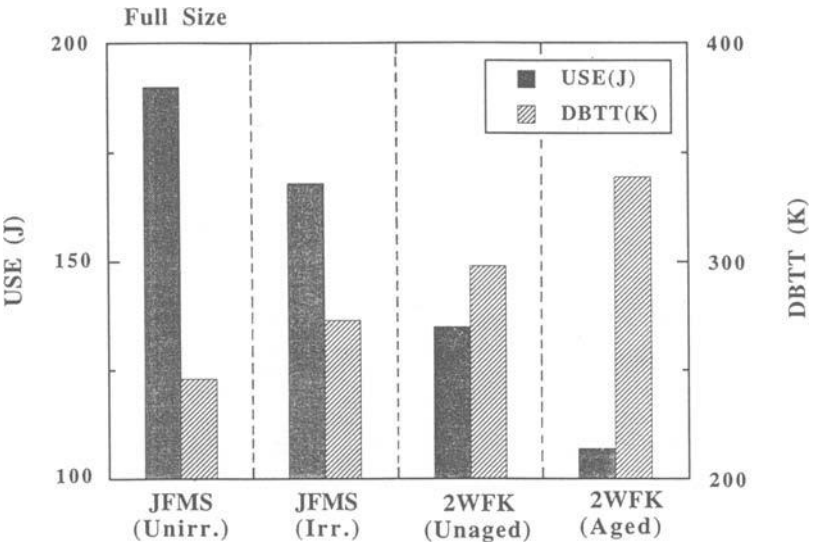


FIG. 1--Comparison of USE and DBTT for full size specimens of unirradiated and irradiated JFMS and unaged and aged 2WFK.

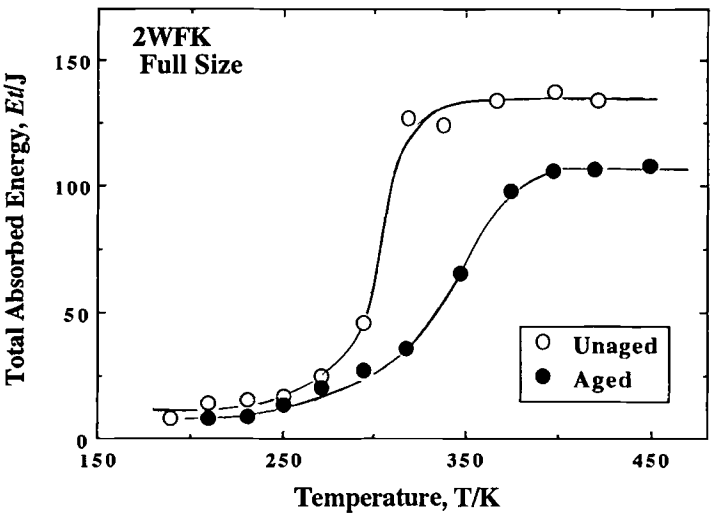


FIG. 2--Temperature dependence of total absorbed energy for full size specimens of unaged and aged 2WFK.

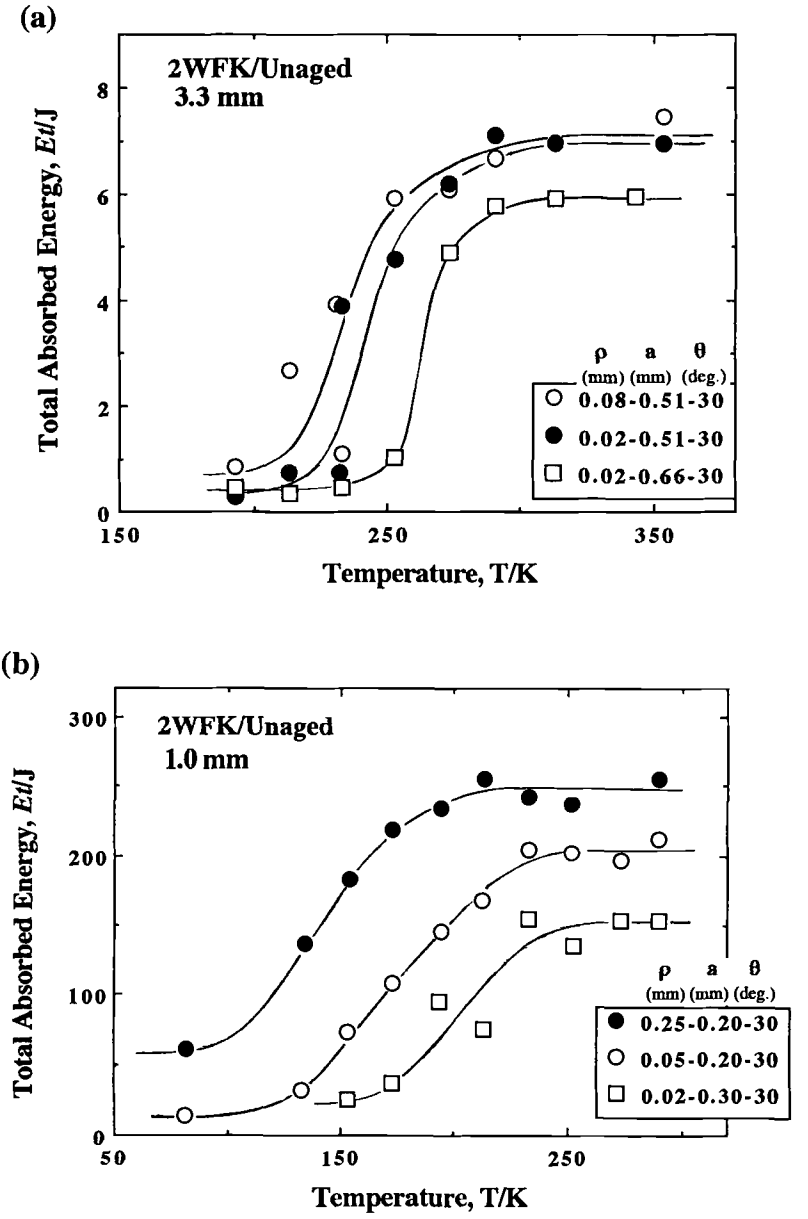


FIG. 3--Notch dimension dependence of total absorbed energy vs temperature curves for 3.3 mm (a) and 1.0 mm (b) specimens of unaged 2WFK.

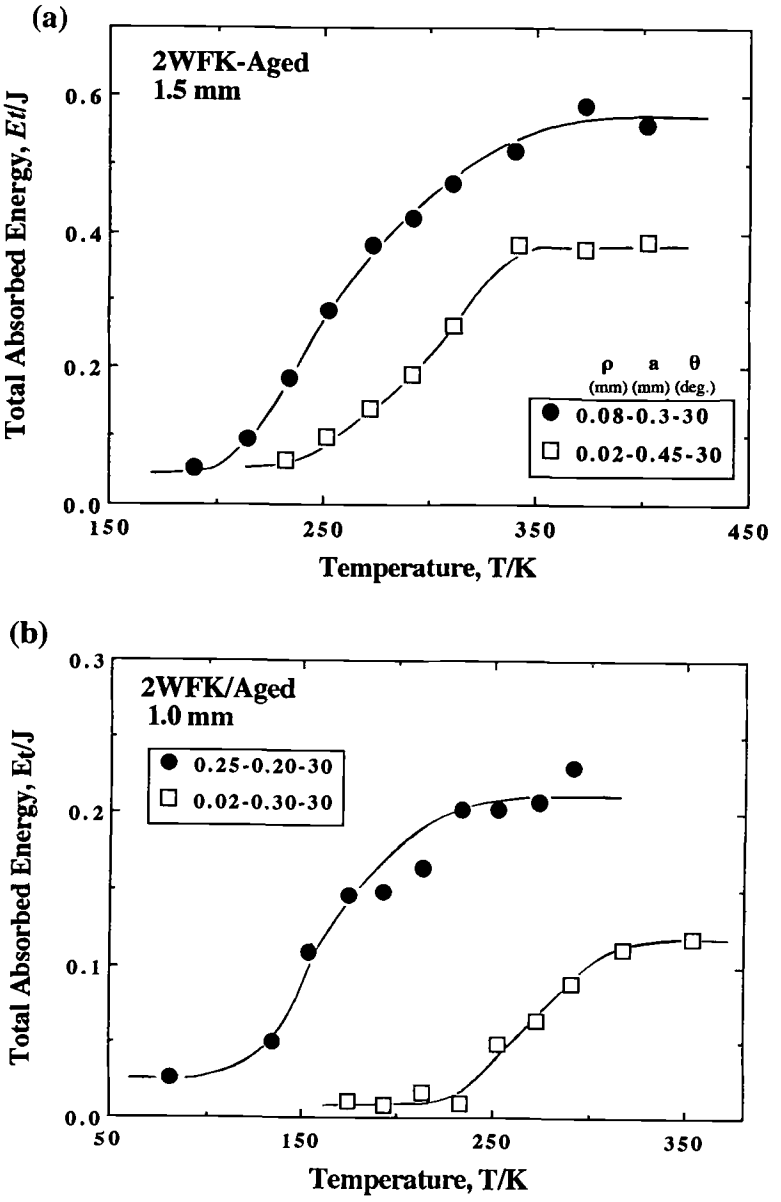


FIG. 4--Notch dimension dependence of total absorbed energy vs temperature curves for 1.5 mm (a) and 1.0 mm (b) specimens of aged 2WFK.

4(b), where the USE has an appreciable dependence on notch root radius. This trend is essentially the same as that observed in unirradiated and irradiated JFMS [11, 12].

The values of USE and DBTT based on energy absorption were determined and are listed in Table 2. The DBTT was calculated as the temperature of one half the USE.

TABLE 2--Values of unnormalized and normalized USE, DBTT and elastic stress concentration factor, K_t, for Charpy specimens of unaged and aged 2WFK.

Specimen type	Size	Kt	USE (J)	USE/$(Bb)^{3/2}$ (J/mm^3)	USE/Bb^2 (J/mm^3)	DBTT (K)
U-1	Full size	3.80	135.3	0.189	0.211	298
U-2		3.55	7.22	0.258	0.281	235
U-3	3.3 mm	6.45	7.02	0.251	0.273	242
U-4		8.00	5.90	0.230	0.257	261
U-5		3.27	1.45	0.254	0.284	229
U-6	2.0 mm	5.57	1.43	0.249	0.279	243
U-7		7.04	1.03	0.219	0.262	246
U-8		2.90	0.681	0.282	0.315	188
U-9	1.5 mm	4.99	0.657	0.272	0.304	212
U-10		6.27	0.461	0.270	0.279	222
U-11		1.70	0.245	0.343	0.383	127
U-12	1.0 mm	3.11	0.205	0.286	0.320	172
U-13		4.37	0.150	0.256	0.306	198
A-1	Full size	3.77	107.3	0.150	0.168	339
A-2	3.3 mm	3.57	5.51	0.197	0.215	289
A-3	2.0 mm	8.57	0.867	0.185	0.221	305
A-4	1.5 mm	2.92	0.554	0.229	0.257	254
A-5		6.30	0.381	0.223	0.231	291
A-6	1.0 mm	2.05	0.211	0.294	0.329	264
A-7		4.76	0.115	0.197	0.235	158

In a previous paper we showed that when all of the USE for miniaturized specimens of unirradiated JFMS were normalized by Bb^2 or $(Bb)^{3/2}$ (B is the specimen thickness, b is the ligament size), the normalized USE was independent of specimen size and notch dimension and agreed with that of full size specimens within the range of ±15% [11]. These volumetric parameters were originally employed by Corwin and coworkers [3] and are known to be related to the extent of plastic deformation below the notch after general yield or an approximation of the volume of plastic deformation at the crack tips [5, 7]. On the other hand, Louden et al. [7] proposed that when full size USE values are below approximately 150J, the normalizing of USE by Bb^2/LK_t (L is the span, K_t is the elastic stress concentration factor) may lead to a better correlation than that by Bb^2. In this study, therefore, all of the measured USE values were normalized by Bb^2 or $(Bb)^{3/2}$ and were plotted against K_t (Figs. 5 and 6). Here we used the value of K_t reported by Nishida [15].

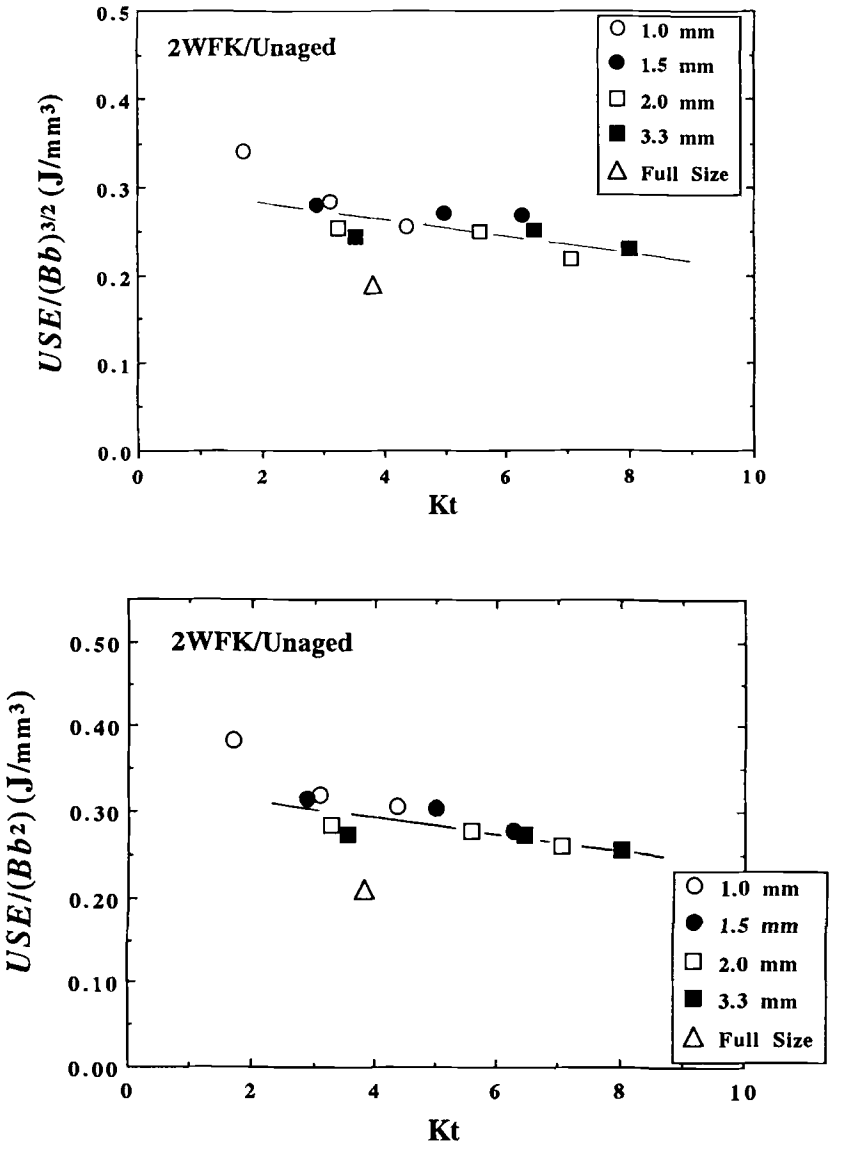


FIG. 5--Dependence of normalized USE on elastic stress concentration factor K_t for full size and miniature specimens of unaged 2WFK.

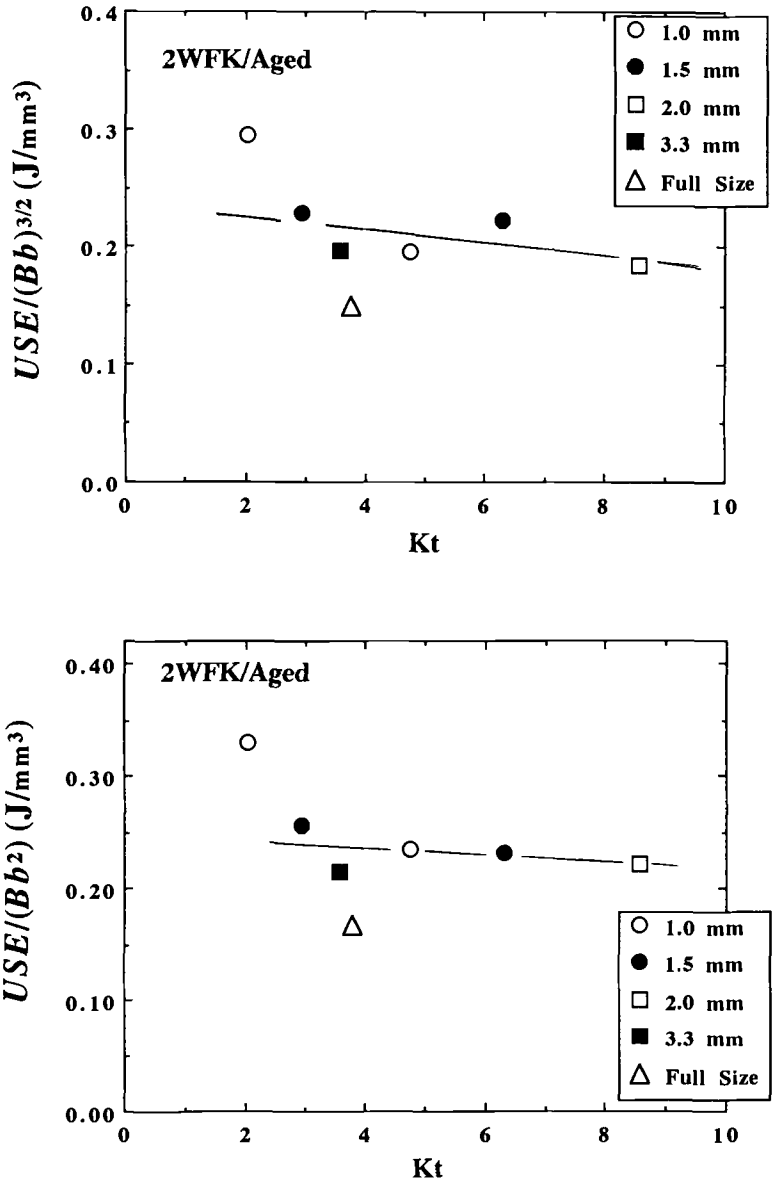


FIG. 6--Dependence of normalized USE on elastic stress concentration factor K_t for full size and miniature specimens of aged 2WFK.

The reason why the K_t values by Nishida were used instead of the well known Neuber's formula [16] was described in a previous paper [11] and is here again mentioned: The previous experimental result that the DBTT of unirradiated JFMS rose with increasing notch depth and decreasing notch root radius may indicate that Kt increases as the notch depth increases and notch root radius decreases. However, in the Neuber's formulae cited so far, Kt increases with increasing ligament size which is the minimum specimen width, thus increases with decreasing notch depth and with decreasing notch root radius. This discrepancy in the effect of notch depth is probably due to the fact that the Neuber's formulae were theoretically obtained for a very wide plate having a very deep notch, where not the notch depth but the ligament size is important. In the present case of notch depth being 20-30% of the specimen width, however, the effect of notch depth will be more significant than that of ligament size. In addition, the Neuber's formulae do not incorporate the effect of notch angle.

It is seen from the figures that for 2WFK-U and 2WFK-A the normalized USE of the miniaturized specimens appears to be independent of specimen size except for the 1 mm specimen the notch root radius of which was as large as 0.25 mm. This means that the observed dependence of unnormalized USE on specimen size resulted from the dependence of the USE on ligament size and the higher normalized USE of the 1 mm specimen indicates that the estimated fracture volume used as a normalization parameter, Bb^2 or $(Bb)^{3/2}$, is an underestimate and that the actual fracture volume is larger, as was discussed in unirradiated JFMS [11]. Three results that are not observed in unirradiated JFMS are noticeable. One is that the normalized USE of miniaturized specimens tends to decrease with increasing Kt. The Kt dependence of normalized USE is somewhat higher than that observed in irradiated JFMS [12]. However, one can easily see that if Bb^2/LK_t is used as a normalizang parameter instead of Bb^2, the difference between the normalized USE for each size of Charpy specimens becomes much more significant (Fig. 7). Second is that the plot of USE/Bb^2 against Kt appears to give less data scattering for each size of miniaturized specimens than the plot of USE/$(Bb)^{3/2}$ against Kt. Quite similar result was also obtained in neutron irradiated JFMS. This result may be attributed to the fact that Bb^2 always gives smaller volume than $(Bb)^{3/2}$. Third is that the normalized USE for full size specimens does not agree with that of miniaturized specimens; the former is considerably lower than the latter. The ratio of the full size to miniature normalized USE for 2WFK is lower than that for irradiated JFMS. This indicates that the normalization parameter, Bb^2, is an overestimate of the fracture volume for full size specimens of these ferritic steels and that the actual fracture volume should be smaller. These results suggest that the observed difference in the effect of specimen size on the USE between the different alloy and irradiation conditions occurs by a larger reduction in specimen volume associated with fracture for full size specimens than predicted using the volumetric parameters Bb^2 or $(Bb)^{3/2}$.

To demonstrate this concept, the ratio, α, of the normalized USE by Bb^2 of full size specimens to that of miniaturized specimens was calculated for 2WFK-U and 2WFK-A. Figure 8 shows α for miniaturized specimens except for the 1 mm specimen having a large notch root radius of 0.25 mm as a function of the unnormalized full size USE. In the figure the results on unirradiated and irradiated JFMS are included. It should be noted that α decreases with decreasing unnormalized USE for full size specimens and their relationship appears to be represented by a curve that is concave upward than by a linear one. Such a relationship is essentially independent of specimen size. Most of the miniature specimen data reported to date in the literature are for 3.3 mm specimen. Therefore α for 3.3 mm specimens was calculated for all of the ferritic steels reported to date in the literature. The results are listed in Table 3 including 2WFK and unirradiated and irradiated JFMS, where the value of α given is for a normalization factor of Bb^2. Figure 9 shows α against the

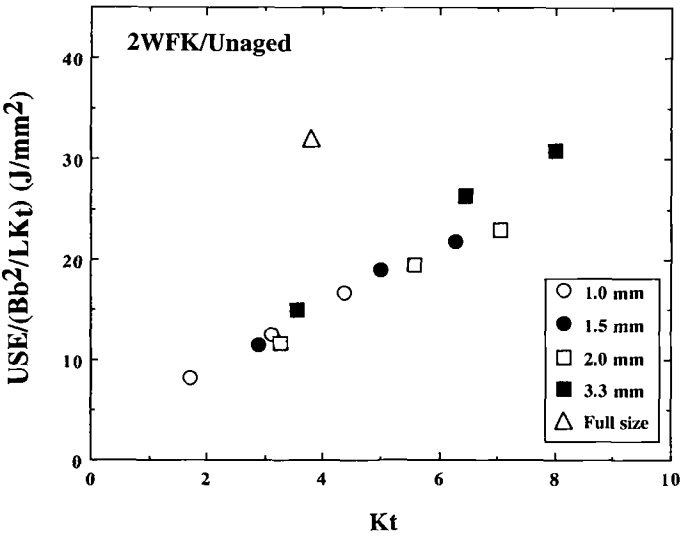


FIG. 7--Plot of USE normalized by Bb^2/LK_t against elastic stress concentration factor K_t for full size and miniature specimens of unaged 2WFK.

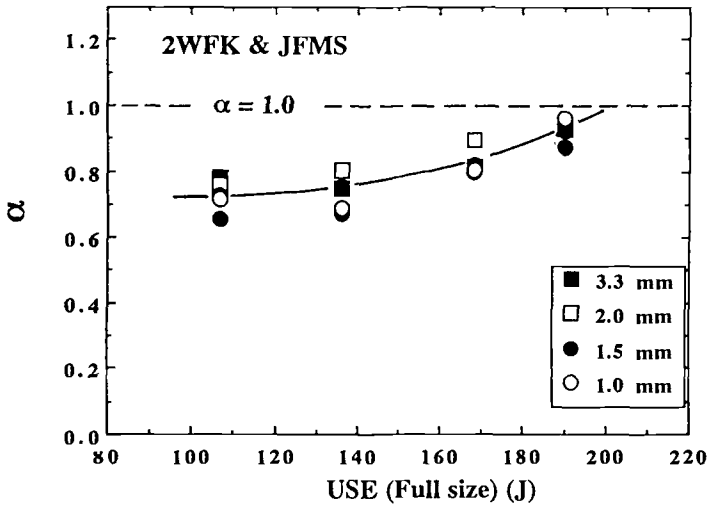


FIG. 8--Plot of the ratio, α, of USE/Bb^2 of full size specimens to that for miniature specimens against the unnormalized USE of full size specimens in unaged and aged 2WFK, including the results of unirradiated and irradiated JFMS.

unnormalized full size USE for the data given in Table 3. It is obvious that α increases monotonically with increasing full size USE without saturating to $\alpha = 1$. The relationship between α and unnormalized USE of full size specimens is again represented by a curve that is concave upward, except for precracked HT-9 [7]. In the precracked HT-9, the ligament size was assumed to be the same as that for notched (un-precracked) specimens [7], suggesting that there is a possibility of overestimation of Bb^2 which can make the data point shift away from the solid curve. Finally, in order to evaluate the USE of full size specimens from that of miniaturized specimens we replotted the unnormalized USE of full size specimens against the normalized USE of miniaturized (third size) specimens. The result is shown in Fig. 10. The unnormalized USE of full size specimens is seen to be uniquely related to the normalized USE of miniaturized specimens, as represented by a solid curve. The relationship is approximately expressed by

$$(USE)_{full} = 1260 \times (USE/Bb^2)^2_{mini} + 165 \times (USE/Bb^2)_{mini} + 8,$$

where the units of USE and B or b are J and mm, respectively. Therefore we can say that the USE for full size specimens of ferritic steels can be approximately evaluated directly from the miniaturized specimen by using the above relationship. This relationship also means that the effect of specimen size on the USE can be understood in terms of the specimen volume associated with fracture. Therefore, the next step is to evaluate the actual fracture volume to explain the observed relationship.

CONCLUSION

In order to develop the methodology to evaluate the upper shelf energy (USE) for full size Charpy specimens of ferritic steels from miniaturized specimen data, the effects of specimen size and notch dimensions (notch root radius and notch depth) on the USE were investigated for unaged and aged ferritic steels, designated 2WFK-U and 2WFK-A, having relatively low USE values of 135 and 107 J, respectively. Miniaturized specimens were of four different sizes, 3.3 by 3.3 by 23.6 mm, 2.0 by 2.0 by 20 mm, 1.5 by 1.5 by 20 mm and 1.0 by 1.0 by 20 mm and each of them had three variations in notch dimensions. All of the full size and miniaturized specimens were subjected to instrumented Charpy impact tests at temperatures from 81 to 450 K.

The USE for the miniaturized specimens, normalized by Bb^2 or $(Bb)^{3/2}$ (B is the specimen thickness, b is the ligament size), was essentially independent of specimen size and tended to decrease with increasing the elastic stress concentration factor, K_t. The Kt dependence, however, was not significant. The normalization parameter of Bb^2 appeared to give less data scattering for each size of miniaturized specimens than that of $(Bb)^{3/2}$. The normalized USE for full size specimens was lower than that for miniaturized specimens, and the ratio of the full size to miniature normalized USE decreased monotonically with decreasing USE for full size specimens. The plot of full size USE against the normalized USE for the third size specimens of ferritic steels reported to date in the literature showed that the former was uniquely related to the latter. The relationship was approximately expressed by

TABLE 3--Values of USE and normalized USE for full size and 3.3 mm specimens, together with the ratio, α, of USE/Bb^2 for full size specimens to that for 3.3 mm specimens in unaged and aged 2WFK and other ferritic steels reported in the literature.

	Full Size Specimens			Third-Size Specimens			
Alloy	USE (J)	USE/(Bb)3/2 (J/mm3)	USE/Bb2 (J/mm3)	USE (J)	USE/(Bb)3/2 (J/mm3)	USE/Bb2 (J/mm3)	α
9Cr-1Mo-V-Nb Norm & Temp. LT [4]	262	0.366	0.409	9.7	0.347	0.378	1.08
9Cr-1Mo-V-Nb Norm & Temp. TL [4]	200	0.277	0.313	8.8	0.315	0.343	0.913
9Cr-1Mo-V-Nb Quenched LT [4]	111	0.153	0.173	5.7	0.204	0.222	0.779
9Cr-1Mo-V-Nb Quenched TL [4]	72	0.101	0.113	5.1	0.183	0.199	0.568
HT-9 notched [7]	129	0.180	0.202	6.0	0.209	0.227	0.890
HT-9 precrack [7]	44	0.062	0.069	2.0	0.070	0.076	0.911
A302 [5]	62	0.086	0.097	3.4	0.134	0.150	0.647
A508 [5]	118	0.165	0.184	6.5	0.253	0.284	0.648
A508 [5]	68	0.095	0.106	3.9	0.151	0.169	0.627
9Cr-1W [6]	259	0.362	0.405	10.8	0.387	0.420	0.964
9Cr-2W [6]	245	0.342	0.383	9.8	0.351	0.381	1.005
9Cr-4W [6]	221	0.309	0.345	8.8	0.315	0.343	1.006
2.25Cr-W (V) [8]	245	0.342	0.383	9.4	0.328	0.355	1.083
	224	0.313	0.350	9.7	0.340	0.366	0.953
	278	0.389	0.434	9.6	0.335	0.363	1.201
	272	0.380	0.425	9.7	0.339	0.366	1.162
5Cr-2W-V [8]	245	0.342	0.383	10.0	0.349	0.378	1.018
9Cr-W (Mo) [8]	216	0.302	0.338	9.4	0.328	0.355	0.956
	255	0.356	0.398	9.7	0.339	0.366	1.088
	262	0.366	0.409	9.7	0.339	0.366	1.117
	200	0.280	0.313	8.8	0.307	0.332	0.946
12Cr-W (Mo) [8]	192	0.268	0.300	9.0	0.314	0.340	0.886
	115	0.161	0.180	5.9	0.206	0.223	0.810
JFMS Unirr. [11]	190	0.265	0.313	8.2	0.295	0.333	0.898
JFMS Irr. [12]	168	0.235	0.263	8.3	0.297	0.323	0.791
2WFK Unaged	135	0.189	0.211	7.2	0.258	0.281	0.751
2WFK Aged	107	0.150	0.168	5.5	0.197	0.215	0.781

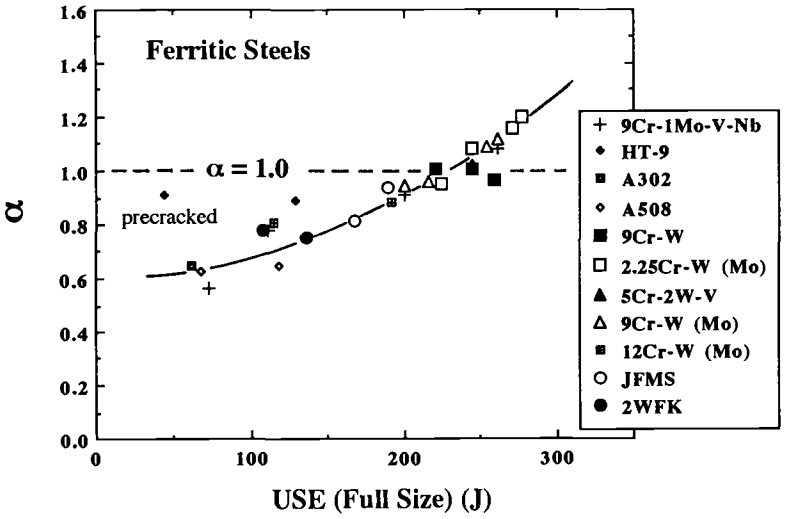


FIG. 9--Plot of the ratio, α, of USE/Bb^2 of full size specimens to that for 3.3 mm specimens against the unnormalized USE of full size specimens in all of the ferritic steels reported to date in the literature.

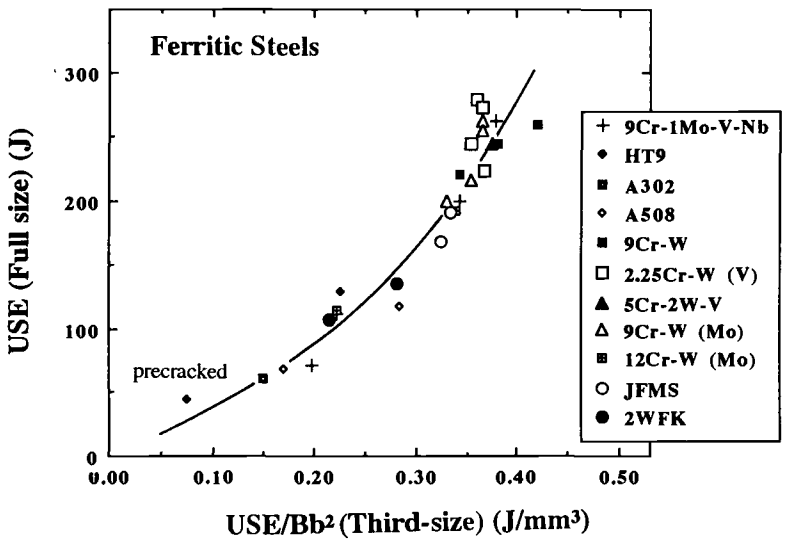


FIG. 10-- Plot of the USE of full size specimens against the USE/Bb^2 of third size specimens in all of the ferritic steels reported to date in the literature.

$$(USE)_{full} = 1260 \times (USE/Bb^2)^2_{mini} + 165 \times (USE/Bb^2)_{mini} + 8,$$

where the units of USE and B or b are J and mm, respectively. This relationship allowed to determine the USE of full size specimens directly from the miniaturized specimen data.

REFERENCES

[1] Hu, W. L. and Gelles, D. S., Proc. Conf. On Ferritic Alloys for Use in Nuclear Energy Technologies, Snowbird, UT, 1983, p. 631.

[2] Hu, W. L., HEDL-SA-2947-FP, 1983.

[3] Corwin, W. R., Klueh, R. L. and Vitek, J. M., J. Nucl. Mater., Vol. 122&123, 1984, P 343.

[4] Corwin, W. R. and Houghland, A. M., The Use of Small Scale Specimens for Testing Irradiated Materials, ASTM ST 888, Ed. Corwin, W. R. and Lucas, G. E., American Society for Testing and Materials, Philadelphia, 1986, p. 325.

[5] Lucas, G. E., Odette, G. R., Sheckherd, J. W., Mcconnell, P. and Perrin, J., The Use of Small Scale Specimens for Testing Irradiated Materials, ASTM STP 888, Ed. Corwin, W. R. and Lucas, G. E., American Society for Testing and Materials, Philadelphia, 1986, p.305.

[6] Abe, F., Noda, T., Araki, H., Okada, M., Narui, M. and Kayano, H., J. Nucl. Mater., Vol. 150, 1987, p 292.

[7] Louden, B. S., Kumar, A. S., Garner, F. A., Hamilton, M. L. and Hu, W. L., J. Nucl. Mater., Vol. 155-157, 1988, p 662.

[8] Alexander, D. J. and Klueh, R. L., Charpy Impact Test: Factors and Variables, ASTM STP 1072, Ed. Holt, J. M., American Society for Testing and Materials, Philadelphia, 1990, p.179.

[9] Kumar, A. S., Louden, B. S., Garner, F. A. and Hamilton, M. L., Small Specimen Test Techniques, ASTM STP 1204, American Society for Testing and Materials, Philadelphia, 1993, p. 47.

[10] Kayano, H., Kurishita, H., Kimura, A., Narui, M., Yamazaki, M. and Suzuki, Y., J. Nucl. Mater., Vol. 179-181, 1991, p 425.

[11] Kurishita, H., Kayano, H., Narui, M., Yamazaki, M., Kano, Y. and Shibahara, I., Mater. Trans JIM, Vol. 34, 1993, p 47.

[12] Kurishita, H., Kayano, H., Narui, M. and Yamazaki, M., SCI. REP. RITU, A-Vol. 40, No. 1, 1994, p 97.

[13] Kurishita, H., Kayano, H., Narui, M. and Yamazaki, M., To be publishied in J. Nucl., Mater., 1994.

[14] Kayano, H., Kurishita, H., Narui, M. and Yamazaki, M., Ann. Chim. Fr. Vol. 16, 1991, p 309.

[15] Nishida, M., "Stress Concentration", 5th Ed., Morikawa Publishers, Tokyo, Japan, 1984, p. 572 (in Japanese).

[16] Neuber, H., "Theory of Notch Stresses", 2nd Ed., Splinger Publishers, Berlin, 1958, p. 71.

G. E. Lucas[1], G. R. Odette[1], K. Edsinger[1], B. Wirth[1], J. W. Sheckherd[1]

ON THE ROLE OF STRAIN RATE, SIZE AND NOTCH ACUITY ON TOUGHNESS: A COMPARISON OF TWO MARTENSITIC STAINLESS STEELS

REFERENCE: Lucas, G. E., Odette, G. R., Edsinger, K., Wirth, B., and Sheckherd, J. W., **"On the Role of Strain Rate, Size and Notch Acuity on Toughness: A Comparison of Two Martensitic Stainless Steels,"** *Effects of Radiation on Materials: 17th International Symposium, ASTM STP 1270,* David S. Gelles, Randy K. Nanstad, Arvind S. Kumar, and Edward A. Little, Eds., American Society for Testing and Materials, 1996.

ABSTRACT: The fracture resistance and micromechanisms of two tempered martensitic steels were characterized over a range of temperatures by both mechanical testing and quantitative fractography. HT-9 and F-82H undergo a fracture mode transition from quasi-cleavage at low temperature to microvoid coalescence at high temperature. The transition in HT-9 is rather gradual, and the transition in F-82H is extremely abrupt. While the toughness of F-82H was higher in all cases, differences between the two steels depended on test type, strain rate and temperature. The results not only demonstrate the inherent non-uniqueness of the so called ductile-to-brittle transition temperature (DBTT), but also call into question the use of Charpy data for ranking the relative performance of various alloys. The similarities in quasi-cleavage fracture and differences in ductile fracture are manifested in the fracture surfaces and are interpreted in terms of the underlying mechanisms and microstructures.

KEYWORDS: martensitic stainless steels, fracture, ductile fracture, quasi-cleavage, ductile-brittle transition temperature, fractography, fracture reconstruction

The demonstrated swelling resistance and high heat flux capacity make tempered martensitic (TM) steels a leading candidate alloy class for application to fusion reactor first wall and blanket structures. However, TM alloys undergo a change from nominally ductile to nominally brittle fracture below a so called ductile-to-brittle transition temperature (DBTT) that may be substantially increased by irradiation. Hence, radiation embrittlement is widely believed to be the major disadvantage of TM steels.

As we have shown elsewhere, however, there is no unique DBTT, and the defect tolerant capabilities of a material must be judged by more structurally relevant measures of

[1] Department of Mechanical Engineering, University of California, Santa Barbara, CA 93106-5070

Copyright© 1996 by ASTM International www.astm.org

strength and strain limits in the presence of cracks [1,2]. Developing and applying appropriate measures requires a more fundamental approach, based on an understanding of underlying fracture processes. To this end we have carried out a comprehensive series of mechanical property tests coupled with detailed fractographic analyses on two leading candidate TM steels which have been, or are being, characterized in a number of irradiation programs: namely, HT-9 and F-82H. HT-9 is a 12Cr-1Mo-W-V steel originally developed for fossil energy plants that has been investigated broadly for both fast reactor and fusion reactor applications [3]. F-82H is an optimized, reduced activation 8 Cr-2W-V steel specifically targeted for fusion applications [4]. It is the immediate precursor to a large International Energy Agency (IEA) heat that will be the focus of research on TM alloys in the next several years [5]. The objective of our study is to compare and contrast various macroscopic and microscopic measures of fracture resistance in the two steels and to interpret the results both in terms of fundamental mechanisms and structural implications.

EXPERIMENT

The composition of the electroslag refined (ESR) heat of HT-9 is given in Table 1. Although there is some ambiguity in the exact heat treatment, it has the microstructure and properties of ESR heat material that has been austenitized at 1050°C for 0.5 h and tempered at 760°C for 0.5h [6]. Previous analysis has shown that this steel has a tempered martensitic structure with prior austenite grains (PAG) of about 55 μm diameter containing martensite laths in packets of about 7-8 μm in diameter. The carbon content of HT-9 is relatively high at 0.23%. The matrix contains a fine scale distribution of Mo_2C and MC precipitates and coarser Cr-rich $M_{23}C_6$ and M_6C carbides. The lath, the lath packet and PAG boundaries are heavily decorated with (mostly $M_{23}C_6$) carbides typically less than 0.2μm in size; there is also a smaller population of relatively large (1μm) carbides along PAG boundaries; the boundary carbides are rich in Cr and contain significant amounts of iron and molybdenum.[7]

The composition of the F-82H steel, obtained courtesy of A. Hishinuma of Japan Atomic Energy Research Institute, is also shown in Table 1. Nickel, molybdenum and niobium contents have been minimized to achieve reduced neutron activation; and tungsten, vanadium and tantalum have been added as replacements -- viz., as strong carbide formers

TABLE 1 -- Compositions of HT-9 and F-82H

Steel	Composition (Wt %)										
	C	Mn	Si	Ni	Cr	Mo	V	W	Ta	S	P
HT-9	.23	.39	.17	.51	12.1	1.04	.28	.45	---	.003	.016
F-82H	.10	.5	.1	---	8.0	---	.2	2.0	.04	.003	.003

and for other metallurgical purposes such as grain size control. The carbon content of F-82H, at 0.10%, is significantly lower than in HT-9. The material was received as 25 mm thick plate which had been normalized at 1040°C for 0.5 h and tempered at 740°C for 1h. The reported microstructure consists of tempered martensite with a prior austenite grain size of about 120 μm. Boundary and matrix precipitation consists primarily of Cr-rich $M_{23}C_6$. Consistent with the lower carbon content, the boundary carbides tend to be finer (on average $\leq$0.15μm) and less numerous than those observed in the HT-9 [8,9]. Although not reported specifically for F-82H, microstructures of steels with similar compositions and heat treatments have been observed to contain significant populations of matrix and boundary carbides, which include, depending on steel composition M_6C (Ta and W-rich) and MC (V and Ta-rich) [10,11].

Round bar tensile specimens 3.2 mm in diameter by 25.4 mm in gage length were cut from the HT-9 plate in the transverse orientation. Flat miniature tensile specimens with gage sections 9 mm x 2 mm x 0.5 mm were punched from coupons cut from F-82H and lapped to 0.5 mm thickness. These miniature tensile specimens have provided data in good agreement with larger specimens in previous experiments [12]. Fracture specimens included standard ASTM E23 blunt-notched Charpy specimens (CVN), subsize Charpy (MCVN) specimens scaled by a factor of one-third in all dimensions, and pre-cracked three-point bend specimens. The three-point bend specimens (3PB) were fatigue pre-cracked at a final $\Delta K \leq 20$ MPa•m$^{1/2}$ to a depth (a) to width (W) ratio of a/W $\approx$ 0.5. They included full thickness (T) Charpy specimens (PCCV) and 0.2T, 0.4T and 0.6T bend bars. In the case of HT-9, 0.15 to 1T compact tension (CT) and disc compact tension (DCT) test specimens were also included in the test matrix.

Tensile tests on HT-9 were conducted at temperatures ranging from -101°C to 66°C at strain rates in the range 10^{-3} to 3 s^{-1} on a servo-hydraulic load frame. Tensile tests on F-82H were performed at strain rates of 10^{-3} s^{-1} over a temperature range of -196°C to 25°C and at 10^{-1} and 10s^{-1} at 25°C. Fracture tests were also carried out over a wide range of loading rates and temperatures from -196 to 350°C. Temperature control was achieved by a number of techniques ranging from a variety of baths to pre-cooling specimen/fixture assemblies. Impact tests were performed on both the CVN and PCCV specimens on an instrumented pendulum impact machine. The MCVN specimens were tested on a drop tower at somewhat lower (~5 times) impact velocities. In all cases load-time data were used to determine both the total and partitioned (e.g., initiation) energies; and for the PCCV specimens, the data were used to obtain either dynamic elastic (K_{Id}) or elastic-plastic toughness (K_{Jd}, assuming crack initiation at maximum loads) [13]. The static, pre-cracked 3PB, CT, and DCT specimens were tested at relatively low displacement rates (~0.008 mm/s) on a servo-hydraulic load frame. Linear elastic toughness, K_{Ic}, was determined according to ASTM Test Method for Plane Strain Fracture Toughness of Metallic Materials (E 399); and critical elastic-plastic energy release rates, J_{Ic}, were determined according to ASTM Test Method for J_{Ic}, A Measure of Fracture Toughness (E 813); in the latter case crack growth (Δa), if any, was measured by unloading compliance (PCCV and 3PB) or electric potential drop (CT, DCT) methods.[14] Some of the data on HT-9 have been taken from previous studies. [7,14-16]

Scanning electron microscopy (SEM) and confocal microscopy (CM) were performed on selected specimens to characterize details of the fracture process. The CM was used to generate quantitative, three dimensional topographic maps of the fracture surfaces. Maps of conjugate fracture surfaces were input to a fracture reconstruction (FR) technique to evaluate

the damage evolution/fracture sequence-of-events ahead of the crack tip as a function of crack tip opening displacement (δ). Details of the CM/FR method are described elsewhere.[17,18]

RESULTS

Mechanical Properties

Tensile and Charpy tests -- Uniaxial yield stress σ_y and ultimate tensile strength (UTS) are plotted in Figure 1 against a strain rate ($\dot{\varepsilon}$) compensated temperature parameter, $P_T = T(K)\log(10^8/\dot{\varepsilon})$. Although not a unique way of correlating tensile properties to temperature and strain rate, P_T has been found useful for other steels [19] and reasonably collapses the dynamic and static data for both HT-9 and F-82H. In spite of differences in composition and heat treatments, the strengths of these two steels are quite similar (note, on average the UTS for the HT-9 is about 50 MPa higher than for the F-82H). The uniform elongations (not shown) ranged from about 12% at room temperature to 15% at -100°C in the HT-9, and from about 7% at room temperature to 10% at -100°C in the F-82H. The strain hardening behavior was also similar, with exponents of about 0.1 to 0.15.

The total absorbed energy (E) as a function of test temperature (T) for the Charpy impact tests is shown in Figure 2a. The HT-9 data show a very broad transition from lower shelf (ending at about -100°C) to an upper (beginning at about 120°C) shelf energy of about 125 J. In contrast, the F-82H shows an extremely abrupt transition at about -50±10°C to an upper shelf energy of over 300 J, consistent with data reported elsewhere [9]. The DBTT indexed at 41J, T_{41}, is about 81°C higher in the HT-9 (25°C versus -56°C for the F-82H). However, the choice of 41J, where the fracture mode involves a mixture of cleavage and microvoid coalescence, as an index for a DBTT is arbitrary. Other DBTT values are obtained using alternate measures, such as: 1) 50% shear fracture appearance; 2) 35 mils (0.89 mm) lateral expansion; and 3) 50% of the upper shelf energy. Values for HT-9 and F-82HA for these various measures are tabulated and compared in Table 2. A more physically meaningful index for a DBTT is at an absorbed energy level of 10 J, T_{10}, which has been found to approximately correspond to the maximum temperature of linear elastic fracture.[20] The T_{10} for F-82H and HT-9 are virtually the same, about -60±5°C.

A better physical measure of fracture resistance is the energy expended up to the initiation of crack extension. Since it is generally difficult to define the exact initiation point, the initiation energy (E_i) is usually defined as the energy absorbed at maximum load [13]. Figure 2b shows that the E_i for F-82H also has an extremely abrupt transition compared to HT-9. The DBTT based on the highest temperature for cleavage initiation (evident as a sharp drop in load in the load-time curve) in blunt notched Charpy impact tests is about 60±6 and -43±3°C, respectively, for HT-9 and F-82H, a difference of about 103°C. Moreover, the ratio of upper shelf initiation energies for F-82H and HT-9 is considerably less than the ratio of total upper shelf energies.

Figure 2c shows the E-T curve for the MCVN tests. Here we have multiplied the actual E by a factor of 27 which is the appropriate continuum mechanics, self-similarity scaling factor for a 1/3-sized specimen. Based on the normalized 41J (≈ 1.5 actual) index, the DBTT's for HT-9 and F-82H are -35±5 and -100±5°C, respectively. Thus, in addition to

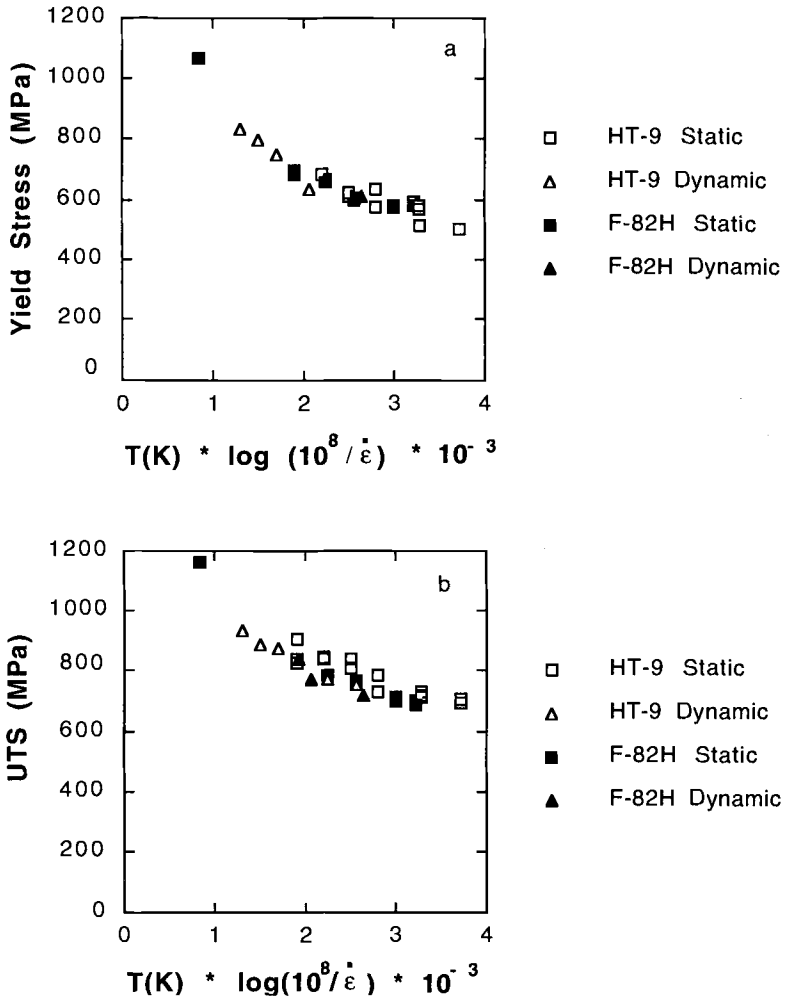


FIG. 1 -- Comparison of a) yield stresses and b) ultimate tensile strengths of HT-9 and F-82H as a function of strain-rate compensated temperature.

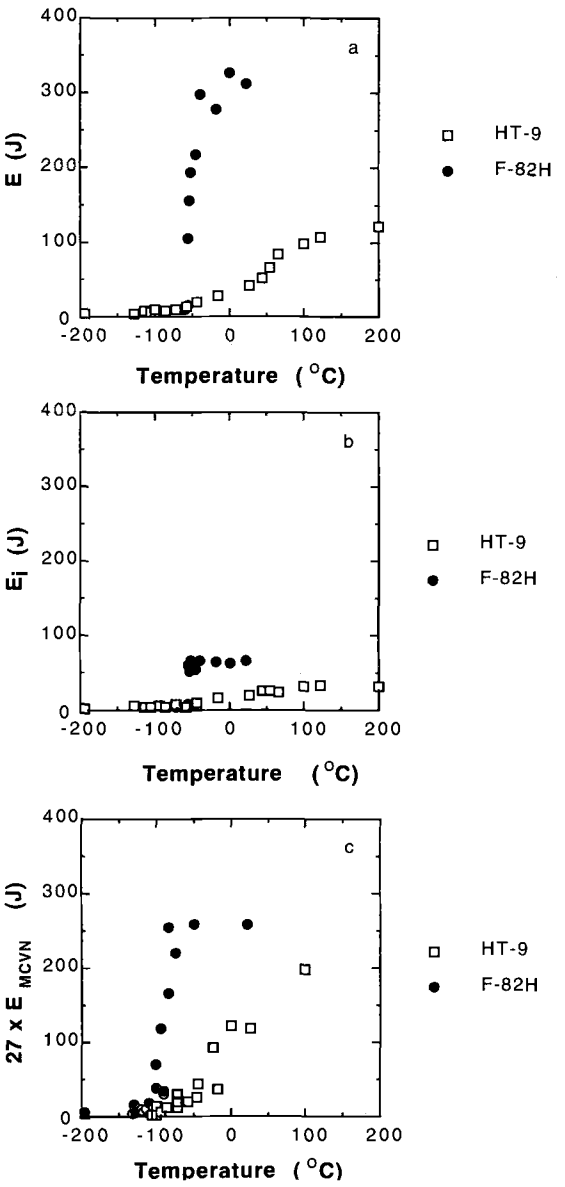


FIG. 2 -- a) Charpy impact energy curves, b) Charpy initiation energies as a function of test temperature, and c) MCVN energy curves for F-82H and HT-9.

TABLE 2 -- Comparison of DBTT Values for HT-9 and F-82H for Various Indices Obtained from Charpy Data

Index	DBTT (°C) HT-9	F-82H
41J absorbed energy	25 + 5	-56 + 5
10J absorbed energy	-60 + 5	-60 + 5
50% shear fracture appearance	34 + 5	-55 + 5
0.89 mm lateral expansion	119 + 5	-56 + 5
50% upper shelf energy	50 + 5	-50 + 5

giving different absolute values of DBTT, the MCVN and CVN tests also yield somewhat different measures of the relative advantage of F-82H based on the same normalized energy index, but for different geometries -- i.e., 65°C for the MCVN versus 81°C for the CVN. More elaborate interpretations of the MCVN data are available [1] but will not be pursued here.

At this point it is important to reiterate that there is no unique DBTT, and to note that any measure of a DBTT from the Charpy test is to some extent arbitrary and extrinsically mediated -- that is, dependent on the details of this particular test as well as the basic properties of the material. However, among the least meaningful indices is 41J of total absorbed energy. In general 41J represents a non-unique combination of two different and, in themselves, not fully defined fracture processes.

The difference between E and E_i represents the energy dissipated during crack propagation. In the upper shelf regime, E is dominated by this propagation energy (more than 70%), and it is larger in F-82H than HT-9. However, ductile tearing in Charpy specimens occurs under enormously complex conditions of massive deformation, loss of crack tip and lateral constraint and out-of-plane deflection in the vicinity of the compressed region under the striker. Hence, it is not surprising that efforts to relate the upper shelf energy to more meaningful measures of fracture resistance, such as upper shelf initiation toughness and tearing modulus, have met with limited success [21]. A potentially better relationship might be obtained between upper shelf toughness and the initiation energy for ductile tearing, since this parameter avoids many of the complications noted above.

Fracture Toughness -- While also beset with a number of questions concerning both measurement and application, fracture toughness clearly provides a far more meaningful and

direct measure of the stress and strain capacity of cracked structures. The variation of static fracture toughness with test temperature for the two steels in this study is shown in Figure 3. We have included some published estimates of the upper shelf toughness data for F-82H from Ref. 20. It is important to emphasize that the data in Figure 3 represent different measures of toughness (K_{Ic} and K_{Jc} and K_{JR})[2] based on, in a number of cases, small specimen tests that may not be strictly valid. However, our discussion will focus on a comparison of the overall K(T) curves rather than details of each data point. In the ductile fracture regime, the fracture toughness may not reach a constant upper shelf, but may exhibit a maximum with temperature. There are insufficient data at this point to characterize this temperature variation; nonetheless, the values of fracture toughness corresponding to ductile initiation can be compared. The HT-9 reaches a ductile initiation toughness of about 200 MPa•$m^{1/2}$ at about 20°C. The static ductile initiation toughness of F-82H is estimated to be on the order of 250 MPa•$m^{1/2}$. Notably, the ductile initiation toughness advantage of roughly 25% for F-82H versus HT-9 compares to a factor of 3 in Charpy upper shelf energy. A fairer comparison would be based on the square root of the Charpy energy; on this basis the square root of the total and initiation energies would predict an F-82H ductile initiation toughness advantage of 70% and 40%, respectively. In either case, such differences in high values of initiation toughness would be irrelevant to the design of thin-walled components.

It is also useful to characterize the transition temperatures indexed by toughness. While various indices could be chosen, fracture toughness is typically indexed at an elastic-plastic, cleavage-initiation level of 100 MPa•$m^{1/2}$. Unfortunately, there are only limited data

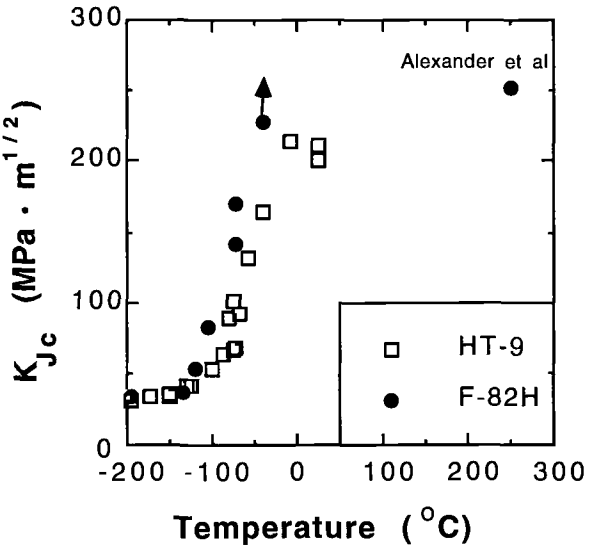


FIG. 3 -- Comparison of static fracture toughness as a function of test temperature.

---

[2] Here J-values have been converted based on the elastic equivalent $K = \sqrt{JE'}$ where E' is the plane strain modulus.

in the transition regime, particularly for F-82H. At -40°C the latter merely blunted up to the maximum available displacement. Hence, as indicated by the arrow in Figure 3, this represents a lower bound on the toughness in Charpy-sized specimens at this temperature; the value may be as high or higher than the toughness of about 250 MPa•m$^{1/2}$ at 250°C. Using these limited values as a guide, we estimate the 100 MPa•m$^{1/2}$ transition temperature for F-82H to be about -100°C±5°C, compared to -75°C ±10°C for HT-9.

The variation of dynamic fracture toughness with test temperature as determined from instrumented PCCV tests is shown in Figure 4. As expected the dynamic loading rates have shifted the curves up in temperature. The F-82H once again undergoes a very steep transition to an initiation toughness of about 310 MPa•m$^{1/2}$. There are insufficient data to establish the temperature dependence of toughness in the ductile fracture regime for the HT-9; however, the maximum toughness of 276 MPa•m$^{1/2}$ suggests the relative advantage of F-82H may be even smaller for dynamic ductile initiation toughness. A greater similarity in the behavior of the two materials is also reflected in the 100 MPa•m$^{1/2}$ transition temperature, which is about 0°C for F-82H compared to about 14°C for the HT-9. The corresponding differences between dynamic and static transition temperatures at 100 MPa•m$^{1/2}$ are about 89°C and 100°C for the HT-9 and F-82H, respectively.[3]

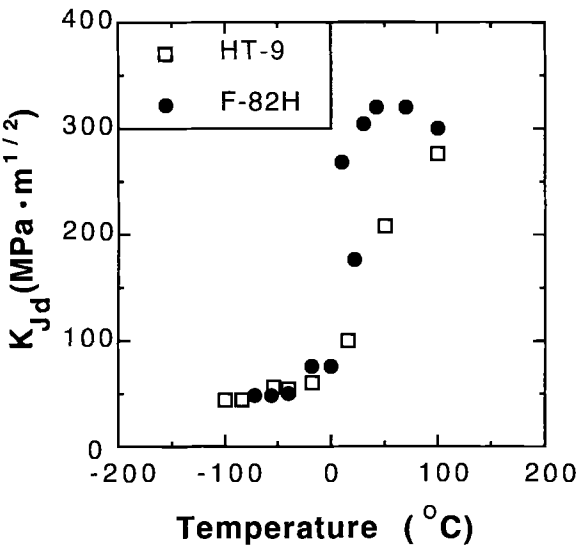


FIG. 4 -- Comparison of dynamic fracture toughness as a function of test temperature.

[3] The shift in the dynamic versus static toughness curves at 100 MPa$\sqrt{m}$ roughly coincides with the difference in temperatures at which the same value of σ_y is obtained in dynamic versus static tests.

Quantitative Fractography

The SEM and confocal microscopy/fracture reconstruction (CM/FR) results are described below for various fracture mechanism regimes. In the fracture reconstructions, the fracture sequences as a function of crack tip opening displacement (δ) are presented as top views down onto the crack plane, and in several cases as side views at the specimen center. In both views, the regions corresponding to material separation are shown in black and the regions corresponding to intact material are shown in white.

Lower Shelf /Lower Knee -- Although not shown, the fracture processes for both HT-9 and F-82H are very similar on the lower shelf below about 45 MPa•m$^{1/2}$, with fracture in both alloys occurring by quasi-cleavage. Quasi-cleavage also dominates the lower knee regime in both steels.

Figure 5a shows a typical SEM fractograph corresponding to a static test of HT-9 at -73°C in the lower knee region. Packets of cleavage facets are separated by thin regions of ductile tearing. The crack plane is characterized by an uneven surface, where out of plane areas of cleavage resulted in large multi-grain/packet "plugs" pulled out of "holes" in the conjugate surface. A corresponding CM/FR reconstruction of a 3PB specimen containing a crack with an a/W $\approx$ 0.4 is shown in Figure 6 for a toughness corresponding to a K_{Jc} of about 68 MPa•m$^{1/2}$. As the pre-crack blunts, stable multiple microcracking (black areas) initiates at a δ of about 14 μm and becomes completely unstable by about 20 μm. The critical condition appears to be controlled by a rapid coalescence of neighboring microcrack/tear ridge regions into a single or few large process zone cracks (PZC) extending over many PAG's. Assuming that $K_{J\delta} \approx (2\sigma_y\, \delta^* E')^{0.5}$, a critical crack opening of 19 μm corresponds to a $K_{J\delta}$ of about 80 MPa•m$^{1/2}$, in reasonable agreement with the mechanical test measurements of K_{Jc} at this temperature.

Figure 5b shows a typical SEM fractograph corresponding to a dynamic test of F-82H at -57°C; and Figure 7 shows a fracture reconstruction for a 3PB static test at -120°C. These tests represent K_{Jc}'s of about 47 and 54 MPa•m$^{1/2}$, respectively, closer to the lower shelf than the corresponding test on HT-9. However, as evident in Figure 5b, the fracture surface is similar; i.e., again cleavage facets separated by tear ridges and a tortuous crack path. Moreover, as seen in Figure 7, a similar sequence of events leading to unstable fracture is observed: the crack blunts up to about 3μm prior to initiation of a small amount of microcracking, followed by unstable crack propagation between about 7-9 μm. A critical δ^* of 8 μm corresponds to a $K_{J\delta}$ of about 53 MPa•m$^{1/2}$, in good agreement with the standard measures of K_{Jc} at this temperature. Note also that several intact ligaments remain in the crack wake (white regions at large δ in Figure 7). These correspond to "plugs" that have been geometrically interlocked in their "holes," resulting in the formation of "hinge" like features propped up out of the fracture plane.

Transition region -- As test temperature increases above the lower knee the same multiple microcrack coalescence instability process is observed. This is demonstrated by the CM/FR of a test on HT-9 at -57°C, shown in Figure 8. However, the tear ridges become thicker as shown in the corresponding SEM micrograph in Figure 9a, and more crack blunting is required to induce PZC instability conditions as seen in Figure 8. The critical crack opening of about 50 μm corresponds to a $K_{J\delta}$ of about 126 MPa•m$^{1/2}$, in good

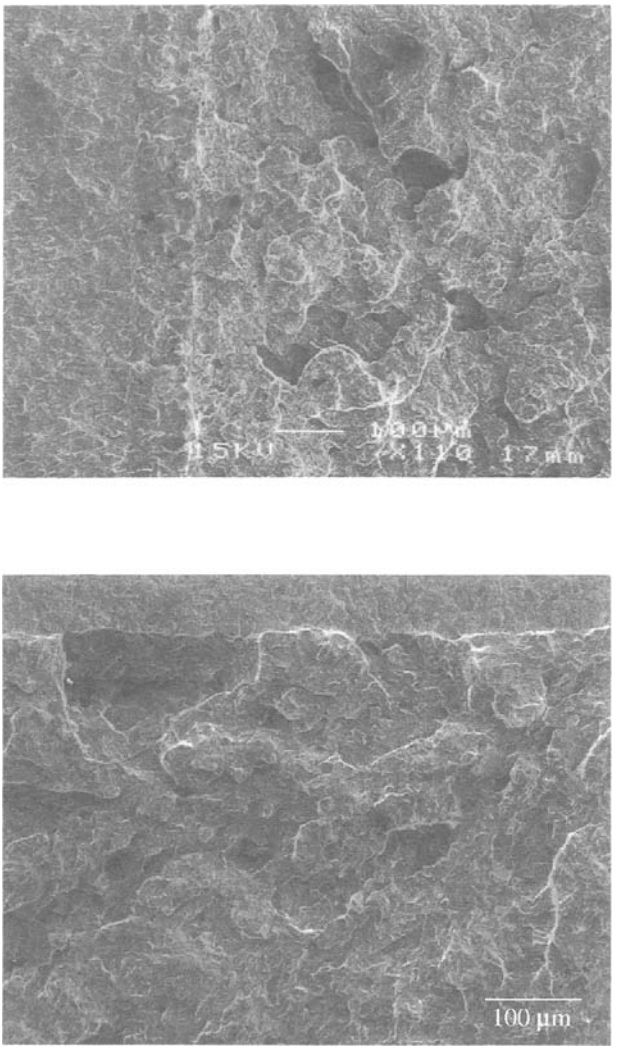


FIG. 5 -- a) SEM fractograph of HT-9 fracture specimen tested under static conditions at -73°C. b) SEM fractograph for an F-82H specimen tested under dynamic conditions at -57°C.

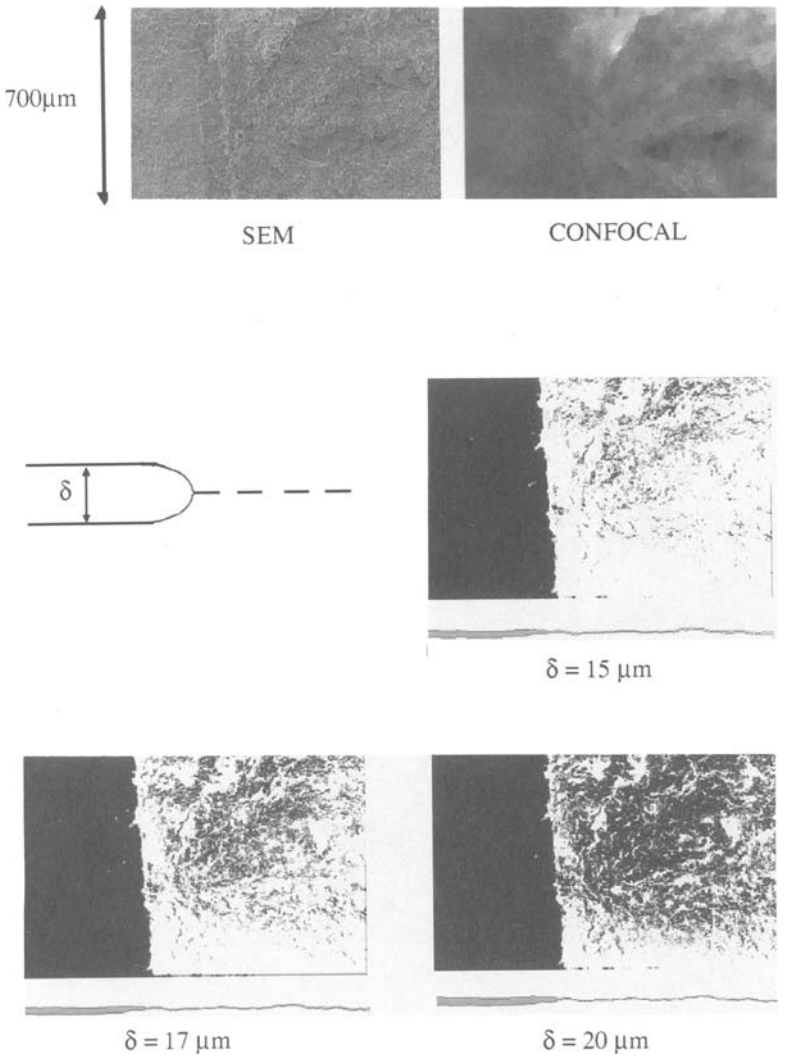


FIG. 6 -- Fracture surface reconstruction of an HT-9 3pB specimen containing a crack with a/w=0.4 tested under static conditions at -73°C.

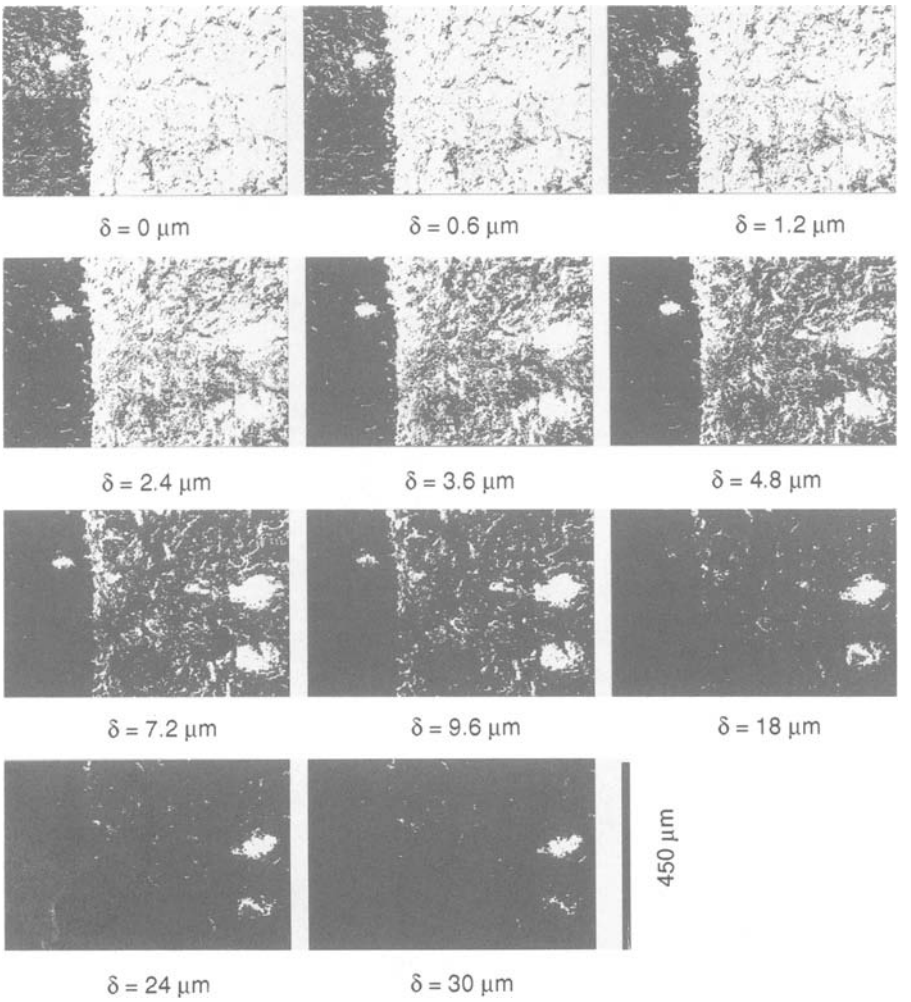


FIG. 7 -- Fracture reconstruction for an F-82H 3pB specimen tested statically at -120°C.

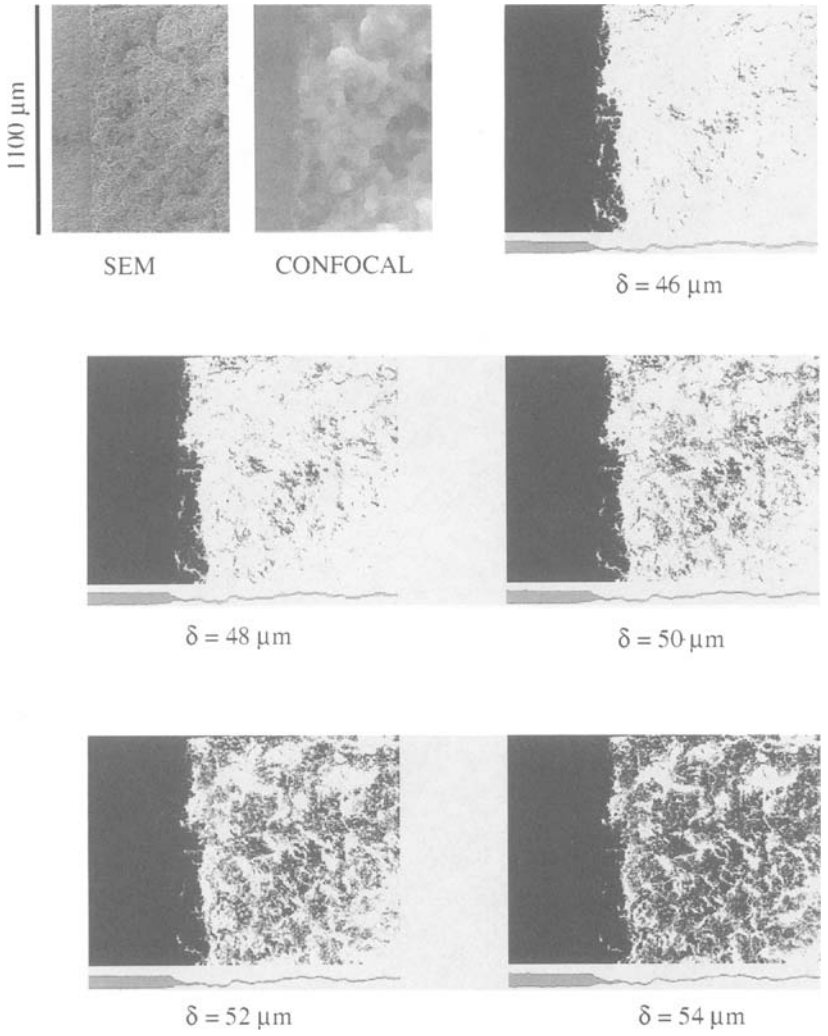


FIG. 8 -- Fracture surface reconstruction for HT-9 tested at -57°C.

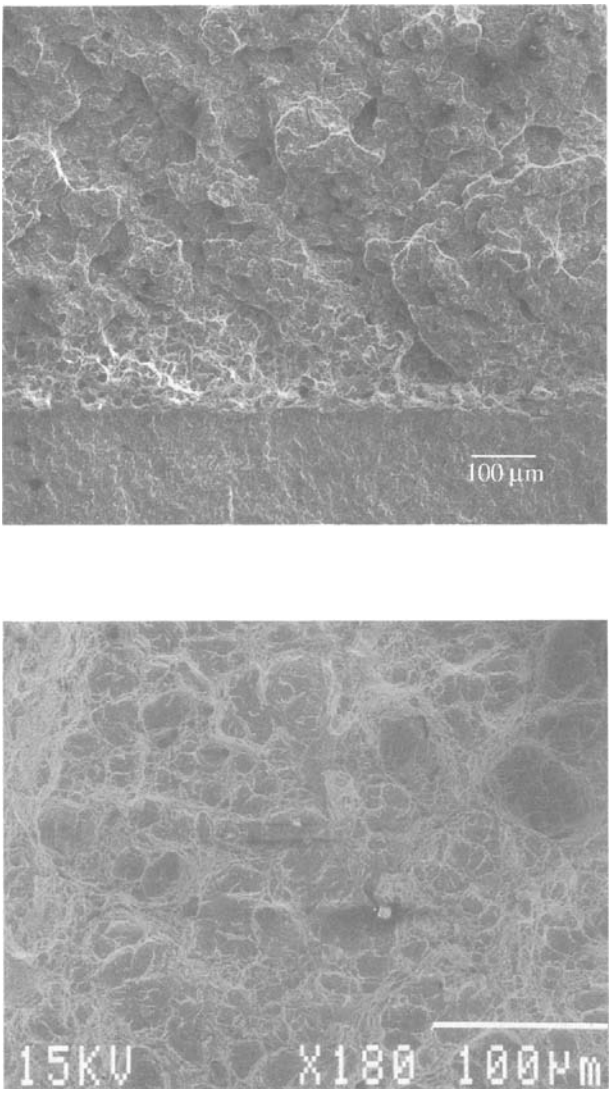


FIG. 9 -- a) SEM micrograph of a region at the root of the pre-crack in HT-9 tested at -57°C; b) SEM fractograph of HT-9 fracture specimen tested under static conditions at -40°C.

agreement with the measured K_{Jc} of 132 MPa•m$^{1/2}$. A qualitatively identical sequence of events is observed for a static test on F-82H at -73°C, as shown in Figure 10; in this case, the critical δ^* is about 65 μm corresponding to a $K_{J\delta}$ of about 141 MPa•m$^{1/2}$ compared to a K_{Jc} of 142 MPa•m$^{1/2}$.

As shown in the SEM micrograph in Figure 9b, by -40°C the fracture process in HT-9 transforms to a mixture of predominantly quasi-cleavage with smaller regions of microvoid growth and coalescence in the fracture plane, in contrast to ductile shear fracture in the tear ridges. The CM/FR shown in Figure 11 demonstrates that the bridging ligaments provided by limited regions of microvoid coalescence also corresponds to the onset of stable crack propagation at an initiation δ^* of about 70 μm. The associated $K_{J\delta}$ is about 140 MPa•m$^{1/2}$ compared to a K_{Jc} of 164 MPa•m$^{1/2}$. The F-82H does not show such a gradual transition to the upper shelf.

Upper shelf/knee region -- The fraction of microvoid coalescence in HT-9 increases with increasing temperature and becomes dominant on the upper shelf. The CM/FR in Figure 12 for static test at 20°C shows that crack growth in HT-9 takes place by a repeated sequence of microvoid nucleation and growth terminated by coalescence with the blunting crack tip. Initiation occurs at a δ^* of about 150 μm corresponding to a $K_{J\delta}$ of about 198 MPa•m$^{1/2}$ compared to a K_{Jc} of about 214 MPa•m$^{1/2}$. However, as shown in the SEM micrographs in Figure 13a, even on the upper shelf, clusters of cleavage facets appear frequently at the center of the large microvoids, suggesting cleavage nucleation of these large microvoids. The growth of the cleavage-nucleated microvoids and linkage by regions with generally finer scale populations of microvoids formed on particles leads to coalescence. Upper shelf processes in F-82H are qualitatively similar, as illustrated in the SEM micrograph in Figure 13b of the stretch region; this shows large voids associated with particles and cleavage facet clusters linked by regions of very fine microvoids leading to coalescence.

DISCUSSION

The results of the previous section can be summarized as follows:

- The behavior of HT-9 and F-82H is similar in the quasi-cleavage regime. As measured by transition temperatures, F-82H has only slight advantages -- i.e., transition temperatures ranging from about 0 to 25°C less than HT-9 depending on the reference index.

- F-82H can have higher fracture resistance in the ductile fracture regime, ranging from factors of less than of 1.15 (dynamic ductile initiation toughness) to about 3 (Charpy upper shelf energy).

- The transition from quasi-cleavage to microvoid coalescence fracture is very gradual in HT-9 and very abrupt in F-82H.

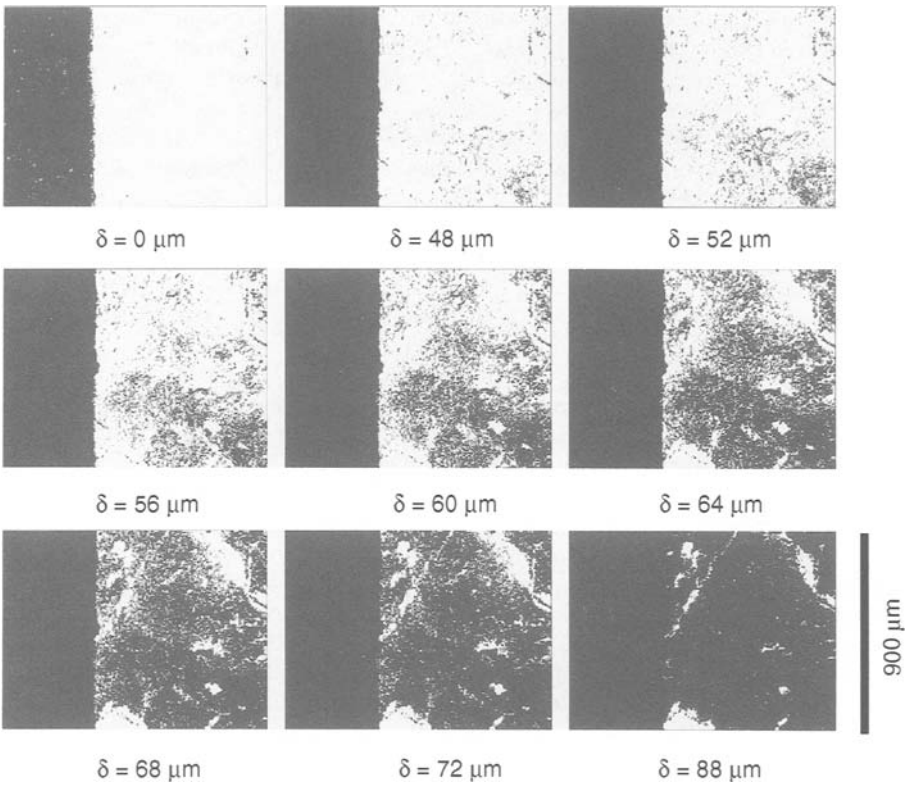


FIG. 10 -- Fracture surface reconstruction for F-82H tested at -73°C.

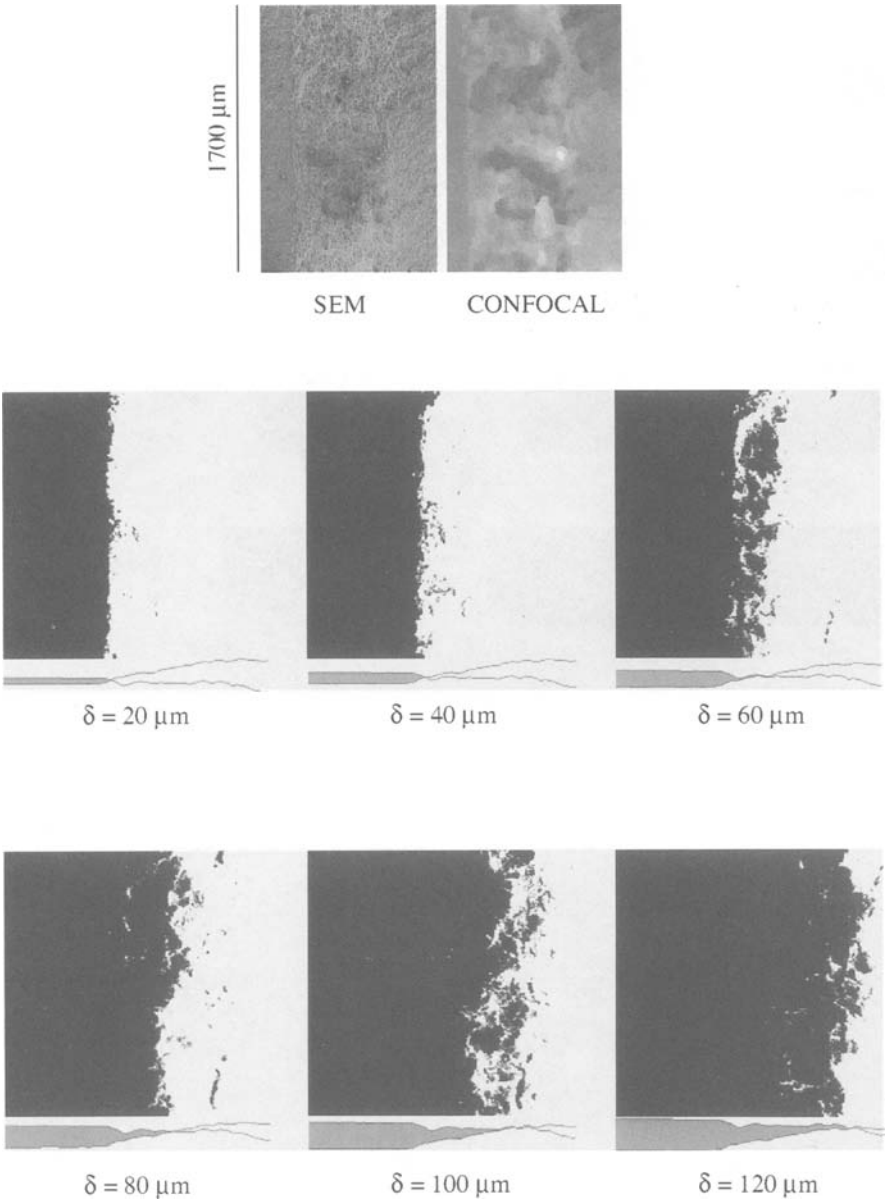


FIG. 11 -- Fracture surface reconstruction for HT-9 tested under static conditions at -40°C

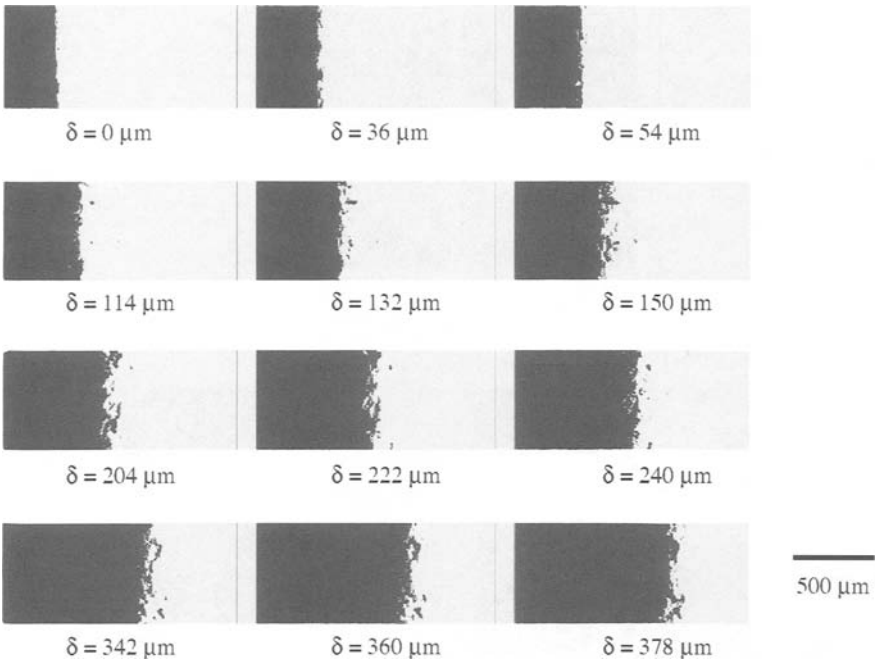


FIG. 12 -- Fracture surface reconstruction for HT-9 tested under static conditions at 20°C

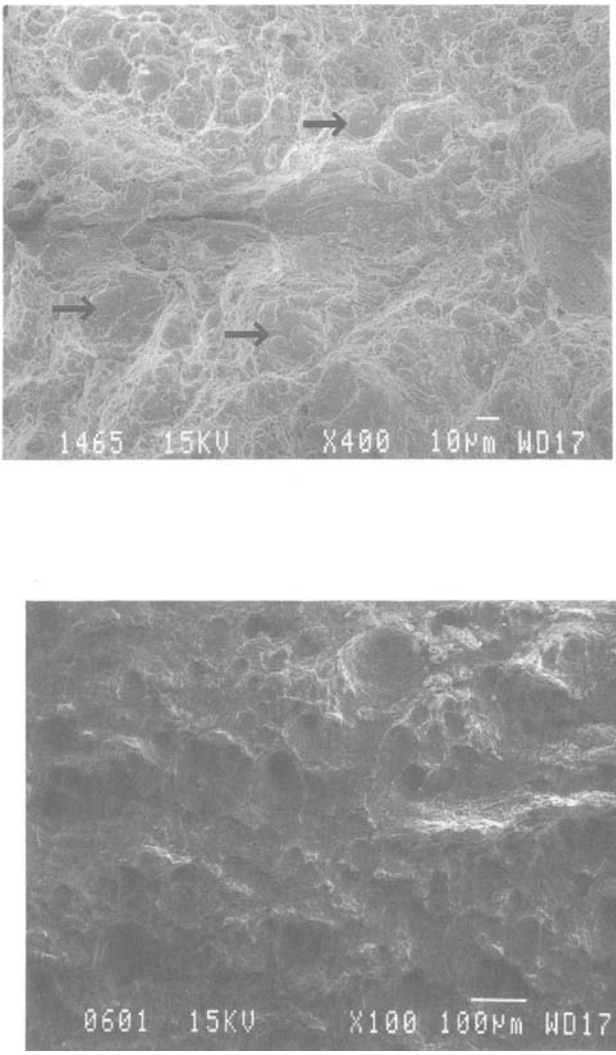


FIG. 13 -- SEM fractographs of a) HT-9 fracture specimen tested under static conditions at 20°C; b) F-82H fracture specimen tested under dynamic conditions at 100°C.

- Primarily as a reflection of the width of the transition regime, mixed mode DBTT indexes show appreciably larger advantages for F-82H, ranging from 65 to 175°C. However, the structural significance of these measures is not clear.

- Both steels manifest qualitatively similar fracture mechanisms in both quasi-cleavage and microvoid coalescence regions. The major differences appear to be: a) a broader transition regime in HT-9, involving a microscopic mixture of the limiting mechanisms; and b) a lower fracture resistance of the HT-9 relative to F-82H in the predominantly ductile fracture regime.

The basic micromechanics of the quasi-cleavage and microvoid coalescence regimes has been described elsewhere.[1] The more pertinent question in comparing these steels is: what gives rise to the large differences in the width of the transition regime? At lower temperatures in the mixed mode regime of HT-9, small regions which ultimately fail by microvoid coalescence contribute to toughness by acting as bridging ligaments that can also sustain stable crack growth. The contribution of the microvoid coalescence regions gradually increases with increasing temperature to the point where the microvoid-associated ligaments give way to cleavage-facet-nucleated microvoids. The absence of the transition regime in F-82H is not understood but might be rationalized on the basis of a synergistic interaction between microcrack formation and linking of microcrack-nucleated microvoids. Both processes appear to be more difficult in F-82H compared to HT-9. Thus the higher strains needed to form microcracks in F-82H also promote the formation of more uniform dilational damage, lowering the peak stresses and preventing the nucleation of more microcracks. By definition isolated microcracks transform to microvoids, rather than unstable or quasi-stable process zone cracks. More isolated microvoids also require larger strains to reach coalescence conditions, which may also be more inherently difficult in F-82H. The larger strains lead to local (dilational) and global (large scale yielding) loss of constraint, further reducing microvoid growth rates and delaying coalescence. Thus, subtle differences in the underlying processes can lead to large differences in regions where they have the potential to interact.

An even more fundamental question is: what is the microstructural basis for these differences? While more detailed microstructural characterization will be needed, we believe the major difference is probably due to the relative compositions and heat treatments of the two alloys and the corresponding differences in carbide populations. The ratio of fine scale carbide formers -- molybdenum + tungsten + vanadium -- to carbon is about 8 for HT-9 compared to 22 for F-82H. The corresponding ratio of chromium, which is associated with coarser carbides, to carbon is roughly similar: that is, 53 for HT-9 versus 80 for F-82H. These compositional factors lead to a greater proportion of finer matrix and boundary carbides in F-82H, and the lower C content results in an overall lower volume fraction of carbides. The greater quantity of coarse matrix and boundary carbides in the HT-9 promote both quasi-cleavage microcrack nucleation and the nucleation of the finer scale secondary microvoids leading to coalescence of the large microvoids.

Details of the mechanisms aside, the results of this study clearly demonstrate the non-uniqueness of both absolute and relative values of the so-called DBTT. This is illustrated in Figure 14a, which compares the numerous measures of DBTT for the various indices described in the Results section for HT-9 versus F-82H. Variations of almost 200°C (e.g.,

tracking the solid bars from top to bottom) were found for HT-9 depending on the specimen size and choice of reference index, while the variations for F-82H were substantially less. Corresponding differences in material ranking by DBTT (solid versus hatched bars) ranged from relatively small (top of the bar chart) to more than 150°C (bottom of the bar chart) depending only on the reference index. Similar differences in the measures of ductile fracture resistance are shown in Figure 14b; again differences between HT-9 and F-82H (solid versus hatched bars) varied by factors of only slightly more than 1 to about 3. However, the exact values in this high toughness regime are largely irrelevant in a structural sense. Clearly, a more quantitative and structurally relevant approach is needed.

CONCLUSIONS

While simple standard test methods yield widely divergent measures of fracture resistance, even greater differences can be expected for actual structures characterized by complicated configurations and loading conditions. We believe that a much more rigorous and reliable approach to structural integrity assessment can be based on a combination of macromechanics and micromechanics; neither alone is sufficient [1]. The basic concept is to combine finite element simulations of the evolution of multiaxial crack tip stress and strain fields with local measures of the conditions leading to crack extension (initiation or stable growth). The effects of variations in stress states can be directly modeled, even in complex geometries which deviate from small scale yielding conditions. Thus, this approach also opens the way to far more rigorous use of small specimens. Local measures of fracture resistance may involve simple stress-volume (distance) or strain-volume criteria or more complex statistical cleavage or microvoid growth models. Calibration of the fields and local fracture parameters to one, or ideally more than one, specimen geometry can be used to interpolate or extrapolate to other structurally relevant geometries. This approach can also be used to specify qualitative/quantitative criteria for failure: elastic-plastic cleavage initiation at a specified toughness level corresponding to a specified stress and strain margin; the occurrence of some stable crack growth prior to cleavage instability; and ductile tearing. Not only would such criteria give physical relevance to specified safety margins, but they would also be readily incorporated into statistical/probabilistic-based safety assessment. We believe that the local approach is critical to the intelligent and effective use of not only TM steels but also for essentially all other candidate structural materials for fusion applications.

ACKNOWLEDGEMENTS

This work has been supported by the Office of Fusion Energy, Department of Energy, under grant number DE-FG03-87ER-52143. The authors would like to acknowledge the assistance of A. Hishinuma of JAERI in acquiring the F-82H steel and E. Donahue in the preparation of the manuscript.

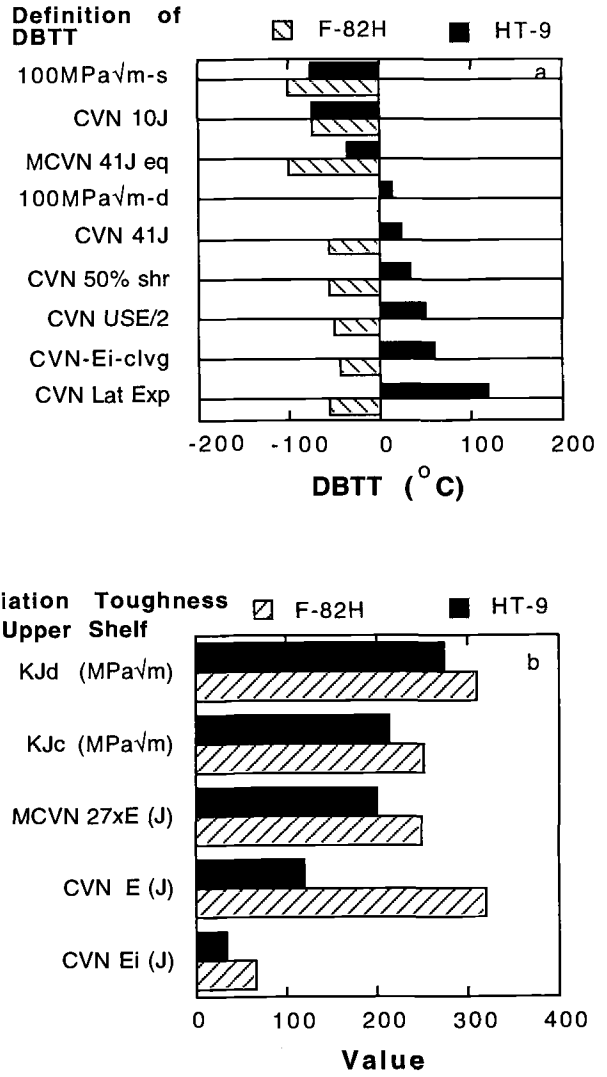


FIG. 14 Comparison of a) transition temperatures and b) ductile initiation toughness and upper shelf energy values in F-82H and HT-9 for a variety of test types and indices.

REFERENCES

[1] Odette, G. R., "On the Ductile to Brittle Transistion in Martensitic Stainless Steels," J. Nucl. Mater., 212-215, 1994, p45.

[2] Odette, G. R., Chao, B. L., Lucas, G. E., "On Size and Geometry Effects on the Brittle Fracture of Ferritic and Temepered Martensitic Steels," J. Nucl. Mater., 191-194, 1992, p827.

[3] Klueh, R. L., Ehrlich, K., Abe, F., "Ferritic/Martensitic Steels: Promises and Problems," ibid., p116.

[4] Tamura, M., Hayakawa, H., Tanimura, M., Hishnuma, A., Kondo, T., "Development of Potential Low Activation Ferritic and Austenitic Steels," J. Nucl. Mater., 141-143, 1986, p1067.

[5] Proceedings IEA Working Group Meeting on Ferritic/Martensitic Steels, ORNL, May 20-21, 1993.

[6] Lechtengerg, T.A., ADIP Quarterly Progress Report, DOE/ER-0045/8, Department of Energy, 1982, p363.

[7] Elliott, C., Lucas, G. E., Maiti, R., Odette, G. R., "Microstructure of HT-9 as a Function of Heat Treatment," J. Nucl. Mater., 141-143 , 1986, p794.

[8] Kohno, Y., Gelles, D., Kohyama, A, Tamura, M., Hishinuma, A., "Irradiation Response of Reduced Activation Fe-8Cr-2W Martensitic Steel F-82H After FFTF Irradiation," J. Nucl. Mater. , 191-194, 1992, p868.

[9] Tamura, M., Hayakawa, H., Yoshitake, A., Hishinuma, A., Kondo, T., "Phase Stability of Reduced Activation Ferritic Steel 8%Cr-2%W-0.2%V-0.4%Ta-Fe," J. Nucl. Mater., 155-157, 1988, p620.

[10] Klueh, R. L. , Kai, J.-J., Alexander, D. J. this publication.

[11] Kimura, A. and H. Matsui, "Neutron Irradiation Effects on the Microstructure of Low-Activation Ferritic Alloys," J. Nucl. Mater., 212-215, 1994, 701.

[12] Lucas, G. E., Odette, G. R., Maiti, R., Sheckherd, J. W., "Tensile Properties of Irradiated Pressure Vessel Steels," ASTM-STP-956, American Society for Testing and Materials, 1987, p379.

[13] Server, W. L., "Impact Three-Point Bend Testing for Notched and Precracked Specimens," J. Test. and Eval., 6, 1, 1978, p29.

[14] Elliott, C., Enmark, M., Lucas, G. E., Odette, G. R., Rowcliffe, A., "Development of Disc Compact Tension Specimens and Test Techniques for HFIR Irradiations," J. Nucl. Matls, 179-181, 1991, p434.

[15] G. R. Odette, G. E. Lucas, R. Maiti, J. W. Sheckherd, "The Effects of Strength and Geometry on Cleavage Fracture Stress and Strain Limits of Martensitic Stainless Steels," J. Nucl. Mater., 133/134, 1986, p849.

[16] G. E. Lucas, G. R. Odette, J. W. Sheckherd, M. K. Krishnadev, "Recent Progress in Testing Subsized Specimens for Fusion Reactor Materials Development," Fus. Tech., 10, 3 parts 2A&2B, 1986, p728.

[17] Edsinger K., Odette, G. R., Lucas, G. E., "The Use of Confocal Microscopy and Fracture Surface Reconstruction to Obtain Structurally-Relevant Fracture Parameters," Proceedings of the IEA International Symposium on Miniaturized Specimens for Testing Irradiated Materials, KFA Julich, September 22-23, 1994, p150.

[18] Edsinger K., B. Wirth, Odette, G. R., Lucas, G. E., this publication.

[19] Steichen, J. M. and Williams, J. A., J. Nucl. Mater. 57, 1975, p303.
[20] Odette, G. R., Lombrozo, P. M., Wullaert, R. A., "The Relationship Between Irradiation Hardening and Embrittlement of Pressure Vessel Steels," Effects of Radiation on Materials: 12th International Symposium, ASTM STP 870, F. A. Garner and J. S. Perrin, Eds., ASTM, Philadelphia, PA, 1985, p840.
[21] Rolfe, S. T. and Barsom, J. M., Fracture and Fatigue Control in Structures, Prentice Hall, New Jersey, 1977, p174.
[22] Alexander, D., Pawel, J. E., Grossbeck, M. L., Rowcliffe, A. F., this publication.

Austenitic Steels

Oleg V. Borodin, Victor V. Bryk, Victor N. Voyevodin, Ivan M. Neklyudov[1],
Valentin K. Shamardin, Victor S. Neystroev[2]

MICROSTRUCTURAL EVOLUTION OF AUSTENITIC STAINLESS STEELS IRRADIATED IN A FAST REACTOR

REFERENCE: Borodin, O. V., Bryk, V. V., Voyevodin, V. N., Neklyudov, I. M., Shamardin, V. K., and Neystroev, V. S., "**Microstructural Evolution of Austenitic Stainless Steels Irradiated in a Fast Reactor,**" *Effects of Radiation on Materials: 17th International Symposium, ASTM STP 1270,* David S. Gelles, Randy K. Nanstad, Arvind S. Kumar, and Edward A. Little, Eds., American Society for Testing and Materials, 1996.

ABSTRACT: Analysis of the microstructure of the stainless steels 16Cr15Ni3MoNb and 18Cr10NiTi, irradiated at temperatures where changes in phase stability occur due to radiation-induced segregation, shows that the stability of second-phase particles depends on the structure of particle-matrix interface.

KEYWORDS: radiation-induced segregation, phase transformation, swelling, microchemical evolution, dislocation structure

Austenitic stainless steels (16Cr15Ni3MoNb, 18Cr10NiTi ,etc.) used as basic core structural materials undergo irreversible structural-phase changes leading to radiation-induced swelling especially at neutron fluence of $(3-5)\times 10^{27} m^{-2}$ typical for operation of existing and designed fast-neutron reactors and fusion facilities [1].

Until the present changes in qualitative and quantitative (number density and mean size) characteristics of microstructure during irradiation for dislocations and dislocation loops, voids , helium bubbles [2,3,4,5] were well known. There is a complete classification of second phase precipitates [6,7]. Conditions and ways of their formation have been determined [8]. Attempts to

[1]Research scientist, senior research scientist, head of laboratory, head of department, respectively, Department of Physics of Radiation Damage and Radiation Materials, National Scientific Center Kharkov Institute of Physics & Technology, 310108 Kharkov, Ukraine
[2] Head of laboratory, senior research scientist, respectively, Institute of Atomic Reactors, Dimitrivgrad, Russia

Copyright© 1996 by ASTM International www.astm.org

link these microstructure changes with material properties have been made [1,9]. One of the most important problem is the description of the solid state behavior under irradiation at a fundamental level - in terms of point defects and crystal lattice atoms. Although in this field, there are undoubted achievements (for example, inverse Kirkendall effect investigation), a complete description is not possible at the present. When developing radiation-resistant alloys and steels for fast reactors, particular attention is given to the establishment of interconnections between the microstructure and properties of a material.

This paper presents the results of electron-microscopy and X-ray spectrum analysis of the defect structure of 16Cr15Ni3MoNb and 18Cr10NiTi steels irradiated with fast neutrons.

MATERIALS AND EXPERIMENTAL PROCEDURE

The materials used in this investigation are: wrappers of heat-produce assembly (HPA) of BOR-60 fast reactor manufactured from steel type 18Cr10NiTi annealed at 800°C for 2h and at 600°C for 1h, and fuel pin cladding from steel type 16Cr15Ni3MoNb annealed at 1050°C for 1/2h. Chemical compositions for these steels are presented in table 1. Wrapper of the HPA was irradiated with neutrons up to maximum fluence $12.6 \times 10^{26} m^{-2}$ (E>0.1MeV), corresponding to a dose level of 68 dpa. The irradiation temperature varied in the range of 320 to 600°C. Distributions of the temperature and fluence along the wrapper are given in fig. 1. Fuel pin cladding from 16Cr15Ni3MoNb steel was irradiated with neutrons up to a maximum fluence $12.6 \times 10^{26} m^{-2}$ (E>0.1MeV), corresponding to 70 dpa. The specimens investigated were cut from the cladding irradiated in the temperature range 385 to 600°C. Distributions of the temperature and fluence along the fuel pin cladding are given in fig.1.

TABLE 1 -- Chemical composition of investigated steels wt%

steel	C	Si	Cr	Ni	Mo	Nb	Mn	Ti	Sc	S	P
Cladding Cr16Ni15	0.53	0.21	15.5	15.4	2.8	0.55	0.66	-	0.09	0.001	0.002
Wrapper Cr18Ni10	0.09	0.36	17.9	10.1	-	-	1.22	0.46	0.05	0.009	0.032

The procedures of preparation and examination of the specimens have been described elsewhere [3].

RESULTS

Initial Structures

18Cr-10Ni-Ti -- In the initial state 18Cr10NiTi steel has a two-phase structure. Together with austenite grains (d=15 ηm) δ-ferrite grains were found . The volume fraction of δ-ferrite is 3 to 5%. The elements of the austenite grain structure were annealing twins, second phase precipitates (carbonitrides of titanium), and dislocations. These TiX precipitates with average size of 0.08 μm and concentration of $7 \times 10^{18} m^{-3}$ have lattice parameters 0.428 to 0.432 nm, depending on their composition. Most of the perfect dislocations were split up into partial ones

with the formation of stacking faults, indicating a low stacking fault energy for this steel. The total dislocation density was $6 \cdot 10^{12} m^{-2}$.

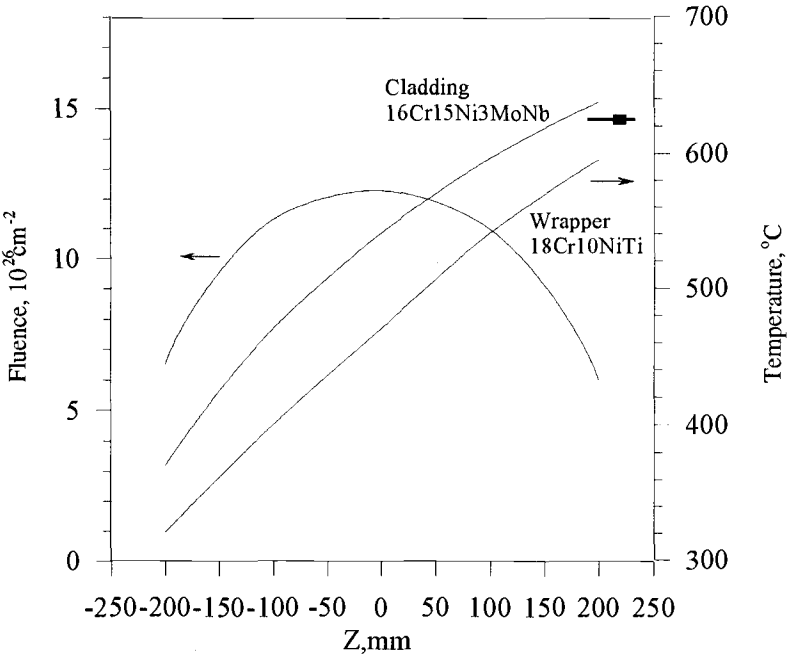


FIG. 1--Fluence and dose distribution along active zone

16Cr-15Ni-3Mo-Nb -- Unlike 18Cr10NiTi steel, 16Cr15Ni3MoNb steel, has a single-phase structure. This is connected with the high content of austenite-forming elements, particularly Ni. The main elements of the microstructure were carbonitrides of niobium, dislocations, stacking faults, and annealing twins. Mean size of the NbX precipitates is 0.05 μm and their concentration is $\approx 9 \times 10^{18} m^{-3}$. The dislocation density was $6.6 \times 10^{12} m^{-2}$ for the initial state of this steel.

Irradiated Structures

The structure of the irradiated specimens is characterized by presence of dislocations, voids, and second phase precipitates.

Fig.2 demonstrates data on fuel pin diameter measurement and changes in density of the specimens cut from fuel pin cladding. The density measurement error was 0.4%. The coincidence of results on fuel pin diameter measurements and density change measurements indicate that swelling plays the main role in size changes of the materials in the core of the BOR-60 reactor. Non-elastic volume changes did not exceed 0.3% in this case. Similar results were obtained under examinations of fuel pins irradiated in standard regimes with various dose levels [10,11].

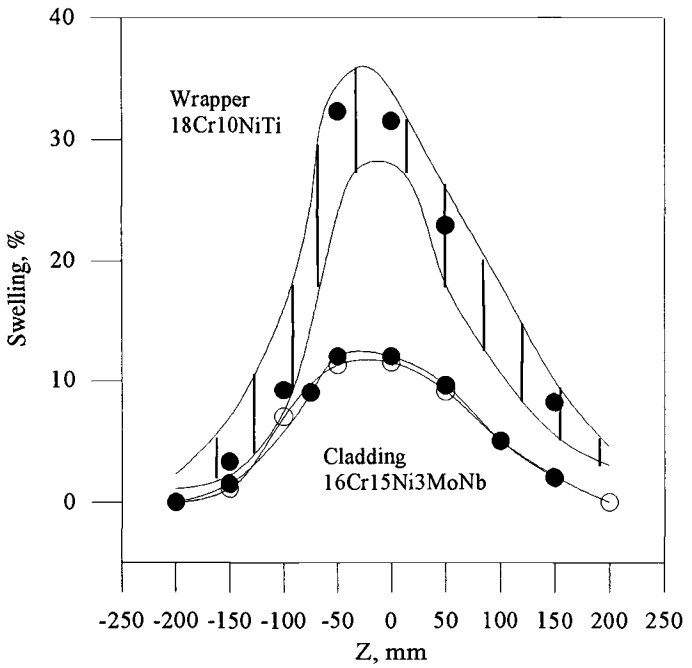


FIG.2-- Swelling of cladding and wrapper along active zone
● - data of TEM investigation
○ - data of diameter measurement
|| - data of density change

18Cr-10Ni-Ti Wrapper

Dislocation structure -- A dislocation network was observed for all values of irradiation dose and temperature that were examined. The dislocation density, determined from micrographs under two-beam condition (220) decreased with increase in temperature (Table 2).

TABLE 2 -- Dislocation concentrations along wrapper

	Z, mm					
	-150	-50	50	150	200	300
Dose, dpa.	54	68	66	54	40	11
T_{irr}, ^{o}C	360	430	500	560	580	600
ρ, $10^{14} m^{-2}$	6.3	5.4	4.2	2.7	1.4	1.2

Isolated faulted Frank loops with Burgers vector $a/3\langle 111\rangle$ were observed together with the dislocation net formed from perfect dislocations type $a/2\langle 110\rangle$ at low irradiation temperature (<430 ^{o}C). At an irradiation temperatures above 580 ^{o}C, a significant fraction of dislocations that form the net were partial Shockley ones generated from perfect dislocations according to a reaction of

$$a/2\langle 110\rangle = a/6\langle 210\rangle + a/6\langle 120\rangle \quad (1)$$

Typical electron-microscopy fringe contrast indicated the presence of stacking faults (Fig.3). At lower temperatures such dislocation reaction was not observed.

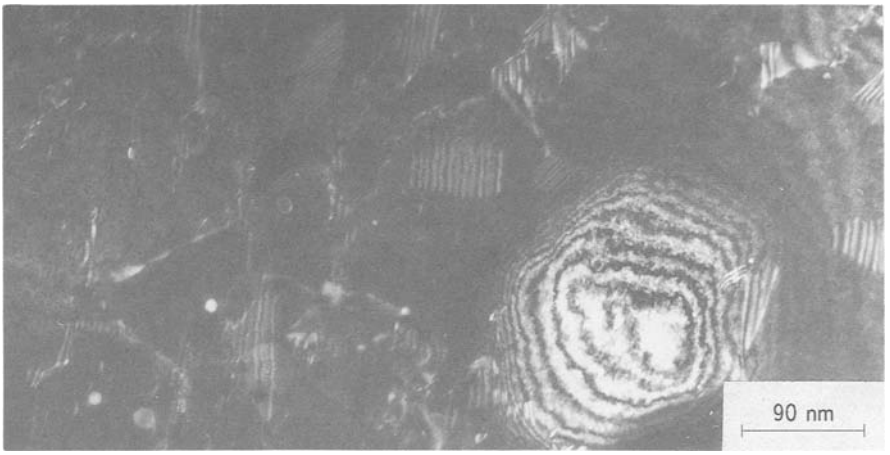


FIG. 3--Stacking faults in irradiated steel 18Cr10NiTi (D=40 dpa, Tirr=580°C)

Void structure -- The basic void parameters are given in table 3. In fig.4 it will be seen that isolated voids, precipitate-attached voids, and void-free precipitates are present in the irradiated material. Irradiation at 580 to 600 °C leads to the formation of two types of vacancy voids in the specimens: cubic shape ones limited with {100} planes and octahedron cutted with {110} planes shape voids , which are ordinary ones for swelling austenitic chromium-nickel steel (Fig.5). It is a characteristic feature that cubic shape voids are not attached to precipitates, and that octahedron ones are found in association with precipitates.

TABLE 3 -- Swelling parameters for wrapper (steel 18Cr10NiTi)

N	T_{irr}, °C	Dose, dpa.	$\bar{d}$, nm	d_{min}, nm	d_{max}, nm	ρ $10^{20}m^{-3}$	volume fraction %
1	360	54	28.1	4	80	19.6	3.3
2	430	68	38.9	8	100	14.5	9.2
3	500	66	90.2	20	200	5	32.3
4	560	54	100.2	18	260	3.5	31.5
5	580	40	137.0	30	300	1.4	23
6	600	11	121.1	28	208	0.7	8.2

Precipitates -- In spite of the great amount of the investigations of structure-phase condition for irradiated steel 18Cr10NiTi a complete identification of the observed second phase precipitates was not conducted. Electron diffraction and X-ray spectrum analysis showed, that despite the difference in sizes and morphology of the phases, most were G-phase precipitates (Fig.6). Fine (3 to 5 nm in size) titanium monocarbides were observed within grains at irradiation

temperature of 580 to 600°C. Coarse primary titanium carbonitrides and δ-ferrite grains were found in separate regions of the specimens. At irradiation temperature of 500 ^{O}C together with G-phase silicides form which contain much Ni and have non-cubic structure in the case of irradiation. At temperature below 450 ^{O}C there silicides are dominant.

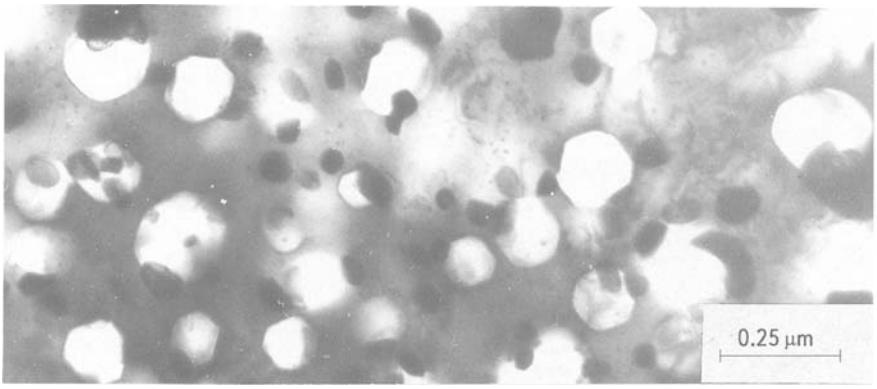


FIG. 4--Microstructure of irradiated steel 18Cr10NiTi (D=66 dpa, Tirr=500°C)

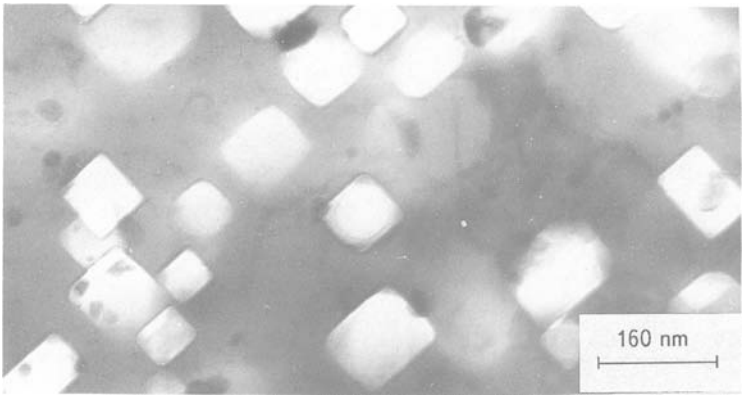


FIG. 5--Cubic voids in irradiated steel 18Cr10NiTi (D=40 dpa, Tirr=580°C)

TABLE 4 -- Precipitates parameter in irradiated steel 18Cr10NiTi

N	T_{irr},,^{O}C	Dose, dpa.	$\bar{d}$, nm	d_{min}, nm	d_{max}, nm	ρ $10^{20}m^{-3}$	volume fraction %
1	360	54	8.6	4	64	63.2	0.65
2	430	68	15.5	8	80	45.1	0.86
3	500	66	23.5	8	64	9.3	1.0
4	560	54	46.0	12	180	3.8	4.0
5	580	40	63.0	12	200	1.7	5.0
6	600	11	56.0	12	200	1.4	2.9

The basic parameters for these precipitates are given in table 4. G-phase- precipitate is the typical phase for 18Cr-10Ni-Ti steel which is the double silicide type A_6-M_{16}-X_7 [12], where A- Ti, Cr, Mn; M- Ni, Fe; X- Si, B, C. It has cubic lattice type Fm3m with parameter 1.115 to 1.145 nm depending on its composition. The composition and morphology of silicides and carbonitrides are shown in table 5. According to those data, with the increase in the irradiation temperature, the silicide composition changes with increase in Ni content and decrease in that of Si. The silicides located on interfaces contain more Ni in comparison with those in the matrix. During irradiation initial carbonitrides change their composition by increasing the both Ni and Si content

TABLE 5 -- Phase composition in irradiated steel 18Cr10NiTi

Phase	T_{irr} °C	Composition, wt %							
		Si	Ni	Sc	Ti	Mn	Cr	Fe	Rem.
MX		-	0.5	0.3	97	-	0.5	1.5	initial
			0-1	0-0.5	95-99		0-1	0-3	
MX	600	5	42	0.8	30.5	0.2	5.5	15.5	primary
		3-7	34-48		22-39	0-0.4	5-6	15-16	
MX	360	9	27.4	3.5	41	0.9	4.7	13.4	primary
		7-14	21-33	0-7	33-55	0.5-2	3.5-6	11-16	
MX	600	-	1	-	95	-	1	3	secondary
			0-2		93-100		0-1.5	0-4	
G	600	12.5	62	0.4	7.7	2.4	5.4	10	within
		11-14	60-64	0-1	4-13	0-5	4-6	5-12	grain
G	360	23	38.4	-	6.9	2.2	7.4	22.2	within
		20-25	37.41		4-10	0-5	5-10	20-23	grain
G	600	8.5	71.9	0.3	6.9	2.4	3.6	6.7	on GB
		8-10	70-73	0-1	5-8	1-5	2-5	5-8	
G	360	8.5	53.1	0.1	6.9	2.4	3.6	9.5	on GB
		8-10	50-55	0-0.4	5-8	1-5	2-5	7-11	

Remark: upper line - average content
lower line - observed range

16Cr-15Ni -3Mo-Nb Cladding

Dislocation structure -- At temperatures < 400 °C the main microstructure elements were perfect dislocation loops with mean size of 25 nm, distributed homogeneously within grains (Fig.7). At temperatures > 400 °C a developed dislocation network was observed with dislocation density of $5.1 \times 10^{14}\ m^{-2}$ at 455 °C (Fig.8), which decreased to $1.7 \times 10^{14}\ m^{-2}$ at 600 °C. At irradiation temperature of 600 °C faulted Frank loops were observed (Fig. 9).

Void structure -- The void structure in 16Cr15Ni3MoNb steel was similar to that in irradiated steel 18Cr10NiTi (Fig.10). At temperatures below 400 °C voids were not observed.

Precipitates -- The phase composition in 16Cr15Ni3MoNb steel is more various than in 18Cr10NiTi steel. At temperatures > 500 °C, in addition to G and MX precipitate Laves was observed mainly on grain boundaries . And a low quantity of γ'-phase was observed too. The changes in content of G and MX precipitates are similar to those observed in 18Cr10NiTi steel (Table 6).

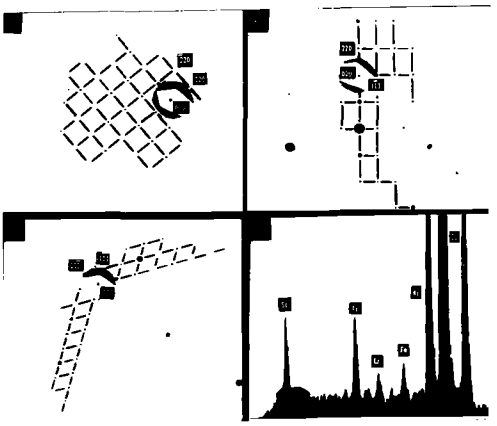


FIG. 6--Electron diffraction patterns from G-phases (z=[100] (a), z=[110] (b), z=[112] (c), and EDS-spectrum (d)

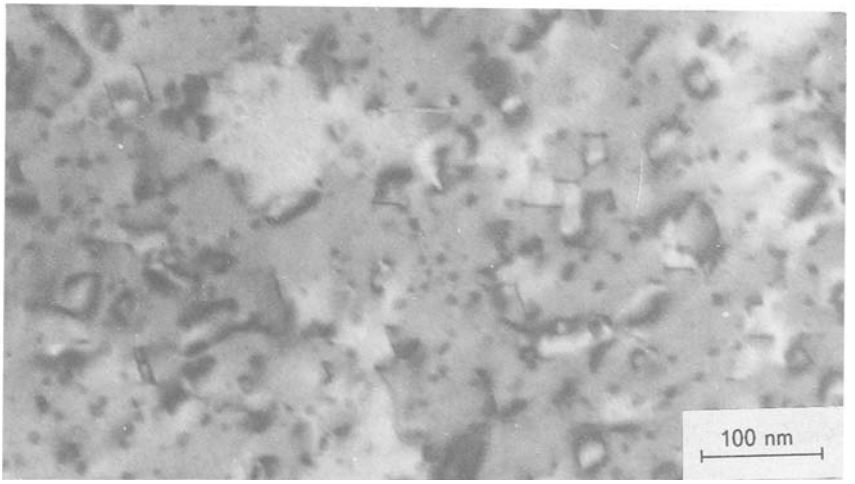


FIG. 7--Dislocation loops in irradiated steel 16Cr15Ni3MoNb (T=385 °C, D= 52 dpa)

DISCUSSION

In figures .4 and 10 it is seen that there is not regularity in the distribution of voids and precipitates: both isolated voids and G-phase precipitates , and void-precipitate complexes (precipitate-attached voids) are present. This indicates that voids and precipitates nucleate separately, and only during their growth under irradiation they form complexes.

A significant feature of the dislocation structure is the formation of split dislocations at 580 to 600 ^{o}C. Segregation of solutes to dislocations arising during irradiation leads to a local decrease in stacking fault energy causing the formation of partial dislocations type $a/6<210>$.

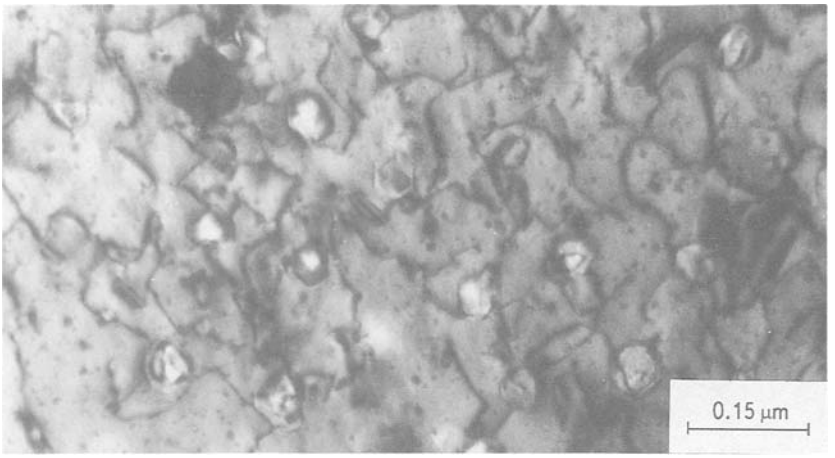


FIG. 8--Network dislocation in 16Cr15Ni3MoNb (D=66 dpa,.T=525 °C)

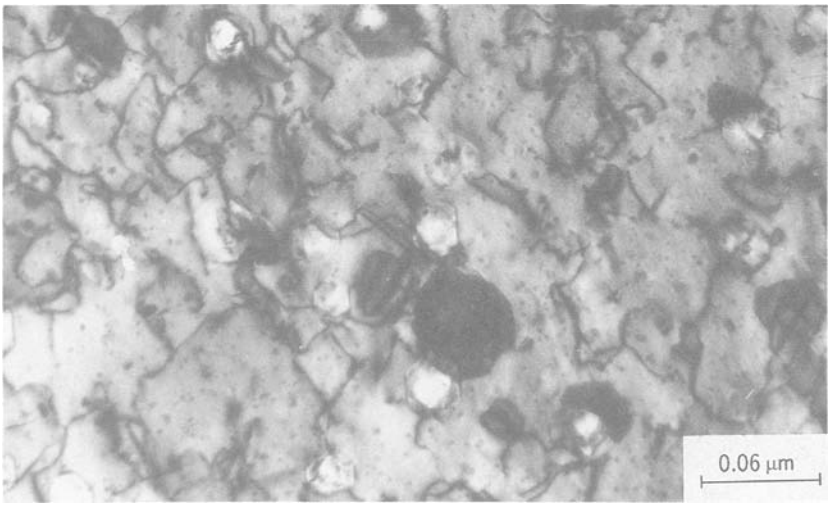


FIG. 9--Frank loops in irradiated 16Cr15Ni3MoNb (D=35 dpa, T=600 °C)

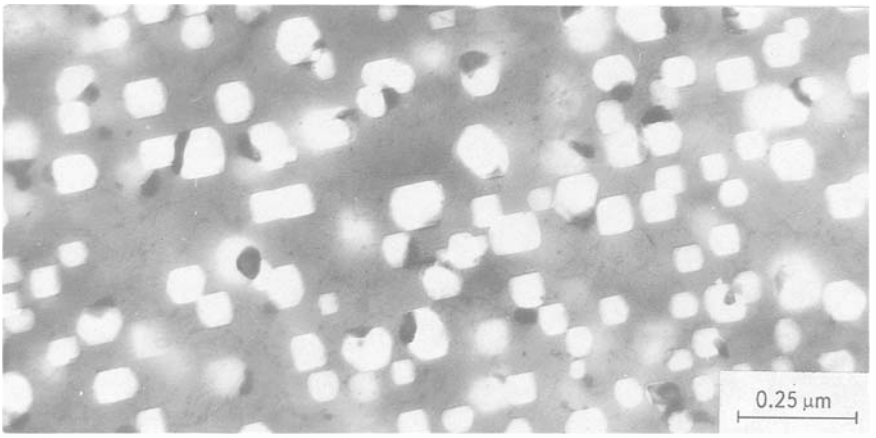


FIG. 10-- Microstructure of irradiated steel 16Cr15Ni3MoNb (T=455 °C, T=70 dpa)

TABLE 6 -- Phase composition in irradiated steel 16Cr15Ni3MoNb

Phase	Tirr °C	Composition, wt %						
		Si	Cr	Fe	Ni	Nb	Mo	
MX	-	0.3	-	1	0.5	88	0.6	
		0-0.8		0.5-2	0-1	87-89	0-1	
MX	455	2	5	10	9	62	3.5	≤0.5 μm
		1-3	3.5-8	5-16	6-11	54-70	1.5-5	
MX	525	2	7	10	10	70	1	≤0.5 μm
		0.5-2.5	5-11	1-20	5-16	47-80	0-2	
MX	525	0.5	1	4	2.5	85	3	≥0.5 μm
		0-1	0-2	1.5-6.5	2-3	80-90	1.5-5	
MX	555	3	4	10	14	68	4	≤0.5 μm
		2-4	3-6	6-16	12-16	63-73	2.5-5.5	
MX	555	1	2.5	5	7	77	2	≥0.5 μm
		0.5-2	0-4	1-11	1-16	65-91	1.5-3	
G	455	10.6	13.5	19	35	9.2	7	
		9-12	12-14.5	9-25	34-37	9-10	6-7.3	
G	525	10.5	11.5	18	44	10	5.5	-//-
		10-12	9-13.5	13-21	41-49	9-10.5	3-7	
G	555	10	8.5	21	40	14.7	5.3	-//-
		9-11	7.5-9	20-22	39-42	12-15	4-7	
G	455	15	7	9	55	8	6	on GB
		11-16	5-8	8-14	50-59	6-9	4-8	
G	525	13	5.5	8	57	10	5	-//-
		12-13.5	5-6.5	7.5-10	55-60	8.5-11	2-8	

Remark: upper line - average content
lower line - observed range

Thus, during neutron irradiation of 16Cr15Ni3MoNb and 18Cr10NiTi steels processes of nucleation and evolution of dislocations, voids, silicides (G-phase, etc.) and MX carbonitrides were observed. Besides, there was no a noticeable interconnection between nucleation of voids and precipitates. G-phase is the main radiation-induced phase in the temperature range 500 to 600 ^{O}C. Its composition is determined by the partial diffusion coefficients of elements forming the precipitate at a given temperature. During irradiation, primary carbonitrides MX are enriched in Ni and Si. The segregation of solutes to dislocations and the formation of atmospheres of these atoms at 580 to 600 ^{O}C leads to a local decrease in stacking fault energy, a result of two is that perfect dislocations are split into Shockley dislocation

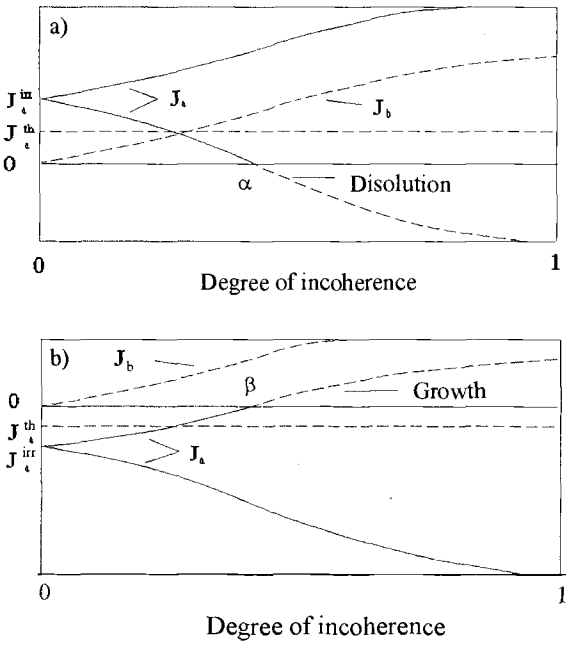


FIG. 11--Schematic picture of phases stability depending on type matrix-phase boundaries:
a) thermally stable precipitates
b) thermally unstable precipitates

In spite of the variety of experimental data described here, it is possible to choose a number of general features of phase evolution of multicomponent materials. In all cases, the behaviour of precipitates under irradiation depends on the structure of precipitate-matrix interface and alters with the changing of precipitate-matrix conjugation. After irradiation at a high dose, precipitates having a coherent interface or interfaces with low degree of incoherence are observed in the material. Such precipitates can exist in the initial specimens or can occur during irradiation. The higher stability of coherent precipitates is explained by the fact that a coherent interface has no defect sites and does not absorb point defects. Therefore, in the environment of the coherent precipitates located far from point defect sinks, segregation effects do not occur, i.e., the composition of the alloy does not change during irradiation. It means that the stability condition for coherent precipitates is not violated - thermally stable precipitates do not dissolve during

irradiation [13]. Under loss of coherence (in the process of precipitate growth) on precipitate-matrix interface sinks of point defects arise (for example, misfit dislocations). In consequence of the interconnection between alloy component flux and point defect flux to precipitate-matrix interface (inverse Kirkendall effect [14,15]) the growth rate of the incoherent precipitate changes. For binary alloys the condition of incoherent precipitate stability is formulated conveniently by introducing the notion of radiation-modified incoherent solubility [16]. It is defined as the average solute concentration when precipitate growth rate becomes equal to zero. Perhaps, the radiation-induced solubility depends on an incoherence degree which is characterized by sink strength on precipitate-matrix interface. The relation between thermal and radiation-induced solubilities depends on the relation between diffusion coefficients of an alloy [16]. In binary alloys segregation effects lead to either, dissolution of incoherent precipitates, or accelerated growth of them. It is true for coherent precipitates located near and at the point defect sinks as well.

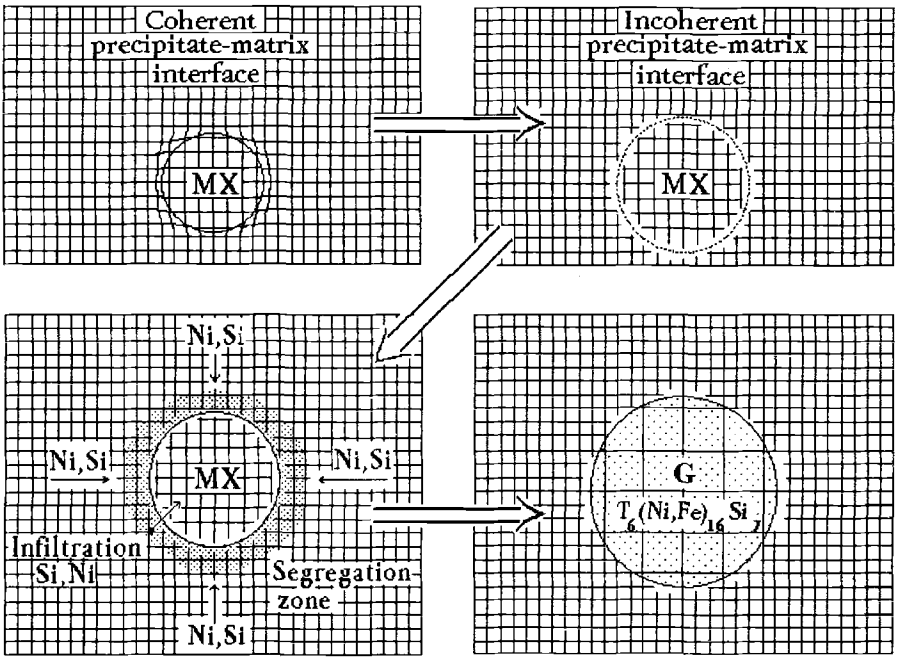


FIG.12--Scheme of transformation MX-type precipitate under irradiated

In alloys containing three or more components the new effect arises. Elements that are not a part of a precipitate can segregate to a coherent boundary of the precipitate. Infiltration of these elements into precipitate could lead to phase transition with changing of both stoichiometry and lattice type. Probably, this mechanism, G-phase precipitates form from of phosphides and coarse carbonitrides.

Above mentioned reasoning may be obviously illustrated with the aid of graphs. In fig.11, the flux of A-component controlled precipitate growth versus incoherence degree of interface of

this precipitate is represented schematically. First, let's consider the thermally stable precipitates case (Fig.11a). In the absence of irradiation flux of A-component, J_A^{th} to precipitate is greater than zero and does practically not depend on interface type. Under irradiation, the flux of A-component changes due to two reasons: firstly, diffusion mobility of components enhances in consequence of non-equilibrium point defect generation; secondly, supplementary mechanism of migration of them towards or away from precipitate boundary appears (segregation). Under the ideal conjugation between the lattices of precipitate and matrix (zero degree of incoherence) irradiation only accelerates the A-component transfer; sign of the flux is not changed ($J_a^{irr} \rangle J_a^{th}$). With increasing the incoherence degree the segregation contribution grows. The total flux either increases monotonically or decreases. In the latter case (when the flux becomes equal to zero (α-point), and the precipitate loses its stability), the incoherence degree depends on displacement production rate and temperature. During irradiation near the incoherent precipitate, redistribution of elements that are not a part of the precipitate occurs. With increasing the incoherence degree, the flow of these elements enhances. For example, in accordance with the case showed in fig.11 accumulation of B-element near precipitate interface occurs. Then this element diffuses into the precipitation. Accordingly, to that excess of the solubility limit of the B-element in the precipitate a phase-transition takes place when incoherence degree can be changed. The precipitate can undergo a number of transitions as a result of whether this precipitate is dissolved or transformed into a precipitate that is in equilibrium with the segregation profiles of alloy components.

Fig.11b corresponds to thermally unstable precipitate in the case of $J_a^{in} \langle 0$ (designations are those as in fig.3a). It is evident that under comparatively high degree of incoherence the unstable precipitate could become a stable one during irradiation. But similar to the previous case, the critical value of incoherence degree depends on the irradiation conditions.

Let's follow the evolution of the MX type carbide (Fig.12). In the initial condition of steel NbC contains mainly Nb with insignificant additions not exceeding 10 %, and has incoherent boundary. During irradiation, the flow of solute atoms to interface leads to changes both in the precipitate itself, and in its environment. In due course the precipitate composition can change the substantially. Transformation of the phase structure takes place into G, so that solute flux to interface decreases. G-phase has a lattice isomorphic to matrix, but precipitate-matrix interface is not completely coherent. Due to steel components segregation to the partly incoherent interface in the precipitate environment such local composition of matrix maintains that the G-phase is stable. Secondary radiation-induced precipitates MX formed as coherent phases, and up to loss the coherence keep their composition nearly invariable. After the loss of coherence, evolution of the secondary precipitates is similar to the primary MX precipitates.

According to a great number of investigations of irradiated austenitic steels doped with strong carbideformers, one may assert that in a temperature range of 500 to 550 °C the main stable phase is G-phase. In type 316 stainless steels as well $M_{23}X_6$, M_6X with lattice isomorphic to matrix one (parameter of the lattice is close to three parameters of a_γ), and γ' with L1 Structure Type and parameter closed to a_γ are observed. At higher temperature in addition to the above mentioned phases in austenitic stainless steel Laves, σ- and χ-phases which are thermally stable and have not a good coherency with matrix are observed. Apparently at these temperatures the radiation-induced segregation does not have a significant influence on second phase stability (Fig.11a).

The mechanisms of evolution of a phase composition described above, work in the temperature range where irradiation gives a rise of segregation processes. With increasing of the

displacement production rate, the high-temperature boundary of this range is shifted to more high temperature region. Accordingly, the region of stability of incoherent phase enlarges [13].

CONCLUSION

As it is seen from above mentioned results, type of interphase boundary plays a significant role in formation of phase composition. The validity of this model is confirmed by results obtained under irradiation of ferritic steels and alloys [8,17]. One may use some principles of this model for development of commercial alloys. Formation of suitable initial structure and microalloying increase "lifetime" of phases which effect on swelling suppression and corresponding physical-mechanical properties [18].

ACKNOWLEDGMENT

The research described in this publication was made possible in part by Grant No UA 8000 from the International Science Foundation.

REFERENCES

[1]. T.P. Chernyaeva, V.F.Zelenski, and I.M.Neklyudov, Radiation defects and swelling of metals (in Russian), Kiev, Naoukova Doumka, 1987
[2] V.N. Voyevodin, V.F.Zelenski, and I.M.Neklyudov, Effects of Radiation on Materials: 14th International Symposium, Volume 1, ASTM STP 1046, American Society for Testing and Materials, Philadelphia, 1989, pp. 193-196.
[3] O.V. Borodin, at al., Atomnaya Energia (in Russian), V.66, 1990, pp. 159-163.
[4] V.F.Zelenski, et al, Physica Chimiya Obrabotki Materialov (in Russian), 4(1991), pp. 5-12.
[5] F.A. Garner, Proceedings of Symposium on Optimizing Materials for Nuclear Applications, The Metallurgical Society Los Angeles, California, February 27-29, 1984, pp.
[6] P.J. Maziasz, Journal of Nuclear Materials, 205(1993), pp. 118-145.
[7] A.S. Bakaj, et.al., Proceedings of International Conference on Radiation Material Science, Alushta, 1990, V.2, pp. 156-163.
[8] O.V. Borodin, at al., Materials Science Forum, Copyright Trans Tech Publications, Switzerland, pp. 299-305.
[9] V.F.Zelenski, et.al., Some Problems Radiation Damage Physics in Materials (in Russian), Kiev, Naoukova Doumka, 1979.
[10] V.S. Neustroev, at al., Proceedings of International Conference on Radiation Material Science (in Russian), Alushta, 1990, V.3, 70-78.
[11] A.V. Povstyanko, at al., Proceedings of International Conference on Radiation Material Science (in Russian), Alushta, 1990, V.3, 79-87.
[12] H.J. Goldschmidt, Interstitial Alloys, V.1-2, London, Butterworths, 1967.
[13] A.S. Bakaj, and A.A. Turkin, Fizika Metallov i Metallovedenie, (in Russian) 3(1991), p.67.
[14] A.D. Marwick, Journal of Physics., 8(1978), p.1849.
[15] H. Wiedersich, P.R. Okamoto and N.Q. Lam, Journal of Nuclear Materials, 83(1979), p.98.
[16] A.S. Bakaj, and A.A. Turkin, Journal of Nuclear Materials, 152(1988), p.331.
[17] O.V. Borodin et al, Physica Chimiya Obrabotki Materialov (in Russian), 6 (1994),pp.14-24
[18] Porter, D.L., Wood, E.L., and Garner, F.A., Effects of Radiation on Materials: 14th International Symposium, Volume II, ASTM STP 1046, American Society for Testing and Materials, Philadelphia, 1990, pp. 551-569.

Hiroshi Kawanishi[1], Margaret L. Hamilton[2] and Frank A. Garner[2]

EFFECTS OF HELIUM/DPA RATIO, ALLOY COMPOSITION AND COLD WORK ON MICROSTRUCTURAL EVOLUTION AND HARDENING OF ^{59}Ni-DOPED Fe-Cr-Ni ALLOYS NEUTRON-IRRADIATED AT 465°C

REFERENCE: Kawanishi, H., Hamilton, M. L., and Garner, F. A., **"Effects of Helium/dpa Ratio, Alloy Composition and Cold Work on Microstructural Evolution and Hardening of ^{59}Ni-doped Fe-Cr-Ni Alloys Neutron-Irradiated at 465°C,"** *Effects of Radiation on Materials: 17th International Symposium, ASTM STP 1270,* David S. Gelles, Randy K. Nanstad, Arvind S. Kumar, and Edward A. Little, Eds., American Society for Testing and Materials, 1996.

ABSTRACT: Three ternary austenitic alloys(Fe-15Cr-25Ni, Fe-15Cr-25Ni-0.04P, Fe-15Cr-45Ni in both annealed and cold worked conditions) were irradiated at 465°C to 0.15, 0.28, and 0.42 dpa at above core position in the Fast Flux Test Facility utilizing the Materials Open Test Assembly to study the separate and synergistic effects of He/dpa ratio, phosphorus addition, nickel content and cold work level on microstructural evolution and hardening. The helium/dpa ratio was varied by isotopic doping with ^{59}Ni to enhance the production rate of helium. The helium production rate was evaluated to be 62 appm He/dpa in the ^{59}Ni-doped specimens and 0.26 appm He/dpa in the undoped specimens.
Transmission electron microscopic examinations revealed that alloy composition affected significantly the evolution of microstructure during irradiation. Phosphorus addition prevented the formation of Frank loops through the precipitation of phosphide. Nickel content influenced the nucleation of cavities. Helium production rate influenced the densities of dot-typed clusters in 25Ni alloys and cavities in 45Ni alloys.

KEYWORDS: helium, helium/dpa ratio, phosphorus, cold work, Fe-Ni-Cr alloy

Isotopic tailoring with ^{59}Ni is the technique initiated by Simons et al. to vary helium production rate without introducing variations in other important material or irradiation parameters[1]. When alloys are prepared with and without isotope ^{59}Ni, side by side irradiation can realize the

[1]Research Associate, Department of Quantum Engineering and Systems Science, University of Tokyo, 7-3-1 Hongo, Bunkyo-ku, Tokyo 113, Japan.
[2]Senior Scientist and Staff Scientist, respectively, Pacific Northwest Laboratory, P.O. BOX 999, MS PB-15, Richland, WA 99352, USA.

Copyright© 1996 by ASTM International www.astm.org

substantial variations of helium production rate where the helium production rate is adjustable depending on the ^{59}Ni content and neutron spectra in a reactor position, and irradiating them in the appropriate reactor position. It is very advantageous to apply this technique to nickel-bearing alloys, such as austenitic steels, since doped ^{59}Ni is not regarded as an impurity[2,3]. Another advantage of utilizing ^{59}Ni is that, when applied to fast reactor irradiations, the production rate of helium is kept nearly constant throughout irradiation, unless neutron environments change in doped specimens[4].
The study is one of a series of the works regarding three ternary austenitic alloys(Fe-15Cr-25Ni, Fe-15Cr-25Ni-0.04P, Fe-15Cr-45Ni in both solution-annealed and cold-worked conditions) irradiated in the Materials Open Test Assembly (MOTA) of the Fast Flux Test Facility (FFTF). The objective is to study the separate and synergistic effects of He/dpa ratio, phosphorus addition, nickel content, and cold work level on density change, microstructural evolution, and mechanical strength[5-7]. The present work provided data on microstructures as well as strengths of the alloys irradiated at 465°C to a relatively low dose of 0.42 dpa. The correlation between microstructure and hardening was discussed.

EXPERIMENTAL PROCEDURE

3-mm disks of the alloys were prepared, which were nominally Fe-15Cr-25Ni, Fe-15Cr-25Ni-0.04P, and Fe-15Cr-45Ni (wt.%) in both 20% cold-worked(CW) and solution-annealed(SA) conditions at 1030°C for 30 min. Half of the alloy was produced by doping nickel enriched in 2%-^{59}Ni; the details in the ^{59}Ni acquisition were described by Simons et al.[1].
The irradiations were carried out side by side for both doped and undoped specimens at 465°C to 0.15, 0.28, and 0.42 dpa at above core position (Level 8) in the FFTF/MOTA where the irradiation was continued for approximately two years to reach 0.42 dpa, and the damage rate was evaluated to be about 3×10^{-8} dpa/s[5]. The helium/dpa ratio was determined to be 0.26 and 62 appm/dpa from the post-irradiation measurement of helium levels for the undoped and doped specimens, respectively. The irradiation conditions for the specimens are summarized in table 1.

Table 1 Irradiation conditions of specimen.

COMPOSITION (nomimal,wt.%)	TMT*	IRRADIATION TEMPERATURE	DOSE (dpa)	He/dpa RATIO (appm/dpa)
Fe-15Cr-25Ni	SA			62(^{59}Ni-doped)
Fe-15Cr-25Ni-0.04P	and	465°C	0.15, 0.28, 0.42	and
Fe-15Cr-45Ni	CW			0.26(undoped)

TMT*(Thermo-Mechanical Treatment), SA*; Solution-Annealed, CW*; Cold-Worked.

Microstructures were examined using a JEM 200CX electron microscope. The microscopy of dislocation loops or precipitates was conducted in bright field images. The examination of small-sized clusters was made under weak beam imaging conditions (**g**=200; **g**, 5**g**) since such clusters were rather difficult to be observed in bright field contrasts due to their small sizes. Vickers hardness measurements were carried out for a separate 3-mm disk with a load of 1 kg. The early results were partially presented in papers[8-9].

RESULTS

Microstructure

The feature in 25Ni alloys(SA) was that small-sized clusters were formed by irradiations in addition to dislocation loops. The density and size of dislocation loops increased and the cluster density decreased with irradiations. Fig. 1 is the microstructures of (a) dislocation loops and (b) clusters in the SA ^{59}Ni-doped 25Ni alloys irradiated to 0.42 dpa. The loops were identified to be of interstitial-type from inside-outside imaging technique. Fig. 2 is the histogram for the cluster size with dose in the SA 25Ni alloys. Three features can be pointed out; the first is that very small-sized clusters(<2nm) were densely populated at 0.15 dpa in undoped and doped alloys, the second is that the clusters disappeared with further irradiations resulting in the decrease of cluster density at 0.42dpa, and the third is that the doping with ^{59}Ni enhanced the density of clusters. No cavities were formed in the doped and undoped 25Ni alloys.

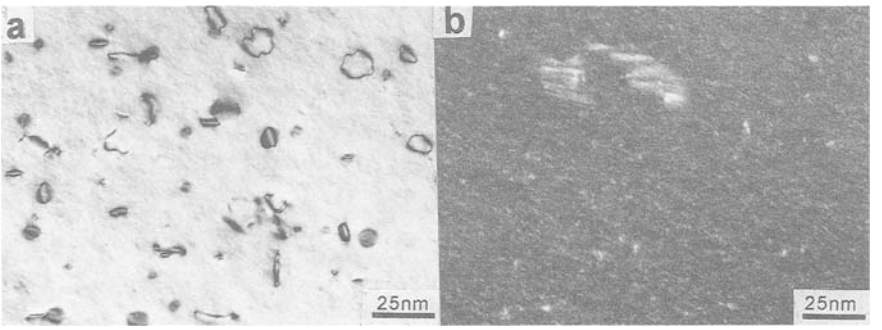


FIG.1 (a) Bright field image for dislocation loops and (b) dark field image for clusters in SA ^{59}Ni-doped 25Ni alloy at 0.42 dpa. The clusters are observed as white dots in (b).

In CW 25Ni alloys clusters (<2nm) were newly produced at 0.28 and 0.42 dpa, while dislocation densities were reduced with irradiations. It was

concluded that no clusters existed at 0.15 dpa. Fig.3 is the dark field image of clusters in the CW undoped 25Ni alloys at 0.28 and 0.42 dpa, where the clusters are observed as tiny white dots. It is clearly shown that the cluster size is larger at 0.42 dpa.

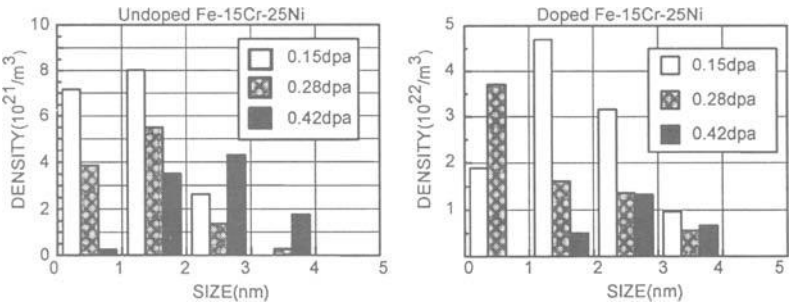


FIG.2 Cluster size histogram in Fe-15Cr-25Ni with dose. It is noted that small-sized clusters disappear partially with irradiation, and that the density is increased by doping with ^{59}Ni.

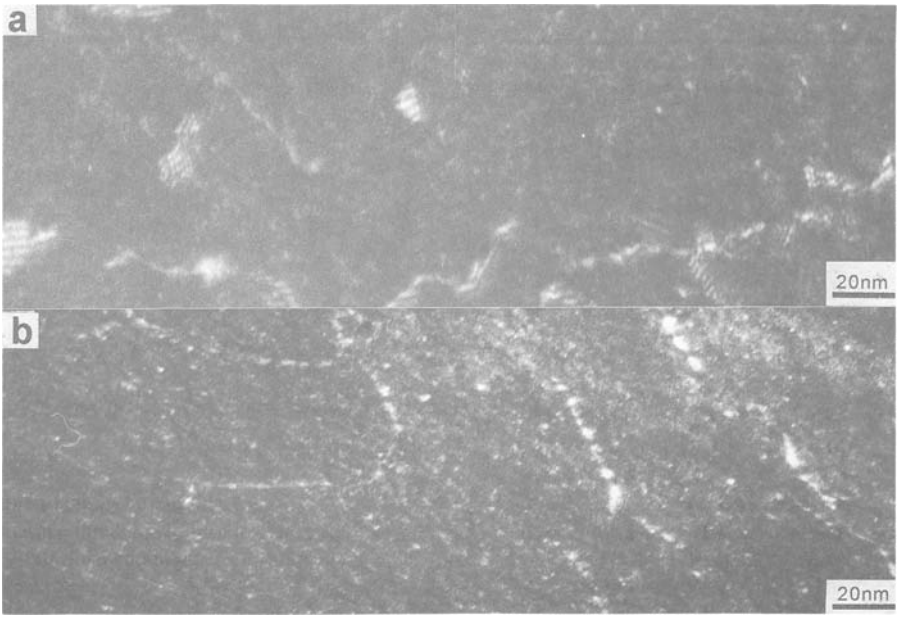


FIG.3 Dark field image of CW undoped 25Ni at (a)0.28 and (b) 0.42 dpa where clusters are observed as white dots. Fringe contrasts in (a) are believed to be due to the segregation of interstitial impurities on dislocation and small loop.

Thin platelet of M_2P (phosphide) was precipitated along <001> directions on (110) planes of the matrix in SA 25Ni-0.04P alloys(fig. 4). Though the thickness and size of the platelet seemed to be slightly increased with

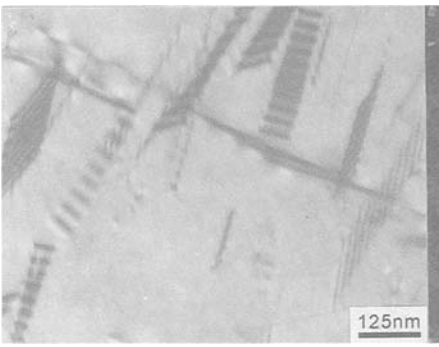


FIG. 4 Phosphide in SA undoped 25Ni-0.04P alloy irradiated to 0.42 dpa.

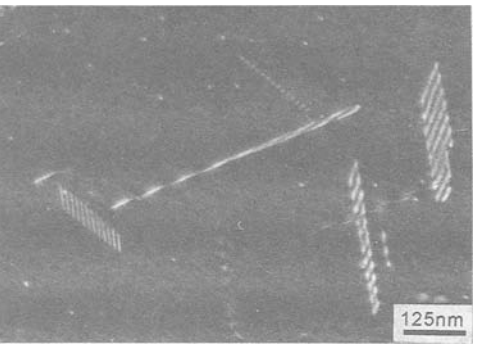


FIG. 5 Dark filed image showing the formation of clusters in SA undoped 25Ni-0.04P alloy at 0.42 dpa. The clusters are observed as white dot.

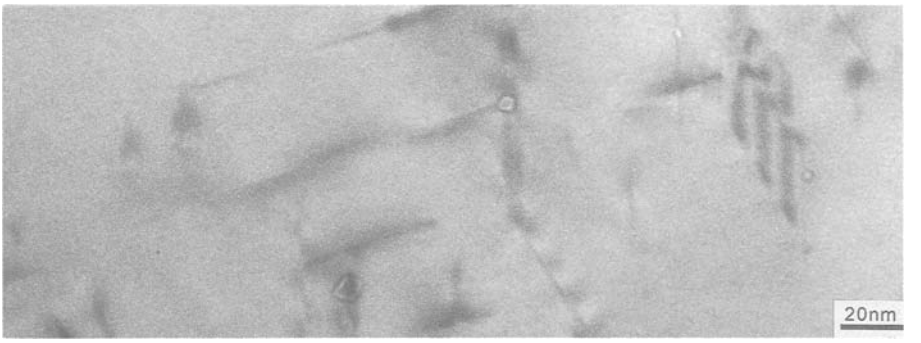


FIG. 6 Cavities on phosphide in SA undoped 25Ni-0.04P at 0.42 dpa.

irradiation, it was unsuccessful to evaluate the density and size quantitatively due to their irregular shape. Fig. 5 shows the occurrence of clusters in the SA 25Ni-0.04P alloy in addition to phosphide. The cluster size was considered to be kept almost constant, though the density($\sim 10^{17}/m^3$) slightly increased with irradiations. The dislocation density due to the clusters was evaluated to be less than $10^9/m^2$ at 0.42dpa. No dislocation loop was observed in the 25Ni-0.04P alloys. Cavities were observed only in the SA 25Ni-0.04P alloys irradiated to 0.42 dpa. The cavities, irrespective of their sizes, were always formed on phosphide. Fig. 6 shows the formation of cavities on phosphide in the SA undoped 25Ni-0.04P at 0.42 dpa. Examinations showed that the doping with

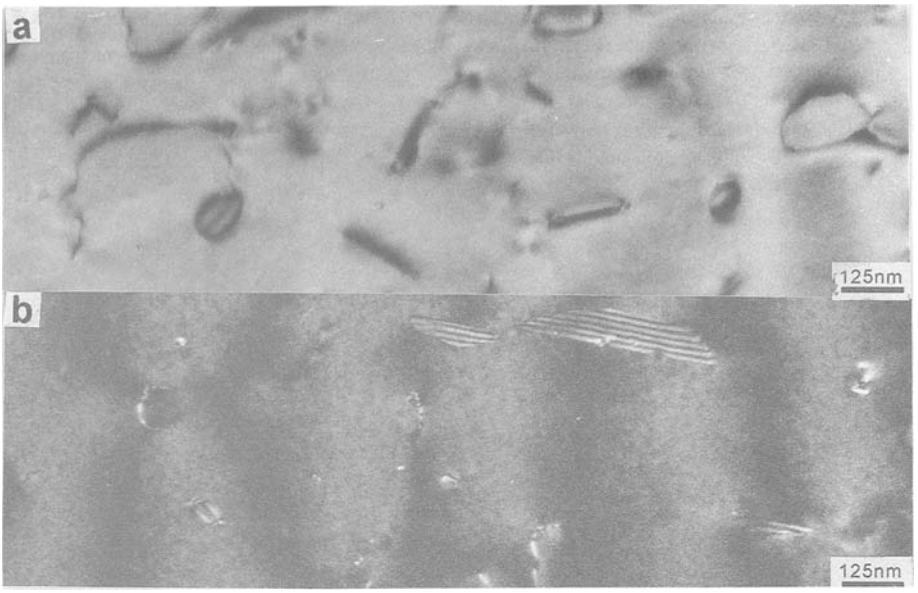


FIG. 7 (a) Loop evolutions and (b) dark field image in SA doped 45Ni alloy at 0.42 dpa, where no clusters are observed.

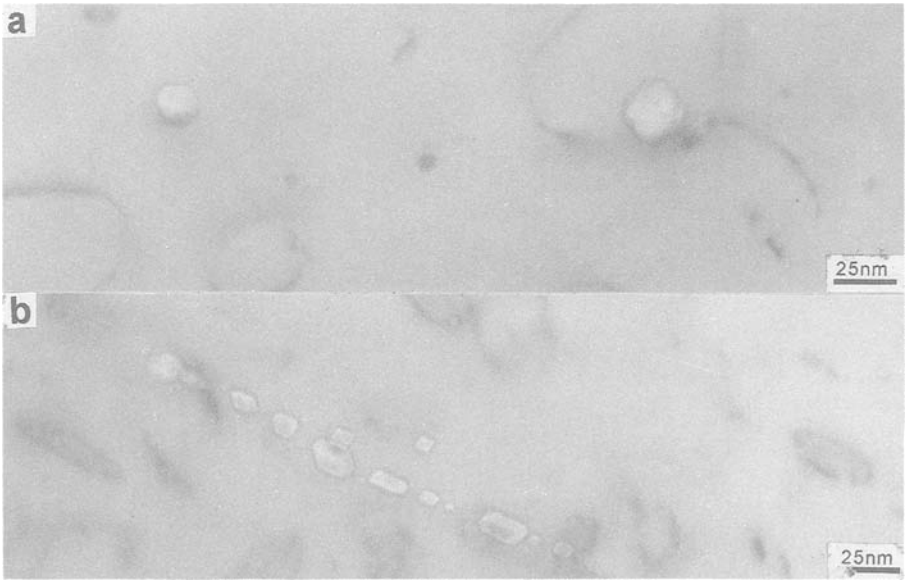


FIG. 8 Cavities in (a) undoped and (b) doped SA 45Ni alloy at 0.42 dpa. ^{59}Ni-doping decreases cavity size and increases density.

^{59}Ni increased the density and decreased the size for cavities. The cavity density for the SA doped 25Ni-0.04P was very low(~2 x $10^{10}/m^3$) and the swelling was estimated to be less than 10^{-13} %; it should be noted that fig. 6 is a selected area where the cavities are locally segregated over an average. Cold work completely prevented the precipitation of phosphide and cavities in the 25Ni-0.04P alloys.
In SA 45Ni alloy, it is characteristic that the density and size for dislocation loops in the 45Ni alloy was higher than those in the 25Ni alloy as seen in fig. 7. No clusters of dot-type as seen in the 25Ni alloys were produced at any dose(fig. 7(b)). No cavities were observed in the alloys at 0.15 and 0.28 dpa. The cavities at 0.42 dpa were inevitably formed on dislocations. The cavity density and the swelling was on the order of $10^{10}/m^3$ and 10^{-10} %, respectively. The doping with ^{59}Ni reduced the cavity size while the density was increased similar to the case of the 25Ni-0.04P. Tangled dislocations in the CW 45Ni alloy gradually decreased in density during the irradiation at 465°C to 0.42 dpa.

Hardness Measurements

The results of hardness measurements are presented in fig. 9. ^{59}Ni doping increased hardness in every alloys, compared to undoped alloys. It was pointed out for SA alloys that the hardness in the SA 25Ni alloy decreased after 0.15 dpa, though the degree was small, in spite of the increase of dislocation density due to the nucleation and growth of loops. On the other hand, the hardness in CW doped 25Ni alloy was increased from 0.28 to 0.42 dpa.

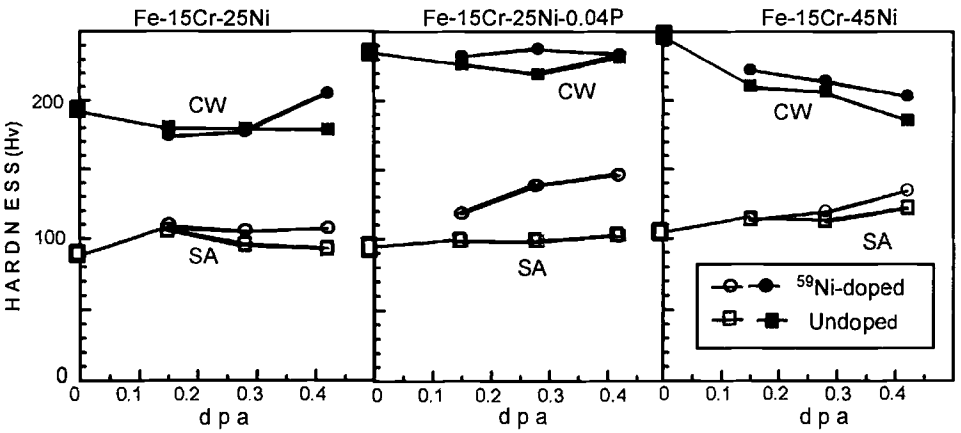


FIG.9 Hardness as a function of dpa for alloys irradiated at 465°C. Note that softening is observed after 0.15 dpa in SA 25Ni alloys, and that hardening occurs effectively by ^{59}Ni-doping in SA 25Ni-0.04P alloy.

Furthermore, it was characteristic that the hardness was almost unchanged during irradiations in CW 25Ni-0.04P alloys, whereas the SA doped 25Ni-0.04P alloys showed a high hardening by irradiations compared to SA undoped 25Ni-0.04P. The hardness in the SA and CW 45Ni alloys increased and decreased with irradiation, respectively.

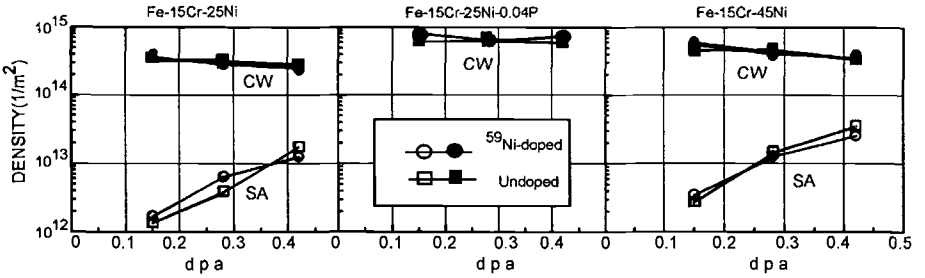


Fig 10 Dislocation density as a function of dpa, Data for SA 25Ni-0.04P are excluded due to no formation of dislocation loops and a low density of clusters during irradiation.

DISCUSSION

The formation of clusters was strongly influenced by a higher helium production rate by ^{59}Ni doping in SA 25Ni alloys as seen in fig. 2. Furthermore, the clusters were observed to be formed at o.28 and 0.42 dpa in CW 25Ni alloys. The production and annihilation of such clusters were considered to be important for understanding the strength behaviors by irradiation. The results as for the 25Ni alloys were partially reported[9], which indicated that the hardness decrease in the SA 25Ni alloy was successfully explained by taking into account both cluster formation and dislocation evolution. The nature of clusters has not been determined directly from electron microscopic techniques such as 2½D method. Yoshida et al. examined similar small defect clusters in 316 stainless steels irradiated at 60 and 200°C by 14 MeV neutrons and concluded that the clusters were of interstitial type[10]. Maziasz also identified the loops of interstitial-type in austenitics irradiated at 200°C[11]. However, the clusters observed in the present study were considered to be of vacancy-type from the following two points: The first one was that relatively large clusters sometimes showed SFT (Stacking Fault Tetrahedra) images. The second was that the clusters did not form the denuded zone near grain boundaries, while the loops observed in this study clearly showed the denuded zone(~50nm in width) parallel to grain boundary, suggesting the different nature of the loop and cluster. In contrast to 25Ni alloys, such clusters were never found in both SA and CW 45Ni alloys. Loop number

densities were higher by a factor of about 2 in SA 45Ni alloys than those in SA 25Ni alloys. It was investigated that higher nickel enhanced the mobility of self-interstitials in Fe-Ni-Cr system[12]. This means that self-interstitials tend to form loops easily or to eliminate the clusters or small loops of vacancy-type for higher nickel alloys, being consistent with the present observations in the 45Ni alloys. The doping with ^{59}Ni clearly enhanced the hardening of alloys as shown in fig. 9.

No remarkable difference in dislocation density was found between the doped and undoped alloys as shown in fig. 10, where no data were shown as for SA 25Ni-0.04P. This is due to no formation of dislocation loop and a low density of cluster produced during irradiations. As for the CW 25Ni-0.04P alloys, the hardness change was small and the dislocation density was almost constant with the irradiation. The hardness in the CW 25Ni-0.04P alloy was qualitatively understood from the dislocation density(figs. 9 and 10). On the other hand, no dislocation loop were produced and the density of cluster was very low in SA 25Ni-0.04P alloy. In addition, The doping with ^{59}Ni was effective for the hardening. However, the cluster density was comparable between the doped and undoped alloys and could not explain the remarkable hardening. Though it was speculated that the hardening may be ascribed to the density increase and size decrease for cavities in the SA doped 25Ni-0.04P alloy, the density of cavities observed was very low, and was not sufficient statistically to discuss the hardening mechanism. This point remains to be further studied together with the effects of helium production rate on the formation of phosphide. The hardening in the SA 45Ni alloy was attributed to the nucleation and growth of dislocation loop with irradiations, while the softening in the CW 45Ni alloys was caused by the density decrease of tangled dislocations(figs. 9 and 10).

The addition of phosphorus produced phosphide in the SA 25Ni-0.04P alloys at 465°C. It was clearly shown that the precipitation of phosphide prevented the nucleation of loops at 465°C, compared to phosphorus-free alloys. This suggested that the interface between phosphide and matrix acted as a strong sink for point defects produced, and that phosphorus remarkably lowered the efficiency of loop nucleation[13]. Lee et al. indicated that the phosphorus stimulated loop nucleation and the precipitation of phosphide on small dislocation loops[14]. The present results were not always consistent with Lee's result. This may arise from the difference in alloy compositions and total fluence between the experiment by Lee et al. and the present study, though the irradiation temperature was comparable. The nucleation site for cavities was concluded to be phosphide in the experiments by Lee et al. and Watanabe et al.[14,15]. In fact, all cavities, irrespective of their sizes, were found to be associated with phosphide in the present study. It was explicitly shown that helium increased the nucleation sites for cavities in both SA 25Ni-0.04P and 45Ni alloys; this was well known for austenitics[16,17]. The

nucleation sites for cavities were identified to be loops or segments of dislocations in SA 45Ni alloys without exception in the present study. This was characteristic in austenitic steels when the dose was relatively low as previously reported[18]. No phosphide was detected on dislocations or in the matrix in CW 25Ni-0.04P alloy, where the dislocation density was kept almost constant as seen in fig. 10, suggesting that the hardness behavior(fig. 9) was understood from the dislocation density.

CONCLUSION

The major conclusions are summarized as follows:

(1) Helium is effective for hardening with irradiation.
(2) Dot clusters are formed in addition to loops of interstitial-type in 25Ni alloy. Density and size of dot clusters are important for understanding strength behavior.
(3) Phosphide is formed and the formation of clusters is delayed in SA 25Ni-0.04P alloy. Cavities are produced on phosphide.
(4) Dislocation loops are formed without the formation of clusters in 45Ni alloy. Cavities are nucleated on dislocations.
(5) Hardening is explained by the density of dislocation and the density and size of clusters in 25Ni alloy, and by dislocation density in 45Ni and CW 25Ni-0.04P alloy.

REFERENCES

1. Simons, R.L., Garner, F.A. and Matumoto, W.Y., J.Nucl.Mater. 141-143 (1986)pp.1057-1060.
2. Mansur,L.K., Rowcliffe, A.F., Grossbeck,M.L. and Stoller, R.E.,J.Nucl. Mater.139(1986)pp.228-238.
3. Kawanishi,H., Garner,F.A. and Simons, R.L., J. Nucl. Mater. 179-181 (1991)pp.511-514.
4. Greenwood, L.R., Garner, F.A. and Oliver,B.M., J. Nucl. Mater.(1992) pp.1051-1055.
5. Garner, F.A. and Brager, H. R., J. Nucl. Mater.154-157(1988)pp.833-837.
6. Stubbins, J.F. and Garner, F.A., J.Nucl.Mater. 179-181(1991)pp.523-525.
7. Stubbins, J.F. and Garner, F.A., J.Nucl.Mater.191-194(1992)pp.1300-1304.
8. Garner,F.A., Hamilton, M.L., Greenwood,L.R., Stubbins, J.F. and

Oliver, B.M., Effect of Radiation on Materials: ASTM STP 1175, A.S. Kumar, D.S. Gelles, R.K. Nanstad and E.A. Little, Eds., American Society for Testing and Materials, Philadelphia, 1993, pp.921-939.

9. Kawanishi, H. and Garner, F.A., J. Nucl. Mater. 212-215(1994)pp.498-502.
10. Yoshida, N., Heinisch, H.L., Muroga, T., Arai, K. and Kiritani,M., J. Nucl.Mater.179-181(1991)pp.1078-1082.
11. Maziasz, P.J., J. Nucl. Mater. 191-194(1992)pp.701-705.
12. Dimitrov, C. and Dimitrov, O., J.Nucl.Mater. 152(1988)pp.21-29.
13. Watanabe, H., Aoki, a., Murakami, H., Muroga, T. and Yoshida, N., J. Nucl.Mater.155-157(1988)pp.815-822.
14. Lee, E.H. and Packan, N.H., Effect of Radiation on Materials: 14th International Symposium, ASTM STP 1046, N.H. Packan, R.F. Stoller, and A.S. Kumar, Eds., American Society for Testing and Materials, Philadelphia, 1989, pp.133-146.
15. Watanabe, H., Muroga,T. and Yoshida, N., Effects of Radiation on Materials: ASTM STP 1175, A.S. Kumar, D.S. Gelles, R.K.Nanstad and E.A. Little, Eds., American Society for Testing and Materials, Philadelphia,1993, pp.951-963.
16 Kawanishi, H., Nodaka, M., Sekimura, N. and Ishino, S., J.Nucl.Mater. 122&123(1984)pp.284-288.
17. Stubbins, J.F., Nevling, J.E., Garner, F.A., and Simons, R.L., Effects of Radiation on Materials: 14th International Symposium, ASTM STP 1046, N.H. Packan, R.F. Stoller, and A.S. Kumar, Eds., American Society for Testing and Materials, Philadelphia, 1989, pp.147-159.
18. Kawanishi, H. and Ishino, S., J.Nucl.Mater.155-157(1988)pp.806-809.

Shamardin, V. K., Neustroev, V. S., Povstyanko, A. V., Bulanova, T. M., Ostrovsky, Z. E.[1], Kuznetzov, A. A., Kursevitch, I. P., Nikolaev, V. A.[2]

Swelling, Mechanical Properties and Structure of Austenitic High-Nickel Alloy Irradiated in a Fast Reactor

REFERENCE: Shamardin, V. K., Neustroev, V. S., Povstyanko, A. V., Bulanova, T. M., Ostrovsky, Z. E., Kuznetzov, A. A., Kursevitch, I. P., Nikolaev, V. A., **"Swelling, Mechanical Properties and Structure of Austenitic High-Nickel Alloy Irradiated in a Fast Reactor,"** *Effects of Radiation on Materials: 17th International Symposium, ASTM STP 1270,* David S. Gelles, Randy K. Nanstad, Arvind S. Kumar, and Edward A. Little, Eds., American Society for Testing and Materials, 1996.

ABSTRACT: Specimens from fuel assembly wrappers and control rod cases of 0.07C-15Cr-35Ni-3Mo-B-Zr-Y alloy were investigated after irradiation in the BOR-60 and BN-600 reactors up to a maximum damage dose of about 110 dpa at temperatures between 340 to 550°C.

Maximum swelling occurs at 420 to 430°C with 6% at a dose of about 80 dpa and 13.5% at a dose of 108 dpa. The maximum change in strength properties and corresponding decrease of ductility occur at an irradiation temperature of 385°C. With increasing testing temperature the ductility increases from 3-6% up to 22% at 450°C for the material irradiated at 60-80 dpa.

Frank dislocation loops with an average diameter of 25 nm (concentration is $2x10^{16}$ cm^{-3}), voids having diameter between 20 to 23 nm (concentration is $(6-7)x10^{14}$ cm^{-3}) and semicoherent needle-like precipitates with an average length of 21 nm, oriented to several directions, were observed in the alloy structure irradiated to 60 dpa at 430°C.

Analysis of the experimental data was performed and the service life time of the investigated alloy was estimated for use as a material for control rod cases of the BOR-60 reactor.

KEYWORDS: high-nickel alloys, mechanical properties, neutron irradiation, radiation swelling.

[1]Head of laboratory, Leading Research Worker, Senior Research Worker, Research Worker, Senior Research Worker, Research Institute of Atomic Reactors, 433510 Dimitrovgrad, Ulyanovsk Region

[2]Senior Research Worker, Senior Research Worker, Head of Laboratory, Central Research Institute of Structural Materials, 193167 St.-Petersburg, Russia, Naberezhnaya Reki Monastyrki, 1

Copyright© 1996 by ASTM International www.astm.org

The relatively higher resistance to radiation swelling of three-component Fe-Cr-Ni alloys is known [1-3] to depend on the nickel content. Also known to be important, alloying with elements - titanium, niobium, aluminium - which influence the solid solution decomposition and have a high lattice mismatch factor [4],

$$\varepsilon = \frac{R_n - R_0}{R_0}$$

where R_n - radius of alloying atom,
R_0 - radius of matrix atom
efficiently changes resistance to swelling of the given alloys.

According to the proposal suggested by Prof. A.M.Parshin [5] swelling suppression is related to peculiarities of structural transformations in the incubation period of solid solution decomposition and the recombination of point defects in the elastically deformed areas associated with secondary phases.

The strong nickel effect on swelling of austenitic steels and alloys, according to F.Garner [6], is related to its effect on the efficient diffusion of vacancies and, hence, on void nucleation. Other factors as:

a) the susceptibility Fe-Cr-Ni alloys to spinodal-like decomposition-formation under irradiation in the structure of areas with different nickel and chromium contents [7],

b) reduction of the lattice parameter and material densification,

c) additional strengthening [8].

Compositions having nickel content near 35% are particularly susceptible to such a decomposition [9].

In the former USSR a precipitation-strengthened Fe-15Cr-35Ni-2Mo-1Nb-Ti-Al-B austenitic alloy (SA) was widely used for fast reactor applications. Steel of this composition is characterized by a high resistance to swelling [10], <2% at a fast neutron fluence of $1x10^{23}$ cm^{-2} (E>0.1 MeV) within the temperature range 400-650°C; it is however susceptible to radiation embrittlement [11]. The last aspect was the reason for development of similar composition with solid solution strengthening and modification due to microalloying with boron, zirconium, yttrium and other surface-active elements that alloy grain boundaries and have a refining effect in the process of melting [12].

V.E.Zelenski et al. [13,14] showed that even a small quantity of yttrium, scandium etc. available in the solid solution markedly changed the mobility of atoms, elastic stress dislocation fields and interfacing energies and, hence, changed the nature and kinetics of precipitation. Ref.[15] demonstrated the efficiency of combined boron and rare earth additives to stainless steel from the standpoint of resistance to swelling and embrittlement up to damage doses of about 80 dpa.

Based on this work a Fe-15Cr-35Ni-3Mo alloy was proposed having microadditives of boron, yttrium and zirconium [16]. In this paper main attention is paid to investigation of mechanical properties of the given alloy after neutron

irradiation at high fluences and at temperatures characteristic of the opertaion conditions for the fast reactor control rod cases.

MATERIAL AND METHODS OF INVESTIGATION

Table 1 presents the chemical composition of the alloy under investigation, its thermal treatment, specimen types and irradiation parameters. The main features of the alloy are the additions of 0.01% of boron, 0.05% of zirconium, 0.01% of yttrium and 0.009% of phosphorus in the composition. Cylindrical specimens were used having a gauge diameter of 3 mm and length of 15 mm. In addition, a number of flat specimens was produced from previously irradiated products by electro-discharge machining (Table 1).

Mechanical properties were determined at a deformation rate of 1 mm/min. In most cases the testing temperature was equal to that of the irradiation temperature . Density was measured by the immersion method. The measuring accuracy achieved was ± 0.3%.

Structural examinations were performed with the EM-125 electron microscope. The average diameter of dislocation loops,

Table 1

Chemical composition, thermal treatment and irradiation conditions

Chemical composition	Thermal treatment conditions	Specimen type	Reactor	T_{irr} °C	Max. dose, dpa
Fe-0.05C-14.6Cr-35.6Ni-2.79Mo-0.31Si-1.75Mn-0.01B-0.05Zr-0.01Y-0.009P-0.01S	1 hr solution treated at 1050°C, cooling in air SA cold worked CW (20%)	Specimens,15 mm gauge length, ∅ 3 mm	BOR-60	400-440	60
		The same	BN-600	385-490	108
		Fuel assembly wrapper, 44·1 mm	BOR-60	320-570	50
		AZ-1 control rod cladding, 44·1 mm	BOR-60	330-460	55
		Control rod cladding, 84 x 3	BN-600	365-500	57

vacancy voids and second phase precipitates was determined with a 10% error; an error of their density measurements is 30% and that of volume fraction measurements for voids and phases is between 30 to 35%.

INVESTIGATION RESULTS

The results on swelling and mechanical properties of Fe-15Cr-35Ni-3Mo-B-Zr-Y alloy as specimens and components will be described separately in accordance with as presented in Table 1.

SPECIMENS IRRADIATED IN THE BOR-60 REACTOR

The specimens were irradiated in four material science assemblies. The irradiation temperature ranged from 400 to 440°C. The damage dose ranged from 18 to 64 dpa (Table 1).

Fig.1 presents the swelling results. No difference was determined in swelling of solution-annealed and aged (20% CW + 1 h aging at 800°C) alloy. The annealing time does not effect swelling. Swelling suppression due to cold-worked deformation (20%) is evident within the damage dose range up to 50 dpa.

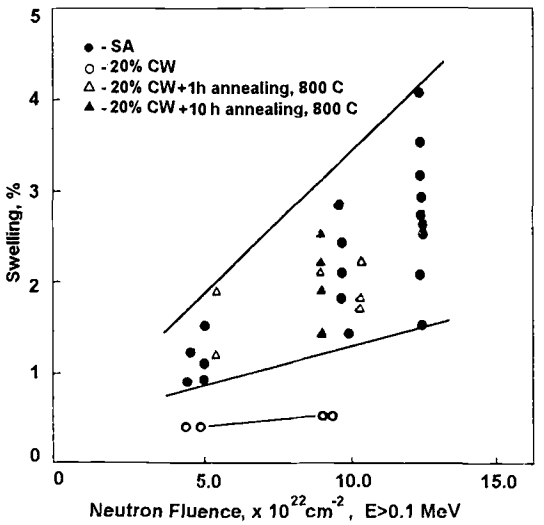


FIG.1 Dose dependence of alloy swelling as a function of the initial structural state after irradiation in BOR-60 at a temperature 450°C.

Fig.2 presents the dose dependence of the yield strength and the uniform elongation of the 15Cr-35Ni alloy at testing temperatures of 500 to 550°C. There was no significant difference between the yield strength properties of the four thermo-mechanical (TMT) conditions studied. Increased scattering and, on the whole, lower ductility values are characteristic of the alloy ductility in cold-worked state (Fig.2).

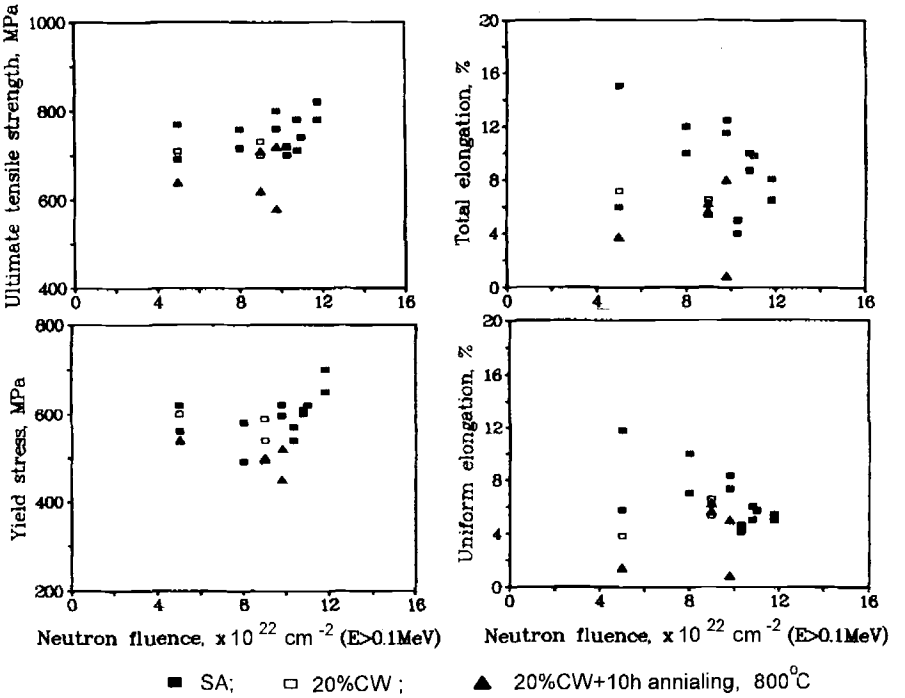


FIG.2 Dose dependence of mechanical properties of an alloy at T_{test}=500-550°C ($T_{irr.}$=400-420°C).

After irradiation at a fluence of 10.8×10^{22} cm^{-2} (E>0.1 Mev) at 450°C (Fig.3) with increasing testing temperature approaching 800°C the total elongation values approach zero.

SPECIMENS IRRADIATED IN THE BN-600 REACTOR

Following an incubation dose of ~50 dpa, the swelling rate is ~0.28 %/dpa (Fig.4). Fig.5 indicates that swelling is a maximum for the region of 400-430°C.

The maximum changes in the strength properties and, correspondingly, the maximum value of the total elongation is observed at an irradiation temperature of 390°C (Fig.6).

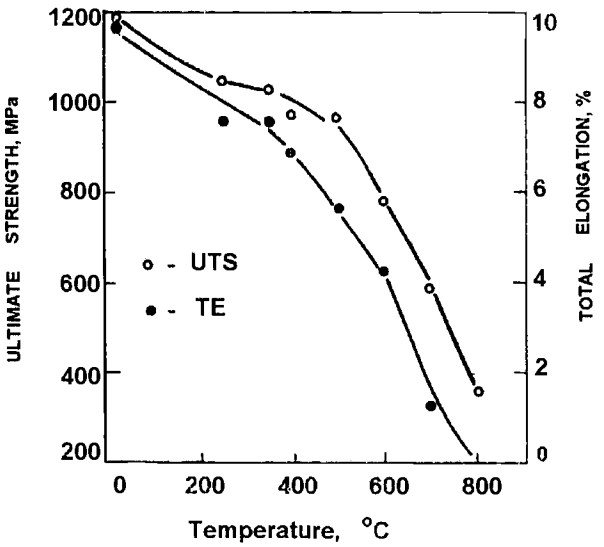


FIG.3 Temperature dependence of ultimate strength and total elongation for an alloy irradiated with fast neutron fluence of $10.8x10^{22}cm_{-2}$ (E>0.1 MeV) at 450°C.

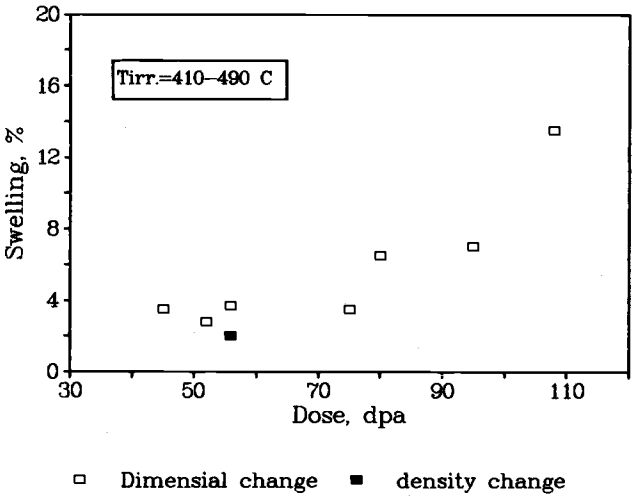


FIG.4 Dose dependence of the alloy (SA) swelling after irradiation at 410-490°C in BN-600.

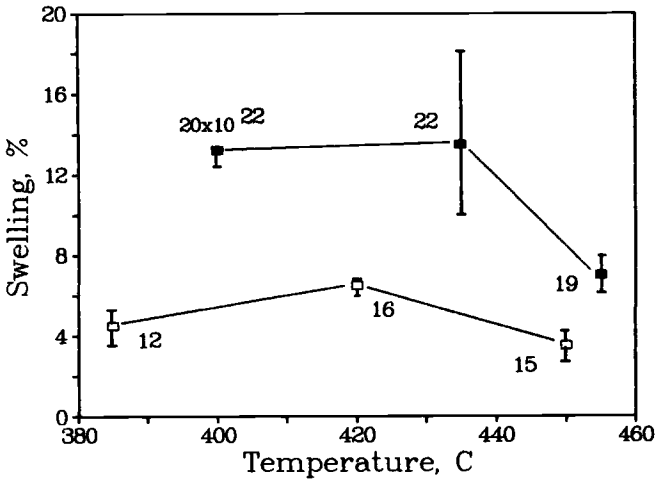


FIG.5 Temperature dependence of the alloy (SA) swelling after irradiation in BN-600.

After irradiation at all temperatures ductility remains at a sufficiently high level within the dose range 60 to 80 dpa (fast neutron fluence range from 1.2 to 1.65 x 10^{23} cm^{-2} E>0.1 MeV). With increasing irradiation temperature from 385 to 450°C a sharp rise of the total elongation value from 3-6% to 23% is observed.

EXPERIMENTAL HEXAGONAL FUEL ASSEMBLY WRAPPER OF THE BOR-60

Fig.7 presents the measurement data on the dimensions of the hexagonal wrapper (44x1 mm) of the alloy (20 % CW + 1 h at 800°C) irradiated up to the maximum fluence of 10.3 x 10^{22} cm^{-2} (E>0.1 MeV) within the temperature range from 320 to 570°C. The maximum deformation value did not exceed 0.5 mm corresponding to a swelling value of 3.4%. The tension testing results (Fig.7, Table 2) demonstrate the suitability of the alloy for manufacturing fast reactor control rod cases as well as for their potential for operation at higher fast neutron fluences.

AZ-1 CONTROL ROD CASE FROM THE BOR-60 REACTOR

Maximum swelling of 1.4% was noted above the core center that correlates with the temperature maximum of swelling of 420°C defined in the BN-600. Mechanical testing of specimens in the temperature range from 20 to 650°C (Fig.8) testifies to the similarity of the strength and ductility values at the center level and in the lower part of the core.

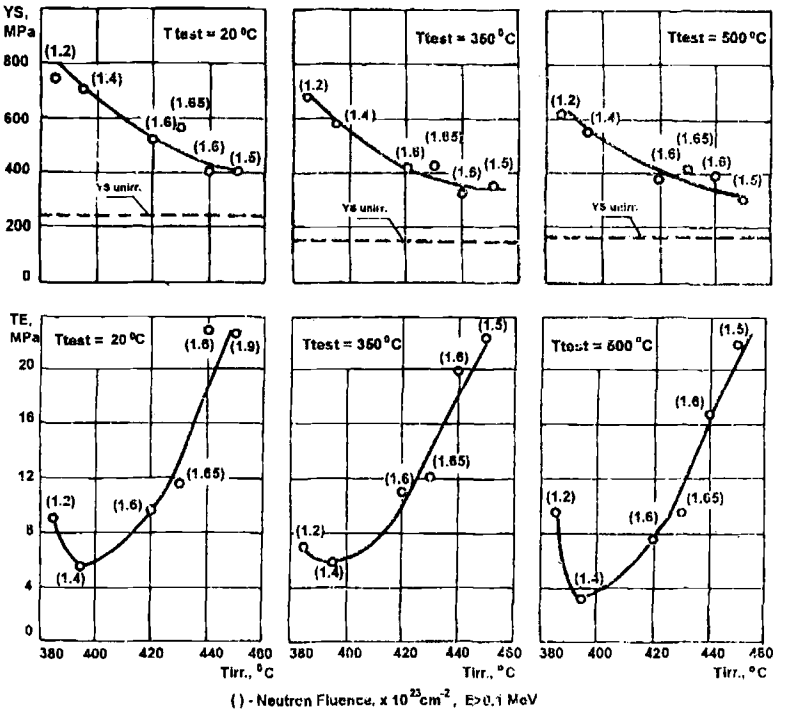


FIG.6 Yield stress and uniform elongation of the alloy as a function of irradiation and test temperature.

Table 2

Mechanical properties of the alloy specimens of the BOR-60 fuel assembly hexagonal wrapper (20% CW + 1 hr at 800°C)

Position from core center, mm	$T_{irr.}$ °C	T_{test} °C	Fluence, $x10^{22}$ n/cm_2	UTS, MPa	YS, MPa	UE, %	TE, %
-325	310	100	2.3	930	910	1.1	1.1
-75	380	250	9.8	660	590	6.9	6.9
-125	350	750	8.8	310	270	4.8	4.8
-25	410	750	10.2	320	290	4.5	4.5
+225	550	750	5.0	350	280	5.9	5.9

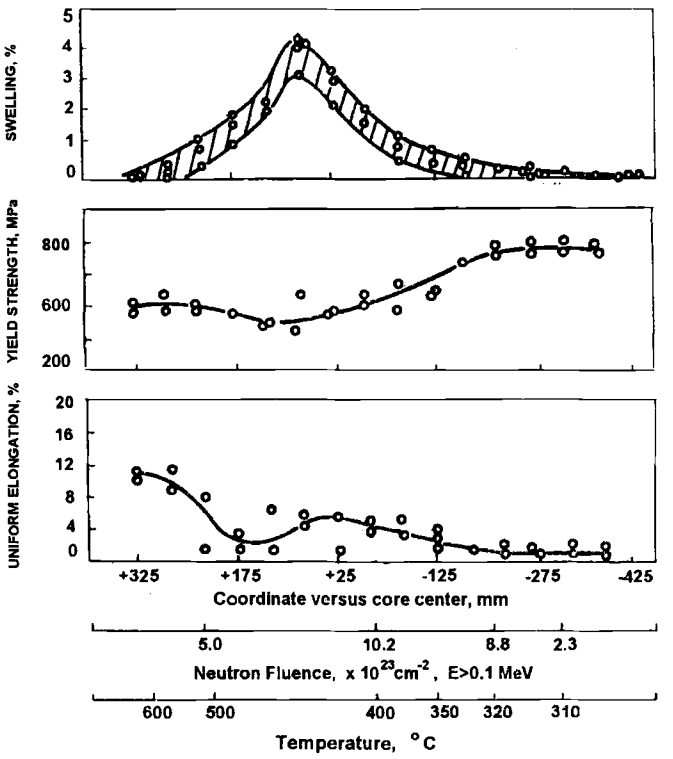


FIG.7 Measurement results on the deformation of 44x1 mm hexagonal tube (experimental fuel assembly) and its mechanical properties after irradiation in BOR-60 up to the maximum neutron fluence of $10.3 \times 10^{22} cm^{-2}$ (E>0.1MeV) at temperatures between 320 to 570°C.

In the upper part of the core at an irradiation temperature of about 460°C lower strength and high ductility values were noted. There are some anomalies in the change of the strength equal or higher than 400°C.

BN-600 CONTROL ROD CASE

The tensile properties (Fig.9) of the alloy were determined using specimens with a 200 mm gauge length located symmetricly about the core center. At all testing temperatures the total elongation did not decrease below 4%. Following irradiation to $1.2 \times 10^{23} n/cm^2$ (E>0.1 MeV) at ~440°C diametral and density measurements yielded swelling values of 3.5% and 2.6%, respectivly.

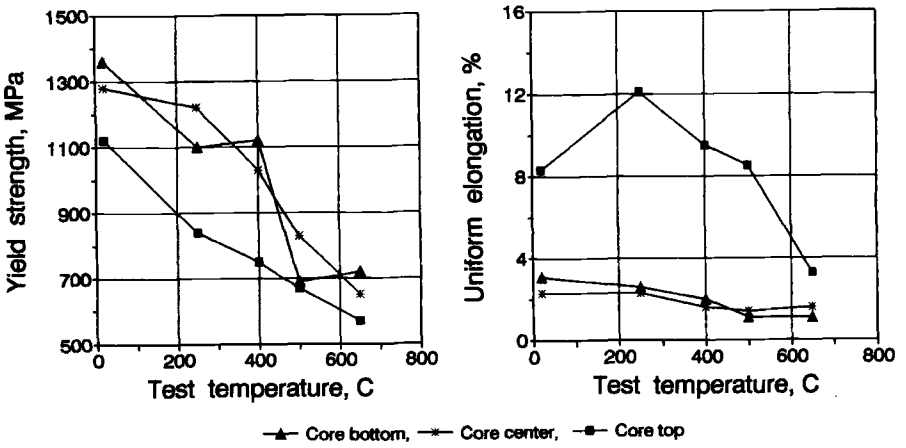


FIG.8 Temperature dependence of yield strength and uniform elongation of the material for AZ-1 control rod cladding of BOR-60.

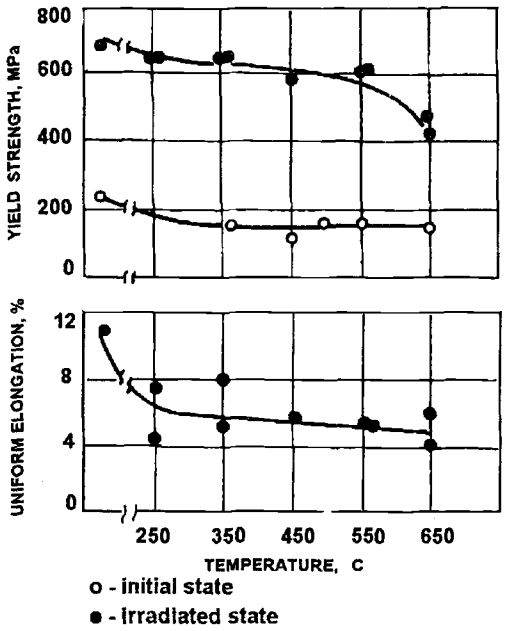


FIG.9 Temperature dependence of mechanical properties of the material for experimental claddings irradiated in BN-600 up to maximum neutron fluence of $12x10^{22}cm^{-2}$ (E>0.1 MeV) at $T_{irr.}$=440°C.

TEM EXAMINATION RESULTS

The TEM examination of structure was performed with specimens of the BOR-60 control rod cases cut out at the level of the core center. Irradiation to 54 dpa at 430°C produced three major microstructural components:

a) dislocation loops (Fig. 10a)

b) vacancy voids (Fig. 10b)

c) fine-dispersion needle-like matrix precipitation (Fig.10c)

The average diameter of dislocation loops is estimated to be about 25 nm and their concentration is $2 \times 10^{16} cm^{-3}$. As Fig.10 shows, in certain foil orientations the loops have stacking fault contrast, i.e. they are faulted Frank loops. The average void diameter is 20-23 nm and the void concentration - $(6\text{-}8) \cdot 10^{14} cm^{-3}$.

Swelling estimated from TEM data is ~ 0.4%. Needle-like precipitates are oriented to several directions. The average needle length is 21 nm, estimated from the orientations that give the maximum needle length projection. This value is underestimated as only projections were measured but not the real needle length. The maximum precipitation length is 75 nm. This value is underestimated as only projections were measured but not the real needle length. The maximum precipitation length is 75 nm. The needle concentration is estimated as $1 \times 10^{16} cm^{-3}$. The analysis of microdiffraction pictures of the matrix with the needle-like precipitations (Fig.10c) shows that they do not produce self-reflection. Streaking of the matrix reflections (Fig.10c) indicates that the needle-like precipitates are coherent with the martix and only in some cases (Fig.10c) they are incoherent and have significant phase contrast differing from that of the matrix.

There are patches of continuous second phase precipitation probably, of a composite carbide, (Fig.10d), occuring on some grain boundaries.

DISCUSSION

Fig.11 shows that the swelling of the solution-strengthened 15Cr-35Ni-3Mo alloy, additionally alloyed with boron, yttrium, phosphorus and zirconium is compared to annealed 18Cr-10Ni steel.

Swelling suppression in our experiments is explained by a complex of mechanisms whose effects have been well demonstrated in the experimental works [19,22]. We recognized the presence of the needle-like precipitates (Fig.10b) in the structure, representing, perhaps, composite phosphides of M_2P type. The fact that such precipitates were detected at 420°C, i.e. at the temperature significantly lower than those at which these precipitations were observed in steels of the 16Cr-17Ni type, confirms the dependence of this mechanism on the content of nickel and other elements in steel. Phosphide precipitates of this shape have been shown to trap helium atoms [19]. They accelerate defect recombination at the precipitation-matrix interface, stabilize the network of dislocations, limit radiation-induced segregation and inhibit formation of G-phase [21] enriched in nickel and silicon.

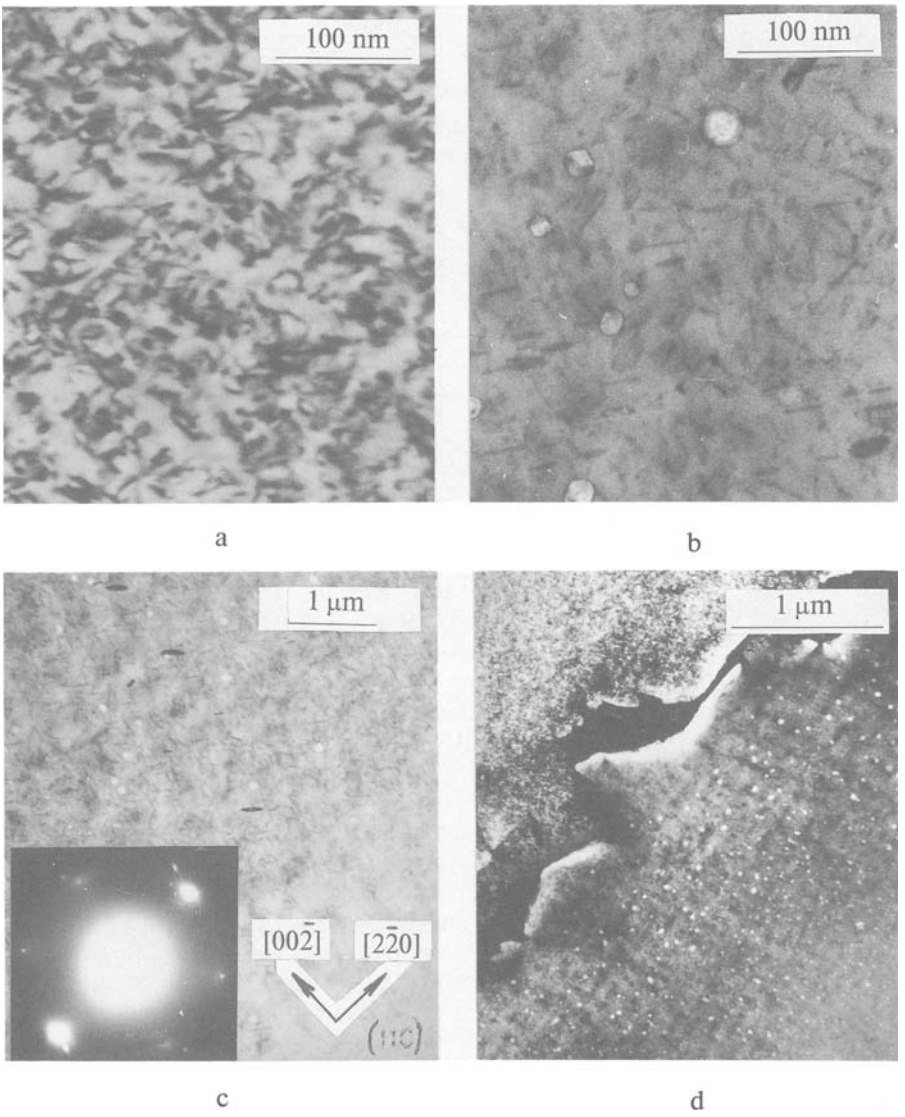


FIG.10 Microstructure of Fe-15Cr-35Ni-3Mo-B-Zr-Y alloy after irradiation at about 430°C up to 54 dpa

a - dislocation loops,

b - vacancy voids and needle-like precipitates,

c - needle-like precipitates and microdiffraction picture,

d - boundary precipitates.

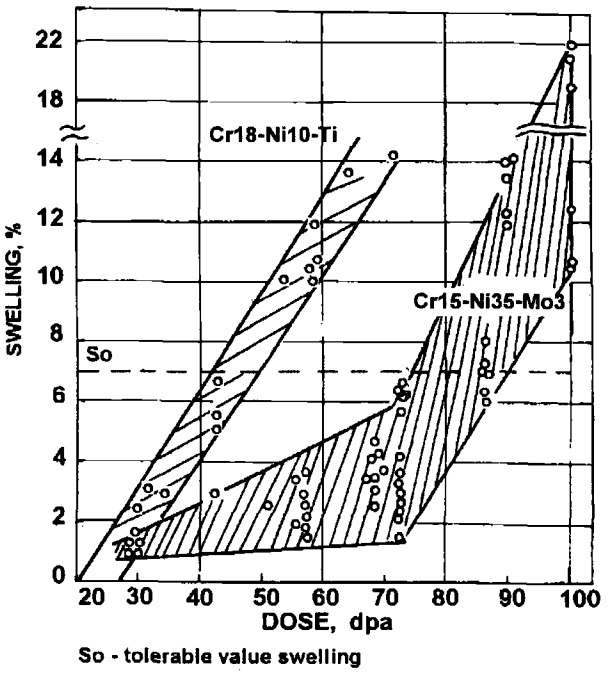


FIG.11 Summarized dose dependence of swelling of Fe-15Cr-35Ni-3Mo-B-Zr-Y alloy irradiated in BOR-60 and BN-600 within the temperature range 410 - 480°C.

Swelling of the investigated alloy is related not only to vacancy void formation but also to the redistribution of alloying elements which changes the lattice parameter. Thus, paper [8] shows that irradiation of Fe-34.5Ni-15.1Cr alloy in EBR-II at a fluence of 2.5 x 10^{22} cm^{-2} (E>0.1 MeV or 12.5 dpa) and 550°C led to alloy densification, according to immersion testing data. These anomalies are explained by a spinodal-like decomposition of Fe-Cr-35Ni compositions in the course of irradiation. The minimum irradiation temperature, at which this phenomenon was observed, was 400°C according to the data on radiation strengthening [8].

As it was already mentioned [8] the process of spinodal-like decomposition provides an additional strengthening component for alloys with 24.5 to 45.3% nickel content at damage dose rate between 10.5 to 12.5 dpa and $T_{irr.}$=450°C. The following facts are of interest with respect to the effect of spinodal-like decomposition under irradiation on the change in mechanical properties of the alloy. Fig.3 shows changes in the character of smooth decrease in strength with increasing test temperature of alloy specimens in the range 380-450°C. The curve characterizing the change in the properties of the AZ-1 control rod cases, at the

level lower than the core center, ($T_{irr.}$ <400°C) indicates the introduction of an additional mechanism into the temperature changes of the strength characteristics whereas the curves for the core top and core center material do not.

The probable mechanism influencing the behavior of the irradiated alloy at $T_{irr.}$> 380-400°C is spinodal-like decomposition of solid solution (Fig.6). The values of radiation strengthening and decrease of the total elongation achieve their maximum at irradiation temperatures between 390-400°C. These temperatures are in good conformity with the low value of the irradiation temperature at which the effect of spinodal-like decomposition of the solid solution in Fe-15Cr-35Ni systems is still assumed.

An increase of ductility within the irradiation temperature range 400-460°C (Fig.6 for T_{test} =500°C; Fig.8 - the curve corresponding to the top of the core) is consistent with the effect of spinodal-like decomposition of solid solution on the ductility parameters of Fe-15Cr-35Ni-Y-Zr-B alloy. The micrographs of the electron-microscopy (Fig.10) reveal irregularities on the foil surface that is an indirect foil surface that is an indirect indication of non-uniform etching due to spinodal -like decomposition of the solid solution.

The criterion of the service life of control rod cases and fuel assembly wrappers is an increase of the manufacturing gap between the neihgbouring fuel assemblies of 1 mm for BOR-60. A certain level of mechanical properties must also be maintained taking into consideration that control rod cases are operated in the absence of the external loading, the gap will be determined by radiation swelling and its tolerable value must not exceed 7%.

As Fig.11 shows, the various thermomechanical conditions of the 15Cr-35Ni-Y-Zr-B alloy have almost two times as much service life as those of 18Cr-10Ni steel considering the embrittlement and swelling maxima which occur for the latter within the temperature range 450-550°C [23]. The change-over to new material will provide significant improvement of the operational safety of the case.

CONCLUSION

1. Small additions of yttrium, boron and zirconium of the Fe-15Cr-35Ni-3Mo composition with a phosphorus content of 0.009% suppress swelling at irradiation temperatures between 380 to 490°C. The incubation period of swelling is about 50 dpa and the swelling rate is 0.28 %/dpa.

2. The character of changes in the temperature dependence of swelling and mechanical properties after irradiation within a vide dose and temperature range is consistent with the process of spinodal-like decomposition of the solid solution in the high-nickel alloy under irradiation ($T_{irr.}$>400°C).

REFERENCE

[1] Johntson, W.G., Rosolowski, J.H., Turkalo, A.M., Lauritzen, T. Journal of Nuclear Materials, Vol.54, N1, 1974, pp.24-40.

[2] Johnston, W.G., Lauritzen, T., Rosolowski, J.H., Turkalo, A.M. Proc. Conf. Radiation Damage in Metals, Cleveland Metals Park, OH: ASTM, pp.227-266.

[3] Parshin, A.M. Voprosy Atomnoj Nauki i Tekniki, Ser.: Fizika Radiats. Povregdenij i Radiats. Materialovedenie, V.3, 1980, pp.20-29.

[4] Parshin, A.M. Structura i radiatsionnoe raspuhanie stalej i splavov, Moskva, Energoatomizdat, 1983.

[5] Parshin, A.M. Radiatsionnaya Povregdaemost konstruktsionnyh materialov i puti ee oslableniya, Leningrad, 1985.

[6] Garner, F.A. Journal of Nuclear Materials, Vol. 122-123, 1984, pp.459-471.

[7] Brager, H.R., Garner, F.A. "Microsegregation Observed in Fe-35.5Ni-7.5Cr Irradiated in EBR-II. Effects of Radiation on Materials: 12th International Symposium, ASTM STP 870, F.A.Garner, and J.Perrin, Eds., American Society for Testing and Materials, Philadelphia, 1985, pp. 139-150.

[8] Brager, H.R., Garner, F.A. and Hamilton, M.L., Journal of Nuclear Materials, Vol. 133-134, 1985, p.594.

[9] Garner, F.A. McCarthney, J.M., Russell, K.G., and Hoyt, J.J., Journal of Nuclear Materials, Vol.205, 1993, p.411.

[10] Nikolaev, V.A., Kursevich, I.P., Gukov, O.N., and Lapin, A.N. Atomnaya Energiaya, Vol.59, Vyp.3, 1985, p.200.

[11] Votinov, S.N., Prohorov, V.I. et al. Properties of Heat-Resisting Steels after High Temperature Irradiation, Trans. Jap. Inst. Met. Suppl., Vol.9, 1968, p.238.

[12] Lanskaya, K.A. Garoprochnye stali. Metallurgiya, Moskva, 1969.

[13] Zelensky, V.F., and Nekludov, I.M. Radiation Materials Science (Proceedings of the International Conference on Radiation Materials Science, Alushta, May 22-25, 1990), Kharkov, Vol.2, 1990, pp. 45-57.

[14] Zelensky, V.F., Nekludov, I.M. et al. Voprosy Atomnoj Nauki i Tekniki, Ser.: Materialovedenie i Novye Materialy, V.2 (46), 1992, p.24-40.

[15] Neustroev, V.S., Shamardin, V.K., Povstyanko, A.V., et al."Effect of microalloying with Boron and Rare-Earth Metals on Swelling and Mechanical Properties of Fe-16Cr-15Ni Steels", Effects of Radiation on Materials: 15th International Symposium, ASTM STP 1125, R.E.Stoller, A.S.Kumar, and D.S.Gelles, Eds., American Society for Testing and Materials, Philadelphia, 1992, pp. 1122-1131.

[16] Kuznetzov, A.A., Kursevich, I.P., Nikolaev, V.A. et al. Radiaton Material Science (Proceedings of the International Conference on Radiation Materials Science, Alushta, May 22-25, 1990), Kharkov, Vol.2, 1990, pp.117-126.

[17] Vasina, N.K., Kursevich, I.P., Shamardin, V.K. et al. Atomnaya Energiya, Vol.59, Vyp.4, 1985, p.265-267.

[18] Uvarov, N.V., Sokursky, Yu.N., Panteleev, K.L., Krivova, V.I. Voprosy Atomnoj Nauki i Tekniki, Ser.: Fizika Radiats. Povregdenij i Radiats. Materialovedenie, V.2(46), 1989, p.3-16.

[19] Lee, E., and Packan, N. "Swelling Suppression in Phosphorus-Modified Fe-Cr-Ni Alloys During Neutron Irradiation", Effects of Radiation on Materials: 14th International Symposium (Volume 1), ASTM STP 1046, N.H.Packan, R.E.Stoller, and A.S.Kumar, EDS., American Society for Testing and Materials, Philadelphia, 1990, pp. 133-146.

[20] Garner, F.A., and Kumar, A.S. "The Influence of Both Major and Minor Element Composition on void Swelling in Austenitic Steels", Effects of Radiation on Materials: 13th International Symposium (Part 1), ASTM STP 955, F.A.Garner, N.H.Packan, and A.S.Kumar, Eds., American Society for Testing and Materials, Philadelphia, 1987, pp.289-314.

[21] Dubuisson, P., Maillard, A., Delalande, C. et al. "The Effect of Phosphorus on the Radiation-Induced Microstructure of Stabilised Austenitic Stainless Steels", Effects of radiation on Materials: 15th International Symposium, ASTM STP 1125, R.E.Stoller, A.S.Kumar, and D.S.Gelles, Eds., American Society for Testing and Materials, Philadelphia, 1992, pp.995-1014.

[22] Watanabe, H., Mugora, T., and Yoshida, N. "The Effect of Phosphorus on Microstructure of Fe-16Cr-17Ni Austenitic Ternary Induced by Fast Neutron Irradiations in Annual Progress Report for Monbusho DOE Collaboration, Fusion YEAR 1991, August 1992.

[23] Neustroev, V.S., and Shamardin, V.K. Atomnaya Energiya, Vol.71, 1991, pp.345-348.

Itaru Shibahara, Naoaki Akasaka and Shoji Onose

EFFECTS OF METALLURGICAL VARIABLES ON SWELLING OF MODIFIED 316 AND HIGHER Ni AUSTENITIC STAINLESS STEELS

REFERENCE: Shibahara, I., Akasaka, N., and Onose, S., **"Effects of Metallurgical Variables on Swelling of Modified 316 and higher Ni Austenitic Stainless Steels,"** *Effects of Radiation on Materials: 17th International Symposium, ASTM STP 1270,* David S. Gelles, Randy K. Nanstad, Arvind S. Kumar, and Edward A. Little, Eds., American Society for Testing and Materials, 1996.

ABSTRACT: The effects of solute elements and cold-work on swelling in modified 316 and higher Ni advanced austenitic stainless steels developed for FBR core material were investigated together with the posted model alloys. The Si, P, B, Ti, Nb modified and cold-worked steels exhibited an improved swelling resistance. In the temperature range between 400 and 500℃, the swelling was suppressed significantly by an addition of 0.8 wt% Si. The beneficial effect of Si appears to be reduced in the steels without Ti and Nb tending to form γ' precipitates. In the temperature range between 500 and 600℃, a needle-like phosphide precipitates played an important role in suppressing void growth. Additions of Ti and/or Nb were found to stabilize the phosphide phase and extended the swelling incubation period. In the improved austenitic steels, the synergistic effect of cold-working and P,B,Ti,Nb additions act beneficially to stabilize the dislocation structure and to form finely dispersed precipitates during irradiation.

KEYWORDS: swelling, austenitic steel, phase stability, microstructure, minor elements, alloy design, fast reactor, fuel cladding

The requirement for high burnup fuel in the Japanese fast breeder reactor development program has motivated development of advanced austenitic steels applicable at service temperatures in the range 400 to 700℃ and neutron exposures beyond 3×10^{27}n/m^2 (E>0.1MeV), corresponding to about 150 dpa (displacement per atom). The main effort was directed to improve creep rupture strength and swelling resistance [1][2]. The first resulting material was a 20% cold-worked modified 316 stainless steel optimized within the chemical composition range of the Japanese Industrial Standard (JIS) SUS316, with a nominal composition of Fe-16Cr-14Ni-0.05C-2.5Mo-0.8Si-0.025P-0.004B-0.1Ti-0.1Nb

Fuels and Materials Division, O-arai Engineering Center, Power Reactor and Nuclear Fuel Development Corporation, O-arai, Ibaraki, 311-13, Japan

Copyright© 1996 by ASTM International www.astm.org

[3]. This material has been designated PNC316.

Further improvement has been made by increasing the nickel and titanium contents beyond the JIS specifications [3]. The second generation advanced austenitic steel for near term application has been selected to be Fe-15Cr-20Ni-0.25Ti-0.1Nb, designated PNC1520, in which the other elements and also the cold-work level are kept the same as in PNC316.

The improved swelling behavior of PNC316 has been attributed to the formation of fine phosphide precipitates which nucleate cavities and extend the swelling incubation period in the temperature range between 470 and 620℃ [4-5]. In this paper the swelling characteristics and microstructural evolution during fast neutron irradiation in PNC316 and PNC1520 are investigated in conjunction with that of developmental steels and simple model alloys. The effects of alloying elements and other metallurgical variables on the swelling resistance are discussed from the view point of practical alloy development for fast reactor core applications.

Experimental Procedure

Chemical compositions of the materials used in this experiment are shown in Table 1. The developmental 316 steels (316-0.01P and -0.03P) contain phosphorus and lesser amounts of silicon and boron: titanium and niobium levels are negligible compared with that of PNC316. Developmental advanced austenitic steels and PNC1520 have higher titanium than PNC316 and variations of silicon, niobium and nickel contents. The simple model alloys contain about the same amount of silicon or phosphorus as that of the complex alloys.

Table 2 summarizes the specimen forms, irradiation test vehicles, maximum neutron doses and swelling evaluation methods. The model alloys are provided in sheet form. Disk specimens of 3 mm in diameter were taken from the sheet and provided for irradiation. Other complex alloys were irradiated as cladding tube samples, which were cold-worked to 16-20% reduction in cross-sectional area.

The swelling specimens sectioned from the cladding tubes were mainly irradiated in the FFTF/MOTA [6]. The irradiation temperatures ranged from 405 to 670℃ and the maximum neutron dose was as high as 212 dpa in PNC316 at 405℃. The specimens were periodically discharged and diameter measurements were made prior to reinsertion into the reactor. The swelling was obtained from the diameter change assuming isotropic deformation. Irradiations were also conducted in JOYO/CMIR (Core Materials Irradiation Rig) for PNC316, PNC1520 and model alloys. PNC316 was also irradiated in a material irradiation rig in the Phenix reactor. These specimens were examined by transmission electron microscopy (TEM) using a JEOL 4000FX. Chemical analysis was conducted using an EDX (Energy Dispersive X-ray Analyzer). Specimens examined by TEM were irradiated at neutron doses of up to 48 dpa in JOYO, and up to 92.5 dpa for PNC316 in Phenix.

Table 1 Chemical composition of modified 316 and advanced austenitic steels including developmental and model alloys.

Alloy	Chemical Composition (wt%)										
	Cr	Ni	C	Si	P	B	Mn	Mo	Ti	Nb	Fe
PNC316	16.52	13.84	0.052	0.82	0.028	0.0031	1.84	2.49	0.080	0.079	bal.
PNC1520	15.05	19.73	0.064	0.75	0.028	0.0031	1.91	2.56	0.25	0.11	bal.
(Developmental Cladding)											
316-0.01P	16.78	13.68	0.056	0.49	0.010	0.0008	1.56	2.49	0.005	0.01	bal.
316-0.03P	17.5	13.05	0.058	0.53	0.029	0.0012	1.94	2.40	0.003	0.002	bal.
1515-Ti-low Si	15.10	15.61	0.060	0.46	0.029	0.0048	1.77	2.45	0.32	-	bal.
1520-Ti	15.29	19.61	0.061	0.81	0.026	0.0043	1.57	2.46	0.18	-	bal.
1520-Ti-Nb-low Si	14.89	19.66	0.057	0.41	0.026	0.0044	1.72	2.55	0.280	0.090	bal.
1525-Ti	15.09	24.41	0.060	0.85	0.020	0.0049	1.47	2.34	0.210	-	bal.
(Model Alloy)											
M1520	15.01	20.17	0.0061	<0.005	0.0009	-	<0.001	-	-	-	bal.
M1520-P	15.09	20.32	0.0092	0.009	0.024	-	0.003	-	-	-	bal.
M1520-Si	14.88	20.31	0.0054	0.48	0.0011	-	<0.001	-	-	-	bal.

Table 2 Specimen form , irradiation rigs and swelling evaluation method.

Alloy	Specimen Forms	Cold-work Level(%)	Irradiation Rigs	Maximam Dose(dpa)	Swelling Evaluation Method
PNC316	Cladding	20	FFTF/MOTA	212	Dimensional Change
			Phenix/P-4	93	Immersion Density
					TEM
PNC1520	Cladding	16	FFTF/MOTA	148	Dimensional Change
(Developmental Cladding)					
316-0.01P	Cladding	20	JOYO/CMIR	84	Dimensional Change
316-0.03P	Cladding	21	JOYO/CMIR	84	Dimensional Change
1515-Ti-low Si	Cladding	16	FFTF/MOTA	185	Dimensional Change
1520-Ti	Cladding	16	FFTF/MOTA	148	Dimensional Change
1520-Ti-Nb-low Si	Cladding	18	FFTF/MOTA	148	Dimensional Change
1525-Ti	Cladding	16	FFTF/MOTA	148	Dimensional Change
(Model Alloy)					
M1520	Sheet	S.A	JOYO/CMIR	27	TEM
M1520-P	Sheet	S.A	JOYO/CMIR	27	TEM
M1520-Si	Sheet	S.A.	JOYO/CMIR	27	TEM
PNC316ST	Sheet	S.A.	JOYO/CMIR	27	TEM
PNC1520ST	Sheet	S.A.	JOYO/CMIR	27	TEM
PNC316-CR Sheet	Sheet	20	JOYO/CMIR	48	TEM
PNC1520-CR Sheet	Sheet	20	JOYO/CMIR	48	TEM

S.A.: solution annealed

Results

Swelling characteristics

Both PNC316 and advanced austenitic steel cladding exhibited maximum swelling at 405℃, which is at the lower limit temperature of this experiment. The dose dependence of swelling at 405℃, shown in Fig.1, indicates significant extension of the transient regime of swelling in higher nickel advanced austenitic steel cladding. However, the 0.5 wt% silicon steels (1515-Ti-low Si, 1520-Ti-Nb-low Si) show a very similar dose dependence regardless of nickel content. Swelling data reported by Puigh and Garner [7] for 20% cold-worked steel cladding of 0.5 wt% silicon and negligible phosphorus (the 1st-core 316 and PCA (Fe-14Cr-17Ni-0.5Si-0.3Ti: heat K280) irradiated in FFTF/MOTA) was also found to exhibit almost the same fluence dependence as the present 0.5 wt% silicon steels at 405℃ [5]. In the high silicon steels, an extension of the transient regime of swelling with increasing nickel content is obvious. The swelling of PNC1520 and 1520-Ti, (the former contains 0.11 wt% Nb), is comparable. Thus, an effect of niobium addition is not apparent.

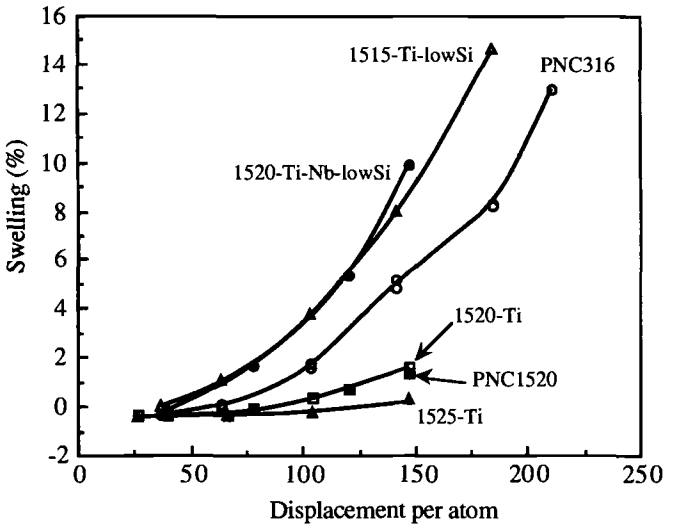


Fig. 1 Dose dependence of swelling in 16-20% cold-worked advanced austenitic steel cladding irradiated at 405°C in FFTF/MOTA.

The temperature dependence of swelling in 316-0.01P, 316-0.03P and PNC316 cladding are compared at 60 dpa in Fig. 2. Also shown in in Fig. 2, swelling data of the 1st-core 316 [7] are indicated for a reference. The most significant difference in the swelling behavior between standard and PNC316 stainless steels is the reduction of swelling at around 550℃. At this temperature the swelling in 20% cold-worked 316 stainless steel decreases with increasing phosphorus content [4-5]. A similar trend can be observed between the 1st-core 316, 316-0.01P and 316-0.03P, in which the phosphorus

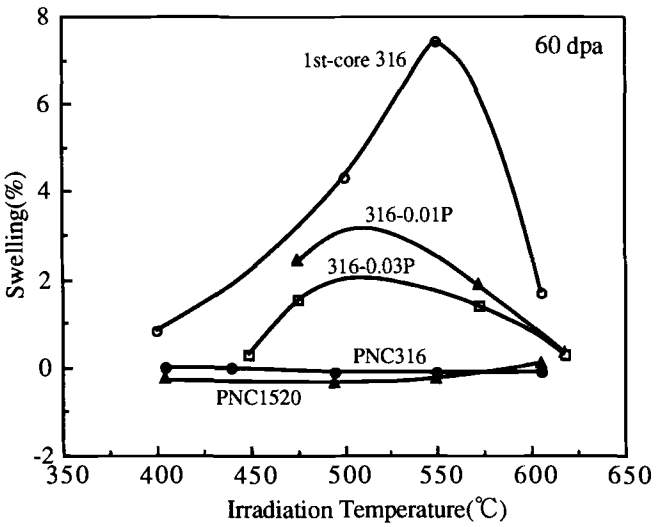


Fig. 2 Temperature dependence of swelling in 20% cold-worked P,B modified (316-0.01P,-0.03P) and P,B,Si,Ti,Nb modified (PNC316, PNC1520) austenitic steel cladding compared with 1st-core 316 (data from Ref.7) at 60 dpa.

increased from 0.003 wt% (1st-core 316) to 0.029 wt% (316-0.03P). With the same phosphorus content as 316-0.03P, a further decrease in swelling is observed in PNC316 which contains an increased amount of silicon and titanium. In this alloy, swelling at 550℃ was negligible even after 125 dpa.

In Fig.3, the temperature dependence of swelling in advanced austenitic steel cladding containing both phosphorus and titanium are compared at 125 dpa. In all cladding except for 1525-Ti, appreciable swelling is observed only at temperatures below about 500℃. The maximum swelling of the 1525-Ti obtained in this experiment was only 0.24% at 147.5 dpa at 405℃. In the lower temperature regime, the effect of silicon is again apparent. Increased nickel content reduces swelling only in the high silicon steels.

Fig.4 shows the swelling of solution annealed model alloys and also solution annealed PNC316ST and PNC1520ST sheet samples. Simple phosphorus or silicon addition in the Fe-Cr-Ni ternary alloys reduce the swelling at 572℃. At 476℃, the silicon addition also reduce the swelling, but phosphorus caused increased swelling. The solution annealed PNC316ST and PNC1520ST show similar behavior and the swelling peak temperature appears to be above 500℃, which is similar to the 20% cold-worked 316-0.01P and 316-0.03P cladding. The difference in the swelling between PNC316ST and PNC1520ST may be attributed to the difference in nickel content. It should be noticed that when we compare the swelling in model alloys and PNC1520ST (both contain about the same amount of nickel and chromium), the swelling of PNC1520ST is even greater than that of the phosphorus or silicon doped model alloys at 572℃.

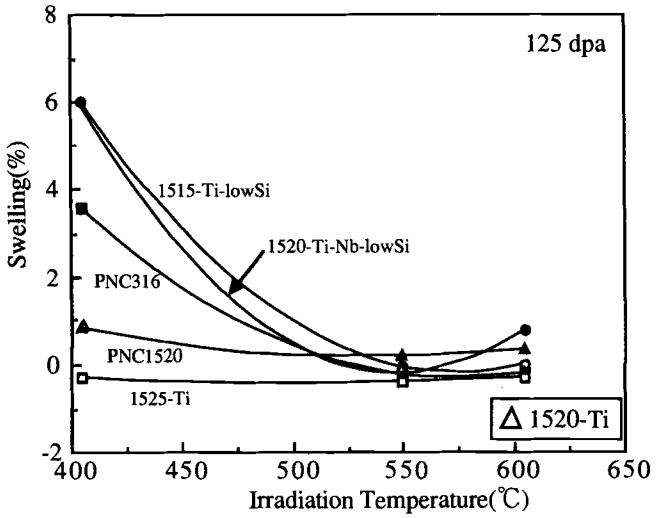


Fig. 3 Temperature dependence of swelling in 16-20% cold-worked advanced austenitic steel cladding at 125 dpa.

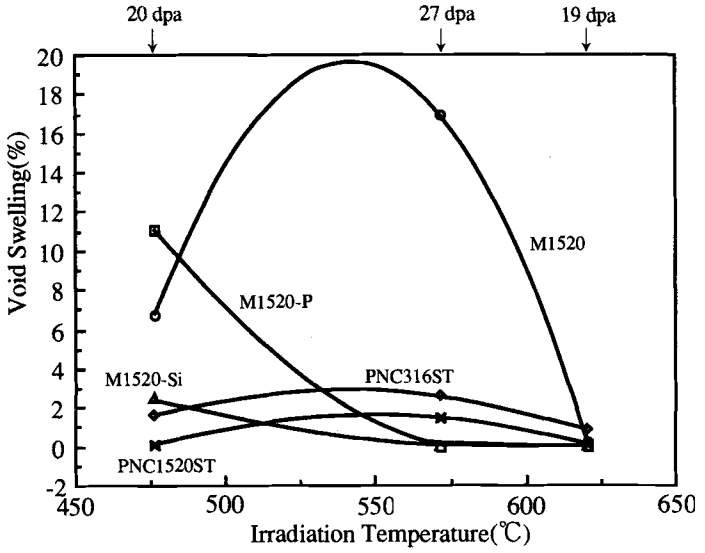


Fig. 4 Temperature dependence of swelling in model alloys irradiated in JOYO/CMIR.

Microstructures

The microstructures of PNC316 and PNC1520 cladding are compared at around 580℃ in Fig. 5. No significant differences between the microstructure of these steels was observed. At temperatures between 470 and 620℃, a high density of needle-like phosphide precipitates form, and fine MC formed on dislocations and a small amount of blocky M_6C precipitates were observed [4]. Gamma-prime and G phase did not form at any temperature. Large Laves phase was occasionally observed at temperatures higher than 600℃. The temperature range of the phosphide precipitation appears to correspond to the swelling suppression regime shown in Fig. 3. The phosphide phase was stable to high doses and small cavities were often observed at the interface of the phosphide. The small cavities attached to phosphide precipitates are also indicated in Fig.5 with those average sizes.

The microstructure of 316-0.03P cladding is shown in Fig. 6. This material contains a lesser amount of silicon than PNC316, but contains no titanium or niobium. Voids were observed over all of the temperature range between 450 and 620℃ and needle-like precipitates were not detected. At lower doses where void did not develop, the needle-like precipitate was frequently observed also with tiny cavities attached to the precipitate-matrix interface [4]. The needle-like precipitate in 316-0.03P was less in number density and greater in length than that in PNC316. At 576℃, M_6C blocky precipitates with attached

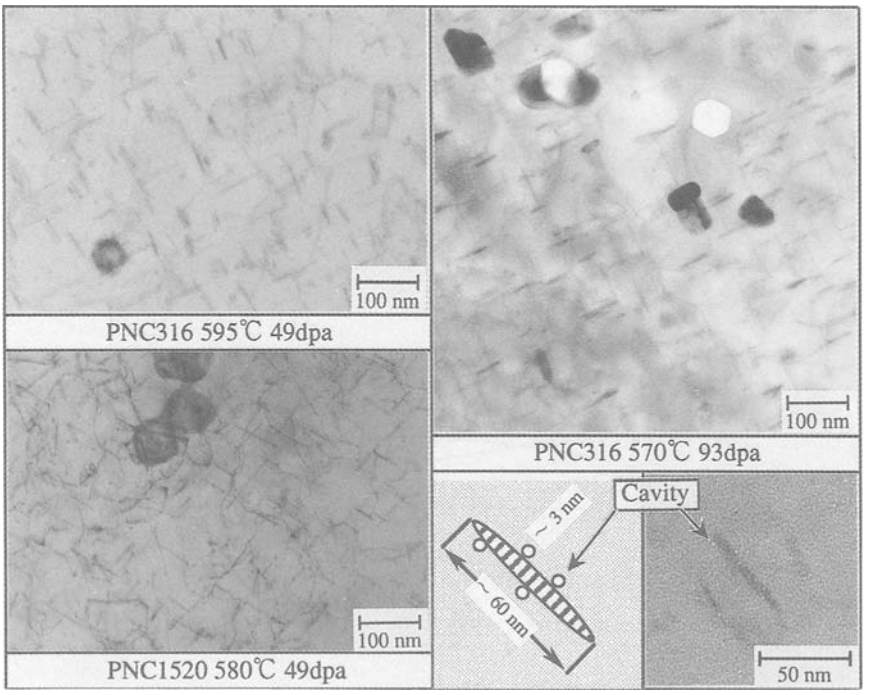


Fig. 5 Microstructures of PNC316 and PNC1520 irradiated at around 580°C.

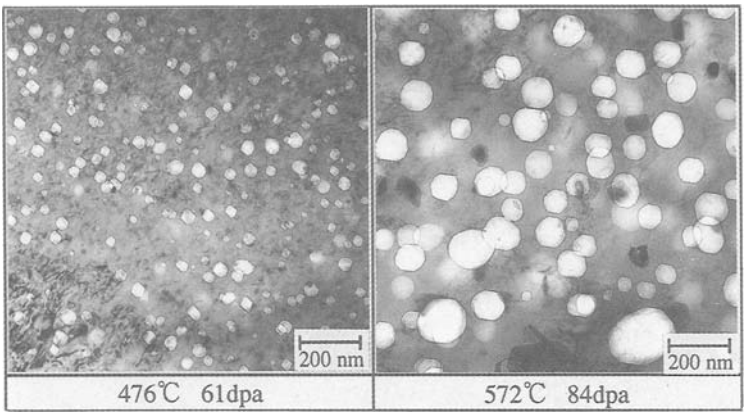


Fig. 6 Microstructures of irradiated 316-0.03P.

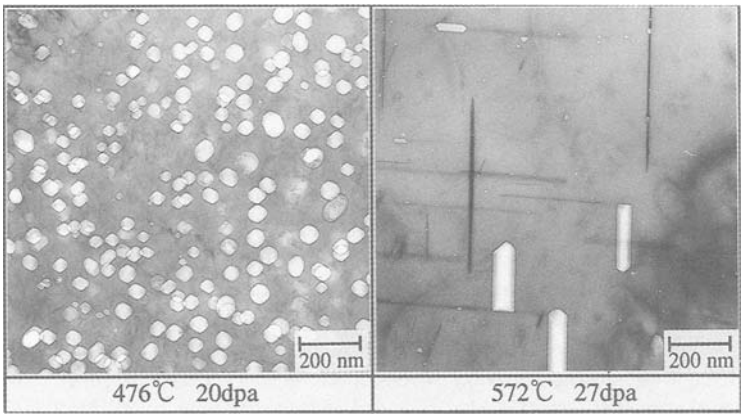


Fig. 7 Microstructures of irradiated 1520-P model alloy.

voids were observed. At 618℃, large voids attached to coarse Laves and M_6C phases were found. At 476℃, extensive γ' precipitate and uniform void formation are observed. At temperature below 476℃, voids and γ' densities tended to decrease.

The microstructure of the M1520-P model alloy is shown in Fig. 7. At 476℃, a large number of voids were uniformly distributed and no precipitates were observed. At 572℃, long needle-like phosphides form and tiny cavities were observed at the precipitate-matrix interface. Sometimes, rod-like elongated voids are observed along the needle-like phosphides and occasionally the phosphide was observed to be partially dissolved at positions where the rod-like voids developed.

Microstructure of M1520-Si model alloy in Fig. 8 shows γ' and voids at 476℃. At 572℃, cavities were observed associated with strain contrast and void growth appeared to

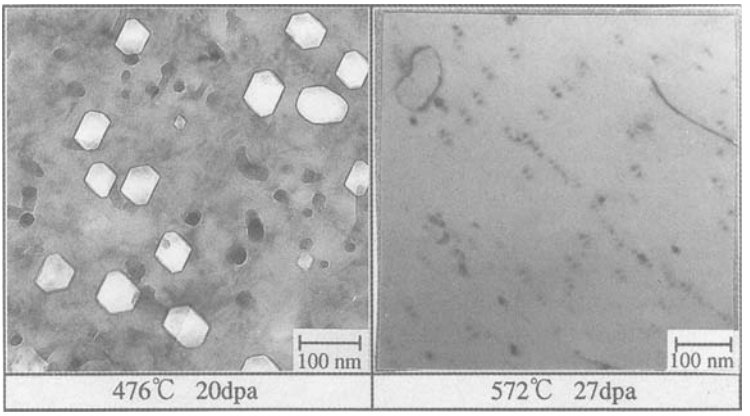


Fig. 8 Microstructures of irradiated 1520-Si model alloy.

be suppressed. The strain contrast may be due to the irradiation induced segregation of silicon.

Fig. 9 compares the microstructure of PNC316ST, PNC316CR-sheet and PNC316 cladding at temperature around 560℃. The latter two materials were cold-worked to approximately 20% reduction in cross-sectional area. In the solution annealed PNC316ST, coarse Laves phase and attached large voids were found to exist. The needle-like precipitate was thin and sparsely distributed. An EDX analysis showed enrichment of molybdenum, silicon, phosphorus and nickel in the large precipitates, and the nickel content in the matrix were therefore reduced from about 14 wt% to 9 wt%. The PNC316 cladding did not show such significant phase changes. In PNC316CR-sheet, the number density of blocky precipitates was larger and needle-like precipitates were longer and their number density was smaller than that of PNC316 cladding. Dislocation structures and densities shown in Fig. 10 for cold-rolled sheet and cold-drawn cladding tube of PNC316 and PNC1520 indicate the recovery of dislocations in PNC316CR-sheet is extensive compared to that of PNC316 cladding. The dislocation structures in PNC1520CR-sheet is less stable than in the PNC1520 cladding, but more stable than in the PNC316CR-sheet. The dislocation density of PNC1520 cladding is almost comparable to that of PNC316 cladding. The improved stability in PNC1520 is considered to be due to the increased amount of titanium which forms fine MC type precipitates on dislocations.

Discussion

Low temperature regime

At temperatures below the phosphide precipitation boundary ($\sim$ 470℃), precipitates were not observed in PNC316 cladding. Generally, the γ' and G as well as the η (M_6C) and τ ($M_{23}C_6$) phase precipitates have frequently been observed in 316 class stainless steels in the temperature range between 400 to 500℃ [8-9]. As demonstrated elsewhere

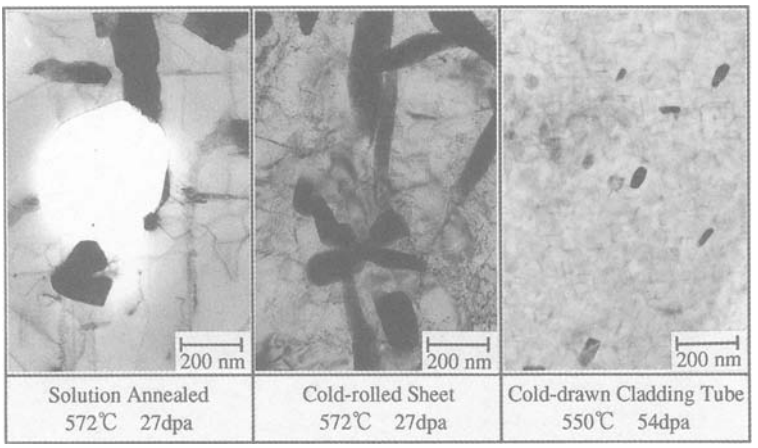


Fig. 9 Microstructures of solution annealed or cold-worked PNC316 after irradiation at around 560°C.

[8-9] and also in the present study for M1520-Si model alloy and 316-0.03P cladding, γ' formation were observed to be coincide with the void development. The mechanism of the suppression of γ' formation in PNC316 cladding is still not clear, but apparently titanium or niobium addition might be effective, because significant amount of γ' was found to develop in the Ti/Nb free 316-0.03P.

The effect of silicon at low temperatures has been reported in simple ternaries, in which the swelling tends to decline above 0.2 wt% and saturate between 0.5 to 1 wt% silicon content [10]. But in this experiment, increasing silicon from 0.5 wt% to 0.8 wt% in PNC316 and the advanced austenitics reduced the swelling significantly at 405℃. An increased level of nickel also reduced the swelling in 0.8 wt% silicon alloys. However in 0.5 wt% silicon alloys, the effect of nickel and other elements, such as titanium and phosphorus, was not obvious [5], i.e., an apparent nickel-independent swelling plateau was observed which is similar to that observed in Fe-Cr-Ni ternary alloys [10]. Nickel and silicon in solid solution are known to increase effective vacancy diffusion and reduce void nucleation [11-13]. The role of silicon, on a per atom basis, appears to be larger than nickel as predicted [12].

The possible effects of phosphorus in the high silicon alloys in the low temperature regime can not be determined due to the lack of high dose data on high Si, no-P material for comparison with PNC316. Improvement by addition of up to 0.16 wt% phosphorus has been demonstrated in cold-worked 316Ti at 450℃ [14]. At this temperature, increased phosphorus up to about 0.09 wt% appears to reduce swelling without formation of phosphide precipitates. The increased swelling in 15Cr-20Ni-0.03P model alloy (M1520-P) at 476℃ corresponds to the reported non-monotonic effect of phosphorus [10], in which the swelling has a maximum at about 0.02 wt% phosphorus. This phenomena appears to be typical in simple model alloys, but in any case further reduction of swelling is expected in the advanced austenitic steels by increasing phosphorus content above 0.03 wt%. The upper limit of phosphorus content will be determined by the detrimental effect

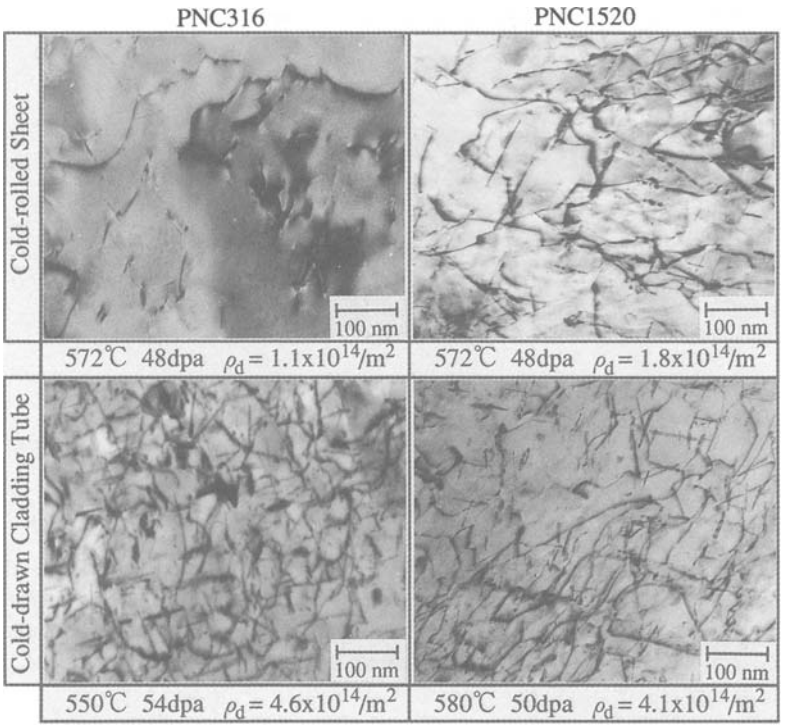


Fig. 10 Dislocation structures compared in cold-rolled sheet and cold-drawn cladding tube of PNC316 and PNC1520 after irradiation around 580°C. (ρ_d : Dislocation density)

of phosphorus on weldability.

High temperature regime

At temperatures greater than 500℃, phosphorus, titanium and silicon-bearing cold-worked austenitic steels showed significant suppression in void swelling. The temperature range of phosphide formation appears to correspond to that of swelling suppression [4]. Also, the coincidence of void development and disappearance of the phosphide phase which was demonstrated in 316-0.03P and M1520-P model alloy, support the importance of phosphide formation and its stability during irradiation. The improved swelling suppression in PNC316 is related to the enhanced formation of stable phosphide precipitates, which is promoted by the strong phosphide formers, i.e., titanium or silicon [8, 15]. Finely dispersed phosphides can effectively trap helium bubbles and retard the conversion of bubbles to voids. This is thought to occur via a helium dilution over a larger number of cavities [16]. The condition of bubble to void conversion may depend on the helium accumulation as well as other circumstances that may change vacancy

supersaturation level for the bias-driven growth of the attached bubbles. The rod-shape void developed along the needle-like phosphide suggest the precipitate-matrix interface serves a channeling path for the point defects into the attached cavities.

Direct cavity trapping at MC precipitates [17-18] could not be detected in this experiment. Niobium has been reported, based on a thermal aging experiment, to replace the titanium in the phosphide phase and leaves the titanium in the matrix to play its role as a swelling inhibiter [14]. In this experiment the direct effect of niobium and titanium appears to be less significant than the role of phosphide.

Effects of cold-working

Cold-working is essential to extend phase stability during irradiation in the complex steels. The swelling of solution annealed PNC316ST and PNC1520ST was even larger than in simple phosphorus- or silicon-added Fe-15Cr-20Ni ternaries due to a scavenging effect caused by the significant development of Laves phase in complex alloys at high temperatures. The stability of the cold-work-induced dislocation structure plays an important role by limiting segregation [19]. The titanium addition in 316 stainless steel and the increased titanium content in PNC1520 (up to the carbide stoichiometric content) stabilizes the dislocation structure by fine MC precipitation, which is reflected in the high dislocation density in PNC316 compared to that of the titanium-free 316-0.03P after irradiation at high temperatures [4]. The dislocation structure in cold-rolled sheet of PNC1520, which was more stable than that of PNC316, also reflect the effect of increased MC precipitation.

The material form was also found to be important in determining the dislocation structure. The cladding and duct materials are fabricated essentially by tube drawing method. The swelling have been confirmed to show the same behavior in the two forms, but the present experiment revealed that the dislocation structure in simple cold-rolled PNC316 sheet is rather unstable compared to that of the cold-drawn cladding or duct. This point is very important in material development for applications to reactor components.

Alloy design

The design of PNC316 was based on a concept to provide a fine dispersion of carbide precipitates by controlled additions of boron and phosphorus in conjunction with dislocations introduced by cold-working [1-2]. The concept was also applied to the higher nickel PNC1520 [3]. These modifications significantly improved the high temperature creep strength by keeping the high dislocation density [2] even at 650℃, 20,000h. The swelling resistance of the PNC alloys was found to be improved in accordance with increasing creep strength [3-4]. A similar modification of cold-worked D9 alloy (Fe-13.5Cr-15.5Ni-2Mo-2Mn-0.75Si-0.25Ti) has been shown to lead to a significant improvement in creep strength and swelling resistance [20]. The Japanese prime candidate alloys (JPCA) for fusion reactors also incorporated the controlled phosphorus and boron alloying [21].

It has been shown frequently that there is a strong relationship between swelling and precipitates. The effect of precipitation on swelling has been described through changes in

the diffusive or other physical properties of the matrix due to precipitation-induced changes in chemical composition of the matrix [19]. The other effects associated with precipitates themselves have been pointed out to be also important, e.g., the helium trapping and the pinning of dislocations by finely dispersed particles [22]. It was suggested that the helium dilution mechanism over a large number of cavities, trapped at the precipitate-matrix interface, might offer a key for alloy design for swelling resistance in high helium environment [23]. Along this line, principles for the design of radiation-resistant alloys were laid out based essentially on the critical conditions for the bias-driven cavity growth that dominate the extension of the transient regime of swelling [24-25].

The present results indicate the improvement both in creep and swelling characteristics arises from the same metallurgical modifications (cold-working and controlled P, B, Ti, Nb additions) to produce fine dispersion of precipitates during creep or irradiation. The improvement of creep strength is mainly due to the fine MC precipitates on dislocations. The swelling in the higher temperature regime appears to be suppressed primarily due to the cavity trapping by finely dispersed phosphide precipitates. It also appears that the MC precipitates on dislocations contribute to the improved swelling by inhibiting the dislocation climb during irradiation. The dense dislocation structure also provide a large number of sites for segregation and precipitation. Thus, a fixed number of segregating solute atoms is diluted among more sites. Under this environment, a certain precipitation reaction may be eliminated or a growth of precipitates may retard. Significant difference in the phase stability between the solution annealed and cold-worked conditions, as was shown in Fig.9, typically indicates the close relation of precipitation and dislocations.

An important point for an alloy design is to provide fine stable precipitates during irradiation. The stability of the precipitates depends on the phase nature and RIS (radiation induced segregation) environment [26]. In the present materials irradiated in FBR conditions, the phosphide precipitates of the cold-worked PNC316 and PNC1520 appear stable at leased up to 125 dpa at around 500℃. The improved stability is considered to be due to an incorporation of titanium and/or niobium into phosphides [27, 14]. Also the stabilized dislocations contribute to form suppressed-RIS environment and reinforce an stable existence of phosphide precipitates. The addition of boron may partly contribute to the structural stability.

The contents of carbon, titanium and niobium in PNC1520 was selected to the stoichiometric ratio for MC carbides which produces the maximum in creep rupture strength. An earlier experiment by carbon ion irradiation indicated that titanium, niobium or carbon only in solution was effective in reducing swelling [28]. By contrast, a good swelling resistance was achieved for DIN 1.4970 (Fe-15Cr-15Ni-1.75Mn-1.2Mo-1.0Si-0.1C-Ti) through understabilization [29]. The US D9, US PCA and Japanese PCA alloys contain stoichiometric Ti/C contents [20-21]. The French 316-Ti or -Ti+Nb steels modified by phosphorus and 15-15Ti alloys contain overstabilized or stoichiometric M/C contents, respectively [14, 30]. There seems to be some controversy about the optimum M/C ratio, although considerable care must be taken to evaluate the ion irradiation results [31] and also pay attention to pre-irradiation heat treatment procedures. The (Ti+Nb)/C ratio of slightly greater than unity appears to be reasonable when phosphide incorporate titanium or niobium during irradiation. Another beneficial effect of niobium has been recognized in retarding grain growth at high temperature which allows an increased solution annealing temperature to obtain a good solid solution [3]. During irradiation,

solute elements gradually precipitate to form finely dispersed microstructures in conjunction with the dislocations introduced by cold-working.

The increase of silicon and/or nickel contents are known to modify the diffusive nature of the matrix and are considered to work beneficial for reduced swelling from a view point to provide an improved environment in the matrix. But these elements are detrimental to high temperature creep strength. A higher content of silicon increases the number density of undissolved carbides during solution treatment [2]. Moreover, the growth rate of carbides, Laves and sigma phases tend to be enhanced during high temperature creep by increased silicon content and cause a decrease in strength [2]. Increasing nickel, beyond 20-30 wt%, also decreases the creep strength by increasing coarse carbide precipitation [2]. The alloy PNC316 and PNC1520 have been optimized to keep both superior swelling resistance and a higher creep strength in the cold-worked condition. In this sense, the swelling resistance can further be improved by increasing the nickel content, even though the creep strength may not be improved significantly.

Various mechanisms have been proposed, sometimes with controversy, concerning about the effects of various alloying elements on swelling. A dominant suppression mechanism in complex alloys may depend on the circumstances of the matrix, because several competing processes are acting and one of these may become dominant when the other processes are suppressed. In PNC316 and the advanced austentic alloys, cold-working and controlled precipitation, make the role of phosphide dominant at higher temperatures. Although swelling suppression has been demonstrated in PNC316 and the advanced austenitics to neutron doses as high as 125 dpa at around 500℃ (relevant temperatures of high neutron flux in fast reactor fuel), care must be taken for higher dose application, because of a possible breakaway of some of the competing processes and dissolution of phosphide precipitates.

Increases in nickel for base-line modification and optimization of titanium, niobium and phosphorus for stable precipitate formation could yield a further improvements in the development of austenitic steels.

Conclusions

In phosphorus-bearing 20% cold-worked austenitic stainless steel, titanium and silicon improve the swelling resistance significantly. This is mainly due to the formation of stable phosphide precipitates, that trap helium bubbles and retard the conversion of bubbles to voids in the temperature range between 500 and 600℃. The fine dispersion and stability of phosphides, for which titanium and niobium additions and/or increased amount of silicon are important, control the duration of transient regime of swelling.

In the lower temperature regime, increased amounts of silicon and nickel also result in significant improvement. In low silicon alloys the swelling is insensitive to other alloying elements, but at high silicon contents, where void nucleation is increasingly more difficult, the role of nickel becomes important. Cold-working is very effective to suppress the phase instability. The primary role of titanium is to maintain a high dislocation density by the precipitation of fine MC precipitates on dislocations and provide a suppressed-RIS environment.

The current PNC1520 is more stable and swelling-resistant than PNC316 due to the

increased titanium and nickel contents. Further improvement in swelling resistance could be attained by increasing nickel and phosphorus in conjunction with titanium and niobium optimization.

Acknowledgements

We are pleased to thank the staff of Westinghouse Hanford Company for their cooperation with irradiation testing in FFTF. We also thank Mr. M. Sekine for his TEM examination and Drs. T. Maruyama and S. Ukai for their discussion on this manuscript.

References

[1] Kondo, Y., Yukitoshi, T., Yoshikawa, K., Nagai, N., Ohta, S., Fujiwara, M., Yoshida, S., Tanaka, C., Uematsu, K., and Suzuki, K., Radiation Effects in Breeder Reactor Structural Materials, TMS-American Institute of Mining, New York (1977) 253.

[2] Fujiwara, M., Uchida, H., Ohta, S., Yuhara, S., Tani, S., and Sato, Y., Radiation-Induced Changes in Microstructure: 13th Symp.(Part I), ASTM STP 955 (1987) 127.

[3] Itaki, T., Yuhara, S., Shibahara, I., Kubota, H., Itoh, M., and Nomura, S., Materials for nuclear reactor core application, BNES, London (1987) 203.

[4] Shibahara, I., Ukai, S., Onose, S., and Shikakura, S., J. Nucl. Mat. 204 (1993) 131.

[5] Shibahara, I., Akasaka, N., Onose, S., Okada, H., and Ukai, S., J. Nucl. Mat. 212-215 (1994) 487.

[6] Puigh, R.J. and Schenter, R.E., Effects of Radiation on Materials: 12th Conf., ASTM STP 870 (1984) 795.

[7] Puigh, R.J. and Garner, F.A., Radiation-Induced Changes in Microstructure: 13th Int. Symp. (Part I), ASTM STP 955 (1987), p.154.

[8] Maziasz, P.J., J. Nucl. Mat. 169 (1989) 95.

[9] Maziasz, P.J., J. Nucl. Mat. 205 (1993) 118.

[10] Garner, F.A. and Kumar, A.S., ibid [7] 289.

[11] Garner, F.A. and Wolfer, W.G., J. Nucl. Mat. 102 (1981) 143.

[12] Esmailzadeh, B. and Kumar, A.S., Effects of Radiation on Materials: 12th Int. Symp., ASTM STP 870 (1985) 468.

[13] Coghlan, W.A. and Garner, F.A., ibid [6] 315.

[14] Dubuisson, P., Maillard, A., Delalande, C., Gilbon, D., and Seran, J., Effects of Radiation on Materials : 15th Int. Symp., ASTM STP 1125 (1992) 995.

[15] Watanabe, H., Muroga, T., and Yoshida, N., Effects of Radiation on Materials: 16th Int. Symp., ASTM STP 1175 (1993) 951.

[16] Lee, E.H., and Packan, N.H., Effects of Radiation on Materials: 14th Int. Symp., Vol.1 ASTM STP 1046 (1989) 133.

[17] Gold, R.E., Bloom, E.E., Clinard, Jr, F.W., Smith, D.L., Stevenson, R.D., and Wolfer,W.G., Nucl. Technology 1 (1981) 1.

[18] Sekimura, N. and Ishino, S., J. Nucl. Mat. 169 (1989) 95.

[19] Garner, F. A., Phase Stability During Irradiation, TMS-AIME (1981), 165.

[20] Hamilton, M.L., Johnson, G.D., Puigh, R.J., Garner, F.A., Maziasz, P.J., Yang, W.J.S., and Abraham, N., Residual and Unspecified Elements in Steel, ASTM STP 1042 (1989) 124.
[21] Tanaka, M.P., Hamada, S., Hishinuma, A., and Maziasz, P.J., J. Nucl. Mat. 155-157 (1988) 801.
[22] Rowcliffe, A.F., and Lee, E.H., J. Nucl. Mat. 108&109 (1982) 306.
[23] Lee, E.H. and Mansur, L.K., J. Nucl. Mat. 141-143 (1986) 695.
[24] Mansur, L.K., Lee, E.H., Maziasz, P.J., and Rowcliffe, A.P., J. Nucl. Mat. 141-143 (1986) 633.
[25] Lee, E.H. and Mansur, L.K., Metal. Trans. A 23A (1992) 1977.
[26] Maziasz, P.J., J. Nucl. Mat. 122&123 (1984) 472.
[27] Maziasz, P.J., MiCon 86: Optimization of Processing, Properties, and Service Performance Through Microstructural Control, ASTM STP 979 (1988) 116.
[28] Terasawa, M., Shimada, M., Kakuma, T., Yukitoshi, T., Shiraishi, K., and Uematsu, K., ibid [1] 687
[29] Hershbach, K., Shneider, W., and Ehrlich, K., J. Nucl. Mat. 203 (1993) 233.
[30] Seran, J.L., Levy, V., Dubbuison, P., Gilbon, D., Millard, A., Fissolo, A., Touron, H., Cauvin, R., Chalony, A., and Boulbin, E.L., ibid [15] 1209.
[31] Lee, E.H., Rowcliffe, A.F., and Kenik, E.K., J. Nucl. Mat. 83 (1979) 79.

Wolfgang Schüle[1]

ON THE FUNDAMENTALS OF RADIATION DAMAGE IN FCC MATERIALS, A REVIEW

REFERENCE: Schüle, W., **"On the Fundamentals of Radiation Damage in FCC Materials, A Review,"** *Effects of Radiation on Materials: 17th International Symposium, ASTM STP 1270,* David S. Gelles, Randy K. Nanstad, Arvind S. Kumar, and Edward A. Little, Eds., American Society for Testing and Materials, 1996.

Abstract: A short historical report is given on the formation of the one-interstitial model (OIM) which was introduced by F. Seitz and H. B. Huntington in the late fifties. In the early sixties J. F. Brinkman and A. Seeger suggested the two-interstitial model (TIM) after many new experimental and theoretical results became available and raised a continous discussion on the validity of the two models.

A few of the many experimental results obtained on radiation damage in fcc metals and alloys over the last thirty-five years are discussed and it is shown that all these results only support the TIM. It could further be shown that the migration activation energies of point defects decrease with increasing high energy particle flux, that dynamic crowdions can change lattice sites 50,000 times before their energy is dissipated to the lattice, that the recombination volume α between self-interstitials and vacancies is one order of magnitude larger than assumed so far etc.. These and many other features of point defects are discussed and the extended version of the TIM, namely the modified two interstitial model (MTIM), is presented.

It is further shown that the rate equations to calculate point defect concentrations built up during irradiation with high energy particles are powerful ways to understand and explain radiation damage. However, the advocates of the OIM in the past used only the steady state solutions of the rate equations which are only mathematical solutions and do not reflect physical reality.

Correlated self-interstitial-vacancy pairs annihilate in recovery stages I and II and correlated crowdion-vacancy pairs annihilate in the broad recovery sub-stage I_D in such materials in which crowdions are stable. Crowdions migrate in the tiny sub-recovery stage I_E, self-interstitials in recovery stage III, and vacancies in recovery stage IV.

The implications and importance of the application of the MTIM for the development of radiation resistant materials are outlined.

Keywords: radiation damage models, rate equations, interstitials, vacancies, crowdions, dynamic crowdions, micro-structure

[1] Senior scientist, European Union, Joint Research Center Ispra, Institute of Advanced Materials, 21020 Ispra (Va), Italy, and
Professor at the Institut für Angewandte Physik der Johann Wolfgang Goethe-Universität Frankfurt, Robert Mayer Straße 2-4, D-60054 Frankfurt, Germany.
Present address: Via Bosco 23, I-21038 Leggiuno (Va), Italy

Copyright© 1996 by ASTM International www.astm.org

INTRODUCTION

If a fcc material, e. g. copper, is irradiated with high energy particles of sufficient energy atoms of the lattice will be displaced, and vacancies and interstitial atoms will be created in equal numbers. In a fcc metal only one single vacancy configuration is imaginable. Empty lattice sites are vacancies around which the neighbouring atoms are relaxed. Many different stable configurations for interstitial atoms are possible in fcc metals, e. g. crowdions, an interstitial configuration consisting of an additional atom in a close packed lattice direction e. g. in <110>-directions and so called split interstitials in the <100>-dumbbell configuration [1]. It is evident that a crowdion type defect can only be produced by irradiating a solid with high energy particles whereas interstitials of the dumbbell configuration which below are called self-interstitials can be produced by irradiation with high energy particles and also by plastic deformation.

Over the last thirty-five years many different radiation damage models have been evaluated (see e. g. reference [1]) of which only the one interstitial model (OIM) and the two interstitial model (TIM) have survived [2,3]. The TIM was further developed leading to the modified two interstitial model (MTIM), which was developed by the present author [4]. These various models will be discussed in more detail in the following.

The various types of point defects created, e. g. after irradiating with high energy particles at the temperature of liquid helium, migrate and annihilate during subsequent annealing in five characteristic annealing or recovery stages in each of which one or more types of point defects characterized by their migration activation energy annihilate. This classification was introduced in 1955 by van Bueren [5] and until now has been found to be valid for each fcc metal (and fcc alloy) investigated namely as copper, silver, gold, aluminium, nickel etc. with specific differences for each metal. This means that the identification of certain point defects is possible by comparing results obtained for two or more different metals.

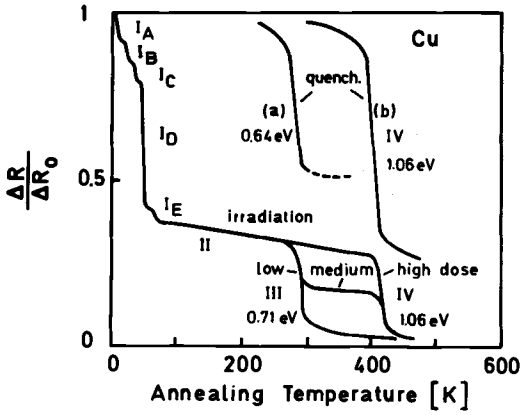


Fig. 1
The recovery of the electrical resistivity of copper is plotted schematically versus the annealing temperature after irradiation with high energy particles and after quenching from "low" (curve (b)) and "high" (curve (a)) temperatures, respectively. After "low" dose irradiation only recovery stage III, after a "medium" dose irradiation recovery stages III and IV, and after a "high" dose irradiation only recovery stage IV is found. The displayed recovery stage II is only found after "low" dose irradiation (recovery stage II_A is not shown).

The recovery spectra obtained for copper and for gold after irradiation with high energy particles and after quenching are displayed in Figs. 1 and 2,

respectively. Again the spectra of these two metals are very similar. However, a characteristic difference in the two spectra is noticed which concerns the two sub-stages I_D and I_E. These two sub-stages were never observed in gold and are only present in pure copper and many other pure metals. If undersized or oversized atoms are added to copper these two sub-stages vanish and the recovery spectrum of copper doped with for example beryllium looks exactly like that of gold.

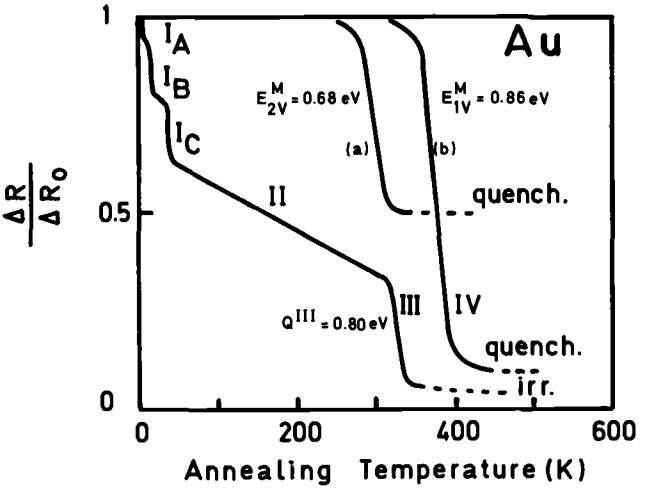


Fig. 2 The recovery of the electrical resistivity of gold is plotted schematically versus the annealing temperature after a "low" dose irradiation with high energy particles, and after quenching from "low" (curve (b)) and "high" (curve (a)) temperatures, respectively.

In the OIM crowdions are not stable, and self-interstitials migrate and annihilate in the sub-stage I_E in e. g. copper and nickel. This sub-stage is not present in gold and no assignment for self-interstitials is made in the OIM. Finally vacancies migrate and annihilate in recovery stage III in the OIM.

In the TIM and in the MTIM - in the following we will use only the up to date version of these two models, namely the MTIM - crowdions migrate and annihilate in recovery sub-stage I_E in copper and nickel. A sub-stage I_E is not found in gold and crowdions are not stable in gold in the MTIM. Finally self-interstitials and vacancies migrate in recovery stages III and IV, respectively, in the MTIM.

In the following discussion we will sometimes use results to explain radiation damage features which are discussed in detail in a later section of this work. We will also not refer to all the individual publications which are listed in the four review articles of references [1-4] except in some instances when a publication appears to be very important or for publications which are almost forgotten or have not been cited so far.

Most of the scientists working in the field of radiation damage still believe in the validity of the OIM, nevertheless - as we will show - the majority of the results are evidence that only the MTIM is correct.

HISTORICAL OVERVIEW

In the very first investigations on the recovery of the electrical resistivity of copper only two main recovery stages were observed, namely recovery stage I between the temperature of liquid helium and 85 K and recovery stage III below ambient temperature (Figs. 1 and 2). Even the sub-stages of recovery stage I were not noticed. The interpretation appeared to be very simple. It was assumed that the more mobile defects recombine in recovery stage I with the less mobile defects. The less mobile defects escaping recombination in recovery stage I were assumed to annihilate in recovery stage III. Huntington and Seitz [6] and Huntington [7] calculated the migration activation energy of vacancies in copper and obtained a value of $E_{IV}^{M} \approx 1.0$ eV. In 1953 Huntington [8] calculated the migration activation energy of interstitials and a value of about $E_{II}^{M} \approx 0.1$ eV was derived. Consequently, Seitz [1] attributed the appearance of recovery stage I to the migration and annihilation of self-interstitials recombining with vacancies and the appearance of recovery stage III to the migration and annihilation of freely migrating vacancies escaping recombination with intertsitials.

This reasoning is correct in principle as long as the migration activation energy of self-interstitials is smaller than that of single vacancies. However, the recovery stage or the sub-stage of a recovery stage, which is attributed to the recombination of self-interstitials of the dumbbell configuration with vacancies, should be very large with respect to all the other recovery-stages. The order of reaction for this recovery stage, that is for the recombination of interstitials with vacancies must be two.

Already in 1959 Corbett, Smith, and Walker [9] found a sub-structure in recovery stage I when irradiating copper with 1.4 MeV electrons. These measurements have been repeated since then in many different laboratories using high energy electrons, protons or neutrons as irradiating particles. Not only pure copper, but copper doped with various amounts of different elements, and gold, silver, nickel, aluminium etc. were systematically investigated. Also the shape of the recovery spectrum was carefully studied as a function of the irradiation dose. In 1963 Seeger recognized that mainly two different sub-structures of recovery stage I exist which are represented by copper and gold, respectively [10].

In gold there are many sub-recovery stages in recovery stage I, namely recovery stages I_A, I_B, I_C, etc., which are commonly attributed to the annihilation of correlated Frenkel defects, namely to correlated interstitial-vacancie pairs, the separation of which is increasing with increasing alphabetic order of the sub-stages. For all the recovery stages a first order reaction was observed. The amount of recovery of each sub-stage decreases with increasing alphabetical order after recovery stage I_B or I_C and finally a continuous recovery spectrum is found in recovery stage II (garbage annealing)[2] until the beginning of recovery stage III. The magnitudes of recovery stages I, II, and III are about equal.

---

2 After low dose irradiations an almost linear decrease of the electrical resistivity is found during annealing for recovery stage II. After higher

However, no sub-recovery stage in recovery stage I is found in gold which has a 2nd-order reaction that could be attributed to the recombination of self-interstitials with vacancies. If we follow the reasoning of Seitz [1], we are obliged to assume that in gold self-interstitials recombine with vacancies in recovery stage III. Stage III is a large recovery stage, and a 2nd-order reaction has been determined for it in annealing experiments.

The finding that vacancies annihilate in recovery stage IV after quenching is also in agreement with this interpretation [11]. Again a 2nd-order reaction is found for the annihilation of vacancies in recovery stage IV. This means that vacancies annihilate via di-vacancy formation and that the migration activation energy of di-vacancies must be much smaller than that of single vacancies.

In summary nearest correlated Frenkel defects annihilate in recovery stage I, further distant correlated Frenkel defects annihilate in recovery stage II, self-interstitials recombine with vacancies in recovery stage III and vacancies annihilate in recovery stage IV. The number of main recovery stages found in gold is also observed in all other fcc materials and there are some specific features which are characteristic for each metal. Apart from these specific features there is *a priori* no reason why the attribution of certain types of point defects to certain recovery stages in all other materials should be different from gold. There are many data available for many different fcc metals that our conclusions can easily be verified.

The main difference between gold and e. g. copper concerns the appearance of recovery sub-stages I_D and I_E in copper. Recovery sub-stage I_D follows a lst-order reaction and recovery sub-stage I_E a reaction order of about two. It is very clear that recovery sub-stage I_E must be due to a new interstitial type defect which is different from the self-interstitial migrating and annihilating in recovery stage III and that consequently recovery sub-stage I_D must be due to the annihilation of correlated Frenkel defects consisting of a vacancy and the new type of interstitial. It is also very clear that the smallest sub-stage I_E among all recovery stages, which can often not even be detected, can not be attributed to self-interstitials if we follow the suggestions of Seitz, according to whom the recovery stage due to the annihilation of self-interstitials should be the largest of all the recovery stages and in addition should exhibit a 2nd-order reaction. In order to overcome these difficulties the advocates of the OIM believe that self-interstitials migrate in recovery sub-stages I_D and I_E and that no recovery stage IV would exist which could be attributed to vacancy annihilation [2].

We will show in the context of this paper that the main body of data concerning properties of point defects in fcc materials was already available at the beginning of the sixties.

If we attribute the appearance of recovery sub-stage I_E to the annihilation of a second type of interstitial, then there is no *a priori* reason why this sub-stage should be the smallest recovery stage found. In other words even if sub-stage I_E were a large recovery stage we would be forced to assume that the appearance of this sub-stage, which is only found after high energy particle irradiations and not after plastic deformation,

---

dose irradiations a pronounced sub-stage is found in recovery stage II which is attributed to the annihilation of di-interstitials formed during irradiation when an existing interstitial encounters a dynamic crowdion, and which is named recovery sub-stage II_A.

would be due to the annihilation of a second type of interstitial stable in copper and not stable in gold and meta-stable with respect to self-interstitials. We will show in the context of this work that the meta-stable interstitials are crowdions which annihilate to a great extent spontaneously during irradiation or which convert during irradiation into stable self-interstitials.

ON RECOVERY STAGES

It is well known that about 95 % of all radiation damage obtained during irradiation with e. g. high energy electrons is formed via dynamic crowdion propagation, i. e., via replacement collision sequences [12-14]. About one half of the radiation damage consists of correlated interstitial-vacancy pairs of various distances and the other half of free interstitials and vacancies. About 90 % of the radiation damage consists of correlated Frenkel defects, namely of interstitial-vacancy and of crowdion-vacancy pairs irradiating materials, in which crowdions are stable, below about 80 K. Thus in these materials only 10 % of the radiation damage consists of free interstitials and vacancies. This means that in gold in which crowdions are not stable, recovery stage I is very small, and that in copper, in which crowdions are stable, recovery stage I is by far the largest recovery stage.

Recovery sub-stages I_A, I_B, and I_C are commonly attributed to the annihilation of correlated Frenkel defects consisting of interstitial-vacancy pairs. We will list and discuss many experimental results which show that correlated Frenkel defects consisting of crowdion-vacancy pairs annihilate in the broad recovery sub-stage I_D, and almost free crowdions annihilate in the tiny recovery sub-stage I_E.

The almost linear decrease of the electrical resistivity observed in recovery stage II (garbage annealing) is attributed to the annihilation of further distant Frenkel defects consisting of interstitial-vacancy pairs. After relatively high irradiation doses a sub-stage II_A is observed which is assigned to the annihilation of di-interstitials.

Finally many experimental results are mentioned which show that self-interstitials and vacancies annihilate in recovery stages III and IV, respectively.

DYNAMIC AND STATIC CROWDIONS

Radiation Enhanced Self-Diffusion due to Thermally Activated Point Defects

Before we discuss further details of dynamic and static crowdions and the possible reactions of these defects with existing defects in the lattice we will just mention a few arguments excluding the assignment of the sub-stage I_E-defects to self-interstitials.

The radiation enhanced self-diffusion coefficient due to self-interstitials is [4,15]:

$$D_{II}^{irr.} = a_o^2 f_{II} \sqrt{\frac{K_{II}^{eff} \nu_o \exp.-(E_{II}^M / k T)}{\alpha}} \qquad (1)$$

where a_o is the lattice parameter, f_{1I} the correlation factor, $K_{II}^{eff.}$ the production rate of self-interstitials, ν_o the pre-exponential factor, E_{1I}^{M} the migration activation energy of interstitials, k the Boltzmann constant, T the irradiation temperature, and α the recombination volume between vacancies and self-interstitials.

If we compute the radiation-enhanced self-diffusion coefficient by means of equation (1) for a migration activation energy of self-interstitials E_{1I}^{M} = 0.12 eV, which is the value assumed in the OIM for copper, or silver, or nickel, etc. [2], we obtain for an irradiation temperature of $T_{irr.}$ = 500 K a self-diffusion coefficient ($D_{II}^{irr.} \approx 10^{-15}$ [$cm^2 s^{-1}$]) which is more than four orders of magnitude larger than that measured for nickel [15]. If the radiation-enhanced diffusion coefficient is computed for the migration activation energy of self-interstitials (MTIM), which is that obtained for stage III recovery, then the measured and computed coefficients are in agreement [15].

This means that the contribution of the sub-stage I_E interstitials to radiation-enhanced self-diffusion is negligibly small with respect to that of self-interstitials which are mobile in recovery stage III (MTIM).

On the Number of Replacement Collision Sequences of Dynamic Crowdions

The radiation damage rates obtained for gold [16] are plotted in Fig. 3. The decrease of the radiation damage rate indicates that radiation-produced defects already annihilate during irradiation. It is essential to note that the decrease of the radiation damage rate is also observed at very low irradiation temperatures at which point defects are not mobile. Consequently, only dynamic crowdions can account for the observed decrease of the radiation damage rate with increasing point defect concentration. Dynamic crowdions recombine with vacancies if they meet a vacancy on their way through the lattice or they form di-interstitials if they meet an already existing self-interstitial. We obtain for the effective production rate of interstitials, $K_{1I}^{eff.}$:

$$K_{II}^{eff.} = K_{II}^{irr.} (1 - \alpha c_{1V} N - \varepsilon c_{II} N - \ldots.) \qquad (2)$$

where $K_{1I}^{irr.}$ is the initial radiation damage rate and ε the recombination volume between two self-interstitials which is certainly smaller than the recombination volume α between vacancies and self-interstitials.

Gilhaus [17], Schüle [4], and Gilhaus and Schüle [18,19] measured radiation damage rates in gold and in pure copper, in commercial copper, and in copper doped with beryllium, and determined the product $N \cdot \alpha$. Surprisingly, very large numbers are found namely $N \cdot \alpha = 6 \cdot 10^7$ (equation (2)) for all the materials except for copper doped with beryllium.

We have shown that the recombination volume α between vacancies and interstitials must be as large as about α = 1200 atomic volumes [15] and thus the number of replacement collision sequences is about N = 50,000. This means that dynamic crowdions travel in a sink free material more than 100,000 Å. The number N decreases about reciprocally to the concentration of beryllium added to copper and achieves a value of N = 15 in copper containing 763 ppm beryllium [18].

The initial radiation damage rate in copper containing 763 ppm beryllium is maintained for irradiation temperatures which are just below the recovery stage III temperature region. Quasi-dynamic steady state defect

concentrations are obtained during irradiation with high energy particles when self-interstitials annihilate due to thermal activation.

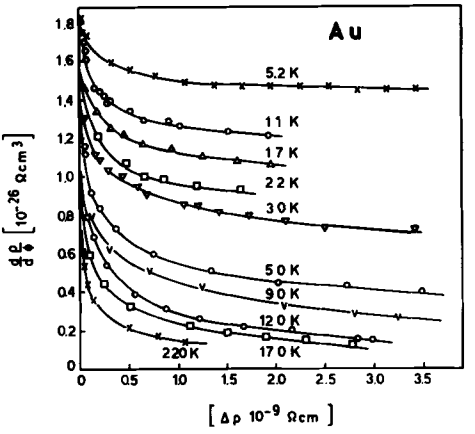


Fig. 3
The change of the radiation damage rate of gold is plotted versus the accumulated point defect concentration as measured by means of the electrical resistivity for various irradiation temperatures (after reference [16]).

The huge number of displacements of dynamic crowdions is for several reasons a very important feature in radiation damage.

Most of the radiation damage rate measurements were performed on specimens which are too thin so that many radiation induced dynamic crowdions annihilate spontaneously at the surface of the specimen.

Studies of radiation damage by means of TEM-techniques were again often performed on such thin specimens so that no confident conclusions with respect to bulk behaviour can be obtained.

The radiation damage obtained by means of Monte Carlo computations was found to be one order of magnitude too large with respect to results of experimental findings. For the number of replacement collision sequences of a dynamic crowdion only N = 10 was used in the computations instead of N = 50,000.

It is also worth considering the behaviour of dynamic crowdions in the development of radiation resistant materials. In materials not containing large amounts of undersized atoms such as beryllium and/or silicon in copper, or in nickel, or in stainless steel alloys, the effective production rates of point defects are about one order of magnitude smaller than in materials doped with certain elements. During irradiation the dynnamic crowdions annihilate "spontaneously" with vacancies and other point defects.

Self-Diffusion due to Dynamic Crowdions

The following equation has been derived for the self-diffusion coefficient due to dynamic crowdions [4]:

$$D^{dyn.} = 0.5 a_o^2 K_{II}^{irr.} N \qquad (3)$$

where $K_{II}^{irr.}$ is the production rate of dynamic crowdions, which is the initial production rate of interstitials, and N is the number of replacement collision sequences of dynamic crowdions necessary for them to lose their kinetic energy to the lattice.

Dynamic crowdions can cause tracer diffusion or inter-diffusion, and they can dissolve e. g. precipitates. The dynamic crowdion mechanism is also known as radiation mixing.

The radiation-enhanced self-diffusion and inter-diffusion coefficients were measured for many different elements and alloy systems in the temperature range between the temperature of liquid helium and the temperature below the recovery stage III temperature region of the respective materials (see e. g. references [20,21]). It was found that the diffusion cooefficients are independent of the irradiation temperature over the entire temperature region and that they depend linearly on the magnitude of the high energy particle flux [4]. At high irradiation temperatures the measured diffusion coefficients were orders of magnitude smaller than the diffusion coefficients due to self-interstitials having a migration activation energy of E_{11}^{M} = 0.12 eV [OIM] and below the temperature region corresponding to the temperature region of recovery stage I the measured diffusion coefficients are many orders of magnitude larger than the computed diffusion coefficients.

If we interpret the results in terms of equation (3), we find values for the number of replacement collisions between N = 15 and N = 150. These numbers are many orders of magnitude smaller than the those, obtained from measurements of the radiation damage rate (see section "On the Number of Replacement Collision Sequences of Dynamic Crowdions"). In all these experiments very high fluxes of very high energetic particles corresponding to displacement rates of 10^{-3} to 10^{-4} dpa$\cdot$s^{-1} were used. The number of replacement collision sequences may have been reduced i) because of the formation of many interstitial clusters during irradiation that act as stops for dynamic crowdions or ii) because of too large concentrations of undersized atoms in the materials through which dynamic crowdions are converted into stable self-interstitials, or iii) because of focussons that disturb the focussing of dynamic crowdions.

This means that the present available diffusion data measured below the recovery stage III temperature region confirm the dynamic crowdion mechanism, but they do not confirm the large numbers of replacement collision sequences that were derived from measurements of the radiation damage rate[3].

Evidence for Correlated Crowdion-Vacancy Pairs

If a partially ordered Cu_3Au alloy is irradiated at the temperature of liquid helium, the electrical resistivity increases because of a decrease in the degree of order [22] which is caused by dynamic crowdions (Fig. 4). The electrical resistivity recovers during subsequent annealing at the end of recovery stage I, which is sub-stage I_D, and the original degree of order existing before irradiation is once more obtained. The electrical resistivity changes found during annealing are shown in Fig. 4. All these changes are again due only to changes in the degree of order, and the resistivity changes due to the annihilation of point defects are negligibly small. We suppose that the increase of the degree of order in sub-stage I_D is due to the annihilation of crowdion-vacancy pairs, i. e. crowdions return to their place of origin thus restoring the original degree of order existing before irradiation. This means that the defect moving in this temperature region can increase the degree of order regardless of the type of defect. However, if Cu_3Au is

[3] Note added in proof: Recent results of investigations of radiation enhanced diffusion of Ni^{63}-diffusion in nickel and in copper (1.85 MeV electrons and 8.86 μAcm^{-2}) lead to replacement collision numbers for both metals of N $\approx$ 40,000 (ICFRM-7, Obninsk, Russia, 1995).

irradiated at 100 K then no change of the electrical resistivity is observed, i. e. no increase of the degree of order is obtained. This means that the defects that become thermally activated in recovery stage I, i. e. recovery sub-stage I_D, cannot increase the degree of order beyond the value existing before irradiation. Thus, this defect cannot enhance diffusion, and this is a typical feature of defects which can only migrate one-dimensionally, e. g. crowdions. Therefore crowdions are stable in Cu_3Au alloys.

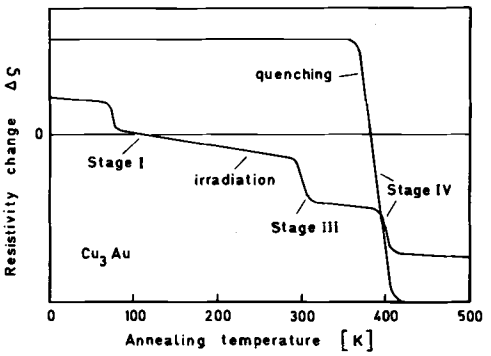


Fig. 4
The recovery of the electrical resistivity of Cu_3Au after irradiation and after quenching is schematically plotted versus the annealing temperature. The changes of the electrical resistivity are due to changes in the degree of order and not to the annihilation of point defects (see reference [23]).

In a real display of the measured data recovery sub-stages I_A, I_B, and I_C are also found. Their magnitudes are negligibly small compared to that of the sub-stage I_D recovery. The first three sub-stages are commonly attributed to the annihilation of correlated interstitial-vacancy pairs. We believe that this assignment is also correct for Cu_3Au alloys because the annihilation of correlated interstitial-vacancy pairs cannot change the degree of order.

With further increasing annealing temperature the electrical resistivity decreases in the same two temperature regions (Fig. 4) which are known as recovery stages III and IV in copper. Ordering is also observed in recovery stage IV after quenching from "low" temperatures (Fig. 4). Thus we conclude that vacancies migrate and annihilate in recovery stage IV after quenching and also after irradiation thereby increasing the degree of order.

Only three types of defects are produced by high energy particle irradiation, namely correlated crowdion-vacancy pairs, self-interstitials, and vacancies able to increase the degree of order during their migration. Thus the increase in the degree of order in recovery stage III (Fig. 4) must be caused by migrating self-interstitials.

The activation energies which are determined for recovery stages III and IV, respectively, are in agreement with those determined for copper [24,25]. From investigations of radiation-enhanced diffusion in Cu_3Au alloys the same activation energies are found for recovery stages III and IV, respectively. It was further found that the ordering rate during irradiation in an almost disordered alloy is mainly determined by a vacancy diffusion mechanism, and the diffusion rate is mainly determined by an interstitialcy diffusion mechanism in an almost ordered alloy [26]. In an almost ordered alloy, interstitials must jump about 600 times more often than vacancies to increase the degree of order by the same amount.

A dispersed type of order develops in gold-silver alloys during a slow cooling or during irradiation [27]. An increase of the degree of order is connected with a total increase of the electrical resistivity which consists

of a superposition of two electrical resistivity contributions. The electrical resistivity decreases because of an increase of the degree of atomistic order within the ordered particles and increases because of the scattering of electrons at the boundaries of the ordered particles, the size of which decreases with decreasing temperatures. If such a material is irradiated with high energy particles at the temperature of liquid helium the electrical resistivity increases because only the atomistic degree of order within the ordered particles decreases because of dynamic crowdion propagation (Fig. 5). However, the size of the ordered particles is hardly changed by dynamic crowdions. Thus, if irradiated gold-silver alloys are annealed the atomistic degree of order existing prior to irradiation is restored at about 80 K through the annihilation of crowdion-vacancy pairs in recovery sub-stage I_D. With increasing annealing temperature, however, only an increase of the electrical resistivity is found in the temperature region of recovery stage III, because of three-dimensionally migrating interstitials [29,30]. One-dimensionally migrating point defects, i. e. dynamic crowdions or the annihilation of correlated crowdion-vacancy pairs, can only cause changes in the degree of atomistic order and not in the size of the ordered particles in contrast to three-dimensionally migrating self-interstitials, which can cause both an increase in the degree of atomistic order and a decrease in the size of the ordered particles. This means that in some instances the type of order developing in an alloy material can be identified by irradiation and annealing experiments.

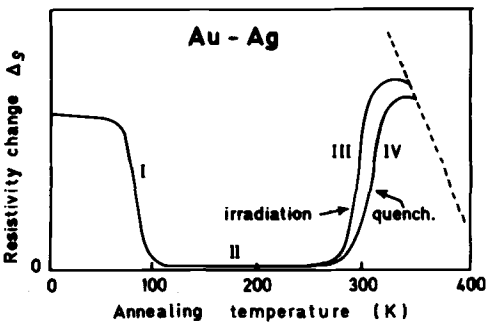


Fig. 5
The recovery of the electrical resistivity of an Au-15at.%Ag alloy irradiated with high energy electrons is plotted versus the annealing temperature (After reference [28]).

It is known that in copper-nickel alloys a negative short range order develops during slow cooling or during irradiation with high energy particles. Dynamic crowdions or the annihilation of correlated crowdion-vacancy pairs cannot cause a measurable change in the ordering structure. In fact, the annealing spectrum of copper-nickel alloys is exactly that of pure nickel or pure copper.

Correlated Crowdion-Vacancy Pairs and Vacancies

Thermal annealing of neutrino recoil-induced Frenkel defects in copper was observed by means of perturbed angular correlation techniques [31]. Sixty percent of the 117 MHz signal resulting from probe atoms next to vacancies is recovered in the temperature region of recovery sub-stage I_D, and the rest of

the signal (40%) is recovered when annealing at 300 K. There are no recovery sub-stages I_A, I_B, I_C, and I_E. The recoil energy resulting from decay atoms was 29 eV per decay, just enough to produce one Frenkel defect per decay via <110>-replacement collision sequences, i. e. via dynamic crowdions. The concentration of the decay atoms was of the order of 10^{-9} (molar fraction) and thus the concentration of Frenkel defects was much lower than this concentration because many of the dynamic crowdions must have reached the surface of the well annealed 20,000 Å thick copper foil, since dynamic crowdions can travel more than 100,000 Å in well-annealed copper. This means that the copper foil contained correlated vacancy-crowdion pairs and vacancies and almost no self-interstitials.

The 117 MHz signal vanishes or is recovered when a vacancy next to the probe atom disappears. Vacancies belonging to correlated vacancy-crowdion pairs vanish when thermally activated crowdions recombine with their own vacancies (sub-stage I_D) or when vacancies jump away from the probe atoms (temperature region of recovery stage III). Vacancies in copper having a migration activation energy of $E^M_V = 1.06$ eV jump about once at 300 K during annealing. This means that the recovery of the 117 MHz signal at 300 K is not due to the annihilation of vacancies.

About the Initial Radiation Damage Rate in Copper and the Activation Energy to Transform Crowdions into Stable Self-Interstitials.

The main radiation damage rate data available in the literature for copper were compiled [4] and are again displayed in Fig. 6. Curve (a) is obtained for copper containing beryllium and corresponds qualitatively exactly with that found for gold [4]. It has already been mentioned that the recovery spectrum of copper doped with beryllium is exactly that of gold (Fig. 2).

For the initial radiation damage rate of pure copper, curve (b) is obtained. This curve has a minimum at about 80 K. Almost all radiation damage is obtained via dynamic crowdion propagation and above an irradiation temperature of about 65 K, i. e. above the temperature region of recovery sub-stages I_D and I_E, crowdion-vacancy pairs and free crowdions annihilate spontaneously. However, we conclude from the observed increase of the production rate between 80 and 140 K (curve (b)) that the rate of crowdions, which are still stable at 80 K, converting to stable and almost immobile self-interstitials, increases with increasing irradiation temperature. Self-interstitials do not annihilate spontaneously during irradiation between 80 and 140 K because they are not sufficiently mobile in this temperature region. They only become sufficiently mobile, so they are able to annihilate due to thermal activation in the temperature region corresponding to recovery stage III. Thus the initial radiation damage rate increases with increasing irradiation temperature because the rate of defects annihilating during irradiation decreases with increasing irradiation temperature.

The activation energy for the transformation of crowdions into self-interstitials can be derived from the increase of the initial radiation damage rate observed between 80 and 140 K, and a value of $E^C_C = 0.14$ eV results. This means that the migration activation energy of crowdions in copper is slightly smaller than the conversion energy, and thus below a certain temperature crowdions are stable and their properties can be determined. We conclude that

the conversion energy in gold must be smaller than the migration activation energy of crowdions so that for a simple reason crowdions cannot be observed in gold.

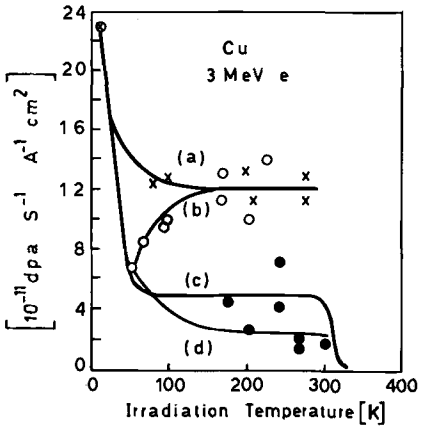


Fig. 6
The radiation damage rate of pure and doped copper, of annealed and pre-irradiated copper is plotted versus the irradiation temperature. Curve (b) is obtained for well annealed pure copper, curve (a) for copper doped with undersized or oversized atoms, curve (c) for copper previously irradiated with protons at ambient temperature, and curve (d) for copper which was slightly deformed during mounting prior to irradiation.

The features concerning stable crowdions are not essential for the development of radiation resistant materials. However, dynamic crowdions can cause structural changes in materials, they can contribute to self- and inter-diffusion, they can dissolve existing precipitates, and perhaps their contribution to irradiation creep is more important than that of thermally activated self-interstitials. Dynamic crowdions can be observed in any material. However, the number of jumps of dynamic crowdions before they convert into stable self-interstitials depend on the defect structure of a material itself.

About the Conversion of Dynamic Crowdions into Self-Interstitials through Additions of Undersized Elements

The number of replacement collision sequences of dynamic crowdions in copper was determined as a function of the concentration of beryllium [18]. It was found that this number is reciprocally proportional to the concentration of beryllium in copper, decreasing from N = 50,000 in pure copper to about N = 15 in copper containing 763 ppm beryllium.

The recovery spectrum of pure copper after irradiation with high energy particles is shown in Fig. 1. It is essential to remember the magnitude of sub-stages I_D and I_E, and of recovery stage III, respectively. If beryllium is added to copper then with increasing amount of beryllium the magnitude of the sub-stages I_D and I_E decreases and that of recovery stage III increases accordingly. If copper contains 763 ppm beryllium, recovery sub-stages I_D and I_E are no longer found, and the amount of the recovery of recovery stage III has obtained the maximum value [32-33]. Thus the resulting recovery spectrum is identical with the recovery spectrum of gold (Fig. 2). The activation energy determined for the recovery stage III of pure copper does not change in a measurable way if beryllium is added to copper [2,18].

Identical results are obtained if gold instead of beryllium is added to copper [34]. The same results obtained for copper and for copper doped with beryllium with respect to the recovery spectra are also observed for nickel and for nickel doped with silicon, respectively [35]. However, the recovery spectra of pure copper and pure nickel, which are almost identical, do not change if almost equally sized elements are added, e. g. Zn, Ni, Sn etc. to copper [34] or Zn, Cu, Sn etc. to nickel [33].

It is again evident that dynamic crowdions exist and that they can be converted to self-interstitials if they meet undersized or oversized atoms on their way through the lattice or they push the undersized atoms into a self-interstitial position and occupy the lattice position of the undersized or oversized atom. The number of replacement collision sequences of dynamic crowdions is not greatly influenced if almost equally sized atoms and equally weight atoms are added.

The finding that the activation energy of recovery stage III is not changed or hardly changed if various elements are added to copper [32-34] or nickel [35,36] or aluminium [37] etc., is also very important. The conclusion is that the binding energies between self-interstitials and impurities are in most instances very small, i. e. below the detection limit. This conclusion is important because for a long time the advocates of the OIM assumed that in recovery stage III in addition to vacancies, self-interstitials would be released from impurities and annihilate, too. The consequence of this assignment is that each element must have almost the same binding energy to self-interstitials namely $E^{B}_{imp.} = 0.71 - 0.12 = 0.59$ eV in the case of copper and $E^{B}_{imp.} = 1.03 - 0.12 = 0.91$ eV in nickel. This is very unlikely and not maintained nowadays by the advocates of the OIM.

It has been noticed that the binding energies of impurities to point defects are usually very small in many different elements and alloys (MTIM). This feature simplifies the reasoning in developing radiation resistant materials. If the mobilities of point defects could be manipulated by adding impurities then it would be an aim to find materials in which the effective migration activation energies of self-interstitials and vacancies would be about equal. In this case the rate of formation of interstitial clusters and of vacancy clusters during irradiation with high energy particles would be much smaller than observed in the materials available at present.

Properties of Vacancies and of Di-Vacancies in Copper

Properties of vacancies in copper and in many other fcc metals and alloys have been investigated for more than thirty-five years in many laboratories all over the world [2]. The self-diffusion coefficient of copper was determined over a range of eleven orders of magnitude [4,38]. In the "low" temperature region a straight line in the Arrhenius plot (Fig. 7) is obtained and attributed to self-diffusion due to vacancies. An upwards curvature in the "high" temperature region in the Arrhenius plot is found (Fig. 7) which is assigned to a contribution of di-vacancies to vacancy diffusion increasing with increasing temperature. The activation energies due to vacancy and di-vacancy self-diffusion derived from measurements of the self-diffusion

coefficient (Fig. 7) are Q_{1V}^{SD} = (2.09 ± 0.01) eV and Q_{2V}^{SD} = (2.50 ± 0.03 eV), respectively. The activation energy of self-diffusion, Q_{1V}^{SD}, determined for copper, is perhaps the most precisely known property of vacancies. For the activation energies of self-diffusion due to vacancies and di-vacancies the following equations are valid:

$$Q_{1V}^{SD} = E_{1V}^{F} + E_{1V}^{M} \tag{4}$$

$$Q_{2V}^{SD} = 2\,E_{1V}^{F} + E_{2V}^{M} - E_{2V}^{B} \tag{5}$$

where E_{2V}^{M} and E_{2V}^{B} are the migration activation and the binding energies of di-vacancies, respectively.

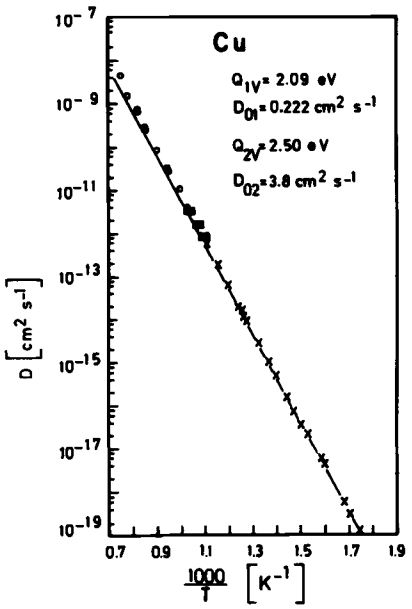


Fig. 7
The logarithm of the self-diffusion coefficient of copper is plotted versus the reciprocal temperature (O Rothman and Peterson; ■ Weithase and Noack; × Schüle [38]).

This means that the migration activation energy or the formation energy of single vacancies can be obtained by equation (4) if one or the other value is known, respectively. Thus each of the two energies can be obtained more than four times from three independent experiments, namely from quenching, irradiation, and from at-temperature experiments.

We will show that the formation energy of vacancies in copper is obtained with an accuracy of ± 0.01 eV and since the self-diffusion coefficient due to di-vacancies is known with an accuracy of ± 0.03 eV the sum $E_{2V}^{M} - E_{2V}^{B}$ is known with an accuracy of ± 0.04 eV.

4.1 Quenching Experiments

The very first reliable results of quenching experiments in copper were reported as early as 1965 [39]. It was realized that it was much more difficult to quench copper than gold, or silver, or aluminium. In all these elements the recovery of the electrical resistivity after quenching was observed in a very broad temperature range below that corresponding to recovery stage IV, e. g. between 470 and 250 K in copper. Also many different activation energies were determined for the recovery after quenching, depending on the quenching temperature and on the quenching rate. The activation energy determined as a higher limit was attributed to the migration activation energy of vacancies, $E_{1V}^{M} = 1.06$ eV. The recovery of the electrical resistivity followed a 2nd-order reaction, implying that vacancies annihilate by forming di-vacancies having a much smaller migration activation energy than that of vacancies. In fact, the activation energy determined as a lower limit was attributed to the di-vacancy migration activation energy which yields a value of $E_{2V}^{M} = 0.64$ eV. At the same time a binding energy of di-vacancies of $E_{2V}^{B} = 0.20$ eV was derived from the recovery features. A confirmation for the validity of the derived values is obtained by comparing these values with the activation energies of self-diffusion by means of relations [4] and [5].

The formation energy of vacancies in copper was also obtained from quenching experiments in 1965 [40]. The value obtained, namely $E_{1V}^{F} = 1.03$ eV, is in perfect agreement and consistent with self-diffusion data [38] and the migration activation energy determined after quenching [39].

Quenching experiments were performed in the sixties and seventies in many different laboratories in order to obtain information on the formation and the migration activation energies of vacancies in copper. In most of these laboratories no measurable concentration of vacancies could be obtained. In 1977 Bourassa and Lengeler [41] reported results from quenching 5 mm thick copper rods. They obtained a quenched-in resistivity that was one order of magnitude smaller than that reported earlier [39,40], and they measured an activation energy for the recovery stage after quenching of 0.76 eV which they attributed to the migration activation energy of vacancies. They derived for the resistivity per vacancy in copper $\rho_o = 0.62 \cdot 10^{-4}$ Ωcm with the assumption that the concentration of vacancies at the melting temperature of copper as determined by Simmons and Balluffi [42] would be $c_V^{ett.} = 1.9 \cdot 10^{-4}$ (molar fraction). Recently, the concentration of vacancies in thermal equilibrium was re-determined by Hehenkamp et al. [43] and a value four times larger namely $c_V^{ett.} = 7.6 \cdot 10^{-4}$ was measured. With this value the resistivity due to vacancies would be $\rho_o = 0.155 \cdot 10^{-4}$ Ωcm. This value is about one order of magnitude smaller than the value derived from irradiation experiments for which $\rho_o = 1.6 \cdot 10^{-4}$ Ωcm was obtained [44].

However, an incorrect value for the resistivity of a vacancy derived by Bourassa and Lengeler [41] was the only value accepted by the advocates of the OIM until now [2], and all the other values obtained before and after 1976 were never cited and considered at all.

Vacancies in Thermal Equilibrium and the Electrical Resistivity of Vacancies

In 1977 we tried to determine the formation energies of vacancies in copper by measuring the electrical resistivity *in situ* between ambient temperature and the melting temperature of copper [45]. Assuming that the electrical resistivity of a vacancy would be $\rho_o = 1.6 \cdot 10^{-4}$ Ωcm an effective concentration of vacancies at the melting temperature of copper of $c_V^{eff.} \approx 7.0 \cdot 10^{-4}$ was obtained which is the concentration that has been determined again recently [4,43].

Measurements of the electrical resistivity in situ on copper were recently repeated [46] assuming that the electrical resistivity of a vacancy in copper is $\rho_o = 1.9 \cdot 10^{-4}$ Ωcm the properties of vacancies and of di-vacancies resulting from the data correspond exactly to those obtained from the Hehenkamp et al. data [4]. These electrical resistivity data can also be interpreted in the following way. Assuming that the Hehenkamp et al. data are correct then we can conclude that the electrical resistivity per vacancy is $\rho_o = 1.9 \cdot 10^{-4}$ Ωcm and that the rule of Matthiessen is fulfilled in copper [46].

The evaluation of the Hehenkamp et al. data [43] in combination with all the data discussed in previous section of this paper yield the following properties of vacancy type defects in copper: $E_{1V}^F = 1.03$ eV, $E_{1V}^M = 1.06$ eV, $E_{2V}^M = 0.64$, $E_{2V}^B = 0.20$ eV, $\rho_o = 1.9 \cdot 10^{-4}$ Ωcm, $S_{1V}^F = 1.4$ k, and $S_{2V}^F = 4.9$ k.

It is essential that these properties of vacancies can also be obtained from measurements performed in thermal equilibrium. The migration activation energy found for vacancies after quenching or after irradiation with high energy particles are dismissed by the advocates of the OIM with the argument that these values are not due to single vacancies but to the dissolution of vacancy clusters etc..

It does hardly matter whether the electrical resistivity of a vacancy is assumed to be $\rho_o = 1.9 \cdot 10^{-4}$ Ωcm or $\rho_o = 1.6 \cdot 10^{-4}$ Ωcm. However, the value $\rho_o = 1.9 \cdot 10^{-4}$ Ωcm is the first measured value whereas the other value has been obtained from either estimations or from computations [1,44].

Vacancies after Irradiation

The variation of the concentration of interstitials and vacancies can be calculated by chemical rate equations:

$$\frac{dc_{II,IV}}{dt} = K_{II,IV}^{eff} - \alpha c_{II} c_{IV} (\nu_{II} + \nu_{IV}) - \beta c_S c_{II,IV} \nu_{II,IV} \qquad (6)$$

where $K_{II,IV}^{eff}$ is the effective production rate of defects which varies interstitials with the concentration of e. g. accumulated point defects according to equation (2), where $\nu_{II,IV}$ are the mobilities of interstitials and vacancies, respectively, c_S the concentration of randomly distributed sinks, and ß the recombination volume between point defects and sinks.

The rate equations were extended assuming that the sink concentration increases with irradiation time and that the sinks are interstitial clusters. The results of such a computation are shown in Fig. 8 for copper containing

763 ppm beryllium [17-19]. Thus the initial production rate of point defects is maintained during irradiation (equation (2)). The values for the various parameters used in the computation are listed in the figure. It is seen that the concentration of vacancies always increases, the concentration of self-interstitials first increases, and then decreases to very small values. The concentration of interstitial clusters also increases, saturating after a certain irradiation dose.

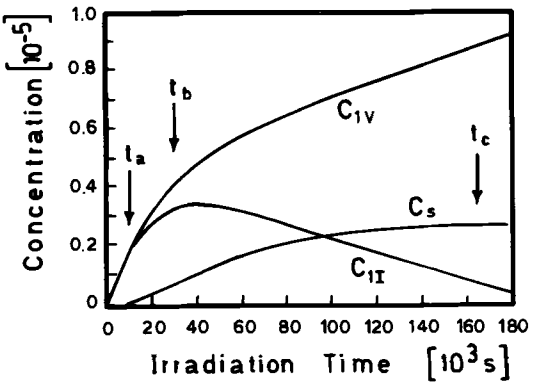


Fig. 8
The calculated changes of the concentration of vacancies, interstitials, and clusters of interstitials by means of extended rate equations (6) are plotted versus the irradiation time ($T_{irr.}$ = -40°C, E_{II}^{M} = 0.68 eV, $K_{II,IV}$ = 10^{-10} dpa·s^{-1}, and α = 1200 atomic volumes).

The change of the electrical resistivity measured during irradiation at $T_{irr.}$ = - 39.65 °C is shown in Fig. 9. It is evident that the measured curve is almost identical with the curve computed for the vacancy concentration (Fig. 8). If the irradiation is stopped at an irradiation time, t_a, then the concentration of interstitials and vacancies are about equal, and the concentration of interstitial clusters is still negligibly small (Fig. 8). If such an irradiated specimen is annealed, then interstitials recombine with vacancies in recovery stage III and only recovery stage III will be observed (Fig. 10). If the irradiation is stopped at an irradiation time, t_b, then there is a surplus of vacancies with respect to self-interstitials and recovery stages III and IV are observed during annealing (Fig. 10). After very long irradiation times, t_c, the concentration of interstitials is negligibly small with respect to that of vacancies and in this case only recovery stage IV is found (Fig. 10).

It is evident that the appearance of recovery stages III and IV depends on the previously accumulated irradiation dose and also on the irradiation temperature. For irradiation temperatures below the temperatures used in the present experiments, much higher irradiation doses are necessary so that only recovery stage IV can be observed. We have shown that recovery stages III and IV are also found in pure copper for corresponding irradiation doses [4]. Therefore, it is understood by the author that the advocates of the OIM do not recognize the presence of recovery stage IV after irradiation [2].

The activation energy determined for recovery stage IV for copper doped with 763 ppm beryllium is Q_{IV} = 1.07 eV and within the error limits, in complete agreement with the migration activation energy for vacancies determined in quenching or in at-temperature experiments for pure copper. Therefore the migration activation energy of vacancies is a

fixed quantity and does not vary due to an unknown physical effect after irradiation as postulated by advocates of the OIM (stage III dilemma).

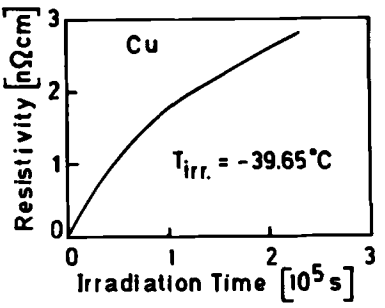


Fig. 9
The increase of the electrical resistivity of copper doped with 763 ppm beryllium is plotted versus the irradiation time. The irradiation temperature was $T_{irr.}$ = - 39.65 °C and the electron flux $\phi = 4.52\ \mu Acm^{-2}$.

The activation energies determined for recovery stages III and IV for copper doped with 763 ppm beryllium are 0.72 and 1.07 eV, respectively, and within the error limits in agreement with the activation energies obtained in recovery stages III an IV in pure copper [17-19]. Therefore we conclude that the binding energies between beryllium atoms and interstitials and vacancies, respectively, are very small.

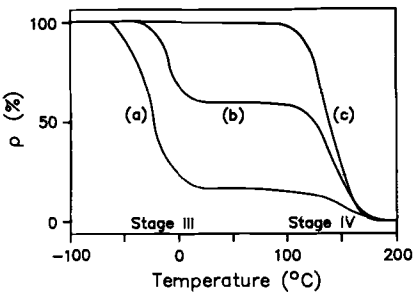


Fig. 10
The recovery spectra of the electrical resistivity of irradiated copper doped with 763 ppm beryllium is plotted versus the annealing temperature. Irradiation doses are labeled with t_a, t_b, and t_c, respectively; see Figs. 8 and 9.

Many investigations have been carried out in the past thirty-five years not only for copper but also for nickel and aluminium, for example, in order to determine the individual binding energy of impurities to interstitials and vacancies, respectively. It has been recognized that the activation energies of recovery stages III after irradiation with high energy particles are hardly changed with respect to temperature and activation energy for many different additions or only very slight increases in the recovery temperature and in the activation energy were found. The increases in the activation energy were of the order of a few hundredths of an eV characteristic for the type of impurities [35-37].

The binding energies of impurities to vacancies were determined in the past in many quenching experiments and these energies were also very small,

varying from a few hundredths to a few tenths of an eV depending on the type of impurity.

On Positron-Annihilation Experiments

Positron annihilation spectroscopy has been proved to be a powerful tool for the investigation of the properties of vacancies. It was already very surprising that the presence of vacancies could be proved by this technique. However, the positron annihilation signal is not linearly proportional to the concentration of vacancies, at least not in the concentration range of vacancies in thermal equilibrium at high temperatures. Consequently the high-temperature data are obtained only by extrapolation.

Secondly, positron annihilation experiments were evaluated as if no di-vacancies were present even at high temperatures and the measured activation energy, which is an effective formation energy of vacancies, is assumed to be the formation energy of vacancies.

The chemical rate equations (6) are powerful tools to describe e. g. the variation of the concentrations of point defects during irradiation. They are valid for other reactions in chemistry, biology, and also in nuclear physics etc.. In the case of the positron annihilation experiments the yield or the magnitude of the signal resulting from the annihilation of positrons with electrons can also be calculated by means of the rate equations (6), if for the concentrations of interstitials and vacancies the concentrations of positrons and electrons are inserted. However, the magnitude of the vacancy signal also depends on the fractions of positrons annihilating with other electrons in the lattice. And it has been shown [4] - this will be discussed in detail in a later section of this work - that the dynamic steady state solutions of the rate equations, which were only considered so far, are only mathematical solutions that often do not reflect physical reality.

The advocates of the OIM quote that the many results reported on studies of the formation energy of vacancies, e. g. in copper by positron-annihilation spectroscopy, would be in favour of their radiation damage model [2]. The effective formation energy of vacancies in copper resulting as an avarage from all the measured data is $E_V^{eff} \approx 1.23$ eV. This value is attributed to the formation energy of single vacancies in the OIM. Such a formation energy of vacancies does not fit predictions of either the OIM or the MTIM.

PROPERTIES OF SELF-INTERSTITIALS

Self-interstitials can be assigned to stage III recovery unambiguously if the assignment of vacancies to recovery stage IV and that of crowdions, a meta-stable interstitial configuration with respect to self-interstitials, to recovery stage I_E is accepted, and when the homology of the five recovery stages found in each fcc material is noticed. There are many experimental data available that show that self-interstitials migrate and annihilate in stage III recovery when they are present [17-19]. Many of these experiments have already been discussed in previous sections. However, there are many important findings that further support the assignment of self-interstitials to recovery stage III.

On the Dumbbell Configuration of Self-Interstitials

Evidence that self-interstitials migrate and annihilate in recovery stage III was already obtained in 1960 for nickel by measurements of the ferromagnetic after-effect and of internal friction [47-49]. It was found that the activation energy for the alignment of self-interstitials in nickel was $E_{aln.} = 0.81 \pm 0.01$ eV and smaller than the migration activation energy of interstitials for which a value of $E_{II}^{M} = 1.03 \pm 0.01$ eV was obtained. Self-interstitials are the only defects imaginable where the alignment energy, $E_{aln.}$, is not the same as the migration activation energy, E_{II}^{M}.

Radiation Enhanced Diffusion

The diffusion coefficient due to radiation enhanced diffusion is:

$$D_{irr.}^{SD} = a_o^2 \sum_n f_n c_n \nu_n \qquad (7)$$

where f_n is the correlation factor for defect type n. The concentration of defect type n can be derived from the rate equations (6). It has been shown many times previously that the steady state solutions of the rate equations (6) are mathematical solutions and that they do not reflect physical reality [4]. The steady state solution of these equations is:

$$c_{1V} = \frac{c_S \beta}{2\alpha} - \left(\frac{c_S^2 \beta^2}{4\alpha^2} - \frac{K_{1V}}{\alpha \nu_{1V}} \right)^{\frac{1}{2}} \qquad (8)$$

The concentration of vacancies resulting formally from equation (8) for irradiation temperatures below the temperature corresponding to recovery stage III is larger than the number of lattice atoms and for "high" irradiation temperatures the concentration of vacancies $c_{1V} \rightarrow 0$. Unfortunately the advocates of the OIM never calculated the concentration of vacancies and interstitials in their computations for irradiation creep, swelling, or precipitate formation during irradiation with high energy particles.

In the OIM approach equation (8) is used in the approximation for $c_S \rightarrow 0$. In this case the activation energies resulting from investigations of radiation enhanced diffusion would be half the migration activation energy of vacancies. If the sink concentration for point defects is negligibly small then the third terms in the rate equations (6) can be neglected and the activation energy of the radiation enhanced diffusion coefficient is half the migration activation energy of self-interstitials (equation (1)). Thus the OIM approach confuses self-interstitials with vacancies.

A square root flux dependency of the diffusion rate is only observed if the dynamic steady state defect concentrations are determined by the mobility of self-interstitials [4]. This square root dependency is found in well-annealed materials up to very high temperatures e. g. up to 400°C in nickel [15] or up to 500°C in Ni-10.6%Cr alloys [50]. If self-interstitials had a migration activation energy of $E_{II}^{M} = 0.12$ eV (OIM) then their concentration in dynamic equilibrium during irradiation, c_{1I}, would be so small already at an irradiation temperature of $T_{irr.} = 20°C$ that the condition for pair recombination would not be fulfilled namely that $c_{1I} > c_S$.

We have shown in many examples that in pure metals, as well as in each alloy investigated, the steady state defect concentration built-up during irradiation is determined by self-interstitials migrating freely in recovery stage III. This means that the activation energy determined for this defect is the same as that determined for the recovery stage III during annealing after a low temperature irradiation. Further, in all these materials, the migration activation energy of vacancies was determined after quenching and in all these materials vacancy annihilation could be assigned to recovery stage IV.

The diffusion mechanisms causing structural changes in the materials during irradiation with high energy particles were determined in many instances [4]. There are examples where structural changes during irradiation are caused mainly by an interstitialcy diffusion mechanism or mainly by a vacancy diffusion mechanism or by both mechanisms. If both diffusion mechanisms are active during irradiation, then not only the migration activation energy of self-interstitials, but also that of vacancies result from investigations of radiation-enhanced diffusion. In addition the number of jumps interstitials must jump more often than vacancies to cause the same structural change during irradiation was derived [4,51].

On Radiation Induced Structural Changes

Atom mobility is increased by irradiation often by many orders of magnitude with respect to the mobilities of atoms without high energy particle irradiation. This means that when irradiating with high energy particles structural changes can be obtained in due laboratory times, which are only obtained without irradiation after a very long thermal treatment. In these instances the phase diagram is maintained during irradiation.

The formation of radiation-induced structures during irradiation is discussed in the following section. These structural changes are mainly formed by an interstitialcy diffusion mechanism, and as a consequence the known phase diagrams are no longer valid. Instead new phase diagrams are valid during irradiation with high energy particles [4].

The formation of α-ferrite in stainless steel alloys does not occur below a characteristic temperature for a certain composition if no nucleation sites are provided in the alloy. For example, if a stainless steel material is cold-worked then during subsequent annealing α-ferrite formes, and then surprisingly, after prolonged annealing again dissolves. If an annealed stainless steel alloy is irradiated, then α-ferrite is formed for sufficiently low irradiation temperature, and the phase boundary valid without irradiation is also maintained during irradiation even in the composition range, which is shown as a dashed line in the phase diagram. Apparently radiation produced interstitials provide the stainless steel materials with nucleation sites for α-ferrite formation. Nevertheless, the rate of formation of this phase is rather determined by a vacancy diffusion mechanism during irradiation with high energy particles [52].

Interstitial Cluster Formation in Pure Metals and in Alloys of Equally Sized Component Atoms

Interstitial clusters are formed in any metal or metallic material of fcc or bcc type below a characteristic temperature which is the temperature of the center of recovery stage IV of the respective material [53]. Extensive studies on this phenomenon were performed on α-copper-zinc alloys [54] and the

results obtained are in agreement with those obtained for pure copper [55] or on other copper-alloys [56,57].

The transition temperature below which such interstitial clusters are formed can be calculated by means of rate equations (6). It is found that the transition temperature is T_t = 158°C for α-copper-zinc alloys [4,54] in agreement with the experimental findings. This transition temperature depends mainly on the migration activation energy of vacancies. Below 158°C the life-time of vacancies in copper or in α-copper-zinc alloys depends on the time until interstitials recombine with them; above 158 °C the life-time of vacancies depends mainly on their own mobility.

The transition temperature below which interstitial clusters are formed is also the transition temperature for vacancy cluster formation [56,57].

Interstitial Cluster Formation in Materials Containing Undersized Atoms

Undersized atoms diffuse during irradiation mainly via an interstitialcy diffusion mechanism. This means that most interstitials will consist of undersized atoms if the undersized atoms are sufficiently small with respect to atoms of the base materials, e. g. silicon in nickel or in stainless steel alloys or beryllium in copper. Consequently, the interstitial clusters that are formed during irradiation will consist of mainly or only undersized atoms and are small precipitates. However, for concentrations of undersized atoms in the 100 ppm range the transition temperature for the formation of interstitial clusters is maintained with respect to the transition temperature for the formation of interstitial clusters in the base material [58].

If the concentration of undersized atoms is increased to 1 or 2 or even 10 %, e. g. silicon in nickel, then the transition temperature during irradiation is drastically increased above the transition temperature corresponding to the base material without additions [58]. The transition temperature during irradiation will then achieve that transition temperature which is the highest one for precipitate formation without irradiation with high energy particles.

ON THE MIGRATION ACTIVATION ENERGIES DURING IRRADIATION

It was recognized in 1984 when measuring radiation enhanced diffusion in α-copper-zinc alloys that the migration activation energy of interstitials decreases as the flux of the high energy particles increases [59]. The result is shown in Fig. 11. This means that the radiation-enhanced diffusion coefficient is also enhanced because of a decrease of the migration activation energy of interstitials with increasing irradiation flux. The decrease of the migration activation energy of interstitials of about 0.15 eV (Fig. 11) causes an additional increase in the diffusion coefficient by a factor twenty, increasing the high energy particle flux by four orders of magnitude. This is in physical terms a huge effect, important in experiments in which an attempt is made to simulate radiation damage accumulating in a nuclear reactor over twenty years in a short time using high flux sources.

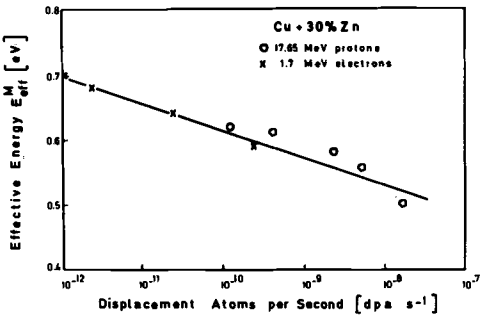


Fig. 11
The effective migration activation energy of interstitials is plotted versus the production rate of point defects for 1.70 MeV electrons and 17.65 MeV protons [4].

The result reported in 1984 [59] has since been confirmed for many different alloy systems [50,51] and also for nickel [15].

CONCLUSIONS

An overview has been presented of radiation damage and point defect behaviour in fcc metals with specific reference to the identification of point defects and processes responsible for the various annealing stages.

The data reviewed and the arguments presented provide a strong support for the modified two-interstitial model (MTIM), but are not consistent with the one-interstitial model (OIM).

Suggestions are also given based on the MTIM which should be taken into account when developing radiation resistant materials.

REFERENCES

[1] J. W. Corbett, Electron Radiation Damage in Semiconductors and Metals, Solid State Physics, Supplement 7, F. Seitz and D. Turnbull, Eds., Academic Press New York and London, 1966.

[2] H. J. Wollenberger, Physical Metallurgy, Part II, R. W. Cahn and P. Haasen, Eds., North Holland Physics Publishing, Amsterdam 1983, pp. 1139-1221.

[3] A. Seeger, Proceedings of the International Conference on Fundamental Aspects of Radiation Damage in Metals, Gatlinburg, October 6-10, 1975, M. T. Robinson and F. W. Young Jr., Eds., CONF.-751006-P1, pp. 493-517.

[4] W. Schüle, Zeitschrift für Metallkunde, Vol. 85, 1994, pp.78-91.

[5] H. G. van Bueren, Zeitschrift für Metallkunde, Vol. 46, 1955, p. 272.

[6] H. B. Huntington and F. Seitz, Physical Review, Vol. 61, 1942, p. 315.

[7] H. B. Huntington, Physical Review, Vol. 61, 1942, p. 325.

[8] H. B. Huntington, Physical Review, Vol. 91, 1953, p. 1092.

[9] J. W. Corbett, R. B. Smith, and R. M. Walker, Physical Review, Vol. 114, 1959, p. 1452.

[10] A. Seeger, Proceedings of the International Conference on Crystal Lattice Defects, Kyoto-2 September 7-12, 1962, Journal of the Physical Society of Japan, Vol. 18, Suppl. III, 1963, pp. 260-266.

[11] W. Schüle, A. Seeger, D. Schumacher, and K. King, physica stato solido, Vol. 2, 1962, pp. 1199-1220.

[12] R. M. Silsbee, Journal of Applied Physics, Vol. 28, 1957, p. 1246.

[13] G. Leibfried, Journal of Applied Physics, Vol. 30, 1959, p. 1388.

[14] J. B. Gibson, A. N. Goland, M. Milgram, and G. H. Vineyard, Physical Review, Vol. 120, 1960, p. 1229.

[15] W. Schüle, Radiation Effects and Defects in Solids, Vol. 114, 1990, pp. 309-313.

[16] H. E. Schepp, "Untersuchung der Defektproduktion in elektronenbestrahltem Gold zwischen 5 K und 220 K", Kernforschungsanlage Jülich, Germany, Report Jül-866-FF, 1972.

[17] H. Ch. Gilhaus, "Untersuchungen über Erzeugung und Diffusion atomarer Fehlstellen in Kupfer im Temperaturbereich oberhalb von 173 K", Dissertation Universität Frankfurt, Germany, 1993.

[18] H. Ch. Gilhaus and W. Schüle, Radiation Effects and Defects in Solids, in press.

[19] H. Ch. Gilhaus and W. Schüle, "Dynamic Crowdions, Interstitials, and Vacancies in Copper", Joint Research Center Ispra, European Commission, Report EUR 16007 EN, 1994.

[20] M. - P. Macht, A. Müller, V. Naundorf, and H. J. Wollenberger, Nuclear Instruments and Methods in Physics Research, Vol. B16, 1986, p. 148.

[21] J. M. Williams, to be published.

[22] W. Schüle, Proceedings of the International Conference on Physics of Irradiation Effects in Metals, Siófok, Hungary, May 20-24, 1991, G. Szenes, Ed., Materials Science Forum, Vols. 97-99, 1992, pp. 133-140.

[23] A. Alamo, C. H. De Novion, and G. Desarmot, Radiation Effects, Vol. 88, 1986, p. 69.

[24] W. Schüle and R. Scholz, Proceedings of the Yamada Conference V on Point Defects and Defect Interactions in Metals, J.-I. Takamura, M. Doyama, and M. Kiritani, Eds., Kyoto, Japan, 16-20 November 1981, University of Tokyo Press, J.-I. Takamura, M. Doyama, and M. Kiritani, Eds., 1982, pp. 257-260.

[25] W. Schüle, Ibidem ref. [24], pp. 667-669

[26] G. Oleownik and W. Schüle, Proceedings of an International Conference on Fundamental Aspects of Radiation Damage in Metals, Gatlinburg, USA, October 6-10, 1975, USERDA, M. T. Robinson and F. W. Young Jr., Eds., CONF.-751006-P1, pp. 341-348.

[27] K. Ziesemer and W. Schüle, Acta Metallurgica, Vol. 33, 1985 pp. 587-593.

[28] B. Srušil, H. Haas, and H. Wollenberger, Radiation Effects, Vol. 5, 1970, p. 273.

[29] W. Schüle, W. Frank, and A. Seeger, Radiation Effects, Vol. 10, 1971, pp. 123-127.

[30] M. D. Giardina, W. Schüle, W. Frank, and A. Seeger, Radiation Effects, Vol. 12, 1972, pp. 277-280.

[31] H. Metzner, R. Sielemann, S. Klaumünzer, and E. Hunger, Physical Review B, Vol. 36, 1987, p. 9535.

[32] A. Kraut, "Die Wechselwirkung von Kupfer-Zwischengitteratomen mit Fremdatomen", Kernforschungsanlage Jülich, Germany, Report Jül-896-FF, 1972.

[33] B. W. F. von Lensa, "Entwicklung einer Elektronenbestrahlungsanlage mit hoher Dosisleistung für Restwiderstandsproben und Durchführung von Bestrahlungsexperimenten an verdünnten Cu-Legierungen zwischen 200 K und 450 K", Kernforschungsanlage Jülich, Germany, Report Jül-1426, 1977.

[34] J. Bewerunge, "Die Kinetik des Aufbaus von Zwischengitteratom-agglomeraten in elektronenbestrahlten verdünnten Kupferlegierungen und die Wechselwirkung von Zwischengitteratomen mit Versetzungsringen in Kupfer", Kernforschungsanlage Jülich, Germany, Report Jül-1615, 1979.

[35] A. Bartels, F. Dworschak, and M. Weigert, Journal of Nuclear Materials, Vol. 137, 1986, p. 130.

[36] P. Simson and R. Sizmann, Zeitschrift für Naturforschung, Vol. 17a, 1962, p. 228.

[37] S. Ceresara, T. Federighi, and F. Pieragostini, Physics Letters, Vol. 6, 1963, p. 152.

[38] W. Schüle, Proceedings of the Yamada Conference V on Point Defects and Defect Interactions in Metals, J.-I. Takamura, M. Doyama, and M. Kiritani, Eds., Kyoto, Japan, November 16-20, 1981; University of Tokyo Press, J.-I. Takamura, M. Doyama, and M. Kiritani, Eds., 1982, pp. 551-553.

[39] F. Ramsteiner, G. Lampert, W. Schüle, and A. Seeger, physica stato solido, Vol. 8, 1965, pp. 863-879.

[40] R. R. Hasiguti, Y. Nakao, and H. Kimura, Journal of the Physical Society of Japan, Vol. 20, 1965, p. 553.

[41] R. R. Bourassa and B. Lengeler, Journal of Physics F: Metal Physics, Vol. 6, 1976, p. 1405.

[42] R. W. Simmons and R. W. Balluffi, Physical Review, Vol. 129, 1993, p. 1533.

[43] Th. Hehenkamp, W. Berger, J.-E. Kluin, Ch. Lüdecke, and J. Wolff, Physical Review B, Vol. 45, 1992, p. 1998.

[44] H. Wenzl, Proceedings of the International Conference on Vacancies and Interstitials in Metals, A. Seeger, D. Schumacher, W. Schilling, and J. Diehl, Eds., Jülich, September 23-28, 1968, Vacancies and Interstitials in Metals, North Holland Publication Company, Amsterdam, 1970, pp. 363-423.

[45] R. Scholz and W. Schüle, Physics Letters, Vol. 64A, 1977, pp. 340-341.

[46] W. Schüle, to be published.

[47] A. Seeger, P. Schiller, and H. Kronmüller, Philosophical Magazine, Vol. 5, 1960, p. 853.

[48] H. Kronmüller, A. Seeger, and P. Schiller, Zeitschrift für Naturforschung, Vol. 15a, 1960, p. 740.

[49] A. Seeger, H. Kronmüller, P. Schiller, and H. Jäger, Radiation Damage in Solids, D. S. Billington, ed., Academic Press, New York, USA, 1963, p. 809.

[50] M. Gieb, J. Heieck, and W. Schüle, Proceedings of the 17th International Symposium on the Effects of Radiation on Materials, Sun Valley, Idaho, USA, June 20-23, 1994, David S. Gelles, Randy K. Nanstad, Arvind S. Kumar, and Edward A. Little, Eds., Journal of Nuclear Materials, Vol. 225, 1995, pp 85-96.

[51] W. Schüle, 13th International Symposium on the Effects of Radiation on Materials, F. A. Garner, N. H. Packan, and A. S. Kumar, Eds., Seattle, Wa, USA, June 23-25, 1986, ASTM Book STP-955, Part I, 1987, pp. 14-26.

[52] W. Schüle and H. Hausen, Sixth International Conference on Fusion Reactor Materials (ICFRM-6), Stresa, Lago Maggiore, Italy, September 27-October 1, 1993, H. Stamm, M. Victoria, D. G. Rickerby, and K. Ehrlich, Eds., Journal of Nuclear Materials, Vols. 212-215, 1994, pp. 388-392.

[53] M. Kiritani, Progress in the Study of Point Defects, M. Doyama and S. Yoshida, Eds., University of Tokyo Press, 1977, pp. 247-327.

[54] W. Schüle, International Conference on Physics of Irradiation Effects in Metals, Siófok, Hungary, May 20-24, 1991, G. Szenes, Ed., Materials Science Forum, Vols. 97-99, 1992, pp. 223-228.

[55] N. Y. Jin, F. Phillipp, A. Seeger, physica stato solido (a), Vol. 116, 1989, p. 91.

[56] S. J. Zinkle, Journal of Nuclear Materials, Vol. 150, 1986, p. 140.

[57] S. J. Zinkle, 15th International Symposium on Effects of Radiation on Materials, Nashville, Tennessee, USA, June 19-21, 1990, R. E. Stoller, A. S. Kumar, and D. S. Gelles, Eds., ASTM Book STP 1125, 1992, pp. 813-834.

[58] A. Barbu and G. Martin, Journal of Applied Physics, Vol. 51, 1980, p. 6192.

[59] W. Schüle and R. Scholz, Radiation Effects, Vol. 81, 1984, pp. 115-128.

Mychailo B. Toloczko[1], Glenn E. Lucas[1], G. Robert Odette[1], Roger E. Stoller[2], and Margaret L. Hamilton[3]

AN INVESTIGATION OF MICROSTRUCTURES AND YIELD STRENGTHS IN IRRADIATED AUSTENITIC STAINLESS STEELS USING SMALL SPECIMEN TECHNIQUES

REFERENCE: Toloczko, M. B., Lucas, G. E., Odette, G. R., Stoller, R. E., and Hamilton, M. L., **"An Investigation of Microstructures and Yield Strengths in Irradiated Austenitic Stainless Steels Using Small Specimen Techniques,"** *Effects of Radiation on Materials: 17th International Symposium, ASTM STP 1270,* David S. Gelles, Randy K. Nanstad, Arvind S. Kumar, and Edward A. Little, Eds., American Society for Testing and Materials, 1996.

ABSTRACT: Transmission electron microscopy (TEM) specimens of a first core heat of 316 stainless steel, in both the solution annealed and 20% cold worked condition, were irradiated to 46 dpa at 420°C, to 49 dpa at 520°C, and to 34 dpa at 600°C in FFTF/MOTA. Prior to irradiation, some of the specimens were pre-implanted with approximately 100 appm of helium over one-third of the specimen thickness. Microstructures and mechanical properties of these specimens were examined. Microstructural data was taken from unimplanted zones and were consistent with data in the literature for unimplanted 316 SS. Where possible, irradiation hardening of the alloys was experimentally evaluated by microhardness and shear punch. For comparison, irradiation hardening was also calculated using a barrier hardening model and the microstructural data. Experimentally measured values of yield stress were in agreement with the range of values reported in the literature regardless of helium pre-implantation and were similar to the calculated values.

KEYWORDS: austenitic stainless steel, irradiation hardening, microstructure, microhardness, shear punch

[1] Department of Chemical and Nuclear Engineering, University of California, Santa Barbara, CA 93106
[2] Oak Ridge National Lab, PO Box 2008, Oak Ridge, TN 37831-6151
[3] Pacific Northwest Laboratory, PO Box 999, Richland, WA 99352

Copyright© 1996 by ASTM International www.astm.org

INTRODUCTION

While austenitic stainless steels have historically been considered as structural materials for fusion reactors, they are limited for use in high temperature, long exposure situations by relatively poor thermomechanical properties and a tendency to undergo significant void swelling at high doses. Nonetheless, they are still of interest for near term devices such as ITER. Hence, it is still important to develop a fundamental understanding of the relationship between the damage microstructure that evolves during irradiation and the changes in key mechanical properties. Moreover, there is significant interest in using small specimen techniques for extracting mechanical properties in fusion reactor materials, as this will be particularly important for utilizing a high energy neutron source in conjunction with developing an engineering data base for fusion machines beyond ITER; and the utility of small specimens is enhanced when they are combined with a fundamental understanding of microstructural evolution and microstructure-property relations.

Hence, it was the purpose of this study to investigate the microstructure and mechanical properties of a set of irradiated austenitic stainless steel specimens using both microhardness and shear punch techniques and to relate the observed microstructures to the measured yield stress changes. The examinations were performed on a set of specimens that had originally been prepared for a helium effects experiment. However, due to a long time interval between irradiation and examination and a mix-up in the records, the specimens were believed to be fully implanted with helium when indeed only one-third of the specimen thickness was implanted, a fact that was discovered rather late in the analysis. In spite of this, the data obtained were found to be useful in providing a microstructure-property link for small specimen data on a material of technological interest, and hence they are reported here.

EXPERIMENT

TEM specimens for irradiation were fabricated from 316 austenitic stainless steel (First Core heat 81585) in two material conditions: 1) solution annealed (SA) at 1050°C for 0.5 hours and 2) 20% cold worked (CW). Prior to final cold working, the sheet stock was annealed at 1050°C for 0.5 h. Coupons of each material were lapped to a final thickness of 0.25 mm. Specimens were punched from the lapped coupons and laser-engraved with an identification code.

Prior to irradiation, some of the specimens were cold pre-implanted with helium. The details are described elsewhere [1]. The implantation resulted in a uniform distribution of helium over 1/3 of the thickness. A schematic showing the location of the pre-implanted helium in a typical disk punched from a pre-implanted coupon is shown in Fig. 1. On average, the helium concentration was 100 appm within the pre-implanted zone. A few of the solution annealed specimens were given an addition pre-irradiation aging treatment of 800°C for 2 h. The effect of this implantation on the results reported here was small, since for reasons described below, the implanted zones were not directly analyzed. Nonetheless, the specimen designations reflecting this preparation are retained here for completeness.

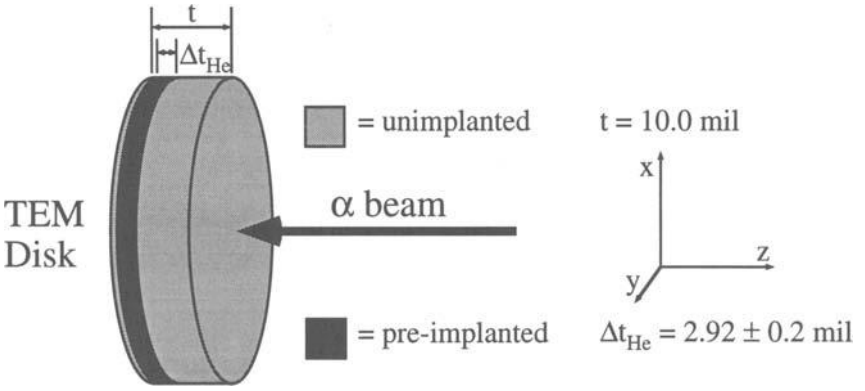


FIG. 1--Schematic showing location of helium in pre-implanted specimens.

Specimens were loaded into TEM packets and placed in the Materials Open Test Assembly (MOTA) test vehicle for irradiation in Fast Flux Test Facility (FFTF)/MOTA 1B (cycle 4) and FFTF/MOTA 1C (cycles 5 and 6) to 46 dpa at 420°C and to 49 dpa at 520°C, and in FFTF/MOTA 1C to 34 dpa at 600°C. Following irradiation, the specimens were subjected to densitometry, transmission electron microscopy (TEM), microhardness, and shear punch testing.

Using equipment located at Pacific Northwest Laboratory (PNL), densitometry was performed on one specimen from each experimental condition (pretreatment, fluence, temperature). The resolution of this technique is ± 0.16% density. Specimens for transmission electron microscopy were prepared by twin jet polishing in a 12% sulfuric/88% methanol solution at approximately 22 V and -15°C. Visual inspection and confocal microscopic measurements of the hole position indicate that perforation occurred close to the thickness center, and hence, examination of irradiated material occurred in regions that were not helium pre-implanted. Specimens were examined using microscopy facilities located at PNL and, to a lesser degree, at UCSB. A JEOL 1200EX was employed at PNL, while a 2000FX was used at UCSB. Image-mode magnification calibrations were performed on a periodic basis using a standard grating. Diffraction-mode magnification calibrations were also performed when required. Only the specimens irradiated to ~50 dpa at 420°C and 520°C were examined in detail. Quantitative measurements were made of the size and number densities of faulted loops, cavities, and precipitates. Network dislocation densities were also measured. Specimens irradiated to 34 dpa at 600°C contained a high density of large voids resulting in poorly polished specimens that were difficult to examine quantitatively.

Diffracting conditions for each defect type were kept the same from specimen to specimen. Thickness was estimated using stereo micrographs, and measured values were found to fall between 100 nm and 200 nm. Cavities sizes were found by measuring the distance between [110] void facets. Measurements were converted to spherical diameters using an equivalent sphere formula which accounts for the method of the cavity size measurement [2]. Measured precipitate dimensions were converted to effective precipitate

diameters based on their projected area in the micrographs. Faulted loops were imaged using the (111) stacking fault streaks, and when possible, measured sizes were gathered from two different (111) planes. Faulted loops were viewed nearly on edge producing an elliptical appearance, and consequently their shapes could not be determined. Hence, the average shape is assumed to be circular and the ellipse major axis taken to be the diameter. Network dislocation densities were measured with the (111) g vector operating. A multiplication factor of 2.0 was included in the dislocation density formula to account for partial invisibility of the network dislocations when working with a (111) g vector. Measurement uncertainties were estimated to be 20% for thickness, 5-10% for extended defect sizes, 30% for cavity and faulted loop densities, 100% for precipitate density, and 50% for network dislocation density.

Using a Vickers indentor and 300 g load, microhardness measurements were made at room temperature on a semi-automated microhardness tester described elsewhere [3]. Prior to indentation, disk specimens were attached to a stainless steel holder and given a light polish with 0.3 μm Al_2O_3 grit. Uncertainties in the diamond pyramid hardness (DPH) number were in the range ± 10 kg/mm^2. Microhardness measurements were performed on the side opposite the helium pre-implanted zone, and tests are thought to be largely representative of unimplanted material. The sampling depth of a Vickers microhardness indentor is approximately three times the length of the indentation diagonal. Nearly all diagonal measurements were between 40 μm and 50 μm putting the maximum sampling depth at 150 μm which is about 30 μm short of the helium pre-implanted zone.

Shear punch tests were also performed at room temperature on a fixture described in detail elsewhere [4]. Briefly, standard TEM disks with uniform thicknesses ranging from 0.20 mm to 0.25 mm were held in a die mounted in a screw-driven, instrumented load frame, and a flat-faced 1 mm diameter cylindrical punch was driven through the specimen at a crosshead speed of 2.12 x10^{-3} mm/s. The resulting load-displacement curve had features similar to that of a uniaxial tensile test; hence, an effective yield stress ($\sigma_{eff,y}$) was determined by dividing the load at deviation from linearity (P_y) by $2\pi rt$, where r is the average of the punch and die radii and t is the specimen thickness. Similarly, an effective maximum stress ($\sigma_{eff,max}$) was determined by dividing the maximum load (P_{max}) by $2\pi rt$. Since only one shear punch test was done for each irradiated specimen condition (pre-treatment, fluence, temperature), statistical uncertainties could not be determined. However, previous experience has shown that scatter is less than about 5% [4,5]. Since the shear punch test sampled both unimplanted and implanted zones, values of effective stress reflect some composite strength of the two regions.

For microhardness and shear punch calibration purposes, additional TEM disks and miniature tensile specimens were fabricated from coupons of unirradiated material prepared from the same heat of material used in the fabrication of the irradiated materials. Sheet stock was rolled to thicknesses ranging from 0.215 mm to 0.280 mm with gradients in thickness less than 0.0015 mm/mm across the sheet stock. The thermomechanical condition was varied from solution annealed to 40% cold worked to a precipitation strengthened condition to provide a range of strengths and strengthening mechanisms thought to be at least partially representative of the irradiated materials. Miniature tensile specimens with a gage section 2.030 mm wide x 0.250 mm thick x 9.000 mm long were punch fabricated from the coupons, and TEM discs were spark machined (EDM). Both microhardness and shear punch tests were performed on the disk specimens, and the

miniature tensile specimens were tested in uniaxial tension at a strain rate of 10^{-3} s^{-1} on an automated tensile tester described elsewhere [6]. All tests were performed at room temperature. The results were used to establish correlations between tensile properties, microhardness, and shear punch stress as described later.

RESULTS

Swelling

Swelling was determined from both densitometry and microscopy. Density swelling, S_ρ, was determined from the usual formula

$$S_\rho = \frac{\rho_{initial}}{\rho_{final}} - 1 \qquad \text{[fractional]} \qquad (1)$$

where ρ is the density of the specimen. Void swelling was calculated from

$$S_v = \frac{V_{final} - V_o}{V_o} = \frac{1}{V_{final} / V_{void} - 1} \qquad \text{[fractional]} \qquad (2)$$

where $(V_{final} - V_o)/V_o$ is the fractional volume change due to void swelling, and V_{void}/V_{final} is the fraction of space occupied by voids in the material. The results for the irradiated specimens are plotted in Fig. 2. Recognizing that the data at 600°C are at a lower dose, the swelling behavior of the SA material exhibits the classic bell-shaped temperature

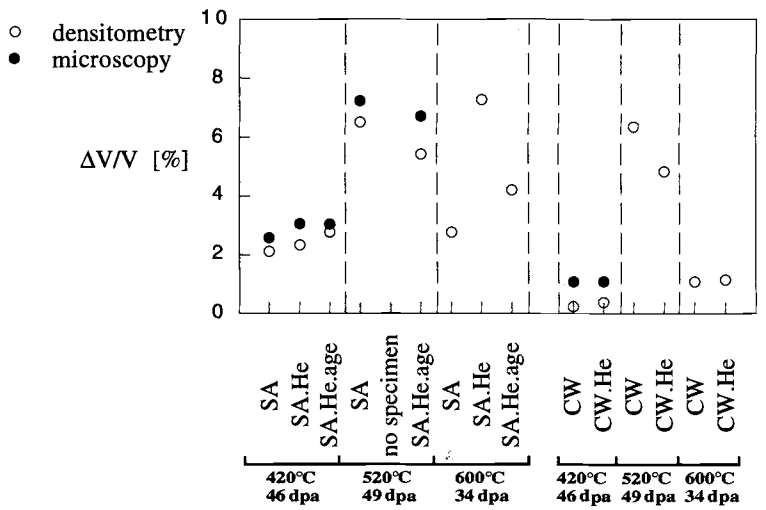


FIG. 2--Swelling versus temperature as calculated from densitometry and microscopy.

dependence of 316 SS, with peak swelling near 520°C. The swelling of the CW material follows the trends of the SA material, but is somewhat smaller, especially at the lower irradiation temperature (420°C) where the pre-existing dislocation network recovers more slowly and suppresses void formation longer. These data are quantitatively consistent with trends reported in previous studies [7-16]. In all cases, S_v is systematically higher than S_ρ, but the difference is not dependent on helium pre-implantation. Small differences between S_v and S_ρ are often attributed to the effect of precipitation on S_ρ [7]. Ascertaining the effects of helium pre-implantation on the observed swelling is confounded by: a) the fact that only 1/3 of the specimen thickness was pre-implanted; b) differing amounts of helium were pre-implanted in each specimen[4]. Nonetheless, the overall effect of implantation appears to be small.

Microstructural Evolution

For reasons described earlier, microstructural observations are largely representative of unimplanted material, although for unaged, pre-implanted specimens, some pre-neutron irradiation damage was introduced by the pre-implantation process.

After thinning, enough deformation was present in the unirradiated control specimens that diffracting conditions permitted only a qualitative analysis. In the SA controls, a low dislocation density was observed and assumed to be on the order of 10^8 cm^{-2}. The CW material had a dense dislocation network and is assumed to be on the order of 10^{12} cm^{-2}. The SA.He control showed a moderate density of black spot damage assumed to be small dislocation loops. Diameters of approximately 2 nm were measured; this is consistent with the other studies where it has been shown that black spot damage is a by-product of helium pre-implantation displacement damage [7,8,17].

The observed irradiated microstructures were broadly consistent with changes reported in unimplanted austenitic stainless steels irradiated in fast reactors: the major microstructural features consisted of faulted loops, network dislocations, cavities, and precipitates. Characteristics of each defect type are detailed below.

In Fig. 3, the dislocation densities observed at ~50 dpa are plotted as a function of irradiation temperature. Following irradiation, the network dislocation density was observed to increase in the SA material and to decrease in the CW material. Production and recovery processes typically result in the dislocation density, ρ_n, approaching a near steady state value, independent of starting condition but inversely proportional to the irradiation temperature. At 420°C and 46 dpa, where SA and CW dislocation densities have both been measured, the dislocation densities are indeed similar, with ρ_n in the CW material slightly larger than in the SA material. The dislocation density for SA decreases with increasing irradiation temperature. The observed network densities fall within the trend bands in the literature for these doses and temperatures [7-9,11,18].

For austenitic stainless steels in the irradiation temperature range 400-600°C, the average faulted loop size, d_L, typically reaches a saturation value (bounded by the critical size for unfaulting) at 10-20 dpa, while loop densities, n_L, typically peak and then begin to gradually decrease starting at about the same dose. d_L is also seen to increase and n_L

[4] For instance, the largest apparent effect is in the SA.He specimen irradiated at 600°C; but this specimen only contained 2 appm of pre-implanted helium compared to the 8-10 appm helium produced during neutron irradiation.

decrease with increasing irradiation temperature [7-9,11,18]. As shown in Fig. 4, the observed value of d_L at ~50 dpa increases and n_L decreases with irradiation temperature. The net result is a decreasing faulted loop dislocation density as a function of temperature as shown in Fig. 3. At 420°C, d_L is nearly identical in the CW and SA material, but n_L is slightly larger in the CW material. The observed loop sizes and loop densities fall within the data trends in the literature [7-9,11,18].

It has been observed that the cavity size, d_v, typically increases with dose and with higher irradiation temperatures. The cavity density, n_v, usually increases to a saturation value by about 10 dpa at 400°C and 20 dpa at 600°C, while higher irradiation temperatures tend to decrease the saturation value of n_v [7-9,11]. As shown in Fig. 5, the cavity parameters in this study follow these trends. At ~50 dpa, d_v increases with temperature, and n_v decreases with increasing irradiation temperature. Helium bubbles were observed at 520°C in the SA material. The bubble density was approximately equal to the cavity density, however they were most often found in clusters near precipitates or cavities. The cavity sizes and densities observed in this study were consistent with values reported in the literature [6-9,11-14].

Precipitate sizes, d_p, and number densities, n_p, were estimated from bright field images. Assuming the bright field diffraction conditions allow a random sampling of all precipitates present, then sizes measured by this method should be comparable to actual sizes while the precipitate number densities will be less than but probably within an order of magnitude of the actual values. Compositions were not measured, but precipitate-cavity association was examined. Fig. 6 shows that average precipitate diameter, d_p, and number

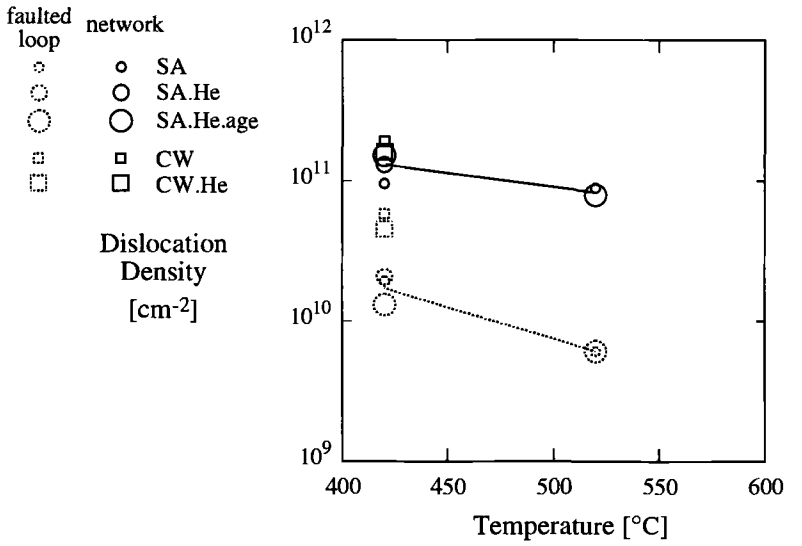


FIG. 3--Dislocation densities plotted as a function of irradiation temperature at approximately 50 dpa.

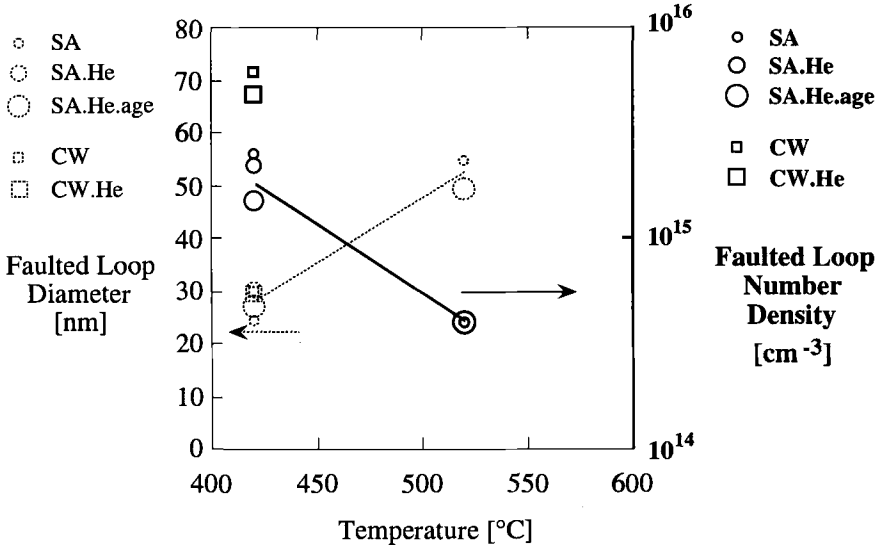


FIG. 4--Variation of faulted loop diameter and number density with irradiation temperature at approximately 50 dpa.

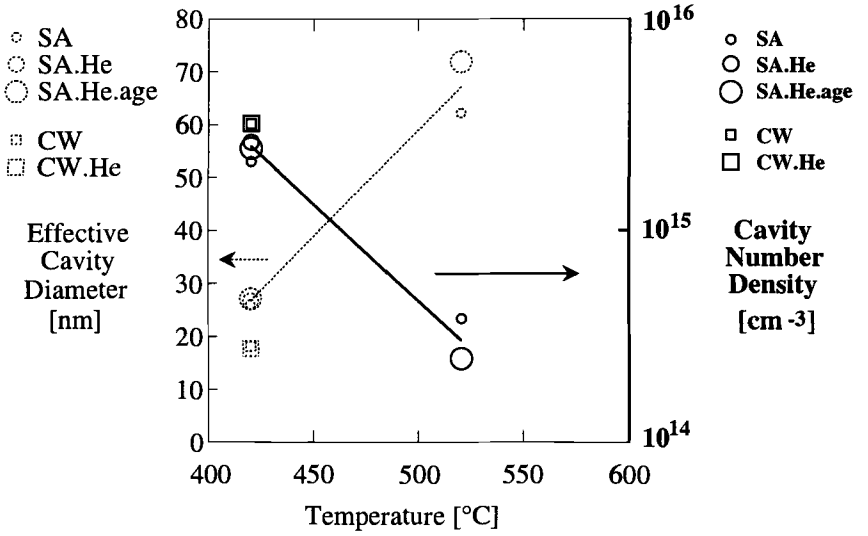


FIG. 5--Variation of cavity diameter and number density with irradiation temperature at approximately 50 dpa.

density, n_p, follow the same temperature-dependent trends as the other extended defects: i.e., d_p increases with irradiation temperature while n_p decreases with increasing irradiation temperature for both SA and CW material. At both irradiation temperatures, there was a strong association between voids and precipitates. A rough analysis suggests that at least half of the voids are associated with precipitates (suggesting heterogeneous nucleation of these voids on precipitates), and likewise at least half of the precipitates are associated with voids. Due to partial precipitate invisibility conditions, it is possible that most, if not all cavities are associated with precipitates.

In summary, defect parameters (sizes and densities) observed in this study are consistent with data trends reported in the literature for unimplanted austenitic stainless steels irradiated under similar conditions. The network dislocation density decreased with temperature, and for all extended defects, size increased while number density decreased with increasing irradiation temperature in the range 420-520°C.

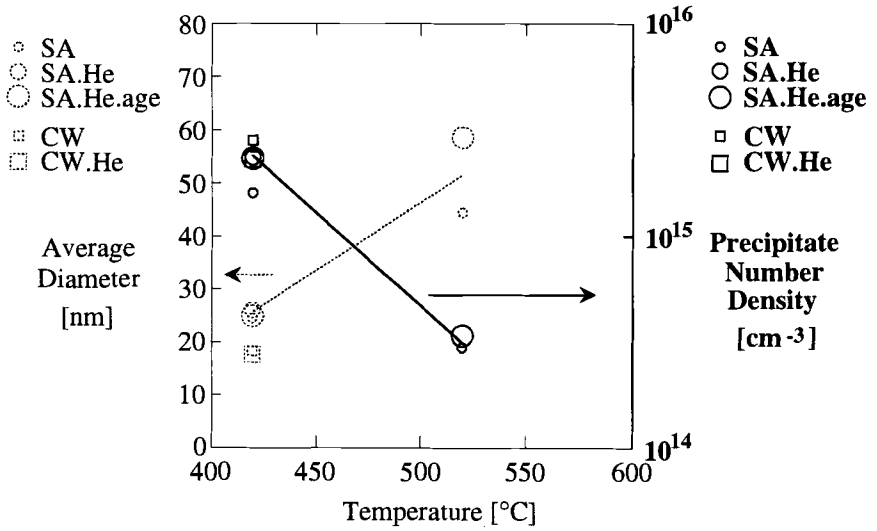


FIG. 6--Variation of precipitate size and number density with irradiation temperature at approximately 50 dpa.

Mechanical Properties

The correlation curves for the microhardness and shear punch tests developed from tests on unirradiated materials are shown in Fig. 7. As shown in Fig. 7a, the Vickers diamond pyramid microhardness (DPH) correlated linearly with uniaxial yield stress, σ_y, and almost linearly with ultimate tensile strength, UTS; a least squares regression provides

$$\sigma_y \text{ [MPa]} = 2.69 \text{ DPH [kg/mm}^2\text{]} - 125 \quad (3a)$$

$$\sigma_u \text{ [MPa]} = 2.11 \text{ DPH [kg/mm}^2\text{]} + 223 \quad (3b)$$

Correlation coefficients were 0.99 for both regressions. Fig. 7b shows the correlation between $\sigma_{eff,y}$ (= $P_y/2\pi rt$) and σ_y, and between $\sigma_{eff,max}$ (= $P_{max}/2\pi rt$) and UTS. Again, over the range of interest, both uniaxial yield stress and ultimate tensile strength correlated linearly with the respective σ_{eff}'s, and a least squares linear regression provides

$$\sigma_y \text{ [MPa]} = 1.70\ \sigma_{eff,y} \text{ [MPa]} + 60 \quad (4a)$$

$$\sigma_u \text{ [MPa]} = 2.41\ \sigma_{eff,max} \text{ [MPa]} - 516 \quad (4b)$$

The slopes of these correlations are similar, although not identical, to the slopes obtained in previous shear punch correlation studies (1.66-2.0) which were based on a wider range of materials and yield/ultimate strengths [4].

Equations 3a and 4a were used to convert the microhardness and shear punch data obtained on the unirradiated (control) and irradiated specimens into uniaxial yield stresses, and these yield stresses are plotted in Figs. 8a and 9a as a function of dose. The lines (solid for CW and dashed for SA) drawn from the unirradiated yield stress to the average of the irradiated values are simply to guide the eye; however, they do reflect observed trends reported in the literature in which the yield stress change saturates by about 10-20 dpa in this irradiation temperature regime [16,19-24]. Also shown in Figs. 8b and 9b are the same yield stresses superimposed on the data trends observed in the literature for yield stress at high dose as a function of irradiation temperature.

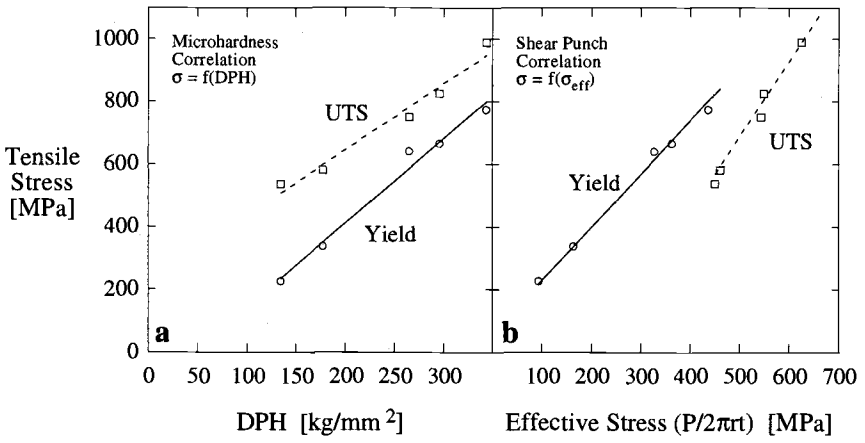


FIG. 7--Uniaxial yield and ultimate tensile strength versus: a) microhardness or b) shear punch effective stress for the unirradiated calibration materials. Lines show linear regression fits.

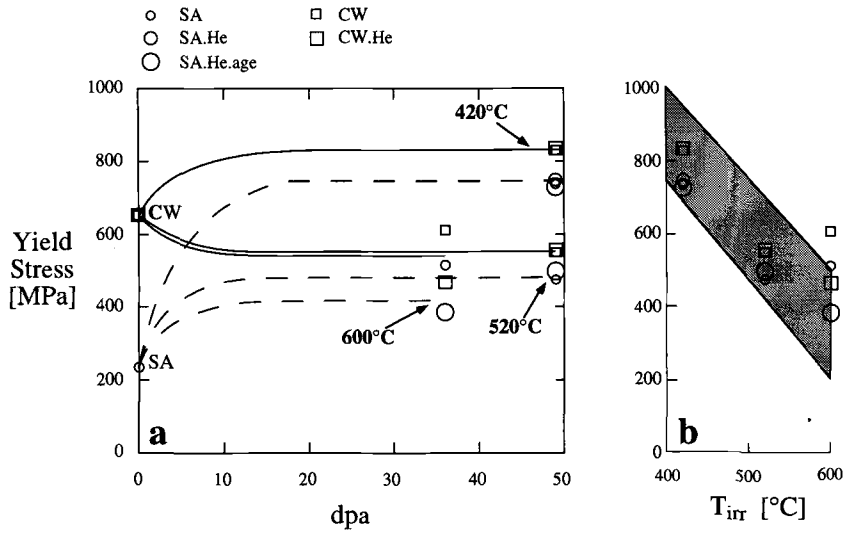


FIG. 8--a) dose dependence and b) temperature dependence of uniaxial yield stress determined from microhardness tests. Guidelines in a) and shaded regions in b) are based on data trends from the literature.

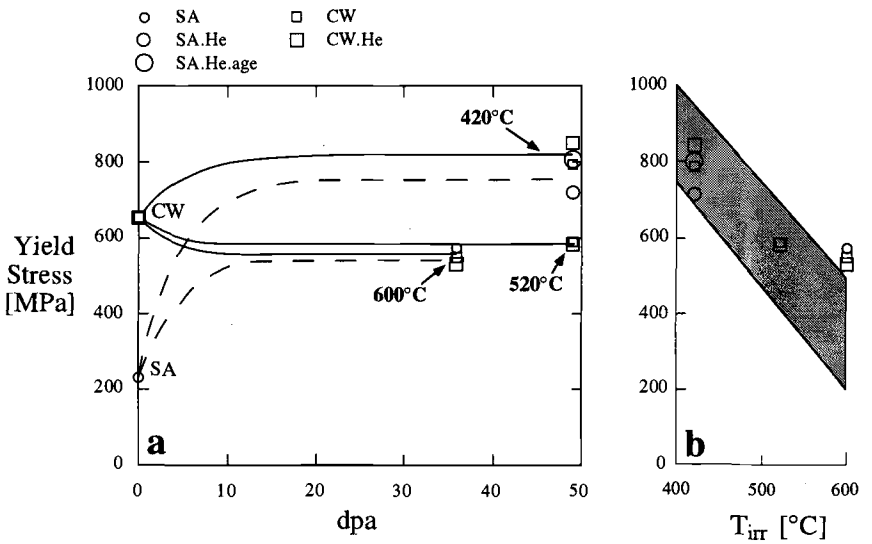


FIG. 9--a) dose and b) temperature dependence of uniaxial yield stress determined from shear punch tests. Guidelines in a) and shaded regions in b) are based on data trends from the literature.

Yield stresses determined from both microhardness and shear punch tests appear to agree quantitatively with previous observations of yield stress in irradiated austenitic stainless steels in the following ways: 1) at 420°C, both SA and CW material harden with irradiation, but at 520°C and 600°C the SA material hardens while the CW material softens; 2) the yield stresses of the SA and CW material, while considerably different in the unirradiated condition, are similar at high dose; 3) the yield stresses at high dose decrease with increasing irradiation temperature, although the differences between the 520°C and 600°C shear punch data are somewhat smaller than would be expected from tensile data in the literature.

There do not appear to be any significant systematic effects of pre-implanted helium on the mechanical property changes. This is not particularly surprising for the microhardness data, since the indentation sampled only unimplanted material and there were no obvious differences in the microstructures of the specimens with and without helium in the unimplanted regions. In the case of the shear punch data, the implanted and unimplanted zones contribute to the total strength in a composite way that was not determined. However, the small effects of helium pre-implantation suggest that the implanted zone (~1/3 of the volume sampled) did not have strength changes that were significantly different than the unimplanted region (~2/3 of the volume sampled.)

DISCUSSION

Mechanical Properties

For a limited number of specimen conditions, sufficient microstructural information was obtained to permit an estimate of yield stress. In previous studies [25-30], microstructure-yield stress relationships have been achieved assuming the total yield strength to be of the form

$$\sigma_y = \sigma_{y,int} + \sqrt{\sum_i \sigma_{sr,i}^2} + \sum_j \sigma_{lr,j} \tag{5}$$

Here $\sigma_{y,int}$ is the intrinsic yield strength of a solid solution with an austenitic stainless steel composition. $\sigma_{lr,j}$ are contributions to hardening from long range barriers, such as grain boundaries, $\sigma_{y,gb}$, and dislocation networks, $\sigma_{y,disl}$. For austenitic stainless steels, these contributions are generally treated by assuming the yield stress of the solution annealed material, $\sigma_{y,o}$, is equal to $\sigma_{y,int} + \sigma_{y,gb}$ and that $\sigma_{y,disl}$ can be evaluated mathematically like a short range obstacle but added in like a long range obstacle. The individual hardening contributions of the short range obstacles, $\sigma_{sr,i}$, are treated by a barrier hardening model such that

$$\sigma_{sr,i} = \frac{M\alpha_{c,i}Gb}{L_i} \tag{6}$$

where M is a factor (3.0 for face centered cubic materials) relating shear stresses on a slip plane in a single crystal to the applied tensile stress necessary to activate slip in a polycrystal [31], $\alpha_{c,i}$ is the strength of obstacle type i, G is the shear modulus of the matrix, b is the Burgers vector of the moving dislocation, and L_i is the square lattice spacing of obstacle type i. The individual contributions have generally been combined by assuming a root mean square (rms) superposition model. However, Foreman and Makin [32] have shown that the efficiency of a random array compared to a square array decreases with obstacle strength and that an rms superposition may not be valid when considering a mix of short range obstacles of differing strength.

Hence, a computer model based on the methodology of Foreman and Makin was used to estimate the hardening contribution of the short range obstacles to the yield stress of the irradiated austenitic stainless steels. Here, short range obstacles were taken to be cavities, loops, and precipitates[5]. In the model, a dislocation is driven under the action of an applied shear stress along a glide plane containing a population of obstacles. Below the critical shear stress, τ_c, the dislocation bows between and may release from some obstacles until reaching an equilibrium configuration. The applied stress is incremented until the dislocation passes unimpeded through the obstacle field -- the final applied stress is taken to be τ_c. The yield stress contribution from the short range obstacles is the product of τ_c and M.

The planar defect densities were taken to be the product of defect number density and size, nd, for cavities and precipitates, and 0.56nd for faulted loops. Average diameters and number densities of each obstacle type used are shown in Figs. 3-6. The obstacle positions on the glide plane were assigned randomly. The dislocation was released from an obstacle if its bowing angle exceeded a critical angle, θ_c, given by

$$\alpha_c = \cos(\theta_c / 2) \tag{7}$$

Values for α_c were adjusted within the ranges reported for the various microstructural defects observed to obtain the best fit to the experimental data. The final α_c values used were: $\alpha_{void} = 1.0$, $\alpha_{precip} = 0.6$, and $\alpha_{FL} = 0.3$. Likewise, the network dislocation contribution to the hardening was taken to be

$$\sigma_{y,disl} = M\alpha_c qGb\sqrt{\rho_n} \tag{8}$$

where α_{disl} was found to be 0.2 and q, the random array efficiency for obstacles of this strength, was taken from Foreman and Makin [32] to be 0.46. Finally, G was set equal to 75 GPa, and b to 2.55×10^{-10} m.

The resulting predictions are compared to measured values of yield stress determined from both shear punch and microhardness measurements in Fig. 10. The model predictions track the experimentally-based values reasonably well. The barrier hardening calculations suggest the major contributions to hardening come from the dislocation

[5] Although a strong cavity-precipitate association was observed, cavities and precipitates were nevertheless treated separately because of the subjectiveness in estimating the strength of a combined cavity-precipitate obstacle.

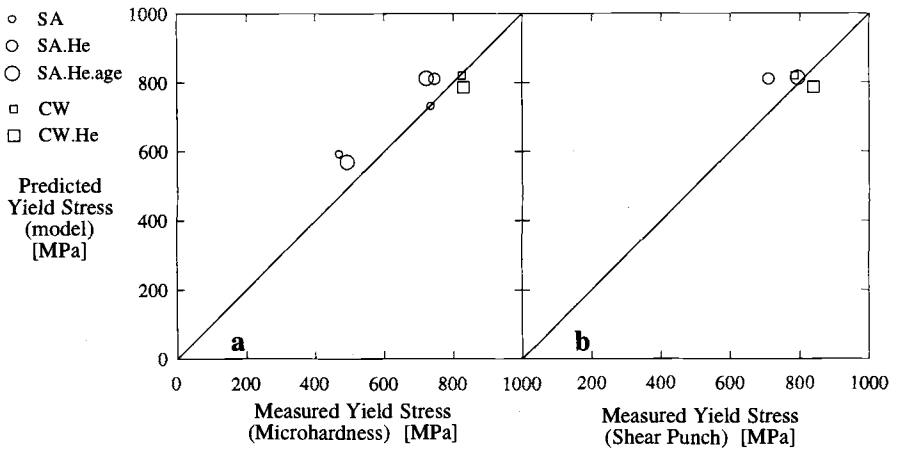


FIG. 10--Comparison of the uniaxial yield stress predicted from the barrier hardening model with values determined from: a)microhardness tests and b) shear punch tests.

network and voids. Voids are estimated to contribute about twice as much strengthening as dislocations.

SUMMARY

A first core heat of 316 stainless steel in both the CW and SA condition was irradiated to ~50 dpa at 420°C and 520°C and to 34 dpa at 600°C. Some specimens were pre-implanted with helium into about one-third of the specimen thickness prior to irradiation. The partial pre-implantation confounded the analysis of helium effects on the results, but overall the effect of helium on swelling or mechanical properties did not appear to be large. The observed swelling as a function of temperature followed the typical bell shaped curve for 316 SS with the swelling peak at 520°C. At 420°C and 520°C where irradiation-induced microstructural defects were characterized, network dislocation densities, faulted loop, cavity, and precipitate sizes and number densities were consistent with trends reported in the literature for unimplanted materials. Yield stress changes as determined by microhardness and shear punch techniques were similar and both agree with data trends for unimplanted materials. Using a computer based barrier hardening model and the microstructural data, the calculated yield stresses were within 100 MPa of the values measured by microhardness and shear punch techniques. The barrier hardening analysis suggests that the major hardening comes from voids and dislocations.

ACKNOWLEDGMENTS

This work was funded by the Department of Energy, Office of Fusion Energy under grants DE-FG03-87ER-52143 and DE-AC06-76RLO-1830. Support for R.E. Stoller was provided in part by Division of Materials Science, U.S. DOE under contract DE-AC05-84OR-21400.

REFERENCES

[1] Toloczko, M.B., Master's Thesis, Department of Chemical and Nuclear Engineering, University of California Santa Barbara, to be published.

[2] Gelles, D.S., Claudson, R.M., and Thomas, L.E., "Quantitative Analysis of Void Swelling", Fusion Reactor Materials Semiannual Progress Report, DOE/ER-0313/3, Published March 1988, pp. 131-136.

[3] Lucas, G.E., Mader E., and Odette, G.R., "Effects of Metallurgical Variable and Irradiation Conditions on the Kinetics of Post-Irradiation Annealing of Pressure Vessel Steels", Proceedings of Fourth International Symposium on Environmental Degradation of Materials in Nuclear Power Systems - Water Reactors, NACE-TMS/AIME-ANS, August 6-10 1989, Jeckyll Island, GA (1990) 2-1.

[4] Lucas, G.E., Odette, G.R., and Sheckard, J.W., "Shear Punch and Microhardness Tests for Strength and Ductility Measurements", The Use of Small-Scale Specimens for Testing Irradiated Material, ASTM STP 888, W.R. Corwin and G.E. Lucas, Eds., American Society for Testing and Materials, Philadelphia, 1986, pp. 112-140.

[5] Hamilton, M.L., Toloczko, M.B., and Lucas, G.E., "Recent Progress in Shear Punch Testing", Miniaturized Specimens for Testing of Irradiated Materials, IEA International Symposium, P. Jung and H. Ullmaier, Eds., Forschungszentrum Jülich GmbH, 1994, pp. 46-58.

[6] Odette, G.R., Lucas, G.E., Stoller, R.E., and Phythian, W., "On the Effect of Flux and Composition on Irradiation Hardening at 60°C", these proceedings

[7] Maziasz, P.J., "Effect of Helium Content on Microstructural Development in Type 316 SS Under Neutron Irradiation", ORNL-6121, 1985.

[8] Stoller, R.E., "Microstructural Evolution in Fast-Neutron-Irradiated Austenitic Stainless Steels", Ph.D. Thesis, UC Santa Barbara, 1987.

[9] Lucas, G.E., "The Evolution of Mechanical Property Change in Irradiated Austenitic Stainless Steels", Journal of Nuclear Materials, Vol. 206, 1993, pp. 287-305.

[10] Brager, H.R., and Garner, F.A., "Microstructural and Microchemical Comparisons of AISI 316 Irradiated in HFIR and EBR-II", Journal of Nuclear Materials, Vol. 117, 1983, pp. 159-176.

[11] Zinkle, S.J., Maziasz, P.J., Stoller, R.E., "Dose Dependence of the Microstructural Evolution in Neutron Irradiated Austenitic Stainless Steel,", Journal of Nuclear Materials, Vol. 206, 1993, pp. 266-286.

[12] Garner, F.A., and Gelles D.S., "Neutron-Induced Swelling of Commercial Alloys at Very High Exposures", Effects of Radiation on Materials: 14th International Symposium (Vol. II), ASTM STP 1046, N.H. Packan, R.E. Stoller, and A.S. Kumar, Eds., American Society for Testing and Materials, Philadelphia, 1990, pp. 673-683.

[13] Maziasz, P.J., and Grossbeck, M.L., "Swelling, Microstructural Development, and Helium Effects in Type 316 Stainless Steel Irradiated in HFIR and EBR-II", Journal of Nuclear Materials, Vol. 103 & 104, 1981, pp. 987-992.

[14] Brager, H.R., and Garner, F.A., "Comparison of Swelling and Microstructural/Microchemical Evolution of AISI 316 Irradiated in EBR-II and HFIR", Journal of Nuclear Materials, Vol. 103 & 104, 1981, pp. 993-998.

[15] Katoh, Y., Kohno, Y., and Kohyama, A., "Microstructural Response of Titanium Modified Austenitic Stainless Steels to Neutron Exposure of 70 dpa in FFTF/MOTA", Journal of Nuclear Materials, Vol. 212-215, 1994, pp. 464-470.

[16] Garner, F.A., and Toloczko, M.B., "High Dose Effects in Neutron Irradiated Face-Centered Cubic Metals", Journal of Nuclear Materials, Vol. 206, 1993, pp. 230-248.

[17] Harkness, S.D., Kestel, B.J., and McDonald, S.G., "Effect of Cyclotron-Injected Helium on Void-Formation Characteristics of Type 304 Stainless Steel", Journal of Nuclear Materials, Vol. 46, 1973, pp. 159-168.

[18] Garner, F.A., and Wolfer, W.G., "A Model for the Evolution of Network Dislocation Density in Irradiated Metals", Effects of Radiation on Materials: Eleventh Conference, ASTM STP 782, H.R. Brager and J.S. Perrin, Eds., American Society for Testing and Materials, Philadelphia, 1982, pp. 1073-1087.

[19] Johnson, G.D., Garner, F.A., Brager, H.R., and Fish, R.L., "A Microstructural Interpretation of the Fluence and Temperature Dependence of the Mechanical Properties of Irradiated AISI 316", Effects of Radiation on Materials: Tenth Conference, ASTM STP 725, D. Kramer, H.R. Brager, and J.S. Perrin, Eds., American Society for Testing and Materials, Philadelphia, 1981, pp. 393-412.

[20] Holmes, J.J., and Straalsund, J.L., Proceedings of International Conference on Radiation Effects in Breeder Reactor Structural Materials, The Metallurgical Society of AIME, Scottsdale, New York, 1977, pp. 53-63.

[21] Bagley, K.Q., Barnaby, J.W., and Fraser, A.S., Proceedings of Conference on Irradiation Embrittlement and Creep of Fuel Cladding and Core Components, British Nuclear Energy Society, London, 1972, pp. 143-153.

[22] Hamilton, M.L., Okada, A., and Garner, F.A., Tensile Behavior and Swelling of Ternary Austenitic Alloys Irradiated in Different Neutron Spectra", Journal of Nuclear Materials, Vol. 179-181, 1991, pp. 558-562.

[23] Hamilton, M.L., and Garner, F.A., "The influence of Helium on Mechanical Properties of Model Austenitic Alloys Determined Using ^{59}Ni Isotopic Tailoring and Fast Reactor Irradiation", Journal of Nuclear Materials, Vol. 191-194, 1992, pp. 1239-1243.

[24] Garner, F.A., Hamilton, M.L., Greenwood, L.R., Stubbins, J.F., and Oliver, B.M., "Isotopic Tailoring with ^{59}Ni to Study Helium Generation Rates and Their Effect on Tensile Properties of Neutron-Irradiated Fe-Cr-Ni Alloys", Effects of Radiation on Materials: 16th International Symposium, ASTM STP 1175, A.S. Kumar, D.S. Gelles, R. Nanstad, and E.A. Little, Eds., American Society for Testing and Materials, Philadelphia, 1993, pp. 921-939.

[25] Odette, G.R., and Frey, D., "Development of Mechanical Property Correlation Methodology for Fusion Environments", Journal of Nuclear Materials, Vol. 85&86, 1979, pp. 817-822.

[26] Garner, F.A., Hamilton, M.L., Panayotou, N.F., and Johnson, G.D., "The Microstructural Origins of Yield Strength Changes in AISI 316 During Fission or Fusion Irradiation", Journal of Nuclear Materials, Vol. 103&104, 1981, pp. 803-808.

[27] Simons, R.L., and Hulbert, L.A., "Correlation of Yield Strength with Irradiation-Induced Microstructure in AISI 316 Stainless Steel", Effects of Radiation on Materials: Twelfth International Symposium, ASTM STP 870, F.A. Garner and J.S. Perrin, Eds., American Society for Testing and Materials, Philadelphia, 1985, pp. 820-839.

[28] Grossbeck, M.L., Maziasz, P.J., and Rowcliffe, A.F., "Modeling of Strengthening Mechanisms in Irradiated Fusion Reactor First Wall Alloys", Journal of Nuclear Materials, Vol. 191-194, 1992, pp. 808-812.

[29] Brown, L.M., "Precipitation and Dispersion Hardening", Strength of Metals and Alloys, ICSMA-5, Vol. 3, 1979, pp. 1551-1571.

[30] Friedel, J., "Dislocations", Pergamon Press, New York, 1964.

[31] Courtney, T.H., "Mechanical Behavior of Materials", McGraw-Hill, 1990, ch. 4.

[32] Foreman, A.J.E., and Makin, A.J., "Dislocation Movement Through Random Arrays of Obstacles", Canadian Journal of Physics, Vol. 45, 1967, pp. 511-517.

Marc G. Horsten[1] and Martin I. de Vries[1]

IRRADIATION HARDENING AND LOSS OF DUCTILITY OF TYPE 316L(N) STAINLESS STEEL PLATE MATERIAL DUE TO NEUTRON-IRRADIATION

REFERENCE: Horsten, M. G. and De Vries, M. I., **"Irradiation Hardening and Loss of Ductility of Type 316L(N) Stainless Steel Plate Material Due to Neutron-Irradiation,"** *Effects of Radiation on Materials: 17th International Symposium, ASTM STP 1270,* David S. Gelles, Randy K. Nanstad, Arvind S. Kumar, and Edward A. Little, Eds., American Society for Testing and Materials, 1996.

ABSTRACT: Type 316L(N) stainless steel plate material has been irradiated up to 10 dpa at temperatures of 80, 225, 325, and 425°C in the High Flux Reactor (HFR) of Petten. Tensile tests have been performed in the temperature range from RT to 575°C at a conventional strain rate of $5x10^{-4}$ s^{-1}. The results of the tensile tests are analyzed in terms of irradiation hardening and loss of ductility due to irradiation. Tensile properties saturate in the early stage (within 0.65 dpa) at the lowest applied irradiation temperature. It is indicated that the most severe degradation of tensile ductility occurs in the temperature range of 275 to 350°C. Comparison with literature data revealed a large scatter in irradiation hardening at irradiation temperatures above 325°C.

KEY WORDS: neutron irradiation, tensile properties, strength, ductility, elevated temperature, stainless steel, microstructure

INTRODUCTION

Type 316 stainless steel is the primary candidate austenitic structural material for fusion first wall constructions. The tensile properties are basic data for the design analyses of fusion devices. A lot of data on irradiation hardening and loss of ductility of Type 316 stainless steel are available from fast reactor studies, see for example [1-5]. These studies are focussed mainly on temperatures above 400°C. Future fusion devices like ITER are anticipated to operate in the intermediate temperature range up to 450°C. Accumulated damage levels may range from 0.5 to 25 dpa. Several studies have indicated that the most severe degradation of ductility and toughness properties of

[1]Netherlands Energy Research Foundation, ECN Nuclear Energy, PO Box 1, 1755 ZG, Petten, The Netherlands.

Copyright© 1996 by ASTM International www.astm.org

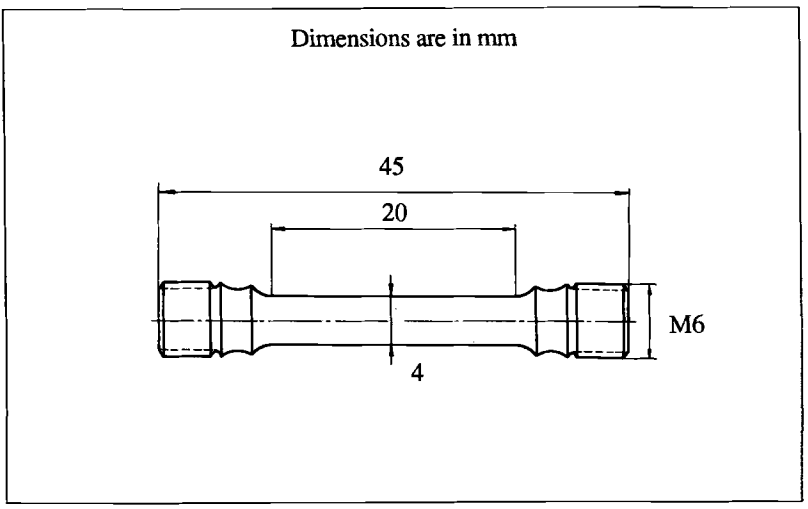


FIG. 1--Tensile test specimen.

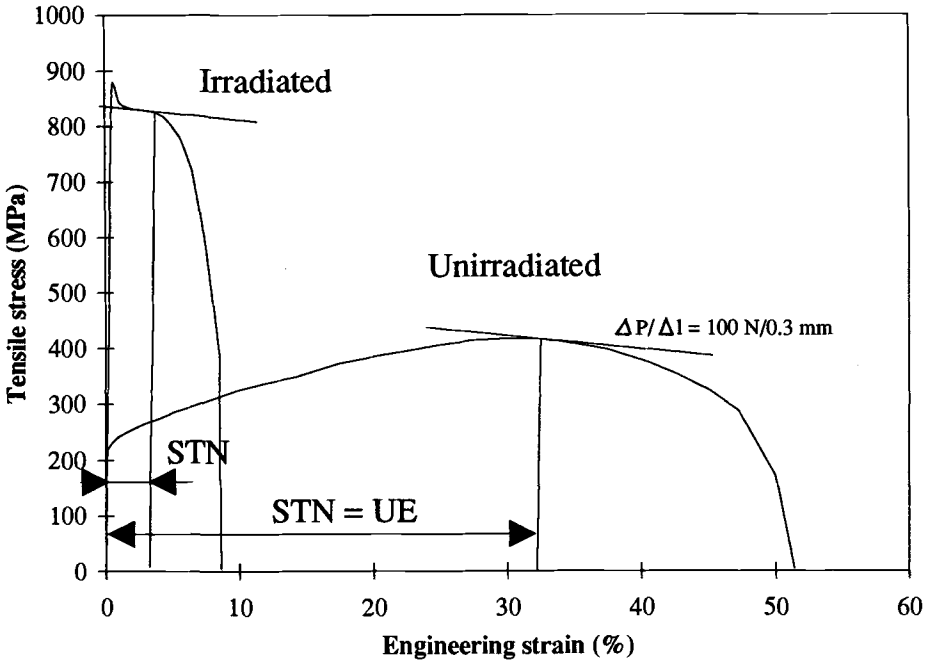


FIG. 2--General shape of tensile stress-strain curve of Type 316L(N) material after irradiation at 225-325°C, (STN=strain to necking,UE=uniform elongation).

austenitic stainless steel occur in the temperature range from 250 to 350°C [6-8]. There is hardly any information on the irradiation behaviour at lower temperatures.

EXPERIMENTAL PROCEDURE

Materials and Specimens

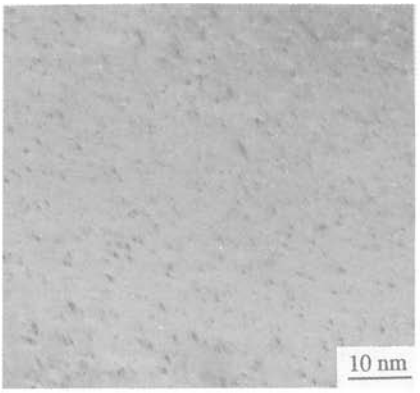
The material tested was AISI Type 316L(N) stainless steel plate material, fabricated by Creusot-Loire Industries in France according to standard practice for material 316L-SPH (Super-PHenix) [9] and refered to as the European Reference Heat (ERH). Two ERH heats were used in this study with only minor differences in chemical composition, ERHI and ERHII. The nominal chemical composition of the material is shown in Table 1. The microstructures of the two heats exhibited only minor differences, which was reflected by the tensile properties in unirradiated condition as will be shown in a later section of this paper. The materials were hot rolled to 30 mm plate and solution annealed at 1100°C for 1 hour. Small cylindrical tensile specimens 4 mm in diameter with a 20 mm gage length (Fig. 1) were machined from the plates with the gage length perpendicular to the rolling direction.

TABLE 1--The chemical composition of Type 316L(N) material in weight-%.

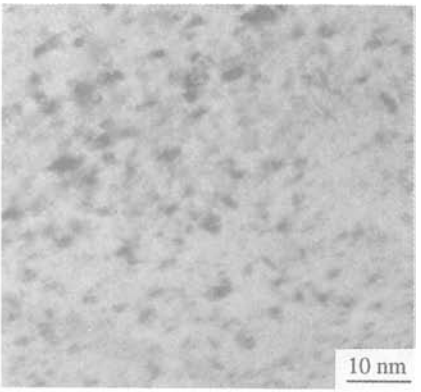
Material	C	Si	Mn	P	S	Cr	Ni	Mo	N	Cu	B
ERH	0.02	0.38	1.77	0.02	0.01	17.5	12.3	2.4	0.07	0.15	0.0017

Irradiation Experiments

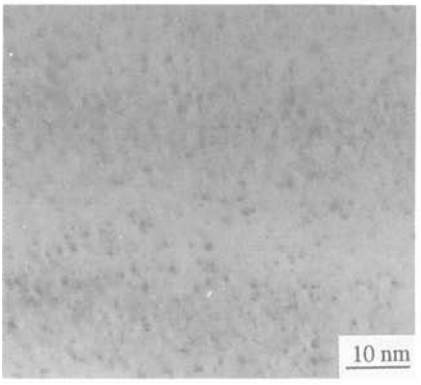
The specimens were irradiated in the HFR of Petten at temperatures of 80, 225, 325, and 425°C with target dose levels of 0.5, 3, 5 and 10 displacements per atom (dpa). ERHII material was used for the low dose irradiation experiment (0.5 dpa) at 80°C and the high dose irradiation experiment (5 dpa) at 225°C. ERHI material was used for all other irradiation experiments. A special irradiation rig was designed to simulate fusion operation conditions as closely as possible during HFR irradiation. The measured damage levels after irradiation to 0.5 dpa at 80°C ranged from 0.44 to 0.97 dpa. The large helium content after about 0.5 dpa is mainly due to the burn up of the boron, according to the transmutation reaction ^{10}B (n, α) ^{7}Li, below about 1 dpa. Above 1 dpa the helium production is mainly determined by the two stage nickel reaction ^{58}Ni (n, γ) ^{59}Ni (n, α) ^{56}Fe. The helium/dpa ratio decreases from 30-40 to about 14 at 5-10 dpa, which is considered to be a fusion representative condition. Temperature stability during irradiation at 80°C was about ±15°C, while the stability at higher temperatures was ±25°C.



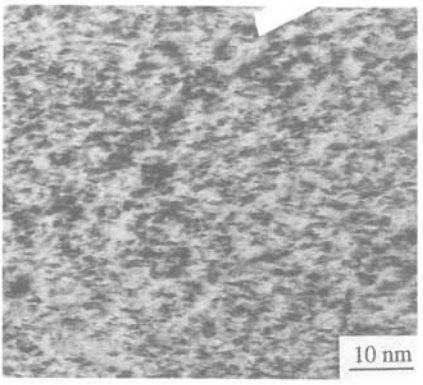
(a) 0.65 dpa at 80°C



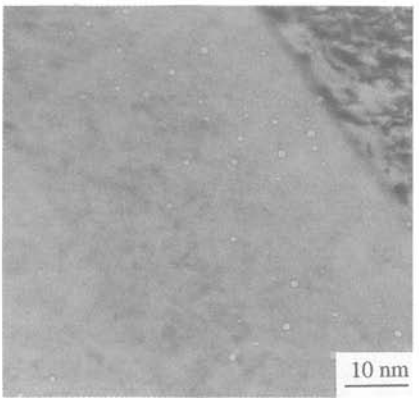
(b) 5 dpa at 80°C



(c) 0.65 dpa at 225°C



(d) 10 dpa at 225°C



(e) 10 dpa at 425°C

Fig. 3--Microstructures of irradiated Type 316L(N) stainless steel.

Tensile Tests

The tensile tests were performed on an Instron 1362 servo-mechanical testing machine installed in a hot cell at ECN in Petten. The specimens were heated in air to the desired temperature in a three zone resistance furnace. The tests were performed at temperatures of 23 to 575°C at a conventional strain rate of $5x10^{-4}$ s^{-1}. Load-displacement curves were registered during the test, resulting in engineering stress-strain curves. The 0.2% offset yield stress (0.2%YS), the ultimate tensile strength (UTS), the uniform elongation (UE), and the total elongation (TE) were determined from these curves.

Tensile stress-strain curves from specimens irradiated to damage dose levels above 3 dpa at temperatures of 225 and 325°C produced difficulties in defining an adequate uniform elongation due to deviant yield behaviour, see Fig. 2. The conventional uniform elongation measured at the maximum load during a tensile test does not provide proper information on the plastic strain prior to necking of the irradiated material. The maximum load is reached directly after the elastic part of the tensile curve and is followed by a lower plateau stress during which the specimen continues to deform plastically prior to necking. Necking of the specimen occurs when the load starts to decrease rapidly. Strain to necking (STN) in this work is defined as the plastic strain at the onset of necking of the specimen and is measured at a characteristic value of the load decrease rate as measured backwards from the end of the tensile curve ($\Delta p/\Delta l$=100 N/0.3 mm), equal to the characteristic slope after reaching the ultimate tensile strength of unirradiated material [10]. In further presentation of results and discussion strain to necking is used whenever appropriate.

Microstructural and Fracture Examination

The damage structure of irradiated specimens was investigated using a transmission electron microscope (TEM). Thin samples were prepared from a non-loaded part of test specimens. Scanning electron microscopy (SEM) was performed to determine the fracture type after tensile testing.

RESULTS AND DISCUSSION

Post-irradiation Examination

The microstructure of irradiated Type 316L(N) stainless steel is shown in Fig. 3. Irradiation temperature and dose level are indicated on the photographs. Irradiation to 0.65 dpa at 80°C results in a 'black dot' type of damage structure (Fig. 3a). Increasing the damage dose level to 5 dpa at this low irradiation temperature coarsened the 'black dot' damage and some loops have occured (Fig. 3b). This minor difference in microstructure means that a fairly stable damage structure is reached. Irradiation to 0.65 dpa at 225°C results in a similar damage structure (Fig. 3c), as was observed after irradiation at 80°C (Figs. 3a and 3b). A very dense small loop type damage structure has occurred after irradiation to 10 dpa at 225°C (Fig. 3d). A similar microstructure is

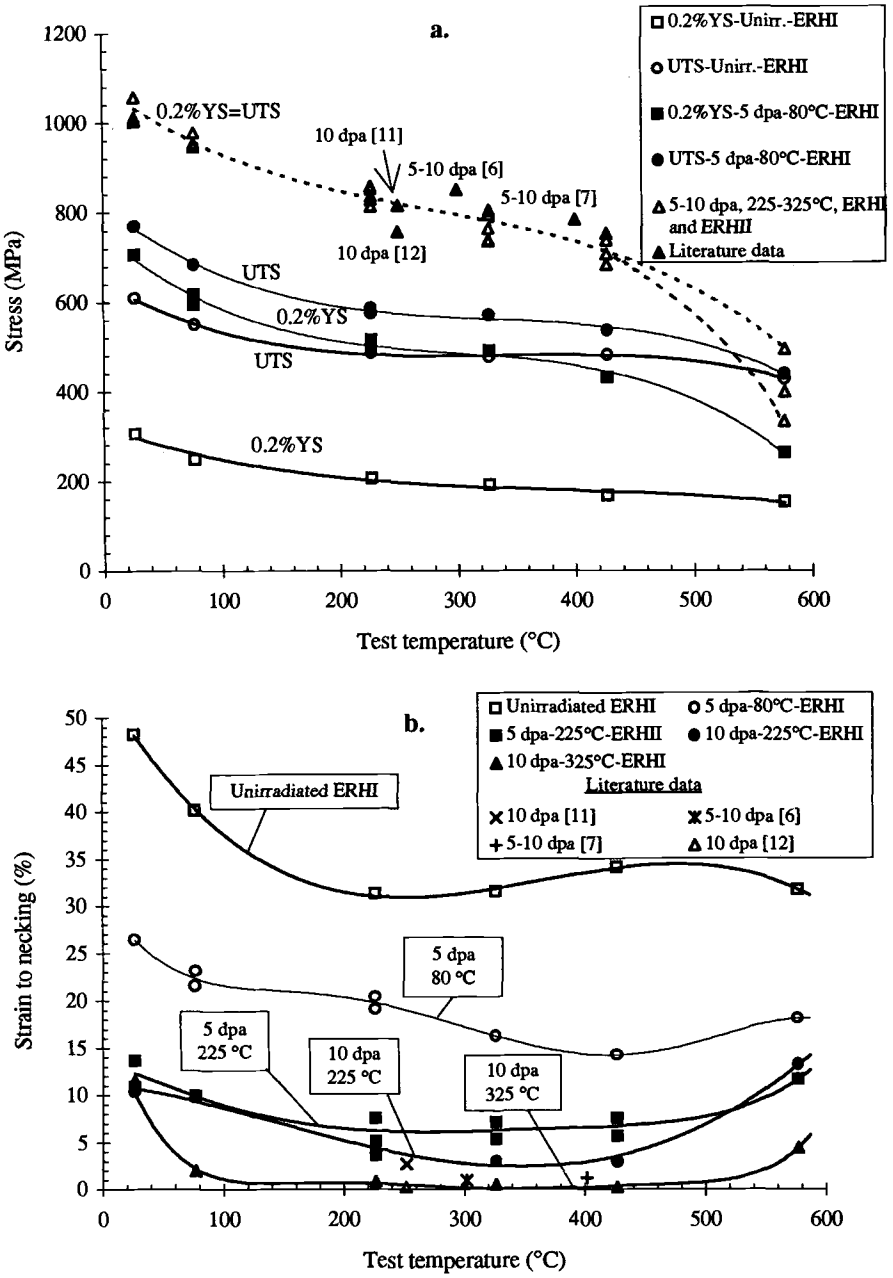


FIG. 4--Effect of irradiation on the tensile properties of ERH material, (a) strength and (b) strain to necking.

observed after 10 dpa at 325°C. A helium bubble and loop type damage structure appears during irradiation at 425°C to 10 dpa (Fig. 3e).

Tensile properties of Unirradiated Material

The tensile properties of unirradiated ERHI and ERHII materials between RT and 575°C are reported in Table 2. The total elongation of ERHII is slightly higher than that observed for ERHI and the 0.2% yield stress, the ultimate tensile strength and the uniform elongation of ERHII are slightly lower than those of ERHI. A discrepancy in this trend is observed at 80°C, where the uniform and total elongation of ERHII appear to be considerably lower than those observed for ERHI.

TABLE 2--Tensile properties of unirradiated ERHI and ERHII material.

Heat	Test temperature (°C)	0.2% YS (MPa)	UTS (MPa)	UE (%)	TE (%)
ERHI	23	305	608	48.2	62.1
	80	299	549	40.1	52.9
	225	247	486	31.3	41.0
	325	229	476	31.5	40.2
	425	205	481	34.1	41.7
	575	187	427	31.7	39.2
ERHII	23	316	598	47.7	63.2
	80	277	535	31.1	46.2
	225	216	467	29.6	42.2
	325	198	462	30.6	42.5
	425	184	459	30.9	41.7
	575	164	408	26.8	41.1

Tensile Properties of Irradiated Material

The specimens irradiated at 80, 225, and 325°C have been tested over the temperature range from RT to 575°C. The tensile stress and ductility of the materials are shown as a function of test temperature in Figs. 4a and 4b respectively. Some data points have been added from the literature [6, 7, 11, 12]. The 0.2% yield stress increased about 300 MPa after irradiation to 5 dpa at 80°C (Fig. 4a). Test temperatures in excess of 400°C annealed a large part of the radiation damage, reducing the irradiation hardening considerably. Material irradiated at 80°C shows work hardening of about 80 MPa over the whole temperature range. Irradiation at this low temperature reduces the strain to necking by about a factor of 2 (Fig. 4b), but still a ductility of 15-25% strain to necking remains, reflecting the ability of the material to work harden. The specimens irradiated at 225 and 325°C to damage levels of 5 and 10 dpa showed deviating yield behaviour as described before, where 0.2% yield stress and ultimate tensile strength

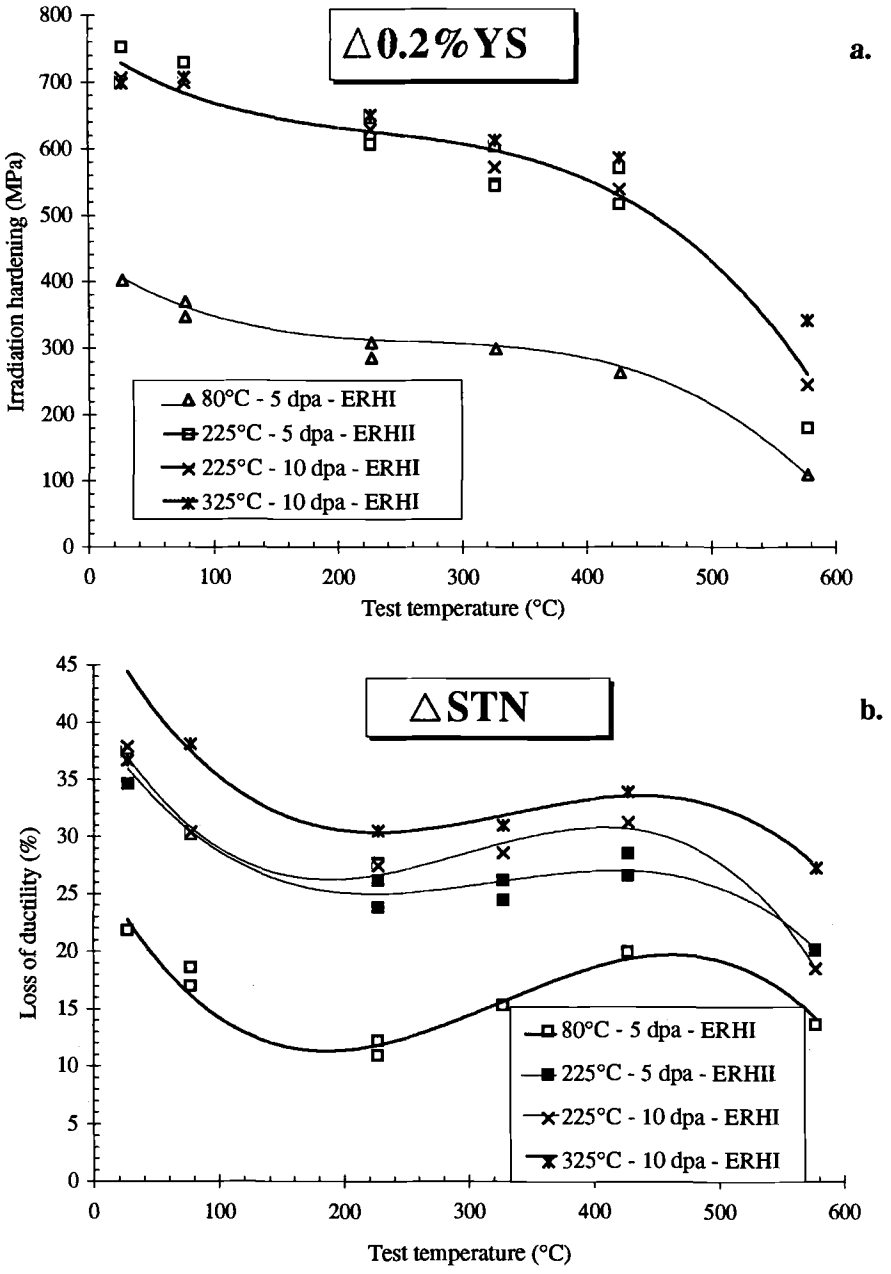


FIG. 5-- Irradiation hardening (a) and loss of ductility (b) of ERHI and ERHII as a function of test temperature.

coincide. The tensile stresses of material irradiated at 225 and 325°C form a band with a width of ±40 MPa up to a test temperature of 400°C as shown in Fig. 4a. The irradiation hardening decreases with increasing test temperature and 'normal' yield behaviour, work hardening, and increasing ductility are observed (Fig. 4b) at temperatures in excess of 400°C. A strong reduction in strain to necking is observed after irradiation to 5 dpa at 225°C. Increase of damage level to 10 dpa further decreases the strain to necking to values lower than 5% in the temperature range from 200 to 400°C. The most severe degradation of tensile ductility is observed after irradiation to 10 dpa at 325°C, where strain to necking has reduced to practically zero in the temperature range from 80°C to 450°C. The strength and ductility results obtained compare well with literature data with equal test and irradiation temperature as shown in Figs. 4a and 4b.

The irradiation hardening and loss of ductility of specimens irradiated at different temperatures is shown as a function of test temperature in Figs. 5a and 5b respectively. In the figures only high dose irradiation experiments are shown, but low dose experiments show similar trends. Irradiation hardening decreases with increasing temperature (Fig. 5a). The lowest irradiation hardening is observed at test temperatures above 400°C. At these temperatures the irradiation-induced defects are annealed and thermally activated processes make dislocations pass obstacles, in this way reducing the hardening effect. It appears that specimens irradiated at temperatures up to 325°C have a maximum loss of ductility at around 425°C (Fig. 5b). This is mainly due to a local maximum in ductility in the unirradiated condition (Fig. 4b), but a minimum in ductility at a test temperature of 425°C is also observed after 5 dpa at 80°C, which contributes to the increase in loss of ductility as well.

Dose Level Dependence

The irradiation behaviour of Type 316L(N) stainless steel at 80 and 225°C is shown in Figs. 6a and 6b. Strength and ductility are given as a function of damage dose level respectively. The variation in actual damage level at about 0.5 dpa at 80°C did not result in a large variation in strength and ductility values, indicating that saturation of the changes had already occurred in a very early stage of the irradiation, which is supported by the microstructural observation. This is consistent with other observations [13], where saturation of irradiation hardening was observed after about 0.2 dpa at temperatures below 100°C. A considerable amount of work hardening remains even after irradiation to 5 dpa at 80°C. Consequently, a considerable ductility remains of about 25% strain to necking.

The change in tensile properties saturates after 5 dpa at a temperature of 225°C. The rate of irradiation hardening in the very early stage of irradiation is smaller than that observed at 80°C (~330 MPa/dpa *versus* ~430 MPa/dpa), but the increase continues, with an ever decreasing rate, up to 5 dpa. At about 3 dpa the 0.2% yield stress is equal to the ultimate tensile stress, corresponding to the appearance of deviating yield behaviour as described before [11, 14]. The accompanied ductility decreases considerably (Fig. 6b).

Odette and Lucas [6] have studied the irradiation hardening of several 300 series stainless steels at 300°C and found a fitted saturation stress level of (850±100) MPa.

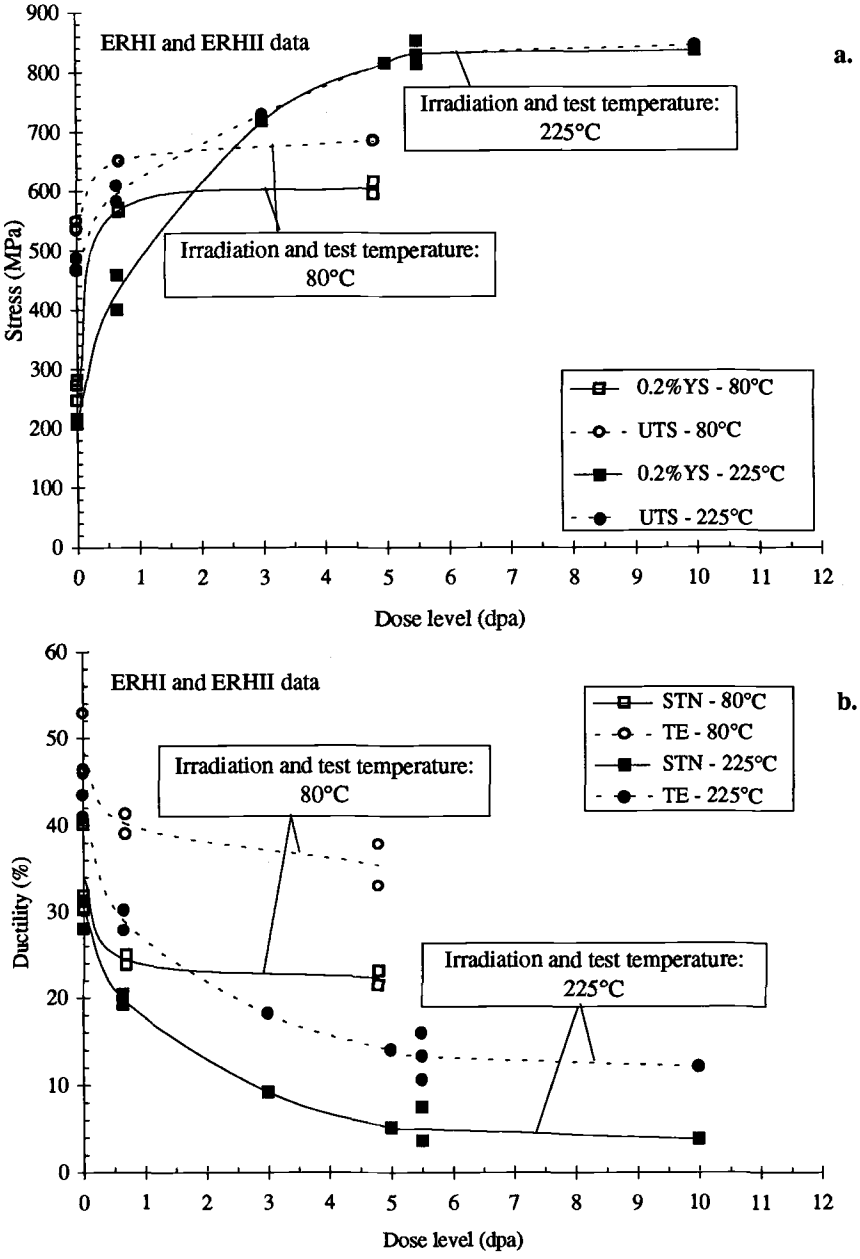


FIG. 6--Dose dependence of tensile properties of ERH material, (a) strength and (b) ductility.

The stress level observed in this work is (800±40) MPa at 300°C, which fits in the lower part of the band obtained by Odette and Lucas.

Temperature Dependence

The irradiation hardening (Δ0.2%YS) and loss of ductility (ΔSTN) are shown in Figs. 7a and 7b as a function of irradiation (and test) temperature. The specimens irradiated to 10 dpa at 425°C were not tested at 425°C. Instead, the data point at 425°C is interpolated from data points obtained at test temperatures of 225, 500, and 575°C. Data points from other 316L heats [15] and some literature data have been added for comparison. Figure 7a clearly indicates the minor additional irradiation hardening at 80°C when the damage dose level is increased from 0.65 to 5 dpa. Increasing the temperature to 225°C results in lower irradiation hardening at low dose levels. However, as indicated before, the irradiation hardening continues to increase up to 5 dpa. Irradiation to 10 dpa at 325°C results in a slightly lower irradiation hardening. A low dose data point from a different Type 316L heat has been added to show that the trend as observed for the low dose irradiation hardening data at lower temperatures continues up to 325°C. It is unknown, however, how the hardening evolves during irradiation at this temperature. The trend of maximum irradiation hardening and loss of ductility in the temperature range of 250 to 350°C is also observed in the literature [6, 7, 11-13]. Irradiation hardening decreases strongly at temperatures above 325°C, which is attributed to *in situ* annealing effect during irradiation [10]. This is also observed by others [6]. This *in situ* annealing process is strongly determined by temperature as the dominant parameter. Small temperature variation may give a large variation in irradiation hardening, which is in accordance with the scatter observed in irradiation hardening in the temperature range of 350 to 450°C.

Parallel to the observed irradiation hardening at 80°C, the loss of ductility increases only slightly when the damage dose level is increased from 0.65 to 5 dpa, see Fig. 7b. Although the low dose irradiation hardening decreases with temperature, the loss of ductility increases with temperature. Still a considerable increase in loss of ductility is observed with increasing the damage dose level from 5 to 10 dpa at 225°C. Figure 7b also demonstrates that the most severe degradation of tensile ductility is observed at an irradiation temperature of 325°C. A considerable loss of ductility is observed in the temperature range from 350 to 450°C. The evolution of the ductility in this temperature range can not be demonstrated due to a lack of low dose irradiation data in this temperature range.

Fracture appearance

All irradiation and test conditions revealed ductile dimple fracture surfaces, one of which is shown in Fig. 8. Although a 'nil-ductility' region is observed between 250 and 350°C, the fracture surface appearance is still of a ductile nature. Brittle fractures fractures due to channeling have been reported in austenitic stainless steels after very high dose levels (50-150 dpa) at temperatures below 450°C [4], whereas high temperature (>450°C) embrittlement due to intergranular fracture was observed after low dose levels down to less than 0.1 dpa [2]. The experimental conditions in this work

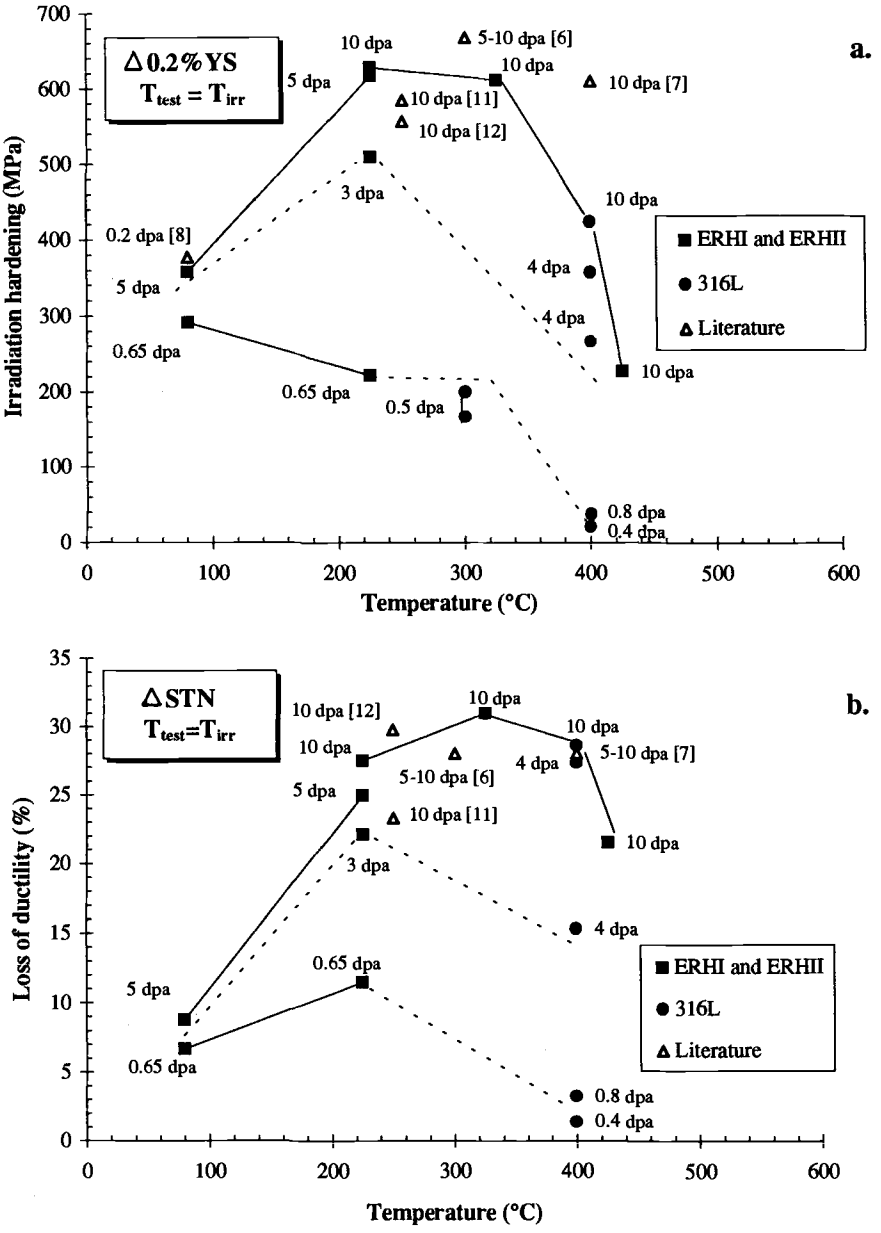


FIG. 7--Irradiation effects on tensile properties as a function of temperature, (a) irradiation hardening and (b) loss of ductility.

(temperatures below 450°C and intermediate dose levels) appear to be outside the indicated regions for brittle tensile fracture.

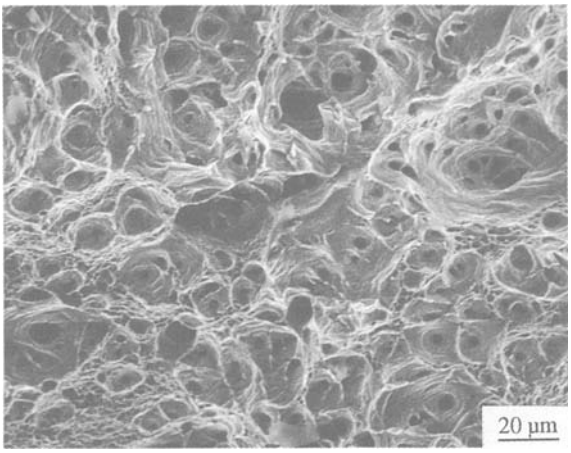


FIG. 8--Fracture appearance of specimen irradiated to 10 dpa at 325°C and tensile tested at $5x10^{-4}$ s^{-1} and 325°C.

CONCLUSIONS

The following conclusions were drawn:

1. Only small variations in tensile properties existed between Type 316L(N) heats in the unirradiated condition.
2. Irradiation hardening and loss of ductility saturated in the early stage (<0.65 dpa) of irradiation at 80°C. Still, a considerable ductility remains, even after 5 dpa.
3. The material lost the ability to work harden after 3 dpa at irradiation temperatures of 225°C.
4. Saturation of irradiation hardening and loss of ductility was reached after 5 dpa at 225°C.
5. The most severe degradation of tensile properties was encountered in the temperature range of 275-350°C after 10 dpa. Evolution of the irradiation effects is unknown in this condition.
6. A large scatter in irradiation hardening and loss of ductility was observed at irradiation temperatures of 400 to 450°C; this is attributed to a strong temperature dependence of tensile properties.
7. All irradiation and test conditions revealed ductile dimple fracture surfaces.

REFERENCES

[1] Fish, R.L. and Hunter C.W., *Irradiation effects on the microstructure and properties of metals, ASTM STP 611,* Wheeler, J.B., Hoersch, H.M. and McGlinchey, J. Eds., American Society for Testing and Materials, 1976, pp 119-138.

[2] De Vries, M.I. et al., *Effects of Radiation on Structural Materials, ASTM STP 683,* Sprague, J.A. and Kramer, D. Eds., American Society for Testing and Materials, 1979, pp 477-489.

[3] Johnson, G. D., Garner, F. A., Brager, H. R., and Fish R. L., *Effects of Radiation on Materials: Tenth Conference, ASTM STP 725*, Kramer, D., Brager, H. R., and Perrin, J. S., Eds., American Society for Testing and Materials, 1981, pp 393-412.

[4] Hamilton, M.L. et al., *Influence of Radiation on Material Properties, ASTM STP 956,* Garner, F.A., Henager, C.H., and Igata, N. Eds., American Society for Testing and Materials, 1987, pp 245-270.

[5] Fissolo, A. et al., *Effects of Radiation on Materials, ASTM STP 1175,* Kumar, A.S., Gelles, D.S., Nanstad, R.K., and Little, E.A. Eds., American Society for Testing and Materials, 1993, pp 646-663.

[6] Odette, G. R. and Lucas, G. E., *Journal of Nuclear Materials 179-181,* 1991, pp 572-576.

[7] Jitsukawa, S., Grossbeck M. L. and Hishinuma, A., *Journal of Nuclear Materials 191-194,* 1992, pp 790-794.

[8] Jitsukawa, S. et al., *Journal of Nuclear Materials 191-194*, 1992, pp 771-775.

[9] Design and Construction Rules for Mechanical Components of FBR Nuclear Islands, RCC-MR, AFCEN June 1985 Edition.

[10] Horsten M. G. and de Vries, M. I., *Journal of Nuclear Materials 212-215,* 1994, pp 514-518.

[11] Elen, J. D. and Fenici, P., *Journal of Nuclear Materials 191-194*, 1992, pp 766-770.

[12] Vandermeulen, W., Hendrix, W., Massaut, V., Van der Velde, J. and De Raedt, Ch., *Test results report Fafuma of SCK/CEN Belgium,* FT/MOL/90-03, N6/292/WVM/ig, September 1990.

[13] Mattas, R.F. et al., *Journal of Nuclear Materials 191-194*, 1992, pp 139-145.

[14] Grossbeck, M. L., *Journal of Nuclear Materials 179-181,* 1991, pp 568-571.

[15] Tjoa, G. -L., Boskeljon, J., D'Hulst, D. S. and de Vries, M.I., *ECN-report ECN-I--94-007*, February 1994.

Shiro Jitsukawa[1], Akimichi Hishinuma[1] and Masahide Suzuki[1]

Fatigue Crack Propagation by Channel Fracture in Irradiated 316 Stainless Steel

REFERENCE: Jitsukawa, S., Hishinuma, A., and Suzuki, M., **"Fatigue Crack Propagation by Channel Fracture in Irradiated 316 Stainless Steel,"** *Effects of Radiation on Materials: 17th International Symposium, ASTM STP 1270,* David S. Gelles, Randy K. Nanstad, Arvind S. Kumar, and Edward A. Little, Eds., American Society for Testing and Materials, 1996.

ABSTRACT: Fatigue crack growth rates (da/dN) in an irradiated cold worked 316 stainless steel were obtained at temperatures of 298, 573 and 673 K. Specimens were prepared from a duct material, which irradiated at 683 K to 20 displacements per atom in an experimental fast breeder reactor.

Fatigue loading caused channel fracture to occur in the irradiated material. This was accompanied by acceleration of da/dN. Both the increment of da/dN and the fraction of channel fracture in fracture surface became larger with stress intensity factor range at temperatures of 573 and 673 K, but they were not at 298 K. Results indicate that irradiation induced channel fracture increased da/dN.

KEYWORDS: irradiation, fatigue crack growth, channel fracture, stress intensity factor range (ΔK), 3 16 stainless steel, fatigue, Frank loop, unfaulting

Austenitic stainless steel is one of the candidate materials for the first wall structure of next generation fusion experimental devices, such as the International Thermonuclear Experimental Reactor (ITER). First wall material will be exposed to high energy neutrons produced by deuterium-tritium burning. Pulse operation of the device and a high heat flux from fusion plasma will produce large alternating thermal stress in the materials. Operating temperature of the first wall is estimated to range below 700 K. Evaluation of the effect of irradiation on fatigue properties of austenitic stainless steel at temperatures below 700 K is, therefore, important.

In the temperature range below 700 K, it has been reported by de Vries, Vandermülen and the present authors that channel fracture by fatigue loading occurred in austenitic stainless steels irradiated in fast breeder reactors [*1, 2, 3*]. Grossbeck conducted low cycle fatigue tests at 703 K on a cold worked 316 stainless steel irradiated in the High Flux Isotope Reactor (HFIR) in Oak Ridge National Laboratory, and reported that transgranular cleavage-like fracture occurred by irradiation [*4*]. He suggested, however, that the cleavage-like fracture occurred mainly because of a large amount of helium produced during the irradiation in HFIR. Figure 1 shows fracture surface by channel fracture during fatigue crack growth in a cold worked 316 stainless steel irradiated in a fast breeder reactor [*3*]. The authors also indicate that crack nucleation is enhanced by channel fracture. This caused crack branching at the notch root to retard crack propagation with the stress intensity factor range (ΔK) varying from 40 to 60 MPa·m$^{1/2}$. However, the enhanced crack nucleation by irradiation induced channel fracture increases fatigue crack growth rate (da/dN) when ΔK is small enough not to cause crack branching.

[1] Department of Materials Science and Engineering, Japan Atomic Energy Research Institute, Tokai-Mura, Ibaraki-Ken 319-11 Japan

Copyright© 1996 by ASTM International www.astm.org

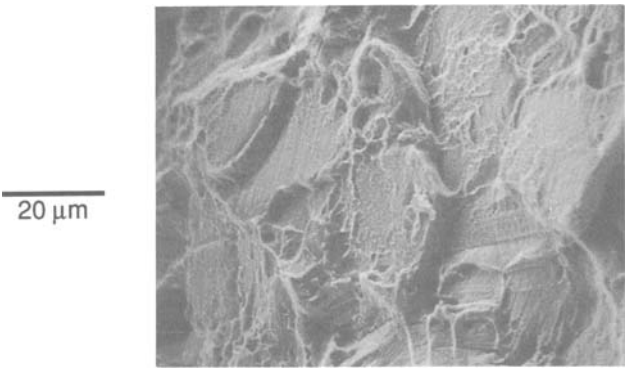


FIG. 1 *Fracture surface created by channel fracture during fatigue crack growth [3]. Channel fracture occurred by fatigue loading in a CW316 specimen irradiated to 20 dpa at 683 K. Test was performed at 673 K with a load cycling frequency of 0.8 Hz. The fracture surface was created with ΔK of about 40 MPa·m$^{1/2}$.*

Fatigue crack growth rates in an irradiated 316 stainless steel were obtained at a load cycling frequency of 40 and 60 Hz with ΔK ranging from 7 to 50 MPa·m$^{1/2}$. The test temperatures were 298, 573, and 673 K. Fracture surfaces by fatigue crack growth (FCG) were examined by a scanning electron microscope to analyze the effect of irradiation induced channel fracture.

Experimental Procedure

Specimens were fabricated from a duct of 10 % cold-worked 316 austenitic stainless steel (CW316), which was irradiated to a fluence level of 4 x 10^{26} neutrons (n)/m^2 at 683 K in an experimental fast breeder reactor (JOYO). The neutron irradiation produced a displacement damage level of 20 displacements per atom (dpa). The chemical composition of the duct material is given in Table 1.

Table 1 *Chemical composition of the CW316 (in wt%)*

C	Si	Cr	Ni	Mn	P	S	Mo	Co	B	Fe
0.05	0.6	16.4	13.5	1.6	0.03	0.006	2.2	0.32	0.0004	Bal.

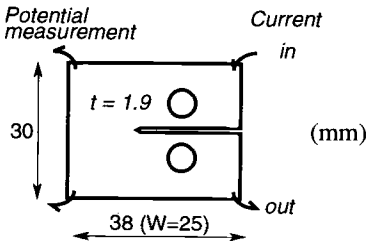


FIG. 2 *Configuration of the fatigue crack growth specimen.*

The geometry of the specimen is shown in Fig. 2. Notch length, a_0, was selected to be $a_0/W = 0.3$ and 0.4 where specimen width, W = 25 mm. In ASTM Test Method for Measurements of Fatigue Crack Growth Rates (E 647), the recommended length, L, for a compact tension (CT) specimen is 1.25W [5]. The length for the present specimen is, however, longer than the recommended size. The effect of length on the compliance of specimen was experimentally evaluated to be negligible. Therefore, the stress intensity factor range, ΔK, was calculated using the equation given in ASTM E 647.

Two feedback-controlled fatigue testing machines installed in hot cells were used for the tests. The INSTRON 1603 electromagnetic resonance and Shimadzu EF 10 hydraulic-servo fatigue testing machines were operated at cyclic frequencies of 60 and 40 Hz, respectively. Sinusoidal load (P) wave form with stress ratio ($R = P_{min}/P_{max}$) of 0.1 was used for the tests. Tests were carried out in air at temperatures of 298, 573, and 673 K.

Crack lengths were measured by 4-point electropotential drop technique. The electrodes were welded at the points near the corners of the specimen, as indicated in Fig. 2. Crack lengths were calculated from the potential values by a computer during the tests using equations developed from the experimental crack length-potential calibration measurements. Potential fluctuations, due mainly to temperature changes, were measured to be equivalent to or less than 1×10^{-7} m in crack length.

FCG tests with ΔK-decreasing method were performed at a load cycling frequency of 60 Hz. Specimens with a_0/W of 0.3 were used for the tests. Normalized K gradient with crack length, C of 0.208, where $C = -1/K\ dK/da$ was employed. The value of C was four times as large as the upper bound of the value range recommended in ASTM E 647, however it had little effect on the da/dN for unirradiated CW316 specimens. After a crack extension to a_0/W of 0.4, load amplitude (ΔP) and mean load (P_{mean}) were kept constant, and the crack was propagated under constant load amplitude. For the ΔK-decreasing tests at 573 and 673 K, initial and minimum ΔP values were about 700 and 320 N, respectively. Values for the tests at 298 K were 900 and 450 N. FCG tests with constant load amplitude were also carried out at a load cycling frequency of 40 Hz. Specimens with a_0/W of 0.4 were used for the tests. The ΔP of 800 N was employed. The da/dN values were obtained in the range defined by a form of $W - a \geq 4/\pi\ (K_{max} / \sigma_y)^2$ where, σ_y is yield stress. Yield stress levels before irradiation were about 600 MPa at temperatures of 298, 573, and 673 K. Irradiation increased the stress levels by about 200 MPa.

After the tests, fracture surfaces were observed with scanning electron microscope (SEM) in a hot cell.

Experimental Results

Results of Tests at 573 and 673 K

Fatigue crack growth rates by ΔK-decreasing tests at temperatures of 573 and 673 K were obtained with ΔK ranging from 7 to 25 $MPa \cdot m^{1/2}$. Figure 3 shows da/dN-ΔK relations of irradiated and unirradiated CW316 specimens. In ΔK range above 10 $MPa \cdot m^{1/2}$, da/dN for irradiated specimens increased with ΔK up to about 6 times as high as those for unirradiated specimens.

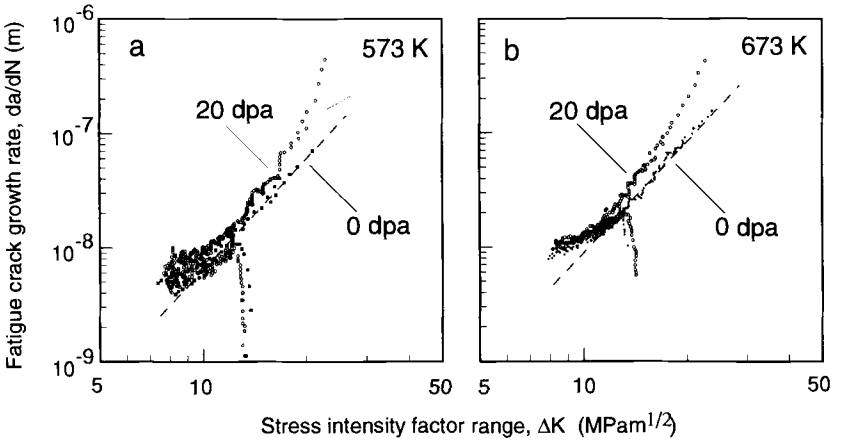


FIG. 3 *The da/dN-ΔK relations of irradiated and unirradiated CW316 at 573 and 673 K with ΔK ranging from 7 to 25 MPa·m$^{1/2}$. In ΔK range above 10 MPa·m$^{1/2}$, da/dN for irradiated specimens increased with ΔK up to about 6 times (573 K tests) as high as those for unirradiated specimens.*

Fracture surfaces created by FCG at 573 K are shown in Fig. 4. The ΔK values at positions labeled A, B, C, and D were 8, 13, 18, and 22 MPa·m$^{1/2}$, respectively. Crack propagated from left to right side in the figure. Notch root is seen at the left end of Fig. 4a. Topography of the fracture surface changed with ΔK. Fracture surface for the ΔK range below 12 MPa·m$^{1/2}$ (Fig. 4a) was rather flat, however it lost flatness with ΔK (Fig. 4b). In the ΔK range above 13 MPa·m$^{1/2}$, the fracture surface was composed of several planes. Those planes were formed along crack growth direction but were not perpendicular to loading direction. Such a fracture surface created at 673 K, and the schematic illustrations of the fracture surface are shown in Fig. 5.

Fraction of channel fracture (FCF) in the fracture surface was also increased with ΔK in the range above 12 MPa·m$^{1/2}$. This is also seen in SEM images labeled A, B, C, and D in Figs. 4a and b. Figure 6 shows the relation between FCF and ΔK. The da/dN-ΔK relation in Fig. 3 and the curves in Fig. 6 indicate that da/dN increased with FCF. It is also shown in Figs 4 and 6 that fracture surface lost flatness with increasing FCF in addition to ΔK. It should be noted, however, that the variation of FCF along specimen thickness was not small depending on ΔK and the crack length.

Fracture surfaces were formed with channel fracture and river pattern-like regions. An example is seen at position A in Fig. 4a. FCF was of about 10% at position A. The river pattern-like region was accompanied by transgranular fracture, and it is readily observed in unirradiated austenitic stainless steels. Similar fracture surface created by FCG at a ΔK of about 20 MPa·m$^{1/2}$ was also reported by de Vries for irradiated and unirradiated 304 stainless steel specimens, which tested at 823 K at a relatively high frequency of 10 Hz[7].

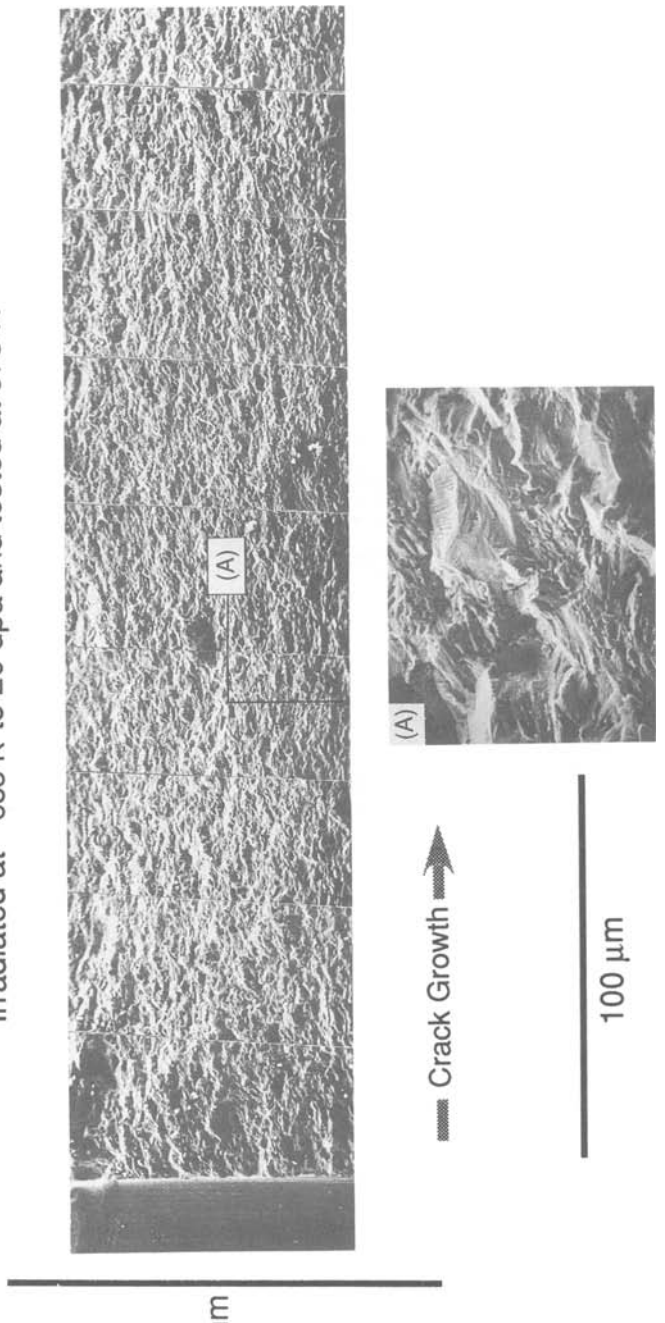


FIG. 4a *Fracture surfaces created by FCG at 573 K. The ΔK values at positions labeled A, B, C, and D were 8, 13, 18, and 22 MPa·m$^{1/2}$, respectively (to be continued).*

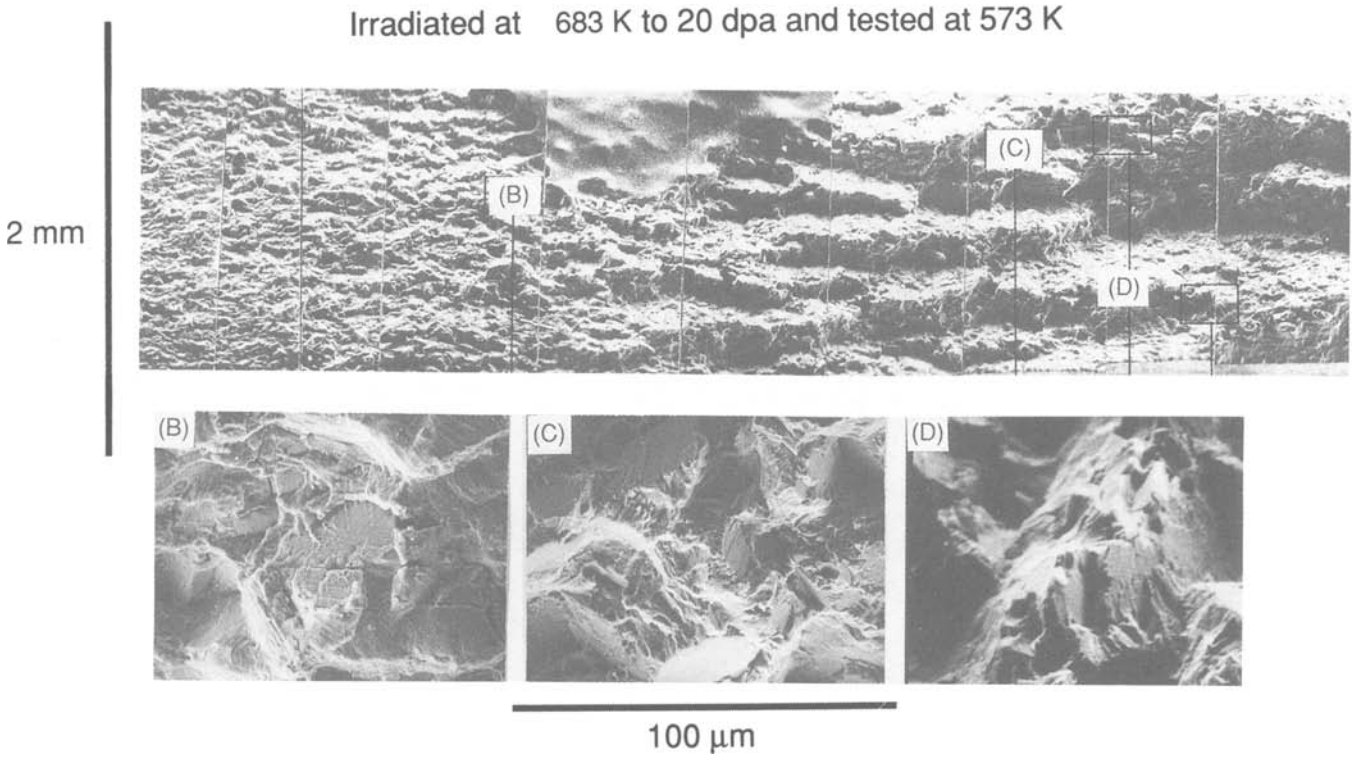


FIG. 4b (Continued) *Crack propagated from left to right side in the figure. Notch root is seen at the left end (a). Topography of the fracture surface changed with ΔK: Fracture surface for the ΔK range below 12 MPa·m$^{1/2}$ was rather flat (a), however it lost flatness with ΔK (b).*

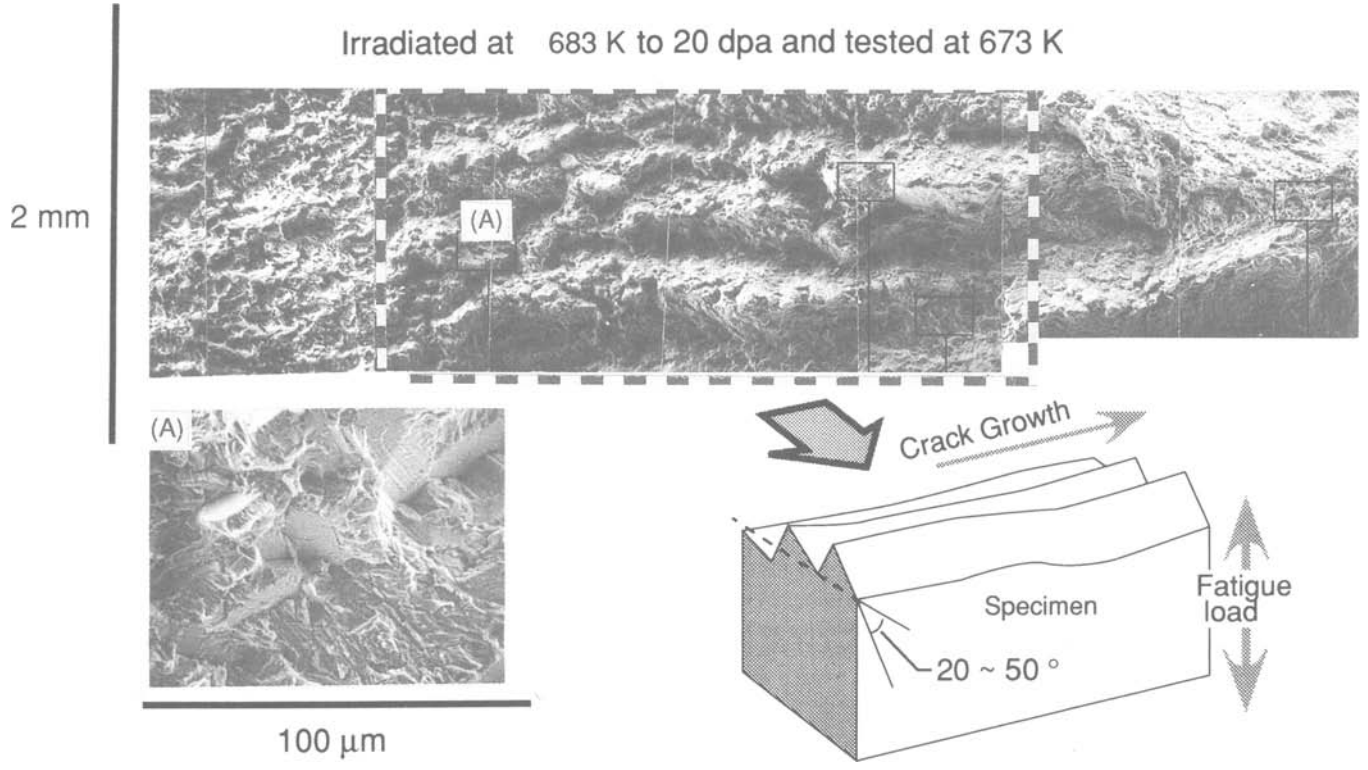


FIG. 5 *Fracture surface created at 673 K and the schematic illustration of the fracture surface. The fracture surface was composed by several planes. These sub-planes were formed along crack growth direction but were not perpendicular to the loading direction, as illustrated (bottom). ΔK at position A was about 13 MPa·m$^{1/2}$.*

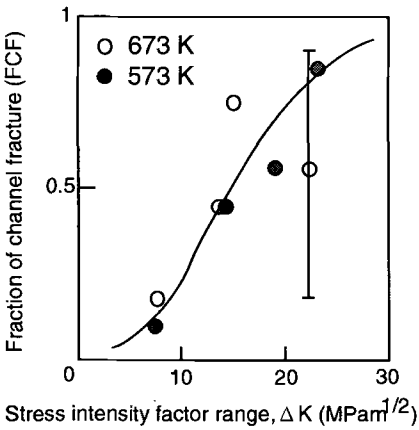


FIG. 6 *Relation between the fraction of channel fracture in the fracture surface (FCF) and ΔK. FCF increased with ΔK. Curves for FCF and the da/dN-ΔK relation in Fig. 3 indicate that da/dN increased with FCF. Compared with Fig. 4, it can be seen that fracture surface lost flatness with FCF in addition to ΔK.*

Results of the Tests at 298 K

The da/dN-ΔK relations were obtained at 298 K for irradiated and unirradiated CW316. The results for ΔK-decreasing tests with ΔK ranging from 10 to 30 MPa·m$^{1/2}$ are shown in Fig. 7a. Irradiation caused a slight reduction in da/dN. A small irradiation effect on da/dN might result from rather low ΔK, therefore tests with higher ΔK were also carried out. Figure 7b shows da/dN-ΔK relations for constant load amplitude test with ΔK ranging from 20 to 53 MPa·m$^{1/2}$. The irradiation effect on da/dN was also small; moreover the irradiation effect diminished with ΔK.

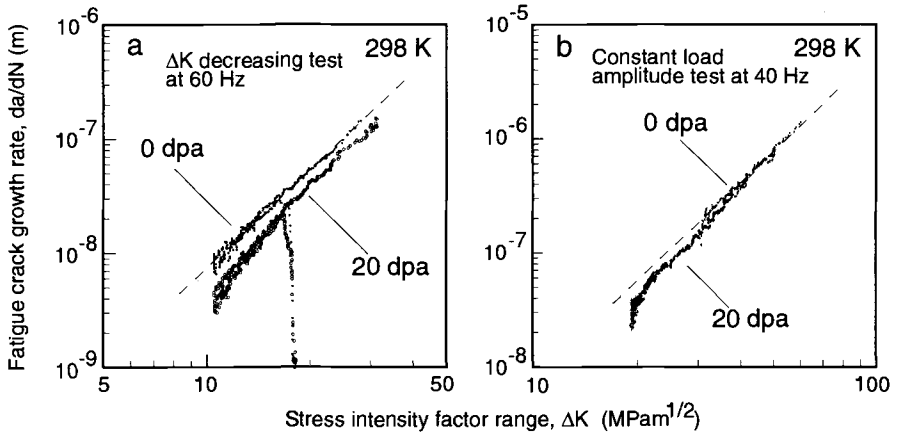


FIG. 7 *The da/dN-ΔK relations obtained at 298 K for irradiated and unirradiated CW316. The results for ΔK-decreasing tests with ΔK ranging from 10 to 30 MPa·m$^{1/2}$ (a) and the results for constant load amplitude tests with ΔK ranging from 20 to 53 MPa·m$^{1/2}$ (b) are shown. Irradiation caused a slight reduction in da/dN. The irradiation effect diminished with ΔK.*

On the whole, the fracture surface of irradiated specimen was rather flat like that obtained from 573 and 673 K tests with ΔK below 12 MPa·m$^{1/2}$. Figures 8a and b show fracture surfaces formed by ΔK-decreasing test. The ΔK values for Figs. 8a and b were 11 and 18 MPa·m$^{1/2}$, respectively. Crack propagated from left to right, as indicated in the figure. The fracture surface in Fig. 8a was composed by river pattern-like and channel fracture regions. The fracture surface looks similar but slightly rougher compared to that in Fig. 4a (bottom). FCF was equal to or smaller than 10%. With increasing ΔK, FCF decreased to zero, and striations became clear. The striations are seen in Fig. 8b.

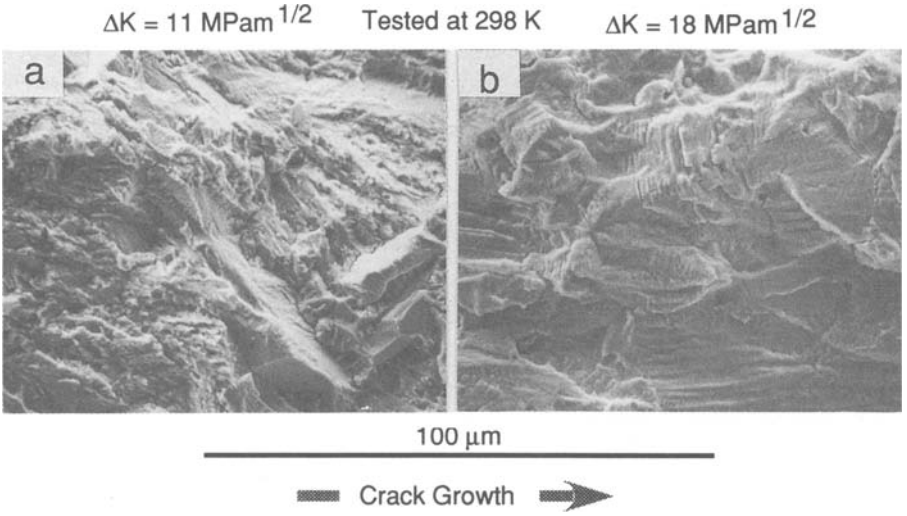


FIG. 8 *Fracture surfaces formed by a ΔK-decreasing test at 298 K. The ΔK values for (a) and (b) were 11 and 18 MPa·m$^{1/2}$, respectively. The fracture surface at ΔK of 11 MPa·m$^{1/2}$ was composed by river pattern-like and channel fracture regions (a). This fracture surface looks similar to but slightly rougher compared to that in Fig. 4a. FCF was equal to or smaller than 10%. FCF decreased to zero with increasing ΔK, and striations became clear. The striations are seen (b).*

Discussion

Channel Fracture and da/dN

When the fraction of channel fracture was not large, da/dN in irradiated specimens was almost similar to that in an unirradiated specimen. On the other hand, da/dN increased with FCF. Change of stress state around crack tip from plane strain to plane stress conditions often causes to increase da/dN. This is prone to occur for the specimens with softer material. Therefore, the acceleration of da/dN in irradiation hardened specimen was not likely caused by the stress state change.

Ratios of da/dN in irradiated and unirradiated specimens, $da_i/dN/da_u/dN$, are plotted against FCF in Fig. 9. In the figure, results of the tests at 573 and 673 K are plotted. The relationship between da/dN ratio and FCF suggests that da/dN by channel fracture, da_{ch}/dN, must be larger than that by river pattern-like fracture and by the fracture with striation mechanism. A least square fitting analysis for the experimental values at 573 and 673 K was conducted supposing da_i/dN was modeled by the rule of mixture of da_{ch}/dN and da_u/dN about FCF. The results indicated that da_{ch}/dN was about eight times as fast as da_u/dN.

Plots for the results at 573 K seem to fit rather better for the curve with $da_{ch}/dN/da_u/dN$ (= A in Fig. 9) of 16 than that with the ratio of 8. This may indicate that da_{ch}/dN rather strongly depends on the temperature. It seems that, however, further examination is required

to evaluate the temperature dependence because of the rather large dispersion of FCF depending on ΔK and the crack length.

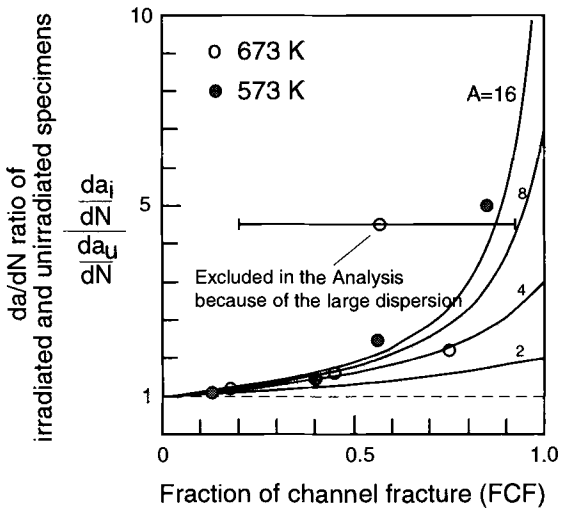


FIG. 9 *Ratios of da/dN in irradiated and unirradiated specimens, $da_i/dN/da_u/dN$, and FCF. Results of the tests at 573 and 673 K are plotted. The relation between the da/dN ratio and FCF suggests that da/dN by channel fracture, da_{ch}/dN, must be larger than those by river pattern-like fracture and by the fracture with the striation mechanism. Curves are calculated results supposing da_i/dN is modeled by the rule of mixture of da_{ch}/dN and da_u/dN about FCF. Constants A stand for $da_i/dN/da_u/dN$ in the calculation. A least square fitting analysis for the experimental values, indicating da/dN for the channel fracture was about 8 times as fast as da_u/dN.*

Temperature and Frequency Dependencies of Channel Fracture

It was indicated by the present authors that plastic deformation by fatigue loading preferentially occurred in the channels, and accumulated deformation in the channels led to fracture of the materials, accelerating fatigue crack nucleation [*3*]. A similar mechanism was also suggested by de Vries and Vandermülen [*1, 2*].

Suzuki et al. indicated that both dislocation channeling and unfaulting of the radiation produced Frank loops were not easy at room temperature in a 316 stainless steel [*8*]. Unfaulting leads Frank loops to react with gliding dislocation, and this reduces number density of Frank loops to form channels. Caillard et al. reported that unfaulting of Frank loops tended to occur because of temperature changes, and suggested that unfaulting was controlled by a thermally activated process [*9*]. These indicate that dislocation channeling tends to occur with increasing temperature but tends to be suppressed with strain rate. Indeed, FCF in the specimens tested at 298 K was smaller than those for specimens tested at 573 and 673 K. A high load cycling frequency may suppress the channel fracture by fatigue loading.

Fracture Surface and Crack Propagation Mode

Fracture surface with large FCF was formed by several planes. These sub-planes extended along crack growth direction but were not perpendicular to loading direction, as

shown in Fig. 5. Accumulation of plastic deformation in the channel leading fracture of the channel is associated with shear deformation, and therefore tends to form fracture surface not perpendicular to the loading direction. With increasing channel fracture, it is encouraged to form sub-planes inclined to the loading line. In this way, crack propagated on each plane in mode I + III, although interference between each plane imposed some limit against shear deformation. These suggest that irradiation effect on da/dN by channel fracture will be larger in modes with shear deformation: I + II, I + III, II and III, compared with simple mode I.

ΔK Dependence of Channel Fracture

The fraction of channel fracture increased with ΔK in the ΔK range above 12 MPa·m$^{1/2}$. Stress, strain, and size of the plastic zone at crack tip also increase with ΔK. In the fracture surfaces, channel surfaces with sizes ranging from 10 to 100 μm are seen, but channel surfaces smaller than 10 μm are seldom found. Minimum size of channel surface and crack tip deformation, which is proportional to ΔK might induce the ΔK dependence of FCF. It should be also noted that channel fracture was suppressed and striation mechanism became dominant in the ΔK range larger than 70 MPa·m$^{1/2}$, as indicated by the present authors [*3*].

Conclusions

(1) The da/dN in irradiated specimen increased by channel fracture. The da/dN on channel fracture was analyzed to be about 8 times faster than that of the unirradiated specimen.
(2) Channel fracture tended to occur with temperature. This may result from the dependence of dislocation channeling on temperature governed by a thermally activated process of unfaulting of irradiation produced dislocation loops.
(3) Irradiation effect on da/dN by channel fracture will be larger in modes with shear deformation: I + II, I + III, II and III, compared with mode I.
(4) The fraction of channel fracture in fracture surface increased with ΔK. Minimum size of channel surface might cause the ΔK dependence of channel fracture.

Acknowledgments

The authors wish to thank Drs. K. Shibahara, K. Sato, S. Onose, and other staff members of the Power Reactor and Nuclear Fuel Development Corp. for their effort to supply duct material. One of the authors (S.J.) would like to thank Profs. of S. Nunomura, Y. Higo, T. Iseki, A. Sato, M. Kato and Y. Mishima of the Tokyo Institute of Technology for their discussions and encouragement.

References

[1] M. I. de Vries, " Effects of temperature and strain rate on the low cycle fatigue properties of neutron irradiated stainless steel DIN 1.4948," Effects of Radiation on Materials: Eleventh Conference, ASTM STP 782, H. R. Brager and J. S. Perrin, Eds., American Society for Testing and Materials, 1982, pp. 665-689

[2] W. Vandermülen, H. Chen, W. Hendrix and J. Ketels, " Observations on the fatigue rupture mechanism of neutron-irradiated AISI 316L," J. of Nucl. Mater., 172 (1990) 247-246

[3] S. Jitsukawa, A. Umino, I Takahashi, S Iida, M. Adachi, K. Suzuki and A. Hishinuma, " Effects of Hold Time and Frequency on the Fatigue Crack Growth Rate of Irradiated Cold-Worked Type 316 Stainless Steel," Effects of Radiation on Materials: 15th International Symposium, ASTM STP 1125, R. E. Stoller, A. S. Kumar, and D. S. Gelles, Eds., American Society for Testing and Materials, Philadelphia, 1992, pp. 1083-1094

[4] M. L. Grossbeck and K. C. Liu, Nucler Technology, Vol. 58, 1982, pp. 538-547

[5] " Standard test method for measurement of fatigue crack growth rate," (E647) in Annual book of ASTM standards, Vol. 03.01, American Society for Testing and Materials, Philadelphia, 1990, pp. 648-668

[6] K. Watanabe, S. Jitsukawa, S. Hamada, T. Kodaira, A. Hishinuma, " Weldability of Neutron-Irradiated Type 316 Stainless Steel," Fusion Engineering and Design (in press).

[7] M. I. de Vries and D. J. Michel," Fatigue Crack Growth in Neutron Irradiated Type 304 and Type 316 Stainless Steels," Effects of Radiation on Materials: Twelfth International Symposium (part II), ASTM STP 956, F. A. Garner, C. H. Henager, Jr., and N. Igata, Eds., American Society for Testing and Materials, 1987, pp. 147-190

[8] M. Suzuki, A. Sato, T. Mori, J. Nagakawa, N. Yamamoto and H. Shiraishi, " In situ deformation and unfaulting interstitial loops in proton-irradiated steels," Philosophical Magazine A, 1992, Vol. 65, No. 6, 1309-1326

[9] D. Caillard, J. L. Martin and B. Joffrey, " Creep under irradiation of 316 steel in the high voltage electron microscope," Acta Metallurgica, Vol. 28, 1980, pp. 1059-1067

David J. Alexander,[1] Janet E. Pawel,[1] Martin L. Grossbeck,[1] Arthur F. Rowcliffe,[1] and Kiyoyuki Shiba[2]

FRACTURE TOUGHNESS OF IRRADIATED CANDIDATE MATERIALS FOR ITER FIRST WALL/BLANKET STRUCTURES

REFERENCE: Alexander, D. J., Pawel, J. E., Grossbeck, M. L., Rowcliffe, A. F., and Shiba, K., **"Fracture Toughness of Irradiated Candidate Materials for ITER First Wall/Blanket Structures,"** *Effects of Radiation on Materials: 17th International Symposium, ASTM STP 1270,* David S. Gelles, Randy K. Nanstad, Arvind S. Kumar, and Edward A. Little, Eds., American Society for Testing and Materials, 1996.

ABSTRACT: Disk compact specimens of candidate materials for first wall/blanket structures in ITER have been irradiated to damage levels of about 3 dpa at nominal irradiation temperatures of either 90 or 250°C. These specimens have been tested over a temperature range from 20 to 250°C to determine J-integral values and tearing moduli. The results show that irradiation at these temperatures reduces the fracture toughness of austenitic stainless steels, but the toughness remains quite high. The toughness decreases as the test temperature increases. Irradiation at 250°C is more damaging than at 90°C, causing larger decreases in the fracture toughness. Ferritic-martensitic steels are embrittled by the irradiation, and show the lowest toughness at room temperature.

KEYWORDS: fracture toughness, austenitic stainless steels, disk compact, ferritic stainless steels, first wall/blanket structure, embrittlement, tearing modulus

Work is under way at Oak Ridge National Laboratory (ORNL) to evaluate the fracture toughness of candidate materials for first wall/blanket structure applications in the International Thermonuclear Experimental Reactor (ITER). A variety of austenitic stainless steels are being examined, as well as several additional materials. Specimens were fabricated from material in several different conditions, including annealed or cold

[1]Metals and Ceramics Division, Oak Ridge National Laboratory, Oak Ridge, TN 37831-6151.

[2]Japan Atomic Energy Research Institute, Tokai-Mura, Japan.

Copyright©1996 by ASTM International www.astm.org

worked, as well as weldments. These specimens have been irradiated in the High Flux Isotope Reactor (HFIR) at ORNL. To date, three capsules have been designed, fabricated, and irradiated to dose levels of approximately 3 dpa; this approaches the expected accumulated dose at the end of the Basic Performance Phase of operation of ITER. The helium concentration generated as a result of transmutation of nickel was about 50 appm; this is in the range expected for the ITER first wall blanket and shield structure after a neutron exposure of about 3 dpa. These capsules were designed for irradiation temperatures of either 60 to 125°C (capsules HFIR-MFE-JP-18 and -19) or 250 to 300°C (HFIR-MFE-JP-17) [1-3]. These temperatures covered the expected range of operating temperatures for stainless steel components in different ITER designs. All of the capsules have been successfully irradiated and disassembled. Some of the results of earlier testing have already been reported [4,5]. This paper presents the final results for all of the fracture toughness tests.

EXPERIMENTAL PROCEDURE

Four major alloy types were included in this experiment: American and Japanese type 316 steels (designated US316 and J316, respectively), a European type 316L steel (EC316L), and the JPCA alloy. The compositions of the alloys are given in Table 1. Specimens were in solution annealed (SA), cold-worked (CW), or welded conditions. The J316 material was also tested after a thermomechanical treatment in which it was strained, aged, and recrystallized (SAR). There were a total of 12 variants of the austenitic materials in composition and thermomechanical treatment. The EC316L was welded using 16-8-2 filler metal (see Table 1) and gas tungsten arc (GTA) welding with argon cover gas. Both the plate and the filler wire were provided by Joint Research Centre-Ispra from the European Fusion Stockpile. The JPCA and J316 plate material were supplied by the Japan Atomic Energy Research Institute. The JPCA specimens were welded with filler wire with a composition similar to the base metal (see Table 1) for the GTA welding. The US316 material was an air-melted heat from the U.S. fusion program, reference heat X15893. Two ferritic-martensitic steels were also included in this experiment, HT-9 and F82H.

In order to utilize the HFIR target region for the irradiations, the specimen size was severely limited. Therefore, a small disk compact specimen was selected for the fracture toughness experiments. Techniques were developed for generating the J-integral resistance (J-R) curve using either unloading compliance (UC) or potential drop (PD) to monitor crack extension [6,7]. Initial trials showed that either method could be used to develop useful fracture toughness data from these small specimens [6-8]. As a result of the success of the laboratory trials, it was decided to use the unloading compliance technique for testing the irradiated specimens.

The disk compact specimens [designated 0.18T DC(T)] were 12.5 mm in diameter by 4.63 mm thick. All specimens were fabricated from the middle of the thickness of the parent plates of material, with the notch oriented so that crack growth would occur parallel

TABLE 1--Specimen alloy compositions and processing

Alloy	Composition (wt %)											
	Fe	Ni	Cr	Ti	Mo	Mn	Si	C	N	V	W	Ta
JPCA	Bal	15.95	14.3	0.21	2.4	1.6	0.54	0.064	0.003	--	--	--
US316	Bal	12.4	17.3	--	2.1	1.7	0.67	0.061	--	--	--	--
EC316L	Bal	12.3	17.4	--	2.3	1.8	0.46	0.024	0.06	--	--	--
J316	Bal	13.95	16.77	--	2.31	0.23	0.04	0.038	0.011	--	--	--
16-8-2 weld wire	Bal	8.98	16.28	--	2.16	1.82	0.060	0.036	0.029	--	--	--
JPCA weld wire	Bal	16.06	14.39	0.23	2.44	1.77	0.35	0.057	0.0095	--	--	--
HT-9	Bal	0.51	12.1	--	1.04	0.57	0.17	0.20	0.027	0.28	0.45	--
F82H	Bal	0.05	7.65	--	--	0.49	0.09	0.093	0.0018	0.18	1.98	0.038

JPCA Annealed: Solution annealed (1120°C/1 h/water quench).
JPCA Cold Worked: Annealed + cold worked 20%.
J316 Annealed: Solution annealed (1060°C/15 min/water quench).
J316 Cold Worked: Annealed + cold worked 20%.
J316 Strained, Aged, Recrystallized: 1150°C/1 h + 60% cold work + 650°C/15 h +800°C/15 h.
EC316L Annealed: Solution annealed.
US316 Annealed: Cold worked 50% + annealed (1050°C/1 h).
US316 Cold Worked: Annealed + 20% cold work.
HT-9: 1050°C/1 h/air cooled + 780°C/2.5 h/air cooled.
F82H: 1040°C/0.5 h + 740°C/1.5 h/air cooled.

to the rolling direction (T-L orientation). The specimens were fatigue precracked at room temperature to a crack length to specimen width ratio (a/W) of roughly 0.5 and then side grooved 10% of their thickness on each side, prior to irradiation. Filler pieces were inserted in the loading holes and in the notches to reduce disturbances in the flow of cooling water over the specimens in the capsule and to improve the uniformity of heat transfer across the specimens.

The low-temperature capsules (HFIR-MFE-JP-18 and -19) [2] were shrouded type capsules with the fracture toughness specimens directly cooled on their flat faces by reactor cooling water. Predicted temperatures over the crack-tip region of the fracture toughness specimens ranged from approximately 60 to 85°C near the ends of the capsule to 65 to 125°C near the middle. For convenience, specimens from these capsules are referred to as 90°C specimens. The higher temperature capsule (HFIR-MFE-JP-17) [3] was of the shrouded type cooled by reactor cooling water flowing between a cladding tube that contained the specimens in a helium atmosphere and a shroud tube. This capsule featured a unique thermal design in that, over the middle portion of the test length, aluminum cooling spacers of varying thicknesses were employed between the fracture toughness specimens to achieve predicted specimen temperatures for the crack region between 250 and 300°C. For convenience, specimens from this capsule are referred to as 250°C specimens. Capsules JP-18 and -19 completed their irradiations in October 1991, and capsule JP-17 completed its irradiation in February 1992 [3]. After disassembly of the capsules, the inserts in the individual specimens were pushed out of the loading holes using an arbor press and punch. The filler in the notch was removed with the aid of a hammer and a thinned screwdriver blade.

Tests were conducted in general accordance with American Society for Testing and Materials standards E 813-89, Standard Test Method for J_{Ic}, A Measure of Fracture Toughness, and E 1152-87, Standard Test Method for Determining J-R Curves. The equations in E 1152-87 were used for the J calculations. The specimens were tested with a computer-controlled testing and data acquisition system [9]. Tests in the laboratory used an 89-kN capacity servohydraulic test machine. In the hot cell, a 445-kN capacity servohydraulic testing machine with a 22-kN load cell was used. All tests were run in strain control. The displacements were measured with an "outboard" clip gage that seated in grooves machined on the outer edge of the specimen along the load line [6,7]. This arrangement provided very good load-displacement and UC results. Test temperatures from 90 to 250°C were maintained within ±2°C of the desired temperature with a split-box furnace that enclosed the specimen and the grips during the test. Temperature was monitored throughout the testing with a thermocouple that was held in contact with the specimen by a spring-loaded clip. Tensile data from specimens included in the capsules were used for calculations in the J-R analyses.[1] Estimated values were taken from literature data when necessary.

---

[1]Pawel, J. E., unpublished research, Oak Ridge National Laboratory, 1994.

After testing, the specimens were heat tinted by placing them on a hot plate and heating them until a noticeable color change had occurred. The specimens were cooled to room temperature and then broken open. The initial and final crack lengths for the unirradiated specimens were measured with an optical measuring microscope. For the irradiated specimens, photographs of the fracture surfaces were fastened to a digitizing tablet to measure the crack lengths.

Materials with very high toughness and low yield strength, such as the annealed austenitic stainless steels, proved to be more difficult to test than material with lower toughness such as HT-9. The soft, tough materials showed enormous crack-tip blunting before stable crack growth began. This resulted in gross changes in the specimen geometry, and so the crack length predictions were not very accurate. The J-R curve was much steeper than the calculated blunting line. In these cases, the data were used to calculate a blunting line. A straight line was fit by eye through the initial portion of the data points, and a second line was drawn parallel to the first but offset by an amount corresponding to a crack extension of 0.2 mm following ASTM E 813-89. The candidate toughness value J_Q was then determined from the intersection of the data with this offset line. In cases where the data rose very steeply, the test was terminated before there was enough crack growth to cross the second exclusion line (drawn corresponding to a crack extension of 1.5 mm as defined in ASTM E 813-89). As a result, no tearing modulus value could be calculated. Materials with lower toughness, such as the cold-worked austenitic stainless steels, behaved in a much more conventional manner. For these materials, the data followed the calculated blunting line quite closely, so no additional construction was required. These specimens also showed very good agreement between the measured and predicted final crack lengths.

RESULTS AND DISCUSSION

The results of the testing are given in Tables 2 to 6. These tables also include the tensile values used in the analyses. Radiation increases the yield and ultimate tensile strengths, with irradiation at 250°C causing a greater increase than at 90°C. The yield and tensile strengths decrease as the test temperature increases. The critical stress intensities calculated from the candidate J values for the various alloys are summarized in Figs. 1 to 8 as a function of test temperature. These figures show that the toughness of the austenitic steels is very high. In general, the toughness decreases as the test temperature increases, but remains very high.

Both before and after irradiation, the fracture toughnesses of the solution annealed materials, as shown in Figs. 1, 3, and 5, are very high (K_J > 150 MPa$\sqrt{m}$) in the test temperature range. The toughness decreases slightly as the temperature increases, but remains very high, even after irradiation and testing at 250°C. The EC316L and J316 annealed steels show only a slight decrease in toughness (50 to 100 MPa$\sqrt{m}$) after irradiation. The JPCA annealed material undergoes a larger decrease in toughness (100 to 200 MPa$\sqrt{m}$) after irradiation (Fig. 5). Even in this case, the toughness is still high,

TABLE 2--Fracture toughness and tensile properties of EC316L

Material	Specimen	Irradiation temperature (°C)	Test temperature (°C)	J_Q (kJ/m^2)	K_J[a] (MPa$\sqrt{m}$)	T	σ_y (MPa)	σ_u (MPa)	E (GPa)
EC316L Annealed	FA14	Unirradiated	22	847	404	NA	296[b]	579	193
	FA22	Unirradiated	100	889	407	NA	283[b]	517	186
	FA5	Unirradiated	200	697	353	NA	214[b]	448	179
EC316L Annealed	FA16	90	25	781	388	107	625	700	193
	FA3	90	25	800	393	93	625	700	193
	FA21	90	25	634	350	135	625	700	193
	FA6	90	100	671	353	129	607[b]	676	186
	FA11	90	100	574	327	92	607[b]	676	186
	FA17	90	200	548	314	221	525	600	179
EC316L Annealed	FA2	250	25	417	284	39	850	860	193
	FA10	250	100	387	268	38	800	810	186
	FA9	250	250	257	214	47	741[b]	748	179
	FA18	250	250	353	252	42	741[b]	748	179
EC316L PERP[c]	FS4	Unirradiated	90	831	393	NA	283	517	186
EC316L PERP[c]	FS1	90	90	512	309	102	607	676	186
EC316L Weld	FB3	Unirradiated	22	772	386	NA	310[b]	614	193
	FB14	Unirradiated	90	710	363	NA	221[b]	476	186
	FB17	Unirradiated	250	610	331	NA	241[b]	448	179
EC316L Weld	FB4	90	90	341	252	109	627[b]	703	186
EC316L Weld	FB5	250	250	160	170	29	741	748	179
	FB13	250	250	152	165	23	741	748	179

[a] $K_J^2 = J_Q E$.
[b] Data from tensile test from these experiments.
[c] PERP = Specimens oriented so that crack growth was perpendicular to the rolling direction.

TABLE 3--Fracture toughness and tensile properties of J316

Material	Specimen	Irradiation temperature (°C)	Test temperature (°C)	J_Q (kJ/m^2)	K_J[a] (MPa$\sqrt{m}$)	T	σ_y (MPa)	σ_u (MPa)	E (GPa)
J316 Annealed	FC8	Unirradiated	22	790	391	NA	100	450	193
	FC24	Unirradiated	90	959	423	NA	90[b]	427	186
	FC21	Unirradiated	250	843	388	NA	62[b]	372	179
J316 Annealed	FC12	90	90	737	370	100	689[b]	696	186
	FC16	90	250	620	333	99	600	625	179
J316 Annealed	FC10	250	90	453	291	59	825	850	186
	FC2	250	250	333	244	55	750	775	179
J316 SAR[c]	FM5	Unirradiated	22	595	339	103	525	650	193
	FM8	Unirradiated	90	548	319	63	517[b]	634	186
	FM9	Unirradiated	250	392	265	107	455	559	179
J316 SAR[c]	FM11	90	90	263	221	36	690	696	186
J316 SAR[c]	FM2	250	250	170	175	28	750	775	179
J316 CW[d]	FD7	Unirradiated	22	870	410	71	717[b]	765	193
	FD5	Unirradiated	90	591	332	101	593[b]	641	186
	FD1	Unirradiated	250	328	243	89	572[b]	607	179
J316 CW[d]	FD12	90	90	479	299	46	827[b]	841	186
	FD8	90	250	302	233	40	725	750	179
J316 CW[d]	FD10	250	90	271	225	40	889[b]	938	186
	FD11	250	250	138	157	18	821[b]	827	179

[a] $K_J^2 = J_Q E$.
[b] Data from tensile test from this experiment.
[c] SAR = Strained, aged, and recrystallized.
[d] CW = Cold worked 20%.

TABLE 4--Fracture toughness and tensile properties of JPCA

Material	Specimen	Irradiation temperature (°C)	Test temperature (°C)	J_Q (kJ/m^2)	K_J[a] (MPa$\sqrt{m}$)	T	σ_y (MPa)	σ_u (MPa)	E (GPa)
JPCA Annealed	FF10	Unirradiated	22	616	345	NA	331[b]	600	193
	FF13	Unirradiated	100	706	363	158	269[b]	510	186
	FF20	Unirradiated	200	498	299	82	269[b]	483	179
JPCA Annealed	FF6	90	25	349	260	23	750	770	193
	FF5	90	25	355	262	41	750	770	193
	FF16	90	100	310	240	34	717[b]	738	186
	FF15	90	100	312	241	31	717[b]	738	186
	FF2	90	200	225	201	46	614[b]	634	179
JPCA Annealed	FF3	250	25	271	229	18	900	950	193
	FF11	250	100	133	157	13	862[b]	910	186
	FF18	250	250	123	148	14	779[b]	827	179
JPCA EBW[c]	FR7	Unirradiated	250	619	333	NA	269	483	179
JPCA EBW[c]	FR11	90	90	885	406	101	717	738	186
JPCA EBW[c]	FR12	250	250	315	238	52	779	827	179
JPCA CW[d]	FE6	Unirradiated	22	365	266	45	625	650	193
	FE3	Unirradiated	90	306	239	55	600[b]	627	186
	FE1	Unirradiated	250	181	180	82	524[b]	572	179
JPCA CW[d]	FE8	90	90	167	176	24	931[b]	952	186
JPCA CW[d]	FE7	250	250	124	149	8	868[b]	896	179
JPCA Weld	FG10	Unirradiated	22	655	356	NA	331	600	193
	FG13	Unirradiated	90	1020	436	NA	269	510	186
	FG1	Unirradiated	250	959	415	NA	269	483	179
JPCA Weld	FG8	90	90	316	242	46	717	738	186
JPCA Weld	FG12	250	250	234	205	27	779	827	179

[a] $K_J^2 = J_Q E$.
[b] Data from tensile test from these experiments.
[c] EBW = Electron beam weld.
[d] CW = Cold worked 20%.

TABLE 5--Fracture toughness and tensile properties of US316

Material	Specimen	Irradiation temperature (°C)	Test temperature (°C)	J_Q (kJ/m^2)	K_J[a] (MPa$\sqrt{m}$)	T	σ_y (MPa)	σ_u (MPa)	E (GPa)
US316 Annealed	FK16	Unirradiated	22	234	213	79	262[b]	607	193
	FK6	Unirradiated	90	235	209	76	186[b]	510	186
	FK8	Unirradiated	250	213	195	88	152[b]	462	179
US316 Annealed	FK7	90	90	156	171	17	500	550	186
US316 Annealed	FK10	250	250	36	80	6	650	700	179
US316 CW[c]	FL13	Unirradiated	22	35	82	4	683[b]	793	193
	FL8	Unirradiated	90	34	80	0	662[b]	724	186
	FL9	Unirradiated	250	28	71	-	572[b]	648	179
US316 CW[c]	FL15	90	90	22	64	0	848[b]	862	186
US316 CW[c]	FL5	250	250	15	52	0	825	850	179

[a] $K_J^2 = J_Q E$.
[b] Data from tensile test from these experiments.
[c] CW = Cold worked 20%.

TABLE 6--Fracture toughness and tensile properties of ferritic-martensitic alloys

Material	Specimen	*Irradiation* temperature (°C)	Test temperature (°C)	J_Q (kJ/m^2)	K_J[a] (MPa$\sqrt{m}$)	T	σ_y (MPa)	σ_u (MPa)	E (GPa)
HT-9	FH11	Unirradiated	22	484	316	104	476[b]	696	207
	FH3	Unirradiated	90	470	307	91	414[b]	621	200
	FH4	Unirradiated	250	415	283	131	427[b]	627	193
HT-9	FH1	90	90	283	238	41	903[b]	917	200
HT-9	FH5	250	25	5	31	-	950	1000	207
	FH6	250	250	140	164	17	876[b]	931	193
F82H	FI3	Unirradiated	250	334	254	122	448[b]	531	193
F82H	FI4	250	25	117	156	-	950	975	207
	FI1	250	250	197	195	22	855[b]	855	193

[a]$K_J^2 = J_Q E$.
[b]Data from tensile specimen from these experiments.

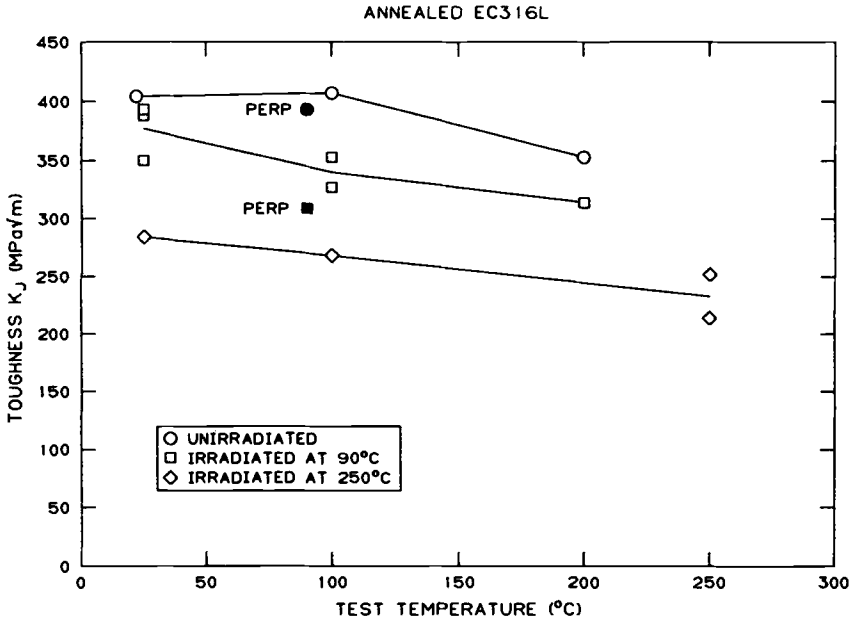


FIG. 1--Fracture toughness values for annealed EC316L. Also shown are data (solid symbols) for two specimens oriented perpendicular to the rolling direction (PERP).

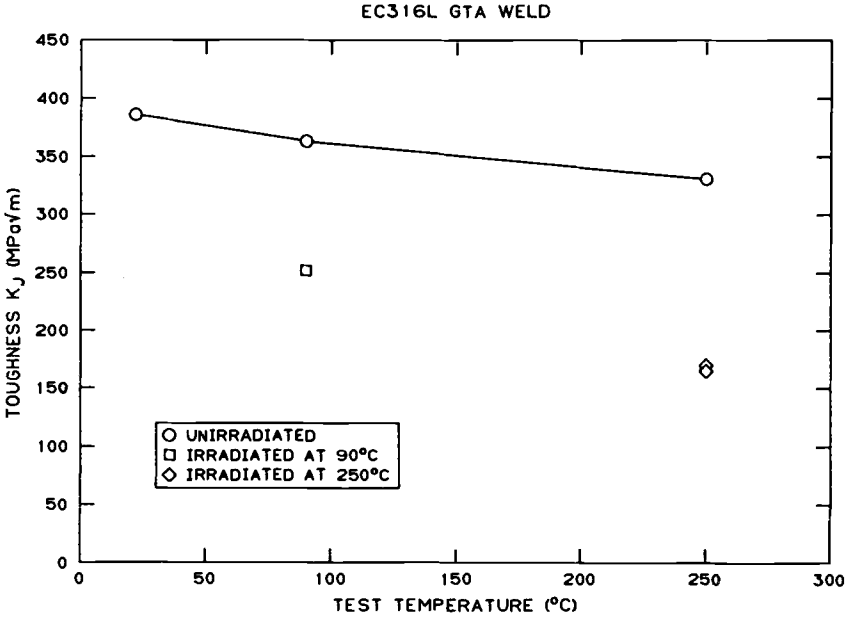


FIG. 2--Fracture toughness values for the gas tungsten-arc (GTA) weldment in EC316L base metal.

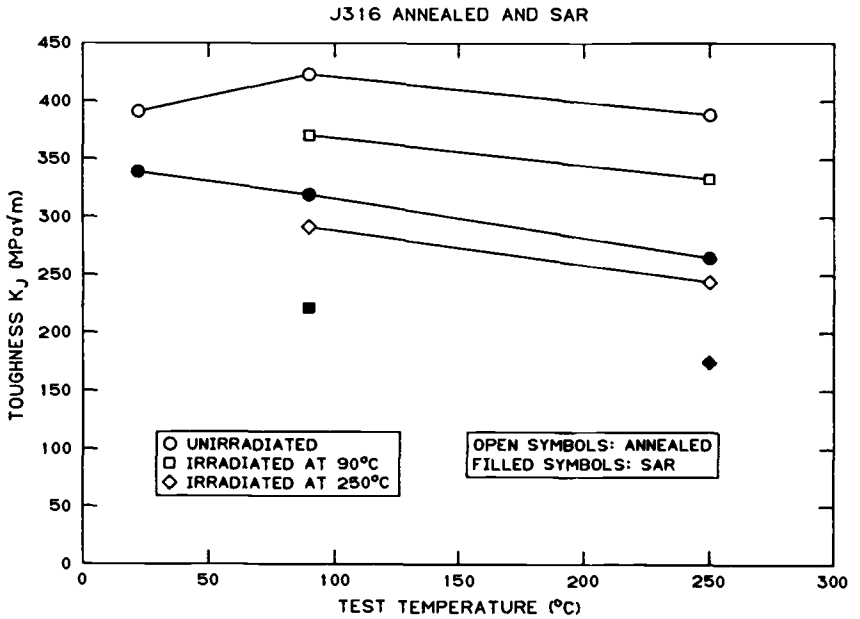


FIG. 3--Fracture toughness values for J316 in the annealed condition (open symbols) and the strained, aged, and recrystallized (SAR) condition (solid symbols).

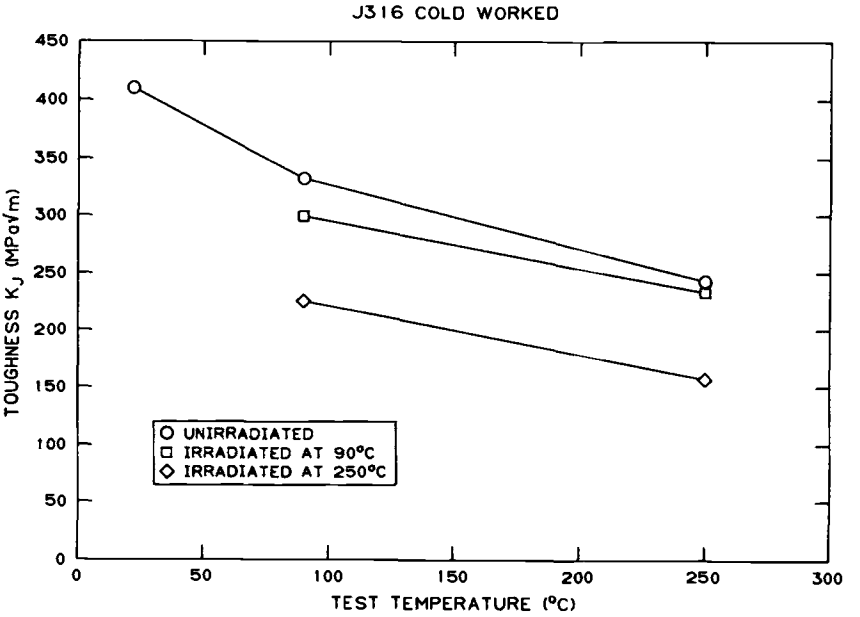


FIG. 4--Fracture toughness values for cold-worked J316.

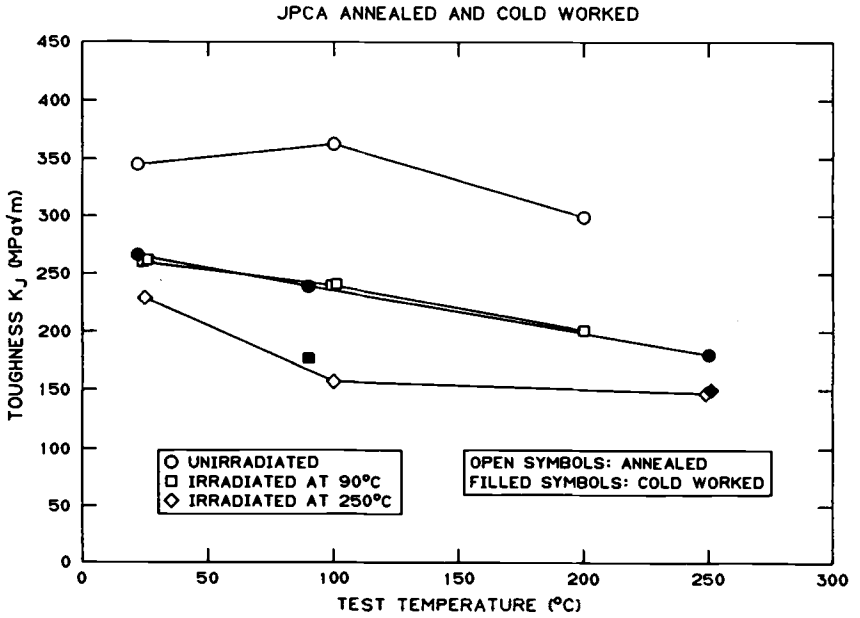


FIG. 5--Fracture toughness values for JPCA in the annealed condition (open symbols) and after 20% cold work (solid symbols).

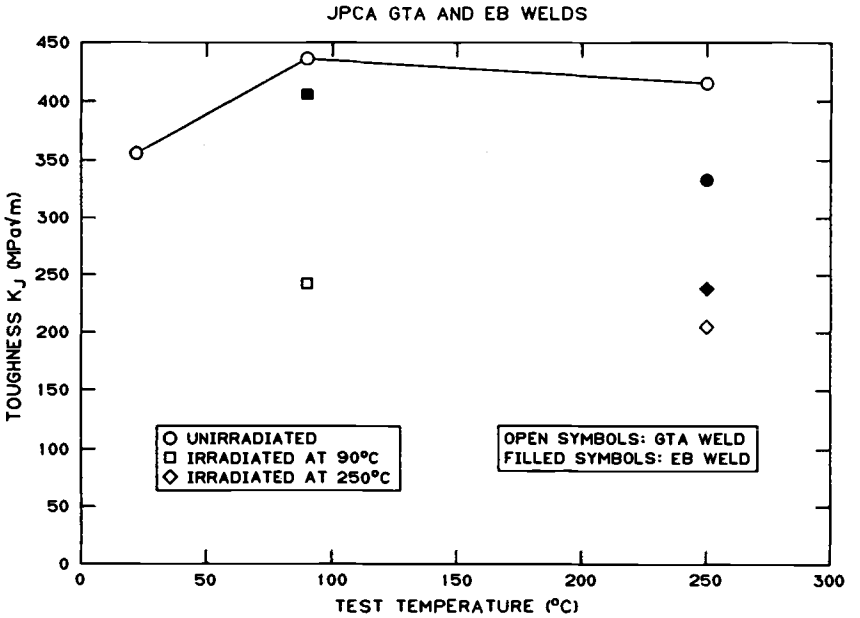


FIG. 6--Fracture toughness for the gas tungsten-arc (GTA) weldment (open symbols) and electron-beam weldments (solid symbols) in JPCA.

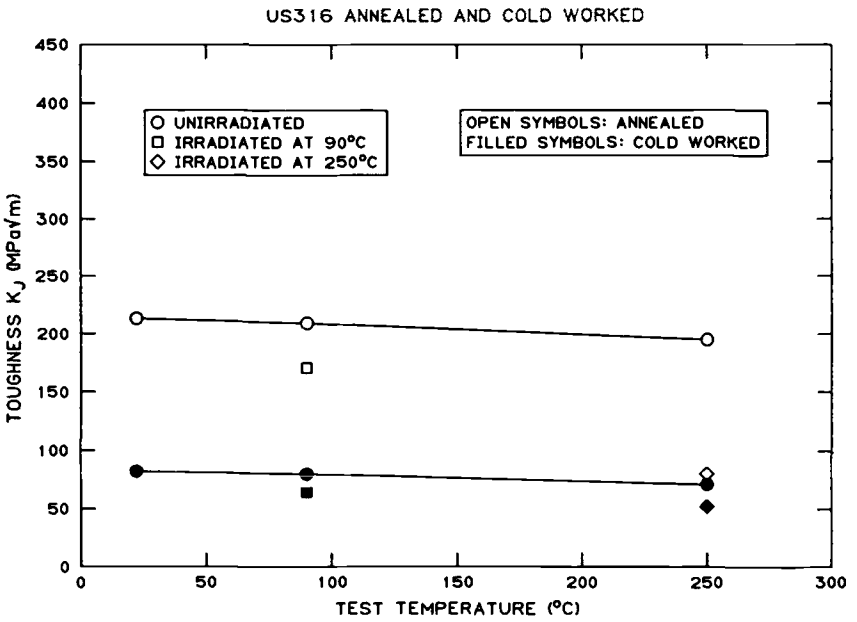


FIG. 7--Fracture toughness for US316 in the annealed condition (open symbols) and after 20% cold work (solid symbols).

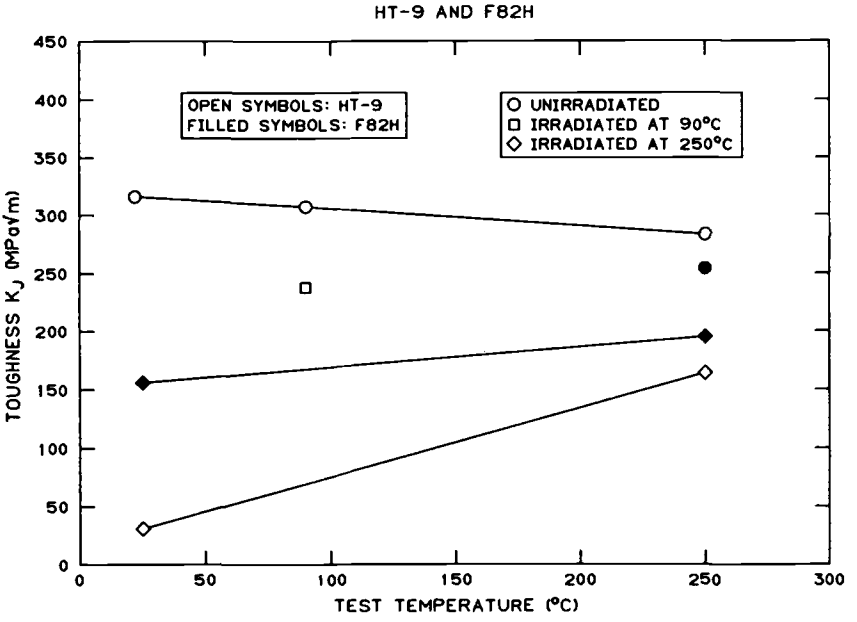


FIG. 8--Fracture toughness for ferritic-martensitic steels HT-9 (open symbols) and F82H (solid symbols).

with a K_J value of 150 MPa$\sqrt{m}$ (Table 4). The US316 material has the lowest toughness both before and after irradiation (Fig. 7). This heat of material was air melted and contains an unusually high volume fraction of nonmetallic inclusions which are likely to promote rapid microvoid growth and coalescence.

The fracture toughness of the cold-worked material is generally lower than that of the annealed material, typically by about 75 to 100 MPa$\sqrt{m}$, both before and after irradiation. One exception is the JPCA material irradiated and tested at 250°C, for which the annealed and cold-worked materials had almost identical toughnesses (see Table 4). In all cases, the fracture toughnesses of the cold-worked JPCA and J316 materials remain high. The US316 material, which had the lowest toughness of the austenitic steels in the solution annealed condition, also had by far the lowest toughness values of the cold-worked materials, about 65 MPa$\sqrt{m}$. This material also had very low values of tearing modulus (Table 5).

Electron beam welds of JPCA (Table 4, Fig. 6) and GTA welds of JPCA (Table 4, Fig. 6) and EC316L (Table 2, Fig. 2) proved to be very tough, both before and after irradiation. The JPCA GTA welded material had approximately the same toughness as the JPCA SA material ($K_J \cong 240$ MPa$\sqrt{m}$) after irradiation and testing at 90°C, while the JPCA EB-welded material had an even higher toughness.

The EC316L material contained a small volume fraction (~3%) of ferrite stringers running along the rolling direction of the plate. However, it was found that specimens with the crack propagation direction parallel to the direction of the delta ferrite stringers had essentially the same toughness as specimens with the crack propagation perpendicular to the stringer direction. These specimens are identified as "PERP" (since they were oriented perpendicular to the rolling direction) in Table 2 and Fig. 1.

The J-R curves for specimens of EC316L, J316, and JPCA, all in the annealed condition, are shown in Figs. 9 to 11. The J316 material shows the smallest degradation in toughness and the JPCA alloy shows the greatest decrease. After irradiation, the J-R curves have a lower slope, which reflects the lower values of tearing modulus given in Tables 2 to 4. The toughness level decreases with increasing test temperature.

The fracture toughness of the ferritic materials is also reduced by these irradiations. The F82H alloy is more resistant to damage than the HT-9 material. Both of these alloys show high toughness at high test temperatures (250°C) with lower toughness at 25°C (Fig. 8). The HT-9 specimen irradiated at 250°C fractured in a brittle manner when tested at room temperature. The load-displacement trace was linear, and the value of the fracture toughness (31 MPa$\sqrt{m}$) is so low that it satisfies the specimen thickness validity criteria for plane strain fracture toughness, despite the very small specimen size. The F82H specimen irradiated at 250°C and tested at 25°C also showed a lower toughness than when tested at 250°C, but the load-displacement curve showed considerable nonlinearity and the final fracture, although unstable, occurred at a high toughness level of 156 MPa$\sqrt{m}$.

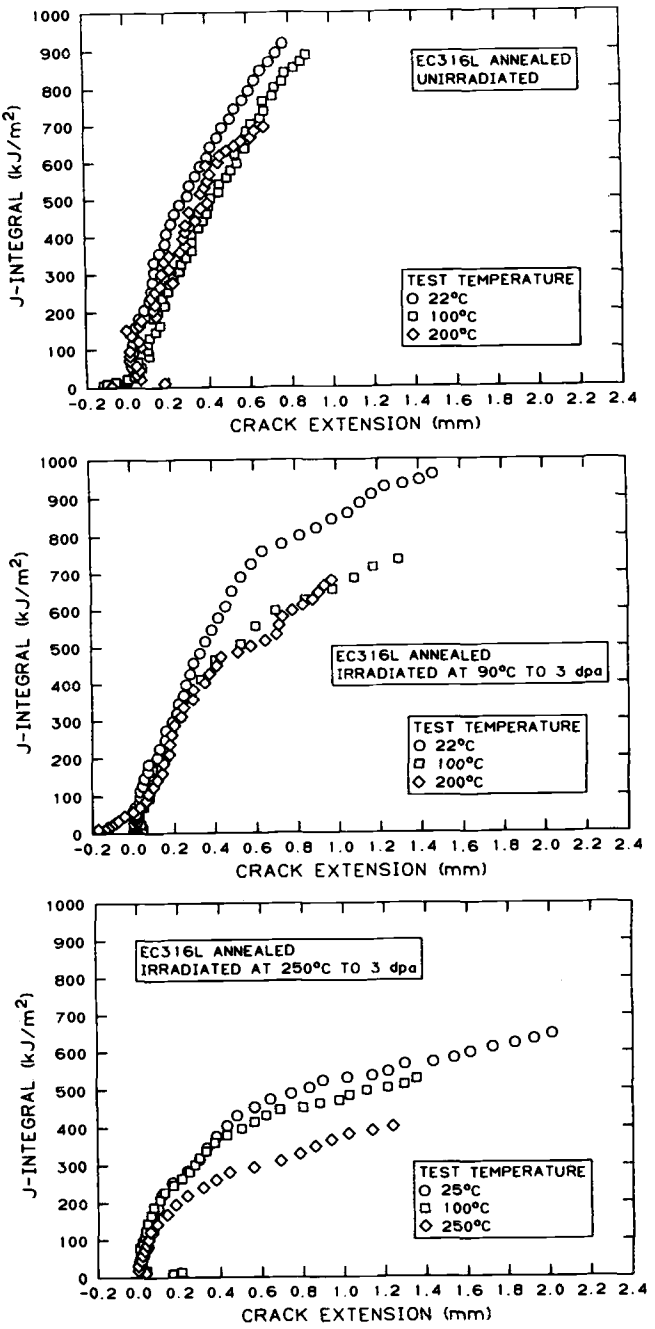


FIG. 9--J-R curves for annealed EC316L material in the unirradiated condition (top), and after irradiation at 90°C (middle) and 250°C (bottom).

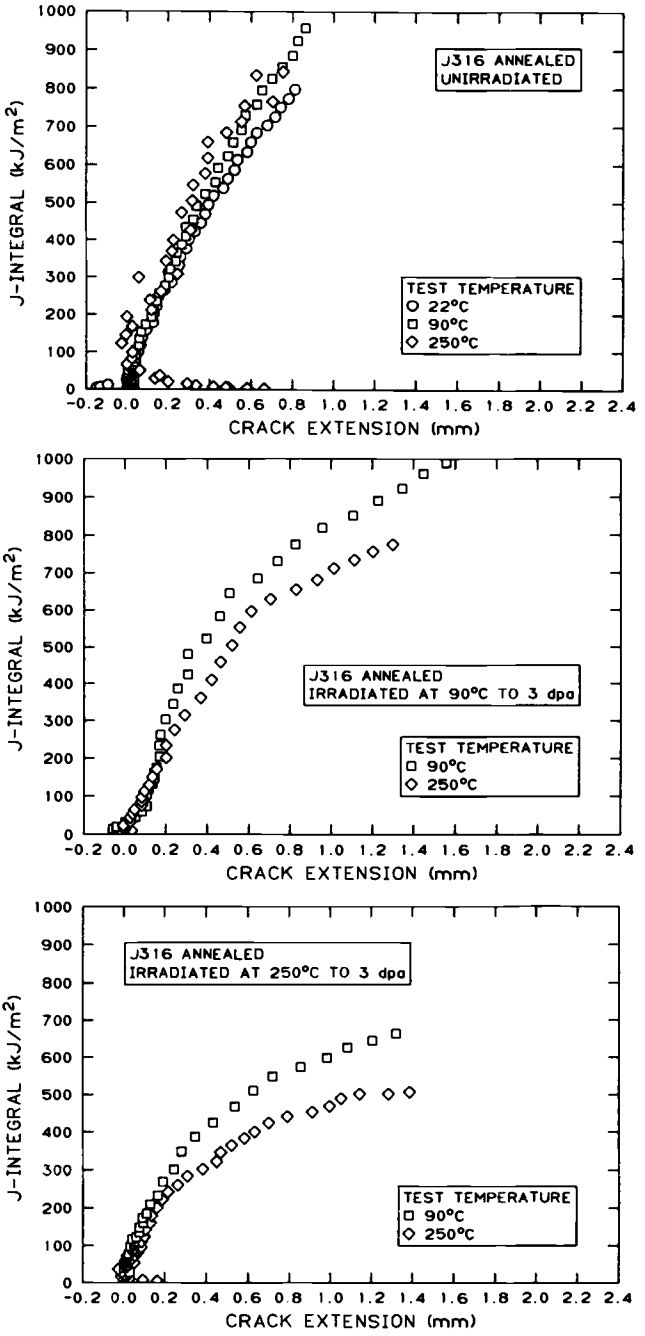


FIG. 10--J-R curves for annealed J316 material in the unirradiated condition (top), and after irradiation at 90°C (middle) and 250°C (bottom).

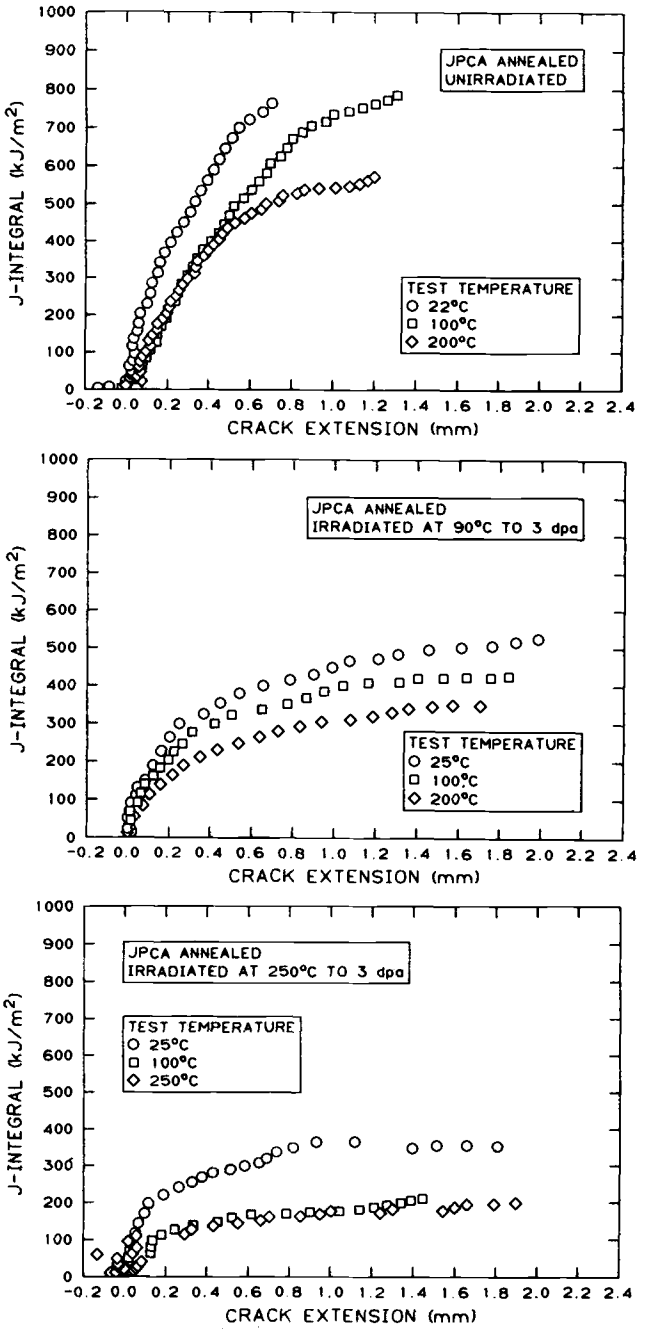


FIG. 11--J-R curves for annealed JPCA material in the unirradiated condition (top), and after irradiation at 90°C (middle) and 250°C (bottom).

Comparison with Literature Data

There are surprisingly little data available for comparison with these results. These stainless steel alloys are very tough, and so the fracture toughness is not usually a concern. Odette and Lucas [10-12], Tavassoli [13], and Boutard [14] have recently surveyed the available data for the effects of low temperature irradiation (<400°C) on the mechanical properties, including the fracture toughness, of austenitic stainless steels. There are very little data that are directly comparable to the present work, but the overall trend of the data shows that although irradiation reduces the fracture toughness, it still remains high, in agreement with the present results.

Several researchers have reported fracture toughness tests of unirradiated austenitic stainless steels, including 304 and several variants of 316 and similar steels [15-21]. At room temperature, the fracture toughness values reported for 316L range from about 200 to 400 kJ/m^2 [15,16] to well over 1000 kJ/m^2 [17-19]. Toughnesses of 304 are generally greater [15,20]. The fracture toughness decreases at higher test temperatures [18,19,21]. Irradiation to low doses has little effect on the toughness [16,20,21] but does degrade the toughness at higher doses [15,19,20].

A trend line of toughness versus irradiation dose is shown in Fig. 12, adapted from the review article by Lucas [22]. This represents data for a variety of wrought materials irradiated at temperatures from 290 to 430°C, slightly higher temperatures than in the present work. After a rapid initial decrease, the minimum toughness values (note that K_J values are shown) approach 50 MPa$\sqrt{m}$ for doses beyond 10 dpa. Also shown are data from Sindelar et al. [20] for a 1950s-vintage type 304 stainless steel irradiated at 100 to 155°C to doses up to 2 dpa. The data from the present work fall into two groups. Results from the higher irradiation temperature (250 to 300°C) are consistent with the published data represented by the trend line which indicates toughness values in the range of 200 to 250 MPa$\sqrt{m}$ for doses up to 3 dpa. For the lower irradiation temperature (60 to 125°C) the reduction in fracture toughness is significantly less with the data falling well above the trend line. This is likely the result of a different microstructural response to irradiation, and a reduced level of irradiation hardening for the same dose as compared to higher temperature irradiation. The data of Sindelar et al. [20] fall well below the present data for low temperature irradiation, likely reflecting the greater sensitivity to irradiation damage of the 1950s-vintage heat of type 304 stainless steel.

The fracture toughness of welds in austenitic stainless steels has also been examined [15,16,18-20,23,24]. In general, the welds show lower initial toughnesses and a greater response to irradiation than do the base metals.

Jitsukawa has reported fracture toughness measurements on the JPCA material [25]. In the solution-annealed condition the toughness ranged from 770 to 1000 kJ/m^2. It decreased to 300 to 340 kJ/m^2 after 15% cold work and to 165 to 175 kJ/m^2 after 40% cold work. These values are similar to the present results.

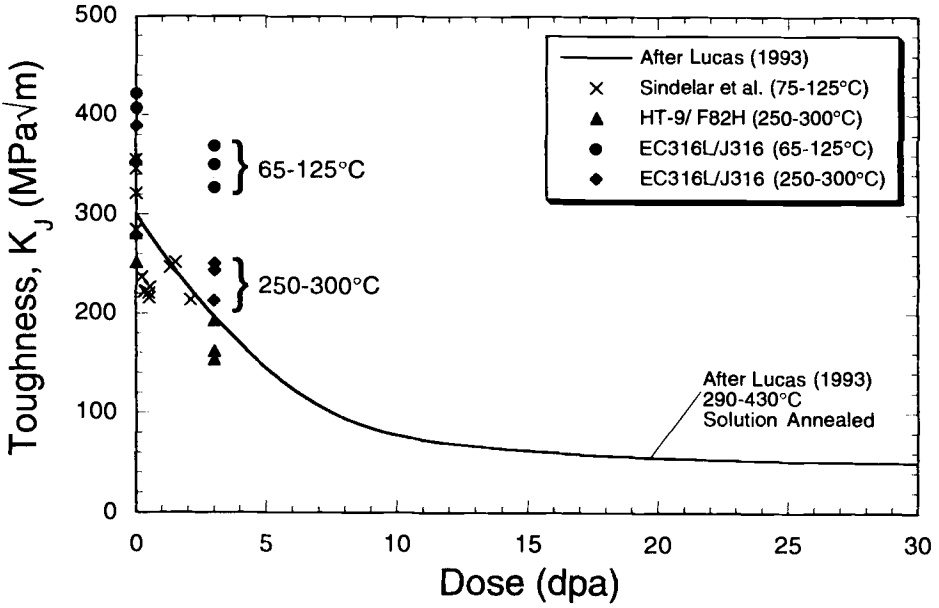


FIG. 12--Trend line of fracture toughness versus irradiation dose in dpa, adapted from Lucas [22], for a range of austenitic stainless steels, irradiation temperatures, and test temperatures. Also shown are data from the present work and results from Sindelar et al. [20] for comparison.

Huang and Hamilton [26] have summarized their work on the effects of irradiation on the toughness of HT-9. The limited results for unirradiated material show toughness values that decrease from 100 to about 50 kJ/m^2 as the test temperature increases from 24 to 316°C. After irradiation at 55°C to 5 dpa, the toughness decreases to about 50 kJ/m^2 for test temperatures from 25 to 205°C. This is very different from the present results, which show fracture toughnesses of over 400 kJ/m^2 for unirradiated material tested from 25 to 250°C. The apparent reason for the difference is the different heat treatments used in the two investigations, as reflected in the very different yield strengths. The material tested by Huang was tempered at 750°C for 1 h, while the present work used 780°C for 2.5 h. As a result, the yield strength at room temperature for Huang's material was 621 MPa as compared to the present 476 MPa (see Table 6). The lower yield strength agrees with the higher toughnesses. After irradiation at 90°C to 3 dpa, the yield strength at 90°C for the material in the present work rises to 903 MPa, similar to the value reported by Huang of 954 MPa for material irradiated to 5 dpa at 55°C and tested at 93°C, but the toughness of the present material is still much higher (283 kJ/m^2) than Huang observed (52 kJ/m^2 at 93°C).

The toughnesses for unirradiated HT-9 reported by Huang are similar to data from Hawthorne [27]. Other data from Hawthorne et al. [28] generated with precracked Charpy specimens show higher toughnesses of about 230 MPa$\sqrt{m}$ for specimens in the upper-shelf (i.e. higher toughness) regime. These latter data also show that irradiation at 93°C is much more damaging than irradiation at 288 or 300°C. The present work shows that irradiation at 250°C is more damaging than irradiation at 90°C for austenitic alloys. The present results suggest this is also true for the ferritic alloys in this study, but the data are too sparse to provide a definitive answer.

The fracture toughness of F82H has been measured by Li et al. [29]. They reported a value of about 430 kJ/m^2 at room temperature. This specimen had a narrow slit rather than a fatigue precrack. With a conventional precrack, the fracture toughness was lower, about 280 kJ/m^2 [30]. Although the heat treatments are slightly different, these values are similar to the limited data from the present work.

Comparison of Results with ASTM Validity Requirements

It should be pointed out that nearly all of the J-R data generated with this small disk compact specimen do not satisfy all of the validity requirements of the ASTM standards, and so, these data are not valid. ASTM E 1152-87 sets three limits based on the specimen size. The maximum J-integral measurement capacity is given by the smaller of

$$J_{max} = b\sigma_y/20 \text{ , or} \quad (1)$$

$$J_{max} = B\sigma_y/20 \text{ ,} \quad (2)$$

where b = initial ligament size,
B = specimen thickness, and
σ_y = flow stress (average of yield and ultimate tensile stresses).

If the crack length to specimen width ratio (a/W) is 0.5, these limits are identical, as b will equal B for this specimen, in this case. For nearly all of the data, the measured J-integral values greatly exceed this limit. Only the lowest toughness materials have J-integral values low enough to satisfy these conditions. However, there is another even more limiting condition. The maximum allowable crack extension is limited to 0.1b. For an initial a/W value of 0.5, which was the intent, the resultant maximum allowable crack extension is only 0.46 mm, well short of the second exclusion line at 1.5 mm of crack extension. If the initial crack length is longer, as was nearly always the case, even less crack extension is allowed. Examination of the J-R curves in Figs. 9 to 11 shows that, for tough materials, these crack extensions are still on the blunting line, and stable tearing has not even begun to occur. Even for lower toughness conditions, i.e. annealed JPCA material

irradiated at 250°C (bottom of Fig. 11), only a few of the data points are valid, and the bulk of the J-R curve is beyond the limit of validity. The values given in Tables 2 to 6 have been generated by using all the data between the first and second exclusion lines to determine the curve fit for calculation of J_Q, even though these data are not valid according to ASTM E 1152-87.

It must be emphasized that the J-R data, despite being invalid according to ASTM E 1152, are not incorrect. The size limitations imposed are conservative, and the J-integral values are quite likely still true measures of the materials' toughness, as long as the limits are not exceeded by too great a margin. Previous work [7] has shown that the 0.18T DC(T) specimens gave results similar to data from 12.7-mm-thick compact [0.5T C(T)] specimens for the US316 material, and Jitsukawa [25] found good agreement between data generated with the 0.18T DC(T) specimen and 10-mm-thick compact [0.4T C(T)] specimens for 15% cold-worked JPCA material. The J-R curves are applicable to structures of the same thickness as the specimens. Additional work is needed to provide more information about specimen size effects for these tough materials.

The J-R curves are of great value in elucidating the materials' responses to irradiation. The J-R curves show how these materials are embrittled by irradiation as a function of irradiation temperature and damage level. They also show which materials are most resistant to embrittlement, and give an indication of the rate at which embrittlement will occur for the present irradiation and material conditions. These are very useful pieces of information for evaluating candidate structural materials for ITER applications.

CONCLUSIONS

Specimens of several austenitic stainless steels and two ferritic-martensitic steels have been irradiated in HFIR to about 3 dpa at nominal irradiation temperatures of 90 or 250°C. For the austenitic stainless steels, irradiation reduces the fracture toughness, and irradiation at 250°C is more damaging than irradiation at 90°C. The fracture toughness decreases with increasing test temperature, for all the austenitic materials. The annealed materials have higher toughnesses than the cold-worked materials. The toughness of the cold-worked materials is still high, with the exception of the US316 material. The welds also have high toughnesses. For the ferritic-martensitic materials, the specimens irradiated at 250°C and tested at room temperature fail in an unstable manner. The F82H has a higher toughness than the HT-9 alloy.

ACKNOWLEDGMENTS

This research was sponsored by the Office of Fusion Energy, U.S. Department of Energy, under Contract DE-AC05-84OR21400 with Lockheed Martin Energy Systems. The fracture toughness testing was performed by Ronald L. Swain. We appreciate helpful

reviews of the manuscript by Fahmy M. Haggag and Philip J. Maziasz. The manuscript was prepared by Julia L. Bishop.

REFERENCES

[1] Longest, A. W., Heatherly, D. W., Thoms, K. R., and Corum, J. E., "Design and Fabrication of HFIR-MFE-JP Target Irradiation Capsules," in *Fusion Reactor Materials Semiannual Progress Report for Period Ending March 31, 1991*, DOE/ER-0313/10, p. 3.

[2] Longest, A. W., Heatherly, D. W., Wolfe, J. E., Thoms, K. R., and Corum, J. E., "Fabrication and Irradiation of HFIR-MFE-JP-17, -18, and -19 Target Irradiation Capsules," in *Fusion Reactor Materials Semiannual Progress Report for Period Ending September 30, 1991*, DOE/ER-0313/11, p. 30.

[3] Longest, A. W., Heatherly, D. W., Thoms, K. and Corum, J. E., "Fabrication and Irradiation of HFIR-MFE-JP-17, -18, and -19 Target Irradiation Capsules," in *Fusion Reactor Materials Semiannual Progress Report for Period Ending March 31, 1992*, DOE/ER-0313/12, p. 24.

[4] Alexander, D. J., Pawel, J. E., Grossbeck, M. L., and Rowcliffe, A. F., "Fracture Toughness of Irradiated Candidate Materials for ITER First Wall/Blanket Structures: Preliminary Results," *Fusion Reactor Materials Semiannual Progress Report for Period Ending March 31, 1992*, DOE/ER-0313/14, p. 277.

[5] Pawel, J. E., Alexander, D. J., Grossbeck, M. L., Longest, A. W., Rowcliffe, A. F., Lucas, G. E., Jitsukawa, S., Hishinuma, A., and Shiba, K., "Fracture Toughness of Candidate Materials for ITER First Wall, Blanket, and Shield Structures," in *Fusion Reactor Materials Semiannual Progress Report for Period Ending September 30, 1993*, DOE/ER-0313/15, p. 173.

[6] Alexander, D. J., "Fracture Toughness Measurements with Subsize Disk Compact Specimens," in *Fusion Reactor Materials Semiannual Progress Report for Period Ending March 31, 1992*, DOE/ER-0313/12, p. 35.

[7] Alexander, D. J., "Fracture Toughness Measurements with Subsize Disk Compact Specimens," in *Small Specimen Test Techniques Applied to Nuclear Reactor Vessel Thermal Annealing and Plant Life Extension, ASTM STP 1204*, W. R. Corwin, F. M. Haggag, and W. L. Server, Eds., American Society for Testing and Materials, Philadelphia, 1993, p. 130.

[8] Elliot, C., Enmark, M., Lucas, G. E., and Odette, G. R., "Development of Disc Compact Specimens and Test Techniques for HFIR Irradiations," in *Fusion Reactor Materials Semiannual Progress Report for Period Ending September 30, 1990,* DOE/ER-0313/9, p. 7.

[9] Nanstad, R. K., Alexander, D. J., Swain, R. L., Hutton, J. T., and Thomas, D. L., "A Computer-Controlled Automated Test System for Fatigue and Fracture Testing," in *Applications of Automation Technology to Fatigue and Fracture Testing, ASTM STP 1092,* A. A. Braun, N. E. Ashbaugh, and F. M. Smith, Eds., American Society for Testing and Materials, Philadelphia, 1990, p. 7.

[10] Odette, G. R., and Lucas, G. E., "Effects of Low Temperature Neutron Irradiation on the Properties of 300 Series Stainless Steel," in *Fusion Reactor Materials Semiannual Progress Report for Period Ending March 31, 1989,* DOE/ER-0313/6, pp. 313-35.

[11] Odette, G. R., and Lucas, G. E., "The Effects of Intermediate Temperature Irradiation on the Mechanical Behavior of 300-Series Austenitic Stainless Steels," *Journal of Nuclear Materials*, Vol. 179-81, 1991, pp. 572-76.

[12] Odette, G. R., and Lucas, G. E., "Deformation and Fracture in Irradiated Austenitic Stainless Steel," *Journal of Nuclear Materials*, Vol. 191-4, 1992, pp. 59-57.

[13] Tavassoli, A. A., *Assessment of Austenitic Stainless Steels*, N.T. SRMA 94-2061, F.A. 3591-ITER, CEA, CEN-Saclay, 91191 Gif Sur Yvette, France, June 1994.

[14] Boutard, J. L. "Structural Materials Requirements and Related R&D for ITER Plasma-Facing Components," *Journal of Nuclear Materials*, Vol. 179-81, 1991, pp. 1179-84.

[15] Dufresne, J., Henry, B., and Larsson, M., "Fracture Toughness of Irradiated 304 and 316L Stainless Steels," in *Effects of Radiation on Structural Materials, ASTM STP 683*, J. A. Sprague and D. Kramer, Eds., American Society for Testing and Materials, Philadelphia, 1979, pp. 511-28.

[16] Bernard, J., and Verzeletti, G., "Elasto-Plastic Fracture Mechanics Characterization of Type 316H Irradiated Stainless Steel up to 1 dpa," in *Effects of Radiation on Materials" Twelfth International Symposium, ASTM STP 870*, F. A. Garner and J. S. Perrin, Eds., American Society for Testing and Materials, Philadelphia, 1985, pp. 619-41.

[17] Balladon, P., Meritier, T., and Rabbe, P., "Influence of Microstructure on the Ductile Rupture Mechanisms of a 316L Steel at Room and Elevated Temperatures," in *Fracture Mechanics: Fourteenth Symposium - Vol. II: Testing and Applications, ASTM STP 791*, J. C. Lewis and G. Sines, Eds., American Society for Testing and Materials, Philadelphia, 1983, Vol. II, pp. 496-513.

[18] Tavassoli, A. A., "Effect of Neutron Irradiation on Mechanical Properties of Permanent Near Core Structures," in *Effects of Radiation on Materials: 14th International Symposium (Vol. II), ASTM STP 1046*, N. H. Packan, R. E. Stoller, and A. S. Kumar, Eds., American Society for Testing and Materials, Philadelphia, 1990, Vol. II, pp. 684-99.

[19] Joseffsson, B., and Bergenlid, U., "Tensile, Low Cycle Fatigue, and Fracture Toughness Behavior of Type 316L Steel Irradiated to 0.3 dpa," *Journal of Nuclear Materials*, Vol. 212-15, 1994, pp. 525-29.

[20] Sindelar, R. L., Caskey, G. R., Thomas, J. K., Hawthorne, J. R., Hiser, A. L., Lott, R. A., Begley, J. A., and Shogan, R. P., "Mechanical Properties of 1950s Vintage Type 304 Stainless Steel Weldment Components, After Low Temperature Irradiation," in *Effects of Radiation on Materials: 16th International Symposium, ASTM STP 1175*, A. S. Kumar, D. S. Gelles, R. K. Nanstad, and E. A. Little, Eds., American Society for Testing and Materials, Philadelphia 1993, pp. 714-46.

[21] de Vries, M. I., "Fatigue Crack Growth and Fracture Toughness Properties of Low Fluence Neutron Irradiated Type 316 and Type 304 Stainless Steels," in *Influence of Radiation on Material Properties: 13th International Symposium (Part II), ASTM STP 956*, F. A. Garner, C. M. Henager, Jr., and N. Igata, Eds., American Society for Testing and Materials, Philadelphia, 1987, Vol. II, pp. 174-90.

[22] Lucas, G. E., "The Evolution of Mechanical Property Change in Irradiated Austenitic Stainless Steel," *Journal of Nuclear Materials*, Vol. 206, 1993, pp. 287-305.

[23] Mills, W. J., "Fracture Toughness of Stainless Steel Welds," in *Fracture Mechanics: Nineteenth Symposium, ASTM STP 969*, T. A. Cruse, Ed., American Society for Testing and Materials, Philadelphia, 1988, pp. 330-55.

[24] Mills, W. J., "Fracture Toughness of Irradiated Stainless Steel Alloys," *Nuclear Technology*, Vol. 82, 1988, pp. 290-303.

[25] Jitsukawa, S., "Comparison of Elastic-Plastic Fracture Toughness of Irradiated and Cold-Worked JPCA Using Miniaturized RCT Specimens," in *Miniaturized Specimens for Testing Irradiated Materials, IEA International Symposium*, P. Jung and H. Ullmaier, Eds., Forschungszentrum Julich GmBH, D-52425, Julich, Germany, 1995, pp. 117-22.

[26] Huang, F. H., and Hamilton, M. L., "The Fracture Toughness Data Base for HT-9 and Modified 9Cr-1Mo Irradiated in Several Reactors up to ~100 dpa," in *Fusion Reactor Materials Semiannual Progress Report for Period Ending March 31, 1989*, DOE/ER-0313/6, pp. 161-75.

[27] Hawthorne, J. R., "Fracture Resistance Testing of Alloy HT-9 in the Unirradiated Condition," in *Alloy Development for Irradiation Performance Quarterly Progress Report for Period Ending December 31, 1980*, DOE/ER-0045/5, pp. 122-41.

[28] Hawthorne, J. R., Reed, J. R., and Sprague, J. A., "Fracture Resistance of Two Ferritic Stainless Steels After Intermediate Temperature Irradiation," in *Effects of Radiation on Materials: Twelfth International Symposium, ASTM STP 870*, F. A. Garner and J. S. Perrin, Eds., American Society for Testing and Materials, Philadelphia, 1985, pp. 580-604.

[29] Li, H., Jones, R. H., Hirth, J. P., and Gelles, D. S., "Effect of Loading Mode on the Fracture Toughness of a Reduced Activation Ferritic/Martensitic Stainless Steel," *Journal of Nuclear Materials*, Vol. 212-15, 1994, pp. 741-45.

[30] Li, H., Jones, R. H., Hirth, J. P., and Gelles, D. S., "Dependence of Mode I and Mixed Mode I/III Fracture Toughness on Temperature for a Ferritic/Martensitic Stainless Steel," in *Fusion Materials Semiannual Progress Report for Period Ending September 30, 1994*, DOE/ER-0303/17, pp. 99-109.

Kiyoyuki Shiba [1], Tomotsugu Sawai [1], Shiro Jitsukawa [1], Akimichi Hishinuma [1] and Janet E. Pawel [2]

IRRADIATION BEHAVIOR OF WELDMENTS OF AUSTENITIC STAINLESS STEEL MADE BY VARIOUS WELDING TECHNIQUES

REFERENCE: Shiba, K., Sawai, T., Jitsukawa, S., Hishinuma, A., and Pawel, J. E., **"Irradiation Behavior of Weldments of Austenitic Stainless Steel Made by Various Welding Techniques,"** *Effects of Radiation on Materials: 17th International Symposium, ASTM STP 1270,* David S. Gelles, Randy K. Nanstad, Arvind S. Kumar, and Edward A. Little, Eds., American Society for Testing and Materials, 1996.

ABSTRACT: An austenitic stainless steel, 316F, irradiated in the High Flux Isotope Reactor to doses of about 8 to 33 dpa at 400° and 500°C was investigated. Electron beam (EB) welding and metal inert gas (MIG) welding techniques were used to make weldment specimens. Weldment specimens were made from their weld metal or weld joint (including heat affected zone) regions of the weldments. Base metal was also studied for comparison. Microstructures of these specimens were observed by TEM.

Tensile tests were carried out at the nominal irradiation temperature in vacuum. Solution annealed 316F showed the large irradiation hardening at 400°C, while the change in yield stress observed at 500°C was not so large. Weldments specimens had the same temperature and dose dependence as the base metal. The differences between EB and MIG after irradiation were small, compared to the differences before irradiation, except for the slight less ductility of MIG weldments. The defect microstructures of weldments were the same as base metal.

KEYWORDS: Austenitic stainless steel, Weldments, HFIR irradiation, Tensile properties, Electron beam welding, Metal inert gas welding

Austenitic stainless steel is one of the candidate materials for nuclear fusion reactor applications. Many studies on irradiation behavior of austenitic stainless steels have been reported, however, information concerning the effect of radiation on weldments is limited

[1] Engineer, senior engineer, senior engineer and group leader, respectively, Department of Materials Science and Engineering, Japan Atomic Energy Research Institute, Tokai-mura Ibaraki-ken 319-11, Japan

[2] Research staff member, Metals and Ceramics Division, Oak Ridge National Laboratory, P.O. Box 2008, Oak Ridge, TN 37831-6376, USA.

Copyright© 1996 by ASTM International www.astm.org

[1]. Because the weldments will be exposed to a neutron environment as part of the structural components of the first wall and blanket, the irradiation response of weldments will be a critical factor. The microstructural segregation that occurs during solidification after welding could cause a change in the irradiation response of the weldment [2,3]. The weldments themselves have several structurally distinct regions such as heat affected zones and weld metal that could show a variation in properties. Environmental effects also have to be considered. While titanium modified type 316 austenitic stainless steels (PCAs) have been proposed for fusion applications, these materials are not suitable for welding. Also, because the PCAs were developed for use in helium cooled reactors, they do not have good corrosion resistance in water. In addition to these factors, the overall weldability of the candidate materials needs to be improved. In the present study, the irradiation behavior of several different weldments of a modified type 316 austenitic stainless steel was examined.

EXPERIMENTAL PROCEDURE

The alloy investigated was austenitic stainless steel (316F) in solution annealed and cold worked conditions. All material was solution annealed for 15 minutes at 1060°C. Some of the material was then 20% cold worked. The chemical composition of this alloy is given in TABLE 1. This alloy is a modified type 316 stainless steel for fusion reactor applications. The main feature of the chemical composition is the low level of impurities such as Si, P, S. Both P and S were reduced to improve the weldability. Carbon is also at a low level to reduce potential for sensitization as a result of welding.

Electron beam (EB) welding and metal inert gas (MIG) welding techniques were used to make weldments. EB welding was carried out without filler metal. The chemical composition of filler metal for MIG welding is listed in TABLE 1. Welding conditions of both techniques are listed in TABLE 2. In addition, some modified techniques were used. Filler metal was used to produce delta ferrite in the weld metal for EB (designed 5% and 10% δF EB). This delta ferrite in the weld metal provides higher strength and better toughness in the weldments. The pulse MIG welding was used to reduce the thermal input. The modified weldments were irradiated primarily for swelling measurements.

Three types of specimens, base metal (BM), weld metal (WM) and weld joint (WJ), were prepared from the weldments. These specimens were fabricated from weldments as shown in FIG. 1. The fusion line is located at the middle of specimen and the width of the weld metal region is 2 - 3 mm and 5 - 10 mm from the center of the weld metal for the EB and MIG, respectively.

These steels were fabricated as SS-3 type sheet tensile specimens which are 25.4 mm in length, 4.95 mm in width, and 0.76 mm in thickness. The gage section of this specimen was 7.62 mm in length and 1.52 mm in width.

These tensile specimens were irradiated in the High Flux Isotope Reactor (HFIR) target position capsules HFIR-MFE-JP-10, -11, -13, -16 and -14 at 400° and 500°C. The details of irradiation were given elsewhere [4]. The peak fluence of fast neutrons (E > 1 MeV) was about 2.0 x 10^{26} neutrons/m^2 for JP-10, -11, -13 and -16, and about 3.8 x 10^{26} neutrons/m^2 for JP-14. These fluences correspond to 18 and 34 dpa in atom

TABLE 1--Chemical compositions of 316F and filler metals for weldments

Alloy	C	Si	Mn	P	S	Cr	Ni	Mo	N	Fe
316F	0.038	0.04	0.23	<0.003	0.002	16.8	14.0	2.3	0.011	bal.
Filler										
MIG	0.031	0.32	1.84	0.003	0.005	17.1	14.1	2.6	0.023	bal.
5% δF	0.033	0.17	0.68	0.003	0.002	20.6	9.24	2.5	-	bal.
10% δF	0.029	0.17	0.67	0.003	0.002	23.1	6.52	2.5	-	bal.

displacement damage. The neutron flux varies in the axial direction of capsule, so that the displacement damage of each specimen varied, depending on its position relative to the reactor centerline. The analyses of the flux monitors are not completed, therefore the irradiation information used in this paper is approximate. Helium production due to the two step reaction of nickel was also calculated [5].

An Instron universal testing machine was used for tensile testing. Tensile testing was carried out at the nominal irradiation temperature in vacuum for each specimen. The strain rate was $1x10^{-3}$ /s. The 0.2% proof stress (YS), ultimate tensile stress (UTS), uniform elongation (Eu) and total elongation (Et) were calculated from the engineering charts. Optical microscopy was performed for some specimens to measure the fracture surface area to obtain the reduction of area (RA).

Microstructural observation by TEM was also performed on TEM disks irradiated in the same capsules.

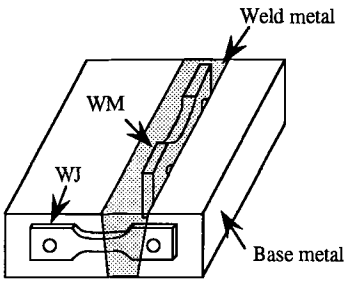


FIG. 1--Sampling location of weldments specimens (WM and WJ) from weld joint.

TABLE 2--Welding conditions of 316F EB and MIG weldments

	EB (standard, 5 & 10% δF)	MIG
Voltage	90 kV	11 V DC
Beam current	80 mA	200 A
Traveling speed	400 mm/min with φ3mm circle vibration	80 -100 mm/min
Pre-heat	none	none
Shield gas	in vacuum	Argon

Results and discussions

The tensile properties of unirradiated and irradiated materials are shown in TABLE 3.

Tensile Properties of Base Metal

316F showed large irradiation hardening at 400°C. The elongation, especially the uniform elongation, was low. True stress-strain analysis showed almost no work hardening ability. This means that the specimen hardened to a maximum, almost saturation, so that local deformation occurred immediately after yielding. however, the RA value of the specimen irradiated to 18 dpa at this temperature was not cruel. Work hardening continues after the start of necking until fracture [6], and the engineering

elongation after the occurrence of necking can not reflect ductility correctly. RA value could be a better index of ductility than elongation, because it includes the information during necking. Therefore, it seems that 316F retains relatively high ductility, in spite of the large irradiation hardening. The low elongation at 400°C was caused by high yield strength and local deformation.

TABLE 3--Tensile results of 316F weldments

Alloy			Temp	Irradiation		Tensile properties					
				Dose	He	YS	UTS	Eu	Et	RA	FS
			℃	dpa	appm	MPa	MPa	%	%	%	MPa
SA	EB	BM	400	0	0	169	442	41.3	51.0	86.4	1415
				8	310	625	631	0.5	8.5	N/A	N/A
				18	970	644	672	3.2	10.7	52.7	936
				33	2090	676	702	1.3	5.7	N/A	N/A
			500	0	0	242	409	26.3	37.7	86.1	1407
				8	310	295	433	20.8	25.8	51.4	583
				18	970	327	444	15.0	17.8	22.4	422
		WM	400	0	0	222	393	26.0	24.3	89.0	1762
				10	440	591	593	0.6	11.2	N/A	N/A
				18	970	661	665	1.3	7.3	54.4	965
				33	2090	607	665	1.8	7.0	N/A	N/A
				33	2090	594	665	1.3	4.7	N/A	N/A
			500	0	0	203	394	30.7	27.7	76.0	845
				8	310	213	348	20.5	27.7	56.5	481
				18	970	311	421	15.7	20.9	44.0	584
		WJ	400	0	0	220	378	16.3	25.0	90.1	1942
				8	310	554	558	1.0	7.3	71.6	1213
				18	970	618	632	1.3	10.3	68.6	892
				33	2090	638	646	0.8	6.5	N/A	N/A
			500	0	0	217	371	15.3	25.0	93.2	2336
				8	310	280	374	7.8	15.9	67.0	525
				18	970	300	376	7.7	13.7	72.7	984
SA	MIG	WM	400	0	0	389	440	10.3	18.0	82.0	1424
				8	310	540	581	2.8	10.2	50.2	826
			500	0	0	344	410	9.0	15.7	77.2	984
				8	310	316	428	11.3	17.8	60.3	657
		WJ	400	0	0	376	431	7.3	14.0	83.2	1491
				8	310	561	594	1.8	6.8	47.9	843
			500	0	0	372	445	12.0	19.0	78.9	1273
				8	310	294	400	9.8	15.0	54.9	600
CW	EB	BM	400	0	0	543	567	2.0	11.3	84.8	2118
				16	870	760	785	0.7	7.8	56.7	1073
			500	0	0	546	587	4.3	12.7	85.3	1683
				18	970	462	558	8.7	14.6	N/A	N/A
		WJ	400	0	0	231	354	8.3	17.0	90.3	1745
				16	870	625	631	1.5	9.5	68.0	1076
			500	0	0	227	358	8.7	16.3	88.2	1686
				18	970	414	459	3.2	9.0	N/A	N/A
SA	5% δF	EB	WJ	400	0	0	347	412	12.3	21.0	95.4	1679
					12	550	604	605	0.3	8.6	N/A	N/A

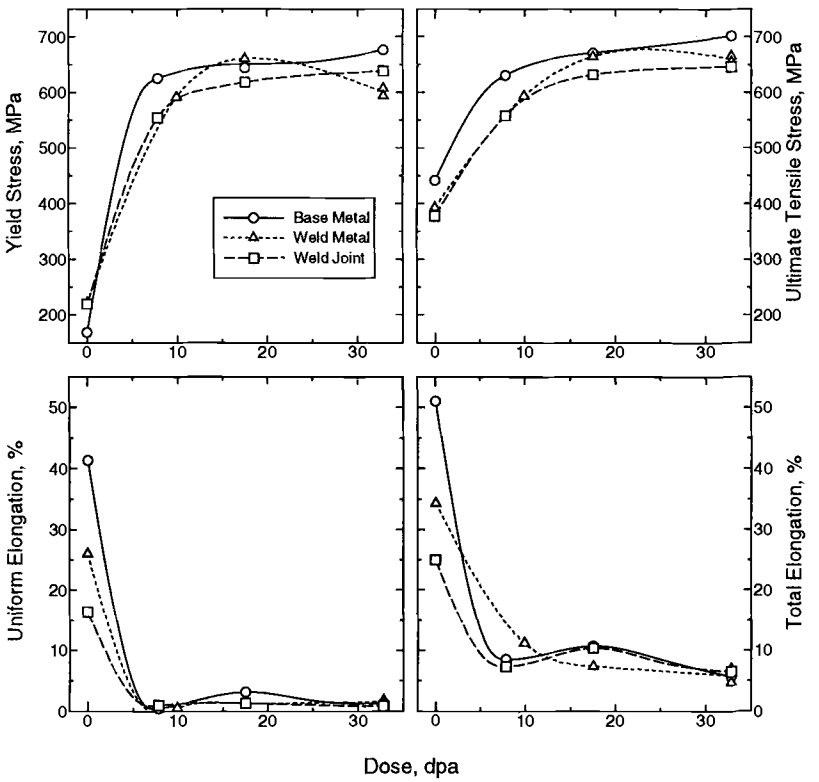


FIG. 2--Tensile properties of 316F base metal and EB weldments irradiated in HFIR target position at 400°C as a function of fluence.

FIG. 2 shows the 400°C tensile properties as a function of fluence. Both strength and elongation were constant in the range 8 to 33 dpa. It seems that the irradiation hardening occurred at a relatively early period of irradiation and any effect of precipitates caused by aging is unlikely.

The increase of strength was not very large at 500°C, but the elongation was much less than half that of the unirradiated specimen. The reduction of in the RA value at 18 dpa was particularly large. 316F showed constant strength between 8 and 18 dpa, but at 18 dpa specimens has less elongation and RA.

Tensile Properties of Weldments

Solution Annealed Electron Beam welded material

As with the BM, 316F WM and WJ showed high irradiation hardening at 400°C. The uniform elongation was quite low, and no work hardening ability was observed,

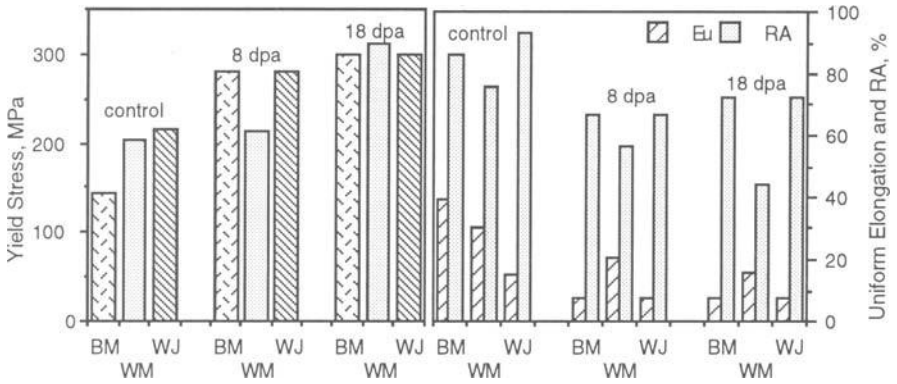


FIG. 3--Yield stress, uniform elongation (Eu) and reduction of area (RA) of EB weldments of 316F irradiated in HFIR target position at 500°C.

implying that they were hardened almost to the saturation level. However, the strength increased slightly with fluence after 8 dpa.

The irradiation hardening at 500°C was small. Both strength and elongation of the weld joint are the same as the base metal after irradiation, as shown in FIG. 3.

EB weldments showed similar properties to BM in all test conditions in general. The weldments have higher strength and lower elongation before irradiation, because of residual stress incurred during welding, but the difference before irradiation disappeared after irradiation. The elongation of WJ specimens were lower than BM and WM, but this is caused by local deformation due to the non-uniform structure of the weld joint specimen. The RA value of weldments were the same as BM or higher than BM, and no special weakness caused by welding was observed. In particular, the RA value of WJ specimens were good. The higher ductility of EB weldments over BM has been seen in other irradiation experiments [1,7,9] and fracture toughness of JPCA EB weldments is high [10].

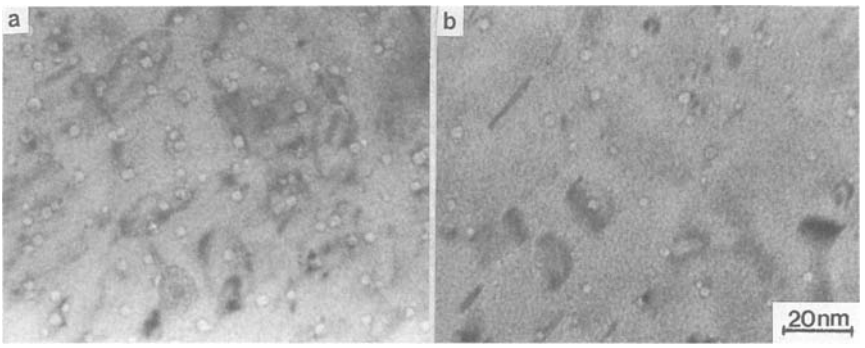


FIG. 4--Cavities in 316F solution annealed electron beam weldment after irradiation in HFIR target position to 18 dpa. (a) base metal at 400°C and (b) weld metal at 400°C.

The microstructures of BM and EB WM irradiated at 400°C are shown in FIG. 4. Both BM and EB WM contain helium bubbles, dislocation loops and tiny black-dot type defect clusters. The size of bubbles are about 3 - 4 nm and those of loops are about 20 - 30 nm, further quantitative analysis is in progress [8]. A solidification structure was observed in EB and MIG weld metals specimens by TEM, but the microstructural evolution in initially or finally solidified area [3] showed no significant difference at this temperature. As shown in FIG. 6, immersion density measurements showed a slight difference in swelling of WM irradiated to 29 dpa at 400°C with the swelling of WM being higher than the BM. The previous research on the swelling behavior of welded material reported some defferences in microstructural evolution between base metal and weld material by HVEM irradiation [2,3]. That was caused by the non-uniform composition due to welding. The HFIR irradiation produces much helium during irradiation, because of its high thermal flux. The high concentration of helium generates high density of small bubbles in the relatively early stage of irradiation and this helium bubble formation dose not depend on the composition of material. This high He/dpa rate of HFIR irradiation much affects to the microstructural evolution rather than the compositional homogeneity.

Solution Annealed MIG welded material

MIG weldments were irradiated at 400° and 500°C. MIG weldments had higher strength and lower elongation than EB weldments before irradiation. No particular difference in strength between EB and MIG was observed after irradiation at 400°C, but the uniform elongation of MIG weldments were higher than EB. However, the RA values of the MIG weldments were lower than those of the EB. MIG WM and WJ had the same properties at both 400° and 500°C. The MIG WJ specimen has a wider weld metal region and HAZ than the EB WJ specimen. The elongation of the EB WJ specimens were small because of local deformation in the narrow WM region. Therefore, the ductility of WJ specimens can not be compared by elongation simply. RA value is better than elongation for this ductility comparison. The RA of EB WJ was better than MIG at 400°C, but EB has less advantage at 500°C as shown in FIG. 5.

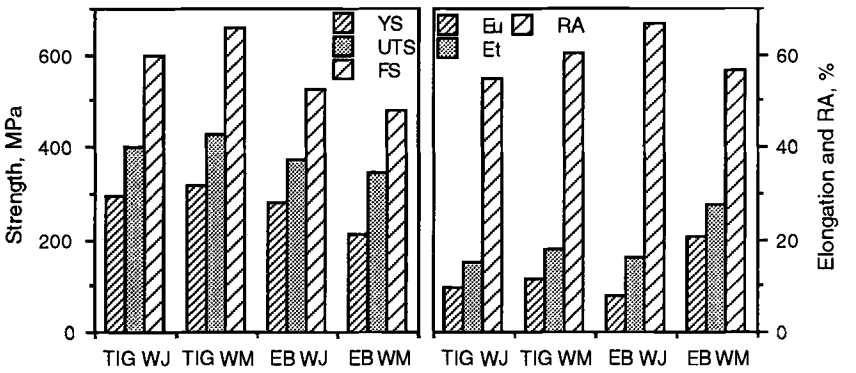


FIG. 5--The comparison of MIG weldments and EB weldments irradiated to a dose of 8 dpa at 500°C in HFIR target position

Cold Worked Electron Beam welded materials

The yield strength of cold worked BM was decreased after irradiation with the recovery of elongation at 500°C, however, the yield strength of CW specimen was still higher than solution annealed specimens. It means that the influence of cold work before irradiation is still apparent after irradiation. This decrease of yield strength and the recovery of elongation was caused by the recovery of cold worked structure due to the enhanced aging effect. The aging may cause segregation and precipitation, though, no precipitates was observed at any temperature. 316F has low levels of impurities such as Si, P, S, but we could not confirm the effect of impurities on the microstructural evolution.

The tensile properties of both SA WJ and CW WJ were the same at 400°C. The strength of CW WJ was lower than CW BM, but it was higher than SA BM. At 500°C, the CW WJ specimen broke in the weld metal region. This was predicted because the weld metal region of the cold worked material would be expected to have strength similar to the SA WJ (EB) material. Because the CW WJ had a yield strength about 100 MPa higher than the SA WJ (EB), the weakest section of the CW WJ specimen was in the weld metal region.

Other weldments

The presence of delta-ferrite in the weld metal gives higher strength and toughness to weldments in the unirradiated condition. Some weldments including delta-ferrite were irradiated and the swelling behavior of these specimens was investigated. FIG. 6 shows the swelling by precision density measurement. At 400°C, swelling decreased with the increase of delta-ferrite in the weld metal, while the opposite tendency was seen at 500°C. No measurable swelling was obtained for all specimens irradiated to 17 dpa at both 400° and 500°C . One specimen including 5% delta-ferrite was examined by tensile test at 400°C (see TABLE 3). It had low uniform elongation, but the tensile properties were generally the same as standard EB welding.

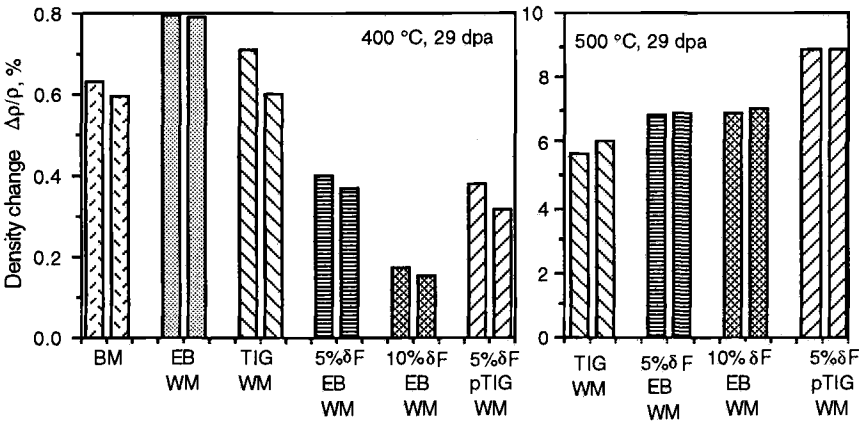


FIG. 6--Swelling ($\Delta\rho/\rho$) by precision density change of 316F weld metals from various weldments irradiated in HFIR target position.

Summary

316F irradiated in HFIR target positions up to 34 dpa at 400° and 500°C was investigated. The followings are the summary of this investigation;

1. Large irradiation hardening accompanied with low elongation were observed at 400°C. Excellent ductility and very little irradiation hardening were observed at 500°C.

2. Welded specimens had similar properties to the base metal specimens in all test conditions. The differences in the different weld types were very small.

3. Irradiated CW BM had higher strength than SA, however the tensile properties of CW EB WJ was similar to SA WJ.

ACKNOWLEDGMENTS

Research sponsored by the Japan Atomic Energy Research Institute and the Office of Fusion Energy, U.S. Department of Energy, under contract DE-AC05-84OR21400 with Martin Marietta Energy Systems, Inc. The authors are grateful to L.T. Gibson, W.S. Eatherly, and R.L. Martin for tensile testing and TEM specimen preparation.

REFERENCES

[1] S. Jitsukawa, P.J. Maziasz, T. Ishiyama, L.T. Gibson and A. Hishinuma, J. Nucl. Mater. 191-194 (1992) 771-775.
[2] T. Sawai, K. Fukai, T. Kodaira, T. Nishida, M. Nayama and A. Hishinuma, J. Nucl. Mater. 155-157 (1988) 861-865.
[3] T. Sawai, K. Fukai, S. Hamada, K. Suzuki and A. Hishinuma, J. Nucl. Mater. 141-1143 (1986) 444-447.
[4] J.E. Pawel and R.L. Senn, Fusion Reactor Material Semiannual Progress Report, DOE/ER-0313/12, Office of Fusion Energy (1992) 15-23.
[5] L.R. Greenwood, J. Nucl. Mater. 115 (1983) 137-142.
[6] S. Jitsukawa, M.L. Grossbeck and A. Hishinuma, J. Nucl. Mater. 191-194 (1992) 790-794.
[7] K. Shiba, S. Jitsukawa, J.E. Pawel and A.F. Rowcliffe, Fusion Reactor Material Semiannual Progress Report, DOE/ER-0313/15, Office of Fusion Energy (1993) 181-186.
[8] T. Sawai, to be published.
[9] A. Hishinuma, S. Jitsukawa and M.L. Grossbeck, Fusion Reactor Material Semiannual Progress Report, DOE/ER-0313/11, Office of Fusion Energy (1991) 163-166.
[10] J.E. Pawel, D.J. Alexander, M.L. Grossbeck, A.W. Longest, A.F. Rowcliffe, G.E. Lucas, S. Jitsukawa, A. Hishinuma and K. Shiba, Fusion Reactor Material Semiannual Progress Report, DOE/ER-0313/15, Office of Fusion Energy (1993) 173-180.

Serguei A. Fabritsiev[1] and Jaap G. van der Laan[2]

HELIUM EFFECTS ON THE REWELDABILITY AND LOW CYCLE FATIGUE PROPERTIES OF WELDED JOINTS FOR TYPE Cr16Ni11Mo3Ti AND 316L(N) STAINLESS STEELS

REFERENCE: Fabritsiev, S. A., van der Laan, J. G., **"Helium Effects on the Reweldability and Low Cycle Fatigue Properties of Welded Joints for Type Cr16Ni11Mo3Ti and 316L(N) Stainless Steels,"** *Effects of Radiation on Materials: 17th International Symposium, ASTM STP 1270,* David S. Gelles, Randy K. Nanstad, Arvind S. Kumar, and Edward A. Little, Eds., American Society for Testing and Materials, 1996.

ABSTRACT: The reweldability of austenitic alloys has been studied for flat specimens of Cr16Ni11Mo3Ti (Russian) and 316L(N)-SPH (European Union) which have been implanted with helium using cyclotron facilities. Specimens with typical thicknesses of 1 mm have been implanted up to helium concentrations of 50, 100, 300 and 860 appm on both sides. Electron beam welding of Cr16Ni11Mo3Ti resulted in weld cracking for specimens with the highest helium concentration of 860 appm, unlike the 316L-SPH material in similar conditions. A reduction in fatigue life in low cycle fatigue was found to be more significant for welded joints of Cr16Ni11Mo3Ti material.

KEY WORDS: Austenitic stainless steel, electron beam welding, helium implantation, helium bubble growth, HAZ cracking, weld cracking, low cycle fatigue

INTRODUCTION

The feasibility of welding neutron irradiated modules and tubes for repair or replacement purposes is one of the key problems in life time estimates for austenitic steel, intended for use as structural material in the first wall, blanket and vacuum vessel of the International Thermonuclear Experimental Reactor (ITER) [1]. According

[1]D.V. Efremov Institute of Electrophysical Apparatus, 189631, St. Petersburg, Russia

[2]Netherlands Energy Research Foundation, ECN Nuclear Energy, P.O.Box 1, 1755 ZG, Petten, the Netherlands

Copyright© 1996 by ASTM International www.astm.org

to theoretical estimations approximately 0.5-5 appm of helium, as a result of n,α-reactions, will be accumulated in type 316 steel for a neutron dose of $2*10^{20}$n/cm^2, which is foreseen in the so-called 'physics phase' of ITER [2,3]. Actually, the amount of accumulated helium may be appreciably higher due to the diffusion and subsequent decay of tritium in the material [4]. The helium accumulation resulting from low-Z impurities (boron) by thermal neutrons will also contribute, which is often not accounted for in calculations [5]. This matter is rather complex because of the impossibility to ensure a maximum helium accumulation rate of 10 appm/dpa required for ITER, in fast neutron reactors, where the rate of helium generation is considerably lower, i.e. about 0.2 appm/dpa.

Results of previous experiments on welding of austenitic materials irradiated in the EBR-II reactor were not unambiguous [6,7,8]. In some cases, cracking could be observed in materials irradiated to doses up to 10^{21}-10^{22} n/cm^2, however sometimes no cracks were seen at all.

Besides, high activity of irradiated materials impedes high quality welding and subsequent study of the sample structure. Apparently, this has been the reason that the most serious and extensive studies on helium influence on weldability were carried out with helium introduced by tritium decay [9,10,11]. This method enables to introduce from 0.01 appm up to 1000 appm of ^{3}He into steel samples of considerable thickness. This permitted for example Robinson et al. [12] to estimate helium influence on fracture toughness in low temperature tests and to show that it was reduced by more than a factor of two when 100 appm of helium was introduced.

Special fracture features of type 316 steel samples were studied in detail in references [10-13], with helium contents of 0.1 to 500 appm and subsequent welding. The first cracks were shown to appear in the heat affected zone (HAZ) already for helium contents of 4 appm. With helium contents above 10 appm large cracks were observed along the whole length of the weld. However, the applied methodology, being rather attractive, has disadvantages. Firstly, the influence of tritium on helium embrittlement is difficult to isolate. Secondly and more important, the helium introduction into steel by tritium decay is not accompanied by defect generation.

Under neutron irradiation in ITER helium is produced in threshold (n,α)-reactions, accompanied by the formation of a number of defects. As a result the helium-vacancy complex formation greatly differs in these two cases : tritium decay yields a rather high rate of helium production and low density of non-equilibrium defects while in case of neutron irradiation a relatively low helium production rate occurs together with a high concentration of non-equilibrium defects. This is the first reason to use a cyclotron for introduction of helium. However, usually thick specimens are required and cyclotron injection allows only thin samples to be implanted with helium.

This paper contains results of the investigation of helium effects on the weldability of austenitic steel and mechanical properties of the welds. In particular it deals with experiments on two materials : Cr16Ni11Mo3Ti and 316L(N) steel. The chemical composition of these materials is given in table 1 and typical mechanical properties are listed in table 2.

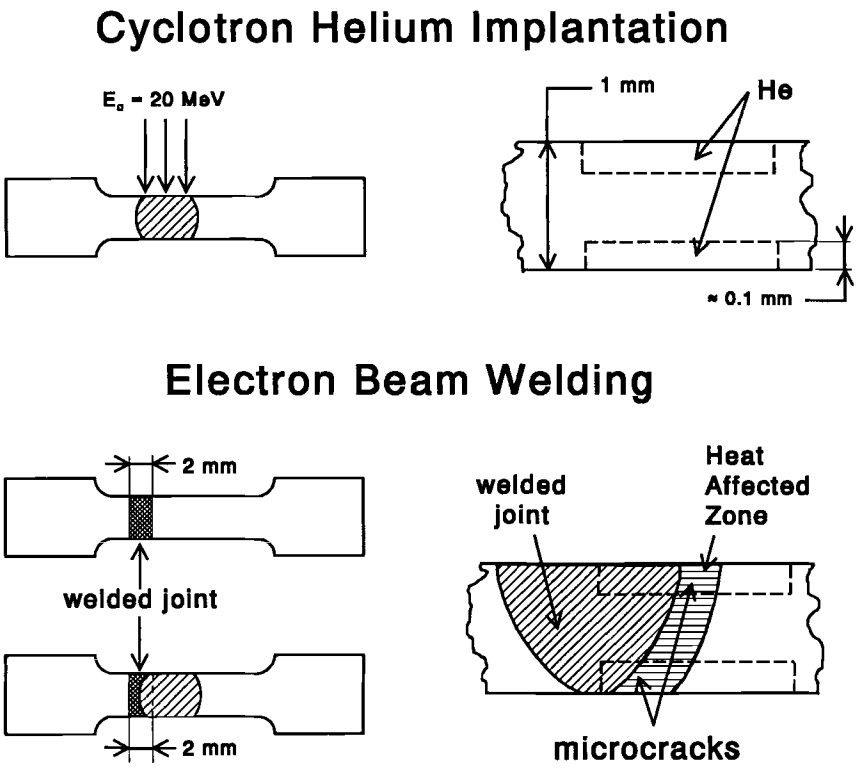


FIG. 1--Method of cyclotron helium implantation and electron beam welding of flat stainless steel specimens.

Table 1.
Chemical composition of Cr16Ni11Mo3Ti and 316L(N) steels (weight percent)

	C	Si	Mn	P	S	Cr	Ni	Mo	N	Cu	Co	Ta	B	Ti	Fe
Cr16Ni11Mo3Ti	.036	.38	1.17		.018	16.0	11.5	2.25		.09			.0003	.95	bal.
316L(N)	.020	.35	1.75	.019	.001	17.2	12.2	2.4	.077	.09	.079	<.001	.0011		bal.

Table 2.
Typical mechanical properties for Cr16Ni11Mo3Ti and 316L(N) steels

Material	Yield Strength MPa	Ultimate Strength MPa	Uniform Elongation %	Total Elongation %	Grain size μm	Hardness HV MPa
Cr16Ni11Mo3Ti	215	580	20	65		
316L(N) (ERHII)	315	600	47	63	85	170

EXPERIMENTAL METHOD

The technique of helium injection, sample welding and low cycle fatigue (LCF) testing was discussed in detail earlier [14]. For the assessment of mechanical properties LCF testing in reverse bending was chosen, since in bending the highest degree of deformation is localized in the surface layers of a flat specimen. In this area cracks emerge and develop perpendicular to the specimen surface, resulting eventually in fracture. The high temperatures occurring in the welding process may induce pores and microcracks in the helium containing area. In LCF testing the maximum deformations are realized in this region and subsequently microcracks emerge and develop (Fig. 1). Thus, all the main fracture factors are present in the near-surface layers of specimens: helium implanted by cyclotron, in the welding joint and HAZ and the maximum deformation from LCF in reverse bending applied for an assessment of mechanical properties.

In the present work 1 mm thick specimens were used (Fig. 1). Specimens were implanted with helium in the St.Petersburg cyclotron facility MGC with a helium ion energy of 20 MeV on both sides. The implantation technique ensured a uniform helium concentration across the 90 μm implantation depth. This uniformity was radiographically checked. Specimens were implanted with helium concentrations of 50, 100, 300 and 860 appm over an area of 15 mm diameter. The specimen temperature during implantation was less than 100°C.

A device for automatic electron beam welding was developed for this type of specimens, providing for a single-pass welding of 6 specimens in one batch. In this way the specimens are welded under identical conditions. The welding prodecure applied ensures a high level of mechanical properties of the welded joint, as was found previously by testing of control (i.e. non-welded) and welded specimens : the number of cycles to fracture of both the welded and control specimens was about the same [14]. Helium implanted and control specimens were exposed to e-beam welding using the above welding device. The surfaces of welded specimens were examined by optical microscopy and SEM for the appearance of microcracks in weld and HAZ.

Welded specimens with and without helium were tested for LCF in reverse bending at room temperature. The amplitude of deformation at the specimen 'outer fiber' was chosen to vary as ±0.6%, ±0.9 or ±1.2%. SEM and TEM investigations of the microstructure and fracture character of these samples were performed.

RESULTS

1. Effect of helium on microstructure of welded joints

SEM investigations of the surfaces of Cr16Ni11Mo3Ti and 316L(N) steel specimens after welding revealed the following effects of the helium on the structure of the welded joint (No microcracks in the HAZ and weld were observed in specimens with no helium, Fig. 2d):

In Cr16Ni11Mo3Ti steel with 86 appm helium contents microcracks appear in the HAZ. No cracks are observed in the weld at this helium concentration. In specimens with a helium concentration of 430-860 appm interdendritic microcracks develop in the weld (Fig. 2a). In some cases these cracks are rather long, up to 300-500 μm (Fig. 2b). These cracks typically result from coalescence of smaller cracks (Fig. 2c).

Investigation of 316L(N) steel specimens after welding showed this material to be extremely resistant to microcracking in the welded joints. Microcracks were neither found in the HAZ nor in the weld of 316L(N) steel specimens with 50-300 appm helium contents (Fig. 2e). Very small microcracks appear only in the welds of specimens with 860 appm helium contents (Fig. 2f).

Investigations of the microstructure of welds in Cr16Ni11Mo3Ti and 316L(N) steel with TEM further substantiate microstructural differences by helium implantation between these two materials.

TEM investigations of 316L(N) steel demonstrated, that the helium injection and subsequent welding results in the formation of helium porosity in these samples. The pore density increases with increasing helium concentration. The pore size is larger in areas which have experienced higher temperatures. The largest pores were observed in the weld (Fig. 3 a,b). Helium bubbles were observed, first of all, on the boundaries of δ-ferrite. In general there are no helium bubbles within dendrites in the weld, and only a few are found in the HAZ. Large helium bubbles are observed mainly on the grain boundaries. Helium bubbles with 20-30 nm diameter are found as well in the matrix, and are typically located at dislocations (Fig. 3c).

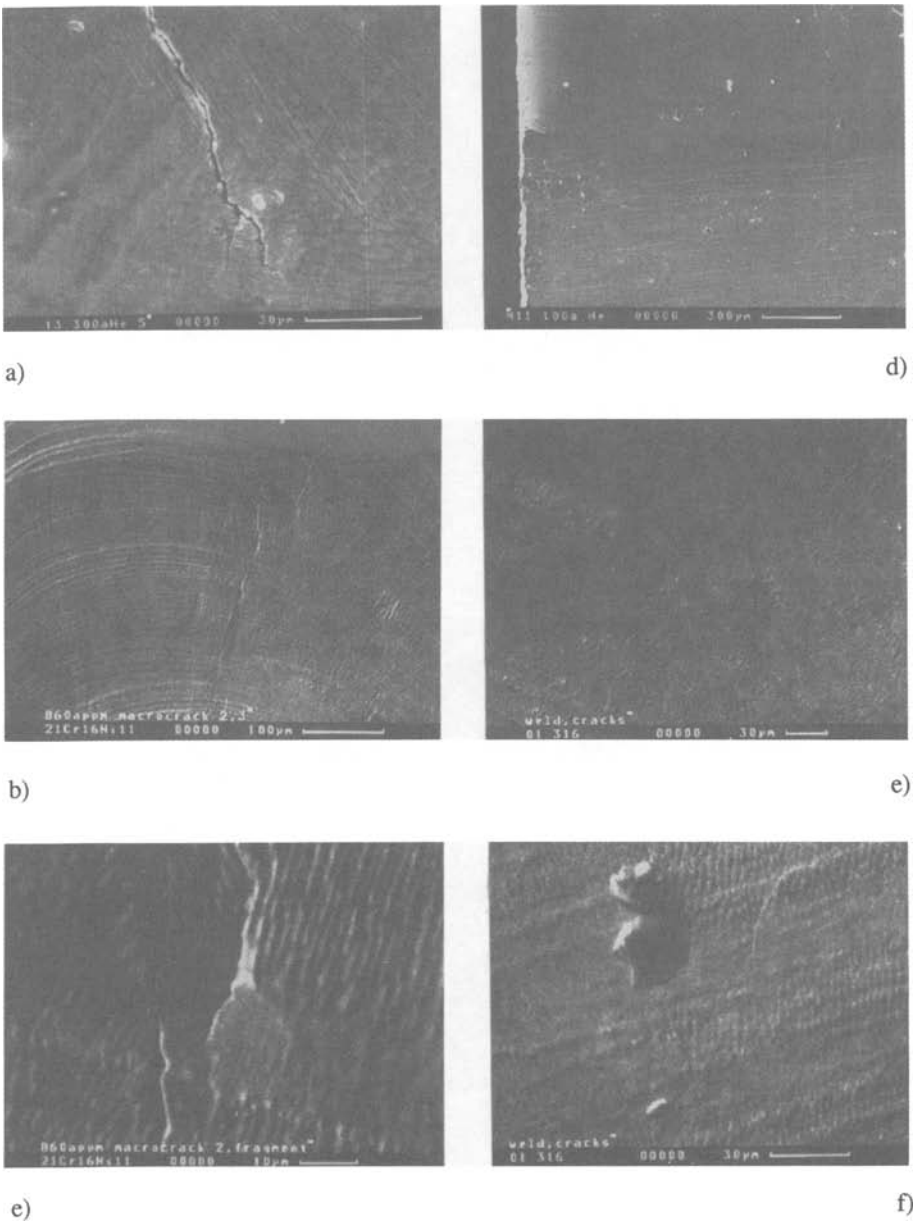


FIG. 2--SEM micrographs of weld surfaces of welded stainless steel specimens for : (a) Cr16Ni11Mo3Ti implanted with 300 appm He; (b) and (c) Cr16Ni11Mo3Ti with 860 appm He; (d) 316L(N) without He; (e) 316L(N) with 50 appm He and (f) 316L(N) with 860 appm He

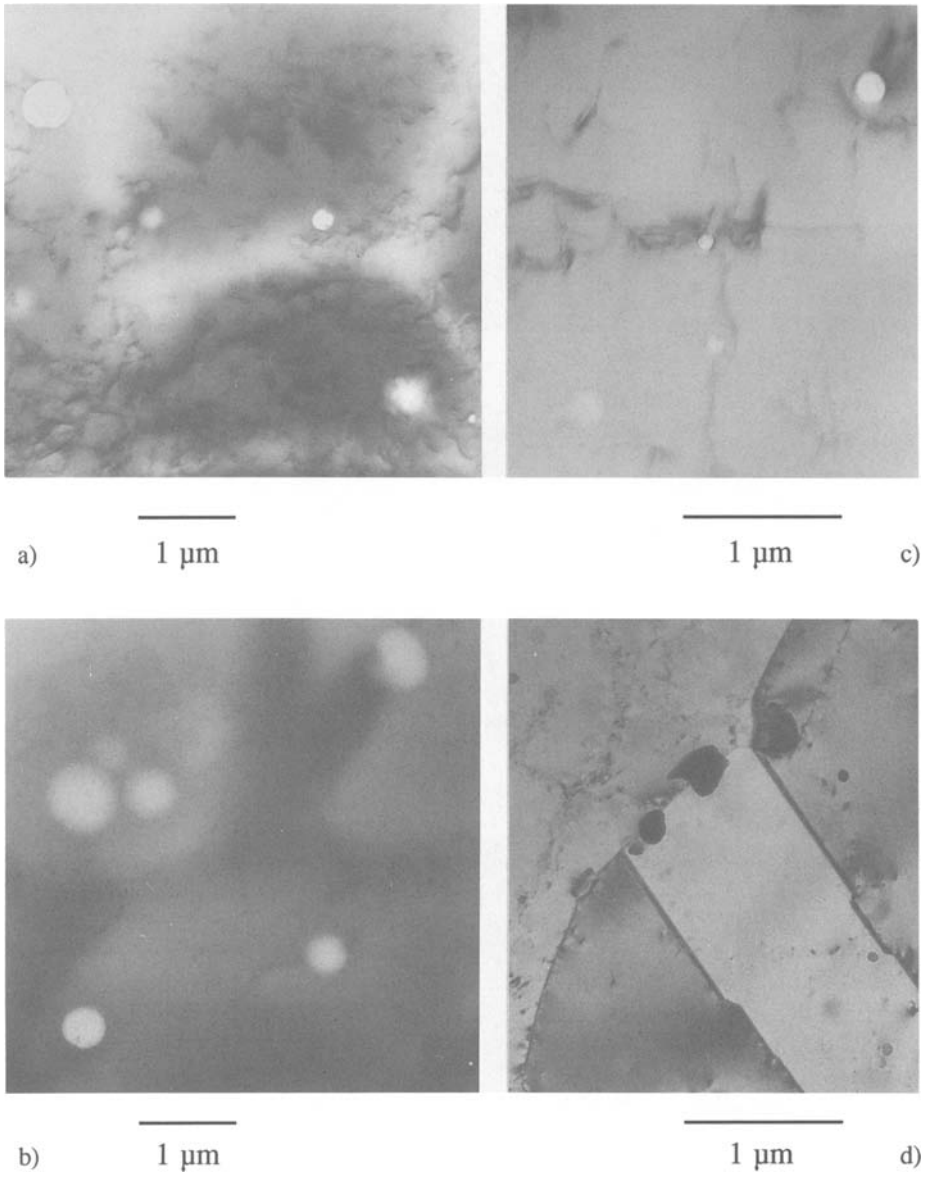


FIG. 3--TEM micrographs of welded specimens of (a) bubbles in weld of 316L(N) with 100 appm He; (b) bubbles in weld of 316L(N) with 860 appm He; (c) bubbles in the HAZ of 316L(N) with 100 appm He and (d) suppression of recrystallisation in the HAZ of Cr16Ni11Mo3Ti steel with 43 appm He

In 316L(N) steel the transient heating during welding induces the formation of porosity, which, as the TEM and SEM investigations suggest, retards rather weakly the processes of high-temperature plastic deformation. The appearance of large helium bubbles on the grain boundaries in the HAZ and the cells in the weld is partly attributed to helium removal from the matrix by moving grain boundaries. Helium mobility along the boundaries seems high. As a result, large bubbles are observed on the grain boundaries in the HAZ and the cells in the weld. These bubbles may retard boundary movements. However, some retardation of the recrystallization was actually observed only at the highest helium concentration of 860 appm. It is important to note that the structure of the entire HAZ and weld is rather uniform. A smooth transition from weld to HAZ is observed, their structures are rather similar. In the HAZ grains are decorated with large helium bubbles along the boundary. In the welds small-sized dendrites are decorated by large helium bubbles.

TEM investigations on Cr16Ni11Mo3Ti steel show that the helium injection and welding contribute to a high density of carbides (Fig. 3d). Small sized carbides (of TiC, M_6C, $M_{23}C_6$ type, as identified by TEM) seem to suppress the recrystallization processes in the specimens during welding, even at a helium concentration of 43 appm. With increasing helium concentration the carbide density in the steel increases and the grain recrystallization and grain growth in HAZ is completely suppressed. As a result, the grain size in HAZ is very small, 1-3 μm. Attempts to investigate the weld of Cr16Ni11Mo3Ti steel failed for specimens with helium concentration above 43 appm, as well as for specimens after fracture in LCF. During electrolytic thinning microcracks in the weld perforated the TEM specimens.

No evidence for large (10-30 μm) helium bubbles in welds of 316L SA steel was found, as in that case the TEM samples could not have been prepared. In helium containing Cr16Ni11Mo3Ti steel a lot of small-sized carbides precipitate during welding. The carbide density is about 10 times as high as the maximum density of helium bubbles in 316L SA steel. Besides, the carbide particles are hard and cannot be cut or displaced by the grain boundaries whereas bubbles can. Such a kind of simulation of ageing by helium in austenitic steels and alloys was observed earlier both in cyclotron-implanted samples and neutron-irradiated samples [15]. As a consequence, plastic deformation processes, recrystallization and polygonization in the HAZ are nearly completely suppressed, even at a helium concentration of 86 appm.

Throughout the HAZ grain boundaries are observed as well as noncoherent twin boundaries pinned on the carbide particles. Thus, Cr16Ni11Mo3Ti steel has a high-strength HAZ, which resists plastic accommodation of stresses in the weld. As a consequence, stresses in the weld during cooling down are high, resulting in a fast growth of helium bubbles in the weld and their coalescence into microcracks. These microcracks then accommodate welding stresses in the welded specimen.

2. Low cycle fatigue of welded joints of helium inplanted specimens

The results of LCF testing of welded Cr16Ni11Mo3Ti and 316L(N) steel specimens with helium showed a considerable difference in the behavior of these two

materials, see Fig. 4 and 5). Cr16Ni11Mo3Ti steel, when welded, displays a decrease in a number of cycles to fracture even for a helium concentration of 86 appm. Fracture is localized in the heat-affected zone (HAZ), similar to the welded specimens without helium. At high helium concentrations (430 and 860 appm) the number of cycles to fracture for this material decreases by a factor of 5-10 after welding (Fig. 4), and fracture occurs in the weld.

Steel 316L SA displays a weak sensitivity to helium injection up to helium concentrations of 300 appm (Fig. 5). Only at the maximum helium concentration of 860 appm a relatively small decrease in number of cycles to weld fracture is observed (by a factor of two). The fracture is still localized in the HAZ.

Figure 6 shows the change in the number of cycles to fracture for welded specimens as a function of helium concentration. It can be seen that Cr16Ni11Mo3Ti steel displays a steady decrease in the number of cycles to fracture with an increase in helium concentration. The effect is observed to be the largest for the maximum deformation amplitude. The 316L(N) steel behaves quite differently. At a deformation amplitude $\Delta\varepsilon = 0.9\%$ an effect of helium on the number of cycles to fracture of the welded joint could not be observed at all. A slight decrease in the number of cycles to fracture at the maximum deformation amplitude $\Delta\varepsilon = 1.2\%$ is observed only at high concentrations of injected helium. Thus, the LCF testing of the welded specimens with helium revealed a higher fatigue endurance of 316L SA steel in comparison to Cr16Ni11Mo3Ti steel.

Analysis of the loading diagrams during the LCF tests shows, that the number of cycles to fracture is controlled essentially only by the time (number of cycles) to the appearance of critical cracks. Final fracture occurs during the next 50÷100 cycles. Thus, for specimens with microcracks induced by the welding process, the time to fracture is controlled by the coalescence and growth of these microcracks under loading. The properties of the near-surface layer, implanted with helium and containing the microcracks determine the LCF behaviour of the whole specimen.

The fractographic investigations for Cr16Ni11Mo3Ti steel samples, when welded and tested for LCF, revealed, that in samples with 43-86 appm He the fracture in the near-surface layer is intergranular (Fig. 7a). The fracture is localized in HAZ. Throughout the thickness of the sample fracture is typically transcrystalline. At higher helium concentrations (430-860 appm He) fracture is localized in the weld (Fig. 7b). In the near-surface layers fracture is observed on the dendrite boundaries. Closer to the sample center (accross the thickness) large pores can be observed (up to 50 μm in diameter, Fig. 7c). The appearance of these pores is likely to be attributed to mixing of liquid metal during welding and coalescence of small helium bubbles.

Investigation of fracture surfaces of 316L(N) specimens after welding and LCF testing demonstrated, that for helium concentrations up to 300 appm fracture characteristics donot depend on the presence of helium. Even in the near-surface layers the fracture has a combined transcrystalline-intercrystalline nature (Fig. 7d). In LCF testing microcracks develop both in the weld (in the area close to the HAZ, Fig. 7e) as well as directly in the HAZ (Fig. 7f). In general these cracks are similar to those in the

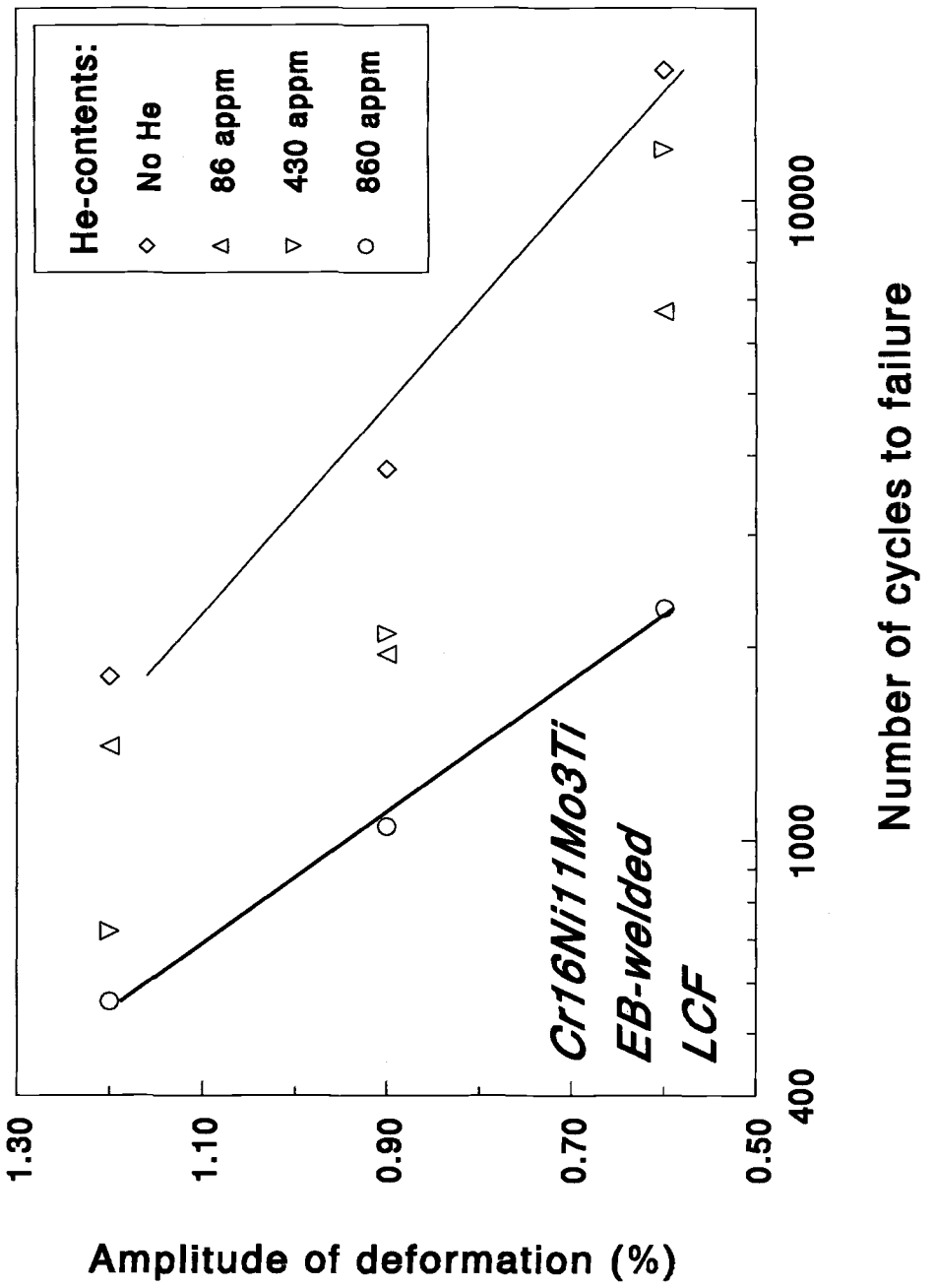


FIG.4--Fatigue life curves of Cr16Ni11Mo3Ti steel with various helium contents in reverse bending tests performed at room temperature.

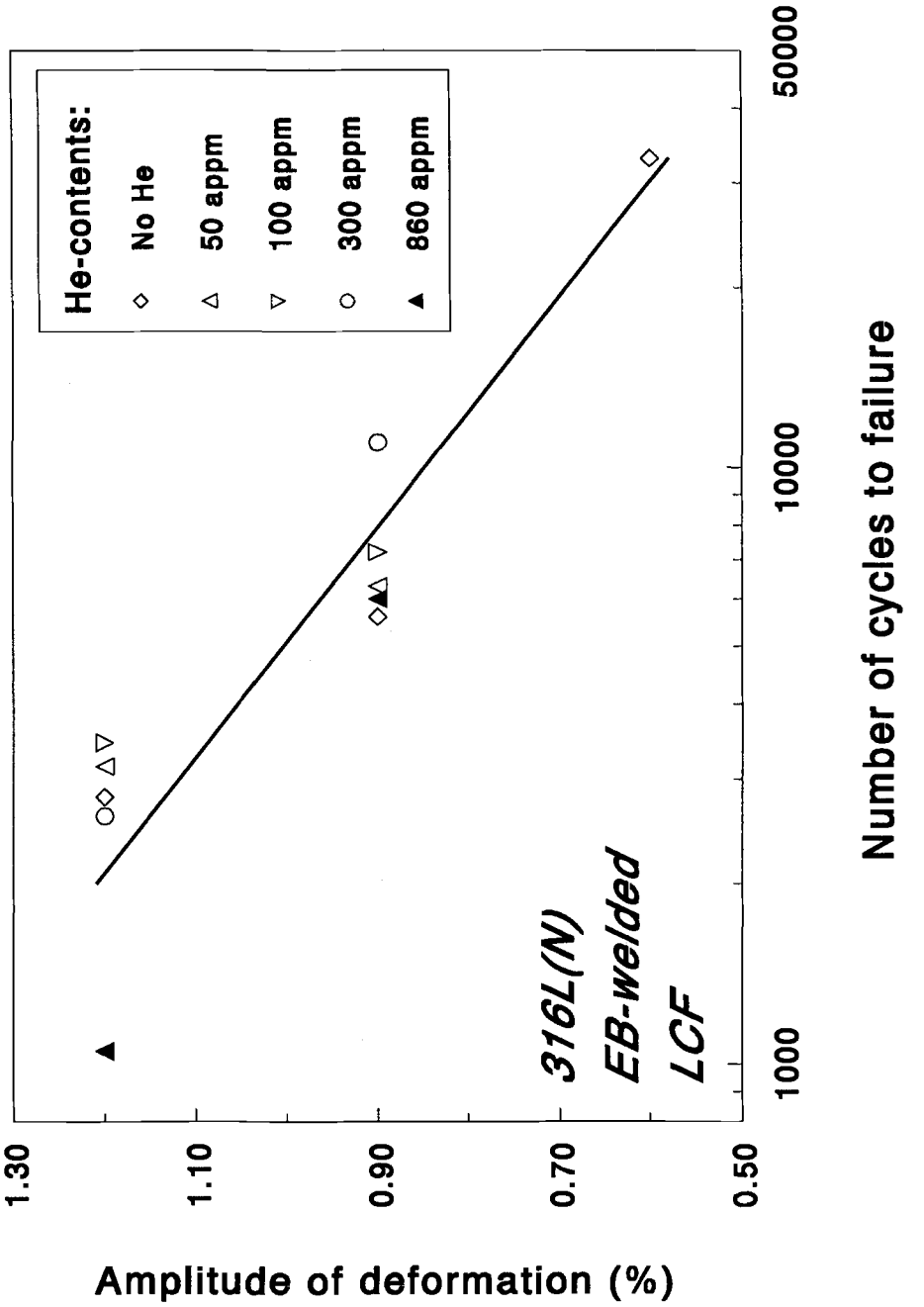


FIG.5--Fatigue life curves of 316L(N) steel with various helium contents in reverse bending tests performed at room temperature.

samples without helium.

DISCUSSION

The experimental results presented show that the investigation technique developed allows the estimate of helium effects on the degradation of the structure and mechanical properties of the welded joints of stainless steel. In this sense, the combination of the helium implantation technique on a cyclotron and the assessment of mechanical property changes during LCF testing in reverse bending turns out to be successful. First cracks appear in the near-surface layers of the sample, i.e. in the area with helium.

The results show, that the effect of helium on the microstructure of welded joints of Cr16Ni11Mo3Ti steel differs considerably from that of 316L(N) steel. In 316L(N) steel the helium injection results in the production of helium pores in the HAZ and weld. Grain recrystallization and grain growth develop rather actively for helium concentrations up to 300 appm. A weak suppression of the recrystallization is observed only in the samples with 860 appm He content.

It may be concluded, that in 316L(N) steel the effect of helium on the appearance and development of intergranular cracking is considerably less as compared to Cr16Ni11Mo3Ti, for helium concentrations up to 300 appm, and sligthly less for helium contents of 860 appm. The results suggest that plastic accommodation of welding induced stresses is effectively reducing microcracking, even in the long run, and a high level of mechanical properties is maintained.

In Cr16Ni11Mo3Ti steel the helium injection gives rise to a sharp intensification of ageing processes and carbide precipitation during weld cooling. Carbides retard the grain growth, displacement of dislocation networks and large-angle boundaries. Therefore, helium suppresses the processes of high-temperature plastic accommodation of the stresses which occur during welding. As a consequence, microcracks appear in the HAZ and weld, and reduce the mechanical integrity of the welded joint of this steel.

The results of LCF testing clearly show the presence of microdefects, caused by welding, and its effects on the mechanical properties of the welded joint.

CONCLUSION

The reweldability of Cr16Ni11Mo3Ti and 316L(N) austenitic stainless steels has been studied by electron beam welding of helium implanted specimens and subsequent low cycle fatigue tests. The testing technique presented allows for the estimation of the helium effect on the structure and mechanical properties of the welded joints for the two steels. The investigation of the structure of welded joints by SEM has revealed, that 316L(N) steel is highly resistant to the appearance of cracks in the welded joint up to helium contents of 300 appm. In helium implanted Cr16Ni11Mo3Ti steel microcracks appear in both HAZ and weld, even at helium concentrations of 86 appm and higher.

From the comparative study of the welded joint microstructure of the two

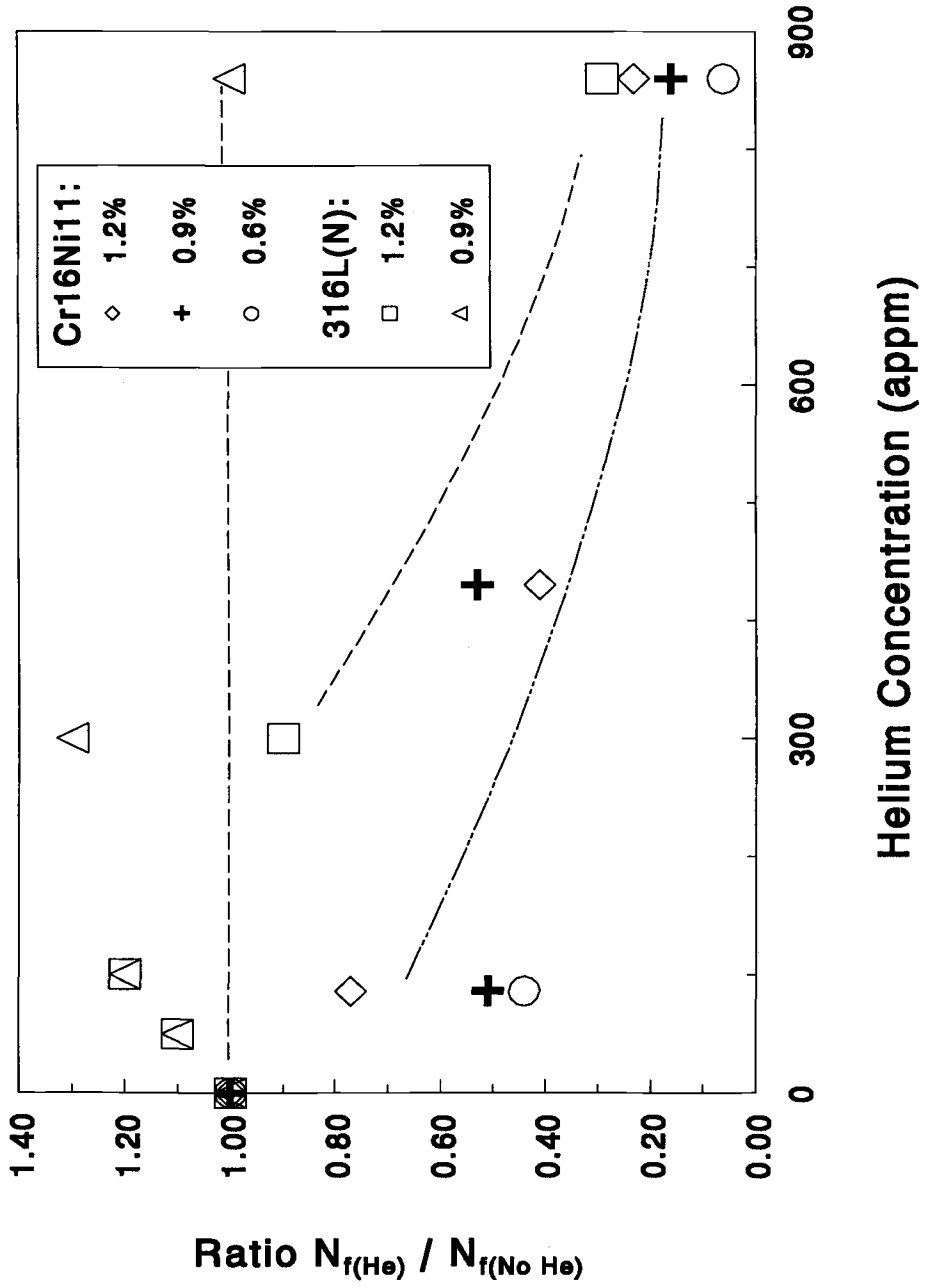


FIG.6--Effect of helium on the number of cycles to failure N_f for EB welded Cr16Ni11Mo3Ti and 316L(N) steels, displayed as the ratio $N_{f(He)}$ to $N_{f(No\ He)}$.

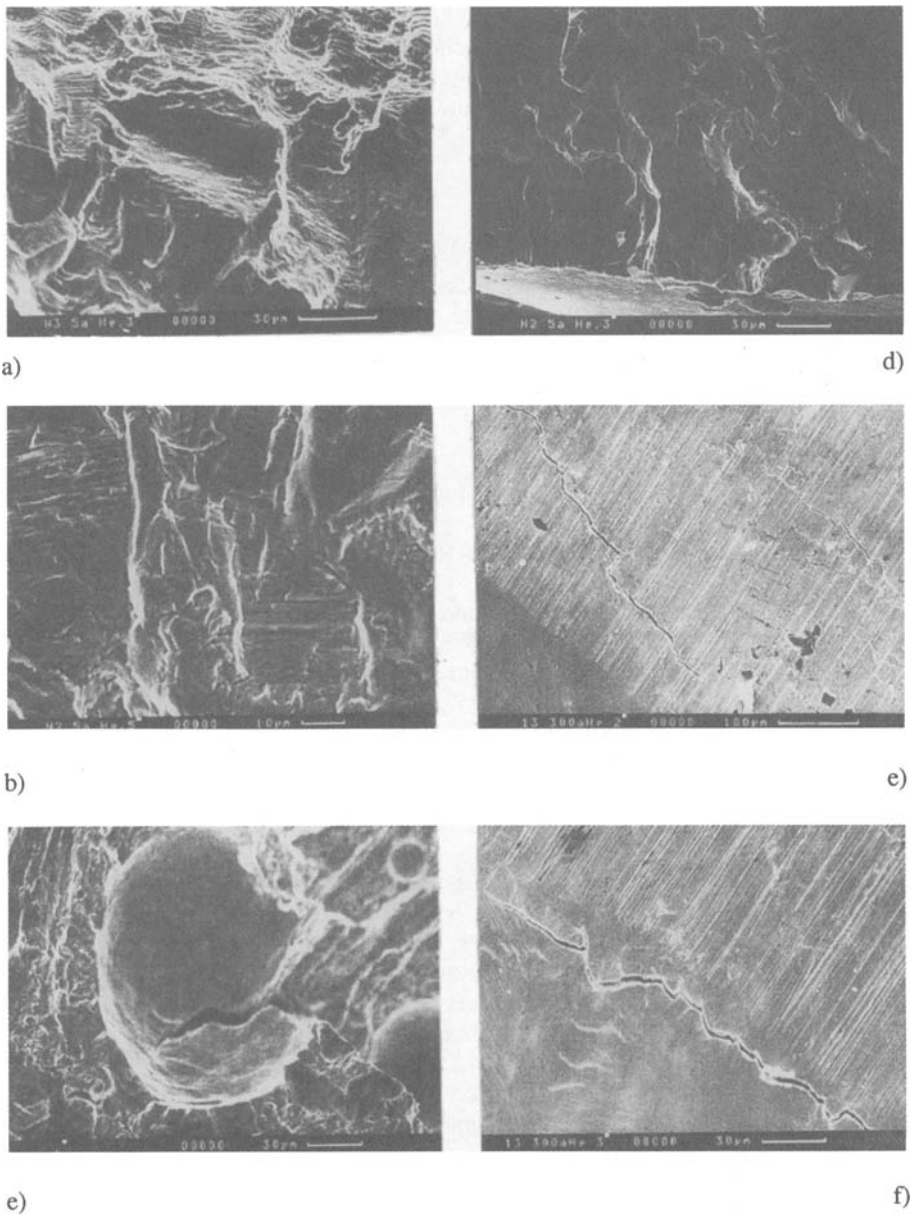


FIG. 7--SEM micrographs of fracture surfaces of (a-c) Cr16Ni11Mo3Ti steel with (a) 43 appm He (fracture in HAZ); (b) 430 appm He, (fracture in weld); (c) 860 appm He, (fracture in weld) and (d-f) fracture surfaces of 316L(N) steel with (d) 300 appm He, (fracture in HAZ); (e) 300 appm He (weld-HAZ boundary after LCF-test with cracks in Weld) and (f) 300 appm He (weld-HAZ boundary after LCF with cracks in HAZ).

materials by TEM it appears that the embrittlement of Cr16Ni11Mo3Ti steel is mainly determined by helium-related mass precipitation of carbides in the HAZ during welding. Stress accommodation in welded joints occurs by the growth of microcracks.

Thus, the LCF life time of the 316L(N) steel welded joints turns out to be less sensitive to the helium injection than that of Cr16Ni11Mo3Ti steel.

ACKNOWLEDGEMENT

The authors like to thank in particular F.A. van den Berg (ECN) for the transmission electron microscopy, and M.G. Horsten and B. van der Schaaf for helpful discussions.

REFERENCES

[1] *ITER Concept Definition Volume 1*, International Atomic Energy Agency, Vienna (1989).

[2] Greenwood, L.R., Garner, F.A., and Heinish, H.L, *Journal of Nuclear Materials* Vol. 191-194, (1992), p. 1096.

[3] Greenwood, L.R., Kneff, D.W. and Skawronski, R.P., *Journal of Nuclear Materials* Vol. 122-123 (1984) p. 1002.

[4] Yamamoto, S., Ishida, Y., Sekimura, N. and Mori, M., *Journal of Nuclear Materials* Vol. 191-194, (1992), p. 759.

[5] Karasev, A.N. and Fabritsiev, S.A., *Voprosy Atomnoi Nauki i Tehniki, Termojadernyi Sintez* Vol. 12, No.3 (1992), p. 54.

[6] Maloney, J.P., Baker, D., Kennedy, W.R., Day, W.A., McClaim, J.B., Fraser, W.G., McKenney, D.H., Huxford, H.R., Meyer, C.A., Kehr, K.E, Mittelberg, R.E. and Walls, J.Z. *"Repair of a Nuclear Reactor Vessel"* E.I.du Pont de Nemours & Co., Inc., Savannah River Laboratory, Aiken, SC, June 1969.

[7] Atkin, S.D., *ADIP Semi-annual Progress Report*, (September 1981) p. 110.

[8] Hall Jr., M.M., Hins, A.G., Summers, I.R. and Wakker, D.E., " Weldment: Physical Metallurgy and Failure Phenomena", *Proceedings of the Fifth Botton Landing Conference*, (General Electric Co, Schenectady, New York, 1978) p. 365.

[9] Kanne, W.R., Angermann, C.L. and Eberhard, B.J., *DP-1470, E.I.du Pont de Nemours & Co.*, Inc., Savannah River Laboratory, Aiken, SC.,1987.

[10] Lin, H.T., Goods, S.H., Grossbeck, M.L. and Chin, B.A., *ASTM STP 1046*, N.H.Packan, R.E Stoller and A.S.Kumar editors, Philadelphia, 1989, p.301.

[11] Goods, S.H., and Yang, N.Y.C., *Metallurgical Transactions A* Vol.23A, March 1992, p.1021.

[12] Robinson, S.L., *Journal of Nuclear Materials* Vol. 152, (1988), p.212

[13] Lin, H.T. and Chin, B.A., *Journal of Materials Science* Vol.26, (1991), p.263

[14] Fabritsiev, S.A., "Effect of the annealing and welding on the structure and mechanical properties of neutron and helium ion irradiated austenitic materials", paper submitted for publication to *Journal of Materials*.

[15] Zhdan, G.T., Ibragimov, Sh.Sh., Kozhevnikov, O.A., Reutov, V.F., Fabritsiev, S.A., Jaroshevich, V.D., *Atomnaja Energiya* Vol.66 No1, pp.28-33, January, 1989.

Ali-Asghar Tavassoli,[1] Charles Picker,[2] and John Wareing[3]

DATA COLLECTION ON THE EFFECT OF IRRADIATION ON THE MECHANICAL PROPERTIES OF AUSTENITIC STAINLESS STEELS AND WELD METALS

REFERENCE: Tavassoli, A-A., Picker, C., and Wareing, J. **"Data Collection on the Effect of Irradiation on the Mechanical Properties of Austenitic Stainless Steels and Weld Metals,"** *Effects of Radiation on Materials: 17th International Symposium, ASTM STP 1270,* David S. Gelles, Randy K. Nanstad, Arvind S. Kumar, and Edward A. Little, Eds., American Society for Testing and Materials, 1996.

ABSTRACT: Data on the influence of low dose 400-550°C irradiation on the mechanical properties of structural steels (Types 304, 316, 316L, 316H and 316L(N) and associated weld metals) at temperatures from 20°C to 750°C, have been compiled from published literature and the results of British, Dutch, French and German laboratories. Properties evaluated include tensile, impact, creep, fatigue, and creep-fatigue. The preliminary results, which cover the dose range from 0 to 5 displacements per atom (and/or up to 9 appm helium) are presented as comparisons between irradiated and unirradiated control data, covering a range of strength and cyclic properties. The results show that low dose irradiation can have a significant influence on the properties, i.e.:

- increases in tensile proof strength,
- reductions in tensile ductility,
- decreases in impact energy,
- reductions in creep-rupture strength and ductility, and
- reductions in creep-fatigue endurance.

By considering the influence of irradiation temperature and dose level, the results are rationalised in terms of irradiation hardening and grain boundary embrittlement mechanisms.

KEYWORDS: Pressurised Water Reactor, Fast Breeder Reactor, internal structures, irradiation, tensile, toughness, creep, creep-fatigue, embrittlement, grain boundaries.

[1] Manager, Commissariat à l'Energie Atomique, DTA/M2RI/DECM, CE-Saclay, 91191 Gif sur Yvette Cedex, France.

[2] Manager of FBR, AEA Technology, Risley, Warrington, Cheshire WA3 6AT, England.

[3] Formerly with AEA Technology, Risley, Warrington, Cheshire WA3 6AT, England, now with DTA/M2RI/DECM/SRMA, CEA, CE-Saclay, 91191 Gif sur Yvette Cedex, France.

Copyright© 1996 by ASTM International www.astm.org

The influence of irradiation on the mechanical properties of materials has been known for many years. Most studies prior to the 1970's concentrated on the relatively high doses of relevance to core components of nuclear reactors. However, it has been recognised for some time that the doses to which the core peripheral components of sodium cooled fast reactors are exposed would also cause some degree of degradation in the mechanical properties. Since these near core items are not usually designed to be removable, studies were subsequently made to assess the effect of more modest irradiation doses.

For design purposes, and those of life assessment, it is important to specify the maximum dose level to which structural components can be subjected without undergoing either a significant change in properties or an unacceptably large change in properties. The aim of the present investigation, which has been funded by the Commission of the European Communities under the auspices of the Fast Reactor Co-ordinating Committee, Working Group Codes and Standards, has been to collect relevant data on the influence of low dose irradiation on mechanical properties.

Data have been collected from British, French, German and Dutch laboratories, together with published information from the open literature (mainly US). The study has concentrated on the austenitic stainless steels (Types 304, 316, 316L, 316H and 316L(N)) and their associated weld metals in the temperature range 20 to 750°C and dose ranges from 0 to 5 dpa (and/or up to 9 appm helium, obtained in several reactors, but most in Phénix and HFR) (1). The scope of the data, in terms of the number of test points for each type of mechanical property is shown in Table 1. The unirradiated data are from specimens to provide control data for the irradiated specimens and do not represent the entire data set for unirradiated materials available from other sources.

The paper outlines the comparisons between the mechanical properties of irradiated and unirradiated control material. The properties studied are tensile, impact toughness, stress rupture, fatigue and creep-fatigue. The data have been subdivided by mechanical property for base and weld metal, further sub-divisions (e.g. by material type or irradiation temperature) have been made for some but not all properties at this stage. Throughout the study, a low test temperature does not necessarily imply a low irradiation temperature. However to make a meaningful comparison, care has been taken to compare data having the same irradiation and test temperature.

This paper is unable to include all the information available, but attempts to summarise the main findings. A later investigation is to examine in detail the material and irradiation factors that affect mechanical properties. Ultimately, a design recommendation will be made on the dose level at which irradiation effects become significant.

TABLE 1--Number of data points

	Tensile Base	Tensile Weld	Impact Base	Impact Weld	Fatigue & C-Fatigue Base	Fatigue & C-Fatigue Weld	Stress Rupture Base	Stress Rupture Weld	Total
Unirr	66	41	24	22	32	27	194	41	447
Irr	108	70	43	49	87	27	182	33	599

RESULTS

Tensile Properties

Base metal--Data on 0.2% proof stress (PS), ultimate tensile strength (UTS), uniform and total elongation and reduction in area were collected for Types 304 and 304L, 316 and 316L(N) steels, although most of the data (nearly half of the irradiated materials' data) were from Type 316 steel. The irradiation dose ranged from about 0.2 dpa to 5 dpa, with test temperatures of 20 to 750°C.

In order to illustrate the emerging trends, data are subdivided so as to illustrate the effect of the maximum dose under investigation (4 to 5 dpa at 400°C) on tensile strength at temperatures from ambient to 750°C, and also the effect of dose level (0 to 5 dpa) on the strength at 400°C. Also examined is the concurrent effect of irradiation on strain at failure.

Fig. 1 shows the effect of irradiation on the yield stress of Types 304L and 316L(N) steels at temperatures from ambient to 750°C; unirradiated data are shown for comparison.

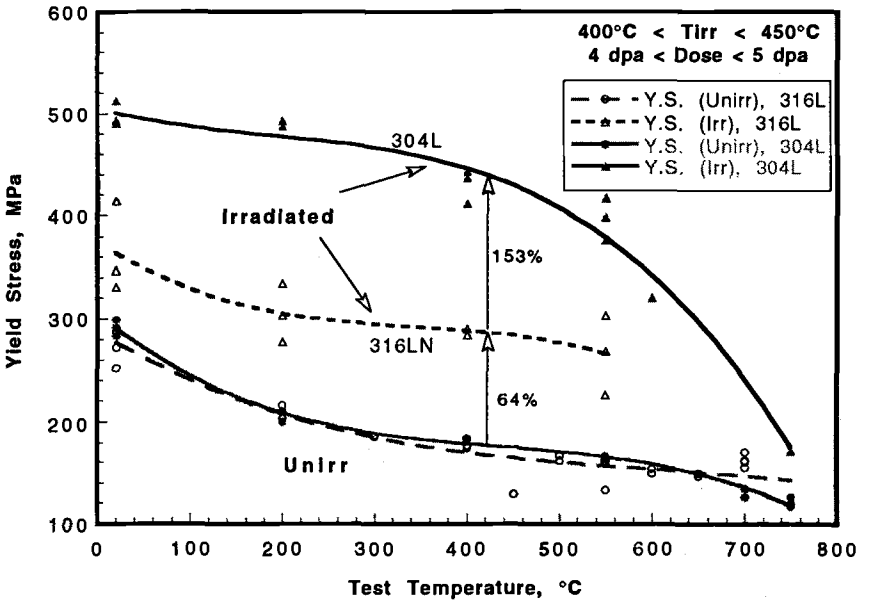


Figure 1. The effect of irradiation at ≈400°C on the yield stress of Types 304L and 316L(N) stainless steels in the temperature range 20 to 750°C.

The irradiation temperature for all of the tests was between 400 and 450°C and the dose level was between 4 and 5 dpa. The unirradiated

yield strengths of the two steels are fairly similar in magnitude and decrease as the test temperature is increased. Irradiated Type 304L steel exhibits a significant increase in strength at test temperatures up to 450°C. At 400 to 450°C (where irradiation and test temperatures are equal) there is a 153 % increase over the unirradiated value. Above this temperature the difference in strength levels decreases so that at 750°C, they approach each other. Data are shown for Type 316L(N) steel at test temperatures from ambient to 550°C. It can be seen that the trend is similar to that for Type 304 L steel but irradiation hardening is less significant, i.e., only 64% increase was obtained at the irradiation/test temperature.

The effect of irradiation and test temperature on UTS is shown in fig. 2. Here the trends mirror those for yield strength, i.e., for Type 304L steel, irradiation at 400-450°C, causes an increase (of the order of 30%) for test temperatures in the range 400 to 450°C. At higher test temperatures this strength difference decreases so that at 750°C it has virtually disappeared. For Type 316 L(N) steel, irradiation under similar conditions causes a 15% increase in UTS for test temperatures up to ~450°C. At higher temperatures the difference is expected to decrease.

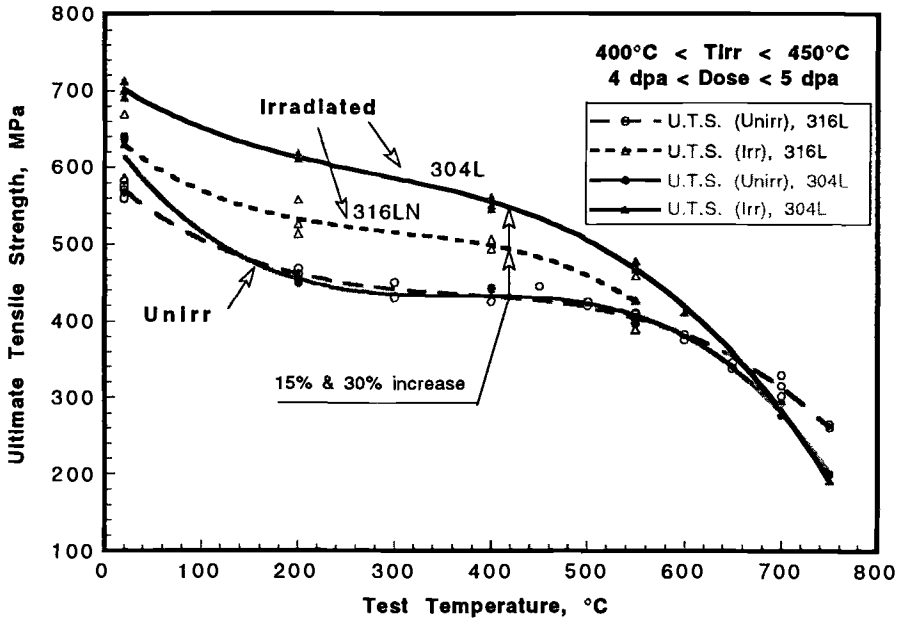


Figure 2. The effect of irradiation at ≈400°C on the ultimate tensile strength of Types 304L and 316L(N) stainless steels in the temperature range 20 to 750°C.

Fig 3 illustrates the effect of irradiation at 400 to 450°C and test temperature on the failure strain for both Types 304L and 316L(N) steels. Unirradiated properties of the two steels are similar both in absolute levels and their variation with temperature. Elongation initially reduces with increasing test temperature but reaches a plateau at 400 to 500°C, after which it increases with increasing temperature. For Type 304L steel, the elongation of irradiated material is reduced by

some 62% for test temperatures in the range of 400 to 450°C. Unlike unirradiated materials and despite the diminishing hardening observed for YS and UTS, elongation continues to decrease as the temperature is increased to 750°C. The trend for Type 316L(N) steel is similar but the reduction in elongation of irradiated material is only 34% of the unirradiated equivalent.

Turning to the effect of dose level on tensile properties, fig. 4 illustrates the effect of irradiation on the tensile properties of Type 304L stainless steel, irradiated and tested at ~400°C. Here, both the 0.2% yield strength, the ultimate strength, and elongation are plotted as a function of dose in the range 0 to 5 dpa. Yield stress rapidly increases in the dose range 0 to 4 dpa, and a doubling of the unirradiated strength level occurs. From 4 to 5 dpa, there is a much slower increase and possibly a saturation of yield stress at higher doses. Ultimate strength shows a less marked increase with dose and increases to 130% of the unirradiated value at a dose of 5 dpa. Both uniform and total elongations decrease steadily with increasing dose and reach absolute levels of 18 and 10%, respectively, at 5 dpa.

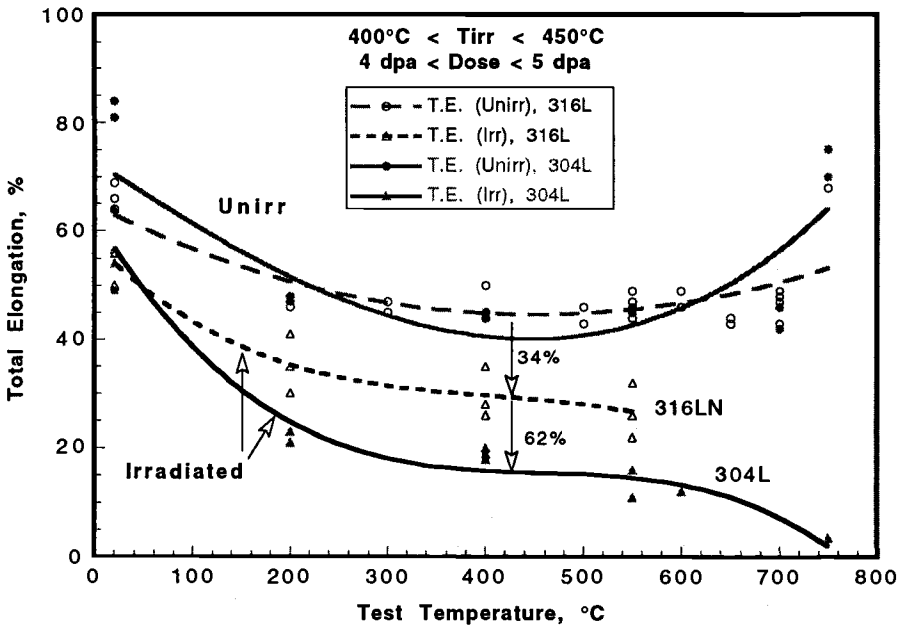


Figure 3. The effect of irradiation at ≈400°C on the tensile ductility of Types 304L and 316L(N) stainless steels in the temperature range 20 to 750°C.

The effect of low dose irradiation on tensile strength in the temperature range 400-450°C can be explained in terms of irradiation-induced hardening by the formation of point defects etc., which restrict dislocation movement. At low test temperatures (up to 400 to 450°C) this type of hardening persists. At more elevated temperatures, where thermal

recovery processes can take place, irradiation hardening is gradually lost and unirradiated material strength is fully recovered at very high temperatures (2).

The reduction in strain at failure (with respect to unirradiated material) observed at lower test temperatures reflects the irradiation-induced strengthening. However, at the more elevated test temperatures, continuous decreases in ductility can no longer be attributed to this phenomenon. Instead, as confirmed by fractographic examination, the dominant mode of rupture changes from transgranular to intergranular. The exact mechanism for grain boundary embrittlement is not yet fully understood but helium formation and irradiation induced grain boundary segregation have been proposed (3) (4). The amount of helium at above which a reduction in ductily has been reported varies significantly, but 0.1 appm is a good approximation.

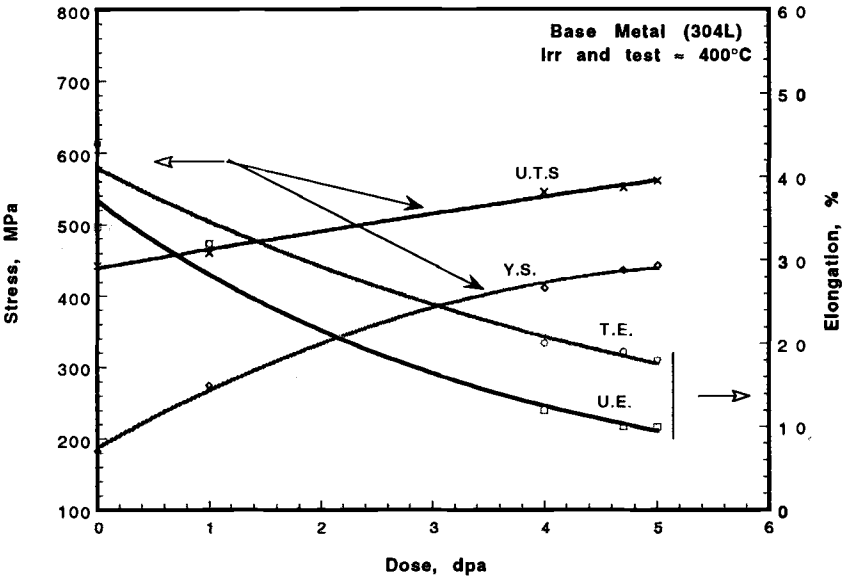


Figure 4. Effect of irradiation dose level at ≈400°C on the tensile properties of Type 304L stainless steel at 400°C.

Weld Metal--Data were collected for the weld metals that are used for joining Types 316, 316L, 316L(N), 304 and 304L steels. These are 19Cr-12Ni-2Mo, 16Cr-8Ni-2Mo, 17Cr-8Ni-2Mo and 18 Cr-10Ni (Type 308L used for welding Type 304L steel), weld metals. Again the majority of the data (half of the data on irradiated steel) was for Type 316 steel weld metal. The irradiation dose ranged from about 0.2 dpa to 5 dpa with test temperatures from 20 to 750°C. As above, the irradiation temperature was between 400 and 450°C.

The property changes observed that were due to irradiation, both in terms of the effects of test temperature and the dose level at 400°C, were similar to those described for the base metal. However, the changes

were less pronounced due to the high yield and tensile strength and low ductility of the unirradiated material. The weld metal ductility remained lower than the base material at all of the dose levels under investigation.

IMPACT PROPERTIES

Base metal and weld metal--Impact toughness data were collected for 316, 316L and 304L steel. The irradiation dose ranged from 0 to 5 dpa, with test temperatures from 20 to 550°C. Data were also collected for 316, 308L and 304L weld metals; irradiation doses varied from 0 to 5 dpa and test temperatures from 20 to 550°C. As above, the irradiation temperature was between 400 and 450°C.

Because of the variety of data from different materials, it is as yet difficult to assess completely all the significant effects. However, if a subset of these data is considered, it is possible to discern the effect of dose on impact properties. Fig 5 illustrates data from Type 304L base metal and Type 308 weld metal, irradiated at temperatures between 400 and 450°C and tested at 400°C. Here, Charpy V-notch energy (standard 10x10x55 mm specimens) is plotted against dose. Note that unirradiated weld metal is inherently less tough than base metal (its impact energy is one third that of base metal) and that for both materials, impact energy decreases as dose level increases in such a way that the differential is maintained for the dose levels investigated. As far as plant operation is concerned, it is the behaviour of the weld metal that is of most interest. Here it will be observed that a dose level of 0.7 dpa has little effect. However dose levels of 4 and 5 dpa reduce the impact energy from 80 (at 0.7 dpa) to 30 J/cm^2.

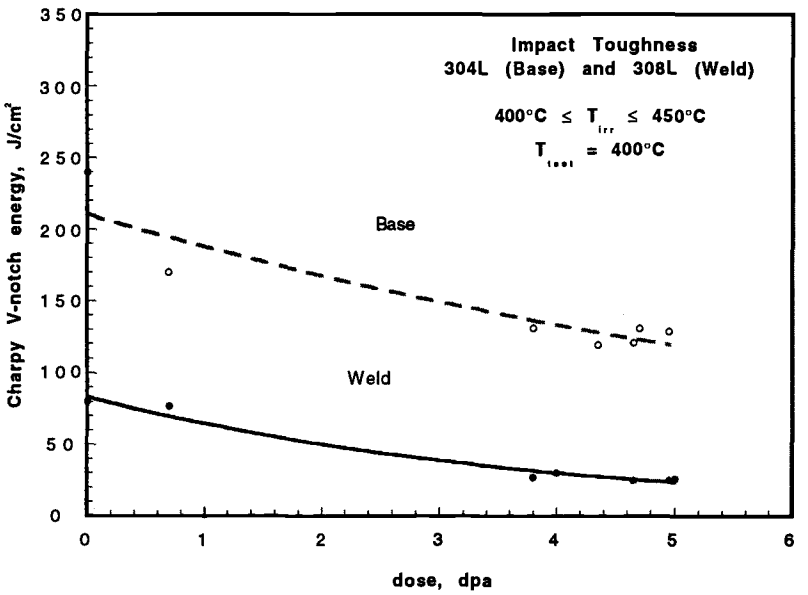


Figure 5. Effect of irradiation dose level at 400-450°C on impact toughness of Type 304L base and Type 308L weld metals at 400°C.

STRESS RUPTURE

Base metal--Stress rupture data on the time to 1% creep strain, the time to begin tertiary creep, rupture time, minimum creep rate, elongation and reduction in area were collected only for Types 304 and 316 steels. The irradiation dose was <0.01 to 2.7 dpa, the irradiation temperatures generally of the order of 550°C and the test temperature 450 to 650°C.

Data are shown in fig. 6 for 304 steel as stress versus time-to-rupture for tests performed at 550°C. Some scatter is observed in both the unirradiated and irradiated data. For unirradiated material, this is a manifestation of variations associated with different product forms of the same cast and differences in the response of different casts. One lot (a forging) exhibits unusually low values after irradiation. This is probably specific to this product and not representative of the steel behavior. The main point to note is that even at very low doses (0.5 dpa) creep resistance is reduced. Although the data shown in figure 6 are for Type 304 steel and the current trend is to use Type 316LN for better creep resistance, as pointed out earlier, in the context of tensile strength properties, the main cause of this degradation is grain boundary embrittlement. An indication of irradiation damage can be obtained through the amount of helium that is formed within the steel. At these very low dose levels, boron is the major source of helium (interaction of thermal neutrons with ^{10}B), and hence its concentration in the steel is an important factor (3).

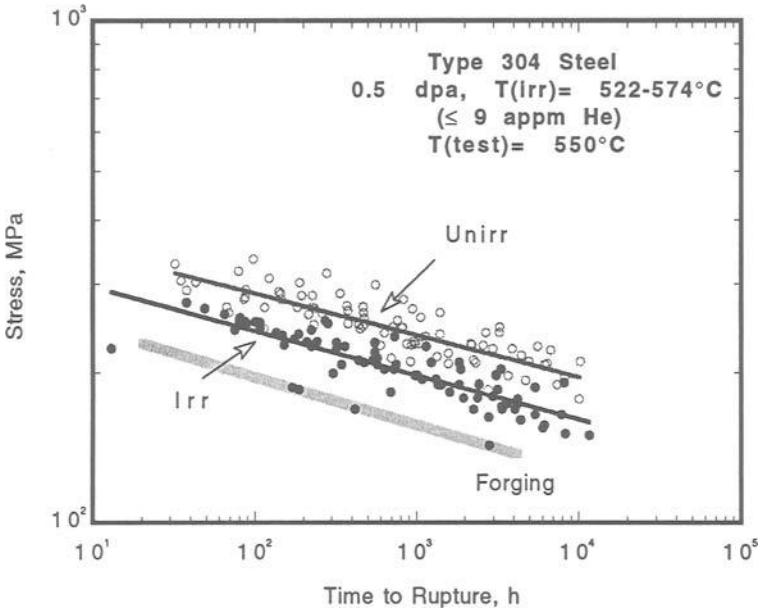


Figure 6. Effect of irradiation on stress rupture behaviour of Type 304L stainless steel at 550°C.

Irradiation also causes a significant decrease in elongation for all test temperatures, this being typically by a factor of 2 for Type 304 steel at temperatures ≳ 550°C, as exemplified by 550°C data in fig. 7, and by an increasing factor (of up to 8) for the highest temperature (i.e. 650°C). A similar pattern of decreasing ductility with irradiation for progressively higher test temperatures was also found for reduction of area.

Weld metal--Only data from Type 316 weld metal were collected. More precisely the data collected are for Type 17-8-2 weld metal used in UK. The irradiation temperature was ≈ 550°C, dose ranged from <0.01 to 2.7 dpa (2 to 44 appm He) and the test temperature was 538 to 600°C.

Although the rupture time at 538°C was decreased by irradiation by a similar amount to the base metal at 550°C, there was no significant effect at 600°C (see fig. 8). However, the elongation (fig. 9) and reduction of area were in general (except for the two points at 2 dpa) significantly decreased by irradiation at 600°C. Notice the significant scatter in the reported data in figures 7 through 9, in part due to variations in the experimental conditions.

The observed difference between the creep behavior at 538°C and 600°C is believed to be due to the enhancement of intergranular failure after irradiation for the former. With increasing test temperature, or creep rupture time (low creep stresses), failure mode of unirradiated material becomes also increasingly intergranular. As a result, the observed effect of irradiation at 600°C is essentially due to the difference in the resistance of grain boundaries before and after irradiation.

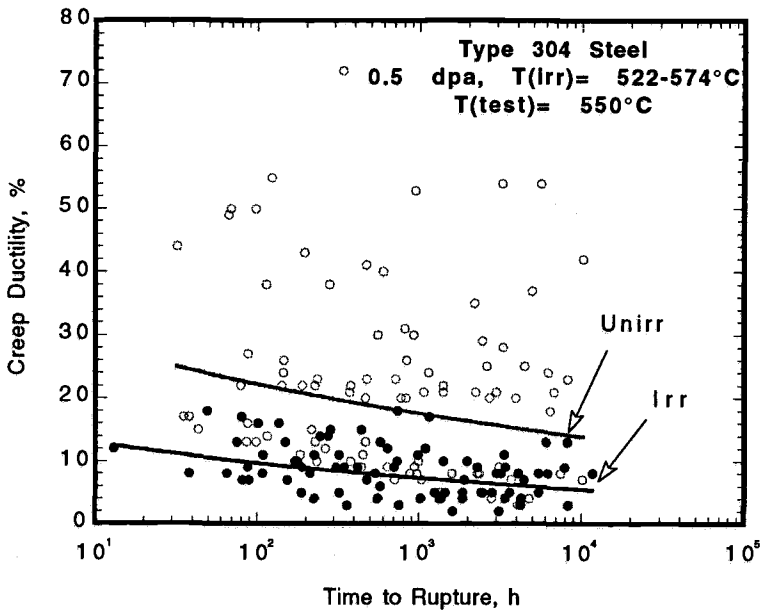


Figure 7. Effect of irradiation on ductility of Type 304L stainless steel at 550°C.

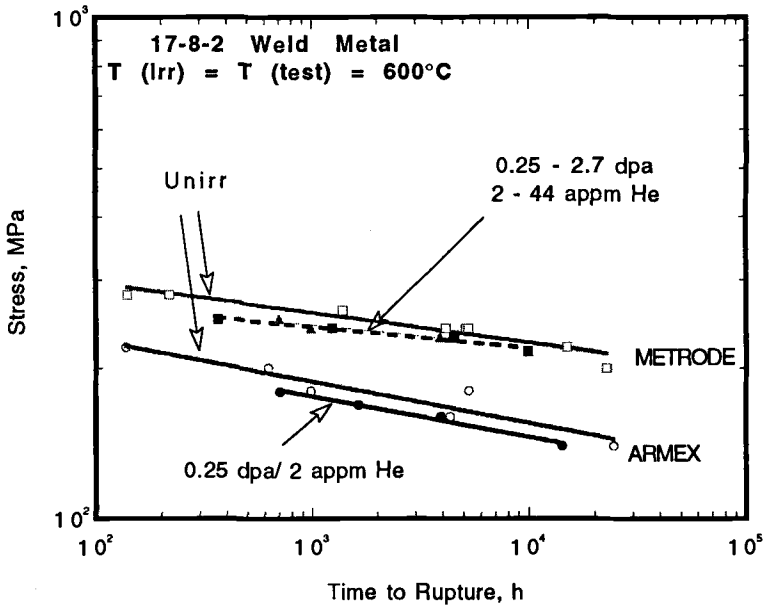


Figure 8. Effect of irradiation on stress rupture behavior of Type 316 weld metal at 600°C.

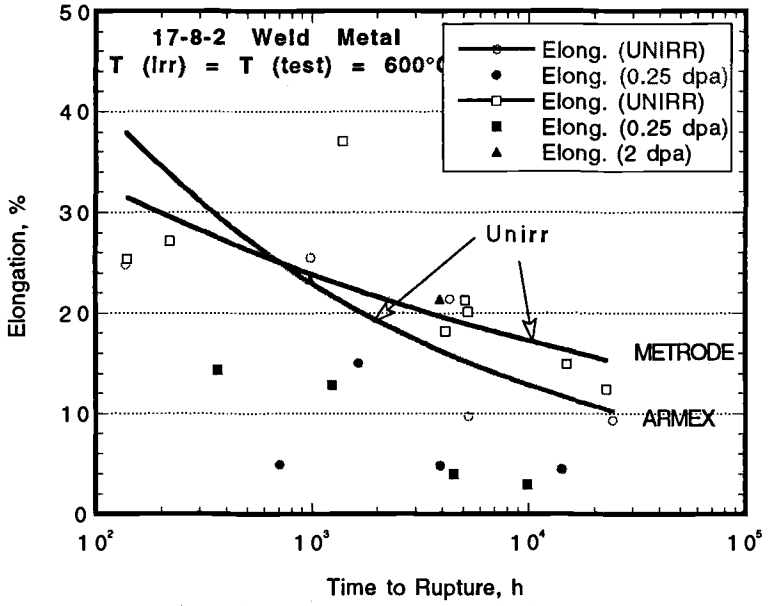


Figure 9. Effect of irradiation on creep ductility of Type 316 weld metal at 600°C.

FATIGUE AND CREEP-FATIGUE

Base metal--Cyclic data (including plastic and total strain range, stress range, hold time and cycles to failure) were collected for types 316 and 304 steel for temperatures from 450 to 700°C. The total strain ranges were from 0.006 to 0.02, with hold times of up to 48 hours for creep-fatigue tests. Irradiation temperatures were usually 550°C and doses varied from 0.01 to 5 dpa.

Continuous cycling fatigue data, in terms of total strain range against cycles to failure, show little effect on fatigue life. Fig. 10 shows data at 550°C. At the highest temperature considered, however (700°C), there is a factor of 2 reduction in fatigue life for irradiated material. This observation is not unexpected for the following reason: Fatigue failure in unirradiated material changes from a transgranular mechanism to an increasingly intergranular process as the temperature increases (5). It is only at the higher temperatures (in this case 700°C), where failure is normally intergranular, that irradiation influences fatigue life (e.g. due to helium formation).

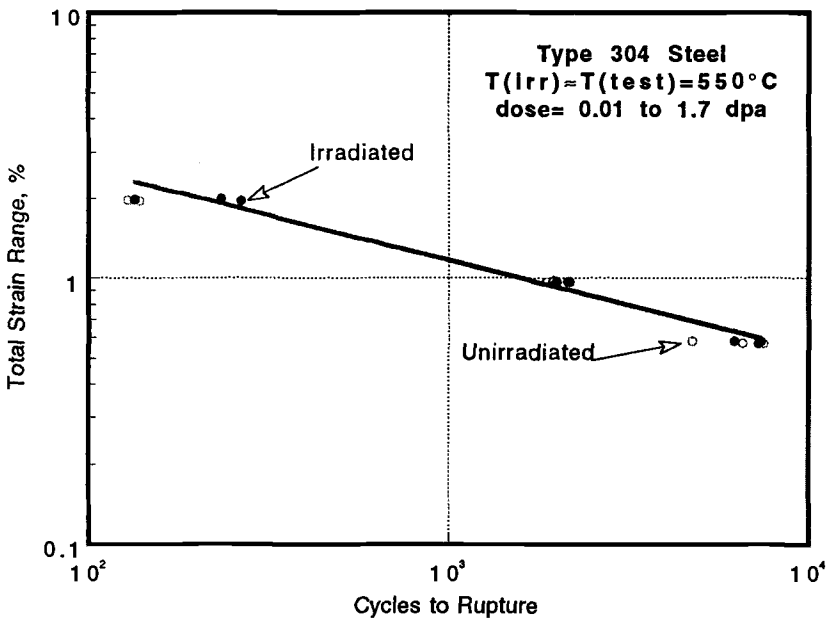


Figure 10. Effect of irradiation on the fatigue properties of Type 304 stainless steel at 550°C.

The effect of a tensile hold period on endurance is shown in fig. 11 and fig. 12 for Types 316 and 304 steels respectively, as plots of cycles to failure against hold time at constant applied total strain ranges. For Type 316 steel, fig. 11, the endurance for both unirradiated and irradiated material decreases as the hold period is extended. The

endurance for the irradiated material is always less than that of unirradiated material for all hold times. For hold times in excess of a few minutes, this difference is of the order of a factor of 2. Similar data are shown in fig. 12 for Type 304 steel at total strain ranges of 1.5 and 0.6%. Note again that the endurance of irradiated material is always less than that of unirradiated material and that endurance continues to decrease as the hold period is extended. The reduction factor for data on irradiated specimens vis a vis data on unirradiated specimens is up to an order of magnitude.

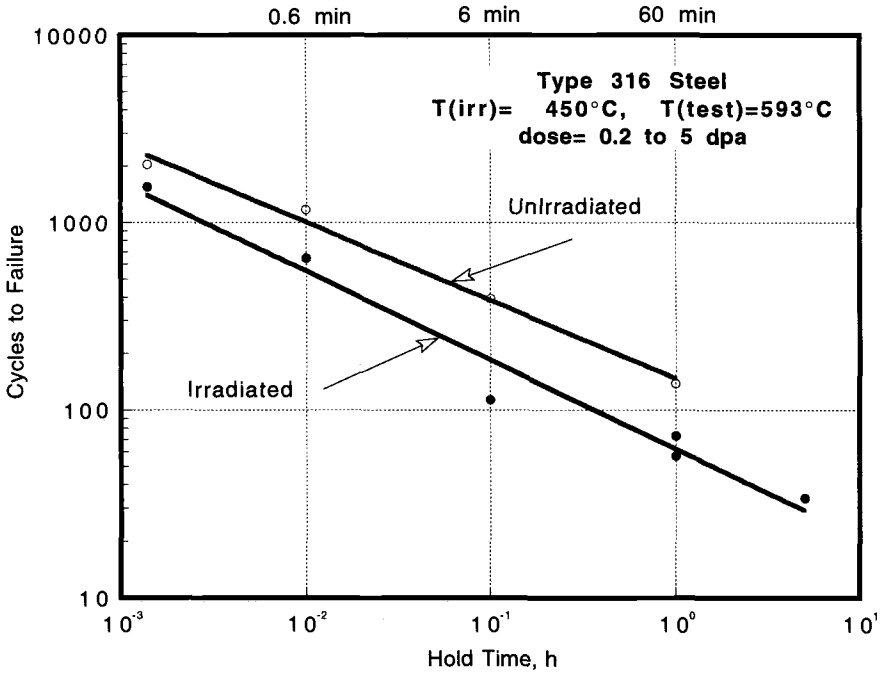


Figure 11. Effect of tensile hold time on the fatigue endurance of irradiated and unirradiated Type 316 stainless steel at 593°C. Total strain range was 1%.

Since the high temperature creep-fatigue life is related to creep rupture ductility, results shown here mirror creep rupture properties (6). These are influenced by irradiation, and ductility is reduced by grain boundary embrittlement, e.g. helium bubble formation. This grain boundary embrittlement is responsible for either an enhancement of fatigue crack growth rate (7) at high strain ranges, or a change in failure mechanism from fatigue- to creep-dominated failure at low strain ranges (6). Under both circumstances endurance is decreased. The present data include long hold times at high strain ranges, and shorter hold times at lower strain ranges. There are as yet few data for the combination of low strain range and long hold time that occurs during plant operation. Under these circumstances failures in unirradiated creep-resistant casts of 316L(N) steel become intergranular. For these situations, the large difference between unirradiated and irradiated

creep-fatigue life is expected to diminish. Experimental verification of such an eventuality is one of the current European goals.

Weld metal--The only data collected were for fatigue tests on an irradiated 18 Cr-11 Ni weld metal, for total strain ranges from 0.006 to 0.02, temperature from 450 to 550°C and dose levels between 0.01 and 0.8 dpa. There were no data available for creep-fatigue tests.

Little effect of irradiation on fatigue life was noticed, as shown in fig. 13, which shows data at 550°C.

DISCUSSION AND CONCLUSIONS

Low dose irradiation is shown to significantly influence mechanical properties, for example by increasing the proof strength and decreasing the creep rupture strength, creep rupture ductility and creep-fatigue endurance. The extent of the changes depends on the irradiation and test temperature and can be summarised as follows:

Mechanical Property	Influence of Irradiation
Tensile	Increase in 0.2% proof stress (at temperatures up to ~400°C), decrease in ductility
Impact Toughness	Decrease in impact energy
Stress Rupture	Significant decrease in rupture strength and ductility
Fatigue	Little effect
Creep-Fatigue	Significant decrease in endurance

Strength and impact energy changes result from low temperature (<450°C) irradiation hardening whilst creep and creep-fatigue property changes are mainly due to high temperature (>550°C) grain boundary embrittlement effects.

The observed changes in properties as a result of low dose irradiation do not necessarily require a modification of existing design codes, because the latter contain important safety margins. However, further work is in progress to evaluate the significant factors and the dose limits above which the effect of irradiation on mechanical properties must be taken into account.

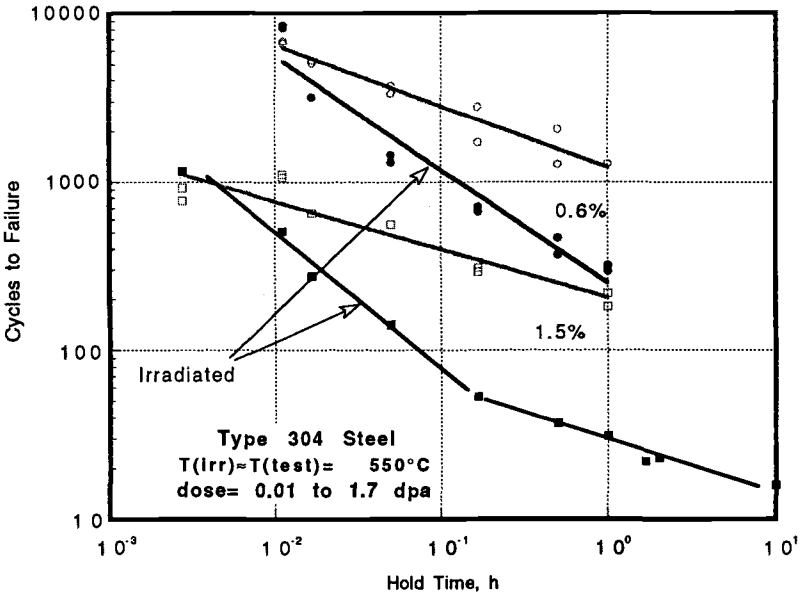


Figure 12. Effect of hold time periods on the fatigue endurance of irradiated and unirradiated Type 304 stainless steel at 550°C.

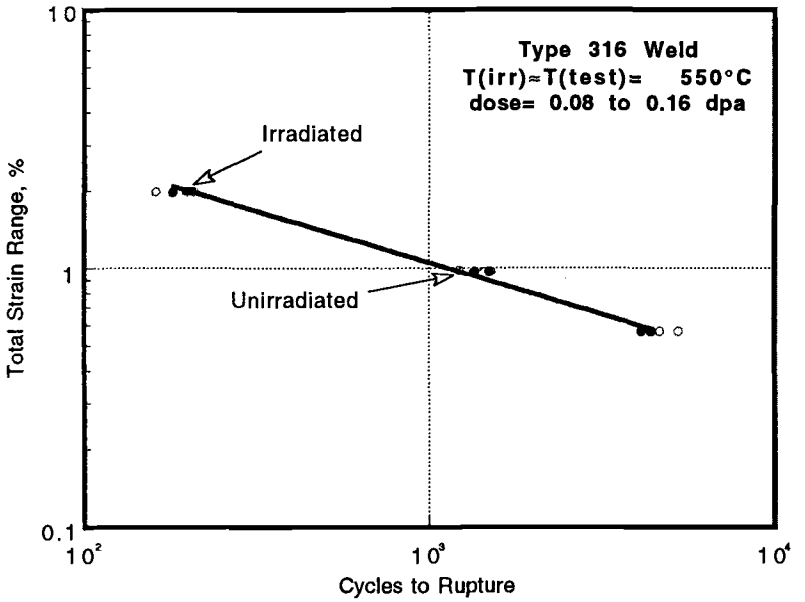


Figure 13. Effect of irradiation on the fatigue properties of Type 316 weld metal at 550°C.

ACKNOWLEDGEMENTS

The role of Dr. V. B. Livesey of AEA Technology and Dr. W. Ohly of Siemens-KWU in carrying out, with Dr. Tavassoli, the original study reported here is gratefully acknowledged.

REFERENCES

[1] Livesey, V. B., Ohly, W. and Tavassoli, A-A., "Evaluation of the effects of low dose irradiation on the mechanical properties of structural steels.", Final Report of Commission of European Communities, Study Contract RA1-0143-UK, Final Report, Oct. 1991.

[2] Tavassoli, A-A, "Effect of neutron irradiation on mechanical properties of permanent near core structures.", Effects of irradiation on materials: 14th International symposium (Volume II), ASTM STP 1046, N. H. Packan, R. E. Stoller and A. S. Kumar, Eds. American Society for Testing and Materials, Philadelphia, 1990, pp. 648-699.

[3] van der Schaff, B., and Marshall, P., "The effect of boron on the development of helium induced creep embrittlement in Type 316 stainless steel.", Conference on the dimensional stability and mechanical behaviour of irradiated metals and alloys, 11-14 April 1983, Brighton, U.K.

[4] Jacobs, A. J., Wozaldo, G. P. , Nakata, K., and Kasahara, S., "The correlation between grain boundary composition in irradiated stainless steel with IASCC resistance.", 6th International symposium on environmental degradation of materials in nuclear power systems-water reactors, Aug. 1-5, 1993, San Diego.

[5] Wareing, J., Tomkins, B., and Sumner, G., "Extent to which material properties control fatigue failure at elevated temperature.", Fatigue at elevated temperature, ASTM STP 520, A. E. Carden, A. J. McEvily and C.H. Wells, Eds. American Society for Testing and Materials, Philadelphia, 1972, pp. 123-138.

[6] Wareing, J., "Mechanisms of high temperature fatigue and creep-fatigue failure.", Fatigue at elevated temperature, R. P. Skelton, Ed., Applied Science, London, 1983, pp. 135-185.

[7] Jitsukawa, S., Umino, A., Takahashi, I., Iida, S., Adachi, M., Suzuki, K., and Hishinuma, A., "Effect of hold time and frequency on the fatigue crack growth rate of irradiated cold worked Type 316 stainless steel.", Effects of irradiation on materials: 15th International Symposium (Volume I), ASTM STP 1125, R; E. Stoller, A. S. Kumar and D. S. Gelles, Eds., American Society for Testing and Materials, Philadelphi, 1992, pp 1083-1094.

Other Materials

Boris A. Kalin,[1] Ivan I. Chernov,[2] Alekseij N. Kalashnikov,[3] and Boris G. Solovyev[4]

BUBBLE MICROSTRUCTURE EVOLUTION AND HELIUM BEHAVIOR IN He^+ IMPLANTED Ni-BASE ALLOYS

REFERENCE: Kalin, B. A., Chernov, I. I., Kalashnikov, A. N., and Solovyev, B. G., "**Bubble Microstructure Evolution and Helium Behavior in Ni-Base Alloys,**" *Effects of Radiation on Materials: 17th International Symposium, ASTM STP 1270,* David S. Gelles, Randy K. Nanstad, Arvind S. Kumar, and Edward A. Little, Eds., American Society for Testing and Materials, 1996.

ABSTRACT: Behavior of ion-implanted helium in Ni as a function of alloying element concentration (Al or Ti) and irradiation conditions (at 20 or 750°C) have been investigated by means of thermal desorption spectrometry (TDS) and transmission electron microscopy (TEM).

Substitution elements in solid solution were demonstrated to have substantial influence on the evolution of implanted helium, shifting the TDS spectrum peaks to higher temperature region and increasing the quantity of helium remaining in the samples after long-time postirradiation annealing. TEM investigations showed that in the case of postirradiation annealing, helium bubbles are formed earlier in quenched alloys than in those annealed. In the high-temperature irradiated alloys, the bubbles

[1]Professor, [2]Associate Professor, [3]Researcher, [4]Post-Graduate Student, Department of Physical Problems of Materials Science, Moscow State Engineering Physics Institute, Moscow 115409, Russia

Copyright© 1996 by ASTM International www.astm.org

formed are smaller in size and higher in density than in the case of postirradiation annealed samples irradiated at room temperature. Alloying elements reduce bubble diameter and increase bubble number density. This is especially typical for concentrations of alloying elements that exceed the ultimate solubility in nickel.

KEYWORDS: nickel base alloys, helium bubbles, microstructure, trapping and release of helium

---

The problem of helium in structural materials of nuclear and thermonuclear reactors is important because of its role in radiation effects, often leading to degradation of material properties. A great amount of work to study helium behavior in various materials (pure metals, structural steels and alloys) has been performed over the last decades including studies on the trapping and release peculiarities of gas implanted by various methods (for example [1-9]), helium bubble formation and growth mechanisms [10-16], helium contribution to radiation induced swelling (for example [17]) and changes of mechanical properties [9, 13, 17-21], bubble formation features at grain boundaries and within grains of a material [22-24] etc. However problems related to the role of alloying elements on helium behavior, including helium bubble formation mechanisms, have not been adequately studied. Few efforts in that area are known at the present time. They include the influence of carbon [25-27] and aluminium and titanium [26, 27-29] in nickel, carbon and boron [6, 9, 30] and titanium [31-33] in steel as a function of introduced gas and creation of helium bubble microstructure.

This paper presents the experimental data related to the effect of alloying elements in Ni (Al up to 7.5 % and Ti up to 8.3 %) on the parameters controlling formation of bubble structure and the trapping and release of ion-implanted helium.

MATERIALS AND EXPERIMENTAL DETAILS

Binary alloys of the nickel-aluminium (Ni-Al) and nickel-titanium (Ni-Ti) systems containing (in wt.%) 0.1, 1.0, 2.0, 2.8, 4.2, 4.6, 6.1, 7.5 %Al and 0.1, 1.0, 4.2, 8.3 %Ti as well as commercial age hardening steel 04C15Cr35Ni2MoNbTiAlB were studied. Alloys were prepared from high-purity Ni (99.99%) according to the technique described in Ref. [34]. The samples were given two heat treatments after repeated rollings with intermediate homogenizing annealings to final thickness of 0.2 mm:

- quenched in cold water from 1100°C after exposure for 1h in vacuum (WQ);

- WQ + annealed in vacuum at 750°C for 1 h following by furnace cooling (WQ+A).

The samples 55x5x0.2 mm in size were irradiated under identical conditions (in a special cartridge) with a surface scanning 40-keV helium-ion beam up to a fluence of 5×10^{20} m^{-2}, at a target temperature of either 20 or 750°C.

The microstructural investigations were performed with either a Philips EM-400T or a JEOL-200CX transmission electron microscope (TEM). TEM specimens were prepared by jet electrical polishing from the unirradiated side.

The details of trapping and release of the implanted helium were studied by means of a helium partial pressure meter, with residual pressure never exceeding 10^{-4} Pa during dynamic evacuation [35], even with sample heating rates, α, of 0.83, 2.5 and 10 K/s. The effective activation energy of gas release, E, at the TDS peak was calculated from the peak shift as a function of the heating rate (tempering technique [36]) according to the expression:

$$E = k\,(Tm_1 \times Tm_2/(Tm_2 - Tm_1)\,\ln[(\alpha_2/\alpha_1)(Tm_1/Tm_2)^2]\,,$$

where α_1 and α_2 are the heating rates; Tm_1 and Tm_2 are the peak temperatures for two different heating rates α_1 and α_2, respectively; k is Boltzmann's constant.

Measurements of the specific electrical resistance, ρ, and microhardness, H_μ, were carried out using classical techniques [28, 37].

RESULTS

Microhardness and specific electrical resistance for the WQ and WQ+A alloys have been measured to obtain a more accurate definition of Al and Ti solubility in nickel.

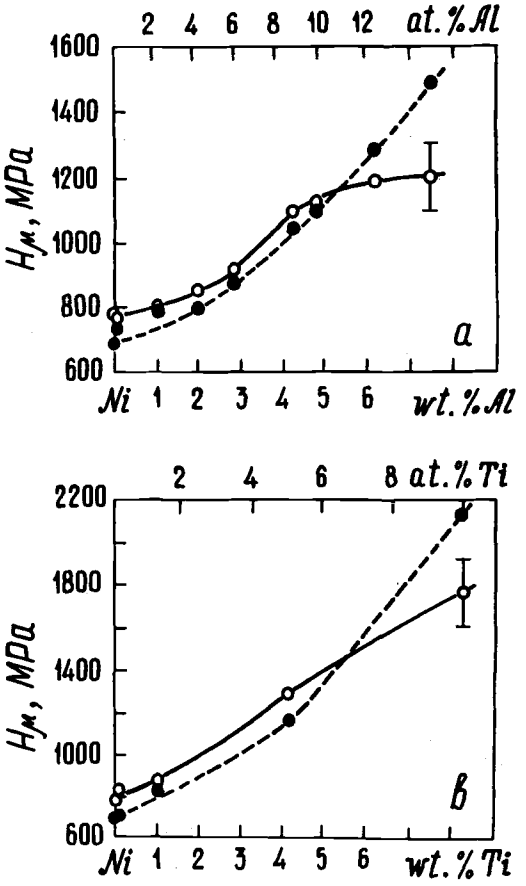


Fig.1--Microhardness of Ni-Al (a) and Ni-Ti alloys: WQ (o) and WQ+A (•). Microhardness of steel is 1460 (WQ) and 1730 MPa (WQ+A), respectively.

Fig.1 shows that the microhardness of samples increase continuously with alloying, but at a slightly lower rate below 5% Al or Ti, and at a considerably higher rate with alloy content above 5% in the WQ+A (i.e. aged) alloys as compared with the WQ ones. The curves for H_μ in the WQ and WQ+A conditions intersect at about 5% for both Al and Ti variation. As can be seen in fig.2a, electrical resistivity increases with increasing alloy content also. This is in good agreement with other researchers' data [38, 39] presented in the same diagram. Furthermore, an inflection is observed at approximately 5% Al on the dependence of ρ versus Al content. Above this concentration, the slope increases. This indicates that the equilibrium solubility limit for Al and Ti in Ni corresponds approximately to about 5%.

TEM studies showed that WQ alloys are homogeneous solid solutions of Al or Ti in nickel (alloys with 6.1 and 7.5% of Al and 8.3% of Ti content are supersaturated solid solutions in accordance with the equilibrium binary Ni-Al and Ni-Ti constitution diagrams [40, 41] and in agree with the above data). The steel contains a small amount of M(C,N) type primary carbonitrides.

Fig.2b shows the electrical resistivity change for WQ+A alloys, $\Delta\rho/\rho$, relative to the resistivity for properly annealed (25h, at 750°C) pure nickel. As can be seen from this figure, $\Delta\rho/\rho$ in WQ nickel is 15% higher than in the WQ+A condition. Addition of only 0.1% Al, leads to the same effect as in WQ alloys. In the alloys with a high concentration of Al, $\Delta\rho/\rho$ decreases, especially for alloys with 6.1 and 7.5 % Al, nevertheless remaining above that for pure nickel. This is because a portion of the dopant is removed from solid solution into growing particles of secondary γ'-Ni_3Al phase as the supersaturated alloys decompose in the course of the initial heat treatment (aging at 750°C for 1h). For example, in alloy Ni-7.5Al, the average size of γ'-phase particles visible in TEM is about 10 nm at a particle density of $2X10^{20}$ m^{-3}, after heat treatment [29].

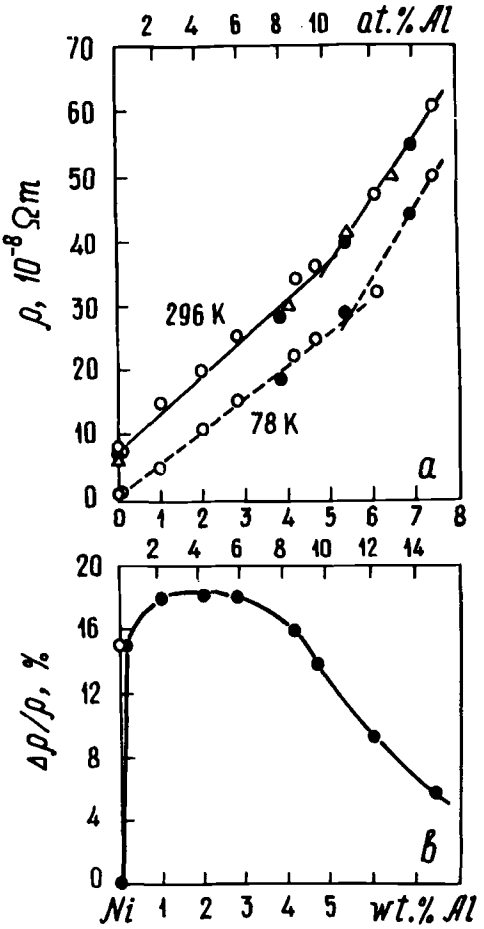


Fig.2--Specific electrical resistivity of Ni-Al WQ alloys (a) at room temperature (296 K) and at temperature of liquid nitrogen (78 K) according to data [38] (•), [39[(Δ) or obtained in the course of our experiments (o) and electrical resistance change of these alloys (b) in respect to resistance of pure Ni annealed at 750°C for 25 h: WQ (o) and WQ+A (•). Resistivity of steel is 124×10^{-8} and 114×10^{-8} Ωm at 296 and 78 K, respectively.

WQ + He^+-irradiation at 20°C

After ion-irradiation at room temperature a cluster-loop structure can be observed only in the alloys. As the alloying

element concentration is increased, the size of the defects decreases while their density increases. TDS measurements of helium show that approximately the same quantity of gas is trapped in all alloys of a given system irradiated at 20°C irrespectively of dopant concentration. The trapping coefficient is close to one for the ion fluence used [42], in good agreement with other data [6, 8]. But after long-time postirradiation annealing (25h, 750°C), dopant concentration influenced significantly by the quantity of helium remaining in samples (fig.3). As much as 30-40% of the initially trapped gas is retained at this temperature in solid solutions of Al in Ni which is higher than the quantity of helium retained both in pure Ni and in the decomposing alloy of Ni-7.5Al (only about 5-7%). This allows the assumption that the substitution alloying elements in nickel are the strongest traps for implanted helium atoms or that they create microstructure which prevents gas release during heating.

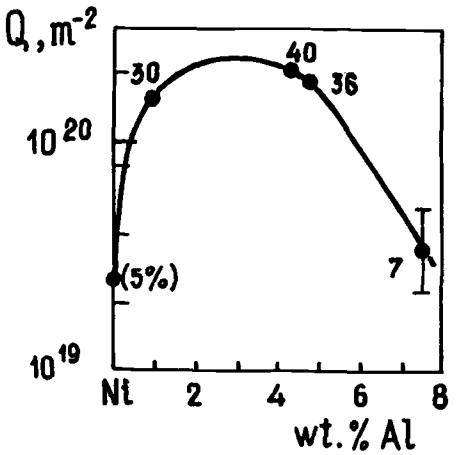


Fig.3--Amount of helium retained in Ni-Al alloys irradiated up to fluence of 5×10^{20} m^{-2} at 20°C after 25 h annealing at 750°C.

Bubbles visible in TEM are formed after exposure at 750°C for 0.15 h in the samples implanted with helium in the WQ condition (fig.4). The bubble diameters increase and their density decreases with increasing annealing times up to 1 h as expected

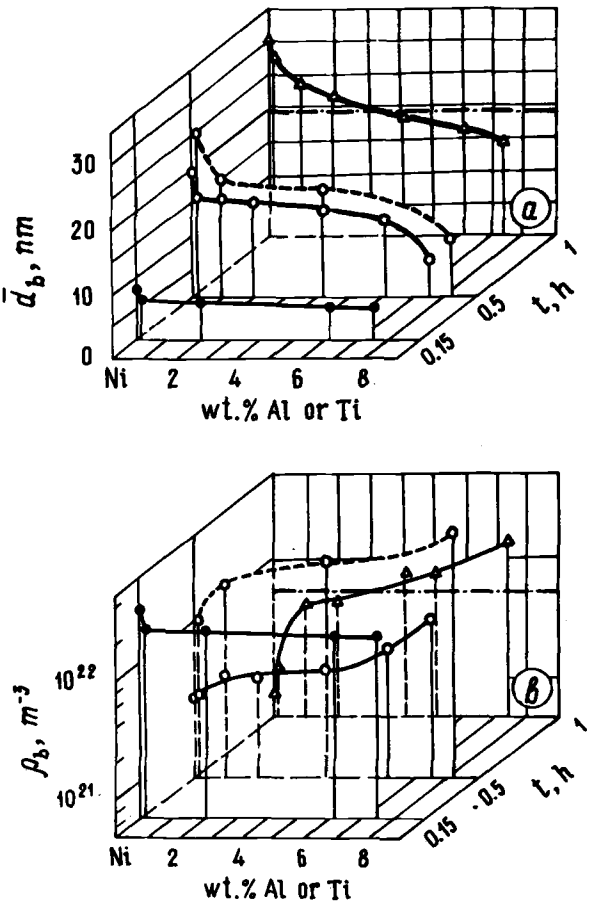


Fig.4--Mean diameter (a) and density (b) of bubbles in alloys irradiated at 20°C after annealing at 750°C as a function of alloying element concentration and annealing time: Ni-Al alloys (———), Ni-Ti alloys (------) and steel (-·-·-·). Initial state: WQ.

[16, 24, 29]. Also, as can be seen in fig.4, the bubble parameters are affected by alloy dopant content: mean bubble diameter, $\bar{d}_b$, decreases and bubble density, ρ_b, increases with increasing of Al or Ti concentration in nickel. It should be noted that the bubbles in Ni-Ti alloys are larger in size and have higher density than those in Ni-Al alloys irradiated and annealed under identical

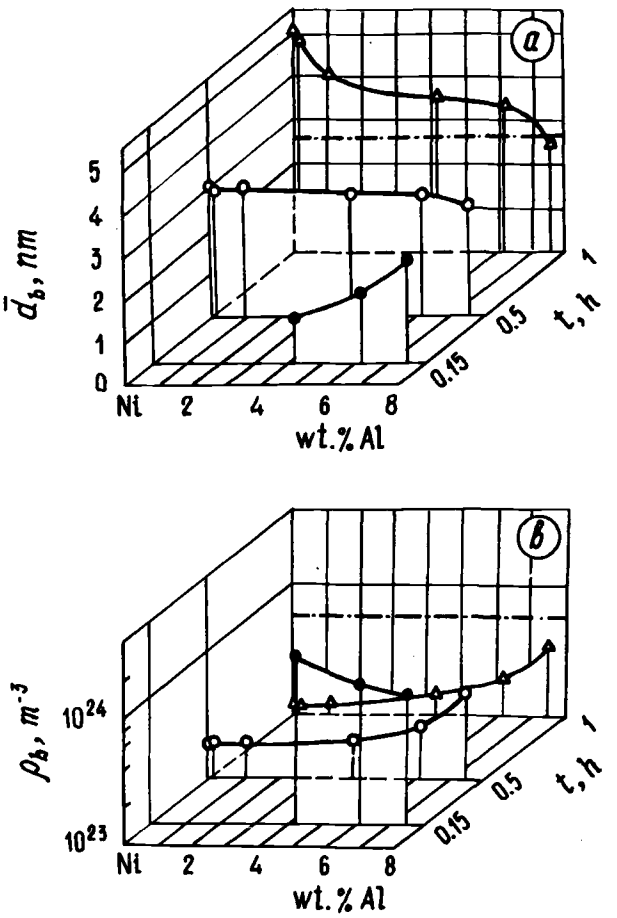


Fig.5--Mean diameter (a) and density (b) of bubbles in alloys irradiated at 20°C after annealing at 750°C as a function of alloying element concentration and annealing time: Ni-Al alloys (———) and steel (-·-·-·-). Initial state: WQ+A.

conditions. The bubble parameters for steel approximately correspond to those for alloys with 3-3.5 % Al (after a 1h anneal).

WQ+A + He^+-irradiation at 20°C

The same influence of alloying elements is typical for alloys irradiated in an initial annealed (WQ+A) state (fig.5). But the

important feature of pretreatment on the bubble microstructure parameters is creation of smaller bubbles at higher density than that for the WQ samples (figs. 4 and 5). For example, in the case of the 0.5h postirradiation anneal, $\bar{d}_b$ = 2.5-3 nm for WQ+A samples and $\bar{d}_b$ = 8-20 nm for WQ samples, number densities being about 10^{23} and 10^{21} m^{-3}, respectively. It is noteworthy that with this heat treatment (WQ+A), helium bubbles appear earlier in decomposing alloys during postirradiation annealing as compared with nickel and solid solution alloys, within 0.15 h (fig.5). However with a longer postirradiation annealing, the bubbles forming in pure Ni and solid solution alloys grow considerably faster, and after 1h annealing the bubble mean diameters in Ni are about 2 times greater than in the Ni-7.5Al alloy (fig.5a), just as in the previous case (fig.4a).

WQ + He^+-irradiation at 750°C

Fig.6 shows the change in bubble parameters in the WQ Ni-Al alloys due to high-temperature irradiation as a function of Al content. As in two cases presented above (figs.4 and 5) aluminium decreases $\bar{d}_b$ and increases ρ_b in the alloys.

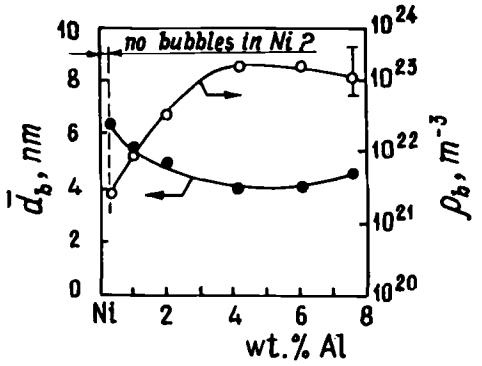


Fig.6--Bubble parameters in Ni-Al alloys irradiated at 750°C up to fluence of $5x10^{20}$ m^{-2}. Initial state: WQ.

A salient feature in this case is that the bubbles formed during high-temperature irradiation (0.15h, 750°C) have smaller

diameters (about 4-6 nm) and higher density (10^{22} - 10^{23} m^{-3}) (fig.6) than the bubbles developed during postirradiation annealing within the same time span (irradiation at 20°C + 0.15h annealing at 750°C) with $\bar{d}_b$ = 6-8 nm and $\rho_b = 10^{22}$ m^{-3}, respectively (fig.4). Unlike the data presented in paper [29], where large bubbles were discovered in pure Ni irradiated by He^+ ions at 750°C, no bubbles were found in the course of repeated TEM investigations of Ni irradiated under the same conditions. Only a well-developed defects and loops were observed.

The TDS study of implanted helium shows that the gas release spectrum for a given fluence for any irradiation mode is characterized by only one maximum located in a high temperature region (for a heating rate 10 K/s). With a low heating rate (0.83 K/s), 1-2 additional resoluable peaks appear. The location of a peak on the temperature scale depends on alloy concentration and heating rate. As can be seen from TDS spectrum maximum temperatures presented in figs. 7 and 8, the peaks shift to higher temperatures with increasing alloy concentration. It is interesting to note that in the alloys irradiated at room temperature, almost monotonic growth of the peak temperature with dopant concentration can be observed (fig.7) while the reverse shift of peaks can be observed for the case of high-temperature irradiation and for high alloy concentration at heating rates of 2.5 and 10 K/s (fig.8).

For an identical heating rate (α = 2.5 K/s), the alloys of the Ni-Ti system have higher peak temperature than those of the Ni-Al system (fig.8). This could be an indication that Ti atoms having a greater size factor promote stronger retention of helium in nickel. It should also be noted that dispersion-hardening steel decomposing with precipitation of secondary γ'-$Ni_3(Al,Ti)$ phase (other intermetallic phases appear on the later stages of aging [43]) have approximately the same peak temperature as Ni-7.5Al or Ni-8.3Ti decomposing alloys.

Another important peculiarity of ion implantation on helium behavior is that, with the same heating rate, the gas release for high-temperature irradiated samples starts considerably later in comparison with alloys irradiated at room temperature (figs. 7 and 8). For example, the temperatures of the main peaks for pure

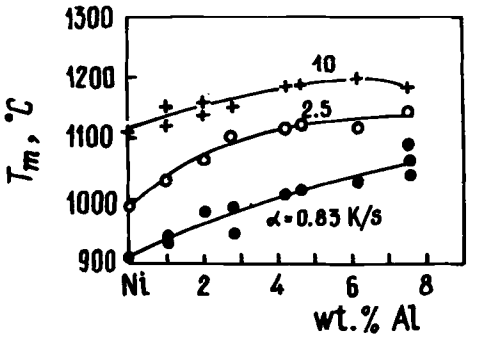


Fig.7--The temperature of maximum gas release rate from WQ Ni-Al alloys irradiated at 20°C as a function of Al content in the condition of three even heating rates: α = 0.83, 2.5 and 10 K/s.

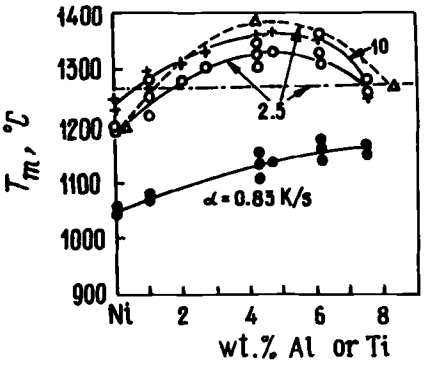


Fig.8--The temperature of maximum gas release rate from WQ alloys irradiated at 750°C as a function of alloying element content in the condition of three even heating rates: α = 0.83, 2.5 and 10 K/s. Alloys: Ni-Al (———), Ni-Ti (------) and steel (-·-·-·-).

Ni differ by almost 200°C when α = 2.5 K/s and are about 1200 and 1000°C respectively.

In the relation of gas release effective activation energy, E, to Al concentration in Ni three peculiarities can be observed (fig. 9). Firstly, with the increase of Al content in the alloys irradiated at 20°C E grows monotonically. This is also the case

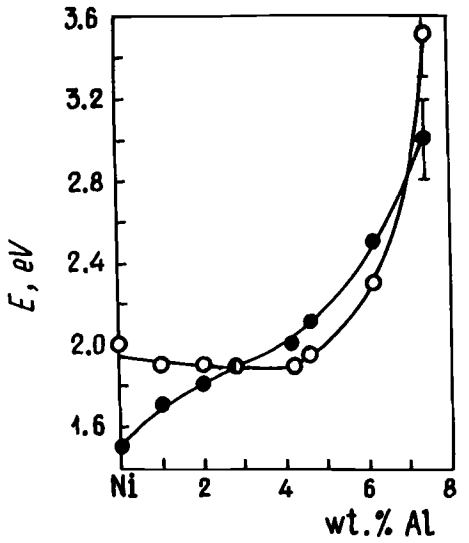


Fig.9--Effective activation energy of helium release from Ni-Al alloys irradiated at 20°C (•) and 750°C (o) versus Al content.

with the alloys irradiated at 750°C but only in the conditions where Al concentration exceeds 5%. Secondly, E for various irradiation temperatures differs significantly in pure Ni and in the Ni-7.5Al decomposing alloy. For Ni, E = 2 and 1.5 eV and for the Ni-7.5Al alloy E = 3.5 and 3 eV for the temperatures 20 and 750°C respectively. Thirdly, despite the fact that an intensive gas release from the samples implanted at high-temperature begins later than from the samples implanted at room temperature, the effective activation energies for gas release from solid solution alloys (< 5% Al) actually coincide in both cases.

DISCUSSION

We begin the discussion of the results gained in the course of experiments by clarifying the initial state of materials. In WQ alloys, atoms of Al or Ti occupy a substitution position in the nickel crystal lattice. Having considerable size misfit with atoms of Ni, they create local deformation fields in the crystal. This is the

main factor which contributes to alloy strength (microhardness) and specific electrical resistivity increase with increasing alloy concentration (figs.1 and 2).

Annealing of WQ samples causes a decrease in the concentration of quenched vacancies and structural relaxation of the lattice. This manifests itself in a H_μ decrease in Ni and in solid solution alloys (< 5% Al or Ti), and yet H_μ is higher in WQ+A (i.e. aged) alloys than in WQ alloys for concentrations over 5% Al or Ti. This indicates that the nickel lattice is hardened by formation of zones of segregations or/and precipitation of secondary γ'-Ni_3Al or η-Ni_3Ti particles. As this takes place, the magnitude of H_μ for Ni-Ti alloys exceeds the relevant values for Ni-Al alloys both for solid solutions and for decomposing alloys for identical concentration of alloying elements, as can be seen in fig.1. This shows the development of large dilatation in the Ni lattice as a result of doping by Ti because the relative misfits of atomic radii, $|r_{Ni} - r_{Me}|/r_{Ni}$, for Ti and Al are 16.9 and 15.3% respectively [43].

The presence of a point of inflection on the diagram illustrating ρ as a function of dopant concentration in the region of concentrations corresponding to ultimate solubility of Al in Ni at room temperature (about 5% [41]) is evidence of the overlapping of crystal lattice local dilatation stress fields in supersaturated solid solutions. It also shows non-additiveness of the effect of total stress created by individual atoms in comparison to the sum of the stress fields created by the same atoms (effect of mutual amplification). It is obvious that such a large influence of Al and Ti atoms as well as the effect of the initial heat treatment on the Ni matrix characteristics should also influence the defect and implanted helium behavior and gas bubble parameters. However it is also clear that their influence on helium behavior and on the bubble development are very complicated and are affected by many factors. Therefore, in each case, a special investigation is required [9].

If, in the general case, helium trapping is envisaged as a model filling in vacancies with gas atoms due to the high density of injected helium (as in our situation) and relatively low temperatures, then from the V-He_m complexes (where V is a vacancy, He is helium atom) a pressure is exerted on the

surrounding lattice and, hence, the distortion of the lattice around the complex increases [12, 17, 22, 44]. Calculations show [45-47] that after some critical number of helium atoms per vacancy being reached, addition of the next gas atom to the complex can perform by pushing out an atom (I) to an interstitial position according to the reaction He_mV + He -> $He_{m+1}V$ + I. This process continues with the formation of large complexes of He_mV_n type. Such complexes can grow further by pushing out interstitial loops [12, 44, 46, 47].

The centers for such complexes in pure Ni are usual vacancies (radiation-induced or structural, for example, quenched-in vacancies). However in alloys where Al or Ti atoms create elasticly-distorted zones in the Ni lattice, such centers could also be represented by substitution atoms because their compressive areas "attract" vacancies or their complexes which trap implanted gas atoms during irradiation. Almost identical relative resistivity changes in the WQ nickel and the WQ+A Ni-0.1Al alloy compared to fully annealed nickel (fig.2b) confirm this assumption indirectly. This should lead to an increased density of He_mV_n complexes and hence to increased numbers of self-interstitial atoms or/and loops per unit of time.

In fact, TEM studies confirm an increase of interstitial loop density with increasing dopant concentration in alloys irradiated with helium ions at room-temperature. Such complicated complexes including alloying element atoms, vacancies and helium atoms can be more stable thermally than He_mV_n complexes in Ni because, as seen in fig.3, after long time annealing at 750°C the alloys retain 6-8 times as much helium in comparison with undoped nickel. In our opinion, this means that one of the mechanisms of helium retention in alloys is by conservation in complexes containing alloying element atoms. In such cases the dissociation temperature of these complexes should be higher than 750°C. There are no direct data available in the literature on He-Al-V or He-Ti-V high stability complexes. However results from Refs. 7, 48, and 49 confirm the plausibility of this idea. It is difficult to reliably assess the mechanisms of gas release at this temperature (750°C) since in TDS investigations, the starting point

for helium release from Ni under even heating occurs at considerably higher temperatures for a given fluence ($5x10^{20}$ m^{-2}) [4-6, 8].

In the case of long-time isothermal annealing at an elevated temperature (25 h, 750°C) bubbles increase in size but with considerable reduction in density [14, 16, 50]. In the case of Ostwald ripening, gas release can be performed in the course of bubble redissolution (migration of untrapped helium atoms from one trap to another). In the case of bubble growth by means of migration and coalescence, gas release can be a result of bubble dissolution via grain boundaries and surfaces [8]. The realization of one or another of these mechanisms depends on a number of factors, [9, 16] and unambiguous determination is quite difficult. Nevertheless, the role of alloying elements is obvious (fig.3), and accordingly, the second mechanism for helium retention in alloys can be associated with a significant reduction in the Ni atom diffusion coefficient in the case of aluminium doping (fig.10). In this situation bubble dissolution and migration and coalescence will be suppressed because point defects are involved in both processes.

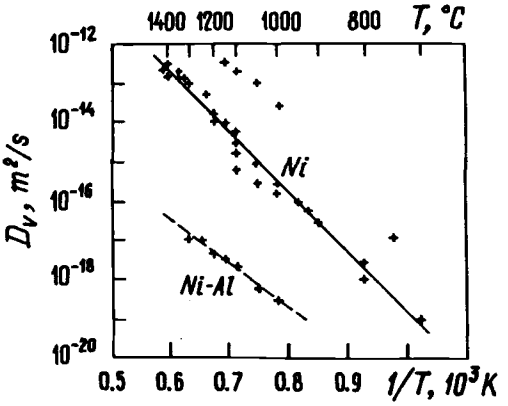


Fig.10--Temperature relationship of Ni self-diffusion coefficient (———) and diffusion coefficient of Ni in Ni-Al alloys (------) for Al content of 12.2-19 at.%. The dispersion of experimental points is shown on the basis of data taken from different sources of Refs [39 and 51].

It is generally known, [24] that complexes in Ni with the highest thermal stability dissociate at temperatures of about 620-650°C (according to data from [7] at 580°C). The deficit of vacancies disappears at temperatures above 700°C, first at the expense of free helium vacancies and then due to thermal vacancies coming, for instance, from the nearest free surface of a sample [24, 52]. TEM examination shows that in the case of a 750°C anneal of WQ samples irradiated at 20°C, helium bubbles appear after only a few minutes (fig.4). It seems reasonable to say that delay in bubble growth in WQ+A alloys (fig.5) is apparently caused by a vacancy deficit because in the WQ+A alloys, vacancy concentration is lower by many orders less than in WQ cases since the vacancy concentration varies proportionally with $\exp(E^f/kT)$, where E^f is the formation energy for vacancies. It is felt [9, 14, 16, 47] that at the earliest stages of annealing, bubble nucleation require only a very short time and follows an Ostwald ripening mechanism (dissolution and reabsorption of gas atoms and vacancies from complexes). Alloying elements provide more centers for bubble nucleation as can be seen in the course of experiments (figs.4 and 5). For the most part, migration and coalescence is the controlling mechanism for bubble coarsening at high concentration of implanted gas and/or relatively short annealing times (our case) [14, 16]. But a peculiarity of bubble formation in our experiments is the immediate proximity of bubble zone near the sample surface (the average depth of the bubble zone is about 100 nm). At an annealing temperature of 750°C the existence of this bubble zone indicates that vacancies (thermal) have had sufficient time to reach the zone from the free surface, as was shown in Refs. [24, 52]. As can be seen in fig.11 taken from Ref. [52], a low temperature branch of the curve plotting mean bubble diameter, $\bar{d}_b$, against annealing temperature, determines a "primary" porosity. For temperatures over 600-700°C, a "secondary" porosity emerges. It is caused by growth of bubbles at the expense of the thermal vacancy flow from surface. However due to the fact that Al doping substantially suppresses the diffusion mobility of nickel atoms (fig.10), the growth of "secondary" porosity in Ni-Al alloys is delayed in comparison with pure nickel (fig.11). Two experimental points for

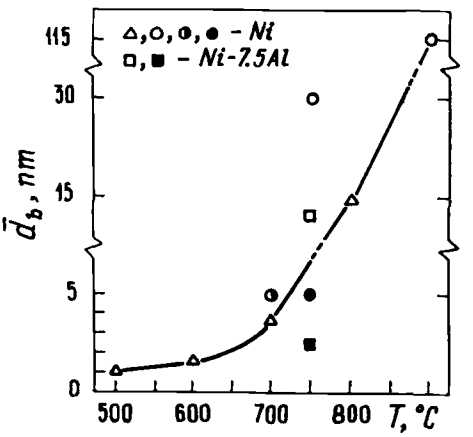


Fig.11--Mean bubble diameter as a function of the isochronal annealing temperature of Ni irradiated with 40-keV He^+ ions up to fluence of $1x10^{20}$ m^{-2} at T<100°C (△,○) [52], as well as of WQ (○,□) and WQ+A (●,■) Ni (○,●) and Ni-7.5Al alloy (□,■), irradiated up to fluence of $5x10^{20}$ m^{-2} at 20°C (data from our research).

WQ and WQ+A nickel presented in this figure do not coincide with the curve demonstrated in Ref. [52]. However this is quite natural because, firstly, the bubble sizes are determined both by the purity of the nickel used [25-27] and its initial heat treatment (microstructural state), (figs. 4 and 5). Secondly, the concentration of implanted helium in our experiments was five times higher than in the work referenced.

Diffusive mobility of vacancies and helium atoms could take place under high-temperature irradiation ($T > 0.3T_m$, where T_m is melting temperature). Bubble growth in this case could occur on based two mechanisms: diffusive-controlled absorption of gas atoms and vacancies (or mobile complexes) or/and by coalescence in the course of migration. The controlling mechanisms depends on the conditions of bubble growth. In our case, high temperature irradiation at 750°C, i.e. about $0.6T_m$ for Ni, when vacancy concentration is close to that of thermal equilibrium irrespectively of irradiation, the bubbles grow only at the expense of the helium influx and always remain in a state close to equilibrium. It has

been shown [9, 12, 29, 53] that bubble formation conditions for the case 0.15 h of irradiation at 750°C are not equivalent to that for postirradiation annealing (irradiation at 20°C + 0.15 h annealing at 750°C). In the latter case, helium bubbles develop more intensively (figs. 4 and 6). Nevertheless, alloying significantly influences bubble parameters at high temperatures. In particular, $\bar{d}_b$ decreases, although not as much as during postirradiation annealing (figs. 4-6), but ρ_b increases almost by an order of magnitude (fig.6). Such a substantial increase in ρ_b in comparison with the small change in $\bar{d}_b$ could be explained only by the fact that Al atoms are additional centers for bubble nucleation and bubble growth occurs as helium atoms are continuous delivered.

Many researchers consider [2, 4-6, 8, 9] that the only intensive peak in the TDS spectrum of gas release from materials irradiated by helium ions up to fluences of $<10^{21}$ m^{-2} is a result of gas release by mechanism of bubble migration and coalescence and transportation to the grain boundaries or to the sample surface because, as was shown in a number of experiments [9], the effective activation energy of gas release for this peak is not dependent on the implanted ion energy, i.e. on the helium implanting depth. As this takes place, it is often observed [5, 8, 54, 55] that a so-called "pin-hole" or "porous" surface structure develops. There are ample grounds to assume that bubble migration at this temperature occurs under conditions of high volume diffusion [6, 8-10, 56]. Under such conditions the observed peak temperature shift into regions of high temperatures can easily be explained because Al suppress the mobility of Ni atoms while the mobility of Al atoms in Ni under identical conditions is also low (fig.10).

Other question, regarding the samples irradiated at room temperature, is why does gas release start earlier, with a peak temperature that increases continuously with increasing alloying concentration, whereas under high temperature irradiation, gas release starts later and as a function of Al or Ti concentration, a reverse shift of the peak takes place (figs.7 and 8)?

In the case of low temperature irradiation, almost all implanted helium is trapped (the trapping coefficient is close

to 1 [8, 42]) and a lot of vacancies condensed in various He_mV_n or other complexes. Under subsequent heating a break-down of these complexes occurs (before about 700°C), releasing a great amount of helium and vacancies, and forming of bubbles (at temperatures above 600-700°C) which grow continuously. There is no shortage of vacancies and therefore bubble growth can continue due to influx of vacancy and helium (for the growth of individual bubbles) and by their migration and coalescence. In this case any specific structural changes do not take place in supersaturated alloys: secondary phase particles (or preprecipitates) which can be formed at 600-800°C are completely dissolved well before the temperatures of intensive gas release are reached. To put it differently, alloying elements in solid solution influence the gas release mechanism (both migration and coalescence), raising the peak temperature monotonically with increasing alloy concentration (fig.7).

At high irradiation temperature the trapping coefficient is much lower than unity [42], and almost all implanted helium is concentrated in the equilibrium bubbles. Therefore, bubbles can grow only as a result of migration and coalescence (delivery of thermal vacancies into the bubble growth zone can be neglected because heating time is not sufficient to ensure the possibility that they reach the depth where the bubble zone lies [52]). It is likely that this is the main reason for the fact that gas release from the samples irradiated at high temperature starts later. Also, in the course of high-temperature irradiation (including the time at temperature prior to irradiation) precipitation of secondary γ'- or η- phases takes place in Ni supersaturated solid solutions of Al and Ti as solute atoms leave the solid solution. This could be the cause for the reverse shift of the peak temperature with Al and Ti concentrations of more than 5% (fig.8) because the transfer from solid solution to secondary phase particles removes atoms from the process for bubble coalescence. Of course, even heating beyond 850°C a process of dissolution from these secondary phases back into the nickel matrix takes place. However, if solute atoms can return to solid solution from precipitates at low heating rates (α = 0.83 K/s), then there is no reverse peak shift, but when the heating rates are higher, α = 2.5 K/s and, especially, at

α = 10 K/s all particles of secondary phase had not a chance to dissociate, and a reverse shift of the peak temperature takes place, particularly distinct at α = 10 K/s (fig.8).

According to the data of various authors [8, 39, 51], the activation energy of volume diffusion in Ni reaches values of 2.6-2.9 eV. This coincides with activation energies for gas release from saturated alloys (fig.9), indicating a good argument for a volume diffusion mechanism favouring for bubble migration, as it was proposed in Refs [8, 8-10, 16, 56]. However for the alloys with relatively low doping (<5% of Al) and for pure Ni the values of E are lower than the volume diffusion activation energy of nickel. This indicates that bubble migration can be carried out under a surface diffusion controlling mechanism also in relatively pure metals [14].

CONCLUSION

Based on experimental results concerning the influence of alloying on bubble microstructure parameters and ion-implanted helium behavior in nickel, it can be inferred that substitution atoms (Al and Ti) are high-effective traps for helium atoms, directly or by means of vacancy trapping with the creation of stable complexes which incorporate vacancies, helium and solute atoms. These atoms increase bubble nucleation density and decrease bubble size. Also, Al and Ti decrease the coefficient of Ni self diffusion by 2-3 orders of magnitude. This hinders the migration and coalescence of bubbles and transport to the surface, and, accordingly, shifts gas release peaks to the region of higher temperature.

REFERENCES

[1] Kornelsen, E. V., Radiation Effects, Vol. 13, 1972, pp. 227-236.
[2] Reed, D. J., Harris, F. T. , Armour, D. G., et al., Vacuum, Vol. 24, No. 4, 1974, pp. 179-186.
[3] Caspers, L. M., and Van Veen, A., Physica Status Solidi (a), Vol. 68, 1981, pp. 339-350.
[4] Ehrenberg, J., Scherzer, B. M. U., and Behrish, R., Radiation Effects, Vol. 78, No. 1-4, 1983, pp. 405-416.

[5] Chernov, I. I., Kalin, B. A., Guseva, M. I., et al., Surface. Physics, Chemistry, Mechanics, Vol. 11, 1983, pp. 75-83 (in Russian).
[6] Karasev, V. S., and Kovirshin, V. G., Atomic Energy, Vol. 55, No. 6, 1983, pp. 362-370 (in Russian).
[7] Van Veen, A., Materials Science Forum, Vol. 15-18, No. 1, 1987, pp. 3-24.
[8] Zelenskij, V. F., Nekludov, I. M., Ruzhitskij, V. V., et al., Journal of Nuclear Materials, Vol. 151, 1987, pp. 22-26.
[9] Zaluzhnij, A. G., Sokurskij, Yu. N., and Tebus, V. N., "Helium in Reactor Materials," Energoatomizdat, Moscow, 1988.
[10] Tyler, S. K., and Goodhew, P. J., Journal of Nuclear Materials, Vol. 92, No. 2-3, 1980, pp. 201-206.
[11] Singh, B. N., and Foreman, A. J. E., Journal of Nuclear Materials, Vol. 103-104, 1981, pp. 1469-1474.
[12] Trinkaus, H., Radiation Effects, Vol. 78, No. 1-4, 1983, pp. 189-211.
[13] Ullmaier, H., Nuclear Fusion, Vol. 24, No. 8, 1984, pp. 1039-1083.
[14] Chkausely, V. F., Physics of Metals and Metal Science, Vol. 66, No. 4, 1988, pp. 722-726 (in Russian).
[15] Trinkaus, H., Scripta Metallurgica, Vol. 23, 1989, pp. 1773-1780.
[16] Schroeder, H., Fichtner, P. F. P., and Trinkaus, H., Materials Science Forum, Vol. 97-99, 1992.
[17] Zelenskij, V. F., Nekludov, I. M., and Chernyaeva, T. P., "Radiation Defects and Swelling of Materials," Naukova Dumka, Kiev, 1988.
[18] Higgins, P. R. B., and Roberts, A. C., Nature, Vol. 206, No. 4991, 1965, pp. 1249-1250.
[19] Agapova, N. P., Africanov, I. N., Butra, F. P., et al., Atomic Energy, Vol. 41, No. 5, 1976, pp. 314-321 (in Russian).
[20] Shroeder, H., Kesternich, W., and Ullmaier, H., Nuclear Engineering and Design/ Fusion, Vol. 2, No. 1-2, 1985, pp. 65-95.
[21] Kalin, B.A., Skorov, D. M., and Yakushin, V. L., "Problems of Materials Selection for Thermonuclear Reactors," Energoatomizdat, Moscow), 1985.
[22] Ullmaier, H., Radiation Effects, Vol. 78, No.1-4, 1983 pp.1-10.

[23] Ryazanov, A. I., Arutyunova, G. A., Chuev, V. I., et al., Journal of Nuclear Materials, Vol. 135, No. 2-3, 1985, pp. 232-245.

[24] Chernikov, V.N., Trinkaus, H., Jung, P., and Ullmaier, H., Journal of Nuclear Materials, Vol. 170, 1990, pp. 31-38.

[25] Kalin, B. A., Reutov, I. V., and Chernov, I. I., Atomic Energy, Vol. 72, No. 6, 1992, pp. 559-565 (in Russian).

[26] Kalin, B. A., Bogachev, A. G., Chernov, I. I., et al., Atomic Energy, Vol. 73, No. 3, 1992, pp. 203-209 (in Russian).

[27] Kalin, B. A., Chernov, I. I., Bogachev, A. G., et al., Materials Science Forum, Vol. 97-99, 1992, pp. 373-378.

[28] Chernov, I. I., Kalin, B. A., and Kalashnikov, A. N., Atomic Energy, Vol. 72, No. 2, 1992, pp. 171-175 (in Russian).

[29] Kalin, B. A., Chernov, I. I., Kalashnikov, A. N., et al., Effects of Radiation on Materials: 16th International Symposium, ASTM STR 1175, American Society for Testing and Materials, Philadelphia, 1994, pp. 838-850.

[30] Suzuki, K., Katano, Y., Agura, T, et al., Journal of Nuclear Materials, Vol. 133-134, 1985, pp. 585-589.

[31] Coghlan, W. A., and Mansur, L. K., Journal of Nuclear Materials, Vol. 122-123, 1984, pp. 495-501.

[32] Aruga, T., Katano, J., and Shiraishi, K., Journal of Nuclear Materials, Vol. 122-123, 1984, pp. 1401-1405.

[33] Kolk, G. J., and Van Veen, A., Journal of Nuclear Materials, Vol. 127, No. 1, 1985, pp. 56-66.

[34] Kalashnikov, A. N., Kalin, B. A., Reutov, I. V., et al., Physics of Metals and Metal Science, Vol. 7, 1990, pp. 203-206 (in Russian).

[35] Kalin, B A., Markin, A. V., Volkov, A. A., et al, Atomic Energy, Vol. 59, No. 2, 1985, pp. 150-151 (in Russian).

[36] Carter, G., Vacuum, Vol. 12, 1962, pp. 245-250.

[37] Shmatko, O. A., and Usov, Yu., U., "Structure and Properties of Metals and Alloys: Electrical and Magnetic Properties of Metals and Alloys," Naukova Dumka, Kiev, 1987.

[38] Williams, R. O., Trans. AIME, Vol. 215, 1959, pp. 1026.

[39] Jung, P., Ansari, M. I., Klein, H., and Meertens, D., Journal of Nuclear Materials, Vol. 148, No. 2, 1987, pp. 148-156.

[40] Barabash, O. M., and Koval, Yu. H., "Structure and Properties of Metals and Alloys: Cristal Structure of Metals and Alloys," Naukova Dumka, Kiev, 1986.

[41] Lifshitz, V. G., "Metallography," Metallurgiya, Moscow, 1990.

[42] Kalin, B. A., Chernov, I. I., Solovyev, B. G., and Kalashnikov, A. N., Physics of Metals and Metal Science, 1995, (to be published in Russian).

[43] Gulyaev, B. B., Kamishanchenko, N. Y., Nekludov, I. M., et al., "Structure and Properties of Metals," Metallurgiya, Moscow, 1993.

[44] Donnelly, S. E., Radiation Effects, Vol. 90, No. 1-2, 1985, pp. 1-47.

[45] Wilson, W. D., Radiation Effects, Vol. 78, No. 1-4, 1983, pp. 11-24.

[46] De Hosson, J. Th. M., Radiation Effects, Vol. 78, No. 1-4, 1983, pp. 25-36.

[47] Kalin, B. A., and Chernov, I. I., Abroad Atomic Technology, Vol. 9, 1985, pp. 3-15 (in Russian).

[48] Melius, C. F., Wilson, W. D., and Bisson, C. L., Harwell Symposium on Inert Gases in Metals and Ionic Solids, AERE Report 9733, 1980, pp. 15.

[49] Van Veen, A., Buters, W. Th. M., Armstrong T. R., et al., Nuclear Instruments and Methods, Vol. 209-210, 1983, pp. 10551061.

[50] Rothaut, J., Schroeder, H., and Ullmaier, H., Philosophical Magazine, Vol. A47, No. 5, 1985, pp. 781-790.

[51] Larikov, L. Nl., and Isaijev, V. I., "Structure and Properties of Metals and Alloys: Diffusion in Metals and Alloys," Naukova Dumka, Kiev, 1987.

[52] Chernikov, V. N., Zakharov, A.P., and Kazanskij, P. R., Doklady AN USSR, Vol. 304, No. 4, 1989, pp. 870-874 (in Russian).

[53] Ibragimov, Sh. Sh., Kirsanov, V. V., and Reutov, V. F., Problems of Atomic Science and Technology. Series: Phisics of Radiation Damages and Radiation Materials Science, Vol. 2(5), 1977, pp. 65-70 (in Russian).

[54] Erents, S. K., and McCracken, G. M., Radiation Effects, Vol. 18, No. 3-4, 1973, pp. 191-198.

[55] Sinha, M. K., Das, S. K., and Kaminsky, M., Journal of Applied Physics, Vol. 49, 1978, pp. 170-172.

[56] Walker, G. K., Journal of Nuclear Materials, Vol. 37, No. 2, 1970, pp. 171-176.

James F. Stubbins[1] and Frank A. Garner[2]

SATURATION OF SWELLING IN NEUTRON IRRADIATED PURE NICKEL AND ITS DEPENDENCE ON TEMPERATURE AND STARTING DISLOCATION MICROSTRUCTURE

REFERENCE: Stubbins, J. F. and Garner, F. A., **"Saturation of Swelling in Neutron Irradiated Pure Nickel and Its Dependence on Temperature and Starting Dislocation Microstructure,"** *Effects of Radiation on Materials: 17th International Symposium, ASTM STP 1270,* David S. Gelles, Randy K. Nanstad, Arvind S. Kumar, and Edward A. Little, Eds., American Society for Testing and Materials, 1996.

ABSTRACT: Pure nickel was irradiated in EBR-II without active temperature control to two exposures levels (14 and 31 dpa) at target temperatures of 425, 500, and 600°C in three starting conditions: annealed, 30% cold worked, 30% cold worked and aged at 650°C for 10 hr. The same material conditions were irradiated with active temperature control in FFTF to 33-36 dpa at 430, 520, and 600°C. Post-irradiation density measurements show that in the annealed condition swelling tends to saturate at levels strongly dependent on irradiation temperature. In EBR-II at 600°C, saturation occurs before 12 dpa but swelling is still increasing slowly at 425 and 500°C. The tendency toward saturation of swelling is enhanced by cold working. In addition, the temperature dependence of the saturation level is strongly decreased by cold-working. The maximum swelling under most irradiation conditions is on the order of 8%. In the isothermal FFTF irradiations, the effectiveness of cold working in promotion of swelling is much less pronounced at the higher irradiation temperatures, particular at 600°C. These results are consistent with most evidence from other neutron and charged particle irradiation studies on pure nickel. In comparing the results of these and previous studies, it appears that the saturation is linked to a progressive collapse of the dislocation network when voids begin to dominate the microstructure.

KEYWORDS: pure nickel, neutron irradiation, EBR-II, FFTF, microstructure, swelling

[1] Professor, University of Illinois, Urbana, IL 61801 USA
[2] Senior Staff Scientist, Pacific Northwest Laboratory, Richland, WA 99352 USA

Copyright© 1996 by ASTM International www.astm.org

In earlier work [1,2], a review and study of the effects of irradiation on the swelling behavior of nickel was carried out. This work was motivated by the interest in the selection of nickel as a base material for comparison of irradiation effects in a variety of neutron spectra and in other irradiation environments. The previous work, however, showed that irradiation behavior of nickel is very sensitive to several material and irradiation variables. In particular, when irradiated over a temperature range of 420 to 600°C in fission reactor spectra, the microstructural evolution and swelling were highly sensitive to the material starting condition, and also exhibited a saturation in swelling with the saturation level also sensitive to starting microstructure and irradiation temperature. Therefore, the use of nickel is thought to be questionable for comparison of widely disparate irradiation environments. While most of the basis of comparison between different irradiation conditions focused on swelling alone, previous studies demonstrated that large differences in post-irradiation bulk swelling and microstructure are found for the same high purity Ni heat when irradiated in different initial thermal-mechanical treatment conditions [2,3]. The swelling behavior determined in the previous work is shown in Figures 1 and 2. The present work examines the microstructure from the higher dose level of the EBR-II experiment, and also examines the microstructures from an independent experiment conducted on the same material conditions in FFTF.

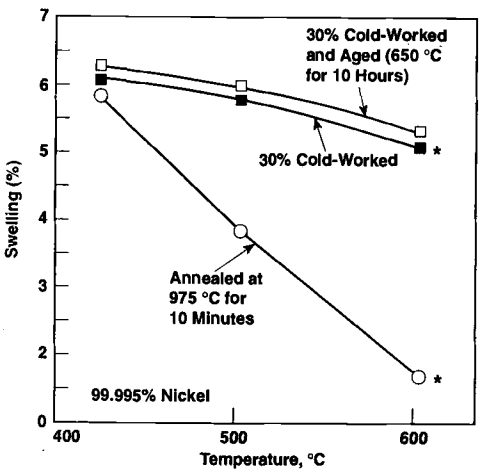


Figure 1, Swelling of pure nickel irradiated in EBR-II to 14 dpa measured by immersion density [2]. (The asterisks indicate point irradiated to 12 dpa.)

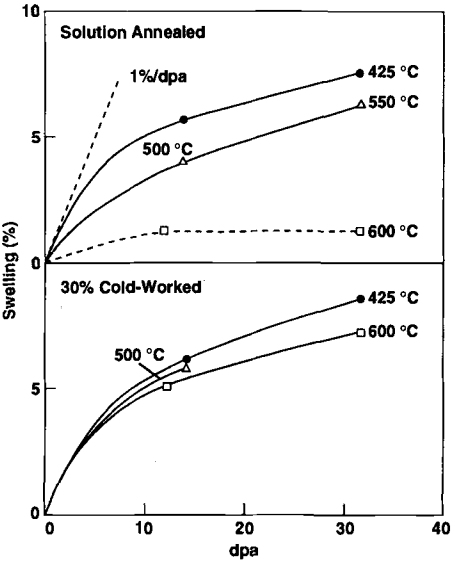


Figure 2, Swelling determined by density change of pure nickel irradiated in EBR-II as a function of initial material condition, irradiation temperature and dose [3].

EXPERIMENTAL

High purity (99.995%) nickel in three thermal-mechanical treatment conditions was irradiated in EBR-II at target irradiation temperatures of 425, 500, and 600°C without active temperature control to doses of 14 and 31 dpa. (The 14 dpa results were reported previously [2].) Material in the same thermal-mechanical treatment conditions was also irradiated at 430, 520 and 600°C with active temperature control in FFTF to a dose of 33-36 dpa. An additional lower temperature, lower dose experiment was also carried out in FFTF with the same materials conditions: 12.3 dpa at 375°C. The thermal-mechanical treatment conditions were solution annealed, cold worked, and cold worked and aged. In addition, for the FFTF irradiation some of the annealed specimens were re-annealed. The specific treatment conditions are given in Table 1.

Table 1, Thermal-Mechanical Treatment Conditions for Nickel

Condition	Treatment History
Solution Annealed (SA)	975°C for 10 min, water quench
Cold Worked (CW)	30% cold rolled
Cold Worked and Aged (CWA)	30% cold rolled, 650° for 10 hrs, water quench
Re-annealed	SA+1000°C for 1/2 hr, water quench

Swelling in all irradiation conditions in both the EBR-II and FFTF experiments was initially determined by immersion density measurements known to be accurate to ± 0.2% change in density. The microstructures of most of the initial and irradiated materials conditions for each of the two experiments were examined using a JEOL JEM 1200EX transmission electron microscope operated at 120 kV.

RESULTS AND DISCUSSION

The results of the new immersion density measurements of swelling for the FFTF irradiations are shown in Figure 3.

The additional swelling data, measured by immersion density, for the 375°C, 12.3 dpa irradiations in FFTF are given in Table 2.

Table 2, Swelling Data for Pure Ni Irradiated to 12.3 dpa at 375°C in FFTF

Condition	Immersion Density Swelling (%)
Solution Annealed	2.61
Re-annealed	2.96
Cold Worked	2.16
Cold Worked and Aged	2.70

The swelling results in FFTF show that, while similar trends exist with respect to the initial starting condition, the cold worked and cold worked and aged conditions show

a greater temperature sensitivity than was observed in the EBR-II irradiations. Cold worked conditions swell more than the solution annealed conditions, but drop to much lower swelling levels, particularly at 600°C, than were found in the EBR-II irradiations.

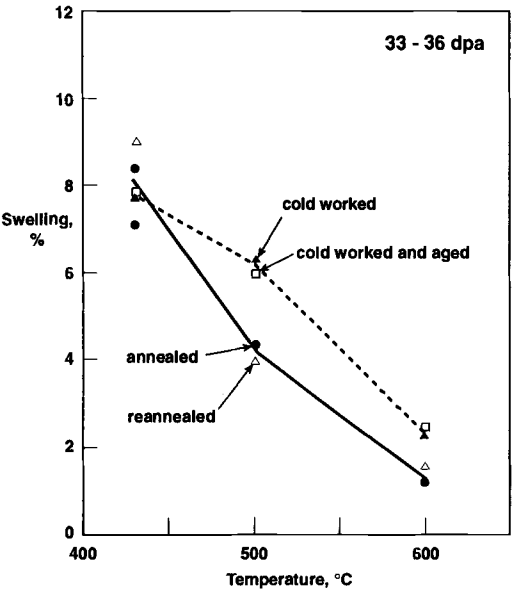


Figure 3, Swelling determined by density change of pure nickel irradiated in FFTF to 33-36 dpa as a function of initial material condition and irradiation temperature.

Due to some indication in the previous EBR-II study that the residual dislocation structure in the annealed material might have been higher than would be typical of a well annealed condition [2], specimens of the solution annealed condition were re-annealed in a more complete manner (see Table 1) and irradiated in FFTF along with the other conditions. As the swelling results from FFTF indicate, there were no significant differences in the response of the annealed and the annealed plus re-annealed conditions. This confirms that the irradiation response of the original "annealed" material is fully representative of the annealed condition.

Selected microstructural parameters from the TEM analysis of the unirradiated and irradiated solution annealed and 30% cold worked materials conditions are presented in Table 3 for the 425 - 430 and 600°C irradiation temperatures.

The present results are consistent with the earlier findings, and confirm that the starting microstructure plays a critical role in determining the swelling and irradiation-induced microstructural evolution in nickel, particularly at temperatures of 500°C and above.

Most notable among the microstructural parameters in Table 3 is the increase in void number densities and decrease in average void size with dose in the cold worked condition at irradiation temperatures of 500 and 600°C and in the solution annealed case at 600°C. These changes are probably due to a refinement of the void structure which first develops at lower doses. This is presumably related to the changes in the dislocation structures with dose. The earlier results also showed that very low dislocation densities developed in the solution annealed condition at 600°C. This is thought to be due to the instability of the dislocation structure at this temperature. Without sufficient obstacles (including voids) for pinning the structure, the dislocation structure evolves or collapses to a low level where the magnitude is determined by the void structure as it develops. It is not surprising that the interconnection of the dislocation and void structures results in a refinement of the void sizes and thereby supports continued void nucleation during irradiation.

Table 3, Microstructural Parameters

Condition	Immersion Density Swelling (%)	TEM-Measured Swelling (%)	N_v 10^{19} (m^{-3})	d_v (nm)	Dislocation Density ($10^{13} m^{-2}$)
Solution Annealed					
Unirradiated	--	--	--	--	4.6
EBR-II, 425°C, 14 dpa	5.8	4.1	24.5	62	3.0
EBR-II, 425°C, 31 dpa	7.5	8.2	19.5	69	2.0
FFTF, 430°C, 33 dpa	7.9	8.2	36.0	56	~1
EBR-II, 600°C, 14 dpa	2.0	1.8	1.3	124	<0.2
EBR-II, 600°C, 31 dpa	2.2	1.1	6.0	56	<0.2
FFTF, 600°C, 33 dpa	1.4	0.8	20.0	33	<0.2
Cold Worked					
Unirradiated	--	--			>20
EBR-II, 425°C, 14 dpa	6.1	7.6	7.6	111	1.8
EBR-II, 425°C, 31 dpa	8.4	2.6	20.5	42	3.0
FFTF, 430°C, 33 dpa	7.8	6.0	15.0	68	~1
EBR-II, 600°C, 14 dpa	5.1	7.0	0.48	268	~1
EBR-II, 600°C, 31 dpa	7.1	8.1	23.4	62	2.0
FFTF, 600°C, 33 dpa	2.5	3.5	8.6	63	~1

The major difference between the microstructures in the high dose EBR-II and FFTF experiments is the apparent differences in the dislocation densities in the cold worked conditions. The cold worked material at both fluences in the EBR-II irradiations contained high dislocation densities. These dislocations are always associated with the void structure such that the two are intertwined. The presumption is that the void population stabilizes the dislocation network so that it is unable to climb or glide out of the matrix at elevated temperatures. The cold worked and aged structure is similar.

However, in the FFTF irradiation of the cold worked and the cold worked and aged material, similar high dislocation densities were not evident. Apparently in this case, the void population which was initially nucleated was not sufficient to tie up the dislocations. Thus swelling must have developed at a somewhat more rapid pace compared to the solution annealed material, but then slowed as the dislocation structure was lost. These differences are apparent when comparing the microstructure of the two irradiations in Figures 4 and 5. Note in Figure 5 that the void population in the cold worked material irradiated in FFTF at 600°C (Fig. 5d) shows a bimodal void population with the smaller voids similar in size to those found the solution annealed case (Fig. 5b). The larger voids are presumably those which were nucleated during the initial stages of irradiation.

Possible reasons for the lack of dislocation stability under irradiation were discussed previously [2]. One major consideration is the high stacking fault energy of Ni which inhibits the formation of partial dislocations, and thus leaves dislocations much more mobile even with high levels of deformation. It is thought that this is a leading factor in the irradiation-induced collapse of the dislocation structures in this material. This is in contrast to stainless steels where higher levels of dislocations are formed and are stable at high levels of deformation.

It is not clear what initial differences in temperature and flux history occurred in the two irradiations, EBR-II versus FFTF, to affect the cold work dislocation structures in different manners. It is apparent however, that due to those differences, two widely different swelling and microstructural results occurred. This underlines the difficulty of using pure Ni for spectral comparisons since, in this case, similar starting condition result in vastly different responses.

The swelling and microstructural evolution near 425 to 430°C are similar between the two irradiation environments, and similar for all starting microstructural conditions. Apart from a few differences, the void sizes and number densities are similar between the two irradiations at nearly the same dose, and similar between the solution annealed and 30% cold worked condition at the same dose. This indicates that the irradiation-induced microstructures have converged to similar forms by about 10 dpa. This is further confirmed by the lower temperature, 375°C, results shown in Table 2. In all of those cases, the swelling had reached similar values by 12.3 dpa, even though the overall swelling values are smaller than those found at 425 - 430°C. Based on these lower temperature irradiation results, it would then be expected that similar irradiation behavior beyond the present dose levels at temperatures of around 400°C would be expected.

CONCLUSIONS

Based on microstructural examination of pure nickel irradiated to approximately 33 dpa in both EBR-II and FFTF at approximately 425, 520, and 600°C, it is possible to draw the following conclusions:

1. For irradiation temperatures at and above 500°C, the resulting swelling is highly dependent on the starting material condition.

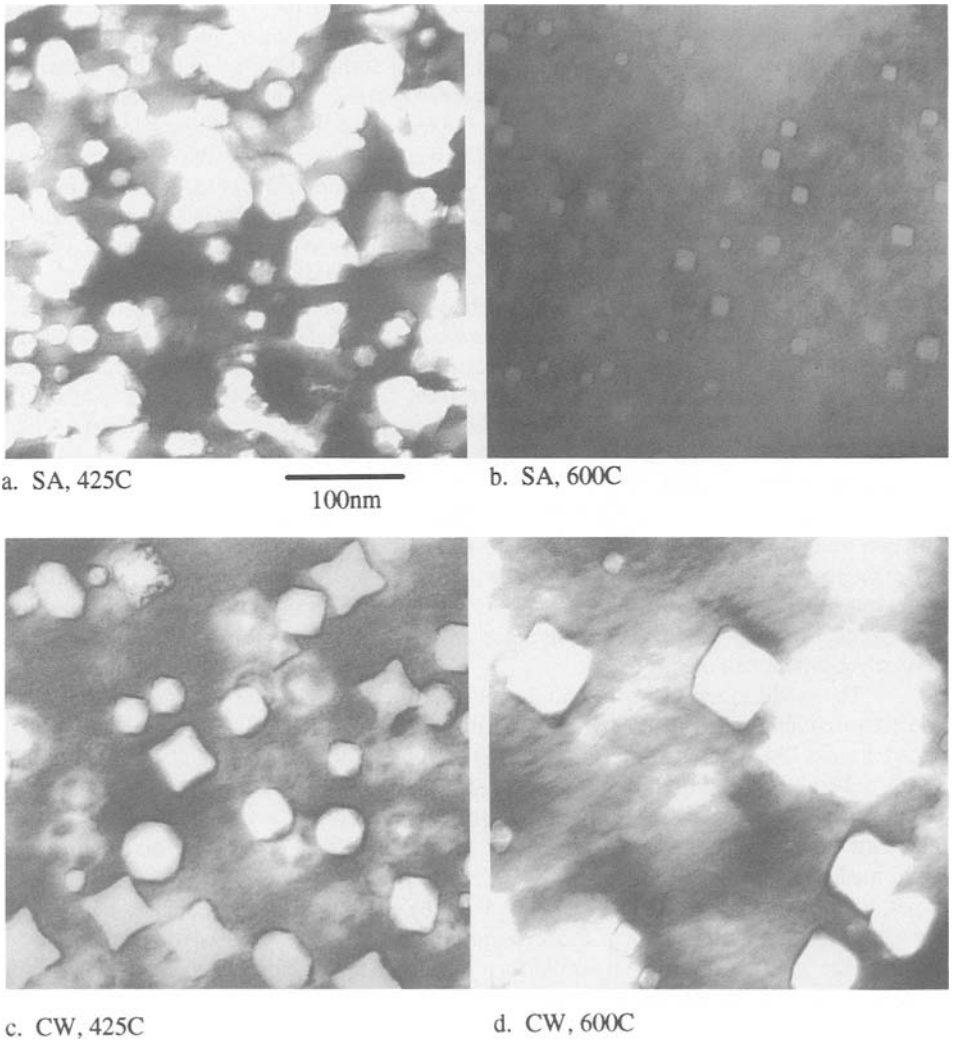


Figure 4, Pure Ni specimens irradiated in FFTF to 31 dpa a.) solution annealed, 425°C b.) solution annealed, 600°C, c.) 30% cold worked, 425°C, and d.) 30% cold worked, 600°C.

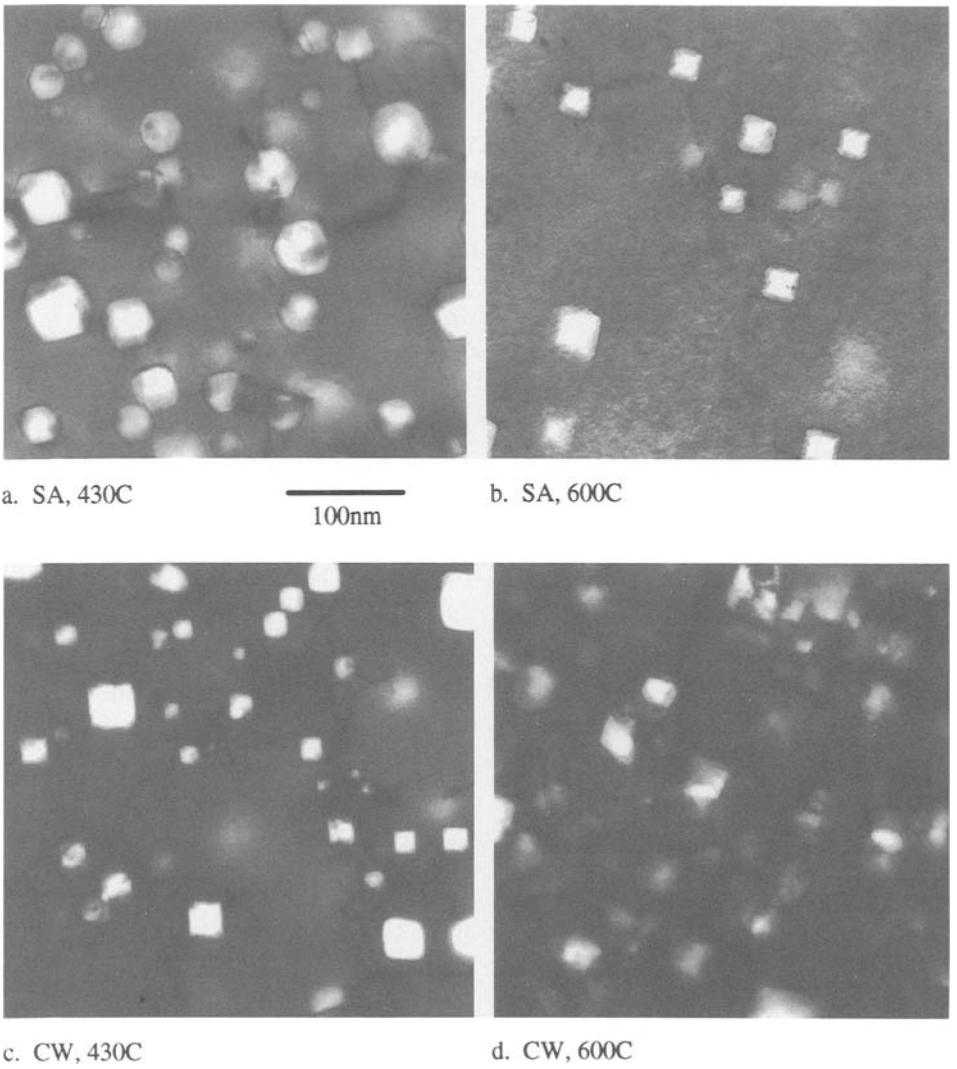


Figure 5. Pure Ni specimens irradiated in EBR-II to 31 dpa a.) solution annealed, 430°C b.) solution annealed, 600°C, c.) 30% cold worked, 430°C, and d.) 30% cold worked, 600°C.

2. Even when the starting material condition is the same, the eventual swelling may be much different for irradiation at elevated temperature. This is due to the relative instability of the dislocation microstructure at such temperatures.

3. Near 430°C, all material conditions and both irradiation environments produce similar microstructures. The initial differences in starting dislocation densities are lost by about 10 dpa at this temperature range.

4. The fall in swelling rate in nickel with dose in the temperature range of 400 to 600°C appears to be due to the relative rates of dislocation collapse and stability of the void-dislocation ensemble which evolves under irradiation. It does not appear to be due to any void ordering phenomena.

5. The variability of the instantaneous swelling rate and the total swelling at saturation with material starting condition and with irradiation temperature makes nickel unsuitable for spectral comparison purposes.

ACKNOWLEDGMENTS

This work was supported by the US Department of Energy.

REFERENCES

[1] Garner, F. A. "Influence of Material and Environmental Variables on the Neutron-Induced Swelling of Nickel, Fusion Reactor Materials," Semiannual Progress Report for Period Ending March 31, 1990, DOE/ER-0313/8 (1990).

[2] Stubbins, J. F., and Garner, F. A. "Swelling and Microstructure of High Purity Nickel Irradiated with Fast Neutrons in EBR-II," J. Nucl. Mater., 191-194 (1992) pp. 1295-99.

[3] Garner, F. A. "Evaluation of Microstructure in Face-Centered Cubic Metals", J. Nucl. Mater., 205 (1993) 98-117.

Jeffrey A. Dunlap[1], Michael J. Borden[2], Walter F. Sommer[2], and James F. Stubbins[1]

EFFECT OF IRRADIATION IN A SPALLATION NEUTRON ENVIRONMENT ON TENSILE PROPERTIES AND MICROSTRUCTURE OF ALUMINUM ALLOYS 5052 AND 6061

REFERENCE: Dunlap, J. A., Borden, M. J., Sommer, W. F., and Stubbins, J. F., **"Effect of Irradiation in a Spallation Neutron Environment on Tensile Properties and Microstructure of Aluminum Alloys 5052 and 6061,"** *Effects of Radiation on Materials: 17th International Symposium, ASTM STP 1270,* David S. Gelles, Randy K. Nanstad, Arvind S. Kumar, and Edward A. Little, Eds., American Society for Testing and Materials, 1996.

ABSTRACT: The Accelerator Production of Tritium (APT) and the Accelerator Transmutation of Waste (ATW) programs require structural materials which retain good mechanical properties when exposed in a spallation neutron irradiation environment. One group of materials likely to withstand the environment anticipated for these systems is the aluminum alloy series. To characterize this class of materials in a prototypical irradiation environment, Al5052 (Al-2.7Mg) and Al6061 (Al-1.1Mg-0.5Si) in hardened and annealed conditions were irradiated to a fluence of 4.2×10^{20} neutrons/cm^2 at ~100°C in a spallation neutron source. Following irradiation, tensile tests and post-test examinations were performed to determine the influence of irradiation and test temperature on mechanical properties and fracture mode. It was found that, the properties of these two aluminum alloys were not significantly affected by the irradiation exposure conditions examined here. Thus these materials may be acceptable as structural materials for APT and ATW applications. This conclusion is based on limited mechanical properties testing, supported by other information in the literature on the performance of these materials in other irradiation environments.

KEYWORDS: aluminum alloys, neutron irradiation, tensile testing, microstructure, spallation neutrons, Al6061, and Al5052

[1] Graduate Student and Professor, University of Illinois, Urbana, IL 61801 USA
[2] Scientists, Los Alamos National Laboratory, Los Alamos, NM 87545 USA

Copyright© 1996 by ASTM International www.astm.org

Accelerator-driven spallation neutron sources are currently being developed to drive a number of applications. The Accelerator Transmutation of Waste (ATW) and the Accelerator Production of Tritium (APT) are among a variety of possible technologies which would be based on such a source. The irradiation environment to which structural materials will be subjected in these systems is considered to be very similar to those presently found at the Los Alamos Meson Physics Facility (LAMPF), particularly with respect to the neutron energy distributions. This environment includes a number of neutrons at high energies produced from proton spallation events with high-Z targets. Neutrons are produced with energies up to the initial proton energy which initiates the spallation event, in most cases at or above 600 MeV. The LAMPF proton energy is nominally 800 MeV, though somewhat lower operating energies have also been employed. Materials for use in ATW, APT or other similar technologies must be able to withstand significant irradiation damage in this neutron environment.

The amount of data for materials subjected to an environment as described above is extremely limited. This is due to the small number of facilities which can produce such a neutron energy spectrum and the limited number of experiments performed in such facilities. The purpose of this study is to expand the amount of data available for certain aluminum alloys in this environment. These aluminum alloys were irradiated in the LAMPF-Los Alamos Spallation Radiation Effects Facility (LASREF). The exposures produced here are prototypic of the exposure the alloys would receive in ATW, APT or similar applications.

Aluminum alloys have been studied in previous experiments and have been found to have a low absorption cross section for thermal neutrons, high thermal conductivity, excellent fabricability and joinability, low activation, and generally good performance in irradiated systems [1]. For these reasons, aluminum and its alloys were considered as an attractive material for use in APT and ATW applications.

It is known that the dominant radiation effect on aluminum alloys is the thermal neutron-based silicon transmutation reaction (SiTR):

$$^{27}\mathrm{Al}\,(n,\gamma)\,^{28}\mathrm{Al}$$
$$^{28}\mathrm{Al} \rightarrow {}^{28}\mathrm{Si} + \beta$$

The general effect of this transmutation is typically to increased the strength and reduce the ductility of aluminum alloys.

EXPERIMENTAL PROCEDURE

Specimen Preparation

Two aluminum alloys were chosen for this experiment, an Al-2.7Mg aluminum alloy very similar in composition to the aluminum alloy 5052 (referred to here as Al5052) and aluminum 6061. Compositions are given in Table 1. These materials were examined in the annealed (O) condition and in the hardened condition H38 for Al5052 and T6 for Al6061. Sheet material was machined into subsize tensile samples 0.25 mm thick with a gauge section of about 30.5 mm. These samples were then irradiated in a spallation neutron environment to a fluence of about 3.4 - 4.2 x 10^{20} neutrons/cm^2. The target irradiation temperature was 120°C,

though the specimens experienced extended irradiation in the latter part of the exposure at 90°C.

Table 1, Aluminum Alloy Compositions (wt.%)

Alloy	Al	Mg	Si	Cu	Cr	Fe	Mn
5052	bal.	2.72	0.16	0.023	0.005	0.25	0.26
6061	bal.	1.13	0.50	0.21	0.22	0.42	0.048

Mechanical Property Measurement

Tensile tests were performed on both irradiated and unirradiated specimens at room temperature and 100°C. The strain rate was controlled to 1mm/s and the extension was monitored by an LVDT attached to the hydraulic piston. Post-test verification of strain measurements was done by cross-checking strains with a caliper. From the stress-strain data, yield strength, ultimate tensile strength, uniform elongation and total elongation were measured. The strain hardening exponent, n, and the strength coefficient, K, were determined according to the relationship $\sigma = K\varepsilon_p^n$, where ε_p is the plastic strain.

Electron Microscopy

Scanning electron microscopy (SEM) was used to determine the effects of irradiation and test temperature on the fracture modes of these alloys. Transmission electron microscopy (TEM) was utilized to determine the effects of test temperature and to study the general microstructure of the unirradiated alloys.

RESULTS and DISCUSSION

Measurements from the stress-strain curves are given in Table 2. These properties compare favorably to those given in the literature. Table 3 gives the values for the plastic strain hardening properties. Also given is the uniform elongation for comparison with the strain hardening exponent with which a theoretical correlation exists.

Aluminum 6061

For the 6061 alloy, the O temper shows an unexpected higher yield strength at 100°C. Other than that, the data are in good agreement with those recorded in handbooks [2]. Farrell and King also show an increase in yield strength for this alloy as the test temperature increased from 50°C to 150°C [3].

Irradiation induced little effect on the Al6061 alloy performance. With the exception of the O temper, test temperatures in the range from room temperature to 100°C also have little effect on this alloy. The dose received by these samples was relatively low, 3.4 to 4.2 x 10^{20} neutrons/cm^2, much lower than the doses where these alloys exhibit significant hardening in fission neutron irradiation environments [3, 4].

The present studies can be compared to the work of Farrell and King [3] for Al6061 in the T6 and O tempers, and Weeks et al. [4] for Al6061 in the T6 temper. Both these studies provide information about Al6061 in fission reactor environments. A comparison of the

studies is given in Figure 1 where tensile data for Al6061-T6 are shown as a function of thermal fluence. For the present study and that by Weeks et al., the data are for room temperature tests. The Farrell and King data are for 50°C tests. The present results follow trends similar to those found by Farrell and King and by Weeks et al., but are somewhat different in absolute value. Some of the differences, particularly the post-yield properties, can be attributed to the specimen geometry which differed across studies. Notably in all studies, there are no significant changes in the tensile properties for exposures less than about 1×10^{21} neutrons/cm^2.

Table 2, Strength and Ductility measurements for Al 5052 and Al 6061

	Yield Strength	Ultimate Tensile	Elongation	
			Total	Uniform
unirradiated, tested at room temperature				
Al 6061-T6	232	310	12	10.5
Al 6061-O	48.7	128	25	23
Al 5052-O	95.5	207	23	21.7
Al 5052-H38	293	335	5.8	5.3
unirradiated, tested at 100°C				
Al 6061-T6	259	305	12	10.3
Al 6061-O	62.2	129	22	20.4
Al 5052-O**	104	215	23	21.7
Al 6061-T6	259	305	12.3	10.3
irradiated, tested at room temperature				
Al 6061-T6	244	305	10.1	9.5
Al 6061-O	54.0	147	20.9	19
Al 5052-O	101	213	23.2	22
Al 5052-H38	263	320	8.8	8.7
irradiated, tested at 100°C				
Al 6061-T6	221	287	10.2	8.3
Al 6061-O	63.3	137	17.1	16.1
Al 5052-O	113	221	22.7	21.7
Al 5052-H38	259	318	6.4	5.8

* unirradiated values are an average of 10 tests, irradiated values are an average of 2 tests.
** average of 9 tests.

Table 3: Plastic strain data for Al 6061 and Al 5052*.

Alloy	Strain Hardening	Strength Coefficient,	Uniform Elongation
unirradiated, tested at room temperature			
Al 6061-T6	0.10	426	10.5
Al 6061-O	0.32	272	23.1
Al 5052-O	0.38	483	21.7
Al 5052-H38	0.09	453	5.3
unirradiated, tested at 100°C			
Al 6061-T6	0.11	435	10.3
Al 6061-O	0.34	295	20.4
Al 5052-O**	0.33	458	21.66
Al 5052-H38	0.05	382	10.27
irradiated, tested at room temperature			
Al 6061-T6	0.10	418	9.5
Al 6061-O	0.35	342	19.3
Al 5052-O	0.39	513	22.0
Al 5052-H38	0.11	453	8.7
irradiated, tested at 100°C			
Al 6061-T6	0.10	394	8.3
Al 6061-O	0.32	325	16.1
Al 5052-O	0.34	477	21.7
Al 5052-H38	0.13	498	5.8

* unirradiated values are an average of 10 tests, irradiated values are an average of 2 tests.
** average of nine tests.

Above 1 x 10^{21} neutrons/cm^2, strength increases and ductility decreases for these alloys. There exists a strange functional relationship between these properties and fast neutron dose. This is due to the fact that transmutation of silicon dictates the changes in structural properties of these alloys and this transmutation correlates with thermal fluence rather than fast fluence. In the Weeks et al. studies, the largest thermal fluence was found at the location of intermediate fast fluences. At the location of the highest fast fluences, the thermal fluence was much more moderate, thus lower Si production and less influence on tensile properties.

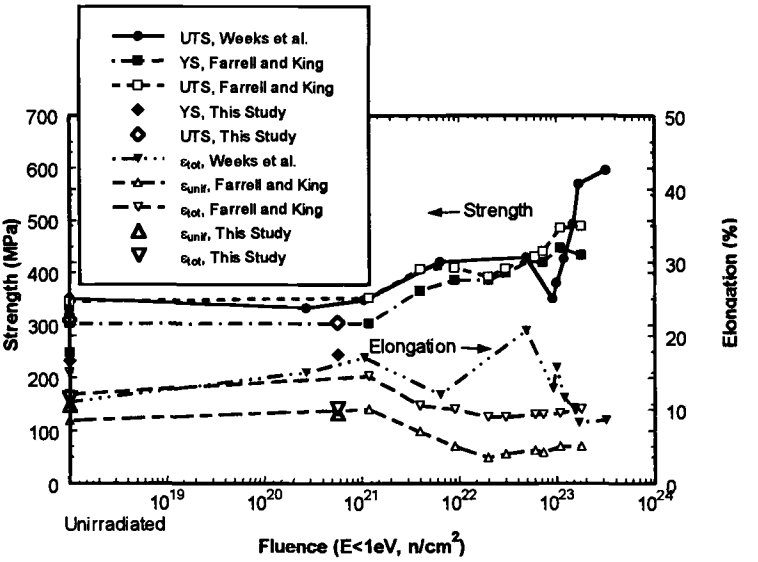


Figure 1. Strength and elongation vs. thermal fluence for Al 6061-T6 at room temperature

For the T6 temper at 100°C, data from the present study are compared to those of Farrell and King after irradiation at 55 to 60°C in Figure 2. Again, changes in properties below 1 x 10^{21} neutrons/cm^2 are insignificant. The data from the present study are similar to those obtained by Farrell and King.

The Al6061 - O temper was also studied by Farrell and King [3]. In this case, it is difficult to directly compare the results of that study to the present study because the first irradiated data point in the Farrell and King study is at a fluence of over 1 x 10^{21} neutron/cm^2. Farrell and King found a significant increase in strength and loss of ductility at fluences at and above this level. The present study shows no significant changes at a dose above 1 x 10^{20} neutrons/cm^2 but below 1 x 10^{21} neutrons/cm^2. The same types of behaviors are found for the O temper at 100°C.

Since the significant contribution to mechanical property changes in this alloy is attributed to the SiTR, it is not surprising that the present results show little change. The transmutation process is supported by thermal neutrons, hence the fission spectra are more damaging than the harder spectrum found in spallation sources. Even when the thermal part of the spallation spectrum is taken into account, the extent of the SiTR is small for the conditions studied here. The influence of other transmutation reactions which require high energy neutrons, in particular the production of hydrogen and helium, is not evident in the present results. This is a useful observation since there is concern that these transmutation products, and others, could play a significant role in mechanical properties alteration as exposure times increase.

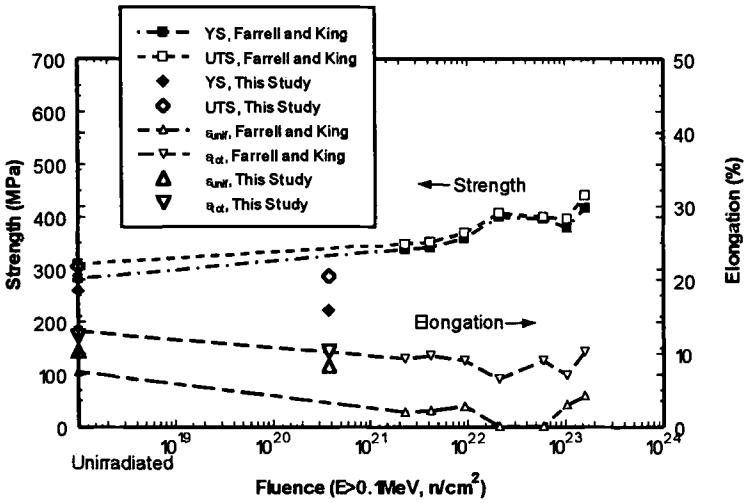


Figure 2. Strength and elongation vs. fast fluence for Al 6061-T6 at elevated temperature

Aluminum 5052

Strength and ductility properties measured for the Al5052 alloy are in good agreement with the literature, with the exception of the total elongation which is lower in the present work than is typically found in handbooks [2]. This is likely due to the decreased elongation experienced by the miniature sheet tensile samples used in this experiment compared to the elongation experienced by ASTM standard sheet and bar specimens.

Irradiation has only a small effect on strength and ductility properties. There was also little effect on these properties at a test temperature of 100°C. The fluence in this experiment reached only about 3.4 - 4.2 x 10^{20} neutrons/cm^2. In the Farrell experiment [5], the dose was higher, about 1 x 10^{21} neutrons/cm^2, and hardening was observed.

The results from the experiments performed by Farrell at 50°C are compared to the room temperature results of the present work in Figure 3 for the O temper. The results are similar to those obtained for Al6061. For values of fluence below 1 x 10^{21} neutrons/cm^2, the mechanical properties are not affected by irradiation, since significant amounts of the SiTR have not been produced. Farrell found that Al5052 shows a greater increase in strength than alloy 6061 at high fluences, which is attributed to the finely distributed Mg_2Si which forms from free magnesium and transmutation-induced silicon. This conclusion agrees with the results found by King and Jostens [6]. The ductility loss which accompanies the increase in strength was also observed by Lijbrink et al. in alloy 5154 and was attributed to the formation of Mg_2Si along grain boundaries [7].

For the H temper, no other radiation studies are available for comparison. The effect of radiation and temperature on mechanical properties is small. It would, again, be expected that this alloy would experience an increase in strength and loss of ductility if the fluence of thermal neutrons were to be increased and significant amounts of transmuted silicon produced.

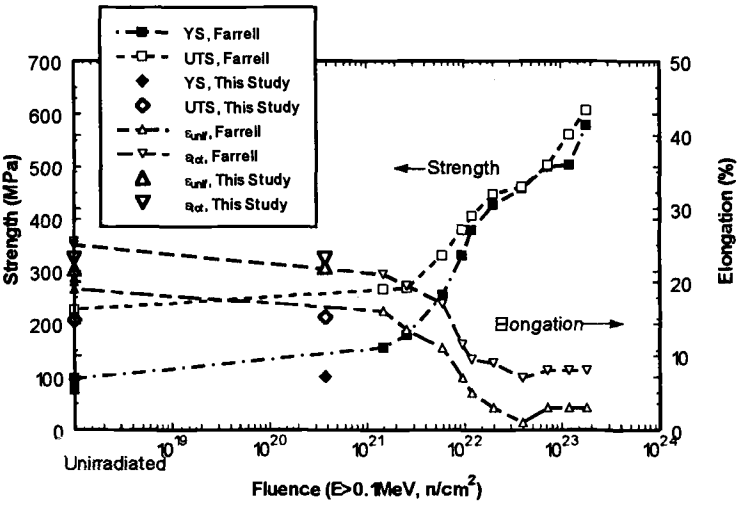


Figure 3. Strength and elongation vs. fast fluence for Al 5052-O at room temperature

Plastic Deformation Properties

Beyond the proportional limit, these alloys tends to behave according to the relationship $\sigma = K\varepsilon_p^n$. The strain hardening exponent, n, and the strength coefficient, K, were determined in this study, principally to determine if the deformation characteristics were affected by the irradiation exposure.

Values for these properties are comparable to those found previously [8]. The value of the strain hardening coefficient is lower for the alloys in the T6 and H38 tempers than for the respective annealed conditions, as would be expected. The values for the O temper are higher than those found by Low and Garofalo, but are a good indication of the ductility of the present alloys. None of the values were significantly affected by irradiation or test temperature.

Values for the strain hardening exponent should correlate with the value for the uniform elongation. The present results show a drop-off of uniform elongation as the strain hardening exponent increases. This drop-off at higher strain hardening values is due to the fact that, in thin sheets, localized necking may occur before the value for the stress reaches the ultimate tensile strength [9]. This results in smaller measured values of uniform elongation and other post-yield properties in sheet materials, particularly those with high ductilities.

Electron Microscopy

SEM fractography of the tensile specimen fracture surfaces indicated that there are no significant differences in the fracture morphologies for any given alloy condition, either as a function of test temperature or irradiated vs. unirradiated. This is consistent with the tensile properties results and the plastic strain range properties which implied that the changes in the alloy conditions were negligible for the fluence and test temperatures studied here.

Fractography showed that ductile dimple fracture surfaces are found in every case. This is consistent with the tensile test results, particularly with the measured values of the uniform and total elongation.

Weeks, Czajkowski and Farrell found that irradiation to a much higher dose decreased the amount of ductile fracture and increased the amount of brittle transgranular fracture in Al6061-T6, although some ductility remained [10]. Farrell and Richt [11] found that this was also the case in their study. They estimated the ductile and brittle fracture percentages to be about 50% each.

Although in the present experiment, the irradiation did not affect the alloy microstructure, changes have been seen by others at higher doses. King and Jostens found that irradiation created two additions to the microstructure: dislocation loops and a high concentration of small Mg_2Si precipitates [6] in Al5052. These findings are in agreement with those of Farrell [5] and Jostens and King [12] in other previous work.

Farrell and King found that, at higher fluences in 6061-T6, the SiTR formed fine amorphous silicon precipitates in addition to the Mg_2Si in the form of needles [3]. These precipitates created dispersion hardening and were responsible for the observed increase in strength and the loss of ductility. The denuding of the Mg_2Si precipitate around grain boundaries found at high fluences by King et al. [13] was not seen at the lower doses of the present study. This is likely due to the fact that the SiTR is governed by the thermal fluence which is low in the present experiment. The lack of grain boundary denuding in the present work was evident from the SEM examination of fracture surfaces [1].

CONCLUSIONS

For the materials tested here (Al6061-T6, Al6061-O, Al5052-O, and Al5052-H38), irradiation in a spallation neutron environment to low fluences has no measurable effect on their physical and mechanical properties. The same is true for a change in test temperature from room temperature to 100°C. The present results are consistent with those obtained for similar alloys and heat treatment conditions exposed to fission neutron spectra to much higher doses. In those studies, higher thermal neutron fluence increased the amounts of Si through the SiTR which, in turn, affected properties. However, neither the fast nor the thermal fluence in the present experiment was sufficiently high to produce changes related to variations in accrued radiation damage from the high energy end of the neutron spectrum or Si production from the thermal neutron spectrum. No other unexpected effects which would be attributable to the high energy neutron tail in a spallation source were found.

ACKNOWLEDGMENTS

This work was supported by the US Department of Energy.

REFERENCES

[1] *APT Materials Safety Experiments, Technical Report.* LA-UR-93-2850, Los Alamos National Laboratory, 1992.

[2] ASM Handbook, Volume 2, Properties and Selection: Nonferrous Alloys and Special Purpose Materials. The Materials Information Society, 10th Edition, 1992.

[3] Farrell, K. and King, R.T., "Tensile Properties of Neutron-Irradiated 6061 Aluminum Alloy in Annealed and Precipitation-Hardened Conditions," Effects of Radiation on Structural Materials, ASTM STP 683, J.A. Sprague and D. Kramer, Eds., American Society for Testing and Materials, 1979, pp. 440-449.[JS1]

[4] Weeks, J.R., Czajkowski, C.J., and Tichler, P.R., "Effects of High Thermal and High Fast Fluences on the Mechanical Properties of Type 6061 Aluminum on the HFBR," Effects of Radiation on Materials: 14th International Symposium (Volume II), ASTM STP 1046, N.H. Packan, R.E. Stoller and A.S. Kumar, Eds., American Society for Testing and Materials, Philadelphia, 1990, pp. 441-452.

[5] Farrell, K. "Microstructure and Tensile Properties of Heavily Irradiated 5052-O Aluminum Alloy," J Nuc Mat, 97 (1981) 33-43.

[6] King, R.T and Jostens, A. "Irradiation Damage in a 2.2 Pct Magnesium-Aluminum Alloy," Met Trans A, 6A (April 1975) 863-868.

[7] Lijbrink, E., Grol, H.J. van, Dekker, F. and Witzenburg, W. van. "Effects of Neutron Irradiation on the Mechanical Properties of a 5154-O Type Aluminum Alloy," Effects of Radiation on Materials: 11th Conference, ASTM STP 782. H.R. Brager and J.S. Perrin, Eds., American Society for Testing and Materials, 1983, pp. 765-778.

[8] Low, J.R. and Garofalo, F. "Precision Determination of Stress-Strain Curves in the Plastic Range," Proc. SESA, 4:2 (1947) 16-25.

[9] Støren, S. and Rice, J.R. "Localized Necking in Thin Sheets," J Mech. Phys. Sol., 23 (1975) 421-441.

[10] Weeks, J.R., Czajkowski, C.J. and Farrell, K. "Effects of High Thermal Neutron Fluences on Type 6061 Aluminum," Effects of Radiation on Materials: 16h International Symposium, ASTM STP 1175, A.S. Kumar, D.S. Gelles and R.K. Nanstad, Eds., American Society for Testing and Materials, Philadelphia, 1993.

[11] Farrell, K. and Richt, A.E. "Postirradiation Properties of the 6061-T6 Aluminum High Flux Isotope Reactor Hydraulic Tube," Properties of Reactor Structural Alloys after Neutron or Particle Irradiation, ASTM STP 570, American Society for Testing and Materials, 1975, pp. 311-325.

[12] Jostens, A. and King, R.T. "Transmutation-Produced Mg2Si Precipitation in an Irradiated Al-2.5% Mg Alloy," Scripta Metallurgica, 6 (1972) 44--452.

[13] King, R.T., Jostens, A. and Farrell, K. "Neutron Irradiation Damage in a Precipitation-Hardened Aluminum Alloy," Effects of Radiation on Substructure and Mechanical Properties of Metals and Alloys, ASTM STP 529, American Society for Testing and Materials, 1973, pp. 165-180.

Margaret L. Hamilton,[1] Mychailo B. Toloczko,[2] Dan J. Edwards,[1] Walter F. Sommer,[3] Michael J. Borden,[3] Jeffrey A. Dunlap,[4] James F. Stubbins,[4] Glenn E. Lucas[2]

CORRELATION BETWEEN SHEAR PUNCH AND TENSILE DATA FOR NEUTRON-IRRADIATED ALUMINUM ALLOYS

REFERENCE: Hamilton, M. L., Toloczko, M. B., Edwards, D. J., Sommer, W. F., Borden, M. J., Dunlap, J. A., Stubbins, J. F., and Lucas, G. E., **"Correlation Between Shear Punch and Tensile Data for Neutron-Irradiated Aluminum Alloys,"** *Effects of Radiation on Materials: 17th International Symposium, ASTM STP 1270,* David S. Gelles, Randy K. Nanstad, Arvind S. Kumar, and Edward A. Little, Eds., American Society for Testing and Materials, 1996.

ABSTRACT: As part of a study to determine the potential for using aluminum alloys as structural components in accelerators used to produce tritium, tensile specimens and transmission electron microscopy (TEM) disks of two aluminum alloys in two tempers were irradiated with neutrons from spallation reactions in the Los Alamos Spallation Radiation Effects Facility (LASREF) at the Los Alamos Meson Physics Facility (LAMPF) at 90 to 120°C to a fluence of ~4 x 10^{20} n/cm^2. Tensile and shear punch tests were performed on the irradiated alloys as well as on a similar unirradiated control matrix with a larger number of specimens, and a correlation between shear and tensile properties was developed for the unirradiated alloys and the irradiated alloys. Comparison of the correlations for the unirradiated and irradiated alloys showed that small differences in the correlations existed, however for purposes of estimation of uniaxial tensile properties, either correlation was found to be adequate.

KEYWORDS: shear punch, aluminum alloys, tensile-shear correlation

[1]Senior scientist and research scientist, respectively, Pacific Northwest National Laboratory, Richland, WA 99352

[2]Graduate student and professor, respectively, Department of Nuclear Engineering, University of California at Santa Barbara, Santa Barbara, CA 93106

[3] Technical team leaders, Los Alamos National Laboratory, Los Alamos, NM 87545

[4]Graduate student and professor, respectively, University of Illinois, Urbana IL 61801

Copyright© 1996 by ASTM International www.astm.org

Aluminum alloys are being considered for blanket and target structural applications in the Accelerator Production of Tritium (APT) Program at Los Alamos National Laboratory[1]. The irradiation environment will consist of high energy protons along with neutrons having a broad spectrum of energies. Aluminum alloys were selected for a feasibility study because of their low absorption of thermal neutrons, their high thermal conductivity, their fabricability and joinability, their structural performance under prototypic and other irradiation conditions, and their low activation under such conditions.

Irradiations were performed in the Los Alamos Spallation Radiation Effects Facility (LASREF), an accelerator thought to have an irradiation environment similar to the APT accelerator environment. Irradiations in LASREF are constrained by a relatively small test volume with steep flux gradients. The limitation on volume and homogeneity of irradiation environment prompted the use of small specimen geometries and test techniques to extract mechanical properties data. Miniaturized tensile specimens and shear punch specimens were used to estimate the mechanical properties.

Within this context, the purpose of this study was to examine the relationship between the uniaxial strength data and the shear punch strength data collected from this experiment. It has been found empirically that the yield and maximum loads in a shear punch test can be linearly correlated with the uniaxial yield and ultimate tensile strengths, respectively, and that the shear punch displacement at failure can be related to uniaxial reduction in area. For this study, miniature tensile specimens and TEM disks were available in both unirradiated and neutron irradiated conditions permitting a comparison of correlations obtained from either unirradiated or neutron irradiated specimens.

EXPERIMENTAL METHOD

The alloys tested were 6061, in both an annealed (O) and precipitation strengthened (T6) condition, and an Al-2.7Mg alloy, also in an annealed (O) and in a strengthened (similar to H38) condition. The Al-2.7Mg alloy is similar to 5052, and in keeping with previous reports on the APT development program, it will be referred to as 5052. The specimens were irradiated in LASREF at temperatures ranging from 90 to 120°C. The total neutron fluence was ~3.4 - 4.2 x 10^{20} n/cm^2 (E > 0.1 MeV) with about 1% of the neutrons having E > 1 MeV.

Shear Punch Testing

The TEM disk specimens for shear punch testing were punch fabricated from sheet stock having a nominal thickness of 0.254 mm (0.010 inches) thick. Each disk had a nominal diameter of 2.79 mm (0.110 inches). All irradiated specimens were flattened prior to shear punch testing in a device that applied a small load to the

specimens located in a recessed die with a depth of 0.254 mm (0.010 inches).[1] The unirradiated specimens were not flattened prior to testing, but the clamping of these specimens in the shear punch fixture had nearly the same effect. Specimen thickness was measured using a calibrated dial micrometer attached to a flat anvil. A radiused micrometer tip was selected to minimize measurement errors induced by specimen curvature. The thickness of each specimen was measured at least six times in different places on the specimen. Three representative measurements were recorded.

The shear punch test utilizes a cylindrical punch with a flat end to deform a lightly clamped disk to failure. The disk material is forced to deform primarily in a small region corresponding roughly to the region below the clearance between the punch and die. Shear punch tests were performed with a 1.00 mm (0.0395 inches) diameter punch. The guide hole for the punch, located in the upper half of the fixture, consisted of a bushing with a 1.02 mm (0.0400 inch) inner diameter. The die, located in the lower half of the fixture, consisted of a similar bushing with a 1.04 mm (0.0410 inch) inner diameter. Hence the resulting radial thickness of the clearance region was ~0.02 mm (0.0008 inches). The specimens were centered over the die on the lower fixture half with the deburred side (the cupped side, where applicable) facing up. A set of three shims having a thickness slightly less than or equal to the disk thickness ($0.000 \text{ mm} \leq t_{disk} - t_{shim} \leq 0.013$ mm [0.0005 in], where t_{disk} and t_{shim} were the thicknesses of the TEM disk specimen and the shim, respectively) were placed around the periphery of the lower fixture half, where they would be between the two fixture halves. The upper fixture was placed on top of the assembly with the assistance of a set of alignment pins and holes. The two fixture halves were bolted together until the upper fixture half just bottomed out on the shims. This arrangement was nominally identical to that used in the original shear punch work [2]. Punch tests were performed in a screw-driven Instron test machine at a crosshead speed of 0.002 mm/s (8.3×10^{-5} in./s).

Shear punch tests were performed on both unirradiated control specimens and the LASREF-irradiated specimens at both room temperature (20°C) and 100°C (±2°C). Room temperature tests were performed to facilitate comparison to data available on these alloys after irradiation in mixed spectrum fission reactors, whereas tests at 100°C were selected as being representative of the expected operating temperature in APT

---

[1]The TEM disks were unavoidably bowed slightly during the fabrication process and had to be flattened prior to testing. The effect of bowing and subsequent flattening was evaluated previously using a matrix of unirradiated 316 stainless steel (SS) and HT9 specimens, half of which were fabricated by punching and half of which were fabricated by electrodischarge machining [unpublished results]. Tests on these specimens showed small increases in the yield strength (~5%) in the solution annealed 316 SS, with the strengthening effect diminishing to zero in the 20% cold worked 316 SS specimens. The effect was negligible in all the HT9 specimens and in precipitation strengthened 316 SS specimens. Based on the results from the steels, it is anticipated that the effect of bowing and flattening the aluminum TEM specimens was also small.

structural elements as well as being representative of the LASREF irradiation temperature. Room temperature tests were performed in air. Elevated temperature was achieved by resistance heating the fixture in an argon-filled, insulated test chamber. Heat-up time was ~30 minutes. Specimen displacement during a test was assumed to be equal to crosshead travel. Ten tests were done for each of the four unirradiated alloy/TMT conditions, and one or two tests were done for each of the four neutron irradiated alloy/TMT conditions.

Uniaxial Tensile Testing

Sheet specimens were used that measured nominally 0.25 mm (0.010 in.) in thickness, 18 mm (0.710 in.) in gauge length, and 3 mm (0.120 in.) in gauge width. Tensile tests were performed on a standard hydraulic tensile frame at a nominal strain rate of 5.6×10^{-3} s^{-1}.The elevated temperature tests were carried out in a heated air furnace chamber where the specimen was brought to uniform temperature in ~10 minutes. Displacement was controlled by an LVDT attached to a hydraulic piston, and load was monitored with a standard load cell. Uniaxial tensile tests were performed at room temperature and at 100°C on both unirradiated control specimens and LASREF-irradiated specimens. Ten tests were done for each of the four unirradiated alloy conditions. Two tests were done for each of the four neutron irradiated alloy conditions. Other details of the tensile tests and a discussion of the results are described elsewhere in these proceedings [3].

RESULTS AND DISCUSSION

Shear Punch Data

The average strengths determined from the tensile and shear punch tests are given in Table 1. The tensile data are described in more detail in [3]. The shear punch strengths were determined for both yield and maximum conditions according to

$$\tau_{eff} = \frac{P}{2\pi rt} \tag{1}$$

where τ_{eff} is the effective shear stress, P is the load, t is the average specimen thickness, and r is an effective radius defined as the average of the punch and die radii, or 0.511 mm (0.0201 in) for the punch used in these tests. The term effective shear stress is used since the shear punch test produces a stress state in the material that is not pure shear [2]. The effective shear yield stress was determined from the load at the point where the load-displacement trace deviated from linearity, and the effective ultimate shear stress was determined for the maximu load. Standard deviations are given only for those conditions where more than two specimens were tested.

TABLE 1--Average shear punch and tensile data

MATERIAL	YIELD STRENGTH (MPa)		MAXIMUM STRENGTH (MPa)	
	UNIRRAD[a]	N IRRAD[b]	UNIRRAD[a]	N IRRAD[b]
Shear punch, room temperature				
6061-O	44 ± 4[c]	-[d]	91 ± 2	-
6061-T6	131 ± 5	140	188 ± 3	193
5052-O	71 ± 6	62	142 ± 3	139
5052-H38	136 ± 4	119	180 ± 3	182
Shear punch, 100°C				
6061-O	45 ± 3	-	90 ± 2	-
6061-T6	122 ± 6	135 ± 0	182 ± 3	187 ± 2
5052-O	83 ± 3	70 ± 6	146 ± 2	148 ± 3
5052-H38	137 ± 7	127 ± 5	178 ± 3	179 ± 0
Tensile, room temperature [1]				
6061-O	49	54	128	147
6061-T6	232	244	310	305
5052-O	96	101	207	213
5052-H38	293	263	335	320
Tensile, 100°C [1]				
6061-O	62	63	129	137
6061-T6	259	221	305	287
5052-O	104	113	215	221
5052-H38	259	259	305	318

[a]8-10 tests per condition
[b]One test per condition
[c]Standard deviation
[d]Indicates no test performed or test data invalid

The shear punch data are plotted against the average tensile data given in Table 1 in Fig. 1 (yield) and Fig. 2 (ultimate), with the corresponding regression lines. The data clustered in the lower left quadrant of these two figures were obtained on the annealed alloys, while the data clustered in the upper right quadrant were obtained on the strengthened alloys. The data can be fit with a linear regression, consistent with earlier work on shear punch testing [2]. The difference between properties observed at room temperature and at 100°C was slight, indicating that the microstructure is reasonably stable at 100°C, at least for short periods of time.

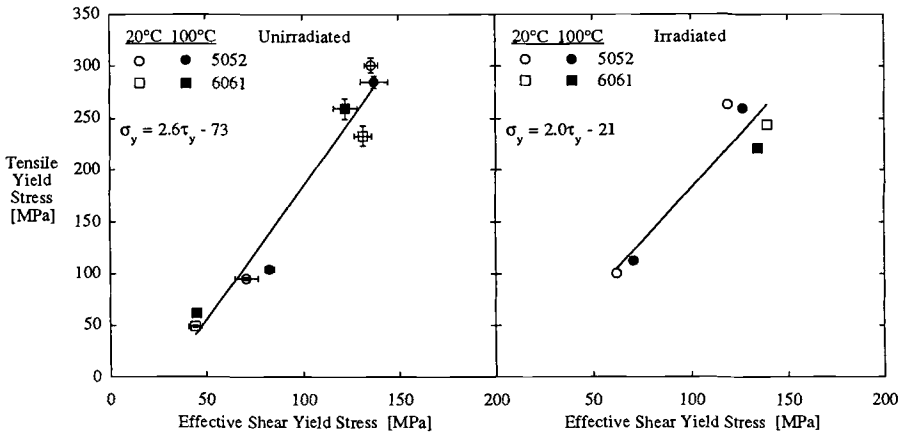


FIG. 1--Average tensile yield versus shear punch yield strength for unirradiated and neutron irradiated alloys 5052 and 6061, with the corresponding regression lines.

Inspection of the data in Table 1 reveals that, with three exceptions, trends in strength differences between tensile specimens tested at 20°C and 100°C are also observed in the shear punch specimens tested at 20°C and 100°C. Very little change in strength is observed following neutron irradiation: the largest shift observed was 38 MPa, while the majority of alloy conditions shifted by less than 20 MPa. Also worth noting is the fact that the strength observed at 100°C was sometimes greater than that observed at room temperature, for both shear punch and tensile strengths. While the differences are small but reproducible within this experiment (i.e., there were multiple specimens tested in each case, for which the data clustered fairly closely [3]), this is atypical of aluminum alloys [4].

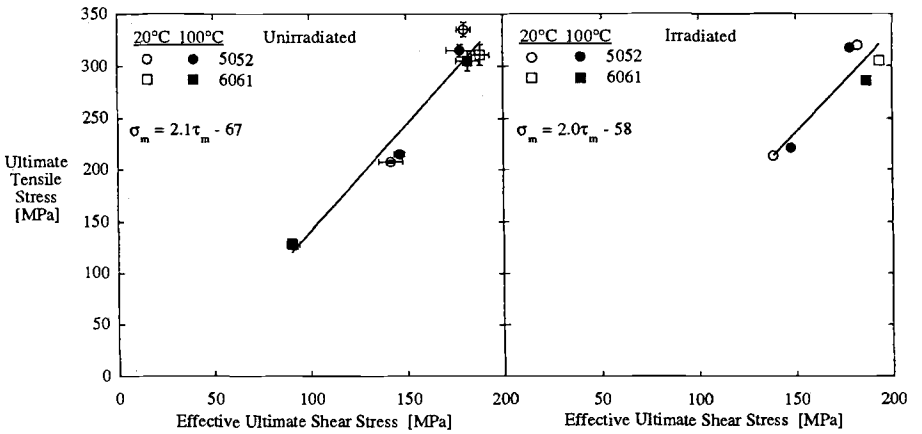


FIG. 2--Average tensile maximum versus shear punch maximum strength for unirradiated and neutron irradiated alloys 5052 and 6061, with the corresponding regression lines.

Correlation Development

The data given in Table 1 for unirradiated materials were used to develop a correlation relating the shear punch strength to the tensile strength with the goal of using the correlation to predict the tensile strength of these alloys in the irradiated condition from shear punch tests on irradiated materials. The data obtained on irradiated materials provide an opportunity to test the inherent assumption that the same relationship between shear punch and tensile strength applies in the irradiated and unirradiated conditions.

Separate regression lines of the form $\sigma = C\tau_{eff} + K$ were fit to the data on irradiated and unirradiated specimens, where σ is the uniaxial tensile stress and τ_{eff} is the effective shear stress. A linear fit to the data typically does not pass through the origin and K is therefore non-zero. Since there was no significant distinction between data obtained at room temperature and at 100°C, the data from the two temperatures were grouped together. The regressions obtained for the yield and maximum load conditions in the unirradiated material were

$$\sigma_y = 2.6\tau_y - 73 \qquad \text{and} \qquad \sigma_m = 2.1\tau_m - 67 \qquad (2), (3)$$

where both σ and τ are in MPa, and the r^2 values for both regressions was 0.98. The corresponding regression equations for the irradiated materials were

$$\sigma_y = 2.0\tau_y - 21 \qquad \text{and} \qquad \sigma_m = 2.0\tau_m - 58 \qquad (4), (5)$$

with r^2 values of 0.93 and 0.91, respectively. These regression lines are shown in Figs. 1 and 2. While the correlations for the unirradiated and irradiated materials are somewhat different, the latter are based on relatively few data, and the uncertainty range on the fit parameters largely accounts for these differences. Moreover, the differences between actual values of the irradiated material tensile properties and estimates obtained from shear punch data using either correlation are similar, as is shown in Figure 3, where tensile strength for the irradiated specimens is shown with the values predicted using the two correlations. The error in the yield stress predictions is consistently slightly larger than that in the ultimate strength predictions. However the errors are not large, and the errors in the predictions made using the unirradiated material correlations are similar to the errors in the predictions made using the irradiated material correlations. Thus the irradiated materials appear to exhibit the same relationship between tensile and effective shear strengths as do the unirradiated materials. This is neither unreasonable nor surprising given the fact that only small changes in strength occurred with irradiation.

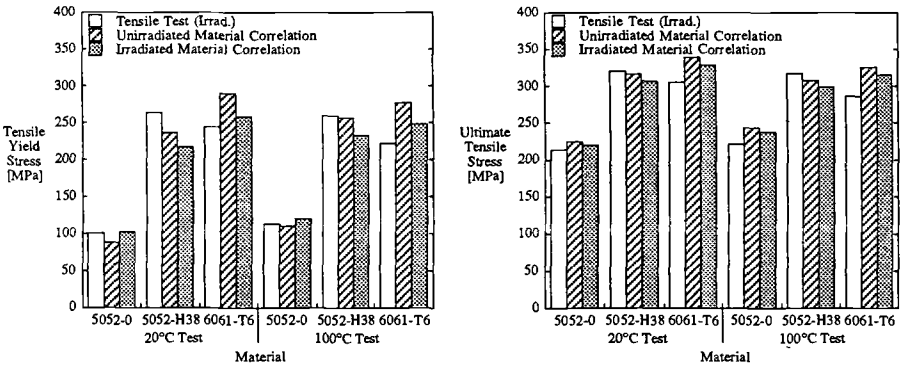


FIG. 3--Tensile strength predicted using correlations based on unirradiated as well as irradiated materials data.

The results presented here can be compared with the previous work of Lucas et al. [2]. The correlations here are in a slightly different form than those presented by Lucas et al., where the effective shear stress was defined as

$$\tau_{eff} = \frac{P-F}{2\pi rt} \tag{6}$$

and F was considered to be the frictional drag created during testing. In practice, F was chosen so that the linear correlation between tensile and effective shear strength intercepted the origin, yielding correlations of the form

$$\tau_{eff} = m\sigma. \quad (7)$$

Comparing equations (6) and (7) with the current work, it is evident that K is equivalent to $F/(2\pi rt)$ and m is equivalent to 1/C. Lucas et al. examined the tensile and effective shear properties for a variety of materials that included copper, brass, steel, aluminum, and stainless steel. They found that when the data were normalized such that the intercept was zero, as in equation (7), all the data could be fit to a single correlation with a value of m such that C = 1/m = 1.85 and C = 1/m = 1.61 for the yield and ultimate correlations respectively. The slopes obtained in the current work are slightly greater (i.e., 2.6 and 2.1, respectively [unirradiated] or 2.0 and 2.0 [irradiated]). In another study [4] where data from a larger variety of materials (including the aluminum alloys presented here) were fit to a single correlation, similar values of the correlation constants were obtained: C = 1.8 and 2.2 for yield and ultimate correlations, respectively. Again, while much of the difference can be attributed to uncertainty in the fit parameters, or arises from data scatter and/or quantity, some of the variability in the constants obtained can probably also be attributed to variations in the experimental apparatus and specimen geometry.

The ultimate tensile and effective shear strength data obtained in the current work were compared in Fig. 4 to a larger set of tensile and shear strength data on aluminum alloys from Reference [5]. The aluminum alloys range from the 1000 to the 7000 series and include alloys strengthened by a number of mechanisms. The data were obtained on standard-size specimens significantly larger than those used in this work, in blanking or single-shear tests (on sheet) or double-shear tests (plate). Although there is some scatter, the data appear to obey essentially the same relationship between tensile and shear strength as the current data, with a slope of C = 1.7.

CONCLUSIONS

A matrix of aluminum alloys comprising 6061 and 5052 in both annealed and strengthened conditions was used to study the relationship between uniaxial tensile and effective shear strengths obtained in the shear punch test on both unirradiated and neutron irradiated specimens. Separate correlations that describe the relation between tensile and effective shear strength were developed from data on unirradiated and irradiated specimens. Good predictions of the tensile strength of the irradiated materials were also obtained using the effective shear strength of the irradiated material in the correlation for unirradiated material behavior. Comparison of the ultimate strength data obtained here with a larger body of similar data on aluminum alloys showed that the current data obey the same relationship as the larger body of data. The correlation developed to describe the current data was similar to

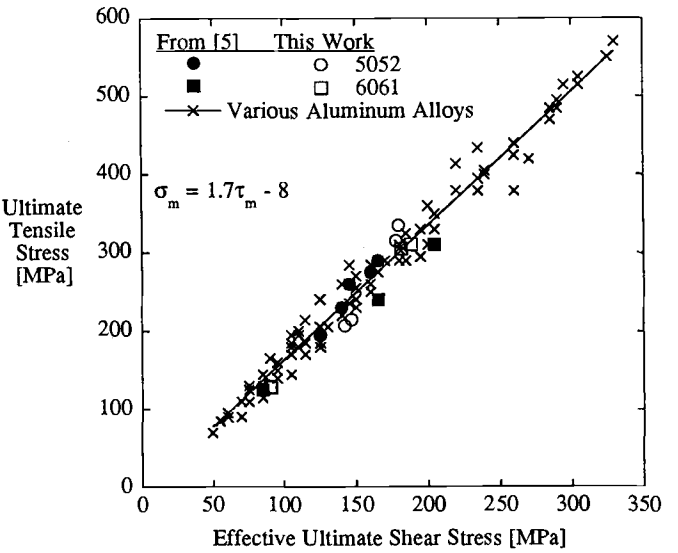


FIG. 4--Comparison between maximum tensile and maximum shear strength data from the current study and from Ref. [5].

correlations for ultimate strength data covering a range of materials that included aluminum, steel, stainless steel, copper, vanadium, and brass.

REFERENCES

[1] APT Materials Safety Experiments Technical Report, LA-UR-93-2850, Los Alamos National Laboratory, September 1993.

[2] Lucas, G. E., Odette, G. R., and Sheckherd, J. W., "Shear Punch and Microhardness Tests for Strength and Ductility Measurements," The Use of Small-Scale Specimens for Testing Irradiated Material, ASTM STP 888, W. R. Corwin and G. E. Lucas, Eds., American Society for Testing and Materials, 1986, pp. 112-140.

[3] Dunlap, J. A., Borden, M. M., Sommer, W. F., and Stubbins, J. F., Effect of Irradiation in a Spallation Neutron Environment on Tensile Properties and Microstructure of Aluminum Alloys 5052 and 6061," Effects of Radiation on Materials: 17th Volume, ASTM STP 1270, David S. Gelles, Randy K.

Nanstad, Arvind S. Kumar, and Edward A. Little, Eds., American Society for Testing and Materials, Philadelphia, 1996.

[4] Hamilton, M. L., Toloczko, M. B., and Lucas, G. E., "Recent Progress in Shear Punch Testing," Miniaturized Specimens for Testing of Irradiated Materials, Hans Ullmaier and Peter Jung, Eds., Forschungszentrum Jülich GmbH, January 1995, pp. 46-58.

[5] Metals Handbook, 10th edition, volume 2, (1990), American Society for Metals, Metals Park, Ohio, p. 49-51.

H. M. Chung,[1] B. A. Loomis,[1] and D. L. Smith[2]

EFFECT OF DYNAMICALLY CHARGED HELIUM ON MECHANICAL PROPERTIES OF VANADIUM-BASE ALLOYS*

REFERENCE: Chung, H. M., Loomis, B. A., and Smith, D. L., **"Effect of Dynamically Charged Helium on Mechanical Properties of Vanadium-Base Alloys,"** *Effects of Radiation on Materials: 17th International Symposium, ASTM STP 1270*, David S. Gelles, Randy K. Nanstad, Arvind S. Kumar, and Edward A. Little, Eds., American Society for Testing and Materials, 1996.

Abstract: One property of vanadium-base alloys that is not well understood in terms of their potential use as fusion reactor structural materials is the effect of simultaneous generation of helium and neutron damage under conditions relevant to fusion reactor operation. In the present Dynamic Helium Charging Experiment (DHCE), helium was produced uniformly in the specimen at linear rates ranging from ≈0.4 to 4.2 appm helium/dpa during irradiation to 18–31 dpa at 425–600°C in the Li-filled capsules. Results of postirradiation tests of mechanical properties of V-4Cr-4Ti, an alloy identified to be most promising, are presented. Effects of helium on tensile strength and ductility at 420–600°C were insignificant for irradiation at these temperatures. However, postirradiation ductilities measured at 20–200°C were higher than those of the non-DHCE specimens (negligible helium generation), whereas strengths were lower, indicating that different types of hardening centers were produced during DHCE and non-DHCE. Ductile-brittle transition behavior of the DHCE specimens was determined from multiple bend tests on TEM disks and broken tensile specimens. No brittle behavior was observed at temperatures >–175°C. In contrast to tritium-trick experiments in which grain-boundary coalescence of helium is pronounced in the absence of displacement damage, no intergranular fracture was observed in tensile or bend-tested DHCE specimens.

Key words: vanadium-base alloys, V–4Cr–4Ti, helium, displacement damage, tensile properties, cleavage, intergranular failure, ductile–brittle transition behavior

Recent attention in the development of vanadium-base alloys for application in fusion reactor first wall and blanket structure has focused on V-4Cr-4Ti, an alloy reported to exhibit an excellent combination of mechanical and physical properties before and after irradiation [1–6]. One of the unresolved issues in the performance of the alloy, however, has been the effect of fusion-relevant simultaneous generation of helium and neutron damage (at a ratio of 4–5 appm helium/displacement per atom [dpa]) on mechanical properties. Helium effects determined for other vanadium-base alloys by means of less fusion-relevant simulation approaches, such as tritium-trick [7–13], cyclotron-injection [14–18], and boron-doping [18–21] techniques, have been inconsistent with regard to concentration of helium bubbles on grain boundaries and the concomitant propensity for intergranular fracture. In the unique Dynamic Helium Charging Experiment (DHCE), the fusion-relevant helium-to-dpa ratio is simulated realistically by utilizing transmutation of controlled amounts of ^{6}Li and a predetermined amount of tritium-doped mother vanadium immersed in ^{6}Li + ^{7}Li [22–24]. This report describes mechanical properties of V–4Cr–4Ti irradiated to 18–31 dpa at 425–600°C in the DHCE (0.4–4.2 appm He/dpa).

MATERIALS AND PROCEDURES

The elemental composition of V–4Cr–4Ti (ANL Identification BL–47), determined prior to irradiation, is given in Table 1. A 30-kg alloy ingot, multiple-vacuum-arc-melted from high-purity titanium and vanadium, was extruded at ≈1150°C and annealed at ≈1050°C several times after 8–10 passes of rolling at 400°C between the annealings. Final forms of the product were annealed plates and sheets 3.8–, 1.0–, and 0.3–mm in thickness.

[1]Metallurgists, Energy Technology Division, and [2]Director, Fusion Power Program Division, respectively, Argonne National Laboratory, Argonne, IL 60439.

Copyright© 1996 by ASTM International www.astm.org

Tensile and TEM disks were annealed at 1050°C for 1 h in an ion-pumped high-vacuum system. The annealed disks were ≈95% recrystallized and exhibited an average grain size of ≈14 μm. Phase structures of the alloy, characterized before and after irradiation in a non-DHCE (425-600°C, 24-34 dpa, <0.1 appm He), have been described in detail elsewhere [4]. The only secondary phase present in the as-annealed specimens was Ti(O,N,C), which is present normally in titanium-containing vanadium alloys with O+N+C > 400 wppm.

Table 1. Chemical composition of V-4Cr-4Ti alloy

	Alloy Composition	Impurity Composition (wppm)							
ANL ID	(wt.%)	O	N	C	Si	S	P	Nb	Mo
BL-47	V-4.1Cr-4.3Ti	350	220	200	870	20	<40	<100	<100

The specimens were irradiated in the Fast Flux Test Facility (FFTF), a fast reactor located in Richland, Washington, at 420, 500, and 600°C to neutron fluences (E > 0.1 MeV) ranging from 3.7 x 10^{22} n/cm^2 (≈18 displacements per atom, or dpa) to 6.4 x 10^{22} n/cm^2 (≈31 dpa). Helium in the specimens was produced by utilizing transmutation of controlled amounts of ^{6}Li and a predetermined amount of tritium-doped "mother" vanadium immersed in ^{6}Li + ^{7}Li [22-24]. Table 2 summarizes the irradiation temperature, weight of the mother vanadium, fraction of ^{6}Li, and tritium and lithium inventory charged in each of the seven DHCE capsules before irradiation. Table 3 summarizes the actual postirradiation parameters determined from tensile and disk specimens of the V-4Cr-4Ti alloy, i.e., fast neutron fluence, dose, and helium and tritium contents measured shortly after the postirradiation tests. Helium and tritium were determined by mass spectrometry at Rockwell International Inc., Canoga Park, California.

Table 2. Capsule-loading parameters of the Dynamic Helium Charging Experiment.

Capsule	Irradiation Temp.	Weight (g)			Fraction of ^{6}Li	Initial Tritium Charge[a]	
ID No.	(°C)	Mother V[a]	Specimen[b]	Lithium	(%)	(Ci)	(mmol)
4D1	425	1.5468	5.86	0.765	5.0	99	1.70
4D2	425	1.5536	5.38	0.765	4.5	70	1.20
5E2	425	1.5657	5.38	0.670	1.0	26	0.45
5D1	500	1.5727	5.77	0.938	6.5	73.5	1.26
5E1	500	1.5651	5.82	0.952	1.0	57	0.98
5C1	600	1.5656	5.82	0.808	8.0	16.4	0.28
5C2	600	1.5466	5.95	0.955	8.0	18	0.31

[a] Letter from C. E. Johnson to K. Pearce, April 23, 1991; 1 mmol = 58.3 Ci.
[b] Excluding tritium-charged mother vanadium.

Tensile properties were measured at 20-200°C and at the irradiation temperatures in flowing argon at a strain rate of 0.0011 s^{-1}. Most of the tensile specimens tested at 20-200°C were not degassed at 400°C for 1 h, a customary procedure to expel tritium and hydrogen, although some were examined after degassing in high vacuum. Fracture behavior was determined by repeatedly bending a TEM disk or a piece of broken tensile specimen while submerged in low-temperature baths of liquid nitrogen or mixtures of dry ice and acetone. Temperature of the surrounding liquid was measured with a calibrated thermocouple. Each side of a bend specimen was firmly held by two grips in the test bath and the middle portion of the disk was bent repeatedly until fracture. Thus, specimen constraint was similar to that in a four-point bend test. Depending on irradiation conditions and test temperature, 3 to 62 bends were required to produce fracture at -196 to 50°C. Cold-work accumulated in the specimen as the number of bends increased. After fracture, morphology of the fracture surface was examined quantitatively by SEM. A few dozen SEM fractographs were taken at ≈200-300 X, and a composite of the whole fracture surface was made. Four types of fracture morphology were observed: cleavage, quasicleavage, ductile-dimple, and fibrous ductile fracture. From the fracture surface composite, the percentage of ductile-fracture morphology was measured.

Table 3. Summary of irradiation parameters of Dynamic Helium Charging Experiment and helium and tritium contents of V-4Cr-4Ti specimens

Capsule ID No.	Irradiation Temp. (°C)	Fluence (E >0.1 MeV) (10^{22} n cm^{-2})	Total Damage (dpa)	Calculated Helium (appm)-to-dpa Ratio[a] at EOI[b] (Assumed k_a or k_w)[c] k_a=0.073 (k_w=0.01)	Measured Helium Content[d] (appm)	Actual Helium-to-dpa Ratio (appm/dpa)	Measured Tritium Content[e] (appm)
4D1	425	6.4	31	3.8	11.2–13.3	0.39	27
4D2	425	6.4	31	2.8	22.4–22.7	0.73	39
5E2	425	3.7	18	2.1	3.3–3.7	0.11	2
5D1	500	3.7	18	4.4	14.8–15.0	0.83	4.5
5E1	500	3.7	18	3.1	6.4–6.5	0.36	1.7
5C1	600	3.7	18	1.1	8.4–11.0	0.54	20
5C2	600	3.7	18	1.1	74.9–75.3	4.17	63

[a] L. R. Greenwood "Revised Calculations for the DHCE," April 30, 1993.

[b] Beginning of irradiation (BOI) May 27, 1991; end of irradiation (EOI) March 19, 1992; 203.3 effective full power days (EFPD), hot standby at ≈220°C until November 1992.

[c] Equilibrium ratio (k_a by atom, k_w by weight) of tritium in V alloy to that in the surrounding liquid lithium.

[d] Measured June 1994.

[e] Measured August 1994.

TENSILE PROPERTIES

Yield strength, ultimate tensile strength, uniform elongation, and total elongation measured on tensile specimens irradiated at 425°C–600°C to 18–34 dpa in the DHCE (helium generation rates 0.4–4.2 appm He/dpa) are summarized in Figs. 1A–1D, respectively. In the figure, similar properties measured on nonirradiated specimens and specimens irradiated in non-DHCE (negligible helium generation) have also been plotted as function of irradiation/test temperature. For each DHCE or non-DHCE specimen tested at 20–200°C, corresponding irradiation temperature is given in the figure.

After irradiation to ≈24–34 dpa in non-DHCEs, ductility of V-4Cr-4Ti retained significantly high ductility, i.e., >8% uniform elongation and >10% total elongation. After irradiation in the present DHCE, the alloy retained uniform and total elongations of >10% and >12%, respectively, regardless of the irradiation temperature (425–600°C), dose (18–31 dpa), helium generation rate (0.4–4.2 appm He/dpa), and test temperature (20–600°C).

Tensile properties measured at >400°C were essentially same as those measured on non-DHCE specimens, showing that the effect of helium was insignificant. Regardless of the specimen degassing treatment at 400°C, ductilities of the DHCE specimens measured at 20–200°C (after irradiation at 425, 500, and 600°C), were higher than those of the similar non-DHCE specimens, whereas strengths were lower. Although the mechanisms leading to the higher ductility and lower strength of the DHCE specimens are not understood at this time, these consistent observations indicate that different types of hardening centers are produced during DHCE and non-DHCE irradiation.

The dependence of uniform and total elongation on irradiation and test temperature, shown in Figs. 1C and 1D, respectively, is in distinct contrast to similar results obtained from tritium-trick experiments. In the latter type of experiments, total elongation measured at room temperature and at 700–800°C was significantly lower than that measured at 500–600°C. This was because of strong susceptibility to intergranular cracking that has been attributed to extensive coalescence of helium bubbles on grain boundaries [10]. However, neither fully nor partially intergranular failure was observed in the present tensile specimens irradiated in the DHCE and tested at 20–600°C (including the specimen irradiated in Capsule 5C2 at 600°C at a helium generation rate of 4.2 appm He/dpa), and no ductility degradation similar to that in the tritium-trick experiments was observed. This is shown in Fig. 2 where ratio of total strain with and without helium is plotted as a function of irradiation and test temperature for tritium-trick and DHCE.

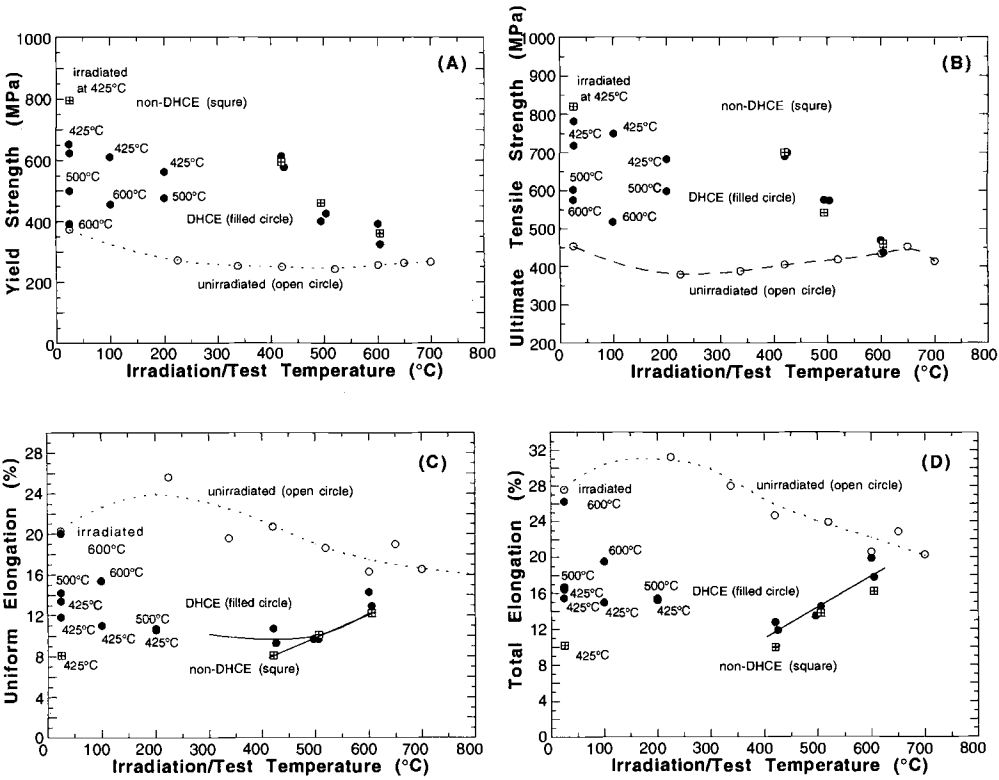


Fig. 1. Yield strength (A), ultimate tensile strength (B), uniform elongation (C), and total elongation (D) of V–4Cr–4Ti after irradiation at 420–600°C to 18–34 dpa in the DHCE (0.4–4.2 appm He/dpa) and in non-DHCE (negligible helium generation).

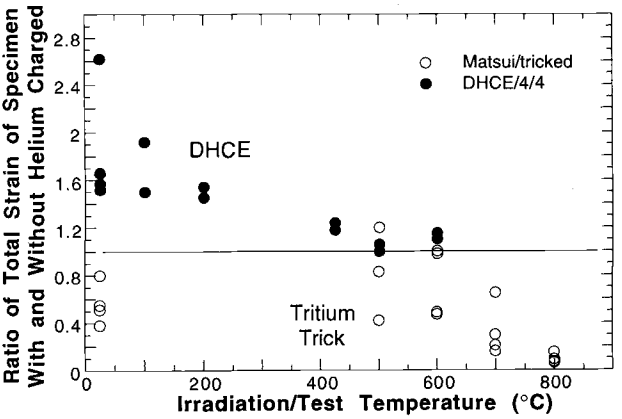


Fig. 2.

Ratio of total strain in specimens with and without helium as function of irradiation and test temperature. Results obtained from tritium-trick experiment and DHCE are shown for comparison.

DUCTILE-BRITTLE TRANSITION BEHAVIOR

Fracture behavior of the alloy was investigated by multiple-bending tests on irradiated miniature specimens. Because of limitation in the capsule space, no Charpy-impact specimens could be irradiated in the present DHCE. Therefore, to extract best information on ductile-brittle transition behavior of the alloy from available specimens, a TEM disk (0.3-*mm* thick) or a broken piece (0.7- to 1.0-mm thick) of a tensile specimen was bent repeatedly submerged in a low-temperature bath (typically 3-62 times) until fracture. Then, ductile and cleavage morphologies were characterized quantitatively. As reported previously [2,5], brittle fracture of V-4Cr-4Ti did not occur at temperatures >-196°C in impact tests on one-third-size Charpy specimens either in the nonirradiated condition or after irradiation to 24-34 dpa at 425-600°C in non-DHCE (negligible helium). Consistent with this behavior, only ductile fracture was observed from the present multiple-bend tests on disk and broken tensile specimens of the alloy either unirradiated or irradiated in non-DHCE. This is shown in Figs. 3 and 4, respectively.

The percentage of fracture surface of disk and broken tensile specimens (irradiated at 425-600°C to 18-31 dpa in the DHCE) with ductile-fracture morphology is plotted as a function of test temperature in Figs. 5A and 5B. The figures show effects of simultaneous displacement damage (18-31 dpa, Table 3), helium generation (at rates of 0.4-4.2 appm helium/dpa), and tritium (2-63 appm) uptake on ductile-brittle transition behavior. For purpose of comparison, similar results obtained for nonirradiated and irradiated non-DHCE specimens (containing negligible amounts of helium, tritium, and hydrogen) are also shown. Despite the difference in specimen thickness, ductile-brittle transition behavior of the disk and broken tensile specimens was similar.

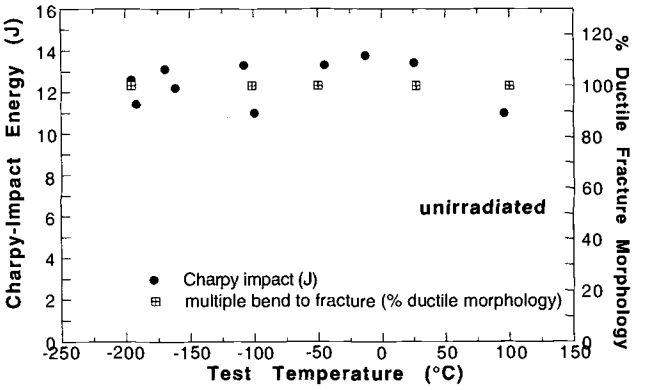


Fig. 3.

Comparison of Charpy-impact energy and percentage of ductile fracture surface morphology of TEM disks (determined after multiple bend until fracture) of unirradiated V-4Cr-4Ti, plotted as a function of test temperature.

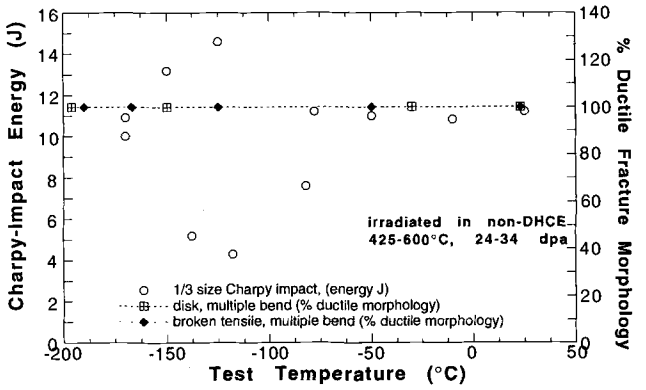


Fig. 4.

Comparison of Charpy-impact energy and percentage of ductile fracture surface morphology of TEM disks and broken pieces of tensile specimens (determined after multiple bend until fracture) of V-4Cr-4Ti irradiated in non-DHCE, plotted as a function of test temperature.

The results in Fig. 5 show that the percentage of brittle cleavage measured from fracture surfaces produced near −190°C was more pronounced in specimens irradiated at 425°C than in specimens irradiated at 500–600°C. As in non–DHCE irradiation , no brittle behavior was observed at temperatures >−170°C for DHCE specimens in which helium generation rate was ≈0.3–4.2 appm helium/dpa (Table 3). Predominantly brittle cleavage fracture morphologies were observed only at −196°C in some specimens irradiated to 31 dpa at 425°C during DHCE. The results in Figs. 5 indicate that the DBTTs for specimens irradiated at 425°C and 500–600°C are −175 and −200°C, respectively. As in case of tensile tests at 20–600°C, no intergranular fracture was observed in any specimens fractured at −196 to 50°C by multiple bending.

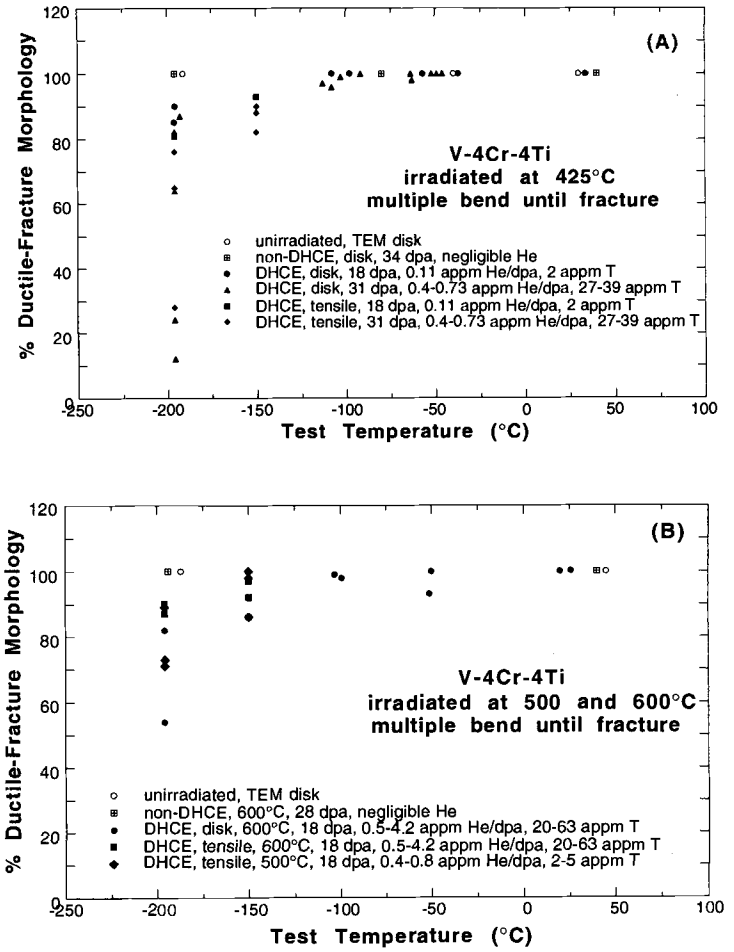


Fig. 5. Percent ductile-fracture morphology vs. test temperature of V-4Cr-4Ti TEM disks and broken tensile specimens irradiated at (A) 425°C and (B) 600°C and fractured subsequently by multiple bending at −196°C to 50°C.

DISCUSSION

An important finding from the DHCE was that the actual (measured) contents of helium and tritium in the V–4Cr–4Ti specimens were significantly lower than those calculated previously on the basis of assumed equilibrium ratio (k_w = 0.01, by weight) of tritium in the alloy to that in the liquid lithium (Table 3). Except for specimens irradiated in Capsule 5C1 and 5C2 at 600°C, actual helium/dpa ratios (i.e., 0.36–0.83) were several times lower than those calculated on the basis of an equilibrium ratio of k_w = 0.01. This indicates that the level of hydrogen and tritium in the lithium–cooled V–4Cr–4Ti first wall/blanket structure, and hence the effect of hydrogen and tritium on fracture toughness, will be significantly lower than previously assumed.

As described in a separate paper [23], densities of helium bubbles or microvoids were negligible in all specimens irradiated in DHCE, except for a limited amount of helium bubbles in specimens irradiated at 425°C that were distributed more or less uniformly in grains and on grain boundaries. In most of specimens only a few helium bubbles were observed at the interface between the grain matrix and some Ti(O,N,C) precipitates that are normally present in V–Ti and V–Cr–Ti alloys. Even in specimens irradiated at 600°C at the highest helium generation rate of ≈4.2 appm He/dpa (Capsule 5C2), no microvoids could be detected in either grain matrix or grain boundaries. The absence of intergranular fracture morphology in the present DHCE specimens seems to be consistent with these microstructural characteristics of helium bubble distribution. However, despite the observation of absence of intergranular failure in specimens irradiated at 600°C at a helium generation rate up to ≈4.2 appm He/dpa, a more comprehensive data base is needed for irradiation at 300–425°C with higher helium–dpa ratios (i.e., the fusion–relevant ratio of 4–6 appm He/dpa).

The uniform and total elongations of the DHCE specimens measured at 20–200°C were significantly greater than similar room–temperature elongations measured on specimens irradiated in either non–DHCE (Fig. 1) or tritium–trick experiments (Fig. 2). This is also consistent with the absence of coalescence of helium bubbles on grain boundaries in the specimens irradiated in DHCE. Also, this observation indicates that different types of hardening centers are produced in the alloy during DHCE and non–DHCE irradiation at 425–600°C. Although the nature of the hardening centers produced during DHCE is not understood at this time, helium atoms are believed to play an important role in the hardening mechanism.

In a series of studies on thermal desorption behavior of helium from unalloyed vanadium and V–5Ti irradiated with helium ions of various energy levels, van Veen et al. [24] and Buitenhuis et al. [25] concluded that helium–oxygen–vacancy and helium–nitrogen–vacancy (and probably helium–vacancy–carbon as well) complexes formed in the irradiated material. These investigators further deduced that the complexes are stable at low temperatures (<250°C) but dissociate into helium atoms and oxygen–vacancy and nitrogen–vacancy complexes at 270–310°C, leading to a prominent helium desorption peak at ≈280°C that was observed consistently in their experiments. Desorption peaks at ≈770°C and ≈1250°C, observed only after irradiation with helium ion to higher doses, were attributed to clusters of helium atoms and helium bubbles, respectively. These clusters and bubbles of helium are believed to be unstable only at the high temperatures. During the degassing treatment in the present study in which DHCE specimens were heated to 405°C at a rate of ≈0.2°C/s, desorption peaks were observed consistently at ≈280°C, although helium desorption was not positively identified by mass spectroscopy, as done by van Veen et al. and Buitenhuis et al.

Based on these observations, it is likely that stable helium–vacancy–impurity complexes were also present in the present DHCE specimens during the tensile tests at 20–200°C. In contrast, in specimens irradiated in non–DHCE under similar conditions, vacancies and impurities (such as oxygen, nitrogen, and carbon) are not expected to form such complexes in the absence of appreciable helium atoms. Rather, the impurity atoms in solution and vacancies or vacancy clusters will be scattered more or less randomly in interstitial and vacancy sites, respectively. Dislocation motion would then be more difficult, and hence ductility would be lower in the non–DHCE than in the DHCE specimens; this seems to be in accordance with the results shown in Fig. 1.

CONCLUSIONS

1. Effects of dynamically charged helium, neutron damage, and retained tritium on DBTT of V–4Cr–4Ti were determined after irradiation in the Dynamic Helium Charging Experiment (DHCE). TEM disks and broken pieces of tensile specimens, irradiated at 425–600°C to 18–31 dpa and at helium generation rates of 0.4–4.2 appm helium/dpa, were fractured by repeated bending while submerged in low-temperature baths. Ductile–brittle transition temperature, based on quantitative SEM fractography of ductile and brittle fracture surface morphologies, was no higher than −175°C in these specimens.

2. Tensile ductility of V–4Cr–4Ti irradiated in DHCE remained significantly high at 20–600°C, i.e., >10% uniform elongation and >12% total elongation. Tensile properties measured at >420°C were essentially the same as those measured on non-DHCE specimens (negligible helium), showing that effects of helium were insignificant. For tests at 20–200°C, ductilities of the DHCE specimens (irradiated at 425–600°C) were higher than those of non-DHCE specimens irradiated under otherwise similar conditions, whereas strengths were lower. These observations indicate that different types of hardening centers are present at 20–200°C in the DHCE specimens (probably helium–vacancy–impurities complex, impurities being oxygen, nitrogen, and carbon) and in non-DHCE specimens (defects and defect clusters, impurities in interstitial sites). The dependence of uniform and total elongation on irradiation and test temperature is in distinct contrast to similar results obtained on specimens in which helium atoms were produced by the tritium-trick method.

3. Neither partial nor predominantly intergranular fracture was observed in tensile tests at 20 to 600°C or multiple-bending tests at −196 to 50°C.

4. Measured helium and tritium contents in the V–4Cr–4Ti specimens indicate that the equilibrium ratio of tritium (in the alloy to that in the liquid lithium) is significantly smaller (probably ≈0.001 by weight) than that assumed previously (≈0.01 by weight). This indicates that the level of tritium and hydrogen in the lithium-cooled V–4Cr–4Ti first wall/blanket structure, and hence the effect of tritium and hydrogen on fracture toughness, would be significantly lower than previously assumed.

ACKNOWLEDGMENTS

Successful completion of the Dynamic Helium Charging Experiment, a complex and difficult irradiation test, was possible only through many years of effort and contributions from many investigators in the United States and Japan: F. W. Wiffen, H. Matsui, K. Abe, C. E. Johnson, R. G. Clemmer, J. P. Kopasz, L. R. Greenwood, M. L. Hamilton, K. L. Pearce, R. Ermi, A. Ermi, H.-C. Tsai, R. V. Strain, D. Donahue, J. Gazda, and L. J. Nowicki. The authors are grateful in particular to L. R. Greenwood and B. M. Oliver for their calculation and measurement, respectively, of helium and tritium contents.

REFERENCES

[1] B. A. Loomis, L. Nowicki, and D. L. Smith, "Effect of Neutron Irradiation on Tensile Properties of V–Cr–Ti Alloys," in Fusion Reactor Materials, Semiannual, Prog. Report, DOE/ER-0313/15, Oak Ridge National Laboratory, Oak Ridge, TN (1994), pp. 219–222.

[2] B. A. Loomis, H. M. Chung, L. Nowicki, and D. L. Smith, "Effects of Neutron Irradiation and Hydrogen on Ductile-Brittle Transition Temperatures of V–Cr–Ti Alloys," ibid., pp. 253–257.

[3] H. M. Chung, B. A. Loomis, L. Nowicki, J. Gazda, and D. L. Smith, "Irradiation-Induced Density Change and Microstructural Evolution of Vanadium-Base Alloys," ibid., pp. 223–231.

[4] H. Matsui, M. Tanno, J. Gazda, and H. M. Chung, "Microstructural Stability of V-4Cr-4Ti During Neutron Irradiation," ibid., pp. 240–246.

[5] H. M. Chung, J. Gazda, L. Nowicki, J. E. Sanecki, and D. L. Smith, "Effects of Fabrication Variables on Impact Properties and Microstructure of V–Cr–Ti Alloys,"

ibid., pp. 207–218.

[6] H. M. Chung, B. A. Loomis, and D. L. Smith, "Thermal Creep Behavior of V–5Cr–5Ti and V–10Cr–5Ti Alloys," in Fusion Reactor Materials, Semiannual. Prog. Report, DOE/ER-0313/14, Oak Ridge National Laboratory, Oak Ridge, TN (1993), pp. 309-317.

[7] D. N. Braski, in Influence of Radiation on Material Properties, ASTM-STP 956 (1986), pp. 271-290.

[8] D. N. Braski, J. Nucl. Mater. 141-143 (1986) 1125.

[9] D. N. Braski, in Reduced Activation Materials for Fusion Reactors, ASTM-STP 1047 (1988), pp. 161-178.

[10] H. Matsui, M. Tanaka, M. Yamamoto, and M. Tada, J. Nucl. Mater. 191-194 (1992) 919.

[11] M. Satou, K. Abe, and H. Matsui, J. Nucl. Mater. 191-194 (1992) 938.

[12] W. van Witzenburg, A. Mastenbroek, and J. D. Ellen, J. Nucl. Mater. 103-104 (1981) 1187.

[13] M. P. Tanaka, E. E. Bloom, and J. A. Horak, J. Nucl. Mater. 114 (1981) 895.

[14] M. L. Grossbeck and J. A. Horak, in Influence of Radiation on Material Properties, ASTM-STP 956 (1986), p. 291.

[15] J. M. Vitek, D. N. Braski, and J. A. Horak, J. Nucl. Mater. 141-143 (1986) 982.

[16] W. van Witzenburg and E. de Vries, in Effects of Radiation on Materials, ASTM-STP 1125 (1990).

[17] L. L. Horton and K. Farrell, J. Nucl. Mater. 122-123 (1984) 687.

[18] H. Kawanishi and S. Ishino, in Reduced Activation Materials for Fusion Reactors, ASTM-STP 1047 (1988), pp. 179-189.

[19] H. Kawanishi, Y. Arai, and S. Ishino, J. Nucl. Mater. 191-194 (1992) 933.

[20] D. L. Smith, H. Matsui, L. R. Greenwood, and B. A. Loomis, J. Nucl. Mater. 155-157 (1988) 1359.

[21] D. L. Smith, B. A. Loomis, H. Matsui, M. L. Hamilton, K. L. Pearce, J. P. Kopasz, C. E. Johnson, R. G. Clemmer, and L. R. Greenwood, in Fusion Reactor Materials, Semiannual. Prog. Rep. DOE/ER-0313/10, Oak Ridge National Laboratory, Oak Ridge, TN (1991), p. 159.

[22] H. Tsai, H. M. Chung, B. A. Loomis, and D. L. Smith, "Status of Dynamic Helium Charging Experiment (DHCE)," in Fusion Reactor Materials, Semiannual. Prog. Report, DOE/ER-0313/15, Oak Ridge National Laboratory, Oak Ridge, TN (1994), pp. 247–252.

[23] H. M. Chung, B. A. Loomis, and D. L. Smith, "Swelling and Structure of Vanadium–Base Alloys Irradiated in the Dynamic Helium Charging Experiment," in this proceedings.

[24] A. van Veen, H. Eleveld, and M. Clement, "Helium Impurity Interactions in Niobium and Vanadium," in Proc. Sixth Intl. Conf. on Fusion Reactor Materials, September 27–October 1, 1993, Stresa, Italy, in press.

[25] T. Buitenhuis, A. Fedorov, and A. van Veen, "Thermal Desorption Investigation of V–5Ti Alloy," IRI–131–94–005, Delft University of Technology, The Netherlands, 1994.

H. M. Chung,[1] B. A. Loomis,[1] and D. L. Smith[2]

SWELLING AND STRUCTURE OF VANADIUM-BASE ALLOYS IRRADIATED IN THE DYNAMIC HELIUM CHARGING EXPERIMENT

REFERENCE: Chung, H. M., Loomis, B. A., and Smith, D. L., **"Swelling and Structure of Vanadium-Base Alloys Irradiated in the Dynamic Helium Charging Experiment,"** *Effects of Radiation on Materials: 17th International Symposium, ASTM STP 1270*, David S. Gelles, Randy K. Nanstad, Arvind S. Kumar, and Edward A. Little, Eds., American Society for Testing and Materials, 1996.

Abstract: Combined effects of dynamically charged helium and neutron damage on density change, void distribution, and microstructural evolution of V and V-4Cr-4Ti alloys have been determined after irradiation to 18-31 dpa at 425-600°C in the Dynamic Helium Charging Experiment (DHCE). The results were compared with those from a non-DHCE in which helium generation was negligible. For V-4Cr-4Ti specimens irradiated to ≈18-31 dpa at 425, 500, or 600°C with a helium generation rate of 0.4-4.2 appm helium/dpa, only limited number of helium bubbles were observed either at some Ti(O,N,C) precipitate interfaces, in localized regions of grains, or near grain boundaries. Neither extensive coalescences of helium bubbles on grain boundaries, typical of some alloys irradiated in tritium-trick experiments, nor dense helium bubbles within grains, typical of unalloyed V or alloys not containing Ti, were observed. Under the conditions of DHCE, most of dynamically produced helium atoms seem to be trapped by irradiation-induced defects and defect clusters within grains or fine Ti_5Si_3 precipitates, which prevents significant bubble nucleation or growth. Density changes measured on specimens irradiated in DHCE or non-DHCE were low (<0.5%) for all the irradiation conditions investigated (425-600°C, 18-34 dpa, and <4.2 appm He/dpa).

Key words: vanadium-base alloy, V-4Cr-4Ti, helium, neutron displacement damage, density change, void swelling, fusion reactor first wall

Recent attention in the development of vanadium-base alloys for application in fusion reactor first wall and blanket structure has focused on V-4Cr-4Ti, an alloy reported to exhibit an excellent combination of mechanical and physical properties before and after irradiation [1-6]. One of the unresolved issues in the performance of the alloy, however, has been the effect of fusion-relevant simultaneous generation of helium and neutron damage (at a ratio of 4-5 appm helium/displacement per atom [dpa]) on density change and void swelling. Helium effects determined for other vanadium-base alloys by means of less fusion-relevant simulation approaches, such as tritium-trick [7-13], cyclotron-injection [14-18], and boron-doping [18-21] techniques, have been inconsistent with regard to concentration of helium bubbles on grain boundaries and the concomitant propensity for intergranular fracture. In the unique Dynamic Helium Charging Experiment (DHCE), the fusion-relevant helium-to-dpa ratio is simulated realistically by utilizing transmutation of controlled amounts of ^6Li and a predetermined amount of tritium-doped mother vanadium immersed in ^6Li + ^7Li [22-24]. This report describes results of microstructural characterization and density measurement primarily of V-4Cr-4Ti specimens irradiated to 18-31 dpa at 425-600°C in the DHCE.

MATERIALS AND PROCEDURES

The elemental compositions of the unalloyed V (ANL Identification BL-19) and V-4Cr-4Ti (BL-47), determined prior to irradiation, are given in Table 1. Most of the investigations were focused on V-4Cr-4Ti. Postirradiation examination of other alloys was limited at this time. Fabrication procedures of the alloy ingots and annealed plates and sheets have been reported elsewhere [25].

[1]Metallurgists, Energy Technology Division, and [2]Director, Fusion Power Program Division, respectively, Argonne National Laboratory, Argonne, IL 60439.

Copyright© 1996 by ASTM International www.astm.org

TEM disks, punched from 0.3-mm-thick cold-worked sheets to investigate density change, void swelling behavior, and microstructural characteristics, were annealed at 1050°C for 1 h in an ion-pumped high-vacuum system. The annealed disks were ≈95% recrystallized and exhibited an average grain size of ≈14 μm. Phase structures of the alloy, characterized before and after irradiation in a non-DHCE (425-600°C, 24-34 dpa, <0.1 appm He), have been described in detail elsewhere [4]. The only secondary phase present in the as-annealed specimens was Ti(O,N,C), which is present normally in titanium-containing vanadium alloys with O+N+C > 400 wppm [26].

Table 1. Chemical composition of the vanadium-base alloys investigated

	Nominal Composition	Impurity Composition (wppm)							
ANL ID	(wt.%)	O	N	C	Si	S	P	Nb	Mo
BL-19	V	1101	161	360	–	–	–	–	–
BL-47	V-4.1Cr-4.3Ti	350	220	200	870	20	<40	<100	<100

The specimens were irradiated in the Fast Flux Test Facility (FFTF), a fast reactor located in Richland, Washington, at 420, 500, and 600°C to neutron fluences (E > 0.1 MeV) ranging from 3.7 x 10^{22} n/cm^2 (≈18 displacements per atom, or dpa) to 6.4 x 10^{22} n/cm^2 (≈31 dpa). Helium in the specimens was produced by utilizing transmutation of controlled amounts of ^{6}Li and a predetermined amount of tritium-doped "mother" vanadium immersed in ^{6}Li + ^{7}Li [22-24]. Table 2 summarizes the irradiation temperature, weight of the mother vanadium, fraction of ^{6}Li, and tritium and lithium inventory charged in each of the seven DHCE capsules before irradiation. Table 3 summarizes the actual postirradiation parameters determined from tensile and disk specimens of the V-4Cr-4Ti alloy, i.e., fast neutron fluence, dose, and helium and tritium content measured shortly after the postirradiation tests. Helium and tritium were determined by mass spectrometry at Rockwell International Inc., Canoga Park, California.

Table 2. Capsule-loading parameters of the Dynamic Helium Charging Experiment.

Capsule	Irradiation Temp.	Total Weight (g)			Fraction of ^{6}Li	Initial Tritium Charge[a]	
ID No.	(°C)	Mother V[a]	Specimen[b]	Lithium	(%)	(Ci)	(mmol)
4D1	425	1.5468	5.86	0.765	5.0	99	1.70
4D2	425	1.5536	5.38	0.765	4.5	70	1.20
5E2	425	1.5657	5.38	0.670	1.0	26	0.45
5D1	500	1.5727	5.77	0.938	6.5	73.5	1.26
5E1	500	1.5651	5.82	0.952	1.0	57	0.98
5C1	600	1.5656	5.82	0.808	8.0	16.4	0.28
5C2	600	1.5466	5.95	0.955	8.0	18	0.31

[a] Letter from C. E. Johnson to K. Pearce, April 23, 1991; 1 mmol = 58.3 Ci.
[b] Excluding tritium-charged mother vanadium.

The retrieved TEM specimens, which contained helium, tritium, and neutron displacement damage, were cleaned ultrasonically in alcohol prior to density measurement and microstructural analysis. Most of the examined TEM disks were not degassed at 400°C for 1 h, a customary procedure to expel tritium and hydrogen from Charpy-impact and tensile specimens. Several TEM disks were examined after degassing in an ion-pumped high vacuum. However, except for hydrogen and tritium contents, none indicated any appreciable difference either in void or helium bubble distribution, density, and microstructure from undegassed specimens that should contain tritium and hydrogen in addition to helium. The irradiated specimens were jet-thinned for TEM in a solution of 15% sulfuric acid-72% methanol-13% butyl cellosolve maintained at -5°C. TEM was conducted with a JEOL 100CX-II scanning transmission electron microscope operating at 100 keV or with a Philips CM-30 analytical electron microscope operating at 200 keV. Density change was determined on small pieces (weight 70-110 mg) cut from the shoulder regions of irradiated tensile specimens (0.7- to 1.0-mm thick). Weights were

measured in air and in research-grade CCl_4. Uncertainty limits of density change measured on tensile specimens were significantly smaller than those measured on TEM disks (≈0.3-mm thick, ≈10 mg in weight).

Table 3. Summary of irradiation parameters of Dynamic Helium Charging Experiment and helium and tritium contents of V-4Cr-4Ti specimens

Capsule ID No.	Irradiation Temp. (°C)	Fluence (E >0.1 MeV) (10^{22} n cm^{-2})	Total Damage (dpa)	Calculated Helium (appm)-to-dpa Ratio[a] at EOI[b] (Assumed k_a or k_W)[c] k_a=0.073 (k_W=0.01)	Measured Helium Content[d] (appm)	Actual Helium-to-dpa Ratio (appm/dpa)	Measured Tritium Content[e] (appm)
4D1	425	6.4	31	3.8	11.2–13.3	0.39	27
4D2	425	6.4	31	2.8	22.4–22.7	0.73	39
5E2	425	3.7	18	2.1	3.3–3.7	0.11	2
5D1	500	3.7	18	4.4	14.8–15.0	0.83	4.5
5E1	500	3.7	18	3.1	6.4–6.5	0.36	1.7
5C1	600	3.7	18	1.1	8.4–11.0	0.54	20
5C2	600	3.7	18	1.1	74.9–75.3	4.17	63

[a] L. R. Greenwood "Revised Calculations for the DHCE," April 30, 1993.
[b] Beginning of irradiation (BOI) May 27, 1991; end of irradiation (EOI) March 19, 1992; 203.3 effective full power days (EFPD), hot standby at ≈220°C until November 1992.
[c] Equilibrium ratio (k_a by atom, k_W by weight) of tritium in V alloy to that in the surrounding liquid lithium.
[d] Measured June 1994.
[e] Measured August 1994.

MICROSTRUCTURE AND HELIUM BUBBLE DISTRIBUTION

Voids or helium bubbles in specimens of unalloyed V, irradiated to ≈18–31 dpa at 425–600°C in the DHCE and containing 9–34 appm He, were observed in high density in the unalloyed V. However, they were insignificant in specimens of V–4Cr–4Ti irradiated in the same DHCE capsules (helium contents 4–75 appm). For unalloyed V specimens irradiated to ≈31 dpa at 425°C (≈15 appm He) and to ≈18 dpa at 600°C (≈11 appm He), dense voids or helium bubbles were observed as shown in Fig. 1 (bubble diameter ≈5–20 and 10–50 nm, respectively, for irradiation at 425 and 600°C). However, despite the high number density, helium bubbles were distributed more or less uniformly within the grains and near grain boundaries, and no evidence of grain-boundary coalescence of bubbles characteristic of "tritium-tricked" specimens was observed (Fig. 1A).

A summary of microstructural characterization of voids or helium bubbles in the DHCE specimens of V–4Cr–4Ti is given in Table 4. Voids or helium bubbles in the DHCE specimens of V–4Cr–4Ti irradiated at 500 or 600°C were negligible, and it was difficult to find any void either within grains or on grain boundaries. In specimens irradiated to ≈18 dpa at 600°C and retrieved from Capsules 5C1 (0.54 appm He/dpa) and 5C2 (4.2 appm He/dpa), a few helium bubbles were observed only at interfaces of a limited number of Ti(O,N,C) precipitates. This is shown in Fig. 2. Also shown in the figure are dark-field morphologies and distributions of Ti_5Si_3 that precipitated at 600°C in the alloy under DHCE (0.5–4.2 appm He/dpa) and non-DHCE (negligible helium generation) conditions. Void swelling and other microstructural characteristics of the DHCE specimens irradiated to ≈18 dpa at 500°C were very similar to those of the counterpart specimens irradiated at 600°C. When irradiated at 500–600°C, virtually all of the dynamically produced helium atoms seem to have been trapped in the grain matrix without significant chance for bubble nucleation or growth, except at Ti(O,N,C) precipitate interface.

For DHCE specimens irradiated to ≈31 dpa at 425°C in Capsules 4D1 (helium generation rate ≈0.4 appm He/dpa) and 4D2 (≈0.8 appm He/dpa), some helium bubbles (≈5 nm in diameter) were observed within grains as well as on some of the grain boundaries. This is shown in Fig. 3. Voids and helium bubbles in these specimens were distributed more or less uniformly in the grains and near grain boundaries (Fig. 3A), in contrast to virtual concentration of all helium bubbles on grain boundaries in tritium-trick

experiments. This observation, similar to that from the unalloyed vanadium, seems to indicate that most of the helium atoms produced dynamically at 425°C were also trapped within the grains, preventing extensive formation of continuous helium bubbles on grain boundaries. In Fig. 3B, a limited number of small helium bubbles, distributed more or less uniformly in the grains and on the grain boundary, are visible.

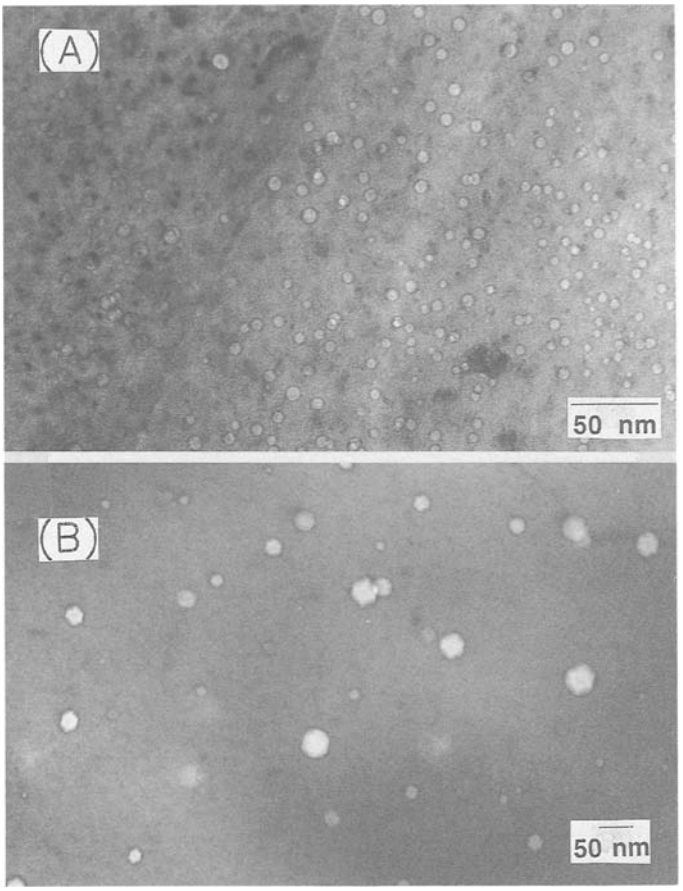


Figure 1.

Void and helium bubble distribution in unalloyed vanadium irradiated in DHCE at: (A) 425°C, ≈31 dpa, ≈15 appm He (Capsule 4D1); and (B) 600°C, ≈18 dpa, ≈11 appm He (Capsule 5C2).

Table 4. Summary of void distribution in V–4Cr–4Ti irradiated in the DHCE.

Capsule ID No.	Irradiation Temp (°C)	Fluence (E >0.1 MeV) (10^{22} n cm^{-2})	Total Damage (dpa)	Helium–to–dpa Ratio (appm/dpa)	Voids within Grains	Voids on Ti(O,N,C) Interface	Voids on Grain Boundaries
non–DHCE	425, 500, 600°C		24–34	–	none	none	none
4D1	425	6.4	31	0.39	some	some	some
4D2	425	6.4	31	0.73	some	some	some
5E2	425	3.7	18	0.11	none	none	none
5D1	500	3.7	18	0.83	none	some	none
5E1	500	3.7	18	0.36	none	some	none
5C1	600	3.7	18	0.54	none	some	none
5C2	600	3.7	18	4.17	none	some	none

Some of the specimens irradiated to 31 dpa at 425°C were also characterized by extremely thin (≈5 nm) shells of voids that surround some of the Ti(O,N,C) precipitates. An example of the helium shells is shown in Fig. 3B. The shells are believed to be composed of continuous helium bubbles similar to those shown in Fig. 2A. These observations clearly show that helium atoms are effectively trapped at the interface of Ti(O,N,C) precipitates. Few helium bubbles were found within grains, on grain boundaries, or at the interface of Ti(O,N,C) precipitates in specimens irradiated to 18 dpa at 425°C in Capsule 5E2 (≈0.11 appm He/dpa).

As in non-DHCEs [4], there was no evidence of precipitation of Ti_5Si_3 from analyses by TEM for irradiation at 425°C in the DHCE. However, presence of clusters of Ti and Si, precursor of preciptates too fine to be detected by TEM, cannot be ruled out. Presence or absence of clusters of Ti and Si in the DHCE specimens irradiated at ≈425°C could be determined best by means of atom-probe field ion microscopy (APFIM). It is also possible that Ti_5Si_3 precipitates at higher dose at ≈425°C. If Ti_5Si_3 precipitation was indeed significant for 425°C irradiation, void swelling would have been suppressed more significantly [27].

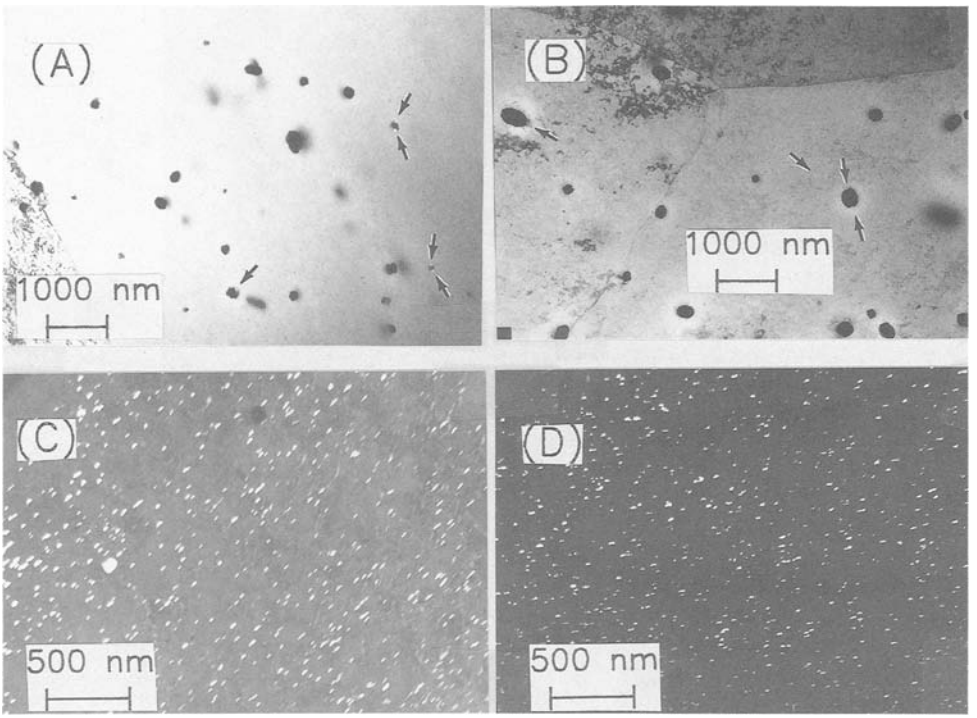


Figure 2. TEM microstructure of V-4Cr-4Ti irradiated at 600°C to ≈18 dpa in DHCE, showing only a few voids near Ti(O,N,C): (A) Capsule 5C1, 0.5 appm He/dpa; (B) Capsule 5C2, 4.2 appm He/dpa. (C) and (D) show dark-field images of Ti_5Si_3 that precipitated during irradiation under DHCE (Capsule 5C1) and non-DHCE conditions (600°C, 28 dpa, <0.003 appm He/dpa), respectively.

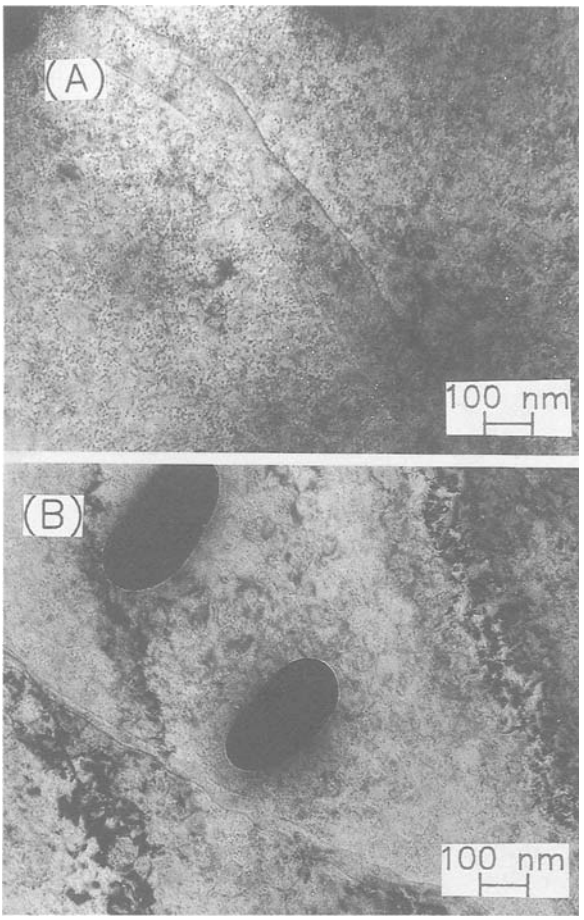


Figure 3. TEM microstructure of V-4Cr-4Ti irradiated at 425°C to ≈31 dpa in DHCE: (A) helium bubbles distributed more or less uniformly in grains and near a grain boundary (Capsule 4D1); (B) thin helium shells surrounding Ti(O,N,C) and limited bubbles in grains and near a grain boundary (Capsule 4D2).

DENSITY CHANGE

Density could be determined more accurately from measurement on broken tensile specimens (0.7- to 1.0-mm thick, 70-100 mg) than on TEM disks (0.3-mm thick, ≈10 mg). This is shown in Fig. 4 in which data scattering in baseline density measured on unirradiated V-4Cr-4Ti is compared. Results of density change measurements (i.e., decrease in density) for V-4Cr-4Ti is given in Fig. 5. The helium contents of the DHCE specimens are also given in the figure (see Table 1). For comparison, density changes determined for similar irradiation conditions in non-DHCEs [3], are also shown in the figure. Density changes measured for the non-DHCE and DHCE specimens were low (<0.5 %). The small density change seems to be consistent with the negligible number density of voids or helium bubbles. Density changes measured for the DHCE specimens irradiated at 425°C were somewhat higher than those for specimens irradiated at 500-600°C.

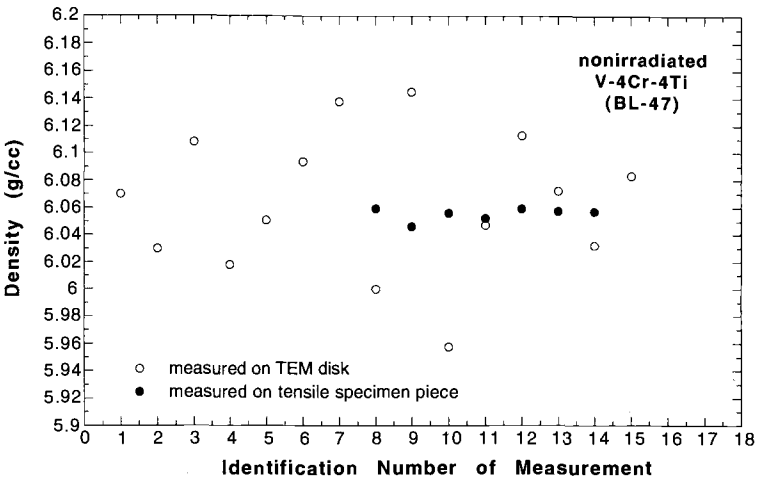


Figure 4. Comparison of densities measured from TEM disks (≈10 mg in weight) and broken tensile specimens (≈70–100 mg) of unirradiated V–4Cr–4Ti, showing significantly more accurate data from tensile specimens.

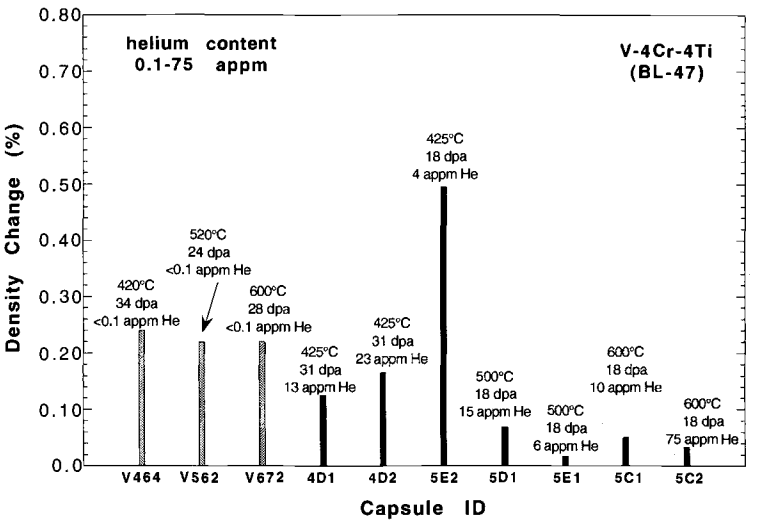


Figure 5. Density changes of V–4Cr–4Ti after irradiation to 18–34 dpa at 420–600°C in DHCE (0.4–4.2 appm He/dpa) and non-DHCE (<0.003 appm He/dpa).

DISCUSSION

Microvoids or helium bubbles were negligible in all specimens of V–4Cr–4Ti irradiated in the DHCE at 500–600°C, including the specimens irradiated in Capsule 5C2 to ≈18 dpa at 600°C and containing ≈75 appm helium (≈4.2 appm He/dpa, Fig. 2B). Only a few helium

bubbles were observed at some Ti(O,N,C) precipitate interfaces. Similar observation of preferential formation of voids near blocky precipitates [presumably Ti(O,N,C) precipitates] was reported by Braski in V-3Ti-1Si specimens that were preimplanted with 82 appm helium using the tritium-trick technique and then irradiated to 40 dpa at 600°C [8].

Van Veen and his coworkers also proposed that Ti(O,N,C) precipitate interfaces act as preferential sinks for helium [28]. From a series of measurements of thermal desorption analyses by mass spectroscopy, they identified a helium desorption peak at a surprisingly low temperature of ≈280°C in V-5Ti specimens that were irradiated and implanted with helium ions. Desorption peaks at ≈770°C and ≈1250°C, observed only after irradiation with helium ion to higher doses, were attributed to clusters of helium atoms and helium bubbles, respectively. These clusters and bubbles of helium are believed to be unstable only at the high temperatures. Some of the desorption peaks near ≈280°C were sharp and narrow and some were weak and broad. Furthermore, Van Veen and his coworkers attributed the former and the latter types of peaks near ≈280°C to helium–vacancy–impurity (O, N, and C) complexes, produced within the grains and near Ti(O,N,C) precipitate interfaces, respectively, which subsequently dissociated into helium and vacancy–impurity complexes upon heating to ≈280°C or higher.

Although most of the disk and tensile specimens investigated in this work were examined as-retrieved without heating at the customary degassing temperature of ≈400°C, some of the DHCE specimens were heated to ≈405°C at a rate of 0.2°C/s in high vacuum. During the heatup, desorption peaks were observed consistently at ≈280°C, although a positive identification of helium desorption was not made from a mass spectroscopic analysis. Some of the specimens exhibited an additional weak desorption peak at ≈390°C. Strong desorption peaks are commonly observed at ≈390–400°C when dissolved hydrogen atoms are expelled from unirradiated vanadium alloys. Therefore, the weak ≈390°C peak of the present DHCE specimens is most likely due to desorption of tritium and hydrogen. No apparent effects of the degassing treatment at 400–405°C were observed on microstructure (characterized by TEM), density, helium content measured, or tensile properties [25]. At this time, therefore, a conclusive identification of the origin of the desorption peak at ≈280°C from our DHCE specimens cannot be given (i.e., helium–vacancy–impurity complexes in grains, helium near specimen surface, or rapid hydrogen or tritium desorption in absence of surface oxide film in specimens irradiated in lithium).

One of the important findings from the DHCE was that the actual (measured) helium and tritium content of V-4Cr-4Ti specimens was significantly lower than that which was calculated on the basis of the assumed equilibrium ratio (by weight) of $k_w = 0.01$ of tritium in the specimen to that in the liquid lithium (Table 3). Except for specimens irradiated in Capsules 5C1 and 5C2 at 600°C, actual helium/dpa ratios were several times lower than those calculated. This could be interpreted to indicate that k_w is significantly lower than previously thought (at least several times or even by an order of magnitude), in particular for irradiation at 425°C. An implication of this observation is that only insignificant amount of tritium would be retained in V-4Cr-4Ti that is irradiated in lithium environment, although presence of insulator coating (such as CaO or AlN) would complicate the permeation of tritium from the first wall to lithium.

For irradiation at 500–600°C, microvoids or helium bubbles were absent within the grains and on grain boundaries in all of the DHCE specimens, in which ultrafine Ti_5Si_3 precipitated at high density. Even in specimens irradiated at 600°C at the highest helium generation rate of ≈4.2 appm helium/dpa (Capsule 5C2), no microvoids could be detected either within the grains or on grain boundaries of V-4Cr-4Ti. This shows that V-4Cr-4Ti is very resistant to void swelling, grain-boundary coalescence of helium bubbles, and density change when irradiated at 500–600°C, at least at a helium generation rate of ≤4.2 appm He/dpa.

For irradiation at ≈420°C, diffuse helium bubbles in relatively low number density were observed within grains and near grain boundaries of V-4Cr-4Ti. Some regions of the grains and grain boundaries seemed to contain more helium bubbles than adjacent regions or other portions of the grain boundaries. However, there was no clear evidence of coalescence of helium bubbles or voids on grain boundaries. This observation on V-4Cr-4Ti seems to have been corroborated by the similar observation on the unalloyed vanadium

irradiated at ≈425°C; even for the unalloyed vanadium specimens containing extremely dense helium bubbles or voids, there was no evidence of grain-boundary coalescence (Fig. 1A). This is in distinct contrast to the well-known propensity for grain-boundary coalescence of helium bubbles that is commonly observed in tritium-trick experiments. These characteristics of DHCE seem to indicate that most of the helium atoms produced in V-4Cr-4Ti at 425°C were trapped by irradiation-induced vacancies or vacancy-impurity complexes, a finding that is in accordance with the findings of Buitenhuis et al. [28]. However, considering the relatively low helium generation rates (<0.8 appm He/dpa) measured in the specimens irradiated at ≈425°C, it is desirable to demonstrate the above finding for higher helium generation rates (e.g., 5-7 appm He/dpa) from a modified DHCE at 300-450°C. In the modified DHCE in this temperature range, it would be desirable to increase the enrichment ratio of ^{6}Li significantly and minimize the initial tritium charge in the mother vanadium alloy. This is because, with an initially high tritium charge in the mother vanadium, and hence, in the liquid lithium, a significant amount of tritium is suspected to diffuse at the early stage of reactor startup to grain boundaries of V-4Cr-4Ti and remain there at ≈400°C, a situation similar to a tritium-trick experiment.

Neither partially nor fully intergranular failure was not observed in any of the V-4Cr-4Ti specimens irradiated in the DHCE and subsequently tested in uniaxial tension at 23 to 600°C or in multiple bending tests at -196 to 50°C [25]. Even in specimens irradiated at 425°C and fractured in brittle manner during multiple bending tests at -196°, cleavage and ductile tearing were observed but intergranular fracture surface morphology was absent. These observations, consistent with the characteristics of helium bubble distribution described above, are also in distinct contrast to the propensity for intergranular failure that is commonly observed in tritium-trick experiments.

CONCLUSIONS

1. Effects of dynamically charged helium and neutron damage on void swelling, density change, and microstructural characteristics of V-4Cr-4Ti and unalloyed vanadium were investigated after irradiation in the Dynamic Helium Charging Experiment (DHCE). Despite of formation of dense microvoids and helium bubbles after irradiation at 425-600°C to 18-31 dpa, no evidence of grain-boundary coalescence of voids or helium bubbles were observed in the unalloyed vanadium. This is in distinct contrast to the propensity for grain-boundary coalescence of helium bubbles that is commonly observed in tritium-trick experiments. Therefore, tritium-trick is not a vaild method of testing helium effects in vanadium-base alloys.

2. Microvoids or helium bubbles were negligible in all specimens of V-4Cr-4Ti irradiated at 500-600°C to ≈18 dpa with helium generation rates up to ≈4.2 appm He/dpa in the DHCE. Only a few helium bubbles were observed at some Ti(O,N,C) precipitate interfaces.

3. For irradiation at ≈425°C (0.4-0.8 appm He/dpa), diffuse helium bubbles in relatively low number density were observed within grains and near grain boundaries of V-4Cr-4Ti. Although some regions of the grains and grain boundaries contained more helium bubbles than adjacent regions, there was no evidence of coalescence of helium bubbles or voids on grain boundaries. Most of the helium atoms produced in V-4Cr-4Ti at 425°C seem to have been trapped by irradiation-induced vacancies or vacancy-impurity complexes. However, considering the relatively low helium generation rates observed for the experiments at 425°C, a further verification of the above finding is desirable for higher helium generation rates (5-7 appm He/dpa) from a modified DHCE at 300-450°C.

4. Neither partially nor fully intergranular failure was observed in the V-4Cr-4Ti specimens irradiated in the DHCE and subsequently tested in uniaxial tension at 23 to 600°C or in multiple bending tests at -196 to 50°C. These observations, consistent with the characteristic helium bubble distribution described above, are also in distinct contrast to the propensity for intergranular failure that is commonly observed in tritium-trick experiments.

5. Density change of V-4Cr-4Ti irradiated to 18-31 dpa at 425-600°C (helium generation

rate 0.4–4.2 appm He/dpa) were <0.5 %. The alloy seems to be resistant to void nucleation and growth, grain-boundary coalescence of helium bubbles or voids, and density change when irradiated under these conditions.

6. Helium and tritium contents in the V–4Cr–4Ti specimens indicate that the equilibrium ratio of tritium (in the alloy to that in the liquid lithium) is significantly smaller than that assumed previously (≈0.01 by weight). This implies that only insignificant amount of tritium and hydrogen would be retained in V–4Cr–4Ti that is irradiated in lithium environment, although presence of insulator coating (such as CaO or AlN) would complicate the permeation of tritium and hydrogen from the first wall to lithium.

ACKNOWLEDGMENTS

The successful completion of the complex and difficult Dynamic Helium Charging Experiment was possible through many years of contributions from F. W. Wiffen, H. Matsui, K. Abe, C. E. Johnson, R. G. Clemmer, J. P. Kopasz, L. R. Greenwood, M. L. Hamilton, K. L. Pearce, R. Ermi, A. Ermi, H.-C. Tsai, R. V. Strain, J. Gazda, and L. J. Nowicki. The authors are grateful to L. R. Greenwood and B. M. Oliver for calculation and measurement, respectively, of helium and tritium contents.

REFERENCES

[1] B. A. Loomis, L. Nowicki, and D. L. Smith, "Effect of Neutron Irradiation on Tensile Properties of V–Cr–Ti Alloys," in Fusion Reactor Materials, Semiannual. Prog. Report, DOE/ER-0313/15, Oak Ridge National Laboratory, Oak Ridge, TN (1994), pp. 219–222.

[2] B. A. Loomis, H. M. Chung, L. Nowicki, and D. L. Smith, "Effects of Neutron Irradiation and Hydrogen on Ductile-Brittle Transition Temperatures of V–Cr–Ti Alloys," ibid., pp. 253–257.

[3] H. M. Chung, B. A. Loomis, L. Nowicki, J. Gazda, and D. L. Smith, "Irradiation-Induced Density Change and Microstructural Evolution of Vanadium-Base Alloys," ibid., pp. 223–231.

[4] H. Matsui, M. Tanno, J. Gazda, and H. M. Chung, "Microstructural Stability of V-4Cr-4Ti During Neutron Irradiation," ibid., pp. 240–246.

[5] H. M. Chung, J. Gazda, L. Nowicki, J. E. Sanecki, and D. L. Smith, "Effects of Fabrication Variables on Impact Properties and Microstructure of V–Cr–Ti Alloys," ibid., pp. 207–218.

[6] H. M. Chung, B. A. Loomis, and D. L. Smith, "Thermal Creep Behavior of V–5Cr–5Ti and V–10Cr–5Ti Alloys," in Fusion Reactor Materials, Semiannual. Prog. Report, DOE/ER-0313/14, Oak Ridge National Laboratory, Oak Ridge, TN (1993), pp. 309-317.

[7] D. N. Braski and D. W. Ramey, in Effects of Radiation on Material Properties, ASTM-STP 870, F. A. Garner and J. S. Perrin, Eds., American Society for Testing and Materials, Philadelphia, 1985, pp. 1211–1224.

[8] D. N. Braski, in Influence of Radiation on Material Properties, ASTM-STP 956, F. A. Garner, C. H. Henager, and N. Igata, Eds., American Society for Testing and Materials, Philadelphia, 1987, pp. 271-290.

[9] D. N. Braski, J. Nucl. Mater. 141-143 (1986) 1125.

[10] D. N. Braski, in Reduced Activation Materials for Fusion Reactors, ASTM-STP 1047, Philadelphia (1988) pp. 161-178.

[11] H. Matsui, M. Tanaka, M. Yamamoto, and M. Tada, J. Nucl. Mater. 191-194 (1992) 919.

[12] M. Satou, K. Abe, and H. Matsui, J. Nucl. Mater. 191-194 (1992) 938.

[13] M. Tanaka and H. Matsui, Mater. Trans., JIM, 34 (1993) 1083.

[14] W. van Witzenburg, A. Mastenbroek, and J. D. Ellen, J. Nucl. Mater. 103-104 (1981) 1187.

[15] M. P. Tanaka, E. E. Bloom, and J. A. Horak, J. Nucl. Mater. 114 (1981) 895.

[16] M. L. Grossbeck and J. A. Horak, in Influence of Radiation on Material Properties, ASTM-STP 956, Philadelphia (1986) 291.

[17] J. M. Vitek, D. N. Braski, and J. A. Horak, J. Nucl. Mater. 141-143 (1986) 982.

[18] W. van Witzenburg and E. de Vries, in Effects of Radiation on Materials, ASTM-STP 1125, Philadelphia (1990).

[19] L. L. Horton and K. Farrell, J. Nucl. Mater. 122-123 (1984) 687.

[20] H. Kawanishi and S. Ishino, in Reduced Activation Materials for Fusion Reactors, ASTM-STP 1047, Philadelphia (1988) pp. 179-189.

[21] H. Kawanishi, Y. Arai, and S. Ishino, J. Nucl. Mater. 191-194 (1992) 933.

[22] D. L. Smith, H. Matsui, L. R. Greenwood, and B. A. Loomis, J. Nucl. Mater. 155-157 (1988) 1359.

[23] D. L. Smith, B. A. Loomis, H. Matsui, M. L. Hamilton, K. L. Pearce, J. P. Kopasz, C. E. Johnson, R. G. Clemmer, and L. R. Greenwood, in Fusion Reactor Materials, Semiannual. Prog. Report. DOE/ER-0313/10, Oak Ridge National Laboratory, Oak Ridge, TN (1991), p. 159.

[24] H. Tsai, H. M. Chung, B. A. Loomis, and D. L. Smith, "Status of Dynamic Helium Charging Experiment (DHCE)," in Fusion Reactor Materials, Semiannual. Prog. Report. DOE/ER-0313/15, Oak Ridge National Laboratory, Oak Ridge, TN (1994), p. 247.

[25] H. M. Chung, B. A. Loomis, and D. L. Smith, "Effect of Dynamically Charged Helium on Mechanical Properties of Vanadium–Base Alloys," in this proceeding.

[26] M. Satou and H. M. Chung, in Fusion Reactor Materials, Semiannual. Prog. Rep. DOE/ER-0313/13, Oak Ridge National Laboratory, Oak Ridge, TN (1993), p. 227.

[27] H. M. Chung, B. A. Loomis, and D. L. Smith, in Effects of Radiation on Materials, ASTM-STP 1175, A. S. Kumar, D. S. Gelles, R. K. Nanstad, and T. A. Little, Eds., American Society for Testing and Materials, Philadelphia, 1993, pp. 1185–1200.

[28] T. Buitenhuis, A. Fedorov, and A. van Veen, "Thermal Desorption Investigation of V–5Ti Alloy," IRI–131–94–005, Delft University of Technology Report, The Netherlands, 1994.

V.F. Urbanic[1] and M. Griffiths[2]

CORROSION RESPONSE OF PRE-IRRADIATED Zr-2.5Nb PRESSURE TUBE MATERIAL

REFERENCE: Urbanic, V. F. and Griffiths, M., **"Corrosion Response of Pre-Irradiated Zr-2.5Nb Pressure Tube Material,"** *Effects of Radiation on Materials: 17th International Symposium, ASTM STP 1270,* David S. Gelles, Randy K. Nanstad, Arvind S. Kumar, and Edward A. Little, Eds., American Society for Testing and Materials, 1996.

ABSTRACT: Out reactor corrosion testing of Zr-2.5Nb pressure tubes in moist air at 573 K has shown that the pre-irradiated samples, i.e. those fabricated from tubes removed from power reactors, were more corrosion resistant than their unirradiated counterparts. The pre-irradiated materials had lower pre-transition corrosion rates, longer times to transition and lower post-transition rates than unirradiated material. As the samples were prepared equally in each case by polishing to bare metal, it is clear that the microstructural changes produced during irradiation are responsible for the improved corrosion response. For this reason X-ray diffraction (XRD) and analytical electron microscopy (AEM) have been used to characterise microstructural and microchemical changes produced by neutron irradiation of Zr-2.5Nb pressure tubes during service.

There is a positive effect of irradiation in improving the corrosion response down to fluences of at least 1 x 10^{25} n/m^2 (E>1 MeV). However, despite the reduction in corrosion, the amount of deuterium absorbed, as a fraction of the total deuterium generated by the corrosion process, was about ten times higher for the irradiated material than for the unirradiated material.

The results of the analyses indicate that improvements in corrosion behaviour may be linked with decreases in the Nb concentration in the α-Zr matrix due to Nb precipitation during irradiation. However there is no clear indication as to the cause of the increased deuterium uptake.

KEYWORDS: zirconium, niobium, zirconium alloys, corrosion, deuterium uptake, radiation damage, dislocation density, lattice parameters.

The early cold-worked Zircaloy-2 pressure tubes in CANDU reactors were replaced by cold-worked Zr-2.5Nb in the early 1970's. The main advantage in using Zr-2.5Nb, apart from superior strength, is the lower rate of corrosion and deuterium uptake compared with the Zircaloy-2 pressure tubes [1].

Zr-2.5 Nb pressure tubes for CANDU reactors are formed by extrusion at a temperature of about 1090K. They are then 27% cold-drawn to give a final tube length of 6.3 metres with a final tube thickness of about 4.5 mm and inside diameter of about 104 mm. The tubes contain a mixture of

[1]Senior staff scientist and [2]staff scientist, Atomic Energy of Canada Limited, Chalk River Laboratories, Chalk River, Ontario, Canada, K0J 1J0.

Copyright© 1996 by ASTM International www.astm.org

a- and c-component dislocations in densities of about 4 and 1 x 10^{14} l/m^2 respectively and have a dual-phase alpha/beta structure. The alpha phase grains are platelets (containing between 0.6 - 1 wt% Nb in solution) with aspect ratios of about 1,10,40 in the radial, transverse and longitudinal directions respectively. They are mostly oriented with prism {11$\bar{2}$0} and {10$\bar{1}$0} planes perpendicular to the radial and longitudinal directions respectively, and basal (0001) planes perpendicular to the transverse direction (Fig. 1(a)). The α-grains are stacked together and separated by a non-equilibrium beta phase containing about 20 wt% Nb (and about 1 wt% Fe in high Fe tubes). A final autoclaving treatment results in partial decomposition of the β-phase with the formation of Nb-depleted ω precipitates in a Nb-enriched matrix (up to about 40 wt%); the average composition in the β-phase remains at about 20 wt%. The β-phase itself has a characteristic texture with (200) planes oriented perpendicular to the radial direction and the (110) planes oriented perpendicular to the longitudinal and transverse directions (Fig. 1(b)).

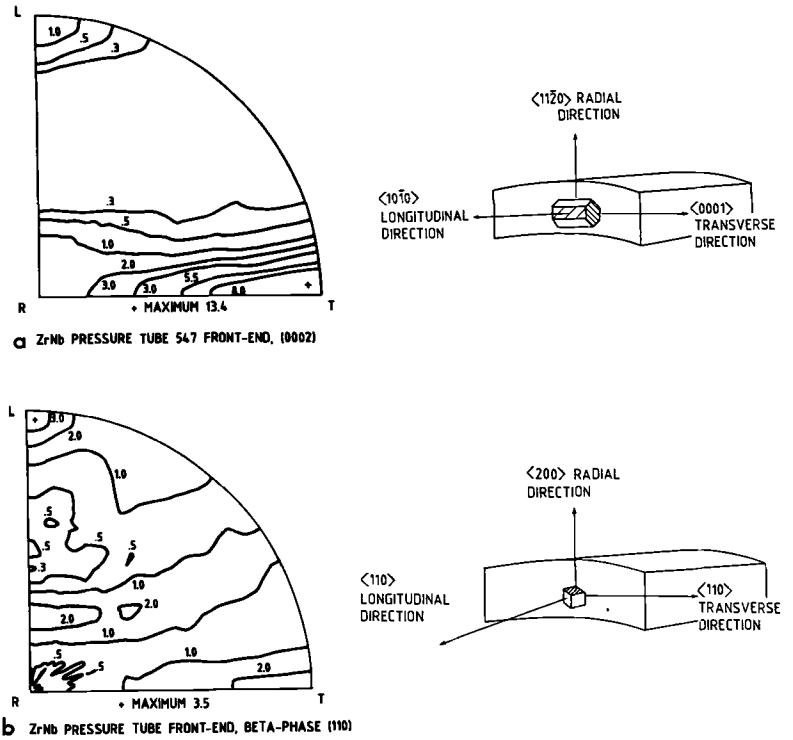


FIG. 1--Schematic diagrams and pole figures illustrating the crystallographic orientation of: (a) α-phase; and (b) β-phase in a typical Zr-2.5 Nb cold-worked pressure tube.

A typical microstructure for Zr-2.5Nb pressure tubing is illustrated in Figure 2. The width of the beta phase in the radial direction is about one tenth that of the alpha phase. The width of the alpha phase is about 0.3 μm at the end of the tube corresponding with the back-end of the extrusion and 0.5 μm at the end of the tube corresponding with the front-end of the extrusion. The grain size varies along the length of the tubes

because the tubes cool during the extrusion process so that the front-end is extruded at a higher temperature compared with the back-end thus affecting the final grain size. Silicides are often present in the tubes and generally have a small amount of Fe and Nb associated with them [2].

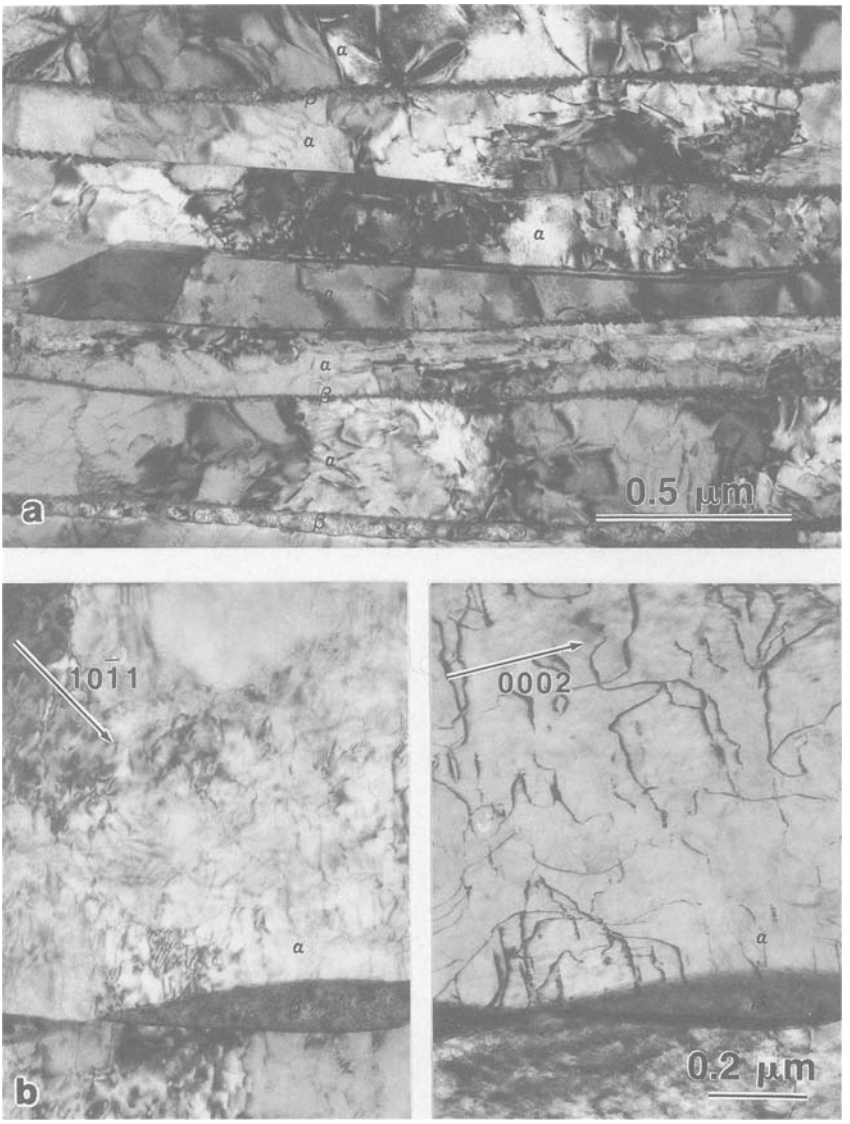


FIG. 2--Typical microstructure observed in Zr-2.5Nb pressure tube materials looking along the longitudinal axis of the tube: (a) grain structure showing α- and β-phases; (b) dislocation structure showing **a**- and **c**-type dislocations with a diffracting vector of 10$\bar{1}$1, and **c**-component dislocations only with a diffracting vector of 0002.

Previous work has shown that corrosion and duterium uptake rates are relatively low in Zr-2.5Nb pressure tubes compared with other zirconium alloy reactor components [1,3]. However considerable effort is expended to monitor and minimise corrosion, not because corrosion itself is a problem for pressure tube performance but because of the requirement for low deuterium uptakes, deuterium uptake generally increasing with increasing corrosion. Previous work has indicated that the corrosion response of Zr-2.5Nb improves with irradiation [4,5], and this has been attributed to changes in the microstructure. The aim of the current work is to investigate in more detail the relationship between the evolving microstructure and corrosion rates and also to determine whether there is any effect of irradiation on the deuterium uptake.

EXPERIMENTAL METHOD

Corrosion samples were prepared by cutting 6 cm x 1 cm slices from the centres of five irradiated pressure tubes or 3 cm x 1 cm slices out of the corresponding pressure tube offcuts perpendicular to the radial direction. The offcut samples were shorter because the offcuts themselves were short. Each sample was then milled to a thickness of about 1 mm, then chemically polished with a solution of 10% HF + 15% HNO_3 + 30% H_2SO_4 + 45% H_2O to remove any damaged layer introduced by the milling operation. Three samples from each location were prepared (for reproducibility). Dimensions and weights were measured prior to testing. The samples were then corroded in moist air at 573 K (100 cm^3/min passed through a D_2O bubbler) for a period of up to 700 days. During the heat-up and cool-down stages the heating assembly was purged with dry argon.

The corrosion was measured as a weight gain for each specimen using a Metler AE163 balance to an accuracy of 0.01 mg and normalised according to unit area from the measured dimensions. Visual examinations were performed after each exposure to check for obvious changes in appearance.

At the end of the corrosion tests, deuterium analysis was performed on tested samples by hot-vacuum-extraction mass spectroscopy using archive materials as controls.

X-ray diffraction (XRD) and analytical electron microscopy (AEM) have been used to characterise microstructural and microchemical changes produced by neutron irradiation in Zr-2.5Nb pressure tubes. Both unirradiated and irradiated materials were prepared and examined. For the irradiated materials care had to be taken to minimise the volume of material used because of the residual radioactivity in the samples.

XRD specimens that were about 1 cm^2 area x 0.5 mm thick were prepared by cutting slices out of the tube perpendicular to each of the three principal tube axes (Fig. 1). Each specimen was then chemically polished to remove any damaged layer introduced by the preparation. In this case at least 0.025 mm was removed being the depth of damage for the diamond wheel used to cut the specimen. TEM specimens were prepared by punching 3mm diameter discs out of 0.1 mm thick slices. Foils were then made by electropolishing with a solution of 10% perchloric acid in methanol at about 230 K with a current density of about 1 A/cm.

The microstructure of a typical cold-worked Zr-2.5Nb pressure tube is illustrated in Fig. 2. Dislocation densities were determined from line-broadening analysis of X-ray diffraction peaks from the hcp α-phase corresponding to prism planes (a-component dislocations) or basal planes (c-component dislocations), [6]. Crystallographic planar spacings were determined from the peak positions using the average of peak maximum and centre of gravity measurements. The α-phase <a> lattice parameters were calculated from the $(11\bar{2}0)$ or $(10\bar{1}0)$ interplanar spacings and the [c] lattice parameters were calculated from the (0002) interplanar spacings.

The Nb concentration in the bcc β-phase of Zr-2.5 Nb pressure tubes was estimated from the position of the (200) and (110) peaks measured using radial normal (RN) and longitudinal normal (LN) specimens respectively [7]. The diffraction angle was then compared with calibration curves obtained from standard samples of Zr-20Nb (water quenched from the β-phase) and pure Nb. The state of the dislocation structure and β-phase morphology was studied by TEM. The longitudinal normal orientation of the foil is the best orientation in which to image the c-component dislocations and β-Nb precipitates in the α-phase using a 0002 diffracting plane, or to image a-type loops using a $11\bar{2}0$ diffracting plane.

The $LN(10\bar{1}0)_\alpha$, $TN(0002)_\alpha$, $LN(110)_\beta$ and $RN(002)_\beta$ X-ray diffraction lines were analysed using a Rigaku rotating anode diffractometer. The $RN(11\bar{2}0)_\alpha$ diffraction lines were measured using a Siemens diffractometer. CuK_α radiation (wavelength=0.154 nm) was used in each case. The specimens were rotated in the focusing plane to increase the scanning area and sample as many grains as possible.

TEM analysis was performed using Philips EM300G (100 kV) and CM30 (300 kV) electron microscopes. Microchemical analyses were obtained by Energy Dispersive X-ray Analysis (EDXA) using a Link ISIS analyser system and Ultra Thin Window (UTW) detector and by Parallel Electron Energy Loss Spectrometry (PEELS) using a Gatan Peels analyser. The spatial resolution for microchemical analysis was about 10 nm.

RESULTS

Corrosion Tests

All corrosion samples initially had bright, shiny surfaces prior to testing. After the tests, both types of samples had different appearances. The unirradiated samples had developed oxide films that were grey-white in colour whereas the pre-irradiated samples had developed dark black oxide films (Fig. 3) suggestive of a lower rate of oxidation.

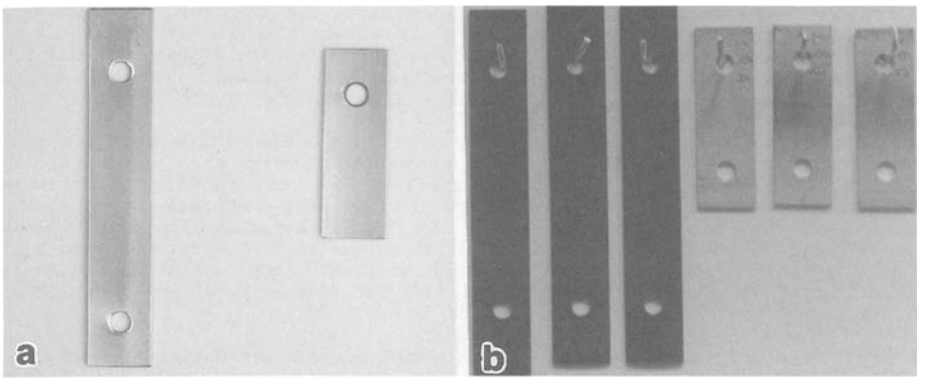


FIG. 3--Comparison of unirradiated and pre-irradiated surface appearance for Zr-2.5Nb pressure tube materials before and after corrosion testing: (a) before testing; (b) after testing. The shorter unirradiated specimens are clearly more oxidised compared with the longer pre-irradiated specimens.

Fig. 4 shows the weight gain results as a function of the test time. Each data point represents the average weight gain of two or three samples for the unirradiated tube material and of three samples for the pre-irradiated tube material. A number of features are evident from the data in Fig. 4. First, there is a large difference in the oxidation rates, with the pre-irradiated material being much lower than the unirradiated material. Second, the unirradiated material shows a kinetic transition to a linear rate between 80 - 100 days exposure whereas any transition in the pre-irradiated material is less obvious. Third, the tube-to-tube variation in oxidation is greater for the unirradiated material compared to the pre-irradiated material.

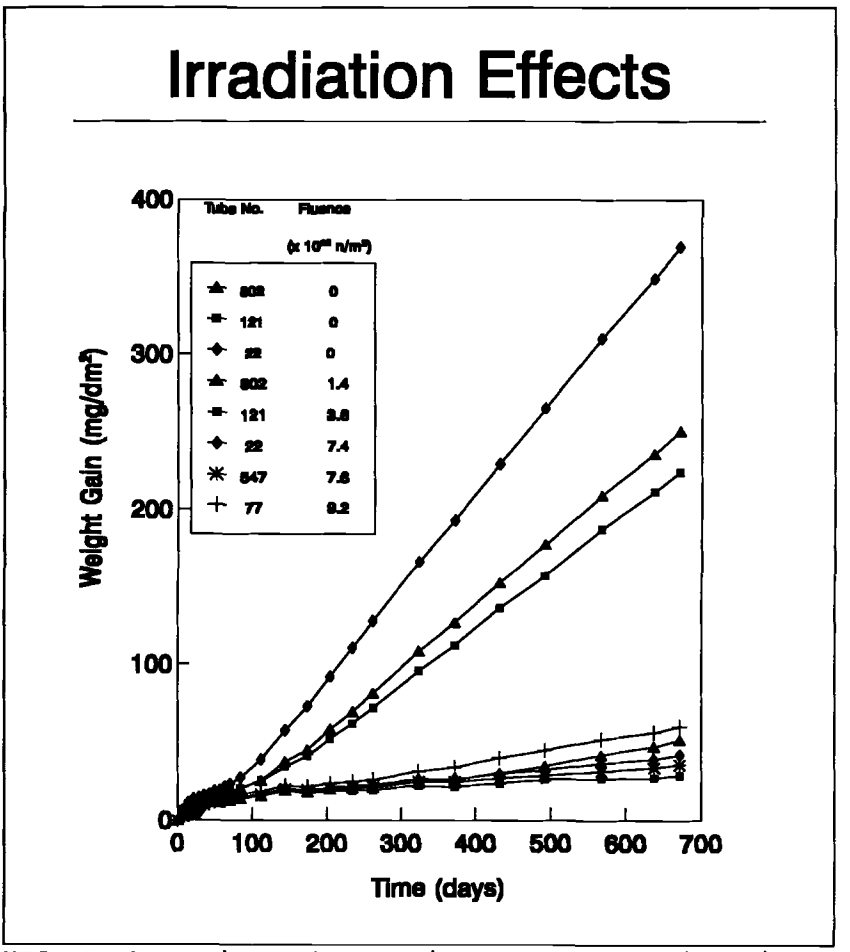


FIG. 4--Comparison of corrosion response for irradiated and unirradiated Zr-2.5Nb pressure tubes tested in moist air at 573 K.

When the weight gain data are plotted on a log-log scale (Fig. 5), three distinct kinetic regions become evident for most tubes. At weight gains less than 10 mg/dm^2, the oxidation rate is rapid and close to linear, particularly for the pre-irradiated material. The next stage, up to 20 - 30 mg/dm^2 weight gain, the kinetics behaviour is intermediate between cubic and parabolic. Beyond about 30 mg/dm^2, the rates become linear. Besides displaying lower weight gains throughout the test duration, the pre-irradiated materials show longer times to transition if the transition weight gain is exceeded.

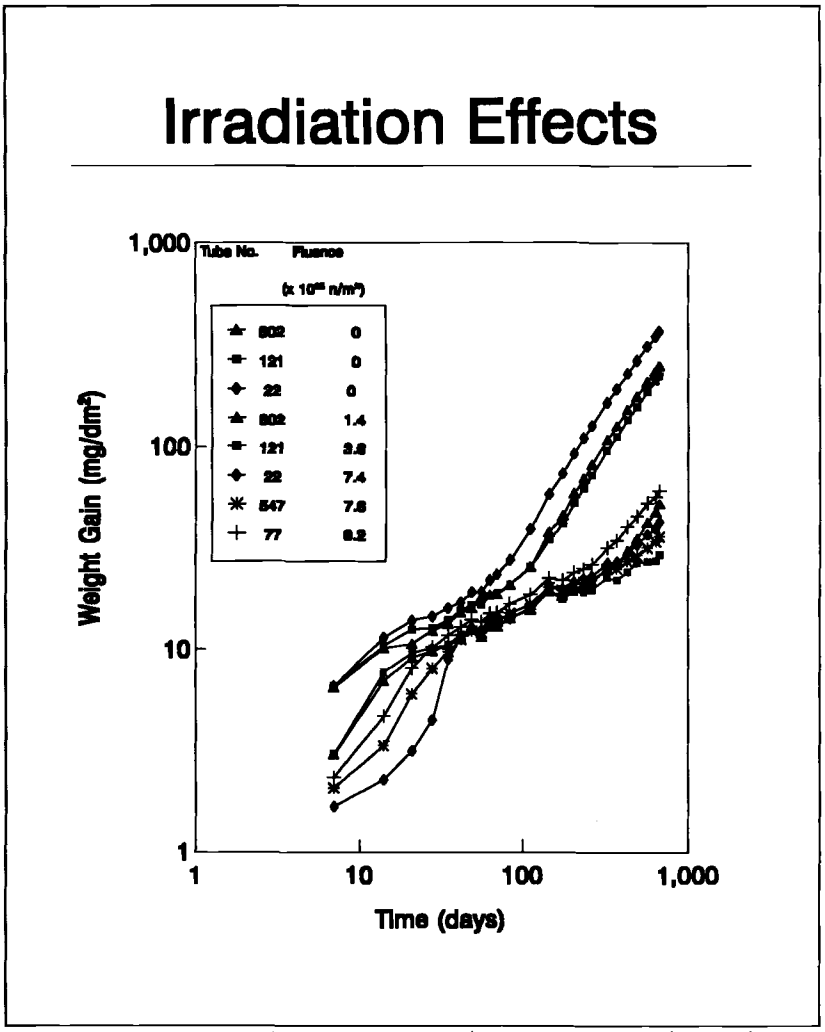


FIG. 5--Log-log plot of corrosion data for irradiated and unirradiated Zr-2.5Nb pressure tubes tested in moist air at 573 K.

Fig. 6 shows the deuterium pickup as a function of time for selected samples from the test. Although some unirradiated samples were analyzed after relatively short exposure times, the pre-irradiated samples were only analyzed after the total 712 day exposure. The results show that for the unirradiated material, deuterium uptake was initially rapid but levelled off to a low rate, despite the transition to more rapid linear kinetics after about 100 days exposure. On the other hand, all pre-irradiated material picked up more deuterium than their unirradiated counterparts despite the much lower oxidation rates observed for the former. Table 1 compares this contrasting behaviour for oxidation and Table 2 compares deuterium pickup for both material types after the 712 days exposure to moist air. Although the amount of oxidation of the pre-irradiated material was 5 - 9 times less than that of the unirradiated material, the percent theoretical uptake was 16 - 23 times greater (0.3 - 0.5 % for the unirradiated and 4.8 - 7.9 % for the pre-irradiated material).

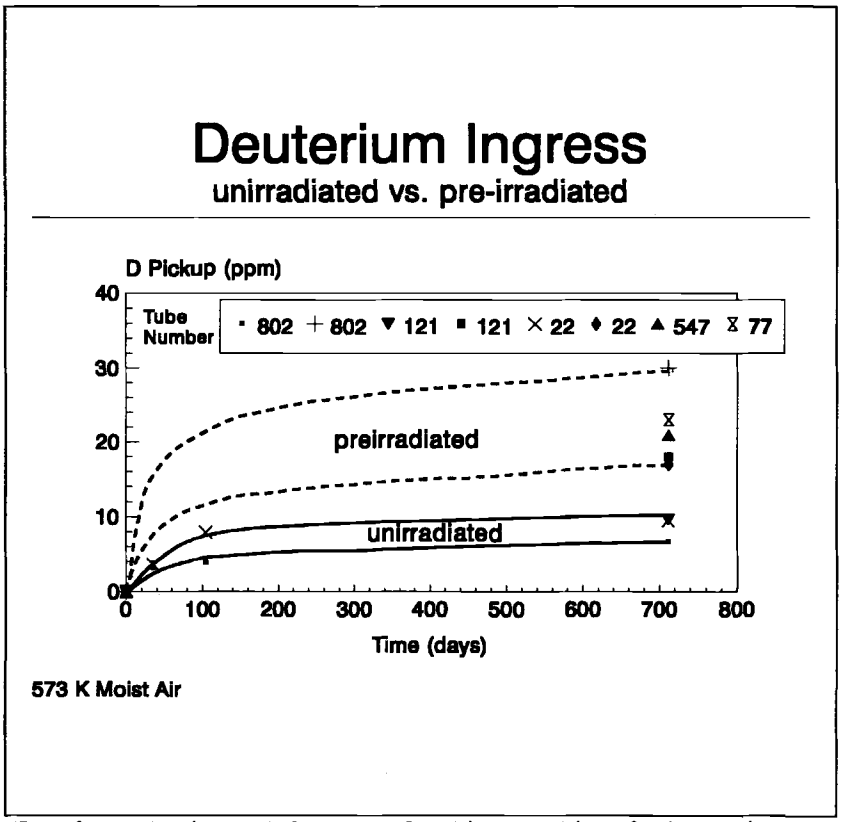


FIG. 6--Deuterium uptake as a function of time during moist air corrosion tests at 573 K for irradiated and unirradiated Zr-2.5Nb pressure tube materials.

TABLE 1--Irradiation Effects on Oxidation of Zr-2.5Nb pressure tube material (tested in 573 K D_2O saturated air for 712 days).

Tube	Fluence	Oxide Thickness (μm)	
	n/m^2	unirrad.	preirrad.
P4F17	$1.4x10^{25}$	18.3	3.8
B2X14	$3.6x10^{25}$	16.4	2.0
P4N16	$7.4x10^{25}$	26.8	3.0
P3J09	$7.6x10^{25}$	na*	2.6
P3L09	$9.2x10^{25}$	na*	4.3

* not available for testing

TABLE 2--Irradiation Effects on Deuterium Uptake of Zr-2.5Nb pressure tube material (tested in 573 K D_2O saturated air for 712 days).

Channel	D Pickup (μg/g)		Theoretical Uptake (%)	
	unirrad.	preirrad.	unirrad.	preirrad.
P4F17	7	29	0.3	6.9
B2X14	10	18	0.5	7.9
P4N16	10	17	0.3	5.1
P3J09	na	21	na*	7.3
P3L09	na	23	na*	4.8

* not available for testing

Microstructure Evolution

Dislocation Structure--Irradiation results in the production of a high density of small (about 15 nm diameter) a-type dislocation loops (Fig. 7). There is no clear evidence for c-component loop formation, however, small 5-10nm diameter defects, that appears to be precipitates, are observed with the same diffraction conditions used to image the c-component dislocations (Fig. 8).

X-ray diffraction analysis shows that there is an increase in a-type dislocation density with neutron fluence, i.e. in the core of the reactor (Fig. 9). The broadening does not appear to be very dependent of tube orientation, i.e. front or back-end of the extrusion at the inlet. The variation in a-type dislocation density (prism plane broadening) along the tubes can be attributed to a-type dislocation loop formation with a higher density of loops at the cooler inlet end (about 520K) compared with the outlet end (about 580K). There is a general sharpening in the basal lines in the irradiated part of the tubes that can be explained by splitting of c-component dislocations. The degree of sharpening tends to be higher at the front-ends of tubes and there is

a peak at the tube centres that can best be attributed to increased climb of **c**-component dislocations with increasing fluence (Fig. 10). In general, dislocation density changes tend to saturate by fluences of about 1 x 10^{25} n/m^2 although there may be long term lower rate increases occurring at higher fluences.

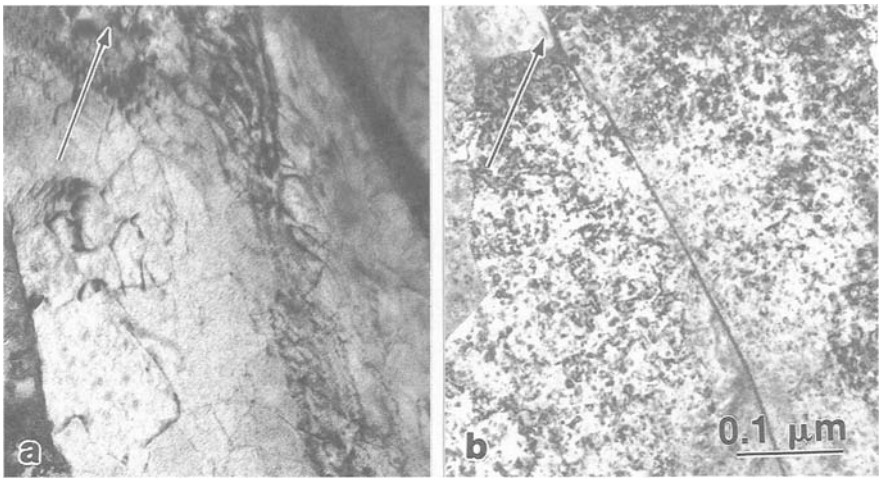


FIG. 7--Typical **a**-type dislocation structure observed in Zr-2.5Nb pressure tubes: (a) before; and (b) after irradiation to a fluence of about 9 x 10^{25} n/m^2 at 543 K; diffracting vector = $10\bar{1}1$.

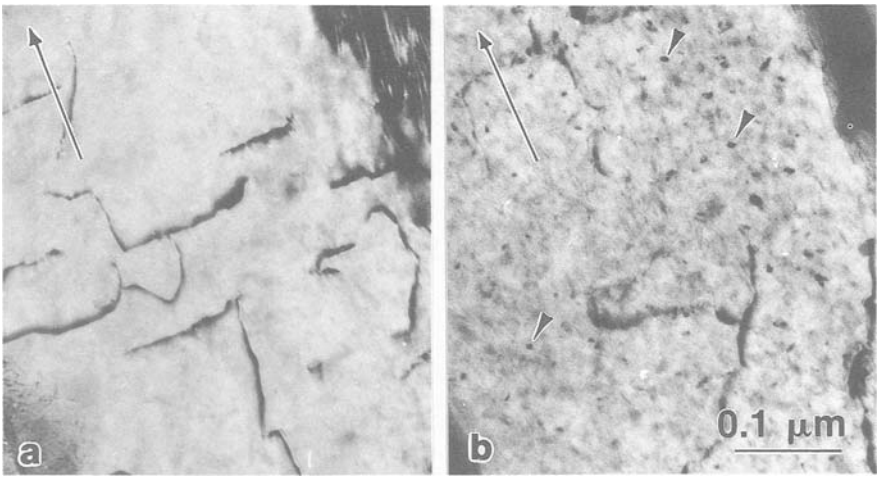


FIG. 8--Typical **c**-type dislocation structure observed in Zr-2.5Nb pressure tubes: (a) before; and (b) after irradiation to a fluence of about 9 x 10^{25} n/m^2 at 543 K; diffracting vector = 0002. Small Nb-rich precipitates are arrowed in (b).

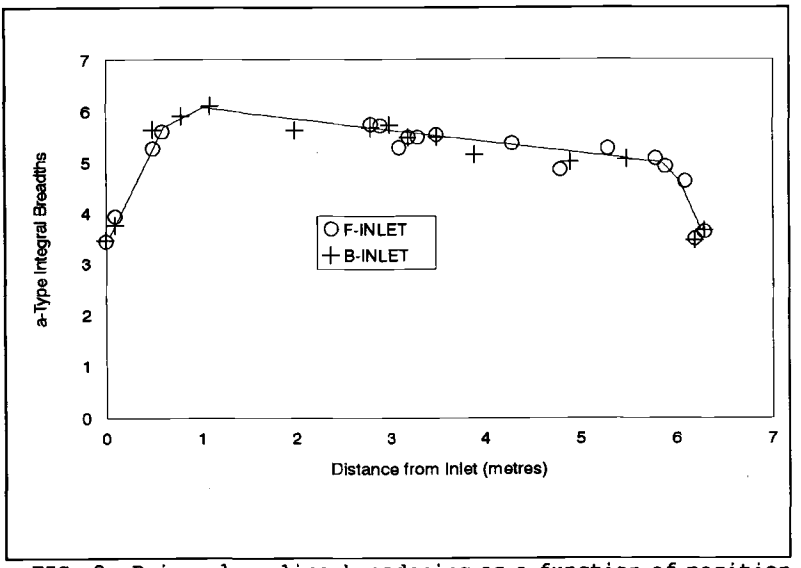


FIG. 9--Prism plane line-broadening as a function of position in reactor. Integral breadths are given in units of 10^7 1/m.

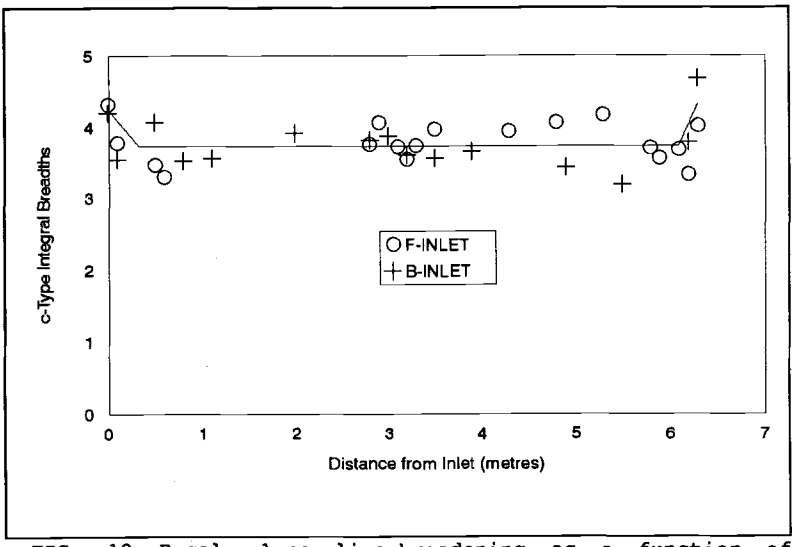


FIG. 10--Basal plane line-broadening as a function of position in reactor. Integral breadths are given in units of 10^7 1/m.

Phase Structure--Small precipitates form in the α-phase during irradiation (Fig. 8). They are generally very small (5-10 nm) and of insufficient volume to give coherent X-ray diffraction. EDX-analysis indicates that they are Nb-rich (Fig. 11), as one might expect for precipitates forming from a solid solution supersaturated with Nb [9,10]. Precipitation of Nb from the α-phase should produce β-Nb (85-90% Nb) according to the phase diagram and this is consistent with the electron diffraction pattern. There are no observations of Nb precipitation in the α-phase in out of flux sections of pressure tube indicating that the precipitates are the result of irradiation. Pressure tube sections irradiated to a fluence of 0.35 x 10^{25} n/m^2 at 547 K showed no evidence for precipitation in the α-phase whereas precipitates were observed in sections irradiated to a fluence of 0.95 x 10^{25} n/m^2 at 563 K.

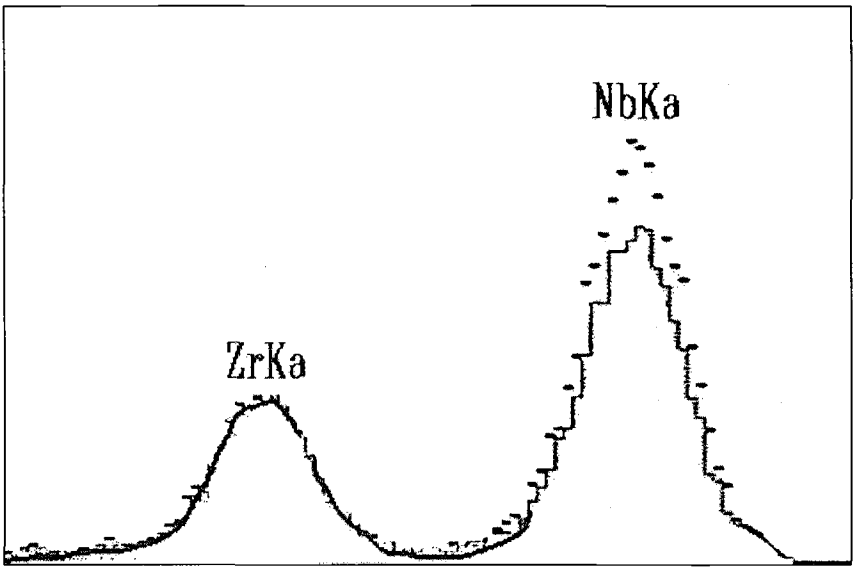


FIG. 11--X-ray spectra obtained from a sample of Zr-2.5Nb pressure tubing after irradiation to a fluence of about 9 x 10^{25} n/m^2 at 543 K. The spectra were obtained using an electron probe on the matrix (full line) and the small Nb-rich precipitates shown in Fig. 8 (dotted line).

There is no change in the crystal structure of the pre-existing silicide precipitates (analysed as Zr_6Si) apart from an apparent increase in Fe (and possibly Nb) at the precipitate/matrix interface.

If one represents the lattice parameters as a strain relative to a stress-free state (a_o=0.3232 nm, c_o=0.5149 nm), there is a general expansion of the α-phase lattice in the irradiated part of the tubes which can be attributed to the precipitation of Nb from supersaturated solid solution [5]. The expansion is especially relevant to the Nb case because similar measurements for a Zircaloy-2 pressure tube - show a lattice contraction with irradiation [5]. There is no corresponding expansion for out-of-flux sections of the Zr-2.5Nb pressure tubes [5], indicating that the lattice expansion is an irradiation-induced phenomena. Lattice parameter changes usually saturate by fluences of about 1 x 10^{25} n.m^{-2} (Fig. 12) and can be attributed to the precipitation of Nb from supersaturated solid solution in the α-phase.

The β-phase is originally a single phase non-equilibrium structure containing about 20 wt% Nb. It transforms to an Nb- and Fe-depleted ω-phase and an enriched β-phase (20-45 wt% Nb and about 1 wt% Fe) during the final autoclaving treatment of the pressure tubes prior to installation in the reactor. The autoclaving is generally for 24 hours at 673 K but can be up to 120 hours in multiples of 24 hours. Nb and Fe segregation is also observed at the α/β-interface in as-fabricated tubes [5]. The composition of the β-phase changes significantly with multiple autoclaving treatments and therefore is a source of variability from tube to tube. The β-phase transformation produces a complex structure in the β-phase making it difficult to distinguish unirradiated and irradiated β-phase from TEM images (Fig. 13).

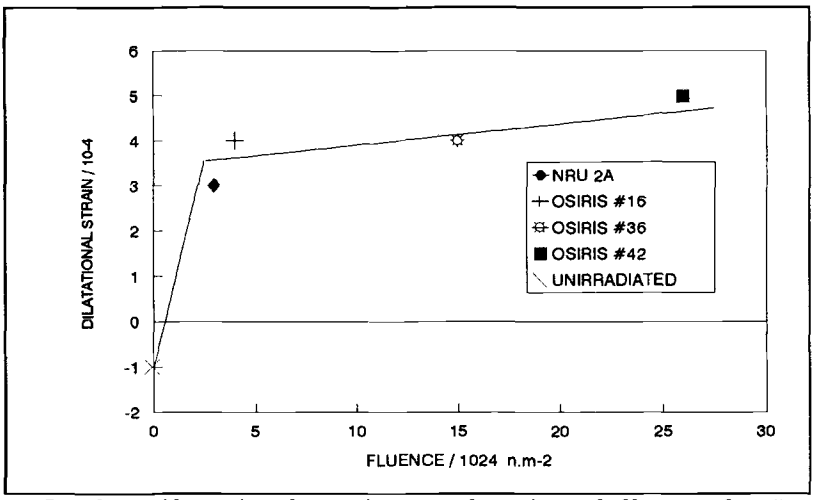


FIG. 12--Dilatational strain as a function of fluence for Zr-2.5Nb pressure tube samples irradiated at 523 K.

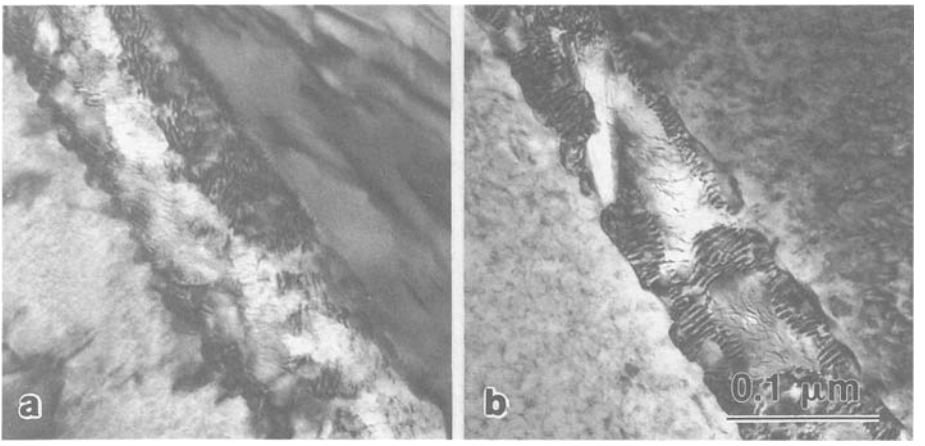


FIG. 13--β-phase structure in Zr-2.5Nb pressure tubes; (a) before; and (b) after irradiation to a fluence of about 9 x 10^{25} n/m^2 at 543 K.

Additional decomposition of the β-phase during service in reactor can be monitored by X-ray diffraction and is illustrated as a function of position in Fig. 14 using (110)-lines and Fig. 15 using (200)-lines. There is Nb enrichment of the β-phase during service which increases on traversing from the inlet to outlet in the pressure tubes. The tubes sampled had been in service for between about 2-10 years. It is clear that the change in composition is very temperature sensitive and there appears to be no enhancement with irradiation. In fact irradiation appears to supress any thermal changes and may in fact cause mixing or disordering as is evident from lattice parameter measurements on test specimens. This radiation-induced mixing is consistent with the results reported by Faulkner et al. showing disolution of ω-particles during HVEM irradiation at 573 K [8].

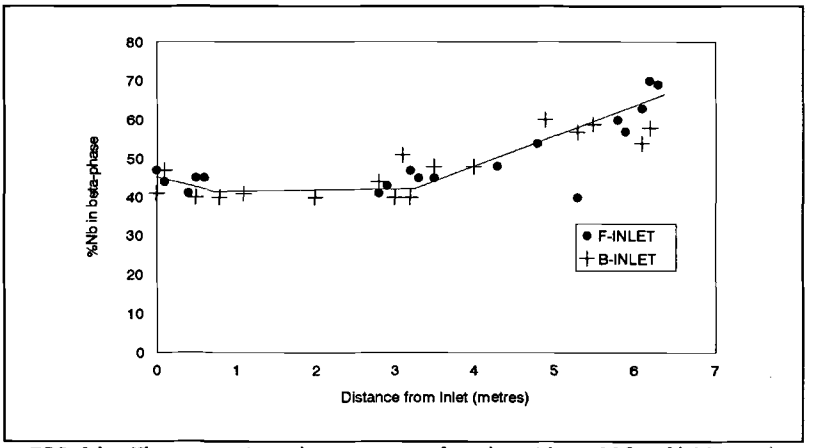


FIG 14--Nb concentration measured using the (110) diffracting planes for the β-phase in Zr-2.5Nb pressure tubes as a function of position in reactor (2 - 12 years service).

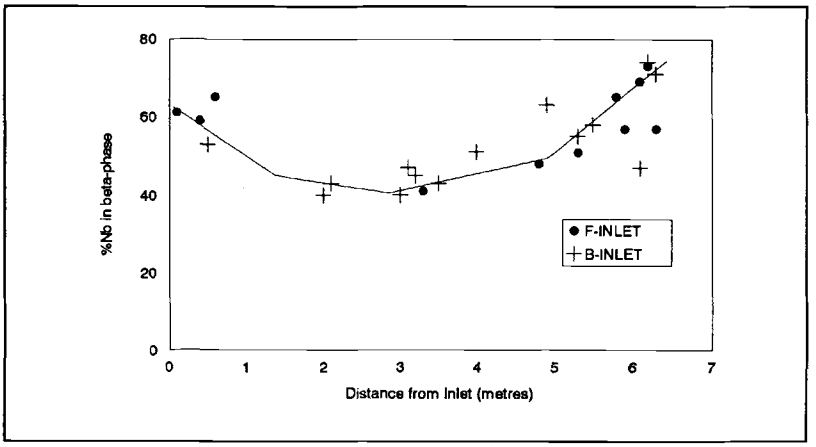


FIG 15--Nb concentration measured using the (200) diffracting planes for the β-phase in Zr-2.5Nb pressure tubes as a function of position in reactor (2 - 12 years service).

The Fe content in the β-phase typically varies from about 0.5 to 1.0wt% for low (500 ppm) to high Fe (1000 ppm) tubes. The Fe itself is not distributed homogeneously throughout the material and, like the Nb within the β-phase filaments, is only homogeneous within a given section of β-phase filament in the as-extruded state [5]. As the tube is autoclaved, internal decomposition within the β-phase filaments occurs and the Fe and Nb are redistributed. For example, the Fe (and Nb) is often segregated at the α/β interface in autoclaved pressure tubes (24 hours at 673 K). This effect is particularly marked in double and triple autoclaved tubes [5]. During irradiation, the Fe is depleted gradually from the β-phase and is reduced to levels almost indistinguishable from the α-phase after irradiation to fluences >3 x 10^{25} $n.m^{-2}$ at about 540 K[5]. The Fe appears to be uniformly distributed throughout the material although some secondary precipitation is also evident at interfaces and grain boundaries [5,9]. A Nb-rich phase at the α/β-interface is clearly defined in the irradiated material (the initial Nb-enrichment being suplemented from the α- and β-phases during the period of operation in reactor). Depletion of Fe from the β-phase has been measured in irradiated sections of pressure tubes (Fig. 16) but not in the zero-to-low flux sections at the tube ends (Fig. 17). It can be concluded that the Fe depletion is a radiation-induced effect. It is unlikely to be a radiation-enhanced effect because thermal treatment results in decomposition of the β-phase and precipitation of the Fe [5]. This conclusion is further supported by the fact that the Fe diffuses back into the β-phase during post-irradiation annealing at 773 K.

Changes in microstructural parameters for the materials tested in this study are consistent with all pressure tube specimens irradiated under the same conditions, i.e. position in reactor and service time.

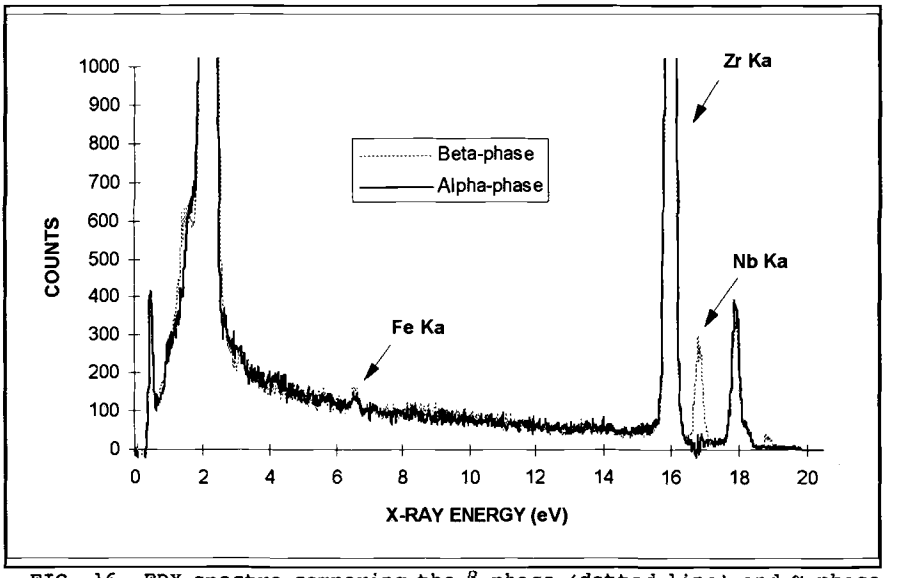


FIG. 16--EDX spectra comparing the β-phase (dotted line) and α-phase (solid line) in a Zr-2.5Nb pressure tube after irradiation to a fluence of 7 x 10^{25} n/m^2 at 553K.

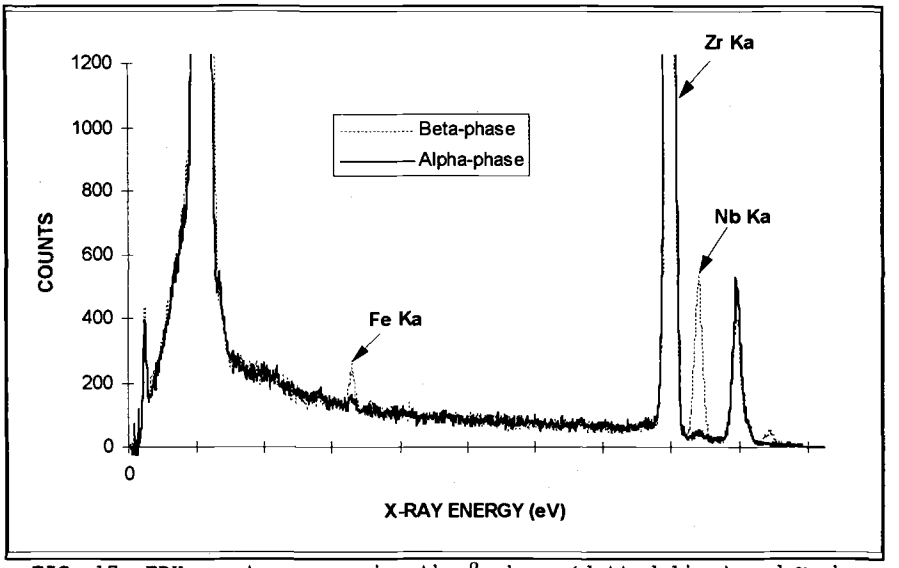


FIG. 17--EDX spectra comparing the β-phase (dotted line) and α-phase (solid line) at the zero-to-low flux outlet-end of a Zr-2.5Nb pressure tube after about 10 years service at 563K.

DISCUSSION

The difference in the appearance of the oxide films on the two types of materials tested was consistent with the observed differences in the recorded weight gain curves. The lower oxidation rates for the pre-irradiated materials indicate that the microstructure and microchemical changes occurring during irradiation are beneficial from the viewpoint of oxidation. It appears that the changes responsible for the reduction in oxidation are essentially complete by a fluence of about 1.4×10^{25} n/m^2. In addition, the tube-to-tube variability displayed by the unirradiated archive material is reduced substantially by the microstructural changes that evolve during irradiation. It has been speculated, [3,4], that the benefit stems from two possible sources; first, the thermal decomposition of the β-Zr phase and second, the reduction in the Nb concentration of the α-Zr grains due to irradiation enhanced precipitation of the β-Nb particles. Thermal decomposition of the β-Zr phase alone is known to improve the corrosion resistance of cold-worked Zr-2.5Nb pressure tubes that had been aged at 673 K and 773 K and subsequently tested in high temperature water [3]. This is because the β-Zr phase is less resistant to oxidation than the α - Zr phase [10], and decomposition to a more equilibrium microstructure improves its oxidation resistance. On the other hand, a reduction in Nb concentration of alpha-prime structures, produced by water quenching, has also been shown to be beneficial for water corrosion of Zr-Nb binary alloys [11]. In cold-worked Zr-2.5Nb microstructures, irradiation-induced precipitation of β-Nb would reduce the concentration of Nb in the matrix of the α-Zr grains. It has been argued that the effect of the irradiation enhanced precipitation of β-Nb

may be the dominant of the two since the extent of thermal decomposition of the β-Zr in the irradiated material did not seem to be sufficient for the improvements in oxidation being observed [4], however additional testing is required to confirm this. In addition, the role of the irradiation damage itself or the implications of the changes in physical properties it produces must be studied further before a firm concensus can be established.

The exact mechanism responsible for the observed increase in deuterium pickup for the pre-irradiated material is not yet fully understood. The presence of the irradiation enhanced β-Nb precipitates that evolve during irradiation however, may be contributing to the deuterium pickup mechanism in a way similar to the intermetallics in the Zircaloys. In the Zircaloys in has been argued that the intermetallics can act as pathways for electron transfer across the thin barrier film at the metal oxide interface thus allowing discharge of protons at the intermetallic surfaces and eventual entry of atomic deuterium into the substate probably via migration along the intermetallic boundaries [12]. If the small β-Nb particles remain only partially oxidized in the oxide film, they could enhance the electronic conduction through the film promoting the discharge of deuterium ions and thereby increasing the amount of deuterium atoms available for diffusion through the film into the alloy substrate. The enriched β-Zr that evolves through thermal decomposition of the β-Zr phase may also play a similar role in promoting deuterium pickup once the decomposition process has advanced beyond a critical stage. Again the relative contributions from each of these two suggested processes is unknown and additional work is required to evaluate the extent of each.

The main material variables that have been identified as possibly affecting corrosion in Zr-alloys are: (i) the presence and distribution of precipitates (especially Fe-rich) [12]; (ii) dislocation density [4]; (iii) solute concentration (Sn, Nb, Fe etc.) [4,12]. All of these change with irradiation. The mechanisms of corrosion are insufficiently understood to determine whether these changes will be beneficial or detrimental. There is some evidence that decreasing the supersaturation of Sn in Zircaloys [12] and Nb in Zr-2.5Nb alloys [4,11] improves the corrosion resistance of these alloys. Irradiation could be beneficial in both cases by enhancing the rate of precipitation of Sn and Nb from supersaturated solid solution [13,14,15].

The improved corrosion properties in Zr-2.5Nb pressure tubes due to irradiation can best be correlated with Nb precipitation in the α-phase of Zr-2.5Nb. Apart from TEM evidence, lattice parameter measurements could be used as a measure of Nb content in the α-phase. Measurements of irradiated Zr-2.5 wt% Nb pressure tubes show that the lattice parameter changes have saturated (equilibrium is reached) after fluences of about 1 x 10^{25} n/m^2. One could speculate that the Fe dispersal or the β-phase stability are important but, in the absence of suitable corroborating data, there is very little justification in correlating any other microstructural change with improved corrosion and/or increased deuterium uptake. Further work is in progress testing: (i) zero-to-low fluence material from the outlet-ends of the pressure tubes, for which there is β-phase decomposition but no other changes; and (ii) heat-treated samples, for which the dislocation structure has recovered to the as-fabricated state, and Fe has returned to the β-phase but the α-phase still retains the β-Nb precipitates.

SUMMARY

Samples taken from the centres of pressure tubes that had been in operation at temperatures between 523 K and 573 K for various times were tested along with their corresponding offcuts, where available. The

results show that the pre-irradiated samples are more corrosion resistant than their unirradiated counterparts.

Corresponding log-log plots of the same data show that the pre-irradiated material has lower pre-transition corrosion rates, longer times to transition and lower post-transition rates than unirradiated material. Corrosion of all pre-irradiated material was similar implying a saturation of the irradiation effect at a fluence of at least 1×10^{25} n/m^2 (E>1 MeV).

Despite the reduction in corrosion, the amount of deuterium absorbed, was higher in the irradiated material. The deuterium uptake expressed as a fraction of the total deuterium generated by the corrosion process, was about ten times higher for the irradiated material than for the unirradiated material. These results indicate that there is a clear change in both the corrosion response and deuterium uptake as a result of irradiation. As each material was prepared to a bare metal surface prior to testing, clearly the microstructural changes caused by the radiation are responsible for the behavioural difference.

CONCLUSIONS

1. The oxidation kinetics for Zr-2.5Nb in 573 K moist air show three distinct stages with a well defined transition to a final linear rate.

2. Pre-irradiated, cold-worked Zr-2.5Nb has a microstructure which is more oxidation resistant in moist air than its unirradiated counterpart.

3. The reduction in oxidation for pre-irradiated material is believed to be due to the evolution to a more equilibrium microstructure during neutron irradiation.

4. Despite the reduction in oxidation, the absolute amount of deuterium absorbed during oxidation in moist air increases because the percent theoretical deuterium pickup is considerably higher for the pre-irradiated material.

Acknowledgements

The authors would like to thank Fuel Materials Branch staff for their technical assisstance in performing the corrosion tests, A. Shaddick for technical assistance in preparing this report, R.R. Hosbons for some irradiated test specimens. The work was performed under contract to the Candu Owners Group.

REFERENCES

[1] Urbanic, V.F., Cox, B. and Field, G.J., "Long-Term Corrosion and Deuterium Uptake in CANDU-PHW Pressure Tubes", Proceedings of the Seventh International Symposium on Zirconium in the nuclear Industry, ASTM STP 939 (1987) p. 189.

[2] Griffiths, M., Phythian, W. and Dumbill, S., "Comment on Fe Distribution in Zr-2.5Nb Pressure Tubing", Journal of Nuclear Materials, Vol. 207 (1993) p. 353.

[3] Urbanic, V.F., Warr, B.D., Manolescu, A., Chow, C.K. and Shanahan, M.W. "Oxidation and Deuterium Uptake of Zr-2.5Nb Pressure Tubes in CANDU-PHW Reactors", Proceedings of the Eighth International Symposium on Zirconium in the Nuclear Industry, ASTM STP 1023 (1989) p. 20.

[4] Urbanic, V.F. and Gilbert, R.W., "Effect of Microstructure on the Corrosion of Zr-2.5 Nb Alloy", IAEA Technical Committee Meeting on Fundamental Aspects of Corrosion of Zirconium Based Alloys, Portland, Oregon (1989) p. 262.

[5] Griffiths, M., Chow, C.K., Coleman, C.E., Holt, R.A., Sagat, S. and Urbanic, V.F., "Evolution of Microstructure in Zr-Alloy Core Components during Service", Proceedings of the Sixteenth International Symposium on the Effects of Irradiation on Materials, ASTM STP 1175 (1993) p. 1077.

[6] Griffiths, M., Winegar, J.E., Mecke, J.F. and Holt, R.A., "Determination of Dislocation Densities in HCP Metals using XRD and TEM", Advances in X-Ray Analysis, Vol. 35A, Plenum Press, New York, (1992) p. 593.

[7] Griffiths, M., Winegar, J.E., Mecke, J.F., Holden T.M. and Holt, R.A., "A Comparison of X-ray and Neutron Diffraction for the Determination of Residual Stress and Chemical Composition in Zr-Alloy Tubes", Advances in X-Ray Analysis, Vol. 35A, Plenum Press, New York, (1992) p. 475.

[8] Faulkner, D. and Nuttall, K., "The effect of Irradiation on the Stability of Precipitates in Zr-2.5Nb Alloys", Journal of Nuclear Materials, Vol. 67 (1977) p. 131.

[9] Perovic, V., Perovic, A., Weatherley, G.C., Brown, L.M., Purdy, G.R., Fleck, R.G. and Holt, R.A., "Microstructural and Microchemical Studies of Zr-2.5Nb Pressure Tube Alloy", Journal of Nuclear Materials, Vol. 205 (1993) p. 251.

[10] Urbanic, V.F., Chan, P.K., Katamian, D. and Woo, O.T. "Growth and Characterisation of Oxide Films on Zr-Nb Alloys",Proceedings of the Eighth International Symposium on Zirconium in the Nuclear Industry, ASTM STP 1245 (1994) p. 116.

[11] Dalgaard, S.B., "The Corrosion Resistance of Zr-Nb and Zr-Nb-Sn Alloys in High Temperature Water and Steam - Part II", AECL-1308 (1961).

[12] Cox, B., "Oxidation of Zirconium and its Alloys", Advances in Corrosion Science and Technology, Plenum Press, New York, Vol. 5 (1976) p. 173.

[13] Griffiths, M., Gilbert, R.W. and Carpenter, G.J.C., "Phase Stability, Decomposition and Redistribution of Intermetallic Precipitates in Zircaloy-2 and -4 During Neutron Irradiation", Journal of Nuclear Materials, Vol. 150 (1987) p.53.

[14] Coleman, C.E., Gilbert, R.W., Carpenter, G.J.C. and Weatherly, G.C., "Precipitation in Zr-2.5Nb During Neutron Irradiation", Proceedings of AIME Symposium on Phase Stability during Irradiation, Eds. J.R. Holland, L.K. Mansur and D.I. Potter, Pittsburgh (1980) p.587.

[15] Griffiths, M., "A Review of Microstructure Evolution in Zr-Alloys during Irradiation", Journal of Nuclear Materials, Vol. 159 (1988) p. 190.

Special Procedures and Techniques

Karl Ehrlich[1], Siegfried W. Cierjacks[2], Stefan Kelzenberg[3], and Anton Möslang[4]

THE DEVELOPMENT OF STRUCTURAL MATERIALS FOR REDUCED LONG-TERM ACTIVATION

REFERENCE: Ehrlich, K., Cierjacks, S. W., Kelzenberg, S., and Möslang, A., **"The Development of Structural Materials for Reduced Long-Term Activation,"** *Effects of Radiation on Materials: 17th International Symposium, ASTM STP 1270,* David S. Gelles, Randy K. Nanstad, Arvind S. Kumar, and Edward A. Little, Eds., American Society for Testing and Materials, 1996.

ABSTRACT: A reliable calculation of neutron-induced activation of materials requires the inclusion of all kinematically allowed reactions and subsequent reaction chains. While neutron-induced reactions have been sufficiently covered in the past, sequential (x,n) reactions with charged particles x, produced in a first-step reaction, were neglected. To include this type of reaction three new libraries and a preparatory code were developed to produce pseudo cross sections for the European reference code FISPACT. Inventory calculations with the updated FISPACT code, done for all stable elements, showed for 30 elements an increase of at least one of the radiological quantities activity, dose rate and decay heat. Two types of candidate structural materials were investigated: Ferritic-martensitic steels and vanadium-based alloys. While V-Cr-Ti alloys without impurities are known to have far superior long-term activation properties, a realistic assumption of technically achievable amounts of tramp elements leads nearly to the same level of activation as for the optimized ferritic-martensitic steels.

[1]Professor Dr., Kernforschungszentrum Karlsruhe, Department Head in the Institute for Materials Research (IMF I), P. O. Box 3640, D-76021 Karlsruhe, Federal Republic of Germany

[2]Dr., senior research scientist at Kernforschungszentrum Karlsruhe, IMF I, who initiated the introduction of sequential reactions, died in October 1992

[3]Diploma Physicist, ibidem

[4]Dr., Research Scientist, Section Head, ibidem

Copyright© 1996 by ASTM International www.astm.org

KEYWORDS: long-term activation, KFKSPEC, KFKSTOPP, KFKXN, PCROSS, FISPACT, pseudo cross section, sequential (x,n) reactions, long-term activation, dose rate, decay heat, ferritic-martensitic steels, vanadium alloys

INTRODUCTION

Because of the very different requirements in fusion reactor technology new materials have to be developed for the various components. The work in our institute concentrates on structural materials for the first wall and blanket structures. One important aspect is the activation of the candidate materials because of safety and environmental impact conditions. Two timescales are to be considered. The short-term activation, immediately after the shut down, is of interest for maintenance and loss-of-cooling events. The long-term activation, after several years of cooling, is essential for the recycling of the material or for waste disposal. Extensive calculations are necessary to investigate materials properties in terms of radiological quantities as activity, γ-dose rate, decay heat and biological hazard. To improve the calculations a new code PCROSS and three additional libraries KFKSPEC, KFKSTOPP and KFKXN were created to include sequential (x,n) reactions. As a first step all stable elements from hydrogen to bismuth were investigated with respect to sequential (x,n) reactions. Then the work concentrated on long-term activation properties of structural materials for the first wall and the blanket.

CODES AND LIBRARIES

In a fusion environment radioactivity and other radiological quantities are mainly induced by the high-energetic neutrons of the fusion reaction which interact inelastically with the nuclei of the structural material. Reliable predictions of materials activation require the inclusion of all kinematically allowed reactions and subsequent reaction chains. The European Activation SYstem (EASY) [1] with the European reference code FISPACT [2], in the meantime also proposed for ITER calculations, was developed to cover all neutron-induced reactions and reaction chains. The inventory code FISPACT calculates the changes in the materials composition by nuclear transmutation and decay. The code needs extended libraries with nuclear reaction cross sections and decay data for all possible reactions and isotopes and a neutron spectrum relevant for the material to be investigated. The libraries used are the European Activation File (EAF) version 2 [3] with cross sections for about 11 000 reactions on 667 target isotopes and the library UKDECAYX with decay data for 1377 isotopes. As a reference [4] a neutron spectrum from the European study on a reference tokamak reactor for the first wall (zone 12) was taken for our calculations.

Other input parameters besides the neutron spectrum are the neutron flux or the neutron wall loading, the material composition, the irradiation time and the cooling time steps. Starting from every new inventory FISPACT determines the following radiological quantities: activity, γ-dose rate, decay heat and biological hazards.

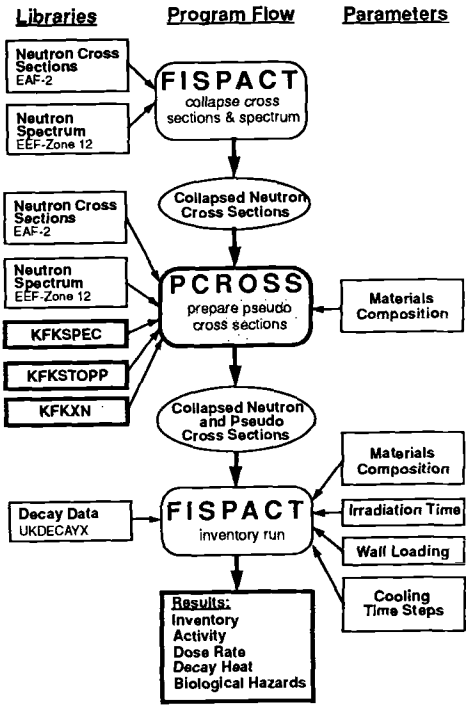


FIG. 1–Flow chart of the FISPACT code, including sequential (x,n) reactions. The hatched areas indicate the modifications introduced by KfK for sequential reactions.

Although FISPACT includes long chains of neutron-induced reactions and decays, it cannot consider sequential (x,n) reactions with charged particles x = p, d, t, ^{3}He and α coming from primary neutron-induced reactions. Preliminary calculations [5] showed, however, that there exist cases where the sequential charged particle reactions have to be taken into account. Hence for systematic investigations it was necessary to develop a new code PCROSS and three additional libraries KFKSPEC, KFKSTOPP and KFKXN in order to include the sequential (x,n) reactions in the existing FISPACT code. The purpose of the new code PCROSS [6,7] is to provide cross-section-like numbers - called pseudo cross sections - as input for FISPACT so that there is no need to change FISPACT itself. The pseudo cross sections are cross sections describing a two-step process. The first step is the production of charged particles by primary neutrons. The second step is the reaction of the charged particles with other nuclei. The calculation of the pseudo cross sections proceeds in two steps.

A charged particle flux is calculated under the assumption that there is essentially no change of this quantity during irradiation. Then the pseudo cross sections are determined by multiplying the charged particle flux with the charged particle reaction cross sections and normalize it to the number of incoming neutrons. In an additional step the pseudo cross sections are merged with the neutron cross sections in one file as input for FISPACT. Figure 1 gives a schematic flow chart of the calculational procedure with PCROSS and FISPACT including sequential reactions.
Doing this requires a huge quantity of data. The neutron cross sections needed to determine the charged particle flux are taken from the EAF library for reasons of consistency. In addition normalized energy spectra and differential ranges for the intermediate charged particles are necessary. They are provided by two new data libraries produced in KfK: KFKSPEC for the energy spectra and KFKSTOPP for the differential ranges. The charged particle reaction cross sections needed for the second step of the calculation are included in the third new library KFKXN [8]. The differential ranges in the library KFKSTOPP were computed by the well established code PRAL [9] further improved by the authors. The file contains data for all elements from hydrogen to curium (Z = 1-96). The spectra and reaction cross sections provided in KFKSPEC and KFKXN were determined by the code ALICE [10] because experimental data are scarcely available. Unfortunately, theoretical predictions might have larger uncertainties. The libraries KFKSPEC and KFKXN cover all isotopes included in EAF.

INVESTIGATION OF ALL STABLE ELEMENTS FOR THE EFFECT OF SEQUENTIAL (X,N) REACTIONS

With the tools described above inventory calculations were performed for all stable elements from hydrogen to bismuth (Z = 1-83). The elements technetium (Tc, Z = 43) and promethium (Pm, Z = 61) were not considered since they have no stable isotopes. One kg of a pure element in its natural isotopic abundance was assumed for this type of calculation. Further input parameters were a neutron wall loading of 5 MW/m^2 and an irradiation time of 2.5 years leading to an integral wall loading of 12.5 $MWyr/m^2$. The decay behaviour was calculated for cooling times between 10^{-3} and 10^6 years. Studying the effects of sequential (x,n) reactions, we compared the activity, the surface γ-dose rate and the decay heat calculated with and without sequential reactions. We found in general an increase of more than 10 % in at least one of the three quantities for 30 cases. For 17 elements the increase is greater than one order of magnitude. Table 1 shows those elements for which sequential (x,n) reactions increase one or more of the three radiological quantities. In addition the factor of increase and the radioisotope as source of the additional contribution are given. The value given in the table is the maximum factor between 10^{-3} and 10^6 years after shutdown and it is strongly time-dependent (see Figure 2).

TABLE 1–Effect of sequential (x,n) reactions in single element inventory calculations on three radiological quantities.

Element	Activity		γ-Dose Rate		Decay Heat	
	Factor of Increase	Radio-isotope	Factor of Increase	Radio-isotope	Factor of Increase	Radio-isotope
Li	only (x,n)	^{10}Be	only (x,n)	^{10}Be	only (x,n)	^{10}Be
B	1.2	^{14}C	—		—	
N	—		$5.5 * 10^3$	^{18}F	—	
O	—		41	^{18}F ^{22}Na	—	
F	—		$1.8 * 10^{11}$	^{22}Na	1.1	^{22}Na
Ne	—		14	^{22}Na ^{26}Al	2.3	^{22}Na
Na	$6.6 * 10^4$	^{26}Al	$1.5 * 10^9$	^{26}Al	$8.2 * 10^5$	^{26}Al
Mg	29	^{26}Al	29	^{26}Al	29	^{26}Al
V	$1.9 * 10^5$	^{53}Mn	$1.8 * 10^3$	^{54}Mn	$2.5 * 10^4$	^{53}Mn
Cr	89	^{53}Mn	1.1	^{54}Mn	89	^{53}Mn
Mn	—		16	^{60}Fe/^{60}Co	—	
As	—		$1.9 * 10^2$	^{81}Kr	—	
Y	$9.7 * 10^2$	^{92}Nb ^{93}Mo	$4.6 * 10^4$	^{92}Nb ^{94}Nb	$1.0 * 10^3$	^{92}Nb ^{94}Nb
Zr	—		6.6	^{92}Nb	—	
Rh	—		1.1	^{108m}Ag	—	
Xe	—		24	^{138}La	—	
Cs	—		$1.5 * 10^3$	^{138}La	—	
Pr	—		1.9	^{146}Pm	—	
Nd	—		1.3	^{166m}Ho	1.2	^{166m}Ho
Sm	1.2	^{166m}Ho	1.2	^{166m}Ho	1.2	^{166m}Ho
Eu	1.1	^{166m}Ho	1.8	^{166m}Ho ^{176}Lu	1.9	^{166m}Ho ^{176}Lu
Gd	—		1.3	^{176}Lu	1.3	^{176}Lu
Tb	1.1	^{176}Lu	1.3	^{176}Lu	1.3	^{176}Lu
Dy	—		1.1	^{176}Lu	1.1	^{176}Lu
Ho	1.1	^{176}Lu	1.1	^{176}Lu	1.1	^{176}Lu
Re	1.1	^{193}Pt	—		—	
Pt	3.2	^{202}Pb/^{202}Tl	$4.3 * 10^4$	^{202}Tl	18	^{202}Tl
Au	$3.2 * 10^4$	^{202}Pb/^{202}Tl	$1.3 * 10^6$	^{202}Tl	$6.0 * 10^5$	^{202}Tl
Hg	1.1	^{202}Pb/^{202}Tl	1.3	^{202}Tl	1.3	^{202}Tl
Tl	—		17	^{202}Tl ^{207}Bi	1.4	^{207}Bi

For a better illustration Figure 2 shows several selected cases. The most dramatic effect of sequential (x,n) reactions is found for the element fluorine. The increase in γ-dose rate due to the contribution of sequential reactions reaches as much as 11 orders of magnitude. In the case of vanadium the effect in activity and dose rate results from the production of different radioisotopes (see Table 1) and occurs in different time regions (see Figure 2). Gold shows that sequential (x,n) reactions affect not only light and medium, but also heavy elements.

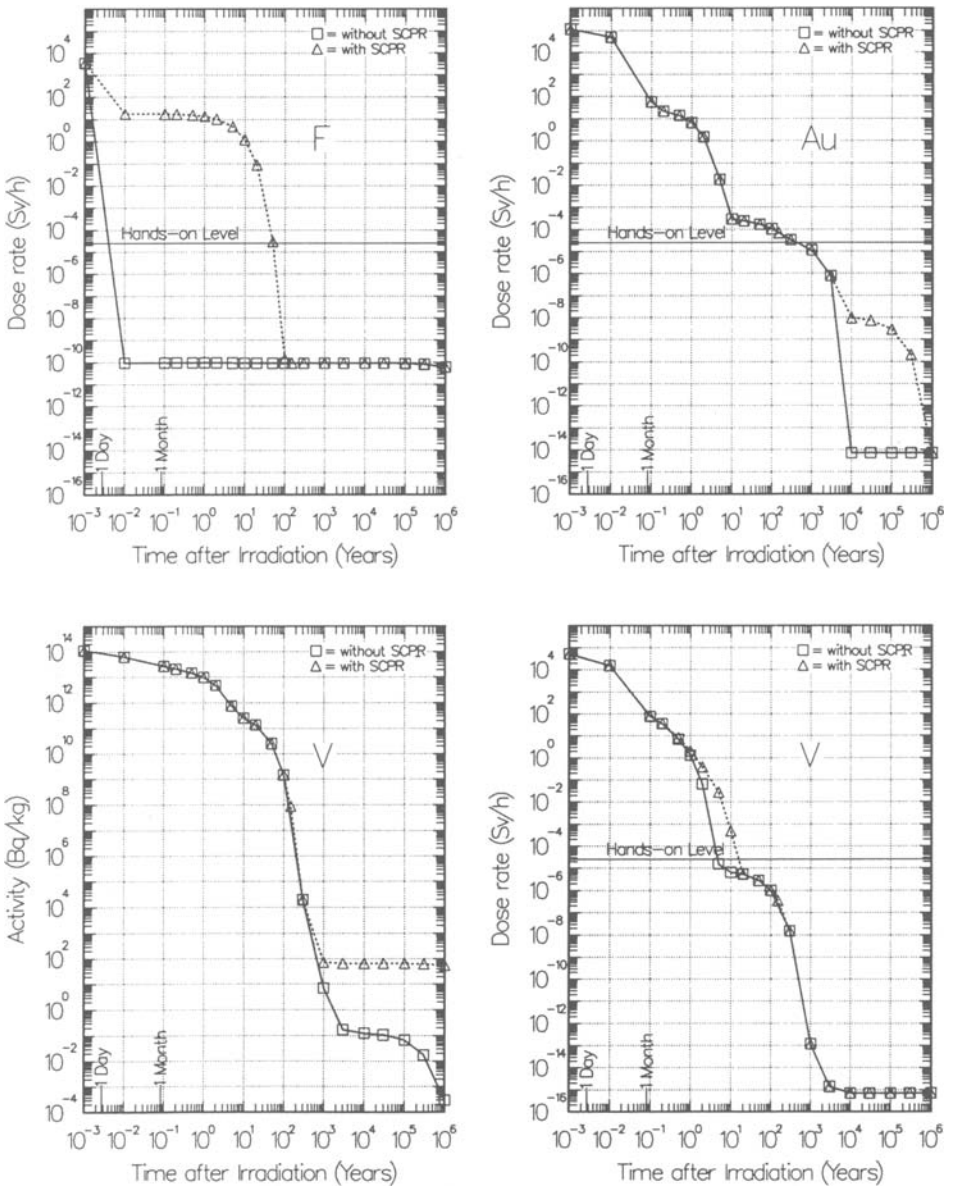


FIG. 2–Calculated results for fluorine (F), vanadium (V) and gold (Au). Different radiological quantities are compared as functions of cooling time with and without sequential (x,n) reactions (SCPR).

IMPORTANCE OF BASE MATERIALS, ALLOYING ELEMENTS AND IMPURITIES FOR THE LONG-TERM ACTIVATION OF MATERIALS FOR FUSION

A first guide line for the selection of alloys with low long-term activation can be derived by a comparison of the radiological properties of elements which form the basis for existing technical materials. Such a comparison is given in Figure 3 for important elements like silicon, titanium, vanadium and iron after irradiation with fusion neutrons to an integrated wall loading of 12.5 MWy/m^2. Ceramic composites of type silicon carbide (SiC/SiC_f), which are used in the aircraft industry and possess many advantageous properties will not reach the hands-on level of radioactivity (25 $\mu Sv/h$) even after very long decay times. The same statement is true for aluminium alloys which are not indicated in this plot. Iron, the base metal for the best-known class of technical materials - the steels - reaches the hands-on level after 100 years and would hence fulfill the requirement for a possible material recycling and waste deposition in form of shallow land burial. Only the elements vanadium (V) and chromium (Cr) show a far better behaviour, both with respect to the time to reach

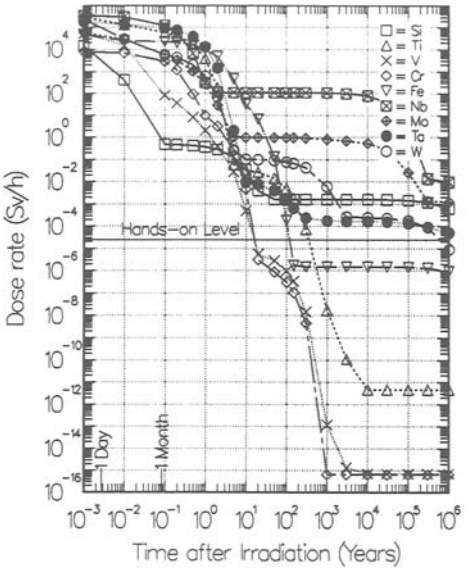


FIG. 3–γ-Dose rate of important base metals and alloying elements after irradiation with fusion neutrons of 12.5 $MWyr/m^2$

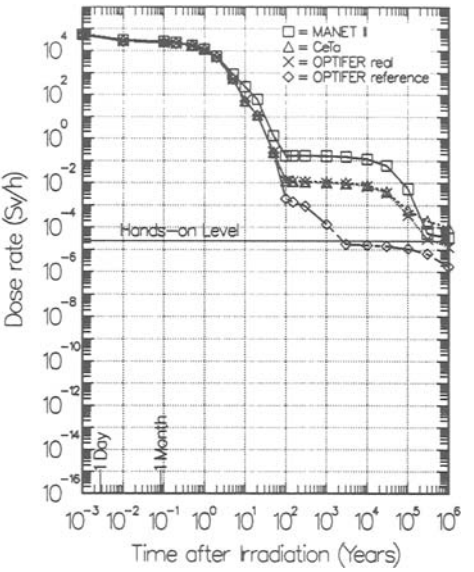


FIG. 4–Optimization of ferritic-martensitic steels.

the hands-on level ($\sim$ 20 years versus 100 years for iron) as well as to the lowest steady state level of radioactivity (10^{-15}Sv/h versus 10^{-6}Sv/h in iron) after 3 000 years and 1 000 years respectively. The prospect of developing chromium-based alloys with otherwise good technical properties are, however, extremely poor. Another option could be titanium-based alloys if a low long-term radioactivity is an essential prerequisite for alloy selection. Titanium alloys are well developed and applied in the aircraft industry. However, hydrogen embrittlement could rule out this class of alloys for fusion application. These facts are the real reason why at present in most fusion programmes only optimized iron-based ferritic-martensitic steels and vanadium alloys are considered as structural materials for fusion. The further considerations concentrate therefore on these two classes of alloys.

Ferritic-Martensitic Steels

Ferritic-martensitic 9 - 12 % CrMoV(Nb) steels possess a number of advantageous properties for fusion reactor applications [11]. Their optimization in Europe (the MANET programme) as well as in other countries has led to far better creep- and fracture toughness properties. One drawback of the commercial alloys is that major alloying elements like nickel (Ni), molybdenum (Mo), niobium (Nb) and aluminium (Al) were found to be deleterious with regard to long-term activation, which is evident if, for example, the γ-dose rates of niobium and molybdenum in Figure 3 and their concentrations are taken into account. The replacement of these elements by other major alloying elements like tungsten (W) and tantalum (Ta) with a similar metallurgical function was the starting point for the 8 - 10 % CrWVTa alloys in different research programmes [12,13]. To demonstrate the status of a common development of our institute reached together with the steel company Saarstahl GmbH, a comparison of the γ-dose rate for the conventional 10.5 % CrMoVNb steel 'MANET II' with two laboratory melts of 9 - 10 % CrWVTa alloys 'CeTa' and 'OPTIFER real' on the basis of the actual chemical compositions is given in Figure 4 [14]. The long-term dose rate of 'MANET II' is governed by the radioisotope ^{94}Nb with a half-life time of 20 000 years. In the steels 'CeTa' and 'OPTIFER real' the elements nickel, molybdenum, niobium and aluminium were replaced by tantalum(Ta), tungsten(W) and cerium (Ce) in a first step. The decrease of one order of magnitude in the long-term γ-dose rate corresponds to an equivalent reduction of the niobium content in these experimental alloys. The lowest achievable γ-dose rate of the new 8 - 10 % CrWVTa alloy is indicated by 'OPTIFER reference' in Figure 4. In this reference alloy all impurity elements were reduced to a level where they no longer play a role and the long-term dose rate is only governed by the activation of the new alloying element tungsten. The dose rate is 2 to 4 orders of magnitude lower than the activation of 'MANET II' but 1 to 3 orders of magnitude higher than that of pure iron, dependent on the cooling time after the irradiation. Assuming that all critical elements (especially niobium!) can be reduced to the level of tolerance for the iron-based alloys as defined in Table 2, the minimum achievable long-term activation is governed by the decay characteristics of pure iron (see Figure 3).

TABLE 2–Concentration equivalent for some critical elements

Element	Concentration Equivalent [weight-ppm]			
	Hands-on Level[a] 300 y after Irradiation	Iron[b] 300 y after Irradiation	Vanadium[c] 300 y after Irradiation	Vanadium[d] 10 000 y after Irradiation
Al	86.1	5.24	$5.17 * 10^{-2}$	$2.52 * 10^{-9}$
Si	$1.56 * 10^{4}$	948	9.35	$4.57 * 10^{-7}$
Cl	$2.71 * 10^{3}$	165	1.63	$8.80 * 10^{-8}$
K	211	12.8	$1.27 * 10^{-1}$	$1.46 * 10^{-6}$
Ca	$2.88 * 10^{3}$	175	1.73	$3.73 * 10^{-6}$
Co	$1.96 * 10^{3}$	119	1.18	$5.72 * 10^{-8}$
Ni	$2.44 * 10^{5}$	$1.48\ 10^{4}$	146	$7.10 * 10^{-6}$
Zr	$2.85 * 10^{3}$	173	1.71	$1.17 * 10^{-7}$
Nb	$2.32 * 10^{-1}$	$1.41 * 10^{-2}$	$1.39 * 10^{-4}$	$9.37 * 10^{-12}$
Mo	27.5	1.67	$1.65 * 10^{-2}$	$1.37 * 10^{-9}$
Pd	3.48	$2.12 * 10^{-1}$	$2.09 * 10^{-3}$	$8.19 * 10^{-4}$
Ag	$8.13 * 10^{-2}$	$4.94 * 10^{-3}$	$4.88 * 10^{-5}$	$2.28 * 10^{-5}$
Cd	37.8	2.30	$2.27 * 10^{-2}$	$1.06 * 10^{-2}$
Eu	9.62	$5.85 * 10^{-1}$	$5.77 * 10^{-3}$	$3.31 * 10^{-6}$
Gd	1.94	$1.18 * 10^{-1}$	$1.16 * 10^{-3}$	$7.63 * 10^{-8}$
Tb	$2.23 * 10^{-1}$	$1.36 * 10^{-2}$	$1.34 * 10^{-4}$	$3.15 * 10^{-9}$
Dy	$7.89 * 10^{-2}$	$4.80 * 10^{-3}$	$4.73 * 10^{-5}$	$6.23 * 10^{-10}$
Ho	$1.00 * 10^{-1}$	$6.08 * 10^{-3}$	$6.00 * 10^{-5}$	$7.88 * 10^{-10}$
Er	3.22	$1.96 * 10^{-1}$	$1.93 * 10^{-3}$	$2.48 * 10^{-8}$
W	582	35.4	$3.49 * 10^{-1}$	$2.98 * 10^{-6}$
Re	78.1	4.75	$4.68 * 10^{-2}$	$1.42 * 10^{-6}$
Os	8.51	$5.17 * 10^{-1}$	$5.11 * 10^{-3}$	$2.89 * 10^{-4}$
Ir	25.6	1.56	$1.54 * 10^{-2}$	20.7
Bi	1.95	$1.19 * 10^{-1}$	$1.17 * 10^{-3}$	$8.94 * 10^{-11}$

[a] 25 μSv/h
[b] 1.52 μSv/h
[c] $1.5 * 10^{-2}\mu$Sv/h
[d] $7.26 * 10^{-10}\mu$Sv/h

In Table 2 the term "concentration equivalent" of an element is defined as the mass in weight-ppm which would after the irradiation of 12.5 MWyr/m^2 and a decay time of 300 years and 10 000 years respectively lead to the γ-dose rate indicated in the head of each column. Whereas the hands-on level of 25 μSv/h is an independent value and has already been used by Khursheed [15] to calculate concentration equivalents, the other three dose levels refer to pure iron and vanadium respectively. As will be discussed later this material-based definition gives a better feeling for the allowable concentration levels of unwanted impurities for steels and vanadium alloys.

Development of Vanadium-Chromium-Titanium Alloys and the Role of Impurities

As already mentioned, vanadium (V), chromium (Cr) and titanium (Ti) are the best choice for materials with an extremly low long-term activation. V-5Cr-5Ti alloys and V-3Ti-Si alloys were already very early developed and investigated in research programmes for nuclear applications, as summarized under [e.g. 16]. However, these investigations were mainly concentrated on conventional properties like high-temperature creep and general irradiation behaviour. The attractiveness of vanadium alloys for fusion technology [e.g. 17] was based also on the argument of intrinsically low long-term neutron activation. Our calculations performed on "pure" alloys V-5Cr-5Ti and V-3Ti-1Si in Figure 5 show already that by the addition of 1 % silicon this advantage is completely lost. But even for pure vanadium-chromium-titanium alloys a strong increase of long-term activation by several orders of magnitude can be caused by impurities. Under the assumption of a realistic minimum of impurities which has recently been elaborated by a technical review for vanadium-chromium-titanium alloys [18] and which is listed in Table 3 the calculated long-term dose rate increases by 6-7 orders of magnitude (see Figure 6) and approaches nearly the level of the optimized iron-based martensitic steel 'OPTIFER reference'.

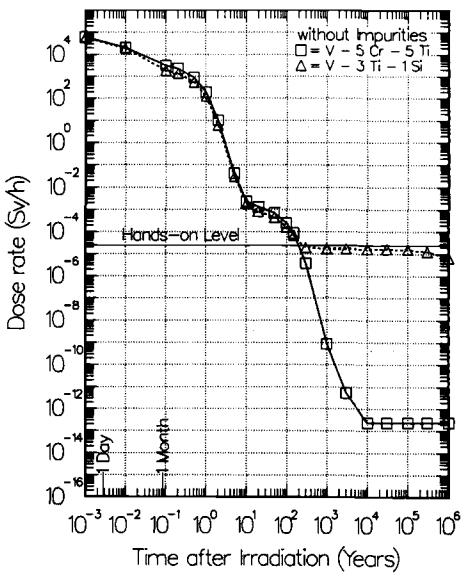


FIG. 5–Dose rates calculated for two intrinsic pure vanadium based alloys.

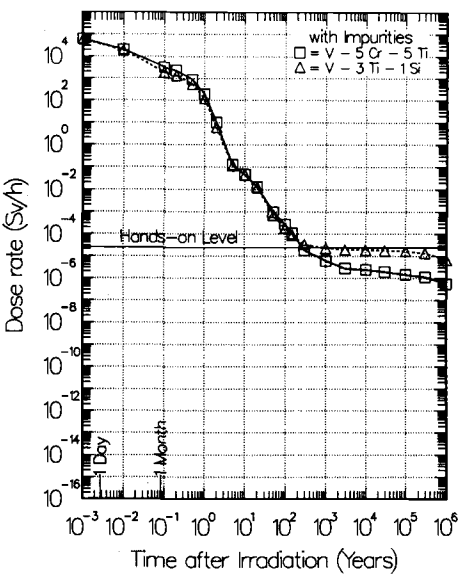


FIG. 6–Dose rates calculated for two vanadium based alloys including impurities.

As a general conclusion, the impurity control in vanadium-chromium-titanium alloys is even more important than for iron-based alloys. This is also reflected in the analysis of the dominant radioisotopes and their period of dominance in the decay behaviour of the V-5Cr-5Ti alloy with impurities, collected in Table 4.

TABLE 3–Impurities taken into account for the vanadium based alloys.

Element	Concentration [weight-ppm]	Element	Concentration [weight-ppm]	Element	Concentration [weight-ppm]
Al	3.0	Co	0.02	Ag	0.03
Si	300.0	Ni	0.03	Cd	0.02
Cl	7.0	Cu	0.3	Ba	0.2
K	15.0	Zr	0.08	Bi	0.007
Ca	15.0	Nb	0.01		.
Fe	3.0	Mo	0.15		.

TABLE 4–Dominant radioisotopes with half-lives and production reaction for the alloy V-5Cr-5Ti with impurities.

Radio isotope	Half-Live	Period of Dominance	Dominant Reaction
^{52}V	3.75 min	End of Irradiation	^{51}V(n,γ)^{52}V
^{48}Sc	1.82 d	0.001 - 0.01 y	^{51}V(n,α)^{48}Sc
^{46}Sc	83.8 d	0.1 - 2 y	^{46}Ti(n,p)^{46}Sc
^{60}Co	5.272 y	5 - 20 y	^{59}Co(n,p)^{60}Co
^{42}Ar	33 y	50 - 150 y	^{48}Ti(n,α)^{45}Ca(n,α)^{42}Ar
^{108m}Ag	127 y	300 y	^{107}Ag(n,γ)^{108m}Ag
^{94}Nb	20 000 y	1 000 - 10 000 y	^{93}Nb(n,γ)^{94}Nb
^{26}Al	716 000 y	30 000 - 10^6 y	^{27}Al(n,2n)^{26}Al

SUMMARY AND CONCLUSIONS

The introduction of sequential (x,n) reactions into the inventory code FISPACT has shown that for 17 out of 81 investigated elements at least one of the calculated radiological quantities is increased by more than one order of magnitude (Table 1). Vanadium, chromium and manganese as base metals or major alloying elements as well as nitrogen as an interstitial element and yttrium as a deoxidation element belong to this category. Impurity or tramp elements like silver, bismuth and rare earth metals which were already earlier identified as critical elements [15,19] are not affected by sequential reactions.

For the ferritic-martensitic steels discussed above, the activation characteristics of pure iron represents the best achievable target in the design of steels with reduced activation. For the optimized alloys, where niobium, molybdenum and nickel were replaced by tungsten and tantalum, a reasonably low long-term activation below the hands-on level of dose rate can be achieved if the concentrations of critical tramp

elements are below those levels compiled in Table 2 first column. This is probably manageable, if specific new ways of steelmaking for "pure" alloys are used.
The class of vanadium-chromium-titanium alloys offers theoretically a break-through to a class of alloys with an extremely low long-term activation, even if the sequential (x,n) reactions are taken into account. In order to achieve this low level of radioactivity in practice the tramp element concentrations should be extremely low as indicated in Table 2 columns three and four. If, however, realistic tramp element or impurity concentrations are used for the calculations the actual advantage of vanadium-chromium-titanium alloys in comparison to the optimized ferritic-martensitic steels (see Figure 7) diminishes to about one order of magnitude with regard to the long-term radioactivity level.

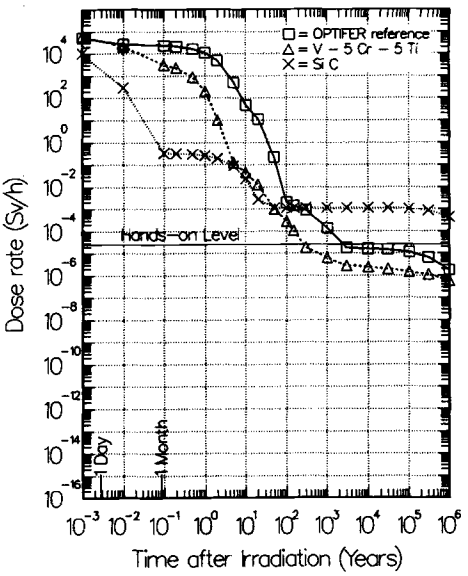


FIG. 7–Dose rates calculated for three candidate structural materials.

Finally the complex situation for the development of low activation materials in general is also demonstrated in Figure 7, where the ceramic composite material SiC/SiC_f is added for comparison. As can be deduced, the very beneficial low γ-dose rate for SiC/SiC_f at short times after shut down is totally reversed for the case of long decay times. This is one of the reasons why the development of "low activation materials" is a very complex objective for the fusion materials community.

REFERENCES

[1] R. A. Forrest and J. Kopecky, "EASY 1.0 The European Activation System," Advisory Group Meeting on FENDL-2, Vienna (November 1991).

[2] R. A. Forrest and D. A. J. Endacott, "FISPACT-User Manual," Harwell Report AERE-M3654 (March 1988).

[3] J. Kopecky, H. Gruppelaar and R. A. Forrest, "European Activation File for Fusion," International Conference on Nuclear Data for Science and Technology, Jülich, Germany, May 1991, Petten Report ECN-RX-91-050.

[4] P. I. H. Cooke, R. Hancox and W. R. Spears, "A Reference Tokamak Reactor," Culham Report, CUL-R 298, (1990).

[5] S. Cierjacks and Y. Hino, "The Importance of Sequential reactions on Element Activation of Fusion Reactor Materials," Journal of Nuclear Materials No. 170 (1990) pp.134-139.

[6] S. Ravndal, P. Obložinský, S. Kelzenberg, S. Cierjacks, "User Manual for the KfK Code PCROSS," Report KfK 4873 (August 1991).

[7] S. Ravndal, P. Obložinsk y, S. Kelzenberg, S. Cierjacks, "Reference Manual for the KfK Code PCROSS," Report KfK 4956 (Dezember 1991).

[8] S. Cierjacks, P. Obložinsk y, S. Kelzenberg and B. Rzehorz, "Development of a Novel Algorithm and Production of New Nuclear Data Libraries for the Treatment of Sequential (x,n) Reactions in Fusion Materials Activation Calculations," Fusion Technology, Vol. 24 No.3, pp. 277-287 (November 1993)

[9] J. F. Ziegler, J. P. Biersack and U. Littmark, "The Stopping and Range of Ions in Solids," Pergamon Press, New York (1985).

[10] M. Blann, "Code ALICE/85/300," UCID-20169, Lawrence Livermore National Laboratory (1984).

[11] R. L. Klueh, K. Ehrlich and F. Abe, "Ferritic-Martensitic Steels: Promises and Problems," Journal of Nuclear Materials, No. 191-194, pp. 116-124 (1992).

[12] K. Ehrlich, M. Schirra, "Entwicklungsarbeiten an Nb-Stabilisierten Martensitischen 9 - 12 % Chromstählen für Anwendungen in der Energietechnik," 15. Vortragsveranstaltung Langzeitverhalten warmfester Stähle und Hochtemperaturwerkstoffe, Düsseldorf, 6. November 1992.

[13] K. Ehrlich, S. Kelzenberg, H.-D. Röhrig, L. Schäfer and M. Schirra, "The Development of Ferritic-Martensitic Steels with Reduced Longterm Activation," Proceedings of the Sixth International Conference on Fusion Reactor Materials, Stresa, Italy, September 27 - October 1, 1993, Journal of Nuclear Materials, (to be published).

[14] Proceedings of the IEA-Workshop on Ferritic-Martensitic Steels, Tokyo, Japan, October 26-28, 1992, F. Abe, A. Hishinuma, A. Kohyama, M. Suzuki, Editors, (March 1993).

[15] Amjad Khursheed, "Neutron - Induced Activation of Materials for the First Wall of Conceptual Fusion Reactors," Ph. D. Thesis, Imperial College, London (February 1989).

[16] M. Rühle, H. U. Borgstedt und M. Schirra, "Vanadinlegierungen für die Kerntechnik," Zeitschrift für Metall, Teil I: No. 2 pp. 140-147 (1979), Teil II: No. 3 pp. 265-266 (1979), Teil III: No. 5 pp. 455-465 (1979).

[17] B. A. Loomis, A. B. Hull and D. Smith, "Evaluation of Low Activation Vanadium Alloys for Use as Structural Material in Fusion Reactors," Journal of Nuclear Materials, No. 179-181, pp. 148-154 (1991).

[18] "Production of High-Purity Vanadium, Chromium and Titanium for Use in Low Activation Materials," Report Euratom Contract NET/89-797, Johnson Matthey, Royston (1993).

[19] D. Murphy and G. J. Butterworth, "Production of High-Purity Vanadium, Chromium and Titanium for Use in Low Activation Materials", Journal of Nuclear Materials No. 191-194, pp. 1444-1449 (1992).

Mirco Große[1], Frank Eichhorn[2],Jürgen Böhmert[1],Gerhard Brauer[3]

CHARACTERIZATION OF IRRADIATION-INDUCED PRECIPITATES BY SMALL ANGLE X-RAY AND NEUTRON SCATTERING EXPERIMENTS

REFERENCE: Grosse, M., Eichhorn, F., Böhmert, J., Brauer, G., **"Characterization of Irradiation-Induced Precipitates by Small Angle Scattering Experiments,"** *Effects of Radiation on Materials: 17th International Symposium, ASTM STP 1270,* David S. Gelles, Randy K. Nanstad, Arvind S. Kumar, and Edward A. Little, Eds., American Society for Testing and Materials, 1996.

ABSTRACT: The nature of the irradiation-induced precipitates in the VVER-440-type steel 15Kh2MFA has been investigated by the combination of small angle neutron scattering and anomalous small angle X-ray scattering. Information about the chemical composition of the irradiation-induced precipitates was obtained by the method of contrast variation . ASAXS experiments with variation of the X-ray energy near the energy of the vanadium K-absorption edge prove the content of vanadium within the irradiation-induced precipitates. The scattering density of the precipitates is lower than the scattering density of the iron matrix. The chemical shift of the vanadium-K_α-absorption-edge and the results of the variation of the contribution of the magnetic scattering in the SANS experiment show, that vanadium does not precipitate in an elementary state. These results can be explained by assuming the precipitates are vanadium carbide.

KEY WORDS: pressure vessel steel, radiation hardening, embrittlement, small angle neutron scattering, anomalous small angle X-ray scattering, microstructure

The deterioration of the mechanical properties of reactor pressure vessel (RPV) steels during their irradiation in a nuclear power plant, known as neutron embrittlement, is a very complex process. Therefore, it is usual to evaluate the embrittlement empirically by means of testing of surveillance specimens. In addition, a physically based understanding of the irradiation-induced structural modifications and the changes of the properties resulting from that is indispensable in order to evaluate the current state of RPV safely. Basis of the understanding is the modelling of neutron embrittlement. Any model has to consider:

- the nature of the irradiation-caused microstructural changes,
- the influence of irradiation and metallurgical parameter variation on the microstructure,

[1] Research scientist and leader of the Neutron embrittlement division, Research Center Rossendorf Inc.; Inst. for Safety Research, P.O.Box 510119, D-01314 Dresden, Germany
[2] Research scientist, Research Center Rossendorf Inc.; Inst. for Ion Beam Physics and Material Research, P.O.Box 510119, D-01314 Dresden, Germany
[3] Leader of the Positron Group of TU Dresden at Research Center Rossendorf, P.O.Box 510119, D-01314 Dresden, Germany

Copyright© 1996 by ASTM International www.astm.org

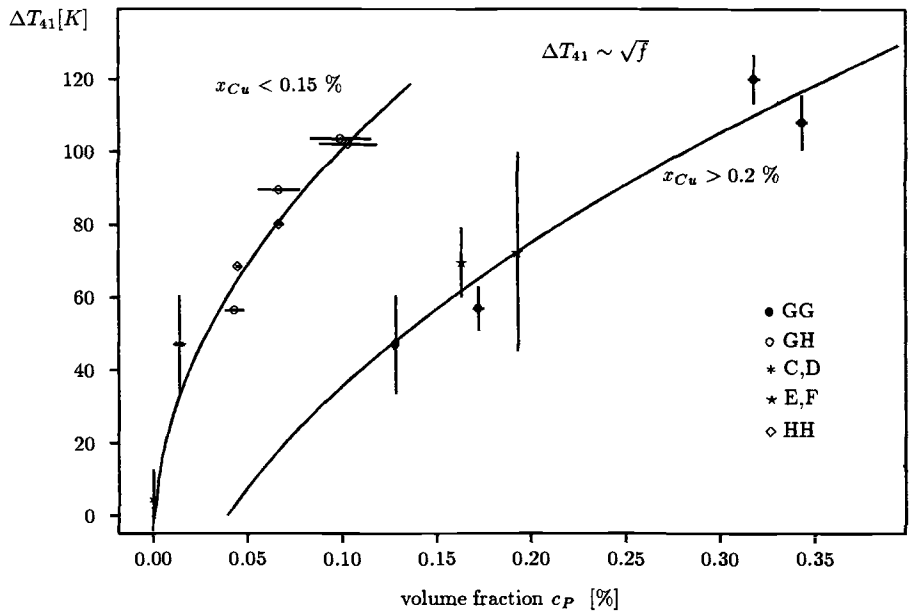


Figure 1: Correlation between volume fraction of irradiation-induced precipitates c_P and shift of the ductile - brittle transition temperature ΔT_{41} for 15Kh2MFA steel with different chemical composition [4]

- the micromechanical modelling of the fracture process and
- the correlation of the micromechanical process with the macroscopic strength and toughness parameters.

According to the literature, e.g. [1] and references therein, neutron embrittlement has to be attributed to the following structural processes:

- lattice defect production caused by neutron displacement cascades
- formation of ultrafine, Cu-rich precipitates
- ultrafine phosphide formation
- ultrafine carbide formation
- temper embrittlement caused by P segregation.

It is largely accepted that the second mechanism is the dominant process [2].

Fig. 1 shows the correlation between the increase of the ductile - brittle transition temperature ΔT_{41} and the volume fraction of irradiation-induced precipitates c_P estimated in prior small angle neutron scattering (SANS) experiments [3] for heats of the VVER-440-type reactor pressure vessel steel 15Kh2MFA, differing in their content of copper impurities [4]. In contrast to ASTM-type RPV steels the VVER-440-type steel is free of Ni, but contains V. The mode of the influence of c_P on ΔT_{41}

depends on the content of copper impurities. The mode with the higher slope of the curve ΔT_{41} *vs.* c_P is representative for heats with low copper content (< 0.15 %) and the mode with the smaller slope for heats with a copper content >0.20 %. The materials are irradiated to different fluences. For the same fluence the volume fraction of irradiation-induced precipitates strongly depends on the copper content. In materials with high copper content much more precipitates are formed during the irradiation than in heats with small one. For a detailed discussion of the correlation between volume fracton of irradiation-induced precipitates and ductile - brittle transition temperature see reference [4].

For an understanding of the differences in the neutron embrittlement behaviour of the steel 15Kh2MFA knowledge about the nature of the irradiation-induced precipitates is necessary. Kočik et al. [5] carried out investigations at this material by means of transmission electron microscopy (TEM) and found dislocation loops, a refinement of vanadium carbide particles and black dots, smaller than 8 nm in size, which could not be identified. Positron annihilation and Mößbauer spectroscopy were used in [6, 7]. Their results are indirect, but they suggest that the major defect types are irradiation-induced carbides.

In this paper first results of the investigations of the nature of irradiation-induced precipitates by combining the results of anomalous small angle X-ray scattering experiments with the results of former small angle neutron scattering are given.

CHARACTERIZATION OF THE CHEMICAL COMPOSITION BY METHODS OF CONTRAST VARIATION IN SMALL ANGLE SCATTERING EXPERIMENTS

In order to characterize the nature of the irradiation-induced precipitates the combination of small angle neutron and X-ray scattering using contrast variation techniques was employed. For a better understanding of the interpretation of the results, some theoretical foundation about small angle scattering experiments are given now.

Neglecting particle correlation effects, the intensity of the small angle scattering $I(Q)$ is given by [8]:

$$I(Q) = a \cdot \mid n_P \cdot f_P - n_M \cdot f_M \mid^2 \frac{1}{n_M} c_p \cdot V_p \cdot S_1(Q) \tag{1}$$

with:

Q	scattering vector
a	calibration factor
$f_{P,M}$	mean scattering length (atomic form factor) of the particle or matrix, respectively
$n_{P,M}$	mean number density in the particle or matrix, respectively
c_P	volume fraction of the particles
V_P	volume of the particle
$S_1(Q)$	specific structure factor; Guinier - approximation (spherical particles): $S_1(Q) = e^{-\frac{Q^2 R_G^2}{3}}$ (valid for $Q \cdot R_G \approx 1$)
R_G	radius of gyration

f_P contains information about the chemical composition and n_P depends on the structure of the inhomogeneities. The separation of these two quantities is possible by methods of contrast variation.

i) In the case of non-ferromagnetic precipitates in a ferromagnetic matrix the contrast variation in the SANS experiment can be performed by variation of the contribution of the magnetic scattering. The magnetic scattering length of the atoms in a non-ferromagnetic precipitate is equal to zero. In this case, an intensity contribution $I^m(Q)$ caused by magnetic scattering is got in addition to the intensity caused by nuclear scattering $I^n(Q)$. This intensity contribution is, according to Eq. (1), given by

$$I^m(Q) = a \cdot \mid n_M \cdot f_M^m \mid^2 \sin^2 \alpha \frac{1}{n_M} c_p \cdot V_p \cdot S_1(Q) \tag{2}$$

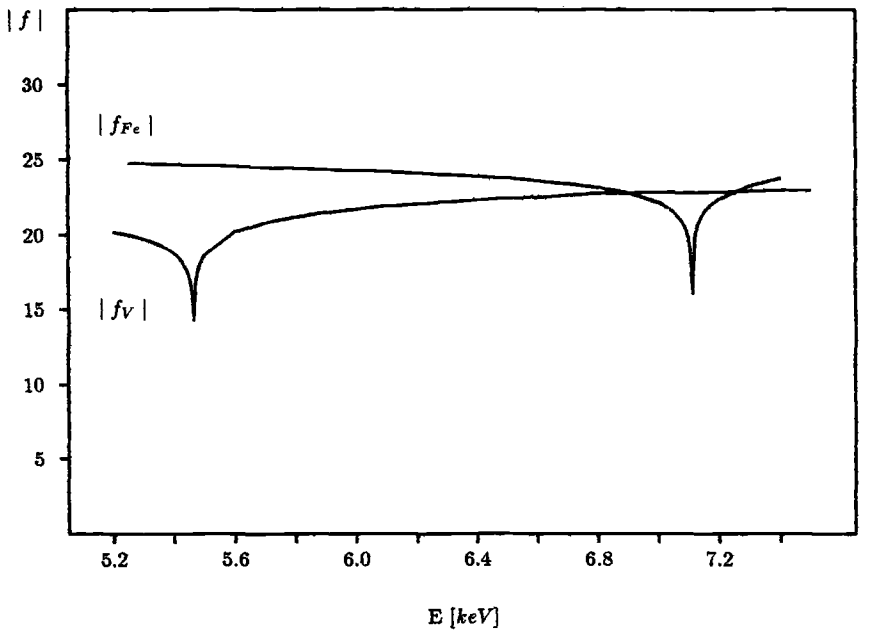


Figure 2: Energy dependence of the atomic form factors of iron and vanadium

with α being the angle between Q and the magnetization M of the specimen. In the case of $\alpha = \frac{\pi}{2}$ the magnetic scattering fully contributes to the intensity, in the case of $\alpha = 0$ this contribution equals to zero. Information about the chemical composition can be obtained from the "A-ratio". The A-ratio is given by Eq. (3) and (4) [3].

$$A = \frac{I^n(Q) + I^m(Q)}{I^n(Q)} = \frac{I(Q, \alpha = \frac{\pi}{2})}{I(Q, \alpha = 0)} \tag{3}$$

$$A = \frac{| n_P \cdot f_P - n_M \cdot f_M |^2 + | n_M \cdot f_M^m |^2}{| n_P \cdot f_P - n_M \cdot f_M |^2} \tag{4}$$

In the case of ferromagnetic inhomogenities in a ferromagnetic matrix the magnetic scattering length of the atoms in the precipitates are not equal to 0 and must be known. Then the intensity contribution by magnetic scattering can be calculated similar to Eq. (1). In this case the A-ratio can be calculated, in contrast to Eq. (4), by

$$A = \frac{| n_P \cdot f_P - n_M \cdot f_M |^2 + | n_P \cdot f_P^m - n_M \cdot f_M^m |^2}{| n_P \cdot f_P - n_M \cdot f_M |^2} \tag{5}$$

ii) In the small angle X-ray scattering (SAXS) experiment element specific contrast variation can be performed by use of the anomalous scattering effect at X-ray energies near the energies of the absorption edges of the elements of interest.

The atomic form factor at small angles is given by [8]

$$f(E, Q \to 0) = Z + f'(E) + if''(E) \tag{6}$$

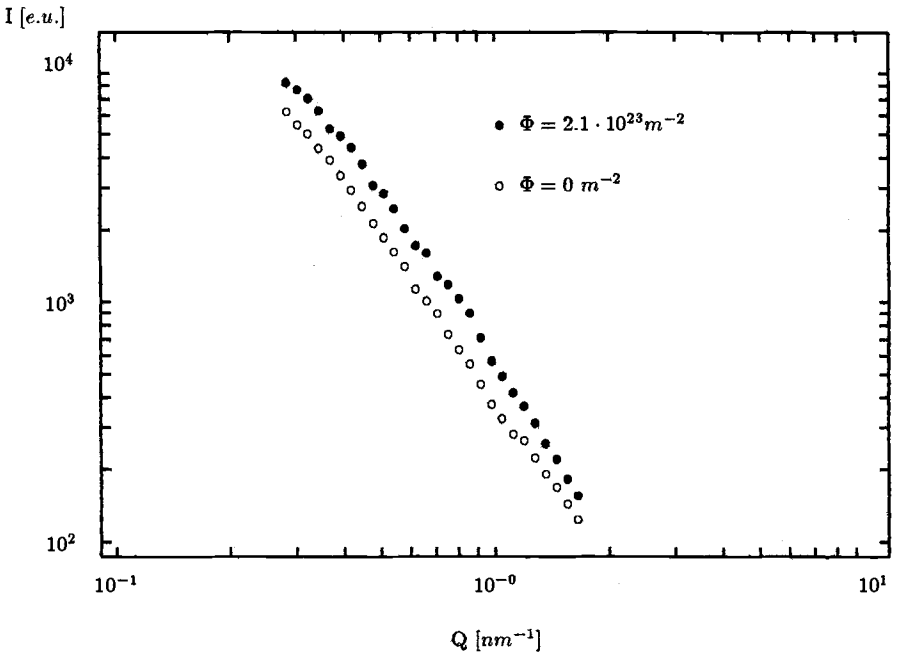


Figure 3: Small angle X-ray scattering patterns at an X-ray energy of 5.471 keV of the material in irradiated (•) and unirradiated (o) state

with Z being the element number and f' and f'' the contributions of anomalous scattering. As an example, in Fig. 2 the energy dependence of the atomic form factor of vanadium and iron, respectively, is shown. The curves were calculated with the help of the program F_ PRIME, which is a part of the data analysis software of the JUSIFA facility of HASYLAB Hamburg. The mean atomic form factor of the steel matrix f_M should correspond to the atomic form factor of iron to a good approximation.

$I(E)$ strongly depends on E at energies near the energies of the absorption edges of the elements which are contained in the precipitate. A variation of the SAXS intensity at energies near the absorption edge of an element, which does not follow the energy dependence of the mean atomic form factor of the matrix, is the proof of this element being present within the precipitate.

MATERIALS AND MEASUREMENTS

Specimens for the present investigation were prepared from VVER-type 15Kh2MFA RPV steel manufactured in industrial scale by SKODA Concern Corporation (Czech Republic). Its chemical composition (in wt.%) is: 0.16 C, 0.19 Si, 0.013 P, 0.014 S, 0.34 V, 2.84 Cr, 0.42 Mn, 0.09 Ni, 0.1 Cu, 0.63 Mo, Fe balance. The material used in the SANS experiments was irradiated at the Hungarian Nuclear Power Plant Paks to neutron fluences of $3.2 \cdot 10^{23}$, $8.0 \cdot 10^{23}$ and $14.0 \cdot 10^{23}$ (E>1.0 MeV) at $270°C$, whereas the material used in the ASAXS experiments was irradiated at the research reactor of the Czech Nuclear Research Institute Řež to a fluence of $2.1 \cdot 10^{23} m^{-2}$ (E>0.5 MeV) at $306°C$. The irradiation conditions of the SANS and ASAXS experiments are not fully the same. For the

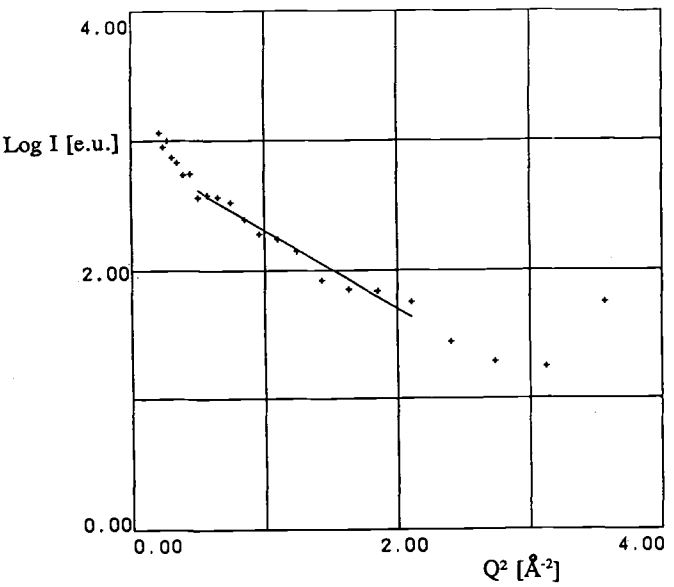


Figure 4: Guinier plot of the difference intensity at an X-ray energy of 5.471 keV

discussion of the results it is assumed, that the differences in the irradiation conditions don't produce qualitative differences in the nature of the irradiation-induced precipitates.

The SANS experiments were performed at the SANS-2 facility at the FRG-1 reactor at Geesthacht (Germany). A detailed description of the SANS experiments and results is given in [3].

The ASAXS experiments were conducted at the JUSIFA facility at the synchrotron laboratory HASYLAB at Hamburg (Germany) [9]. The thickness of the irradiated specimen was 11 μm and of the unirradiated one 13 μm. The X-ray beam cross section was $1 \cdot 1$ mm^2. For contrast variation an energy range of 5.25 to 7.112 keV was used. This energy range covers the energies of the vanadium, chromium, manganese and iron K-absorption edges. Measurements at higher energies, e.g. at energies near the copper K-absorption edge, were not successful up to now because of the high iron fluorescence radiation at this energies, which gives a background intensity several orders of magnitude higher than the SAXS intensity to be measured.

RESULTS

In order to separate the scattering effect of the irradiation-induced precipitates,measurements at irradiated material were compared with those in the unirradiated condition (Fig. 3). The difference $\Delta I(Q)$ between these two patterns is caused by the irradiation-induced precipitates.

The volume fraction c_P of the irradiation-induced precipitates has been estimated from the magnetic small angle neutron scattering intensities, on the basis that the precipitates are non-ferromagnetic, no other assumptions about the structure and chemical composition are necessary (see Eq.(2)). The values of c_P depend on the fluence. They are smaller than 0.2 % for the heats with low copper content. If the assumption, that the precipitates are non-ferromagnetic, is not fulfilled, the volume fraction of the precipitates would be underestimated.

In order to investigate the effect of contrast variation the SAXS intensity at the scattering vector Q=0 was calculated by extrapolation of the linear part of the curve $Log(\Delta I(Q))$ *vs.* Q^2 (Guinier-Plot), because S(Q=0) is equal to 1 (see Eq.(1)). Fig. 4 shows the guinier plot of $\Delta I(Q)$ at an X-ray energy of 5.471 keV as an example. For the linear fit in the Guinier plot the same Q-range was used for all energies. The radii of gyration calculated from the slope of the fitted curves are the same for all

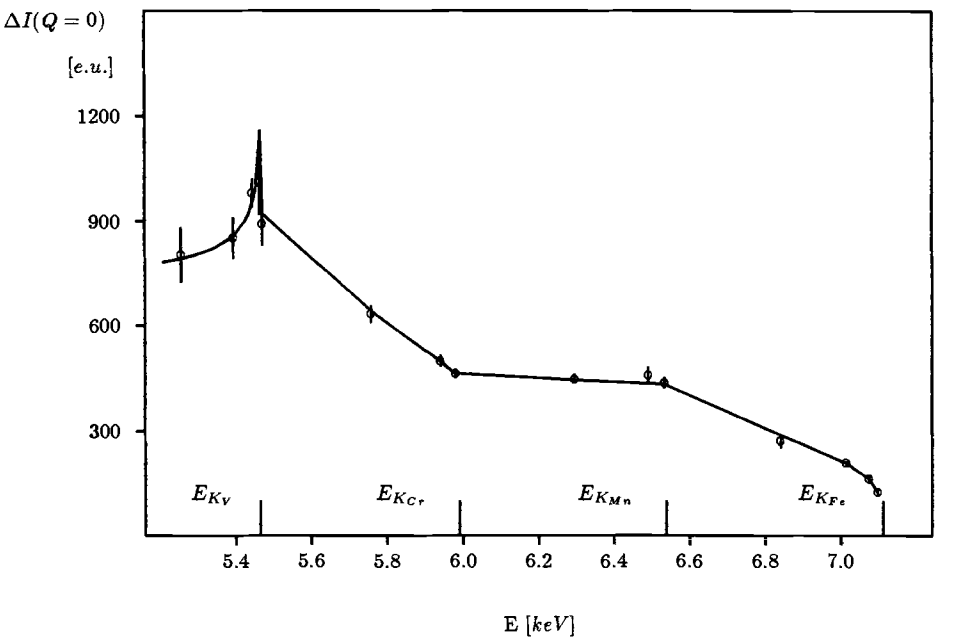


Figure 5: Energy dependence of the SAXS intensity I(Q=0)

energies regarding a variance of 10%. They are consistent with the results of the SANS experiments [3].

Fig. 5 shows the energy dependence of $\Delta I(Q = 0)$. The solid line is calculated for energies smaller than the the energy of the vanadium-K_α-absorption-edge by a fit on the basis that the irradiation-induced precipitates including vanadium. At higher energies the solid line is only a trend curve. The calculation of a physically based curve can be only done if the exact structure of the precipitates is known, because the imaginary part of the atomic form factor of vanadium has to be taken into account (at energies smaller than the absorption edge the imaginary part is nearly zero).

A significant intensity variation is noted at energies near the vanadium-K_α-absorption-edge, which points out that the irradiation-induced precipitates in this steel are vanadium rich. No intensity variation was found at energies near the chromium and manganese absorption edges. This shows that the chromium or manganese content of the precipitates can be neglected. The intensity variation near the iron K-absorption edge is caused by the variation of the mean atomic form factor of the steel matrix. The intensities decrease at energies near of the iron K-absorption edge. This means that the difference between the scattering densities of precipitate $n_P f_P$ and steel matrix $n_M f_M$ decrease with decreasing $n_M f_M$. The scattering density of the precipitate must be smaller than the scattering density of the matrix.

The exact position of an absorption edge depends on the chemical valence state of the element under investigation. There is a nearly linear dependence of the "chemical shift" on the valence. Fig. 6 shows - as a zoom - the energy dependence of $\Delta I(Q = 0)$ near the vanadium K-absorption edge in comparision with the position of metallic vanadium, or carbides of the composition V_4C_3 and VC, respectively. Due to the large error bars of the intensity values $I(Q = 0)$ and the few data points obtained up to now, it is impossible to estimate the exact position of the absorption edge. However, valences the metallic state or between the metallic state and a valence of +3 seem to be possible. This would exclude the composition VC.

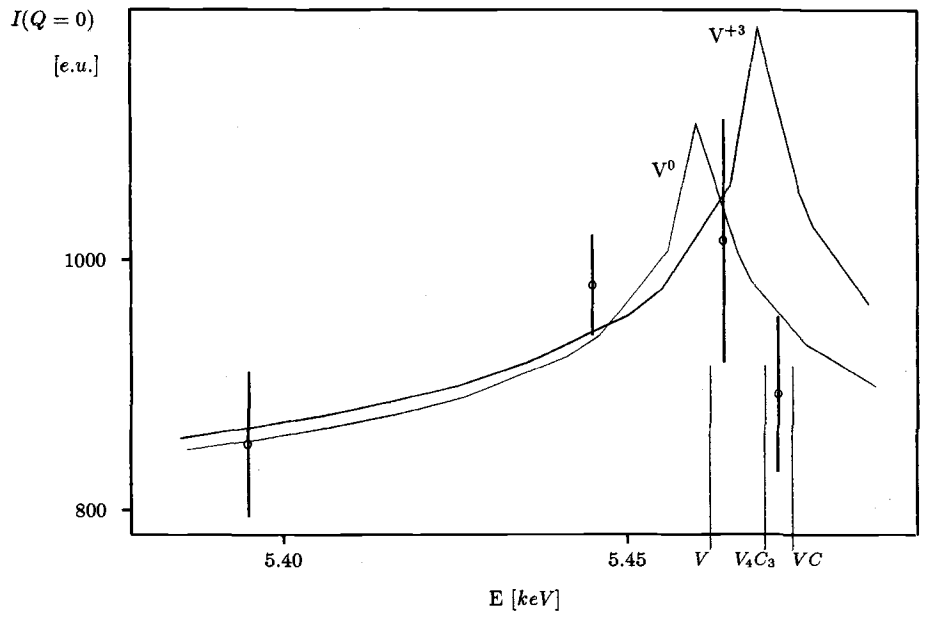


Figure 6: Position of the K-absorption edge of vanadium in the irradiation-induced precipitates (the solid curves are calculated for vanadium valences of 0 and +3, respectively)

The slope of the curve $I(Q=0)$ *vs.* E depends on the ratio of the mean number density of precipitate and matrix $\frac{n_P}{n_M}$. Because of the uncertainty of the position of the absorption edge and of the content of possible additional elements, e.g. C, Fe, Cu, within the precipitates, the ratio $\frac{n_P}{n_M}$ can be limited to the case $0.4 \leq \frac{n_P}{n_M} \leq 0.55$. Any more precise estimation needs to be based on further experiments.

DISCUSSION

The fact that the irradiation-induced precipitates in the steel 15Kh2MFA contain vanadium in a significant manner is noteworthy, because no empirical data about the influence of vanadium on neutron embrittlement are known up to now.

Which kind of vanadium rich precipitates is formed during the irradiation process can be investigated by a comparison of the A-ratio estimated in the SANS experiments with theoretical A-values, calculated for several possible kinds of vanadium rich precipitates (see Tab. 1). For the material with low copper content irradiated to three different fluences, A-ratios of 1.8 to 1.9 were found. The A-ratio is independent of the fluence.

Pure vanadium:– – Vanadium has a coherent nuclear neutron scattering length close to zero. Therefore, pure vanadium has the same A-ratio like voids (A=1.4). Due to the experimental A-value of 1.8 to 1.9 the case of pure vanadium or a mixture of vacancies and V atoms can be excluded.

Vanadium carbide:– – The A-ratio of 1.8 to 1.9 agrees well with V_4C_3 (A=1.9), but not with stochiometric VC (A=2.4) or with the vanadium rich mixing carbide $V_{0.86}Cr_{0.09}Mo_{0.04}Fe_{0.01}C$ found

Kind of precipitate	A-ratio
measured value	1.8..1.9
fcc-copper	11.0
bcc-copper	7.0
voids	1.4
pure vanadium	1.4
VC ($NaCl$ structure)	2.4
VN ($NaCl$ structure)	4.4
$V_{0.86}Cr_{0.09}Mo_{0.04}Fe_{0.01}C$	2.7
V_4C_3 ($NaCl$ structure)	1.9
V_4N_3 ($NaCl$ structure)	2.5
$\alpha' - FeV$ ($CsCl$ structure, ferromagnetic)	2.1

Table 1: Comparision of the measured A-ratio with calculated A-ratio of some possible kinds of precipitates

in the unirradiated state [10] (A=2.7). By the chemical shift of the vanadium K-absorption edge, the existence of V_4C_3 precipitates is supported to a higher degree than the existence of VC particles. The ratio $\frac{n_P}{n_M}$ of the mean number densities in the precipitates and in the matrix, respectively, is 0.7 for the vanadium carbides VC and V_4C_3 with $NaCl$ structure. It is higher than the experimental data. A plausible explanation of this fact would be that the bulk $NaCl$ structure was not completely arised. The assumption of vanadium carbides with V vacancies agrees also well with the results of former positron annihilation spectroscopy experiments [6].

Vanadium nitrides and carbo-nitrides:– – The A-ratios calculated for VN (A=4.4) and V_4N_3 (A=2.5) are significantly higher than 1.9. Therefore, perfect or defected vanadium nitrides can be excluded. Vanadium carbo-nitrides, i.g. $V_4(C,N)_3$, having a small content of nitrogen only could still explain the experimental A-ratio of 1.8 to 1.9, because the replacement of nitrogen by carbon atoms reduces the A-ratio linearly to the value discussed above.

Fe-V phase:– – $\alpha - FeV$ and $\alpha' - FeV$ are ferromagnetic phases. Only for the ordered phase $\alpha' - FeV$ with $CsCl$ structure information about the magnetic moments of the lattice places, needed for the calculation of the magnetic scattering length, were found. The A-ratio of this phase, calculated to be 2.1, is near to the experimental value. The assumption of FeV as the irradiation-induced precipitates also agrees with the chemical shift and the ratio $\frac{n_P}{n_M}$ of the number densities in the precipitates and matrix, respectively. In the case of ferromagnetic FeV precipitates their volume fraction, estimated formerly assuming only non-ferromagnetic precipitates, would be underestimated and thus corrected by the small factor of 1.06.

The assumption that copper rich precipitates contain manganese, too, in order to explain the small A-ratio must be excluded. The experimental ASAXS results at energies near the Mn K-absorption edge give no hint to the existence of such precipitates.

CONCLUSION

For the first time the high content of vanadium in the irradiation-induced precipitates in the VVER-440 type RPV steel 15Kh2MFA was detected by anomalous small angle X-ray scattering. Manganese could not be detected.

The assumption of vanadium rich carbides provides the best agreement with the results of magnetic contrast variation in small angle neutron scattering experiments and the chemical shift of the vanadium K-absorption edge. The assumption of the formation of a ferromagnetic $\alpha' - FeV$-phase agrees fairly good with the experimental results too.

The first assumption agrees well with conclusions drawn from earlier positron annihilation spectroscopy investigations at this material [6].

ACKNOWLEDGEMENTS

This work was sponsored by the Saxony Ministry of Science and Art. The authors would like to thank H.-G. Haubold and G. Goerigk from the KFA Jülich (Germany) for their support in the ASAXS measurements and help in the analysis of the ASAXS data. We are grateful to J.Kočik from the NRI Řež for his support in the sample preparation.

REFERENCES

[1] Radiation Embrittlement of Nuclear Reactor Pressure Vessel Steel: An International Review (Fourth Volume), ASTM STP 1170, L.E.Steele, Editor, American Society for Testing and Materials, Philadelphia, 1993, pp. 99-117

[2] Lukas,G.E., Odette,G.R. Lombrozo,P.M., Sheckhard,J.W.:
"Effects of Composition, Microstructure and Temperature on Irradiation Hardening of Pressure Vessel Steels", Effects of Radiation on Materials: 12th International Symposium, ASTM STP 870, F.A.Garner, J.S.Perrin, Editors, American Society for Testing and Materials, Philadelphia, 1985, pp. 900-930

[3] Brauer,G.; Eichhorn,F.; Frisius,F.; Kampmann, R.:
"Investigation of neutron irradiated Soviet type reactor pressure vessel steels by small angle neutron scattering", Effects of Radiation on Materials: 16th International Symposium, ASTM STP 1175, Arvid S. Kumar, David S. Gelles, Randy K. Nanstad and Edward A. Little, Editors, American Society for Testing and Materials, Philadelphia, 1993, pp. 503-515

[4] Große,M.; Böhmert,J.;Viehrig,H.W.:
"Correlation between Volume Fraction of Irradiation-induced Precipitates and Toughness of Cr-Mo-V alloyed VVER Pressure Vessel Steel", J.Nucl.Mat., 1994, (in press)

[5] Kočik,J., Keilová,E.:
"Radiation Damage Structure of VVER (Cr-Mo-V type) RPV Steels", J.Nucl.Mat. **172**, 1990, 126-129

[6] Brauer,G.; Liszkay,L.; Molnar,B.; Krause,R.:
"Microstructural aspects of neutron embrittlement of reactor pressure vessel steels - A view from positron annihilation spectroscopy", Nuclear Engineering and Design, Vol. 127, 1991, pp 47-68

[7] Brauer,G., Matz,W., Liszkay,L., Molnar,B., Krause,R.:
"Positron Annihilation and Moessbauer Studies of Neutron Irradiated Reactor Pressure Vessel Steels", Material Science Forum 97-99, 1992, pp 379-385

[8] Haubold,H.-G.: "Röntgenkleinwinkelstreuung an Synchrotronstrahlungsquellen", 23. IFF--Ferienkurs "Synchrotronstrahlung zur Erforschung kondensierter Materie", Juelich 1992, pp 29.1-29.31

[9] Große,M., Böhmert,J., Eichhorn,F., Haubold,H.-G., Goerigk,G.: "Resonante Röntgenkleinwinkelstreuung zur Untersuchung bestrahlungsinduzierter Ausscheidungen im Stahl 15Ch2MFA" HASYLAB annual report, 1993, pp. 497-498

[10] Janovec,J., Güth,A., Vyrostkava,A., Stefan,B.: "Umwandlung der Karbidphasen beim Anlassen eines niedriglegierten Cr-Mo-V-Stahls", Neue Hütte Vol. 34, 1989, pp. 91-96

Gerhard Brauer[1], Andreas Kolitsch[2], Henk Schut[3] and A. van Veen[3]

VARIABLE ENERGY POSITRON MEASUREMENTS AT NITROGEN ION BOMBARDED STEEL SURFACES

REFERENCE: Brauer, G., Kolitsch, A., Schut, H., and van Veen, A., **"Variable Energy Positron Measurements at Nitrogen Ion Bombarded Steel Surfaces,"** *Effects of Radiation on Materials: 17th International Symposium, ASTM STP 1270,* David S. Gelles, Randy K. Nanstad, Arvind S. Kumar, and Edward A. Little, Eds., American Society for Testing and Materials, 1996.

ABSTRACT: Nitrogen ion bombardment of steel samples has been studied by utilizing the Delft variable energy positron beam facility. The energy of the beam was varied between 250 eV and 25 keV and a line-shape parameter S describing the annihilation radiation has been measured. By use of the VEPFIT fitting programme, up to five different layers, each having different densities, could be identified and characterized. The results show that carbon layers deposited during nitrogen implantation can be observed. A relation between the measured depth profiles of nitrogen, carbon and oxygen by Elastic Recoil Detection Analysis (ERDA) and the results of positron annihilation is given and discussed. The wear and friction properties of the steel surfaces before and after nitrogen implantation are presented.

KEYWORDS: tool steel, nitrogen implantation, carbon surface layer, variable energy positron beam, elastic recoil detection analysis, wear resistance

---

Ion implanters without mass separators and vacuum systems based on oil diffusion pumps are potential sources of target contamination due to hydrocarbon cracking products, especially in connection with long implantation times. The deposition of an additional carbon layer may have a large influence on the wear and friction behaviour of ion implanted steels. Therefore, methods to characterize thin layers are required in order to study this effect in more detail.

Recently, the influence of the simultaneous deposition of carbon layers during the implantation of nitrogen ions into specimens of 210Cr46 tool steel has been reported in some detail /1/. Depth profiles of C, N, and O atoms were measured in the near surface region of the specimens

---

[1] Group leader, Positron group of TU Dresden at Research Centre Rossendorf, Inc., D-01314 Dresden, Germany
[2] Research scientist, Institute for Ion Beam Physics and Material Research, Research Centre Rossendorf, Inc., D-01314 Dresden, Germany
[3] Research scientist and Professor, respectively, Interfaculty Reactor Institute, TU Delft, Mekelweg 15, NL-2629 JB Delft, The Netherlands

Copyright© 1996 by ASTM International www.astm.org

using elastic recoil detection analysis (ERDA) and correlated with the wear resistance measured by means of a pin-on-disk arrangement.

Positron annihilation spectroscopy (PAS) is a powerful tool for the investigation of bulk properties of materials as well as the defects therein with electron densities less than average, vacancies and vacancy clusters (voids) in particular. In special cases, it can also give useful information about precipitates /2, 3/. In recent years variable energy positron beams became available which allow the study of properties of layered structures. Here we report the basic principle of such measurements and their application to the problem of carbon layers deposition during ion implantation.

POSITRON ANNIHILATION TECHNIQUE

The energy shift from 511 keV due to the non-zero momentum of the annihilating positron-electron pair results in a broadening of the photo-peak as observed in a measured annihilation photon spectrum. This broadening is characterized by the so-called S(shape)-parameter. This parameter is defined as the ratio of the number of counts in a fixed central region of the 511 keV peak and the total number of counts in the peak. The regions are chosen so as to obtain a maximum sensitivity of S to the Doppler broadening, which in practice corresponds to S-parameter values of about 0.5. Since S is an overall parameter of the shape of the 511 keV peak, it reflects the total momentum available in the positron annihilation process. Free or unlocalized positrons can annihilate with both core and conduction electrons, whereas a positron trapped in a vacancy has a higher probability to annihilate with a conduction electron. As a result, the high-momentum contributions to the 511 keV peak are reduced and the peak becomes narrower, thus leading to a higher S-parameter value as compared to a defect free (reference) specimen.

In a typical positron beam Doppler-broadening measurement, positrons are implanted with selected energies ranging from about 100 eV to 30 keV /4/. These energies are well above the thermal energy given by $k_B T$. After the implantation, the positron looses its kinetic energy in a variety of interactions with the lattice, such as scattering, ionisation and electron and phonon scattering. This slowing down process finally results in a depth distribution of implanted or "stopped" positrons. A mathematical description of this implantation profile, denoted by P(E,z), has been obtained from Monte Carlo calculations. It has been parameterized by a so-called Makhov profile /5/:

$$P(E,z) = (m * z^{m-1}) / (z_o^m) * \exp(-(z/z_o)^m) \quad (1)$$

where P(E,z)dz is defined as the fraction of positrons implanted with energy E that will be stopped at a depth z and z+dz. The penetration parameter z_o is related to the mean implantation depth z_m by:

$$z_m = z_o \, \Gamma(1 + 1/m) \quad (2)$$

It is assumed that:

$$z = (\alpha/\rho) * E^n \quad (3)$$

with ρ = the density of the material and α = a constant. The values of the profile parameters n and m are normally chosen as 1.62 and 2, respectively /6/.

The processes to which thermal positrons are subjected, via implantation, diffusion, drift due to electric fields, trapping and annihilation, can be combined in the one-dimensional steady-state diffusion equation:

$$D_+(d^2(z))/dz^2 - d(\nu_d(z)c(z))/dz - (\nu_t n_t(z) + \lambda_b)c(z) + I(E,z) = 0 \qquad (4)$$

Here D_+ = the positron diffusion coefficient, $c(z)$ = the positron distribution as a function of the depth z, ν_d = the positron drift velocity, n_t = the defect density, ν_t = the trapping rate of defects for positrons, λ_b = the positron annihilation rate and $I(E,z)$ = the energy and depth dependant positron implantation rate. This equation forms the basis of the computer program VEPFIT, developed for modelling and fitting positron beam experimental data /7/. The positron diffusion length L_+ is related to the diffusion coefficient D_+ via:

$$L_+ = (D_+/\lambda_b)^{1/2} \qquad (5)$$

In case of materials with an uniform defect distribution the positron diffusion length reduces to an effective diffusion length $L_{+,eff}$ due to trapping in defects:

$$L_{+,eff} = (D_+/(\lambda_b + \kappa_t))^{1/2} \qquad (6)$$

with the positron trapping rate into defects, κ_t, defined as $\nu_t n_t$.

EXPERIMENTAL

Positron beam--The positron annihilation Doppler broadening experiments have been performed with the Delft Variable Energy Positron beam /8, 9/. This apparatus consists of a 70 mCi ^{22}Na source (90 % positron decay events, half life 2.6 y) placed in a vacuum chamber. The ^{22}Na source emits positrons with a typical β-decay energy spectrum with an end point energy of 0.54 MeV. These fast positrons are moderated to thermal energies in a 7 μm thick 99.95 % pure polycrystalline tungsten foil in transmission moderation geometry. The moderator foil reemits the positrons with an energy of about 3 eV. These now slow positrons are preaccelerated to an energy of 115 eV and transported in vacuum to the final accelerator stage and subsequently to the sample chamber. The maximum attainable acceleration voltage is 30 kV and the efficiency of the conversion from fast to slow positrons is of the order 10^{-4} resulting in a beam of approximately 10^5 slow positrons per second. The positron transport from the source chamber to the sample chamber is achieved by a 10mT static magnetic field produced by 14 coaxial solenoids positioned in a Helmholtz configuration. The diameter of the positron beam is approximately 10 mm.

A grid is located in front of the sample. By applying a positive voltage (typically 10-50 V) to this grid the reemitted positrons from the sample are forced to return to the sample surface. A negative grid voltage in combination with an E x B filter removes these positrons from the sample area. The specimens are mounted on a sample holder which can carry five specimens with dimensions of 20 x 20 mm^2. The sample holder is connected to a linear motion feedthrough and by moving it vertically, one of the specimens is positioned in the positron beam. The specimens can be heated in situ by accelerated electrons emitted by a tungsten filament. The temperature of the specimens is measured with a Chromel/Alumel thermocouple.

The photon detection system consists of an intrinsic Ge-detector with a measured resolution of 1.75 keV and a relative efficiency of 33.1 % at 1.33 MeV. Pulses from the preamplifier are fed into a fast main amplifier connected to a 450 MHz Analog-to-Digital convertor (ADC). To improve long term stability, a two-point stabilizer has been added, which corrects for small changes in the gain and offset of the spectrometer system. The output of the ADC is accumulated in the spectrum buffer of a

Multi-Channel-Analyser located in a 16 MHz 386DX IBM compatible computer. The width of the spectrum is 4096 channels. During a measurement, the acceleration voltage and thus the positron energy is adjusted automatically to predefined values. This is achieved by sending output signals from a Digital-to-Analog convertor in the computer to the high voltage power supply connected to the accelerator stage.

Sample preparation--Six polished samples of 210Cr46 tool steel were

TABLE 1--Conditions of nitrogen implantation of the tool steel samples

Parameter	Implantation
Ions	N^+, N_2^+
	100% N_2 gas inlet
	80% N_2+20% air inlet
	60% N_2+40% air inlet
Energy	$E=50$ keV
Beam current density	$I=4\ \mu A\ cm^{-2}$
Ion fluxes	$F=8\times10^{17}$ ions cm^{-2}
Irradiation time	$t=600$ min
Baffle temperature	25 °C water cooled
	40 °C water cooled
	60 °C water cooled
Vacuum	10^{-3} Pa

TABLE 2--Sample preparation

Sample number	Baffle temperature (°C)	Gas inlet for ion source
1	25	100% N_2
2	40	100% N_2
3	25	80% N_2+20% air
4	40	80% N_2+20% air
5	25	60% N_2+40% air
6	40	60% N_2+40% air

implanted with 50keV nitrogen ions under different vacuum conditions using an oxygen admixture of the ion source gas at the Research Centre Rossendorf (see Tables 1, and 2, respectively). An unimplanted, polished steel specimen as well as samples 2 and 4, respectively, have been used for the variable positron beam studies.

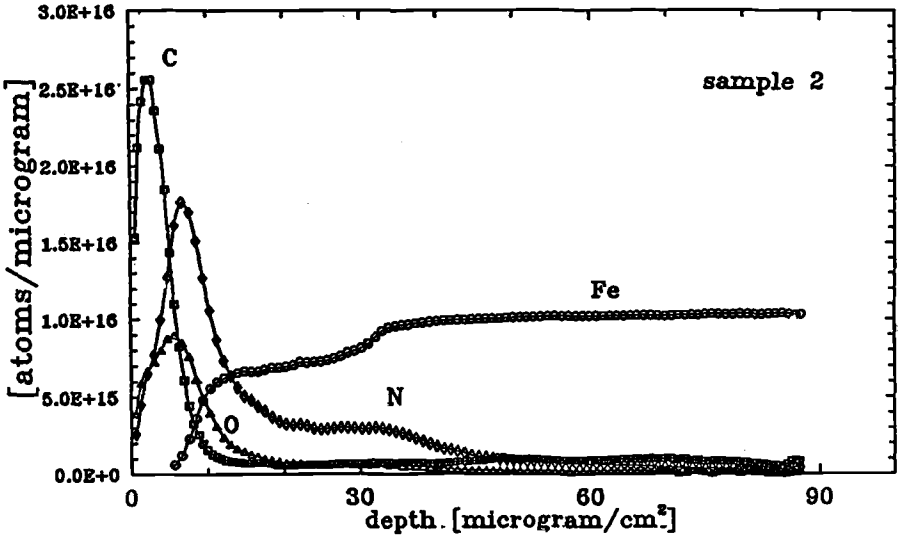


Fig. 1--Depth profiles of carbon, oxygen, nitrogen, and iron, respectively, measured by ERDA in sample 2

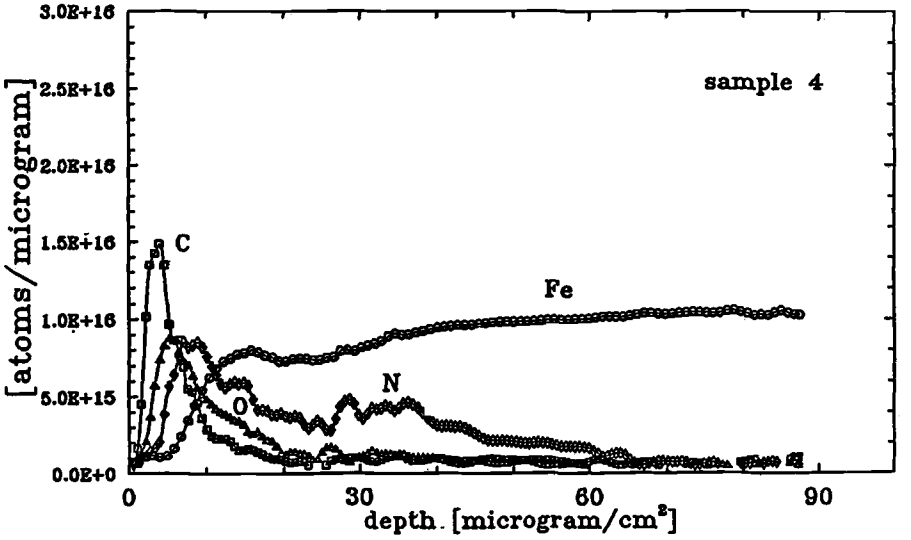


Fig. 2--Depth profiles of carbon, oxygen, nitrogen, and iron, respectively, measured by ERDA in sample 4

RESULTS AND DISCUSSION

The application of Bragg-curve spectroscopy to ERDA of carbon layers deposited on steel surfaces is described in ref./1/. Resulting depth profiles of carbon, oxygen, nitrogen and iron for specimens 2 and 4 are shown in Figs. 1 and 2, respectively. Furthermore, the wear behaviour of all steel samples has been examined using a pin-on-disk arrangement. The volume abrasion was determined in relation to the sliding distance of a fixed, hardened (HRC=60) bearing ball with 3 mm diameter on the rotating steel disk. In these experiments, the pin ball moved on the disk with a velocity of 1 m s^{-1} and a load of 0.8 N. The wear tests were performed at 303 K in air without lubrication. The results are shown in Fig.3.

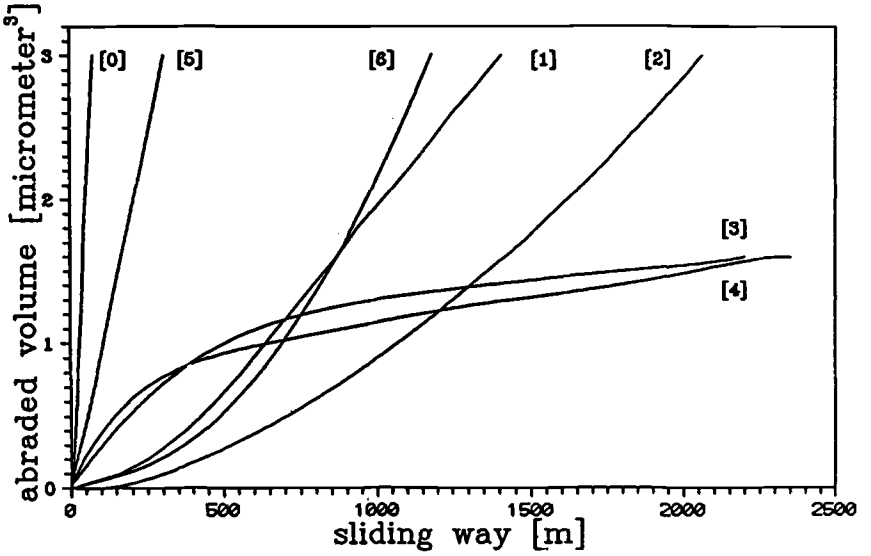


Fig. 3--Volume abrasion vs. sliding distance for non-implanted (sample 0) and nitrogen implanted (samples 1-6) 210Cr46 steel

The results of the positron beam Doppler broadening measurements on the implanted samples 2 and 4 as well as the unimplanted reference sample (in the as-received (polished) state and after annealing for 30 min at a temperature of 770 K) are presented in Fig. 4. The lines in this figure represent the fits to the data using the VEPFIT programme. In VEPFIT, a model is applied in which the samples are represented by a layered structure composed of materials with different densities. The number of layers depends on the sample preparation. Fitting parameters for the different layers are the S-parameter, the position of the boundary between two adjacent layers (d) and for the reference sample, the positron diffusion length (L_+). The effect of annihilation of epithermal positrons is accounted for in the top layer only ($S_{epithermal}$). A summary of the fitting results is given in Table 3.

Reference sample--The measurement on the as-received, polished reference specimen shows a rapid decrease for positron energies increasing from 0 to 4 keV. From 4 keV to about 10 keV the S-parameter slightly increases and for higher positron energies a slow decrease is observed. In order to obtain a satisfactory fit at least two layers had to be assumed. The relatively short diffusion length and somewhat higher S-parameter value

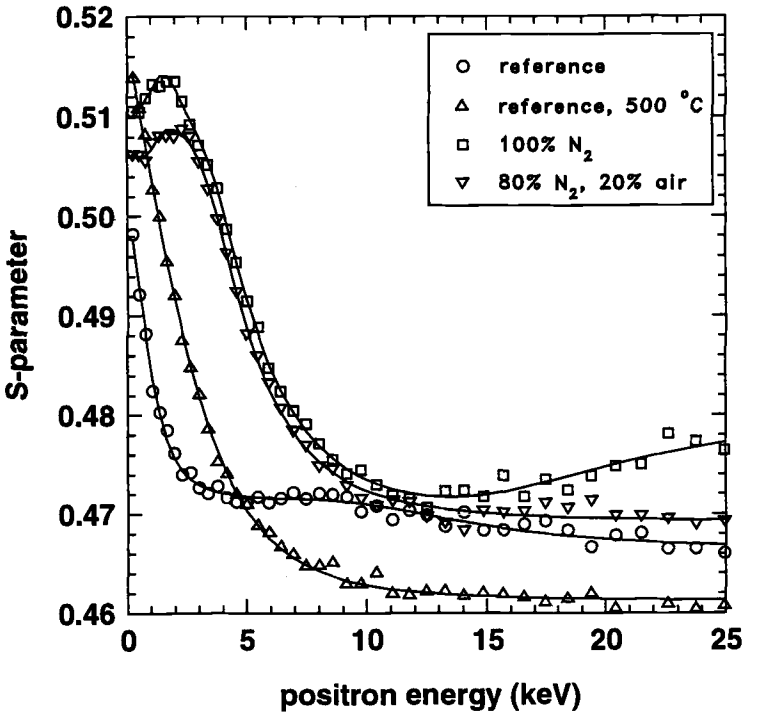


Fig. 4--Doppler broadening lineshape parameter S as a function of incident positron energy for different steel samples

as compared to the bulk value) in the top layer (layer 1) are indicative for the presence of small vacancy-type defects in this layer. These defects are likely to produced during the mechanical polishing of the sample. Therefore, the sample was annealed for 30 min at a temperature of 770 K. The effect of annealing is seen by a reduction of the S-parameter for the bulk and by an increase of the positron diffusion length from 9 to 30 nm. Moreover, the measured data could be fitted with a model consisting of one single layer. These observations confirm the assumption that small vacancy-type defects are present in the as-received, polished sample.

Sample 2--The implantation of 50 keV N^+ ions from a 100 % nitrogen atmosphere results in a strong increase of the S-parameter in the near surface region. With a positron implantation energy of about 10 keV, the S-parameter approaches the value measured for the as-received, polished reference sample. Above 15 keV, an increase of S is observed. Based on the ERDA depth profiling results /1/, the positron data were fitted assuming a structure composed of five layers. The density of the top layer is set to 2.5 g cm^{-3} (carbon), the second layer is believed to have a density of about 5.5 g cm^{-3} (possibly iron oxide + N), while the density of the deeper layers is set to the density of iron. Because of the relatively large number of layers only the position of the layer boundaries and S-parameters have been fitted. The fit gives an S-value of 0.512 for the top layer. This value is in agreement with results of

measurements on carbon layers sputtered onto Si substrate. At the moment it is not clear, why positron energies above 15 keV (in this model

Table 3--Summary of the VEPFIT fitting results. The parameters with superscript[f] as well as the densities are fixed parameters.

		reference + 500 °C	reference as polished	100% N_2	80% N_2 + 20% air
$S_{surface}$		0.5023(6)	0.4825(13)	0.5065(78)	0.5059(80)
$S_{epithermal}$		0.5157(10)	0.5010(11)	0.5123(49)	0.5065(50)
layer 1	S	0.4612(2)	0.4712(3)	0.5127(20)	0.5058(22)
	L(nm)	29(1)	9(2)	5[f]	5[f]
	d(nm)	∞	342(30)	28(4)	26(5)
	ρ(g/cm^3)	7.86	7.86	2.5	2.5
layer 2	S		0.4662(4)	0.5230(38)	0.5129(26)
	L(nm)		25[f]	5[f]	5[f]
	d(nm)		∞	39(4)	41(6)
	ρ(g/cm^3)		7.86	5.5	5.5
layer 3	S			0.5049(7)	0.5059(8)
	L(nm)			5[f]	5[f]
	d(nm)			82(3)	75(4)
	ρ(g/cm^3)			7.86	7.86
layer 4	S			0.4698(3)	0.4692(2)
	L(nm)			14[f]	14[f]
	d(nm)			656(26)	∞
	ρ(g/cm^3)			7.86	7.86
layer 5	S			0.4811(8)	
	L(nm)			14[f]	
	d(nm)			∞	
	ρ(g/cm^3)			7.86	

corresponding to a depth larger than 650 nm) result in a higher S value than that found for the bulk.

Sample 4--The S-parameter curve measured for this sample has the same overall shape as the one observed for sample 2. The differences are the lower fitted values for the two top layers and the absence of the rise in S for high positron energies. The latter enabled a fit with a model consisting of four layers only. It was found, however, that the fitted positions of the remaining layer boundaries correspond to those found for sample 2.

In Fig. 5 the fitted S-parameter values for the four measurements are shown as a function of depth below the surface. This figure shows that the implantation leads to an overall increase of the S-parameter up to a depth of about 75 nm suggesting the presence of vacancy-type defects in the nitrogen implanted region connected with and/or in addition to the formation of chemical (nitrogen) compounds. Annealing studies could help to clearify this problem. As theoretical support, the very recently calculated positron properties of several carbides and nitrides which have been extensively discussed in connection with the application of PAS to the problem of neutron embrittlement of reactor pressure vessel steels /10, 11/, may also provide valuable insights.

From Fig. 5 it becomes clear that the layer structure found by ERDA /1/ in the implanted steel samples can be detected by variable positron beam experiments as well. ERDA is known to be a very useful method to detect light elements (low z number) within a heavier matrix (high z number) whereas variable energy positron measurements are well suited for the detection of vacancy-type defects produced by ion implantation in

multilayer systems. Here we need to know the specific trapping rate ν_t for positrons at vacancies in steel. If we adopt the diffusion length

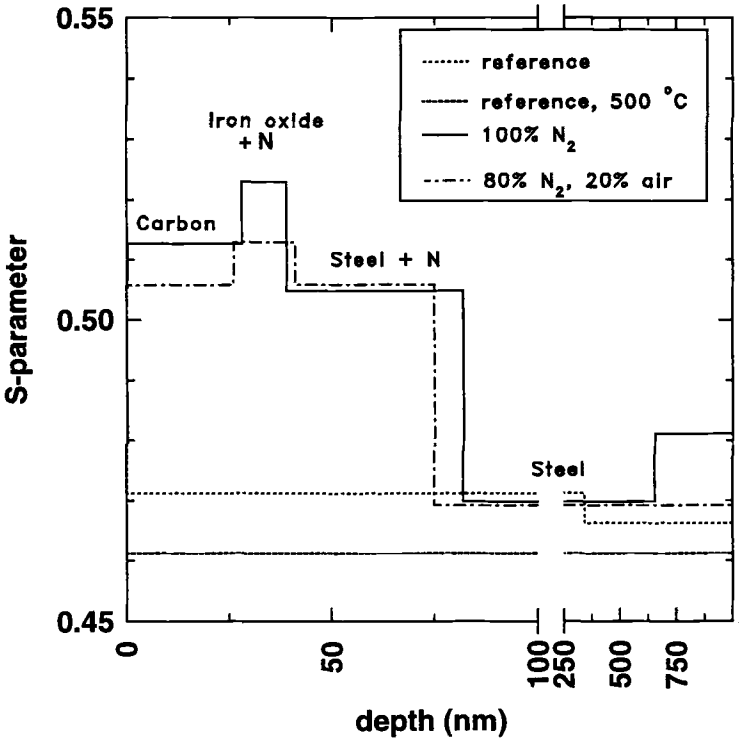


Fig.5--Doppler broadening lineshape parameter S as a function of implantation depth

measured for the 737 K reference sample as the "defect free" diffusion length L we can use equations 5 and 6 to calculate the vacancy concentration by:

$$\kappa_t = n_t \nu_t = \lambda_b \, (L^2/L_{eff}^2 - 1) \qquad (7)$$

Numbers on diffusion lengths are found in Table 3. However, it is still impossible from the present measurements to draw definite conclusions concerning the different wear behaviour due to different ion implantation conditions (Fig. 3).

CONCLUSIONS

The present study has shown that variable positron beam experiments are well suited to the study of ion implanted materials and the detection of carbon layers co-deposited with the ion implantation into the steel. This suggests the combined use of this method and ERDA for future studies of multilayer systems produced by ion implantation.

It has been shown that monoenergetic positrons are extremely sensitive regarding the detection of vacancy-type defects near the surface of the as-received, polished reference sample. However, due to this sensitivity, any more detailed analysis of the measured data is somewhat hampered by the presence of these defects and the rather complex structure due to the formation of carbon and iron oxide layers. Therefore, in future experiments it should be possible to overcome these difficulties by a more careful sample preparation in order to obtain still more detailed results.

These results show, that for the explanation of the wear resistance behaviour it is necessary to analyse the phase state, lattice parameters and chemical bonding especially of the carbon layer.

REFERENCES

/ 1/ Kolitsch, A., Hentschel, E., and Richter, E., "Depth profiles of carbon, nitrogen and oxygen on carbon coated steel surfaces made by ion beam assisted deposition", Diamond and Related Materials, Vol. 2, 1993, pp 1175-1178

/ 2/ "Positrons in Solids", Topics in current physics, Vol. 12, P. Hautojärvi, Editor, Springer, Berlin, 1979

/ 3/ "Positron Solid-State Physics", Proc. International School of Physics "Enrico Fermi", Course LXXXIII, Varenna on Lake Como, 1981. W. Brandt and A. Dupasquier, Editors, North Holland, Amsterdam, 1983

/ 4/ Schultz, P.J. and Lynn, K.G., Rev. Modern Physics, Vol. 60, 1988, pp 701-779

/ 5/ Valkealahti, S. and Nieminen, R.M., Appl. Phys. A, Vol. 32, 1983, pp 95-106, and Appl. Phys. A, Vol. 35, 1984, pp 51-59

/ 6/ Vehanen, A., Saarinen, K., Hautojärvi, P., and Huomo, H., Phys. Rev. B, Vol. 35, 1987, pp 4606-4610

/ 7/ van Veen, A., Schut, H., de Vries, J., Hakvoort, R.A., and IJpma, M.R., in: "Positron Beams for Solids and Surfaces", AIP Conf. Proc., Vol. 218, P.J. Schultz, G.R. Massoumi, and P.J. Simpson, Editors, New York, 1990, pp 171-196

/ 8/ Schut, H., "A variable energy positron beam facility with applications in materials science", Thesis, Delft University of Technology, Delft, 1990

/ 9/ Hakvoort, R.A., "Applications of positron depth profiling", Thesis, Delft University of Technology, Delft, 1993

/10/ Puska, M.J., Sob, M., Brauer, G., and Korhonen, T., "First-principles calculation of positron lifetimes and affinities in perfect and imperfect transition-metal carbides and nitrides", Phys. Rev. B, Vol. 49, 1994, pp 10947-10957

/11/ Brauer, G., Puska, M.J., Sob, M., and Korhonen, T., "Positron affinity for precipitates in reactor pressure vessel steels", Nuclear Engineering and Design, Vol. 158, 1995, pp 151-158

Christian BRILLAUD[1] , Thierry MEYLOGAN[1] and Paul SALATHE[1]

USE OF LASER EXTENSOMETER FOR MECHANICAL TESTS ON IRRADIATED MATERIALS

REFERENCE: Brillaud, C., Meylogan, T. and Salathe, P., **"Use of Laser Extensometer for Mechanical Tests on Irradiated Materials,"** *Effects of Radiation on Materials: 17th International Symposium, ASTM STP 1270,* David S. Gelles, Randy K. Nanstad, Arvind S. Kumar, and Edward A. Little, Eds., American Society for Testing and Materials, 1996.

ABSTRACT: Techniques have been developed by EDF's hot laboratory in Chinon for performing mechanical tests on irradiated materials. Some of these techniques aim to facilitate strain measurements, which are particularly difficult to perform on irradiated specimens at high temperatures or on subsize specimens.

Recent progress has been driven by laser technology combined with software development. The use of this technique, which allows strain measurements without contact on the specimen, is described for tensile (especially on subsize specimens), fatigue and creep tests.

KEY WORDS: laser, extensometer, strain, measurement

Mechanical characterization of materials requires an accurate measurement of the deformation of the specimen during the test. The most frequently used devices are resistance strain gage extensometers, LVDT (linear variation differential transformer) inductive transducers and, more rarely, capacitive transducers. All these devices have limitations in use, particularly with respect to temperature. Adhesives of strain gage extensometers are unable to withstand a temperature greater than 150°C ; above this temperature, intermediate devices, which are complex or brittle must be used to transmit the measurement outside the furnace. The accuracy of LVDT transducers is not always compatible with test specifications. In general, calibration under test conditions of all these devices remains a delicate operation, when it can be carried out at all. These are not the only difficulties encountered by laboratories ; there is also the geometry of the specimens, which does not always allow conventional extensometers to be used, or which necessitates a wide variety of transducers to cope with the various types of tests to be carried out. Finally, tests which must be performed in hostile environments, in particular on irradiated materials, involve the installation and calibration of extensometers in hot cells by remote handling, which is a difficult, even impossible, operation.

[1] Electricité de France - Groupe des laboratoires - Service Contrôle des Matériaux Irradiés
B.P. 23 - 37420 AVOINE - FRANCE

Copyright© 1996 by ASTM International www.astm.org

All these difficulties often mean that, instead of carrying out deformation measurements directly on the specimen, laboratories use alternative techniques which are never entirely satisfactory from an experimental point of view. For these reasons, the EDF's hot laboratory (*Service Contrôle des Matériaux Irradiés - SCMI*) decided to develop an extensometry technique which was capable of satisfying the requirement for mechanical characterization of irradiated materials from power plant components such as fuel rod or rod cluster cladding tubes, thimble tubes, the pressure vessel or internal structures, etc. The technique chosen is ombroscopy [*1*]. The equipment used to develop the technique is based on a commercial laser used in production control.

Laser metrology

Measuring principle

Measurement by ombroscopy consists of placing the object to be measured, which must be opaque and convex in shape, in the parallel beam of a laser transmitter. The shadow projected by the object is registered by the receiver, and then measured (Fig. 1).

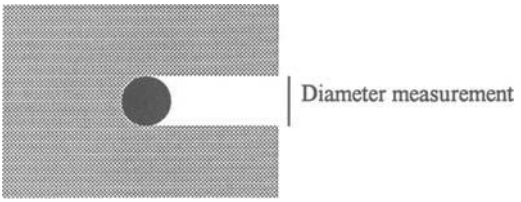


FIG. 1—*Ombroscopy principle.*

The transition from an area of shadow to an illuminated area is called a edge. An object generates two edges, and the receiver measures the distance between the two edges to give its size. Several objects can be placed simultaneously in the laser beam; by measuring the distance between the various successive edges of the illuminated or dark segments, the device can give the size of the objects and the distances between them (Fig. 2).

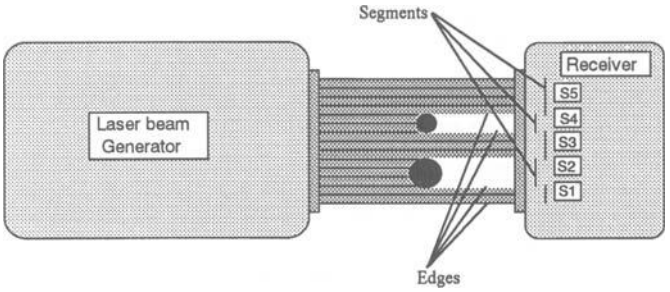


FIG.2—*Principle of size and distance measurements.*

Description of the equipment

The laser device includes a helium-neon type laser transmitter and a receiver, which must be aligned with one another. A processor controls the operation of the device and also data processing.

The laser transmits a beam of visible red light with a diameter of 0.25 mm which is reflected by a revolving mirror located at the focal point of a lens (Figure 3).

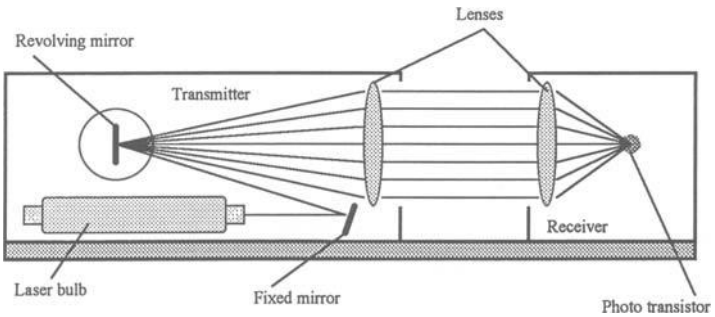


FIG. 3—*scheme of laser device.*

The beam, whose displacement is made parallel by its passage through the lens, has a high scanning frequency, which enables us to obtain a patch 50 mm wide, in which the object to be measured is placed.

The receiver lens collects the beam transmitted and converges it onto a phototransistor, located at the image focus, which transmits a 5 volt analog signal when it is illuminated, or 0 volts when it is not (Fig. 4). The processor carries out a time measurement, based on the signal transmitted by the phototransistor between the different edges.

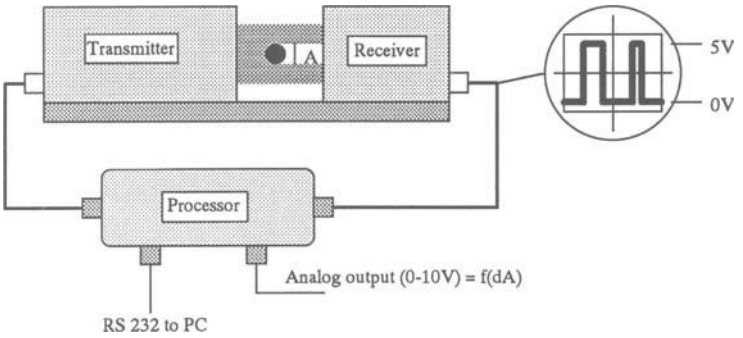


FIG. 4—*Scheme of the equipment.*

This measurement of time is converted into a distance which corresponds to the length of the various illuminated or dark segments thanks to a prior calibration using standard gages. Objects, or the distance between them, can be measured by this way. The device supplies the measurement in the form of a digital or analog signal. The average of several measurements is required to obtain a good accuracy. The measurement frequency used is 600 Hz.

Based on commercially available equipment, this measuring technique was adapted by the SCMI to a certain number of tests as described below.

Extensometry for mechanical tests

During a mechanical test, the deformation of the specimen subjected to an imposed load (tensile, shear etc.) is a particularly important piece of information. When combined with the stress, its allows the material's behaviour to be characterized.

Strain measurement requires the definition of a reference length, which depends on the geometry of the specimen to be tested. This reference length must be selected on the specimen in an area in which the deformation is homogeneous (for example, the calibrated part of a tensile specimen). Monitoring of deformation during the test is traditionally carried out using mechanical gage extensometers equipped with blades for attachment to the specimen to be tested. The distance between the blades determines the reference length.

When the laser is used for extensometry, the reference length is identified by a segment of the patch resulting from the intersection of the laser beam and the object to be measured. Change in length of this segment provides data on the deformation of the sample.

The tubular geometry of specimen, for types of test such as creep under internal pressure or burst test, leads to choose the diameter of the tube as the reference length. In this case, the sample is placed perpendicular to the plane of the laser patch and the segment measured for monitoring of deformation is the "dark" segment of the patch (Fig. 1).

Measurement of axial deformation by laser extensometry during a tensile test is more delicate since, contrary to the previous case, the reference length is not clearly identified. Two locators, or targets, used to define the area of deformation measurement, must thus be placed on the calibrated length (i.e. the length of homogeneous deformation). These targets, which are machined at the same time as the specimen, cut the laser beam into 5 segments, 3 of which are "illuminated" and 2 "dark" (Fig. 5).

In this case, the axis of the specimen is parallel to the plane of the laser patch. The deformation is monitored by recording the variations of the central illuminated segment.

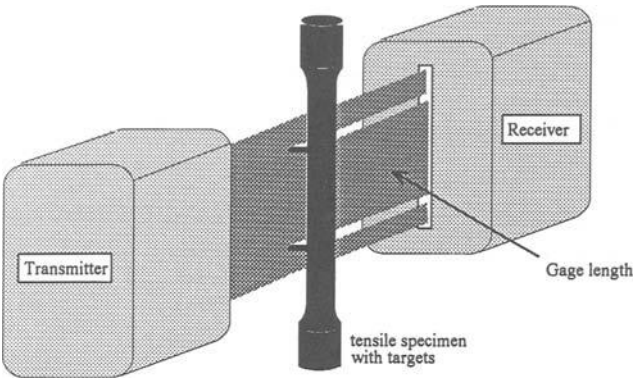


FIG. 5—*Scheme of strain measurement on tensile test.*

Practical examples of use

Extensometry by laser ombroscopy is currently used for most tensile tests and for internal pressure creep tests on fuel rod cladding tubes.

For tensile tests on cylindrical specimens, targets are fixed by spot welding a metal wire 0.2 mm in diameter at each end of the gage length. For example, Figure 6a shows a photograph of a tensile specimen used for surveillance of pressure vessel steel under irradiation. The device developed for welding the targets onto the specimen in the hot cell is shown in Figure 6b.

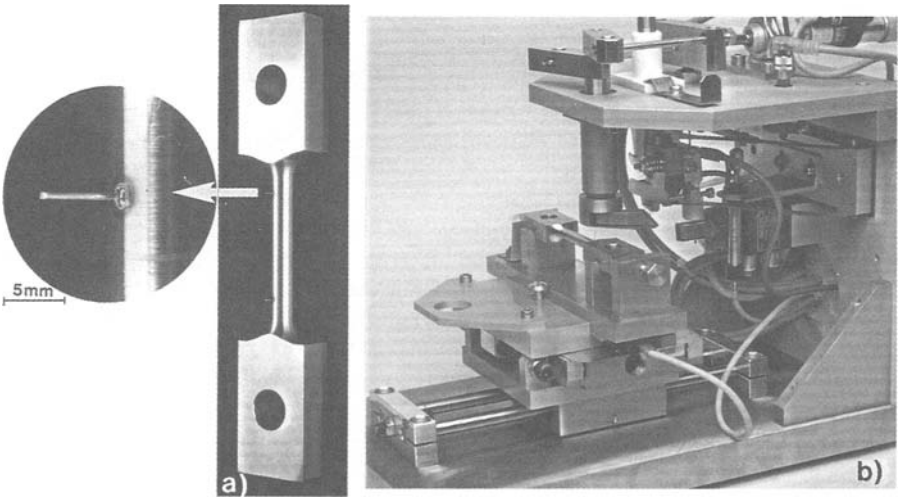


FIG. 6—*(a) tensile specimen and target detail, (b) device for welding the targets.*

Two other types of tensile specimens have been adapted to laser extensometry. The targets are machined directly on the specimen, during the electroerosive machining process. This involves the double wing specimen used to characterize the fuel cladding tubes (Fig. 7a), as well as a subsize tensile specimen used to characterize bolts taken from the internal reactor structures (Fig. 7b).

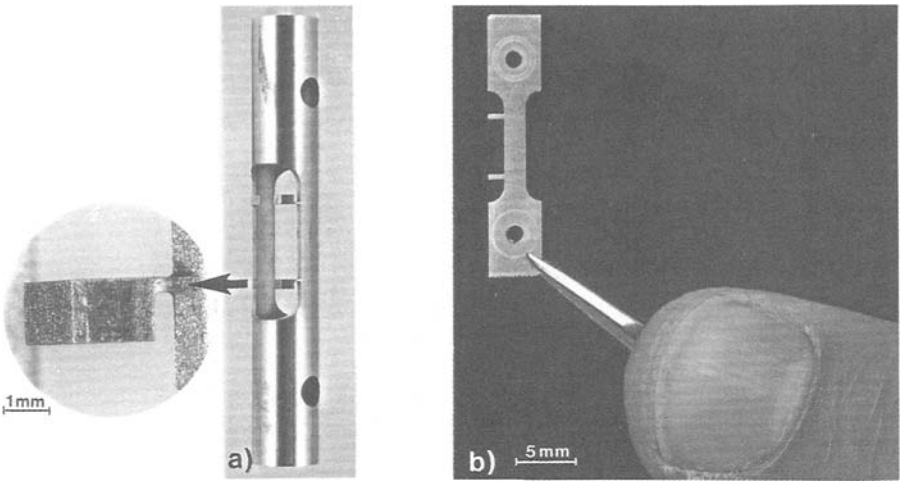


FIG. 7—*An example of target on double wing specimen (a) and subsize specimen (b).*

In the case of creep tests on fuel cladding tubes, the deformation is measured directly on the external diameter of the specimen. The device was designed to allow simultaneous testing of 5 samples "stacked" in the same plane. A microcomputer is used to acquire the data, as well as controlling the movement of the laser, at time intervals suited to the creep rate (Fig. 8).

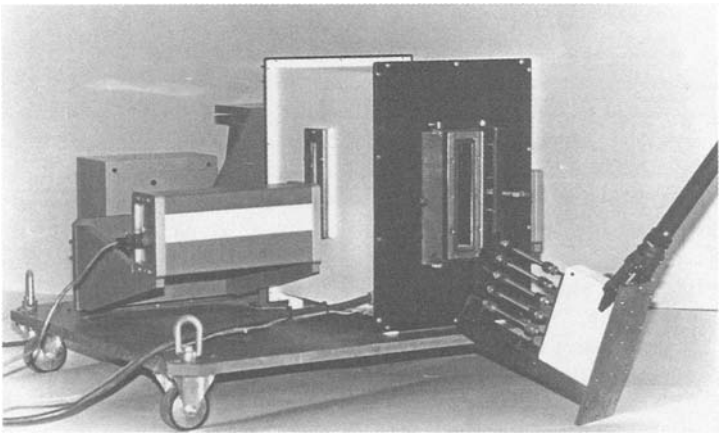


FIG. 8—*Photograph of creep test device.*

Temperature tests

The furnaces used are designed to allow the passage of the laser patch and to carry out tests up to a temperature of 400°C. For tensile tests, a tubular type furnace is used, which opens into two half-cylinders in a longitudinal plane. A space has been incorporated into the closure plane of the furnace between the two half-cylinders for the passage of the laser patch directly in front of the specimen (Fig. 9).

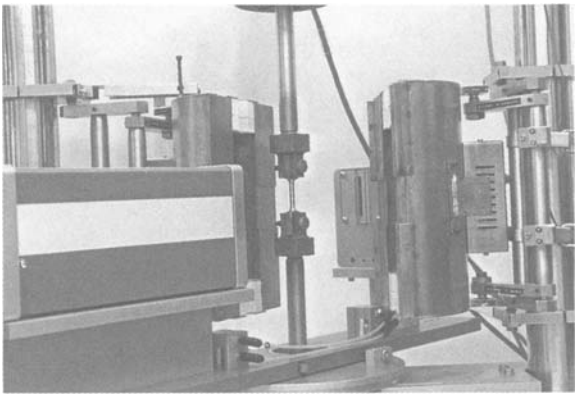


FIG. 9—*Device for tensile test in environmental chamber with laser extensometer.*

Very accurate alignment of the various parts (transmitter, receiver, furnace and specimen) is essential. For creep tests, the furnace is a parallelepiped with a window on either side of the specimens, for the passage of the laser patch. In order to avoid reflections towards the transmitter and the receiver creating interference, the glass in the windows is not set perpendicular to the axis of the beam.

Dynamic tests

The use of laser extensometry for dynamic tests is more delicate. By its design (revolving mirror), the signal received by the receiver is a discontinuous signal, whose period depends on the type of mirror (number of faces) used and the rotation speed of the motor. The type of laser described in section 1 is referenced as a "600 Hertz" laser, as the time between two successive signals received is 1/600 seconds, or approximately 1.7 ms. During this period, no measurements are carried out, although the specimen continues to deform. Recording variations in the deformation of a specimen placed in the laser patch thus leads to a signal sampled at a frequency of 600 Hz. This frequency constitutes one of the limitations of the laser in measuring deformation for high-speed tests. In fact, the Shannon condition states that a signal must be sampled at a frequency **at least** twice the **maximum** frequency of the signal to be measured. Then, it is possible to rebuild the real signal from the sampled signal without loss of information. At a sampling frequency of 600 Hz, signals whose frequency spectrum extends up to 300 Hz can thus, in theory, be recorded. In practice, for simple readouts or temporal processing (calculating maxima,

slopes, build-up times etc.), a factor of 10 is generally assumed between the sampling frequency and the maximum frequency of the signal to be measured in order to obtain a sufficient number of measuring points.

Fatigue tests

Laser extensometry can be used for monitoring the deformation of a specimen under cyclic stress. However, in addition to the limitations regarding test frequency described above, the effect of averaging, intended to improve the measurement accuracy, must also be taken into account. Considering a sinusoidal variation in the deformation of the specimen during a fatigue test, averaging of the laser leads to the following:

a reduction in the sampling frequency by a factor n (n being the number of points on which averaging is carried out),
filtering of the sinusoidal deformation signal.

With regard to the first point, compliance with the Shannon condition lead to the following relationship :

$$f_{test} < \frac{600}{2n}$$

Averaging 16 points thus leads to a maximum test frequency of 19 Hz. Above this value of 16 points, the deformation signal will be undersampled, and it will no longer be possible to obtain the deformation value.

The effect of filtering is reflected in an attenuation of the signal amplitude, which depends on its frequential components (harmonics). In the case of a sine wave of frequency f, attenuation of the peak-to-peak amplitude occurs.

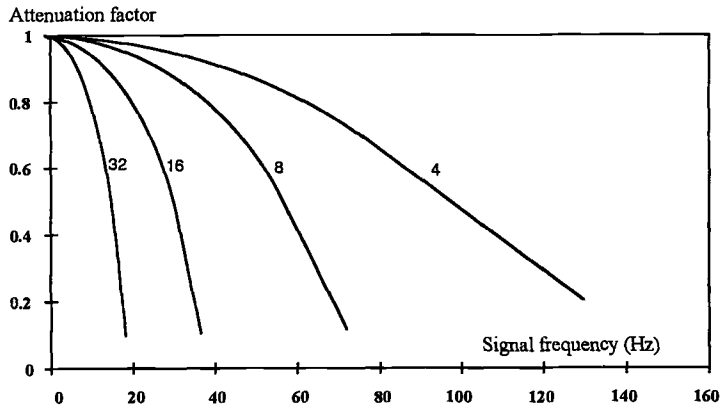


FIG. 10—*Attenuation factor versus signal frequency for different averaging (4, 8, 16 and 32 points).*

The diagram in Figure 10 gives the attenuation curves for various averaging values.

To return to the actual deformation value during the fatigue test, it will thus be necessary to :

oversample the laser signal, if necessary, to obtain a sufficient number of points to be able to describe perfectly the deformation signal. The signal can be reconstructed by using the Shannon formula :

$$x(t) = \sum_{k=-\infty}^{k=+\infty} x(k\Delta t) \frac{\sin\left[\pi\left(\frac{t}{\Delta t} - k\right)\right]}{\pi\left(\frac{t}{\Delta t} - k\right)}$$

Where :

t	=	time value of recalculated point,
Δt	=	laser sampling rate,
$x(k\Delta t)$	=	signal value at time $k\Delta t$,
$x(t)$	=	signal value at time t.

take into account the effect of attenuation due to averaging.

Accuracy of measurements

The accuracy of laser measurement will be determined under static conditions by prior calibration. At room temperature, and with averaging of 64 points, the amplitude of the fluctuations around the mean value is approximately one micron. If the number of averaging points is reduced, this amplitude increases.

At high temperature, the convection currents inside the furnaces cause disturbances in the measurements. The amplitude of the fluctuations, again with averaging of 64 points, then rises to approximately 5 microns. The uncertainty regarding the mean values of the signals at room temperature and under high temperature conditions is nonetheless very low, and of the same order of magnitude, provided that sufficient points are included for the required accuracy.

Conclusion and outlook

The ombroscopy technique has been adapted to the measurement of strain for mechanical characterization of materials in order to solve some difficulties which have been encountered, particularly regarding tests on irradiated materials in a hot laboratory. The main advantages of this technique are the followings :

a single piece of equipment capable of coping with the most frequent mechanical tests,

the absence of contact with the specimens, and thus ease of use in hot cells, particularly for tests at high temperature,
the possibility of measuring deformations on small specimens during mechanical tests.

The prospects for future development include:
the use of this technique for toughness tests on CT specimens
the possibility of using analog signals to control test machines
increased measuring accuracy.

Reference

[1] E. Vrignaud - Contrôle dimensionnel par nappe laser - Application aux empreintes élastomères et crayons combustible. Groupe de travail "Laboratoires chauds et télémanipulations" des Communautés Economiques et Européennes. 15-16 Juin 1993 Avoine France.

Author Index

A

Akasaka, N., 858
Alamo, A., 761
Albertini, G., 206
Alexander, D. J., 945
Amayev, A. D., 232
Augendre, H., 375

B

Backfisch, W., 458
Batawi, E., 721
Bethmont, M., 320, 375
Biemiller, E. C., 138
Bischler, P. J. E., 260
Böhmert, J., 1123
Bolton, C. J., 103, 119
Borden, M. J., 1047, 1057
Borodin, O. V., 817
Boydon, F. M. D., 331
Brachet, J. C., 761
Brauer, G., 637, 1123, 1134
Briguet, C., 721
Brillaud, C., 375, 1144
Brumovsky, M., 522
Bryk, V. V., 817
Bulanova, T. M., 842
Buswell, J. T., 103, 119

C

Carsughi, F., 206
Carter, R. G., 138
Chaouadi, R., 531
Chernov, I. I., 1013
Chung, H. M., 1068, 1077
Cierjacks, S. W., 1109
Coppola, R., 206
Cuddy, L. J., 637

D

De Meester, P., 531
DeVan, M. J., 660
De Vries, M. I., 919
Druce, S. G., 119
Dunlap, J. A., 1047, 1057

E

Edsinger, K., 670, 706, 790
Edwards, D. J., 1057
Ehrlich, K., 1109
Eichhorn, F., 1123
English, C. A., 119

F

Fabritsiev, S. A., 980
Fabry, A., 138, 294, 442, 458, 531
Foreman, A. J. E., 119
Freyer, P. D., 86
Frund, J.-M., 320

G

Gage, G., 331
Garner, F. A., 831, 1038
Gavillet, D., 721
Gérard, R., 294
Gorynin, I. V., 248
Griffiths, M., 1088
Grossbeck, M. L., 945
Grosse, M., 1123

H

Hall, J. B., 660
Hamilton, M. L., 831, 902, 1057
Harbison, L. S., 59
Hasegawa, M., 220, 623
Helm, J. L., 363
Hishinuma, A., 753, 933, 971
Horsten, M. G., 919
Housin, B., 320

I

Iskander, S. K., 277, 690

Copyright© 1996 by ASTM International www.astm.org

J

Jitsukawa, S., 933, 971
Jones, R. B., 103, 119, 569

K

Kalashnikov, A. N., 1013
Kalin, B. A., 1013
Kam, F. B. K., 500, 591
Kawanishi, H., 831
Kayano, H., 775
Kelzenberg, S., 1109
Kimura, A., 220, 623
Kizaki, M., 351
Klingensmith, R. D., 547, 606
Kolitsch, A., 1134
Koyama, K., 623
Kryukov, A. M., 232
Kurishita, H., 775
Kursevitch, I. P., 842
Kuznetzov, A. A., 842

L

Levit, V. I., 232
Little, E. A., 739
Loomis, B. A., 1068, 1077
Lott, R. G., 86
Lowe, A. L., Jr., 68, 487, 660
Lucas, G. E., 547, 606, 670, 706, 790, 902, 1057

M

Maillard, A., 761
Manahan, M. P., 637
Marmy, P., 721
Martinko, J., 637
Matsui, H., 220, 623
McElroy, R. J., 68, 119, 331
Meylogan, T., 1144
Mizuta, S., 775
Moskovic, R., 103
Möslang, A., 1109

N

Nanstad, R. K., 277, 384, 690
Narui, M., 775
Neklyudov, I. M., 817
Nesterova, E. V., 248
Neustroev, V. S., 842
Neystroev, V. S., 817
Nikolaev, V. A., 3, 248, 842
Novosad, P., 522

O

Odette, G. R., 547, 606, 670, 706, 790, 902
Onizawa, K., 351
Onose, S., 858
Ostrovsky, Z. E., 842

P

Pavinich, W. A., 59
Pawel, J. E., 753, 945, 971
Peters, J., 721
Petrova, T., 138
Phythian, W. J., 191, 331
Picker, C., 995
Platonov, P. A., 232
Povstyanko, A. V., 842
Priest, R. H., 103
Puzzolante, J.-L., 294, 442, 458

R

Rabouille, O., 761
Remec, I., 591
RézaiAria, F., 721
Rowcliffe, A. F., 945
Royer, J., 761
Rustichelli, F., 206
Rybin, V. V., 3, 248

S

Salathe, P., 1144
Sawai, T., 971
Schüle, W., 874
Schut, H., 1134
Séran, J. L., 761
Shamardin, V. K., 817, 842
Sheckherd, J. W., 790
Shiba, K., 753, 945, 971
Shibahara, I., 775, 858
Shibamoto, H., 220, 623
Smith, D. L., 1068, 1077
Sokolov, M. A., 232, 277, 384, 690
Solovyev, B. G., 1013

Sommer, W. F., 1047, 1057
Soular, P., 320
Stallmann, F. W., 500
Stefanon, M., 206
Stoller, R. E., 25, 547, 902
Stubbins, J. F., 1038, 1047, 1057
Suzuki, M., 351, 753, 933

T

Tavassoli, A.-A., 995
Toloczko, M. B., 902, 1057
Touron, H., 761
Tulke, K., 458

U

Urbanic, V. F., 1088

V

Van der Laan, J. G., 980
Van de Velde, J., 138, 294, 442, 458, 531
Van Ransbeeck, T., 138, 294, 458
Van Veen, A., 1134
Van Walle, E., 294, 415, 442, 458, 531
Vatter, I. A., 119
Verstrepen, A., 138, 294
Victoria, M., 721
Voyevodin, V. N., 817

W

Wang, J.-A., 500, 591
Wareing, J., 995
Wild, R. K., 260
Williams, T. J., 191, 569
Wirth, B., 670, 706, 790

Y

Yamaguchi, S., 220, 623
Yuya, H., 220, 623

Z

Zd'árek, J., 522

Subject Index

A

Accelerator Production of Tritium, 1047
Accelerator Transmutation of Waste, 1047
Activation, 1109
Aluminum alloys, 1047, 1057
American Society of Mechanical Engineers codes, 320
Annealing, 3, 248, 277, 660, 1038
  aluminum alloys, 1047
  damage state differences, 86
  embrittlement mitigation, 232
  fracture toughness effects, 690
  helium bubble, 1013
  model alloys, 623
  post-irradiation, 331
  recovery, 86, 277
ASTM standards
  A302B, 138, 637
  A508, 320
  A533B, 531
  A588, 331
  E8, 442

B

Binary alloy, 3
Blanket structure, 945
BN-600, 842
BOR-60, 842
Boron-10 dope, 753
Brown modulus hardening model, 191

C

Carbides, 220
Carbon, 623
  surface layer, 1134
Cavity, 739, 831
  growth, 531
Channel fracture, 933
Charpy data, 790
Charpy impact, 363, 375, 487, 531
  test, 775
Charpy shift, 103, 331, 351, 637
Charpy specimen, 706
  examination, 260
Charpy tensile specimens, 442
Charpy tests, 375, 761
Charpy transition temperature recovery, 232
Charpy-V notch
  bars, 458, 670
  shift, 351
  specimens, 138, 294, 384
  tests, 191, 320, 415, 761
  transition temperature, 277
  transition temperature shift, 68
Chromium, 721
Cladding, fuel, 858
Cleavage, 790, 1068
Cleavage fracture, 706
Cleavage initiation, 670
Cluster, 3, 547
  helium influence on, 831
  point defect, 25
Coarsening, 86
Composition effects, 547, 606
Concentration factor, elastic stress, 775
Constraint effects, 670
Copper, 547, 606
  alloy, 220, 623
  dependence, 637
  embrittlement, 103
  precipitates, 25, 59, 191, 220, 331, 569
  steels, 351
  welds, 68, 277, 294
Corrosion, 1088
Crack propagation, fatigue, 933
Crack tip opening displacement, 706
Creep properties, 995
  creep-fatigue, 995
Creep tests, 1144
Crowdions, dynamic, 874
Curve fitting, 363

D

Damage, 103, 119, 945, 1088
  black spot, 220
  copper effect on, 59
  cross sections, 68
  displacement, 1068
  ductile, evolution, 531
  gamma ray, 547
  low temperature, 331
  matrix, 569
  models, 138, 874
  neutron displacement, 1077
  states, differences, 86
  structures, 220
  studies, 206
Density, 1038
  change, 1077
  dislocation, 1088
Detection analysis, 1134
Deuterium uptake, 1088
Dislocation density, 1088
Dislocation loops, 842
Dislocation structure, 817, 858, 1038
Displacement damage, 1068
Displacement rate, 25, 591
Doel I and Doel II, 294, 442
Doel IV, 531
Dose rate, 191, 1109
  dependency, 119
  effect, 351
Dose use, 569
Ductile brittle transition
  behavior, 1068
  temperature, 721, 790
Ductile fracture, 531, 637, 790
Ductility, 637, 753, 919, 995
  helium effects on, 1068
  temperature effects on, 842
Dynamic Helium Charging Experiment, 1068, 1077

E

Elastic Recoil Detection Analysis, 1134
Elastic stress concentration factor, 775
Electron beam welding, 971, 980
Elongation, 753
Embrittlement, 86, 294, 569, 637
  evaluation by fracture reconstruction, 706
  ferritic-martensitic, 945
  iron-based alloys, 3
  irradiation, 68, 86, 103, 138, 320, 351
    beltline materials, 522
    steel, 606
  phosphorus segregation and, 119
  predictions, 25
  radiation, 232, 500, 591
Erosion, 487
Error analysis, 487
European standards, 458
Extensometer, 1144

F

Fast Flux Test Facility, 831, 1038
Fatigue crack propagation, 933
Fatigue, 995
  load, 933
  low cycle, 980
  tests, 721, 1144
Finite element, 531
  modeling, 670
First wall/blanket structure, 945
Fisher model, 68
Fitting functions, 363, 375
Flow stress, 637
Flow structure, 248
Fluence, 232, 1047, 1057, 1088
  end-of-license, 637
  monitors, 591
Flux, 547
  neutron flux, 351, 522
Fracture appearance transition temperature, 68
Fracture, cleavage, 706
Fracture, ductile, 790
Fracture energy, 458
Fracture initiation, 670
Fracture, intergranular, 103, 260
Fracture reconstruction, 670, 706, 790
Fracture toughness, 138, 415, 458, 660, 690
  temperature effects, 945
  tests, 721

Frank loops, 831, 933

G

Gamma rays, 547, 591
Gamma scanning, 522
Grain boundary, 995, 1077
  segregation, 103, 119, 260

H

Hardening, 25, 68, 191, 248, 351, 831
  barrier, model, 902
  composition influence on, 3
  irradiation, 547, 606, 623, 902, 919
  neutron irradiation, 331
  radiation, 569, 1123
Hardness, 902
  measurements, 294, 637, 761
  micro-Vickers, 623
Heat affected zone, 294, 500
  cracking, 980
Heat treatment effects, 606
Heavy Section Steel Irradiation Program, 384
Helium, 591, 753, 831, 902
  bubble growth, 980
  bubbles, 206
  damage, 1077
  Dynamic Helium Charging Experiment, 1068
  implantation, 980
  ion-implanted, 1013
High Flux Isotope Reactor, 547, 591, 753, 971
High Flux Reactor, 919
Hyperlogistic functions, 363

I

Impact testing, 384, 775, 995
  Charpy, 363, 375, 487
Intergranular failure, 190, 260, 1068
Intergranular fracture, 103, 260
International Thermonuclear Experimental Reactor, 933, 945
Interstitials, 874
Iron alloys, 3
  iron-copper alloys, 220

J

J-integral, 945

L

Laser, 1144
Lateral expansion, 458
Lateral shift method, 232
Lattice parameters, 1088
Lead, 522
Linde 80 welds, 59, 68, 138, 660
Load-deflection response, 138
Low activation materials, 721

M

Manganese, 547
Materials Open Test Assembly, 831
Metal inert gas welding, 971
Metallography, 248
Microscopy, 59
  confocal, 670, 706
Microstructure, 86, 103, 874, 919
  aluminum alloys, 1047
  austenitic stainless steels, 902
  characterization, 59
  defect, weldments, 971
  dislocation, 1038
  effects, 547
  evolution, 220, 637, 817, 831, 1013
  support steel, 331
  WWER-440, 248
Micro-void coalescence, 260
Modeling, 191
  barrier hardening, 902
  copper precipitation, 25
  damage, 138
  damage, radiation, 874
  finite element, 670
  irradiation embrittlement, 68, 86, 103
  irradiation hardening, 220
  mechanistic, 331
  micromechanical, 531
  one-interstitial model, 874
  phosphorus segregation, 119
  point defect clustering, 25
  radiation embrittlement, 59

Modulus hardening model, 191
Molybdenum, 547

N

Neutron activation dosimeters, thermal, 591
Neutron displacement damage, 1077
Neutron fluence, 232, 690
Neutron flux, 351, 522
Neutron-induced activation, 1109
Neutron irradiation, 842
Neutron scattering, 59, 191, 206
Nickel, 547, 606, 831, 842, 1038
  alloys, 1013
Niobium, 1088
Nitrogen implantation, 1134
Notch depth, 775

O

Optical microscopy, 59
Oxide-dispersion-strengthened ferritic steel, 739
Oxygen, 1134

P

Particle-matrix interface, 817
Phase stability, 858
Phase transformation, 817
Philippsburg, 442, 458
Phosphorus, 103, 119, 547, 606, 831
  segregation, 260
Plant life management, 415
Point defect concentrations, 874
Positron annihilation, 623, 1134
Power Reactor Embrittlement Data Base, 500
Precipitates, 206, 1077
  copper, 25, 59, 103, 331, 569
  formation, 3
  irradiation-induced, 1123
  phosphide, 858
  vanadium, 1123
Proton irradiation, 220, 623

R

RCC-M, 320
Reconstitution, 415, 442, 458, 522
Recovery, annealing, 86, 277

S

Sampling strategies, 375
Scanning, 522
Scanning electron microscopy, 706
Scattering
  neutron, 59, 191, 206
  small angle neutron, 1123
  small angle X-ray, 1123
Segregation
  grain boundary, 103, 119
  phosphorus, 260
  radiation-induced, 817
  zone effects, 320
Shear punch, 902, 1057
Size distribution, 206
Small angle neutron scattering, 191, 206, 1123
Small angle X-ray scattering, 1123
Solid solution, 3
Spallation neutrons, 1047
Standards (See also ASTM standards)
  European, 458
Steel, 68, 375, 384, 547
  A302B, 138
  A508, 320
  A533B, 351, 531
  austenitic, 831, 842, 858, 971
  austenitic stainless, 817, 902, 945, 980, 995
  embrittlement evaluation, 706
  Fe-C-Cu alloys, 220, 623
  Fe-Ni-Cr, 831
  ferritic, 591, 739, 775
  ferritic/martensitic, 753, 945, 1109
  ferritic stainless, 945
  low alloy, 191
  martensitic, 721, 761
  martensitic stainless, 790
  ODS ferritic, 739
  plate, 569, 919
  SA-508, 660
  SA-533, 660
  stainless, 817, 919, 933, 980
  support structure, 331
  tool, 1134

VVER-440, 1123
WWER-440, 232, 248, 522
Strain, 1144
Strain localization, 637
Stress concentration factor, elastic, 775
Stress intensity factor range, 933
Stress relief, 606
Support structures, 331
Surveillance program, 522
Swelling, 817, 842, 1038
resistance, 858
void, 739, 1077

T

Tearing modulus, 945
Temperature dependence, 119, 606
Tensile tests, 531, 721, 761, 1144
ductility, 919
proof strength, 995
properties, 753, 919, 971
spallation neutron environment, 1047
specimens, 442
strength, 1068
ultimate, 753
tensile-shear correlation, 1057
Test Reactor Embrittlement Data Base, 500
Thermal aging, 294, 320, 637, 660, 690
Thermal dependence, swelling, 1038
Thermal desorption spectrometry, 1013
Thermomechanical treatment, 739
Toughness, 670, 790, 995
ferritic-martensitic steel, 945
properties, 277
segregation zone effects, 320
Transition curves, 458
Transition electron microscopy, 902
Transition temperature, 277, 458, 547
Charpy, 232
ductile to brittle, 384, 721
fracture appearance, 68
measurements, 375
nil ductility, 363
shift, 351, 487
Transmission electron microscopy, 59, 248, 1068
aluminum alloys, 1057
helium bubble investigation, 1013
microstructure analysis, 971
Trend curve, 103, 138
dose use, 569
validation, 260
Tritium, 1057, 1068, 1077

U

UK Magnox Embrittlement Model, 68
Uncertainty evaluation, 375
Upper shelf energy, 277, 363, 384, 487
fulfillment, 458
miniaturized vs. full-size specimens, 775
single cycle heat effect on, 637
weld material, 531

V

Vacancies, 874
Vanadium-based alloys, 1068, 1077, 1109, 1123
Voids, 206, 637, 842, 1038
growth, 858
swelling, 739, 1077

W

Wear resistance, 1134
Welds, 86, 248, 569, 971
copper, 277
cracking, 980
EB, 761
Linde 80, 59, 68, 138
materials, 500
metals, 995
nickel, 294
stud gun, 442
submerged arc, 59, 103, 119, 191, 260, 660
TIG, 761
upper shelf, 690

upper shelf, low, 690
welding techniques, 415, 971
Wrappers, fuel assembly, 842
WWER-440 reactor vessel, 232, 248, 522

X

X-ray diffraction, 1088
X-ray scattering, small angle, 1123

Y

Yield, 442
Yield strength, 25, 59, 68, 351, 384, 637
Yield stress, 706, 753, 902

Z

Zirconium, 1088

ISBN 0-8031-2016-8